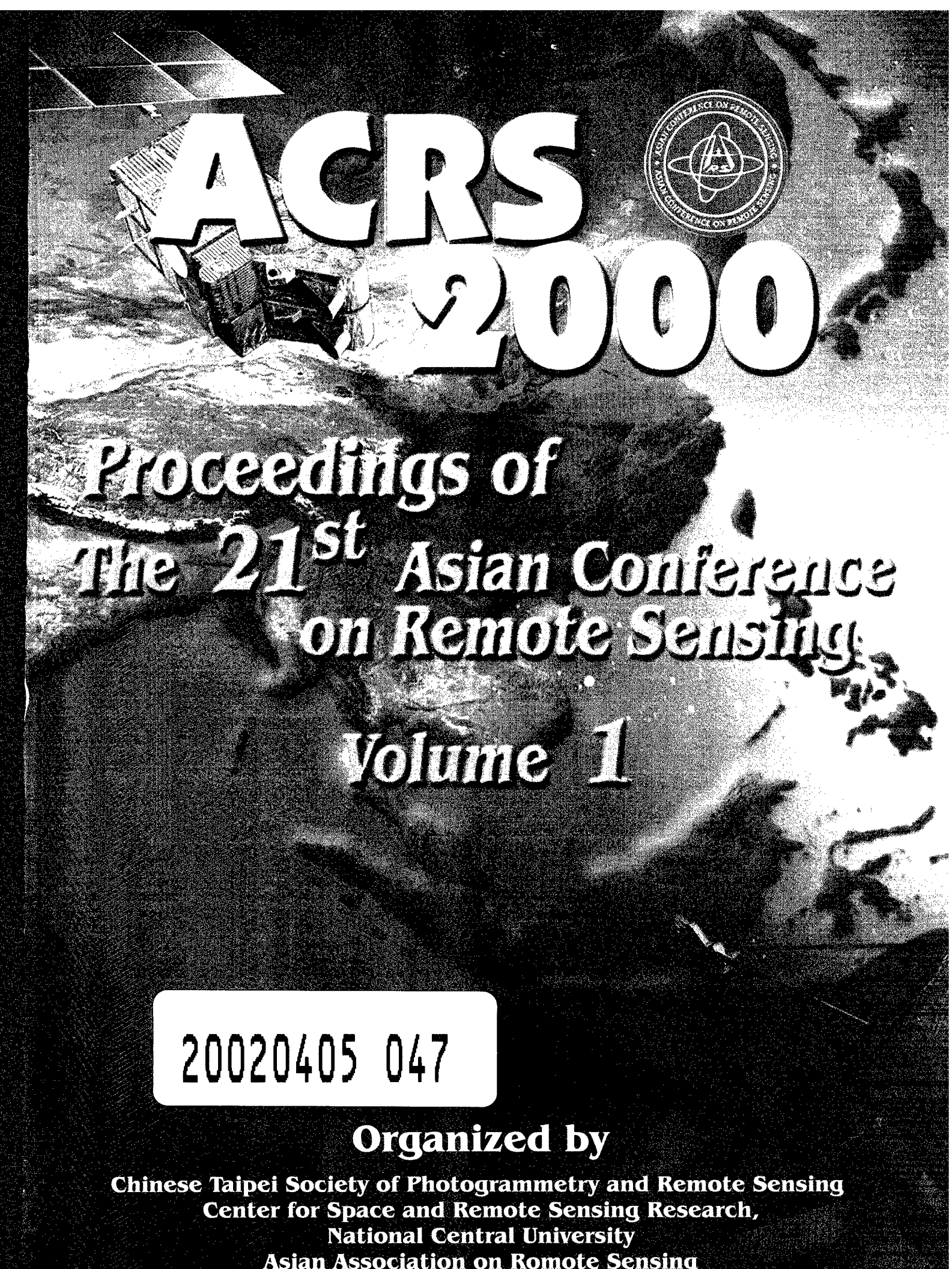


ACRS 2000

Proceedings of The 21st Asian Conference on Remote Sensing

Volume 1

20020405 047

Organized by

Chinese Taipei Society of Photogrammetry and Remote Sensing
Center for Space and Remote Sensing Research,
National Central University
Asian Association on Romote Sensing

REPORT DOCUMENTATION PAGE

Form Approved OMB No. 0704-0188

Public reporting burden for this collection of information is estimated to average 1 hour per response, including the time for reviewing instructions, searching existing data sources, gathering and maintaining the data needed, and completing and reviewing the collection of information. Send comments regarding this burden estimate or any other aspect of this collection of information, including suggestions for reducing this burden to Washington Headquarters Services, Directorate for Information Operations and Reports, 1215 Jefferson Davis Highway, Suite 1204, Arlington, VA 22202-4302, and to the Office of Management and Budget, Paperwork Reduction Project (0704-0188), Washington, DC 20503.

1. AGENCY USE ONLY (Leave blank)	2. REPORT DATE	3. REPORT TYPE AND DATES COVERED
	2000	Conference Proceedings, 4-8 December 2000

4. TITLE AND SUBTITLE

Proceedings of the 21st Asian Conference on Remote Sensing (ACRS 2000), Volume 1

5. FUNDING NUMBERS

F6256201M9011

6. AUTHOR(S)

Conference Committee

7. PERFORMING ORGANIZATION NAME(S) AND ADDRESS(ES)

Center for Space and Remote Sensing Research
National Central University
Chung-Li
Taiwan

8. Performing Organization Report Number

N/A

9. SPONSORING/MONITORING AGENCY NAME(S) AND ADDRESS(ES

AOARD
Unit 45002
APO AP 96337-5002

10. SPONSORING/MONITORING AGENCY REPORT NUMBER

CSP-001014

11. SUPPLEMENTARY NOTES

Conference held: December 4-8, 2000, Taipei International Convention Center, Taipei, Taiwan. Organized by: Chinese Taipei Society of Photogrammetry and Remote Sensing, Center for Space and Remote Sensing Research, National Central University, Asian Association on Remote Sensing. Volume 1 pages 1 - 620 . Volume 2 pages 621-1214. ISBN 957-02-7241-4.

12a. DISTRIBUTION/AVAILABILITY STATEMENT

Approved for public release; distribution is unlimited.

12b. DISTRIBUTION CODE

A

ABSTRACT (Maximum 200 words)

The 21st Asian Conference on Remote Sensing (ACRS 2000) was held 4-8 December 2000 in Taipei, Taiwan. 210 Papers are included in the proceedings, Vol. 1 & 2. Technical sessions included: Agriculture & Soil, Water Resources, Coastal Zone Monitoring, Digital Photogrammetry, Environment, Forest Resources, GIS & Data Integration, Hazard Mitigation, Image Processing, Education & Profession, Global Change, Landuse, Mapping from Space & GPS, SAR/InSAR, Oceanography, Hyperspectral & Data Acquisition Systems, and AirSAR/MASTER.

14. SUBJECT TERMS

AOARD, Taiwan, Image processing, IR sensors, Global positioning systems, Infrared technology, Hazard Mitigation

15. NUMBER OF PAGES

16. PRICE CODE

17. SECURITY CLASSIFICATION OF REPORT	18. SECURITY CLASSIFICATION OF THIS PAGE	19. SECURITY CLASSIFICATION OF ABSTRACT	20. LIMITATION OF ABSTRACT
UNCLASSIFIED	UNCLASSIFIED	UNCLASSIFIED	UL

Proceedings of

The 21st Asian Conference on Remote Sensing

Volume 1

December 4-8, 2000
Taipei International Convention Center
Taipei, TAIWAN

Organized by

Center for Space & Remote Sensing Research, National Central University
Chinese Taipei Society of Photogrammetry and Remote Sensing
Asian Association on Remote Sensing

AQ F02-06-1091

Proceedings of

The 21st Asian Conference on Remote Sensing

Volume 1

ISBN

957-02-7241-4

Copyright @2000

Center for Space & Remote Sensing Research, National Central University

Chinese Taipei Society of Photogrammetry and Remote Sensing

Asian Association on Remote Sensing

All rights reserved. Reproduction of this volume or any parts thereof (excluding quotation for use in preparation of reviews, technical and scientific papers) may be made only after obtaining the specific approval of the publishers. The publishers are not responsible for any opinions or statements made in the papers.

Published by

Center for Space & Remote Sensing Research, National Central University

Chinese Taipei Society of Photogrammetry and Remote Sensing

CONFERENCE ORGANIZING COMMITTEE

Honorary Chairman
Chao-Han Liu
(National Central University)

Secretary General of Asian Association on Sensing
Shunji Murai
(University of Tokyo)

General Chairman
A. J. Chen
(Chinese Taipei Society of Photogrammetry and Remote Sensing)

Steering Committee
Bruce Forster; John van Genderen; Armin Gruen; Chin-Chao Koh; Lim Hock; Nik Nasruddin Mahmood; Nguyen Dinh Duong; Ryutaro Tateishi; Tong Qinxi; Suvit Vibulsresth

General Vice-Chairman
S. C. Wang
(National Cheng Kung University)

Technical Committee
L. C. Chen, Chairman; C. F. Chen; K. S. Chen; T. C. Chen; Y. K. Chen; C. C. Cheng; W. H. Ho; M. K. Hsu; Y. C. Liao; Y. A. Liou; J. K. Liu; T. Y. Shih; L. C. Tsai; J. Wu

Local Organizing Committee
G. R. Liu (National Central University), Chairman; C. F. Chen; K. S. Chen; Y. A. Liou; L. C. Tsai; W. L. Wei; J. Wu

Secretariate
Mei-Yuan Lai; Wei-Ling Wei

ACRS 2000

The 21st Asian Conference on Remote Sensing

We wish to thank the following for their contributions to the success of this conference:

NATIONAL SCIENCE COUNCIL
MINISTRY OF EDUCATION
COUNCIL OF AGRICULTURE
MINISTRY OF THE INTERIOR
WATER RESOURCES BUREAU
U.S. AIR FORCE OFFICE OF SCIENTIFIC RESEARCH, ASIAN OFFICE OF AEROSPACE RESEARCH AND DEVELOPMENT (U.S. AFOSR/ AOARD)

EXHIBITORS' LIST

1. Chinese Taipei Society of Photogrammetry and Remote Sensing
2. System & Technology Corporation
3. MacDonald Dettwiler
4. Radarsat International
5. Datron/Transco Inc.
6. Intergraph Co. (Taiwan)
7. Control Signal Co. Ltd.
8. PCI Geomatics
9. ImageSat International
10. The Earth Geographic Publishing Co. Ltd.
11. Matra Systems & Information
12. Spot Image Co.
13. L-3 Communications
14. RITI Taiwan Inc.
15. Hitron Technology Inc.
16. Geoinfor Scientek Consultant Inc.
17. National Space Development Agency of Japan, (NASDA) Bangkok Office
18. Asian Institute of Technology
19. Applanix Corporation
20. China Arial Survey Co.
21. Taiwan Space Imagery Inc.
22. Hitachi Software
23. Remote Sensing Technology Center of Japan (RESTEC)
24. Productivity Group Inc.

PROGRAM OUTLINES

Date	Time	Agenda		
Dec. 4 Mon.	8:30-9:30	Registration		
	9:30-10:00	Opening Ceremony (including award presentations)		
	10:00-10:30	Coffee Break		
	10:30-11:00	Keynote Speech (1)	Possibility and Limitation of Satellite High Resolution Data Prof. Armin Gruen Institute for Geodesy and Photogrammetry, ETH	
	11:00-11:30	Keynote Speech (2)	Recent Advances in Radar Remote Sensing of Vegetation Prof. Kamal Sarabandi Department of Electrical Engineering and Computer Science, University of Michigan	
	11:30-12:00	Keynote Speech (3)	Progress of Photogrammetry and Remote Sensing Prof. Deren Li President, Wuhan Technical University of Surveying and Mapping	
	12:00-13:30	Lunch		
	13:30-15:00	TS-D1/Room 102	TS-H1/Room 101D	
	15:00-15:30	Coffee Break		
	15:30-17:00	TS-E1/Room 102	TS-I1/Room 101D	ST/Room 101C-2
	18:00	Welcome Reception		Ends@17:30
Dec. 5 Tue.	8:30-10:00	TS-H2/Room 102	TS-M/Room 101D	SS1/Room 101C-2
	10:00-10:30	Coffee Break		
	10:30-12:00	TS-A/Room 102	TS-K/Room 101D	SS2/Room 101C-2
	12:00-13:30	Lunch		
	13:30-15:00	TS-I2/Room 102	TS-L1/Room 101D	SS3/Room 101C-2
	15:00-15:30	Coffee Break		
	15:30-16:00	Briefing by each Poster Presenter (PS-1)/Room 101D		BM-1/Room 101C-2 Ends@17:00
	16:00-18:00	PS-1/Room 101C-1 (Finger Food Provided)		
	19:00	General Meeting (1)for National Delegates only		
Dec. 6 Wed.	8:30-10:00	TS-F/Room 102	TS-J/Room 101D	BM-2/Room 101C-2 Ends@17:00
	10:00-10:30	Coffee Break		
	10:30-12:00	TS-B/Room 102	TS-N/Room 101D	
	12:00-13:30	Lunch		
	13:30-15:00	TS-C/Room 102	TS-L2/Room 101D	
	15:00-15:30	Coffee Break		
	15:30-16:00	Briefing by each Poster Presenter (PS-2)/Room 101D		
	16:00-18:00	PS-2/Room 101C-1		
	19:00	Banquet & Culture Night		
	(Technical Tour to CSRSR, one group each in Morning & Afternoon.)			

Date	Time	Agenda		
Dec. 7 Thur.	8:30-10:00	TS-E2/Room 102	TS-P/Room 101D	BM-3/Room 101C-2
	10:00-10:30	Coffee Break		
	10:30-12:00	TS-G1/Room 102	TS-O/Room 101D	BM-4/Room 101C-2
	12:00-13:30	Lunch		
	13:30-15:00	TS-D2/Room 102	TS-I3/Room 101D	BM-5/Room 101C-2 Ends@17:00
	15:00-15:30	Coffee Break		
	15:30-16:00	Briefing by each Poster Presenter (PS-3)/Room 101D		
	16:00-18:00	PS-3/Room 101C-1 (Finger Food Provided)		
	19:00	General Meeting (2) for National Delegates only		
	19:00	Students Night for Students only		
Dec. 8 Fri.	8:30-10:00	TS-I4/Room 102	TS-G2/Room 101D	
	10:00-10:30	Coffee Break		
	10:30-12:00	Closing Ceremony/Room 102 (including Best Paper Awards)		

Remarks: TS: Technical Session; SS: Special Session; PS: Poster Session, BM: Business Meeting
ST: Student Session

Session Name-Discipline Correspondence:

A	: Agriculture & Soil	J	: Education & Profession
B	: Water Resources	K	: Global Change
C	: Coastal Zone Monitoring	L 1 ~ L 2	: Landuse
D1~D2	: Digital Photogrammetry	M	: Mapping from Space & GPS
E1~E2	: Environment	N	: SAR/InSAR
F	: Forest Resources	O	: Oceanography
G1~G2	: GIS & Data Integration	P	: Hyperspectral & Data Acquisition Systems
H1~H2	: Hazard Mitigation	S S 1 - S S 3	: Special Sessions (AIRSAR/MASTER)
I 1 ~ I 4	: Image Processing	P S 1 - P S 3	: Poster Sessions

CONTENTS

Paper List iii

Author Index xxi

VOLUME 1

Technical Session A: Agriculture & Soil

A-1 MODELLING TEA (CAMELLIA SINENSIS (L) O. KUNTZE) YIELD USING SATELLITE DERIVED LAI, LANDUSE AND METEOROLOGICAL DATA 1
R.M.S.S. Rajapakse, Nitin K. Tripathi, Kiyoshi Honda

A-2 LAND DEGRADATION DUE TO HYDRO-SALINITY IN SEMI-ARID REGIONS USING GIS AND REMOTE SENSING 7
Nasir Mahmood Khan, Yohei Sato

A-3 ANALYSIS OF SPECTRAL CHARACTERISTICS OF RICE CANOPY UNDER WATER DEFICIENCY 13
Chwen-Ming Yang, Muh-Rong Su

A-4 CLIMATE CHANGE AND AGRICULTURAL FOOD PRODUCTION OF BANGLADESH: AN IMPACT ASSESSMENT USING GIS-BASED BIOPHYSICAL CROP SIMULATION MODEL 19
Afzal Ahmed, Ryosuke Shibasaki

A-5 THE STUDY FOR ASSESSMENT OF SUSCEPTIBILITY TO SOIL LIQUEFACTION IN TAIWAN 23
Horng-Yuh Guo, Chih-Feng Chiang, Tsang-Sen Liu, Jiang-Liung Chu, Jen-Chyi Liu

A-6 ON THE RETRIEVALS OF SURFACE SOIL MOISTURE FROM SIMULATED SMOS AND AMSR BRIGHTNESS TEMPERATURES 29
Shou-Fang Liu, Yuei-An Liou, Wen-June Wang

Technical Session B: Water Resources

B-1 IDENTIFYING OPTIMUM SITES FOR LOCATING RESERVOIRS EMPLOYING REMOTELY SENSED DATA AND GEOGRAPHICAL INFORMATION SYSTEMS 35
K. Wan Yusof, Serwan M. J. Baban

B-2 INTEGRATED GROUND WATER RESOURCES MAPPING IN GURGAON DISTRICT, (HARYANA) INDIA USING REMOTE SENSING AND GIS TECHNIQUES 41
B.V.M. Rao Toleti , B. S. Chaudhary, K. E. Mothi Kumar, G. P. Saroha, Manoj Yadav, Ajeet Singh, M. P. Sharma, A. C. Pandey, P. K. Singh

B-3 IDENTIFICATION AND MAPPING OF NEW MARU-GANGA CHANNEL IN NORTH WEST INDIA OF INDIAN SUB-CONTINENT 47
Narpat Singh Rathore

B-4 USING SPECTRAL MIXTURE MODELING TECHNIQUES TO DERIVE LAND-COVER PARAMETERS FOR DISTRIBUTED SEDIMENT YIELD ESTIMATIONL MODEL 52
Enrico C. Paringit, Kazuo Nadaoka

B-5 GROUNDWATER LEVEL FORECASTING WITH TIME SERIES ANALYSIS 58
Miao-Hsiang Peng, Jin-King Liu, Tian-Yuan Shih

B-6 RESERVOIR TROPHIC STATE EVALUATION USING LANDSAT TM DATA 64
Ke-Sheng Cheng, Tsu-Chiang Lei

Technical Session C: Coastal Zone Monitoring

C-1	ANALYSIS ON THE CONVECTIVE MIXING CHARACTERISTICS OF ESTUARINE RESERVOIR BY LANDSAT TM IMAGES *Takashi Hoshi, Moon Soo Choi, Hideyuki Tonooka*	70
C-2	NEAR REAL TIME MONITORING OF TAIWAN COASTAL WATERS – A MULTIPLE SENSOR APPROACH *I-I Lin, L.S. Wen*	76
C-3	COASTAL ZONE ENVIRONMENT MANAGEMENT WITH EMPHASIS ON MANGROVE ECOSYSTEM, A CASE STUDY OF AO-SAWI THUNG KHLA, CHUMPHON, THAILAND *Surachai Ratanasermpong, Thongchai Charuppat, Dararat Disbunchong, Suwit Ongsomwang*	77
C-4	APPLICATION OF REMOTE SENSING WITH LANDSAT TM DATA FOR MANAGEMENT AND CONTROL OF MANGROVE FOREST –A CASE STUDY IN OKINAWA *Kazuhiro Sato, Munetake Kanetomi*	83
C-5	OBSERVING INTERTIDAL ZONES USING SATELLITE IMAGERY *Rigel Hian Dee Leow, Yihan Tan, Chee Yuen Wan, Christian Melsheimer*	89
C-6	CORAL REEF ECOSYSTEM CHANGE DETECTION BASED ON SPATIAL AUTOCORRELATION OF MULTISPECTRAL SATELLITE DATA *Heather Holden, Chris Derksen, Ellsworth LeDrew*	94

Technical Sessions D1, D2, D3, D4: Digital Photogrammetry

D1-1	KNOWLEDGE-BASED IMAGE ANALYSIS FOR 3D ROAD RECONSTRUCTION *Chunsun Zhang, Emmanuel Baltsavias, Armin Gruen*	100
D1-2	ORTHORECTIFICATION OF STEREO SPOT PANCHROMATIC AND RADARSAT FINE MODE DATA USING ORBITAL PARAMETERS AND DIGITAL ELEVATION MODEL *Mohd Ibrahim Seeni Mohd, Shahruddin Ahmad*	106
D1-3	HIDDEN COMPENSATION AND SHADOW ENHANCEMENT FOR TRUE ORTHOPHOTO GENERATION *Jiann-Yeou Rau, Nai-Yu. Chen, Liang-Chien Chen*	112
D1-4	DEVELOPMENT OF SOFTWARE TO CREATE A RECTIFIED IMAGE OF AN INCLINED PLANE *Ryuji Matsuoka, Naoki Shirai*	119
D1-5	AN ITERATIVE APPROACH TO ACQUIRE LINEAR FEATURES UNDER THE CONSTRAINTS OF THEIR KNOWLEDGE IN OBJECT SPACE *Shih-Hong Chio, Shue-Chia Wang*	125
D1-6	AUTOMATIC ACQUISITION OF 3D SPATIAL DATA IN CITY WITH AIR-BORNE TLS (THREE LINE SCANNER) *Yoshiaki Kagawa, Ryosuke Shibasaki*	131
D2-1	MULTI-RESOLUTION APPROACH TO RADARGRAMMETRIC DIGITAL ELEVATION MODELS GENERATION *Xiaojing Huang, Leong Keong Kwoh, Hock Lim*	135
D2-2	IMPLEMENTATION OF DIGITAL PHOTOGRAMMETRY FOR MONITORING THE TSAOLIN AREA IN TAIWAN *Yeong-Kuan Chen, Jihn-Fa Jan*	141
D2-3	TOPOGRAPHIC MAP REVISION IN DIGITAL PHOTOGRAMMETRIC ENVIRONMENT *K.S.K.Wijayawardana*	147
D2-4	GLOBAL IMAGE COMPOSITE OF ADEOS/OCTS GAC DATA *T. Hashimoto, T. Igarashi, A. Mukaida, R. Higuchi*	152
D2-5	EXTRACTION AND UTILIZATION OF GEOMETRICAL AND CONTEXTUAL INFORMATION IN VERY HIGH RESOLUTION IKONOS SATELLITE IMAGERY *Annie Hui, Soo Chin Liew, Leong Keong Kwoh, Hock Lim*	158

D2-6	THE RECTIFICATION OF HIGH RESOLUTION REMOTE SENSING SATELLITE IMAGERY *Chao-hsiung Wu*	164

Technical Sessions E1, E2: Environment

E1-1	LAND COVER CHANGE AND FLUCTUATION OF LACUSTRINE WATER QUALITY IN OKUTAMA LAKE *Susumu Ogawa, Moe Moriyama*	170
E1-2	VEGETATION MAPPING IN GANGES RIVER BASIN FOR GLOBAL MAPPING PROJECT *Mona Lacoul, Lal Samarakkon, Kiyoshi Honda*	176
E1-3	VERIFICATION OF SURFACE TEMPERATURE FROM LANDSAT 7/ETM+ DATA *Yuzo Suga, Motohide Yoshimura, Shoji Takeuchi, Yoshinari Oguro*	182
E1-4	AN EVALUATION OF DROUGHT RISK AREA IN NORTHEAST THAILAND USING REMOTELY SENSED DATA AND GIS *C. Mongkolsawat, P. Thirangoon, R. Suwanwerakamtorn, N. Karladee, S. Paiboonsak, P.Champathet*	188
E1-5	INVESTIGATION OF EVAPORATE DEPOSITS ON GAVKHONI PLAYA LAKE *R. Ajalloeian, H.R.Pakzad, H.Safaei*	194
E1-6	ESTIMATION OF THE METHANE EMISSION FROM WEST SIBERIAN WETLAND BY SCALING BETWEEN NOAA/AVHRR AND SPOT/HRV DATA *Wataru Takeuchi, Masayuki Tamura, Yoshifumi Yasuoka*	200
E2-1	URBAN CHANGE STUDY USING RS AND GIS *D. Amarsaikhan, M.Ganzorig, M.Saandar*	204
E2-2	ENVIRONMENTS TRANSITION RESEARCH IN YUSAN NATIONAL PARK AFTER EARTHQUAKE AND TYPHOON *Tien-Yin Chou, Chih-Cung Kao, Ying-Huei Chang*	210
E2-3	THE CHARACTERIZATION OF VERTICAL MEAN TEMPERATURE OVER INDONESIA FROM 1994 TO 1998 *Achmad Sasmito, Urip Haryoko, Riris Adriyanto, Nelly Florida Riama, Rosdiana*	216
E2-4	CAPABILITY OF RADARSAT DATA IN MONSOON FLOOD MONITORING *Mardiana Shafiee, Azman Ahmad, Osman Kadir*	222
E2-5	APPLYING AVHRR DATA TO ESTIMATE AND MONITOR AEROSOL OPTICAL THICKNESS *Tang-Huang Lin, Gin-Rong Liu*	228
E2-6	SURFACE TEMPERATURE ANALYSIS OF URBAN AREA USING RS AND GIS *Myung-Hee Jo, Kwang-Jae Lee, Ji-Hyun Shin, Ae -Sook Suh, Sung-Nam Oh*	234

Technical Session F: Forest Resources

F-1	APPLICATION AND VALIDATION OF LWCI (LEAF WATER CONTENT INDEX) TO TROPICAL SEASONAL FOREST REGION *Michio Anazawa, Genya Saito, Haruo Sawada*	240
F-2	APPLICATION OF ECOSYSTEM MANAGEMENT DECISION SUPPORT SYSTEM IN SELECTING SUITABLE SITE FOR TAIWANIA *Su-Fen Wang, Yeong-Kuan Chen, Chi-Chuan Cheng*	246
F-3	FOREST FIRE MONITORING WITH SPOT-4 SATELLITE IMAGERY *Kim Hwa Lim, Leong Keong Kwoh, Soo Chin Liew, Hock Lim*	252
F-4	STUDY ON THE RELATIONSHIP AMONG THE MACHILUS SPECTRAL BEHAVIOR AND LIGHT INTENSITY AND PHYSIOLOGICAL ACTIVITY *Chinsu Lin*	258

F-5	ANALYSIS OF FRAGMENTATION AND ANTHROPOGENIC DISTURBANCES IN THE HIMALAYAN FORESTS: USE OF REMOTE SENSING AND GIS *Subrat Sharma, L.M.S. Palni, P. S. Roy*	264
F-6	MODELING LANDSCAPE CHANGES USING LOGIT MODELS *Li-Ta Hsu, Chi-Chuan Cheng, Yu-Ching Lai*	270

Technical Sessions G1, G2: GIS & Data Integration

G1-1	IMPLEMENTATION OF A GEOGRAPHIC INFORMATION SYSTEM (GIS) TO DETERMINE WILDLIFE HABITAT QUALITY US ING HABITAT SUITABILITY INDEX *Yu Ching Lai, Walter L. Mills, Chi-Chuan Cheng*	276
G1-2	APPLICATION OF GIS TO MEASURE AND EVALUATE LANDSCAPE CHANGES *Chi-Chuan Cheng, Jihn-Fa Jan*	282
G1-3	GIS FOR VISUAL IMPACT ASSESSMENT *Zongyu Zhang, Jin Yeu Tsou, Hui Lin*	288
G1-4	INTEGRATION AND APPLICATION OF SOCIO-ECONOMIC AND ENVIRONMENTAL DATA WITHIN GIS FOR DEVELOPMENT STUDY IN THAILAND *Tran Hung, Yoshifumi Yasuoka*	294
G1-5	HARNESSING INFORMATION TECHNOLOGY FOR (GEO)MANAGEMENT AND DECISION-MAKING *Rowena Bassi Quiambao*	300
G1-6	GIS DATABASE OF THE ENVIRONMENTAL INFORMATION *Sharav Munkhtuya, Batjantsan Enkhtsetseg*	306
G2-1	APPLICATION OF GEOINFORMATICS ON MOUNTAIN LAND HAZARD MAPPING: A CASE OF ANNAPURNA HIMALAYAS, CENTRAL NEPAL. *Krishna Poudel*	312
G2-2	A SURFACE INTERPOLATION FOR LARGE-SCALE REPRESENTATION OF TERRAIN IN AN URBAN AREA *Yohko Shimura, Shaobo Huang, Ryosuke Shibasaki*	318
G2-3	DYNAMIC SPATIAL MODELING USING ROS AND CARRYING CAPACITY FOR ECOTOURISM MANAGEMENT *Kampanart Piyathamrongchai, Nitin Kumar Tripathi*	323
G2-4	A CASE-BASED URBAN PLANNING SUPPORT SYSTEM USING AN INTEGRATED COMBINATION OF GEOGRAPHICAL INFORMATION SYSTEMS AND REMOTE SENSING *Ko-Wan Tsou, Yao-Lin Chang, Yu-Ting Hung*	329
G2-5	AN IMPLEMENTATION OF 3D GIS ON WEB *Tien-Yin Chou, Lan-Kun Chung, Wen-Yuan Ku, Wei-Yuan Lo*	335
G2-6	THE MANAGEMENT SYSTEM DEVELOPMENT OF CAMPUS FACILITY INFORMATION USING WEB-BASED GIS *Myung-Hee Jo, Sung-Joong Park, Mal-Suk Kim, Yun -Won Jo*	341

Technical Sessions H1, H2: Hazard Mitigation

H1-1	INFORMATION TECHNOLO GY AND NATURAL DISAS TER MANAGEMENT IN INDIA *Alok Gupta*	346
H1-2	DETECTION OF DISASTER DAMAGE USING CHANGES OF CITY LIGHTS WITH DMSP/OLS DATA IN ASIA PACIFIC REGION *Izumi Nagatani, Genya Saito, Masafumi Kodama, Xianfang Song, Chris Elvidge*	352
H1-3	HIGH RESOLUTION REMOTE SENSING DATA & GIS TECHNIQUES IN UPDATION OF INFRASTRUCTURE DETAILS FOR FLOOD DAMAGE ASSESSMENT- A CASE STUDY *YK Srivastava, Binod Doley, Dk Pal, RK Das, S Sudhakar,S. Adiga , Kv Venkatachary, SK Srivastava*	358

H1-4	**VISUALIZATION OF WATER LEVELS FROM JERS-1 SAR IMAGES USING STRONG SCATTERS - PHITSANULOK, THAILAND -** *Takako Sakurai-Amano*	366
H1-5	**DROUGHT AND VEGETATION STRESS MONITORING IN THE ARID AND SEMI-ARID REGIONS OF THE MONGOLIA US ING REMOTE SENSING AND GROUND DATA** *Yu. Bayarjargal, Ts. Adyasuren, Sh. Munkhtuya*	372
H1-6	**INTEGRATING REMOTE SENSING AND GIS FOR FIRE HAZARD CATEGORIZATION & RES OURCE ALLOCATION** *Sunil Bhaskar*	378
H2-1	**LANDSLIDES TRIGGERED BY THE CHI-CHI EARTHQUAKE** *Hsuan Wu Liao, Chyi Tyi Lee*	383
H2-2	**DEVELOPMENT OF GIS-BASED BUILDING DAMAGE DATABASE FOR THE 1995 KOBE EARTHQUAKE** *Koichiro Umemura, Osamu Murao, Fumio Yamazaki*	389
H2-3	**AIRBORNE THERMAL IR REMOTE SENSING OF LUSHAN GEOTHERMAL FIELD** *Chi-Nan Wu, Ta-Ko Chen*	395
H2-4	**AUTOMATED DETECTION OF BUILDING DAMAGE DUE TO RECENT EARTHQUAKES USING AERIAL TELEVISION IMAGES** *Hajime Mitomi, Fumio Yamazaki, Masashi Matsuoka*	401
H2-5	**VALIDITY STUDY OF EDES APPLICATION TO TAIWAN CHI-CHI EARTHQUAKE DISASTER** *Masayuki Kohiyama, Haruo Hayashi, Norio Maki, Shin Hashitera*	407
H2-6	**ASIA PACIFIC NETWORK FOR DISASTER MITIGATION USING EARTH OBSERVATION SATELLITE (ANDES) (1) - FOREST FIRE DETECTION** *Taro Shinmura, Haruo Sawada, Izumi Nagatani*	413

Technical Sessions I1, I2, I3, I4: Image Processing

I1-1	**A NEURAL NETWORK MODEL FOR ESTIMATING SURFACE CHLOROPHYLL AND SEDIMENT CONTENT AT THE LAKE KASUMI GAURA OF JAPAN** *Pranab Jyoti Baruah, Masayuki Tamura, Kazuo Oki, Hitoshi Nishimura*	419
I1-2	**URBAN IMAGE ANALYSIS USING ADAPTIVE RESONANCE THEORY** *Supoj Mongkolworaphol, Yuttapong Rangsanseri, Punya Thitimajshima*	425
I1-3	**COLOR IMAGE ENHANCEMENT BASED ON SEGMENTATION REGION HISTOGRAM EQUALIZATION** *Sakreya Chitwong, Fusak Cheevasuvit, Kobchai Dejhan, Somsak Mitatha*	430
I1-4	**PARALLEL COMPUTING IN REMOTE SENSING DATA PROCESSING** *Chao-Tung Yang, Chi-Chu Hung*	434
I1-5	**USING COMPLETE POLARIMETRIC INFORMATION IN FUZZY NEURAL CLASSIFICATION OF SAR IMAGE BASED ON COMPLEX GAUSSIAN DISTRIBUTION** *Chia-Tang Chen, K. S. Chen*	440
I1-6	**COMPARATIVE STUDY ON MODEL FITTING METHODS FOR OBJECT EXTRACTION** *Masafumi Nakagawa, Huijing Zhao, Ryosuke Shibasaki*	446
I2-1	**SOME ADVANCED TECHNIQUES FOR SPOT 4 XI DATA HANDLING** *Nguyen Dinh Duong, Le Kim Thoa, Nguyen Thanh Hoan*	452
I2-2	**THE ANALYTIC OF REMOTELY SENSED DIGITAL IMAGE** *Xianhua Li, Dengrong Zhang, Gelong Yu, Hui Lin, Huosheng Shi*	458
I2-3	**THE STATISTICAL CORRELATION WITH INVARIANT MOMENTS FOR GEOMETRIC CORRECTION IMPROVEMENT** *Sompong Wisetphanichkij, Kobchai Dejhan, Somkid Hanpipatpongsa, Fusak Cheevasuvit, Somsak Mitatha, Chanchai Pienvijarnpong, Chatcharin Soonyeekan*	464

I2-4	**OPTIMIZATION OF ACTIVE AND PASSIVE REMOTE SENSING SYSTEMS USING INFORMATIONAL CRITERION** *Asadov Hikmat Hamid Oglu*	470
I2-5	**MULTISPECTRAL IMAGE COMPRESSION USING FCM-BASED VECTOR QUANTIZATION** *Uthai Sangthongpraow, Yuttapong Rangsanseri*	476
I2-6	**COMPARISON OF TWO TEXTURE FEATURES FOR MULTISPECTRAL IMAGERY ANALYSIS** *Pornphan Dulyakarn, Yuttapong Rangsanseri, Punya Thitimajshima*	481
I3-1	**IMAGE ANALYSIS OF REMOTE SENSING DATA INTEGRATING SPECTRAL AND SPATIAL FEATURES OF OBJECTS** *Joji Iisaka, Takako Sakurai-Amano*	486
I3-2	**A NEW APPROACH FOR AUTOMATIC DETERMINATION OF EDGE CENTER LINES IN A DIGITAL IMAGE** *Jaan-Rong Tsay*	492
I3-3	**GEOMETRIC REGISTRATION METHOD FOR 10-DAY COMPOSITE AVHRR DATA FOR ASIAN REGION** *Ts. Purevdorj, R. Yokoyama*	498
I3-4	**FEATURE EXTRACTION IN RESIDENTIAL AREAS BY KNOWLEDGE MODELLING** *His-Min Chao, John C. Trinder*	504
I3-5	**SUBBAND SAR IMAGE CODING BY USING QUADTREE DECOMPOSITION ON VARIABLE BLOCK TRUNCATION CODE** *Amnach Khawne, Somchai Omsin, Suthichai Noppanakeepong , Krit Wongrujira*	510
I3-6	**OPTIMAL POLARIZATION FOR CONTRAST ENHANCEMENT IN POLARIMETRIC SAR USING GENETIC ALGORITHM** *Ruey-Long Su, K. S. Chen, Jiancheng Shi*	516
I4-1	**A REFLECTANCE RETRIEVAL ALGORITHM FOR LANDSAT TM SATELLITE IMAGE** *C. H. Liu, E. F. Vermote*	522
I4-2	**A SYNERGISTIC AUTOMATIC CLUSTERING TECHNIQUE (SYNERACT) FOR MULTISPECTRAL IMAGE ANALYSIS** *Kai-Yi Huang*	527
I4-3	**AN EFFICIENT ARTIFICIAL NEURAL NETWORK TRAINING METHOD THROUGH INDUCED LEARNING RETARDATION: INHIBITED BRAIN LEARNING** *Joel C. Bandibas, Kazunori Kohyama*	533
I4-4	**FLOODED AREA ASSESSMENT WITH FUSED MULTI-SPECTRAL MULTI-SENSOR BY USING TEXTURE FEATURE ANALYSIS AND NEURAL NETWORK CLASSIFICATION** *Kobchai Dejhan, Sompong Wisetphanichkij, Prasit Kerdyou, Fusak Cheevasuvit , Somsak Mitatha, Chanchai Pienvijarnpong, Chatcharin Soonyeekan*	539
I4-5	**ACCURACY IMPROVEMENT OF THE LAND COVER CLASSIFICATION BY USING TRUNCATED NORMAL DISTRIBUTION** *Tsukasa Hosomura*	545
I4-6	**SELF-ORGANIZING FEATURE MAP FOR MULTI-S PECTRAL SPOT LAND COVER CLASSIFICATION** *Jen-Hon Luo, Din-Chang Tseng*	549

Technical Session J: Education & Profession

J-1	**DEVELOPMENT OF DATA SET FOR ANALYSIS OF LANDSAT TM IMAGES USING WWW BROWSER AND SPREADSHEET** *Kiyotada Sato, Ryuzo Yokoyama*	555
J-2	**SURVEY DEPARTMENT OF NEPAL: TODAY AND TOMORROW** *Krishna Raj Adhikary*	561
J-3	**TELLING STORIES OF JIN-SHAN-MIANN ADJACENT TO HSINCHU SCIENCE-BASED INDUSTRIAL PARK ON A SIMULATED ROCSAT-2 IMAGE** *Ku-Yu Chang, Chih-Li Chang*	567

J-4	**DETERMINATION OF ORIGINAL SIZE OF THE ABHAYAGIRIYA STUPA** *Siri Diyupathi Dampegama*	573
J-5	**REMOTE SENSING ACTIVITIES OF NASDA IN SOUTHEAST ASIA** *Eiichi Muto*	578
J-6	**THE EDUCATIONAL FUNCTION OF SATELLITE IMAGERY** *Shi-Ming Lu*	584

Technical Session K: Global Change

K-1	**DESERTIFICATION MAPPING OF WEST ASIA -A GIS AND REMOTE SENSING APPLICATION** *Hussein Harahseh, Ryutaro Tateishi*	585
K-2	**DEVELOPMENT FOR DATA BASE FOR ECO-SYSTEM CHANGES AND EMISSION CHANGES OF GHG USING REMOTE SENSING AND GIS IN SUMATRA ISLAND, INDONESIA** *Lilik Budi Prasetyo, Genya Saito, Haruo Tsuruta*	591
K-3	**MODELING THE EFFECTS OF RECENT LAND USE CHANGE ON THE CARBON CYCLE IN THE ZHU JIANG DELTA REGION OF SOUTHERN CHINA** *Dennis G. Dye, Thomas Hinchliffe, Curtis E. Woodcock*	597
K-4	**SATELLITE OBSERVATION OF MIGRATION ROUTES AND HABITATS OF MIGRATORY BIRDS LIVING IN WETLANDS IN EAST ASIA** *Masayuki Tamura, Hiroyoshi Higuchi*	603
K-5	**AN OPERATIONAL APPROACH FOR MAPPING BUSHFIRE HISTORY IN THE TROPICAL SAVANNAS OF NORTHERN AUSTRALIA** *Yue Zhang, Peter Whitehead, Waqar Ahmad, Carl Menges*	609
K-6	**RELATIONSHIP BETWEEN CANOPY BRDF AND PHYSICAL PARAMETERS OF 3-D STRUCTURE OF VEGETATION IN NORTHERN WETLANDS IN JAPAN** *Michiru Miyamoto, Kunihiko Yoshino, Keiji Kushida*	615

VOLUME 2

Technical Sessions L1, L2: Landuse

L1-1	**CLASSIFICATION OF REMOTELY SENSED IMAGERY USING MARKOV RANDOM FIELDS** *Brandt Tso, Paul M. Mather*	621
L1-2	**MACHINE LEARNING METHODS TO IDENTIFY MIS LABELED TRAINING DATA AND APPROPRIATE FEATURES FOR GLOBAL LAND COVER CLASSIFICATION** *Jonathan Cheung-Wai Chan, Matthew C. Hansen, Ruth Defries*	628
L1-3	**DEVELOPMENT OF TRUNK-CANOPY BIOMASS AND MORPHOLOGY INDICES FROM QUADPOLARIZED RADAR DATA** *Peter N. Tiangco, Bruce C. Forster*	634
L1-4	**A LAND USE CHANGE STUDY USING CELLULAR AUTOMATA** *Jinn-Guey Lay*	646
L1-5	**IDENTIFICATION OF LANDSLIDES INDUCED BY CHI-CHI EARTHQUAKE USING SPOT MULTISPECTRAL IMAGES** *Yu-Chuan Kuo, Hui-Chung Yeh, Ke-Sheng Cheng, Chia-Ming Liou , Ming-Tung Wu*	652
L1-6	**DETERMINATION OF MAJOR FACTORS AFFECTING THE LAND USE/LAND COVER OF UPPER MAGAT WATERSHED. - A PRELIMINARY STUDY FOR THE LAND USE/LAND COVER CHANGE CASE STUDY OF UPPER MAGAT WATERSHED PHASE - II** *Victorino A. Bato*	658
L2-1	**ADDITIONAL NIGHTTIME AVHRR DATA FOR CLASSIFYING LAND COVER TYPE IN THAILAND** *Chada Narongrit, Mitsuharu Tokunaga, Shunji Murai, Kaew Nualchawee, Apisit Eiumnoh, Suphat Vongvisessomjai*	665
L2-2	**LAND-COVER CHANGE IN CHINA USING TIME SERIES ANALYSIS, 1982 - 1999** *Chien-Pin Lee, Stephen S. Young, Hao Chen*	671
L2-3	**URBAN PLANNING AND MONITORING CHANGES USING ER MAPPER** *Abdullah Mah*	678
L2-4	**INVESTIGATION OF LAND USE IN RELATION TO LANDSLIDE BY USING GIS** *R. Ajalloeian , R.Karami, M.Nikzad*	683
L2-5	**THE STUDY OF KNOWLEDGE-BASED DATABASE ASSIST FOR URBAN LAND USE CLASSIFICATION** *Fu-Jen Chien, Tien-Yin Chou*	689
L2-6	**APPLICATION OF REMOTE SENSING IMAGE DATA IN THE ANALYSIS OF LAND USE MANAGEMENT OF AGRICULTURE IN CHIANAN IRRIGATION PROJECT IN TAIWAN** *You Jenn Ming, Kiyoshi Torii, Yoshiaki Mori, Ryouhei Kada*	695

Technical Session M: Mapping from Space & GPS

M-1	**COVARIANCE PROPAGATION IN GPS/IMU - DIRECTLY GEOREFERENCED FRAME IMAGERY** *Mohamed M. R. Mostafa, Joseph Hutton, Erik Lithopoulos*	701
M-2	**RADARSAT-2 MISSION: OVERVIEW AND DEVELOPMENT STATUS** *Peter Meisl, Alan A. Thompson, Anthony P. Luscombe*	702
M-3	**PERFORMANCE EVALUATION OF RTK GPS WITHOUT SA EFFECT** *Jenn-Taur Lee, Wen-Feng Chen*	708

M-4 EFFECT OF COHERENCE ON DEMS DERIVED FROM SAR INTERFEROMETRY: A CASE STUDY OF MAYON VOLCANO, PHILIPPINES 714
Vu Tuong Thuy, Mitsuharu Tokunaga

M-5 USE OF DIGITAL TERRAIN MODELS FOR THE INFRASTRUCTURE DEVELOPMENT IN SRI LANKA 720
Nihal Wijesekara

M-6 A METHOD OF MAP MATCHING FOR PERSONAL POSITIONING SYSTEMS 726
Kay Kitazawa, Yusuke Konishi, Ryosuke Shibasaki

Technical Session N: SAR/InSAR

N-1 A MULTI-POLARIZED AND MULTI-ANGLE C-BAND RADAR SYSTEM FOR SOIL MOISTURE DETERMINATION UNDER BARE SOIL CONDITIONS 732
Shakil Ahmad Romshoo, T. Oki, K. Musiake

N-2 VERIFICATION OF INSAR CAPABILITY FOR DISASTER MONITORING - A CASE STUDY OF CHI-CHI EARTHQUAKE IN TAIWAN 738
Shoji Takeuchi, Yuzo Suga, Yoshinari Oguro, A. J. Chen, Chinatsu Yonezawa

N-3 SAR INTERFEROMETRY APPLICATIONS IN THE PHILIPPINES USING ERS-1, ERS-2 AND JERS-1: CASE STUDIES IN MAYON AND TAAL VOLCANO 744
J. H. G. Salvador, H. Kanbara,R. Abundo, M. Tsukada, K. Hirose, A. Dayao, E. Corpuz, A. Baloloy

N-4 A STUDY ON DIFFERENTIAL INTERFEROMETRY IN SUBSIDENCE 749
C. T. Wang, H. T. Wang, D. C. Chern , N. Y. Chen, L. S. Liang
Center for Space and Remote Sensing Research, National Central University, Taiwan

N-5 921 CHICHI EARTHQUAKE : PRELIMINARY INTERFEROMETRIC INTERPRETATIONS 755
B. Deffontaines, L. S. Liang, E. Pathier, C. T. Wang, B. Fruneau, C. T. Lee, D. Raymond, J. Angelier, J. P. Rudant

N-6 DOPPLER COEFFICIENT ESTIMATION FOR SYNTHETIC APERTURE RADAR USING SUB-APERTURE INTERFEROGRAM 761
Jim Min Kuo, K. S. Chen

Technical Session O: Oceanography

O-1 SEA SURFACE TEMPERATURE VARIABILITY IN THE SEAS SURROUNDING THE PHILIPPINES IN RELATION TO ENSO EVENTS 767
Erlinda E. Salamante, Cesar L. Villanoy

O-2 EL NINO SOUTHERN OSCILLATION (ENSO) IMPACT ON SEA SURFACE TEMPERATURE (SST) DERIVED FROM SATELLITE IMAGERY AND ITS RELATIONSHIP ON TUNA FISHING GROUND IN THE SOUTH JAVA SEAWATERS 772
Jonson Lumban Gaol, Djisman Manurung

O-3 DERIVATION OF AEROSOL OPTICAL DEPTH OVER THE EAST ASIAN OCEANS WITH ROCSAT-1 OCI IMAGERY 777
Shih-Jen Huang, Gin-Rong Liu

O-4 COMPARATIVE PERFORMANCE OF SST ALGORITHMS IN THE TROPICAL OCEAN USING OCTS DATA 782
K. Abdullah, M. Z. M. Jafri, N. M. Saleh, A. Bahari

O-5 THE USE OF SEAWIFS SATELLITE DATE FOR OCEAN COLOUR DETERMINATION IN FISHERIES APPLICATION 788
Mohd Ibrahim Seeni Mohd, Tadris Ahmad

O-6 CLASSIFICATION OF ALGAL BLOOM TYPES FROM REMOTE SENSING REFLECTANCE 794
Soo Chin Liew, Leong Keong Kwoh, Hock Lim

Technical Session P: Hyperspectral & Data Acquisition Systems

P-1	**VEGETATION SPECTRAL FEATURE EXTRACTION MODEL** *Qian Tan, Hui Lin , Yongchao Zhao , Tong Qingxi , Zhen Lanfeng*	800
P-2	**HYPERSPECTRAL IMAGE COMPRESSION USING THREE-DIMENSIONAL WAVELET TRANSFORMATION** *Yi-Hsing Tseng, Hung-Kuan Shih, Pai-Hui Hsu*	809
P-3	**ESTIMATION OF PHOTOSYNTHETIC RATE OF PLANT FROM HYPER-SPECTRAL REMOTE SENSING OF BIOCHEMICAL CONTENT** *Takahiro Endo, Toshinori Okuda, Masayuki Tamura, Yoshifumi Yasuoka*	815
P-4	**MULTISCALE ANALYSIS OF HYPERSPECTRAL DATA USING WAVELETS FOR SPECTRAL FEATURE EXTRACTION** *Pai-Hui Hsu, Yi-Hsing Tseng*	821
P-5	**MICROWAVE HOLOGRAPHIC - IMAGING REMOTE OBJECTS USING LIGHT - MODULATED SCATTERING TECHNIQUE** *Thammasak Vimonkiattikun, Jirawath Panklang , Anupong Srongprapa*	828
P-6	**APPLICATION OF AIRBORNE HYPERSPECTRAL IMAGING IN WETLAND DELINEATION** *Chung-Hsin Juan, Jonathan D. Jordan, Chih-Hung Tan*	834

Special Sessions SS1, SS2, SS3 : AirSAR/MASTER

SS1-1	**PACRIM 2 AIRSAR DEPLOYMENT TO THE ASIA-PACIFIC REGION AUGUST - OCTOBER 2000: REPORT ON THE DATA ACQUISITION PHASE AND EARLY RESULTS** *A.K. Milne, Ian J. Tapley*	840
SS1-2	**THE USE OF AIRSAR DATA FOR ASSESSING THE POTENTIAL OF FUTURE SPACEBORNE SAR FOR REGIONAL ESTIMATION OF WOODLAND BIOMASS IN AUSTRALIA** *A.K. Milne, N. Cronin, R.M. Lucas, C. Witte, R. Denham*	841
SS1-3	**ESTIMATION OF SOIL MOISTURE WITH VEGETATED SURFACE BY MULTI-TEMPORAL MEASUREMENTS** *Jiancheng Shi*	847
SS2-1	**DEPLOYMENT OF THE MODIS/ASTER AIRBORNE SIMULATOR (MASTER) DURING PACRIM 2** *Ian J. Tapley, A. K. Milne*	852
SS2-2	**ADVANCES IN DIGITAL ELEVATION DATASETS FOR EXPLORATION, TOPOGRAPHIC MAPPING AND DISASTER MANAGEMENT** *Ian J. Tapley*	853
SS2-3	**BENEFITS OF TOPSAR RADAR INTERFEROMETRY IN TROPICAL TERRAINS** *Ian J. Tapley*	857
SS3-1	**ANALYSIS OF POLARIZATION SIGNATURES AND TEXTURAL FEATURES FOR AIRBORNE PI-SAR IMAGES** *Takahiro Yamada, Takashi Hoshi*	860
SS3-2	**A STUDY OF SURFACE DEFORMATION FROM EARTHQUAKE BY DIFFERENTIAL RADAR INTERFEROMETRY** *C. T. Wang, L. S. Liang, K. S. Chen, A. J. Chen*	866
SS3-3	**ANALYSIS OF MULTIPOLARIZATION AND MULTI-BAND RADAR DATA OVER ILOILO CITY AND VICINITIES** *Michael B. Lituanas, Jerry H.G. Salvador, Dulcisimo S. Domingo III, Aeschylus M.J. Valenzuela, Eduardo O. Claridad*	872

Poster Session PS1

PS1-01	AN INTRODUCTION OF ASTER (THE ADVANCED SPACEBORNE THERMAL EMISSION AND REFLECTION RADIOMETER) FOR THE EARTH OBSERVATION *Masatane Kato, Yuichi Maruyama, Makoto Tsukada*	877
PS1-02	PHOTOGRAMMETRIC DIGITAL DATA PROCESSING OF TSAU-LIN BIG LANDSLIDE *Hsin-Hsing Cheng*	883
PS1-03	3D DIGITAL ARCHIVING SYSTEM FOR WORLD HERITAGE *Kazuhisa Inaba, Ryosuke Shibasaki*	891
PS1-04	ON MODELING OF THE SAR-IMAGE SQUINT PARAMETER *J. Wu, C. J. Liu*	897
PS1-05	INTEGRATION OF MULTISENSOR MULTITEMPORAL SATELLITE DATA FOR AGRICULTURAL VEGETATION MAPPING *L. Zhu, R. Tateishi*	903
PS1-06	GLOBAL POSITIONING SYSTEM (GPS) *Venant B. Mugemuzi*	909
PS1-07	POST-CLASSIFICATION AND DETECTION OF SIMULATED CHANGE FOR NATURAL GRASS *Hao-Hsiung Huang, Chiao-Ju Hsiao*	915
PS1-08	CONSTRUCTION OF SATELLITE IMAGE DATA SET BY MULTISPECTRAL AND HYPERSPECTRAL SENSORS *Yuzo Suga, Kenji Takasaki, Shoji Takeuchi*	922
PS1-09	TRACKING AUTOMOBILES USING AIR-BORNE TLS (THREE LINE SCANNER) IMAGES *Ryuichi Murata, Ryosuke Shibasaki*	928
PS1-10	GEO-REFERENCING OF MULTI-SENSOR RANGE DATA FOR VEHICLE-BORNE LASER MAPPING SYSTEM (VLMS) *Dinesh Manandhar, Ryosuke Shibasaki*	932
PS1-11	A PHOTOGRAMMETRIC EVALUATION OF AN APS CAMERA *Tian-Yuan Shih, Chien-Bin Kung*	938
PS1-12	APPLICATIONS OF HYPERSPECTRAL REMOTE SENSING IN URBAN REGIONS *Sunil Bhaskaran, Bisun Datt*	944
PS1-13	IMAGE GEOMETRIC SIMULATION AND ORIENTATION MODELING FOR ROCSAT-2 *Liang-Chien Chen, Yi-Ying Wu*	948
PS1-14	SUPERVISED CLASSIFICATION OF MULTI-TEMPORAL REMOTE SENSING IMAGES *Chi-Farn Chen, Yueh-Tan Li*	954
PS1-15	COMPARING EFFECTS OF DIFFERENT SIZES OF AGGREGATION ON SPATIAL STRUCTURE OF REMOTELY SENSED DATA *Yu-Pin Lin, Tung-po Teng*	960
PS1-16	COMPUTERIZED IONOSPHERIC TOMOGRAPHY USING THE GPS/MET AND NNSS DATA *C. T. Liu, L. C. Tsai, W. H. Tsai*	967
PS1-17	SENSOR INTEGRATION FOR PERSONAL POSITIONING SYSTEM *Yusuke Konishi, Ryosuke Shibasaki*	974
PS1-18	GROUND TRUTH MEASUREMENT SYSTEM USING RC HELICOPTER *Daisuke Hongoh, Hironori Ichikawa, Koji Kajiwara, Yoshiaki Honda*	980
PS1-19	DEVELOPMENT OF THE RETRIEVAL ALGORITHMS FOR ATMOSPHERIC REFRACTIVITY FROM GPS/MET OCCULTATION *Yuei-An Liou, Cheng-Yung Huang*	984
PS1-20	AUTOMATED CARTOGRAPHIC LINE TRACKING *Pakorn Apaphant*	990
PS1-21	BIOMASS ESTIMATION BY THE STEREOPHONIC IMAGE ANALYSIS *Hiroyuki Masubuchi, Koji Kajiwara, Yoshiaki Honda*	996

Poster Session PS2

PS2-01	**OPTICAL REMOTE SENSING USING FIBER BRAGG DEVICE FOR DYNAMIC LOAD MEASUREMENTS** *C. Patimapornchai, V. Jewpraditkul, P. P. Yupapin*	1002
PS2-02	**MAPPING AND MEASURING THE TROPOSPHERE POLLUTANTS ORIGINATED FROM THE 1997 FOREST FIRE IN SOUTH EAST ASIA** *Mazlan Hashim, Kasturi Devi Kanniah, Abdul Wahid Rasib , Lim Chee Ming*	1006
PS2-03	**LAND COVER CHANGE AND LONG-TERM FLUCTUATION OF EVAPOTRANSPIRATION IN OKUTAMA** *Susumu Ogawa, Nobuaki Naito*	1012
PS2-04	**MULTISOURCE DATA FUSION – FUSING OPTICAL AND SAR DATA FOR IRRIGATED RICE AREAS IDENTIFICATION** *J. Worawattanamateekul , X. J. F. Canisius, L. Samarakoon*	1018
PS2-05	**STUDY ON LAND USE MANAGEMENT WITH GEOGRAPHIC INFORMATION SYSTEMS** *Wei-Hsin Ho, Ge-Wen Lee*	1024
PS2-06	**ASSESSMENT OF CROP PRODUCTIVITY FOR MAJOR RIVER BASINS IN ASIA USING GIS AND RS DATA** *Shiro Ochi, Shunji Murai*	1030
PS2-07	**A SYSTEMATIC APPROACH IN REMOTE SENSING EDUCATION AND TRAINING AT UNIVERSITI TEKNOLOGI MALAYSIA** *Kasturi Devi Kanniah, Mazlan Hashim, Mohd Ibrahim Seeni Mohd*	1036
PS2-08	**THE STUDY ON BIOMASS ESTIMATION IN MONGOLIAN GRASSLAND USING SATELLITE DATA AND FIELD MEASUREMENT DATA** *Hirokazu Yamamoto, Koji Kajiwara, Yoshiaki Honda*	1042
PS2-09	**INTEGRATION OF RS AND GIS TO ASSESS HUMAN IMPACT ON ECOSYSTEM CHANGE IN LLANOS AREA (VENEZUELA)** *Yanning Guan, Steven M. de Jong, Johan de Meijere*	1048
PS2-10	**THE PRODUCTION OF PHOTO BASE MAP IN TAIWAN** *Jih-Cheng Ru*	1054
PS2-11	**INTEGRATION OF WEB-BASED GIS AND ONLINE ANALYTICAL PROCESSING** *Yin Shan, Hui Lin , Wai Chee Fu*	1060
PS2-12	**THE STUDY OF PRECIPITATION EFFECTS ON AMSU AND APPLICATION OF AMSU ON TYPHOON MONITORING** *Kung-Hwa Wang*	1065
PS2-13	**PHENOLOGY DETECTION OF FOREST AREA USING SATELLITE DATA** *Asako Nagao, Koji Kajiwara, Yoshiaki Honda*	1071
PS2-14	**UTILIZATION OF LANDSAT-5 IMAGERY FOR SUGARCANE AREA SURVEY AND MAPPING IN THAILAND** *W. Hadsarang, S. Sukmuang*	1075
PS2-15	**APPLICATION OF GIS AND REMOTE SENSING TO ANALYSES LANDSCAPE STRUCTURES** *Kazuyuki Takahashi, Keitarou Hara*	1081
PS2-16	**OBSERVATIONS OF THE DAYTIME INTERNAL BOUNGARY LAYER IN ONSHORE FLOW** *N. Mohd Saleh, M. Z. M. Jafri, K. Abdullah*	1087
PS2-17	**EARTH OBSERVATION SYSTEM** *Vinai Vorrawat*	1093
PS2-18	**INTEGRATING REMOTELY SENSED DATA WITH AN ECOSYSTEM MODEL TO ESTIMATE NET PRIMARY PRODUCTIVITY IN EAST ASIA** *Wenjing Zhao, Masayuki Tamura*	1099

Poster Session PS3

PS3-01	**A R&D PROGRAM FOR PROMPT RESPONSE ABOUT FOREST-PROTECTION INFORMATION WITH PLATFORM DISPLAY SYSTEM** *Gwo-Jern Hwang, Ching-Ming Wu, Ten-Yin Chou, Joou-Shiau Lee*	1104
PS3-02	**APPLICATION OF OPTICAL REMOTE SENSING TECHNOLOGY FOR OIL PALM MANAGEMENT** *Ibrahim Selamat, Zainal Abidin Hasan, Mariamni Khalid*	1112
PS3-03	**APPROACH TO LAND-USE ANALYSIS IN HETAO IRRIGATION PROJECT OF INNER MONGOLIA, CHINA, BASED ON SATELLITE IMAGE DATA** *Takashi Kume, Kiyoshi Torii, Toru Mitsuno*	1118
PS3-04	**DROUGHT MONITORING IN ZAMBIA USING METEOSAT AND NOAA AVHRR DATA** *Kawana Nawa*	1124
PS3-05	**FOREST RESOURCES IN TAIWAN** *Jih-Cheng Ru*	1130
PS3-06	**EARTH SURFACE GEOPHYSICAL PARAMETERS DETERMINATION FROM ATSR DATA** *Yong Xue, Huadong Guo*	1136
PS3-07	**A CREEPING-TYPE LANDSLIDE OBSERVED ON AERIAL PHOTOGRAPHS FOLLOWING THE JI-JI EARTHQUAKE OF TAIWAN ON 21 SEPTEMBER 1999** *Jin-King Liu*	1142
PS3-08	**VOLCANO HAZARD MANAGEMENT USING DIGITAL ELEVATION MODEL** *D. John Prabaharan, Kasturi Devi Kanniah*	1148
PS3-09	**PROSPECT FOR THE METHOD OF URBAN SAFETY ANALYSIS AND ENVIRONMENTAL DESIGN** *Osamu Murao, Fumio Yamazaki*	1155
PS3-10	**THE DEVELOPMENT OF FOREST FIRE FORECASTING SYSTEM USING INTERNET GIS AND SATELLITE REMOTE SENSING** *Myung-Hee Jo, Myung-Bo Lee, Si-Young Lee, Yun -Won Jo, Seong-Ryul Baek*	1161
PS3-11	**CONTRIBUTION FROM REMOTE SENSING IN UPDATING BATHYMETRIC CHART** *K. Abdullah, M. Z. M. Jafri, Z. B. Din*	1167
PS3-12	**REMOTE SENSING OF TOTAL SUSPENDED SOLIDS IN PENANG COASTAL WATERS, MALAYSIA** *K. Abdullah, Z. B. Din, Y. Mahamod, R. Rainis, M. Z. M. Jafri*	1173
PS3-13	**FLOOD HAZARD MAP AND LAND DEVELOPMENT PRIORITY MAP DEVELOPED USING NOAA AVHRR AND GIS DATA** *Md. Monirul Islam, Kimiteru Sado*	1179
PS3-14	**USE OF LANDSAT IMAGES FOR THE IDENTIFICATION OF DAMAGE DUE TO THE 1999 KOCAELI, TURKEY EARTHQUAKE** *Miguel Estrada, Fumio Yamazaki, Masashi Matsuoka*	1185
PS3-15	**NATURAL-SCIENTIFIC APPROACH FOR NATURAL CONSERVATION USING GIS** *Byungyang Choi, Takekazu Koyanagi, Yuji Kuwahara, Kunio Shima*	1191
PS3-16	**GIS APPLICATION ON THE STRATEGY FOR SUSTAINABLE DEVELOPMENT IN PHITSANULOK PROVINCE** *Vicharn Amarakul, Sirirat Sangyong*	1197
PS3-17	**DYNAMIC SIMULATION OF LAND USE/COVER CHANGE BASED ON TIME SERIES SATELLITE IMAGES** *Zhongchao Shi, Ryousuke Shibasaki*	1203
PS3-18	**GROUNDWATER PREDICTION POTENTIAL ZONE IN LANGAT BASIN USING THE INTEGRATION OF REMOTE SENSING AND GIS** *Khairul Anam Musa, Juhari Mat Akhir, Ibrahim Abdullah*	1209

AUTHOR INDEX

Author	page
A :	
Abdullah, Ibrahim	1209
Abdullah, K.	782,1087,1167,1173
Abundo, R.	744
Adhikary, Krishna Raj	561
Adiga, S.	358
Adriyanto, Riris	216
Adyasuren, Ts.	372
Ahmad, Azman	222
Ahmad, Shahruddin	106,683
Ahmad, Tadris	788
Ahmad, Waqar	609
Ahmed, Afzal	19
Ajalloeian, R.	194,683
Akhir, Juhari Mat	1209
Amarsaikhan, D.	204
Anazawa, Michio	240
Angelier, J.	755
Apaphant, Pakorn	990
B :	
Baban, Serwan M. J.	35
Baek, Seong-Ryul	1161
Bahari, A.	782
Baloloy, A.	744
Baltsavias, Emmanuel	100
Bandibas, Joel C.	533
Baruah, Pranab Jyoti	419
Bato, Victorino A.	658
Bayarjargal, Yu.	372
Bhaskaran, Sunil	378,944
Byungyang, Choi	1191
C :	
Champathet, P.	188
Canisius, X. J. F.	1018
Chan, Jonathan Cheung-Wai	628
Chang, Chih-Li	567
Chang, Ku-Yu	567
Chang, Yao-Lin	329
Chang, Ying-Huei	210
Chao, Hsi-Min	504
Charuppat, Thongchai	77
Chaudhary, B. S.	41
Cheevasuvit, Fusak	430,464,539
Chen, A. J.	738,866
Chen, Chi-Farn	954
Chen, Chia-Tang	440
Chen, Hao	671
Chen, K. S.	440,516,761,866
Chen, Liang-Chien	112,948
Chen, Nai-Yu	112,749
Chen, Ta-Ko	395
Chen, Yeong-Kuan	141,246
Chen, Wen-Feng	708
Cheng, Chi-Chuan	246,270,276,282
Cheng, Hsin-Hsing	883
Cheng, Ke-Sheng	64,652
Chern, D. C.	749
Chiang, Chih-Feng	23
Chien, Fu-Jen	689
Chio, Shih-Hong	125
Chitwong, Sakreya	430
Choi, Moon Soo	70
Chou, Tien-Yin	210,335,689,1104
Corpuz, E.	744
Chu, Jiang-Liung	23
Chung, Lan-Kun	335
Claridad, Eduardo O.	872
Cronin, N.	841
D :	
Dampegama, Siri Diyupathi	573
Das, RK	358
Datt, Bisun	944
Dayao, A.	744
Deffontaines, B.	755
Defries, Ruth S.	628
Dejhan, Kobchai	430,464,539
Denham, R.	841
Derksen, Chris	94
Din, Z. B.	1167,1173
Disbunchong, Dararat	77
Doley, Binod	358
Domingo III, Dulcisimo S.	872
Dulyakarn, Pornphan	481
Duong, Nguyen Dinh	452
Dye, Dennis G.	597
E :	
Eiumnoh, Apisit	665
Elvidge, Chris	352
Endo, Takahiro	815
Enkhtsetseg, Batjantsan	306
Estrada, Miguel	1185
F :	
Forster, Bruce C.	634
Fruneau, B.	755
Fu, Wai Chee	1060
G :	
Ganzorig, M.	204
Gaol, Jonson Lumban	772
Gruen, Armin	100
Guan, Yanning	1048
Guo, Horng-Yuh	23
Guo, Huadong	1136
Gupta, Alok	346
H :	
Hadsarang, W.	1075
Hanpipatpongsa, Somkid	464
Hansen, Matthew C.	628
Hara, Keitarou	1081
Harahseh, Hussein	585
Hasan, Zainal Abidin	1112
Hashim, Mazlan	1006,1036
Hashimoto, T.	152
Hashitera, Shin	407
Hayashi, Haruo	407
Haryoko, Urip	216
Higuchi, Hiroyoshi	603
Higuchi, R.	152
Hinchliffe, Thomas	597
Hirose, K.	744
Ho, Wei-Hsin	1024
Hoan, Nguyen Thanh	452
Holden, Heather	94
Honda, Kiyoshi	1,176

AUTHOR INDEX

Author	page
Honda, Yoshiaki	980,996,1042,1071
Hongoh, Daisuke	980
Hoshi, Takashi	70,860
Hosomura, Tsukasa	545
Hsiao, Chiao-Ju	915
Hsu, Li-Ta	270
Hsu, Pai-Hui	809,821
Huang, Cheng-Yung	984
Huang, Hao-Hsiung	915
Huang, Kai-Yi	527
Huang, Shaobo	318
Huang, Shih-Jen	777
Huang, Xiaojing	135
Hui, Annie	158
Hung, Chi-Chu	434
Hung, Tran	294
Hung, Yu-Ting	329
Hutton, Joseph	701
Hwang Gwo-Jern	1104
I :	
Ichikawa, Hironori	980
Igarashi, T.	152
Iisaka, Joji	486
Inaba, Kazuhisa	891
Islam, Md. Monirul	1179
J :	
Jan, Jihn-Fa	141,282
Jewpraditkul, V.	1002
Jo, Myung-Hee	234,341,1161
Jo, Yun -Won	341,1161
Jong, Steven M. de	1048
Jordan, Jonathan D.	834
Juan, Chung-Hsin	834
K :	
Kada, Ryohei	695
Kadir, Osman	222
Kagawa, Yoshiaki	131
Kajiwara, Koji	980,996,1042,1071
Kanbara, H.	744
Kanetomi, Munetake	83
Kanniah, Kasturi Devi	1006,1036,1148
Kao, Chih-Cung	210
Karami, R.	683
Karladee, N	188
Kato, Masatane	877
Kerdyou, Prasit	539
Khalid, Mariamni	1112
Khan, Nasir Mahmood	7
Khawne, Amnach	510
Kim, Mal-Suk	341
Kitazawa, Kay	726
Kodama, Masafumi	352
Kohiyama, Masayuki	407
Kohyama, Kazunori	533
Konishi, Yusuke	726,974
Koyanagi, Takekazu	1191
Ku, Wen-Yuan	335
Kuo, Jim Min	761
Kumar, K. E. Mothi	41
Kume, Takashi	1118
Kung, Chien-Bin	938
Kuo, Yu-Chuan	652
Kushida, Keiji	615
Kuwahara, Yuji	1191
Kwoh, Leong Keong	135,158,252,794
L :	
Lacoul, Mona	176
Lai, Yu-Ching	270,276
Lanfeng, Zhen	800
Lay, Jinn-Guey	646
LeDrew, Ellsworth	94
Lee, C. T.	755
Lee, Ge-Wen	1024
Lee, Chien-Pin	671
Lee, Chyi Tyi	383
Lee, Jenn-Taur	708
Lee, Joou-Shiau	1104
Lee, Kwang-Jae	234
Lee, Myung-Bo	1161
Lee, Si-Young	1161
Lei, Tsu-Chiang	64
Leow, Rigel Hian Dee	89
Li, Xianhua	458
Li, Yueh-Tan	954
Liang, L. S.	749,755,866
Liao, Hsuan Wu	383
Liew, Soo Chin	158,252,794
Lim, Chee Ming	1006
Lim, Hock	135,158,252,794
Lim, Kim Hwa	252
Lin, Chinsu	258
Lin, Hui	288,458,800,1060
Lin, I-I	76
Lin, Tang-Huang	228
Lin, Yu-Pin	960
Liou, Chia-Ming	652
Liou, Yuei-An	29,984
Lithopoulos, Erik	701
Lituanas, Michael B.	872
Liu, C. H.	522
Liu, C. J.	897
Liu, C.T.	967
Liu, Gin-Rong	228,777
Liu, Jen-Chyi	23
Liu, Jin-King	58,1142
Liu, Shou-Fang	29
Liu, Tsang-Sen	23
Lo, Wei-Yuan	335
Lu, Shi-Ming	584
Lucas, R.M.	841
Luo, Jen-Hon	549
Luscombe, Anthony P.	702
M :	
Mah, Abdullah	678
Mahamod, Y.	1173
Maki, Norio	407
Manandhar, Dinesh	932
Manurung, Djisman	772
Maruyama, Yuichi	877
Masubuchi, Hiroyuki	996
Mat, Jafei M.Z.	782,1087,1167,1173
Mather, Paul M.	621
Matsuoka, Masashi	401,1185
Matsuoka, Ryuji	119
Meijere, Johan de	1048

AUTHOR INDEX

Author	page
Meisl, Peter	702
Melsheimer, Christian	89
Menges, Carl	609
Mills, Walter L.	276
Milne, A.K.	840,841,852
Ming, Lim Chee	1006
Ming, You Jenn	695
Mitatha, Somsak	430,464,539
Mitomi, Hajime	401
Mitsuno, Toru	1118
Miyamoto, Michiru	615
Mohd, Mohd Ibrahim Seeni	106,788,1036
Mongkolsawat, C.	188
Mongkolworaphol, Supoj	425
Mori, Yoshiaki	695
Moriyama, Moe	170
Mostafa, Mohamed M. R.	701
Mugemuzi, Venant B.	909
Mukaida, A.	152
Munkhtuya, Sharav	306,372
Murai, Shunji	665,1030
Murao, Osamu	389,1155
Murata, Ryuichi	928
Musiake, K.	732
Musa, Khairul Anam	1209
Muto, Eiichi	578
N :	
Nadaoka, Kazuo	52
Nagao, Asako	1071
Nagatani, Izumi	352,413
Naito, Nobuaki	1012
Nakagawa, Masafumi	446
Narongrit, Chada	665
Nawa, Kawana	1124
Nikzad, M.	683
Nishimura, Hitoshi	419
Noppanakeepong, Suthichai	510
Nualchawee, Kaew	665
O :	
Ochi, Shiro	1030
Ogawa, Susumu	170 ,1012
Oglu, Asadov Hikmat Hamid	470
Oguro, Yoshinari	182,738
Oh, Sung-Nam	234
Omsin, Somchai	510
Ongsomwang, Suwit	77
Oki, Kazuo	419
Oki, T.	732
Okuda, Toshinori	815
P :	
Paiboonsak, S.	188
Pakzad, H.R.	194
Pal, Dk	358
Palni, L.M.S.	264
Pandey, A. C.	41
Panklang, Jirawath	828
Paringit, Enrico C.	52
Pathier, E.	755
Patimapornchai, C.	1002
Park, Sung-Joong	341
Peng, Miao-Hsiang	58
Pienvijarnpong, Chanchai	464,539
Piyathamrongchai, Kampanart	323
Poudel, Krishna	312
Prabaharan, D. John	1148
Prasetyo, Lilik Budi	591
Purevdorj, Ts.	498
Q :	
Qingxi, Tong	800
Quiambao, Rowena Bassi	300
R :	
Rainis, R.	1173
Rajapakse, R.M.S.S.	1
Rangsanseri, Yuttapong	425,476,481
Rasib, Abdul Wahid	1006
Ratanasermpong, Surachai	77
Rathore, Narpat Singh	47
Rau, Jiann-Yeou	112
Raymond, D.	755
Riama, Nelly Florida	216
Rosdiana	216
Roy, P. S.	264
Romshoo, Shakil Ahmad	732
Ru, Jih-Cheng	1054,1130
Rudant, J. P.	755
S :	
Saandar, M.	204
Sado, Kimiteru	1179
Safaei, H.	194
Saito, Genya	240,352,591
Sakurai, Amano Takako	366,486
Salamante, Erlinda E.	767
Salvador, J. H. G.	744,872
Saleh, N. Mohd	782,1087
Samarakoon, Lal	176,1018
Sangthongpraow, Uthai	476
Saroha, G. P.	41
Sasmito, Achmad	216
Sato, Kazuhiro	83
Sato, Kiyotada	555
Sato, Yohei	7
Sawada, Haruo	240,413
Selamat, Ibrahim	1112
Shafiee, Mardiana	222
Shan, Yin	1060
Sharma, M. P.	41
Sharma, Subrat	264
Shi, Huosheng	458
Shi, Jiancheng	516,847
Shi, Zhongchao	1203
Shibasaki, Ryosuke	19,131,318,446,726,891, 928,932,974,1203
Shih, Hung-Kuan	809
Shih, Tian-Yuan	58,938
Shin, Ji-Hyun	234
Shima, Kunio	1191
Shimura, Yohko	318
Shinmura, Taro	413
Shirai, Naoki	119
Singh, Ajeet	41
Singh, P. K.	41
Sirirat, Sangyong	1197
Song, Xianfang	352
Soonyeekan, Chatcharin	464,539

AUTHOR INDEX

Author	page
Srivastava, SK	358
Srivastava, YK	358
Srongprapa, Anupong	828
Su, Muh-Rong	13
Su, Ruey-Long	516
Sudhakar, S	358
Suga, Yuzo	182,738,922
Suh, Ae -Sook	234
Sukmuang, S.	1075
Suwanwerakamtorn, R.	188
T :	
Takahashi, Kazuyuki	1081
Takasaki, Kenji	922
Takeuchi, Shoji	182,738,922
Takeuchi, Wataru	200
Tamura, Masayuki	200,419,603,815,1099
Tan, Chih-Hung	834
Tan, Qian	800
Tan, Yihan	89
Tapley, Ian J.	840,852,853,857
Tateishi, Ryutaro	585,903
Teng, Tung-po	960
Thirangoon, P.	188
Thitimajshima, Punya	425,481
Thoa, Le Kim	452
Thompson, Alan A.	702
Thuy, Vu Tuong	714
Tiangco, Peter N.	634
Tokunaga, Mitsuharu	665,714
Toleti, B.V.M. Rao	41
Tonooka, Hideyuki	70
Torii, Kiyoshi	695,1118
Trinder, John C.	504
Tripathi, Nitin K.	1,323
Tsai, L. C.	967
Tsai, W. H.	967
Tsay, Jaan-Rong	492
Tseng, Din-Chang	549
Tseng, Yi-Hsing	809,821
Tso, Brandt	621
Tsou, Jin Yeu	288
Tsou, Ko-Wan	329
Tsukada, Makoto	744,877
Tsuruta, Haruo	591
U :	
Umemura, Koichiro	389
V :	
Valenzuela, Aeschylus M.J.	872
Venkatachary, KV	358
Vermote, E. F.	522
Vicharn, Amarakul	1197
Villanoy, Cesar L.	767
Vimonkiattikun, Thammasak	828
Vongvisessomjai, Suphat	665
Vorrawat, Vinai	1093
W :	
Wan, Chee Yuen	89
Wang, C. T.	749,755,866
Wang, H. T.	749
Wang, Kung-Hwa	1065
Wang, Su-Fen	246
Wang, Shue-Chia	125
Wang, Wen-June	29
Wen, L.S.	76
Whitehead, Peter	609
Wijayawardana, K.S.K.	147
Wijesekera, Nihal	720
Wisetphanichkij, Sompong	464,539
Witte, C.	841
Wongrujira, Krit	510
Woodcock, Curtis E.	597
Worawattanamateekul, J.	1018
Wu, Chao-hsiung	164
Wu, Chi-Nan	395
Wu, Ching-Ming	1104
Wu, J.	897
Wu, Ming-Tung	652
Wu, Yi-Ying	948
X :	
Xue, Yong	1136
Y :	
Yadav, Manoj	41
Yamada, Takahiro	860
Yamamoto, Hirokazu	1042
Yamazaki, Fumio	389,401,1155,1185
Yang, Chwen-Ming	13
Yang, Chao-Tung	434
Yasuoka, Yoshifumi	200,294,815
Yeh, Hui-Chung	652
Yokoyama, Ryuzo	498,555
Yonezawa, Chinatsu	738
Yoshimura, Motohide	182
Yoshino, Kunihiko	615
Young, Stephen S.	671
Yu, Gelong	458
Yupapin, P. P.	1002
Yusof, K. Wan	35
Z :	
Zhang, Chunsun	100
Zhang, Dengrong	458
Zhang, Yue	609
Zhang, Zongyu	288
Zhao, Huijing	446
Zhao, Wenjing	1099
Zhao, Yongchao	800
Zhu, L.	903

MODELLING TEA (Camellia (L) O. Kuntze) YIELD USING SATELLITE DERIVED LAI, LANDUSE AND METEOROLOGICAL DATA

R.M.S.S. Rajapakse*, Nitin K. Tripathi**, Kiyoshi Honda***
Space Technology Application and Research Program,
Asian Institute of Technology,
P.O. Box 4, Klong Luang, Pathumthani, 12120, Thailand
Tel (66-2)-524-5577 or (66-2)-524-5670
Fax (66-2)-524-5597
Email – stb997175@ait.ac.th

(KEY WORDS: LAI, NDVI, TEA YIELD MODELLING)

Abstract

Tea is very important cash crop for Sri Lanka as it is the number one foreign exchange earner. Monitoring tea yield is vital from both management of tea plantation and commercial purpose. Tea yield depends on various land use and environment parameters. Remote sensing provides useful information on existing crop condition. In this analysis an attempt has been made to predict tea yield using remote sensing and other key parameters in GIS environment.

Leaf area index (LAI) is one main key factor useful in crop growth models that may be derived from optical remote sensing data. The LAI during the plucking stage is an important state variable in tea yield modeling. The LAI is a major factor determining crop reflectance and is often used in crop reflectance modeling. Therefore, the relationship between tea LAI and optical remote sensing parameter (NDVI) was investigated and this is very important in developing yield prediction models for tea. A model with a logarithmic function was adopted to find the relationship between NDVI and measured LAI.

Satellite derived LAI values and existing spatial, meteorological and agronomic variables with statistical regression analysis and analytical capabilities of GIS were used to develop a model for tea yield estimation. Although different methods were tried to find the best model by using multiple regression, a model develop by using weights of considered variables selected as the suitable model for predicting tea yield.

1. Introduction

Tea (*Camellia sinensis (L) O. Kuntze*) plantations are very important for Sri Lanka as in terms of land use and employment, tea industry occupies the foremost place in the island. Develop a model to forecast or estimate tea yield is very useful for decision making in tea industry. Remote sensing and GIS technologies has been used during last decade for this purpose for develop yield prediction models for several annual crops like rice, wheat etc. Therefore, development of a yield prediction model using remote sensing and GIS for tea, a very important perennial crop is pressing need. The lack of previous studies in monitoring tea using remote sensing provided the main

*Master student, AIT and Experimental Officer, Tea Research Institute of Sri Lanka.
**Assistant Professor
***Associate Professor

imputes for this study. LAI plays an important role in both the processes of crop growth and canopy reflectance (Clevers et. al., 1994). Measuring LAI in the field is time consuming. Therefore much relative benefit might be obtained from the estimation of LAI from optical remote sensing data. The normalized difference vegetation index (NDVI) could be considered as a measure of plant productivity (Sellers, 1985). NDVI has been considered a measure of LAI for most of crops (Gong, P. et. al., 1995). Objectives of this study were to develop a model for estimating LAI using optical satellite data and to develop a model for estimating tea yield using LAI, agronomic, landuse and meteorological parameters.

2. Methodology

2.1. Study area

A mid country tea estate situated in Nawalapitiya, Dolosbage planting district of Kandy administrative district in Sri Lanka was selected as the study area. Total land area of the estate is 945ha and 235.25ha is under tea plantation. Balance area is under fuel wood, paddy, vegetables, a tea factory and settlements. Whole estate consists of 50 tea fields respectively. The location of the estate is between 197000mN, 176000mE and 201000mN, 180000mE local coordinates. Several clones of vegetatively propagated tea can be seen in the estate; TRI 2025, TRI 2023, CH13, DN and TRI 2026. All most all seedling tea fields are more than 80 years old. Slope of the estate is less than 53%. Elevation range of the estate varies from 1000m amsl to 1500m amsl. Cumulative annual rainfall of the estate is greater than 2000mm. Average relative humidity of the estate is between 84%-90% and average daily temperature is between 21^0C to 23^0C. The base temperature for tea is 13.5^0C. Therefore this estate has a suitable temperature range through out the year. Daily average sunshine hours of the estate are 5.2 hours.

2.2. Data collection

This study considered both attribute and spatial data. The attribute data was collected from tea estate records, meteorological records and by measuring field-by-field Leaf Area Index. The spatial data is extracted from satellite images and existing maps. These spatial and attribute data were linked within a GIS database. Existing maps were used to prepare digital coverages of field boundaries, landuse, soil boundaries, road and stream network, slope, elevation and aspects. Using inverse distance interpolation (IDW) method annual cumulative precipitation, average daily relative humidity, average daily sunshine hours and average daily temperature maps for the estate were prepared. Tea plantation parameters concerning acreage, variety (clone), planting density, soil cover by the canopy, pruning cycle, planting date and yield were collected. These data were collected from tea estate records.

Each and every tea field leaf samples were collected for measuring LAI. Sampling was done in 50 fields of the estate. Sample size was 1 square meter. Ten random sampling points per field were selected from each field. Leaf

area was measured by using Decagon pseudocolor Ag vision image analyzer. Following equation was used to calculate LAI by point-by-point basis:

$$LAI = \frac{Leaf\ Area}{Sample\ Surface\ Area}$$

However, when considering satellite images actual coverage of tea plant canopy has to be considered. Therefore measured leaf area readings and fields by field plant density records were used to calculate LAI by using following formula. Leaf area and sample ground surface area should be in same units.

$$LAI = \frac{Leaf\ Area}{Sample\ Surface\ Area} * Actual\ Coverage$$

$$\text{Actual Coverage} = \frac{\text{Actual Plant Density}}{\text{Optimum plant density}}$$

Where;

For Vegetatively propagated tea with 0.6mx1.2m spacing;
Optimum tea plant density = 13800 plants per ha
For seedling tea with 0.9mx1.2m spacing;
Optimum tea plant density = 9250 plants per ha
Sample surface area = $1m^2$

2.3. Satellite data

Radiometric normalization was done to remove inherent noise in multi-temporal LANDSAT-TM images. Linear transformation was done for radiometric correction. The IRS-1C LISS III (Linear Imaging Self Scanner) acquired on 12th February 2000 and LANDSAT-TM image acquired on 6th March 1995 were used in the study. After performing geometric correction, radiometric normalization and masking for assigning null value to non vegetation areas of images NDVI values were calculated by using field boundary vector file as ROI (region of interest).

Non-vegetation areas include water, buildings and roads etc. Masking was done by detecting all NDVI responses less than zero and assigning the pixels a null value. NDVI values were calculated with formula expressed below;

$$NDVI = \frac{NIR - VR}{NIR + VR}$$

NDVI is a measure of chlorophyll abundance and energy absorption (Myneni et. al., 1995). Band 4 of LANDSAT-TM and band 3 of IRS-1C receives the maximum of the chlorophyll reflectance, while band 3 of Landsat-TM and band 2 of IRS-1C is the chlorophyll absorption band. Vector layer of the estate field boundary map was overlain and used as regions of interest to get statistics of mean NDVI value for each field.

2.4. Model 1- Model for estimating LAI using satellite derived NDVI

NDVI values derived from IRS-1C satellite image were used for this model development. Out of Landsat-TM and IRS-IC only IRS-1C satellite image

was used for this as it was acquired on one of the sampling date. Several univariate linear and nonlinear prediction models were used. Gong, P. et. al.(1995) also tried several functions for develop a model for estimate coniferous forest LAI using NDVI and conclude a hyperbolic is the best model for estimating LAI using NDVI.

2.5. Model 2 – Model for estimating tea yield

All digital coverages were used for assessing modeling parameters specific to tea plants. In order to estimate LAI from all existing variables multivariate relationships between tea yield and other variables were investigated. These variables were slope, aspect, elevation, age of the tea plantation, type of tea, relative humidity, annual cumulative rain fall, average daily temperature, average daily sunshine hours, soil depth, rock cover percentage of the field and leaf area index. However, average daily temperature and daily sunshine hours parameters were not considered for the model development as temperature and daily sunshine hours do not show any variations in field-by-field basis of the estate. To find the parameter weights univariate relationship between LAI and all existing variables were investigated. Using these correlations weights were assigned to each variable and empirical relationship between average yield and other parameter weights was investigated.

3. Results and Discussion

3.1. Model 1- Model for estimating LAI using satellite derived NDVI

The spectral data corresponding to 40 LAI measured fields were extracted from the IRS-1C February 2000 image. NDVI were calculated for those images. Several linear and non-linear models were tried to the relationship between LAI and NDVI derived from IRS-1C satellite image. Out of all a logarithmic function considers as the best goodness of fit by considering all cases for estimate LAI using satellite images. Models adopted to find the relationship between NDVI and LAI for satellite image presents in Figure 1.

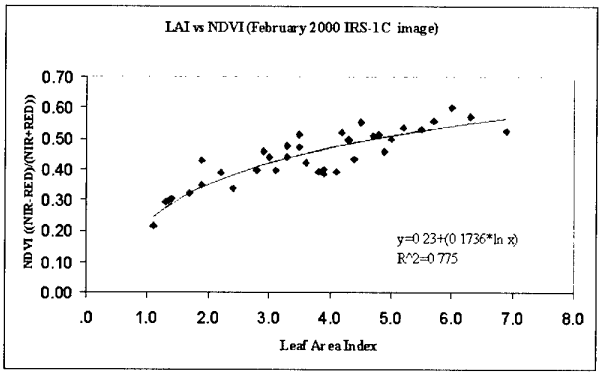


Figure 1 - The relationship between NDVI and LAI for IRS-1C image

3.2. Model 2 – Model for estimating tea yield

Variable weights were assigned by finding the univariate relationship between each variable with yield. Weights for classes within each variable

were assigned by using ARCVIEW analysis technique, which is yield summarized within the zones of reclass of each variable. Class weights were assigned by considering the yield of each tea field summarized within the zones of each variable. After assigning weights for all classes in available variables the relationship between yield and weights of classes were found using backward regression analysis. 5 models were obtained using backward regression analysis technique. Following model considered as the best model because, soil depth and rock cover percentage are very important factors for tea plant growth. Slope is also very important factor but Tea Research Institute of Sri Lanka is not recommending to plant tea in more than 55% slope lands in mid country region and more than 70% slope in up country region. Therefore, this factor is excluded.

Model 2

$$\text{Yield} = -603.923 + 50.124w_d - 23.5w_r - 14.049w_l + 65.845w_i + 513.54w_a + 39.54w_h + 65.695w_f + 46.338w_e$$

For Model 2-3 $r^2 = 0.742$; $F = 1575.083$

Where;

w_d = Soil depth weight
w_r = Rockiness cover weight
w_l = Landuse type weight
w_i = LAI weight
w_a = Age of tea plantation weight
w_h = Relative humidity weight
w_f = Rainfall weight
w_e = Elevation weight

3.3. Model validation and application

Validate the model 1

Model developed for estimate LAI using IRS-1C image was validated using t test by using holdout samples. The calculated t value (0.1367) is less than the tabulated t value (1.7247). Therefore the null hypothesized cannot be rejected and can be conclude that there is no significant difference between actual and measured LAI values. Therefore the model developed for estimate LAI by using satellite image derived NDVI values is valid with 95% significant level.

Validate the model 2 by using holdout samples and February, 2000 IRS-1C image

The selected model 2 was validated using t test by using holdout samples. As the calculated t value (-0.197) is less than the tabulated value (1.745), the null hypothesis of no difference between actual and predicted yield cannot be rejected. Therefore actual yield does not differ significantly with predicted yield using the model developed for predict yield by using measured LAI values, other meteorological, agronomic parameters and is valid with 95% significant level.

After normalized March 1995 Landsat-TM image NDVI values of the tea fields were calculated. Model 2-B-3 was used to estimate 1995 yield. Estimated and actual tea yields were compared using t-test. The calculated t value (1.467) is less than the tabulated t value (1.669). Therefore the null hypothesized cannot be rejected and can be conclude that there is no significant difference between actual and estimated yields. Therefore this model can be used to estimate yield with 95% significant level. Actual tea yield for the whole estate is 1144 made tea kg ha^{-1} $annum^{-1}$for 1995.

Estimated tea yield for the whole estate for year 1995 is 1031 made tea kg ha^{-1} $annum^{-1}$.

4. Conclusion

Logarithmic function gives a good relationship between NDVI and LAI. This model can be adopted to estimate LAI of particular tea field using NDVI value of satellite images. The model develops by using weights of all variables give best correlation of determination. In this multivariate regression analysis all variables were considered. This method gives five models with backward regression and the model with eight variables selected as the best one out of these five as it gives 95% validity with holdout samples and could be able to estimate 1995 yield. Therefore this model (Model 2) is used for estimating tea yield.

5. Acknowledgement:

The authors are grateful to Kahawatte plantation Ltd, Sri Lanka for giving permission to utilize Westhall estate for the study, Institute of surveying and mapping, Diyatalawa, Sri Lanka for providing a GPS system and Tea Research Institute of Sri Lanka for providing necessary facilities to carry out the study.

5. References

Cleves, J.G.P.W., Buker, C., Van Leeuwan, H.J.C., and Bouman, B.A.M. (1994) A Framework for Monitoring Crop Growth by Combining Directional and Spectral Remote Sensing Information, Remote Sensing Enviroment, 50: 161-170

Gong, P., Ruiliang, Pu, and Miller, J.R. (1995) Coniferous Forest Leaf Area Index Estimation along the Oregon Transect using Compact Airborne Spectrographic Imager Data, PE&RS, 61-9:1107-1117

Myneni, R. B., Hall, F. G., Sellers, P. J., & Marshak, A. L. (1995). The interpretation of spectral vegetation indexes. IEEE Transactions on Geoscience and Remote Sensing, 33(2), 481-486

Selleres, P.J., 1985, Canopy reflectance, photosynthesis and transpiration, International Journal of Remote Sensing, 6, 1335-72

LAND DEGRADATION DUE TO HYDRO-SALINITY IN SEMI-ARID REGIONS USING GIS AND REMOTE SENSING

Nasir Mahmood KHAN* and Yohei SATO**
Graduate Student* and Professor**
Department of Biology and Environmental Engineering
Graduate School of Agricultural and Life Sciences, The University of Tokyo
1-1-1 Yayoi, Bunkyo-ku, Tokyo 133-8657, Japan
Tel: +81-3-5841-5344, Fax: +81-3-5841-8169
Email: <aa97093@mail.ecc.u-tokyo.ac.jpt >*

KEY WORDS: Remote Sensing, GIS, Hydro-Salinity, NDVI, Interpolation, FDP

ABSTRACT

Fourth drainage project located in the center of Punjab province of Pakistan was selected as a research field. A newly introduced tile drainage system and remodeled surface drains have gradually reduced the waterlogging problem, however, salinity still remains in patches in the area. The present study describes an attempt to monitor land and water management scenarios that caused deterioration of vast productive land, using satellite data.

IRS-IB LISS-II digital data acquired were digitally analyzed along with other field data sets and topographical maps. False Color Composite and unsupervised classified image shows that most of the waterlogging and salinity problems are located along the drainage canals. The buffering analysis along the drainage and irrigation canals was performed to see the hydro-salinity impact on productivity in terms of its vegetation vigor. The Normalized Difference Vegetation Index (NDVI) tends to be lower along drainage and higher along the irrigation canals. It is probably because of the inequity water distribution and locational disadvantage of the down-stream farmers as well. A contrast example of an enterprise model-farm near the project area was observed which does not show any locational unbalance/inequity but exhibits comparable high NDVI values almost all over the farm area, except fallow lands. The extent of waterlogged soils was also estimated through GIS analysis from more than 150 peizometers locations lying within the study area. It was found that 24.5%, 22.0% and 63.4% of the mapped area was under risk of waterlogging (≤ 200cm) during 1990, 1993, and 1996 respectively. Evidence is presented that the existing drainage system along with use of groundwater for irrigation reduces the extent of waterlogged soils. However, the reuse of poor quality water to supplement irrigation supplies by the downstream farmers and the failure of a few drainage sumps are likely to disturb the water balance resulting into increased risk of waterlogging and salinity in the area.

INTRODUCTION

Environmental land degradation has recently become a global, urgent issue and is now being considered with high priority, specially in the developing counties, to meet food and fiber demands of accelerated population pressure with the limited available resources. Secure balance in the global supply and demand for food has forced humans to develop agriculture in semi-arid to arid lands, which are generally less suitable for agriculture and sensitive to environmental changes. Irrigation systems have always been considered as an effective way of increasing agricultural production since ancient times to bridge the gape of water shortage. Owing to irrigation systems, the farmers

have obtained quite stable productivity but they started facing an acute problem of waterlogging and salinity due to seepage from the huge system in most of the developing countries like Pakistan. The farmers, many local and international organizations are struggling now against the so-called "white death" of their lands. Land degradation due to waterlogging and subsequent salinization has been so enlarged that it is now being regarded as a global environmental problem, desertification. It is, therefore, important to monitor land and water management scenarios causing severe land degradation and low productivity. Remote sensing is one of the key tools in monitoring local, regional and global environmental issues. More recently, much attention has been paid to spatial analysis due to merging of geographic information system (GIS) and satellite images for environmental research and applications. The conventional means are however, not only difficult and time consuming but also laborious due to vagaries of the weather. It is prudent to use such emerging technique with an emphasis to its application in semi-arid areas. The present paper describes an attempt, where in IRS-1B, LISS-II (Indian Remote Sensing Satellite) digital data have been used along with other maps and field data, to monitor land degradation due to hydro-salinity and low agricultural productivity (vegetation condition).

RESEARCH FIELD

A reclamation project called as "FDP" (Fourth Drainage Project) was launched to mitigate the twine menace of waterlogging and salinity, in 1983. The FDP area is located in the center of Punjab province of Pakistan and consists of Schedule-I and Schedule-II units. The Schedule-I area covering about 70,000ha was selected as a research filed, lies between 31° 02' to 31° 45' N and 72° 50' to 73° 22' E (Figure 1). It was estimated that 77% and 43% of the total area was under high watertable conditions and salinity respectively, before the installations of a new tile drainage system (Table 1). Mean annual rainfall of the locality is <350mm out of which nearly 75% occurs during monsoon season (July-September). The mean monthly maximum temperature is between 19.4 - 41.2 C°. The mean annual evaporation is as high as 2100mm. Physio-graphically, the area is nearly level to very gentle slope (average topo-gradient is 0.02%) with mean sea level of 190m. Geologically, the soils are alluvial deposits classified as silt loam, loam, and silt clay loam and loamy sands. There are two cropping seasons i.e. Rabi (winter) and Kharif (summer). Main Rabi crops are wheat, sugarcane, pulses, and fodder while corn, paddy, cotton, sugarcane, and fodder occupy lands in kharif season.

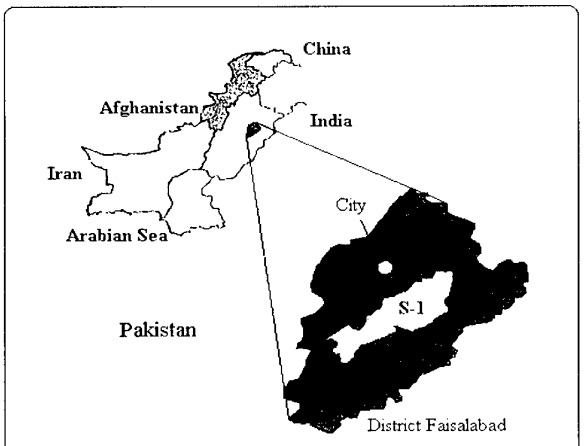


Figure 1. Location of the study area (S-1), Faisalabad, Pakistan.

Table 1. Waterlogging and salinity situation in the Fourth Drainage Project in January 1983.

Status	Salinization			Watertable Position		
Area (%)	Salt Free	Saline-Sodic	Saline-Non Sodic	0.00-1.50m	1.50-3.0m	> 3.0m
	57 %	35 %	8 %	77 %	21 %	2 %

DATA USED

Two types of data have been used in this study, i.e. satellite and field data. Satellite data of IRS-IB, LISS-II (linear image self-scanning spectrometer) in all four bands (B1: 0.04-0.52um, B2: 0.52-0.59um, B3: 0.62-0.68um and B4: 0.77-0.86um) are used for three time periods of year1993. Three different months have been chosen for the satellite data because of considerable variation in salinity as well as in vegetation cover. Topographic maps of survey of Pakistan used in the study were 44 E/3, 44 E/7, 44 E/8 and 44 /16 of scale 1:50,000. Layout maps of irrigation canal and surface drains were also used. The watertable data for more than 150 Piezometer locations (Figure. 2) lies within the S-1 area were used to know the status of soils under waterlogging risk. ILWIS 2.2 for Windows system has been used for all remote sensing and GIS analysis. Information about water and soil quality, soil types, agricultural practices, crop yield, irrigation facilities and necessary ground truth data of the study area will be obtained and used in the remaining part of the study.

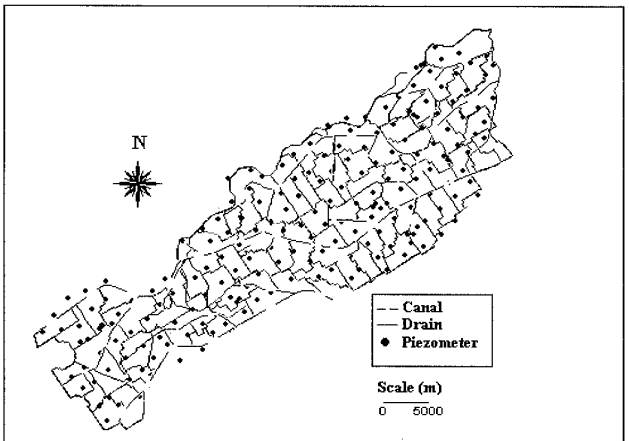


Figure 2 . Piezometers Location Map for ground water-table and quality measurements in the study area.

STUDY APPROACH

The IRS LISS-II digital data were registered to Survey of Pakistan topographical sheets using an image-to-map registration algorithm (UTM map projection with 36.25m ground resolution). About 30 common, well identified and uniformly distributed GCP points were selected from both, the displayed image and topographical sheets. The image was then registered using affine transformation method and the nearest interpolation was used for arrangements of the coordinates of each picture element. The average error was within one picture element in terms of precision after the geometric correction. Following this procedure, the others scenes were registered through image-to-image tie-down algorithm using ILWIS 2.2 for windows. False color composite (FCC) image was generated using band combination of R:G:B = 4:3:2 for better and visual interpretation of salt-affected lands in contrast to other features (Figure 3).

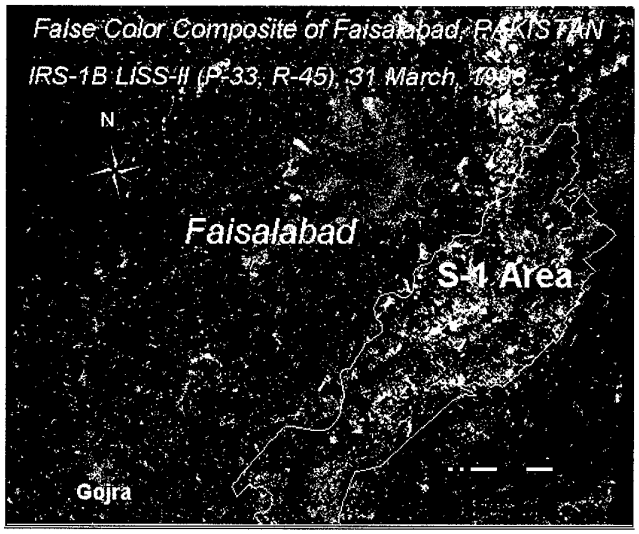


Figure 3. False colour composite image of IRS-IB LISS-II data (31 March, 93).

Unsupervised classification was performed, as the complete site information was not available. It involved various processes like image enhancement, creating composite

files, using cluster/ iso-cluster modules etc. Various salinity indices were also applied based on the concept of spectral response of salt-affected soils. It is to note that spectral response in terms of digital no. (DN) of salt-affected soils is relatively higher than other categories in band-1 (B1) and band-3 (B3). The following two salinity indices namely S.I (Salinity Index) and NDSI (Normalized Differential Salinity Index) proposed by Tripathi et. al. (1997) were applied which relatively give good results in re-classification of salt-affected lands. NDSI is just the reverse of NDVI index for vegetation.

$$S.I = \sqrt{Band\ 1 * Band\ 3} \qquad (1$$

$$NDSI = \frac{Band\ 3 - Band\ 4}{Band\ 3 + Band\ 4} \qquad (2$$

The strongly visible salt-affected lands were then extracted from the final classified image to make a thematic map. The sum of all the extracted salt-affected soils was prepared, considering the rest of area as slightly saline to normal lands (Figure 4). Depth to watertable data for the year of 1990, 1993, and 1996 for more than 150 piezometer, reported by JIID (1997) along with their GPS locations, were used to see the spatial watertable positions in the area. Using moving surface interpolation technique, initially the average watertable positions maps were prepared and analyzed for each year and then a map of "mean watertable positions" based on the three year results, was prepared. It is further grouped as waterlogged and non-waterlogged conditions, assuming an assumption of critical watertable depth of ≤ 200m for the area (Figure 5).

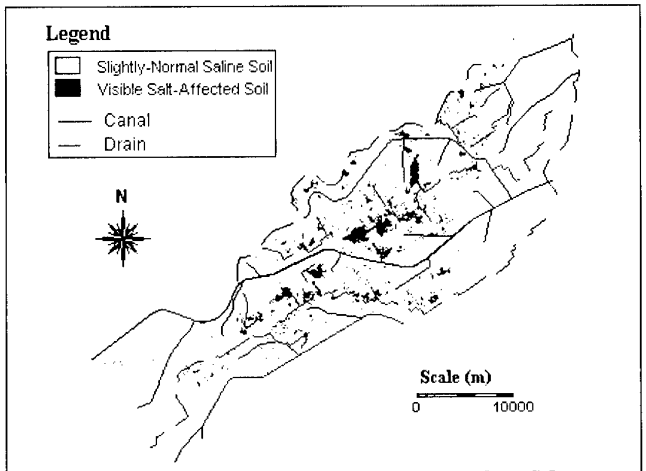


Figure 4 Classified IRS-image of salt-affected lands at S-1 area with relation to canal and drainage network.

Reflectance variations of vegetation on the image are attributed to the different species of vegetation and their densities, which together provide evidence of shallow ground watertable conditions and saline agricultural areas. Favorable growth conditions prevail in regions where the watertable is situated below the area of influence of evapotranspiration, that is, within 10-m depth (Srivastava 1997). An indication of whether scanty vegetation in an area is due to high watertable depth or salinity can be investigated using Normalized Differential Vegetation Index (NDVI)

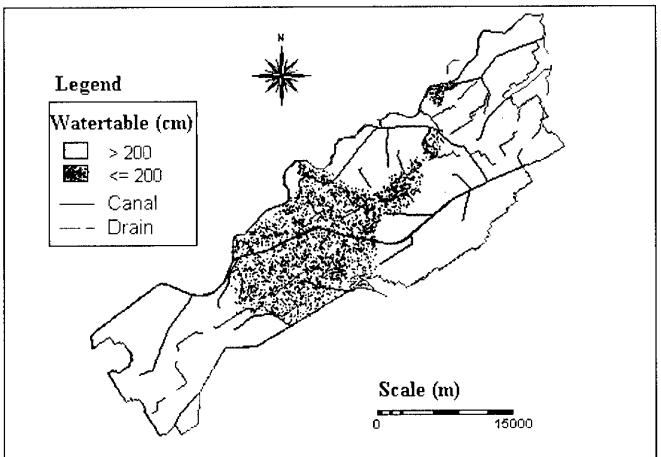


Figure 5. Watertable level showing the areas under the risk of waterlogging.

which easily grasp the state of vegetation. The NDVI for the area can be expressed as:

$$NDVI = (NIR\ Band - Red\ Band) / (NIR\ Band + Red\ Band) \quad (3)$$

The maps of irrigation canals and surface drainage network were digitized in the GIS environment. Some discrepancies of mismatching were found when overlaid on the geo-referenced image. These layers then were corrected with the help of topographic maps and image. It was presumed that the topographic sheets could be the most reliable source of information. Buffering analysis along canal and drain channels was performed for 1000m corridor to see the hydro-salinity impact on productivity in terms of vegetation vigor.

RESULTS AND DISCUSSION

Waterlogging and Salinization

The IRS composite image was systematically visually interpreted with the help of old salinity maps/ information developed in early 80's. It is revealed that salt-affected and waterlogged areas are clearly delineated compared with other land use features in FCC pellet. The most of the salt-affected lands were observed more pronounced near the drainage network as shown in white to light bluish tones. JIID (1997) and Casas (1995) reported similar results. This could be best explained, as the watertable along the drainage canals has found shallower relatively due to low location. The irrigation canals are constructed on relatively high locations comparing to the drainage system to utilize the natural gradient effectively. The occurrence pattern of salt-affected soils through unsupervised classification method was grouped into two main classes i.e. slightly to normal saline and visible salt-affected soils. The existence percentage of salt-affected soils was found to be 7.5 % for the mapped area of S-1 unit. Map of 'mean' depth of watertable shows the extent of waterlogging (area $\leq$ 200cm) in the area. The yearly average watertable analysis indicates the lowering trends during 1990-93 from 24.5 % to 22. %. However, it started increasing tremendously by 39 % in 1996. This situation is quite alarming when comparing the change of watertable for the 7 years period gape. Low with-drawl from the sumps, low natural drainage to the aquifer, deterioration of many vertical drainage system (tube-wells), choking of various sub-surface drainage lines by debris like weed growth and silting have appreciably contributed to the rising of watertable (WAPDA, 1997). All other sources of recharge and discharge of groundwater reservoir are, more or less, the same except the unpredictable rainfall pattern but it hardly cause any big change in the hydraulic balance of the area. Many farmers were reported for re-use of poor quality drainable surplus to supplement irrigation needs. Most of the farmers complained water shortage in the socio-economic survey (WAPDA/SMO, WM&E, 1993-94) for the whole area, especially, big percentage for the tail-end users. Inequity water distribution were also reported among the shareholders of a watercourse at the head, middle and tail reach.

Agro-Productivity in Relation to Hydro-Salinity

The results of the vegetation index (NDVI) were analyzed along the irrigation and drainage channels (the area under easy risk of hydro-salinity) indicated rather scarcity of vegetation as a whole (Figure 6). Relatively healthy growth of the green bio-mass were observed along the canals than that along the drains. Easily visible high NDVI were noted for a private agricultural model farm (Sehgal model farm) near the FDP area for all periodic NDVI images, except fellow lands. It is due the fact that the water management is demand oriented there (3-times more water allocation

i.e. 4.7mm/d than the average of FDP area as 1.54mm/d), thus more flexible with sufficient water supply. The design irrigation allocation (1.8-2.1mm/d) for the area is half of average crop water requirement (JIID, 1997). These results clearly show the possibility of resolving the remaining salinity problem out of area. The NPP (Net Primary Productivity) for natural vegetation corresponding to the annual precipitation range of about 300mm was too small and quite sensitive to changes in the rainfall pattern (JIID, 1997). As NPP is closely related to the agricultural productivity in rainfed farming, it is certain that ample irrigation supplies are necessary to obtain sustainable agriculture in the area.

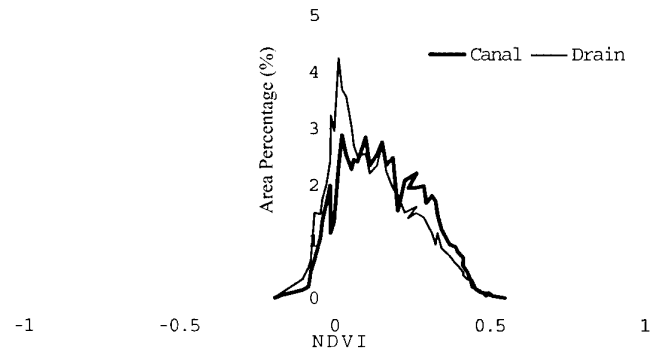


Figure 6. Vegetation status through NDVI within 1000m buffered zone along the irrigation and drainage channels.

CONCLUSION

Composite image and unsupervised classified image shows that most of waterlogging and salinity problems are located along the drainage canals. The existence percentage of salt-affected soils was found to be 7.5 % for the mapped area of S-1 unit. Th situation of waterlogging is quite alarming when comparing the change of watertable for the 7 years period with the lowering trends from 24.5% to 22% (1990-93) and clear increase by 39% in 1996. Evidence is presented that the existing drainage system along with use of groundwater for irrigation reduces the extent of waterlogged soils. However, the reuse of poor quality water to supplement irrigation supplies by the downstream farmers and the failure of a few drainage sumps are likely to disturb the water balance resulting into increased risk of waterlogging and salinity in the area. The vegetation growth analyzed through NDVI tends to be lower along drainage and higher along the irrigation canals due to the inequity water distribution and locational disadvantage of the drains and vice versa. High NDVI values for almost all over the model farm near FDP project area with demand oriented water supply thus gives the solution to resolve the remaining salinity problem. Lastly, it is concluded that the water shortage is one of the fundamental problem in the area to reclaim the soils for sustainable productive lands.

REFERENCES

Casas, S., 1995. Salinity assessment based on combined use of remote sensing and GIS. Use of Remote Sensing Techniques in Irrigation and Drainage, pp. 141-150, FAO, Rome, Italy.

JIID, 1997. Study on Establishment of a New Monitoring System for Land and Water Resources Management in Arid Area. (JIID), Main Report, 254 p.

SMO (M&E Directorate, WAPDA), 1994. Annual report. M&E, FDP Project. Vol.I. Text Pub. 237.

Srivastava, A.,Tripathi,N.K.,and Gokhale, K.V.G.K.,1997. Mapping groundwater salinity using IRS-1B LISS II data and GIS techniques. Int. J. Remote Sensing, vol.18, NO.13,pp.2853-2862.

Tripathi, N.K., Rai, B.K., and Dwivedi, P., 1997. Spatial modeling of soil alkalinity in GIS environment using IRS data.18th Asian conference on remote sensing, Kualalampur, pp.A.8.1-A.8.6.

WAPDA, 1997. Monitoring and Evaluation Fourth Drainage Project, WAPDA, Lahore, Pakistan.

ANALYSIS OF SPECTRAL CHARACTERISTICS OF RICE CANOPY UNDER WATER DEFICIENCY

Monitoring changes of spectral characteristics of dehydrating rice canopy

Chwen-Ming Yang, Muh-Rong Su
Agronomist and Assistant, Department of Agronomy
Taiwan Agricultural Research Institute
189 Chung-Cheng Road, Wufeng, Taichung Hsien, Taiwan 41301
Tel: (886)-4-330-2301ext.135 Fax: (886)-4-330-2806
E-mail: cmyang@wufeng.tari.gov.tw
TAIWAN

KEY WORDS: Spectral characteristics, Rice, Water deficiency, Vegetation index, Red edge

ABSTRACT: Information of spectral characteristics of rice canopy was extracted from ground-based remotely sensed reflectance spectra of hyperspectral resolution during water stress period in the vegetative growth phase. The analyses were focused mainly on the correlation between levels of water deficiency and spectral characteristics or parameters across wavebands of 350-2400 nm. It was shown that reflectance spectrum of rice canopy was sensitive to water stress, while different wavebands had diverse responses to of water deficiency. A dramatic difference of correlation coefficients (r) along the spectral range was found between stress treatments. The correlation between reflectance and stress level can be best represented at wavelength 2113.5 nm, where the reflectance and the reflectance ratio to control were the most significant difference. Among 12 characteristics wavelengths selected to examine their correlation to water deficits, the reflectance of 8 wavelengths had significant linear relationships with stress levels. Results further indicate that changes in red-edge position and slope did not correlate to soil water potential. The relationship between NDVI and soil water potential was significant, the increasing of soil water stress with decreasing value of NDVI.

1. INTRODUCTION

The use of canopy spectral data from remote sensing for agricultural purposes such as crop growth monitoring, yield prediction, and stress evaluation has been widely adopted nowadays. Crop growth models describing the relationship between physiological status of plants and effects of environmental factors were established and modified for various applications. Before any practical utilization in agricultural fields, however, spectral characteristics or parameters should be identified and then be incorporated into algorithms linked to the relationship in this respect. On the other hand, remote sensing may yield information to the actual conditions of a

crop and in turn improving the accuracy and structure of crop growth models.

Currently reflectance from visible and near-infrared regions has been used as variables for estimating physical traits of a crop in modeling. Much more research has also been aimed at combing the reflectance in different wavebands in assessment of growth parameters for minimizing undesirable interference from soil background and atmosphere. Such combinations are the so-called vegetation indices (Clevers, 1988, 1989; Huete, 1988; Kauth and Thomas, 1976; Richardson and Wiegand, 1977). In any case, variables employed for these applications should be able to closely represent growth characteristics or behavior.

On developing of satellite remote sensing in the 1970s, it was broad bands rather than narrow band width were used for spectral detecting due to the limitations of hardware and software techniques. With the advancement of remote sensing technology, when the spectral resolution reached to the order of 10 nm or smaller, it becomes possible to uncover minor differences in spectra data in details (Curran, 1989). Specific features of reflectance spectrum may be extracted in comparable to the specific changes of physical traits or internal chemical compounds for a crop (Elvidge, 1990; Goetz, 1991). Responses of crops to environmental stresses such as nutrient deficiency, drought, frost, and pests may also be distinguished and classified qualitatively as well as quantitatively.

The objectives of this research are to analyze remote sensing data of rice canopy from ground measurements during water stress period in the vegetative growth phase. Information of spectral characteristics was extracted from reflectance spectra of high spectral resolution. The correlation between levels of water deficit and changes in spectral parameters is studied and the potential of applying such relationship for estimating strength and status of water deficiency is evaluated.

2. MATERIALS AND METHODS

The potential of using spectral characteristics for water deficiency evaluation was examined from the ground-based remotely sensed hyperspectral data over rice canopy under varied levels of soil water deficits. Rice (*Oryza sativa* L. cv. Tainung 67) plants were grown on a loam soil at a density of 22 plants m^{-2}, with row spacing of 0.3 m and plant distance of 0.15 m, in opaque plastic containers (1.0 m W × 1.2 m L × 0.55 m H). The 20-d old seedlings were transplanted with 1 plant per hill on 5 April 2000, and the containers were placed in the experimental farm of Taiwan Agricultural Research Institute at Wufeng, Taiwan. Plants were fertilized and well taken care of to avoid the infestations of weeds and pests. When reached to leaf 8 to leaf 9 stage in the vegetative growth phase, containers were divided into three groups and subjected to water-withholding treatments. At this stage, vegetative cover was considered dense with the covering percentage more than 70%.

The collected ground truth was made periodically from 6 days after stress treatments with a portable spectroradiometer (model GER-2600, Geophysical and Environmental Research Corp., New York, USA) on near cloudless days at about solar noon. There were 10 levels of soil water deficits attained from 3 groups of containers during the experimental period, with one control (the well-watered plants) for each group (Table 1). The scanner of spectroradiometer has a 10 degree field-of-view (FOV) and was held at a nadir viewing over rice canopy, at a distance of 1 m, to acquire the reflected radiance within 330-2500 nm. Reflectance spectrum was obtained by comparing the radiance of the target canopy with the radiance of a standard (the so-called Spectrolon). Six measurements of radiance spectra were made from canopy of every treatments and each measurement was set as a mean of 3 individual full-range spectral scans. A mean reflectance spectrum was calculated from those of 6 measurements. As the reflectance above wavelengths of 2400 nm had higher noise and seemed not to affect the objectives of this study, data obtained above 2400 nm were excluded from analysis. Care was taken to prevent the influence of shadow and background.

There were 4 approaches employed to determine spectral characteristics or parameters for evaluation of water deficiency in rice plants. The first approach was to acquire wavelengths of maximum correlation coefficient (r), from the analyzed wavelength domain (350-2400 nm), by computing curve of correlation coefficients for the reflectance from different treatments. The second approach was to compare difference in reflectance relative to the controls. The percent difference in reflectance over the wavelength domain between the stressed plants and the well-watered plants were calculated, and then subjected to a correlation processing as aforementioned to compare the effect of different smoothing intensity on the correlation between the wavelengths. In the third approach, 12 wavelengths were selected from the apparent peaks and valleys appeared in the mean reflectance spectrum of each controls, and characteristics wavelengths were determined from mean value of each of 12 wavelength intervals. The reflectance of 12 characteristics wavelengths from treatments were used to examine for their correlation to levels of water deficits. The final approach was to direct correlate the red edge and the normalized difference vegetation index (NDVI) to soil water potentials. The region of red-edge is defined as wavelengths between red minimum (RED) and near-infrared maximum (NIR). The position of the red-edge is determined by the wavelength of the main inflexion point of the red-edge slope, which is the maximum value of the first order derivatives in the red-edge region. Both the position and the slope of the red-edge changed between levels of stress were tested. The NDVI was calculated by the equation: (NIR-RED)/(NIR+RED).

3. RESULTS AND DISCUSSION

The spectral reflectance in the domain of 350 to 2400 nm from rice canopy under varied water deficits and their correlation to stress levels were graphed in Figure 1. It was shown that

reflectance spectrum was sensitive to water stress, while different wavebands had diverse responses to water deficiency. A dramatic difference of correlation coefficient (r) along the spectral range was found between stress treatments. The curve gives an overall picture of the correlation feature for reflectance spectra in response to water stress. By examining the differences between wave regions, the maximum values of r and the corresponding wavelengths in different regions of reflectance spectra were identified (Table 1). The percent differences in reflectance between the stressed plants and the controls were further compared in Figure 2. It shows that the intensity of the correlation curve is similar, but in less extent, to the aforementioned feature of the processing results. The most pronounced spectral characteristics in relation to water deficits was the reflectance at wavelength 2113.5 nm (r=-0.97).

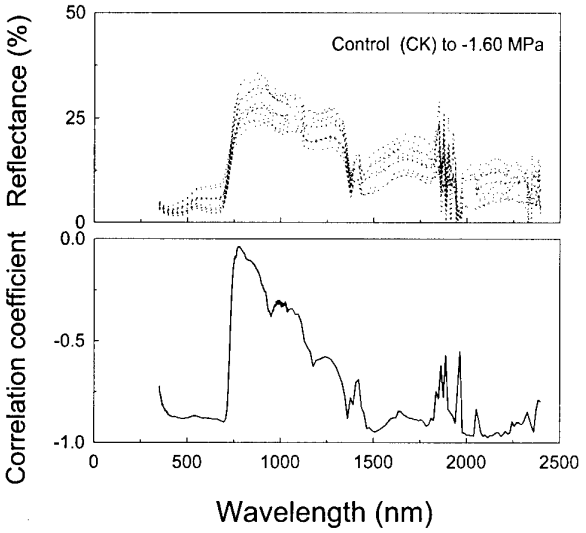


Fig. 1. The spectral reflectance in the domain of 350-2400 nm from rice canopy under varied levels of water deficit and their correlation coefficients to water stress.

Table 1. The wavelengths with maximal correlation coefficients in different wavebands of reflectance spectra and ratio spectra[@] from rice canopies under various levels of soil water deficits.

Item	Region	Waveband	Wavelength	R
Reflectance spectrum	Ultraviolet to visible	350- 740 nm	697.3 nm	-0.90**
	Near-infrared	740-1300 nm	1176.9 nm	-0.63*
	Middle infrared	1300-1800 nm	1508.3 nm	-0.95**
	Shortwave infrared	1800-2400 nm	2113.5 nm	-0.98**
Ratio spectrum	Ultraviolet to visible	350- 740 nm	692.8 nm	-0.87**
	Near-infrared	740-1300 nm	1176.9 nm	-0.51
	Middle infrared	1300-1800 nm	1508.3 nm	-0.90**
	Shortwave infrared	1800-2400 nm	2113.5 nm	-0.97**

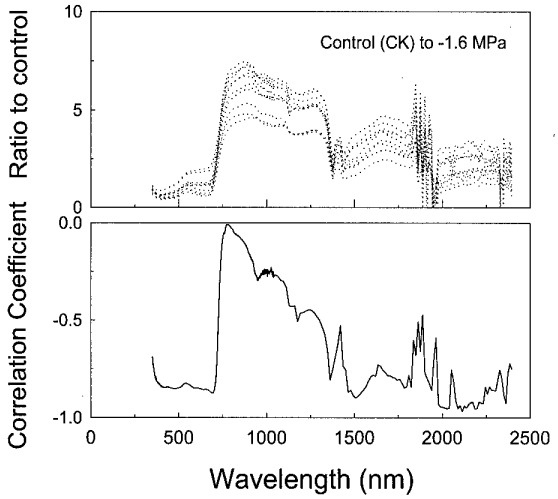


Fig. 2. The reflectance difference to the controls in the domain of 350-2400 nm from rice canopy under varied levels of water deficit and their correlation coefficients to water stress.

@ Reflectance ratio of the spectrum from stressed canopy to that from well-watered canopy.

From the apparent peaks and valleys of reflectance spectra measured in the well-watered plants during the experimental period, 12 characteristics wavelengths were identified (Table 2). Among these characteristics wavelengths selected to examine their correlation to water deficits, the reflectance of 8 wavelengths had significant linear relationships with stress levels; the coefficients all greater than 0.61. The reflectance at 2245 nm had the highest r value (0.80), but not as good as at 2113.5 nm. Based on such results, it suggests that soil water stress did not change dramatically the overall pattern of reflectance spectrum of rice canopy.

Table 2. The correlation coefficients for the 13 characteristics wavelengths selected from reflectance spectra of rice canopy in response to soil water deficits[@].

Correlation coefficient	Characteristics wavelength (nm)											
	486	553	660	881	1192	1270	1376	1406	1435	1676	1810	2245
r	0.78**	0.76**	0.78**	0.03	0.36	0.35	0.61*	0.50	0.68**	0.76**	0.78**	0.80**

[@] The 13 levels of soil water deficits were -0.36, -0..51, -0.64, -0.73, -0.86, -1.45, -1.50, -1.53 and –1.60 MPa plus CK1, CK2 and CK3. (r=0.50).

It has been reported that the absorption maximum of chlorophyll in the visible band and the near-infrared shoulder of the red-edge will be changed upon environmental stress (Horler et al., 1983). It is therefore a reasonable prediction that both position and slope of the red-edge may be altered by the impact of water stress. With hyperspectra at intervals less than 10 nm in this study, position and slope of the red-edge acquired were quite reliable and accurate (Figure 3). However, results show that changes in red-edge position and slope did not correlate to soil water potential. Thus, the red-edge is not a good spectral parameter to distinguish levels of water deficit. On the

other hand, the relationship between NDVI and soil water potential was significant (figure 3), the increasing of soil water stress with decreasing value of NDVI.

4. REFERENCES

Clevers, J. G. P. W. 1988. The derivation of a simplified reflectance models for the estimation of leaf area index. Remote Sens. Environ. 25, pp.53-69.

Clevers, J. G. P. W. 1989. The application of a weighted infrared-red vegetation index for estimating leaf area index by correcting for soil moisture. Remote Sens. Environ. 29, pp.25-37.

Curran, P. J. 1989. Remote sensing of foliar chemistry. Remote Sens. Environ. 30, pp.271-278.

Elvidge, C. D. 1990 Visible and near infrared reflectance characteristics of dry plant materials. Int. J. Remote Sens. 11, pp.1775-1795.

Goetz, A. F. H. 1991. Imaging spectrometry for studying earth, air, fire and water. EARSeL Advances in Remote Sensing 1, pp.3-15.

Horler, D. N. H., M. Dockray and J. Barber. 1983. The red edge of plant leaf reflectance. Int. J. Remoter Sens. 4, pp.273-288.

Huete, A. R. 1988. A soil adjusted vegetation index (SAVI). Remote Sens. Environ. 25, pp.295-309.

Kauth, R. J. and G. S. Thomas. 1976. The tasseled cap-a graphic description of the spectral-temporal development of agricultural crops as seen by Landsat. Proc. Symp. On March. Proc. Rem. Sens. Data, Purdue Univ., W. Lafayette, Ind., 4B. pp.41-51

Richardson, A. J., and C. L. Wiegand. 1977. Distinguishing vegetation from soil background information. Photogram. Eng. Remote Sens. 43, pp.1541-1552.

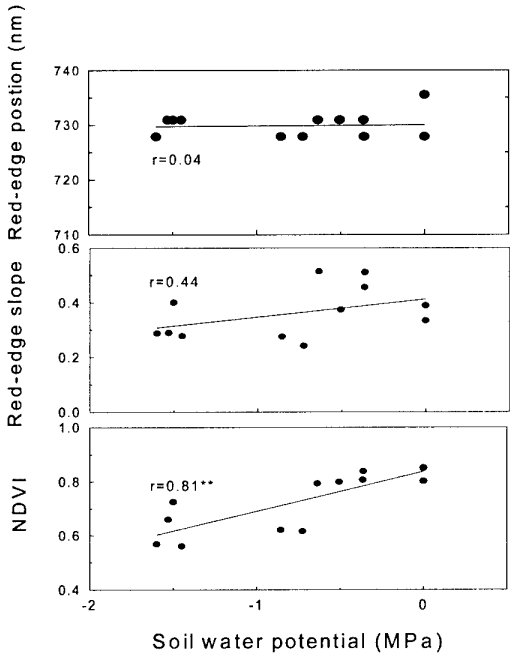


Fig. 3. Changes of position and slope of the red-edge and the normalized difference vegetation index (NDVI) in response to soil water potential.

CLIMATE CHANGE AND AGRICULTURAL FOOD PRODUCTION OF BANGLADESH: AN IMPACT ASSESSMENT USING GIS-BASED BIOPHYSICAL CROP SIMULATION MODEL.

Afzal Ahmed and Ryosuke SHIBASAKI
Center for Spatial Information Science
University of Tokyo, 4-6-1 Komaba
Meguro-Ku, Tokyo 153-8505, JAPAN
Phone: +81-3-5452-6417, Fax: +81-3-5452-6414
Email: afzal@skl.iis.u-tokyo.ac.jp

KEY WORDS: Global warming, crop production, Crop simulation model, Spatial-EPIC

ABSTRACT

Agriculture is always vulnerable to unfavorable weather events and climatic conditions. Despite technological advances such as improved crop varieties and irrigation systems, weather and climate are still key factors in agricultural productivity. Often the linkages between these key factors and production losses are obvious, but sometimes the linkages are less direct. The impacts of climate change on agricultural food production are global concerns, and they are very important for Bangladesh. Agriculture is the single most and the largest sector of Bangladesh's economy which accounts for about 35% of the GDP and about 70% of the labor force. Agriculture in Bangladesh is already under pressure both from huge and increasing demands for food, and from problems of agricultural land and water resources depletion. The prospect of global climate change makes the issue particularly urgent. It is well established that atmospheric concentration of CO_2 is increasing and this would be beneficial for crop growth and productivity. But the nature and magnitude of climatic change associated with the increase of CO_2 and other radioactive trace gases are uncertain. Thus, it is difficult to predict the combined impact of increasing atmospheric CO_2 on agricultural productivity. Crop simulation models are used widely to predict the crop growth and development in studies of the impact of climatic change.

So far, climate-based models for estimating potential productivity are used for this purpose. These models are relatively easy to apply, but they fail to estimate actual productivity and possible effects of mitigation measures. On the other hands, process-based crop models are advantageous to estimate actual productivity, but they are applied to only limited numbers of test sites due to heavy data requirement in applying them for wide areas.

A comprehensive GIS-based biophysical crop simulation model, Spatial-EPIC, was used in order to demonstrate the crop growth response to the combined effects of CO_2 concentration increase and CO_2-induced climate change at the national level. Modeling within a GIS offers a mechanism to integrate the many scales of data developed in and for agricultural research. Rice and wheat cropping system in Bangladesh were studied for this purpose.

INTRODUCTION

The balance of scientific evidence now suggests that over the last century humans have begun to have a discernible influence on the earth's climate, causing it to warm (IPCC, 1996, 1998). Since the beginning of the industrial age, the concentration of CO_2 in the atmosphere has increased from 280 to 350 parts per million (Bazzaz and Fajer, 1992). The increase of CO_2 in the atmosphere has been more rapid in recent years. The major reason for this increase may be attributable to the extensive use of fossil fuels, such as oil, coal and gas. The destruction of

The soil characteristics of Bangladesh were obtained after digitization of survey of Bangladesh soil map with many properties like soil texture, soil pH and soil depth. Weather data were obtained and their surfaces were generated using World Meteorological Organization station falling around 22 in number scattered throughout Bangladesh. Agricultural management data were obtained at district level. All these data were used for whole country simulation at 10 km cell size. The simulation and validation result is not complete yet. These would likely to be presented at the conference.

REFERENCES

BARC: 1991, *Agroecological database,* BARC Computer Center, Bangladesh Agricultural Research Council, Dhaka.

Bazzaz, F. A., Fajer, E. D. (1992). Plant life in a CO2-rich world. Scient. Am. 1992: 1821

Houghton, J. T., Jenkins, G. J., and Ephrauma, J. J.: 1990, Climate Change, The IPCC Scientific Assessment, Cambridge University Press, Cambridege, UK, 365 pp.

IPCC, 1996. Watson, R.T., Zinyowera, M.C., Moss, R.H. (Eds.) Climate Change 1995: Impacts, Adaptations and Mitigation of Climate Change: Scienti"c-Technical Analyses. Contribution of Working Group II to the Second Assessment Report of the Intergovernmental Panel on Climate Change, Cambridge University Press, Cambridge.

IPCC, 1998. Watson, R.T., Zinyowera, M.C., Moss, R.H. (Eds.) The regional impacts of climate change: an assessment of vulnerability. A Special Report of IPCC Working Group II, Cambridge Univer-sity Press, Cambridge.

Jodha N.S., 1989, Potential strategies for adapting to green house warming: Perspective from the developing world, in: Green House warming: Abatement and Adaptation, Rosenberg N.L., Earterling III W.E., Crosson P.R., and Darmstadter J. (eds), RFF Proceedings, Climate Resources Division, pp.147-158

Kimball, B. A., J. R. Mauney, F. S. Nakayama and S. B. Idso,: 1983, Effects of Increasing Atmospheric CO_2 on Vegetation. Vegetatio 104/105:65-70

Satya Priya, Shibasaki Ryosuke and Shiro Ochi (1998) Modeling Spatial Crop Production: A GIS approach, Proceedings of the 19th Asian Conference on Remote Sensing, 16-20 Nov, 1998 held at Manila. pp A-9-1 to A-9-6.

THE STUDY FOR ASSESSMENT OF SUSCEPTIBILITY TO SOIL LIQUEFACTION IN TAIWAN

Horng-Yuh GUO, Chih-Feng CHIANG, Tsang-Sen LIU, Jiang-Liung CHU, Jen-Chyi Liu
Taiwan Agricultural Research Institute, Wufeng, Taichung Hsien, Taiwan

KEY WORDS : Susceptibility of Soil Liquefaction, Pedotransfer Fuctions, GIS

ABSTRACT : Soil liquefaction has been observed in many places after 921 Taiwan Chichi Earthquake. Soil liquefaction resulted in disastrous effects such as tilted buildings, foundation failure and sand volcanoes or sand boils in the fields. It was suggested that government should provide revealing of information regarding the potential hazard of soil liquefaction and teach citizens how to evade soil liquefaction hazard. Responding to this, it is the fact that there is no graphic information (regional map) available about potential hazard of soil liquefaction in disastrous region currently. Liquefaction occurs in saturated soils, that is, soils in which the space between individual particles is completely filled with water. There are a number of different ways to evaluate the liquefaction susceptibility of a soil deposit. Generally, fine-grained soils are susceptible to liquefaction if they satisfy the criteria (Wang.1979) shown in the followings: Fraction finer than 0.005mm$\leqq$15%；Liquid Limit(LL)$\leqq$35%；Natural water content $\geqq$0.9LL ； Liquidity Index$\geqq$0.75. However, there is no quantitative parameter in the soil information here at this moment for applying the criteria to evaluate the susceptibility of soil liquefaction. Pedotransfer fuctions (PTFs) are used to transfer the quantitative criteria to the easily measured soil properties we have in the soil information system. In this study, we evaluated, classified and mapped the in disastrous regions based on three categories in soil information. The map was further verified the reliability in earthquake areas.

INTRODUCTION

Soil liquefaction has been observed in many places after 921 Taiwan Chichi Earthquake. Soil liquefaction resulted in disastrous effects such as tilted buildings, foundation failure and sand volcanoes or sand boils in the fields. Because soil liquefaction occurred places did not coincided with the geometry relationship of the fault, so it is assumed that soil liquefaction is a mysterious phenomenon by some people. It was suggested that government should provide revealing of information regarding the potential hazard of soil liquefaction and teach citizens how to evade soil liquefaction hazard. Responding to this, it is the fact that there is no graphic information (regional map) available about potential hazard of soil liquefaction in disastrous region currently. It is a very difficult task to complete the survey of the potential hazard of soil liquefaction in a short time.

Soil surveys provide information that is useful in multiple disciplines. Soil information system can provide the information of the pattern of the soil cover and its characteristics for us to analyze and display the topics of soil resources management. To evaluate the soil liquefaction hazard completely, a number of necessary and sufficient conditions must be successively examined. However, there is no available parameter in the soil information here at this moment for applying the criteria to evaluate the susceptibility of soil liquefaction. In this study, we transfered and applied the soil information system databases to evaluate, classify and map the susceptibility of soil liquefaction in Taichung, Nantou, Changhua and Yunlin's Plain regions in a short time, and the maps were further verified their reliability in the fields.

REVIEW OF SOIL LIQUEFACTION

Plasticity parameters, which have been expressed in terms of moisture content of the soil (that is, Atterberg limits), have been defined, and standard methods for making the measurements have been established. (ASTM, 1958) Plastic limit, PL, is defined as that the water content on a dry weight basis corresponding to the arbitrary limit between plastic and brittle states of consistency of a soil. Liquid limit, LL, is defined as that the water content on a dry weight basis corresponding to the arbitrary limit between the liquid and plastic states of consistency of a soil. Plasticity index, PI, is the difference between the liquid and plastic limits and represents the range of moisture within which the soil is plastic. Silts and sands have slight or no plasticity indices, which clays have higher indices. Plasticity index in combination with the liquid limit indicates how sensitive the soil is to changes in moisture. (USDI, 1990) Field observations and experimental investigations have pointed out that the consistency of soils varies with texture, organic matter, the amount and nature of the colloidal material, and especially with moisture content. (Hillel, 1980) Liquidity index, LI, is defined as that the ratio of the difference between the nature soil water content and plastic limit to the soil plastic index (PI) of the same soil. If a soil liquidity index is less than 1, that means the soil water content is less than liquid limit. A soil liquidity index is very low or close to 0, that means the soil water content is near to plastic limit and the soil have a high cohesion. (McCarthy, 1997)

Soil liquefaction is a phenomenon in which the strength and stiffness of a soil is reduced by earthquake shaking or other rapid loading. In soil mechanics, liquefaction is the passage from a solid to a liquid state. Liquefaction occurs in saturated soils, that is, soils in which the space between individual particles is completely filled with water. The fluidification of a soil results in a diminution, or disappearance of its shear resistance, which in turn leads to instability problems. The liquefaction of a soil under seismic solicitation requires two types of conditions: (1) Permanent factors: soil characteristics and parameters describing the state of the soil. Soil is known to have susceptibility to liquefaction when it is relatively pulverulent and uncompacted,

under little stress and water-logged. (2) Aggravating factors: the first is an earthquake acting as a trigger. The opportunity to liquefy, when the energy of emitted waves is sufficient. (Monge *et al,* 1998*)*

There are a number of different ways to evaluate the liquefaction susceptibility of a soil deposit. Here they are organized as follows (Kramer, 1996), (1) Historical criteria: Soils that have liquefied in the past can liquefy again in future earthquakes. (2) Geological criteria: Saturated soil deposits that have been created by sedimentation in rivers and lakes, deposition of debris or eroded material, or deposits formed by wind action can be very liquefaction susceptible. (3) Compositional criteria: Liquefaction susceptibility depends on the soil type. Soils composed of particles that are all about the same size are more susceptible to liquefaction than soils with a wide range of particle sizes. (4) State criteria: At a given effective stress level, looser soils are more susceptible to liquefaction than dense soils. For a given density, soils at high effective stresses are generally more susceptible to liquefaction than soils at low effective stresses.

Liqefiable soils can be identified by a combination of several criteria. A simple model to evaluate soil liquefaction was developed by Wang, that is, fine-grained soils are susceptible to liquefaction if they satisfy the criteria shown in the followings: Fraction finer than 0.005mm$\leqq$ 15% ; Liquid Limit(LL) $\leqq$ 35% ; Natural water content $\geqq$ 0.9LL ; Liquidity Index $\geqq$ 0.75. (Wang.1979)

MTERIALS AND METHODS

1. Assessment procedures:

To evaluate, classify and map the susceptibility of soil liquefaction in Taichung, Nantou, Changhua and Yunlin's Plain regions, we use the soil information system of Taiwan, which was constructed 10 years ago by Taiwan Agricultural Research Institute, as a bases. Soil texture, soil drainage classes and available soil depth (90cm to 150cm) are the parameters available to evaluate the permanent factors of soil liquefaction susceptibility. We had to apply pedotransfer function to modify these parameters of the soil information system and meet Wang's model requirement. (Wang, 1979) The map of active faults in Taiwan (CGS, 1998) is another useful information to be used as a aggravate factor of soil liquefaction susceptibility. The nearer the fault lines site is, the more opportunity to liquefy, when the energy of emitted waves is sufficient. MAPINFO geographic information system software was used as an analysis tool. We map the susceptibility of soil liquefaction in Taichung, Nantou, Changhua and Yunlin's Plain regions, and the maps were verified their reliability in the soil liquefaction areas.

2. Pedotransfer of soil data:

The objectives of the identification of liquefiable soil are granulometry and Atterberg limits etc, which have some relationship with soil texture and soil water content characteristics. But these two factors are very difficult to measure. Pedotransfer fuctions (PTFs) are used to transfer the quantitative criteria to the easily measured soil properties we have in the soil information system. So we had to transfer the Wang's criteria of the soil liquefaction into the parameters of the soil information system for further analysis. The followings are pedotransfer Functions (PTFs) for soil liquefaction:

Fraction finer than 0.005 mm< 15% ⇨ Soil texture class (USDA) : Sand, loamy sand and sandy loam

Liquid Limit, LL≦ 35%
Natural water content≧ 0.9 LL
Liquidity Index≧ 0.75
⇨ Soil texture class is coarse, medium coarse and Soil drainage classes: submerged, poor to very

Because the effective depth of the shallow foundation construction is about one meter to five meters, we chose the soil texture of the deepest layer (90cm to 150cm) which the soil information system of Taiwan available.

3. Rating the soil liquefaction susceptibility:

Liquefiable soils are rated and classified by the criteria of soil texture and drainage class as following table:

Table 1. Rating table of soil liquefaction susceptibility (for shallow foundation construction)

SOIL LIQUEFACTION SUSCEPTIBILITY RATING CLASS	Coarse texture (sand, loamy sand, etc)	Medium-coarse texture (sandy loam, very fine sandy loam, etc)	Medium texture (silt loam, loam, etc)	Medium-fine texture (clay loam, silty clay loam, etc)	Fine texture (silty clay, clay, etc)	Gravelly
Well to moderate-well drainage	2	3	4	5	5	5
Imperfect drainage	1	2	3	4	5	5
Poor to very poor drainage	0	1	2	3	4	4
submerged	0	0	1	2	3	3

1. Class 1:more than 90% liquefaction vulnerability ; Class 2:more than 70% liquefaction vulnerability ; Class 3:more than 50% liquefaction vulnerability ; Class 4:more than 30% liquefaction vulnerability ; Class 5:no liquefaction vulnerability.
2. If the site in the faults buffer zones(10Km wide) increases 1 class.

RESULTS AND CONCLUSIONS

Because liquefaction only occurs in saturated soil, its effects are most commonly observed in low-lying areas near bodies of water such as rivers, lakes, bays, and oceans. Parts of Taichung, Nantou, Changhua and Yunlin's Plain regions belong to these kinds of landscapes. Tzo-Sui Alluvial Fan covers the most area in this region. Tzo-Sui River had changed its water way several times in the past two hundreds years, so many abandoned channels spread around this region. Taichung, Changhua and Yunlin plains are also nearby the seashores, these lands have a high potential of soil liquefaction. Taichung Port and wharf facilities are located in areas susceptible to liquefaction, and have been damaged by liquefaction in 921 Chi-Chi earthquake. On level ground, during and after an earthquake, the flowing pore-water rises quickly enough, it can carry sand particles through cracks up to the surface, where they are deposited in the form of sand volcanoes or sand boils. (Kramer, 1996) The buildings and houses on the abandoned river channel are tilt due to soil liquefaction. These phenomena have been observed around the riverbeds and the fields in the Taichung, Changhua and Yunlin plains.

We used Wang's model to evaluate soil liquefaction. Soil particle size and soil water contents are the two major factors concerning soil liquefaction in this model. The criteria of fraction finer than 0.005mm$\leqq$15% means that the part of finer than coarse silt particles is not more than 15% in the soil. The pedotransfer function can be changed this quantitative criteria to that the soil belongs to coarse texture (sands, loamy sands and sandy loams in USDA soil textural class). By the same way, Liquid Limit(LL)$\leqq$35% also indicates that the soil belong to coarse grained soil. Because the coarse grained soil has a low liquid limit. Natural water content$\geqq$0.9LL and Liquidity Index$\geqq$0.75 indicate that the coarse soils have a high water content.

Sands were considered to be the only type of soil susceptible to liquefaction, but liquefaction has also been observed in gravel and silt. (Kramber, 1996) So the different soil texture has the different sensitivity of soil liquefaction. Soil drainage classes can indicate the different levels of soil water contents, which can be used to evaluate the sensitivity of soil liquefaction, too. So in this study, we classified the soil texture classes into five groups and soil drainage classes to four groups, as Table 1. We rated five classes of the soil liquefaction susceptibility for the shallow foundation construction by these two factors. Because the site near the active fault lines has more energy of emitted waves when earthquake occurs, so if the site under the active fault 5 Km buffer zones, the rate increase one class. In this study, we evaluated, classified and mapped the susceptibility of soil liquefaction in disastrous regions based on three categories in soil information. The map was further verified the reliability in earthquake areas. Most of the boundaries of the soil liquefaction susceptibility units match the soil liquefaction regions. The

reliability of the assessment of soil liquefaction susceptibility is very high. The information provided here could be very helpful in the developing plan for evading soil liquefaction hazard.

There are basically three possibilities to reduce liquefaction hazards when designing and constructing new buildings or other structures as bridges, tunnels, and roads. The first possibility is to avoid construction on liquefaction susceptible soils. The maps we drew can be used as a reference to determine the liquefaction susceptibility of a soil. By characterizing the soil at a particular building site according to these criteria one can decide if the site is susceptible to liquefaction and therefore unsuitable for the desired structure. If it is necessary to construct on liquefaction susceptible soil because of space restrictions, favorable location, or other reasons, it may be possible to make the structure liquefaction resistant by designing the foundation elements to resist the effects of liquefaction. The third option involves mitigation of the liquefaction hazards by improving the strength, density, and/or drainage characteristics of the soil. This can be done using a variety of soil improvement techniques. (EERI,1997)

REFERENCES

1. ASTM 1958. Procedures of soil testing, Philadelphia.
2. Central Geological Survey, MOEA 1998 Map of Survey of the active faults in Taiwan. Central Geological Survey Repot No.10, Taipei, Taiwan. (In Chinese).
3. EERI 1997. Adopted from www.eeri.org/EQ_Basics
4. Hillel D. 1980. Fundamentals of soil physics., Academic Press, NY., Pp.347-351.
5. Kramber 1996. Adopted from"www.ce.washington.edu/~liquefaction".
6. McCarthy, D.F. 1997. Basic Geotechnics., (5th ed.)., Prentice Hall, New Jersey., Pp.73-78.
7. Monge, O., D. Chassagneux and P. Mouroux 1998. Methodology for liquefaction hazard studies: new tool and recent applications. Soil Dynamics and Earthquake Engineering. 17(1998):415-425.
8. Siderius, W.1995. Introduction to pedotransfer. Lecture Notes., International Institute for Aerospace Survey and Earth Sciences., Enschede, The Netherlands.
9. USDI 1990 Earth Manual. Second edition. Bureau of reclamation, U.S. Department of the Interior, Pp.25-29.
10. Wang, 1979. Adopted from "www.ce.washington.edu/~liquefaction".

On the Retrievals of Surface Soil Moisture from Simulated SMOS and AMSR Brightness Temperatures

Shou-Fang Liu[1,2], Yuei-An Liou[3], and Wen-June Wang[1]

1. Department of Electrical Engineering, National Central University, Chung-Li 320, Taiwan.

2. Department of Industrial Design, Oriental Institute of Technology, Taipei 220, Taiwan.

3. Center for Space and Remote Sensing Research, National Central University, Chung-Li 320, Taiwan. Email: yueian@csrsr.ncu.edu.tw. Tel: (03) 4227151 ext 7631. Fax: (03) 4254908.

KEY WOEDS: Soil Moisture, L-band Radiometry

ABSTRACT

We present the retrievals of surface soil moisture (SM) by simulated Advanced Microwave Scanning Radiometer (AMSR) and Soil Moisture and Ocean Salinity (SMOS) "simulate" brightness temperatures. The nonlinear mapping from brightness temperatures onto SM is handled by an Error Propagation Learning Back Propagation (EPLBP) neural network (NN). AMSR is a space-borne microwave radiometer operating at 6.9, 10.7, 18.7, 23.8, 36.5, and 89.0 GHz to be launched in November 2001 by the National Space Development Agency of Japan (NASDA). It is designed to scan conically at an incidence angle of 55 degrees. SMOS mission is tentatively scheduled for launching by European Space Agency (ESA) in 2005. Its payload Microwave Imaging Radiometer using Aperture Synthesis (MIRAS) measures brightness temperatures at a wide range of incidences, approximately from 0 to 50 degrees. The well-known Land Surface Process/Radiobrightness (LSPR) model is used to provide SM and AMSR brightness temperatures at both 6.9 and 10.7 GHz for an incidence angle of 55 degrees, and SMOS brightness temperatures at L-band for multiple incident angles of 0, 10, 20, 30, 40, and 50 degrees.

Introduction

Soil Moisture (SM) dominates the partitioning of net radiation energy into sensible and latent heat fluxes, and rainfall into runoff and root-zone storage at the land-air interface. Hence, it plays a crucial role in current hydrologic, climatic, agricultural, and biogeochemical models, and becomes a parameter of great interest in the field of remote sensing. It is linked to radiometric signatures through its influence on microwave emission of the land surfaces (Njoku and Li 1999; Liou et al. 1999a).

In this paper, the retrievals of surface SM from simulated AMSR and SMOS brightness temperatures by a newly developed EPLBP neural network are presented. AMSR is a space-borne microwave radiometer operating at 6.9, 10.7, 18.7, 23.8, 36.5, 50.3, 52.8, and 89.0 GHz to be launched in November 2001 by the National Space Development Agency of Japan (NASDA). It is designed to scan conically at an incident angle of 55 degrees. SMOS satellite is tentatively scheduled for launching by European Space Agency (ESA) in 2005. Its payload, L-band (1.4 GHz) 2D interferometric radiometer, measures brightness temperatures at a wide range of incident angles, approximately from 0 to 50 degrees. The LSP/R model is used to provide time series of SM and brightness temperatures at AMSR's 6.9 and 10.7 GHz channels for an incident angle of 55 degrees, and at L-band of the SMOS for multiple incident angles of

0, 10, 20, 30, 40, and 50 degrees. These multiple incident angles allow us to design a variety of observation modes based on the viewing and instrumental characteristics of the AMSR and SMOS. For example, L-band brightness temperature at any single look angle can be used to infer SM. Meanwhile, it can be combined with either the observation at the other angles to become an L-band 2D or multiple dimensional observation mode, or with the observation at 6.9 or 10.7 GHz to become an integrated AMSR and SMOS observation mode.

LSP/R Model

We have studied radiometric characteristics of land surfaces for the purpose of sensing surface parameters by microwave radiometry for many years. Our approach is to improve the understanding and capability by incorporating land surface processes into microwave emission models. As a consequence, a series of LSP/R models for bare soils and prairie grassland have been developed (Liou and England 1996, 1998a, 1998b; Liou et al. 1999a). Each of these LSP/R models consists of two modules, an LSP module and an R module. The LSP module simulates land-air exchange of energy and moisture to predict temperature and moisture profiles of soil and, if any, vegetation. The R module utilizes predictions of temperature and moisture fields from the LSP module to compute brightness temperatures of the terrain.

The current study utilizes the LSP/R model developed and validated by Liou et al. (1999a) for prairie grassland in South Dakota. The LSP/R model was previously integrated into a Dynamic Learning Neural Network to demonstrate the capability of L-band radiometer in sensing SM (Liou et al. 1999b, 1999c). As the SMOS mission is likely to be carried out in the year of 2005 by ESA, European Space Agency (Kerr et al. 1998), it is of great interest to examine the capability of L-band radiometry in sensing SM based on the SMOS viewing design, and its combination with the viewing designs of the other space-borne sensors such as AMSR and AMSR-E.

The EPLBP Neural Network

Radiometric signatures of a vegetation-covered field reflect an integrated response of the soil and vegetation system to the observing microwave system. This allows one to link surface parameters to the radiometric signatures by

$$\vec{y} = f(\vec{x}) \qquad (1)$$

where $\vec{y}$ is a feature vector of surface parameters (variables of interest), $\vec{x}$ is an observation vector of radiometric signatures, and f is a mapping function.

Neural networks are known for their capability in handling nonlinear mapping problems (Chen et al. 1999; Liou et al. 1999b, 1999c). Hence, they are suitable to characterize the f function for the problems of our interest. One major feature using neural networks is that f does not have to be explicit. Instead, f is simply defined through a training process using a representative data set. The EPLBP neural network is used to handle nonlinear mappings from microwave emissions to the parameter of interest, SM. It encourages different individual networks to get improved in an ensemble to learn different parts or aspects of a training data. The errors associated with each individual networks are negatively correlated through an adjustable penalty parameter λ ($0 \leqq \lambda \leqq 1$). This negative correlation learning is a simple extension to the standard back propagation algorithm of the Rumelhart et al. (1986). Weight updating of all the individual networks is performed simultaneously with equal penalty parameter. Since the correlation is quite often decreased with increasing distance from the individual network of

concern, a distance dependent penalty parameter is expected to simulate the neurons more appropriately than a constant penalty parameter.

The EPLBP algorithm is developed not only to correlate the errors associated with individual network via adjustable penalty parameters, but also to allow the penalty parameter to be distance dependent, that is, the limit of the distance in which neural networks are correlated is tunable. In addition, the value of the penalty parameter within that specific distance of concern is variable with distance from the center of a concerned region. The details for the EPLBP algorithm have been reported by Liu et al. (2001).

Analysis of the Results

A. Observation Modes

The viewing characteristics of AMSR and SMOS provide the basis to define the observation modes. Since there are many observation modes, we will not show all of the results. A more completed summary on the results will be presented in Liou et al. (2001). Results from four observing modes are presented.

1. One integrated 2 AMSR channels observation mode: The observations at both 6.9 and 10.7 GHz channels of the AMSR are used simultaneously to become an integrated 2 AMSR frequency observation mode.
2. One 1D SMOS observation mode: L-band observation at 30 degrees is studied. This observing mode is defined as a 1D L-band mode.
3. One 2D SMOS observation mode: L-band observations at 20 and 30 degrees are utilized as inputs of the retrieval algorithm. This observation mode is defined as a 2D L-band mode.
4. One integrated AMSR and 1D SMOS observation mode: The observation at AMSR's 6.9 GHz is combined with the observation from the 1D L-band mode at 30 degrees to become an integrated AMSR and SMOS observation mode.

B. Comparison of Observation Modes

Based on the above four observational modes, the sensitivity of microwave brightness to SM can be examined by comparing the retrieved SM with the corresponding reference. Note that Gaussian-distributed noises with standard deviation of 2 K are imposed upon the input nodes of the neural network to simulate instrument noises for all observation modes of concern.

Figure 1 shows the retrieved SM from the 2 AMSR frequency observation mode versus the corresponding reference. The correlation between the retrieved SM and the reference with the corresponding root mean squared error (RMSE) in volumetric SM content are also shown in the figure. Overall, the retrieved SM falls onto or near the 1:1 line. The correlation is 81.3 % with RMSE less than 1.76%. The corresponding correlation is near 1 when no noise is imposed upon the input node.

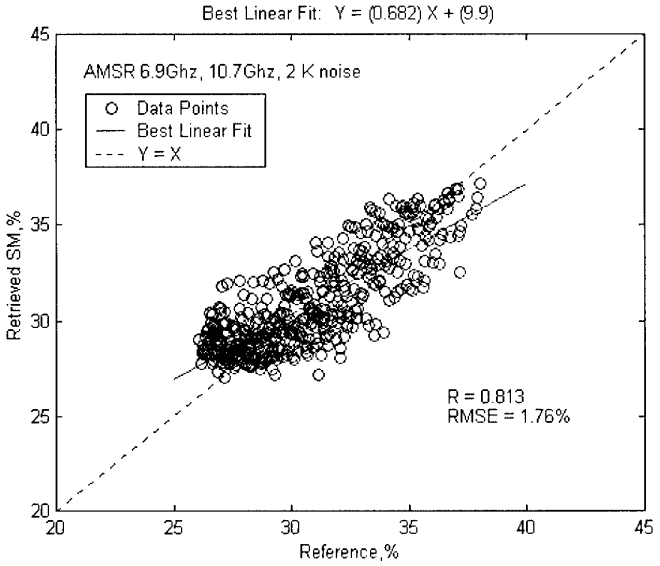


Fig. 1 Retrieved SM from the integrated 2 AMSR frequency mode versus the reference.

Figure 2 shows the retrieved SM for the 1D L-band observation mode at 30 degrees versus the corresponding reference. The retrieved SM is improved significantly compared to that derived from the 2 AMSR frequency observation mode. Figure 3 presents the retrieved SM from the L-band 2D observation mode at 20 and 30 (20-30) degrees versus the corresponding reference. It is observable that the retrieved SM is further improved compared to that from the previous two cases. The correlations between the retrieved SM and the reference is 1 with RMSE as low as 0.025%. A comparison between Figures 2 and 3 clearly demonstrates the advantage of a 2D mode over a 1D mode since the RMSE is reduced significantly.

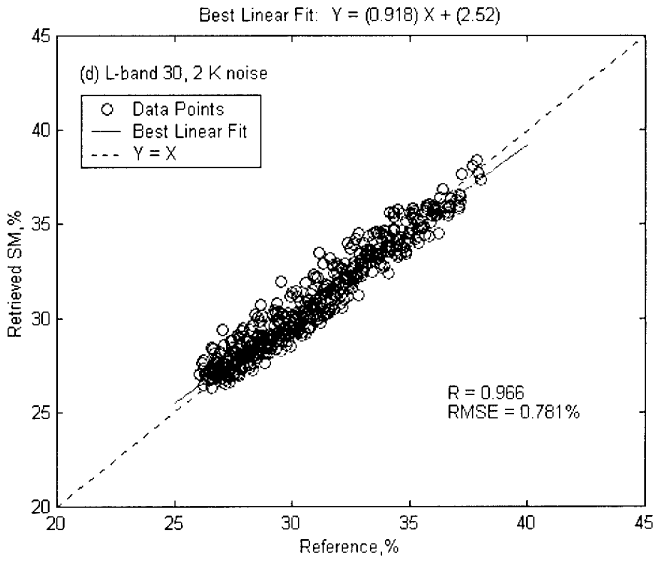


Fig. 2 Retrieved SM for the 1D L-band mode at 30 degree versus the reference.

Figure 4 compares the retrieved SM from the combined 6.9 GHz observation and 1D L-band observation at 30 degree with the corresponding reference. The retrieved SM is improved upon either the 1D L-band observation mode or the integrated 2 AMSR frequency observation mode by different degrees although its quality is slightly worse than the 2D L-band mode. The performance of the combined 10.7 GHz and 1D L-band observation mode is similar to the

combined 6.9 GHz and 1D L-band observation mode. We notice that there is almost no difference in the correlation or RMSE between the two cases. That is, 6.9 and 10.7 GHz observations add approximately equal values onto the SMOS (1D L-band) observations for sensing SM. This statement remains effective when we combine either 6.9 or 10.7 GHz observation with 2D L-band observations with angular differences of 10 degrees. For simplicity, the results from the other cases of combined AMSR and SMOS multiple dimensional observations are not presented.

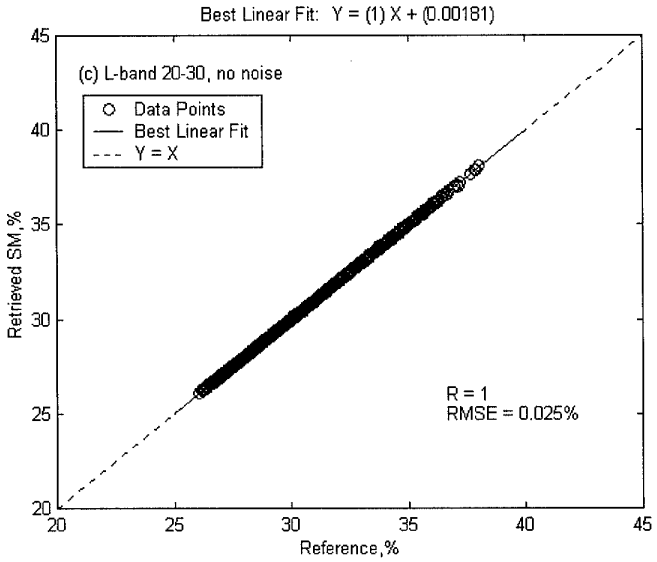


Fig. 3 Retrieved SM for the 2D L-band mode at 20-30 degree versus the reference.

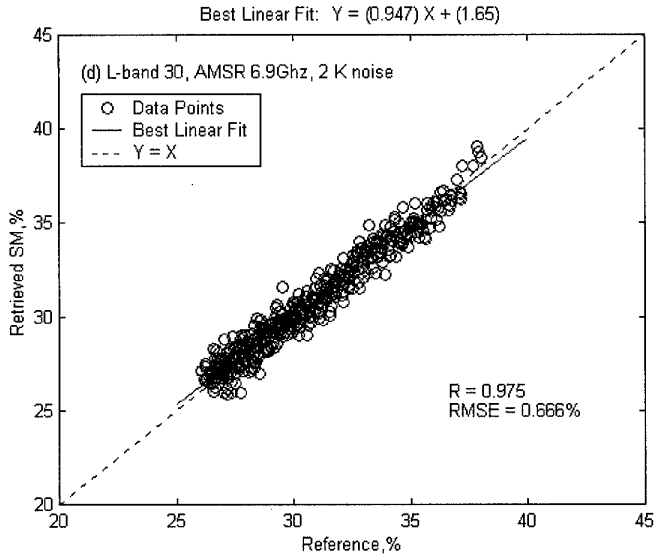


Fig. 4 Retrieved SM from the combined 6.9 GHz and 1D L-band (at 30 degree) mode versus the reference.

V. Conclusions

The capability of the SMOS or the AMSR, and of their integration to measure SM from the space have been studied in this study by incorporating the LSP/R model into the newly

developed EPLBP algorithm. For realization of the concerned problem, the input nodes of the algorithm are added by Gaussian distributed noises with 2 K standard deviations. We have shown that the EPLBP algorithm can manage the nonlinear mapping from microwave brightness temperatures to SM very well. In addition, it has been demonstrated that the EPLBP algorithm is robust since the quality of the retrieved SM remains high even when the Gaussian distributed noise with 2 K standard deviation is imposed upon the input nodes of the retrieval algorithm.

Acknowledgments We appreciate much the National Science Council grant NSC 89-2111-M-008-025-AP3.

Reference :

[1] Chen, K.-S., Y.-C. Tzeng, and P.-C. Chen (1999) Retrieval of ocean winds from satellite scatterometer by a neural network. *IEEE Trans. Geosci. Remote Sens.*, **37(1)**, 247-256.

[2] Kerr, Y. *et al.* (1998), SMOS: Soil Moisture and Ocean Salinity, Full proposal, Answer to the Call for Earth Explorer Opportunity Missions, ESA.

[3] Liou, Y.-A., and England, A. W. (1996) Annual temperature and radiobrightness signatures for bare soils. *IEEE Trans. Geosci. Remote Sensing.* **34**, 981-990.

[4] Liou, Y.-A., and England, A. W. (1998a) A land surface process/radiobrightness model with coupled heat and moisture transport in soil. *IEEE Trans. Geosci. Remote Sensing.* **36**, 273-286.

[5] Liou, Y.-A., and England, A. W. (1998b) A land surface process/radiobrightness model with coupled heat and moisture transport for freezing soils. *IEEE Trans. Geosci. Remote Sensing.* **38**, 669-677.

[6] Liou, Y.-A., E. J. Kim, and A. W. England (1998) Radiobrightness of prairie soil and grassland during dry-down simulations. *Radio Sci.*, **33**, 259-265.

[7] Liou, Y.-A., Galantowicz, J., and England, A. W. (1999a) A land surface process/radiobrightness with coupled heat and moisture transport for prairie grassland. *IEEE Trans. Geosci. Remote Sensing*, **37 (4)**, 1 848-1 859.

[8] Liou, Y.-A., Tzeng, Y. C., and Chen, K. S. (1999b) The use of neural networks in radiometric studies of land surface parameters. *Proc. NSC Part A: Physical Science and Engineering*, **23**, 511-518.

[9] Liou, Y.-A., Tzeng, Y. C., and Chen, K. S. (1999c) A neural network approach to radiometric sensing of land surface parameters. *IEEE Trans. Geosci. Remote Sensing*, **37 (6)**, 2 718-2 724.

[10] Liou, Y.-A., S.-F. Liu, and W.-J. Wang (2001) Retrieving soil moisture from simulated SMOS and AMSR brightness temperatures by a neural network. *IEEE Trans. Geosci. Remote Sensing.* (submitted)

[11] Liu, S.-F., W.-J. Wang, and Y.-A. Liou (2001) An Error Propagation Learning Back Propagation (EPLBP) neural network. *IEEE Trans. Neural Network.* (submitted)

[12] Njoku, E. G., and L. Li (1999) Retrieval of land surface parameters using passive microwave measurements at 6-18 GHz. *IEEE Trans. Geosci. Remote Sensing*, **37(1)**, 79-93.

[13] Rumelhart, D. E., G. E. Hinton, and R. J. Williams (1986) Learning internal representations by error propagation. In D. E. Rumelhart and J. L. McClelland, *Parallel distributed processing: explorations in the microstructures of cognition. I.*, 318-362, Cambridge, MA: MIT Press.

IDENTIFYING OPTIMUM SITES FOR LOCATING RESERVOIRS EMPLOYING REMOTELY SENSED DATA AND GEOGRAPHICAL INFORMATION SYSTEMS.

K. Wan Yusof [1] **and** **Serwan M. J. Baban** [2]

[1] e-mail: apx158@coventry.ac.uk
GRRU Group, Geography,
School of Natural and Environmental Sciences,
Coventry University, Coventry,
Priory Street, CV1 5FB. U.K.
Tel. no: 44 024 76 838444
Fax. no: 44 024 76 838409

[2] e-mail:sbaban2001@yahoo.com
Department of Surveying & Land Information,
The University of the West Indies, St. Augustine,
Trinidad, West Indies
Tel: 001 868 662 2002 ext. 2108
Fax: 001 868 6624414

ABSTRACT

Langkawi Island in Malaysia, faces the possibility of having water shortages in the future, building reservoirs have been promoted as a possible solution to meet future demands for water supply. In this study, a criteria was developed to locate reservoirs taking into consideration all relevant factors including; topography, geology, hydrology, location in relation to both abstraction and supply points, land use/cover types and settlements.

A satellite imagery and digitised geological and elevation maps were analysed and used to generate the necessary data layers to satisfy various conditions within the established criteria. Then, IDRISI, a raster based GIS was employed to implement the criteria using two different methods to combine the information layers. First, the Boolean method which considered all the layers as being equally important to the process and gave them an equal weight. Second, theWeighted Linear Combination (WLC) method which grouped the layers and graded them according to their perceive importance. The Boolean method produced five reservoir sites located at the northern, southern and eastern of the Island. Whilst, the WLC method produced five sites located mainly towards the central area of the Island.

Comparing these outcomes with a field based study with a similar objective on the Island, which identified six suitable reservoir sites, showed that two of the sites located using the Boolean method and four of the sites identified using the WLC method have corresponded well with the field-based study sites.

This study indicates that the developed criteria for locating reservoirs are sensitive to the physical, environmental and economical settings on the Langkawi Island. Furthermore, GIS and remote sensing can be useful tools for generating, manipulating and handling relevant data layers, leading eventually to identifying a number of optimum sites for locating reservoirs and ultimately providing options and, assisting with the planning process.

1. Introduction

A study was conducted in Langkawi Island which faces the possibility of having water shortages in the future as a result of rapid development. The study concluded that the total water demand may increase three times greater in 2010 compared to 1993 (Syed, 1992). Building reservoirs has been promoted as a possible solution to meet the future demand of water supply (Baban and Wan Yusof, 2000). This paper aims to develop and implement a set of criteria to locate reservoir sites on the Langkawi Island using remotely sensed data and GIS.

2. The study area

Langkawi Island lies off the northwest coast of Peninsular Malaysia and located approximately at latitude 6°20'N and longitude 99°40'E (Fig.1). Its annual average rainfall is 2430mm (Shaaban and Sahat, 1995; Wan Yusof and Baban, 1999). Most streams have small catchment areas and they tend to flow downstream rapidly from the mountain to sea. As such their flow tend to cease during periods of dry weather (Syed, 1992).

3. Methodology

Factors influencing reservoir site selection includes topography, hydrology, geology, soil, land use/land cover, road network as well as socio-economic and environmental factors (Gismala *et.al.*, 1996; Murphy, 1977). Based on these factors and the development guidelines by Langkawi District Council (1992), criteria for locating reservoir in the Island was developed (Table 1). The reservoir sites should not be in the vicinity of densely populated areas, must be located on land providing a strong foundation and there should not be any development in the forest reserve areas, hence constraint criteria 1, 2 and 3. Constraint criteria include numbers 4, 5 and 6 will ensure the necessary degree of suitability within the classified areas such as avoiding high grade agricultural land, having the pre-requisite altitude and slope. Constraint 7 was included to account for the projected demand for water supply in the Island. Total water demand was projected to be 70 megalitre/day (Mld) in 2010 (Syed, 1992). As a general guideline, a common dam height is between 15 and 30 m (Morris and Fan, 1997).

Table 1. Reservoir location constraints criteria

Criteria	**Consideration**
The dam and reservoir site must:	
(1) not be located in or within settlement areas	Safety
(2) be on granite and/or metamorphic rock	Safety
(3) avoid forest reserved areas	Resources/Environment
(4) avoid high grade agricultural land value areas	Resources/Economic
(5) be at an altitute of between 25-90 m	Hydraulic/ Economic
(6) be on a gentle slope of 0°-11°	Environmental/Safety
(7) have a sufficient surface area to provide the necessary volume	Consumption/Economic

If two reservoirs were developed, the water demand would each reduce to 35 Mld in 2010. This would require a water storage capacity of 16,425 x 10^3 m^3 yr^{-1} with a maximum surface area of 85.2 ha for dam height of 15 m and a minimum surface area of 25.5 ha for dam heights 50 m.

4. Use of remote sensing and GIS in the site selection process

A land use/cover map of the Langkawi Island was produced from satellite data of 1995 and field data using a Maximum Likelihood Supervised classification (Baban and Wan Yusof, 2000). The land use/cover map was used to extract information and construct layers of information for constraints 1, 4 and 5, i.e. to identify urban areas, to protect agricultural and forest areas respectively. IDRISI, a raster based, GIS was employed to create information layers corresponding to each constraint. In implementing the criteria, these relevant information layers were combined using two different methods. First, the Boolean method which considered all the layers as being equally important and gave them an equal weight. Second, the Weighted Linear Combination (WLC) method which grouped the layers and graded them according to their perceive importance.

In the Boolean method, all the criteria are reduced to constraint Boolean images of areas which are suitable and not suitable. The constraint layers were subsequently overlayed consecutively, by using the OVERLAY multiply function to produce a single suitability Boolean image. Subsequently, the suitable areas in the last Boolean image were regrouped to determine the surface area. The output image was achieved by using the GROUP and AREA functions of IDRISI. The GROUP function was used to assign identifiers to unite groups of pixels and the AREA function was used to calculate the surface area for each group. Finally, the RECLASS function was used to select only those areas (groups) that can comply with the specified surface areas (Table 1) (Fig.2).

In the WLC technique, the criteria are standardised to a continuous scale of suitability from the least to the most suitable, thus giving a flexibility in the site selection (Eastman, 1997). The procedure in the WLC required that the principal eigenvector of the pairwise comparison matrix be computed to produce the best-fit set of weights. Subsequently, the acceptable best fit of the respective weights were used in the Multi Criteria Evaluation function (MCE) to calculate the weighted linear combination (WLC) using the factors (slope, height, land value, and erosion) and constraints (forest reserve, settlement zone, and geological foundation) images. Then using the GROUP, AREA and RECLASS functions again, potential sites with the highest suitability were produced (Fig.3).

5. Results and discussions

A field study to locate reservoir sites on the Langkawi Island based on topography, catchment areas, hydrology, land use/cover, accessibility and socio-economic factors has identified six possible reservoir sites (Fig.4) (Syed, 1992). These areas are the Limbong, Ulu Melaka, Upper Ayer Tawar, Lower Ayer Tawar, Batu Asah and Langkanah. This information has been used to evaluate the outcomes from the two methods employed in this study.

In the Boolean approach, the selected areas were absolute i.e. there were no trade-offs with other constraints criteria. Consequently, suitability in one criterion cannot compensate for a lack of suitability in any other image (Eastman, 1997). In terms of risk, this approach is very conservative. The final outcome of potential sites produced satisfied all the criteria: the reservoir sites selected were within the surface area required, were outside the settlement zone, located at an altitude between 25-90m, were on a gentle slope of 0 to 11°, have a strong foundation on either granite or metamorphic rock, and were not within the forest reserve areas. In Fig.2, two of the potential reservoir sites were located in the northern, one in the western, one in the

southwest and one in the south of the Island. Two of the potential reservoir sites (Kg. Nyior Cabang and Bukit Tekoh) using the Boolean method corresponded well with the field-based study areas (Fig.2, Fig.4).

Using the WLC method, factors assigned to each criterion had been more flexible. This allowed the factors to compensate for each other while maintaining all of the variability in the continuous suitability data (Eastman, 1997). There were five potential reservoir sites produced by this method, these were located around the central region of the Island (Fig.3). These potential sites are more practical due to their central locations, as this will reduce costs in pipeline distribution throughout the Island. Four of the sites (Limbong, Ulu Melaka, Lower Ayer Tawar and Upper Ayer Tawar) identified using the WLC method matched with the field-based study areas (Fig.3, Fig.4).

6. Conclusion

A set of criteria was developed to locate suitable reservoir sites in Langkawi Island. The criteria chosen are comprehensive, taking into consideration all relevant constraints based on hydrology and hydraulics, topography, geology, economy, site location in relation to the points of abstraction and supply and environmental implications. The main considerations being safety, economy and the environment. The inclusion of environmental and social considerations for locating reservoir sites has made the decision-making process more complicated by adding extra information layers. However, the advent of GIS has helped to overcome these multi-criteria considerations in the decision-making process.

Two approaches were considered for reservoir site selection: Boolean and Weighted Linear Combination. The Boolean technique is more direct in its approach to decision making and is very conservative in taking risk. Reservoir sites located by using the Boolean approach were scattered over the Island and two of them corresponded well with the field-based study areas. In the Weighted Linear Combination technique, its flexibility in assigning factors allowing them to compensate for each other thus gave more allowance and effectiveness in the suitability analysis of reservoir site selection. Four potential sites matched those of the field-based study areas water requirement in 2010. The sites were located at Limbong, Ulu Melaka, Lower Ayer Tawar and Upper Ayer Tawar.

Overall, this study has shown that the criteria chosen were sensitive and comprehensive. Furthermore, it has demonstrated the effectiveness of using remotely sensed data in providing the necessary spectral and spatial information for generating information layers for reservoir sites selection criteria. The GIS as a decision-making tool, has facilitated combining various information layers as well as implementing the necessary analysis on the data.

References

Baban S. M. J., and Wan Yusof, K. (2000). Mapping land use/cover distribution in a mountainous tropical island using remote sensing and GIS. *International Journal of Remote Sensing*, (in press).
Eastman, J. R. (1997). Multi-Criteria Evaluation - Boolean and Weighted Linear Combination. In *Tutorial Exercises: Idrisi for Windows Version 2.0*. Clark Labs for Cartographic Technology and Geographic Analysis. Idrisi Production, Clark University, pp. Adv-24 to Adv-34.

Gismalla Y. A and Bruen M. (1996). Use of GIS in reconnaissance studies for small-scale hydropower development in a developing country: A case study from Tanzania. In K. Kovar and H. P. Nachtnebel

(Eds.), *HydroGIS 96: Application of Geographic Information Systems in Hydrology and Water Resources Management, Proceedings of the Vienna Conference. IAHS Publ.* no **235**, 307-312.

Langkawi District Council. (1992). Langkawi Structure Plan 1990 - 2005. Prepared by Langkawi District Council, Section 5, 1-22.

Murphy, M. (1997). Planning and environmental studies. In A. R. Golze (Ed.), *Handbook of Dam Engineering.* Van Nostrand Reinhold Co., London, 1-96

Shaaban, A. J., and Sahat, R. (1996). Hydrological charcteristics and surface water availability of Pulau Langkawi. In *Seminar on Hydrology on Small Islands, Langkawi, Kedah, Malaysia, 29 December, 1996.* Published by the Department of Irrigation and Drainage, Malaysia, Kuala Lumpur, Malaysia, Section 1, paper 1.

Syed, M. (1992). Review of surface water resources and water supply system, detailed design and construction supervision of immediate works in Pulau Langkawi. Water Resources Study- A Final Report, Syed Muhammad, Hooi and Binnie Limited Company, Kuala Lumpur, pp 76.

Wan Yusof, K., and Baban S. M. J. (1999). A preliminary attempt to develop an erosion risk map for Langkawi Island, Malaysia using the USLE, remote sensing and GIS. *Proceedings of the 20th Asian Conference on Remote Sensing, Hong Kong,* Vol.1, 85-90.

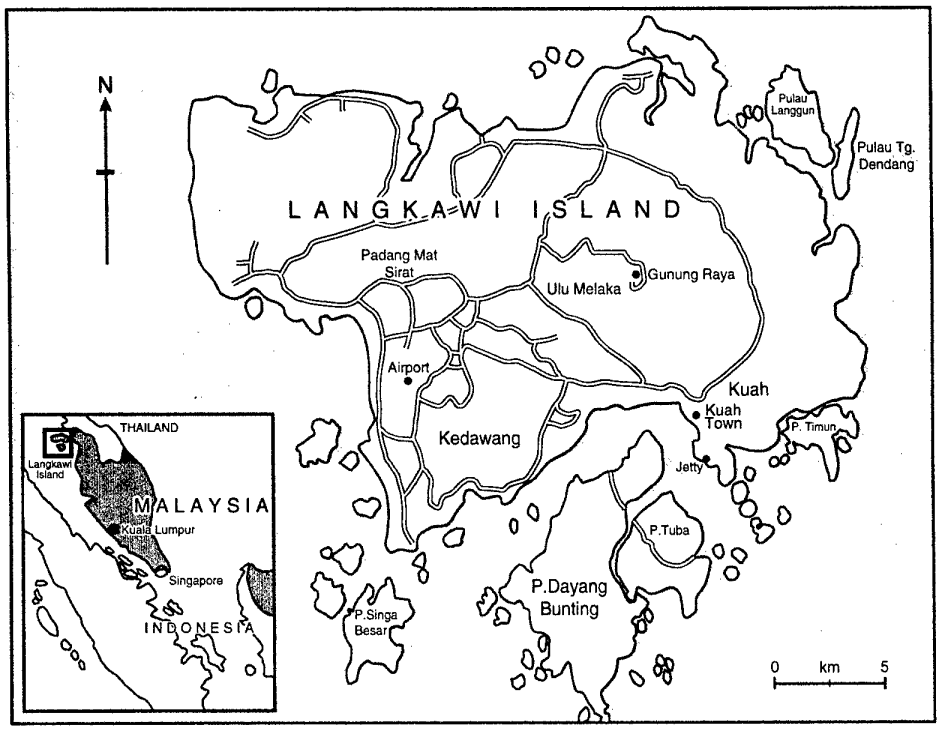


Fig.1 The study area (after Baban and Wan Yusof, 2000)

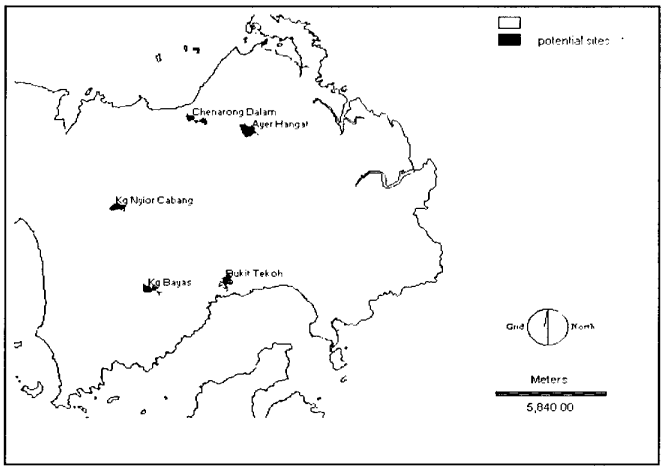


Fig.2 Potential reservoir sites using Boolean method

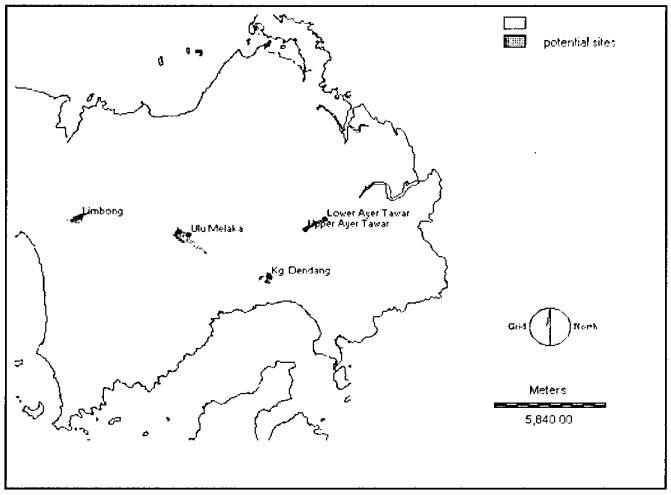


Fig.3 Potential reservoir sites using Weighted Linear Combination (WLC) method

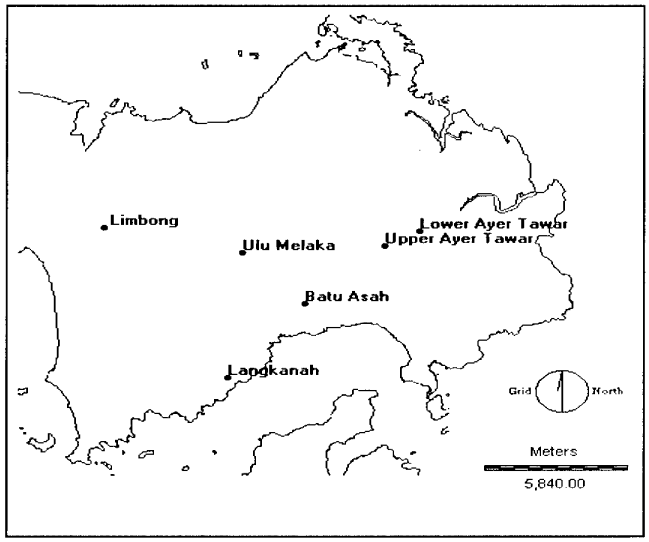


Fig.4 Field-based potential reservoir sites for the Langkawi Island
(Source: Syed, 1992)

INTEGRATED GROUND WATER RESOURCES MAPPING IN GURGAON DISTRICT, (HARYANA) INDIA USING REMOTE SENSING AND GIS TECHNIQUES

B. V. M. Rao TOLETI, B. S. CHAUDHARY, K. E. Mothi KUMAR, G. P. SAROHA, Manoj YADAV, Ajeet SINGH, M. P. SHARMA, A. C. PANDEY and P. K. SINGH
Scientists, Haryana State Remote Sensing Application Centre
(Deptt. of Sci. & Tech., Govt. of Haryana)
CCS HAU Campus, Hisar 125 004, Haryana,
Phone (01662) 31045-47, 32632; FAX 25958
Email: harsac@vsnl.net.in
INDIA

KEY WORDS: Hydrogeomorphology, Ground Water Resources, Integration, Remote Sensing, Geographical Information Systems (GIS)

ABSTRACT: This paper mainly deals with the preparation of Integrated Ground Water Resource (IGWR) map indicating ground water prospects, quality and depth. Indian Remote Sensing Satellite (IRS-1C) geocoded false colour composites of Gurgaon district have been used for preparation of hydrogeomorphological map. The northern part of the district is occupied with quaternary alluvium and southern and south eastern part is occupied by precambrian metasediments of Delhi systems. The land form of this district is formed by fluvial, structural and denudational origins. The main hydrogeomorphic units mapped are alluvial plain, alluvial plain with sand cover, valley fills, interrmontane valley/basin, structural hills, residual hills, buried pediments, linear ridges along with lineaments. Each geomorphic unit is assessed for probable ground water potentiality. Depth to water table and well location data has been collected form Ground Water Cell, Department of Agriculture, Haryana. The prepared hydrogeomorphology, ground water quality and depth maps have been digitized in Arc/Info GIS environment. In order to provide more useful information on ground water resources, the authors have developed a methodology on integrated ground water resource map on 1:50,000 scale using remote sensing and conventional data in GIS environment. The IGWR map thus prepared gives information on ground water potential, quality and depth to water level at any given location. This information is very useful in narrowing down the target areas for siting bore wells. This will result in significant saving of time and cost.

1. INTRODUCTION

Water is the most vital requirement for mankind. Ground water constitutes a major portion of the earths water circulatory system known as hydrologic cycle. Ground water occurs in permeable geologic formation known as aquifer, i.e. formation having structure that can store and transmit water at rates fast enough to supply reasonable amounts to wells. In recent years much progress has been made in the application of remote sensing techniques to ground water. Exploration procedures can ideally adopt remote sensing as the first step to be followed by field geological studies, geophysical prospecting and test drilling. This helps in concentrating the field efforts in areas where greater potential exists and eliminating other zones, thus reducing the cost and time involved in exploration procedures. The advent of Geographical Information Systems (GIS) has added new vistas in the field of ground water resources mapping and management. It helps in the integrating remotely sensed derived data with ancillary data to have more precise and correct information about various factors involved in the ground water resources management. Studies are being targeted in this direction by many authors (Prakash

1993, Roy & Ray 1993, Chaudhary et al 1996 and Ravindran & Jeyram 1997). Present study emphasize on getting the information on ground water prospects, depth and quality from the prepared IGWR map.

2. OBJECTIVES

- To prepare hydrogeomorphological maps on 1:50,0000 scale using satellite data.
- To delineate ground water potential zones by assessing the hydrogeomorphic units on 1:50,000 scale.
- Preparation of integrated ground water resources map derived from hydrogeomorphology, ground water quality and depth to water level maps.

3. STUDY AREA

3.1 Location and Extent

The Gurgaon district is one of the southern districts of Haryana. The district lies between 27^0 39' to 28^0 32' North latitude and 76^0 39' to 77^0 20' East longitude. On its north are the district of Rohtak and the Union territory of Delhi, on its east Faridabad district. Its south the district shares boundary with the state of UP and Rajasthan. On its west lies the district of Rewari and the state of Rajasthan. The total area of the district is 2716 sq. kms. Gurgaon town is situated only 32 kms south west of New Delhi, the capital city of India. The district has sub-tropical, continental monsoon climate. The normal annual rain fall in the district is 553 mm. Temperature starts rising in March. The mean daily maximum temperature is about 41° C in the months of May and June.

3.2 Physiography and Drainage

The district comprises of hills on the one hand and depressions on the other, forming irregular and diverse nature of topography. Two ridges: Firojpur Jhirka - Delhi ridge forms the western boundary and Delhi ridge forms the eastern boundary of the district. These hills are northern continuation of Aravalli hills. The northwestern part of the district is covered with sand dunes lying in the westerly direction due to south western winds. The extension of the Aravalli hills and the presence of sand dunes collectively form the diverse physiography of the district. The drainage of the district are typical of arid and semiarid areas. It comprises of large depressions and seasonal streams. Important depressions of the district are Khalilpur lake, Chandani lake, Sangel - Ujhina lake, Kotla dhar lake and Najafgarh lake. Sahibi and Indrani are two important seasonal streams of the district.

3.3 Geology and Soils

Gurgaon district is occupied by quaternary alluvium and precambrian meta-sediments of Delhi System. The geological formations of Gurgaon district have been extensively studied by R. Chakrapani (1981). Delhi super group is represented by Alwar quartizites, mica schists and pegmatite intrusives of the Alwar series and slates of phyllites and quartzites of the subrecent alluvium and sand dunes. Stratigraphic succession of the area is given in table 1. The soils are sand to loamy sand in sandy plain areas. Sandy loam to clay loam/silty clay loam in alluvial plains, loam sand to loam, calcareous in salt affected plains; silty loam to loam in low lands and loamy sand to loam, calcareous in hills. Taxonomically these soils may be classified as Typic Ustipsamments, Typic Ustorthents, Typic/Udic/Aquic Ustochrepts, Typic Haplaquepts and skeletal/Lithic Ustorthents

4. DATABASE

4.1 Remote Sensing Data:

IRS-1C geocoded standard False Color Composite (FCC), a combination of three spectral bands 2,3 and 4 on 1:50,000 scale have been used in the above study. IRS 1C path row 95/51, 96/50 and 96/51 covers the study area. March/ October 1996 data have been used in the above study.

4.2 Survey of India (SOI) toposheets

The following toposheets on 1:50,000 scale are used in the preparation of base maps onto which the interpretation details are transferred. The district is covered by 12 toposheets numbered- 53D/11, 14, 15, 16; 53H/2, 3, 5; 54A/13, 14 and 54E/1, 2, 5.

4.3 Ancillary Data

The meteorological data, Statistical abstracts, Census handbook, available ground water literature etc. Ground water depth and quality data have been collected from Ground Water Cell, Agriculture Department, Govt. of Haryana.

5. METHODOLOGY

The water on the surface which has a bearing on ground water circulation under ground can be distinguished in the near infrared region owing to low reflection of water. Synoptic view, repetitive coverage and capability to view the scene in several spectral bands, some lying beyond the visible part of the electromagnetic spectrum, are some of the special characteristics that have made remote sensing an effective tool in ground water search. The clue to ground water search is the basis that subsurface geologic elements forming aquifers have almost invariably surface expressions which can be discerned by remote sensing techniques.

Visual interpretation of IRS 1C LISS-III FCC has been carried out by taking in to consideration various image and terrain elements by using a light table. Significant hydrogeomorphic units have been demarcated based on tone, texture, shape, size, pattern, association, etc. Delineation of all linear features have been carried out and with available information, classification of these linear features in to fractures, faults, shear zones, straight lithocontacts has been attempted. Delineation of hydrogeomorphologically significant land forms like valley fills, alluvial fans, piedmont zones, alluvial plains, braided channels, abandoned channels, palaeochannels, flood plain etc. has been carried out in the area covered by unconsolidated sediments. All the delineated hydrogeomorphic landforms are suffixed with lithology type i.e. RD(q) Residual hills quartzitic.

Interpreted maps have been modified by taking into consideration the ground observations. Hydrogeomorphological maps thus prepared has been digitized in Arc/ Info GIS Version 7.1. Ground water depth and quality data have also been digitized . After digitisation, error removal and attributation, groundwater prospects and quality maps have been integrated to prepare ground water prospective zones map. The digitized ground water depth map has been draped on this integrated map thus resulting in to IGWR Map.

6. RESULTS AND DISCUSSION

The details of various geomorphic units and their ground water bearing prospects are given in Table 1.

Table 1 Ground water prospects of various geomorphic units

Geomorphic Units	Description	Ground Water Prospects
Fluvial origin Alluvial Plain	Gently undulating plains consisting of clay, silt, fine to coarse sand of varying lithology with extensive cultivation.	Excellent
Alluvial Plain with Sand cover	Undulating plains comprising sand, silt and clay. Sand is dominant but stabilized.	Good
Palaeo Channel/ Abonded channel	Channels which are cut off from main course of the river which are buried or abonded. Comprises of fluvial deposits. (sand, silt and clay particles)	Very Good
Denudational origin Pediment	Occurring near to structural hills gently slopping area comprising colluvial material and medium to fine grained sand and silt This unit has higher thickness near ridges and laterally merge with alluvial plain.	Moderate to good
Intermontane Valley/Basin	Depression between mountains, formed as broad basin consisting of colluvial deposits covered with alluvium.	Excellent
Valley Fill	Unconsolidated material coarse to fine sand, silt and clay.	Good
Residual hills	Isolated low relief hill formed due to differential weathering consisting of metasediments.	Poor
Structural origin Structural Hills	Structurally controlled steep sides hills associated with folds, faults, fractures and joints these are meta sediments of Delhi super group	Poor to Moderate (moderate along fault planes)
Linear Ridges	Long narrow low lying linear to arcuate hills rising from alluvial plains acting as barriers of ground water flow.	Poor

Ground water quality map has three categories i.e. good (EC varies from 0-2000 micro Mhos); moderate (EC varies from 2000 - 4000 micro Mhos) and poor (EC > 4000 micro Mhos). The digitized Quality map has been integrated with ground water prospects map and an integrated map has been prepared. The integrated map has eight categories. Table 2 (on next page) shows different categories and the area covered by these units.

The IGWR map prepared after the integration of this map with the ground water quality map and draping of depth to water level information various zones have been identified which are shown in Figure 1.

Table 2 Area under various units

Sr. no.	Units	Area	% of the total area
	Prospects (Quality)	(sq. kms.)	
1	Excellent (Good quality)	965.77	35.56
2	Good (Good quality)	190.18	7
3	Moderate (Good quality)	104.77	3.89
4	Poor (Good quality)	44.88	1.65
5	Excellent (Moderate quality)	217.3	8
6	Good (Moderate quality)	78.1	2.92
7	Moderate (Moderate quality)	9.64	0.35
8	Excellent /Good/Moderate/ Poor (Poor quality)	1,105.36	40.63
	Total	**2,716**	**100**

7. ADVANTAGES

The main advantages in using remote sensing and GIS techniques for ground water exploration are : Quick and inexpensive technique for getting information on the occurrence of ground water, aids to select promising areas for further ground water exploration thus reducing field work and provides information on prospects, depth and quality in one map. This type of information is very helpful in the areas where more emphasis is on ground water for the irrigation and drinking purposes such as southern part of Haryana.

8. CONCLUSION

Use of Remote Sensing and GIS technology is very useful for the preparation of ground water prospective areas mapping & management plan on a scientific basis. The information generated on prospects, quality and depth in a single map will help the planners and decision makers for devising sound and feasible ground water development plans.

9. ACKNOWLEDGEMENTS

Authors are thankful to Dr. S. Mohan Chief Scientist, Haryana State Remote Sensing Application Centre (HARSAC), Hisar for giving ideas and making corrections in the final version of the paper. It has improved a lot due to his constructive criticism and valuable suggestions.

10. SELECTED BIBLIOGRAPHY

Chakrapany, R.A.1981. Hydrogeology of Gurgaon District, Haryana, Central Ground Water Board, Ministry of Irrigation, Govt. of India, pp. 43 - 51.

Chaudhary, B. S.; Kumar, M.; Roy, A.K. and Ruhal D.S. 1996. Application of Remote sensing and Geographic Information Systems in Ground water Investigations in Sohna block, Gurgaon District, Haryana (India). In: International Archives of Photogrammetry and Remote Sensing Vienna, Vol. XXXI, Part B6, pp.18-23.

Prakash, S.R. 1993. Identification of ground water prospective zones by using remote sensing and geo-electrical methods in and around Saidnagar area, Dakar Block, Jalaun district, U.P., Indian Society of Remote Sensing 21(4): 217-227.

Ravindran, K.V. and Jeyram A.,1997. Ground water prospects of Shahbad tehsil, Baran district and Eastern Rajasthan: A remote sensing approach. Indian Society of Remote Sensing 25(4): 239-246.

Roy, A.K.; and Ray P.K.C., 1993. Ground water investigation using remote sensing and GIS techniques- A case study in Manabazar-II, Purulia (W.B.). Proceedings National Symposium of North-Eastern region, Guwahati, India pp. 180-184.

District Gazetteer, 1991, District Gurgaon, Haryana.

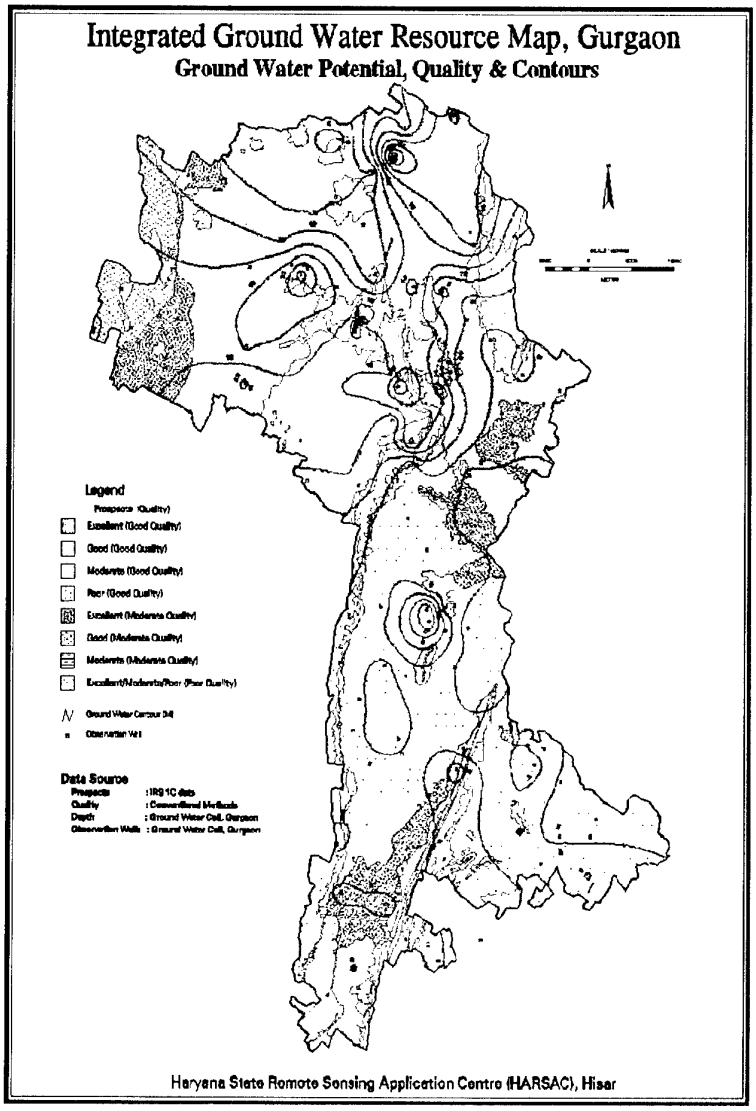


Figure 1. Integrated Ground Water Resources Map

IDENTIFICATION AND MAPPING OF NEW MARUGANGA CHANNEL IN NORTHWEST INDIA OF INDIAN SUB-CONTINENT

Dr. Narpat Singh Rathore
Department of Geography, M.L. Sukhadia University,
Udaipur - 313 001 (Raj.) INDIA
Fax: +91 294 415200, E-mail: kksud@yahoo.com

ABSTRACT

In this study the main focus is upon harnessing the water resource potential of perennial river originating from the Himalayas in order to irrigate the arid and semi-arid part of north-west India. The remote sensing technique offers great scope in providing identification and mapping of link channel for two different rivers which flow in two different directions. The present study is an attempt to use remote sensing technique for preparing the development plan for Indian desert and semi-desert regions through diverting the flood waters of the Himachal Himalayas and Uttrakhand without lifting towards Western Rajasthan and Northern Gujarat Plains. The study revealed that after the implementation of the proposed plan, north-west India will be largest food grain producing and irrigated area of the world. The significance of the plan could be compared to the status of the Kaveri River in South India and Nile River in Egypt.

Study Area : The present study area lies between 21°45' north to 33°00' north latitudes and 70°00' east to 78°00' east longitudes. Geographically this region is the part of desert and semi desert of north-west India in the Indian Sub-continent **(Fig. 1)**. The new Maru-Ganga channel will flow from Punjab, Haryana, Rajasthan and Gujarat states of India. Climatically this region falls in the arid and semi-arid part of north and west India. The characteristic features of the climate of the areas is its dryness, extremes of temperature, erratic nature of the rainfall, high evaporation and wind velocity. The average annual rainfall is only 370 mm. The minimum temperature often falls below freezing point in January and maximum temperature recorded during the month of May and June is 40° to 45° centigrade. The region is swept by dust storms and thunder storms during summer and pre monsoon months. More than ninety per cent of rainfall occurs in the months of July to September every year. Only some amount of rainfall is received by western disturbance in winter season.

Material and Methods: The study area is covered in 15 satellite imagery i.e. different dates in black and white and colour composites transparency and paper prints for visual interpretation. The false colour transparency of million scale was brought on 1:2,50,000 scale to make the study comprehensive. Indian topographical sheets and maps were also used for study purpose. The details of satellite imagery and topographical maps are given in **Table-1**. For the visual interpretation of the remotely sensed data, ground truth collection and field verification are essential to eliminate the doubts and hence, ground truth data have been collected from the field. Apart from the data inferred from the satellite imagery, topographical maps and field survey, the relevant data were also collected from secondary sources

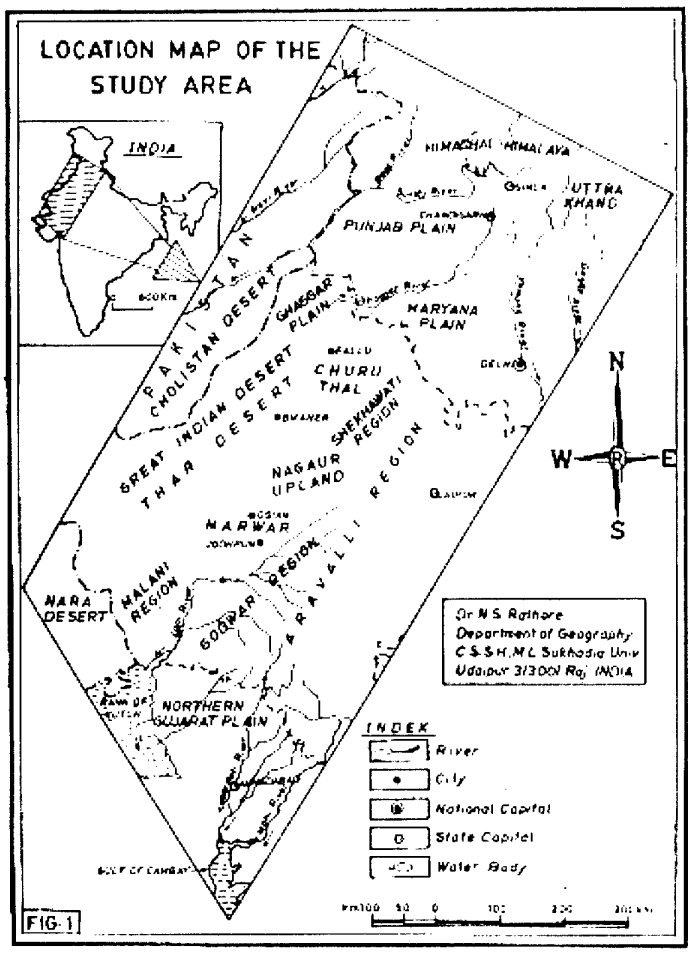


TABLE - 1

Satellite Type	Satellite Imageries		Topographical Sheet No (Survey of India)
	Row No.	Path No.	
IRS-IC WiFS IMAGE (NRSA)	47	30	40 - O and P
	47	31	41 - M and N
	47	32	44 - K,L,N,O, and P
	48	30	45 - A,B,C,D,E,F,G,H,I,J,K and L
	48	31	46 - ABCE and F
	49	31	53 - ABCD
	49	32	National Atlas of India, Plate No.
	49	33	1,3,25,27,28 and 31
	50	33	
	51	33	
LANDSAT - 4 (NRSA)	149	042	
LANDSAT - 2 (NASA)	160	039	
LANDSAT - 1 (NASA)	189	1136	
	189	1373	
	189	1582	

SIGNIFICANCE OF STUDY: The proposed identified new Maru-Ganga river's Channel length will be near about 15 hundred km right from Himachal Himalayas to Gulf of Cambay of Arbian Sea in Gujarat State. However, after the Brahmaputra, Ganga and Godawari rivers the new Maru-Ganga river will be the 4th Major river of India in length. The proposed Maru-Ganga river will be 16th major river in terms of length in the Asian continent and 30th river in the world. This river will carry water of Himalayas through Indian desert and ultimately merge in the Gulf of Cambay in Gujarat State. After implementation of this plan, the north-west India will get permanent relief from natural calamities like flood, famine and drought. After implementation of the plan cattle migration will stop, saline water will be converted into potable water, and under ground water level will rise, protect the cattle wealth of the region, produce additional foodgrains, green vegetable and fruit. The Bhakra, Gang and Indira Gandhi canal command area will get permanent relief from water logging problem. With this plan Bahawalpur region of Pakistan and Delhi Indian national capital region will get relief from flooding during rainy season of Ghaggar and Yamuna river respectively.

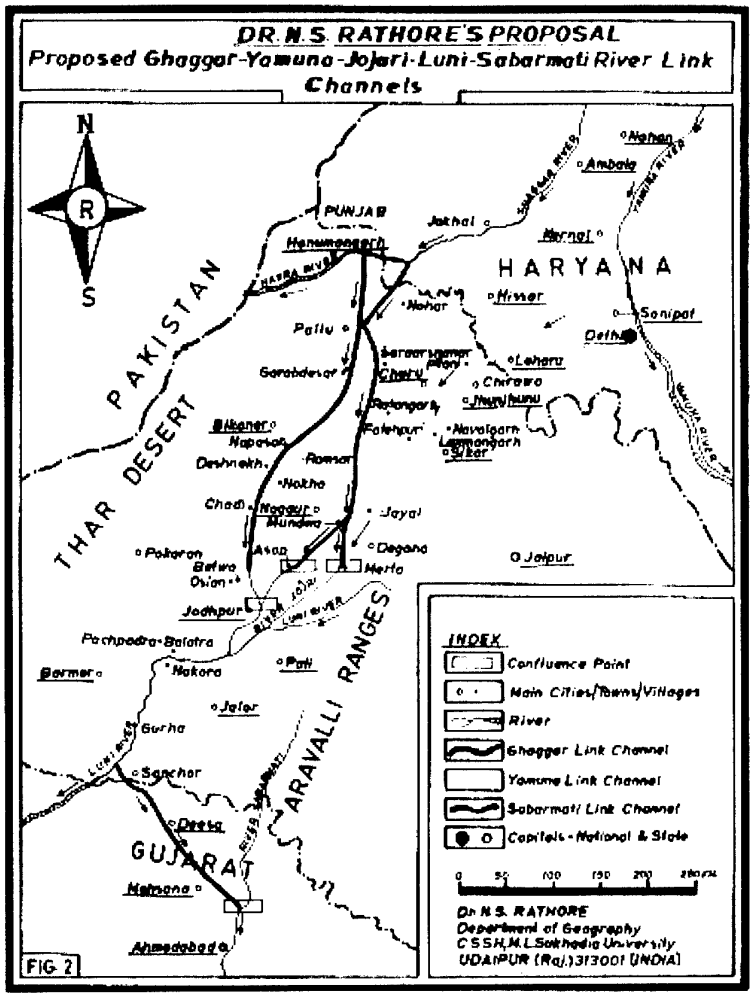
In the Luni-basin and Nothern Gujarat by the implementation of this plan the area will produce large amount of Coconut, Banana, Mango, Date, Green Vegetable, Spices and milk. Due to the availability of solar and wind energy alongwith Himalayan water new Industries can be established in the study area.

ANALYSIS: During the rainy season, large amount of floodwater is available in the Himachal Himalayas and the Uttrakhand region of the Himalayas. This flood water goes waste through the Ghaggar and the Yamuna river respectively into Pakistan and the Bay of Bengal. For the development of the Indian desert and semi desert areas this floodwater can be diverted without lifting towards Rajasthan and the North Gujarat Plain. The floodwater of Punjab rivers and also the Yamuna river can be diverted through three link channels (**Fig. 2**). These link channels are the Ghaggar link channel, the Yamuna link channel and the Sabarmati link channel. Through these channels the Himalayan diverted flood water will reach the Arabian Sea through the Gulf of Cambay. The details of proposed newly identified channels are:

Ghaggar Link Channel: The arid and semi arid regions of Rajasthan and Gujarat state can get many million cubic meters of water through proper management and diversion of Himalayan water. In rainy season large amount of floodwater flows into the Ghaggar river. This flood water can be diverted by the removal of soil from Hanumangarh to Pallu, Napasar, Deshnok, Chadi, Danwara, Jodhpur or Pallu, Sardar Shahar, Tal-Chapper, Nagaur , Asop, Bhopalgarh, Jodhpur or Nagaur to Merta by the removel of soil. By these route the Himalayan water can be dropped into Jojari-Mithari river. Ultimately this diverted water flowing naturally will reach near Salawas or Khejari Khurd and meet with Luni river.

Yamuna Link Channel: In the same rainy season the Uttarakhand region of Himalayas also gets large amount of water due to heavy rain and flood situation occurs in the Yamuna river every year. This flood water of Yamuna river which is released from Tejawala feeder can be diverted from Sonipat by removing the soil of Rohatak, Mahendragarh and Hissar districts of Haryana state and Jhujhunu, Mandawa, Mukundgarh, Sikar, Didwana, Degana and Merta in Nagaur district. The diverted water will reach Merta and join with Mithari-Jojari river. From Merta onwards this Yamuna water which will naturally flow and go towards Ghaggrana; Ghorawat, Pipar and Bisalpur. This Yamuna water will meet with Luni river near Jodhpur at Khejarli-Khurd. However, the Ghaggar and Yamuna diverted flood water will meet near Khejarli Khurd or Luni village with Luni river. This water will reach Samdari, Balotra, Sindari, Dhorimana, Guda and ultimately reach near Sanchore in Jalor district.

Sabarmati Link Channel: However, that proportion of the Himalayan water which is flowing in the Luni river and which goes into Rann of Kachch through delta will remain unharnessed. So by the third channel constructed by the removal of soil from Sanchore to Dissa, Palanpur, Sidhpur, Mesana and Ahmedabad of Gujarat State, the Luni river can be linked with Sabarmati river. By this way, the joining of the Himalayan water with new proposed channel, in the Northwest India of the Indian sub-continent will be called Maru-Ganga.



RESULTS: In the state of Rajasthan the Hanumangarh, Churu, Jhunjhunu, Sikar, Nagaur, Bikaner, Jodhpur, Pali, Barmer and Jalore districts will get additional irrigation of 12 lakhs hectares land, 5 lakhs hectares of grazing land, 50 thousand sq. km underground water will be re-charged and 25 lakhs tons additional foodgrain can be produced every year. In the Gujarat State, Banaskanta, Dissa, Palanpur, Sidhpur and Ahmedabad will also get additional irrigation facilities for 2 lakh hectares, in 10 thousand sq. km underground water level will be re-charged and 5 lakhs tonnes foodgrain will be produced. The proposed river channel will protect wild life and migratory birds of this region and also conserve the environment and eco-system of the surrounding area of the new Maru-Ganga channel. The area which falls between the Thar Desert and Aravalli mountain region like Churuthal, Shekhawati, Shalkh or Nagaur upland, Marwar, Godwar, Malani and northern Gujarat where the agriculture land will be irrigated by the diverted Himalayan water.

CONCLUSION: After implementation of this plan, the rivers of North India will be linked with Southern India rivers through Rajasthan desert with help of newly identified Ghaggar, Yamuna and Sabarmati link Maru-Ganga Channel. Desert soil area linked with fertile black soil region of Southern India through this new plan. To complete the proposed plan it will be possible only with the help of special financial assistance from the Central Government in collaboration with State Government in three stages. In first stage Ghaggar channel, in second stage Yamuna channel and finally the third stage Sabarmati link channel can be made and complete the whole plan. After that the Western India will be largest foodgrain producing and irrigated area of the world. This new river channel will join Himalayas, Desert and sea. In the 21st century the important event will take place if joining of these three major geographical regions of Indian sub-continent by the new identified channel.

ACKNOWLEDGEMENTS: The author is grateful to Dr. J.R. Sharma, Director, Regional Remote Sensing Service Centre, Jodhpur for providing remotely sensed data in the form of Satellite imagery to carry out this work. Author is also thankful to Prof. A.K. Singh, Vice-Chancellor of M.L. Sukhadia University, Udaipur for giving consent and encouragement for research work. I am indebted to Prof. K. K. Sud, Dr. L.S. Rao, Dr. K.N. Joshi for giving valuable comments and suggestions. Thanks are also due to Mr. M.L. Ameta for cartographic work.

REFERENCES

1- OLDHAM, C.F. (1874). Notes on the lost river of the Indian Desert, Calcutta Rev., V.59, pp.1.27.

2- OLDHAM, R.D. (1886). On probable change in the geography of the Punjab and its rivers - a historic-geographical study. Jour. Asiatic Soc. Bengal. V55. pp 322. 343.

3- RAMASAMY, S.M., BAKLIWAL, P.C., and VERMA R.P. (1991). Remote Sensing and River Migration in Western India. Int. Jour. Rem. Sens. V 12,(12), pp.2597-2609.

4- RAO, D.P. (1999). Role of remote sensing in understanding of palaeodrainage evolution, Vedic Sarasvati, Memo. Geol. Soc. India, No.42 pp.237-244.

5- RAO, K.L. (1979). India's Water Wealth, Orient Longman Ltd., New Delhi.

6- RATHORE, N.S. (1989). Rajasthan State, Nehru a Panoramic Profile, M.L. Sukhadia University, Udaipur.

7- RATHORE, N.S. (1992), Natural Resources Base Development. Scientific Publishers, Jodhpur.

8- THUSSU, J.L. and CHOPRA, S. (1994). Channel migration and phenomenon of Terminal Fan Formation in some of the major Streams of the Ghaggar River Basin of Haryama. NW India. Indian Minerals V. 48, No.4, pp.255-272.

USING SPECTRAL MIXTURE MODELING TECHNIQUES TO DERIVE LAND-COVER PARAMETERS FOR DISTRIBUTED SEDIMENT YIELD ESTIMATION

Enrico C PARINGIT[1] and Kazuo NADAOKA[2]
[1]Graduate student, [2] Professor
Department of Civil Engineering
Tokyo Institute of Technology
2-12-1 O-okayama, Meguro-ku, Tokyo 152-8552,
E-mails: ecp@mei.titech.ac.jp, nadaoka@mei.titech.ac.jp
Tel: (81)-3-5734-3486 Fax: (81)-3-5734-2650
JAPAN

KEY WORDS: Sediment yield estimation, spectral unmixing, leaf area index

ABSTRACT: Vegetation and soil properties and their associated changes through time and space affect the various stages of erosional processes. This paper discusses the application of remote sensing techniques in the retrieval of vegetation and soil parameters necessary for the distributed soil loss modeling in small agricultural catchments. To account for the compositional nature of the ground surface as depicted on remotely-sensed data, a linear spectral mixture modeling (LSMM) approach is used to parameterize vegetation and soil optical properties. Results of these parameter estimates were coupled to a DEM-based distributed hydrologic rainfall-runoff model to simulate overland flow and sediment yield for a given rainfall event. Field observations were undertaken to gather spectral and physical measurements of vegetation and to obtain data for soil hydraulic properties. Results of the sediment yield model indicate strong relationship between vegetation abundance and erosion by soil detachment. A general agreement between the simulated and measured sediment discharges is also observed. The method provides a physical basis for incorporating the spatial and temporal variability of various vegetation and soil condition to dynamic processes such as soil erosion and may be applicable to monitor other non-point source pollutants from agricultural watersheds.

1. INTRODUCTION

The risk of soil erosion by water, varies as a function of many factors, but the degree of protection provided by vegetation is one of the most important. Usually erosion rates are computed by means of empirical methods or if treated in terms of physically-based models, are highly idealized, such that effects of vegetation presence become trivialized, mainly due to its high spatial and temporal variation. Leaf area index (LAI) and percentage vegetation cover (PVC), two parameters routinely derived from remote sensing, can provide the necessary details to incorporate vegetation effects to soil losses.

Spectral mixture models are among the popular methods to resolve the optical components of surfaces with diverse land cover types especially useful when the analysis is constrained by the spatial resolution of the available dataset (van Leeuwen et. al, 1997). A desirable feature of mixture models is that they are able to estimate the fractional abundance of vegetation and soils simultaneously, appropriate for purposes which require both information at the same instant such as in the case of erosion analysis. LSMM is most appropriate for crop plants since leaves are relatively dominant, soil reflectance is uniform, topography is minimal and most crowns can

be modeled with simple geometric shapes, the favorable conditions to achieve linear spectral mixing.

This study was conducted to investigate the effect of applying vegetation indexes, particularly LAI and PVC, obtained through spectral mixture analysis of remotely-sensed data, to quantify soil losses, particularly sediment discharge from a predominantly agricultural area during rainfall events with consideration to development stage of vegetation.

2. MATERIALS AND METHODS

2.1 The Study Area

A small catchment test area (11 km^2) was chosen to exemplify the essential points of this research. The study area represents a typical tropical environment prone to high degree of rain-induced erosion. It covers the eastern portion of Ishigaki, an island south of the main Okinawa Island Prefecture in Japan. It is located about 24°23' N latitude, 124°14' E longitude, with topography varying from flat, undulating to hilly terrain currently being subjected to intense agricultural cultivation. Crops consists mainly of tobacco, sugarcane, rice and pineapple. The area is drained through the Todoroki River with outlet to the coastal area, where a special concern is focused on mitigating the effects of sediment discharge on coral reef zones (Dikou and Takeaki, 1999).

2.2 Remote Sensing and Field Observation Data

Field campaigns were conducted on three occasions: early June, early August and early September with various inland data-logging instruments to measure river discharge, turbidity, depth and rainfall in different locations inside the watershed. Spectral signatures for both soil and vegetation were also gathered to parametrize reflectances from 320 to 1080 μm range. Water samples have been previously obtained for turbidity-sediment concentration calibration of the instruments. Soil samples were processed in the laboratory to obtain various hydrologic parameters such as hydraulic conductivity, soil moisture, porosity, grain size and typing. Vegetation structure measures such as plant spacing, layering and leaf dimensions were also recorded.

Due to the absence of remotely-sensed data, both spaceborne and airborne, within the period of field observations, the land cover captured from the aerial photographs taken in 1995 was assumed to be the prevailing land surface condition. The use of an asynchronous data can be justified since the dates of the aerial photography lie within the same season of the year and that no major changes in cropping patterns and infrastructure developments has occurred since.

2.3 Spectral Mixture Modeling of Vegetation and Soil

Spectral unmixing is a deconvolution technique that aims to decompose the mixed reflectance spectrum, $R_i(\lambda)$ of a ground element in an imagery into landcover components based on the LSMM (Settle and Drake, 1993) given by:

$$R_i(\lambda) = \sum_{j=1}^{n} f_j R_f(\lambda)_i + \varepsilon_i \quad \text{and} \quad 0 \le \sum_{j=1}^{n} f_j \le 1 \qquad (1), (2)$$

where $R_f(\lambda)$ is reflectance of end-member spectrum of a homogenous land cover for each band i of n land cover types, and ε_i is the residual noise. The objective is to estimate $\hat{f}_j$, for each land

cover component within a pixel by inversion technique, a typical solution of which is the classical least squares approximation, in matrix notation, $\hat{f}_j = (\mathbf{R}^T\mathbf{R})\mathbf{R}^{-1}\mathbf{R}_f$. However, since there is a constraint to sum up the fractional cover to one by Eq. (2), then a Lagrangian formulation gives the more appropriate solution:

$$\hat{f}_j = \alpha\mathbf{U}\mathbf{j} + (\mathbf{U} - \alpha\mathbf{U}\mathbf{J}\mathbf{U})\mathbf{R}^T\mathbf{R}\mathbf{N}^{-1}\mathbf{R}_f \quad (3)$$

where the $\mathbf{U}=\mathbf{R}^T\mathbf{N}^{-1}\mathbf{R}$, $\alpha = (\mathbf{j}^T\mathbf{U}\mathbf{j})^{-1}$, $\mathbf{J}$ $(=\mathbf{j}\mathbf{j}^T)$ is an n x n identity matrix of n x 1 **j**s with elements =1 consisting of and **N** represents the sensor noise characterized by the variance-covariance matrix. The equivalent f for the soil and vegetation cover are used as the values percentage soil cover (PSC) and PVC respectively. PVC quantifies merely the portion of exposed canopy. In hydrologic modeling as will be shown later, it becomes more important to determine the fractional abundance or sparsity of vegetation, which can be adequately described by LAI. The reflectance model of Gilabert et al. (2000) is modified obtaining:

$$LAI = -ln(PVC)/C \quad (4)$$

C is regarded as a weighing parameter assumed to be invariant with wavelength and assumes complete absorption. Its value rather, varies with angle of light source and plant architecture. An immediate application of LAI is to compute for the interception capacity of a particular canopy for rain expressed as a function of the LAI given by:

$$S_r = S_{r0}LAI / LAI_0 \quad (5), (6)$$

where S_r is the canopy interception capacity (m), S_{r0} and LAI_0 are the maximum canopy interception capacity and leaf area index (m^2 m^{-2}) respectively specific for each vegetation type.

2.4 Runoff Modeling and Sediment Routing

The overland flow runoff routing model utilizes the DEM (digital elevation model)-based diffusion wave equation according to the procedure outlined by Wang and Hjelmfelt (1998) while the sediment yield component is taken from SHESED model of Wicks and Bathhurst (1996). Both models are ideal for small flat watersheds where the main processes affecting sediment yield are soil erosion by raindrop impact and overland flow and sediment transport by overland and bed channel flows. The results of the PVC and PSC computations may be used on the following expression:

$$D_R = k_r F_w (1 - PSC)[(1 - PVC)M_R + M_D] \quad (6)$$

where D_R is the soil detached by raindrop impact (kg m^{-2} s^{-1}), k_r is the raindrop soil erodibility coefficient varying according to the type of soil, F_w is the water depth correction factor, while M_R and M_D are momentum squared for raindrop and leaf drip respectively. Values or the expressions to obtain k_r, F_w, M_R and M_D may be taken from Wicks and Bathhurst (1996) and is still subject to calibration. Application of unmixing results to Eqs. (5) and (6) allow attribute variability within one pixel unafforded in other routing techniques.

2.5 Data Processing and Hydrologic Modeling Steps

The spectral signatures for six full-grown vegetation and three soil types were average-sliced into three ranges equivalent to the spectral sensitivity of a colour film with a minus-blue filter. Thirteen aerial photographs were scanned, registered to a 1:25,000 topographic map at 10 m resampling, and mosaicked, with correction for vignetting effects. Radiometric calibration was performed by obtaining coefficients from fitting the RGB values of homogenous landcover types with their equivalent sliced signatures. These coefficients were then applied to the whole

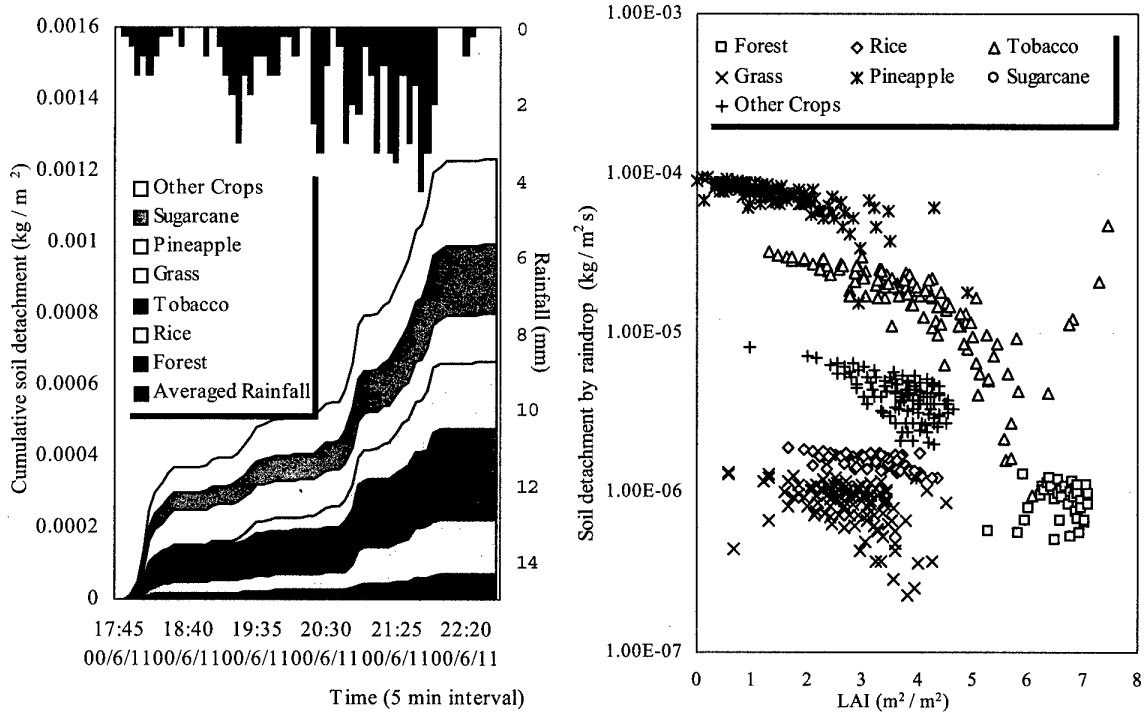
440 x 445 pixel data to generate the radiance image. The sliced signatures also served as values for R_f, the "pure" end-member spectra.

In the unmixing proper, applying the appropriate crop and soil type signatures is determined through the use of agriculture land use and soil series maps with validation for soil sampled from the field. Other field data such as leaf dimensions and number, and plant height, spacing and density for each full grown crop served as an input to compute their respective LAI_0s while values for C were obtained from Gilabert et al.(2000) but may be obtained if leaf samples are brought to the laboratory for an LAI experiment. Built-up areas and bare soil types were masked out and automatically assigned LAI_0s of zero. Selective LAI_0 and C usage likewise makes use of the agriculture land use map.

The DEM and channel routes were obtained by the digitizing the topographic map while data from the four rain gauges were used to generate a continuous distributed rainfall map for four rainfall events by inverse distance interpolation. The hydrologic model was then implemented in computational grid size of 10 meters at 10-second time intervals inside the watershed boundary. Aside from the Courant-Friedrichs-Lewy (CFL) routing scheme stability criterion, the selection of grid size and time interval depended on the consideration for an ideal grid size that minimizes detail loss due to spatial aggregation while maintaining a manageable number of cells for optimal computation time. It is assumed that for a single grid cell, only the fractions of soil and one specific vegetation type are present. Finally, runoff, water and sediment discharge simulation results are compared with observed values by means of regression techniques.

3. RESULTS AND DISCUSSION

3.1 Land Use, LAI Estimates and Soil Detachment Rates



(a) (b)

Fig. 1 In rainfall event 1,(a) cumulative soil detached per unit area; (b) soil detachment rate to increasing LAI for the same land use at maximum rainfall intensity.

The relative contribution of different vegetation types to the accumulated soil detached is shown in Fig. 1(a), with losses averaging 1.22 g m^{-2}. This translates to about 14.1 tons of soil removed for the 5-hour, 36 mm rainfall. From Fig. 1 (b) it can be surmised that the detachment rate of soil due to raindrop impact either by leaf drip or direct rainfall is strongly influenced not only by the fraction of vegetation it encounters but also varies according to the type of vegetation involved and its abundance. It can also be deduced from Fig. 1(b) that the detachment mechanics can be confidently estimated from lesser LAI values and becomes more varied as vegetative cover thickens (i.e. high LAI).

The general trend that low LAI values lead to high soil detachment rates is observed. However, this was not the case for tobacco, pineapple and sugarcane crops, areas which, even with high abundance of leaf cover experience high detachment rates. In contrast, grass fields having lower LAI values yields lower detachment rates. Other surface conditions such as effects of tillage or absence thereof and other forms of disturbances on soil structure may be a plausible explanation for this observation and is subject for further investigation.

The condition for paddy rice fields however should be interpreted with care, since while the soil is open at the early stages of growth, as what is the existing condition at the time of the aerial photography, unlike other crops, it does not react directly with impacting rain by the ponded water which reduces sensitivity to D_R. This may explain the almost level plot of detachment rate against increasing LAI.

3.2 Sediment discharge and turbidity plots

Table 1 presents a summary results of the comparison between observed simulated peak water discharge, sediment discharge and runoff for the four runoff events. Results of the sediment yield discharge modeling on four rainfall events are shown in Fig. 2, with the actual sediment discharge rates plotted from the turbidity sensor at the downstream portion of the river. For all the four rainfall events, the simulated sediment discharge peaks earlier than that measured by the turbidity sensor but all of them occur after the maximum water discharge.

Table 1. Rainfall, modeled sediment discharge and turbidity characteristics of 4 rainfall events.

Peak water discharge ($m^3 s^{-1}$)		Delay in time to peak (min)	Peak sediment discharge $m^3 s^{-1}$		Delay in time to peak (min)	Peak runoff (mm)		Delay in time to peak (min)
Obs.	Sim.		Obs.	Sim.		Obs.	Sim.	
62.24	74.56	7.833	658.92	668.49	16.6	2095	2105	7.33
46.25	54.03	4.666	651.114	562.34	13.3	1667	1707	5.00
21.06	26.36	3.5	552.296	535.58	21.5	1356	1393	2.833
54.64	60.77	5.33	680.025	953.65	3.43	1757	1802	5.17

Linear regression results report of R^2 fits of 0.98, 0.67 and 0.97 between the observed versus the estimated peak runoff, water and sediment discharges respectively, almost all of which tend to match expected values but with discrepancies in timing. Although peak sediment discharge fits poorest, an examination of its time series plot in Fig. 2 suggests a realistic rendition of the sediment behavior in the channel flow. For an uncalibrated watershed, the results of the simulation already yield promising results to warrant further refinement of the input parameters. One data deficiency in the sediment yield model lies with the description of the initial bed conditions and the sediment sources along the channel. For example, the existence of grasses lying within the river beds may be responsible for the delay in discharge peaks but was not considered in the parameterization of channel flow.

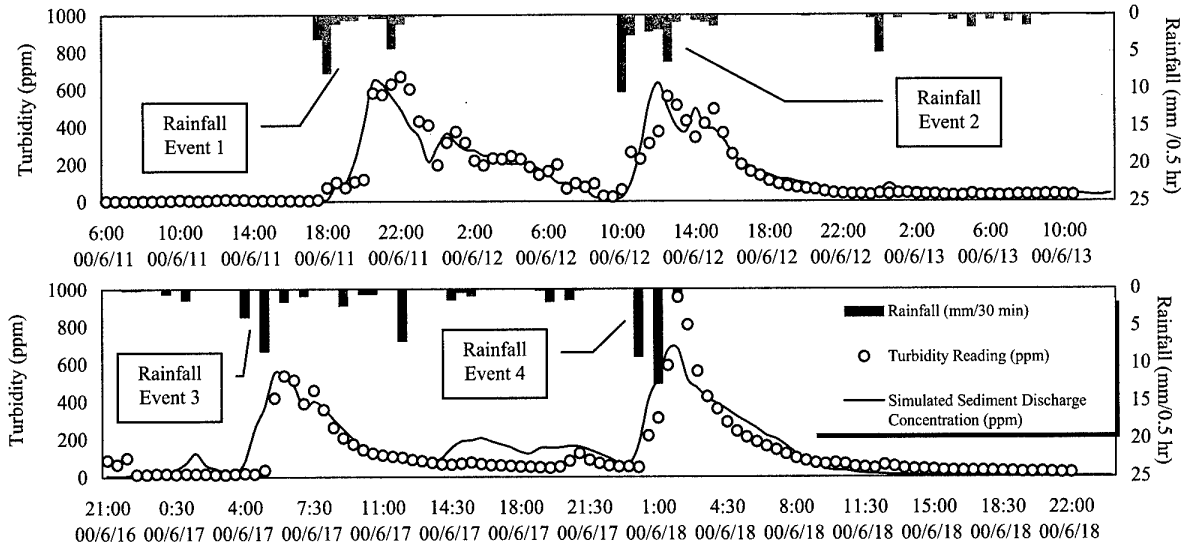


Fig. 2 Comparison of the simulated and measured sediment discharges for the 4 rainfall events.

4. CONCLUDING REMARKS

This paper presented an application of spectral unmixing technique to remotely-sensed data as an input to distributed sediment yield modeling with consideration for spatial variations in topographic, soil and vegetation cover conditions. It was observed that the rate of soil detachment varies with the type of vegetation cover and its abundance. The four rainfall events simulated show a satisfactory reproduction of the observed sediment discharge magnitudes but some discrepancy in the timing of the simulated discharge peak exists.

Future work should take into account the variation of vegetation growth conditions into the unmixing process. This requires acquisition of a time-series spectral signatures for the vegetation and soil cover. The sediment yield model should likewise be modified to incorporate the effects of physical characteristics of the channel bed. Coupled with these innovations, improved and integrated remote sensing and hydrologic methods can be attained and applied to monitor environmental degradation due to soil losses.

5. REFERENCES

Dikou, A., and T. Takeaki, 1999. Red-clay erosion in Okinawa Prefecture, Japan, Current status. Ambio, 28(6), pp. 534-535.

Settle, J.J. and N.A. Drake, 1993. Linear mixing and the estimation of ground cover proportions. International Journal of Remote Sensing, 14(6), pp. 1159-1177.

Gilabert, M. A., F.J. Garcia-Haro and J. Melia, 2000. A mixture modeling approach to estimate vegetation parameters in remote sensing. Remote Sensing of Environment,72(3), pp. 328-345.

Wang, M., and A. Hjelmfelt, 1998. DEM-based overland flow routing model. Journal of Hydrologic Engineering, 3(1), pp. 1-8.

Wicks, J.M. and J.C. Bathhurst, 1996. SHESED: a physically-based, distributed erosion sediment yield component for the SHE hydrological modeling system. Journal of Hydrology, 175, pp. 213-238.

Van Leeuwen, W.J.D, A. R. Huete, C.L Walthall, S.D. Prince, A. Begue and J.L Roujean, 1997. Deconvolution of remotely sensed spectral mixtures for the retrieval of LAI, faPAR and soil brightness. Journal of Hydrology, 188-189, pp. 697-724.

GROUNDWATER LEVEL FORECASTING WITH TIME SERIES ANALYSIS

Miao-Hsiang PENG and Jin-King LIU
Energy and Resources Laboratories, ITRI, Hsin-Chu, TAIWAN
E-mail: 781062@itri.org.tw; JKLiu@itri.org.tw

Tian-Yuan SHIH
Professor, Department of Civil Engineering, National Chiao-Tung University,
Hsin-Chu, TAIWAN
E-mail: tyshih@cc.nctu.edu.tw

KEY WORDS: Autocorrelation Function, ARIMA Model, Land Subsidence, Stochastic Process, Stationality

ABSTRACT: This study investigates the application of time series analysis methods for forecasting groundwater levels. The study site is located in western Taiwan where serious land subsidence has occurred. A series of monthly groundwater level observations made during the period 1993 and 1999 is used for the experiments. Univariate time series models, including ARIMA models and the time series decomposition method, are applied and the resulting accuracy is compared. Empirical results indicate that groundwater level data series in this study are cyclical. ARIMA models generate more accurate forecasts. The forecasting of ARIMA models presents the characteristics of trend and seasonal variation.

1. INTRODUCTION

Groundwater level models provide useful information for land subsidence forecasts. The Univariate Box-Jenkins (UBJ) ARIMA analysis (Box, Jenkins and Reinsel, 1994) has been used in many applications, such as medical, environmental, financial, and engineering applications (Abdel-Aal and Mangoud, 1998; Kumar and Jain, 1999; Mitosek, 2000). A comparative study between ARIMA models and the time series decomposition model for forecasting groundwater levels is discussed in this article.

2. SITE DESCRIPTION AND DATA COLLECTION

Records of groundwater levels were compiled for wells in a monitoring network in the Cho-Shui alluvial fan near southwest Taiwan, starting around 1993. Groundwater-levels were generally measured once a month.

3. ARIMA MODELING OF THE GROUNDWATER LEVEL

The statistical package MINITAB for Windows is employed to develop the ARIMA models. There are four stages in the modeling process (Bowerman and O'Connell, 1993), i.e. identification, estimation, diagnostic checking, and forecasting.

3.1 Identification

The first step is to plot the data for the monthly groundwater-level time series for 7 years (Figure 1). Data for the first 5 years are used for constructing the ARIMA model and the remaining years are reserved for evaluation. A simple linear regression model is used to characterize the trend component. The result of regression analysis is shown in Table 1. The trend of the overall groundwater-level develops through time. A clear seasonal pattern, with low levels from November to April and high levels from February to August, emerges from the data gathered.

Table 1. Results fromthe linear regression model

Site	Intercept (m)	Slope	Mean absolute deviation (m)	Mean squared deviation (m)
IWu	-28.2856	0.0635	2.61	3.22

The first insight into the statistical properties of the time series is shown in Table 2. Performing the first differencing on the groundwater-level series reduces the series mean from -25.46 to 0.03. The first differencing often results in a stationary mean value of approximately zero (Figure 2).

Table 2. Various statistics of the raw data and of the first differencing

Data	Max (m)	Min (m)	Mean (m)	Variance
Raw	-16.95	-31.98	-25.46	11.852
First differencing	5.21	-7.60	0.03	5.478

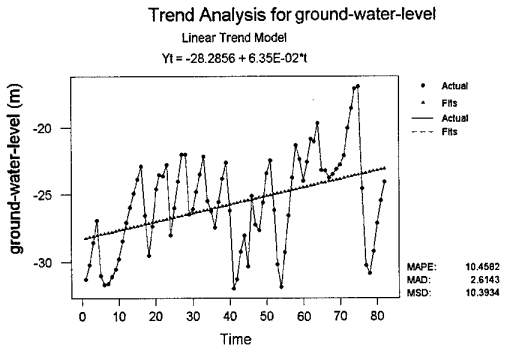


Figure 1. Monthly groundwater-level data and regression model.

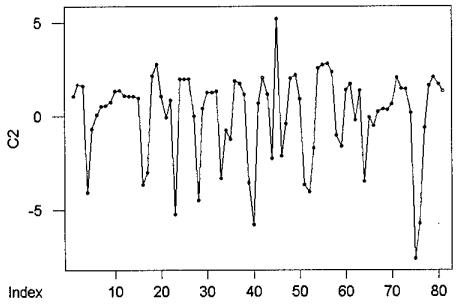


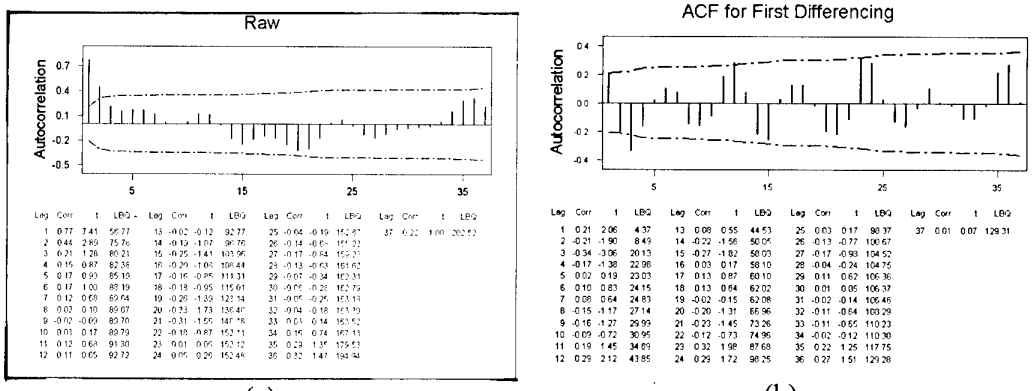
Figure 2. First differencing sequence plot.

Further illustration of the time series is obtained from the estimated autocorrelation function (ACF) and partial autocorrlation function (PACF). As shown in Figure 3, lags up to 37 months long are taken. The acf in Figure 3 dies down slowly in a damped sine-wave pattern, indicating that the raw data is nonstationary. Significant correlations (| t-value | >1.6) exist at the lag 1 and lag 2 phases in Figure 3(a). Spikes exist, indicating that the model can be mixed with the autoregressive and moving average models with each seasonal term.

To remove seasonal nonstationarity of the series, the first seasonal differencing is applied:

$$w_t = E_t - E_{t-1} - E_{t-12} + E_{t-13};\ t=14,15,\ldots \qquad (1)$$

Where w_t is the first seasonal differencing of ground-water level E_t. A spike at the first seasonal lag 12 (| t-value | >1.6) appear on both acf and pacf (Figure 4), indicating that the period of differencing is 12 months.

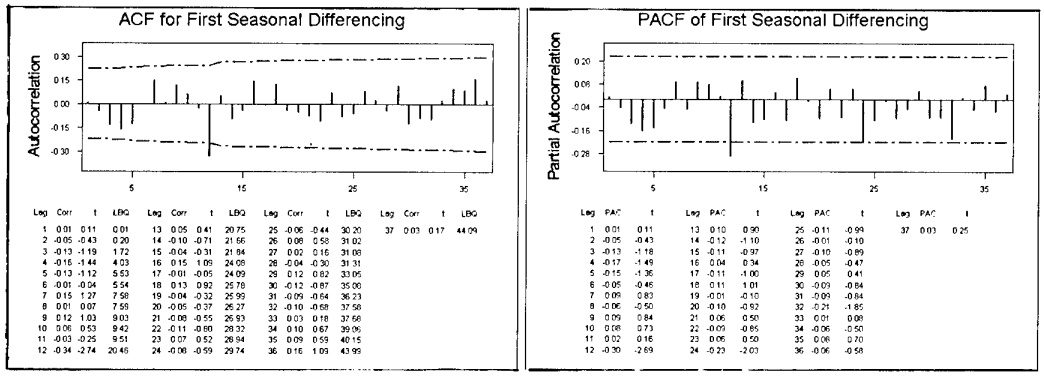


(a) (b)

Figure 3. The autocorrelation function (ACF)

(a) the raw monthly time series;

(b) the time series obtained through the first differencing.



(a) (b)

Figure 4. The autocorrelation function (ACF) and the partial autocorrelation (PACF) for the time series obtained from the first seasonal differencing.

3.2 Estimation

The parameters for each model are estimated with the ARIMA module of MINITAB. The results are summarized in Table 3. The constant terms of all cases are negligibly small since the modeled differencing series has a nearly zero mean. The good quality of the coefficients are significantly greater than zero (| t-value | >2.0) and satisfy the stationarity conditions. Absolute values for all coefficients are also significantly different from 1.

Table 3. Results of estimations for ARIMA models

Model	Parameter	Coefficient	St. Dev.	t-value
$ARIMA(0,1,1)(1,1,0)_{12}$	MA1	0.0028	0.1144	0.02
	SAR12	-0.5768	0.1065	-5.41
	CONSTANT	0.0008	0.2594	0.00
$ARIMA(1,1,0)(1,1,0)_{12}$	AR1	-0.0021	0.1144	-0.02
	SAR12	-0.5727	0.1066	-5.37
	CONSTANT	0.0006	0.2602	0.00
$ARIMA(1,1,1)(1,1,1)_{12}$	AR1	-0.1016	0.8447	-0.12
	MA1	-0.2270	0.8162	-0.28
	SAR1	-0.3225	0.1149	-2.81
	SMA1	0.9192	0.0850	10.82
	CONSTANT	-0.03478	0.03617	-0.96
$ARIMA(1,1,1)(1,1,0)_{12}$	AR1	0.8036	0.0765	10.50
	MA1	0.9794	0.0431	22.74
	SAR12	-0.6026	0.1058	-5.70
	CONSTANT	0.00479	0.01086	0.44
$ARIMA(1,1,0)(0,1,1)_{12}$	AR1	0.1014	0.1173	0.86
	SMA12	0.8729	0.0980	8.91
	CONSTANT	-0.00998	0.05413	-0.18
$ARIMA(0,1,1)(0,1,1)_{12}$	MA1	-0.1158	0.1157	-1.00
	SMA12	0.8631	0.0969	8.90
	CONSTANT	-0.00907	0.06239	-0.15

3.3 Diagnostic checking

The statistical adequacy of the estimated models is then verified. The ACF function for the residuals resulting from a good ARIMA model will have statistically zero autocorrelation coefficients. Figure 5 shows a plot of the residuals for $ARIMA(1,1,0)(1,1,0)_{12}$ model. The residual plot shows small variations around the zero mean. The plot of the estimated residual ACF in Figure 5 indicates that there is no significant autocorrelation, and the model adopted will be acceptable.

3.4 Forecasting

Two ARIMA models were applied to forecast the 21 water level values from January 1998 to September 1999. The forecasts are then compared with the measured data. The forecasted time series and its 95% confidence level error bound are plotted in Figure 5 for both models. It is observed that all measured monthly values fall within the error bound, and the forecasts track the seasonal pattern reasonably well.

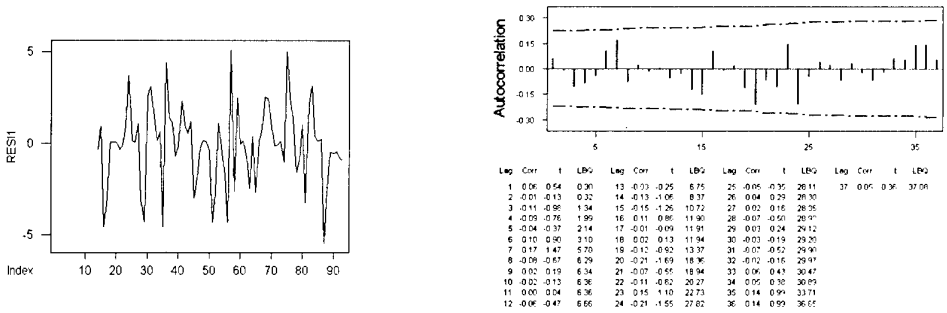


Figure 5. The plot of the residual time series and the residual ACF function.

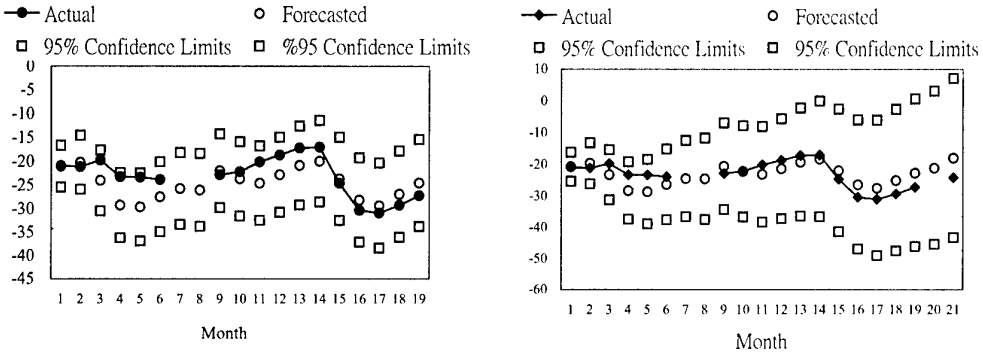


Figure 6. Plots of the actual data and estimates and 95% confidence limits of forecasts for groundwater-level.

(a) the ARIMA(1,1,0)$(1,1,0)_{12}$ model;

(b) the ARIMA(1,1,1)$(1,1,0)_{12}$ model.

4. COMPARISON WITH VARIOUS MODELING TECHNIQUES

Three accuracy indices are computed for six ARIMA models and the decomposition model. As shown in Table 4, the ARIMA(1,1,1)$(1,1,1)_{12}$ model has mean absolute error 2.29m and mean square error 8.33 m^2, and is ranked the lowest among all.

Table 4. Forecasting performance comparison between ARIMA models and decomposition model.

Model type	Mean absolute error (m)	Mean square error (m^2)	Maximum absolute error(m)
ARIMA(1,1,1)$(1,1,1)_{12}$	2.29	8.33	4.86
ARIMA(0,1,1)$(1,1,0)_{12}$	2.84	10.24	5.28
ARIMA(1,1,0)$(1,1,0)_{12}$	2.54	10.25	5.28
ARIMA(1,1,1)$(1,1,0)_{12}$	2.86	11.30	6.34
ARIMA(1,1,0)$(0,1,1)_{12}$	2.75	12.15	6.58
ARIMA(0,1,1)$(0,1,1)_{12}$	2.84	13.25	7.06
Decomposition	3.22	12.02	5.22

5. CONCLUSIONS

The multiplicative combinations of nonseasonal and seasonal ARIMA models have been used to forecast groundwater-levels for land-subsidence areas, located in southwest Taiwan. The forecasting performance of the ARIMA models presents a seasonal trend. The various ARIMA models forecast monthly data for the evaluation with a mean error of about 2.3m to 2.9m. In terms of numerical accuracy measures, the ARIMA model generates more accurate forecasts than the decomposition model. It should be emphasized that the objective is not to determine which forecasting method is the best, but to introduce the various procedures available to check the forecasting.

REFERENCES

1.Abdel-Aal, R.E. and Mangoud, A.M., 1998. Modeling and forecasting monthly patient volume at a primary health care clinic using univariate time-series analysis. Computer Methods and Programs in Biomedicine, 56, pp.235-247.

2.Bowerman, B.L. and O'Connell, R.T., 1993. *Forecasting and Time Series*: *An Applied Approach*, Duxbury Press, Belmont, CA.

3.Box, G.E.P., Jenkins, G.M. and Reinsel, G.C., 1994. *Time Series Analysis, Forecasting and Control*, Prentice Hall, Englewood Cliffs, N.J.

4.Kumar, K. and Jain, V.K., 1999. Autoregressive integrated moving averages (ARIMA) modeling of a traffic noise time series. Applied Acoustics, 58, pp283-294.

5.Mitosek, H.T., 2000. On stochastic properties of daily river flow processes. Journal of Hydrology, 228, pp188-205.

6.Thury, G. and Witt, S.F., 1998. Forecasting Industrial Production Using Structural Time Series Models. Omega Int. J. Mgmt Sci, 26, pp751-767.

RESERVOIR TROPHIC STATE EVALUATION USING LANDSAT TM DATA

Ke-Sheng Cheng and Tsu-Chiang Lei
Associate Professor and Ph.D. Candidate
Agricultural Engineering Department / Hydrotech Research Institute,
National Taiwan University,
Taipei, TAIWAN
Tel: +886-2-2366-1568, Fax: +886-2-2363-5854
E-mail: rslab@ccms.ntu.edu.tw

KEY WORDS: trophic state index, reservoir, random field simulation, remote sensing

ABSTRACT: Reservoir water quality is traditionally monitored and evaluated based on field data collected at limited locations. Whether the limited field data represent the overall trophic state of a vast water body is often disputed. In this study we utilize Landsat TM data to evaluate the overall trophic state of Te-Chi Reservoir in Central Taiwan. Three water quality parameters: chlorophyll-a (*Chla*) concentrations, total phosphorous (*TP*) measurement, and secchi disk depth (*SDD*), are found to have high correlations with transformed spectral features derived from bands 1, 2, 3 and 4 of TM data. Therefore, TM data are used to yield a trophic-state-index (*TSI*) map of the reservoir. Ranges of *Chla*, *TP*, and *SDD* measurements in Taiwan's reservoirs are generally much larger than that of Minnesota's lakes which original *TSI* model was developed; therefore, a modified *TSI* model was proposed for Techi Reservoir. Based on measurements of water quality parameters, *TSI* cutoff values of 66 and 78 are used to signify the reservoir trophic state of eutrophication and hypereutrophication. In order to provide a confidence level for reservoir trophic state evaluation, we employ a two-dimensional random field simulation technique to generate a large pool of *TSI* realizations. Using these realizations, probability distributions of the trophic states of specific reservoir cross-sections and the reservoir as a whole can be estimated. A probabilistic approach of reservoir trophic state evaluation is proposed as follows: the overall reservoir trophic state is considered eutrophic or hypereutrophic if the probability that the overall TSI exceeds the cutoff value (66 or 78) is greater than a predetermined level, say 0.9. Based on this criterion, the trophic state of Te-Chi reservoir is found to be eutrophic in summer and meso-eutrophic in winter.

1. INTRODUCTION

Traditionally the quality and trophic state of water in impoundments have been assessed using limnological methods and laboratory analyses of field-sampled data. Single- and multi-parameter indices were developed for trophic classification of lakes (Brezonik and Shannon, 1971; Beeton and Edmonson, 1972). Carlson (1977) proposed a trophic state index (*TSI*), that

retains the expression of the diverse aspects of the trophic state found in multi-parameter indices yet also has the simplicity of a single parameter index, for water quality assessment of impounded water bodies. Carlson's trophic state index can be computed from any of three interrelated water quality parameters: *secchi disk depth* (*SDD*), *chlorophyll-a concentration* (*Chla*), and *total phosphorous measurement* (*TP*). The index has since then been widely accepted owing to its calculation simplicity and ability to communicate between researchers, government agencies, and local community residents.

Determination of trophic state using field-collected water quality data is time and cost consuming, and whether the limited number of field data can adequately represent the overall quality of a vast water body is often disputed. To circumvent the disadvantages of traditional data-collection method, utilization of remote sensing data for water quality assessment has been investigated. Previous work (Lillesand, et al., 1983; Ekstrand, 1992; Tassan, 1993; Lavery et al., 1993; Han, 1997; Rundquist, 1997; Avard et al., 2000: Thiemann and Kaufmann, 2000) has shown that remote sensing data can not only be used to estimate certain individual water quality parameters, these data can also be related to trophic state indices developed from single or multiple water quality parameters.

Although empirical models have been developed for water quality monitoring using remote sensing data, most of these studies were conducted in coastal or estuarine waters, or used field-spectrometer measurements in inland lakes. Also chlorophyll and sediment concentrations in several Taiwan's reservoirs are found much higher than that reported in above studies. Therefore, the objective of this study is to use TM data to determine water quality of the Te-Chi reservoir, located in Central Taiwan, and give a probability-based decision on the overall trophic state of the reservoir.

2. CARLSON TROPHIC STATE INDEX

Carlson's *TSI* model converts raw data of *SDD*, *Chla*, and *TP* to a standard numerical scale ranging from 0 to 100 based on empirical relationships between water quality parameters. Individual indices are calculated by the following equations:

$$TSI(SDD) = 10(6 - \frac{\ln SDD}{\ln 2}). \quad (1)$$

$$TSI(Chla) = 10(6 - \frac{2.04 - 0.68 \ln Chla}{\ln 2}), \quad (2)$$

$$TSI(TP) = 10(6 - \frac{\ln(48/TP)}{\ln 2}). \quad (3)$$

The units are meters for *SDD* and $\mu g/\ell$ for *Chla* and *TP*. A commonly applied criterion for trophic classification of lakes is: Oligotrophic – TSI $\leq$ 40; mesotrophic – 40 < TSI $\leq$ 50; eutrophic – 50 < TSI.

3. STUDY AREA AND DATA

Te-Chi reservoir, located in Central Taiwan, with a drainage basin of 592 km^2, has multiple functions including water supply for domestic use, irrigation, flood control, and a hydropower plant. The reservoir pool is approximately 14km long and covers an area of 454 hectares. Based on local relationships between water quality parameters, the following modified *TSI* model was developed for Te-Chi reservoir:

$$TSI(SDD) = 10\left(8.605 - \frac{\ln(SDD)}{\ln(1.544)}\right) \tag{4}$$

$$TSI(Chla) = 10\left(8.605 - \frac{1.8571 - 0.3264\ln(Chla)}{\ln(1.544)}\right) \tag{5}$$

$$TSI(TP) = 10\left(8.605 - \frac{2.1775 - 0.4230\ln(TP)}{\ln(1.544)}\right) \tag{6}$$

$$\overline{TSI} = (TSI(SDD) + TSI(Chla) + TSI(TP))/3 \tag{7}$$

TSI cutoff values are 0–52 for oligotrophic, 53–60 for mesotrophic, 61–65 for meso-eutrophic, 66–77 for eutrophic, and 78–100 for hypereutrophic. These categories reflect the reservoir's nutrient and clarity levels.

4. TSI ESTIMATION USING LANDSAT TM DATA

Landsat TM data from four dates (8/23/1993, 10/17/1994, 1/10/1995, and 7/22/1996) were analyzed. Corresponding to each TM image, water quality samples were collected at five cross sections within the reservoir pool. Digital numbers of TM bands 1, 2, 3, and 4 are related to water quality parameters:

$$\ln SDD = 2.925 - 0.629\ln(TM4) - 0.515\ln(TM2) \quad R^2 = 0.78 \tag{8}$$

$$\ln Chla = -1.432 + 1.195\ln(TM4) + 1.239\ln(TM2) \quad R^2 = 0.80 \tag{9}$$

$$\ln TP = 0.675 + 1.4116\ln(TM4) + 0.01387\ln(TM2) \quad R^2 = 0.79 \tag{10}$$

Combining use of Eqs.(4)-(7) and Eqs.(8)-(10) yields pixel-based $\overline{TSI}$ images of the reservoir pool. The overall reservoir trophic state index is expressed as the areal average of $\overline{TSI}$

$$\overline{TSI}_{\Omega} = \frac{1}{\Omega}\int_{\Omega} \overline{TSI}(x)dx \tag{11}$$

where $\overline{TSI}(x)$ represents the pixel-based *TSI* value and Ω the area extent of the reservoir pool.

5. RANDOM FIELD SIMULATION

In order to develop a probabilistic approach of reservoir trophic state evaluation, a geostatistical random field simulation model HYDRO_GEN (Bellin and Rubin, 1996) is utilized to generate six hundred realizations using parameters mean, variance, and variogram obtained from the TM-derived $\overline{TSI}$ image. A brief summary of theoretical background of the HYDRO_GEN is given below.

Let the mean, variance, and covariance function of a Gaussian random field Z(x) be

$$E[Z(x)] = m_Z(x),, \tag{12a}$$

$$Var[Z(x)] = \sigma_Z^2(x) \tag{12b}$$

$$C_Z(x,x') = E\{[Z(x) - m_Z(x)][Z(x' - m_Z(x')]\} \tag{12c}$$

Initially we can generate a realization of $Z(x_0)$, i.e., $z(x_0)$, by a standard random generator. Given $z(x_0)$, the conditional mean and variance of $Z(x_1)$ are, respectively,

$$\begin{aligned} E[Z^c(x_1)] &= E[Z(x_1) \mid z(x_0)] = m_Z(x_1) + \frac{C_Z(x_0,x_1)}{\sigma_Z^2}[z(x_0) - m_Z(x_0)], \\ \sigma_Z^{2c}(x_1) &= \sigma_Z^2 - \frac{C_Z(x_0,x_1)}{\sigma_Z^2} C_Z(x_1 - x_0) \end{aligned} \tag{13}$$

Therefore, a realization of $Z(x_1)$ given $z(x_0)$ can be generated using the above parameters. A general form of HYDRO_GEN is given below:

$$\begin{aligned} E[Z^c(x_N)] &= m_Z(x_N) + \sum_{j=1}^{N-1} \lambda_j(x_N)[z(x_j) - m_Z(x_j)], \\ \sigma_Z^{2c}(x_N) &= \sigma_Z^2 - \sum_{j=1}^{N-1} \lambda_j(x_N) C_Z(x_N - x_j), \\ \sum_{j=1}^{N-1} \lambda_j(x_N) C_Z(x_j - x_q) &= C_Z(x_N, x_q), q = 1,2,\cdots,N-1 \end{aligned} \tag{14}$$

Using Eq. (14) a realization of $Z(x_N)$ given $z(x_j)$, j =1,2,..., N-1, can be generated.

The date-specific $\overline{TSI}$ image derived from a set of Landsat TM data is considered one realization of the embedding random field that characterizes the spatial variation of $\overline{TSI}$. The probability distribution of $\overline{TSI}_\Omega$ is then estimated using these generated realizations. Table 1 demonstrates distribution parameters of $\overline{TSI}_\Omega$ for four Landsat images.

Image Date	31/08/1993	05/10/1994	09/01/1995	22/07/1996
Mean	79.82	71.99	64.98	74.17
Std. Dev.	0.06	0.05	0.03	0.07

Table 1. Distribution parameters of $\overline{TSI}_\Omega$

6. PROBABILISTIC EVALUATION OF RESERVOIR TROPHIC STATE

To circumvent the dispute about the overall trophic state of the reservoir, we adopt a probabilistic approach for reservoir trophic state evaluation. A reservoir is considered eutrophic (or hypereutrophic) if the probability that $\overline{TSI}_\Omega$ exceeds the cutoff value (v_c) of 66 (or 78) is greater than a pre-specified level α, i.e.

$$P\left(\overline{TSI}_\Omega \geq v_c\right) \geq \alpha \tag{15}$$

In this study the level α is set to be 0.90. Overall reservoir trophic states determined by the proposed probabilistic approach were compared against the trophic states determined by using the average *TSI* values at the five data-collection locations. Table 2 indicates that the trophic

state of Te-Chi reservoir tends to be eutrophic or hypereutrophic in summer, and the trophic state may be better in winter, e.g. meso-eutrophic from the 09/01/1955 TM image.

Image Date	31/08/1993	05/10/1994	09/01/1995	22/07/1996
$\overline{TSI}_{\Omega}$ (Trophic State)	79.82 (Hypereutrophic)	71.99 (Eutrophic)	64.98 (Meso-eutrophic)	74.17 (Eutrophic)
5-point $\overline{TSI}$ (Trophic State)	78.35 (Hypereutrophic)	79.71 (Hypereutrophic)	63.51 (Meso-eutrophic)	79.47 (Hypereutrophic)

Table 2. Comparison of reservoir overall *TSI* values.

7. CONCLUSIONS

We demonstrate that reservoir water quality parameters are highly correlated with transformed spectral features of the Landsat TM data, particularly TM2 and TM4. Using the empirical relationships between TM data and three water quality parameters, *SDD*, *Chla*, and *TP*, reservoir *TSI* map can be created. By means of a random field simulation technique, sufficiently large pool of realizations that characterize the spatial distribution of $\overline{TSI}$ is generated, and the probability distribution function of the overall trophic state index $\overline{TSI}_{\Omega}$ can be estimated. Based on the criterion of exceedence probability $P(\overline{TSI}_{\Omega} \geq v_c) \geq 0.9$, we find that the Te-Chi reservoir is eutrophic in summer, and maybe meso-ereutrophic in winter. This preliminary results demonstrate the potential of combining usage of TM data and geostatistical modeling for probabilistic evaluation of environmental topics.

REFERENCES

Avard, M.M., Schiebe, F.R., and Everitt, J.H., 2000, Quantification of chlorophyll in reservoirs of the Little Washita watershed using airborne video, Photogrammetric Engineering and Remote Sensing, 66(2):213-218.

Beeton, A.M. and Edmonson, W.T., 1972. The eutrophication problem. Journal of the Fisheries Research Board of Canada, 29: 673-682.

Bellin, A. and Rubin, Y., 1996, HYDRO_GEN: a new random field generator for correlated properties, Stochastic Hydrology and Hydraulics, 10(4):253-278.

Brezonik, P.L. and Shannon, E.E., 1971. Trophic state of lakes in north central Florida. Water Resources Research Center Publication 13. 102p.

Carlson, R.E., 1977, A trophic state index for lakes, Limnology and Oceanography, 22(2):361-369.

Ekstrand, S., 1992, Landsat TM based quantification of chlorophyll-a during algae blooms in coastal waters, International Journal of Remote Sensing, 13(10):1913-1926.

Han, L., 1997. Spectral reflectance with varying suspended sediment concentrations in clear and algae-laden waters. Photogrammetric Engineering and Remote Sensing, 63(6): 701-705.

Han, L. and Rundquist, D.C., 1997. Comparison of NIR/red ratio and first derivative of reflectance in estimating algal-chlorophyll concentration: a case study in a turbid reservoir. Remote Sensing of Environment, 62: 253-261.

Lavery, P., Pattiaratchi, C., Wyllie, A., and Hick P., 1993, Water quality monitoring in estuarine waters using the Landsat Thematic Mapper, Remote Sensing of Environment, 46:265-280.

Lillesand, T.M., Johnson, W.L., Deuell, R.L., Lindstorm, O.M., and Meisner, D.E., 1983, Use of Landsat data to predict the trophic state of Minnesota lakes, Photogrammetric Engineering and Remote Sensing, 49(2):219-229.

Tassan, S., 1993, An improved in-water algorithm for the determination of chlorophyll and suspended sediment concentration from Thematic Mapper data in coastal waters, International Journal of Remote Sensing, 14(6):1221-1229.
Thiemann, S. and Kaufmann, H., 2000. Determination of chlorophyll content and trophic state of lakes using field spectrometer and IRS-1C satellite data in the Mecklenburg Lake District, Germany. Remote Sensing of Environment, 73: 227-235.

ANALYSIS OF THE CONVECTIVE MIXING CHARACTERISTICS OF ESTUARINE RESERVOIR BY LANDSAT TM IMAGES

Takashi HOSHI
Professor, Department of Computer & Information Sciences,
Ibaraki University, 4-12-1 Nakanarusawa-cho, Hitachi, 316-8511,
Tel: (81)-294 -38-5133 Fax : (81)-294 -38-5282
E-mail: hoshi@cis.ibaraki.ac.jp, JAPAN

Moon Soo CHOI
Graduate Student, Graduate School of Science and Engineering,
Ibaraki University, 4-12-1 Nakanarusawa-cho, Hitachi, 316-8511
Tel: (81)-294 -38-5133 Fax : (81)-294 -23-7586
E-mail: moon@cis.ibaraki.ac.jp, JAPAN

Hideyuki TONOOKA
Research Associate, Department of Computer & Information Sciences,
Ibaraki University, 4-12-1 Nakanarusawa-cho, Hitachi, 316-8511,
Tel: (81)-294 -38-5149 Fax : (81)-294 -38-5282
E-mail: tonooka@cis.ibaraki.ac.jp, JAPAN

KEY WORDS: Freshening Process, Landsat TM, Atmospheric Correction, Numerical Simulation, Convective Mixing

ABSTRACT: The hydraulic characteristics of the estuarine reservoir constructed in the mouth of a river, which is influenced by the complex mechanisms such as convective mechanism, vertical diffusion, and mixing action in the freshening process. The convective mixing mechanism is the most important element in the freshening of estuarine reservoirs introducing desalted fresh water for the control and improvement of water quality. This paper describes for the convective mixing characteristics using satellite image data and a numerical simulation of flows. The satellite image data consist of two kinds of Landsat TM images acquired in different times separately, which are classified for the study area including the Yongam lake and its bay after the geometric and atmospheric correction processing. These results are also compared to a numerical simulation related to the velocity-vector distribution of influent water and field measurement values that show the temporal variations of water quality in the freshening process. Finally, in the analysis hydraulic characteristics in freshening process, we examined the applied possibility of Landsat TM Image data.

1. INTRODUCTION

The Yongam lake located in the southwestern coast of the Korean peninsula (Fig.-1), is a standard estuarine reservoir which had been completed on Dec. 31, 1993 as a part of Yongsan river comprehensive agricultural development projects (Y-1stage). The hydraulic characteristics of the reservoirs constructed in the estuary, which has been influenced by the complex mechanisms, such as the convective freshening in an upper fresh water layer, the vertical diffusion through a density interface of fresh-salt water, and the mixing action from the bottom soil of a lake. The convective mechanism caused by the mixing of inflows, is very important element in the freshening process of the estuarine reservoir as the Yongam lake introducing

desalted fresh water (surplus water) through link canal from adjacent lake.

This article deals with the convective mixing mechanism in the freshening process using Landsat Thematic Mapper(TM), a numerical simulation of flows, and field observations. But, in the use of Landsat image data, three visible bands (485*nm*, 560*nm*, and 660*nm*) observed in the wave length range of visible spectrum have been powerfully affected by the presence of atmosphere, and the analysis of original data becomes difficult. The atmospheric influence must be especially removed in study cases of very small difference of radiance, or surface reflectance or absolute values of temperature, or in researches related to water pollution. And, the atmosphere correction of satellite image data is not much performed because the radiative transfer of electromagnetic wave follows very complicated process.

And then, this study uses the Second Simulation of the Satellite Signal in the Solar Spectrum (6S) of radiative transfer code to make the atmosphere correction possible on the image data without the various information about atmosphere, which is the improved version of 5S developed by the Laboratoire d'Optique Atmospherique. That is a pre-processing process of TM data to analyze the hydraulic characteristics of estuarine reservoir. The corrected data were classified, which were generally compared to the results of the two dimensional numerical simulation of flow fields and field surveys.

2. STUDY AREA AND TOPOGRAPHICAL CHARACTERISTICS

The study area of this study is the Yongam lake located in the middle of three estuarine reservoir in Yongsan river comprehensive agricultural development projects, as shown in Fig. 1. The enclosure dike of Yongam lake was completed on April 8, 1991. The length of the enclosure dike is 2.2 km while the water resources developed in this desalted lake is 153 million m^3 and the water area reclaimed land is 6,730 ha. And the area of the agricultural land adjacent to the water area reclaimed land offered for improvement of irrigation and land consolidation is 5,470 ha. The water resources of Yongam lake is controlled and managed by the management office of Yongam lake opened on May 3, 1994.

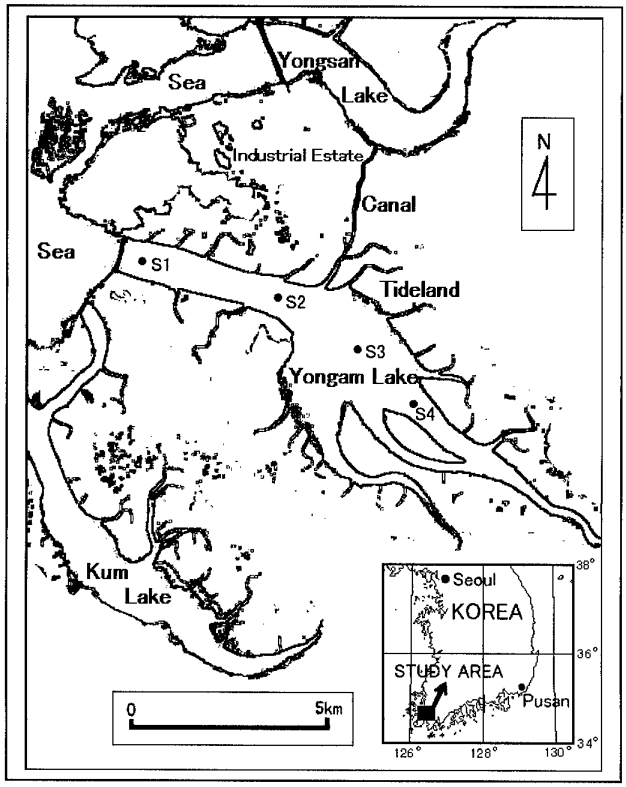


Fig. 1 Location of the Study Area

The Yongam lake is introducing the desalted fresh water through link canal from Yonsan estuary lake because the river basin is narrow and the inflow is small in comparison to the storage capacity of Yongam lake. The excess water of lake is also recycled as fresh water to desalt the salt water of high concentration in Kum lake. At the present time, the link canal to Kum lake has been completed, the desalinization is progressing well by introducing surplus water desalted from Yongam lake.

The characteristics of study area (Yongam lake) is summarized as follows.(i) In the

bottom layer of downstream, there exists the stratified density interface by the density difference of fresh and salt water. The salt water of stagnated high concentration under density interface is difficult to be drained because hydraulic stability is high and fixed. (ii) This area has only small river basin, and the inflow is insufficient for freshening. Therefore, fresh water for desalinization has been introducing from Yongsan estuary lake, if necessary, which can be also drained into Kum lake. (iii)In the freshening process, the convective mixing by the inflow of desalted fresh water is very important freshening mechanism, and the mixed water is excluded by the facilities such as outlet gate, pumps, and siphons.

3. SATELLITE IMAGE DATA AND IMAGE PROCESSING

The Landsat TM images acquired by Landsat 5 on September 22, 1992 and September 28, 1994 were used in this study. These are band 1, band 2, and band 3 operating in the wavelength ranges of blue, green, and red, respectively, with the ground resolution of 30m for each band. The image processing of satellite data includes the geometric correction and the atmospheric correction as a preprocessing of images. The former correct geometric distortion using ground control points (GCP), the latter remove distortion due to the absorption and the scattering of atmospheric constitutes.

In this study, TM bands were cut in the size of 768 lines by 768 pixels after the geometric correction of original data for the areas including three estuarine reservoirs, that is, Yongsan estuary lake, Yongam lake and Kum lake. In the geometric correction, ground control points of TM data are selected on the topographic map of 1:50,000 scale, published in September 1995 in the national geography institute, Korea. The absolute difference between the computed and measured values of the image coordinates was kept down within 1 pixel. The coordinate transformation of which was used Affine transformation equation.

The atmosphere correction in remote sensing that the absorption and the emission of atmospheric energy are regarded as a noise is necessary to correct. The diverse methodologies of atmospheric correction have been proposed. It is classified into three types that consist of the method using radiative transfer code, skylight emission measurements, and regression analysis. The radiative transfer code is used to estimate surface radiance and atmospheric transmittance on the conditions of atmosphere, geometry, and wave number based on radiative transfer equation. The typical codes are MODTRAN (Kneizys *et al.*, 1996) and 6S (Vermote *et al.*, 1994). In addition, the dark object subtract can be also applied when atmospheric affects remove briefly according to study purpose. The method deduct the minimum value of observed DN (Digital Number) values from the image including area that the reflectance is regarded as zero such as wide water area and the shade of clouds. This study uses the radiative transfer code (6S) to execute the atmosphere correction of the image data without a lot of information about atmosphere. When Landsat imagery is used in studies of this nature, there are usually errors associated with the estimation of parameters. The significance of these errors depends on the application of the data. This paper is mainly connected with a synoptic variations in the freshening process of estuarine reservoir, and therefore these errors will not have a significant effect on the objectives of this work (Baban; 1997).

4. METHODOLOGY

The study methods of this paper include the water quality observation of field, the simulation of inflow patterns using a numerical analysis, and the processing of Landsat TM images, to analyze the convective mixing patterns of estuarine reservoir.

4.1 Water Quality Observation

The Yongsan river third-stage office of Rural Development Corporation, Korea has been measuring the water quality of lake periodically twice and three times per year since 1991. The salinity has been investigated at the four points of the vicinity of outlet gate (S1), the outlet of link canal (S2), the central part of lake (S3), and the upstream part (S4), along the center line of Yongam lake, as shown in Fig.-1.

4.2 Numerical Simulation of Flow Fields

A simulation related to the mixing patterns of inflows, which is the two-dimensional simulation of flow fields by adopting finite difference method on general curvilinear coordinate system. The various conditions of grid generation in the simulation process were examined, and the temporal variations of horizontal velocity-vector distribution were applied and visualized for the flow fields of final enclosed freshening reservoir.

4.3 Analysis of Satellite Image data

The analysis of TM image data, which is focused and classified for categories such as inflows and stagnant water related to water bodies and convective mixing patterns on the surface of water, after image processing described in the preceding chapter. However, this study was not carried out for a correlation between water quality categories and image data owing to the lack of water quality data.

5. RESULTS AND DISCUSSION

5.1 Temporal Variations of Water Quality

The Yongam lake has topographical conditions that is not suitable for freshening because the inflow from watershed is not sufficient to desalt, which is the feature of a standard estuarine reservoir. However, the water depth of lake (6~9m) is shallow relatively except downstream area near outlet gate, maximum depth is approximately 23m. The freshening process is progressing satisfactorily by the introduction of desalted fresh water from adjacent Yongsan lake for desalinization. The salinity that is an important criterion evaluating freshening process has been observed since 1991. Table 1 shows the temporal variations of water quality observed under conditions operated normally by means of desalting facilities as outlet gate, desalt siphons, and suction pumps. These are the results investigated in the downstream (S1) of Yonam lake from

Table 1 Water Quality Values in the Downstream Vicinity (S1) of Yongam Lake

year/ month	Temp. ℃	pH	EC μmhos/cm	DO mg/l	COD mg/l	SS mg/l	chl-a mg/m^3	T-N mg/l	T-P mg/l	Cu mg/l
	7.9	7.4	14,600	9.6	2.8	2.8	-	0.784	0.010	0.022
4	30.3	7.8	13,700	6.7	2.5	4.8	-	0.672	0.046	0.020
'94 7	17.5	7.9	9,040	7.7	2.8	6.8	-	0.448	0.024	0.004
10										
3	9.9	8.1	6,690	9.9	6.0	18.4	1.086	0.042	-	0.005
'95 8	25.6	8.3	5,025	6.7	5.0	4.4	1.064	0.002	-	0.005
10	19.5	7.6	3,460	8.4	2.6	8.4	0.672	0.024	-	0.002
5	15.3	7.9	2,860	8.4	4.3	6.0	-	0.392	0.032	0.001
'96 9	26.3	7.3	2,420	6.6	6.0	6.0	-	0.616	0.032	0.001
11	14.6	7.4	2,930	9.1	4.6	4.4	-	0.336	0.017	0.004

Apr. 1994 to Nov. 1996.

When the inflow of fresh water is increased, the salinity decreases because the mixed salt water with inflow is drained through gates. On the contrary, if the inflow is reduced, the salinity rises by the intrusion of seawater from sea dike and outlet gate, and moreover, the salt water under density interface is also diffused and mixed into upper fresh water layer by density currents. Therefore, it is regarded that the convective phenomenon of inflow affects largely water quality in the freshening process of estuarine reservoir.

5.2 Convective Characteristics of flows

This study was used a numerical scheme based on finite difference method with general curvilinear coordinate system, and was carried out two-dimensional numerical simulation to analyze the convective mixing characteristics of flows in the freshening process. Fig. 2 shows the boundary extracted from TM image and the computational grids generated by adopting the multi-block grid generating method which the inlets (Q_1-Q_8) were divided into eight places for watershed and outlet (Q_g) was fixed in the outlet gate of Yongam lake, respectively. Fig. 3 shows velocity-vector distribution simulated for 24 hours in the conditions (a) without (Δt:2) and (b) with (Δt:1) the inflow of fresh water and the open of outlet gate.

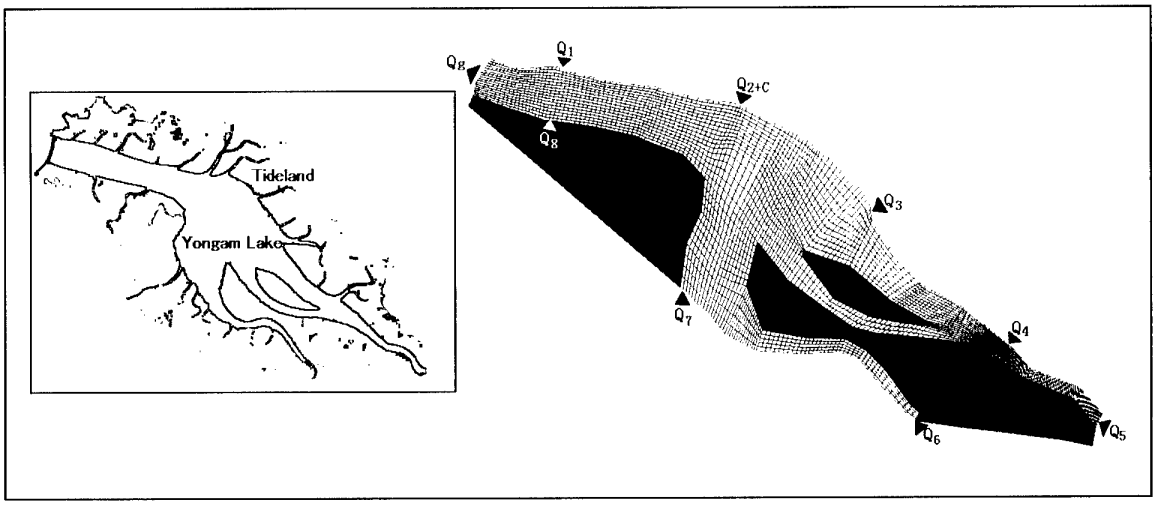


Fig. 2 Boundary of the Study Area Extracted from TM Image and Computational Grids

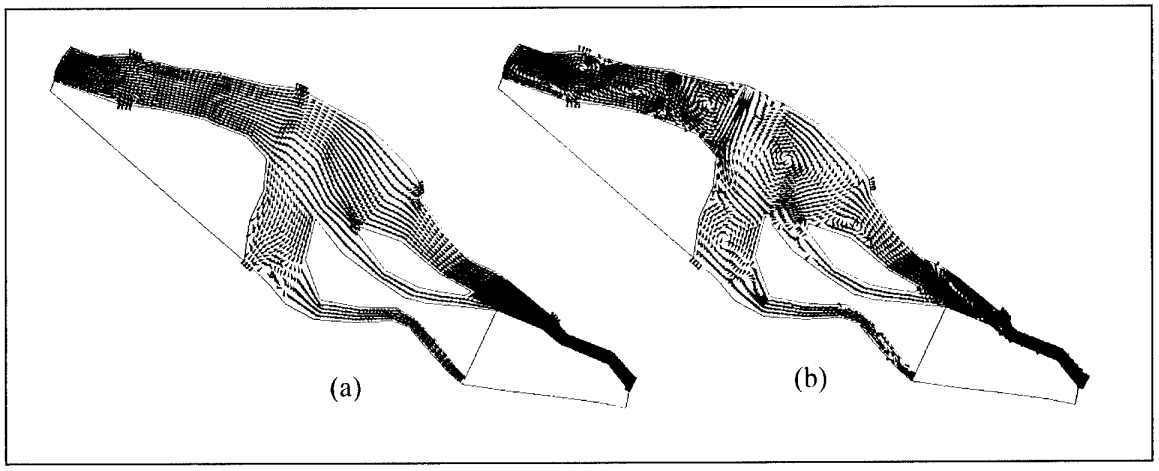


Fig. 3 Velocity-Vector Distribution in Conditions (a) without (t=24h, Δt:2, V_{max}=0.030 m/s) and (b) with (t=24h, Δt:1, V_{max}=0.113 m/s) Desalted Fresh Water

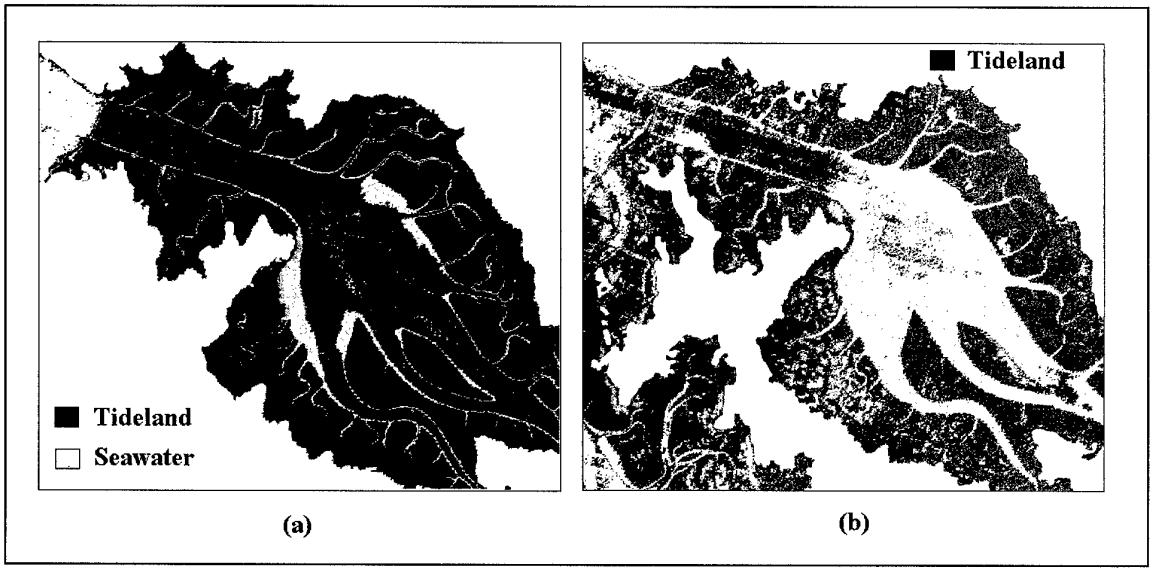


Fig. 4 Classification Images of TM Data Acquired on (a) Sep. 22, 1992 and (b) Sep. 28, 1994

The results indicate that occur the large and small eddies in the most places of Yongam lake including the central part of lake, near outlet gate, and the outlet of link canal. The Eddies affect the convection and rotation of flows, which also accelerate the desalinization of stagnated salt water under density interface. Thus, it was confirmed that the convective mixing mechanism plays an important role in freshening process

5.3 Mixing Patterns in Freshening Process

Fig. 4 is the images classified using TM data of (a) Sep. 22, 1992 and (b) Sep. 28, 1994, respectively, which clearly shows the different patterns of estuarine reservoir, tideland, and seawater. The convective mixing patterns in freshening reservoir seems to be connected with complicated factors such as a suspended matter and its density, eddies related to inflow velocity, inflow discharge, the diffusion and mixing of density currents, and meteorological parameters et al.. The TM image data as shown in Fig. 4 can be applied to the works on the mixing patterns of convective flows on the surface of water and the environmental changes of tideland (or reclaimed land) changed according to the progress of reclamation projects.

6. CONCLUSION

The application with satellite image data and numerical analysis in the field of hydraulic engineering, which is considered as a useful way to analyze various hydraulic problems. Finally, it will be supplemented on the presentation for contents have not explained relating to atmospheric correction.

REFERENCES

Baban, S. M. J., 1997. Environmental Monitoring of Estuaries; Estimating and Mapping Various Environmental Indicators in Breydon Water Estuary, U.K., Using Landsat TM Imagery. Estuarine, Coastal and Shelf Science, 44, pp. 589-598.

Choi, M. and Hoshi, T., 2000. Analysis on the Freshening Process of Freshening Reservoir by Desalt Fresh Water, Annual Journal of Hydraulic Engineering, JSCE, 44, pp. 1251-1256.

Torii, K. and Hoshi, T. et al., 1996. Investigation on Tidal Land Reclamation in Korea Using Satellite Image Data, Proc. of the 17th ACRS, G-4-1~6,.

Near Real Time Monitoring of Taiwan Coastal Waters – A Multiple Sensor Approach

I-I Lin and L.S. Wen
National Centre for Ocean Research, P.O. Box 23-13, Taipei 10617, Taiwan
Tel: 886-2-23655671 (*148)
Fax: 886-2-23644049
Email: linii@odb03.gcc.ntu.edu.tw

Keywords : Near Real Time, Coastal and Estuary Water Monitoring, Multiple Sensor

This research uses SEAWIFS, SPOT, and SAR images to monitor the water quality of the estuarine and surrounding coastal region of a major Taiwan river, Tan-Sue River. Estuaries link rivers with the ocean. In estuaries complex dynamic processes including chemical, physical, geological, and biological processes coexist. They are the sites where most pollutants are introduced into the ocean, especially into coastal waters. Understanding the biogeochemistry of estuarine and coastal waters is an important environmental task. However, this understanding is much hindered by the lack of synoptic and frequent observation. In this research, *in situ* sampling programme is done in conjunction with near real time reception of satellite data. Within 4 hours of data reception, images are reviewed and feature locations are informed to the cruise team to collect water samples. The study site, the Tan-Sue River estuary and the surrounding coastal waters, covers an area of about 100km square. Bi-monthly field sampling in collected sea truth data is ongoing at 20 stations at the study site. The average distance in between the stations is 10km. Sea truth data including chlorophyll-A, dissolved organic matter, and sediments, as well as other basic physical, biogeochemical parameters are collected. Sea truth data are used to develop algorithms in interpreting satellite images. SPOT images (20m spatial resolution) are used to provide detail spatial information of the distribution of pollutants. The potential and applicability of satellite remote sensing in monitoring Taiwan coastal water quality is assessed.

COASTAL ZONE ENVIRONMENT MANAGEMENT WITH EMPHASIS ON MANGROVE ECOSYSTEM, A CASE STUDY OF AO-SAWI THUNG KHLA, CHUMPHON, THAILAND

Dr. Surachai RATANASERMPONG
Ms. Dararat DISBUNCHONG

Remote Sensing Division
National Research Council of Thailand
196 Phaholyothin Rd., Chatuchak, Bangkok 10900
Tel. (66)-2-940-6997 Fax. (66)-2-579-5618
E-mail: ratana@pop.nrct.go.th
THAILAND

Mr. Thongchai CHARUPPAT
Dr. Suwit ONGSOMWANG

Royal Forest Department
Phaholyothin Rd., Chatuchak, Bangkok 10900
Tel. (66)-2-5799484
E-mail: technical5@forest.go.th
THAILAND

KEY WORDS : Mangrove ecosystem, Thailand

ABSTRACT The primary objective of the study on coastal zone environment management with emphasis on mangrove ecosystems was to identify an effective approach for sustainable mangrove forest management using Remote Sensing and GIS technology. The study was conducted by 1) assessing forest land use in 1973, 1987, 1993 and 1998 based on visual interpretation of satellite imagery at the scale of 1:50,000; 2) evaluating forest land use area and change using GIS; and 3) developing a plan for the sustainable forest land use based on additional relevant thematic data.

The major results of this study were the compilation of a relevant thematic database; assessment of forest land use in 1973, 1987, 1993 and 1998; assessment of forest distribution in 1987, 1993 and 1998 as well as the change of land use between 1987-1993 and 1993-1998 and development of a forest land use plan. The mangrove forest can be divided into three principal classes as follows : 1) class I is near to the seashore where the mud is very soft and wet. The dominant species in this class is *Avicennia alba* and *A. officinalis* 2) class II It is the are to the first class. The dominant species are *Rhizophora apiculata* and *R. mucronata.* 3) class III It is mostly consists of mixed species including *Bruguiera cylindrica, Ceriops tagal, Excoecaria agallocha* and *Xylocarpus granatum.*

INTRODUCTION

Mangrove forest is one of the most valuable coastal resources, important for its multiple economic, ecological, scientific and culture resources for present, and future generations. It is an important component of Thailand's coastal zone ecosystem. In addition, mangrove forests are utilized as a source of fuelwood and pole production, they provide a nursery and breeding ground for many commercial fish and prawn species. They also protect against coastal erosion and provide a habitat for some protected species of birds and animals.

In recent decades, the coastal zone has been subjected to the effects of a growing population and economic pressure manifested by a variety of activities such as an aquaculture, tin mining, waste disposal, construction and industrialization. Major coastal resources in Thailand, especially mangrove forest, beaches, coral reefs and marine water have been deteriorated or degraded. In addition, the area of mangrove forest in Thailand has decreased rapidly due to the expansion of shrimp farming.

In order to use coastal resources on a sustainable basis, a proper management planning process is necessary. remote sensing and GIS are the major tools for undertaking the plan. Since 1972, Thailand has used a remotely sensed satellite data for assessment of natural resources in many fields, proving that remote sensing is a useful tool for assessing and monitoring the country's coastal resources, especially mangrove forests. Mangrove forest assessment and monitoring has been conducted continuously in Thailand since 1979.

In 1990, high resolution data of Landsat-TM and SPOT-PLA, which can provide more effective information than Landsat-MSS, was used for mangrove forest land use zoning monitoring. It was found that the Landsat-TM bands 4-5-3/R-G-B with linear stretching technique can be used to differentiate mangrove forest from other vegetation and SPOT-PLA shows a better pattern for shrimp farm and built-up areas. In addition, the combination of TM4-TM5-PLA/R-G-B via digital classification can easily depict the mangrove forest zonation which corresponds to the dominant species (Ratanasermpong, S. and C. Silapathong, 1991)

Therefore the integration of remote sensing and GIS for mangrove forest management is considered as an important tool for the development of effective plans by natural resource managers and planners. The main objective of this study is to demonstrate an effective approach for sustainable mangrove forest management by using remote sensing and GIS technology.

STUDY AREA

Ao Sawi – Thung Kha is located between the latitudes 10° 15′ and 10° 30′ N and the longitudes 99° 7′ and 99° 20′ E, at the mouth of Khlong Sawi and Khlong Thung Kha, in Chumphon province on the south Eastern seaboard of Thailand. It has a total surface area of about 675 sq. km.

The study site has a tropical monsoon climate with two main seasons (wet and dry). The average annual rainfall is 2,010 mm. The peak rainfall month is in November, while the driest month is in March. The wet season is from May to January. The mean annual temperature is 26.90° C, and the highest relative humidity is in October. Tides are diurnal (one high and one low tide a day) with an average amplitude of 1.04 m. The monthly mean sea level is the highest in November and the lowest in March. The monthly discharge from the Chumporn rivers is the highest in August and the lowest in March. The monthly runoff is the highest in November.

The present land use/land cover in the study area is composed of mangrove forest, tropical evergreen forest, freshwater swamp forest, paddy field, rubber plantation, oil palm plantation, mixed orchard, coconut plantation, villages, wetland, wasteland, water bodies and shrimp farms.

METHODOLOGY

The main tasks were to classify the forest land use in 1987, 1993 and 1998 based on visual interpretation of satellite imageries at the scale of 1:50,000. The assessment of land use/land cover and change was then conducted using GIS. Finally, the proposal for sustainable forest land use plan was developed based on extracted and relevant thematic data. A schematic flowchart methodology is shown in Figure 1.

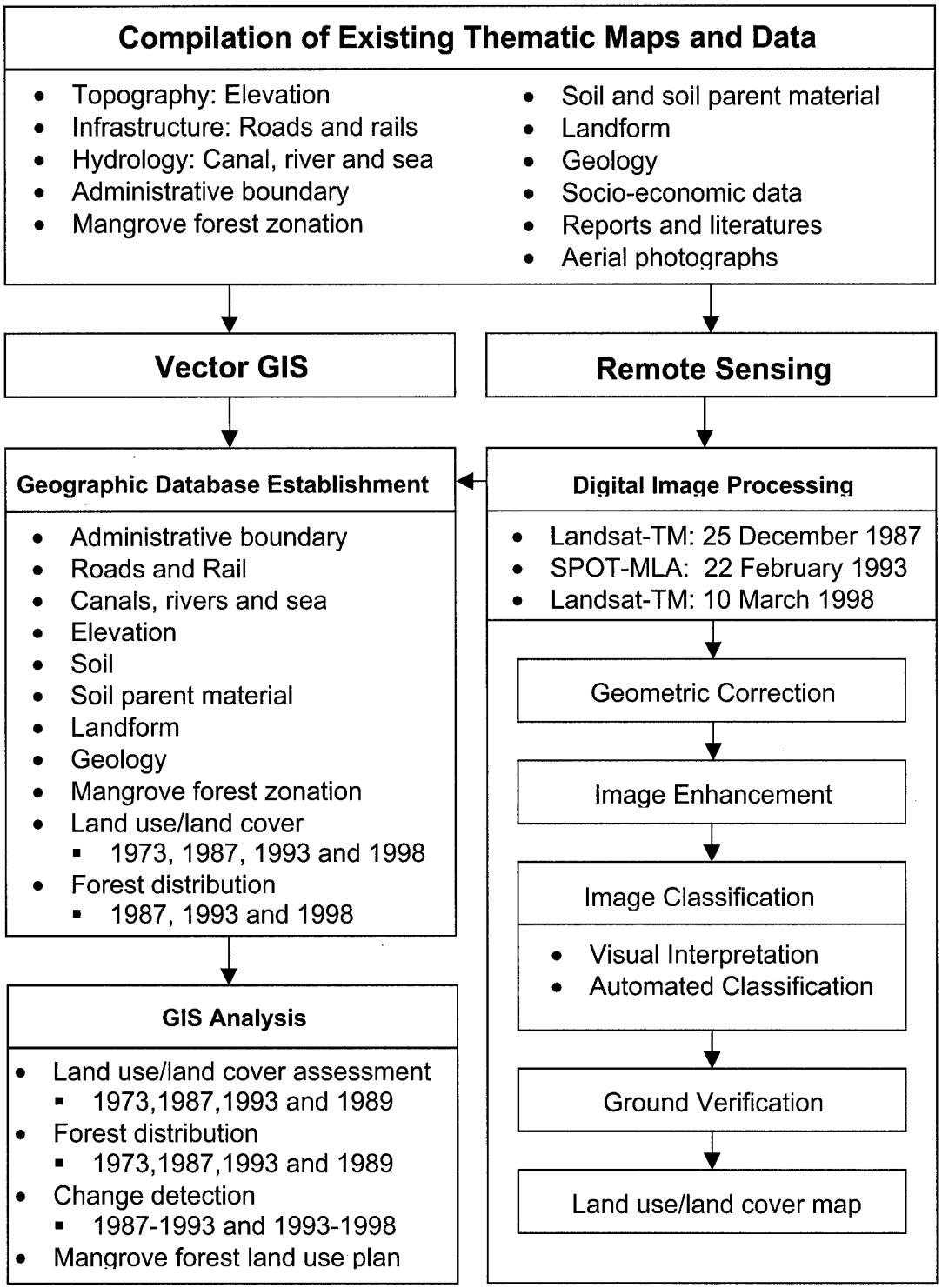


Figure 1 Schematic flowchart of the methodology

ANALYSIS OF GIS

Analysis of GIS was performed under vector GIS of PC Arc/Info. Four main outputs were derived based on the complied and extracted geographic databases as follows:

(1) land use and land cover in 1973, 1987, 1993 and 1998;
(2) forest distribution in 1993, 1987, 1993 and 1998;
(3) change in land use and land cover between 1987-1993 and 1993-1998;

The basic techniques employed in the GIS analysis were overlay operation where two layers were input to extract a new layer. For example, for change in land use and land cover change 1987 and 1993, "the two inputs layers were land use and land cover in 1987 and 1993". The new layer was " change of land use and land cover during 1987 and 1993".

RESULTS

The major results are the compilation of relevant thematic databases, assessment of forest land use and forest distribution in 1973, 1987, 1993 and 1998, as well as change in land use and land cover between 1987-1993 and 1993-1998 and development of a proposed forest land use plan.

Assessment of land use/land cover The land use and land cover categories in 1987, 1993 and 1998 were extracted by visual interpretation of satellite images at a scale of 1:50,000. Categories consist of (1) agriculture area; (2) built-up area; (3) forest area; (4) water bodies; (5) wasteland; (6) wetland and (7) shrimp farms. For land use and land cover categories in 1973 directly interpreted from a topographic map at a scale of 1: 50,000 are composed of (1) agriculture area (2) built-up area (3) forest area (4) water bodies (5) wasteland and (6) wetland. The components of land use and land cover in 1973, 1987, 1993 and 1998 are summarized and compared as shown in Table 1.

Table 1 Comparison of land use and land cover change

Land use/Land cover Classes	*Changed area in ha.*		
	1973-1987	*1987-1993*	*1993-1998*
Agriculture area	10,050.95	-1,752.34	-973.92
Built-up area	436.56	762.70	-7.94
Forest area	-13,785.30	-1,976.15	-237.63
Water bodies	-358.14	25.25	-86.64
Wasteland	1,944.85	721.40	845.99
Wetland	-63.81	0.00	0.00
Shrimp farm	1,774.89	2,219.14	460.15

FOREST DISTRIBUTION

Based on visual interpretation of satellite imageries at the scale 1:50,000, forest area was further classified into three classes according to the their signature appearance on the image and their characteristics. Major forest types are mangrove, evergreen and freshwater swamp forest. The distributions of forest in 1973, 1987, 1993, 1998 . In addition, mangrove forests are further classified based on crown cover into three classes, namely mangrove with more than 75 % coverage, mangrove with 50-75 % coverage and mangrove with less than 50 % coverage.

The component of forest distribution in 1987, 1993 and 1998 are summarized and compared as shown in Table 2. The characteristics and change of forest classes are described as follows:

- **Mangrove with > 75 % coverage.** These mangrove forests mostly consist of *Rhizophora apiculata* and *R. mucronata* situated along the river channels and behind the pioneer species zone(Figure 2). The extent of mangrove forest with density of more than 75 percent increased during 1987 to 1998 and covered an area of 290, 488 and 519 ha, in 1987, 1993 and 1989, respectively. The main cause of increasing area is natural succession and reforestation.

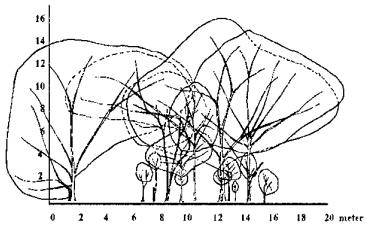


Figure 2 Pioneer species profile

- **Mangrove with 50-75 % coverage.** These mangrove forests mostly consist of pioneer species, *Avicennia alba* and *A. officinalis* situated on the outer fringe facing the sea (Figure 3). The extent of mangrove with density more between 50 to 75 percent decreased slightly during 1987 to 1998. These areas covered an area of 1,267, 1,140 and 1,091 ha, in 1987, 1993 and 1989, respectively. The main cause of decrease is natural succession by *Rhizophora spp.* and die back by sand deposit.

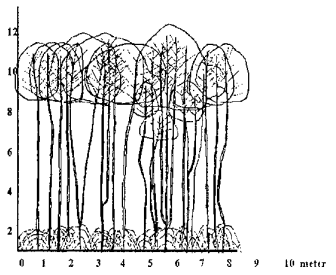


Figure 3 Rhizophora species profile

- **Mangrove with < 50 % coverage.** These mangrove forests mostly consist of mixed species including *Bruguiera cylindrica, Ceriops tagal, Excoecaria agallocha, Ficus sp., Heritiera littoralis, Hibiscus tiliaceus, Intsia bijuga, Xylocarpus granatum*, and *X. moluccensis* situated behind the *Rhizophora* species zone (Figure 4). The extent of mangrove with density of less than 50 percent decreased from 1987 to 1998, covering an area of 3,846, 1,900 and 1,696 ha, in 1987, 1993 and 1989, respectively. The main cause the decrease is the expansion of shrimp farms.

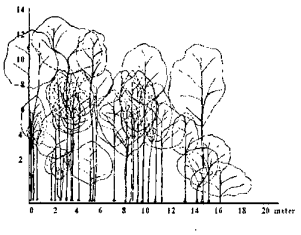


Figure 3 Mixed species profile

- **Evergreen forest.** Evergreen forests situated on the mountainous area decreased from 1987 to 1998. These forests covered an area of 2,691, 2,583 and 2,565 ha, in 1987, 1993 and 1989, respectively. The main cause of the decrease is the expansion of agriculture areas.

- **Freshwater swamp forest.** This forest mostly consists of *Melaleuca leucadendra* situated on flat areas behind the mangrove forest. The extent of swamp forest increased during 1987 to 1993 and decreased between 1993 and 1998. This forest type covered an area of 517, 551 and 527 ha, in 1987, 1993 and 1989, respectively.

Table 2 Comparison of forest distribution change between 1987 and 1998

Forest Distribution Classes	***Changed area in ha.***	
	1993-1987	***1993-1998***
Mangrove: > 75 % coverage	197.68	31.49
Mangrove: 50-75 % coverage	-127.31	-49.13
Mangrove: < 50 % coverage	-1,946.10	-204.45
Tropical evergreen forest	-108.05	-17.62
Freshwater swamp forest	34.06	-24.20
Water bodies	25.25	-86.63
Other area	1,924.47	350.55

CONCLUSION

In conclusion remote sensing appears to be a significant tool for assessment and monitoring of coastal zone resources, especially mangrove forest. In addition, planning and management of forest land use is easily and effectively conducted using GIS. However, the integration of remote sensing and GIS for the development of mangrove forest management plans by natural resource managers and planners is necessary.

REFERENCES

Ratanasermpong, S. and C. Silapathong. 1990. ***Mangrove Forest Zonation by Using High Resolution Satellite Data***. Proceeding of the 11th Asian Conference on Remote Sensing, Guangzhou, China. Volume 1, 6 p.

National Research of Thailand. 1991. ***Remote Sensing and Mangroves Project (Thailand)***. Final Report. IDRC/NRCT/RFD. 183 p.

Ongsomwang, S. 1998. ***Forest Potential Assessment by Using GIS***. Forest Resources Assessment Division, Forest Research Office, Royal Forest Department, Bangkok. 69 p. (In Thai).

The 21st Asian Conference on Remote Sensing
December 4-8, 2000 Taipei, TAIWAN

Application of Remote Sensing with LANDSAT TM Data for Management and Control of Mangrove Forest - A Case Study in Okinawa -

Kazuhiro Sato* and Munetake Kanetomi **

* : College of Agriculture, University of the Ryukyus,
Senbaru 1, Nishihara, Okinawa 903-0129, Japan
Tel.81-98-895-8792, Fax. 81-98-895-8734, E-mail: sato4408@agr.u-ryukyu.ac.jp
** : Air-Graph Co. Ltd., Kamiigusa 1749-1, Kawashima,
Hiki, Saitama 350-0152, Japan
Tel. 81-492-97-7410, Fax. 81-492-97-7414 , E-mail:aan01610@nyc.odn.ne.jp

Key Words: Mangrove forest, Sub-compartments, Stand parameters, Quantitative information

Abstract: We have investigated the application of remote sensing for management and control of mangrove forest. In the process, a mask procedure had been suggested to separate whole area into three large categories of land area, mangrove forest and waters. It was effective to avoid misclassification occurred among three categories in case of whole scene classification, and it was also necessary for estimation of mangrove stand parameters with the regression equations among them and satellite data. A qualitative and quantitative two-ply expression had been tried, for example it was overlaid print of black mark corresponding species on colored map corresponding classified estimated growing stock.
In this paper, we tried to sum up total growing stock in each sub-compartment and to extract properties for the quantitative stand structure of them by overlaying masks on two Okinawan mangrove forests. Such information should be useful for sustainable management and control of mangrove forest.

1. Introduction

We have investigated the application of remote sensing for management and control of mangrove forest that has difficult conditions for field survey. In the process, a mask procedure had been suggested to separate whole area into three large categories of land area, mangrove forest and waters (Sato K. *et al.*, 1997). The intents were to avoid misclassification occurred among the categories in case of whole scene classification, and to estimate quantitative information of mangrove forest based on correlation and regression analysis between satellite data and stand parameters of it. It was succeeded to extract only mangrove forest from the whole scene by the mask procedure. The correlation and regression analysis were done among remote sensing data and stand parameters obtained from complete enumeration at 14 sample plots in southern Okinawa. Remote sensing data were TM data of Landsat 5 and indexes calculated as combination with data of bands (Dwi S. *et al.*, 1997a, 1997b). Digital value of band 4, indexes of B1/B4, B4/(B3+B2), (B4-B3)/(B4+B3) and so on showed significantly high correlation coefficients with some stand parameters of mean DBH(diameter at breast height), mean tree height, mean crown size and growing stock and so on. The mask procedure was effective for the estimation of stand parameters by substitution of remote sensing data in the regression equations. As it became possible to make a data set to correspond only mangrove forest, we tried to apply this way to two mangrove forests in Okinawa, and it was effective to show multiply distribution

of species and resources of mangrove (Kanetomi M. *et al.*, 1998). By this way, it becomes possible to sum up the amount of resources particularly with species or mixture ratio of mangrove forest. This matter increases the usefulness of remote sensing for sustainable management and control of mangrove forest.
Generally the forest is controlled as compartments sectionalized according to topography and a compartment is controlled as sub-compartments according to forest type, site productivity, forest land use and land parcel. In this paper, some trials were described as a case study that were each particular sum of the amount of resources with main tree species or mixture ratio in each sub-compartment and sum of them as whole mangrove forest, and expression as figures of frequency distribution of tree height and DBH for each sub-compartment. Two mangrove forests examined here are located in southern Okinawa. The boundaries were not actual, they were assumed and drawn by the authors for this case study. By this examination, it became clear that this way was useful to grasp quantitative information and properties of stand structure for each sub-compartment of mangrove forest.

2. Data and method

Data used in this paper was same with the data in a series of our examination to apply remote sensing for mangrove forest. Satellite data was TM data of Landsat 5 accumulated May 16th, 1994 and stand parameters were obtained from complete enumeration at 14 sample plots in Ishigaki Is and Iriomote Is., 11 points in May 1995 and 3 points in February 1996. All digital values of band 4 in the data set corresponded to only mangrove forest produced through the mask procedure, were substituted in the regression equation of Y=6.18X-354.2 (r=0.878) between data of band 4 and growing stock. The distribution of main mangrove species and mixed stand by maximum likelihood method was overlaid on the distribution map of estimated growing stock with the above equation as a multiple expression. Quoted and arranged two multiple maps were shown as Figure 1.
Assumed and drawn boundaries were overlaid on the imagery of band 4 and pixels inside a sub-compartment were painted with black or given zero by the reference of the boundaries. Outside pixels were painted white or given 255. By this way, masks were separately made for each sub-compartment. A data set of a sub-compartment was obtained by addition of this mask and data of band 4. Although stand parameters can be estimated with some indexes combined bands, in this paper digital value of band 4 was substituted in regression equations for estimation of growing stock, mean of DBH and tree height. The regression equations were shown with the correlation coefficient in Table 1. In forestry, growing stock of every small stand is expressed as trunk volume per hectare for the convenience of comparison among many stands. Here, growing stock of 1 pixel area was calculated from estimated value multiplied by 9/100 for conversion from per $10000m^2$ to per $900m^2$.

Stand parameter as Y	Regression equation	Correlation Coefficient	Unit for one pixel
Growing stock	Y=6.18X-354.2	0.878	$(9/100)m^3$
Mean DBH	Y=0.1137exp(0.0532X)	0.954	cm
Mean tree height	Y=0.264X-15.4	0.958	m

Remarks Y : stand parameter, X : digital value of band 4, correlation coefficient : significant at 0.1% level (>0.78)

Table 1. Regression equations used in this examination
(arranged Dwi S. *et al.*, 1997a)

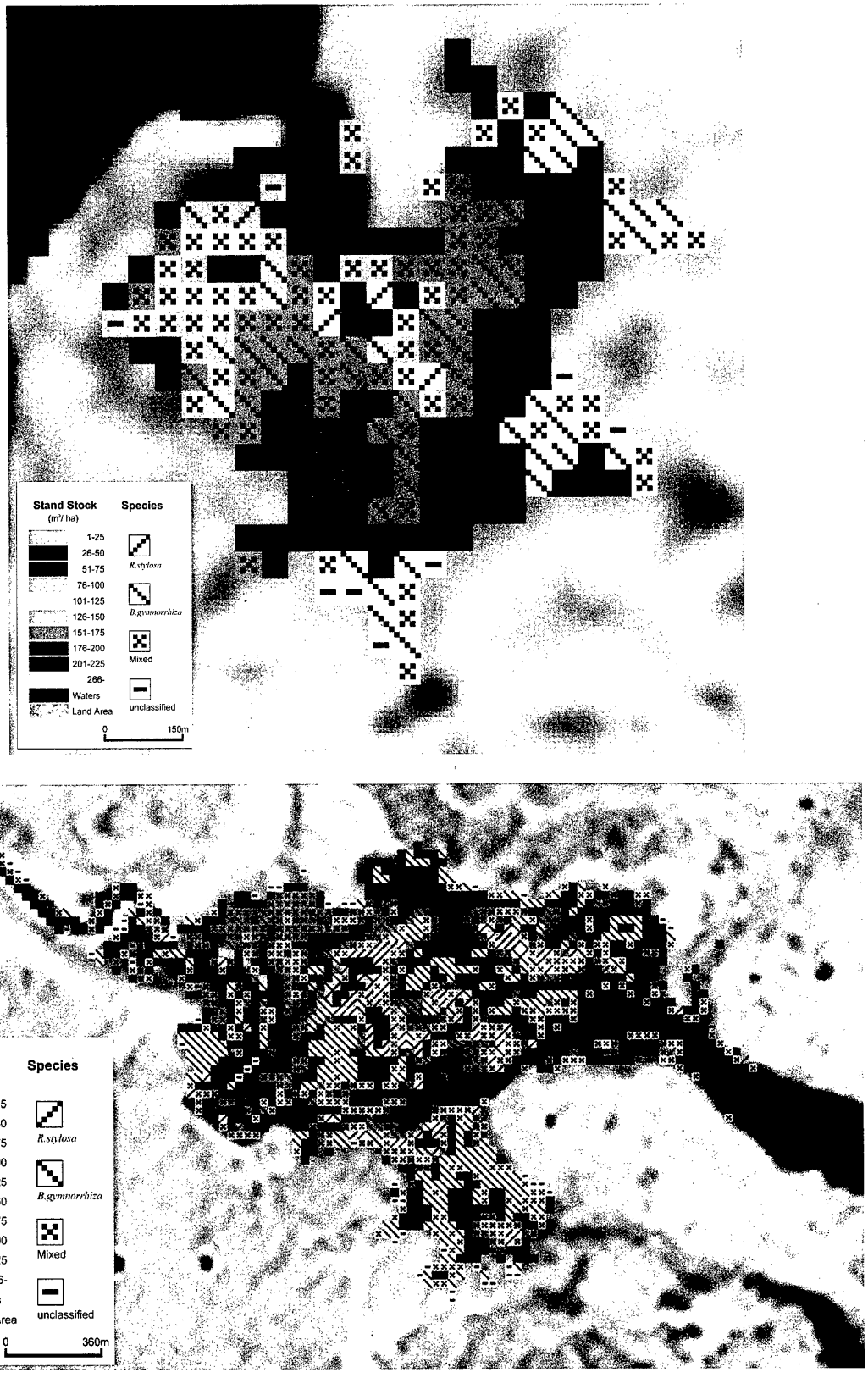


Figure 1. Multiple expression for two mangrove forests (above: Fukido-gawa River, Ishigaki Is. And below: Nakama-gawa River, Iriomote Is.)

(arranged Kanetomi M. *et al.* ,1998)

3. Results and discussion

It was easy to make black pixels as the mask for each sub-compartment by utilization of suitable application software for painting, smearing and drawing after overlay sub-compartment map to an imagery of remote sensing data. Although this procedure was done by hand works here, it was considered that program was not so complicate to make the mask automatically. The procedure to make masks and masks for 4 sub-compartments of mangrove forest in the mouth of Fukido-gawa River, were shown in Figure 2. The data sets were obtained by overlaying each

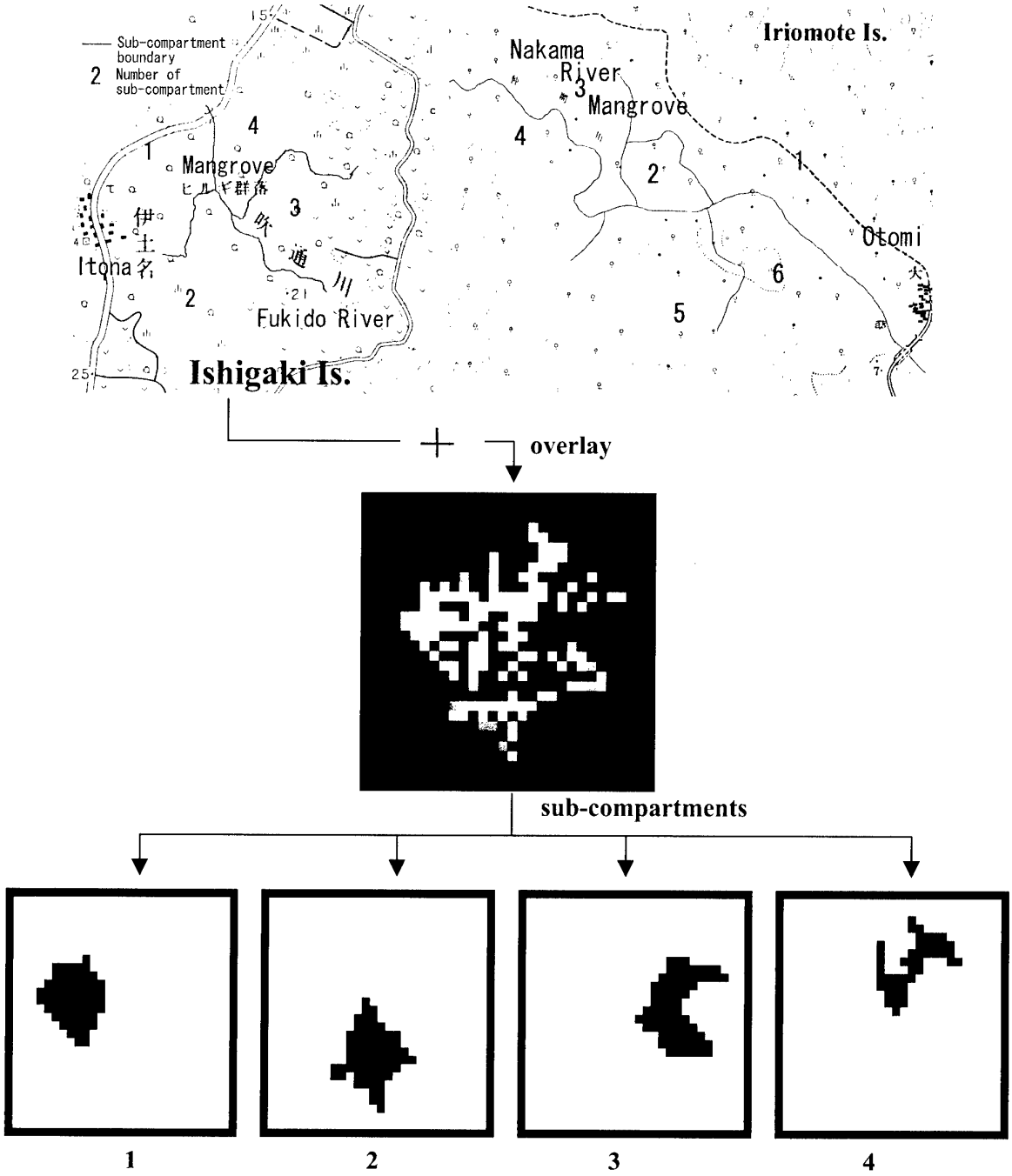


Figure 2. Boundaries of sub-compartments for two mangrove forests and process to make masks for each sub-compartment of Fukido-gawa River

Location	Sub-compartment	Growing stock (m^3)					Area (ha)
		R. s.	*B. g.*	mixed	uncl.	total	
Nakama-gawa River (Iriomote Is.)	1	220.7	4,473.9	3,810.8	253.2	8,758.6	47.52
	2	555.8	2,399.2	1,983.6	0.0	4,938.6	33.21
	3	18.4	1,260.7	3,254.6	276.2	4,809.9	27.00
	4	105.8	1,030.6	1,537.8	374.7	3,048.9	18.72
	5	170.8	3,177.5	2,597.4	594.9	6,540.5	34.02
	6	14.3	52.3	683.0	0.0	749.6	4.95
total		1,085.8	12,394.2	13,867.2	1,499.0	28,846.1	165.42
Fukido-gawa River (Ishigaki Is.)	1	38.2	219.9	481.0	49.4	788.4	5.58
	2	5.4	537.3	481.4	122.4	1,146.5	5.94
	3	9.3	855.4	427.6	69.0	1,361.2	6.48
	4	11.0	174.2	524.5	0.0	709.6	4.05
total		63.9	1,786.8	1,914.5	240.8	4,005.7	22.05

Remarks *R. s.*: stand with dominant species of *Rhizophora stylosa*, *B. g.*: stand with main species of *Bruguiera gymnorrhiza*, mixed : mixed stand with *R. stylosa* and *B. gymnorrhiza*, uncl. : unclassified stand

Table 2. Sum of growing stock of two species and mixed stand in each sub-compartment and whole forest for two mangrove forests in Okinawa

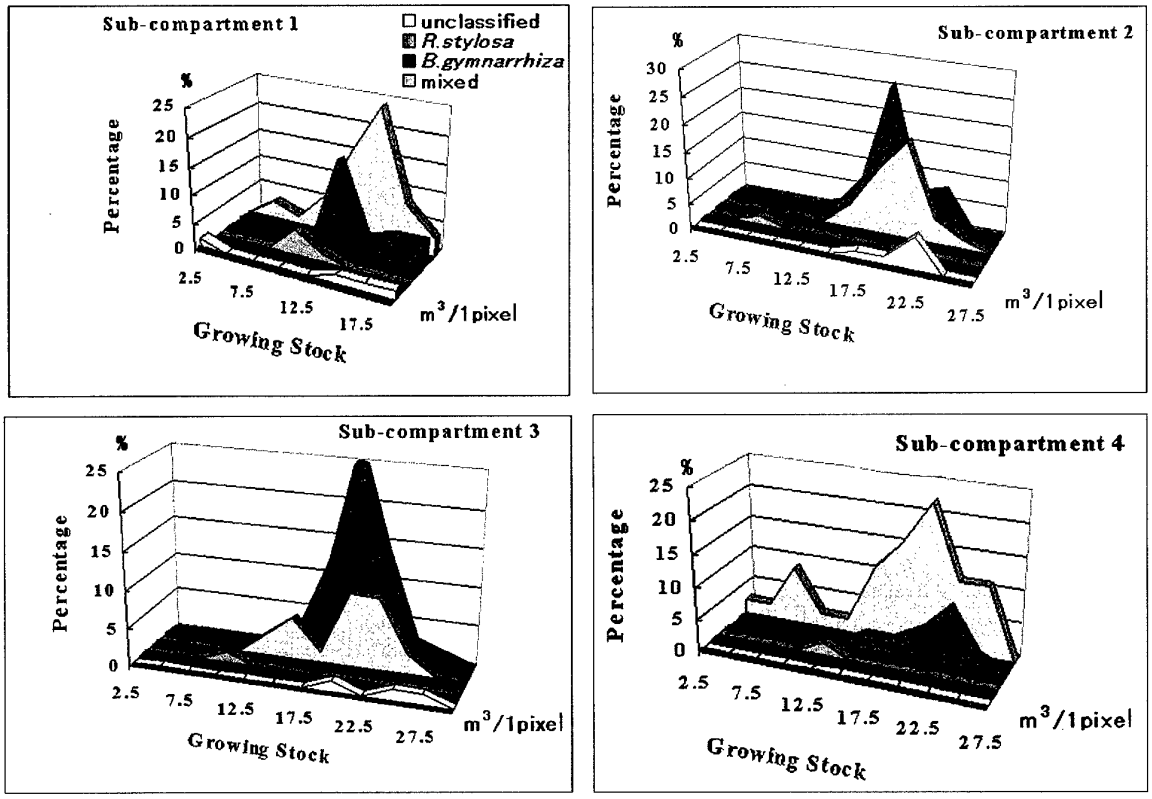


Figure 3. Frequency distribution figures for growing stock in each pixel (Fukido-gawa R.)

mask on remote sensing data. The all data were substituted in the regression equation for growing stock in serial order, and the estimated values were separated with classified main species or mixed stand and summed up separately. For mean of DBH and tree height, same data were substituted in each regression equation in like manner and frequency distribution figures

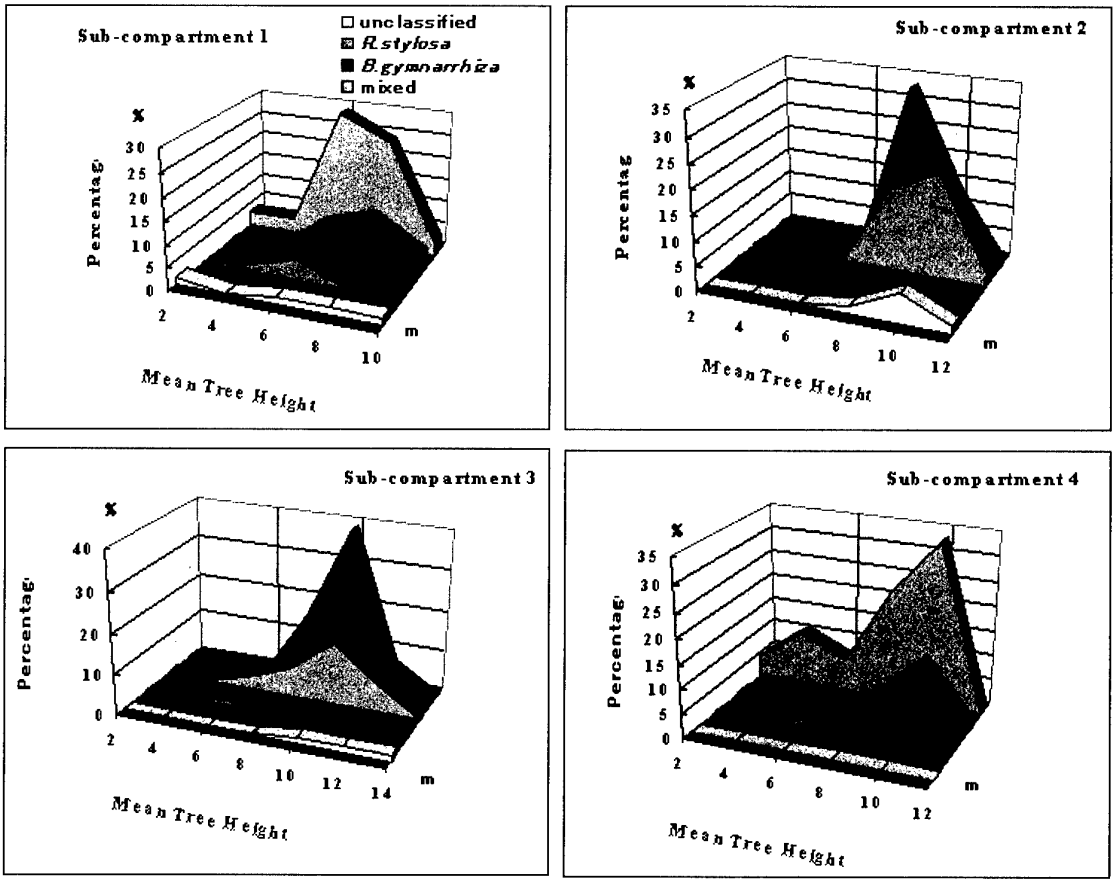


Figure 4. Frequency distribution figures for mean tree height in each pixel (ditto)

were drawn by arrangement of estimated values. The results were shown as Table 2 and Figure 3. Figures for DBH were omitted, as the tendency was similar with the figures for mean tree height in each pixel.

Although the detail in Table 2, Figure 3 and 4 were not investigated from the point of forestry view, the information in them should be useful for management and control of mangrove forest.

4. Conclusion

Results mentioned above clearly showed usefulness of remote sensing for management and control of mangrove forest. Significant high correlation between data of band 4 and growing stock as total of trunk volume suggests possibility of that the amount of absorbed and fixed carbon dioxide also can be estimated by remote sensing. Because it should be converted from the amount of biomass as the total of all parts mangrove estimated by remote sensing data.

References

Dwi S. , Sato K. & Kohda Y. : 1997a, Relationships Between TM Data of Landsat 5 and Stand Parameters on Mangrove Forest in Okinawa, Jour. of Japan Soci. of Photog. and RS, 36 (2), pp.4-12

Dwi S. , Sato K & Kohda Y. : 1997b, Relationships Between Calculated Indexes from TM Data of Landsat 5 and Stand Parameters on Mangrove Forest in Okinawa, Jour. of Japan Soci.of Photog.and RS, 36 (3), pp.6-12

Kanetomi M. , Sato K. & Yamauchi T. : 1998, Expression of Qualitative and Quantitative Information on Mangrove Forest in Okinawa, Proceedings of the 19th Asian Conference on Remote Sensing, Q-13-1-6

Sato K. , Nakajima M. & Hoshi T. : 1997, Conception Qualitative and Quantitative Classification of Mangrove Forest with TM Data of Landsat 5, Proceedings of the 18th Asian Conference on Remote Sensing, G-6-1-6

OBSERVING INTERTIDAL ZONES USING SATELLITE IMAGERY

Rigel Hian Dee LEOW, Yihan TAN, Chee Yuen WAN
Raffles Institution
Raffles Institution Lane
Singapore 575954
SINGAPORE

Christian MELSHEIMER
Centre for Remote Imaging, Sensing and Processing (CRISP)
Block S17, Level 2, Faculty of Science
National University of Singapore
Lower Kent Ridge Road
Singapore 119260
Tel.: (65)-8746587 Fax: (65)-7757717
E-mail: crscm@nus.edu.sg
SINGAPORE

KEY WORDS: Intertidal Zone, SPOT, ERS

ABSTRACT: The strip of land exposed at low tide and submerged at high tide is defined as the intertidal zone. We have studied the intertidal zone of the headland to the west of Rupat Island, Sumatra, using European Remote-Sensing Satellite (ERS) and Système Pour l'Observation de la Terre (SPOT) satellite images. The analysis of images of that area from the year 1996 to 2000 revealed a number of differences and changes that took place throughout that period of time. Most notable were the increase in vegetation on the coastline over time and development and growth of a new island from deposited sediments. Such observations can possibly be used to update maps.

1. INTRODUCTION

The intertidal zone is the coastal transition region between the permanently exposed land surface on one side and the submerged region on the other side. It is alternately exposed and submerged during each tidal cycle. The intertidal zone is subjected to ocean waves and tidal currents and hence can show rapid changes due to erosion and sedimentation. The aim of this paper is to monitor changes in intertidal zones using multitemporal satellite imagery. By comparing the intertidal zones delineated in the satellite images with those marked in existing maps, the accuracy of the existing maps can be assessed, and if necessary, the maps can be updated using information derived from the satellite imagery.

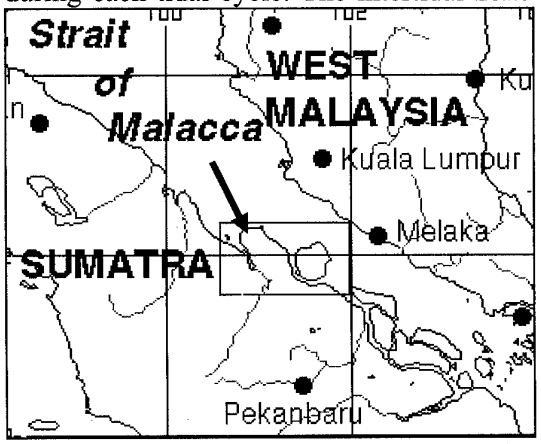


Figure 1: Map of the Straits of Malacca and the surrounding land masses. The arrow marks the location of the area studied.

Our test area is the intertidal zone around a headland near Rupat Island, on the eastern coast of the Riau Province in Sumatra, Indonesia (see Figure 1 and Figure 2). The intertidal zone here is relatively large in area and is easily visible in the high resolution SPOT and ERS SAR images. The

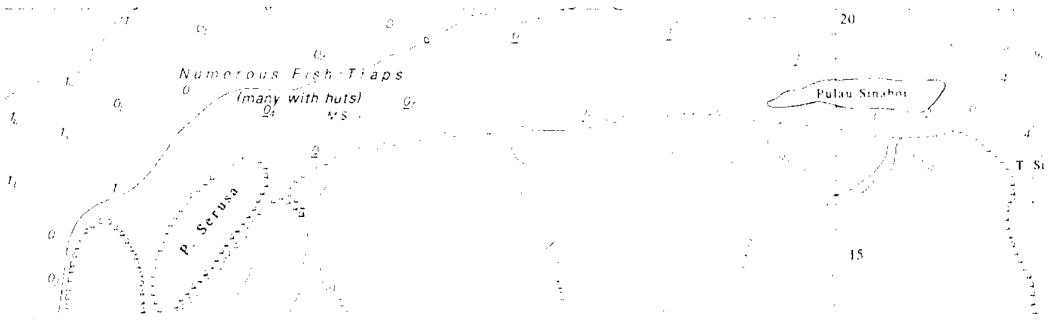


Figure 2: Map of the studied area (adapted from: Hydrographer of the Navy, 1998, Admiralty Charts) on the east coast of Sumatra, Indonesia. Green represents intertidal zone at tide level 0.0 m while yellow represents land.

images used were acquired by the SPOT satellites (SPOT=Satellite Pour l'Observation de la Terre) and by the ERS satellites (ERS=European Remote Sensing sattelite) within a four-year period from 1996 to 2000. Only images acquired near low-tides were used. Tidal levels as given in the figure captions were derived from tide tables (Hydrographer of the Navy, 1996,1997, 1998; Hyddrographic Branch, 1999, 2000). All the images were geometrically corrected and co-registered using prominent land features as ground control points.

2. SPOT AND ERS IMAGES

The satellites ERS-1 and ERS-2 (Kramer 1996) of the European Space Agency (ESA) orbit the earth at an altitude of 780 km and among other sensors carry a synthetic aperture radar (SAR). The SAR operates at a frequency of 5.3 GHz (C-band microwaves) and has a ground resolution of 25 m. It measures the intensity of the microwaves that are backscattered from the ground. This backscatter intensity depends strongly on the roughness of the ground surface: The rougher the surface, the stronger the backscatter intensity, and the brighter the SAR image.
The SPOT satellites (Kramer 1996) of the Centre National d'Etudes Spatiales (CNES) orbit the earth at an altitude of 832 km and each carry two High Resolution Visible scanners (HRV). The HRV collects radiance data in optical and near-infrared wavelengths, either in a broad-band (panchromatic) mode with a ground resolution of 10 m, or in a three-band (multispectral) mode with a ground resolution of 20 m. Here we only consider images taken in multispectral mode. The three spectral bands are 500-590 nm (band 1, roughly: green visible light), 610-680 nm (band 2, roughly: red visible light), and 790-890 nm (band 3, near infrared). We use the common way of displaying the multispectral images as RGB images with band 3 as R, band 2 as G and band 1 as B. Since plants strongly reflect NIR light, vegetation looks red in the images. In contrast, the sea, which absorbs NIR light almost totally, appears in hues of blue and green.

3. OBSERVATIONS AND DISCUSSION

3.1 ERS SAR and SPOT HRV Images of the Intertidal Zone

The intertidal zone in the studied area consists of sand and mud deposits. The landward portion may be covered by mangrove vegetation while the remaining portion is bare (tidal sand and mud flats).
In ERS SAR images (e.g Figure 3), the part of the intertidal zone that is not covered by vegetation (i.e. the tidal flats) looks very dark as it consists of mud and sand and therefore has a smooth surface. In contrast, areas covered by vegetation and wind-roughened water surfaces have significantly higher radar backscatter and appear brighter in ERS SAR images. Under very low wind or calm conditions, the water surface appears very dark and cannot be easily distinguished from sand and mud flats. Note that branched bright lines are visible in some areas

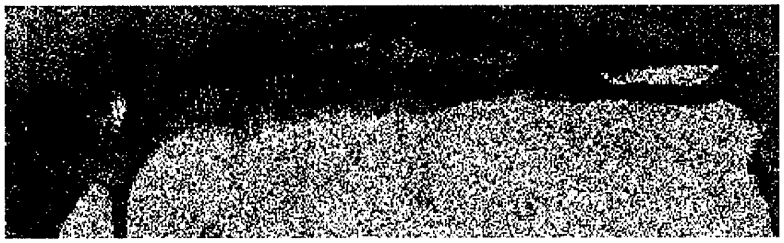


Figure 3: ERS SAR image, 15 Apr 1996, 22:56:10 GMT, Tide Level 0.81m(0.5h after low tide). Image Size 57 km x 18 km (© ESA 1996)



Figure 4: SPOT image, 7 Oct 1999, 04:04:45 GMT, Tide Level 0.85m (1h after low tide). Image Size 57km x 18km (© CNES 1999)

(see Figure 7 and Figure 6). They mark channels and creeks that drain the intertidal zone when the tide is going down. The current creates roughness (ripples) on the sand and mud, thereby increasing the radar backscatter.

In SPOT HRV images, the part of the intertidal zone that is not covered by vegetation (i.e. the tidal flats) appears in shades of greyish brown (see Figure 4). The seaward edge of the intertidal zone is very distinct whenever sun glitter causes the sea to appear brighter. In other cases, the edge may be less distinct. A zoom into the SPOT image (see Figure 5) shows that the tidal flat area has two distinct parts of different colours, light grey and dark grey. The part of the intertidal zone nearer the land is mostly light grey, while the part of the intertidal zone near the sea is mostly dark grey. This happens because the soil nearer the land has been exposed to the air for a longer time, so it is drier and looks lighter than the wet part. Another factor could be that different types and grainsizes of sediments are deposited at different zones.

Note that the landward part of the intertidal zone, when covered by mangrove vegetation, cannot be easily distinguished from vegetation on dry land, neither on ERS SAR nor on SPOT HRV images. Thus what seems to be the landward edge of the intertidal zone is actually the seaward edge of the mangrove vegetation.



Figure 5: SPOT image (subset from Figure 4), 7 Oct 1999, 04:04:45 GMT, Tide Level 0.85m (1h after low tide) Image Size 20 km x 5 km (© CNES 1999)

3.2 Difference in the Shape of the Intertidal Zone

Comparing Figure 7 and Figure 6, there appears to be a change in shape of the intertidal zone. The intertidal zone in the 1996 image (Figure 7) has a smooth seaward edge. In the image taken in 2000 (Figure 6), however, the seaward edge of the intertidal zone is jagged and irregular. A possible cause is a difference in water level in connection with the topography of the intertidal zone. After low water, the lower regions such as channels and creeks get flooded first, resulting in the irregular shape at intermediate tide levels. Another possible cause is that during the 4 years of time difference, waves, currents and sedimentation have actually modified the shape of the intertidal zone.



Figure 7: ERS SAR image, 15 Apr 1996, 22:56:10 GMT, Tide Level 0.81m (0.5h after low tide) Image Size 18 km x 4.5 km (© ESA 1996)

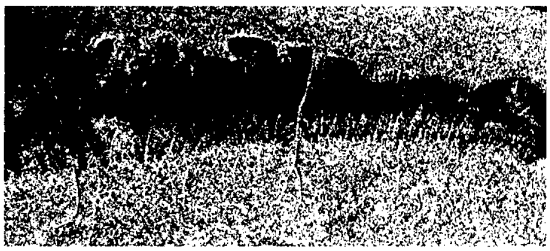


Figure 6: ERS SAR image, 20 Jan 2000, 10:37:51 GMT, Tide Level 0.13m, (10 min before low tide) Image Size 18 km x 4.5 km (© ESA 2000)



Figure 8: SPOT image, 20 Apr 1999, 04:01:46 GMT, Tide Level 2.55m (3h before low tide) Image Size 11 km x 4.8 km (© CNES 1999)

3.3. Extension of Vegetation Along the Northern Coast Over Time

In the SPOT image in Figure 8 (from 1999), the boundary of the vegetation (mangrove) along the coast is clearly visible as the line where the red portion (vegetation) meets the brownish-grey (tidal flats). In the ERS SAR image in Figure 6 (from 2000), there is a slightly curved and distinct line along the northern coast, separating lighter grey (below) from darker grey (above). It roughly coincides with the vegetation boundary found in the above-mentioned SPOT image (Figure 8). Note that the water level at the acquisition time of this SPOT image was quite high (3 hours before low tide). Therefore the stretch of tidal flats visible on that image is much narrower here than in the ERS SAR images (Figure 7 and 7). The vegetation boundary in the image in Figure 7 (from 1996) has a different shape, it is slightly concave. Comparison with the ERS SAR image in Figure 6 (from 2000) shows that the vegetation (probably mangrove) has actually extended seaward within the 4 years.

3.4. Formation of New Island with Vegetation

There seems to be a new island forming between two already existing islands, Pulau Serusa and Pulau Berkey, near the estuary of the Rokan river at the western end of the studied area. According to images taken of that area from 1996 to 1999, what was an offshore intertidal zone in 1996 (see Figure 9) has slowly become a small island in 1999 (see Figure 10).
There are to possible causes: Either (1) the deposition of sediments has increased over the years,



Figure 9: SPOT image, 19 Jul 1996, 03:55:14 GMT, Tide Level 1.68m (2h before low tide) Image Size 5 km x 6 km (© CNES 1996)



Figure 10: SPOT image (subset from Figure 4), 7 Oct 1999, 04:04:45 GMT, Tide Level 0.85m (1h after low tide) Image Size 5 km x 6 km (© CNES 1999)

possibly because of human activity, e.g. deforestation and land clearing upstream, or (2) the erosion has decreased. As the area is silted, vegetation grows on the intertidal zone and consolidates is until it becomes stable and eventually permanently emerges from the water.

3.5. Absence of Intertidal Zone East of Sinaboi Island



Figure 11: ERS SAR image, 20 January 2000, 03:37:51 GMT, Tide Level 0.13m (10min before low tide) Image Size 5 km x 3 km (© ESA 2000)

The SPOT image in Figure 11 shows that a wide intertidal zone only occurs along the seaward side of the western tip of the island Pulau Sinaboi. This suggests that the eastern part of the island is apparently more sheltered from the strong currents in the Straits of Malacca than the western part. Furthermore, the image suggests that apparently there is a strong current in the channel between the island, with the main current direction going towards the west: Whereas there are no significant tidal flats at the banks of that channel, there are extensive tidal flats beyond the western opening of the channel (where the current spreads out and loses its energy). Note also that the extent and shape of the intertidal zone on the map (Figure 2) does not correspond with the extent and shape of the intertidal zone on the image (Figure 11)

4. SUMMARY AND CONCLUSIONS

This study has shown that ERS SAR as well as SPOT HRV multispectral images can be used for observing intertidal flats. SPOT HRV multispectral images have the advantage of clearly showing vegetation, whereas ERS SAR images have the advantage of not being affected by cloud cover, as the microwaves penetrate clouds.

Several changes in the intertidal zone of the study area were observed to have taken place during the four-year period. In one area, the vegetation (probably mangroves) along the coast has extended its boundary towards the sea. In another area, the low-tide coastline has changed its shape from smooth to jagged and irregular. A new island with vegetation growth has been observed to form between two existing islands.

By comparing the intertidal zones delineated in the satellite images with those marked in existing maps, the accuracy of the existing maps can be assessed and if necessary, the maps can be updated using information derived from the satellite imagery.

ACKNOWLEDGMENTS

The first three authors of this paper (R. H. D. Leow, Y. Tan, and C. Y. Wan) are secondary school students at the Raffles Institution, Singapore. This study was performed while they were attached to CRISP, under the supervision of C. Melsheimer, in the framework of the Science Mentorship Program of the Gifted Education Branch, Ministry of Education, Singapore.

REFERENCES

Hydrographer of the Navy 1998. Chart of Malacca Strait – Port Klang to Melaka (Fifth Edition). Admiralty Charts and Publications 1998.

Hydrographer of the Navy 1996, 1997, 1998. Admiralty Tide Tables Atlantic and Indian Oceans 1996, 1997, 1998 (Volume 2).

Hydrographic Branch, Royal Malaysian Navy 1999, 2000. Tide Tables Malaysia 1999, 2000 (Volume 1).

Kramer, H.J., 1996. Observation of the Earth and Its Environment – Survey of Missions and Sensors (Third Enlarged Edition). Springer-Verlag Berlin Heidelberg, Germany.

CORAL REEF ECOSYSTEM CHANGE DETECTION BASED ON SPATIAL AUTOCORRELATION OF MULTISPECTRAL SATELLITE DATA[1]

Heather Holden
Department of Geography
National University of Singapore
(65) 874-6135 (tel.), (65) 777-3091 (fax) heather@nus.edu.sg

Chris Derksen, Ellsworth LeDrew
Waterloo Laboratory for Earth Observations
University of Waterloo, Canada

KEYWORDS: spatial autocorrelation, coral reef monitoring, multispectral discrimination

ABSTRACT

Rather than attempt to remotely identify specific benthic habitats with similar optical properties, a more appropriate use of available satellite technology may be to examine benthic homogeneity of a coral reef ecosystem with the hypothesis that a healthy reef will display great heterogeneity, but a dead algae-covered reef will be relatively homogeneous. Such an approach to ecosystem analysis could prove to be efficient with respect to time, human resources, and data storage, and would produce results that could be directly applied to a realistic management scheme with "minimal regrets". A measure of spatial autocorrelation, the Getis Statistic, used in a case study of SPOT imagery shows potential in evaluating the well-being of a coral reef ecosystem.

INTRODUCTION

Over the past decade, there have been increased efforts to establish better management and conservation measures to protect the diversity of the biologically rich areas of coral reefs and related benthic habitats. Remote sensing can be used as a management tool to map and monitor the geographic extent of coral reefs to a limited degree given the available satellite imagery, but perhaps its true value is in its ability to identify areas of change over time. Analysis of hyperspectral data has produced encouraging results in the discrimination of common and optically similar coral reef substrates such as healthy corals, bleached corals, sea grass, and algae-covered surfaces (Holden and LeDrew, 1998, 1999, 2000; Hardy et al., 1992; Myers et al., 1999; Clark et al., 2000), but at the present time, such high spectral resolution data is unavailable from a satellite platform.

While currently available satellite sensors have global mapping and monitoring capabilities, the accuracy and precision attainable when applied to reef ecosystems is relatively low due to the large pixel size and broad spectral bandwidths of these sensors. Because of the deteriorating global state of coral reef and related benthic ecosystems, however, waiting for the ideal technology for accurate and precise imaging of submerged benthic habitats is not realistic.

Instead, there is a need to utilize the available imaging technology, assess the accuracy and acknowledge the limitations. SPOT HRV, Landsat TM and possibly SeaWiFS data are viable options since they provide moderate spatial resolution (20m, 30m, and 100m respectively) and spectral resolution (2, 6, and 6 useful optical broadbands, respectively) in the visible wavelengths while covering large geographic areas at regular time intervals (revisit times of approximately 26, 16, and 1 day, respectively). The spectral resolution of these sensors is limiting if optically similar substrates, such as healthy coral and algae-covered surfaces, need to be discriminated due to the small number of broad wavebands, however little conclusive research has been conducted to examine the optimal spectral resolution requirements for bottom type detection (See Hardy et al., 1992; Myers et al., 1999; Holden and LeDrew, 1998 and 1999; Clark et al., 2000; Holden and LeDrew, 2000). Additionally, the spatial characteristics are limiting if small features, such as discrete coral heads, need to be definitively located since the pixel sizes are relatively large compared to the size of common coral reef features (techniques such as sub pixel feature identification could minimize this limitation). Similarly, satellite technology may not be appropriate if a high temporal resolution data set is required to examine rapid changes because of infrequent revisit times and cloud-cover issues. The alternative is to conduct (often prohibitively) expensive and logistically complex airborne surveys at a higher spatial, spectral and temporal resolution, which may not be operationally feasible in the developing regions in which coral reefs are found.

[1] 21st Asian Conference on Remote Sensing, Taipei, Taiwan, 4-9 December 2000

An appropriate approach to using available satellite imagery to monitor coral reef ecosystems is the use of benthic homogeneity as indicated by spatial autocorrelation to evaluate the ecosystem (LeDrew et al, 2000). Spatial autocorrelation is defined as the situation where one variable (reflectance value of a pixel in this case) is related to another variable located nearby (surrounding pixels). Spatial autocorrelation is useful since it not only considers the value of the pixel (magnitude of reflectance), but also the relationship between that pixel and its surrounding pixels. Our hypothesis is that a healthy coral reef ecosystem will be heterogeneous, but a dead, algae-dominated coral reef will be relatively spatially homogeneous. This approach does not necessarily facilitate direct identification of substrate type, but it does allow for fast assessment of changes in ecosystem composition over a large geographic area if a time series of imagery is available. The results of such an approach utilizing currently available satellite technology may contribute to more effective management of coral reef resources.

The specific objective of this paper is to perform a case study using a local indicator of spatial autocorrelation (the Getis Statistic) based on SPOT imagery of Bunaken National Marine Park, North Sulawesi, Indonesia. This case study is performed to examine the feasibility of using measures of spatial homogeneity to evaluate changes in benthic habitat over time. The accuracy of the Getis Statistic approach is estimated based on familiarity with the study site and field data collection during time of satellite image acquisition (1997 and 2000).

METHODS

Measures of spatial autocorrelation indicate the strength of the relationship between values of the same variables, and may be either global or local in nature (Goodchild, 1986). Global measures provide a single value that indicates the level of spatial autocorrelation within the variable distribution, while local measures provide a value for each location within the variable distribution. Local indicators of spatial autocorrelation, such as the Getis statistic used here, are therefore able to identify discrete spatial patterns that may not otherwise be apparent by quantifying the spatial dependence between each pixel and a surrounding kernel of defined pixel dimensions (Wulder and Boots, 1998).

The Getis Statistic was first developed for application to point data, and has proven appropriate for identifying spatial "hotspots" (Getis and Ord, 1992). One form of the Getis statistic, G_i^*, has been modified and successfully applied to analysis of remotely sensed data at a range of spatial scales (Wulder and Boots, 1998; Derksen et al., 1998). The calculation of G_i^* using predefined window sizes surrounding a central pixel make it suitable for investigating the distance at which maximum spatial autocorrelation occurs. For its first application to remotely sensed imagery, Wulder and Boots (1998) provide a thorough description of G_i^*, and conclude that its ability to assess the strength of inter-pixel relationships, as well as the magnitude of spatial autocorrelation is valuable for digital image analysis. The equation for G_i^* is:

$$\frac{\sum_j w_{ij}(d)x_j - W_i^* \bar{x}}{s[W_i^*(n - W_i^*)/(n-1)]^{1/2}}$$

where $\sum_j w_{ij}(d)x_j$ is the sum of the variates within distance d of observation i (including i), W_i^* is the count of the pixels within distance d of pixel i, x is the mean, s is the global standard deviation, and n is the total number of observations.

The output values from the above equation can be interpreted similar to standardized Z scores. The largest G_i^* value for all distances (d) considered represents the maximum spatial autocorrelation. If the maximum G_i^* occurs when the window size is small (i.e. 3x3 pixels), then maximum autocorrelation covers a small area, but if maximum G_i^* corresponds to a large window size (i.e. 9x9 pixels), then maximum autocorrelation extends to a larger area. A cluster of high pixel values is represented by a large positive G_i^* value, while a cluster of low pixel values is indicated by a lower G_i^* value.

SPOT HRV imagery (August 1997 and July 2000) of Bunaken National Marine Park, North Sulawesi, Indonesia is used for the case study based on spatial autocorrelation. A common subset of a coral reef within the park was selected from the atmospherically corrected and georeferenced image for the case study corresponding to a region in which extensive fieldwork was performed. For each SPOT band, four distances were considered in the calculation of G_i^*: d=1, d=2, d=3, and d=4, representing increasingly larger kernels or windows. These distances refer to window sizes of 3x3, 5x5, 7x7, and 9x9 respectively. The resultant G_i^* values for each pixel are compared and the largest value retained to compile a Max G_i^* image: the larges Gi* value for all distances represents the maximum spatial autocorrelation. A general overview of the spatial dependence characteristics of the data is provided by

this Max G_i* image, which illustrates clusters of high and low digital numbers. Next, for each pixel, the distance at which the Max G_i* occurs is identified; for pixels where Max G_i* occurs at d=1, spatial dependence is local and the region can be considered heterogeneous, and for pixels where Max G_i* occurs at d>1, spatial dependence is not local therefore the region can be considered homogeneous.

RESULTS

Because identification of specific substrate type may not be the most appropriate and reliable use of available coarse spatial and spectral resolution satellite images, an alternative approach is needed to address the immediate problem of rapidly changing coral reef ecosystems worldwide to aid management of resources. The approach that is tested here is one based on spatial autocorrelation. The hypothesis is that a healthy reef will display relatively great spatial heterogeneity due to the diverse bottom types and benthic habitats, but an unhealthy coral reef will display spatial homogeneity if it is bleached or colonized by macroalgae. This indirect approach to evaluating the overall well being of coral reef ecosystems has the strength of allowing quick and straight forward change detection based on increasing or decreasing diversity/heterogeneity of bottom cover and is not reliant upon substrate identification.

For each band of the SPOT imagery, a series of calculations must be performed to use the Getis statistic to investigate the spatial autocorrelation within the region of interest. The first examination will be of the derived Max Gi* value, which is determined by finding the largest G_i* value among those calculated for the four distances (d=1, d=2, d=3, and d=4) for each pixel. This derived image is found by comparing G_i* for all kernels and assigning the largest value of G_i* to the central pixel of the kernel. A high Max Gi* magnitude indicates a cluster of high digital number values, while a low Max Gi* magnitude indicates a cluster of low digital number values. Max Gi* results for SPOT bands 1 and 2 of the 1997 and 2000 imagery of Bunaken Marine Park are shown in Figure 4 (SPOT band 3 is excluded due to its comparative inability to penetrate the water). The land is masked out of the subscene (shown in black in Figure 4) and not included in the calculations.

The largest G_i* value (i.e. Max G_i*) for all distances represents the maximum spatial autocorrelation such that a cluster of large positive Gi* values reveals high pixel values while a cluster of lower G_i* values reveals low pixel values. For both years, there is great homogeneity observed over the deep-water areas indicated by the extensive G_i* values of zero. There are observable clusters of relatively high G_i* values (G_i* > 37) indicating a conglomeration of high digital number pixel values; this area corresponds to a shallow water zone, which is often exposed at low tide and consists of highly reflective sand and dead coral debris. Surrounding the land mass is a zone of moderate G_i* values (20 < G_i* < 37) revealing areas of maximum spatial autocorrelation between midrange digital numbers; this zone contains healthy coral and a great diversity of benthic habitats.

The next step is to identify exactly which distance (*d*) produces the Maximum Gi*. If the Max Gi* is found at a small distance (d=1 kernel), then spatial dependence is local and similar values are found within close proximity. If Max Gi* occurs at a greater distance (d>1 kernel), then similar pixel values can still be found when larger distances are considered: the spatial dependence is not local. A single binary image for each SPOT band can be used to visualize the spatial autocorrelation (Figure 5). Interpretation of the images in Figure 5 reveals areas that have shifted from a relatively heterogeneous to a homogeneous surface as well as areas that have shifted from a relatively homogeneous to a heterogeneous surface. Examination of the "distance" images for SPOT band 1 reveals that the shallow coral reef area in the south west quadrant has shifted from a relatively heterogeneous healthy reef to a more homogeneous algae-dominated reef, which is confirmed by our observations during field data collection in 1997 and 2000.

The purpose of such an examination is not to identify the specific substrate, but rather to identify regions that have shifted from a heterogeneous surface to a more homogeneous surface, and vice versa. This type of change detection can be done quickly and without the need for extensive field verification, which enables information to be relayed to appropriate decision makers and resource managers for further examination and appropriate action.

CONCLUSIONS

There is little qualitative difference between *in situ* reflectance values of various substrates collected at depth in a coral reef environment, which indicates that interpretation of remotely sensed imagery may yield inaccurate classification results. Significant mixing of several different substrate types within the relatively large pixels of SPOT HRV images (20x20m) compounds the issue of classification inaccuracy. Other complicating factors include the effects of attenuation and multiple scattering from the overlying water column (Holden and LeDrew, In Press), refraction of light at the

air-water interface, scattering and absorption in the atmosphere, and effects of the variable morphology of the substrate with respect to slopes and self-shading.

The interpretation of a derived spatial autocorrelation image based on the Getis Statistic is a simple matter of understanding the series of basic calculations. A measure of spatial autocorrelation, Gi*, is calculated for the central pixel of kernels of increasingly larger size; following this, a single image is compiled whereby for each pixel, for each band, the largest value of Gi* is assigned (Max Gi*). This image reveals the actual value of the Max Gi* for each pixel whereby the magnitude of Gi* provides the interpreter with information regarding the magnitude of reflectance of the particular cluster.

The final step in the process is to answer the question: at which distance, or kernel size, is the Max Gi* found? This information allows the interpreter to take the analysis one step further and determine if the spatial dependence is local or spatially extensive. The interpreter can determine the degree of spatial dependence based on the distance at which the Max Gi* is found such that if it is found when the kernel size is small (d=1) then dependence is local in nature, but if it is found with the kernel is large (d>1), then dependence is not as local and can be considered spatially extensive. This provides the information for the interpreter to infer if the degree of homogeneity or heterogeneity extends over a large or a small area. The main benefits of this approach are that it results in an increased dynamic range of pixel values; it creates an image in which the values are normally statistically distributed; and produces an easily interpretable image to be used as an effective visualization tool.

The case study utilizing readily available satellite imagery based on spatial autocorrelation has produced encouraging results. The next stage will be to operationally use change in spatial autocorrelation to evaluate management decisions within Bunaken National Marine Park, North Sulawesi, Indonesia. For example, zones of limited use have been defined for the park such as "No Take" and "Recreational Use" and it would be useful to know the extent to which these zones are aiding reef recovery or resulting in reef degradation. This approach to image analysis is appropriate for change detection such that the interpreter can determine (1) the degree of spatial autocorrelation (whether homogeneous or heterogeneous), and (2) the area affected (whether spatially extensive, or local in nature). This approach is superior to change detection based on magnitude of reflectance alone because of the value added information of spatial autocorrelation.

REFERENCES

Derksen, C., M. Wulder, E. LeDrew and B. Goodison. 1998. Associations between spatially autocorrelated patterns of SSM/I-derived prairie snow cover and atmospheric circulation. Hydrological Processes. 12, 2307-16.

Getis, A. and J. Ord. 1992. The analysis of spatial association by distance statistics. Geographical Analysis. 24, 189-205.

Goodchild, M. 1986. Spatial Autocorrelation. Norwich: Geobooks.

Hardy, J., F. Hoge, J. Yungel, and R. Dodge. 1992. Remote detection of coral bleaching suing pulsed-laser fluorescence spectroscopy. Marine Ecology Progress Series. 88, 247-255.

Holden, H. and E. LeDrew. 1998. Spectral discrimination of healthy and non-healthy corals based on cluster analysis, principal components analysis and derivative spectroscopy. Remote Sensing of Environment. 65, 217-24.

Holden, H. and E. LeDrew. 1999. Hyperspectral identification of coral reef features. International Journal of Remote Sensing. 20 (13), 2545-2563.

Holden, H. and E. LeDrew. 2000. Accuracy assessment of hyperspectral classification of coral reef features based on first and second derivatives. Geocarto International, 15(2), 5-11.

Holden, H. and E. LeDrew. In Press. The effects of the water column on hyperspectral reflectance of submerged coral reef features. Bulletin of Marine Science.

LeDrew, E., Wulder, M., and H. Holden. 2000. Change detection of satellite imagery for reconnaissance of stressed tropical corals. Proceedings of the International Geophysical and Remote Sensing Symposium, Hawaii, USA, 24-28 July 2000.

Mumby, P., Green, E., Clark, C. and Edwards, A. 1998. Digital analysis of multispectral airborne imagery of coral reefs. Coral Reefs 17, 59-69.

Myers, M., J. Hardy, C. Mazel, and P. Dustan. 1999. Optical spectra and pigmentation of Caribbean reef corals and macroalgae. Coral Reefs. 18, 179-186.

Wulder, M. and B. Boots. 1998. Local spatial autocorrelation characteristics of remotely sensed imagery assessed with the Getis statistic. International Journal of Remote Sensing. 19 (11), 2223-31.

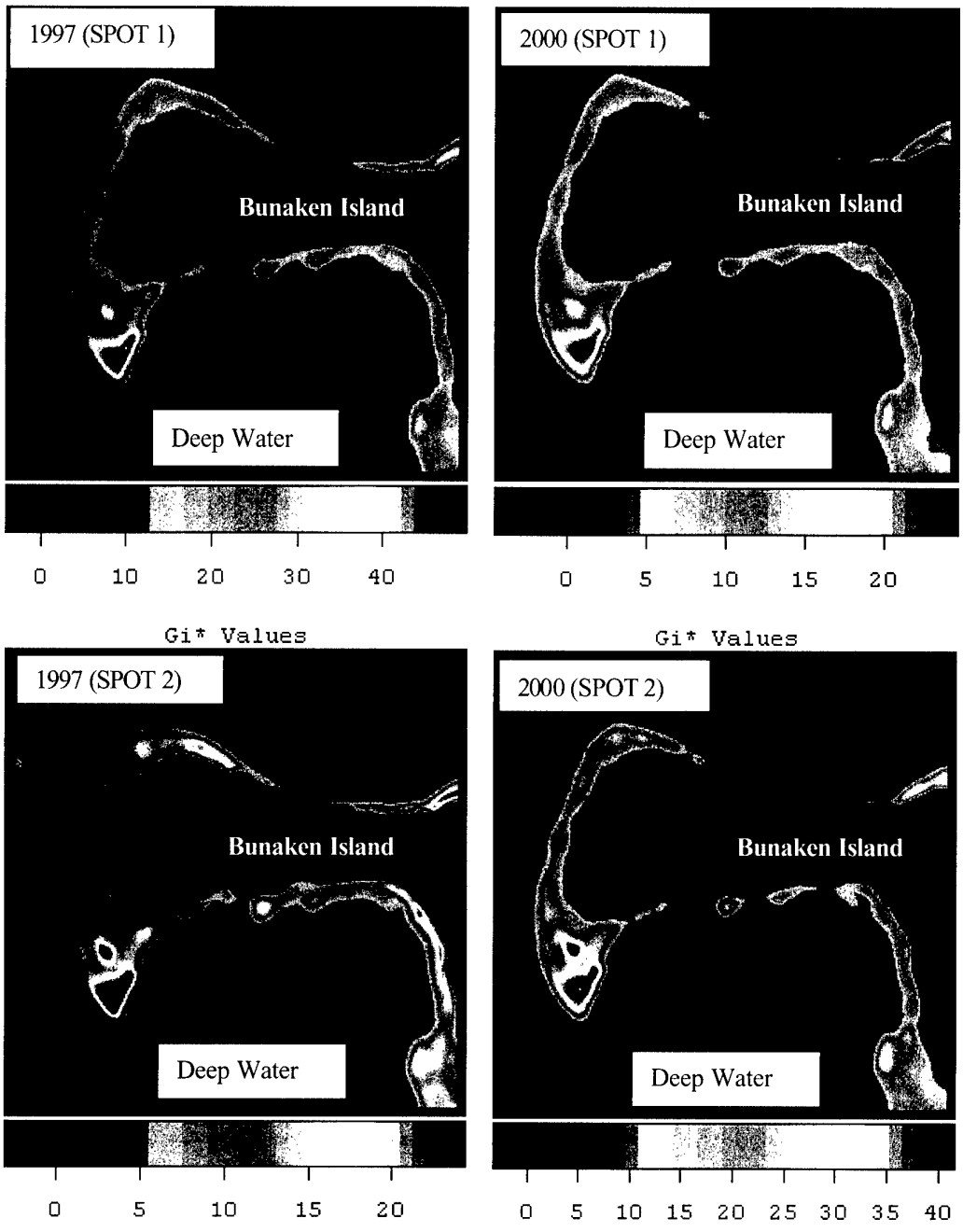


Figure 1. Maximum G* images for SPOT bands 1 and 2 in 1997 and 2000. The size of this SPOT image subset is 256x256 pixels.

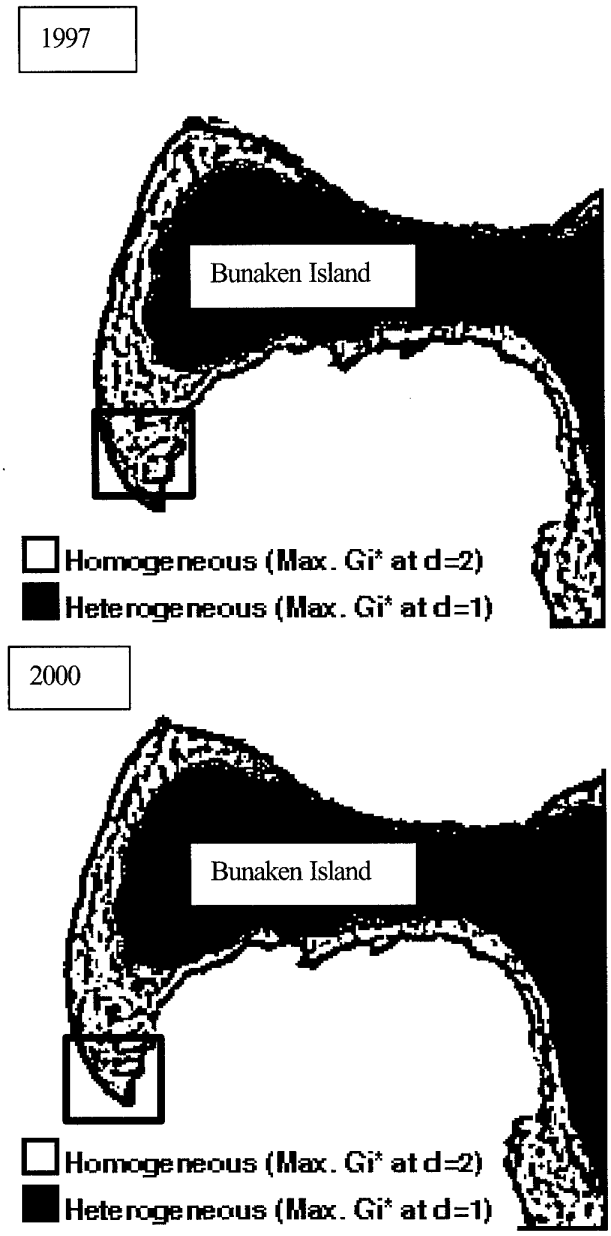


Figure 2. Binary images indicating the distance at which Max G* was found for SPOT 1997 (top) and 2000 (bottom). The size of this SPOT image subset is 256x256 pixels.

KNOWLEDGE-BASED IMAGE ANALYSIS FOR 3D ROAD RECONSTRUCTION

Chunsun ZHANG, Emmanuel BALTSAVIAS, Armin GRUEN
Institute of Geodesy and Photogrammetry
ETH-Hoenggerberg, CH-8093 Zurich, Switzerland
Tel.: +41-1-6332931, Fax: +41-1-6331101
E-mail: {chunsun, manos, agruen}@geod.baug.ethz.ch

KEY WORDS: Road reconstruction, Context, Knowledge base, Spatial reasoning

ABSTRACT: The extraction of road networks from aerial images is one of the current challenges in digital photogrammetry and computer vision. In this paper, we present our developed system for 3D road network reconstruction from aerial images using knowledge-based image analysis. In contrast to other approaches, the developed system integrates knowledge processing of color image data and information from digital geographic databases, extracts and fuses multiple object cues, thus takes into account context information, employs existing knowledge, rules and models, and treats each road subclass accordingly. The key of the system is the use of knowledge as much as possible to increase success rate and reliability of the results, working in 2D images and 3D object space, and use of 2D and 3D interaction when needed. Another advantage of the developed system is that it can correctly and reliably handle problematic areas caused by shadows and occlusions.

1. INTRODUCTION

The extraction of roads from digital images has drawn considerable attention lately. The existing approaches cover a wide variety of strategies, using different resolution aerial or satellite images. Overviews can be found in Gruen et al. (1995, 1997a) and Foerstner and Pluemer (1997). A semi-automatic scheme requires human interaction to provide interactively some information to control the extraction. Roads are then extracted by profile matching (Airault et al., 1996, Vosselman and de Gunst, 1997), cooperative algorithms (McKeown et al., 1988), and dynamic programming or LSB-Snakes (Gruen and Li, 1997b). The automatic methods usually extract reliable hypotheses for road segments through line and edge detection and then establish connections between road segments to form road networks (Wang and Trinder, 2000). Contextual information is taken into account to guide the extraction of roads (Ruskone, 1996). Roads can be detected in multi resolution images (Baumgartner and Hinz, 2000). The existing approaches show individually that the use of road models and varying strategies for different types of scenes are promising. However, all the methods are based on relatively simplistic road models, and most of them do not make use of a prior information, thus they are very sensitive to disturbances like cars, shadows or occlusions, and do not always provide good quality results. Furthermore, most approaches work in single 2D images, thus neglecting valuable information inherent in 3D processing.

In this paper, we present a knowledge-based system for automatic extraction of 3D roads from stereo aerial images which integrates knowledge processing of colour image data and existing digital spatial databases. The system combines different input data that provides complementary, but also redundant information about road existence, therefore it can account for problematic areas caused by occlusions and shadows, and the success rate and the reliability of the extraction results are increased. The system has been developed in the project ATOMI (for details of ATOMI, see Eidenbenz et al., 2000) to improve road centerlines from digitized 1:25,000 topographic maps by fitting them to the real landscape, improving the planimetric accuracy to

1m and providing height information with 1-2m accuracy. We currently use 1:16,000 scale color imagery, with 30cm focal length, and 60% forward overlap, scanned with 14 microns at a Zeiss SCAI. The other input data include: A nationwide DTM (DHM25) with 25m grid spacing and accuracy of 2-3/5-7 m in lowland/Alps, the vectorised map data (VEC25) of 1:25,000 scale, and the raster map with its 6 different layers. The VEC25 data have a RMS error of ca. 5-7.5m and a maximum one of ca. 12.5m, including generalization effect. They are topologically correct, but due to their partly automated extraction from map, some errors exist. In addition, DSM data in the working area was generated from stereo images using MATCH-T of Inpho with 2m grid spacing.

2. EXTRACTION STRATEGY & IMPLEMENTATION

Our approach makes full use of available information about the scene and contains a set of image analysis tools (see Fig. 1). The management of different information and the selection of image analysis tools are controlled by a knowledge-based system. The initial knowledge base is established by the information extracted from the existing geographic data and road design rules. This information is formed in object-oriented multiple object layers, i.e. roads are divided into various subclasses according to road type, land cover and terrain relief. It provides a global description of road network topology, and the local geometry for a road segment. Therefore we avoid developing a general road model, instead a specific model can be derived for each road segment. This model provides the initial 2D location of a road in the scene, as well as road attributes, such as road class, presence of road marks, and geometry (width, length, horizontal and vertical curvature, land cover and so on). A road segment is processed with an appropriate method corresponding to its model, and the knowledge base is automatically updated and refined using information gained from previous extraction of roads. The processing proceeds from the easiest subclasses to the most difficult ones. Since neither 2D nor 3D procedures alone are sufficient to solve the problem of road extraction, we make the transition from 2D image space to 3D object space as early as possible, and extract the road network with the mutual interaction between features of these spaces. More details of the general strategy can be found in Zhang and Baltsavias (2000).

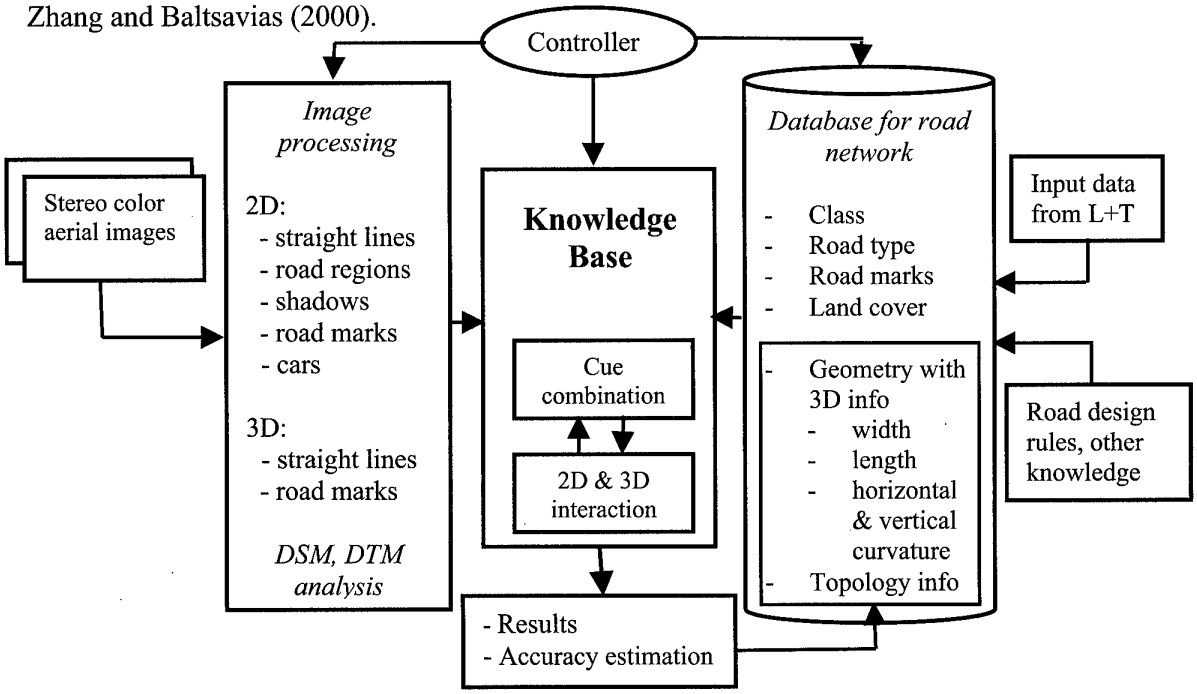


Figure. 1 Strategy of road network extraction in ATOMI.
L+T: Swiss Federal Office of Topography, Bern

When a road segment is selected, the system focuses on the image regions around it and activates a set of image processing tools. Edge pixels are detected with the Canny operator, line extraction and 3D straight line generation are conducted using the methods described in Zhang and Baltsavias (2000).

An unsupervised classification method, ISODATA, is applied in image patches to separate road regions from other objects. For this purpose, 3 bands from different color spaces (derived from original color image) are used: a* from the Lab color space, one band computed with the R and G bands in RGB space as (G-R)/(G+R), and the S band from the HSI color space.

Road marks are a good indication of the existence of roads. In addition, in many cases the correct road centerlines can be derived directly from presented road marks. This is especially useful when the roadsides are occluded or not well defined, such as in cities or city centers. Road marks in high resolution images such as the one used in our work are thin lines with a certain width and distinct color (usually white or yellow), thus the road mark pixels can be roughly detected using color information. The road marks are then extracted by finding thin lines in the detected pixels. The structural matching method developed in Zhang and Baltsavias (2000) is applied to generate 3D road marks. We also detect cars on roads as an additional cue about the road existence, this is still under development.

With the information from existing geographic data and image processing, the knowledge base is established according to the general strategy. Note that one of the important characteristics of the built knowledge base is that all information in it is spatially related, and relations between 2D edges and their corresponding 3D straight lines are kept. The system then extract roads by finding 3D parallel lines that belong to a road and link them in sequence. In case of shadows, occlusions caused by trees and buildings, spatial reasoning is applied using the knowledge base. The main procedures are shown in Fig. 2. The key is the use of knowledge and image context as much as possible, working in 2D images and 3D object spaces, use of 2D and 3D interaction when needed, and reasoning the problematic area. The details of implementation can be found in Zhang (2000).

The system checks extracted lines to find 3D parallel lines. Only lines located in the buffer defined by VEC25, having a similar orientation to VEC25 segments and a certain slope are further processed. Since roads are on the ground, lines above ground are removed by checking with the DHM25. By checking with the image classification results, a relation with the road region (in, outside, at the border) is attached to each line. Two lines are considered as parallel if they have similar orientation in 3D space. The lines of a pair must overlap in direction perpendicular to the lines, and the distance between them must be within a certain range. The minimum and maximum distances depend on the road class defined in VEC25. The found 3D parallel lines are projected into the images and evaluated using multiple knowledge. The region between the projected lines must belong to the class road as determined by the image classification. Image processing tools such as those for road mark extraction are activated to extract additional cues about the road existence in the region.

The parallel lines passing the above check are considered as Possible Road Sides that are Parallel (PRSP). They compose a graph. The nodes of the graph are PRSPs, the arcs of the graph are the relations between PRSPs. Note that in occlusion areas, the arcs also represent the missing parts of a road between a pair of PRSPs. The width of two PRSPs should be similar. If there is no gap between two PRSPs with similar width, i.e. one PRSP shares points with another, and the linking angles between them in 3D space comply with VEC25, they are connected directly. In case of gap existing, the gap area is checked. This is called spatial reasoning in our development.

If the gap is not too long, and 1) within the gap is a road region, e.g. a parking lot right beside road, or 2) within the gap is a shadow, or shadow mixed with road region, or 3) the gap is caused by tree occlusion (determined with image classification result and the data of DSM minus DTM), or 4) within the gap is terrain as determined by the DSM, or 5) road marks are extracted within the gap, and the connecting angles between PRSPs and gap comply with VEC25, a link is made for the two PRSPs.

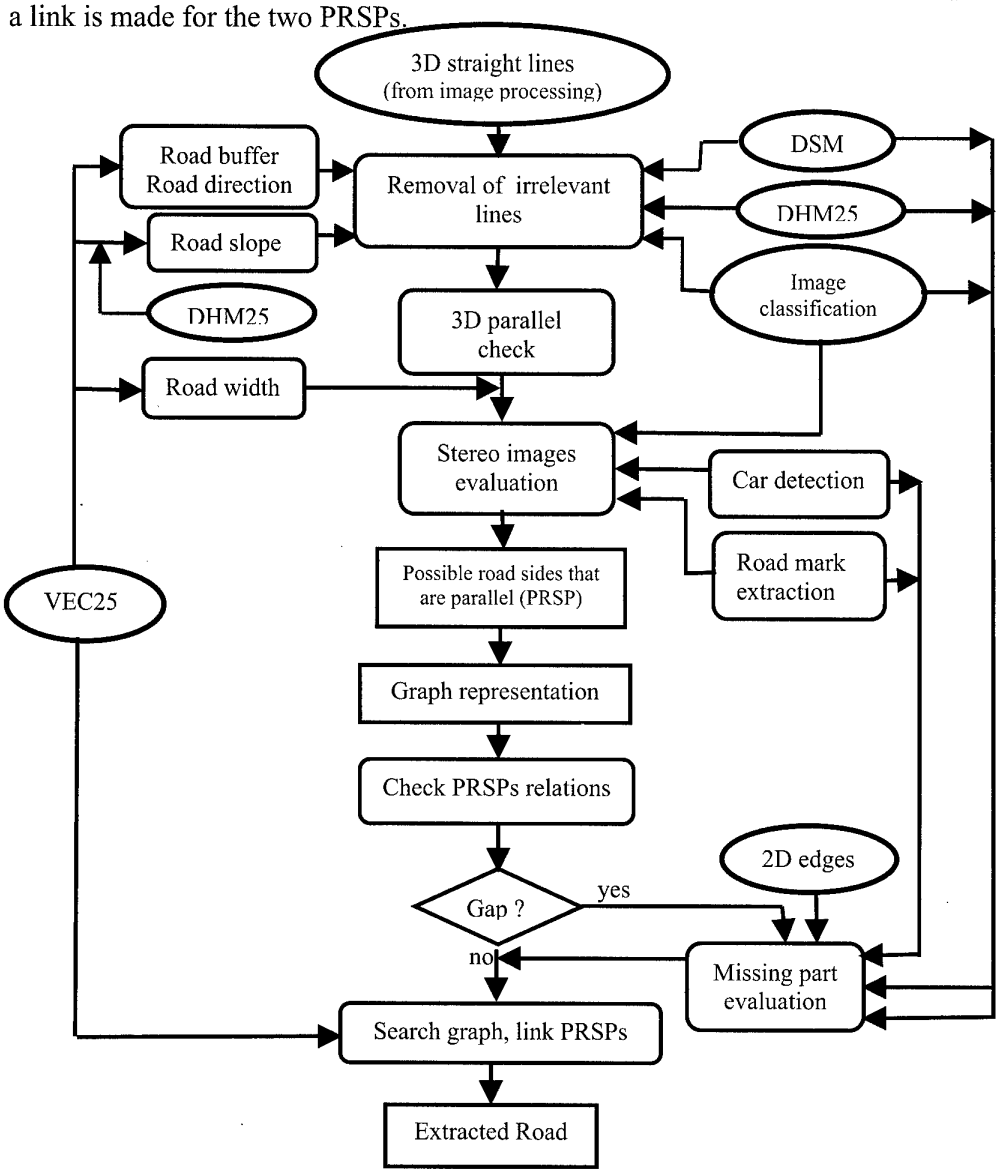


Figure.2 Procedures for road extraction.

A road hypothesis is found by searching the graph using the depth-first method. Each hypothesis is associated with a score that is the summation of the relation measurement of the PRSPs it contains. The hypothesis with the highest score is selected as road.

3. RESULTS

The described system is implemented as a standalone software package with a graphic user interface running on SGI platforms. Fig.3 shows a road image in a rural area where the road is occluded by tree shadows. The extracted road centerline is shown in the same image in red. In Fig.4 we show the road extracted in a suburban area by the developed method. Fig. 5 is an

example where the road is occluded by buildings and shadows. In Fig.6 the roadsides are not well defined, but the correct road centerline can be reliably extracted by the system through road mark extraction.



Figure. 3 Road extraction in rural area with occlusions.

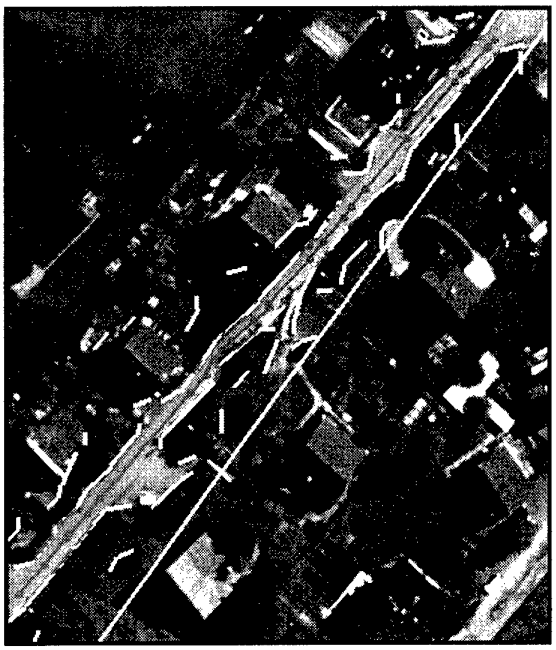


Figure. 4 Road extraction in suburban area.

Yellow: Outdated road centerline from VEC25
White: Extracted straight lines in road buffer
Orange: Found 3D parallel lines
Red: Extracted road centerline

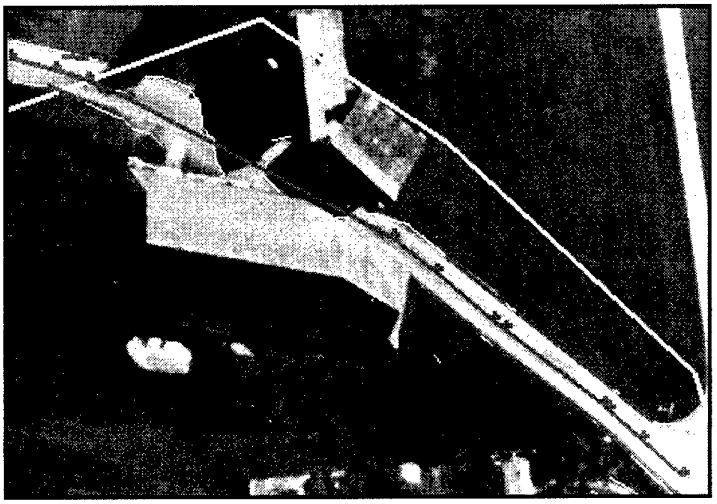


Figure. 5 Buildings occlude the road.



Figure. 6 Road extraction through road mark extraction.

4. DISCUSSION AND CONCLUSION

We presented a knowledge-based image analysis system for road extraction from stereo aerial images. The system has several advantages over other approaches. It uses existing knowledge, image context, rules and models to restrict search space, treats each road subclass differently, checks the plausibility of multiple possible hypotheses, and derives reliable criteria, therefore

provides reliable results. The system contains a set of image processing tools to extract various cues about road existence, and fuse multiple cues and existing information sources. This fusion provides information not only complementary, but also redundant to account for errors and incomplete results. Working on stereo images, the system makes an early transition from 2D image space to 3D object space. The road hypothesis is generated directly in 3D object space. This not only enables us to apply more geometric criteria to create hypotheses, but also largely reduces search spaces, and speeds up the process. The hypotheses are evaluated in 2D images using accumulated knowledge information. Whenever 3D features are incomplete or entirely missing, 2D information from stereo images is used to infer the missing features. By incorporating multiple knowledge, the problematic areas caused by shadows, occlusions etc. can be handled. Our future work will concentrate on road extraction in city and city center. Another important issue is the measurement of reliability of the extraction results. A method will be developed to quantify reliability using accumulated knowledge information. In order to evaluate the extraction results, a metric and method for evaluation will also be developed in future.

ACKNOWLEDGEMENTS

We acknowledge the financial support of this work and of project ATOMI by the Swiss Federal Office of Topography, Bern.

REFERENCES

Airault, S., Jamet, O., Leymarie, F. 1996: From Manual to Automatic Stereoplotting: Evaluation of Different Road Network Capture Processes. IAPRS, Vol.31, Part B3, pp.14-18.

Baumgartner, A., Hinz, H. 2000: Multi-Scale Road Extraction Using Local and Global Grouping Criteria. IAPRS Vol.33, Part B3/1, pp.58-65.

Eidenbenz Ch., Kaeser Ch., Baltsavias E., 2000. ATOMI – Automated Reconstruction of Topographic Objects from Aerial Images using Vectorized Map Information. IAPRS, Vol.33, Part 3/1, pp.462-471.

Foerstner, W., Pluemer L. (Eds.), 1997. Semantic Modeling for the Acquisition of Topographic Information from Images and Maps. Birkhaeuser Verlag, Basel.

Gruen A., Kuebler O., Agouris P. (Eds.), 1995. Automatic Extraction of Man-Made Objects from Aerial and Space Images. Birkhaeuser Verlag, Basel.

Gruen A., Baltsavias E.P., Henricsson O. (Eds.), 1997a. Automatic Extraction of Man-Made Objects from Aerial and Space Images (II). Birkhaeuser Verlag, Basel.

Gruen A., Li H., 1997b. Semi-Automatic Linear Feature Extraction by Dynamic Programming and LSB-Snakes. Photogrammetric Engineering and Remote Sensing, 63(8), pp.985-995.

McKeown, D.M., Denlinger, J.L., 1988: Cooperative Methods for Road Tracking in Aerial Imagery. Proc. of IEEE Computer Vision and Pattern Recognition, Michigan, pp.662-672.

Ruskone, R., 1996: Road Network Automatic Extraction by Local Context Interpretation: Application To the Production of Cartographic Data. Ph.D. Thesis. Marne-La-Vallee University, France.

Vosselman, G., de Gunst, M., 1997: Updating Road Maps by Contextual Reasoning. Automatic Extraction of Man-Made Objects from Aerial and Space Images (II), A. Gruen, E.P. Baltsavias and O. Henricsson (Editors), Birkhäuser Verlag, Basel, pp. 267-276.

Wang Y., Trinder J, 2000: Road Network Extraction by Hierarchical Grouping. IAPRS, Vol.33, Part B3/2, pp.943-949.

Zhang C. and E.P.Baltsavias, 2000: Knowledge-based Image Analysis for 3D Edge Extraction and Road Reconstruction, IAPRS, Vol.33, PartB3/2, pp.1008-1015.

Zhang C., 2000: ATOMI Intermediate Report on Road Extraction. Institute of Geodesy and Photogrammetry, ETH Zurich.

ORTHORECTIFICATION OF STEREO SPOT PANCHROMATIC AND RADARSAT FINE MODE DATA USING ORBITAL PARAMETERS AND DIGITAL ELEVATION MODEL

Mohd Ibrahim Seeni Mohd and Shahruddin Ahmad
Department of Remote Sensing
Faculty of Geoinformation Science and Engineering
Universiti Teknologi Malaysia
81310 Skudai
Johor, Malaysia
Tel: (607) 5502906 Fax: (607) 5566163
E-mail: mism@fksg.utm.my
sahmad@fksg.utm.my

ABSTRACT

Rectification of satellite data using ground control points (GCPs) in a polynomial fit is not practical in areas where well-defined GCPs are limited. This will be the case in many forested areas or in coastal areas. Rectification using orbital parameters of the satellite together with limited GCPs will overcome this problem. This study emphasises on the evaluation of the geometric accuracy of SPOT Panchromatic and Radarsat Fine Mode data using the later technique. The GCPs were obtained by differential Global Positioning System technique with sub-meter accuracy. The accuracy of rectification evaluated using independent check points gave a positional accuracy of 0.4 pixels for SPOT Panchromatic data. The rectification reveals that the optimum number of GCPs is 8 for SPOT Panchromatic data and 10 GCPs for Radarsat Fine Mode data. A digital elevation model derived by digital image matching technique from stereo SPOT Panchromatic and Radarsat Standard Mode data was used to remove relief distortion to produce an orthoimage. The digital elevation model (DEM) accuracy was validated using spot heights derived from contour map in flat and hilly areas. The accuracy of DEM achieved from stereo SPOT data is 26.3 m and stereo Radarsat data is 35.2 m. The final orthoimage of SPOT Panchromatic and Radarsat Fine Mode data was quantitatively evaluated by merging with digital vector data of 1:25,000 scale of the area. The mismatch in details between them is about ±1 pixel.

KEYWORDS: Rectification, Orbital Parameters, Digital Elevation Model, SPOT, Radarsat Satellite Data.

1. INTRODUCTION

Rectification of satellite image by polynomial method is widely used since it is simple. However, this method is not practical in areas where GCPs are very limited and also in images where the elevation ranges from flat to hilly areas. The use of orbital parameters can overcome this problem.

Various studies have been carried out using satellite orbital parameters for the rectification of SPOT Panchromatic (Cheng & Toutin, 1997 and Westin, 1990) and ERS SAR data (Cheng and Toutin, 1997 and Keong, 1995). The results from these studies showed an accuracy of 0.3 pixel from SPOT data and 1 to 2 pixels for ERS SAR data. In the case of stereo SPOT, an accuracy

of 10 m can be achieved (Al-Rousan et al., 1997 and Theodossiou & Dowman, 1990). Toutin (1998) also showed that stereo Radarsat data can produce DEM from various pair of modes and intersection angles with an accuracy of 25 m.

In this study, orbital parameters have been used with limited GCPs to carry out geometrical correction of SPOT Panchromatic and Radarsat Fine Mode SAR data together with DEM generated from the stereo SPOT data and stereo Radarsat Standard Mode SAR data.

2. STUDY AREA AND SATELLITE DATA

2.1 Study area

The test site that has been selected for this study is the Klang Valley area, Malaysia, which covers an area of 60 km by 60 km (Figure 1). The selection of this site is due to the topography which ranges from flat, moderate and hilly areas.

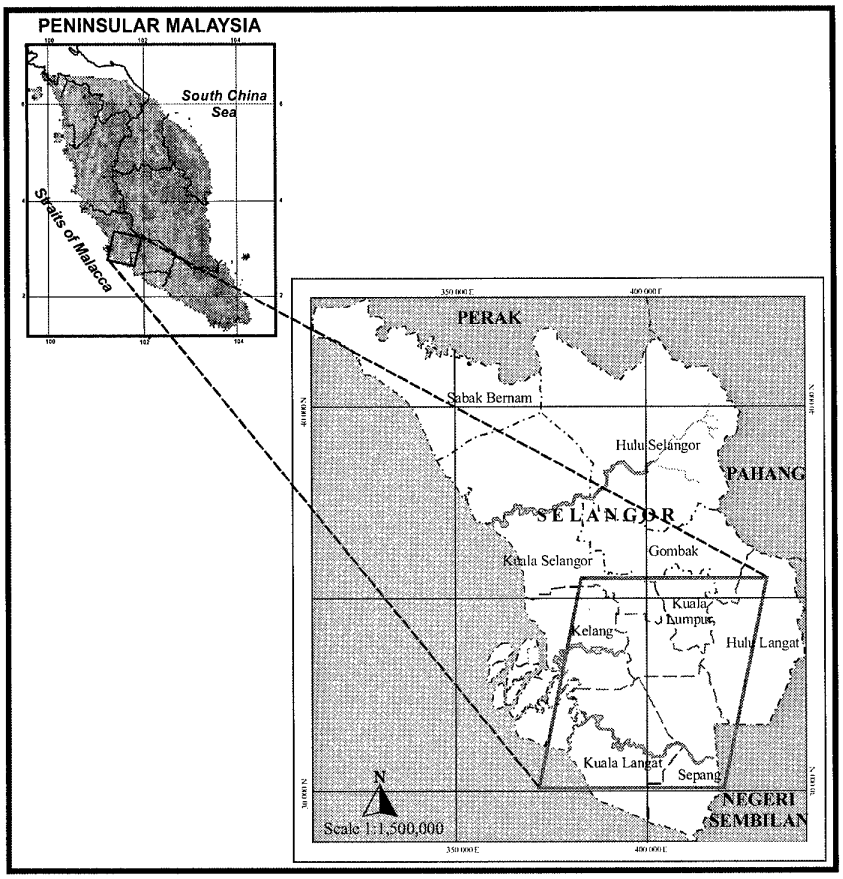


Figure 1: Study area.

2.2 Satellite Data

The characteristics of the satellite data used in this study is given in Table 1. The base height ratio (B/H) value for SPOT stereo pair is 0.8. The value of vertical parallax ratio (VPR) calculated for the Radarsat stereo pair data acquired from the same side of Standard 2 and Standard 7 mode is 0.99.

Table 1: Characteristics of satellite data.

Platform	SPOT		RADARSAT		
Scene Number	270-344	269-343	14297	C0015070	C0015059
Sensor/ Mode	HRV-P	HRV-P	F5F-Mode	Standard Mode (S2)	Standard Mode (S7)
Level of Processing	1 A	1 A	Path Image	Path Image	Path Image
Date	21.4.98	23.1.98	31.7.98	20.12.99	17.12.99
Pixel Size (meter)	10x10	10x10	6.25x6.25	12.5x12.5	12.5x12.5
Viewing Angle (degree)	-30.3°	+15.8°	45.5°–47.7	24°-31°	45°-49°

3. DATA PROCESSING

3.1 Data Collection

GCPs of high accuracy are necessary for rectification of SPOT Panchromatic and Radarsat Fine Mode data due to the high spatial accuracy of the data. For this reason, GCPs collection was carried out using GPS real time differential correction technique. The observations were done using a 12-channel Omni STAR receiver with sub-meter accuracy. A total of 35 GCPs that are uniformly distributed over the image were obtained. In addition, digitised contours from a topographic map with scale of 1:25,000 at 20 m interval are used to validate the DEM that has been generated. Major roads were also digitised to evaluate qualitatively the final orthoimage.

3.2 Geometric Modeling

In this study, the rectification process using PCI/OrthoEngine Version 6.3.0 software is based on collinearity conditions which represent the transformation between the image and ground space. This technique was developed by Toutin (1995) from the Canada Center for Remote Sensing (CCRS). The input for the model are orbital parameters gathered from header file and image coordinates (pixel, line) which correspond to the coordinates (X, Y, Z) of the Malaysian Rectified Skew Orthomorphic (RSO) projection.

The left-hand SPOT Panchromatic and Radarsat Standard Mode images were rectified. The rectified image is transformed and resampled to create epipolar geometry to ensure both images are offset only in the horizontal direction. Image matching was performed to match the corresponding pixel in the right image, i.e a template window and moving this template window in the search area of the epipolar image until the best digital number match is obtained. The correlation coefficient between 0 and 1 is calculated for each pixel, where 0 represents a total mismatch and 1 represents a perfect match. The different center locations of template window with the matched pixel represents the parallax. This parallax value is used to compute the elevation at the center of the template.

4. RECTIFICATION RESULTS

4.1 SPOT Panchromatic Data

The rectification accuracy of scene 270-344 is 0.28 pixels (x direction) and 0.27 pixels (y direction) using all 35 GCPs. In order to find an optimum number of GCPs for the rectification, the following number of points were tested, i.e 4, 6, 8, 10 and 12 points. A few GCPs were also used as check points to evaluate the accuracy of rectification. Table 2 and Figure 3 show the results of the RMSE of GCPs and check points. The accuracy is almost constant when the

number of GCPs used is about 8 and more with a corresponding accuracy of 0.4 pixels at check points. Using 4 GCPs, the accuracy of rectification is 1.36 pixel.

Table 2: RMSE of rectification for SPOT data.

Ground Control Points				Check Points			
No. of GCPs	RMSE (pixels)			No. of CPs	RMSE (pixels)		
	X	Y	R		X	Y	R
4	0.28	0.08	0.29	31	1.32	0.29	1.36
6	0.33	0.19	0.38	29	1.08	0.3	1.13
8	0.27	0.21	0.34	27	0.34	0.3	0.45
10	0.25	0.22	0.33	25	0.32	0.3	0.44
12	0.24	0.21	0.32	23	0.32	0.29	0.43

Note: R = vector

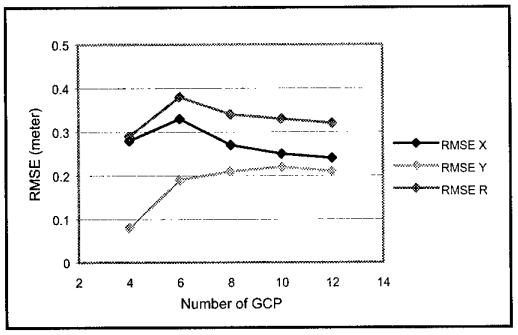


Figure 3: RMSE plot of rectification for SPOT data.

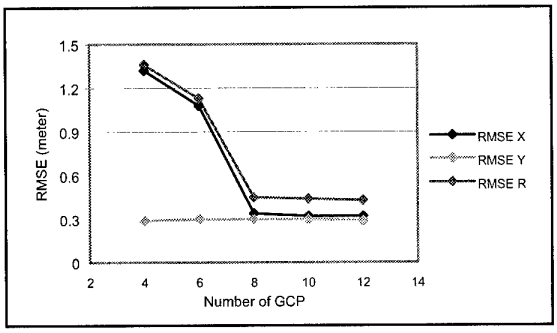


Figure 4: RMSE plot of check points for SPOT data.

4.2 Radarsat Fine Mode Data

GCPs selection for Radarsat Fine Mode rectification is more difficult compared to SPOT due to the speckle. Speckle reduction was performed using Lee and Frost filters in order to enhance the image details for accurate GCPs selection. The rectification of the Radarsat data was carried out by using only 12 GCPs since the other GCPs were not clear on the image. As a result, evaluation of accuracy could not be performed. However, evaluation of accuracy was done after the process of orthorectification. The rectification result shows that the RMSE is 9.06 pixels using 4 GCPs and improves with increase in the number of GCPs. It is possible to obtained RMSE of ±1 pixel with 12 GCPs.

Table 3: RMSE of rectification for Radarsat data.

Number of GCPs	RMSE (pixels)		
	X	Y	R
4	9.03	0.73	9.06
6	1.19	1.16	1.67
8	1.06	1.13	1.55
10	0.75	0.72	1.04
12	0.74	0.70	1.02

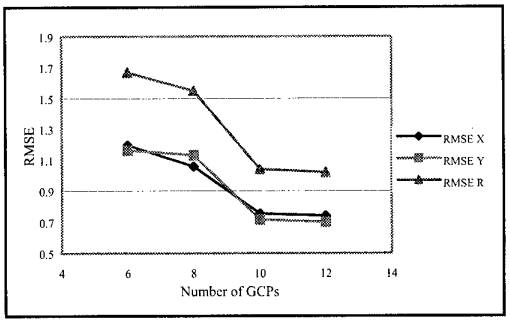


Figure 5: RMSE plot of rectification for Radarsat data.

5. ACCURACY OF DEM

From Table 4, it can be seen that different accuracies have been achieved from DEM generated from stereo SPOT and stereo Radarsat data. Accuracy of both DEMs was validated in

flat/moderate and hilly terrain using check points derived from contours. The flat/moderate area mainly covers urban area and vegetation, whilst most of the hilly area is covered by tropical rain forest. The accuracy of flat/moderate area from SPOT DEM is 32.1 m and for hilly area is 17 m which was evaluated using 100 check points. For the Radarsat DEM the accuracy achieved in flat/moderate areas is 41 m and 26.7 m in hilly area. The results show that both DEMs give better accuracy in hilly area compared to flat/moderate area. The overall accuracy of SPOT DEM is 26.3 m and Radarsat DEM is 35.2 m. This result shows that accuracy of SPOT DEM is better than Radarsat DEM. The difference in accuracy is due to the better spatial resolution of SPOT Panchromatic compared to Radarsat Standard Mode data.

Table 4: Comparison of RMSE of DEMs for different types of terrain.

Types of terrain	RMSE (m) from SPOT	RMSE (m) from Radarsat
Flat/ Moderate	32.1	41.0
Hilly	17.0	26.7
Overall Accuracy	26.3	35.2

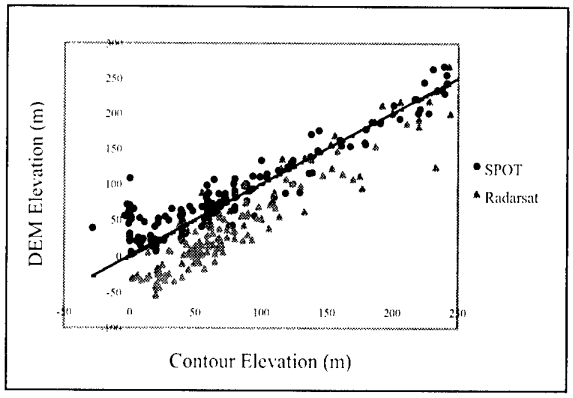


Figure 6: Comparison of accuracy of SPOT and Radarsat DEMs.

6. ORTHORECTIFICATION

Orthorectification is a process to remove the relief distortion using DEM to produce an orthoimage. In areas with cloud cover and homogenous pixels (eg. forest), the SPOT DEM produced 'missing' elevation values. These areas are masked and the corresponding elevations in these areas were replaced by using the elevation from Radarsat DEM. The DEM obtained by combining the SPOT and Radarsat data were used to produce the orthoimage. The accuracy of orthoimage was evaluated by superimposing with digitized digital vector data of the study area. The mismatch in the location of roads and rivers are about 1 pixel (Figures 7 and 8).

7. SUMMARY

The method of rectification using orbital parameters is suitable for areas with limited GCPs. This study shows that the rectification using SPOT Panchromatic data gives an accuracy better than 1/3 pixel, whilst Radarsat data give an accuracy of about 1 pixel. The optimum number of GCPs required for suitable rectification of SPOT Panchromatic data is 8 and Radarsat Fine Mode SAR data is 10. The DEM generated from stereo SPOT Panchromatic data gives an accuracy of 26.3 m and Radarsat Standard Mode data is 35.2 m. The accuracy in the DEM is satisfactory to remove relief distortion to produce an orthoimage with good accuracy for mapping.

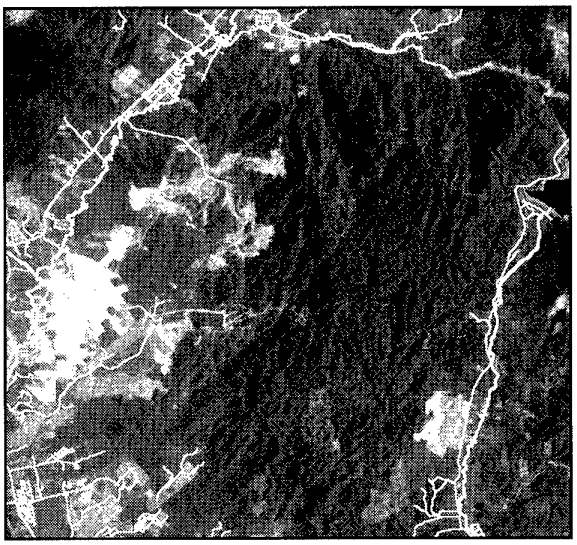


Figure 7: Orthoimage of SPOT Panchromatic data.

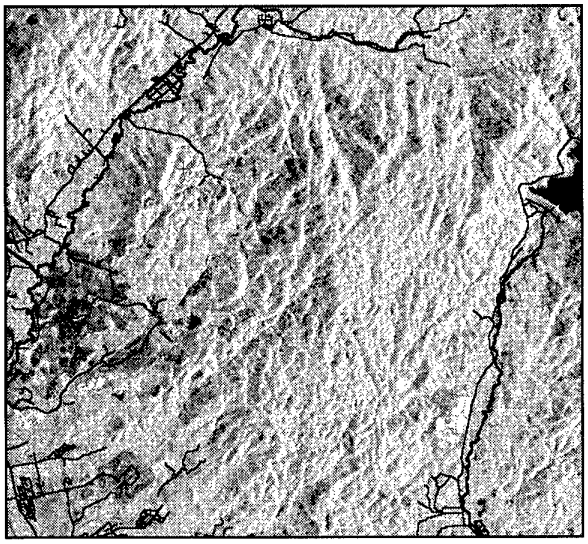


Figure 8: Orthoimage of Radarsat Fine Mode SAR data.

REFERENCES

Al-Rousan, N., Cheng. P., Toutin. T. and Valadan Zoel, M.J., (1997). "Automated DEM Extraction from SPOT Level 1B Imagery". Photogrammetric Engineering & Remote Sensing, Vol. 63, No. 8, August, pp 965-974.

Cheng, P. and Toutin.T., (1997). "On-Site Interactive GPS and Geometric Modelling: A Winning Combination". EOM, April 1997, pp. 35-37.

Keong, K.L., (1995). "Geocoding of Spaceborne SAR Imagery". Proceedings of Seminar on the Integration of Remote Sensing and GIS for Applications in South East Asia, 27-29 March 1995, Kuala Lumpur, Malaysia.

Theodossiou, E.I. and Dowman, I.J, (1990). "Heighting Accuracy of SPOT". Photogrammetric Engineering & Remote Sensing, Vol. 56, No.12, December, pp. 1643-1649.

Toutin, T., (1995). "Multi-Source Data Fusion with an Integrated and Unified Geometric Modelling". Journal EARSel – Advances in Remote Sensing, Vol.4, No 2, pp. 118-129.

Toutin, T., (1998). "Stereo RADARSAT for Mapping Applications. Proceedings of ADRO Final Symposium, Montreal, Canada, October 13-15, 1998.

Westin, T., (1990). "Precision Rectification of SPOT Imagery". Photogrammetric Engineering and Remote Sensing, Vol. 56, No. 2, February, pp. 247-253.

HIDDEN COMPENSATION AND SHADOW ENHANCEMENT FOR TRUE ORTHOPHOTO GENERATION

Jiann-Yeou Rau Nai-Yu Chen Liang-Chien Chen
Tel: 886-3-4227151 Ext. 7651,7627,7622 Fax:886-3-4255535
{jyrau,nychen,lcchen}@csrsr.ncu.edu.tw
Center for Space and Remote Sensing Research
National Central University, Chung-Li
TAIWAN

ABSTRACT

Hidden and shadow areas are major defects in large-scale aerial photos. Both defects severely degrade the interpretability of orthophotos. Abrupt changes of surface height are the primary sources that cause these defects. Thus, the surface height discontinuities, orientation parameters and solar zenith angle are key factors in determining defect extents. An orthographic rectification scheme minimizing these defects is proposed for generating large-scale true orthophotos. Presuming the DBM (Digital Building Model) and the DTM (Digital Terrain Model) are available, the scheme utilizes projection geometry to detect hidden and shadow areas. For hidden areas, lost information is further compensated with the data from the conjugate image. Seamless mosaic technique considering gray value balance is then applied. For shadow areas, dimmed features are enhanced using local histogram matching method to reduce the impact from poor illumination. Experimental results indicate that the proposed scheme minimizes hidden and shadow defects significantly to generate a true orthophoto using aerial quadruplet.

KEY WORDS: True Orthophoto, DBM, Hidden Compensation, Shadow Enhancement.

1. INTRODUCTION

Orthographic rectification process is one important subject in the field of photogrammetry. Despite past achievements, it remains a challenge task to develop an automatic scheme for generating large-scale true orthophotos. First emphasized by Amhar and Ecker [1998], the term □true orthophotos□ conceptually refers to ideal orthographic products. The factors considered in relief displacement removal for true orthophoto generation include not only the terrain variation but also canopies. Of which, buildings are often the most important ones.

A complete orthographic rectification task involves two steps of processing, namely, calculating orientation parameters and performing image rectification provided that a surface model is available. With decades of development, calculating orientations for aerial photograph is now a mature technique. Still, new researches are flourishing to extend existing methods and

concepts to adapt for carriers and devices of the new age [Chen, et. al 1997]. In the retrieval of surface height information, stereoplotter or analytical plotter is conventionally used for measuring terrain or surface height from stereopair. Meanwhile, various schemes based on patch or feature matching methods have been widely explored to automate height extraction [Chen & Rau, 1993]. To generate digitally true orthophotos, DBM is also needed. Mayer [1999] and Shufelt [1999] surveyed the state-of-the-art automatic building extraction techniques. They concluded that a fully automatic system is still a long way to go. While on the other hand, the importance of semi-automatic approaches is increasingly acknowledged [Sahar & Krupnik, 1999] in a number of applications.

Hidden and shadow areas are major defects shown on orthophotos. Usually, the lager the scale of the orthophoto, the more prominent these defects appear. Both defects severely degrade the interpretability of orthophotos. Abrupt changes of surface height are the primary sources that cause hidden and shadow defects. And for most large-scale orthophoto applications, predominate factors causing surface height discontinuities are buildings. Thus, an orthographic rectification scheme minimizing hidden and shadow defects resulted from buildings is proposed to improve the interpretability for such applications. Fig.1 shows the flow chart of the proposed scheme. A master image is selected from the multi-view image set as the rectification object whereas the others serve as slave images to reimburse for the master image the hidden information. Two major parts are included in the proposed scheme. The orthographic rectification method with hidden detection and compensation is performed first, followed by a shadow area detection and enhancement operation. Section 2 and 3 discuss algorithms for these two parts. A case study presented in section 4 demonstrates the effectiveness of the purposed scheme. Finally, section 5 concludes the discussion.

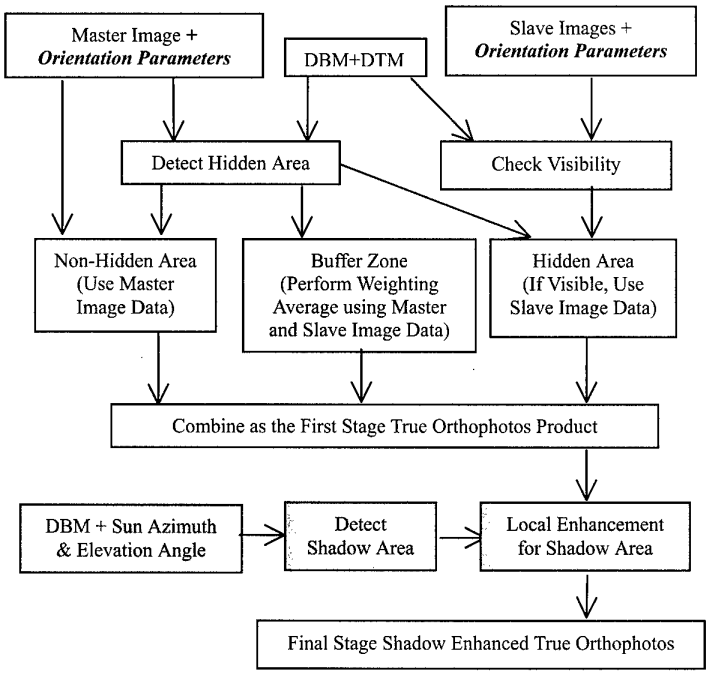


Figure 1, Flow chart of the proposed scheme.

2. ORTHO RECTIFICATION WITH HIDDEN DETECTION AND COMPENSATION

The hidden areas are detected by using Z-buffer and index map. Z-buffer is a matrix set composed of two 2-D matrixes on the image plane. One component of the matrix set is used to record an object location for an image point. The other one stores the distance between the camera and the object and is initialized with a very large value. The index map is also a 2-D matrix on the ground plane to identify if the ground point is hidden. Superimposing DBM on DTM, the coordinates of the surface object may be determined. Applying these coordinates to collinearity condition equation, the projected image coordinates are calculated and rounded to the nearest image grid for each groundel. Meanwhile the projection distance is calculated and compared to the one stored in the Z-buffer. If the distance newly calculated is greater, the corresponding cell in index map is flagged as hidden. On opposite, the location recorded previously is first retrieved from the Z-buffer to locate corresponding groundel for flagging hidden. The Z-buffer is then updated with the new values. As an example, the projection distances of the surface objects X and Z shown in figure 2 are dX and dZ respectively. Because dX < dZ, on index map the cell corresponding to Z will be flagged hidden, and the information regarding X will be stored in the Z-buffer. Since the foregoing detection searches hiddens in horizonal sequence, certain hidden pixels around very steep surface elements may be overlooked. The possibility is illustrated as M portion in fig.2. To solve the problem, along near vertical surfaces pseudo groundels are introduced in the next phase. To determine the number of pseudo pixels, height difference and projection length are used. For instance, if the left building in fig.2 has a height of $50m$, the projection length is 5 image pixels, thus on the vertical walls of the building, pseudo pixels are placed in a spacing no greater than $10m$. Applying again the detecion rules for these pseudo pixels completes the hidden searching. Due to numerical rounding errors, isolated points or lines may occure in the index map. A post moving window processing employs majority rule to refine the index map is necessary.

With hidden detection mechanism, enhancing orthographic rectification process to minimize hidden defect is possible as shown in fig. 1. Index maps flagging groundels hidden from the master and the slave images is constructed. For each groundel nonhidden from the master image, gray value is casted according

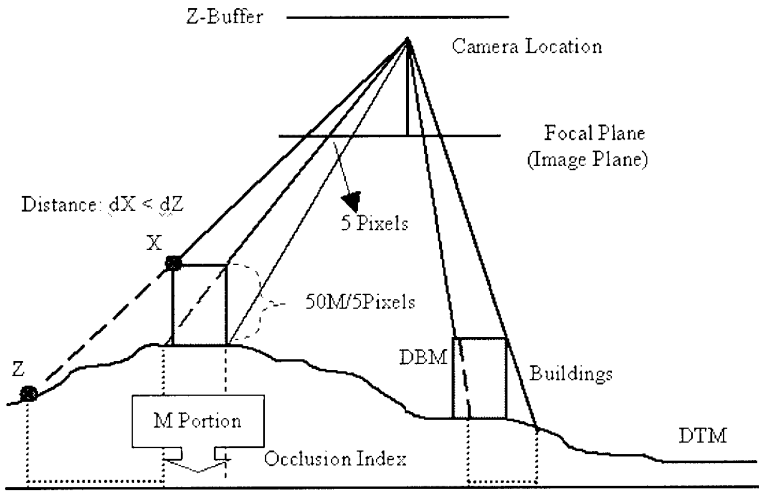


Figure 2, Hidden detection for buildings.

to the projection geometry from the master image. For those hidden ones, the index map of slave images are consulted to check for the possibility of patching. Filling-in directly for hidden areas the data patched from slave images may causes radiometric discontinuities. A seamless mosaic technique is developed to reduce the discontinuity. The buffer zone extended from the boundary of particular hidden area is constructed using a morphology operator named dilation. Within the buffer zone, gray value is calculated from both the master and the slave image by weighting average. The weighting factors are determinated according to the distance between the processing pixel and boundary of the hidden area.

3. SHADOW DETECTION AND ENHANCEMENT OPERATIONS

The technique for shadow detection is similar to that for hidden detection. In place of projection geometry, parallel projection is used. The plane of Z-buffer is built perpendicularly to the direction of the sun. In case of lacking such information, this direction may be estimated from the shadow of tall buildings. As shown in fig.3a, the azimuth angle of the sun may be measured from the direction of the shadow, whereas the zenith angle may be calculated from the ratio of the building height to the shadow length. As shown in fig. 3b, the distance stored in Z-buffer is replaced with the path length between the surface object and the local zero height. For convenience, the path length is recorded in negative quantity. Hence, the searching algorithm used for hidden detection may be re-used for shadow detection.

To level the illumination differences around shadow areas, image enhancement technique should be applied. Around the building areas, characteristics of ground features are often dominated by human activities and are usually quite different from place to place. Hence, local enhancement is preferred. Surrounding the shadow area, a buffer zone is first constructed using dilation operator. If presented, rooftops are further excluded from both the shadow area and the buffer zone. This is to keep the similarity of image contents in the shadow area and those in the buffer zone. The histograms for particular pair of buffer zone and shadow area are calculated accordingly. Considering the formal one as the reference histogram, the gray value transformation table for the shadow area is then constructed with histogram matching method. Thereafter, the shadow enhancement may be accomplished area by area.

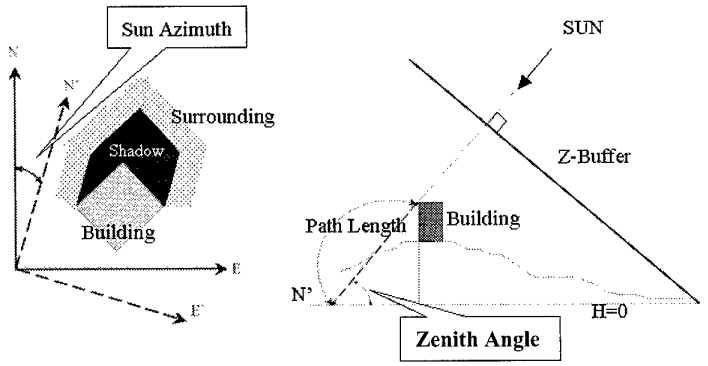


Figure 3, (a) Direction of sun and the buffer-zone surrounding shadow area, (b) Shadow detection, Z-Buffer and path length from local zero height to object.

4. CASE STUDY

To realize the algorithms presented in previous sections, a fully automatic orthographic rectification procedure was developed. Along with the source images, inputs of the procedure include DBM, existing DTM, pre-calculated orientation parameters and direction of the sun. Among the cases studied, the quadruplet covering Fu-Zen University is chosen to illustrate the important features of the proposed scheme. Figure 4 shows the photo data from which the rectangular region highlighted in white box was picked for inspection in the following discussion. The scale of the quadruplet is around $1:5000$, the overlap along and across trip are both about 60%. The photo data was scanned at a spacing of $25\mu m$ to produce digital images with $12.5cm$ nominal ground resolution. By assuming the shape of most buildings may be decomposed into vertical walls and horizontal or slant rooftops, the DBM was constructed numerically from coordinates of all building corners measured from analytical plotter.

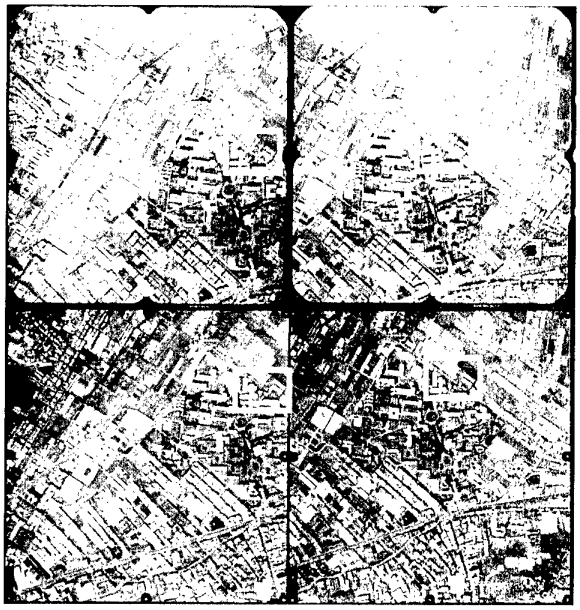


Figure 4, The quadruplet under studying.

For comparison, fig.5 shows for the highlighted area the conventional orthophoto generated from the lower-left and the upper-right scenes. It demonstrates that without hidden detection and relief displacement correction for buildings, locating from these products the right position of a given object would be difficult. It is also problematic for visual interpreter to decide whether a particular feature shown on these products should be appeared. Impacts of shadow defect are also distinctly observed in this figure. Besides the difficulty of recognizing objects in shadow areas, it is sometime a challenge task just distinguishing shadow itself from the other ground features.

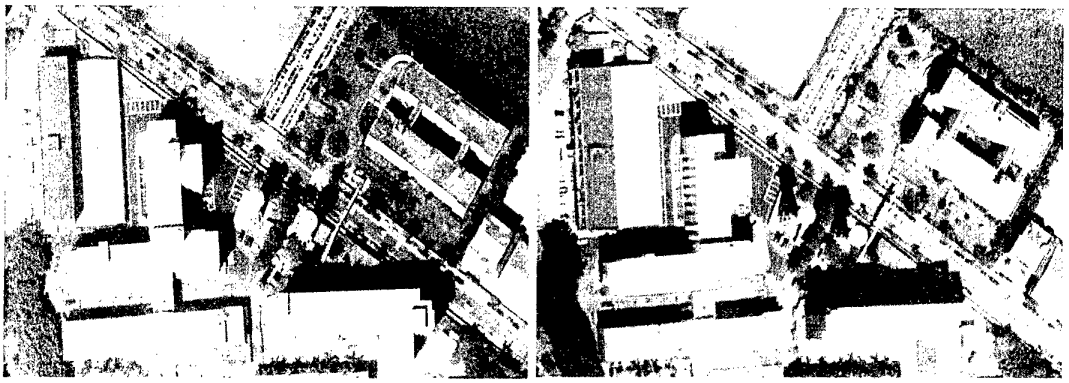


Figure 5,Conventional orthophotos from lower-left and upper-right photo.

With the upper-right scene as the master image, a true orthophoto was generated using the procedure developed in this study. The intermediate results and the final product for the highlighted area are shown in fig.6. Fig.6a shows result with hidden detection and relief displacement correction applied. The hidden areas were left blank to avoid possible confusion. Locating from this product the accurate position for viewable object is possible. As shown in fig.6b, the hidden defect has been significantly reduced after a fill-in operation. Still few small hidden areas exist. For all the master and slave images, the highlighted area is located right to the central line. Chance is that some part of ground features west to tall buildings is hidden from either of the images. A close look at fig.6b, unnatural discontinuity may be observed along the fill-in boundary. This is improved as shown in fig.6c by substituting direct fill-in operation with the seamless mosaic technique. Applying further the local enhancement for shadow defect, the final true orthophoto product as shown in fig.6d is with improvements, especially in the accessibility for objects obscured in shadow areas. Compared to fig.5, the interpretability of fig.6d is significantly improved.



Figure 6, Intermediate and final products.

(a) Relief displacement correction only.

(b) Hidden compensation applied without smoothing.

(c) Hidden compensation using seamless mosaic technique.

(d) Shadow enhancement applied.

5. CONCLUSIONS

In this study an orthographic rectification scheme is proposed to generate large-scale true orthophotos. Provided that the DBM and DTM are available, the scheme minimizes hidden and shadow defects and improves the interpretability of products. The proposed scheme achieves (1) correction of the relief displacement for buildings and terrain, (2) recovering information within the hidden areas from conjugate photos, (3) stitching filled-in data with master image to reduce discontinuity, and (4) compensating illumination difference for shadow areas. A fully automatic procedure has been developed to examine the proposed scheme. Experimental results indicate that reading barricade is significantly reduced and the products retain good precision and reliability. Though some tuning is needed for processing data other than the aerial photos, a primitive course has been laid in this study for further stepping toward the generation of large-scale true orthophoto.

6. REFERENCES

Sahar, L., and A. Krupnik, 1999, "Semiautomatic Extraction of Building Outlines from Large-Scale Aerial Images", *PERS*, 65 (4), pp.459-465.

Shufelt, J. A., 1999, "Performance Evaluation and Analysis of Monocular Building Extraction from Aerial Imagery", *IEEE Trans. on PAMI*, 21 (4), pp.311-326.

Mayer, H., 1999, "Automatic Object Extraction from Aerial Imagery-A Survey Focusing on Buildings", *CVIU*, 74 (2), pp.138-149.

Amhar F., and R. Ecker, 1998, "The Generation of True Ortho-photos Using a 3D building Model in Conjunction with a Conventional DTM", *IAPRS*, Vol.32, Part4 "GIS-Between Visions and Applications", Stuttgart.

Chen, N. Y., H. T. Wang and M. M. Lin, 1997, "Orthographic Correction of Airborne Scanner Imagery for Mountainous Areas", *Proceeding of the 3rd International Airborne Remote Sensing Conference and Exhibition*, held in Copenhagen, Denmark, on 7-10 July, Vol. II, pp. 293-299.

Chen, L. C. and J. Y. Rau, 1993, "A Unified Solution for Digital Terrain Model and Orthoimage Generation from SPOT Stereopairs", *IEEE Trans. on Geoscience and Remote Sensing*, Vol. 31, No. 6,pp. 1243-1252.

DEVELOPMENT OF SOFTWARE TO CREATE A RECTIFIED IMAGE OF AN INCLINED PLANE

Ryuji MATSUOKA
Tokai University Research & Information Center
2-28-4 Tomigaya, Shibuya-ku, Tokyo 151-0063, JAPAN
Phone: +81-3-3481-0611, Fax: +81-3-3481-0610
E-mail: ryuji@yoyogi.ycc.u-tokai.ac.jp

Naoki SHIRAI
Department of Research and Development, Kokusai Kogyo Co., Ltd.
2 Rokuban-cho, Chiyoda-ku, Tokyo 102-0085, JAPAN
Phone: +81-3-3288-5921, Fax: +81-3-3262-6150
E-mail: nshirai@kkc.co.jp

KEY WORDS: image rectification, digital camera, analytical photogrammetry

ABSTRACT: A piece of software to create a rectified image of an inclined plane for geological survey at a construction site has been developed. The major advantage of our software is that it is easy for a nonprofessional to create a rectified image with sufficient quality.
Digital camera images of an inclined plane are utilized for geological survey at a construction site. A target slope is too large to be covered by one image with sufficient spatial resolution. Not less than several, usually more than ten digital images taken for a target slope should be rectified and connected each other to become an image covering the whole of the target slope. At present each acquired image is manually deformed one by one using a piece of photo-retouch software in PC, and deformed images are also manually connected. This work takes time and quality of the produced image depending on skill of an operator is unsatisfactory in some cases.
Accordingly, we decided to develop a piece of software to create a rectified image covering the whole of an inclined plane in a short time and sufficient quality without ground survey of control points. Our software is based on analytical photogrammetry and image processing technologies, and it is designed for an amateur such as a geological engineer without photogrammetric or image processing know-how to operate it easily after short-period training.

1. INTRODUCTION

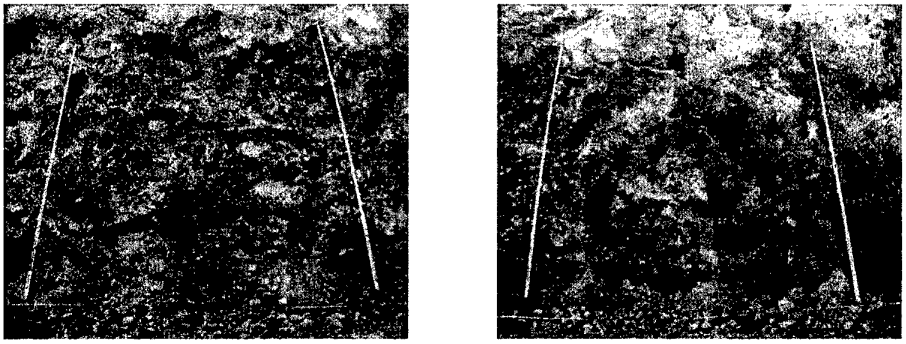
Photographs of an inclined plane have been utilized for geological survey at a site of a massive scale construction such as dam and highway construction. A lot of analog photographs used to be taken at a construction site. As performance of a digital camera becomes better and its price becomes lower in recent years, digital camera images are becoming major at a construction site.

A digital camera image has several advantages; one is that its quality can be examined immediately after exposure without development, and another is that image data can be transferred directly into a computer. However, a major weak point of a digital camera image is its lower spatial resolution. A target inclined plane is too large to be covered by one image with sufficient spatial resolution. Not less than several, usually more than ten digital images are taken for a target slope. They should be rectified and connected each other to become an image covering the whole of the target slope.

Figure 1 shows a pair of adjacent images of an inclined plane. Each image has a pair of scales on both left and right sides. Though a pair of scales was laid in parallel on the slope, a pair of

scales on the image looks not in parallel because a photographer faced obliquely to the target plane. Figure 2 demonstrates a process of creating a rectified image. Each image is deformed and connected each other to become an image covering the whole of the target slope.

At present each acquired image is manually deformed one by one using a piece of photo-retouch software in PC, and deformed images are also manually connected. This work takes time and quality of the produced image depending on skill of an operator is unsatisfactory in some cases. Accordingly, we decided to develop a piece of software to create a rectified image covering the whole of an inclined plane in a short time with sufficient quality.



(a) Left image (b) Right image

Figure 1 A pair of adjacent images of an inclined plane

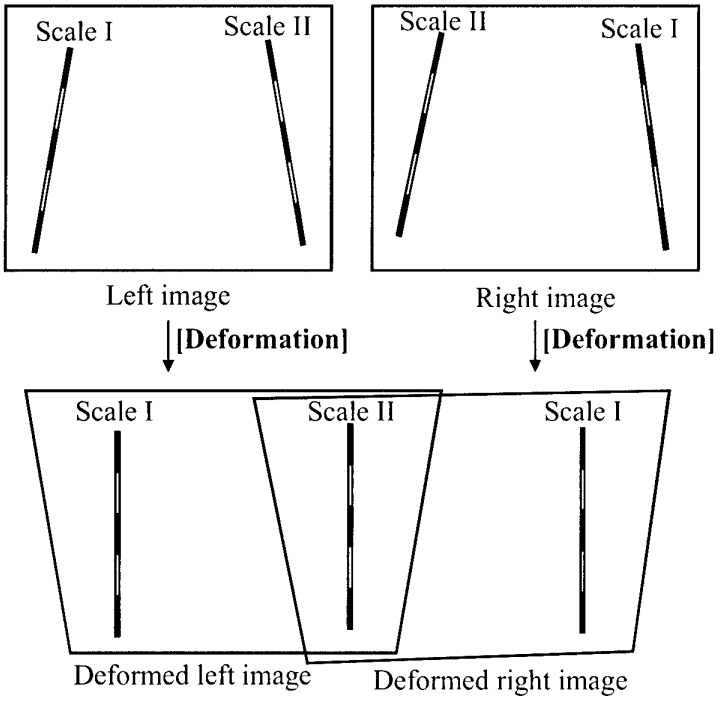


Figure 2 Creating a rectified image of an inclined plane

2. OUTLINE OF DEVELOPED SOFTWARE

2.1 User Requirements

User requests to the software to create a rectified image of a slope were summarized as follows:

(1) Software should be operated easily by an amateur.
The software will be operated by a geological engineer or a civil engineer at a construction site who is not used to photogrammetry nor image processing. Software should be operated easily by an operator without photogrammetric nor image processing know-how.

(2) Field works at a construction site should take a short time.
There is a limited time for geological survey at a construction site. No field works except image acquisition are usually allowed at a site. It should be easy for an amateur photographer to take necessary images. No ground survey of control points should be required.

(3) High spatial accuracy of a rectified image should not be required.
A rectified image of a slope will be utilized for visual interpretation. Geological survey at a construction site allows rather lower spatial accuracy of a rectified image.

(4) No special equipment should be required.
The cost of equipment should be low. All hardware components should be inexpensive, and they should be for all purposes and available on the market.

2.2 Processing flow

In order to answer the above mentioned user requests we developed a piece of software to create a rectified image of a slope based on the assumption that the target slope is a plane. Figure 3 shows the processing flow using our software. Outline of each step will be explained in the following section.

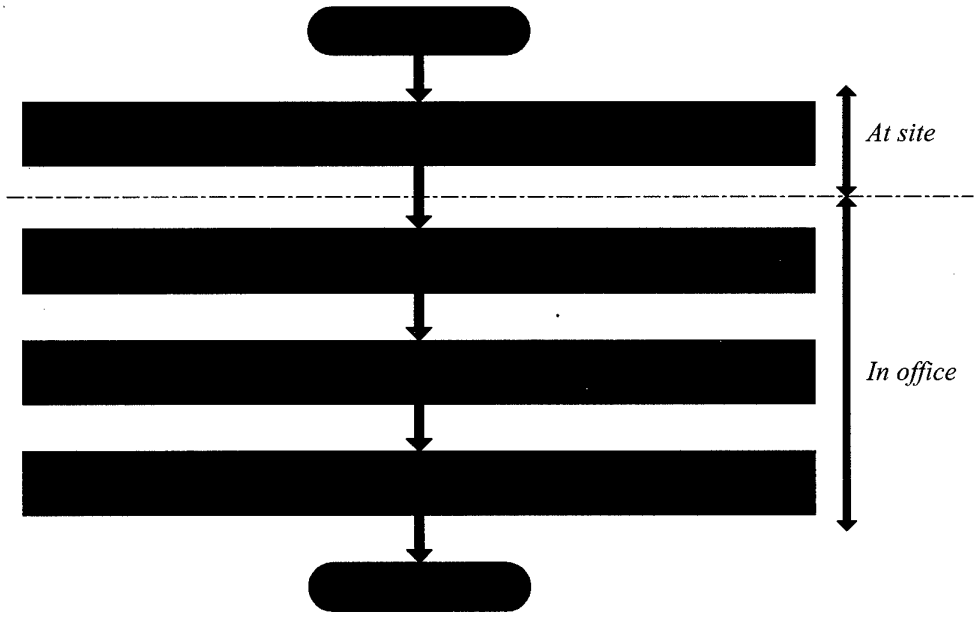


Figure 3 Processing flow using the developed software

2.3 Image acquisition by digital camera

A pair of scales such as staffs in leveling laid in parallel on a target slope is photographed in both sides of an image as shown in Figure 1. This gives geometric controls such as length and straightness in determination of transformation equation of each image. Furthermore this ensures that there is no gap between adjacent images.

Figure 4 illustrates acquisition of a series of images with a pair of scales. Image 1 and Image 3 have Scale I in the left side and Scale II in the right side. In reverse, Image 2 and Image 4 have Scale I in the right side and Scale II in the left side. These movements of Scales I and II are the same as the movements of staffs in leveling.

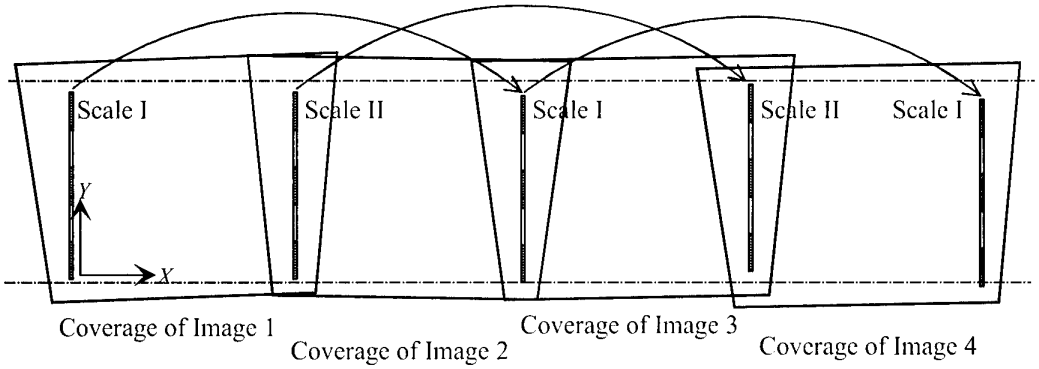


Figure 4 Acquisition of a series of images with a pair of scales

2.4 Measurement of image coordinates of control points

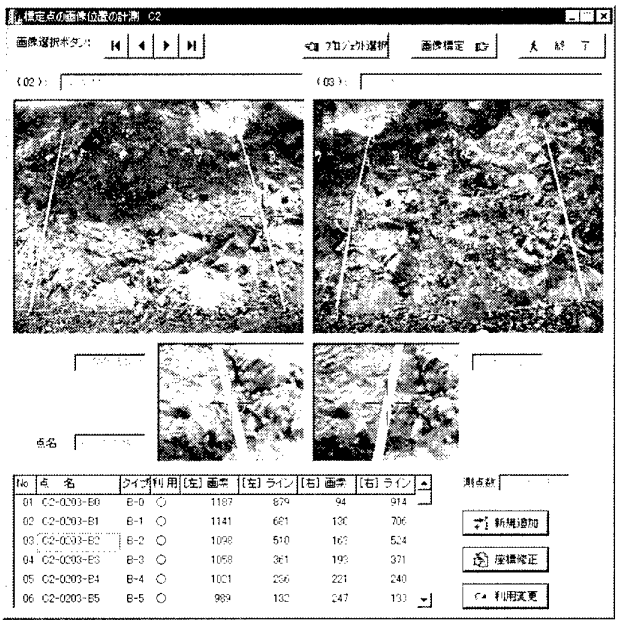


Figure 5 Measurement of image coordinates of control points

Acquired images are transferred into a computer in an office. Two adjacent images are displayed on the computer screen, and an operator clicks at marked points on scales on the screen. Marked points on a scale are treated as control points. Clicked position of each marked point on the image is measured and recorded as image coordinates of the control points. Figure 5 shows a screen for measuring image coordinates of control points. Measurement of image coordinates of control points is the major manual operation of the software.

2.5 Determination of transformation equation

We adopted the following colinearity equation as a transformation equation of a digital camera image:

$$\left.\begin{aligned} u &= -c\frac{a_{11}(X-X_0)+a_{12}(Y-Y_0)+a_{13}(Z-Z_0)}{a_{31}(X-X_0)+a_{32}(Y-Y_0)+a_{33}(Z-Z_0)}+u_0 \\ v &= -c\frac{a_{21}(X-X_0)+a_{22}(Y-Y_0)+a_{23}(Z-Z_0)}{a_{31}(X-X_0)+a_{32}(Y-Y_0)+a_{33}(Z-Z_0)}+v_0 \end{aligned}\right\} \quad \text{.....(1)}$$

$$\begin{bmatrix} a_{11} & a_{12} & a_{13} \\ a_{21} & a_{22} & a_{23} \\ a_{31} & a_{32} & a_{33} \end{bmatrix} = \begin{bmatrix} 1 & 0 & 0 \\ 0 & \cos\omega & -\sin\omega \\ 0 & \sin\omega & \cos\omega \end{bmatrix} \begin{bmatrix} \cos\phi & 0 & \sin\phi \\ 0 & 1 & 0 \\ -\sin\phi & 0 & \cos\phi \end{bmatrix} \begin{bmatrix} \cos\kappa & -\sin\kappa & 0 \\ \sin\kappa & \cos\kappa & 0 \\ 0 & 0 & 1 \end{bmatrix} \quad \text{.....(2)}$$

where (X,Y,Z) and (u,v) are the ground and image coordinates of the point respectively, (X_0,Y_0,Z_0) and (ω,ϕ,κ) are position and attitude of the camera respectively, (u_0,v_0) are the image coordinates of the principal point, and c is the focal length of the camera.

Transformation equations of all images are simultaneously determined by SAPAGO (Simultaneous Adjustment of Photogrammetric And Geometric Observations) developed by the authors. Figure 6 shows geometric constraints of control points used in SAPAGO.

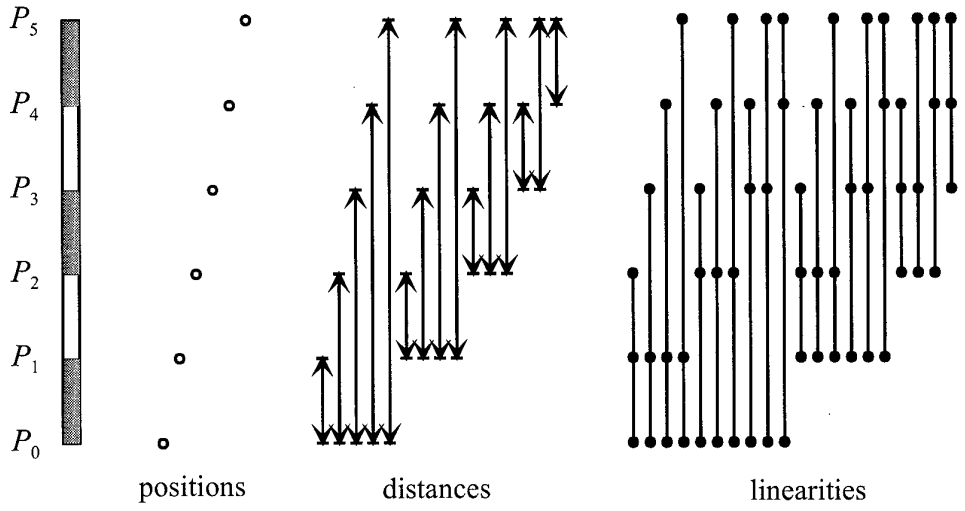


Figure 6 Geometric constraints of control points used in SAPAGO

2.6 Creating a rectified image file

The only work of an operator at this step is to input a size of a pixel of a rectified image to be created. After input of the pixel size of a rectified image a computer executes geometric correction of each image following the determined transformation equation. Finally geometrically corrected images are connected each other to become an image covering the whole of the target slope.

3. EXPERIMENT

We conducted an experiment to investigate performance and user-friendliness of the developed software. The objects of the experiment were four excavation slopes at a dam construction site. Widths of the target slopes range approximately from 10 m to 40m and heights of them range approximately from 5 m to 10m. There were three, three, seven and eight images of the target slopes acquired respectively. Each image covers approximately 7 m wide and 6 m high.

Figure 7 shows a rectified image of one of the target slopes made of a series of three images. Figure 8 shows a rectified image of another target slope made of a series of eight images. There are found some discrepancies between adjacent images in both rectified images. The reason of these discrepancies is that a real target slope is not a plane in the strict sense. Since we assumed that the target slope is a plane with the aim of easy operation, these discrepancies are unavoidable. Fortunately these unavoidable discrepancies are negligible for geological survey at a construction site.

There are found another defect that the outermost images (leftmost image and rightmost image) are slightly distorted. The reason of these distortions is that the outermost images are more weakly constrained than the other inside images. Acquisition of images covering the outside of the target slope lets these distortions avoidable.



Figure 7 Rectified image of a series of three images

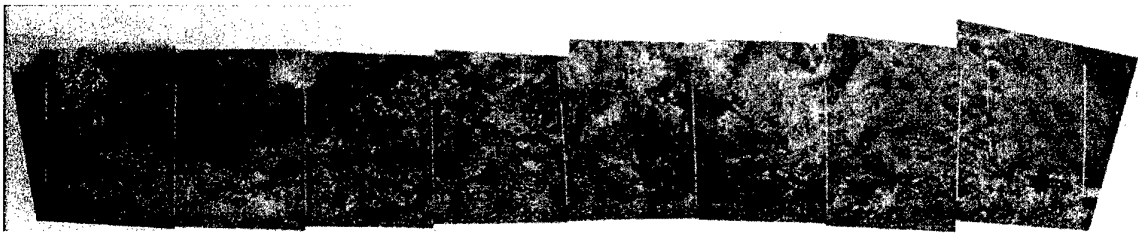


Figure 8 Rectified image of a series of eight images

4. CONCLUSION

We have developed a piece of software to create a rectified image of an inclined plane for geological survey at a construction site. The major advantage of our software is that it is easy for a nonprofessional to create a rectified image with sufficient quality without ground survey of control points. An operator without photogrammetric nor image processing know-how can operate the software easily after brief training, and create a rectified image of the target slope in a short time with requested quality.

ACKNOWLEDGEMENTS

The authors are grateful to Mr. Masayoshi Kuji, a geological engineer of Technology Research Institute of Maeda Corporation for his help at the experiment of the software.

AN ITERATIVE APPROACH TO ACQUIRE LINEAR FEATURES UNDER THE CONSTRAINTS OF THEIR KNOWLEDGE IN OBJECT SPACE

Shih-Hong CHIO and Shue-Chia WANG
Ph.D. Candidate and Professor
Department of Surveying Engineering, National Cheng-Kung University
No. 1, University Road, Tainan, TAIWAN
Tel:(+886)-6-2373876 ext.834; Fax:(+886)-6-2375764
E-mail: p6883102@sparc1.cc.ncku.edu.tw

KEYWORDS: Geometric constraint, Matching, Linking, Object knowledge

ABSTRACT: 3-D linear segments are crucial primitives for reconstruction of man-made buildings. This paper presents one iterative approach to acquire more linear segments from stereo image pair with known orientations under the constraints of their knowledge in object space. The major algorithm in this iterative approach is referred as □Core Algorithm□ which simultaneously match and link linear segments based on their knowledge in object space. This iterative approach consists of four processing procedures. No additional height constraint is used in the first processing procedure. The other three iterative processing procedures will employ average height from relevant 3-D linear segments as additional height constraint to acquire more 3-D linear segments by using Core Algorithm. We hope this iterative approach will increase the amount of the acquisition of 3-D linear segments.

1.Introduction

3-D linear segments are crucial primitives that constitute most of the man-made objects, especially the roof boundaries in the aerial images. Therefore, they are very important for the reconstruction of man-made object. No matter what kind of method is used to acquire those 3-D linear segments, i.e. segment stereo-matching algorithm in [1], it is impossible to obtain all the 3-D linear features. Therefore, this paper would like to presents one iterative approach to acquire more 3-D linear segments under the constraints of their knowledge in object space. The core algorithm of this iterative approach is to simultaneously match and link the linear segments based on their knowledge in object space. Firstly, Core Algorithm is used to those linear segments according to the order of their geometric structure. No additional height constraint from adjacent 3-D linear segments could be imposed in this step. During this first process, when it succeeds, the average height of this acquired 3-D linear segment will be immediately introduced as additional constraint to handle the adjacent linear segments of this successfully processed linear structure by Core Algorithm. This is the second iterative process. Subsequently the same Core Algorithm with height constraint are used in the third iterative process to handle the remaining linear segments that are the members of the successfully processed linear structure. Finally, Core Algorithm together with height constraint will be once more applied to those remaining linear segments that locate at the certain range of those already successfully processed linear segments. We will describe Core Algorithm in Section 2 and this iterative approach in Section 3. The relevant experiments will be shown in Section 4. Finally, short conclusions will be drawn in Section 5.

2.Core Algorithm for Matching and Linking in Object Space

2.1 Available Knowledge of 3-D Linear Segments in Object Space and Their Calculations

As stated before, Core Algorithm will match and link linear segments based on their object knowledge. Hence, this section will describe the relevant knowledge of 3-D linear segments and their calculations.

We assume that man-made 3-D linear segments should be either oblique or horizontal. Since they are man-made, their change rate of height in object space should be reasonable. For one horizontal 3-D linear segment, the real change rate of height should be close to zero *meter per meter* (short for *m/m*). For one oblique 3-D linear segment, the real change rate of height along this line should be constant and within a reasonable limit. These two definitions for change rate of height are the main knowledge of linear segments in object space that will be used as constraints in our method to match and link linear segments. Also, it implies that several linear segments with same change rate of height could be the same one. Of course, if this 3-D linear feature is horizontal, then the same height information will be its another knowledge. Next we will explain how to calculate the change rate of height of one 3-D line.

In Fig.1, one 3-D horizontal linear segment is projected onto stereo images. One 3-D edge piece is defined as every three corresponding edge pixel in series and one 3-D linear segment could be regarded as the composition of several 3-D edge pieces. Each corresponding edge pixel will determine its 3-D coordinate in object space by the space intersection, therefore, the ground coordinates on each 3-D edge piece will be known also; then the individual information on each 3-D edge piece will be calculated accordingly (see Fig. 1). Next the object knowledge, i.e. average change rate of height, for each 3-D linear segment will be determined according to those 3-D edge pieces. Now, the details to calculate will be described below.

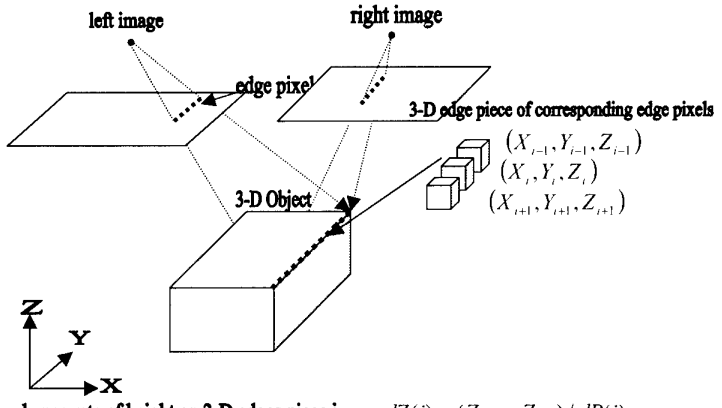


Fig.1: Illustration of calculation of the average change rate of height

Firstly, the horizontal distance (*dP(i)*) of 3-D edge pieces *i* will be defined as shown in Fig.1. It should be limited in terms of pixel resolution and image scale. The limitation of *dP(i)* corresponds to filter the problematic and unreliable individual change rate of height *dZ(i)* along this 3-D linear segment. Those unreliable *dZ(i)* might be caused by noise or by uncertainty of edge points during the edge detection. After the unreliable edge pieces are filtered, average change rate of height *dZ* of this 3-D linear segment will be determined by averaging *dZ(i)* from all reliable 3-D edge pieces (c.f Fig.1). Fig.1 just illustrates how to get the knowledge of horizontal line segments, but it's applicable to oblique 3-D line segment.

2.2 Data Preparation

At the beginning, Poly-Morphic feature extraction method [2], will be used in this research to extract relevant junctions and edge pixels in image space. After using non-optima suppression to them, one simple edge-linking algorithm is used to link the adjacent pixels together to form longer edges by considering the pixel connectivity. Since 3-D linear features are our concerns and they should be straight lines in image space. Therefore, Douglas-Peucker algorithm [3] is applied to get 2-D linear segments by considering the pixel collinearity. In this research, each pixel coordinate on 2-D linear segments should be recorded in order to calculate their knowledge in object space. Therefore, the major purpose of Douglas-Peucker algorithm is not for the data generation or reduction.

For deciding the checking priority of those 2-D linear segments, the feature aggregates, including line structures and junction structures, consisting of junctions and line segments are grouped from geometric proximity and collinearity according to their potential to form man-made buildings. For example, a longer linear segment with junctions near both its endpoints could be more possibility from a roof than a single line segment without anything attached to its endpoints. For our method, the former one should have higher priority to be chosen for processing. More details about the classification of feature aggregates was described in [4]. Then both line structures and junction structures together with flanking attributes, i.e. average gray value, on both sides of linear segments are used to develop this iterative approach to match and link linear segments by considering their knowledge in object space.

2.3 Initial screening of possible candidates

This iterative approach will start from higher priority of line structure and is done along the epipolar direction. Since at the beginning we don't know anything about the object knowledge of any linear segment, for each one in left image probably there are many candidates waiting to be chosen in right image. To demand the correctness of results as possible as it can, it is important to give strong constraints for the initial screening of possible candidates in right image. Therefore, object knowledge, geometric and radiometric properties are all considered simultaneously as follows:

From geometric consideration: the initial correspondence of the linear segments between the stereo images must have the junction point along the epipolar direction. This factor is only considered in the first iterative processing procedure. The subsequent three iterative processes don't take this into account. Instead, this part will be replaced by the constraint of height. Plus, their absolute difference of azimuth between the correspondence is within one threshold.

From radiometric consideration: at least one side of the corresponding flanking regions on possible corresponding 2-D linear segments should have similar gray values, i.e. the difference of their mean gray values should be less than a given threshold.

From the object-knowledge consideration:

1. Besides the constraint of the change rate of height, the number of reliable 3-D edge pieces should be higher than one threshold. It implies the length of this 3-D line should be long enough in object space.
2. The standard deviation of average change rate of height is smallest among the candidates and less than one threshold. This criterion demands more accurate change rate of height.

Finally, the optimal decision is decided by simple weighting equation:

$$Weight = \frac{1}{\lfloor sigma \rfloor} + \frac{1}{\lfloor dG_L \rfloor} + \frac{1}{|dG_R|}$$

Where *sigma*: the sigma of height change rate; dG_L , dG_R: gray difference on the left and right side of line

2.4 Subsequent matching and linking process

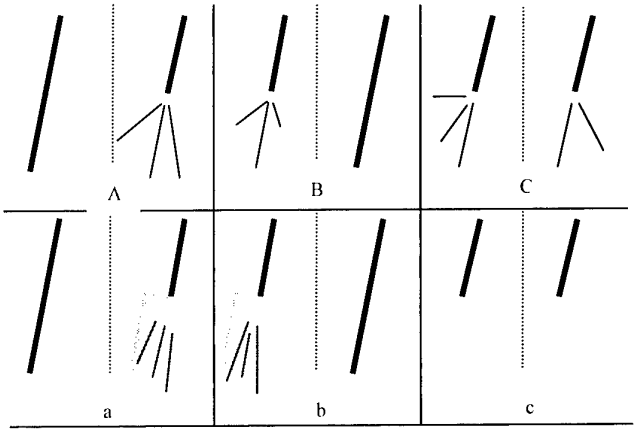
After finding the initial correspondence, the process will proceed by matching and linking the next linear segments according to the status of Fig.2. From possible liking candidates. The following constraints in object space will be considered for the optimal liking linear segment.

1.For length, the number of reliable 3-D edge pieces should be higher than one threshold.

2.For "man-made" 3-D line, the average change rate of height should be within one certain range.

3.For the "same" man-made 3-D linear feature, the absolute value of difference of average change rate on height between linking linear segment and the initial linked linear segment is the smallest among possible candidates and less than one threshold.

The subsequent process proceeds as follows. First, the process will be conducted between the longer linked line segment and the neighboring linear segments of shorter linked linear segments, see Fig.2A and 2B, by the above-mentioned constraints of object knowledge. If the neighboring linear segments could not be found or meet the conditions, the search area formed by the maximum and minimum parallax will be setup.



Left part means left image and right part shows right image.
Thick and Thin lines: already linked and non-linked 2-D lines

Fig.2: Possible six situations during linking process by using the stereo images based on object knowledge

Then the linear segments in this search area, shadow area in Fig 2a and 2b, will be processed under the same constraints of object knowledge. If the linear segments have the same length, as shown Fig.2C and 2c, only the situation in Fig.2C is processed. The process will repeat over and over until no linear segment could be found and linked. From the constraint on the change rate of height, the process would be applied to handle not only the horizontal lines but also the oblique lines.

3.Iterative Approach to Simultaneously Match and Link the Linear Segments

In the iterative approach, Core Algorithm mentioned above is used in each procedure. The iterative processing algorithm is proceeding as follows:

Firstly, this iterative approach will begin from the strongest structures to weaker structure in left image, The strongest structures mean their high possibility to correspond with the imaging of roof boundaries in image space. For example, line structure A in Fig.3 has stronger structure than B ,C and D. That is C and D has the weaker structure in this case.

If the first iterative process succeeds, then not only the object knowledge of 3-D linear segment but also

the average height of this 3-D linear segment will be simultaneously introduced as the constraints in the second iterative process. Besides the additional height constraint, the second iterative process still uses the core algorithm to match and link the linear segments which are the members of this strongest linear structure. The first and second iterative processing procedure will be applied to the linear segments whose structures are from strongest to weakest.

Subsequently the third iterative process is applied to the remaining linear segments that are the members of the successfully processed linear structure. The same Core Algorithm will be also utilized and height constraint is also considered in this step. This process proceeds repeatedly until the remaining linear segments don't meet the requirement. Finally, Core Algorithm together with height constraint will be employed to those remaining linear segments that locate in the certain range of those already successfully processed linear segments repeatedly until no linear segment meets the above requirements.

Therefore, this iterative approach consists of four steps with one core algorithm and one additional height constraint. The geometric constraint in these four steps becomes less and less and the height constraint is also looser and looser. However, the relevant constraint of object knowledge about 3-D linear segments in Core Algorithm is always unchanged no matter which step it uses.

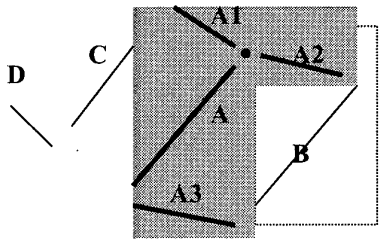


Fig.3: the diagram of iterative approach

Now take the Fig.3 as an example. The further iterative approach will start from the stronger structure **A** which consists of one junction and three neighboring linear segments **A1**, **A2** and **A3**. If the process succeeds, then **A1**, **A2**, and **A3** will be processed at once. In this case, linear segments **A2** is also the neighboring linear segment of the weaker structure **B**. It is assumed that the process didn't succeed in handling linear segment **B** due to fail in finding the corresponding junction in right image. The iterative process will process it again in the third step because linear segment **B** is the adjacent linear segment of linear segment **A2**, which has been successfully processed. Next, linear segment **C** is close enough to successfully processed linear segment **A1**, the process will be initialized again. If the linear segment **C** also is successfully handled, then the linear segment **D** is also processed again due to the same reason. Otherwise, all the process will stop.

Apparently if only the first iterative processing is applied, it might be impossible to obtain the results from linear segment **B**, **C**, and **D**. Because the result is feedback to restrict and guide another process once more to handling others, therefore, it is possible to produce more results. From the above discussion, the iterative approach does increase the amount of successfully matching and linking the linear segments. Next section will give some experiments.

4.Experiments and Results

This section will describe the results of the experiments. The pixel resolution of image pair is 30μm; image scale is about 1:8,000; and their image size is 180*180 and 180*225, respectively.

The associated thresholds for Core Algorithm in object space are described as follows:

The reasonable horizontal distance of 3-D edge piece (*dP(i)*) is set as 0.12m. Beside the threshold for the absolute value of average change rate of height is chosen as 1 *m/m,* the relevant thresholds are set as:

In the initial screening of possible candidates, 10 degrees for the azimuth difference threshold and 20 gray values for the difference of mean gray values of the flanking mate. Plus, 8 for the number of reliable 3-D edge pieces and 3*m/m* for the standard deviation of average change rate of height.

In subsequent matching and linking process, 5 for the number of reliable 3-D edge pieces.0.2 *m/m* for the difference of average change rate of height between candidates and the initial linked linear segment.

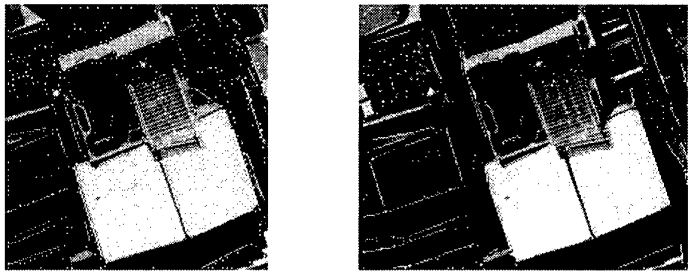


Fig.4: The result of matching and linking in object space according to their geometric priority

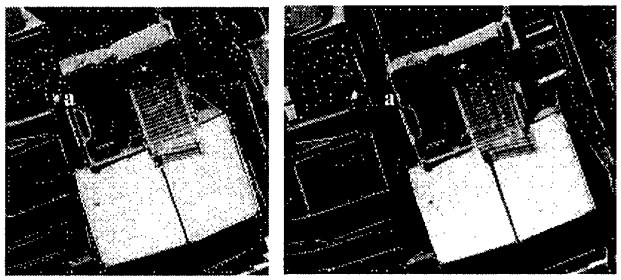


Fig.5: The result of matching and linking in object space via further iterative process: height difference 0.5 m

The result in Fig.4 is acquired only by the first processing procedure of iterative approach. Only 7 linear segments are successfully acquired. Some line segments could not be successfully processed because the geometrical structure can't meet the requirement of initial screening. However, after the concept of iterative approach is used, the results in Fig.5 show that 11 line segments are acquired. Additional 6 linear segments are obtained. The height difference in third and fourth process is set as 0.5m in the test of Fig.5. If the constraint of height difference is relaxing to 5m, two more will be successfully acquired, not shown here due to short space. Therefore, it could say that the concept of iterative approach could be helpful to get more 3-D linear segments. The results prove this concept could be applicable. Only one correspondence seems questionable, indicated by linear segment **a** at the upper left in Fig.5. This case is often happened in the urban images of Taiwan area due to the structures themselves.

5.Conclusions

From the experiment, this iterative approach does increase the number of matched and linked line segments for the next task. Nevertheless the simple weighting criterion is worthwhile to further investigation. Anyway, the increasing amount will be helpful for the subsequent relevant tasks.

References

[1]F. Bignone, "Segment Stereo-Matching and Coplanar Grouping", Technical Report BIWI-TR-165, Institute of communication Technology, Image Science Lab, ETH, Zurich, Switzerland, 1995.

[2] W. Foerstner, "Framework for Low Level Feature Extraction," in C*omputer Vision, ECCV '94,* vol. II, L*ecture Notes in Computer Science, 801,* pp. 383-394, J.O. Eklundh, Eds., Springer-Verlag, Berlin, 1994.

[3] D. H. Douglaus and T. K. Peucker, "Algorithms for the reduction of the number of points required to represent a digitized line or its caricature," Canadian Cartographer, vol. 10, pp.110-122, 1973.

[4] S. H. Chio, S. C. Wang, and B. Wrobel, "A Semi-Automatic System for the Reconstruction of Building Roofs in Dense Urban Areas Using Aerial Stereo Image Pairs," AVN ALLGEMEINE VERMESSUNGS-NACHRICHTEN, pp.167-174, 1999.

Automatic acquisition of 3D spatial data in city with air-borne TLS (Three Line Scanner)

Yoshiaki KAGAWA and Ryosuke SHIBASAKI
Center for Spatial Information Science and
Institute of Industrial Science,
University of Tokyo
4-6-1 Komaba, Meguro-ku, Tokyo 153-8505
Tel: (81) -3-5452-6417 Fax(81) -3-5452-6417
E-mail: kagawa@skl.iis.u-tokyo.ac.jp
JAPAN

KEY WORDS:TLS(Three Line Scanner) , three-dimensional spatial data, laser scanner , stereo matching

ABSTRACT: Recently, automatic generation of three-dimensional data in city from aerial images are needed for three-dimensional GIS and revision of GIS database. Though digital or analogue aerial photograph or sequential CCD image data are conventionally used for this purpose, the accuracy and reliability is not sufficient especially for urban area where height of terrain and building surfaces have abrupt changes. Instead, the authors are developing an integrating sensors consisting of three line scanner (TLS) and laser scanner. TLS is made of three CCD line sensor located in parallel on the imaging plane and has capability of triplet observation, which will have higher accuracy and capability in three-dimensional data generation. By integrating with a laser scanner, reliability of high-resolution three-dimensional city data generation will be improved. In this study, we describe the system configuration and methodology of making three-dimensional data from TLS and the laser scanner using an experimental flight data.

1.Introduction

Recently, three-dimensional data in city are needed, because as compared with two-dimensional data, three-dimensional data can describe detail of city, which enables us conduct more accurate and detailed simulation or analysis on urban areas. Examples of the simulations or analysis are wind simulation around high-rise buildings, fire propagation simulation, flooding analysis and propagation/reflection analysis of electric waves for telecommunication.

Mainly, there are two methods for generation of three-dimensional data. First method is using optical sensor like CCD camera. This method is a successor to traditional analogue

aerial photo. But resolution of two dimensional CCD camera is not very sufficient for generating accurate 3D city data generation. Second method is using laser scanner. Laser scanner is an equipment that radiates laser beam to objects and measure distance form the scanner to the object using the return time of the radiated laser beam. When the position of scanner and angle of radiation of laser are known, three-dimensional coordinates of object can be calculated directly. By swinging the laser beam, many data points are obtained, but the resolution is lower than that of CCD sensor. Although studies on application of the individual technologies are conducted, but the possibilities of the combination of both technologies have never been explored using real data. So, in our study, objective is to develop methodology of making three-dimensional data from optical sensor and the laser scanner using an experimental flight data. And as optical sensor, new hardware -Three Line Scanner was used.

2.Three Line Scanner TLS

Three Line Scanner (TLS) is an optical sensor for aerial survey. Three Line Scanner has three linear CCD located in parallel to get image of three directions -forward, nadir, and backward, which is oriented perpendicular to the flight direction of aircraft. Image is generated due to the aircraft motion by scanning the terrain surface. (Fig1)

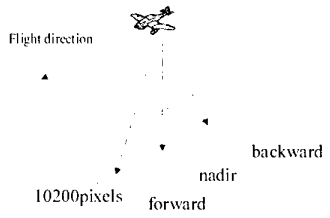


Fig1 : method of getting data with TLS

Differently from CCD frame sensor (two dimensional CCD), the exterior orientation must be computed for each scan-line. The specification of the Three Line Scanner used in this study is shown in Table1. Using linear CCD, the resolution of the image is very high. Single line has 10200 pixels. Ground resolution of the image reaches 5 cm when the flight height is 500m. Flight path and high frequent vibration have a blurring effect on the image, which necessitates the development of stabilizer to absorb the vibration.

Table1 : system specification of TLS

CCD	number of pixel/line	10200 pixels
	pitch of pixel	7 um
number of CCD		3 (monochrome) ,1 (RGB)
number of shades		(4096shades) 12 bit
lens	distance of focus	60mm
angle of stereo		21 °
number of line		500 line/second

3. Laser Scanner

Data of laser scanner is obtained in a synchronized manner with the TLS. Resolution of data is about 50cm. Fig2 shows data of laser scanner. (Location is Roppongi, Tokyo in Japan) Ground resolution of the laser scanner data is approximately 50 cm, which is much lower than that of the TLS, though 3D shape of urban objects can be directly extracted from the laser data. But we can know some objects somewhere from data, then they can be used for auxiliary data.

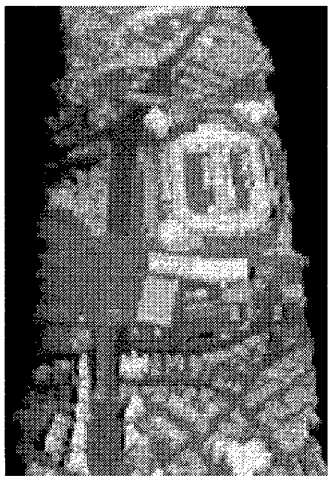


Fig2 : Data of laser scanner seen with bird's eye view

4.Theory

4.1.Posiion and angle data in each line

Flow chart of this study is shown Fig3. First of all, we have to generate accurate data of position and angle in each line. For that, we conducted relative orientation with some ground control points and GPS (Global Positioning System) /INS (Inertial Navigation System) data as auxiliary data. From GPS and INS, position and angle of CCD is obtained directly, but the number of measurement per second are lower than the data acquisition frequency of TLS (500Hz), especially GPS data can be obtained only 5 times per second. And data's reliability is not so high, so we use them as auxiliary data.

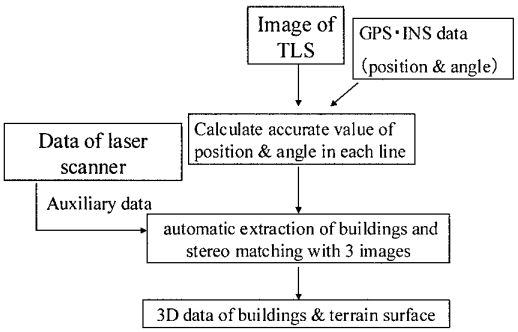


Fig3 : Flow chart of this study

4.2.Automatic extraction of buildings and stereomatching

Fig 4 shows TLS image obtained by a test flight without the stabilizer. Distortions coming from attitude changes of the aircraft prevents the stereo viewing and automatic image matching directly using the raw data. So, we have to rectify these images. For the rectification a horizontal plane located at a mean terrain height is defined. And each pixel of the image is projected on the plane to rectify the distortions. Fig5 is the rectified image. And then, using the rectified



Fig4 : Raw data of TLS

image, buildings are extracted. At first, edges of buildings are extracted from image. With application of wavelet transform, image of edge eliminating noise can be obtained. Then, segmentation is conducted by extracting closed areas. At last, correspondence of an identical object among the three different images are determined in stereo matching process. But there are problems when using only images. For example, wrong correspondence may arise because some buildings may have almost the same characteristics. Another source of wrong correspondence is the occlusion, i.e. a feature in one image may not appear in the other images. Then, in our study, laser scanner data is used for solving these problems.

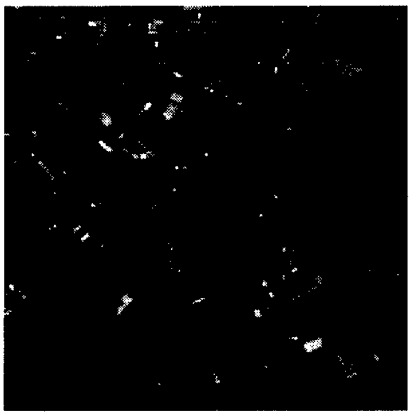


Fig5 : Rectified image of TLS

4.3.Ideas of using laser scanner data to support stereo matching process

Laser scanner data can be used for reducing the range of search for corresponding features area of reference, because the laser scanner data give approximate height of the buildings and terrain surfaces.

And before matching, occluded area can be detected from the coarse 3D data from the laser scanner and the estimated position and attitude of the aircraft. The results of the experiment of integrating TLS data and the laser scanner data will be presented at the conference.

5.Summary

We proposed methodological framework of generating three-dimensional data automatically from data of TLS and laser scanner. For the purpose of generating 3D city model with higher resolution and automation level, TLS image can compensate the low resolution of laser scanner data, while the laser scanner data can assist stereo matching process by providing approximate height of terrain surface and building height. Detailed algorithm should be devised using the experimental flight data. The result will be reported at the conference.

References

• Norbert Haala, Dirk Stallmann and Micheal Cramer, "Calibration of directly measured position and attitude by aero triangulation of three-line-airbone imagery"

• Ryosuke Shibasaki, 1993, "Three Line Scanner", Photogrametry & Remote Sensing Vol.32,No.6 pp26-30

• Zhongchao Shi and Ryosuke Shibasaki,1995,"Application of Wavelet Transform Based Image Segmentation and Stereo Matching for Automated House Detection from Aerial Photograph",Photogrametry & Remoto| Sensing Vol.34, No.5

MULTI-RESOLUTION APPROACH TO RADARGRAMMETRIC DIGITAL ELEVATION MODELS GENERATION

Xiaojing HUANG, Leong Keong KWOH and Hock LIM

Centre for Remote Imaging, Sensing and Processing
National University of Singapore
SOC1 Level 2, Lower Kent Ridge Road, Singapore 119260
Fax: (65)7757717 Email:crshxj@nus.edu.sg

KEY WORDS: Digital Elevation Models, Radargrammetry, Correlation

ABSTRACT: In this paper, we present our work in Digital Elevation Models (DEM) generation with RADARSAT stereopairs, usually form from S2 and S6 standard beam modes, using radargrammetric technique. We introduced a weighted block window for the matching of corresponding patches and a hierarchical multi-resolution approach to improve the DEM generation robustness. Prior to DEM generation, an imaging model based on the satellite and target geometry, and signal acquisition time for RADARSAT has been developed, and the model parameters have been refined to match the local terrain with ground control points (GCPs).

INTRODUCTION

DEM of a region can be generated from stereopairs of satellite images. In tropical areas where cloud free optical images are hard to acquire, DEM generation with radargrammetry using high resolution spaceborne synthetic aperture radar (SAR) images, such as RADARSAT images, is a potential alternative. In this paper, we described the system we developed at CRISP for DEM generation from RADARSAT stereopairs. The main processing steps involved are (a) establishing the SAR imaging model and determining the parameters of the imaging models, (b) automatic DEM generation applying a weighted block window digital correlation and implementing a hierarchical multi-resolution approach.

SAR IMAGING MODEL

In a SAR image, the location on the ground of an image sample (u, v) can be derived from knowledge of the sensor position and velocity [1]. The pixel coordinate u is related to the slant range r from the sensor to the corresponding point on the ground. While the line coordinate v is related to the azimuth time s at which the pulse of the corresponding line is transmitted. These relationships can be expressed as follows:

$$r = r_0 + kr_0 \cdot u \tag{1}$$

$$s = s_0 + ks_0 \cdot v \tag{2}$$

where r_0 is the slant range of the first pixel in the image, kr_0 is the scaling factor in the range direction, s_0 is the azimuth time of the first line in the image, and ks_0 is the scaling factor in the azimuth direction. The preliminary values of r_0, kr_0, s_0 and ks_0 can be obtained from the RADARSAT product leader file.

The SAR range r and line time s of any target is further related to the sensor as follows:

$$r^2 = (\mathbf{r}_s - \mathbf{r}_t)\cdot(\mathbf{r}_s - \mathbf{r}_t) \tag{3}$$

$$f_{dc} = \frac{2}{\lambda}(\mathbf{v}_s - \mathbf{v}_t)\cdot(\mathbf{r}_s - \mathbf{r}_t) \tag{4}$$

where $\mathbf{r}_s, \mathbf{v}_s$ are sensor position and velocity vectors, and $\mathbf{r}_t, \mathbf{v}_t$ are target position and velocity vectors. f_{dc} is the Doppler centroid frequency, and λ is the radar wavelength. For RADARSAT SGF images, f_{dc} is zero since the image is resampled to the zero-Doppler. The target velocity can be determined from the target position since the target is on the earth surface. The sensor position and velocity can be derived from azimuth time s and satellite state vectors given in the image leader file.

Equations (1) - (4) describe the imaging model we use for a SAR image. All imaging parameters can be obtained from the image product leader file. To optimize the imaging model for the local area of interest, some parameters can be refined with GCPs. We choose to only refine equation (1) and (2) with the following expressions:

$$r' = \Delta r + kr \cdot r \tag{5}$$

$$s \leftarrow \Delta s + ks \cdot s \tag{6}$$

where $\triangle r$ and kr are the shift and scaling factor of image slant range, respectively, $\triangle s$ and ks are the shift and scaling factor of image azimuth time, respectively, r¢and s¢are the corrected slant range and azimuth time, respectively. There are thus a total of 4 parameters to be refined for each image. These 4 parameters are solved by least square adjustment techniques, using at least 2 GCPs.

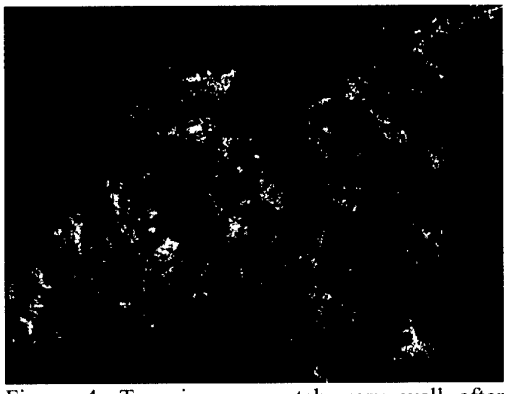


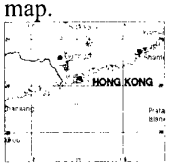
Figure 4. Two images match very well after geocode to accurate topographic map (red for S7 mode, green and blue for S2 mode).

To verify the correctness of the imaging model, we use them to terrain geocode a RADARSAT S2 image (fig 1) and a RADARSAT S7 image (fig 3) of Lantau Island (Hong Kong) with available DEM. The parameters of the imaging model for each image were refined using GCPs obtained from topographic maps. The good agreement of the terrain corrected geocoded images shown in figure 4 (the S2 geocoded image shown in red and the S7 geocoded image shown in cyan) shows the correctness of the model.



Figure 1. Lantau Island in RADARSAT SGF image of S2 mode acquired on 25 Dec 1996

Figure 2. (below) Lantau Island location map.



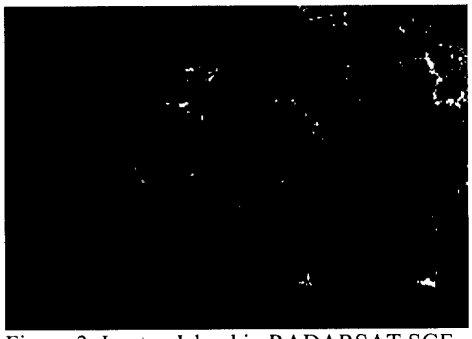


Figure 3. Lantau Island in RADARSAT SGF image of S7 mode acquired on 28 Dec 1996.

DEM GENERATION

The underlying principle for generating the DEM is to find, for each X,Y coordinates, a height H where the normalized cross correlation of two image patches, one from each images, is highest within a range of heights. The location of each image patch is computed from the refined imaging model. A problem in correlating SAR imagery is that there are usually some very dominating high intensity features amongst the majority of average intensity features. When we choose any patch, the correlation results will be biased to these strong intensity features, even though they may be at the far edges or corners of the patch. We reduce this problem by introducing a weighted block window to minimize the contribution of the edge pixels in the correlation computation. The weighted block window chosen is the Welch window [4] in two dimensions. The weighted window w_i in one dimension of pixel i can be expressed as follows:

$$w_i = 1 - [\,(i - N - 1)/(N + 1)\,]^2 \qquad (7)$$

where N is the half window size in one dimension. The full window size in one dimension is $2N+1$. Figure 5 shows the weighted window in one dimension with N = 19. The weighted window w_{ij} in two dimension (i, j) is:

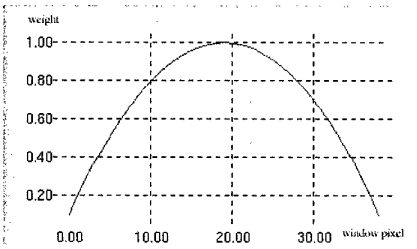


Figure 5. The weighted window in one dimension with N = 19.

$$w_{ij} = w_i \times w_j \ . \qquad (8)$$

HIERARCHICAL MULTI-RESOLUTION APPROACH

To improve the robustness of the DEM generation processing, a hierarchical multi-resolution approach (fig.6) is implemented. The original stereo pair of imagery (12.5m/pixel) were averaged over 16×16 (200m/pixel), 4×4 (50m/pixel) and 2×2 (25m/pixel) pixel-windows. A preliminary DEM is first computed from the correlation of the lowest resolution (200m/pixel) image pair. For the higher resolution computation, the DEM computed at the previous step is used to carry out a geometric correction of the image pair to enhance correlation, hence more accurate height determination. The advantage of using this hierarchical multi-resolution matching technique is that it is easier to find the correct matching of the reduced resolution images because of the removal of the speckle noise and detailed features in the block window.

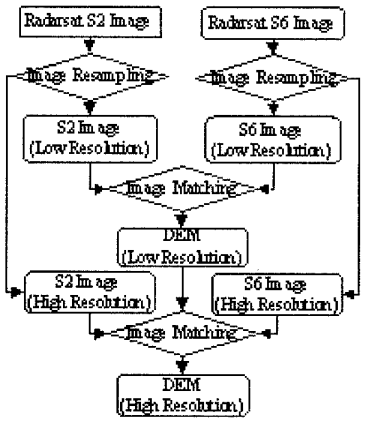


Figure 6. Hierarchical multi-resolution DEM approach.

TEST SITE AND DEM GENERATION

The hierarchical multi-resolution DEM approach was tested with two descending RADARSAT images of S2 and S6 beam modes (fig. 7 and 8) over Brunei. The detailed image description is listed in table 1. The pair of imagery (12.5m/pixel) were averaged over 16×16 (200m/pixel), 4×4 (50m/pixel) and 2×2 (25m/pixel) pixel-windows. The lowest resolution (200 m/pixel) DEM (fig. 9) of the area was first generated from the 200m/pixel image layers. The 50m/pixel resolution DEM (fig. 10) of the same area was later generated from 50m/pixel image layers by using the terrain information of previous DEM. Finally, the highest resolution DEM (fig. 11) of 20m/pixel of the same area was generated from 25m/pixel image layers by using

more detailed terrain information of previous DEM layer. An attempt to generate 10m/pixel resolution DEM by using the original imagery did not produced satisfactory results, probably because of the heavily scattered speckle noise at that resolution that causes de-correlation of the image patches.

Table 1. The description of Radarsat stereo imagery used in the DEM generation.

Stereo Pair	Image Format	Beam Mode	Incidence Angle (degree)	Orbit	Date	Image Pixel (12.5m/pixel)
Image No. 1	SGF	S2	23.8 – 31.1	12110	28 Feb 1998	8953×9000
Image No. 2	SGF	S6	41.4 – 46.7	11381	8 Jan 1998	8675×9000

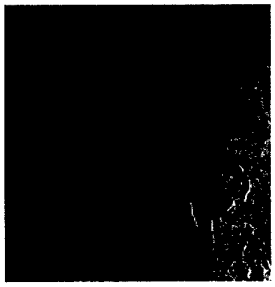


Figure 7. (above) Radarsat image (S2 mode) acquired on 28 Feb 1998. ©CSA 1998

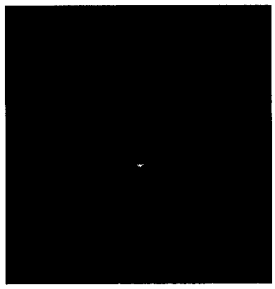


Figure 8. (above) Radarsat image (S6 mode) acquired on 8 Jan 1998.©CSA 1998



Figure 9. DEM with 200m/pixel resolution in an area of 80×100 km^2.
Map projection: UTM 50N Datum: GRS 1980



Figure 10. DEM with 50m/pixel resolution in the same area.
Map projection: UTM 50N Datum: GRS 1980



Figure 11. DEM with 20m/pixel resolution in the same area.
Map projection: UTM 50N Datum: GRS 1980

An example of the correlation at a range of height in the generation of 25m/pixel resolution DEM is shown on figure 12. The locations of the block window centres in the image layers are listed on table 2. It can be seen that a 5m change in height causes a relative shift of 0.22 pixel in the image pair, i.e. 5.5m in distance. As the resolution of the RADARSAT standard image used is 25m, it may suggest that the accuracy of the generated DEM, if the matching accuracy is 1 pixel, will be about 23m.

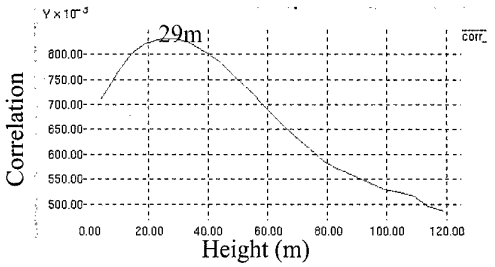
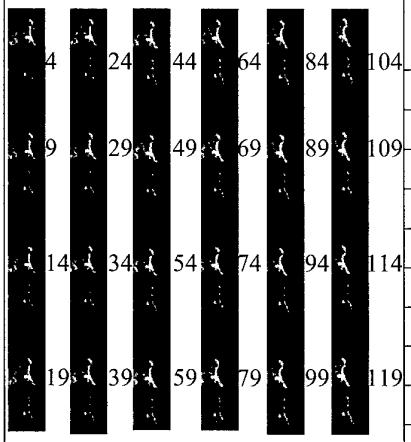


Figure 12. Correlation of weighted block windows changes with a range of height.

Table 2. Image blocks and center pixel coordinates for matching.

Blocks for matching at different heights at (E284460m, N558060m)	Centers of Block windows for matching at different heights Height at (E284460m, N558060m in HongKong Grid)			
	Height (m)	Center position (x, y) in averaged 2×2 S2 image layer (25m/pixel)		Center position (x, y) in averaged 2×2 S6 image layer (25m/pixel)	
		x	y	x	y
	4	3622.661542	767.367137	1547.553400	581.473096
	9	3623.082823	767.367268	1547.754103	581.473225
	14	3623.504114	767.367399	1547.954806	581.473354
	19	3623.925417	767.367530	1548.155510	581.473483
	24	3624.346730	767.367661	1548.356213	581.473612
	29	3624.768055	767.367792	1548.556917	581.473741
	34	3625.189389	767.367924	1548.757621	581.473869
	39	3625.610735	767.368055	1548.958325	581.473998
	...	...	...	...	...
	119	3632.354471	767.369993	1552.170352	581.475902
	Each 5m change	0.42 pixel shift		0.20 pixel shift	
		Relative shift in 25m/pixel layers is 0.22 pixel.			



The accuracy of the DEM generated from RADARSAT images was evaluated by comparing it with a DEM (fig. 13) generated from Stereo SPOT imagery over the same area. The disparity of the two DEMs is shown in figure 14. The histogram of the disparity is shown in figure 15. The mean height disparity between these two is less than 10 meters, while the standard deviation of the disparity is 26 meters.

CONCLUSION

The imaging model based on physical imaging parameters of the SAR is described. The parameters of our model can be refined with 2 GCPs or more. A weighted block window has been implemented to improve the digital correlation of the matching patches and a hierarchical multi-resolution approach is implemented to increase the robustness of the DEM generation process. The high disparity between the DEM generated from RADARSAT and that from SPOT has a standard deviation of 26 meters. More work will be done to reduce this disparity.

REFERENCES

[1] Curlander, John C. and Mcdonough, Robert N., "Synthetic Aperture Radar, Systems & Signal Processing", p370-377, 1991.

[2] J.S. Greenfeld, "An operator-based matching system", *Photogrammetric Eng. Remote Sensing*, 57(8), 1049-1055, August 1991.

[3] Thierry TOUTIN, "SAR image sampling on DEM generation", *IEEE 2000 International Geoscience and Remote Sensing Symposium*, volume III, 794-796, July 2000.

[4] Willian H. Press, etc., "Numerical Recipes in C", p554.

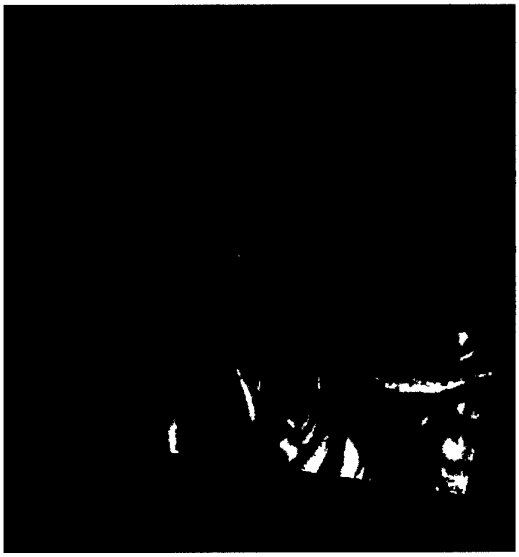


Figure 13. DEM generated from SPOT stereopair with IMAGINE Orthomax software.



Figure 14. The height disparity map between the DEMs generated from RADARSAT stereo pair and SPOT stereo pair.

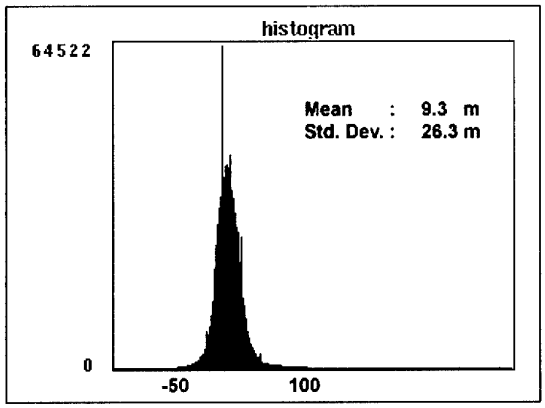


Figure 15. Histogram of the disparity map.

IMPLEMENTATION OF DIGITAL PHOTOGRAMMETRY FOR MONITORING THE TSAOLIN AREA IN TAIWAN

Jihn-Fa JAN (Taiwan)
Assistant Professor, Department of Geography
National Changhua University of Education
1, Jinn Der Road, Changhua 500, Taiwan
Telephone: +886-4-7232105 ext. 2825 Facsimile: +886-4-7211186
E-mail: jfjan@cc.ncue.edu.tw
Jih-Cheng RU (Taiwan)
Director
Agricultural and Forestry Aerial Survey Institute
No. 61-3, Chao-Chou Street, Taipei 106, Taiwan
Telephone: +886-2-23931837 Facsimile: +886-2-23931870
E-mail: nn240918@ms19.hinet.net
Yeong-Kuan CHEN (Taiwan)
Professor, Department of Forestry
National Taiwan University
1, Sec. 4, Roosevelt Road, Taipei 106, Taiwan
Telephone: +886-2-23630231 ext. 3134 Facsimile: +886-2-23639799
E-mail: ykchen@ccms.ntu.edu.tw

KEY WORDS: digital photogrammetry, GIS, digital terrain model.

ABSTRACT: On 21 September 1999, an earthquake of 7.3 on the Richter scale shook the Tsaolin area and caused an enormous landslide. Accompanying the quake, a large natural dam was formed by the fallen rocks and debris. Due to the fragile geological structure in this area, effective measures are needed to prevent devastating floods caused by collapse of the dam. The objective of this research was to apply digital photogrammetry to monitor the Tsaolin area so as to provide valuable information for flood prevention, water resource planning, and hydraulic engineering. In this research, aerial photographs obtained after the earthquake were used to investigate the geomorphic status in the study area. The aerial photographs were converted to digital images using high-resolution scanning device. Using the digital images, the digital photogrammetric technique was applied to collect digital terrain model (DTM) grids and other topographic features of the study area. Furthermore, from the digital terrain models, GIS was applied to derive stream networks, watersheds, aspect, slope, curvature, profile curvature, planform curvature, and several physiographic parameters for this area. The results indicate that, digital photogrammetry is an effective approach for monitoring geomorphic status of a large area. In addition, the digital terrain model generated by digital photogrammetry can be readily applied to produce topographic and geomorphic data that are valuable for various disciplines.

1. INTRODUCTION

In the past few decades, there were three large landslides in the Tsaolin Area, Yunlin County, Taiwan. On 21 September 1999, an earthquake of 7.3 on the Richter scale shook the area and caused another landslide. Accompanying the quake, a large natural dam was formed by the fallen rocks and debris. Due to the fragile geological structure in this area, effective measures are needed to prevent devastating floods caused by collapse of the dam. Any treatment on the area should be based on accurate estimate of the volume of the dam, amount of water, and flow path. However, the road condition and instability of the slope makes surveying the area very difficult and costly.

Photogrammetry has the advantages of acquiring information about a large area very efficiently and cost effectively. Especially for inaccessible areas, photogrammetry is far more superior than traditional ground survey. In recent years, inexpensive computers and advance of computer technologies contributed to the rapid development of digital photogrammetry (Dowman et al., 1992; Heipke, 1995). Successful implementation of digital photogrammetric workstation in mapping have been found in various disciplines (Chen et al., 1998; Skalet et al., 1992). In this research, aerial photographs obtained after the earthquake were used to investigate the geomorphic status in the study area. The aerial photographs were converted to digital images using high-resolution scanning device. Using the digital images, the digital photogrammetric technique was applied to collect digital terrain model (DTM) grids and other topographic features of the study area. The objective of this research was to apply digital photogrammetry to monitor the Tsaolin area so as to provide valuable information for flood prevention, water resource planning, and hydraulic engineering.

2. MATERIALS AND METHODS

2.1 Study area

As shown in Figure 1, the study area, Tsaolin, is located in the Gukon Township of Yunlin County. This area is the upstream region of the Chinsuei Creek, and the elevation ranges between 280 m and 1400 m.

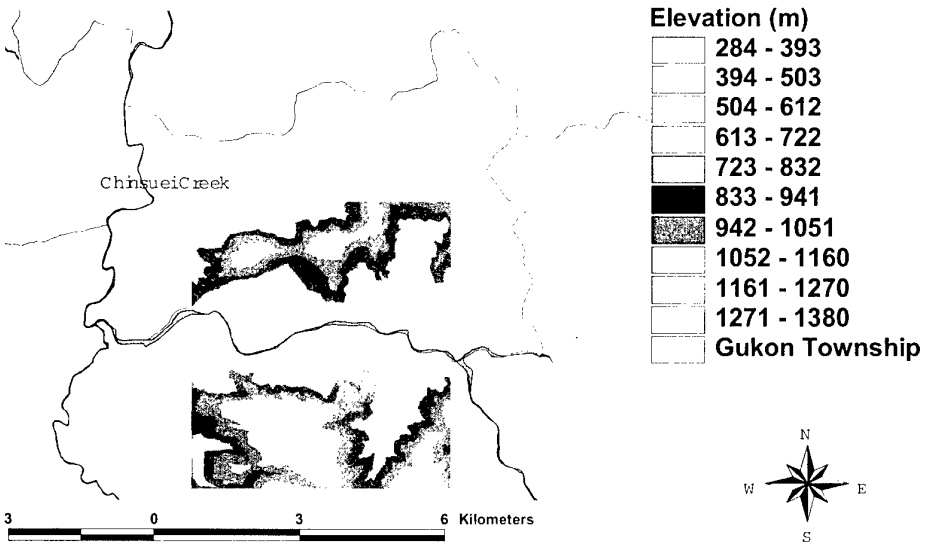


Figure 1. Location map of the study area.

2.2 Materials

A set of aerial photographs of the study area was acquired on December 24, 1999. The aerial camera used was a RMK A TOP 15/23 manufactured by Carl Zeiss. The average flight height was 3,000 meters above mean ground elevation, which yielded 1:19,000-1:21,000 for the scale of the photographs. For these photographs, the percentage of forward overlap and side overlap were about 80% and 30%, respectively. The hardware and software used in the study included Zeiss C-130 analytical stereoplotter, digital photogrammetric workstation (Intergraph ImageStation),

aerial photograph scanner, personal computers, ArcInfo, ArcView GIS, and MicroStation.

2.3 Analysis methods

In order to obtain high-quality mapping products, standard photogrammetric procedure was followed to acquire aerial photographs and process the related data. Figure 2 depicts the workflow of digital photogrammetric processing. In somewhat more detail these steps are described as follows.

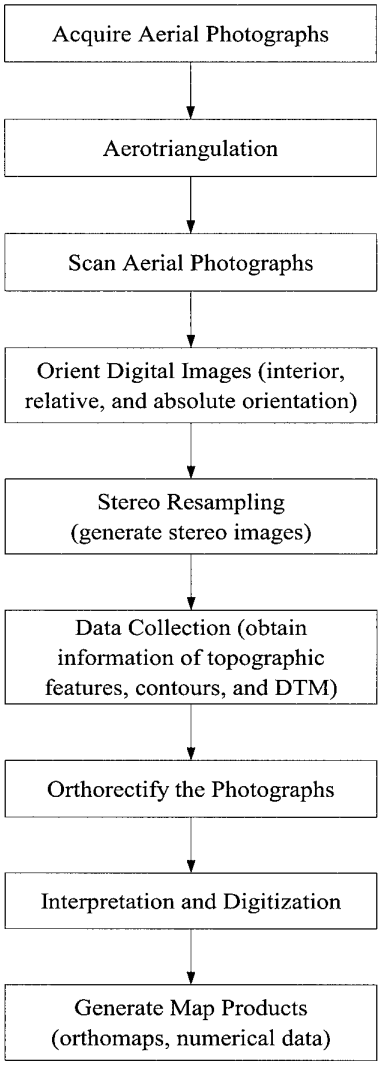


Figure 2. Workflow of digital photogrammetric processing.

For each photograph comprising the stereo models, the control points including ground points of known horizontal position and/or elevation, and natural targets discernible on the photographs were identified. These points were then carefully measured using C-130 analytical stereoplotter. Triangulation was done using PAT-M local adjustment software.

In order to retain as much detail of the original film as possible, high-quality positive films were used to duplicate them. The duplicated positive films were then scanned using Intergraph Photo

Scan system. The resolution used in the scanning process was 15 μm, or approximately 1,700 dots per inch.

The orientation process includes three steps, that is, interior orientation, relative orientation, and absolute orientation. Interior orientation reconstructs the bundle of light rays so that they are geometrically identical to those entered the camera lens at the time of exposure. Relative orientation reproduces the same perspective conditions between a pair of photographs so that the corresponding light rays in these two photographs intercept in space and a stereo model is formed. Follows relative orientation, the process of absolute orientation involves using control points with known horizontal and/or vertical positions to make the stereo model conform in scale and position with respect to the reference plane of the map sheet. At the completion of absolute orientation, the position of any point in the stereo model can be measured at the intersection of two corresponding light rays (American Society of Photogrammetry, 1980). The orientation process was completed using the mensuration software (ISDM) module provided by Intergraph ImageStation.

After completing the orientation process, the original imageries were resampled to generate epipolar images, which were used to form the stereo model. The images were viewed in stereo on the monitor using the CrystalEyes stereo viewing system. While viewing the images in stereo, topographic features of interest such as streams, contour lines, spot heights, and DTM (digital terrain model) grids were collected. The DTM were then used to orthorectify the photographs to produce orthophotos.

Together with other reference data, the images and collected topographic features were analyzed and special features were digitized as needed. The final products of the digital photogrammetric process include orthophotomaps and numerical data (e.g. contour lines, DTM), which may be readily used to build a geographic database for use in GIS (geographic information system).

3. RESULTS

Control points are needed to scale and level the stereo model resulting from relative orientation. For each photograph used in the photogrammetric process, several natural targets distributed evenly over the photograph were identified. Together with existing known ground control points and control points obtained from control survey, all the points were carefully measured using Zeiss C-130 analytical stereoplotter. These points were then used as input to the PAT-M software, which was used to perform aerotriangulation. The scale of the maps to be produced was set to 1:5,000. Consequently, aerotriangulation was performed following the mapping standard.

The photographs were scanned at a resolution of 15 μm. The digital images were compressed to about 150 MB in order to reduce the required storage space. In addition, to facilitate rapid display of the images, overviews of the original images were created. These images were then used for orientation. The control points required for absolute orientation were obtained from aerotriangulation. To insure satisfactory orientation results, by repeatedly examining the results for possible errors the orientation process completed only if the error was less than 15 μm, i.e. no more than a pixel.

After completion of orientation process, stereo images were generated by resampling the original images. While viewing the stereo images in stereo, topographic features including contour lines, spot heights, peaks, and drains were digitized. These topographic features were then used to build a TIN (triangulated irregular network) model. In addition, a GRID model, similar to DTM, was produced from the TIN model. To attain accurate illustration of the relief of the study area, the vertices of contour lines were sampled at 5-meter interval. The pixel size of the GRID model was set to 9 m x 9 m. This pixel size was selected because high quality orthophotomaps can be achieved using the existing map setting system. The GRID model, or DTM, was then used to orthorectify the photographs. Figure 3 shows the shaded relief and an image created by draping orthophoto image on top of the relief.

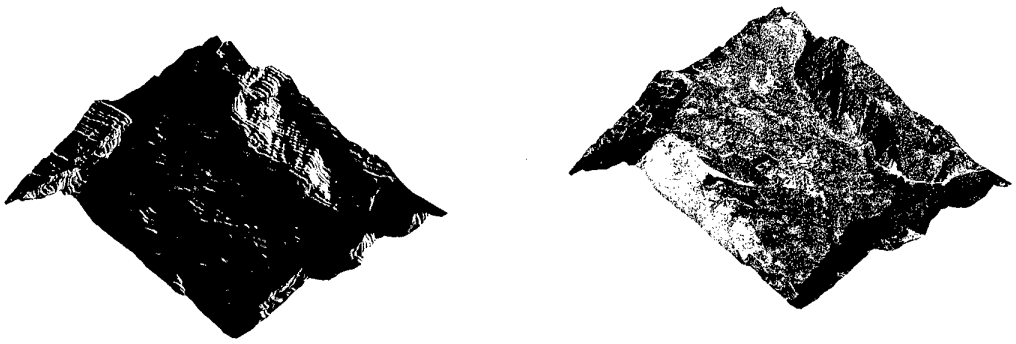


Figure 3. Shaded relief and orthophoto image draped over the relief.

The topographic features and DTM can be used for further analysis by using GIS software. Using the software developed by Jan et al. (2000), several physiographic parameters of the study area such as watersheds, stream networks, stream orders, stream lengths, drainage density, mean elevation, median elevation, bifurcation ratio, streams lengths ratio, stream areas ratio, and stream frequency can be readily derived from the DTM.

4. DISCUSSION

In this study, the aerial photographs were obtained about three months after the earthquake. By examining the photographs, it is apparent that the landscape of the study area has been changed drastically. To understand the impacts of earthquake on the environment, and the risks resulted from the natural dam on the surrounding villages, a large-scale surveying about the area is very needed. This study shows that photogrammetry is very suitable for acquiring information about a large area, particularly when cost, effectiveness, efficiency, and accuracy are all considered.

The digital photogrammetric approach utilizes digital images to do all the measuring and digitizing works, therefore it is essential to have high-quality digital images. Extra caution should be exercised to retain appropriate contrast of the images both during the processes of duplicating film and scanning.

The accuracy of the photogrammetric mapping process highly depend on the accuracy of control points, equipment used for measurement, and most importantly, well-trained people that execute the tasks. To insure satisfactory results, ground survey is necessary to obtain data for the control points. In addition, the results of aerotriangulation provides the basis for model adjustment and further measuring tasks, therefore the aerotriangulation process has to be done carefully.

To estimate the volume of the natural dam and the amount of water, it requires data about the

geomorphic status of the study area prior to the earthquake. Therefore, the photographs obtained before the earthquake can be used for photogrammetric processing. Further study is suggested to monitor the geomorphic changes in the study area in order to prevent disaster from occurring in the future.

5. CONCLUSION

The following conclusions are drawn from this study:

(1) Aerial photogrammetry is an effective approach for acquiring information about a large area, particularly when cost, effectiveness, efficiency, and accuracy are all considered. In addition, the results produced using digital photogrammetric approach can be readily used to establish geographic database, which can be further analyzed with GIS software. Integrated with GIS, digital photogrammetric approach can provide timely and accurate information about an area, which may be valuable for various disciplines.
(2) High-quality digital images are required for use in digital photogrammetric processing. Therefore, the processes of duplicating film and scanning positives should be done with extra caution.
(3) The results of aerotriangulation provide the basis for model adjustment and further measuring tasks, therefore the aerotriangulation process has to be done carefully. When necessary, ground survey should be done to acquire data about the control points.
(4) Further study is suggested to monitor the geomorphic changes of the study area. It is recommended to acquire aerial photographs both prior and after the earthquake in order to monitor temporal changes in this area. Considering the cost and time constraint, as well as the desirable accuracy of the data generated from the mapping process, digital photogrammetric approach and GIS may be most suitable to meet the objective.

REFERENCE

American Society of Photogrammetry, 1980. Manual of Photogrammetry. Eds. Slama, C.C., C. Theurer, and S.W. Henriksen, American Society of Photogrammetry, VA, 1056 p.

Chen, Y.K., J.F. Jan, and H.Y. Lai, 1998. Mapping and establishing topographic layers for GIS in mountainous forest area by digital photogrammetric technique. Quart. Journ. Exp. For. National Taiwan University, 12 (3), pp. 139-156. [in Chinese with English summary]

Dowman, I.J., H. Ebner, and C. Heipke, 1992. Overview of European developments in digital photogrammetric workstations. Photogrammetric Engineering and Remote Sensing, 58 (1), pp. 51-56.

Heipke, C., 1995. State-of-the-Art of digital photogrammetric workstations for topographic applications. Photogrammetric Engineering and Remote Sensing, 61 (1), pp. 49-56.

Jan, J.F., Y.K. Chen, C.C. Cheng, H.Y. Lai, and S.C. Liaw, 2000. Automatic extraction of watershed physiographic parameters using digital terrain model and geographic information system. Proceedings of The 19th Symposium on Surveying Research and Applications, August 24-25, Changhua, Taiwan, pp. 455-464.

Skalet, C.D., Y.G. Lee, and L.J. Ladner, 1992. Implementation of softcopy photogrammetric workstations at the U.S. Geological Survey. Photogrammetric Engineering and Remote Sensing, 58 (1), pp. 57-64.

TOPOGRAPHIC MAP REVISION IN DIGITAL PHOTOGRAMMETRIC ENVIRONMENT

K.S.K.Wijayawardana
Assistant Superintendent of Surveys
Photogrammetric Unit, Survey Department
P.O.Box. 506,Narahenpita, Sri Lanka
Tel: -94-1-588871 Fax: -94-1-585586 E mail: -sgsurv@sri.lanka.net

ABSTRACT

The Survey Department being the national surveying & mapping organisation that provides geo-spatial data to other institutions and individuals for their needs. During the period of 1980-1997, produced 1:50,000 topographical maps for the entire island under as an interim series. Since 1992, 1:10,000 topographic map series has been produced using photogrammetric method. Data available in digital form for all areas to be developed.

This paper describes updating of 1:10,000 map series using digital photogrammetric method. Now department is enriched with 2000dpi scanner and sophisticated software like VirtuZo for softcopy photogrammetry. Digital photogrammetric techniques may introduce or strengthen image-handling procedures such as orthophoto mapping. In this connection new concept was applied to revise the 1:10,000 map series namely the prioritised revision method (revision promptly by factors other than mere change in the landscape as a example of demanding from the customer or knowledge of future development) is used for this purpose.

Orthophotos can play vital role in such a revision as they show the terrain in fine detail. Digital photogrammetric techniques can be used to produce high quality, orthorectified aerial photographs quickly, easily and cheaply. Recently taken vertical photographs at a nominal scale of 1:20,000 available for scanning at a resolution of 25 microns. Interior orientation performed using camera calibration file for relevant year and fiducial marks for each scanned photograph. It is normal to relate the model created to a real world. So, it is necessary to have a number of ground control points, which can be identified in the model. Almost 80% of ground control points of already mapped area were in Microsoft access database. Once produced orthophoto(which can be mosaic for large area) after digital elevation model, then the existing vector data which to be revised can be overlaid on top of the orthophoto. Then new and changed information can be extracted by on screen digitising in Microstation environment.

Such a system will address the concern of the planners for decision making and customers for quality up to date data.

Introduction

Survey Department being the national surveying & mapping organization that provides topographical data to other institutions and individuals for their needs. This data are available in both hard copy and soft copy format. The history of topographic map production goes back to early 1900's. At that time department had established geodetic triangulation network and then the entire country was mapped using plane table method at the scale of one inch to one mile, this is popularly known as One inch map series. During the period of 1980 – 1997 Department has produced 1: 50,000 topographical maps for entire country by combining these one inch maps and 1: 40,000 aerial photographs. Since 1992 topographical maps of 1: 10,000 scale has been produced using 1:20,000 aerial photographs that were taken at early 90's. It implies that most of the available data do not provide updated or recent changes in development. The negative effects of delaying updating have been clearly demonstrated in planning and decision making stage. Updating of topographical maps in traditional way would take long period of time as well as money. As users are more concerned about updated 1:10,000 data, this paper describes updating of 1:10,000 map series using digital photogrammetric method.

Target area

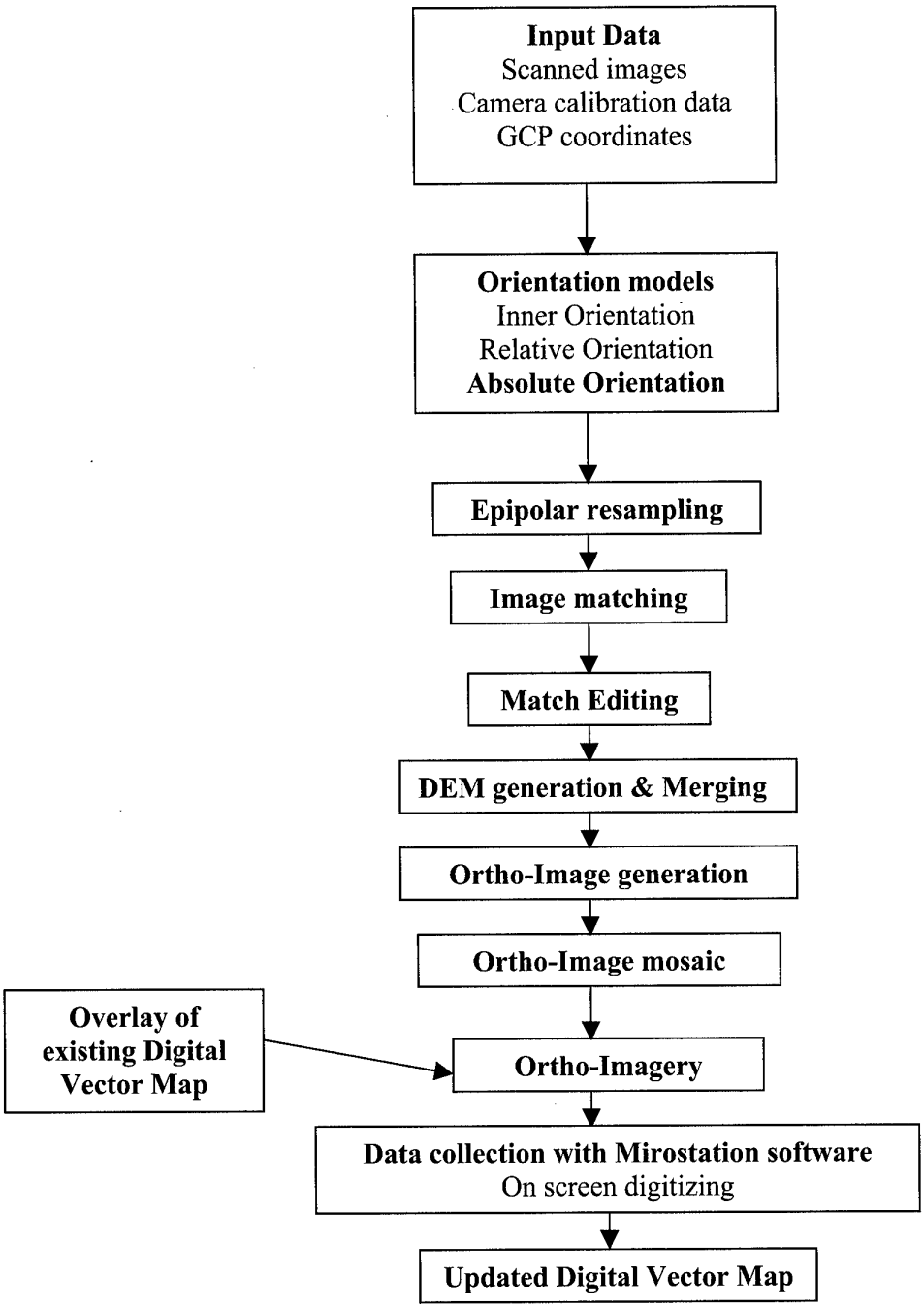
The target area, Horana is situated in the Kalutara District of Western Province of Sri Lanka. Its geographical location is latitude 6^0 41' 34" & 6^0 43' 10" and longitude 80^0 02' 53" & 80^0 05' 03" and that covers 16km^2. Area has been rapidly developed recently as introducing a new industrial zone. Simultaneously other facilities have been developed such as residential areas, commercial areas and new rods etc. In this connection necessity of revision of existing information is very vital.

Data and software/hardware used

Digital vector data set in particular area that was extracted in 1994 as per 1: 10000 data library. Recently taken aerial photographs with a scale of 1: 20,000 for scanning. Sophisticated software such as Vexcel, VirtuZo and MicrostationSE to photographs scanning, orthophoto generation and data extraction respectively. Data collection and analyzing were done by using soft copy photogrammetric instrument with 750MHZ 512MB RAM computer system.

Methodology

Workflow is as follows,



The first step in the map revision process was selecting most recent 1:20,000 scaled aerial photographs for scanning (no matter whether these are diapositives or contacts). Target area was covered two strips with six aerial photographs. All these were scanned 25 micron resolution with sophisticated VX 400 scanner. The scanning surface should be clean and dirt free to produce good quality images. With changing the look up table for each image, output image quality can be improved dramatically. It is important to have all fiducial marks in image for inner orientation. The next phase is to input scanned images and parameters such as camera calibration data and ground control points' coordinates to VirtuZo NT Workstation for further processing.

Next phase is to orient each model. The interior orientation is based on the calibration values and the measured coordinates of the fiducial marks. After completing the inner orientation of a model relative orientation can be performed continuously to obtain the stereoscopic vision. Then performed absolute orientation to transform the stereo model from photogrammetric coordinate system to ground coordinate system.

Once the relative orientation completed, can be specified the working area and do the automatic epipolar resampling to removed the Y- parallaxes from the original imagery. After creating epipolar image, software provides facility to do image matching automatically. The image matching method technique using to VirtuZoNT is an area and feature based, bridge mode technique integrating with the dynamic programming and least squares matching algorithms. As the image matching finished, can be entered editing environment. Software provides variety of editing tools for editing where necessary. Selecting options namely PRODUCT – DEM & ORTHO IMAGE provides by the software, Ortho Imagery can be created for each model. After creating a number of ortho images within a block, single continuous composite image for entire target area can be performed.

Then overlaid the existing vector data on to the composite ortho image. There is an interface between VirtuZo and Microstation software. In this connection, setting lower left & upper right coordinates of vector data set on to an ortho image, overlaid image can be get easily. After that digitizing performed on screen in Microststation environment as per 1: 10,000 data library. Separate level was assigned for new and changed information. Ultimately updated digital vector map available in acceptable accuracy.

Discussion

The 1:10,000 map revision method, which has been adopted by the Survey Department, would take at least one month to revise the particular target area. Even if we spent large amount of money for instrumentation, as a long time basis it would be benefited a lot because it will take only a few days to revise a map. Total time taken to produce ortho image and map revision for target area was three working days with the full time involvement of one person.

In future, revision of 1:10,000 map series in the Survey Department should be as mentioned earlier also target areas be selected according to the prioritized method (revision promptly by factors other than mere change in the landscape as a example of demanding from the customer or knowledge of future development). With regard to developing countries such as Sri Lanka, this system is very suitable because no need to spend much money for hardware/software maintain as well as no need of skill full persons to operate. Eventually, emphasis of developing such a system is benefited country a lot.

Conclusion

This paper is mainly dealt with revision of 1:10,000 map series in digital photogrammetric environment. Map revision is only one product from ortho imagery. As ortho imagery contains all terrain features in details, they can play vital role in land resources survey than conventional old paper maps. Further to map revision ortho images can be used as invaluable large information for earth resource planners as well as geological information system (GIS).

GLOBAL IMAGE COMPOSITE OF ADEOS/OCTS GAC DATA

T.Hashimoto[1], T.Igarashi[2], A.Mukaida[3], R.Higuchi[3]

1) Center for Environmental Remote Sensing (CEReS), Chiba University,
1-33 Yayoi-cho, Inage-ku, Chiba 263-8522, Japan
Tel:+81-43-290-3842, Fax:+81-43-290-3857, e-mail: hashi@ceres.cr.chiba-u.ac.jp
2) Earth Observation Research Center, National Space Development of Japan,
1-9-9 Roppongi, Minato-ku, Tokyo 106-0032, Japan
3) Remote Sensing Technology of Japan,
1-9-9 Roppongi, Minato-ku, Tokyo 106-0032, Japan

KEYWORDS : Image Composite, ADEOS/OCTS, Geometric Correction

ABSTRACT :
The OCTS(Ocean Color and Temperature Scanner) onboard the ADEOS(Advanced Earth Observing Satellite) was the first space borne optical scanner with many channels. It observed mainly the ocean condition, but the data could be used for land monitoring. In case of utilizing optical sensor data for land monitoring, cloud free composite images are very useful. The authors generated the cloud free composite images of OCTS GAC(Global Area Coverage) data for the applications to the land environment. The cloud free composite images from NOAA/AVHRR data are very popular in such applications. Since the characteristics of OCTS are different from those of the AVHRR, the different method is necessary for generating the composite images from the OCTS data. The paper describes the method of generating the image composite of OCTS data and introduces the product as the result.

1. INTRODUCTION

The ADEOS was launched in 1996 by NASDA (National Space Development Agency of Japan). Unfortunately it was terminated 10 months after the launch. The OCTS onboard the ADEOS is an optical mechanical scanner with 12 channels covering visible to thermal infrared region. The orbit of ADEOS satellite is summarized in Table 1 and the main characteristics of the OCTS are shown in Table 2. The GAC data are generated by re-sampling the data with original spatial resolution to the data with ground resolution of about 3.5 kilometers at nadir.

item	value
type	sun synchronous, sub-recurrent
period	101 min.
inclination	98.6 deg.
recurrent period	41 days
Local time at descending node	AM.10:30±15min

Table 1 Summary of ADEOS orbit

item	value
spectral channels	VIS : 6, NIR : 2, TIR : 4
resolution at nadir	680 m
swath angle	± 40 deg.
tilt angle	-20 deg., 0 deg., 20 deg.
quantization bits	10 bits/data

Table 2 Main characteristics of OCTS

The geometric accuracy is very important in the field of land applications like multi-temporal analysis, image composite, etc. The initial checks of ADEOS data indicated that the geometric accuracy of the OCTS imagery was more than 10 kilometers on the ground. The NASDA and some

organizations examined the factors for such terrible errors and found out three factors; 1) the bug of the software for determining satellite position, 2) the insufficiency of the algorithm for getting satellite attitude, 3) the miss-alignments of the sensors. Among them, the first factor was easy to fix. With respect to the second one, a new algorithm adapted to the ADEOS-II satellite has been examined. The third one was corrected using a number of ground control points (GCP) from many OCTS images. The modification of processing system at the ground station lead to the geometric accuracy of the OCTS imagery within a few kilometers which correspond to more than one pixel in the GAC data. But, the accuracy was yet insufficient. The system for precise geometric correction had to be developed.

The Maximum Value Composite (MVC) method utilizing the Normalized Difference Vegetation Index (NDVI) is very popular to generate cloud free composite images from NOAA/AVHRR data (NOAA, 1997). The OCTS was operated with two kinds of gain mode; ocean mode and land mode. The image composites from the OCTS data in the land mode were generated by the MVC as same as the AVHRR data. In case of the ocean mode, however, the NDVI could not be calculated, because some pixels of near infrared channels were saturated. Another method had to be applied to the image composite from the OCTS images in the ocean mode.

2. METHOD FOR IMAGE COMPOSITE

Figure 1 shows the general flow for image composite. The composite image consists of 10,000 pixels by 5,000 lines in Latitude/Longitude production. It contains scan geometry data like solar zenith and azimuth angle, satellite zenith and azimuth angle as well as channel data.

2.1 RADIOMETRIC CORRECTION

The OCTS was operated with two kinds of gain mode as mentioned above. The radiometric correction had to be performed to match the pixel values from both modes onto the same radiometric level. The coefficients for the calibration were prepared through the NASDA's WWW site (NASDA, 2000).

2.2 GEOMETRIC CORRECTION

The geometric correction with high accuracy is essential to generate composite images. The algorithm for precise geometric correction was developed. It was based on the collinearity equation in the photogrammetry (Hashimoto, T., 1997). The navigation data (satellite position and attitude) were treated as the orientation parameters, and they were adjusted utilizing GCPs.

First of all, the coordinates systems used here are defined as follows (see Figure 3);

- (X,Y,Z): ECR(Earth Center Rotation) coordinates where the origin is the gravity center of the Earth, X axis is Greenwich Meridian at the equator, Z axis is North along the spin axis, Y is defined by right-handed rotation,
- (x, y, z): Orbital Coordinates where the origin is the gravity center of the satellite, z axis is nadir, y axis is defined by the outer product of z axis and velocity vector, x is defined by right-handed rotation.

The view vector at the aperture (corresponding to the satellite coordinates) can be defined by the optical-mechanical system of the OCTS as (Bx_s, By_s, Bz_s) . The view vector is transformed into the orbital coordinates using the attitude, (roll, pitch, yaw) = $(\omega, \varphi, \kappa)$, as follows.

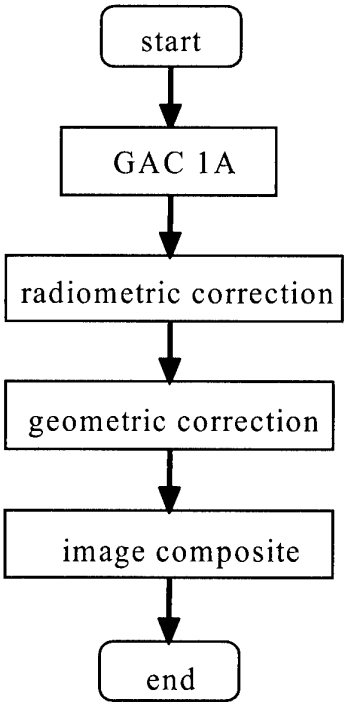


Figure 1 General Flow

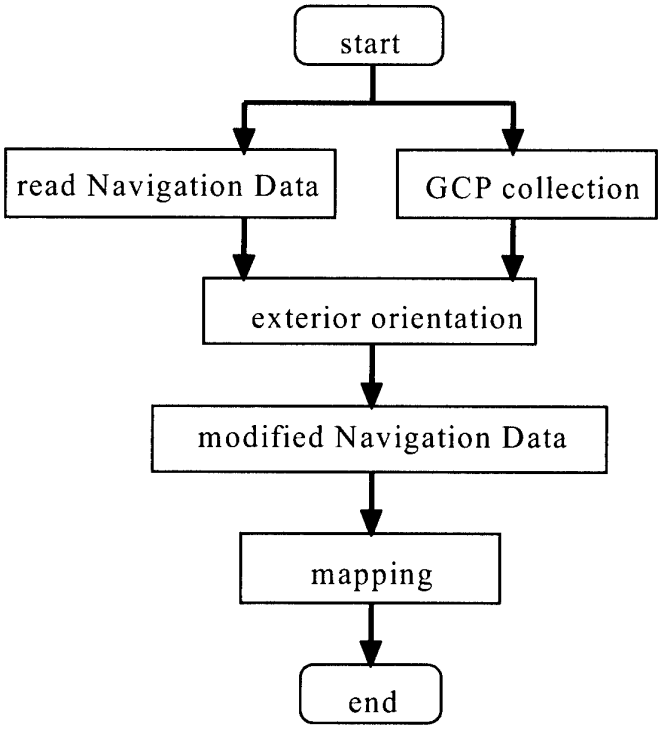


Figure 2 Flow of Precise Geometric Correction

$$\begin{pmatrix} Bx_e \\ By_e \\ Bz_e \end{pmatrix} = \mathbf{P}_1 \cdot \begin{pmatrix} Bx_s \\ By_s \\ Bz_s \end{pmatrix} = \begin{pmatrix} \cos & -\sin & 0 \\ \sin & \cos & 0 \\ 0 & 0 & 1 \end{pmatrix} \begin{pmatrix} \cos & 0 & \sin \\ 0 & 1 & 0 \\ -\sin & 0 & \cos \end{pmatrix} \begin{pmatrix} 1 & 0 & 0 \\ 0 & \cos & -\sin \\ 0 & \sin & \cos \end{pmatrix} \begin{pmatrix} Bx_s \\ By_s \\ Bz_s \end{pmatrix}$$

where (Bx_s, By_s, Bz_s) : view vector in satellite coordinates (1)

(Bx_e, By_e, Bz_e): view vector in orbital coordinates.

The OCTS products contain the satellite position and velocity in ECR. But, the satellite movement can be also expressed using the distance between the Earth center and the satellite center (R), the longitude of ascending node(Ω), the inclination(i), the latitude argument from ascending node on the orbital plane(u) as follows (Hashimoto, T., 1998).

$$\begin{pmatrix} X_r \\ Y_r \\ Z_r \end{pmatrix} = \mathbf{P}_3 \cdot \begin{pmatrix} X_e \\ Y_e \\ Z_e \end{pmatrix} = \begin{pmatrix} \cos\Omega & \sin\Omega & 0 \\ \sin\Omega & -\cos\Omega & 0 \\ 0 & 0 & 1 \end{pmatrix} \begin{pmatrix} 1 & 0 & 0 \\ 0 & \sin i & -\cos i \\ 0 & \cos i & \sin i \end{pmatrix} \begin{pmatrix} -\sin u & 0 & \cos u \\ 0 & 1 & 0 \\ \cos u & 0 & \sin u \end{pmatrix} \begin{pmatrix} X_e \\ Y_e \\ Z_e \end{pmatrix} \quad (2)$$

Both $(\mathbf{P}_s, \mathbf{V}_s)$ and (R, Ω, i, u) are time dependent. The variation ratios of the former are bigger than those of the latter, especially at the equator or the Polar Regions. So the latter is suitable for the expression of satellite movement. In this work, the parameters for satellite movement and attitude are expressed by the polynomials of line number (L) as ;

$$Q = Q_0 + Q_1 \cdot L + Q_2 \cdot L^2 + \cdots, \quad Q = (R, \Omega, i, u, \omega, \phi, \kappa). \quad (3)$$

The coefficients of polynomials for (R, Ω, i, u) and attitude are determined by the regression analysis using the navigation data.

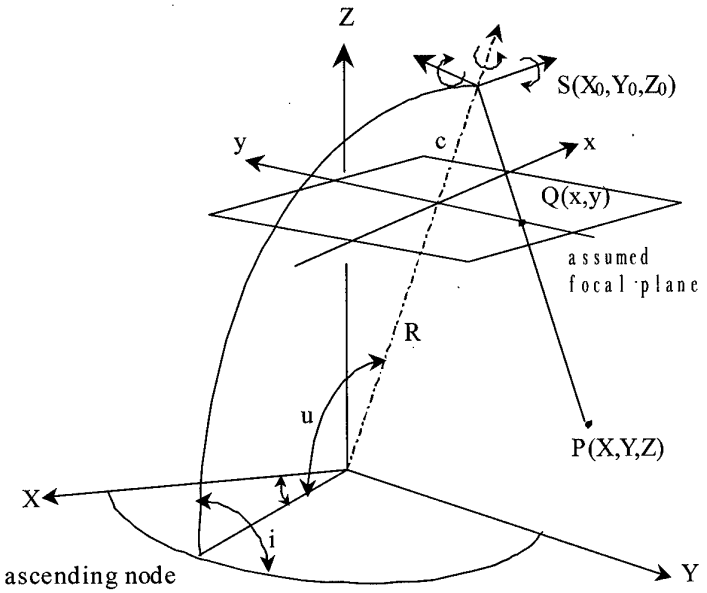


Figure 3. Collinearity condition

The coefficients of polynomials for (R, Ω, i, u) and attitude are determined by the regression analysis using the navigation data.

The view vector and the observed ground point (X, Y, Z) satisfy the collinearity equations as follows (Hashimoto, T., 1997).

$$F_x = -\frac{Bx_s}{Bz_s} - c \cdot \frac{a_1(X - X_o) + a_2(Y - Y_o) + a_3(Z - Z_o)}{a_7(X - X_o) + a_8(Y - Y_o) + a_9(Z - Z_o)} = 0$$

$$F_y = -\frac{By_s}{Bz_s} - c \cdot \frac{a_4(X - X_o) + a_5(Y - Y_o) + a_6(Z - Z_o)}{a_7(X - X_o) + a_8(Y - Y_o) + a_9(Z - Z_o)} = 0 \qquad (4)$$

where $\begin{pmatrix} a_1 & a_2 & a_3 \\ a_4 & a_5 & a_6 \\ a_7 & a_8 & a_9 \end{pmatrix} = (\mathbf{P}_3 \cdot \mathbf{P}_1)^T = \mathbf{P}_1{}^T \cdot \mathbf{P}_3{}^T$, c : assumed focal length.

$$\begin{pmatrix} X_0 \\ Y_0 \\ Z_0 \end{pmatrix} = \begin{pmatrix} \cos\Omega\cos u - \sin\Omega\cos i\sin u \\ \sin\Omega\cos u + \cos\Omega\cos i\sin u \\ \sin i\sin u \end{pmatrix} \cdot R$$

In the equation (4), the parameters (R, Ω, i, u) and (ω, φ, κ) are treated as exterior orientation parameters.

Sufficient numbers of GCPs are necessary for exterior orientation. Conventionally, the GCP has been collected by human interpretation. Such procedure is very time consuming and not proper for daily process. In this work, the GCP collection is realized automatically by the image matching technique. The matching was done using two kinds of templates; one from the Generic Mapping Tool (GMT) coastal data (Wessel, P., 1999) prepared in advance, another from the original image which was binarized to make coast line data. The position of templates was selected as a GCP candidate from the GCP library. The precise navigation data are determined using the GCPs. A rectified image is generated using the newly determined navigation data.

2.3 IMAGE COMPOSITE

The composite process was carried out separately over land regions and ocean regions (see Figure 4). The land/ocean mask prepared in advance determined the separation of both regions. For the land, the MVC would be applied only if channel 7 (near infrared channel) was not saturated. Among the spectral channels of the OCTS data, channel 5 corresponds to the chlorophyll absorption channel (red color region). Generally, the plants containing chlorophyll have smaller reflectance than other ground cover or clouds. When the channel 7 was saturated, the process was carried out by selecting the pixels with the minimum value in channel 5.

Such a minimum value composite method by using channel 5 was also applied to the ocean regions. But, the method could not be applied to the Polar region, because some pixels were illuminated by small Solar radiation and had very small Digital Number (DN) owing to the big Solar zenith angle. To prevent such a case, one of the thermal infrared channels (channel 11) was used. While both the ice/snow and the cloud are cold, the cloud will be colder than the ice/snow. When the channel 7 was saturated in the Polar land region, the pixels with maximum value in channel 11 would be selected. In case that the channel 7 was not saturated, the pixels seem to be illuminated by small Solar radiation. The pixels observed at the minimum solar zenith angle was selected in such a case.

The period for image composite is very important for the analyses with use of them. If the period is too short, it will very difficult to extract cloud free pixels. On the other hands, if it is too long, the results will be less sensitive to the rapid changes of vegetation. Basically, the 10 days composite and the 30 days composite were adopted in this work. The OCTS was operational only about eight months after the initial checkout period. In three months of those 8 months, the OCTS was operated without the tilt function. All observed data were processed for the image composite. After all, 20 images for 10 days composite and 8 images for 30 days composite were generated as shown in Table 3.

3. CONCLUSIONS

(1) The system for the precise geometric correction of ADEOS/OCTS was developed. The algorithm of the geometric correction is based on the principle of collinearity condition.
(2) The new algorithm for generating a cloud free composite from OCTS data was developed. It was applicable to the saturated pixels in near infrared channels.
(3) 20 images for 10 days composite and 8 images for 30 days composite covering all observation period (8 months) were generated. It is very expected that these composite images will be used in some land environmental applications.

ACKNOWLEDGMENT

This work was partially supported by the 'GCMAPS program' conducted by Scientific Technology Agency of Japan.

REFERENCES

Hashimoto, T., 1997. Precise Geometric Correction of ADEOS/OCTS Imagery, Journal of JSPRS, Vol.36, No.5, pp.42-51

Hashimoto, T., 1998. The Estimation of Motion and Attitude of ADEOS Satellite Utilizing the Principle of Exterior Orientation, Journal of JSPRS, Vol.37, No.6, pp.4-13

NASDA, 2000, home page on ADEOS, on http://www.eorc.nasda.go.jp/

NOAA, 1997, NOAA GVI GUIDE, on http://www2.ncdc.noaa.gov/docs/gviug/

Wessel, P., 1999, GMT–The Generic Mapping Tools, on http://www.soest.hawaii.edu/gmt

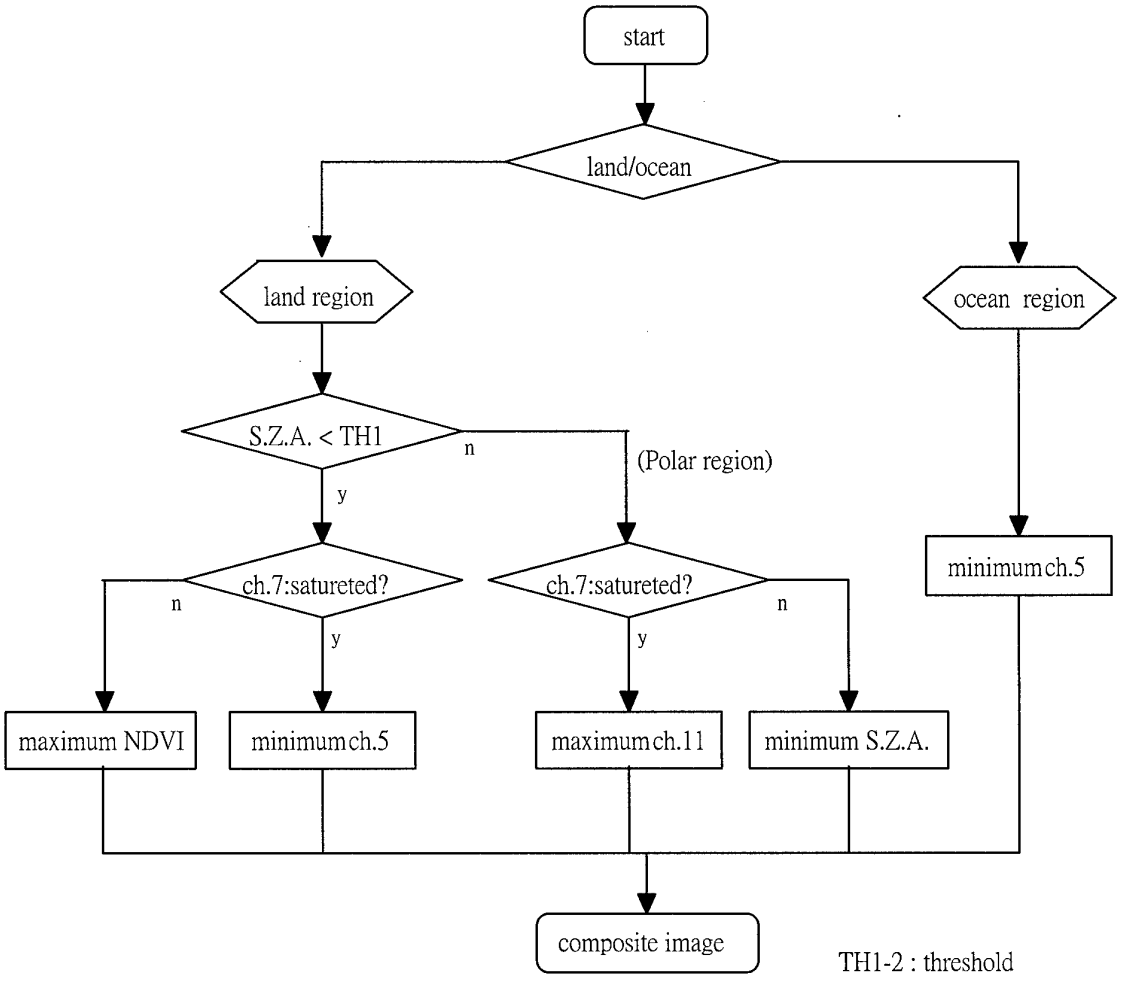


Figure 4 Selection of Pixel for Image Composite

Table 3 Composite images to be generated

No	period	10 days comp.	30 days comp.	tilt	No	period	10 days comp.	30 days comp.	tilt
1	'96.11.01 – 11.12	12	24	yes	12	'97.03.19 – 03.28	10	31	yes
2	'96.11.13 – 11.24	12		yes	13	'97.03.29 – 04.07	10		yes
3	'96.11.25 – 12.06	12	24	yes	14	'97.04.08 – 04.18	11		yes
4	'96.12.07 – 12.18	12		yes	15	'97.04.19 – 04.28	10	32	yes
5	'96.12.19 – 12.29	11	22	no	16	'97.04.29 – 05.09	11		yes
6	'96.12.30 – 01.09	11		no	17	'97.05.10 – 05.20	11		yes
7	'97.01.10 – 01.20	11	23	no	18	'97.05.21 – 05.30	10	32	yes
8	'97.01.21 – 02.01	12		no	19	'97.05.31 – 06.10	11		yes
9	'97.02.13 – 02.23	11	34	no	20	'97.06.11 – 06.21	11		yes
10	'97.02.24 – 03.06	11		no					
11	'97.03.07 – 03.18	12		no					

EXTRACTION AND UTILIZATION OF GEOMETRICAL AND CONTEXTUAL INFORMATION IN VERY HIGH RESOLUTION IKONOS SATELLITE IMAGERY

Annie HUI, Soo Chin LIEW, Leong Keong KWOH, and Hock LIM
Centre for Remote Imaging, Sensing and Processing, National University of Singapore
Blk. SOC1 Level 2, Lower Kent Ridge Road, Singapore 119260
Tel: (65) 8746557 Fax: (65) 7757717 email: crshuia@nus.edu.sg

KEY WORDS: IKONOS satellite, very high resolution imagery, plantations, linear features, building height

ABSTRACT: With the successful launch of the IKONOS satellite, very high resolution imagery (up to 1-m resolution) is within the reach of civilian users. In the one-meter spatial resolution images acquired by the IKONOS satellite, details of buildings, shadows, roads, vehicles, individual trees, and even aggregates of people are visible. The visibility of such details opens up many new applications which require the use of contextual and geometrical information contained in the images. In this paper, we present some examples where geometrical and contextual information are used. These examples include estimating building height from its shadow, automatic delineation of tree crowns for enumerating trees in oil palm plantations, and extraction of linear features for cartographic applications.

1. INTRODUCTION

Very high resolution imagery (up to 1-m resolution) is within the reach of civilian users with the successful launch of the IKONOS-2 satellite in September 24, 1999. The IKONOS satellite provides imagery at two resolution modes: a 1-m panchromatic mode and a 4-m multispectral mode with four (red, green, blue and near infrared) spectral bands. Images of a same area can be acquired simultaneously in the two resolution modes and merged to form a pan-sharpened natural colour image at 1-m resolution.

Many details such as building structures, roads, vehicles, individual tree crowns, and even aggregates of people can be seen clearly in the very-high resolution imagery. Pixel-based methods of image analysis will not work successfully in such imagery. In order to fully exploit the information contained in the imagery, image processing and analysis algorithms utilising the textural, contextual and geometrical properties are required. Such algorithms make use of the relationship between neighbouring pixels for information extraction. Incorporation of a-priori information is sometimes required. A multi-resolutional approach is also a useful strategy when dealing with very high resolution imagery. In this case, pixel-based method can be used in the lower resolution mode and merged with the contextual and textural method at higher resolutions.

In this paper, we examine three examples where contextual and geometrical information are used in extracting information from 1-m resolution IKONOS images: automatic delineation and counting of tree crowns in an oil palm plantation, road extraction in an urban area and estimating building height from shadow.

2. TREE COUNTING IN OIL PALM PLANTATIONS

Oil palm plantation owners have a genuine interest in knowing the number of trees in their plantations for the fact that they need to monitor the production and to assess the value of the plantations. In the buying and selling of plantations, the interested parties evaluate a plantation

not only by its size, but also by the quantity of palms within because knowing the actual number of trees will give them a better assessment of the production rate.

Oil palm plantations range in size from below 40 hectares to as large as 75,000 hectares. The current practice of tree census is to deploy workers into the plantations and count the palm trees manually. The cost of manual counting can be low but the accuracy is doubtful due to various human factors. Though going physically into a plantation to count trees is not a drudgery, it is extremely tedious and hard to verify. The availability of 1-meter resolution IKONOS satellite imagery provides a better alternative. The advantages are both in the bird-eye views it offers and in the convenience of working with digital imagery.

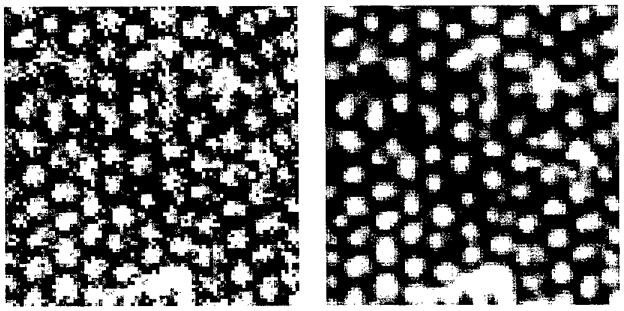


Figure 1 (Left) the appearance of oil palm trees in an IKONOS image, (right) the image after smoothing

The resolution of the IKONOS images is high enough for individual trees to be clearly spotted and enumerated. In these images of young plantations, palm trees generally have dome-shaped intensity profiles after some smoothing. Young trees tend to be well delineated at this resolution because of their distances of separation. As the trees grow bigger, the gaps among individual trees decrease and eventually disappear. However, the dome-shaped profiles remain visible. See Figure 1(a) for a palm tree image and Figure 1(b) for the image after smoothing.

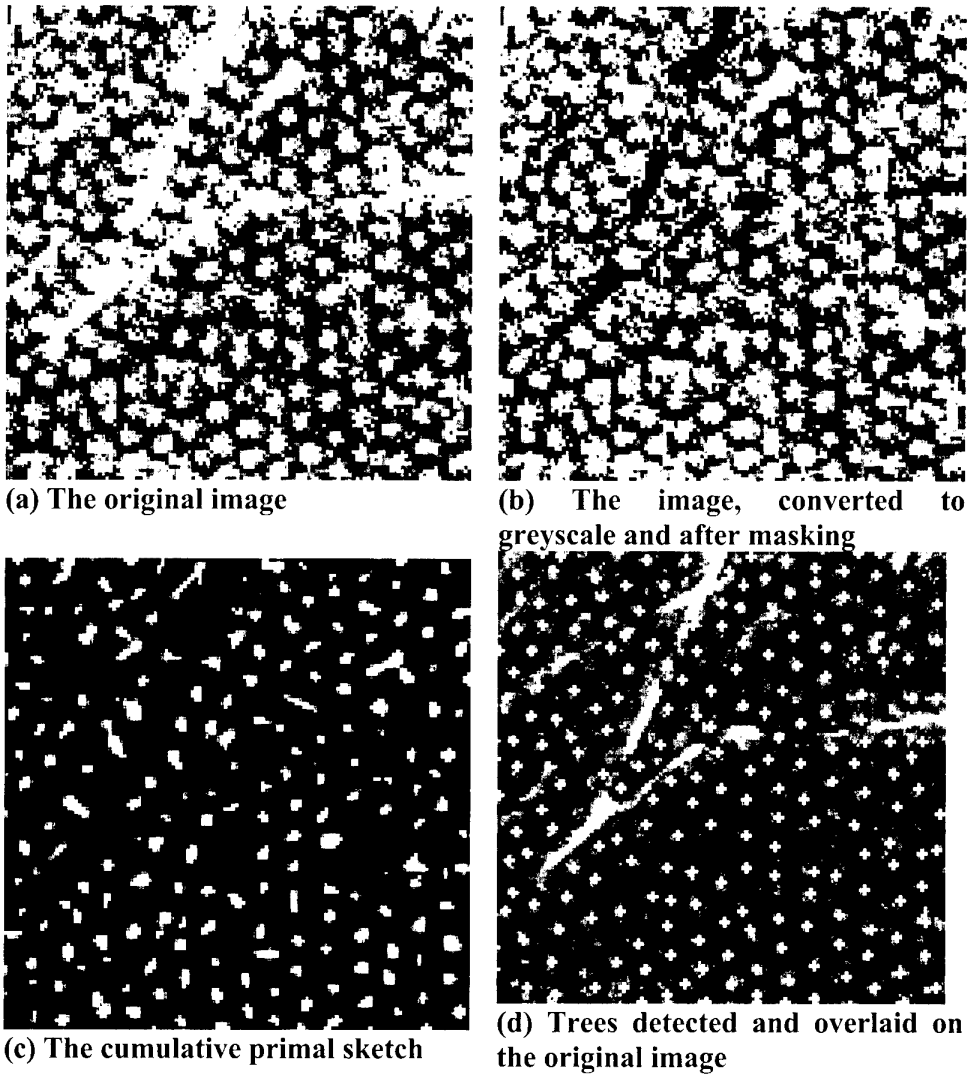
Counting trees in an image is much more manageable as workers can label the trees easily on the image. Verification is much easier. To further reduce the tediousness of the task and to speed it up, tree counting can actually be automated and the human worker needs only to verify the counting and make minor corrections when necessary. There are existing image processing techniques, which can be easily adopted and modified to automate tree counting. One technique which shows excellent results is that adopted from Brandtberg and Walter (1998). This technique is based on the concepts of *edge* and *curvature* in differential geometry. The boundaries of the dome-shaped intensity profiles show up as edge segments. The *curvature primal sketch* is then used to integrate (1) the information from the edge segments detected at a particular resolution, and, (2) the information obtained at various resolutions. The curvature primal sketches obtained at various resolutions are summed together to form a cumulative primal sketch. Peaks in the cumulative primal sketch are filtered using a local maximum filter of the size of a palm tree. Those peaks that pass the filtering are considered to represent trees. The shortcoming of this technique is that it uses only the gradient of intensity and ignores the magnitude of intensity itself. Sometimes, the magnitude of intensity can be a useful piece of information. For instance, tracks and lanes in plantations tend to appear very bright in the image. Such areas can be filtered away by thresholding.

We have tested the performance of this technique with several scenes of the pan-sharpened 3-2-1 bands of the IKONOS images. Though the images are in RGB colours, at this stage we only use the red band. The intermediate result of one of them is presented in Figure 2. The original

scene image is 400 pixels by 400 pixels in size. Figure 2 covers a zoomed-in area. The performance of this technique is verified with human eyes, which spotted 1803 trees in this region. With this technique, 1855 trees are counted by the automatic procedure. The accuracy of the technique is evaluated by the equation:

Accuracy = 1 - |no. of trees automatically counted – actual no. of trees| / actual no. of trees

Using this equation, the accuracy of automatic counting is 97.2%. Of the 1855 trees detected by the algorithm, 1535 are located correctly at the crown centers, 320 are mistaken as trees, and 268 trees are missed. We found that the errors are mainly due to the mis-location of the tree crowns. Instead of locating the trees at the centre of the tree crowns (which can be detected visually) the detected tree locations are displaced away from the crown centres. Hence, an error in mis-location contributes to both the mistaken tree and missing tree errors when validated by a human observer. There are four other scenes tested with this technique. There results are tabulated in Table 1.



(a) The original image

(b) The image, converted to greyscale and after masking

(c) The cumulative primal sketch

(d) Trees detected and overlaid on the original image

Figure 2 Intermediate results of the tree counting experiment

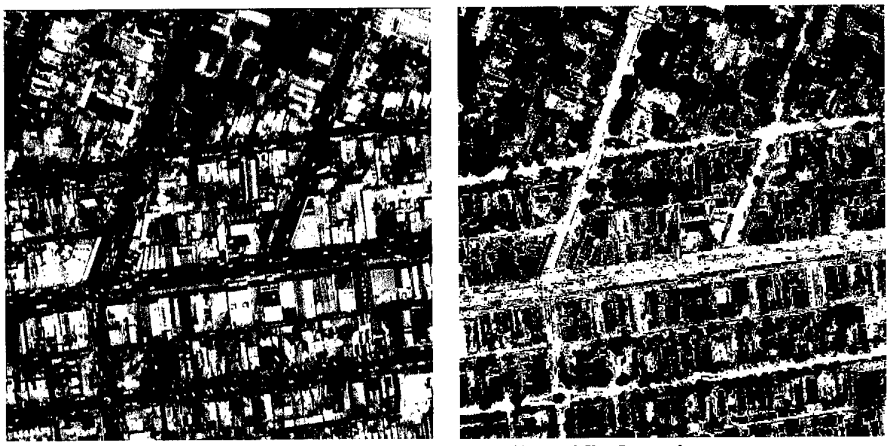
Table 1 Performance of the tree counting technique

Scene	Number of trees counted visually	Number of trees counted automatically	Counting accuracy (%)	Correctly spotted by the technique	Wrongly spotted by the technique	Missed by the technique
1	1012	1018	99.4	928	90	84
2	1823	1697	93.1	1410	287	413
3	1733	1765	98.2	1565	200	168
4	1710	1756	97.3	1490	266	220

3. ROAD EXTRACTION IN URBAN AREAS

Another potential application of the IKONOS image is to extract road-network information of any areas. Roads appear as linear curves at low resolution, but the resolution of the IKONOS image is fine enough for us to observe the details of the road condition and structures that are along the roadside or are on the roads. The presence of these details actually destroys the homogeneity of the roads' geometrical features and thus makes the extraction of roads difficult using techniques such as ridges, semivariograms, and local orientation. Colour images generally offer an advantage over greyscale ones, though there is no standard colour for roads.

We are investigating a semi-automatic method that is based on colour and active contour. First a supervised colour-based region classification is used to extract out regions of the "road colour". Then, active contour is used on the outcome of the classification to extract curves and lines from the regions of the "road colour". The usual active contour method uses intensity change as the internal energy. Instead of intensity change, we use the homogeneity of the region. In this paper, we discuss first the supervised classification. The active contour part is under development.



(a) Original image **(b) Classified regions**

Figure 3: Intermediate results of road extraction

We worked on the 4-3-2 bands of an IKONOS image of a city region. First, the NDVI value is used to determine potential vegetation areas. Regions with positive NDVI values are all put into the class called vegetation. Then, 5 other classes are defined. They are: dull roofs, bright roofs, buildings, dark smooth areas (including shadows and waters), and road. Spectral signatures for these classes are obtained from training sites in the image by the human supervisor. The mean and covariance matix are computed for each class. Subsequently, all the pixels in the image are classified to the class of closest colour using the Mahalanobis distance. Figure 3(b) shows the

classification result of the image of Figure 3(a). Areas belonging to the "road" class are shown in white. All other classes are in black. The network of the roads shows up prominently after classification. However, holes may occur within a road region and sometimes the road can be hidden behind vegetation or other classes.

4. ESTIMATING BUILDING HEIGHT FROM SHADOWS

In conventional stereo processing techniques, heights of buildings can be estimated using two images of the same area acquired at different viewing directions. Building height can also be derived from a single image using a simple geometric method if shadows of the buildings can be located in the image. For example, in Figure 4, the height of the building (H) can be calculated from the length of its shadow (L_s) on the ground and the sun elevation angle (θ_s) using a simple trigonometric relation: $H = L_s \tan(\theta_s)$. Very often, the base of a building in a satellite image is blocked by other surrounding structure such that the shadow length cannot be determined. In this case, it is still possible to determine the building height if both the top of the building (such as point P in Fig. 4) and its shadow (point Q in Fig. 4) can be located in the image. The building height can be obtained by using a geometric relation between the length of the line joining PQ on the image and the building height H.

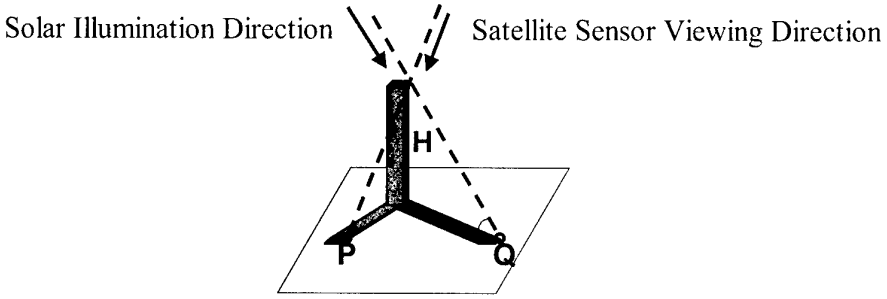


Figure 4: Geometry for estimating building from shadow

For example, Figure 5 shows the Chairman Mao Memorial Hall in Beijing. The top left corner of the roof top and its shadow can be seen clearly. The height of the building can be determined to be about 35 m with one or two meters error.

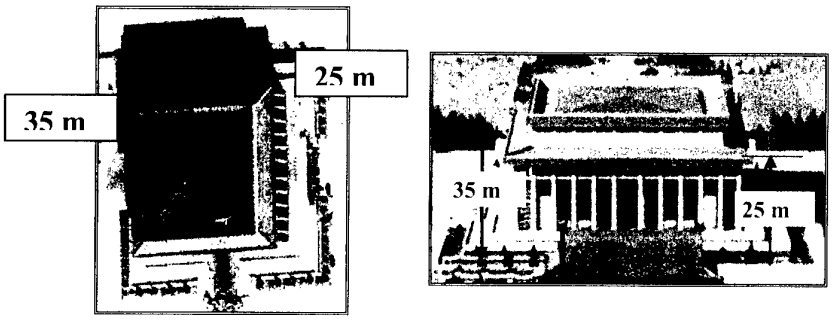


Figure 5: (left) Ikonos image of the Chairman Mao Memorial Hall in Beijing, China; (right) Photograph of the building..

5. CONCLUSION

In this paper, we have presented three potential new applications of the 1-meter IKONOS images. These applications demand the "common sense" type of knowledge that is relatively easy for human. However, due to the tediousness and extensiveness of the tasks, the automation of these tasks is invaluable. We have also shown that the automation of some of these tasks can be easily made possible using some existing tools.

6. REFERENCES

Brandtberg T., and Walter F., 1998. Automated delineation of individual tree crowns in high spatial resolution aerial images by multiple-scale analysis, Machine Vision and Applications (1998) 11:64-73.

Coxeter, H.S.M., 1969. Introduction to geometry, 2nd Ed, New York, Wiley.

THE RECTIFICATION OF HIGH RESOLUTION REMOTE SENSING SATELLITE IMAGERY

Chao-hsiung WU
Assistant Professor, Digital Earth Research Center
Chinese Culture University
55, Hwa-Kang Road, Yang-Ming-Shan, Taipei 111
Tel:(886)-2-28623538 Fax: (886)-2-28623538
E-mail : chwu@derc.pccu.edu.tw
TAIWAN

KEY WORDS : Remote Sensing Image, Geometric Correction, Ortho-Rectification

ABSTRACT : Since the successful launch of the IKONOS in 1999, its high ground resolution has draw attentions from earth resource management communities. This study involves geometric correction of the IKONOS Geo-product image. Two correction models are applied to the image. 1: without ground control, the relative geometrically corrected image shows a visually acceptable picture. 2: with accurate control points and DEMs' yields ortho-rectified image. The results show that this image can be used for map revision at large and medium scale cost effectively. Further investigation of using satellite onboard data to precisely determine the imaging geometry is recommended.

1. INTRODUCTION

Since the advance of earth observation satellites in the late 70's, remotely sensed imagery has been widely used in many fields of earth science. Due to its limited ground resolution, applications in large-scale mapping, planning, zoning and evaluation are not yet readily for business purposes. The successful launch of the U.S. IKONOS in 1999, high ground resolution image is since then commercially available. It provides digital image of 4 meters ground resolution in color and 1 meter in black and white. The revision cycle of 1-3 days makes it possible to periodically monitor the changes of the earth surface in an ever-closer manner. This brings the detailed earth observation scope into a feasible and operational stage that medium/small scale image such as Landsat and SPOT image are not compatible.

The preprocessing of remotely sensed image consists of geometric and radiometric characteristics analysis. By realizing these features, it is possible to correct image distortion and improve the image quality and readability. Radiometric analysis refers to mainly the atmosphere effect and its corresponding terrain feature's reflection, while geometric analysis refers to the image geometry with respect to sensor system.

This paper investigates the geometric characteristics of the IKONOS satellite image. Two scenes were processed and the results were evaluated. Three experiments of various numbers of control points and distribution pattern were conducted to evaluate the planimetric accuracy. The results can be used when this image is to apply at large scale observation and measurement whose geometric requirement is in the order of one meter.

2. Mathematical Model

2.1 Space Transformation

During the satellite imaging process, the projection, the tilt angle, the scanner, the atmosphere condition, the earth curvature and the undulation etc., will cause the satellite image distorted. It is necessary to correction these distortions before one can really use it as a precise measurement in the large scale operations. In this paper, as previously stated, the orbital parameters were unknown. The mathematical model used to compensate the distortion correction is the so-called rubber shifting method. It neglects all the sources of distortions but deal with the present ones with the help of control points. This also makes the correction procedure easier in the circumstance of insufficient parameters. In this study, due to the limitation of the software on hand, one assumption was made in formulating the relationship between image coordinate system and the ground control system. It is assumed that the geometry of the IKONOS imaging system is similar to that of the SPOT, for both scanners are optical system. The import source of the software is image coordinate system. This system is then transform to the photographic coordinate system and again transform to the ground control system.

The transformation model between satellite image coordinate system and the photographic coordinate system is the widely applied Affine transformation or the 6 parameters transformation. The mathematical equation is:

$$\begin{bmatrix} x \\ y \end{bmatrix} = \begin{bmatrix} a_1 & b_1 \\ a_2 & b_2 \end{bmatrix} \begin{bmatrix} u \\ v \end{bmatrix} + \begin{bmatrix} c_1 \\ c_2 \end{bmatrix}$$, Its inverse operation is:

$$\begin{bmatrix} u \\ v \end{bmatrix} = \begin{bmatrix} a_1 & b_1 \\ a_2 & b_2 \end{bmatrix}^{-1} \begin{bmatrix} x-c_1 \\ y-c_2 \end{bmatrix} = \frac{1}{a_1 b_2 - b_1 a_1} \left\{ \begin{bmatrix} b_2 & b_1 \\ -a_2 & b_2 \end{bmatrix} \begin{bmatrix} x \\ y \end{bmatrix} - \left[b_2 c_1 - b_1 c_2 - a_2 c_1 + a_1 c_2 \right] \right\}$$

where

x,y : satellite image coordinates

u,v : photographic coordinate system

a_1~c_2 : transformation parameters

The model used to link the photographic system to the ground control system is the famous condition: the space resection condition, the co-linearity equation as following:

$$x = -f \frac{a_{11}(X-X_0)+a_{12}(Y-Y_0)+a_{13}(Z-Z_0)}{a_{31}(X-X_0)+a_{32}(Y-Y_0)+a_{33}(Z-Z_0)}$$

$$y = -f \frac{a_{21}(X-X_0)+a_{22}(Y-Y_0)+a_{23}(Z-Z_0)}{a_{31}(X-X_0)+a_{32}(Y-Y_0)+a_{33}(Z-Z_0)}$$

in which

x,y : photographic coordinate, f : focal length

X_0,Y_0,Z_0 : exposure station in ground system

X,Y,Z : control point in ground system a_{11}-a_{33} : rotation matrix

In a flat terrain, geometric correction can be implemented by transformation of planimetric control points. While in a hilly area, relief displacement of terrain features are significant and need to be compensated. A 3-dimensional transformation should be introduced and the ortho-rectification procedure is adopted.

2.2 Image Resampling

In image resampling, in general, 3 different approaches can be applied, namely: the nearest neighbourhood, the bilinear interpolation and the cubic convolution. They possess their own characteristics but mainly vary in computation time and fidelity. For those who needs more information about resample techniques can refer to interpolation textbooks.

3. DATA SOURCE

3.1 Satellite Image

The image used in this study is the IKONOS satellite image. IKONOS was launched successfully on 24 September 1999, from California, USA. The orbit height is 681km above sea level, travel at a speed of 7 km/sec. The revision period ranges from 1 to 3 days depending on the imaging angle. The optical scanner provides image swath of 11km. The sensor system allows simultaneously collection of 1 meter resolution black and white (panchromatic) images and 4 meter resolution color (multispectral) images. The sun-synchronous orbit drive the satellite flies over 24° N latitude at 10:00 a.m. everyday, which allows the image shadows falling onto about the same direction of north-west, and hence improves the efficiency of visual interpretation.
Two IKONOS scenes were used in this paper. The first scene is the forbidden city, Beijin. The imaging date was 10/21/1999 and the data volume is 2006 * 2006 pixels. The second scene is Yuan-shan, Taipei. The imaging date was 10/21/1999, and the data volume is 2101 * 2101 pixels. Both scenes were downloaded from the Internet provided by the Space Imaging Co. Thess image have been radiometrically adjusted to improve the radiometric quality by the producer before uploading to the web site. From a general user point of view, the radiometry can be of little improvement, whilst the geometric accuracy is of concerned as long as the control materials are available. For the second scene, the image frame covers part of northern Taipei area, namely Yuan-shan. The geomorphology in this area is mostly flat terrain, while a small portion of hilly mountain located at the right middle with elevation of 110 meter above sea. Tan-shui river flows through at left of the image and Kee-lung river flows from right middle to north. Highway, metropolitan railway, football field and one of the landmark of Taipei, the Grant Hotel, are clearly visible in this image. Due to the image is an Internet sample, the orbit parameters such as satellite position of exposure, geometry of scanner, tilt angle as well as sun angle are unknown. This makes it impossible to apply orbit parameters in precisely determining the geometry of imaging.

3.2 Control Data

The control data used in this research were derived from two different sources.

In the Forbidden City case, due to the lack of ground truth, the control data were read from a 1/15,000 tourism map. It is clear that this map's accuracy is not sufficient for rectification purpose of the IKONOS image. But the geometric condition of the rectangularity for the shape of the Forbidden City was evidently a major constrain from visual inspection of this tourism map. In the Yuan-shan case, a digital 1/1,000 topographic map produced by the Bureau of Urban Development of Taipei City Government was used. It provides approximately 30cm planimetric accuracy and 50cm horizontal accuracy. Compare with the ground resolution of 1 meter of IKONOS image, this digital map provides sufficient control data.

4. EXPERIENCES AND RESULTS

4.1 Case 1

Case 1 refers to the relative geometric rectification of the Forbidden City image. As previously stated, the control points were derived from a tourism map. This map was scanned and converted to a digital form. By superimposing a digital regular grid net on top of the scanned map, relative control points of the test area were derived. In particularly, the right angle corners of the Forbidden City Wall were abstracted and recorded.

Figure 1 shows the original image. It is evident that the corners of the Wall are in skew due to the satellite view angle at the imaging instant. Figure 2 presents the relatively geometric corrected image in which the rectangularity of the Wall corners were maintained.

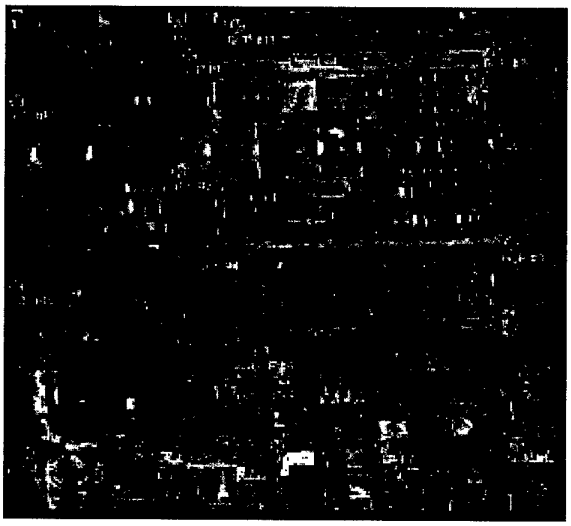


Figure1: Forbidden City (Origin)
Data Source: Space Imaging Co.

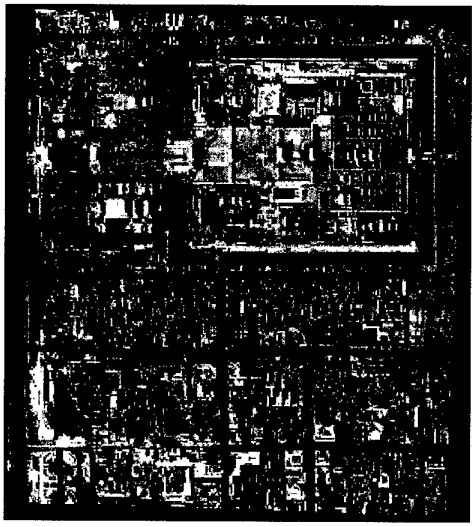


Figure 2: Forbidden City
(Relative Geometrically Corrected)

4.2 Case 2

Case 2 refers to the image rectification with accurate control in various pattern of distribution. Control pattern were classified into 2 types.

The first type is for flat terrain control in which 16 planimetric control points

were selected. Among them 9 points served as the control and the rest of 7 points served as the check points.

The second test refers to ortho-rectification. The correspondent 1/1,000 digital topographic map was served as the DTM. Figure 3 is the origin scene of Yuan-shan. Figure 4 illustrates a portion of the rectified image in which the digital topographic map is on top of it to provide a visual impression of the processing quality.

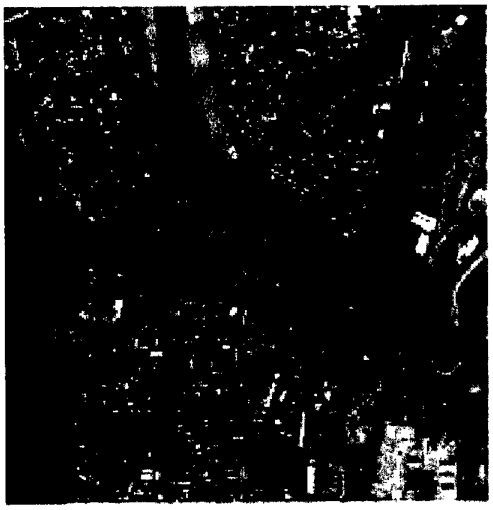


Figure 3: The Yuan-shan (Origin) Data Sources: Space Imaging Co.



Figure 4: Enlarged portion of Yuan-shan

5 DISCUSSION AND CONCLUSIONS

All the results in this study are evaluated by the Root Mean Square Error (RMSE) value. Table 1 shows the control pattern and its error vectors using planimetric control. Table 2 shows the RMSE of the ortho-rectification process.

The RMSE of the control points are all less than 1 pixel. The RMSE of the check points are also under 1 pixel in the flat area. While in hilly terrain, the RMSE increase drastically. These results also coincide with the theory that hilly terrain tend to decrease accuracy of height measurement, which shows at point number 15 with tremendous amount of error.

It is clear that after geometric rectification using accurate controls, the IKONOS image can be utilized in large scale mapping and planning. The image in this paper is adopted freely from the Internet and with little knowledge about the satellite attitude during exposure. It is strongly recommended that with the help of orbital parameters, one can expect a reliable and accurate image available for detailed earth observation. The short revision period of this imaging system also provides the possibility of rapid map updating which in general is a time consume and

costly task.

Table 1: The control pattern and error vectors using planimetric control

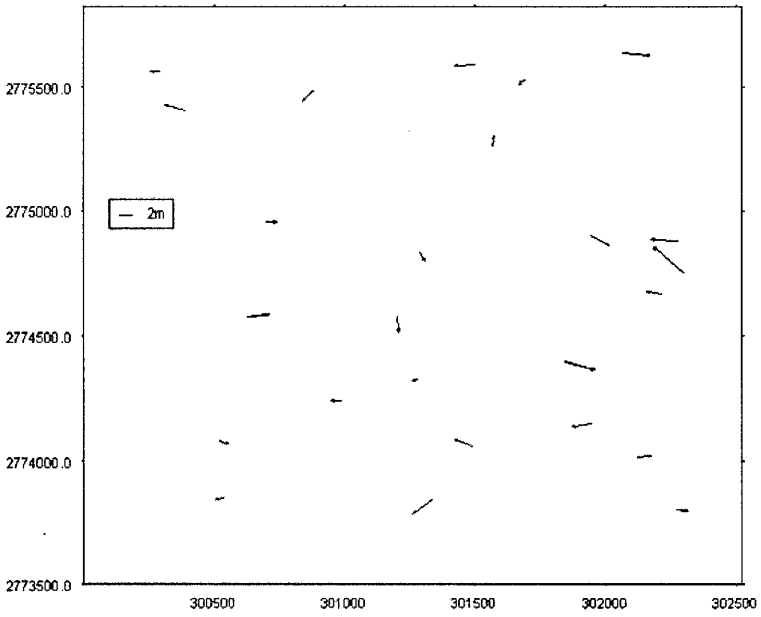


Table 2: The RMSE of control points after ortho-rectification

Pt #	RMSE	Pt #	RMSE	Pt #	RMSE	Pt #	RMSE
1	0.28	10	0.23	4	1.4	9	3.17
2	0.6	11	0.77	6	0.76	12	4.57
3	0.25	13	0.36	7	0.43	14	0.61
5	0.28	16	0.32	8	0.58	15	13.28

6 ACKNOWLEDGEMENT

The images used in this paper are credited to SPACEIMAGING.COM. Thanks to Jen-yu Han, I-hwei Du and Na-wen Tsai for their help in conducting the experiences in this article.

7 REFERENCES

Mayr, 1988, ISPRS Congress preceeding, Commission IV, Kyoto, Japan, pp.430-439.

Lillesand and Kiefer, 2000, Remote Sensing and Image Interpretation, pp.309-438.

Toutin and Cheng, 2000, Densifications of IKONOS, Earth Observation Magazine, V9, No 7, pp.13-21

Visser, 1980, Orthophoto Production and Application, The ITC Journal, 1980-4, pp.638-659.

Wiesel, 1985, Digital Image Processing for Orthophoto Generation, Photogrammetria, 40,pp.69-76.

LAND COVER CHANGE AND FLUCTUATION OF LACUSTRINE WATER QUALITY IN OKUTAMA LAKE

Susumu Ogawa* and Moe Moriyama**
Faculty of Geo-Environment Science, Rissho University
1700 Magechi, Kumagaya, Saitama, 360-0194 Japan
Phone: +81-48-539-1652 Facsimile: +81-48-539-1632
E-mail: *ogawa@ris.ac.jp; **morimoe77@hotmail.com

KEYWORDS: forest basins, lacustrine water, water quality, Landsat TM, land cover

ABSTRACT: Land cover change and fluctuation of lacustrine water quality in Okutama Lake were analyzed using two-date Landsat TM data. The relationship between its forest constitution and water quality was investigated. Most land cover was forest in this area. Forest was composed of evergreen and deciduous trees. Two long-term water quality trends were obtained: soil and sewer origins. The former origin might be derived from the change of forest constitution.

1. INTRODUCTION

Okutama located in the upper Tama River has been managed for stable flow rate and natural environment by protecting and planting forest. On the other hand, land use change with the management abandonment by aged landowners and the reduction policy of paddy fields affected directly on water quality in the river. The purpose of this study is to examine relationship between land cover change and lacustrine water quality from two-date Landsat TM and water quality data for 39 years in the Ogouchi Dam (Aoyama & Nishikawa, 1990; Kazama, Tada & Sawamoto, 1996; Yamada, Shimizu, Inoue & Tachibana, 1999; Kishimoto, Kakuchi, Somiya & Nakamura, 1999).

2. MATERIALS AND METHOD

2.1 Study Area and Data Used

Study area is located in the upper Tama River in Tokyo and Yamanashi prefectures as shown in Figure 1. For calculation of watershed area and watershed separation, digital elevation models '2,500' and '50m-mesh' by the Geological Survey Institute were used.

2.2 Land Cover Classification

Two-date satellite data were used for land cover classification and each area calculation.

With most likelihood method, land cover classification was carried out for 1984 and 1997 as shown in Table 1.

2.3 Watershed Separation

The objective watershed was determined semi-automatically with GIS software from digital elevation models '50m-mesh' by the Geological Survey Institute.

2.4 Water Quality Analysis

Water quality items are water temperature, turbidity, pH, transparency, chlorophyll-a, total nitrogen, and total phosphorus, which were measured at the Ogouchi Dam (Waterworks Bureau, Tokyo Metropolitan Government, 1959-1997). They were analyzed to seasonal and annual changes each item. Moreover, they were calculated for correlation.

3 RESULTS

3.1 Land Cover Change

Table 2 shows land cover classification in the forest of Okutama upper watershed. During the observation, the area of forest and urban increased, while agricultural field decreased as shown in Figure 2. Forest was composed of evergreen and deciduous ones. The latter increased more than the former. Figures 3 and 4 show long-term hydrological observation, which has almost constant trends each variable.

3.2 Water Quality Fluctuation

Figure 5 shows long-term fluctuation for turbidity, transparency, and chlorophyll-a. Transparency and chlorophyll-a increased, while turbidity decreased in trend. In seasonal water quality fluctuation, turbidity and total nitrogen decreased in summer, while chlorophyll-a increased in summer. However, sedimentation increased though turbidity decreased during this period as shown in Figure 6.

3.3 Water Quality Correlation

Table 3 shows correlation between water quality items. Turbidity correlates with total phosphorus positively, but with transparency, chlorophyll-a, and total nitrogen negatively. On the other hand, total nitrogen correlates with water temperature and pH negatively. Chlorophyll-a correlates with transparency, pH, and total inorganic nitrogen (Figure 7) positively. Moreover, sedimentation correlates with the square of flow rate as shown in Figure 8.

4 DISCUSSION

4.1 Land Cover Change

As a result of land cover change, forest and urban area increased, but agricultural fields decreased. The period of satellite data used here corresponds with that of the 8th water supply forest management plan by Tokyo Metropolitan Government from 1986 to 1996. By this plan, the introduction of broadleaf trees into forest led to the change of forest constitution. On the other hand, by the reduction of paddy fields their cultivation area decreased. Moreover, urbanization brought sewer drainage networks to generate sedimentation of soils.

4.2 Water Quality Fluctuation

Long-term fluctuation for water quality in the lake showed two different trends: the decrease of turbidity (increase of transparency) and increase of chlorophyll-a. Turbidity performs transparency reversely, which represents runoff reduction in the watershed physically. On the other hand, the increase of chlorophyll-a means microbial breeding corresponding to the increase of total nitrogen. Moreover, urbanization seemed to make sewer drainage into the lake, which is proved by negative correlation between total nitrogen and rainfall. Rainfall also correlates with total phosphorus, which is inferred from forest runoff.

4.3 Water Quality Correlation

Turbidity correlated with total phosphorus positively, but with transparency, chlorophyll-a, total nitrogen negatively. If turbidity was brought from soils in the watershed, it should depend on rainfall and be affected by the reduction of runoff ratio. In fact, rainfall and turbidity correlated, and the runoff ratio showed decrease trend. On the other hand, total nitrogen showed negative correlation with rainfall. As sewer drainage discharges constantly, it shows negative correlation with rainfall. Therefore, total nitrogen behavior should be derived from sewer drainage. As chlorophyll-a correlates with total phosphorus negatively, its breeding should be controlled by total phosphorus critically. Moreover, chlorophyll-a has positive correlation with total nitrogen annually, but shows negative correlation with it seasonally. It is inferred that chlorophyll-a breeding requires enough total nitrogen supplies and consumes total nitrogen seasonally.

Water quality fluctuation in 1984 and 1997 was controlled not only by land cover change but also other factors. For example, vegetation constitution may contribute water quality, which should be the next theme. Sedimentation behavior may depend on sewer networks development, which should be also the next theme.

5 CONCLUSION

From water quality and satellite data for the Ogouchi Dame for 39 years, relationship between long-term water quality fluctuation and land cover change in the water supply forest watershed was analyzed for the next conclusions.

(1) Land cover classification indicated the increase of forest and urban area, and the decrease of agricultural fields.

(2) Long-term water quality fluctuation showed two trends: the decrease of turbidity and the increase of chlorophyll-a and total nitrogen. The former might be affected by the reduction of runoff rate accompanied with the increase of forest and the decrease of agricultural fields. The latter might be caused by sewer drainage pollution into the Tama River accompanied with urbanization.

(3) From the correlation of water quality items, it was inferred that turbidity was derived from soils with rainfall and chlorophyll-a was controlled by total phosphorus critically to consume total nitrogen.

Water quality fluctuation might be affected by not only land cover change but also other factors: forest constitution change and sewer networks development, which will be the next theme.

ACKNOWLEDGEMENT

The authors thank Waterworks Bureau in Tokyo Metropolitan Government for their cooperation with their data. We also appreciate to Dr. Genya Saito, Mr. Naoki Ishituka, and Dr. Takuhiko Murakami at National Institute of Agro-Environmental Sciences, and Ms. Ikuyo Makino at Tokyo Institute of Technology for their cooperation of remote sensing analysis.

REFERENCES

Aoyama, S., H. Nishikawa, and H. Murai, *Journal of Remote Sensing Society of Japan*, 10, 4, 539-551, 1990.

Kazama, S., T. Tada, and M. Sawamoto, *Annual Journal of Hydraulic Engineering,* 40, 81-86, 1996.

Yamada, T., T. Shimizu, T. Inoue, and H. Tachibana, *Environmental Engineering Research,* 36, 217-224, 1999.

Kishimoto, N., K. Kakuchi, I. Somiya, and T. Nakamura, *Environmental Engineering Research,* 36, 225-236, 1999.

Waterworks Bureau, Tokyo Metropolitan Government, *Annual Report of Ogouchi Reservoir Management,* 1959-1997.

Table 1 Satellite data used

Satellite	Date
LandsatTM	1984/10/26; 1997/10/30

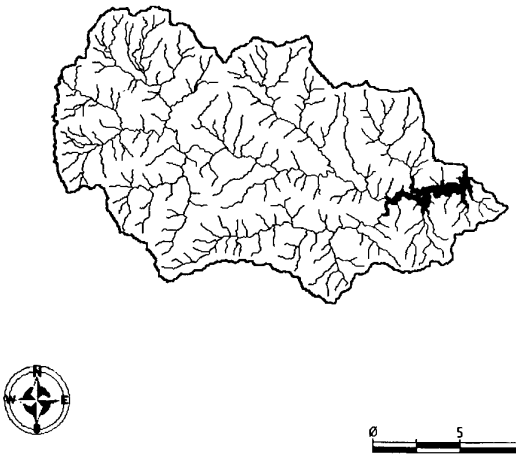


Figure 1 Okutama basin

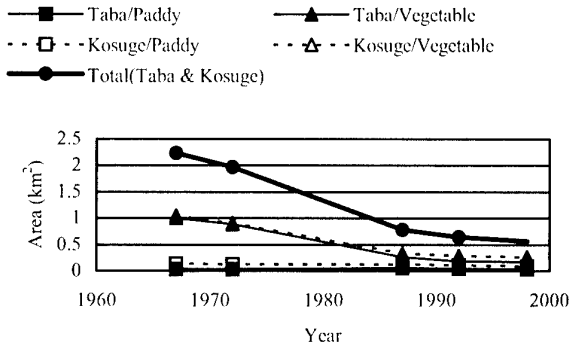


Figure 2 Historical change in agricultural area

Table 2 Land cover area rate in Okutama using Landsat TM (Unit:%)

Year	Forest	Urban Area	Grass	Paddy Field	Vegetable Field	Water
1984	92.8	0.4	2.6	2.1	0.8	1.3
1997	97.2	1.0	0	1.0	0.5	1.3

Table 3 Correlation for water quality items

Items	Turbidity	Transperancy	Chlorophyll-a	Water Temparature	pH	Total Nitrogen	Total Phosphorus
Turbidity	1						
Transperancy	-0.758	1					
Chlorophyll-a	-0.559	0.817	1				
Water Temparature	0.051	0.085	-0.023	1			
pH	-0.048	0.452	0.631	0.232	1		
Total Nitrogen	-0.609	0.320	0.022	-0.586	-0.529	1	
Total Phosphorus	0.694	-0.608	-0.510	-0.058	0.112	-0.335	1
Rainfall	0.487	-0.544	-0.344	-0.048	0.119	-0.485	0.411

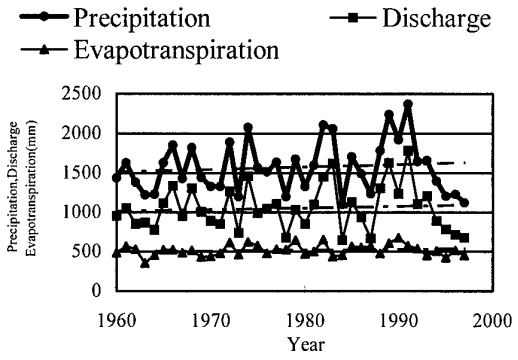


Figure 3 Long-term change in hydrological data

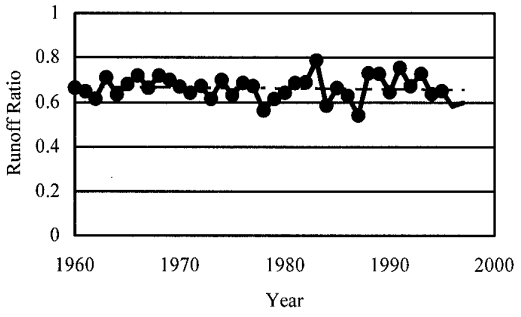


Figure 4 Long-term change in runoff ratio

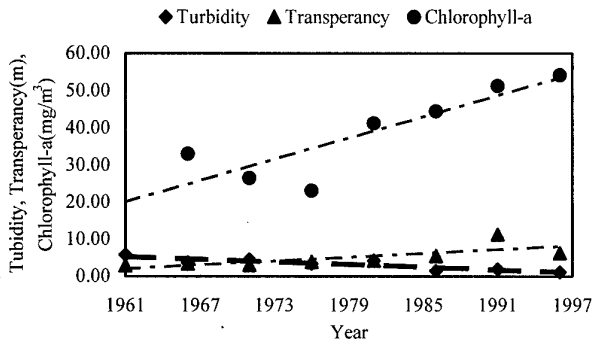


Figure 5 Turbidity, Transparency & Chlorophyll-a

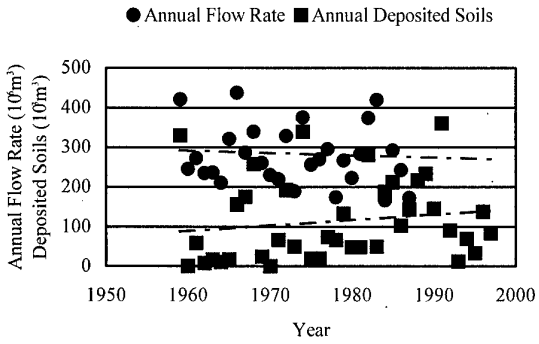


Figure 6 Annual flow rate and sedimentation

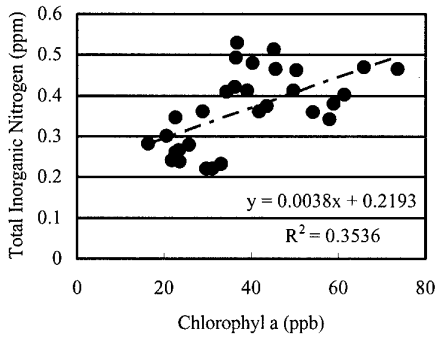


Figure 7 Chlorophyll-a and total inorganic nitrogen

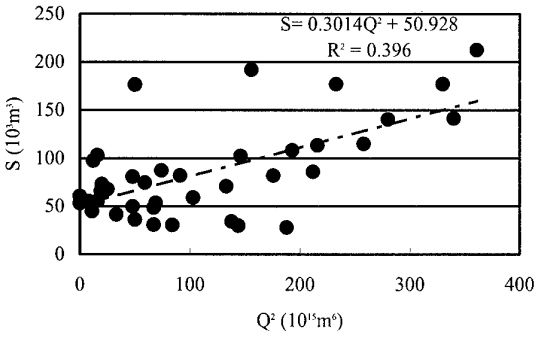


Figure 8 Annual flow rate and sedimentation

Vegetation Mapping in Ganges River Basin for Global Mapping Project

Ms. Mona Lacoul, Dr. Lal Samarakkon and Dr. Kiyoshi Honda
Asian Center for Research on Remote Sensing
Space Technology Applications and Research Program,
Asian Institute of Technology,
Km. 42, Paholyothin Highway, Klong Luang, Pathumthani 12120, THAILAND.
Tel : +66-2-524-6148 Fax : +66-2-524-6147 Email : mlacoul@ait.ac.th

ABSTRACT (paper -196)

This paper describes the preparation of vegetation map of Ganges river basin that could be used for various hydrological analysis that could be useful for water resources planning, flood forecasting and disaster mitigation. This study focuses on vegetation mapping of the Ganges river basin covering from 70° E to 95° E and 35° N to 20° N using NOAA AVHRR.

Initial vegetation cover of the area was prepared by monthly maximum NDVI data. The reason for aggregate daily NOAA-AVHRR data for monthly average was the presence of considerable amount of cloud cover in this region. Having generated the basic vegetation map based on NDVI, it was further classified according to climatic and elevation zones. The final vegetation map represents vegetation classes that are interpreted considering their temporal climatic and altitudinal variation that are needed to be considered for hydrological analysis.

Introduction

At the United Nations Conference on Environment and Development held in Brazil in 1992, Agenda 21, an action program for addressing global environmental challenges while continuing to support sustainable economic development, was resolved. Agenda 21 clearly makes the case that baseline data on key environmental parameters is important. In this course, in 1992, the Ministry of Construction of Japan began to advocate the Global Mapping concept. The fundamental basis of this concept is to develop global scale geographic information through international cooperation. Since its inception in 1992 the Global Mapping concept has obtained support from many countries in the world. Efforts are now being made to implement the development of global scale map products with uniform accuracy and specification under the auspices of an International Steering Committee for Global Mapping (ISCGM). This will facilitate resolving global problems by forming and implementing policies for the issues such as river control, disaster countermeasure and food security. As continuation of development of global map, Ganges River Basin was selected following the successful completion of Mekong River Area.

The Ganges basin contains the largest river system on the subcontinent. The Ganges rises in the southern Himalayas on the Indian side of the Tibet border. Area covered in the study of global mapping of Ganges river basin(approximately 174000 square kilometer) is 20 N to 35 N latitudes and 75 E to 95 E longitudes. The water supply is dependent partly on the rains brought by the southwesterly monsoon winds from July to October, as well as on the flow from melting Himalayan snows, in the hot season from April to June.

In order to monitor global scale vegetation cover, satellite data with frequent repetitive coverage should be available. This could be achieved only with NOAA-AVHRR series of polar orbiting, meteorological satellites. A lot of research is going on to develop techniques for continental and global scale studies of land cover using AVHRR data. One

of such technique is maximum value composting of normalized difference vegetation index (NDVI) for reducing cloud contamination and atmospheric effects. The seasonal variation of NDVI can be used to classify land cover /land use.

Significance of the study

Hydrological analysis, which could provide vital information for water resources planning, flood estimation, desertification analysis etc. requires land cover information as one of the significant parameters or a parameter derived form land cover status. In regional scale studies as in this present study, forest and vegetation cover should be considered with respect to climatic region, elevation condition as vegetation cover in different climatic regions or with the change of elevation could have different characteristics needed to be taken care in hydrological analysis. In order to develop a land cover map satisfying these issues, this study incorporated NOAA-AVHRR data with climatic and elevation information.

Data and Method

NOAA AVHRR maximum NDVI composite
The following flow chart (Fig 1) gives the complete overview of the methodology of analysis of the study.

At first, 10 days composite images of NOAA AVHRR based on maximum normalized difference vegetation index (NDVI) for year 1998 were collected form Asian Institute of Technology. In order to interpret temporal variation pattern, ten days NDVI composites were generated from these data, which is a method accepted globally(Moody & Stranfler, 1994). Due to frequent cloud cover in this region, 10 days temporal resolution of NOAA-AVHRR could not produce cloud-free composites. To overcome this situation, further data aggregation, monthly maximum NDVI was attempted. This step provided cloud free composite for the year 1998 except for the months June, July and August. As these three sense contained significant amount of cloud cover, they were excluded from subsequent analysis.

Multi-temporal NDVI data classification was carried out based on iso-class unsupervised classification method. With few initial evaluation of class distribution it was decided to terminate iso-class groups into 25. The resulting 25 classes were interpreted into vegetation classes using knowledge derived from temporal profiles, elevation, meteorological information as well as existing landuse maps. Basically, the classification scheme developed by International Geographic Information System Examination Committee for Global Mapping was adopted in this stage.

Elevation data
Elevation data freely available from National Imagery Mapping Agency (NIMA) was used for the study. The data is in 30 arc sec, similar to the working pixel NOAA data, but had to transform to the present co-ordinate system.

Meteorological data
10 years meteorological records of Ganges River basin were gathered from different organizations of respective countries. From collected meteorological data, average monthly temperature and average yearly rainfall were calculated for each meteorological

station. These data were interpolated incorporating elevation, representing iso heightal lines. These lines were further interpolated to 30 arc sec cells. Similarly, temperature data were interpolated and converted to 30 arc sec cell data.

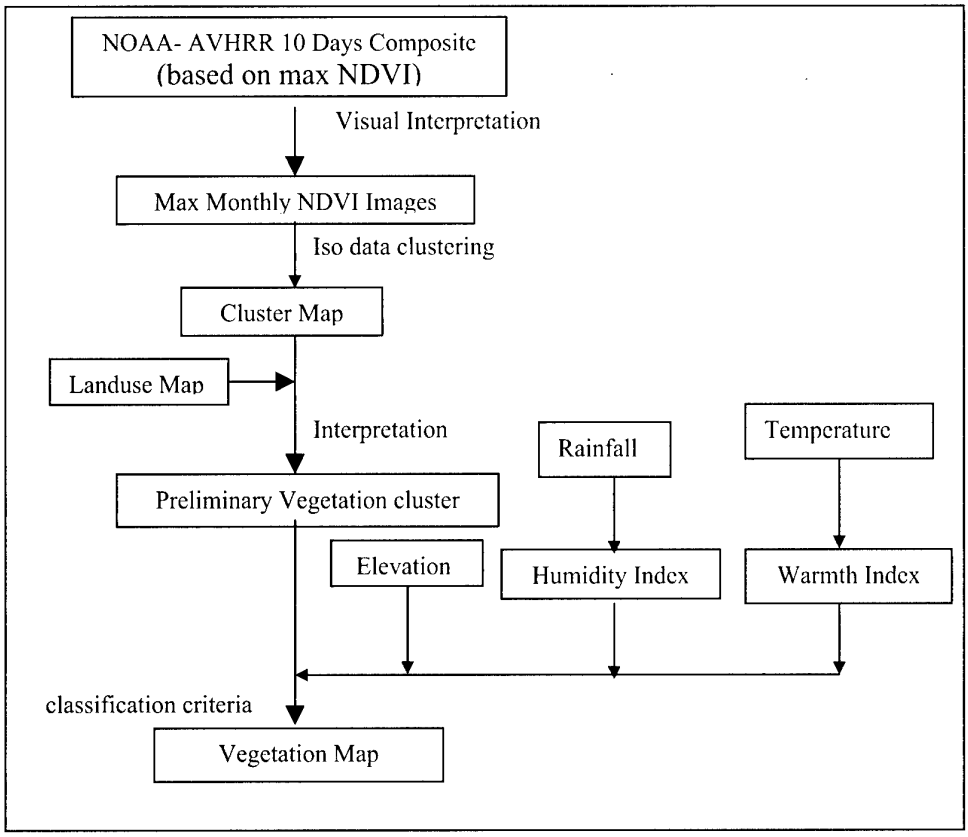


Fig 1: methodology of analysis

Kira's humidity index and Kira's warmth index were calculated using monthly average precipitation and monthly average rainfall data(Chunying, 1999). These indices are given by following equations.

Humidity Index,

$$HI = \frac{P}{WI + 20} \; for WI < 100 \;\&\; P \le 400$$

$$HI = \frac{2P}{WI + 140} \; for WI \ge 100 \;\&\; P \le 400$$

$$if P > 400, then P = P - 400 \; (tropics)$$

$$else P = P - 370 \; (subtropics)$$

Warmth Index,

$$WI = \sum_{m=1}^{12} T$$

$$where T = Tm - 5 if Tm \ge 5$$

$$else T = Tm$$

P: yearly average precipitation(mm)

Tm : average monthly temperature(C)

Results and Discussion

Studying multi-temporal spectral patterns of each of the 25 clustes, 4 preliminary classes were defined. The classes were (i) snow & ice, (ii) bare land and semi bare land, (iii) crop land and (iv) forest.

Among the 25 clusters, 3 classes were found to be generated with pixels arising from scan error during the data acquisition but the total number of pixels in these classes were less .06% of total pixels. These clasess were excluded from further analysis. The remaining 22 classes were identified as forest(3 classes), semibare land (5 classes), bare land (2 classes), snow &ice (1) and crop land (11 classes). The following figure gives monthly variation NDVI of preliminary classes except for three months June, July, and September.

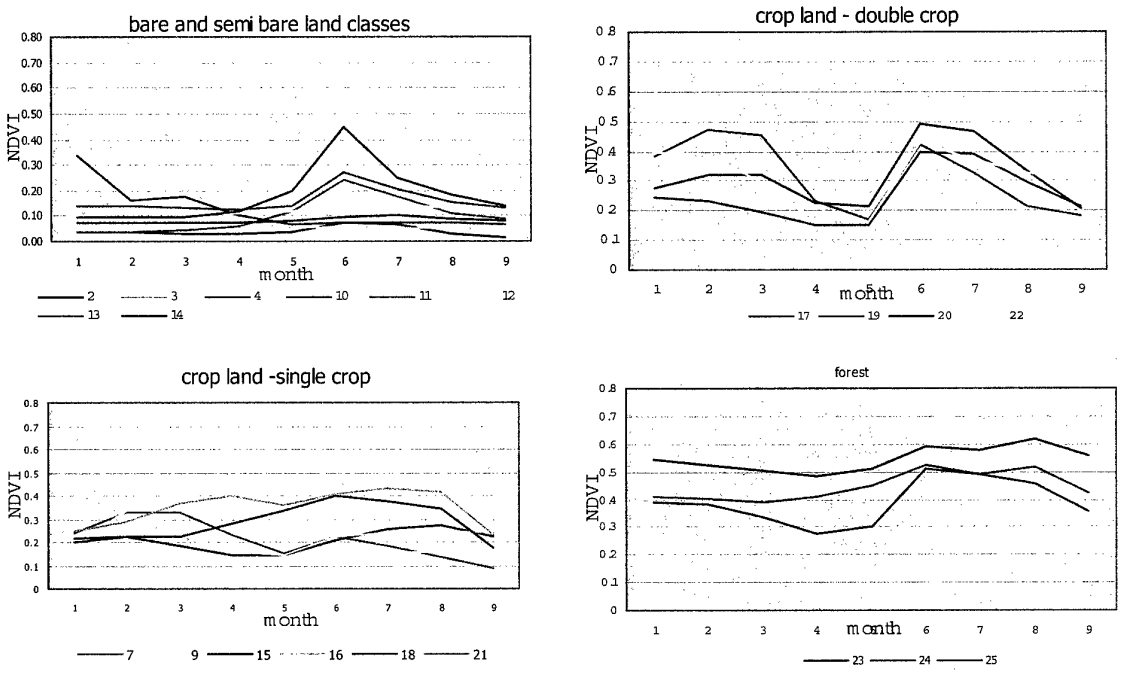


Fig 2: Spectral patterns of different vegetation classes based on Iso-data clustering

The Classes were defined using classification scheme developed by International Geographic Information System Examination Committee for Global Mapping to have conformity with other studies. 11 preliminary classes of crop land in the study area were regrouped into two classes, single crop and double crop based on temporal variance of NDVI.

According to Trwartha&Horn, 1980, approximate altitudinal limit of alpine vegetation on a tropical mountain is above 4000 m elevation. This altitudinal information was used in reclassifying two bare land (2 classes) semi bare land classes (5 classes) into two alpine bare/semi bare land classes and two bare/semi bare land classes.

Elevation and climatic factors were used to classify forest classes into five distinct classes evergreen, deciduous, semi-deciduous, savanna and mixed coniferous - deciduous from

three preliminary forest classes. Semi deciduous forest class was interpreted from original forest class referring to annual average precipitation as below 2000m elevation, semi–deciduous forest is predominant (Wallace, 1991). Similarly, other forest classes except mangrove forest were defined from preliminary forest classes using the criteria listed in the following table (table 1). An existing GIS layer of landuse was used to distinguish mangrove forest from other natural vegetation classes.

Class	Definition	Classification Criteria
snow/ice	Perennial snow (snow and ice throughout the year)	Vegetation index is low(almost constant)
alpine desert	Area of more than 4000m elevation covered with snow or ice	Vegetation index is low throughout the year
alpine vegetation	Shrubs and broadleaf grass location in the area of more than 4000 m elevation	Vegetation index is low but increases for short time period.
bare land	Non vegetated area through out the year	Vegetation index is low (little fluctuation).
semi bare land	Almost non vegetated area	Vegetation index is low but increases for short time period.
crop (1)	Farming land with two cycles per year	Vegetation index is high twice a year.
crop (2)	Farming land with one cycles per year	Vegetation index is high once a year.
evergreen forest	Forest of temperate zone in the area of rich rain in summer or throughout the year	Vegetation index is high throughout a year & 85< WI < 180 & HI>10.
deciduous forest	Forests active in warm season. Whose leaves fall in cold season	Vegetation index is high but decreases in winter & 45<WI<180 & HI > 7.
mixed pine and deciduous forest	Forest mainly locating in mountainous range of Nepal and Bhutan	Vegetation index is high but decreases lower in winter.
semi deciduous forest	Forest in tropical low land with precipitation lower than 2000 mm per year (Wallace E. Akin, 1991)	Vegetation index is medium to high.
savanna	Grass land in severe dry climate with long dry season consisting of mainly rice family plants with scattered trees	Vegetaion is low to middle throughout a year & WI > 180 & WI > 180 & 5<HI<7.

Table 1: definition and characteristics of vegetaion classes used in the study

Conclusions

The vegetation map produced in this study following global map guidelines showed conformity and continuity with adjoining data prepared by different study. This provided integration both studies together to develop regional map covering 75 deg E to 110 deg E and 5 deg N to 35 deg N. Visual comparison of result show good relationship with published maps of the all the countries that the area falls and this justifies temporal NOAA-AVHRR data usages in regional scale vegetation mapping.

Acknowledgements

This study was done under the financial support of Infrastructure Development Institute Ministry of Construction, of Japan

References

Moody and Stranhler, 1994. Global data sets for the land from AVHRR. Int. J. Remote Sensing, 1994. Vol 15, no 17, 3473-3491

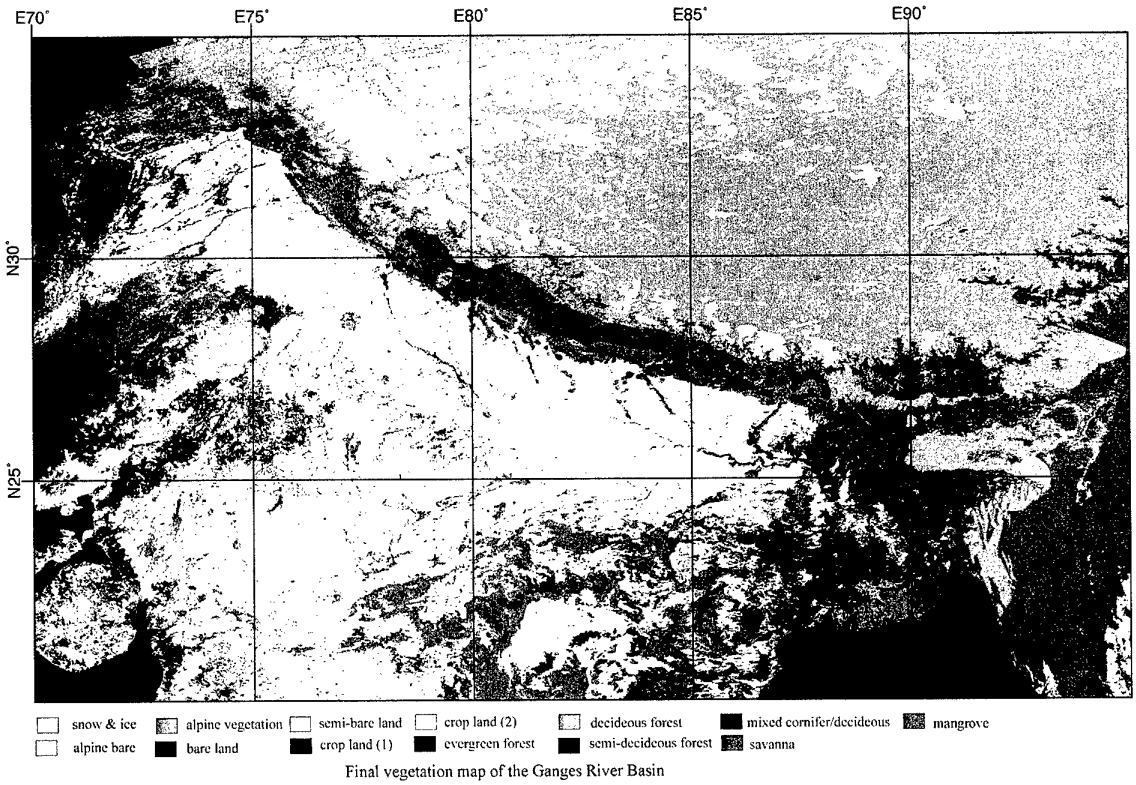
Defries and Townshend, 1994. NDVI derived land cover classification at global scale. Int. J. Remote Sensing, 1994. Vol 15, no 17, 3467-3486

Ministry of Construction, Infrastructure Development Institute, 1999. Study of comprehensive assessment on infrastructure development using global geographic information system(1). Trail production of the global map in the IndoChina Peninsula and construction of the geographic information system using the global map as a spatial data framework.

Trewartha & Horn, 1980. An Introduction to climate (fifth edition)

Wallace, 1991.Global pattern: climate, vegetation and soils. University of Oklohama Press. Norman. Publishing Division of the University

Chunying, 1999. The Application of Kira's Indices to study of vegetation-climatic interactions in China. ACTA Phytoecologica Sinica. 1999 vol. 2, no 2



Final vegetation map of the Ganges River Basin

VERIFICATION OF SURFACE TEMPERATURE FROM LANDSAT 7/ETM+ DATA

Yuzo Suga[1], Motohide Yoshimura[3], Shoji Takeuchi[1] and Yoshinari Oguro[2]
1: Professor, 2: Assistant Professor and 3: Researcher
Hiroshima Institute of Technology, 2-1-1 Miyake, Saeki-ku, Hiroshima 731-5193, JAPAN
Tel & Fax: +81-82-922-5204, E-mail: ysuga@cc.it-hiroshima.ac.jp

KEY WORDS: Surface Temperature, LANDSAT 7/ETM+, Short-wave Infrared, Thermal Infrared

ABSTRACT: The authors conduct a verification study on the surface temperature derived from the short-wave infrared and thermal infrared bands image data of LANDSAT 7 Enhanced Thematic Mapper Plus(ETM+) for the estimation of the thermal condition around the Hiroshima City and Bay Area and the observation of the volcanic activity in Mt. Usu in Japan. As to the thermal infrared band, the approximate functions for converting the spectral radiance into the surface temperature are estimated by considering both typical surface temperatures measured by the simultaneous field survey with the satellite observation and the spectral radiance observed by the ETM+ band 6, and then the estimation of the surface temperature distribution around the Hiroshima City and Bay Area is examined. As to the short-wave infrared band, the detection of the surface thermal anomalies in Mt. Usu is also examined by considering only the surface temperature distribution observed by the ETM+ bands 5 and 7.

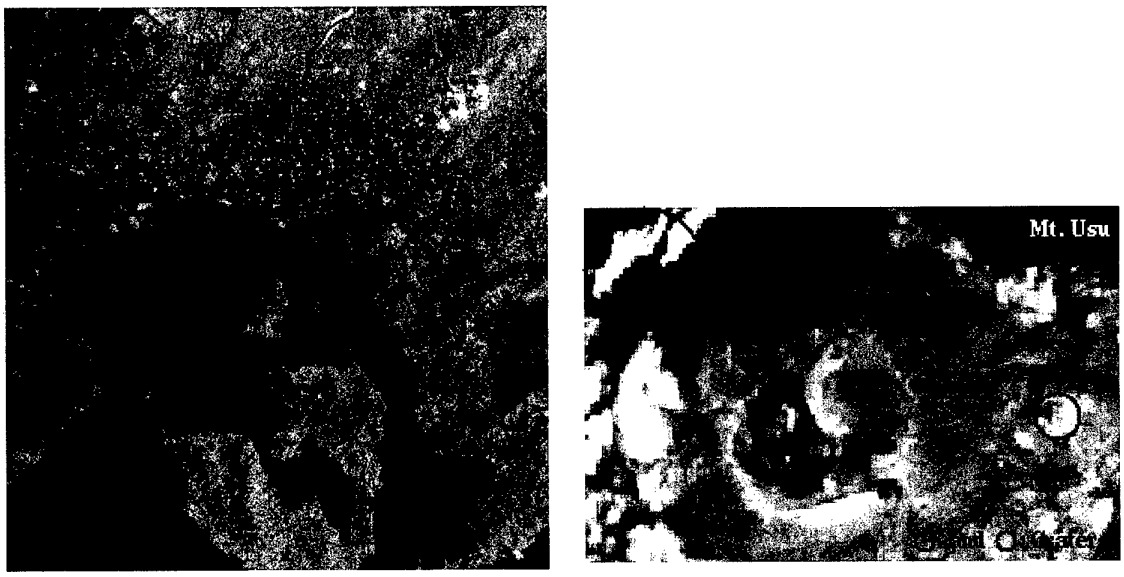
1. INTRODUCTION

LANDSAT 7 was launched on April 15th, 1999 and images large areas of the sunlit Earth daily by revisiting the same areas every 16 days. It has ETM+ sensor, a multi-spectral scanning radiometer with eight bands and being capable of providing high-resolution image information of the Earth's surface. The ETM+ acquires the image data in visible(band 1: 0.45-0.52, band 2: 0.53-0.61, and band 3: 0.63-0.69 μm), near infrared(band 4: 0.78-0.90 μm), short-wave infrared(band 5: 1.55-1.75 and band 7: 2.09-2.35 μm), thermal infrared(band 6: 10.4-12.5 μm), and panchromatic(band 8: 0.52-0.90 μm). The spatial resolution is 15m in the panchromatic band, 30m in the visible, near infrared, and short-wave infrared bands, and 60m in the thermal infrared band and each scene represents the Earth in 183 by 170 kilometers.

Hiroshima Institute of Technology(HIT) in Japan has established LANDSAT 7 Ground Station for receiving and processing the ETM+ data on March 15th, 2000. At the beginning of the research, the authors preliminarily examine the verification study on the surface temperature derived from the short-wave infrared and thermal infrared bands image data of the ETM+. The items of the verification study are the estimation of the thermal condition around the Hiroshima City and Bay Area using the ETM+ band 6 image data and the observation of the volcanic activity in Mt. Usu using the ETM+ bands 5 and 7 image data. The surface temperature estimation is necessary to establish the monitoring systems of the heat islands in urban areas, sea surface temperature, thermal drainage distribution, forest fires, and volcanic activities, etc. by using satellite remote sensing, and those systems provide us with the countermeasures for the environmental issues and the prediction methodologies for the natural disasters. So far, many researchers have reported their verification study on the surface temperature from LANDSAT 5/TM and NOAA AVHRR data(Rothery *et al.* 1988, Rothery *et al.* 1990, Franca *et al.* 1994, Schneider *et al.* 1996, Urai 2000).

2. TEST SITES AND DATA

The test sites for the verification study of the surface temperature from the ETM+ image data are the surroundings of the Hiroshima City and Bay Area and Mt. Usu in Japan. The former is located in the



(a) (b)

Figure 1: (a) LANDSAT 7/ETM+ color composite images(red : band 5, green : band 4 and blue : band 3) including the surroundings of the Hiroshima City and Bay Area(July 22nd, 2000). (b) LANDSAT 7/ETM+ color composite images(red : band 5, green : band 4 and blue : band 3) including Mt. Usu(May 7th, 2000)

western part of Japan islands and there exists the industrial area along the coast. The latter is located in the northern part of Japan islands and it has erupted on March 31, 2000. Figure 1(a) and (b) show the LANDSAT 7/ETM+ color composite images(band 5: red, band 4: green, and band 3: blue) received and processed by HIT on July 22nd and May 7th, 2000, respectively. The factories of the automobile manufacture and steel industry are located in the circled area in Figure 1(a). The smokes emitted from new active craters in Mt. Usu are interpreted in left upper corner of Figure 1(b).

3. SURFACE TEMPRATURE FROM LANDSAT 7/ETM+ DATA

In this paper, the authors conduct a verification study on the surface temperature using the short-wave infrared and thermal infrared bands image data of the ETM+ for the estimation of the thermal condition around the Hiroshima City and Bay Area and the observation of the volcanic activity in Mt. Usu in Japan. For the surface temperature estimation, the radiation emitted from the target on the surface is measured by using the remote sensor such as LANDSAT 5/TM, LANDSAT 7/ETM+, and SPOT 4/HRVIR etc, and Plank's radiation equation can be used to convert the measured spectral radiance to the temperature:

$$L_\lambda = 2\pi h c^2 \lambda^{-5} \tau_\lambda \varepsilon_\lambda / [\pi \{\exp(hc/\lambda kT) - 1\}] \qquad (1)$$

where λ is the wavelength in meters, L_λ is the spectral radiance in W m^{-2} $ster^{-1}$ μm^{-1}, h is Plank's constant, 6.626×10^{-34}Js, k is Boltzmann's constant, $1.380\times 10^{-23}JK^{-1}$, T is temperature in K, c is the speed of light, $2.998\times 10^{8}ms^{-1}$, τ_λ is the atmospheric transmittance and ε_λ is the spectral emissivity. Then the conversion equation from the spectral radiance into the temperature can be obtained as follows:

$$T = c_2 / [\lambda \ln \{(\tau_\lambda \varepsilon_\lambda c_1 \lambda^{-5} / \pi L_\lambda) + 1\}] \qquad (2)$$

where $c_1 = 2\pi hc$ and $c_2 = hc/k$.

LANDSAT 7/ETM+ data are acquired as the 8 bits gray-scale imagery in Level 1G products. The equation and constants for converting the 8 bits digital number(DN) of the image data into the spectral radiance is as follows:

$$L_\lambda = L_{min} + (L_{max} - L_{min}) \times DN / DN_{max} \qquad (3)$$

where L_λ is the spectral radiance in W m^{-2} $ster^{-1}$ μm^{-1} received by the sensor for the pixel in question. L_{min} is the minimum detected spectral radiance for the scene and L_{max} is the maximum detected spectral radiance for the scene. DN_{max} is the maximum value of the gray-level(=255), and DN is the gray-level for the pixel in question. The spectral radiance value is converted from DN in each pixel by using equation (3) and then it can be substituted in equation (2) to compute the temperature.

The satellite level spectral radiance at various temperatures from equation (1) is shown in Figure 3. We can see that the intensity of emitted radiation increases with the peak shifting towards shorter wavelength as the temperature rises. Figure 3 shows that the bands 5 and 7 in the short-wave infrared region can measure the temperature in the range of 250~440℃ and 160~270℃, respectively, and band 6 in the thermal infrared range can measure the temperature in the range of -70~+90℃ in the low gain mode and -30~+60℃ in the high gain mode. Parameters such as the wavelength range, L_{max} and L_{min}, etc. are in *Landsat 7 Science Data User Handbook*(USGS, 2000).

As to the test site of the Hiroshima City and Bay Area, the authors conduct the simultaneous field survey with the satellite observation and measure typical surface temperatures. By considering the ground truth data measured by the field survey and the spectral radiance converted from the DN data of the ETM+ band 6, approximate functions for converting the spectral radiance into the surface temperature are estimated by the least square method. Then the surface temperature distribution around the Hiroshima City and Bay Area is estimated. As to the test site of Mt. Usu, the authors convert the DN data of the ETM+ bands 5 and 7 into the temperature by using equation (2) and (3), and investigate the distribution of the surface thermal anomalies in Mt. Usu. In this paper, the atmospheric transmittance, τ_λ and spectral emissivity, ε_λ are supposed to be 1.0.

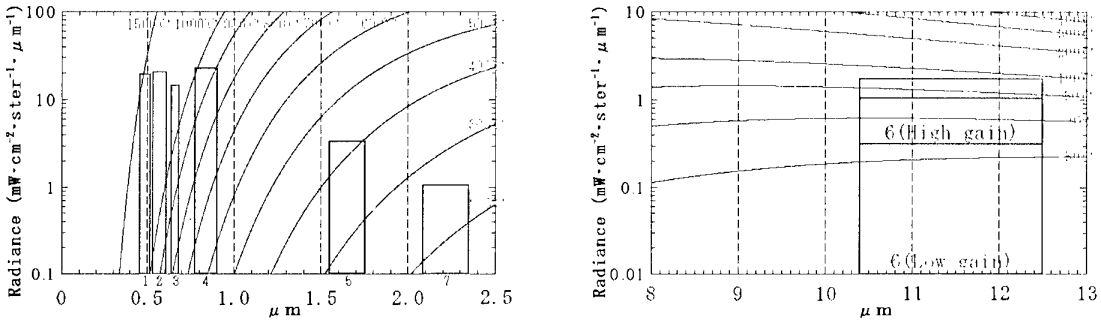


Figure 3: Satellite level radiance at various surface temperatures. Uniform atmospheric transmittance of 1.0 and surface emissivity of 1.0 are assumed. Vertical columns indicate the bands and dynamic ranges of LANDSAT 7/ETM+ sensor(modified Rothery *et.al* 1988 for LANDSAT 7/ETM+).

Table 1: The ground truth data measured by the field survey and the spectral radiance in low and high gain modes observed by the ETM+ band 6 for each land cover.

Land cover	Temperature[℃]	Spectral radiance in low gain and high gain modes [W m^{-2} $ster^{-1}$ μm^{-1}]		Estimated surface temperature[℃]
		Low gain mode	High gain mode	
Sea Surface	25.1	9.0212	9.0182	25.0
Paddy	29.8	9.0880	9.0924	27.8
Grass	35.5	9.4221	9.4259	38.9
Asphalt	46.1	9.6226	9.6112	44.5
Insulation Material	66.3	10.6249	10.6118	66.5

4. SURFACE TEMPERATURE AROUND THE HIROSHIMA BAY

On July 22nd, 2000, the authors conducted the simultaneous field survey in each land cover using portable thermometers in the Hiroshima City with the satellite observation of LANDSAT 7(path: 112 and row: 36). In order to cover the wide range of the surface temperature, sea surface, paddy fields, grass in golf links, asphalt pavement, and the insulation material on a roof of the building were selected for the field and the satellite observations. Table 1 shows the ground truth data and the spectral radiance from the DN data of the ETM+ band 6. The correlation coefficients between typical surface temperatures and the spectral radiance in Table 1 are 0.989 for the low gain mode and 0.988 for the high gain mode. The approximate functions temperature for low gain and high gain modes for converting the spectral radiance into the surface are estimated as follows:

$$L_{lowgain}=3.5785e\text{-}4\times T^2-0.1895\times T+33.7064 \quad (4)$$

$$L_{highgain}=3.5625e\text{-}4\times T^2-0.1888\times T+33.6634 \quad (5)$$

where $L_{lowgain}$ and $L_{highgain}$ are the spectral radiance in low gain and high gain modes, respectively, and T is the surface temperature in K. The surface temperatures for the five land covers estimated by using above functions are also indicated in Table 1. The result supports the fact that the surface temperature is estimated appropriately. Figure 3 shows the surface temperature distribution in the surroundings of the Hiroshima City and Bay Area derived from the ETM+ band 6 image data. The white colored part depicts the cloud in the image. The temperature distribution in Figure 3 is equivalent to the land cover types and the sea surface temperature distribution is also appropriate in comparison with NOAA/AVHRR data. The high temperatures around 70℃ observed in the circled area of the Hiroshima City. There exist the large factories of the automobile manufacture. The high temperatures around 80℃ are also observed in the

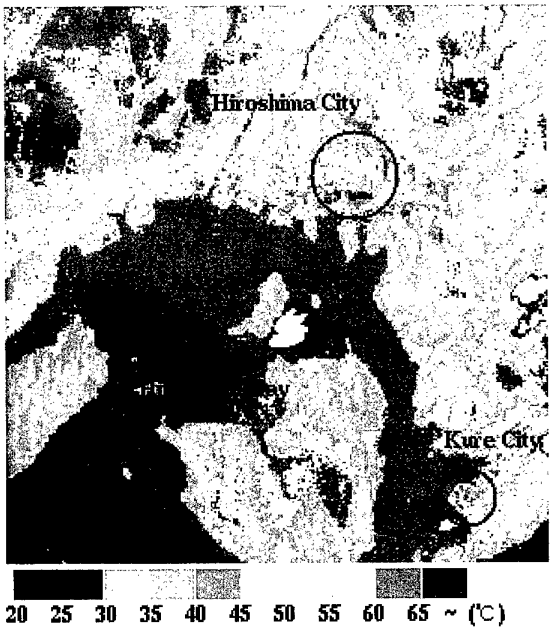
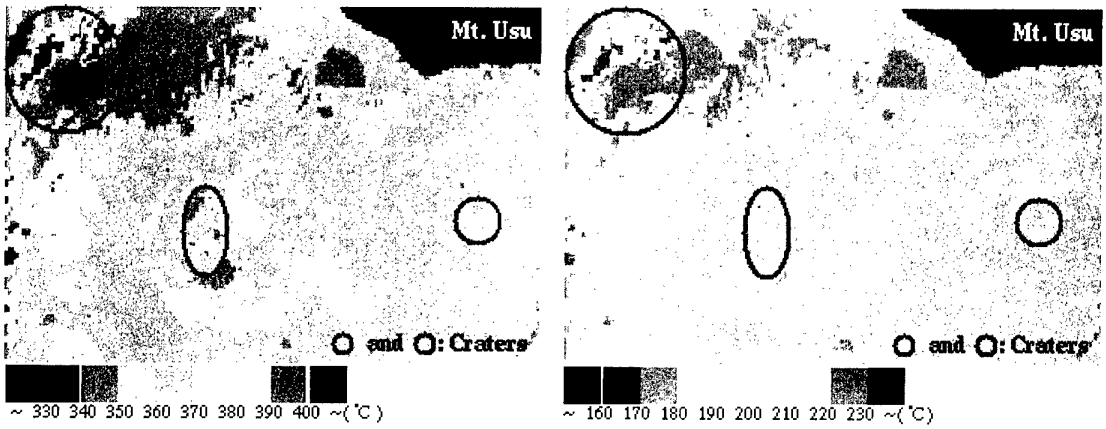


Figure 3: Surface temperature distribution around the Hiroshima City and Bay Area.

circled area in the Kure City. There exist the factories of the steel industry. From these results, it is proved the authors can verify the surface temperature derived from LANDSAT 7/ETM+ band 6 image data.

5. SURFACE TEMPERATURE IN MT. USU

Mt. Usu begun to erupt again on April 31st, 2000. HIT receives and processes LANDSAT 7/ETM+ data(path: 108 and row:30) on May 7th, 2000. The authors examine the detection of the surface thermal anomalies in Mt. Usu using the image data of the bands 5 and 7 in the short-wave infrared region of the ETM+. Figure 4(a) and (b) show the surface temperature distributions in Mt. Usu derived from the bands 5 and 7 image data, respectively. The surface thermal anomalies are found not only in the new but also in the existing craters. The temperatures around 388℃ for the band 5 and 245℃ for the band 7 are found at the new craters in the circled area(red), and the temperatures around 360℃ for the band5 and 225℃ for the band 7 are found at the existing craters in the circled area(blue). From these results, it is proved that the authors can verify the surface temperature derived from LANDSAT 7/ETM+ bands 5 and 7 image data.



(a) (b)

Figure 4: (a) Surface temperature distribution in Mt. Usu derived from the ETM+ band 5 image data. (b) Surface temperature distribution in Mt. Usu derived from the ETM+ band 7 image data.

CONCLUSION

In this paper, the authors conducted a verification study on the surface temperature derived from LANDSAT 7/ETM+ data using short-wave infrared and thermal infrared bands for the estimation of the thermal condition around the Hiroshima City and Bay Area and the observation of the volcanic activity in Mt. Usu in Japan. The authors estimated the surface temperature distribution equivalent to the land cover types around the Hiroshima City and Bay Area and detect the surface thermal anomalies at craters in Mt. Usu. For the further study, the authors plan the modification of approximate functions for converting the spectral radiance into the surface temperature by the field and satellite observation throughout a year and the development of various monitoring systems for the disaster and environmental issues. In this paper, the atmospheric transmittance and spectral emissivity are supposed to be 1.0. Therefore the effect by the atmospheric transmittance and spectral emissivity should be considered in the further study.

REFFERENCES

Rothery D.A., Francis P.W. and Wood C.A., 1988, Volcano monitoring using short wavelength infrared data from satellites. *Journal of Geophysical Research*, **93**, 7993-8008

Rothery D. A. and Francis P. W., 1990, Short wavelength infrared images for volcano monitoring. *International Journal of Remote Sensing*, **10**, 1665-1667

Franca G.B. and Cracknell A.P., 1994, Retrieval of land and sea surface temperature using NOAA-11 AVHRR data in north-eastern Brazil. *International Journal of Remote Sensing*, **15**, 1695-1712

Schneider K. and Mauser W., 1996, Processing and accuracy of Landsat Thematic Mapper data for lake surface temperature measurements. *International Journal of Remote Sensing*, **17**, 2027-2041

Urai M, 2000, Volcano monitoring with Landsat TM short-wave infrared bands: the 1990-1994 eruption of Unzen Volcano, Japan. *International Journal of Remote Sensing*, **21**, 861-872

USGS, 2000, *Landsat 7 Science Data Users Handbook*

An Evaluation of Drought Risk Area in Northeast Thailand using Remotely Sensed Data and GIS

C.MONGKOLSAWAT[1] P.THIRANGOON[2] R. SUWANWERAKAMTORN[2]
N. KARLADEE[1] S.PAIBOONSAK[3] P.CHAMPATHET[1]
[1]Computer Centre [2]Department of Computer Science [3]Faculty of Agriculture
KHON KAEN UNIVERSITY, KHON KAEN 40002 THAILAND
Email : charat@kku.ac.th

Key Words: Drought, GIS, Northeast Thailand

Abstract

In Northeast Thailand, drought has the most profound effect on the way of living and regional economy. It is also a major menace to regional food supplies. By its severity and duration these events can be disastrous not only locally but for the whole economic structure. Hence knowledge of the drought risk area of their occurrence and their course is an essential aspect for planning. Remotely sensed data and GIS is widely accepted as a tool for the establishment of integrated information. Drought risk area, by nature, is a result of interrelated parameters concerned. The objectives of this study were to model the drought risk area with a set of themes using remotely sensed data and GIS.

The study area, Northeast Thailand, covers an area of about 170,000 km^2 or about 1/3 of the total area of the kingdom. The underlining concept of the paper is that the severity of drought can be considered as being a function of rainfall, hydrology and physical aspect of landscape. A set of these themes were studied and reviewed. In terms of the water deficiency, these mainly include meteorological drought, hydrological drought and physical drought. Each theme of the drought consists of a set of logically related geographic features and attributes is used as data input for analysis. Establishment of each theme based on the overlay of the theme or individual theme layer. ***Meteorological drought*** was performed using mean annual rainfall data of minimum 15 years record of 264 stations. ***Hydrological drought*** was analyzed by overlay process of surface water, irrigated area, density of stream within sub-watershed and ground water yield and quality. ***Physical drought*** was formulated from a combination of spatial information of landform, drainage condition and land use by the matrix overlay function. A number of theme layers were extracted either mainly or partly from Landsat TM data of December 1998, these included surface water, land use, land form and drainage condition. In addition, the other theme layers were derived from map produced by the governmental agencies. The matrix overlay operation of the 3 drought risk layers was then performed and yielded the resultant polygonal layer. Each of which is homogeneous area with respect to each of the drought layer, there are then classified into 4 classes of drought risk: very mild, mild, moderate and severe.

The study indicated that high drought risk areas are found in the Southwest and extended to Northwest of the region. The low risk areas are located along the Mekong River. To evaluate its reliability, the resultant drought risk map, produced using GIS was checked against the survey data (NRD2C) of the National Economic and Social Development Board. In addition the drought regions developed were verified with the information acquired by interviewing the sub-district official committees. It is found to be satisfactory. The study confirms that the model developed can greatly enhance drought risk area mapping in the Northeast.

1. Introduction

Northeast Thailand contains one-third of the total population and land area of the kingdom. Over 70% of the population is engaged in agriculture which dominated by rain-fed production. At the present time, less than 6% of the cultivated land in northeast is irrigated,

leaving the majority of farmers operating in rain-fed conditions (Rigg, 1985). In addition, water shortage for domestic consumption is usually identified as principal constraint for the people during the dry season. Lack of water or drought in the region has profound impact that can be listed as economic, social and environmental. The eighth National Economic and Social Development Plan(1992-1996) called for achievement of water resource sustainability (NESDB 1992). The plan describes development issues and problems with the guidelines for developing water resources.

Drought risk area, by nature, is a result of a variety of factors. Drought in general originates from less precipitation over an extended period of time. These include occurrence of no rain in the rainy season, number and amount of rainfall event and other climatic anomalies. Palmer (1965) identified monthly index values for past dry periods to yield an equation for calculating drought severity in four classes. In an operational definition of drought it identifies drought from impact data (i.e. crop damage). The drought pattern should be started with an assessment of rainfall which orignates capital water. It is widely accepted that combination of physical nature of area, amount of rainfall and water resource development leads to identify the drought pattern.

In northeast Thailand, mean annual rainfall is about 1285 mm./annum, the region has yet significant impact of drought in a various part of the region (Wongvitawas 1993). Erratic distribution of rainfall, shallower water reservoir, low water holding capacity of soil and erosion sediment are major causes of drought. Koonthanakulwong (1990) concluded the drought on the basis of the number of days with rainfall less than specified threshold. Anukularmpai et al (1980) applied gamma distribution to predict minimum monthly rainfall in Thailand. Saenjan et al (1990) reported the frequency rainfall occurrence in the northeast and mapped along with a measure of their variability. Department of Environmental Planning and Policy (DEPP) (1996) established the drought risk areas in the northeast using GIS for spatial overlay of variable layers: rainfall index, soil water holding capacity, irrigated area, ground water yield, rainfall probability and land use. There still exists the gap in the methods used and details of the thematic layers established. Another study of rainfall in the northeast made by Siripon et al (2000) concludes that the unevenly distributed rain fall over the rainy season is found extensively and extends longer period in the southwest and the central part of the region. This phenomena is frequently occurred in the second half of June and of September for the areas in southwest and northeast of the region respectively. The information obtained from limited studies still requires a more detail identification of spatial pattern of drought. This is to support the government in allocating water for rural consumption more accurately and at the right place. Computer-based analysis and GIS can addresses this issue with higher accuracy, based on the integration of meteorological, hydrological and physical data of the areas. The purpose of this study is to model drought risk area using GIS with a set of data layers empirically evaluated.

2. Study Area

Northeast Thailand, one of the distinct main physiographic feature of Thailand, covers about one-third of the total area of the kingdom. It lies between the latitude of 14° and 19° N and the longitude of 101° and 106° East. Physiographically, the main area of northeast Thailand is formed by the so-called Korat plateau and a part of central highland. In the Korat plateau, the Phu Phan range lies in Northwest Southeast direction, dividing the plateau into two basins, the larger, Korat basin to the South and the smaller Sakon Nakhon basin to the North. The central highland covers narrow range along the western part of the region.

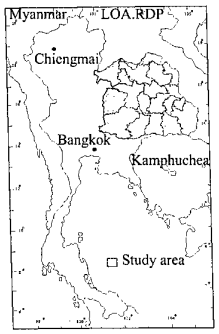


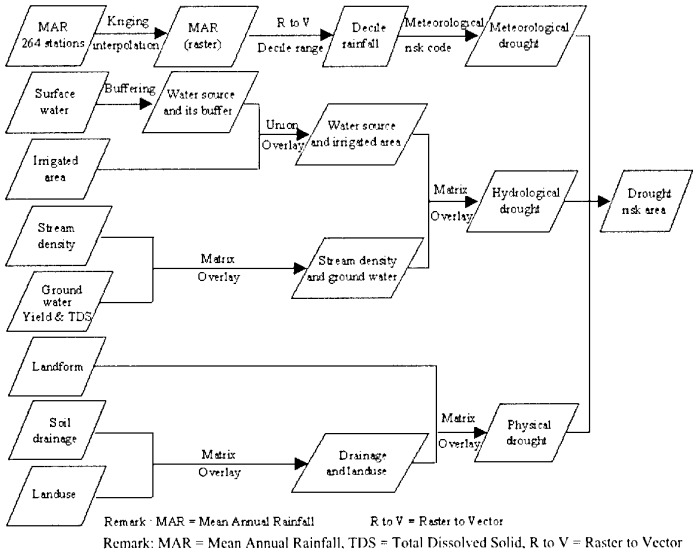
Fig. 1 study area

3. Methodology

The underlining concept of the paper is that the severity of drought is a function of rainfall, hydrology and physical aspect of landscape. Each of which is a thematic data layer that is a result of a analysis of sub layers or individual layer. The three thematic data layers are then combined to ultimately formulate a composite output layer or drought risk area. The schematic chart of this analysis is shown (Fig 2).

3.1 Rain analysis

Daily rainfall data from 264 stations across northeast Thailand covering at least 15 years record were compiled as point database for analysis. Calculation of mean annual rainfall was made at each station. Kriging interpolation was performed to establish spatial mean annual rainfall across the entire northeast Thailand. The threshold of mean annual rainfall was then identified using decile range to create the decile rainfall.



Remark: MAR = Mean Annual Rainfall, TDS = Total Dissolved Solid, R to V = Raster to Vector

Fig 2. Schematic chart of drought analysis

The decile rainfall of 10 classes was grouped into 4 levels of drought severity that so called meteorological drought.

3.2 Hydrological analysis

Input data layers for hydrological drought include surface water source, irrigated area, stream density in subwatershed and ground water yield and quality.

Surface water source and irrigated area were derived from 14 scenes of Landsat TM acquired during December 1998-February 1999 and data collected by the site project of the Royal Irrigation Department respectively. Stream density was calculated from stream length within subwatershed area. Ground water yield and quality at scale of 1:100,000 is available from the Department of Mineral Resources. Each input map layer was digitally encoded in GIS database.

To generate the hydrological drought the matrix analysis was performed for every coincidence of classes in two layers (Fig 2). The variables class and severity of drought are given in table 1.

3.3 Physical landscape Analysis

Land form, drainage condition and land use are input variables for analysis of physical drought. Preparation of land form and land use maps were done using the Landsat TM acquired as above. Drainage condition map was compiled from soil map 1:50,000 of Land Development Department. Digital map of each layer was performed using GIS functions.

The digital output of the physical drought is a combination of 3 input variables. The analysis and procedure were executed the same as those performed for the hydrological drought. (Fig 2 and table 1)

Table 1 variables, class and drought severity

Variables	Class	Drought severity
Mean annual rainfall (Decile range)	0 - 1130.065 mm.	4
	> 1130.065 - 1276.133 mm	3
	> 1276.133 - 1431.076 mm.	2
	> 1431.076	1
Irrigated area and water source	Water source 0 - 0.5 km^2	
	Area beyond water source >0.5 km.	4
	Area beyond water source >0.12 - 0.5 km.	2
	Area beyond water source 0 - 0.12 km.	1
	Water source 0.5 - 5 km^2	
	Area beyond water source >1 km.	4
	Area beyond water source >0.25 – 1 km.	2
	Area beyond water source 0 - 0.25 km.	1
	Water source 5 –10 km^2	
	Area beyond water source >1.5 km.	4
	Area beyond water source >0.5 – 1.5 km.	2
	Area beyond water source 0 - 0.5 km.	1
	Water source > 10 km^2	
	Area beyond water source >3 km.	4
	Area beyond water source >1 - 3 km.	2
	Area beyond water source 0 - 1 km.	1
	Area within irrigated area	1
Groundwater yield and TDS.	3 m^2 / hr. & TDS. > 1500 mg/l	4
	2 - 10 m^2 / hr. & TDS. > 750 - 1500 mg/l	3
	10 –20 m^2 / hr. & TDS. <750 mg/l	2
	>20 m^2 / hr. & TDS. <750 mg/l	1
Stream density	0 – 120.98 m/ km^2	4
	120.99 – 248.17 m/ km^2	3
	248.18 – 406.89 m/ km^2	2
	>406.89 m/ km^2	1
Land form	Mountainous	4
	Dissected erosion surface	3.5
	High terrace	3
	Middle terrace	2.5
	Low Terrace	2
	Flood plain	1
Drainage condition	Excessively drained	4
	Well drained	3.5
	Moderately drained	3
	Somewhat poorly drained	2.5
	Poorly drained	2
	Very poorly drained	1
Land use	Field crop / Deciduous forest / Village	4
	Mixed field crop / Forest and mixed crop	3.5
	Grass land / Shrub / non-use	3
	Mixed paddy / Mixed ever green forest	2.5
	Tree / Fruit tree / Swamp and other	2
	Paddy / Mixed fruit tree / ever green forest	1.5
	Water source / Riparian / Swamp	1

Drought Severity : 1 = Very mild, 1.5 – 2 Mild, 2.5 – 3 Moderate, 3.5 – 4 Severe

3.4 Drought risk area

The resulting thematic data layers were then combined by matrix analysis to produce the drought risk area. The drought risk area represents the integration of meteorological drought, hydrological drought and physical drought which in turn are assigned according to the drought criteria studied.

4. Results and Discussion

Result of the overall drought risk area are shown in Fig 3d and has 4 classes : very mild, mild, moderate and severe. The severe drought area covers mainly in the southwest of region and has approximately 11.20% of the northeast. The moderate drought area extends around those of severe class and has about 32.06%. The some of very mild areas have occurred in the southwest region where water source and irrigated area was developed. The very mild and mild drought areas are found extensively in the eastern and northeastern part of

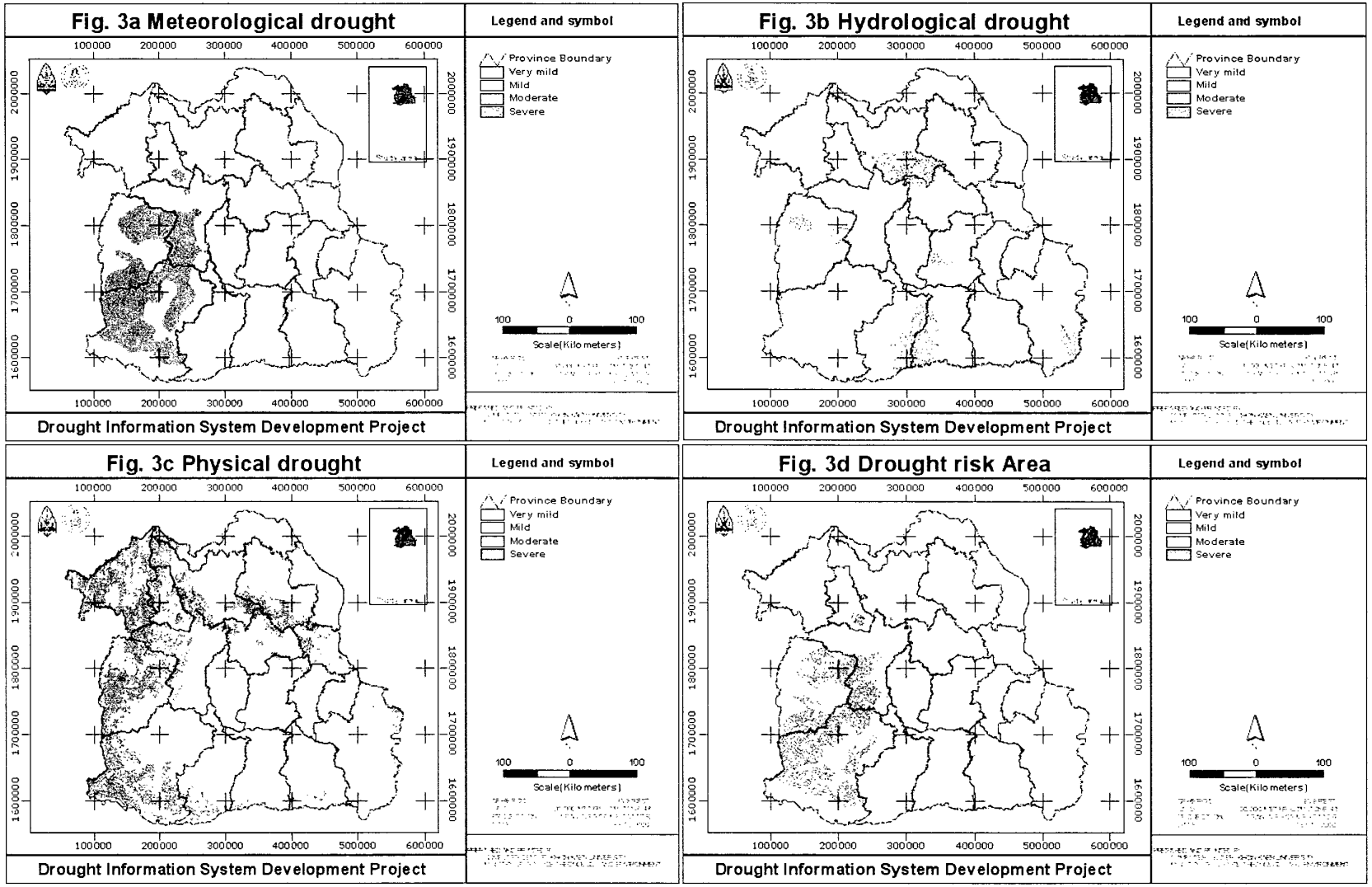


Fig. 3 Meteorological drought, Hydrological drought, Physical drought and Drought risk Area Map

the study area, particularly along the Mekong river. The areas occupied by the different kinds of the droughts are summerized in table 2.

Table 2 Meteorological Drought, Hydrological Drought, Physical Drought and Drought risk Area.

Drought class	Meteorological Drought (%)	Hydrological Drought (%)	Physical Drought (%)	Drought risk Area (%)
Very Mild	5.61	28.12	13.40	29.40
Mild	35.20	20.22	42.78	27.34
Modurate	34.03	38.07	38.61	32.06
Servere	25.16	13.59	5.21	11.20
Total	100.00	100.00	100.00	100.00

The total area = 170,000 km^2

To assess the reliability of resultant map the test areas were check against other information surveyed by The National Economic and Social Development Board (NESDB) or NRD2C survey data. This survey based on the shortage of water in village for agricultural use and domestic consumption. The 26,000 village locations of different water shortage were laid over the drought risk map obtained. Over 80% of village locations of each water deficiency class corresponded to the drought class studied. In addition, information obtained from interviewing the sub-district official committee in relation to result compiled was statistically evaluated and no significantly different.

In conclusion, the result obtained by the integration of a number of variables concerned provides guidelines for drought mitigation plan and allocates water for rural consumption. The information offers not only spatial data of drought severity but also their related attributes. These attributes include variables involved the drought, all drought class and villages drought affected. The computer-based information both locational information and attribute data contribute to develop the decision support system with higher accuracy.

5. References

Anukularmphai. A., Shabiruzzaman, and Ullah. E, 1990. Rainfall and evaporation analysis of Thailand. Bangkok, Div. of Agricultural and Food Engineering, AIT.

DEPP., 1996. Flood and Natural Risk Area in Northeast Thailand Project Bangkok; Min. of Science, Technology and Environment.

Koonthanakulwong. S., 1990. Meteorological drought in Northeast Thailand. Bangkok. Chulalongkorn Univ.

NESDB., 1992. The eight National Economic and Social Development Plan, Office of The Prime Minister, Bangkok.

Palmer., 1965. Meteorological Drought, Office of climatology, Washington D.C., U.S. Weather Bureau, Research paper No 45, 58p.

Rig, D.J., 1985. The role of environment in limiting the adoption of new rice technology in Northeast Thailand. Transs. Inst. Br, Geog. N.S.10. p 481-494.

Saenjan. P., Ganier. B.J., Maclean. P.A., 1990. Patterns of Wet Season Rainfall in Northeast Thailand In Proceedings of the Seminar on Remote Sensing and GIS for Soil and Water Management. Khon Kaen : Khon Kaen University, p 180-p 202.

Siripon. K., and Mongkolsawat. C., 2000. Spatial and Temporal Analysis of Rainfall Pattern in Northeastern Thailand : Application of GIS. Journal of Remote Sensing and GIS Association of Thailand. Vol.1, No.1, p.1-p 18.

Wongvitavas.P., 1993. Rainfall Analysis in Northeastern Thailand. Bangkok Meteorological Dept, Technical Document No.551.577.3-01, 99p.

INVESTIGATION OF EVAPORATE DEPOSITS ON GAVKHONI PLAYA LAKE

R.Ajalloeian(B.Sc, M.Sc, Ph.D)
Department of Geology, Isfahan University, Isfahan-Iran
H.R.Pakzad(B.Sc, M.Sc)
Department of Geology, Isfahan University, Isfahan-Iran
H.Safaei(B.Sc, M.Sc, Ph.D)
Department of Geology, Isfahan University, Isfahan-Iran

KEYWORDS: Aeolian, Evaporate, Facies, Playa, Salina mud, Salt pan,

ABSTRACT: Gavkhoni playa lake as a depression is located at the south-east of Isfahan in central of Iran. This area is between longitudes of E52°,43' - 52°,53' and latitudes of N32° - 32°,21'.The lake was formed as a result of block faulting (graben) since tertiary period. It has been surrounded by volcanic rocks at the north-east part and sedimentary rocks at the south-west part. Also there is an extensive sand dune at the western part of the playa. Ghavkhoni playa is a permanent lake with a closed drainage basin which mainly feded by a permanent river and two ephemeral rivers. Climatologically, this area is dry and its annual precipitation and evaporation are about 80 mm and 3000 mm respectively.
Based on satelite image processing (TM) and field works, this basin can be divided into several subenvironments such as sand flat, mud flat, salina mud flat and salt pan. The most important issue in this area is salt pan which is considerable area and covered more than 70% of the playa lake. According to surface and subsurface investigations, salt pan consist of medium to fine grain terrigenous sediments and evaporates. The thickness of the salt layer ranges between few centimeters to the north and about 1.5m to the south. This paper mostly emphesis on evaporate deposits through the field works and remote sensing studies.

1. INTRODUCTION

Gavkhoni Playa Lake is located to the southeast of Isfahan in the central of Iran. The surface of the playa is about 1470 meters elevation. The Gavkhoni playa lake similar to many other saline lake basins (e.g.. Death valley, California U.S.A. and Howz-e-Soltan) was formed as a graben as the result of block faulting (Krinsley, 1970). Extensive alluvial fans have covered the northeast, south and east of the area. These alluvial fans, which extend from mountains to the margin of the Playa Lake, derive mainly from alteration and erosion of igneous rocks. The Varzaneh aeolian sand field marks the western boundary of this Playa. The margin of the lake to the north is wetter than other area and is covered with bushes.

The Gavkhoni Playa Lake is typical of many permanent lacustrin basins within a closed drainage basin in the central of Iran. Water is delivered to the basin via a permanent river, two ephemeral rivers, numerous diffuse small streams, and direct precipitation on the lake's surface and ground water discharge. The lake receives most of water from northern river (Zayandehrud River). The two temporary rivers enter into the south and the west of the lake and sometimes flood and inundate these parts of the lake. In normal years the ground water contribution and evaporation are the largest components of the hydrologic budget. In this reason the sediment in this playa may be a sensitive indicator of any changes in the hydrological budget. Evaporation exceeds precipitation and inflow.

Extensive evaporation begins in May and continuous till September. It is a hypersaline lake and dominated by sodium and chloride ions but shows wide variations in composition and concentration on a spatial basis. Hydrological, climatological and geological conditions combined for formation of this saline lake.

In this paper it will be present the types of environment and facies including alluvial fan, sand flat, mud flat, saline mud flat and salt pan and also brine evolution in the Gavkhoni saline Playa Lake. In order to recognize the various units in playa lake, the landsat TM data was used (path 163 and row 38). Through the optimum index factor, three banding combination formatting false color composite was selected. For better understanding of specific phenomena, almost the interactive processing was used. Different processing include contrast stretching, filtering and formula was considered. Based on field studies and image processing several units has been recognized. Also for investigation of subsurface sediments and chemical analysis 5 trenches and 10 pits with up to 2 m deep were dug.

2. ENVIRONMENTS AND FACIES

Several major environmental zones can be easily recognized in the basin. They can be defined on the basis of texture, mineralogy, and the ratio of evaporite to clastic. Although the facies are distinct and can be mapped but boundaries are usually graditional. They include alluvial fan, sand dune, interdune, sand flat, saline sand flat, sand beach, mud flat, saline mud flat and salt pan.

2.1 Alluvial fan facies

This facies occurs at the base of the steep slopes of the basin. It grades laterally into the wide sand flat to the west, and mud flat, sand beach and narrow sand flat to the north and east, and narrow sand flat, and mud flat facies to the south of the Gavkhoni playa lake. It consists of a mixture of coarse and fine clastic material that has been derived from the adjacent mountains. They were transported down slope by channalized flow in the upper fan and dominantly by sheet flow on the lower fan. Debris flows also may account for significant downslope movement of sediments. Gypsum crystals are commonly found as cement in the alluvial fans, especially in the southwestern alluvial fan. They are concentrated in surface layer and present mostly in the form of fibrous and twinned crystals. Calcite is another chemical mineral, which is present as fine –grained cement in this facies.

2.2 Sand dune facies

The sand dunes enclose the Playa Lake to west. They grade laterally into the sand flat and salina sand flat to the east and alluvial fan to east. Mineralogical composition of the sand dune grains comprise sedimentary (mainly carbonate), igneous and metamorphic lithics and quartz grains, respectively. Feldspar, heavy mineral grains and shells are found as subordinate. Halite and gypsum are present as trace.

2.3 Interdune facie

Some small and large interdunes are located between the sand dunes. They are low relief areas, where vegetation and sand dunes are absent. Its surface layer is a very thin sand layer weakly cemented by fine salt crystals usually covers the interdunes. It is usually dry, soft, polygonal. The detrital sand-sized grains of unit (1) are as a result of wind activity in dry conditions. Sand- sized grains could be transported to this basin by wind

from the sand dunes. They are deposited over the interdunes from the sand dunes. The presence of gypsum scattered between sediments is a result of reworking, derived from neighborhood saline mud flat.The dispersal halite crystals is probably the result of evaporation on brine pore water in a dry period (Lowenstein & Haride, 1985).

3. SAND FLAT FACIES

This facies extends as a wide area to the west of the Gavkhoni Playa Lake and as narrow bands to the east and south of the lake. It will be explained only about the western sand flat mostly regarding to evaporitic sediments in this paper. The western sand flat is covered with gypsiferous marls. A porous carbonate debris blanket and tuffa covers sediments in some locations. A Soft, porous, puffy surface encrusted with a flaky, thin efflorescence of salt comprises most of the sand flat surface. The two types of gypsum form are known in this facies; rosette, and twin. Rosette gypsum is usually present as wavy layers, interbedded with aeolian sand layers along the western side of the aeolian sand dunes in the sand flat. They are soft and friable, not more than 2 cm thick. Twinned gypsum crystals are found as dispersal in the marl sediments deposited over the sand flat in some places. They have destroyed laminations of the sediments. The sand flat facies grades laterally to saline sand flat and salt pan in the western part of the lake and to mud flat in the other sides of the lakes.

3.1 Sand beach facies

stinct and continuos beach ridges occur at the edge of the salt pan to the east and between the saline mud flat to the north of the Playa Lake as a long narrow zone. The grain size of the sand beach mostly ranges from coarse sand to fine sand. In order to study of sedimentary cycle two pits dug in the marginal sand beach up to 1 m. According to the two pit two facies was observed , gravelly sand and sand facies.

4. MUD FLAT & SALINE MUD FLAT

This zone includes the mud flat and saline mud flat. This facies encircle the lake, except in the western part of the lake. The northern clay flat is wide, where the Zayandehrud river reaches into the playa. In the northern mud flat, some meandering channels drain waters and transport sediment to the playa and form Zayandehrud delta. Mud flat and saline mud flats are chiefly composed of very fine sediments (silt and clay), gypsum and halite crystals. During high water levels in the lake, the mud flats are sites of clastic sedimentation. Ground water table measured during about 3 years in this zone indicates that fluctuations are not considerable and it is approximately fixed. The mud flat is no saturated by brine and is commonly desiccated. It is characterized by polygonal mud cracks. Polygonal desiccation is fairly common and cracked up to a few cm across.

5. SALT FLAT (SALT PAN)

The property of the sediment deposited in the salt pan varies laterally from dominantly clastic facies to dominantly evaporite facies. The salt pan covers the center of the Gavkhoni Playa Lake as an efflorescent crust. It occupies more than % 75 of the playa surface and is the most characteristic feature of this playa lake. It takes place the lowest area of the Gavkhoni closed basin. The flat, salt-encrusted pan is surrounded by a saline-soaked mudflat and sand flat in the east and west permeated with evaporite minerals that grew within the sediments. The saline mud flat in turn grades outward into a dry mudflat and sand flat. The common features of this zone are polygonal halite crusts, efflorescent

halite ridges and popcorns (cauliflower). Brine –saturated sediment underlies the surface. Brine level slightly fluctuates during dry and wet season and it does not fall more than 20 cm below the salt surface. This surface is normally moist. Below the surface the voids in salt and sediment layers are filled with halite/saturated brines. Principal salt found in the salt pan is halite but carnalite, tachyhidrate, and calcium chloride hexahydrate are also present as minor. Halite is in hopper cubic and massive form. The size of halite crystal reaches is up to 20mm in diameter. The salt pan is a result of flooding, evaporation and desiccation. After flooding when the shallow ephemeral lake becomes concentrated by evaporation, the formation stage of salt pan starts. In NaCl rich system of this lake continuous evaporation concentrates the brines until they get saturation with halite. Crystallization starts at the brine surface as small plates and hopper crystals, which sink to the bottom. The individual floating crystals are cemented together where they touch to form rafts. When surface tension is disturbed, the crystals fall to the bottom, forming an accumulation of individual halite crystals and broken rafts on the brine pool floor. These serve as nuclei for further growth and widespread syntaxial overgrowth that takes place on the lake floor, ultimately resulting in the development salt crystals (Lowenstein & Haride, 1985).

When the salt surface was exposed, the halite layers were buckled, broke into polygonal crust, and teepe structures are formed. The buckling was caused by a net volume increase due to thermal expansion. The continued growth of halite immediately beneath the dry surface of the pan causes lateral expansive growth of the surface crust, and leads to disruption of the crust into large polygons rimmed by pressure ridges that override each other like tectonic thrust. Preferential evaporites pumping of subsurface brine take place along the cracks between the polygons and leads to precipitation of a spongy efflorescent halite (Lugli, Schreiber and Triberti, 1999). Next inflowing dilute floodwaters originated from meteoric waters partially dissolve the old surface saline crust before reaching supersaturation. With evaporation halite precipitates over the salt pan. In most cases, rapid evaporation does not allow halite to form as a cubic crystal at the surface of salt crust, although, in other environments hopper- shapped crystals generally record rapid growth rate (Fayazi, 1991). The subsurface sediments and stratigraphy of the salt pan are known from few pits drilled holes. Deep cores drilled near the south of the playa by Geology Survey of Iran the reveal presence of a cyclic stragraphic record of non-evaporites facies. Beds exposed in cores and pits range from a few centimeters to over 12 m thick. The sedimentology facies found in the saline pans through cores and pits consist of layers of crystalline salt and detrital siliciclastic (mud and sand). They range from salt, black mud, loose sand., sandy mud and brown clay facies. In this paper it is described only the first three facies in detail, because there is no sufficient data about other facies.

Salt (unit 1): The thickness of salt crust ranges from a few centimeters to the north and up to150 centimeters to the south. They are usually clear and white in color, but black, pink and green colors are also is marked due to impurities. The surface layer comprises some sand- sized grains. The volume percentage of these sediments is in different places. There are thin layers of dark mud interbedded with crystalline halite layers. The largest number of mud layers separating crystalline halite is observed on the southern margin of the salt pan in close proximity to one of detrital sediment sources. In contrast, the layer of crystalline halite without intermittent mud layer is observed in the central portion of the salt pan where only major floods succeed to reach mud sediments.

Black mud (Unit 2): The black mud layer underlies the salt layer .The thickness of this unit reaches to 10 cm in the lake center and. It consists of gray to black clay and silt. The ratio of clay to silt is high (about 80% clay-sized). Clay minerals include illite, chlorite, kaolinite and smectite. The organic content is approximately high in this layer. Halite as hopper cubic and gypsum as prismatic form are scattered through the gray mud. The size of halite and gypsum crystals is up to 20 mm in diameter. A large number of gastropode and ostracode shells are present in the sediments of this unit.

Sand (Unit 3): This unit is the lowermost layer in one location. It is also exposed in one drilled core below the salt layer and repeated between brown clay layers. It is mostly composed of sand grains. They are well sorted and mostly range between fine sand to medium sand. Mineralogical composition of detrital sediments is composed of mostly sedimentary, igneous lithics and quartz grains. Feldspars and heavy minerals are as subordinate. It consists of gastropoda and ostracoda shells similar to unit 2.

Gpsiferous marl (Unit 4): This unit directly overlies unit 5 in one drilled core. The thickness of this facies is about 2m. It is greenish to dark in color.

Brown mud (Unit 5): This facies is recognizable in one drilled core. It includes two parts, upper and lower part. The upper one underlies immediately gypsiferous marl facies. The lower one is the lowermost layer in this core. This unit ranges from 4m to more than 12m thick.

During spring, minor floodwaters originated from meteoric waters (rainstorm runoff and snow meltwater), cover the saline pan and form a temporary shallow brackish lake. The depth of this lake is usually no more than a few tens of centimeters. Minor flooding is much more common occurrence on saline pans than major flooding, and can create a temporarily undersaturated saline lake without deposition of a detrital mud layer. Repetition of such flooding can result halite crust without detrital mud parting. Also during a major storm flooding stage when muddy floodwaters inundated the pan ,mud layers presumably were deposited in the shallow ephemeral lake. This results to form alternating layers of halite and mud. This sequence record the deposition of halite in a salt pan in the playa center followed by retrogradation of mud flats over the halite beds.

The presence of hopper halite within the mud matrix is a result of fluctuation of brine during the wet and dry period, similar to fluctuations of brine level in Bristol dry lake (Fayazi, 1991). The pink to red color of the halite is due to impregnated by iron oxides between the salt. The black to greenish color of halite especially in the surface layer results impurities of fine -grained detrital sediments.Clay – sized sediments were transported into the playa lake in two ways; 1-Clay in low salinity water is suspended by density stratification and can be transported over wide areas before it flocculates and slowly descended to the bottom (Novorka, 1982). Floodwaters move only clay-sized material out from the shoreline; silt is deposited in deltas near the shore. 2-Aeolian dust storms are an alternative mechanism for transporting silt –and clay sized material for long distance. Fine to medium sand sediments mixtured with salt crystals is derived from aeolian sands in the west of the area. Sand – sized sediments capped by mud most likely reflects a rapid fall aeolian sands in a shallow temporally lake. The change in turn from sand, black mud upward into the salt unit marks the transition from a sand flat, mud-dominated playa to a salt pan. The lack of plant roots reflects that the Playa Lake was poorly vegetated. This feature is indicative of a semi –arid to arid climain the region (Amini, 1997).

6. CONCLUSIONS

To interpret the history and evolution of the lake, it may be insufficient to present a model only with these data. However, with investigation of a 4o m core and up to 2m some trenches and pits of the sediments it can be described sedimentation episodes to some extent in this basin. The material filling the basin is the result of a complex interplay of varying evaporation/ precipitation ratio, quantity and chemistry of groundwater inflow and surface runoff, and drainage basin characteristics.The stratigraphy sequences indicate, in a general way, considerably differing depositional and hydrological conditions and fluctuating water chemistry.

The deposition of intermittent of sand and clay (sand flat and mud flat) suggest that the basin was influenced repeatedly by flooding and desiccation. As a result, during the floods it has been a permanent lake without change in water table and fine- grained sediments deposited in the basin for a long time. In contrast the sand layers most likely derived from aeolian sands during dessication periods for a short time. With increasing aridity, the lake gradually became shallower and more restricted and the only salt pan formed. The salt pan was formed during the latest retrogadation in this playa lake. The absence of a salt unit except the surface layer implies that hypersaline playa conditions probably have been existed only in the latest sedimentation period in this basin. Based on surface and subsurface field data a depositional model for the Gavkhoni Playa Lake has been suggested.

7. REFFERENCES

Amini, A. (1997). Provenance and depositional environment of the upper red formation, Central zone, Iran. Ph.D. Thesis, University of Manchester.

Fayazi, F. (1991). Evaporates of the Howze Soltan lake basin. Ph.D. Thesis, University of East Anglia.

Krinsley, D.B. (1970). A geomorphological and paleoclimatological study of the playa of Iran. U.S. Government printing office Washington D.C. 20, 402.

Lowenstein, T.K. and Haride, L.A. (1985). Criteria for the recongnition of salt-pan evaporates. Sedimentology, 32, 627-644.

Lugli, S.B, Schereiber, C. and Triberti, B. (1999). Giant polygonal in the realmonte mine (Agrigento, sicily): Evidence for the desiccation of a messinian halite basin. J.S.R Vol 69, NO.3, 764-771.

Novorka, S. (1982). Depositional environments of marine- dominated bedded halite Permian San Andres formation, Texas, Sedimentology, 34, 1029-1054.

The 21st Asian Conference on Remote Sensing
December 4-8, 2000 Taipei, TAIWAN

Estimation of the methane emission from west Siberian wetland by Scaling between NOAA/AVHRR and SPOT/HRV data

Wataru TAKEUCHI* Masayuki TAMURA** Yoshifumi YASUOKA*
*Institute of Industrial Science, University of Tokyo
4-6-1, Komaba, Meguro, Tokyo 153-8505, Japan
Tel & Fax: +81-3-5452-6410
E-mail: wataru@iis.u-tokyo.ac.jp
**National Institute for Environmental Studies
16-2, Onogawa, Tsukuba, Ibaraki 305-0053, Japan
Tel: +81-298-50-2479, Fax: +81-298-50-2572

KEY WORDS

remote sensing, spatial resolution, scaling technique, methane emission

ABSTRACT

High spatial resolution data is effective for monitoring the land cover type changes, but it can't cover a wide area because of its narrow swath width. On the other hand, global scale data is indispensable to cover large area, but it is too coarse to get the detail information due to the low spatial resolution. It is necessary to devise a method for the fusion of the data with different spatial resolutions for monitoring the scale-differed phenomena.

In this paper, firstly, we developed a scaling technique to extrapolate the local information on landcover type combination from high spatial resolution data (SPOT/HRV) to more extensive area through low spatial resolution data with wide coverage (NOAA/AVHRR). Over a combined set of HRV and AVHRR data, landcover type of the area was classified into 4 categories with HRV data and AVHRR image density was statistically regressed with the corresponding category mixture ratio from HRV pixels for corresponding AVHRR pixel. With this regression model (scaling model), local information of the category mixture was extrapolated to extensive area with AVHRR data.

Secondly, this method is applied to the wetland categorization by means of the regression analysis (scaling model) relating AVHRR CCT counts in ch.1, 2 and 3 with HRV ch.1, 2 and 3. Then we estimated the methane emission in the west Siberian wetlands by using the methane flux for each land cover type.

1. Introduction

Westen Siberian wetlands are presumed to be large sources of methane (CH_4), which is one of the most important greenhouse gases. In this research, we investigate the land cover conditions in western Siberian wetlands by using remote sensing techniques and estimate wide area methane emissions in wide area by combining the results of satellite observations with grund methane measurements

We used two types of sattelite sensors: SPOT/HRV as a high spatial resolution sensor and NOAA/AVHRR as a low spatial resolution sensor. High spatial resolution data is used for detailed classification of the land cover types in the test site. Global scale data is used to monitor the whole western Siberian wetland (Fig. 1).

The objective of this study are to develop the method for the fusion of the data with different spatial resolution for monitoring the scale-differed phenomena and to examine the relation between ground surface conditions and the greenhouse gases.

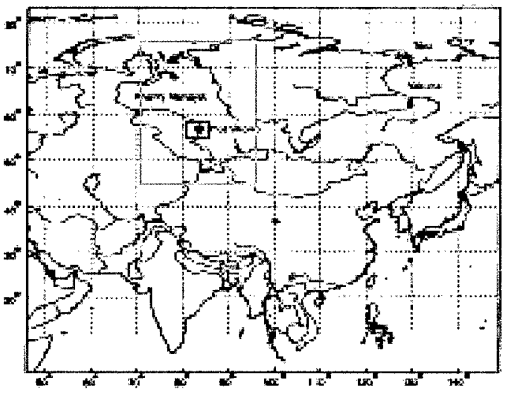


Figure 1: Location of Western Siberian Wetland

2. Comparison of Vegetation Index between AVHRR and HRV

SPOT/HRV data of July 7th, 1995 and NOAA/AVHRR data of July 7th, 1995 over Plotnikovo in western Siberian wetland were geometrically corrected and overlayed so that one pixel of AVHRR covers a set of HRV pixels in a rectangular block of 50x124 (Fig. 2). Spatial resolution of one pixel of AVHRR is around 1.1(km) and that of HRV is around 20(m). Then the relations between each pixel of AVHRR and corresponding block of 55x55 pixels of HRV were statistically investigated in NDVI (Normalized Difference Vegetation Index). NDVI for AVHRR and HRV are defined by

$$NDVI_{AVHRR} = (AV_2 - AV_1)/(AV_2 + AV_1) \quad (1)$$

$$NDVI_{HRV} = (HRV_3 - HRV_2)/(HRV_3 + HRV_2) \quad (2)$$

where AV_1, AV_2, HRV_2 and HRV_3 are the CCT counts for NOAA/AVHRR ch.1 and 2, and SPOT/HRV ch.2 and 3 respectively. Fig. 2 and 3 show the NDVI from NOAA/AVHRR and SPOT/HRV data over the target area. The relation between NDVI value for each AVHRR pixel and an average NDVI value for a corresponding HRV block 50x124 is examined (Fig. 4). Regression analysis between $NDVI_{AVHRR}$ and $NDVI_{HRV}$ shows high correlation between the vegetation index of NOAA/AVHRR and SPOT/HRV (r=0.93).

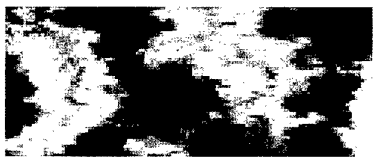


Figure 2: AVHRR/NDVI (50x124 pixels)



Figure 3: HRV/NDVI (2750x6820 pixels)

3. Estimation of category mixing ratio of AVHRR from HRV Data

Scaling model between NOAA/AVHRR and SPOT/HRV was investigated to estimate the mixing ratio of landcover cateogies in each pixel of AVHRR data. With this model, local information from SPOT/HRV data was extrapolated to the whole western Siberian wetland through AVHRR data.

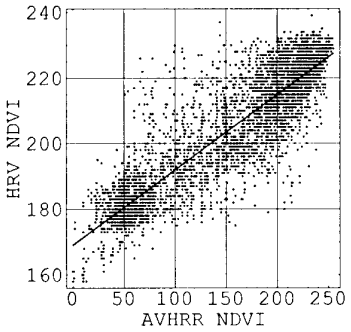


Figure 4: Scatter plot between AVHRR/NDVI and HRV/NDVI

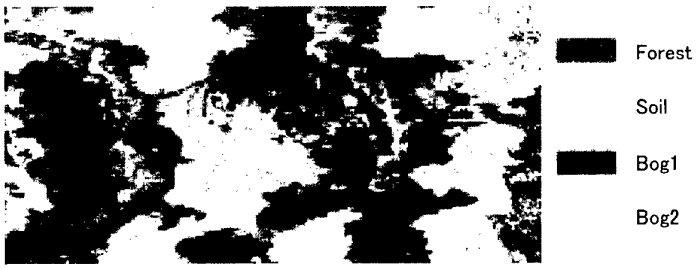


Figure 5: Land cover classification from SPOT/HRV data

First, each pixel of HRV was classified into 4 categories including forest, soil, bog1 and bog2 by using supervised classification (Fig. 5). The mixing ratio in each pixel of AVHRR data is calculated by counting the land cover type in each block of 55x55 pixels of HRV.

Then, AVHRR channel 1, 2 and 3 were correlated with F, S, B1 and B2, which are the coverage ratios for each category mixing ratio of forest, soil bog1 and bog2, using least squares method. The linear equations obtained with high correlation are Eq. 3, 4 and 5.

$$AV_1 = 34.7F + 60.0S + 23.8B1 + 29.2B2, \quad r^2 = 0.63 \tag{3}$$

$$AV_2 = 111F + 132S + 145B1 + 173B2, \quad r^2 = 0.87 \tag{4}$$

$$AV_3 = 87.0F + 96.7S + 42.3B1 + 55.7B2, \quad r^2 = 0.62 \tag{5}$$

This relation shows that the category mixing ratio (F, S, B1, B2) can be solved inversely from Eq. 3, 4, 5 and the following constraint Eqn. 6.

$$F + S + B1 + B2 = 1 \tag{6}$$

This scaling model enables us to extrapolate the local information (category mixing ratio) from SPOT/HRV to more extensive area by using NOAA/AVHRR data.

4. Extrapolation of the result for an extensive area

By applying the model equations 3, 4, 5 and 6, we estimated the category mixing ratio F, S, B1 and B2 for more extensive area through AVHRR data. Figure (6), (7), (8) and (9) shows each category mixing ratio image.

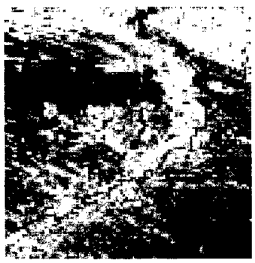


Figure 6: Forest

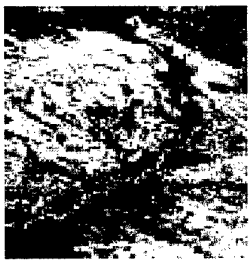


Figure 7: Soil

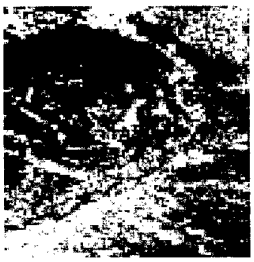


Figure 8: Bog1

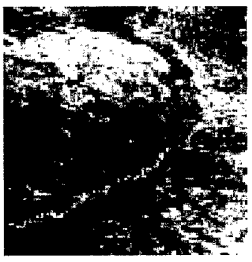


Figure 9: Bog2

5. Estimation of methane emission from the broader wetland

We calculated the methane emission by multiplying the emission rate with area size for each land cover type. The emission rate for forest and soil are zero because it is reported that they do not release much methane.Table 1 shows the mixing ratio, methane emission rate for each landcover type and the methane flux.

Table 1: Estimated methane emission from the extensive wetland

Landcover Type	Area ($10^3 km^2$)	Emission rate($mg/m^2/day$)	Methane flux($10^9 g/day$)
Forest	113.0	0	0
Soil	75.2	0	0
Bog1	79.2	118	93.5
Bog2	35.1	166	58.3
Total	302.5	-	151.8

6. Summary

This study demonstrated that scaling techniques would provide a tool to extrapolate local information from high spatial resolution data to larger scale by using low spatial resolution data. We applied this method to the wetland categorization by means of the regression analysis then estimated the methane emission in the west Siberian wetlands.

Since most of the global issues originate from local events such as extensive logging, monitoring earth surface changes requires that the observation of landcover embraces the terrain from local to global. Linking local with global is one of the key aspects in global environmental issues. The method proposed in this study is expected to play an important role in bridging the local and the global in remote sensing.

References

Y.Yamagata, et al., 1997: Development of Vegetation-Soil-Water Index algorithms and applications, Journal of Remote Sensing, Vol.17(1), pp.54-63 (in Japanese).

M.Sugita and Y.Yasuoka, 2000: Estimation of Land Cover Mixing Ratio within a Pixel by Scaling between NOAA/AVHRR and LANDSAT/TM Data, Journal of Remote Sensing, Vol.20(1), pp.32-42 (in Japanese).

K.Minami, et al., 1994: Soil and Atmosphere, pp.55-84 (in Japanese).

URBAN CHANGE STUDY USING RS AND GIS

D.Amarsaikhan, M.Ganzorig

Institute of Informatics and RS, Mongolian Academy of Sciences,
av.Enkhtaivan-54B, Ulaanbaatar-51
E-mail: informc@magicnet.mn, amaraa66@hotmail.com
MONGOLIA

M.Saandar

MonMap Engineering Services Co., Ltd
r.502, Sarora Hotel, Seoul street 12/6, Ulaanbaatar-46
E-mail: monmap@magicnet.mn, msaandar@mongol.net
MONGOLIA

KEY WORDS: Urban, Ger, Building Parcels, Multi-Temporal, RS, GIS

ABSTRACT

The aim of this study is to investigate the urban changes that have occurred in central part of Ulaanbaatar area, Mongolia over the past few decades and describe the socio-economic reasons for the changes. For this purpose, multi-temporal RS and GIS data sets are used. For the analysis, two classes such as ger area (a Mongolian national house) and building parcels are selected and compared.

INTRODUCTION

In recent years, cities all over the world have experienced rapid growth because of the rapid increase in world population and the irreversible flow of people from rural to urban areas. Specifically, in the larger towns and cities of the developing world the rate of population increase has been constant and nowadays, many of them are facing unplanned and uncontrolled settlements at the densely populated sites or fringes. To prevent from such occasions urban planners need detailed updated maps for thorough planning and management. However, most city planners have a lack of such maps and often they posses old data which is not relevant for current decision making. Even if they do not hold a detailed updated map of the city area a regularly updated map with an acceptable resolution can at least give them an impression about the changes in the city area [3,4,5,7].

Mongolia, as many of the developing countries has a problem with the urban expansion and the growth of population in the main cities. For example, over the last decades Ulaanbaatar, the capital city of Mongolia has significantly expanded due to different development activities and migration of people from rural sites [7]. Various changes have been and are being occurred in the city but there are no regularly updated maps to indicate those changes. In general, it should be interesting to study the urban growth in the capital city comparing the growths occurred before 1990 when Mongolia had centralized economy with the changes occurred during the market economy.

The aim of this paper is to detect the main changes occurred in central part of Ulaanbaatar area before and after 1990 and describe the socio-economic reasons of these changes. For this

purpose, multi-temporal RS and GIS data sets have been used. For the study, two classes such as ger area (a Mongolian national house), and building parcels (parcels of apartments, residential houses and industrial buildings) have been selected and compared. The analysis was carried out using ERDAS and ILWIS-systems and different RS and GIS techniques have been applied.

THE GER

Mongolian dwellings have evolved with nomadic life. The need for a portable dwelling is obvious for people following their herds and seeking new pastures. The history of the Mongol ger goes back to about 2500-3000 B.C. and has continued to be used to the present day. The ger is still used as dwelling everywhere in Mongolia. The walls of the ger are made of narrow birch willows formed into a lattice framework and held together by leather strips. Sections of the lattice are put together in a large circle to form the walls. Each section is approximately five to six feet high and seven to eight feet long. The entire outside surface of the ger is covered with felt, tied in place by ropes made of hair and wool. One layer is sufficient in the summer season. Two or three layers are necessary in winter. The ger is comfortable in all kinds of weather. In hot summer, the root wheel is opened and the felt walls are raised to give ventilation. When it is windy the ger is stable becuase of its shape and is tied to the ground and in cold winter the layers of the left are increased and the door is sealed. The assembling and taking down of any ger are done within half an hour in as fixed order. The gers situated in urban areas are surrounded by fences, whereas the gers of herdsmen in rural sites do not have fences because they move from place to place following good pasture area. The gers of rural herdsmen are shown in figure1.



Figure 1. The gers of rural herds people

THE TEST SITE

As a test site Ulaanbaatar, the capital city of Mongolia has been selected. Ulaanbaatar is situated in the central part of Mongolia on the river Tuul at a height of 1350 m above sea level and currently has approximately 650,000 inhabitants [7]. The city is surrounded by mountains which are spurs of the Hentii range. The temperature of Ulaanbaatar is about 20-25°C above zero in summer but in winter it is usually 15-20°C below zero. The mean precipitation in the city is 233 mm [8].

DATA SOURCES

- A topographic map of 1969, scale1:25.000
- SPOT XS image of 1986
- SPOT PAN data of 1990
- SPOT XS image of 1997
- Census data of Ulaanbaatar.

ANALYSES AND DISCUSSION

In our study, we assumed that there is an operational GIS that stores an old city map and multi-temporal RS data sets. To acquire primary digital data stored within the GIS the selected classes: a ger area (a Mongolian national house) and building parcels were digitized in a UTM map projection from a topographic map of the test area, scale 1:25.000. There have been selected only two classes because on the satellite images it was not possible to distinguish between land parcels related to apartments, residential houses and industrial buildings. The digitized city map is shown in figure2. To define the total area of each class the vector map was rasterized with a pixel size of 10m and then a number of pixels falling into each of the classes has been calculated. The result indicated that in 1969, ger area covered 624ha whereas building parcels occupied 1566ha. Although, we have census data of Ulaanbaatar, it is not possible to directly relate it to our analysis because due to a lack of data, our study area covers more central and western parts and a part of eastern block of the capital city. Therefore, census data has been used to see just general increase of population at different years. As it was seen from the census data, in 1969 the city had 267.400 inhabitants.

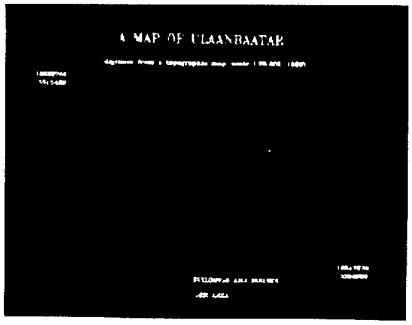


Figure 2. A digitized city map of Ulaanbaatar

As it has been mentioned before, the aim of the study is to compare the changes occurred in central part of the city during the centralized economy with the changes occurred during the market economy. For this purpose, SPOT PAN data of 1990 and SPOT XS image of 1997 could be compared with the digital GIS data. However, for the interpretation it is better to use a colour image if it is available. Therefore, to have more spectral variation of the selected classes, SPOT PAN data was integrated with SPOT XS image of 1986. The processing of the images has been carried out as follows [1,2]:

Initially, all the images were thoroughly analyzed in terms of distortion and brightness. The images were of a good quality but only the panchromatic data had to be radiometrically corrected. Radiometric correction of panchromatic data was done by averaging upper and lower lines of the stripes that had to be corrected. Then, SPOT images of 1986, 1990 and 1997 were successively geometrically corrected to the UTM map projection using the same topographic map of the study area. The ground control points were selected on well defined cross sections of linear features. For the actual transformation, a second order transformation and nearest neighbour resampling approach have been applied and the related RMSs were 0.38, 0.47, 0.58, respectively. Further, from each image the same set of subsets falling into the same image frame has been chosen. To create an integrated colour image the multispectral image was firstly sum normalized in order to eliminate different influences and then multiplied by the intensity of the panchromatic data. After this, the normalized bands have been assigned to RGB colours accordingly (figure3).

It can be expressed by the formula:

R=(NIR/NIR+R+G)*PAN
G=(R/NIR+R+G)*PAN
B=(G/NIR+R+G)*PAN

where NIR,R,G - bands of SPOT-XS, and PAN - panchromatic band.

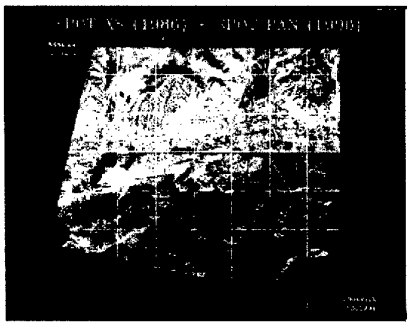


Figure 3. The integrated image of Ulaanbaatar (SPOT XS-86 + SPOT PAN-90)

To create a city map of 1990, on the enhanced image the selected classes were screen digitized and then rasterised with a pixel size of 10m. Moreover, the statistics of each class was calculated. The result indicated that the ger area and building parcels covered 1236ha and 1987ha, respectively, while population of the city had become 574.900. As seen, within a 21 year period, ger area increased by 98% and building parcels increased by 27%, while population had increased by more than 2 times. It has the following reasons:

1) during the centralized economy, due to the industrialization process in the city many people came from rural sites with their gers to the city;
2) gers are surrounded by fences covering usually 600-800sq.m, thus covering large area;
3) during the socialist economy as residential houses mostly building blocks with many floors and flats were built. Although, a few residential blocks could contain families of a whole ger district, they occupy much smaller land parcels than gers' parcels.

A map indicating the changes occurred in Ulaanbaatar area during the centralized economy is shown in figure 4.

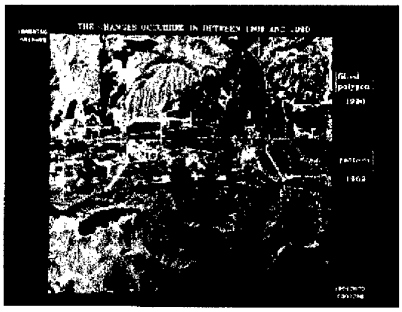


Figure 4. A map indicating the changes occurred in Ulaanbaatar area in between 1969 and 1990

To investigate the changes that have occurred in the city during the market economy a false colour image was created using SPOT XS bands of 1997. For the improvement of the interpretation and the detection of the boundaries between the selected classes of objects, band 3 of the colour image was edge-enhanced using a 3x3 convolution filter (central pixel 10 and other values -1). The created colour image is shown in figure5.

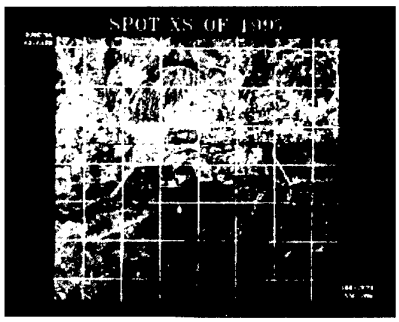


Figure 5. Enhanced image of SPOT XS-97

Then, on the enhanced image the selected classes were screen digitized. Furthermore, the digitized vector map was rasterised with a pixel size of 10m and the total number of pixels falling into each of the classes has been calculated. The result indicated that during a 7 year period ger area had increased by 50% while building parcels had increased by 48%. At the same time, population of the city had become 649.800. The reasons for these changes are:

1) due to the market economy people moved to the area with a good infrastructure;
2) during the market economy income of people has increased and the built houses are mostly cottages or houses with few floors, not like building blocks;
3) due to the new land law which gives a distinct right to land owners [6], the interest of people to own land parcels has increased.

A map indicating the changes occurred in Ulaanbaatar area during the market economy is shown in figure 6.

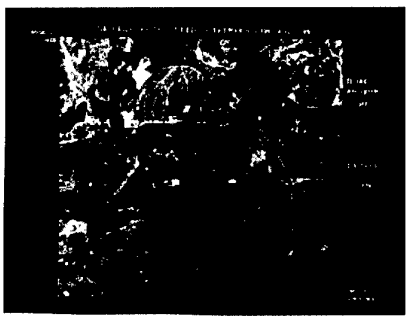


Figure 6. A map indicating the changes occurred in Ulaanbaatar area during the market economy

CONCLUSIONS

The overall idea of the study was to compare the general changes occurred in central part of Ulaanbaatar area during a centralized economy with the changes occurred during a market economy and describe the socio-economic reasons for these changes. For this purpose, multi-

temporal RS and GIS data sets were used. As seen from the analysis, during the centralized economy significant changes occurred in the ger area of the city, while during the market economy significant changes occurred in both areas. Surely, this is just a rough estimation of the changes of the capital city. For the proper estimation, large scale maps and very high resolution satellite data (eg, IKONOS) or aerial photographs covering all areas should be used.

ACKNOWLEDGEMENT

The authors are very grateful to Ms.O.Tsolmongerel and Ms.Sh.Tumentsetseg for digitizing a city map of Ulaanbaatar area, and Dr.P.Galsan for his valuable advice in the study.

REFERENCES

1. Amarsaikhan, D., Tsolmongerel, O., 1997. Some Results Of Using Spatial Enhancement Techniques. Journal of Informatics, Ulaanbaatar, Mongolia, pp61-68.

2. Amarsaikhan, D., Ganzorig, M., Tsolmongerel, O., 1997. Comparison of Spectral Enhancement Techniques. Journal of Informatics, Ulaanbaatar, Mongolia, pp35-39.

3. Dirk Bolt, 1996. An Urban Community Strategy For Implementing Decentralization And Devolution Policies. ITC Journal 1996-1, pp18-28.

4. Hans de Brouwer, Carlos R Valenzuela, Luz M Valencia, Koert Sijmons, 1990. Rapid Assessment of Urban Growth using RS-GIS. ITC Journal 1990-3, pp233-235.

5. Jan Turkstra, 1996. Urban Growth And Land Use Options For Lower-Income Groups: A Case Study Of Villavicencio, Colombia. ITC Journal 1996-1, pp57-64.

6. Land Law of Mongolia, 1994. New Land Law of Mongolia. Ulaanbaatar, Mongolia.

7. Statistics Report, 1999. Statistics Report Intended to the 360th Anniversary of Ulaanbaatar. Ulaanbaatar, Mongolia.

8. Tsegmid, Sh., 1969. Physical Geography of Mongolia. Ulaanbaatar, Mongolia.

ENVIRONMENTS TRANSITION RESEARCH IN YUSAN NATIONAL PARK AFTER EARTHQUAKE AND TYPHOON

Tien-Yin Chou , Chih-Cung Kao , Ying-Huei Chang
Mr., Geographic Information System Research Center
Fung Chia University
Geographic Information System Research Center,Fung Chia University
, 100 WenHwa RD., Taichung
TAIWAN
Tel: +886-4-4516669 ext. 59 **Fax:**+886-4-4519278
E-mail: cckao@gis.fcu.edu.tw

KEY WORDS : Remote Sensing , Geographic Information Systems,

ABSTRACT : It always follows a huge lost after the disaster happens. It's more serious in Yushan National Park cause its wide area. It always takes a lot of people, goods and materials to relieve the victims of a disaster. If we can find out the affect carried by those disaster immediately, we can make better policy decision to rebuild and recovery plan. Our study use Remote Sensing technology and Geographic Information System to analysis the Environments Transition in Yushan National Park after earthquake happened in September 21 in 1999 and the typhoon happened in August 1 in 1996.and find out if any facilities damaged on these two disasters. We attempt to offer a powerful suggestion for National park management organization and will be helpful when they want to rebuild the facilities broken in the disasters.

I.INTRODUCTION

It always follows a huge lost after the disaster happens. It's more serious in National Park cause its wide area. It's more important to distribute the succor resource before we send the People, goods and materials to relieve the victims of a disaster. Our study trying to use remote sensing technology monitor the transitions of land cover after the disasters. And we also analyze the effect of the disaster with the assistance of Geographic information systems. For this purpose, we choice Yushan National Park to deliberate the earthquake happened in September 21 in 1999 and the typhoon happened in August 1 in 1996 effects. We hope our research can offer a powerful suggestion for National park management organization and will be helpful when they want to rebuild the facilities broken in the disasters.

II.METHODOLOGY

Our research wants to find out the relationship between disaster and transitions of land cover.

For this purpose we used Remote sensing technology, Geographic Information Systems, land cover classification theory and environmentally sensitive area correlation studies. First we choose the National park in middle part of Taiwan – Yusan National Park. The central region of Yusan National Park takes 10 hectare, which covered Nanto, Kaohsiung, Hualien and Jangyi four counties. There are four rivers and 100 mountains inside. Just like the other National Park in Taiwan the land cover monitor and management become the biggest problem for the management organization. This problem especially effects after two huge disasters in middle part of Taiwan. Typhoon Hobo effects at August 1, 1996 and the earthquake happened at September 21, 1999.

We Use three SPOT images that pictured in 1993,1996 and 1999. Last two images are pictured just after typhoon and earthquake. And all three images are level 10 standard images. Classify images to four classes to see if anything changes during the disasters. And respectively compare the land cover situation between two images to see what changes since 1993 to 1999 in Yusan National Park. At last, we respectively overlay the land cover map, geologic map, topographic map and stature map to find out the relationship between these land factor and different disasters. According to some reference collected from R.O.C. we also delimit the environment sensitivity area at Yusan National Park.

III.RESEARCH TOPICS

This research aims at the land cover of Yusan National Park after hazard. The research topics are as follows:

1. An analysis of land cover after disaster in Yusan National Park.
2. Land covers transition of Yusan National Park since 1993 to 1999.
3. Bare ground distribution analysis.
4. Disasters Sensitivity analysis.

To do these research topics in traditional methods always takes lots of time. Our research offers a fast and worthy method for environment monitoring and analysis of National Park disaster.

1.Land Cover Analysis

First, We make an image enhancement for classification reference. Than we simply used supervise and Unsupervised methods on classification progress. Caring about mountainous region always have lots of shadow, we separate the image to Shadow part and the other in progress. And we also use air photos and rainy records to modify the misconstruction between real water area and temporary water cause by the big rain during image pictured. After Classification procedure, we progress the image to four classes. They are bare, wood, grass and water. The distribution Area and percentage at 1993,1996 and 1999 are given in table 1.

Table 1. Classification result in

Year / Class	1993		1996 (After the typhoon)		1999 (After the earthquake)	
	Area	Percent	Area	Percent	Area	Percent
Grass	14668.47	14.09	12877.2	12.37	13238.1	12.72
Bare	6583.28	6.33	9356.33	8.99	8543.47	8.41
Wood	81105.24	77.93	79303.5	76.2	78818.6	75.73
Water (river)	1114.14	1.07	1816.08	1.74	1089.73	1.05
Cloud	605.91	0.59	-	-	2326.42	2.24
Total	104077.04	104077.04	104077.04	104077.04	104077.04	104077.04

After classification we make an accuracy assessment according to the data on the spot. The result is user accuracy is 84.62% and producer accuracy is 83.78%.

2. Land Cover Transition analysis

We respectively compare the transition from 1993 to 1996 and 1996 to 1999. The conclusions are as follow:

(1) Transition analysis of 1993 to 1996

In 1993 to 1996, most part of land cover in the Park is similar. It shows that National Park is profit for environment nursling. But it also have 3.94% land cover situation translate from woods to bare land and 2.76% translate from grass to bare land. The big fire happened during these three years may be one of the reason.

(2) Transition analysis of 1993 to 1996

In 1996 to 1999,there are 78.16% land cover didn't change in these years. But similar as 1993 to 1996, there also have a part of plant disappears. Fortunately the transition from bare land to plant is also increase at these three years.

To make a comprehensive survey from 1993 to 1999, Yusan National Park goes through two huge disasters and several fire accidents. It's a pleasure to see that most part of land cover is still remaining as before. But the 3% bare land translate situation is also a big problem needed to be concerned. Consider about the distribution of transitions, we overlay geology, topography and fire accidents distribution maps. It shows that the transitions always happen around the road, river and other human activities area. Obviously human activity is a serious problem in a natural nursing region.

3. Bare ground distribution analysis

Bare land distribution is an important factor of disaster effects in national park. We search and collect the geology, topography, stature and some land use data for bare land analysis by Geographic information Systems. We take out the bare land part from image overlap with other land use maps. The conclusions are as fig1, fig2.

Fig 1 bare land overlap with river at 1996

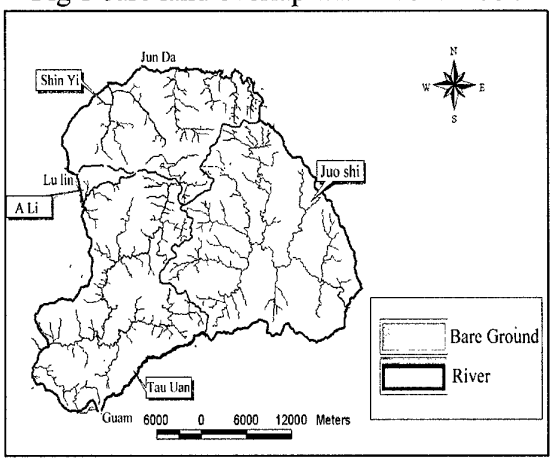
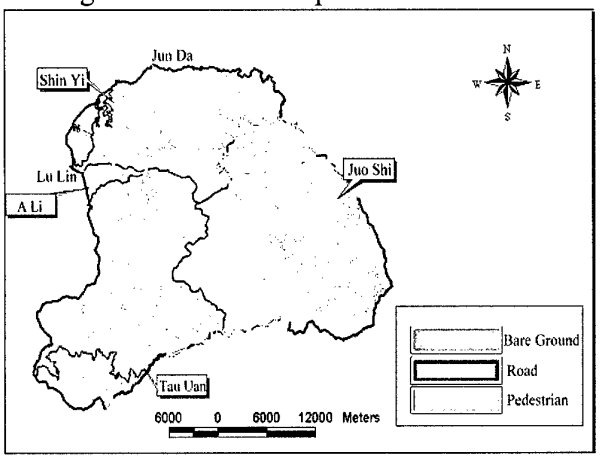


Fig 2 bare land overlap with road at 1999



As the overlap map shows, most bare land distribute around the road and river. Compare the distribution in 1996 and 1999 we also discovered that the bare around the river are critical after typhoon at 1996. The state of affairs shows that big rain must be one critical factor of bare around rivers.

4. Disasters Sensitivity analyses

To take one step ahead, we search and collect some sensitivity delimit correlation researches. And harmony with GIS and Remote Sensing data, we delimit the potential disaster sensitivity region for management organization. According to the regulation of mountainside safeguard and the direction of rock formation we mark off eight kinds of basic land units. To simplify the combination we pay much attention to the gradient factor. So we combine the eight classes to five. The flow chart of environment sensibility is as fig 3 and the result is as fig 4.

Fig 3 Flow chart of environment sensibility

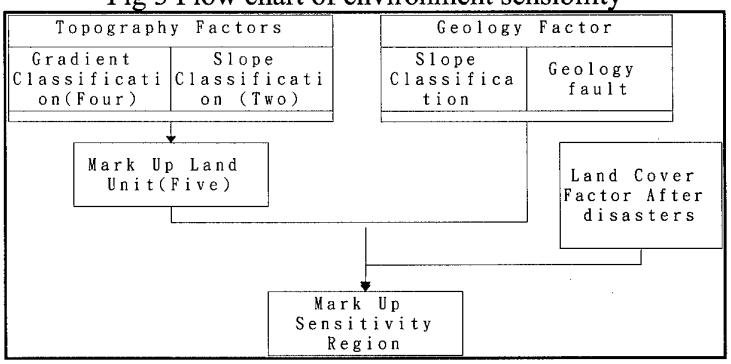
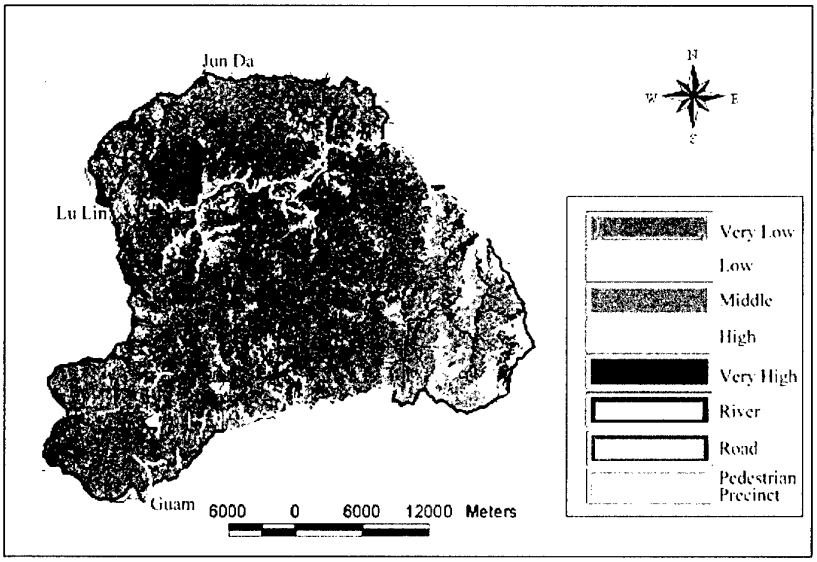


Fig 4 Environment sensibility distribution of Yusan National Park



VI.RESEARCH RESOULT

Our research uses the Remote Sensing and Geographic Information Systems to progress the analysis from the Yusan National Park after Typhoon and the earthquake 921,the analysis from the character of bare lands, and the sensitivity of environment. The conclusion are bellowing:

1. This research applying Remote Search to investigate the covering of land in Yusan National Park from 1996 to 1999. Their precision can be more than 80% in every class. And precision of the class which is about the woods reaches 93.53% and 93.94%. It is known that Remote Search is a kind of excellent way to examine the land use of large area, and also can be applied to the examination and monitoring of the land in high mountain and resources of woods.
2. According to the result of examination of land covering, it is obvious that there's no change between 1993 and 1996 from 83.5% of classifications of land covering around Yusan National Park (There are Woods, Grasses, Bare Lands, and Water), and the rate remains 78.16% between 1996 and 1999. The area of woods occupied 75.73% in 1999. It is clearly to know Yusan National Park is workable about nursing living things and also the importance of establishment of Yusan National Park.
3. It is showed that there are six-degree slope mostly in Yusan National Park according to the examination of its own natural environmental characters. And it is also showing that the terrain is dangerously steep. Also the geology there is fragile and mainly schist and slate .are there.
4. It is showing that the close relationship between the spread of bare lands and pedestrian precinct according to the result of bare lands change analysis. It is deserve to be mentioned that lots of landslip happened after earthquake around the north peak which

slope is bigger then 55%. And the Slide happened after the typhoon is always around the rivers. And these places are also on top of human activities region. It might a warning of the management organization.

V.REFERENCES

1.McCauley, J. D., and B. A. Engel, 1995, Comparison of Scene Segmentations:SMAP, ECHO, and Maximum Likelihood.IEEE Transactions on Geoscience and Reomte Sensing.33(6)

2.Zhu, Z., and D. L. Evans,1994, U.S. Forest Types and Predicted Percent Forest Cover from AVHRR Data, Photogrammetric Enginneering & Remote Sensing, 60(5).

3.Zhuang, X., and B. A. Engel,1991, Improving Classification of Crop Residues Using Digital

4.Land Ownership Data and Landsat TM Imagery. Photogrammetric Engineering & Remote Sensing,57(11).

5.John, J.R.,1986, " Introductory Digital Image Processing", Prentice-Hall, New Jersey.

6.Chapin, S.J. and E. J. Kaiser,1985, "Urban Land Use Planning", University of Illiois Press, Illiois.

7.Hall P., 1992, "Urban and Regional Planning", Routledge, New York.

THE CHARACTERIZATION OF VERTICAL MEAN TEMPERATURE OVER INDONESIA FROM 1994 TO 1998

Achmad Sasmito, Urip Haryoko, Riris Adriyanto, Nelly Florida Riama, Rosdiana
Meteorological Analysis Sub Division
Meteorological and Geophysical Agency
Jl. Angkasa I No.2 Jakarta10720, Indonesia
Ph.62-21-4246321, Fax.62-21-4246703, e-mail:anmet@bmg.go.id

KEY WORDS: vertical mean temperature, radiosonde, aerosol, global warming, cooling

ABSTRACT

Recently climatologists have indicated that the global warming is currently happening as a result of human activities. Such evidences were shown by the increasing trend of surface temperature that taking place at a number of big cities and industrial areas all over the world. This just brings impact on microclimate but it doesn't have much influenced for the atmospheric mean temperature.

In fact, the analysis result of the atmospheric mean temperature based on radiosonde data observed in several big cities in Indonesia show the cooling between -2.73^0 and -5.51^0 from its normal. This indicates that nuclei condensation (aerosol) particles on the atmosphere over Indonesia were quite abundant. It can be related with the fact that Indonesia is an archipelago consists of thousand of islands – 70 % of Indonesian region is ocean.

On the other hand we can assume that the global warming that is usually connected with surface temperature cause the increasing of evaporation from ocean. And these aerosols will be trapped at mixing layer and cannot go higher. So that the propagation of sun radiation will prevent from going through and this cause the cooling temperature of atmosphere in this layer. The problem is how far from the surface that the global warming can affect the atmospheric layer.

1. INTRODUCTION

The symptoms of heat increase of the earth surface have become the growing concerns for scientists. Many theses have been proposed to find the causes of increasing global temperature. The increases have been taking place since the industrial revolution up to now. The main factor considering have role in global warming process is green house gases in the atmosphere.

It is believed that green house gases have an effect to trap heats. When the concentrations of the atmospheric green house gases increases, it will occur heat energy oscillation between earth surface and the atmosphere with green house gases content. The result is the air becomes hot and this condition is identified by the increase of mean temperature. The United State-Global Change Research Information Office (US-GCRIO) predicted that the earth temperature has increased 0.3 – 0.6°C during the last period of 19th century.

The increase of earth surface heat causes smelting of glacier resulting sea level rises. However, besides some regions have earth surface heat increase, the mean temperature in the other regions decreased (cooling process), This is probably because the effects of energy balance process occurring on the globe. If there is a changing action within a certain physical condition such as temperature increase in several areas, re-action will take place in to achieve equilibrium energy in other locations. It is believed that the total energy on the globe is always fixed. There is no energy lost but it can alter to be other form.

This study will explain the fluctuation or variation of vertical mean temperature in Indonesia regions and look the possibilities of global climate change impacts to the boundary layer atmospheric conditions. This study used 1994 to 1998 upper air data from 11 radiosonde stations in Indonesia regions.

2. THEORETICAL OVERVIEW AND DATA

2.1. Theoretical Overview

Atmospheric heating is basically taken place due to the interaction between solar radiation and any gases in the atmosphere. It is known that the atmosphere consists of various gases: permanent and impermanent gases; solid and liquid particles such as aerosol, ice crystal and water rainfall.

The permanent gases: nitrogen; oxygen and argon are almost 99.9% of total gases in the atmosphere. Such gases have fixed volume over 60 kilometers height. It is important to be noticed that CO_2 is also considered as a permanent gas with various level of concentrations due to the result of fossil fuels burning. CO_2 sinks into the ocean or is absorbed by plants by way of photosynthesis.

Atmospheric water vapor content varies every time depending on the atmospheric condition. The variation of water contents in the atmosphere is important because it relates to absorption and emission process of solar radiation. Furthermore, ozone concentration also varies from time to time. The concentration variation can be clearly seen on vertical direction with 15-30 Km height from the earth surface.

Ozone is generally formed in stratosphere layer. In mesosphere area, air temperature also decrease toward height from 50-85 kilometer. The layer above mesosphere area is called thermosphere layer. Air temperature in this layer is about 500° K to 2000° K. The outside of thermosphere layer is exosphere layer.

In meteorology air temperature and humidity in every atmospheric layer up to 20 km height can be determined by releasing radiosonde balloon. The vertically atmospheric mean temperature can be calculated by using the following formula (Bevis, et.al):

$$Tm=(\int(\rho v/T)\,dz)/\int(Pv/T^2)\,dz \qquad (1)$$

Pv and T are water vapor partial pressures (mb) and temperature. pv value is described as follows:

$$\log_{10} pv = -7.90298\,(Ts/T-1) + 5.02808\,\log_{10}(Ts/T) - 1.3816 \times 10^{-7}(10^{11.344(1-T/Ts)} - 1) - 8.1328 \times 10^{-3}\,(10^{-3.49149\,(Ts/T-1)} - 1) + \log_{10} e_{ws} \qquad (2)$$

where T = temperature at certain height in absolute degree (° K); Ts = vapor point temperature (273.6° K) and e_w= saturation water pressure at 273.6° K. (1 atmospheric standard = 1013.246 mb).

In analysis process it is also be used the following deviation method

$$R = Xi - Xs \quad (3)$$

Where R= deviation value; Xi= daily vertical mean temperature data; Xs = vertical mean temperature reference (10.00° C to 12.78° C).

2.2. Data

This study used 1994 to 1998 data from 11 radiosonde stations. The numerical calculation results by using the formula number 1 is the isopleth for vertical mean air temperature in Indonesia regions whereas the deviation of vertical mean temperature toward mean temperature reference is about 10.00 to 12.78° C **(Fig. 1).**

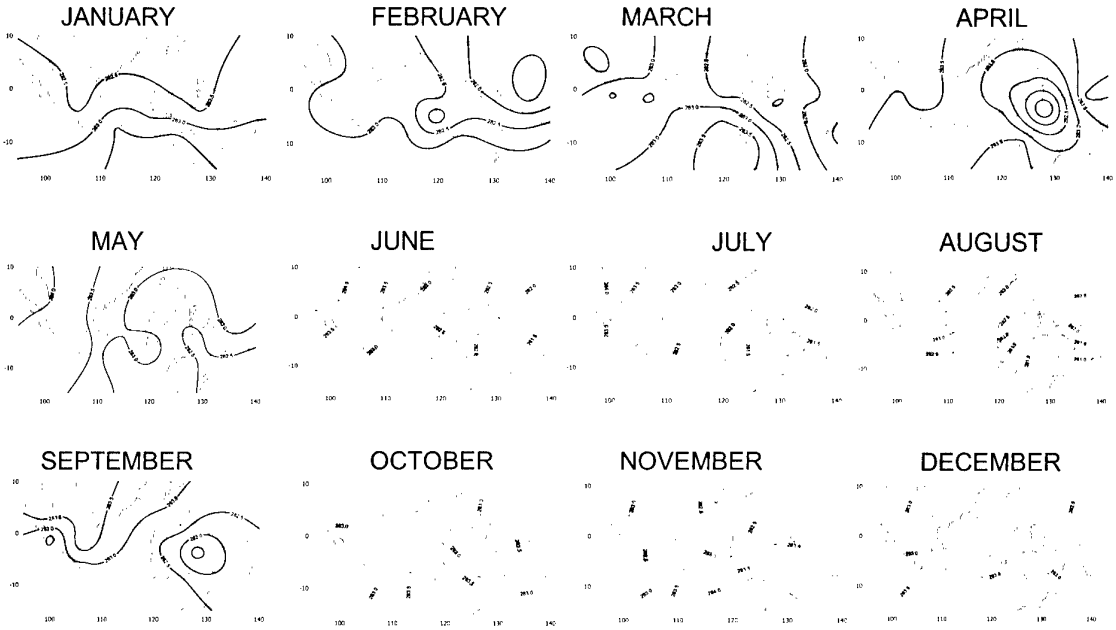


Figure 1. Isopleth for vertical mean temperature

3. ANALYSIS

The observation results for upper-air temperature from the radiosonde can be used to determine water vapor content values in the atmosphere and the air stability. It also can be used to calculate other physical events such as vertical height, mixing depth and vertically atmospheric mean temperature. Davis, et al.(1985) pointed out that vertically atmospheric mean temperature value could be calculated by using the formula 1. The analysis result shows that the vertically atmospheric mean temperature values for every month in Indonesia regions are as follows:

In January, the vertical mean temperature in the south regions of the equator was relatively hotter than such temperature in the north regions of the equator. In the eastern part of Jawa, Ujung Pandang and Nusa Tenggara, the vertical mean temperature is around 280° K.

In February, the vertical mean temperature on this month in the Western part of Indonesia regions was generally higher than the temperature in the Eastern Indonesia. Minimum rate of vertical mean temperature, 283° K, occurred in Sumatera and Jawa.

In March, the temperature pattern in March is nearly similar to the temperature in February. The vertical mean temperature for the Western Indonesia was higher than the temperature in Eastern Indonesia regions, except for the big part of South Sulawesi and Nusa Tenggara.

In April, the vertical mean temperature in Indonesia was generally hot (>282.5° K), yet there was a cell of minimum vertical mean temperature, less than 282.5° K. Maximum air temperature, 283° K, occurred in almost Western Indonesian areas.

In May, the vertical mean temperature was relatively hot, more than 282.5° K. Maximum air temperature, 284° K, took place in the Northern part of Sumatera. Yet the mean temperature, less than 282.5° K, occurred in Tual, Saumlaki and some part of Merauke.

In the Western part of Indonesia, the vertical mean temperature on June was generally hot but the temperature became cooler in the Eastern areas. The maximum value of vertical mean temperature was about 284° K took place in North Sumatera, whereas the minimum rate of vertical mean temperature, 281.5° K, occurred in the Southern part of Irian Jaya.

The vertical mean air temperature pattern on July is the same as the temperature pattern on June. Yet the vertical minimum mean temperature areas are wider. Such areas encompass the southern part of Irian Jaya, Maluku and small part of East Nusa Tenggara. In addition, there is the closing cell of vertical mean temperature, 283.5° K in West Jawa.

In August, the vertical mean temperature pattern in the south equator regions was cooler than the temperature in the north equator areas. The maximum value of mean temperature, 283° K occurred in East Coast areas of Sumatera Island and the Western part of Kalimantan, whereas the minimum rate of mean temperature took place in surrounding Maluku and East Nusa Tenggara.

For September, the vertical mean temperature patterns in the western part of Indonesia: Western Sulawesi; Kalimantan; East and West Nusa Tenggara, and also Sumatera were generally hotter than other places in Indonesia. The minimum rate of vertical mean temperature, 282 °K took place in Ambon.

In October, the vertical mean temperatures in the Eastern regions of Indonesia were commonly cooler than other places in this country. The maximum values of vertical mean temperature happened in East Jawa, Bali, West and East Nusa Tenggara.

In November, Indonesian regions located in the south equator have commonly a higher vertical mean temperature than the northern equator areas. However, North Sumatera and Aceh have a relatively enough high mean temperature as the same as the temperature in the southern equator regions. The maximum vertical mean temperature value, 284° K occurred in East Nusa Tenggara.

In December, the vertical mean temperature patterns in the south equator areas in Indonesia were generally hotter than in the north equator regions. The minimum rate, 282.5° K took place in Biak whereas the maximum one, 283.5° K happened in East Nusa Tenggara and East Jawa.

Besides the analysis resulted the patterns of vertical mean temperature every month in Indonesia, it also gave the deviation rates of the existing vertical mean temperature toward the reference values: 10–12.78° C. The deviation values range from –2.73° C to –5.51° C.

4. DISCUSSION

Analysis results show that the deviation of vertical mean temperature from all radiosonde stations toward the reference values namely 10.00° to 12.78° C were negative. The mean values varied from –2.73° C to –5.51° C. This means that the upper-layer atmosphere in Indonesia has not been influenced yet by the global warming occurrence.

Angell (1999) presented that there was heating process in atmospheric low layer due to surface mean temperature increase while in atmospheric upper layer showed there was cooling process. So if both atmospheric upper and lower layers are compared, it shows that there is action to reach equilibrium condition.

Increased surface temperature due to global warming occurrence can actually cause increased sea evaporation. Aerosol released by the sea evaporation process enters the atmosphere, but the aerosol cannot reach the outer space. The aerosol will be halted in a certain layer in the atmosphere called mixing depth so that there will be a huge number of aerosol in the atmospheric upper layer. As a result, solar radiation reaching the earth surface will be blocked by the aerosol so that air temperature in upper layer is lower than normal temperature. Accordingly, a question then arises, namely how many meters do the distance from the earth surface that the global warming effects has influenced the atmosphere?

It is understandable that surface temperature data is obtained from the measurement conducting at 2 meters height from the earth surface, and the data is usually taken in several big cities. Many studies have actually showed that the occurrence of micro climate change take places only few meters from the earth surface, and such a change much stronger horizontally run than vertically.

Considering the important role of atmospheric conditions, from the earth surface to the tropopause layer, in forming the global weather, it is crucial to understand either surface temperature or upper air temperature due to the global warming effects. Based on analysis results using vertical mean temperature data for 5 years long period (1994-1998), there has been a cooling process in the atmospheric upper-layer in Indonesia regions. This means that global warming event has cooling effects in the upper-layer. Indonesian areas known as tropical maritime continent, with 70% of the areas are sea.

Theoretically, Indonesia has a lot enough of nuclei condensation particles (NaCl) suspending in the atmosphere so that a long the way of solar radiation to reach the earth surface in Indonesia, it will occur a physical process between the solar radiation and aerosols. As a result, a few solar radiation re-radiates back to the outer space so the air temperature in the upper atmosphere becomes relatively low.

5. CONCLUSION

The deviation rates of vertical mean temperature in Indonesia toward the reference values were negative (-2.73o C to –5.51o C). This can be assumed that the upper atmosphere in Indonesia has a lot of nuclei condensation particles (NaCl) coming from sea-water evaporation so that the solar radiation re-radiates back to the outer space. This shows that Indonesia has characteristics as a tropical maritime continent.

The global warming issues due to human activities seem to give effects only in the atmospheric lower-layer while in the atmospheric upper-layer, cooling process takes place. This is indicated by the deviation negative values (-2.73° C to –5.51° C).

6. REFERENCES

Bevis, M., Bussinger,S., Herring, T.A., Rocken, C., Anthes, R.A., and R. H. Ware, 1992. GPS Meteorology: Remote Sensing of Atmospheric Water Vapor Using the Global Positioning System. Journal of Geophysical Research, Vol. 97, No. D14, pp 15.787 - 15.801.

Davis, J.L., A. Herring, T.A., Shapiro, I.I.,A.E. Rogers, A.E., and G. Elgered, 1985.Geodesy by Radio Interferometry: Effects of Atmospheric Modelling Errors on Estimates of Baseline Length. Radio Sci., 20, pp.1953 - 1607.

Herring, T.A., Anthes, R.A., Rocken, C., and R.H. Ware, 1993. GPS Meteorology: Mapping Zenith Wet Delays onto Precipitable Water. Journal of Applied Meteorology,

Liljegren, J.C., Lesht, B.M., Van Hove, T., and C. Rocken, 1999. A Comparison of Integrated Water Vapor from Microwave Micrometer, Balloon-Borne Sounding System and Global Positioning System, Ninth ARM Science Team Meeting Proceedings, San Antonio, Texas (March 22-26, 1999).

Sasmito, A. 1998 : *Characteristic Sea Surface Temperature in Eastern Indonesian Region to Detect of the ENSO Phenomenon*, Paper Presented on Conference of Meteorology and Geophysics for Mitigation of Natural Disaster, Hanoi, Vietnam, October 13, 1998.

Smith, E.K. and S. Weintraub, 1953. The Constant in the Equation for Atmospheric Refractive Index at Radio Frequencies. J. Res. Natl. Bur. Stand, 50, pp.39 - 41.

Ware, R.H., Alber, C., Rocken, C., F. Sonheim, 1997. Sensing Integrated Water Vapor Along GPS Ray Paths. Geophys. Res. Let., Vol. 24, No. 4, pp 417 – 420.

Capability Of Radarsat Data In Monsoon Flood Monitoring

by
Mardiana Shafiee, Azman Ahmad and Osman Kadir

Malaysian Centre For Remote Sensing (MACRES)
13, Jalan Tun Ismail
50480 Kuala Lumpur, Malaysia
Tel: 603 – 2697 3400 Fax: 603 – 2697 3350
http:\\www.macres.gov.my

ABSTRACT

Flood is one of the disaster which distructing of properties and human life. In Peninsular Malaysia, flood often occurred during monsoon period in November and December. During flood event, most of the area covered by cloud and sometime light rain. In this situation, radar sensor was used and is able to penetrate in any type of wheather. These studies investigate the capability of radar using Radarsat data to monitor and mapping the flood event in Kota Baharu, Kelantan. Six scenes of multi temporal (18 Dec 1998, 22 Dec 1998, 25 Dec 1998, 29 Dec 1998, 8 Jan 1999 and 9 Jan 1999) various mode (standard, extended high and fine) of Radarsat data, acquired during flood event and Landsat-5 TM data (29 August 1997) captured during dry session were used. Radar image processing and analysis including special filters were tested. The Radarsat images were combined with Landsat-5 TM and produce the window profile to confirm the flood area. Vector of flood area extracted from the radar images overlay on the Landsat-5 TM to produce the flood mapping. Result indicated that Radarsat images applied with special filter performed better result. It shown better assessment on the movement of flood event. Conclusion from this study, Radarsat images have potential and capable monitoring the flood event and easy to identify the flood area from the flood mapping.

1.0 Introduction

Monsoon floods occur every year in Malaysia during the monsoon, in particularly in the East Coast of Peninsular Malaysia. Information about flood is extremely important as it helps mitigation planning and support activities in both state and national level (Mardiana, et al. 1999). Satellite images has been a useful source of information all this while. In flood studies applications, remote sensing can be used to map extend of flooding, assess flood damages and effect of flood mitigation infrastructure on flood plain hydrology, determine the changes of hydrological regimes in the flood plains and evaluate flood prediction techniques. The optical imaging sensors used in those platforms rely on the sun ray has caused feasible due to the presence of thick and widespread cloud.

To overcome this major setback, the uses of active remote sensing are developed. Such system has the ability to penetrate clouds, strong contrast observed on images between land and water surface areas and its frequent revisit capabilities makes it particularly useful data in monitoring and detecting flood in the region such as Southeast Asia (Honda et. al. 1997).

2.0 Study Area

Kota Bharu is located in the east coast of Peninsular Malaysia. It is under the administrative jurisdiction of Kelantan state government. Map of the study are shown in Figure1.0.

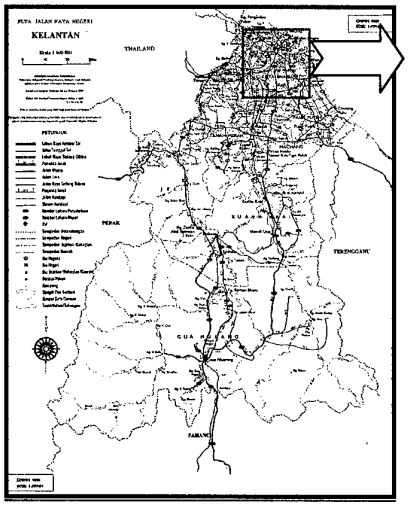


Figure 1.0 Location of the Study Area

3.0 Materials

Our approach for this research involved the use of multi-sensor and multi-temporal satellite data for monitoring monsoon flood in the study area. For the purpose, both VIR and SAR data were utilized in combination with a GIS database. Landsat TM data were selected as VIR data while Radarsat data were selected as SAR data.

3. 1 Satellite Data

Descriptions of all the data sources for this study are summarized in the table 1.0 below.

Table 1.0 Types of Satellite Data Used

Satellite Data	Date of Acquistion	Ground Resolution (m)	Wavelength (μm)	Incident Angle
Landsat TM	29 August 1997	30	0.45 – 12.5	94°
Radarsat Standard 1	18 December 1998	12.5	C-band	20° – 49°
Radarsat Standard 7	22 December 1998	12.5	C-band	20° – 49°
Radarsat Standard 2	25 December 1998	12.5	C-band	20° – 49°
Radarsat Extended High 3	29 December 1998	12.5	C-band	50° – 60°
Radarsat Fine 3	8 January 1999	6.5	C-band	37° - 48°
Radarsat Standard 6	9 January 1999	12.5	C-band	20° – 49°

4.0 Methodology

Both visual and digital image analysis methodologies were employed during the investigation of the remotely sensed data giving greater emphasis for this study. Flowchart of the study shown as figure 2 below .

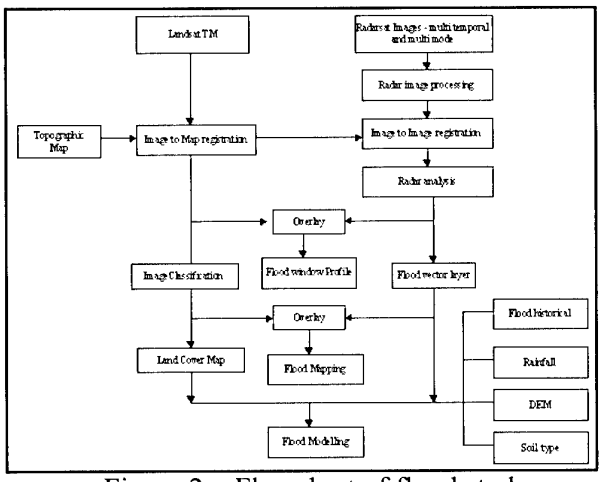


Figure 2 : Flowchart of flood study

4.1 Visual Image Analysis

Visual Image analysis of the entire data source was done primarily for orientation and familiarization with the recognizable features of the study area. The knowledge gained from the procedure was instrumental in the subsequent selection of the training samples for the digital image analysis. Geometric correction and image registration of all data sources were performed before visual analysis.

4.2 Filtering

The best filter is selected based on theoretic all facts that which filter produced an image with lowest standard deviation and mean value compared with original image value. Besides that, the filtered images also judged by visual interpretation. From the observation, Kuan filter are found to be the most suitable filter to be used in this project because it provides the lowest standard deviation value and high visual interpretation compare to others. As a conclusion, the Kuan Filter with 3x3 mask are selected, this is because filter with 5x5 could blur the images visually.

4.3 Geometric correction

Two types of geometric correction was done in this study : *(i)* Image to map registration, *(ii)* Image to Image registration.

4.3.1 Image to Map registration

The Landsat TM scene was first spatially geo-referenced to a UTM map projection using the second order polynomial and resampled with a cubic convolution algorithm. Ground control points (GCPs), are located and then were identified from 1:50,000 scale topographic maps. A total of 74 GCP point were collected and the points are well distributed and well defined on the image. A root mean square (RMS) error of less than quarter pixel (0.25) was accepted for the

correction process. The image is then resample by converting 30 m pixel size to 12.5 m. The geometrically corrected Landsat TM images were crosschecked with the topographic map to optimize accuracy.

4.3. 2 Image to Image registration

Multi temporal and multi mode radarsat images are geometrically corrected using image to image method with validated geocoded Landsat TM image used as a referenced for the registration of other radarsat images. This method consist collecting ground control point pairs from a split-screen display of both the uncorrected and master images. The master file can be any image file that the analyst wishes to regard as a standard, whether or not it has been previously corrected. The root mean square value is set to be less than one pixel. These images are then resampled using cubic convolution algorithm with second order polynomial.

5.0 Data analysis and results

There are two types of analysis method were done in this project : *(i)* Visual Image Analysis, and *(ii)* Digital Image Analysis.

5.1 Visual Image Analysis

Visual image interpretation was done by overlaying single date Radarsat image to Landsat TM . From the process of overlaying, it reveals that the spot of water and the size of the Kelantan river and Tumpat District varies differently according to the date. The significant increase shows the presence of flood in the particular area at figure 3 and figure 4.

5.2 Digital Image Analysis

Multi-temporal Radarsat data were analyzed by displaying the window profile. As we can see on the profile segment for six multi temporal images and multi mode, we could detect the increases and decreases of water level according to the distances. For example, the Radarsat image dated 22nd December 1998 shows a distance 410 meter and 950 meter for the training area Kelantan river/Kota Bahru and Tumpat District. For the same area, Radarsat image dated 29th December 1998 however shows an increase of water level. The distance for Kelantan River was 625 meter while Tumpat District 1.26 km. However, the water level shows reduction in the Fine image dated 8th January 1999 where reading in the area in Kelantan river are 430 meter while 950 meter in Tumpat district (see figure 4). Counting the pixel of the training area in Tumpat District (see figure 5) by masking the vector of predicted flood area, a typical wet area to be found expanding in these three images. The first image (22nd of December 1998) was around 35.5 km^2. In the second image (29th of December 1998) shows a tremendous increase to 119.7 km^2. This area anyway, reduces to a figure of 79 km^2 in the third image (8th of January 1999). These increase/decrease volume of water can be verify by the ground truth data which was gathered by the Department of Irrigation And Drainage (DID) on the study area between the date 29th of December 1998 till 5th January 1999 which flood have been occured during this period.

6.0 Conclusion

Discrimination of flood area can be significantly predicted both visually and statistically using multi-temporal and multi mode of Radarsat images on flood mapping (see figure 3). Radarsat images have potential and capable monitoring the flood event and easy to identify the flood area from the flood mapping. Further research will carried out to integrate with spatial database to obtain a better result of flood mapping and flood modelling.

Reference

Mardiana, S., Azman, A., and Osman, K. (1999) ,"Remote Sensing In Flood Studies", Presented at Seminar on Remote Sensing & Related Technologies for Water Resources, 27 September 1999, Kuching Sarawak.

Honda, K., Canisius, F.X.J., Sah, B.P. (1997) , " Flood Monitoring in Central Plane of Thailand Using JERS-1 SAR data" Proceedings of the 18th Asian Conference on Remote sensing, 20-24 October 1997, Kuala Lumpur.

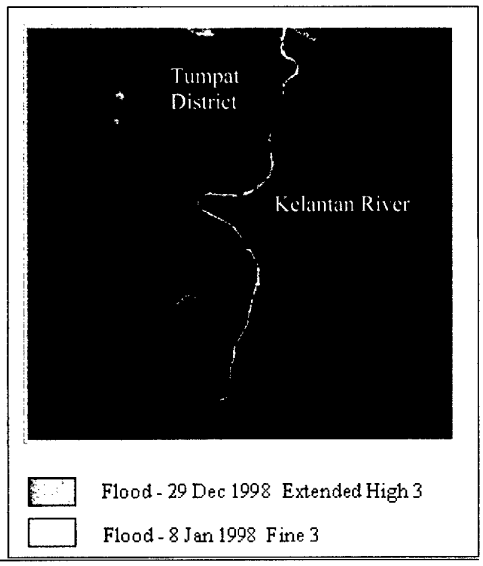


Figure 3 : Flood mapping – Kota Baharu, Kelantan

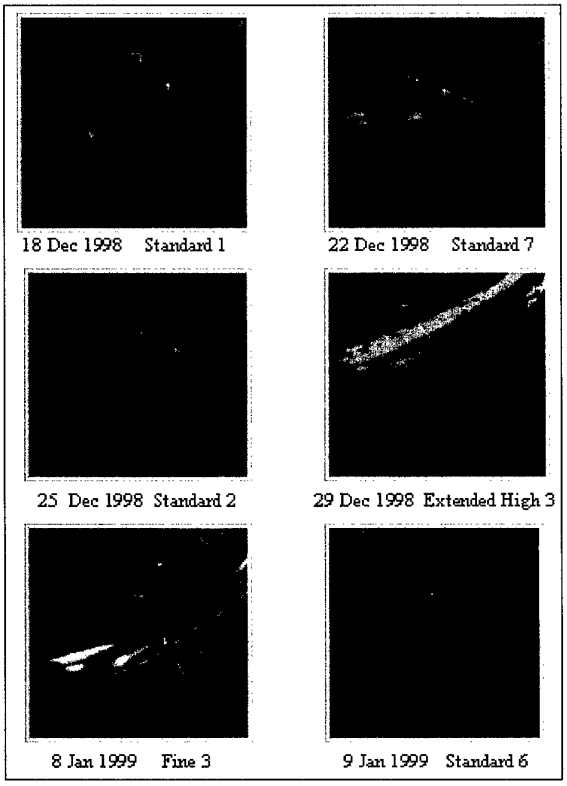


Figure 4 : Kelantan River – Flood monitoring using multi temporal and multi mode Radarsat images (Flood mask from Radarsat images overlay on Landsat TM images).

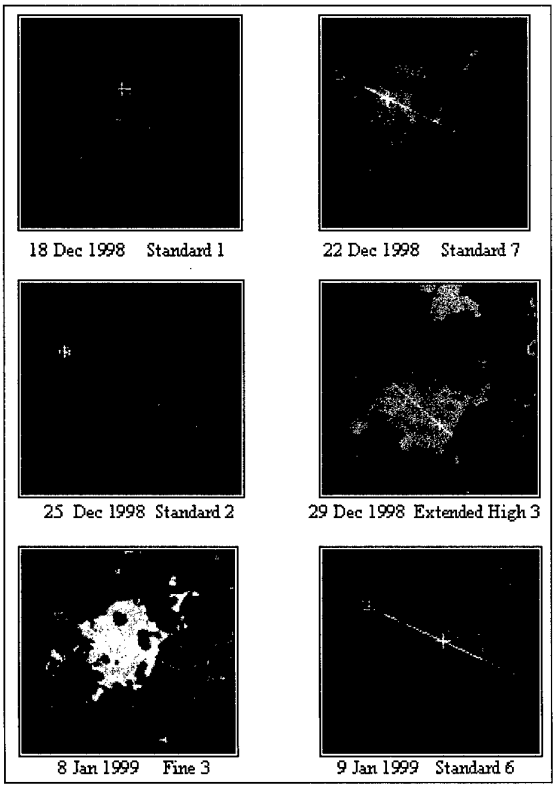


Figure 5 : Tumpat District– Flood monitoring using multi temporal and multi mode Radarsat images (Flood mask from Radarsat images overlay on Landsat TM images).

Applying AVHRR Data to Estimate and Monitor Aerosol Optical Thickness

Tang-Huang Lin* and Gin-Rong Liu**
* Graduate Student, Institute of Space Science
National Central University.
** Professor, Center for Space and Remote Sensing Research
National Central University
Chung-Li, Taiwan 320
E-mail:grliu@csrsr.ncu.edu.tw

Key Words: Remotely sensed data, Atmospheric effect, Contrast reduction method

Abstract: Owing to the existence of atmosphere, the remotely sensed data observed from satellite are affected by the atmospheric effect. The actual information of earth surface are showed only while the effects are correctly removed. Basically the effects are dependent on the atmosphere conditions. In the visible and near IR spectral, the effects are mainly caused by the scattering of atmosphere molecular and aerosol. That is, the aerosol parameters can be retrieved from the remotely sensed data. So, this study improved the aerosol optical depth method developed by previous studies, to retrieve the aerosol optical depth by using AVHRR data. The results revealed that the improvements proposed by this study was accuracy and practical. On the other hand, since the aerosol concentration in the atmosphere is one significant index of the air quality, the distribution of air pollution seems can be monitored effectively with remote sensing data. Therefore, the application of the retrieved aerosol characters for environmental monitoring, such as air pollution, smoke, or dust detection, is also an important sub-topic in this research.

1. INTRODUCTION

In the visible and infrared spectral region, the atmospheric effects mostly come from the atmospheric molecular and aerosol scattering. Generally, these effects are not easy to corrected accurately although we know that they blur the ground truth information, especially for the part of aerosol scattering. There are two main methods have been used for atmospheric effects correction with remote sensing data. One is to pick up low and stable reflective objects, such as clear water body or dark dense vegetation (DDV) targets as the path radiance estimation reference, to reduce the aerosol optical parameter estimation error due to the uncertainty of object reflectance(Ahern et al., 1977; Liu et al., 1996). The other is so-call the "contrast-reduction" method. Assuming that the surface target reflectance are not changed, the

aerosol optical parameter could be estimated by the radiance difference of satellite observations in a series times with a reference datum. Based on that, Tanre et al. constructed the Structure Function (SF) method with the Landsat TM images and got satisfying results in 1988. Holben et al. (1992) also got good results using AVHRR data for aerosol optical depth retrieval by SF method. Sifakis et al. (1992 and 1998) applied the contrast method for SPOT and Landsat TM satellite image to estimate the aerosol optical parameter and monitor the air pollution over urban area.

In this study, the SF method is applied to estimate the aerosol optical depth over Taiwan area from AVHRR data, but some anomalies of the structure function distribution pattern were appeared. The anomalies probably due to the sensor observing geometry, the change of landcover in the multi-temporal images and terrain effect and would induce the significant errors in aerosol optical depth estimation. In order to avoid such errors, the study would introduce the "optimal position number" to remove the distribution anomalies(Liu et al., 1997). The maximum error of estimated aerosol optical parameter is reduced from 61% to 24% after the "optimal position number" is adopted in this study. The result also shows that this improvement is one of the crucial steps in estimating aerosol optical parameter. Not only the estimation accuracy is improved significantly when the "optimal position number" is employed, but also make the structure function more practical.

2. METHODOLOGY

Assume the ground surface observed by satellite is Lambertian, the equivalent ground reflectance observed by satellite is ρ *, and can be expressed as (Tanre et al., 1988)

$$\rho^*(\mu_s,\mu_v,\varphi)=\rho^a(\mu_s,\mu_v,\varphi)+\frac{T(\mu_s)\left[\rho\exp[-\tau/\mu_v]+<\rho>t_d(\mu_v)\right]}{1-<\rho>s} \quad (1)$$

where ρ * is equivalent ground reflectance, $\mu_s=\cos\theta_s$, θ_s is solar zenith angle, $\mu_v=\cos\theta_v$ and θ_v is sensor zenith angle, ρ^a is atmospheric reflectance, ϕ is relative azimuth angle between solar and sensor, τ is atmospheric optical depth, ρ ground surface reflectance, T is total transmittance from solar to ground surface, s is atmosphere albedo, $<\rho>$ is mean surface reflectance, t_d is diffuse transmittance from surface to sensor. Under the following conditions: (1) Ignore the multi-reflectance activities between earth surface and atmosphere; (2) The surface is unchanged in time; (3) The mean surface reflectance is constant, then we can obtain:

$$\frac{M^{*2}(d,t_1)}{M^{*2}(d,t_2)}=\frac{Function[\tau_a(t_1)]}{Function[\tau_a(t_2)]} \quad (2)$$

where M is the structure function defined by Taner et al.(1988),

$$M^2(d)=\frac{1}{N}\sum_i\sum_j(\rho_{i,j}-\rho_{i,j+d})^2 \qquad (3)$$

and Function[τ_a] = $T(\mu_s)\exp[-2\tau/\mu_v]$

The parameters of t_1 and t_2 indicate the two different observation time. From Equation (2), it is clear that the aerosol optical depth will get different values in different distance, *d*, unless the ration of structure function is constant. Basically the mean ration of *d=1* to *d=10* is used in the general cases. In some cases, the errors of estimated aerosol optical depth are large when the correlation of ration in the different *d* number is low.

Applied Equation (3) defined by Tanre et al. to estimate the optical depth over the northern Taiwan area with AVHRR visible data, the structure function distribution of neighboring pixels with different *d* numbers is showed in Figure 1. Assume the difference of surface reflectance is increasing when the distance is increasing, the structure function will is increasing when *d* number is increasing and has the similar distribution pattern (Tanre et al., 1988; Holben et al., 1992). But the structure functions of different dates were changed significantly in Figure 1. It may be caused by the terrain effect, the complex canopy in Taiwan area and the satellite geometric observation. This anomaly will influence the retrieved aerosol optical depth strongly. This study used the result of statistical analysis for determining the "optimal position number" to discard the anomalous structure functions.

Figure 2(a) and 2(b) are the histogram of AVHRR channel 1 digital count difference for different *d* values on 6 and 19 November. Generally the reflectance differences distribution of the neighboring pixels are similar to normal distribution. In Figure 2(a), the distribution is quite irregular when *d*=5, while the distribution is regular and similar to the right wing of normal distribution in Figure 2(b). This anomaly would influent the structure function pattern as illustrated in the Figure 1, square symbols bending anomaly after *d*=5 on 6 November. Then the "optimal position number" is set at *d*=5 in this case study to reduce the errors induced by the structure function anomalies.

3. RESULTS

This study used one set of multi-temporal NOAA-14 AVHRR data to estimate the atmospheric aerosol optical depth. The data set includes 6 AVHRR images acquired during November, 1997 over Chung-Li, Taiwan, shown in Table 1. The size of tested area in this study was about 25 x 25 km at the Northern Taiwan, and landuse includes urban, rural, agricultural and tree area. This tested area is over the neighboring area of National Central University (NCU), and the sunphotometer

observation site(at NCU). The ground measured aerosol optical depth were used for reference and as the checked data to confirm our estimated results.

The results of aerosol optical depth estimated by not using and using "optimal position number" are listed in Table 2 and 3, respectively. The comparison with the sunphotometer measurements showed that the errors induced by the anomalies of structure function distribution were obvious reduced and the maximum errors were reduced from 61% to 24%. It revealed that the application of the "optimal position number" really could improve the estimation accuracy significantly.

4. CONCLUSION

The induce of the "optimal position number", which can reduce errors efficiently, is one of important procedures of applying structure function method to retrieve aerosol optical depth. The result in this study reveals that this improvement is very useful in promising the estimation accuracy and extends the application of the relative satellite images in the different area. Meanwhile, it can reduce the sensitivity of data acquiring time, especially for more longer time interval data, and prolong the applied time interval of referred observation data. Of course, the limitation of the "optimal position number" should be investigated further. This improvement also can be applied in some high time-resolution geostationary satellite images, such as GMS and GOES, to estimate the relative air quality parameters for air quality monitoring.

REFERENCES

[1] Ahern F. J., D. G. Goodenough, S. C. Jain, V. R. Rao, and G. Rochon, 1977: Landsat atmospheric corrections at CCRS, In Proceedings of the Fourth Canadian Symposium on Remote Sensing, Quebec City, May, 583-595.

[2] Holben, E. Vermot, Y. J. Kaufman, D. Tanre, and V.Kalb, 1992: Aerosol Retrieval over Land from AVHRR Data-Application for Atmospheric Correction. IEEE Trans. on Geoscience and Remote Sensing, Vol. 30, No. 2, pp. 212-222.

[3] Liu C. H, A. J. Chen, and G. R. Liu, 1996: An Image-based Retrieval Algorithm of aerosol Characteristics and Surface Reflectance for Satellite Images. INT. J. Remote Sensing, Vol. 17, No. 17, 3477-3500.

[4] Liu G. R, T. H. Lin, and A. J. Chen, 1997: An Improved Method to Determine Aerosol Optical Depth from SPOT Data. COAA '97-First International Ocean-Atmosphere Conference, 18-19 Oct 1997, Washington, D. C., USA.

[5] Sifakis N. I. and P. - Y. Deschamps , 1992: Mapping of Air Pollution Using Satellite Data. Photogrammetric Engineering & Remote Sensing, Vol. 58, No. 10, 1433-1437.

[6] Sifakis N. I., N. A. Soulakellis, and D. K. Paronis, 1998: Quantitative mapping of

air pollution density using Earth observations: a new processing method and application to an urban area. INT. J. Remote Sensing, Vol. 19, No. 17, 3289-3300.

[7] Tanre D., P. Y. Deschamps, C. Devaux, and M. Herman, 1988: Estimation of Saharan Aerosol Optical Depth from Blurring Effects in Thematic Mapper Data. J. Geophys Res., Vol. 93, No. D12, pp 15955-15964.

Table 1. The observation geometry of NOAA-14 AVHRR satellite of the five observations using in this study. (* : reference date)

			Satellite		Solar	
Orbit number	Date	Local Time	Zenith	Azimuth	Zenith	Azimuth
14700	1997/11/06*	06:40	58	193	58	228
14714	1997/11/07	06:29	48	186	56	224
14756	1997/11/10	05:56	3	165	52	215
14770	1997/11/11	05:45	23	158	51	212
14883	1997/11/19	05:58	1	166	54	215
14897	1997/11/20	05:47	21	159	53	213

Table 2. The comparison of the aerosol optical depth estimated by sunphotometer data and AVHRR Channel 1 data, while the "optimal position number" was not used. (* : reference date)

Date	AVHRR CH1 (580-680 nm)	Sunphotometer measurement	Error/ Percentage
1997/11/06*	0.204	0.204	----
1997/11/07	0.473	0.346	0.127 / 38%
1997/11/10	0.345	0.214	0.131 / 61%
1997/11/11	0.430	0.275	0.155 / 56%
1997/11/19	0.489	0.483	0.006 / 1%
1997/11/20	0.349	0.240	0.109 / 45%

Table 3. Same as Table 2, except the "optimal position number" was used.

Date	AVHRR CH1 (580-680 nm)	Sunphotometer measurement	Error/ Percentage
1997/11/06*	0.204	0.204	----
1997/11/07	0.431	0.346	0.085 / 24%
1997/11/10	0.242	0.214	0.028 / 13%
1997/11/11	0.347	0.275	0.028 / 10%
1997/11/19	0.474	0.483	0.009 / 2%
1997/11/20	0.254	0.240	0.014 / 6%

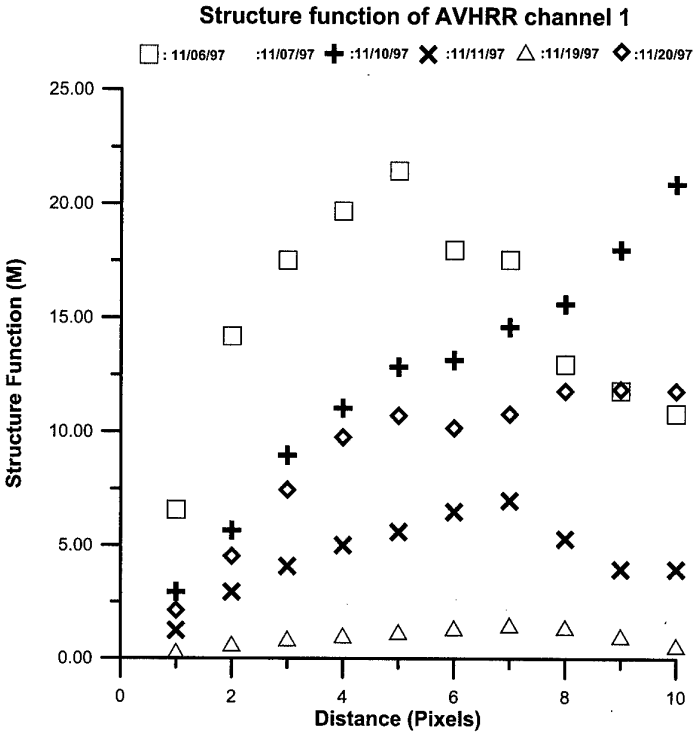


Figure 1. The structure functions derived from AVHRR-14 Channel 1 data, acquired on 6 dates, with different distances, *d*.

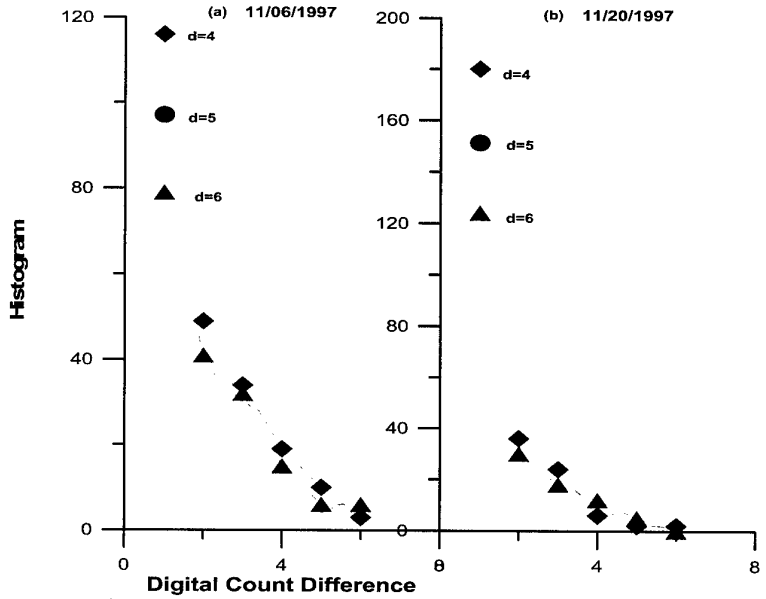


Figure 2. The comparison of digital count different histogram of AVHRR Channel 1 data acquired on 1997/11/06 and 1997/11/20 with *d*=4, 5 and 6. Figure 2(a) shows the curve of *d*=5 shifting right hand side obviously. It means that the difference of ground reflectance property in this AVHRR data is large. The difference is not found in Figure 2(b).

Surface Temperature Analysis of Urban Area using RS and GIS

Myung-Hee Jo · Kwang-Jae Lee · Ji-Hyun Shin · Ae-Sook Suh · Sung-Nam Oh
Department of Geodetic Engineering, Kyungil University
33 Buho-ri, Hayang-up, Kyungsan-si, Kyungsan bukdo, 712-701, Korea
Tel) +82-53-850-7312, Fax) +82-53-854-1272
mhjo@bear.kyungil.ac.kr, leck-j@hanmail.net, jh_justina@hanmail.net
Remote Sensing Research Lab · Applied Meteorological Research Lab
MRI, Korea Meteorological Administration
assuh@metri.re.kr, snoh@metri.re.kr

KEY WORDS : REMOTE SENSING, SATELLITE IMAGE, URBAN HEAT-ISLAND, SURFACE TEMPERATURE, NDVI

ABSTRACT

The aim of this study is to analyze the relationship between urban surface temperature, land cover and NDVI using satellite image and observation data. This study compared and analyzed between Landsat TM band 6 and AWS data for monitoring the establishment of urban heat island using multi temporal images.

There were several methods to estimate the surface temperature from Landsat TM data. However, in this study, it used four theoretical models to extract thermal density value from Landsat TM band 6 image processing: Two-point linear model, linear regression model, Quadratic regression model and Cubic regression model. After simple analyzing between four models and AWS data, in this case, it should be need selection of suitable model through remodeling of four models. Thus, after remodeling, to created suitable regression algorithm for this study.

In summary, the result of analysis between NDVI, land cover classification and surface temperature will regard as one of effective methodologies for to make manifest urban heat island in the future. This study verified some methods of surface temperature estimating from satellite images and extracted the most effective algorithm through the comparing land cover and surface temperature.

INTRODUCTION

These days, a lot of people come together in the city rapidly because of the industrial development, so climatic changes such as a sudden rise in temperature, relative humidity and air pollution have been brought out all over the world. Especially, distinct difference of temperature

between urban and rural, it depends on urban planning, construction of industry and pattern of green distribution, which is called urban heat island, is one of the biggest problems nowadays. Furthermore, previous studies only used meteorological observation data of surface although meteorological type was very difference, depending on topographic of study area and landuse. However modern research are using a technique of remote sensing and GIS(Geographic Information System) because it could be possible to prove to adapt these skills in this kind of study area. Park. I. H(1999) did a evaluation of the heat island in transition zone of three cities in Korea. Also, Griend(1993) analyzed distribution of temperature depending on status of surface with correlative analysis between NDVI and surface temperature using NOAA(National Oceanic and Atmospheric Administration) images. According to Klysik and Fortuniak(1999), urban heat island is a phenomenon, which temperature is distinctly going up, because of the increasing buildings in cities.

The purpose of this study is to verify some methods of surface temperature estimating from satellite images and extracted the most effective algorithm through the comparing land cover and surface temperature.

In this research, first of all, surface temperature was taken by Landsat TM band 6 at 25 places in Seoul and the connection of above it is proved through AWS (Automatic Weather Station) temperature data and regression analysis. Then, temporal variation of urban heat island depending on landuse pattern and NDVI(Normalization Difference Vegetation index) was performed. Finally, urban heat island in Seoul could be synthetically analyzed by comparing the distribution of temperature between green areas and non-green areas through GIS spatial analysis.

MATERIALS AND METHODS USED

In this research, the multi temporal Landsat TM (Apr. 19 1999, Jun. 16.1997, Oct. 22. 1997, Jan. 21 1996) images, temperature data acquired at the point of 23 AWS, 1/5,000 digital map and 1/25,000 topographical map were used to present urban heat islands more precisely. Fig. 1 shows the process of this study.

First, the temperature at every 10 A.M was extracted and classifying each layer using Arc/info GIS Tool prepared the thematic map in study area. Multi temporal Landsat TM(band 5/3/2) images were carried out geometric correction with GCP (Group Control point), which was acquired on 1/25,000 topographical map using Unix ERDAS IMAGINE 8.3.

The training area, which is one of the most important operations in classification, was selected based on "Analyzed distribution of Biotop and construction of ecological city in Seoul city "(Feb. 2000) and Maximum Likelihood Classification classified this area into 10 classes, which is one of supervised classification method.

This research extracted regression equation, which is possible to analyze temperature of study area, through regression analysis between the value of DN(Digital Number) of Landsat TM

band 6 and observation temperature of 23 point of AWS for analysis of distribution of temperature at study area.

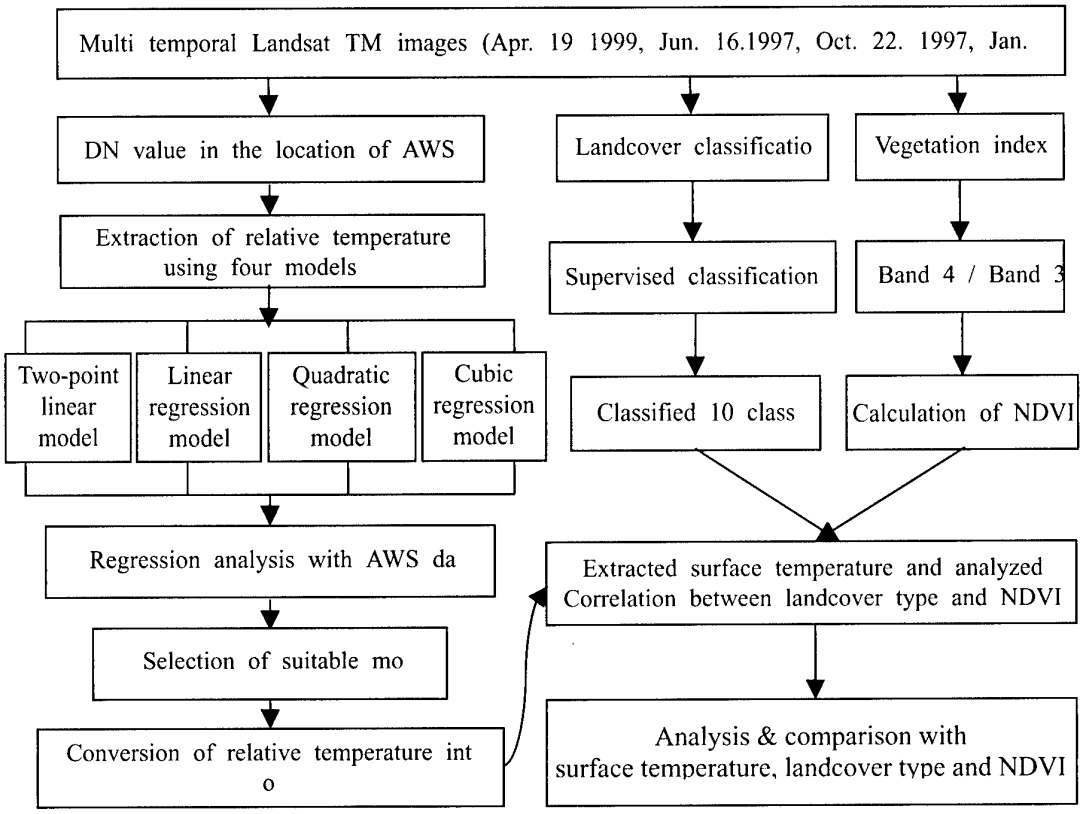


Figure 1. Process of analysis and comparison between heat island, MLC and NDVI

After computing relative temperature using Two-point linear model, linear regression model, Quadratic regression model, cubic regression model, the real temperature was obtained in entire study area through observation temperature and regression analysis. Also, the original vegetation activity has the value of $-1 \sim 1$. However in this study transformed these value into difference images, which have 8 bit value images.

ANALYZING OF HEAT-ISLAND USING LANDSAT TM IMAGE

1. Analysis of surface temperature using the value of DN of Landsat TM band 6

Observing surface temperature from Landsat TM band 6 and each model was relative temperature. So, it was difference between observation of AWS temperature and relative temperature. However, in this study could extract different regression equation because in this case already operated regression analysis between observation temperature and relative temperature. This study used 4 models, which is already existence, for extraction of real

temperature.

- Two-point linear model

  Temperature(°K) = 203.2 + 0.541176 × TM 6

- Linear regression model

  Temperature(°K) = 219.97218 + 0.525959 × TM 6

- Quadratic regression model

  Temperature(°K) = 209.830966 + 0.834313 × TM 6 - 0.001372 × $TM\ 6^2$

- Cubic regression model

  Temperature (°K) = 206.127 + 1.054 × TM 6 - 0.003714 × $TM\ 6^2$ + 6.60655 × 10^{-6} × $TM\ 6^3$

However this case need to calculate from the absolute temperature to the centigrade temperature because it had absolute temperature through these equations.

centigrade temperature (℃) = absolute temperature (°K) - 273.15

Table 1. Regression equations between real temperature and relative temperature

YEAR	Suitable Models	Regression Equation	R^2
Apr. 19. 1999	Quadratic regression model	Y = 1.2643x – 10.79	0.8151
Jun. 16. 1997	Linear regression model	Y = 0.5731x + 14.164	0.8640
Oct. 22. 1997	Quadratic regression model	Y = 1.2439x – 6.7449	0.8036
Jan. 21. 1996	Cubic regression model	Y = 1.1104x – 0.8665	0.7683

- Dependent variable: real temperature
  Independent variable: relative temperature

2. Composition of landcover classification map

In this study classified total 10 classes(Forest, Water, Barren, Traffic facility, Resident area, Commercial area, Factory area Culture area Agriculture area, Special area).

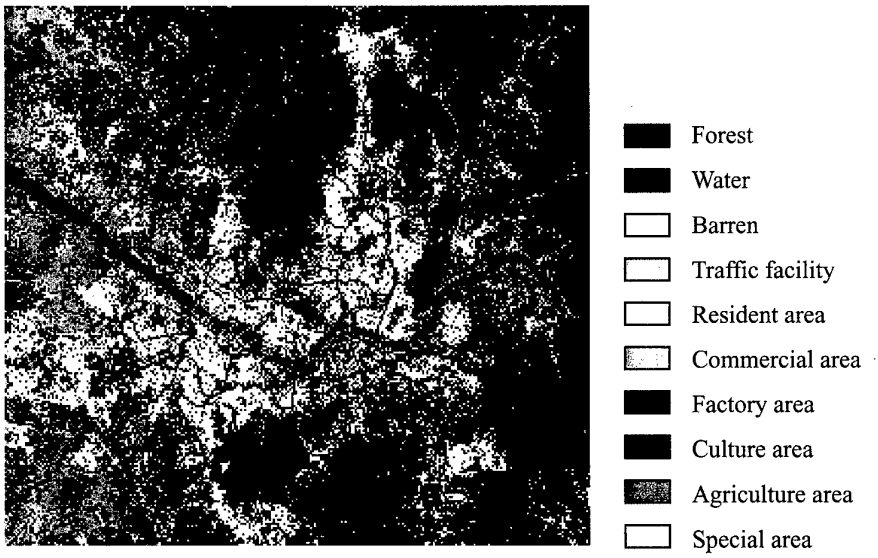


Figure 2.Landcover classification map in Seoul city (Apr. 19. 1999)

3. Extraction of NDVI

This research used the NDVI for to analyze distribution of temperature in green area non-green area. Generally speaking, NDVI have the value of –1(Min) ~ 1(Max) through Equation of NDVI extraction. But, in this case transformed these value into difference images which have 8 bit value images.

$$NDVI = (Band4 - Band3) / (Band4 + Band\ 3)$$

SUMMARY AND CONCLUSIONS

1. Analyzing distribution of surface temperature with classification type

It can be show as Table 2., which is standard value of surface temperature with classification type using Landsat TM band 6.

Table 2. Landcover classification and Surface temperature (unit ℃)

Class	Apr. 19. 1999	Jun. 16. 1997	Oct. 22. 1997	Jan. 21. 1996
Forest	15.986	23.864	12.563	-4.196
Water	3.759	21.634	10.528	0.43
Barren	12.088	26.451	16.834	0.887
Agriculture	13.808	24.498	14.188	-0.619
Urban	20.124	28.504	16.083	-1.22
Factory	19.783	30.382	17.701	0.56

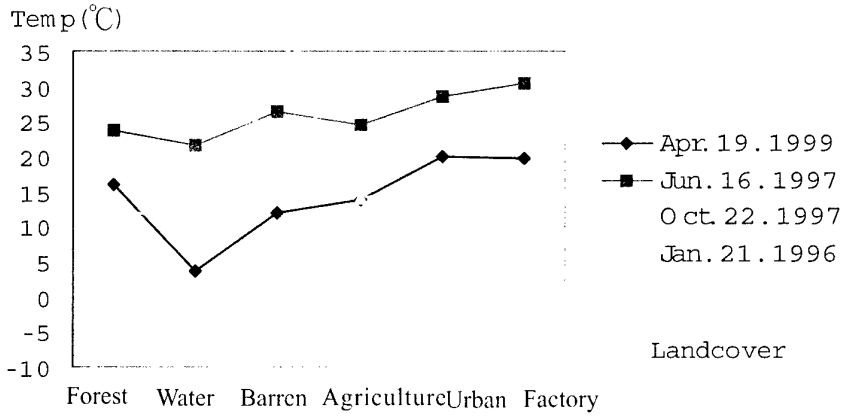


Figure 3. Change detection of temperature with landcover classification

2. Correlation analysis between surface temperature and NDVI using Landsat TM images

This research selected 80 points and calculated Pearson correlation coefficient(R) between surface temperature and NDVI for to study distribution of temperature in green area and non-green area.

Table 3. Correlation analysis of surface temperature and NDVI

YEAR	Regression Equation	R	R^2
Apr. 19. 1999	Y =–6.2073x+214.87	–0.8043	0.6470
Jun. 16. 1997	Y =–21.194x+692.25	–0.9293	0.8636
Oct. 22. 1997	Y =–14.654x+372.87	–0.8414	0.7080
Jan. 21. 1996	Y = 9.14x+135.52	–0.8490	0.7209

REFERENCE

Gallo, K.P> et al, 1993, The use of a vegetation index for assessment of the urban heat island effect, International Journal of Remote Sensing, 14(11):2223-2230.

James E. Vogelmann, 1999, Effects of Landsat Thematic Mapper radiometric and geometric calibrations on selected land cover analyses, Pecora 14 Proceeding, pp143-153.

Jensen, 1996, Introductory digital image processing.

Jauregui, E, 1998, Long-term effect of Mexico City's heat island on potential energy demand for space heating, Journal of Conference on Agriclutural and Forest Meteorology, 23rd.

Kim, H.H, 1992, Urban heat island International Journal of Remote Sensing, Vol.13 No.12, pp2319-2336.

Kyung-Hun Park, Sung-Kwan Jung, 1999, Analysis on urban heat island effects for the metropolitan green space planning, Journal of the Korea Association of Geographic Information studies, Vol.2 No.3, pp 35-45.

Lambin, E. F. & Ehrlich D, 1996, The surface temperature-vegetation index space for land-cover and land-cover change analysis, Int. J. Remote sensing, 17(3): 463-487.

Park, Kyung-Hun, Jung, Sung-Kwan, Oh, jung-Hak, Kim, Hee-Nyeon, Park, Jin-Soo, 1999, Analysis on heat island alleviation effects of vegetation using Landsat TM data, The Korea Association of Geographic Information Studies, pp.131-135.

Park, In-Hwan, Jang, Gab-Sue, Lim, Jong-Yong, 1999, Evaluation of the heat island in transition zone of three cities in Kyungpook, Korea, Korea Society Environmental Impact Assessment, Vol. 8 No.2, pp. 73-82.

Saitoh, T.S, 1998, The present and future state of urban warming in the Tokyo metropolitan area. Japanese Urban Environment, G.S. Golany et al, (ed.), Pergamon press, Chapt, Part•-A, pp.99-116.

Investigation of biotop in Seoul and establishment of guide for construction of ecology city, 2000, Seoul.

APPLICATION AND VALIDATION OF LWCI (LEAF WATER CONTENT INDEX) TO TROPICAL SEASONAL FOREST REGION

Michio ANAZAWA*, Genya SAITO* and Haruo SAWADA**

* National Institute of Agro-Environmental Sciences
3-1-1 Kannondai, Tsukuba, Ibaraki 305-8604, JAPAN
Tel +81-298-38-8192 Fax +81-298-38-8199
E-mail anazawa@niaes.affrc.go.jp
** Forestry and Forest Products Research Institute,
1 Matsunosato, Kukisaki-machi, Ibaraki, 305-8687, JAPAN

Key WORDS: LWCI, Tropical Seasonal Forest, Environmental Gradient Analysis, LAI, Precipitation

ABSTRACT: Leaf Water Content Index derived from Landsat TM is found useful for detecting the leaf water content for tropical seasonal forest in Thailand. Water availability of plant leaves is recognized as the most important key for forming vegetation types in this forest zone, e.g. shedding of the leaves begins from the bottom of the mountain (which is contrary to that of temperate forest) and the gallery forest along water streams keep leaves all the year. Based on this index, water availability map, which shows the seasonal change of foliage moisture within vegetation area was created for Kanchana Buri study site in western Thailand. The dominant forest types are dry-dipterocarp forests (DDF), mixed deciduous forest and bamboo forest. Seven Landsat TM data were used to estimate the leaf water contents at each time. Then, the time sequential analysis and filtering process (Modal filter) was applied to delineate the terrain on the basis of the differences of water availability.

Integrating the DEM data, environmental gradient analysis was conducted to the water availability map for three watersheds, north side, west side and east side. The result shows that not so many deciduous forests are found even in low elevation at north side, deciduous trees are dominant in all elevation at west side and impact of human activities (agriculture) made up quite different vegetation types and land use at east side.

As for Landsat TM data, the correlation between LWCI and ground truth data at the Mae-Klong watershed research center (the meteorological data, etc.) could be analyzed. It was also found to have a tendency of close relation to precipitation and evaporation with the time lag of 1-2 months. In conclusion, this study shows that the LWCI is one of the most useful indices for evaluating terrain condition and understanding the vegetation types which are found in tropical seasonal forest area.

1. INTRODUCTION

Seasonal change is one of the most important information for analyzing growing condition of vegetation and the NDVI derived from satellite remote sensing data is generally used for this purpose. The NDVI, however, is influenced by haze and smoke very much. Therefore, an index is required for monitoring tropical seasonal forest area where smokes caused by fires in agricultural land affect very often.

The change of water condition within forest such as the leaf water content according to seasonal alternation (water stress: wet and dry) seems to play important role in phenological dynamics of tropical monsoon forest, especially in deciduous forest and rain-green forest like teak. As for the monitoring of forest phenology and vegetation activities in this area, it is effective to measure the leaf water content by using remote sensing data. It seems possible to

monitor the change of leaf water content by applying LWCI Index to TM data processed in advance with radiometric rectification.

In this study, improving upon LWCI proposed by Raymond Hunt and et al , we contrived mLWCI(Modified_LWCI). Applying this index to every pixel, the zoning image was created, which shows the regional feature of the water supply condition in dry season.

We intended to develop the leaf water content index (LWCI) into the practical remote sensing index that can catch the water availability of leaves in tropical seasonal forest without receiving the influence of haze such as clouds and fog.

2. STUDY AREA AND DATA USED

(1) Study area

North East of Kanchana Buri, Thailand.

UTM Coordinates (N 1602996 - N 1630496, E 473000 - E 500500)

(2) Data used

(a) 7 scenes of Landsat TM data in dry season from the beginning to the end were selected. These data were obtained from NRCT and NASDA. . The following Table 1 shows acquisition date of Landsat TM.

Table 1 List of acquired Landsat TM data.

Area	Sensor	Path Row	Date
Kanchana Buri	LandsatTM	130 - 50	1989/12/5,1990/4/17,1993/1/30,1993/4/4,1994/1/17, 1994/3/6,1995/2/21(scenes)

(b) DEM data (UTM) of the study site from the geographic map with the scale 1:50,000(derived from 100m contours, pixel size: 30m).

(c) Meteorological data observed at Mae-Klong watershed research station (1993-1997).

3. METHODOLOGY AND ANALYSIS

(1) Definition of LWCI (Leaf Water Content Index)

On the basis of LWCI proposed by Raymond Hunt (1987), we contrived new LWCI intended for practical use, so as to utilize the energy value of remote sensing data instead of measuring reflectance. The index uses TM4 and TM5 spectral bands in which the difference in water content of leaves appears conspicuously (Fig.1).

The formula of new LWCI is as follows,

$$LWCI = \frac{-\log [1-(\alpha \times TM4/A - \beta \times TM5/B)]}{-\log [1-(\alpha \times TM4ft/A\ \beta \times TM5ft/B)]}$$

A: Maximum value of TM4 through whole images

B: Maximum value of TM5 through whole images

α : a correction coefficient(usually 1).

β : the coefficient for converting the energy value into the reflectance(the reflectance value ratio at the season of the minimum water stress in a leaf = the ratio of TM5 to TM4 in the theoretical solar radiation spectrum curve : the representative value: 0.2).

TM4ft & TM5ft: TM4 and TM5 at the season of the minimum water stress (full turgor),that is, these are the maximum value composite image of TM4 derived from all images and the minimum value composite image of TM5 derived from all images.

- Here, instead of reflectance, the energy value (transformed from radiance according to sensor's dynamic range) is used for TM4, TM5, TM4ft and TM5ft, respectively.

(2) Creation of the multi-temporal LWCI Images

By applying LWCI to those geometrically corrected and radiometrically rectified images, 7 LWCI images were created (Fig.2).

(3) Comparison of LWCI with other observed Data

The seasonal change of LWCI and the meteorological data of the Mae-Klong watershed research station were compared (Fig.3). The experimental plot data (LAI, Leaf Litter Production) of MWRS were compared with LWCI. Furthermore, GPS photos at the ground were compared with LWCI Image by using 3D perspective view images.

(4) Water Available Map in Kanchana Buri based on LWCI

The K-means clustering method was applied to the LWCI images to classify the pattern of the LWCI changes in this area. As the result, 21 clusters were identified. These 21 clusters were summarized into 10 categories which show different seasonal change patterns of the LWCI.

The differences of the seasonal changes of LWCI are caused by the water availability and also by the vegetation types. Therefore, a filtering is needed to be applied to the clustering result to minimize the influences of the differences of vegetation types and to get the zoning map on water availability.(Fig.4).

(5) Environmental Gradient Analisis for three watersheds

The study area was topographically divided into three watersheds for analysing the site characteristics by the environmental gradient analysis.

Integrating the DEM data, the environmental gradient analysis(Fig.6) was conducted to the water availability map for three watersheds, north side, west side and east side of the study area(Fig.5).

The ratio of the classes on the LWCI changes were summarized in every 100m interval of the elevation.

4. RESULT AND DISCUSSION

(1) Comparison of LWCI with other observed data.

In Comparison of the seasonal change of LWCI and the meteorological data of the Mae-Klong watershed research station, it seems that the changes of LWCI correspond to precipitation and evaporation with the time lag of 1-2 months(Fig.3). However, it's necessary to collect more data ranging long term (more than 2 years) for analyzing the detail correlation.

(2) Water Available Map and Environmental Gradient Analysis

The results (Fig.6) clearly show as follows,

- In the north side (where the watershed faces the north), the rate of evergreen trees and deciduous trees that do not shed the green leaves is the highest. This indicates that the water availability condition is the best at the north side.
- In the west side, the relation between the elevation and the rate of evergreen is linear. This indicates that the west side has the standard trend of the vegetation types according to the elevation.
- Compared with the north side, it is found that the land use of the west and the east sides are much more advanced (agricultural area, irrigating water etc.).

In tropical seasonal forest zone, LWCI is useful index for zoning water availability of

vegetation area and for analyzing the phenological dynamics dry season. However, in case of comparison among pixels, it is necessary to consider the crown density and other factors that related to leaf density.

5. CONCLUSION

1) The LWCI enables us to examine the relation between the satellite data and the ground truth data owing to its characteristic of physical quantities.

2) The TM channels used for LWCI calculation are channel 4 and 5, which are not susceptible to influences from the atmospheric noise. Therefore, LWCI is suitable for the comparison of seasonal fluctuation of vegetation condition.

3) Regional water condition map can be created using multi-temporal LWCI images. This map may supply the approach to understand water environmental changes in the tropical monsoon forest such as defoliation, evapotranspiration so on that correspond to its phenological dynamics.

4) Integrating various kinds of GIS data such as DEM and satellite LWCI image, it is possible to conduct environmental gradient analysis of a target area to get useful information about the landuse(e.g.vegetation type, planted species, etc.).

ACKNOWLEDGEMENTS

This work was performed on the subject of environmental change analysis with forest monitoring information by the cooperative system for supporting priority research of Japan Science and Technology Agency. We wish to thanks the counterparts of Royal Forest Department and National Research Council of Thailand for collaboration and the data providing.

REFERENCES

Boyd,D.S.,Foody,G,M.,Curran,P.J.,Lucas,R.M.,and Honzak,M.,1996. An assessment of radiance in Landsat TM middle and thermal infrared wavebands for the detection of tropical forest regeneration. Int.J.Remote Sensing,17, pp.249-261.

Raymond Hunt, Jr.E.,Barrett,N.R.,Park,S.N., 1987. Measurement of Leaf RelativeWater Content by Infrared Reflectance.Remote Sensing of Environment,22, pp.429-435.

Inoue, Y., 1993. Non-destructive Estimation of Water Status of Intact Crop Leaves Based on Spectral Reflectance measurements,Jpn.J.Crop Sci., 62(3), pp.462-469.

Sawada H., H. Saito,Y.Hirata and G. Takao., 1995.Characteristics of seasonal changed of forests observed by satellites,Proceedings of the international workshop on "The Changes of Tropical Forest Ecosystems by EL Nino and Others". pp.241-246.

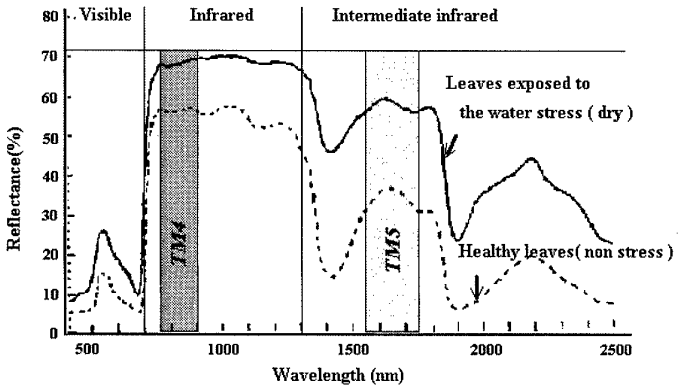


Fig.1 The spectral reflectance curve of the leaves exposed to the water stress and non stress.

---- RWC(Relative water content)=99.2%, —— RWC=12.2%

(Inoue, et al, 1993, material: peanut)

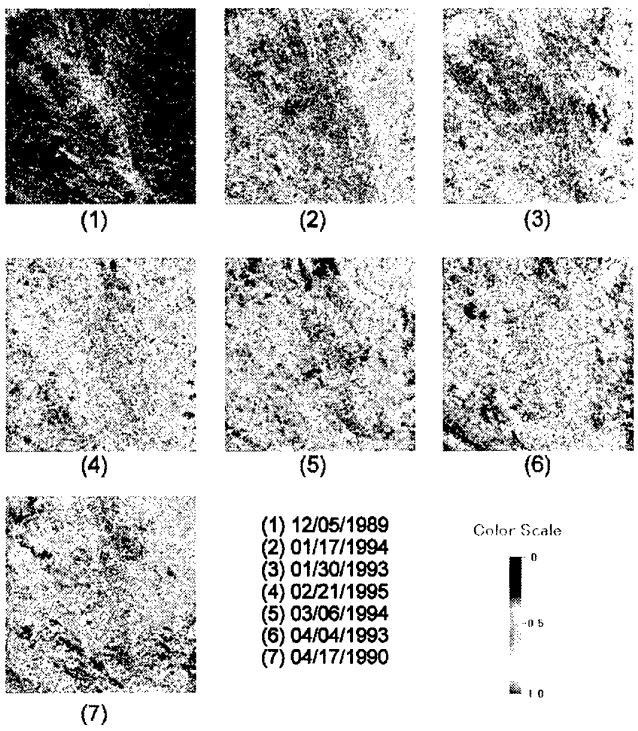


Fig. 2 Seasonal Change Images of LWCI in Kanchana Buri

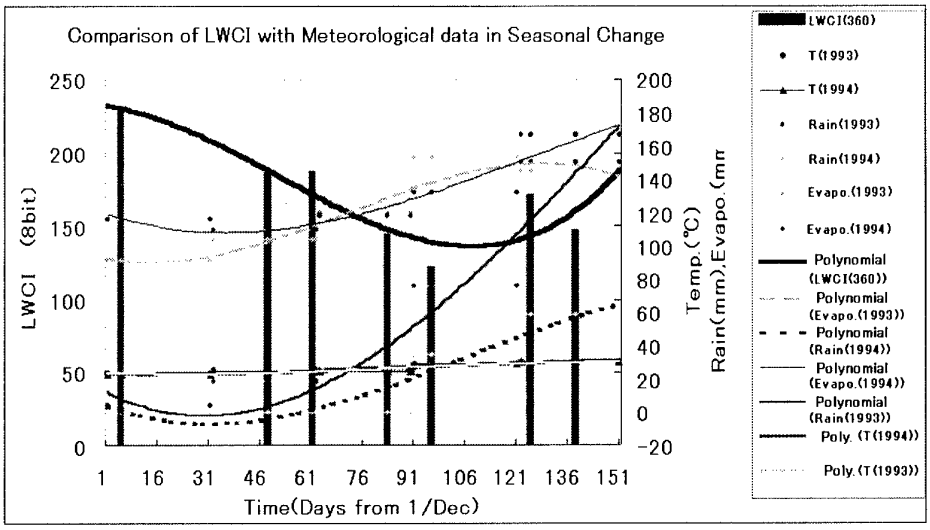
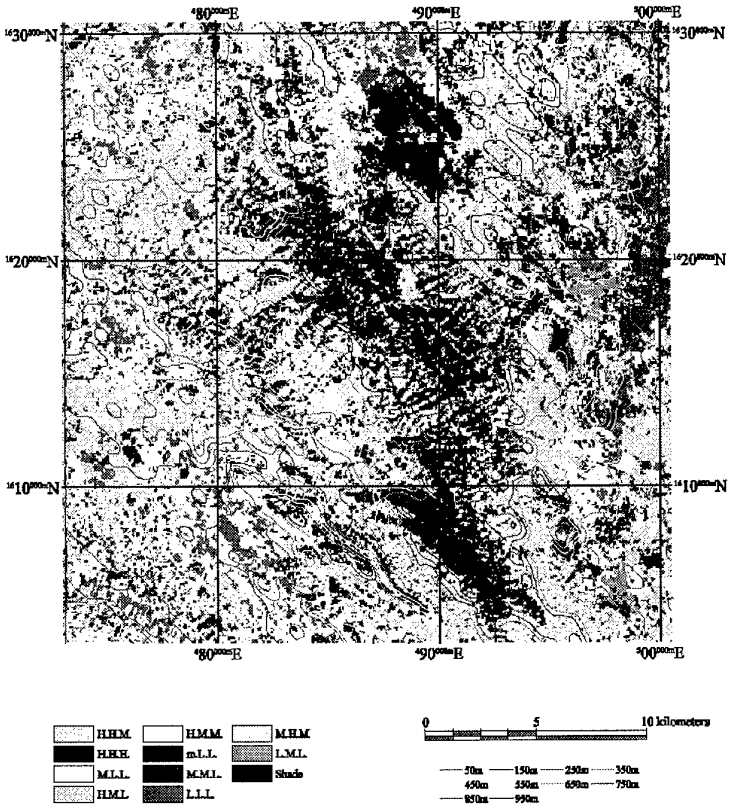


Fig.3 Comparison of LWCI with Meteorological Data in Seasonal Change



Legend: LWCI Change Pattern Class (e.g. H.M.L. means high LWCI value in the early, middle value in the middle, low value in the last stage)

Fig. 4 Water Availability Map derived from LWCI in North East side of Kanchana Buri study area

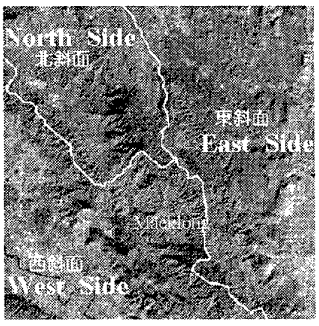


Fig. 5 The Study Area is geographically divided into 3 Watersheds (above)

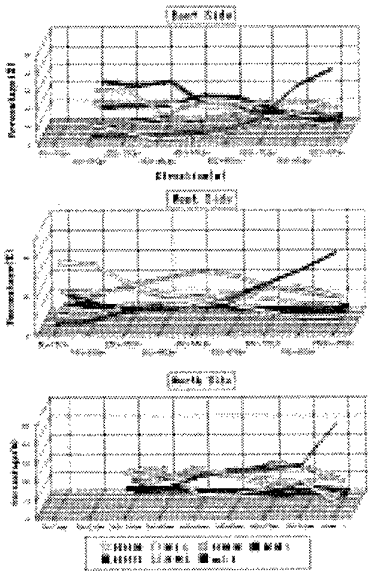


Fig. 6 Correlation between Water Availability Classes and Elevation at the 3 Watersheds (right)

APPLICATION OF ECOSYSTEM MANAGEMENT DECISION SUPPORT SYSTEM IN SELECTING SUITABLE SITE FOR TAIWANIA

Su-Fen WANG (Taiwan)
Graduate student, Department of Forestry , National Taiwan University
Department of Forestry, National Taiwan University,106 Taipei, Taiwan
Telephone: +886-2-23638044 Facsimile: +886-2-23638044
E-mail: d7625009@ms.cc.ntu.edu.tw
Yeong-Kuan CHEN (Taiwan)
Professor , Department of Forestry , National Taiwan University
Department of Forestry, National Taiwan University,106 Taipei, Taiwan
Telephone: +886-2-23639799 Facsimile: +886-2-23639799
E-mail: ykchen@ccms.ntu.edu.tw
Chi-Chuan CHENG (Taiwan)
Deputy Director, Taiwan Forestry Research Institute
53, Nanhai Road, Taipei 100, Taiwan
Telephone: +886-2-23039978 Facsimile: +886-2-23757469
E-mail: cccheng@serv.tfri.gov.tw

KEY WORDS: EMDS, ecosystem management, species determination

ABSTRACT: Ecosystem management has become the mainstream of contemporary forestry. Ecosystem management involves a variety of different issues and is an adaptive management approach that is able to adapt to temporal changes in needs. Therefore, a computer is needed to process complex data, and to integrate knowledge of various disciplines in order to develop decision support system for use in decision making for forestry. EMDS (Ecosystem Management Decision Support) is a decision support system for ecosystem management developed by the USDA Forest Service. The system integrates knowledge-based ecological and geographic database with geographic information system to build a dynamic decision support system that allows the user to easily modify the size of study area and criteria for assessment. Taiwania (*Taiwania cryptomerioides*), distributed in mid-elevation areas, is one of the most important native coniferous species in Taiwan. This species is worthwhile planting because it grows well and rarely gets infected with disease. In this research, the Luikuei Experimental Forest was selected as the study site. Using the topographic and soil data, suitable sites for Taiwania were selected according to the fuzzy logic provided by the EMDS knowledge base. It is expected to improve the traditional map overlaying method, which has the drawback of being not objective when determining the levels for suitability analysis. The results will be used as reference for the forest managers to select tree species for plantation.

1. INTRODUCTION

The main job of forest ecosystem management is to make the forest resource well arranged and used. The ecosystem principles are applied to fit the objectives of economic and social needs. For managers, the process of resource arrangement and using involves a series of decision making. All kinds of decision support systems are being developed as the computer techniques continue to improve. The ecosystem researchers are trying to solve the dynamic and complex problems by computer simulation and analysis.

The purpose of ecosystem management is to maintain the diversity and sustainable development of forest resource. Forest ecosystem management is the guideline of the forest management in

Taiwan now. According to the principle of sustainable management, forest land must be classified for multi-purposes such as economics, protection, and recreation. Long-rotation and deep-root species must be planted for the needs of watershed management.

Taiwania (Taiwania cryptomerioides), distributed in mid-elevation areas, is one of the most important native coniferous species in Taiwan. This species is worthwhile planting because it grows well and rarely gets infected with disease. In this research, the Luikuei Experimental Forest was selected as the study site, and EMDS (Ecosystem Management Decision Support) was used as the tool to perform suitablility analysis for Taiwania. The result was compared with the real situation to evaluate the feasibility of the EMDS in suitablility analysis.

2. MATERIALS AND METHODS

2.1 Study area, data, and tools

The Liukuei experimental forest of the Taiwan Forestry Research Institute was selected as the study area, which is located at Maolin, Kaohsiung County. The study area encompasses 25 forest compartments, and covers about 9616 ha. Average temperature is 16 to 23 degree Celsius, total annual rainfall is about 2150~3748 mm, and elevation is between 350~2400 km. Main forest type is natural broad-leaf forests, and there are coniferous and mixed-forests at high elevation.

The data used in this study are listed as the following:
(1) Soil data: The soil data were collected by the soil inventory team.
(2) DTM: The DTM data was obtained from the Agriculture and Forestry Aerial Survey Institute, with a pixel resolution of 40 40 meter. The slope map, aspect map were derived from the DTM data.
(3) Areial photographs: A 1/5000 scale forest type map was made from aerial photographs. Positive films of the photographs were scanned into digital images and the features of landscape were identified.
(4) The software used in this study were ArcView Version 3.1 and EMDS Version 2.0.

2.2 Analysis method

Topographic and soil characteristics are the main factors that influence the vegetation habitat. Topographic factors include the elevation, slope, and aspect. Elevation affects the temperature, aspect affects the insolation, and slope affects the washout and insolation of the habitat. In this research, elevation, slope, and aspect were grid-based, which were produced from the DTM. Each grid can be treated as a single unit, but it seems too small to characterize the concept of landscape scale for the ecosystem research. It took much more time to process data than using watershed unit. Grid unit is used only when it is specially required or the study area is small, and grid data must be converted to vector format and suitable unit must be selected.

First order watershed was selected as basic unit to establish the database of ecosystem. According to the results of previous researches, environmental factors related to Taiwania growth in different levels were selected to build the dependency network and data links. Data links are frequently used to represent data and evaluate their degrees of membership based on the concept of quantitative fuzzy argument. All the data are standardized to 1~-1, which is called truth-value. Where 1 means the environmental condition is completely suitable for the Taiwania; on the other hand, -1 means not suitable. This dichotomy is improved by fuzzy logic and compensation of ecological factor is better represented by fuzzy algorithm. For example, proper soil will compensate the weakness of topographic condition. This can't be shown in traditional overlay

approach.

Taiwania is distributed between 1000~2000km in elevation in the Luikuei Experimental Forest, but grows better between 1200~1700km. According to the forest type inventory in the study area, the planting sites with better quality are listed as Table 1. It shows that the suitable slope for Taiwania is from 15 degree to 45 degree, but must be constrained under 35 degree when considering the working sites permissible. As for the aspect, though some references show Taiwania was distributed in South, the sunlight was compensated in this study area, because it's nearby tropical. Because Taiwania can be found in all the aspects, so the aspect factor was abandoned in this study.

Table 1. Distribution of Taiwania in the study area.

Forest compartment	Plantation area (ha.)	Elevation (m)	Aspect	Slope (degree)
2	38.5	1500-1600	North-West	20-40
2	40	1500-1600	North-West	20-40
2	12.9	1000	North-West	20-40
3	58	1500-1600	South-West	20-30
3	20	1500	South-East	20-35
3	61.3	1300-1500	South-West	20-35
3	26.5	1400	South-West	20-35
10	24	1400	South-East	20-30
12	24.8	1450	South-East	20-30
12	25	1500	South-East	20-30
12	23.7	1300	South-East	20-30
12	18.5	1500	North-East	15-25
12	19.2	1500	North-West	15-30
12	15	1300	North-West	15-30
13	47.4	1500	North-East	20-40
13	24.1	1600	North-West	20-45
14	41.3	1500	South-East	25-40

Soil type determines soil characteristics such as texture, water drainage, and nutrient. Soil type was selected in this study, and soil inventory book was used as reference to select soil type. Soil types such as Fcs, Mls, Nsa, Nsa-Ycl, Stm, Wss, Ycl, Gts-Mls, Stm-Ycl, Wss-Ycl are with sandy-loam texture, well water drainage and suitable for planting, were selected.

3. RESULTS

When topographic factors were considered, most of the study area were included in the result because the average values were used for first order watershed unit, and the values were too rough to determine the species (Fig. 1). Therefore, soil factors must be selected in species determination.

From another perspective, the species determination is a local and small-scale forest management programming when considering scale, therefore the micro condition of habitat must be considered (soil, micro-climax…etc).

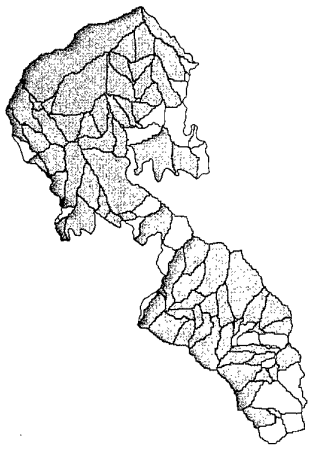


Fig.1 Suitable sites selected using topographic factors.

When soil factors were added to the EMDS assessment, the suitable sites were reduced and more detailed information was shown in the resulting map. (Fig.2)

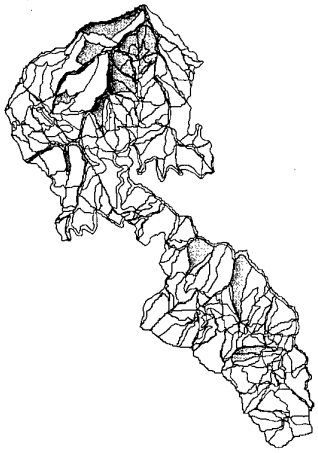


Fig.2 Suitable sites selected using topographic and soil factors.

The results were compared with the real Taiwania distribution (Fig.3). In the northern part of the study area, most areas of distribution match with each other quite well. It shows that it is feasible to apply EMDS in species determination. As to the southwest part of the study area, there are some Taiwania distributed in the real world but are not suitable based on EMDS analysis. Perhaps the Taiwania isn't the suitable species in the southwest part, because the growth of Taiwania there is under average. At last, the southeast part is suitable based on EMDS analysis but no distribution was found in the real world. It suggests that the manager can try to use Taiwania as the planting species in this part.



Fig.3 Distribution of Taiwania in Luikuei Experimental Forest

4. DISCUSSION

Though this study shows the value of EMDS in suitability analysis, there is still some problem with respect to the analysis units. The analysis units in the resulting map are complex, and the locations and boundaries are difficult to define in real world, which may cause the work difficult. The common units must be created in order to build the database for ecosystem decision support system.

First order watershed unit and soil unit were used because the choice of species is a type of small scale ecosystem management. For incorporating the ecological issues at different scales in EMDS, all the units must be converted to match the corresponding watershed unit, which is used as the basic unit.

5. CONCLUSION

The following conclusions can be drawn from this study:

(1) It is feasible to apply EMDS in species determination in Taiwan. As for large scale forest planning, more complex factors must be considered, and more perspectives such as economics, society, must be involved.
(2) Topographic factors are too rough to determinate the species, because the species determination is a local forest programming. Data scale must be selected carefully to match the study issues.

REFERENCE

Cheng, CC. ,1995. GIS application in forest land classification. Taiwan Journal of Forest Science, 10(2), pp. 241-54 [in Chinese with English summary].
Densham, P.J. and M.F. Goodchild, 1989. Spatial decision support system : A research agenda. GIS/LIS Proceedings, Vol. 2. pp. 707-716.
Herrington, L.P. and D.E. Koten,1988. A GIS based decision support system for forest management. GIS/LIS'88 Proceedings, Vol. 2. pp. 825-831.
Jeng H. D., 1994. A Research on Spatial Decision Support System --Designing A System for Land Use Models Building Assistant Environment. [MSc thesis]. National Taiwan University,

Taiwan. [in Chinese with English summary].
Keith M.Reynolds, EMDS User's Guide (Version 2.0)
Lai H.Y., 1995. DTM, GIS applications in planning water conservation protected forest [MSc thesis]. National Taiwan University, Taiwan. 131 p. [in Chinese with English summary]
Meulen, G..G.., 1992. Geographical information and decision support system, Computer, Environment and Urban Systems, 1(16), pp. 187-193.
Robert H.G. et al., 1987. Neutral models for the analysis of broad-scale landscape pattern. Landscape Ecology, 1(1), pp. 19-28.
Salwasser H, and R.D. Pfister, 1994. Ecosystem management: from theory to practice. In: US Department of Agriculture, Forest Service, editor. Sustainable ecological systems: implementing an ecological approach to land management. Gen.Tech.RM-247, Rocky Mountain Forest and Range Experiment Station, 363 p.
Shrestha,B.P. and Duckstein L., 1998. A Multiobjective Decision Support System Multiresource Forest Management. Group Decision and Negotiation, Vol.7. pp. 23-40.
Sharpe, D.M. and Yang, Z., 1991. Design of buffer zones for conservation areas and a prototype spatial decision support system(SDSS). GIS/LIS'91 Proceedings, Vol. 1. pp. 60-70

Forest Fire Monitoring with SPOT-4 Satellite Imagery

Kim Hwa LIM, Leong Keong KWOH, Soo Chin LIEW and Hock LIM

Centre for Remote Imaging, Sensing & Processing, National University of Singapore
Lower Kent Ridge Road, Singapore 119260
Tel: (65) - 874 4411, Fax: (65) – 775 7717, Email: crslimkh@nus.edu.sg

Key Words: Forest Fire, SPOT-4, Calibration and Temperature

ABSTRACT

This paper assesses the advantages of using SPOT-4 in forest fire monitoring. During the active fire period of 4-16 July 2000, many fires were detected in Sumatra, Indonesia. We found that the SPOT-4 432 representation (i.e., SWIR(4), NIR(3), and Red(2) bands in RGB display channels respectively) is especially effective for fire detection as active fire shows up distinctively as bright red patches and smoke plumes appear in faint bluish colour. However, in the usual 321 representation for SPOT-1 and SPOT-2 (i.e., NIR(3), Red(2), and Green(1) bands in RGB display channels), fire can only be detected from its smoke plume. One disadvantage of the SPOT-4 432 representation is that the smoke plumes tend to be too thin for the purpose of determining the size of the plumes. Thus, we propose a new way of displaying the SPOT-4 images. This is achieved by replacing the NIR band by the average of NIR and Green bands in the 432 representation. With this new representation, both the active fires and smoke plumes are clearly visible. Attempts have also been made to estimate the temperature of the active fires from the radiance detected in the SWIR band.

1. INTRODUCTION

Since the 1997/98 forest fire episode in South East Asia, the Centre for Remote Imaging, Sensing and Processing (CRISP) has carried out daily forest fire monitoring using SPOT imagery. The high resolution SPOT images were used to detect individual fires and to determine their nature in terms of the size of the smoke plumes, their locations and the landcover of the affected area. With SPOT-1 and SPOT-2 satellites, any given location in the Southeast Asia region can be observed with a repeat interval of two to three days. Ever since CRISP started acquiring SPOT-4 data in late 1999, together with SPOT-1 and SPOT-2, daily coverage of any given location in the region was made possible.

In this paper, we begin by assessing the advantages of using SPOT-4 in forest fire monitoring. The SWIR band of SPOT-4 is highly sensitive to temperature. The 432 representation (i.e., SWIR(4), NIR(3), and Red(2) bands in RGB display channels respectively) is especially effective for fire detection as active fires show up distinctively as bright red patches and smoke plume appears in faint bluish colour. This feature enables SPOT-4 to detect fires more effectively and efficiently than SPOT-1 and SPOT-2. A new way of presenting the SPOT-4 imagery is presented. The SWIR band lies in the spectral range of 1.58 to 1.78 μm. In this spectral range, radiance received by the satellite consists of both the reflected and the emitted radiances. The emitted radiance originates from the thermal radiation of the earth surface. It is highly dependence on surface temperature. Therefore, if we are able to separate the two portions of radiance, the surface temperature of active fire can be estimated.

2. SPOT-4 IN FOREST FIRE MONITORING

2.1 Forest Fires Monitoring in CRISP

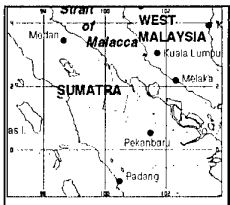
Since the forest fire episode in 1997/98, CRISP has carried out daily forest fire monitoring of the South East Asia region using SPOT imagery. The main objectives of the operation are to detect individual fires and to determine their nature in terms of the size of the smoke plumes, their locations and the landcover of the affected area. Fire detection is carried out by visual inspection of the full resolution SPOT images. In SPOT-1 and SPOT-2, fires can be identified from their smoke plumes that appear bluish white in colour. In most of the cases, they can readily be distinguished from clouds by their characteristic shapes. However, when the smoke is not thick enough or the cloud is too low, it is rather difficult to distinguish between the two. Once the fires are detected, a full SPOT scene covering the fire areas is processed to Level 1B. A fire report containing the locations (lat/lon), smoke plume conditions (length, width and thickness), wind directions of each detected fire is also made. When both the scene and the report are ready, they are sent to Ministry of Environment.

2.2 Fires in SPOT-4

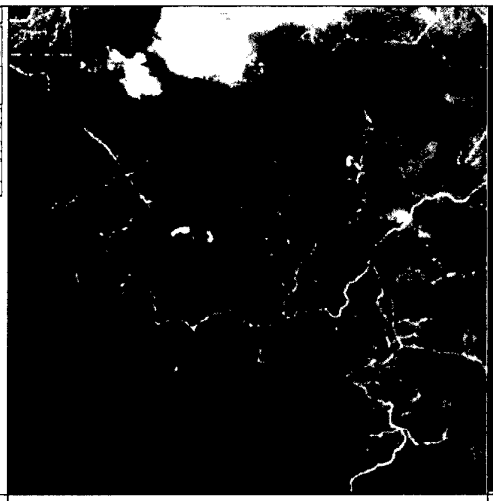
SPOT-4, the fourth member of SPOT family, was launched in March 1998. It was only at late 1999 that CRISP started acquiring the SPOT-4 data. Together with SPOT-1 and SPOT-2, daily coverage of any given location in the region was made possible. The High Resolution Visible and Infra Red Instrument (HRVIR) of SPOT-4 satellite has four channels. The first three channels are identical with those of the previous SPOT system. The fourth channel lies in the spectral range of 1.58 to 1.78 μm, which is the short-wave infrared region of the spectrum. In this spectral range, satellite signal is relatively unaffected by atmospheric conditions. This unique feature has enabled SPOT-4 to capture relatively clear image. The SWIR is also very sensitive to high temperature. This is the major advantage of using SPOT-4 in forest fire monitoring.

One of the most commonly used colour composites of SPOT-4 is the 432 representation which is obtained by putting SWIR (4) in red, NIR (3) in green and RED (2) in blue. In this representation, vegetation appears green, fires appear as bright red patches and smoke plumes appear in faint bluish streaks. As compared to SPOT-1 and SPOT-2's 321 representation (i.e. NIR (3), RED (2) and GREEN (1) in RGB display), in which vegetation appears in red and smoke plumes appear in bluish white, the 432 representation is closer to natural colour. Unlike SPOT-1 and SPOT-2, fires can only be detected from their smoke plumes, which is sometimes rather difficult to be discriminated from cloud or haze. With SPOT-4's 432 representation, active fire that appears bright red in colour can easily be detected from its surrounding green vegetation and brownish burnscar.

During the period of 4-16 July 2000, many fires were detected in Sumatra and Kalimantan of Indonesia. Some of the fires can only be detected by SPOT-4. In figure 1, the big fire on the top left corner is clearly visible in both representations. However, small fires indicated on the right image can only be detected by SPOT-4's 432 representation. In figure 2, in this cloudy image, there is no clear indication of fires on the left image. However, fires still show up distinctively as bright red patches in between clouds.



Fires detected at Sumatra, Indonesia On 07 July 2000



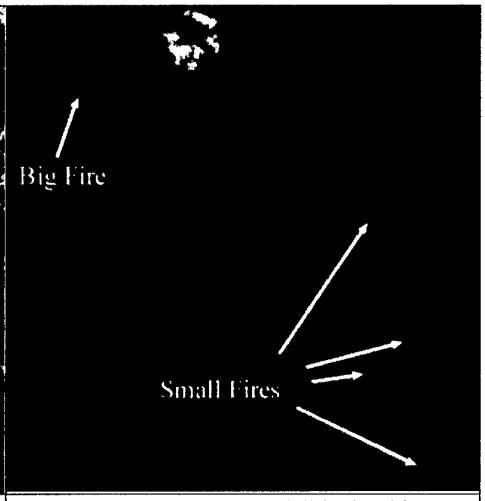
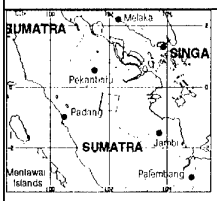


Figure 1

In this standard 321 representation, only big fire (the one at the top left corner) can be identified from its smoke plume.

Small fires still clearly visible in this 432 representation.



Fires detected at Sumatra, Indonesia On 13 July 2000

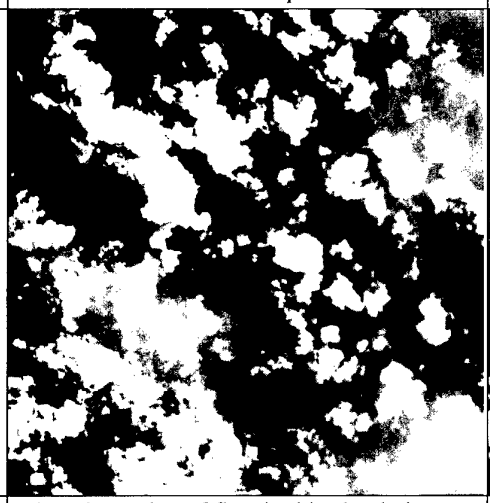




Figure 2

There is no sign of fires in this cloudy image.

Fires showed up distinctively as red patches in between clouds.

2.3 New Representation

One disadvantage of the 432 representation is that the smoke plumes tend to be too thin for the purpose of determining the size of the plumes. Thus, we propose a new way of displaying the SPOT-4 images. This is achieved by replacing the NIR band by the average of NIR and Green bands in the 432 representation. In this manner, both the active fires and smoke plumes are clearly visible. In figure 3, the new way of displaying scheme is applied to the same image displayed in figure 1. The smoke plume of the big fire on the top left corner is now clearly visible as compared to the right image shown in figure 1.

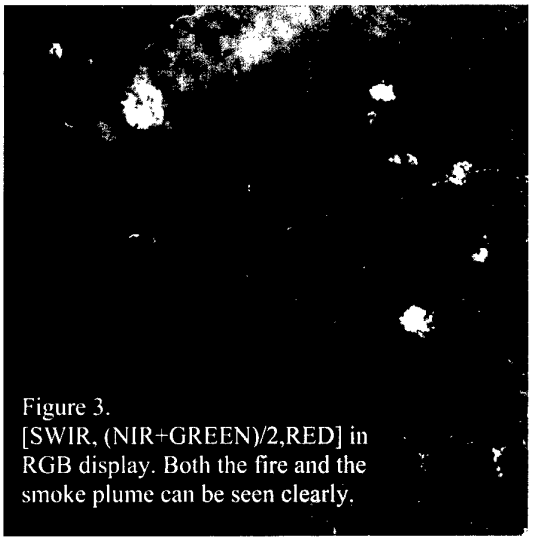


Figure 3.
[SWIR, (NIR+GREEN)/2,RED] in RGB display. Both the fire and the smoke plume can be seen clearly.

3. ESTIMATION OF TEMPERATURE

3.1 Radiance Received

The radiance received by the satellite can be written as

$$L_t(\lambda) = L_p(\lambda) + L_r(\lambda) + L_e(\lambda)$$

where $Lp(\lambda)$ is the path radiance resulting from multiple scattering of solar radiance by air molecules and aerosols, $Lr(\lambda)$ is the solar radiance reflected from the ground and Le is the thermal radiation emitted by earth surface. Both the reflected radiance Lr and emitted radiance Le have suffered from atmospheric attenuation. However, in SWIR band, the atmospheric effect can be ignored as far as this paper is concerned. The emitted radiance can be modelled by Planck's radiation equation

$$L_e(\lambda) = \frac{2hc^2}{\lambda^5 \exp(hc/(\lambda kT - 1))}$$

where h is the Planck constant, c is the speed of light, k is the Boltzmann's constant and T is the absolute temperature. The reflected radiance depends on the ground reflectance and solar radiance falling onto it.

3.2 Radiometric Calibration of SPOT-4

According to the SPOT's interface document, the level 2A image of SPOT-4 can be calibrated to physical radiance by

$$L = X / AG$$

where X is the digital value of level 2A image, A is the absolute calibration coefficient and G is the programmable gain. Both A and G can be found in the leader file.

3.3 Effective Wavelengths

In order to use Planck's equation to estimate the temperature, we need to know what wavelength to use in the equation. The effective wavelength, λe is the one which best fit the following equation

$$\frac{2hc^2}{\lambda_e^5 \exp(hc/(\lambda_e kT - 1))} = \frac{\int f(\lambda) L(\lambda) d\lambda}{\int f(\lambda) d\lambda}$$

where $f(\lambda)$ is the spectral response of the SWIR band as shown in figure 4. The equations are computed with T range from 273 to 373 K. The effective wavelengths for band 4 of instruments HRVIR1 and HRVIR2 are found to be 1649 nm and 1635 nm respectively.

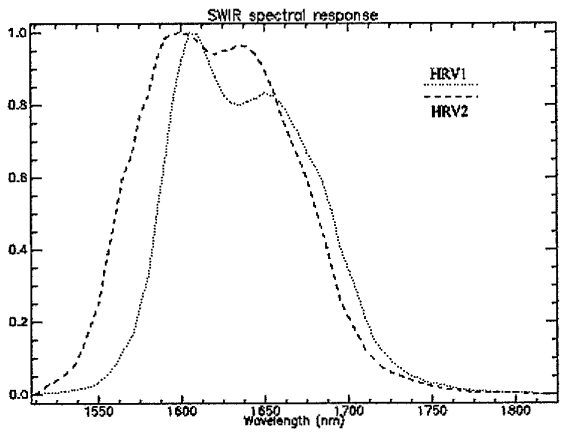


Figure 4 SWIR Spectral responses of the two HRVIR instruments

3.4 Image Used

The image used in our study is the one shown in figure 1. The image was acquired on 7 July 2000 with instrument HRVIR2. The absolute calibration coefficient A is `5.49300` and the programmable gain G is `1.5`. The digital value X of the big fire on the top left corner (refer to figure 1) is about `252`. With this value, the corresponding radiance is computed to be `30.58` W/m2/sr/μm.

3.5 First Attempt in Temperature Computation

We first assume that the emitted radiance *Le* dominates the total radiance. This is motivated by the fact that most of the active fires can easily have temperature up to a few hundred degrees Celsius. Under this circumstance, the emitted thermal radiance is larger than the reflected radiance by a few order of magnitude.

Therefore, the emitted radiance is taken to be `30.58` W/m2/sr/μm. Since the image was acquired using HRVIR2, the effective wavelength λe is `1.636` μm. With these values, the temperature is readily be computed from the Planck's equation

$$T = \frac{hck}{\lambda_e \log(1 + 2hc^2 / \lambda_e^5 L_e)}$$

The temperature computed is `331.34` K that is equal to `58.34` °C.

3.6 Second Attempt in Temperature Computation

In our first attempt, the temperature computed is merely 58 °C which is far below a few hundred °C. This renders our assumption that the emitted radiance dominates the total radiance invalid. Therefore, we need to estimate the reflected radiance *Lr* of the active fire so that we can subtract it from the total radiance.

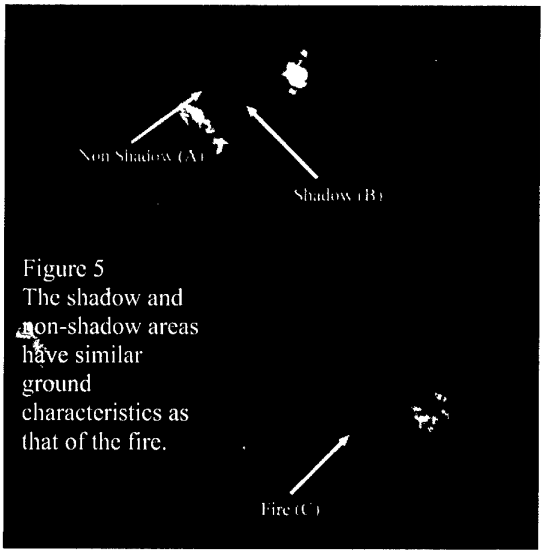


Figure 5
The shadow and non-shadow areas have similar ground characteristics as that of the fire.

In figure 5, the shadow as indicated has a relatively low radiance than the surrounding non-shadow area. Therefore, the total radiance in this area is dominated by the emitted thermal radiance. Hence, we can use it as a reference to estimate the reflected radiance of a similar area.

The total radiances of the two areas A and B as shown in figure 5 can be written as

$$L_t(A) = L_r(A) + L_e(A)$$

$$L_t(B) = L_e(B)$$

Here we have assumed that reflected radiance of area B is negligible as compared to the emitted radiance. Since the two areas have similar ground characteristics, we further assume that the emitted radiances of the two areas are the same. Therefore, we can compute the reflected radiance of these areas by taking the difference between the two total radiances.

We find that the reflected radiance *Lr* of area A is about 9.30 W/m2/sr/μm. Hence we estimate that the emitted radiance *Le* of the fire C is 21.28 W/m2/sr/μm which is obtained by subtracting 9.3 from the total radiance of 30.58. With this value, the temperature of the active fire is found to be 53.34 °C.

The relatively low value of temperature may be due to the fact that in the 20x20m pixel only a small part of the area was actively burning. Therefore, the surface temperature computed is just the average temperature of the entire 20x20m area.

3. CONCLUSIONS

The temperature sensitive SWIR band has rendered SPOT-4 to be more effective and efficient in forest fires monitoring. Even small fires, which do not have smoke plumes at all, can be detected in SPOT-4's 432 representation. Another advantage of SPOT-4 is that the SWIR band is relatively unaffected by atmospheric effects, therefore fires under thin cloud or haze can still be detected. One setback of SPOT-4's 432 representation is that the smoke plumes tend to be too thin for the purpose of determining the size of the plumes. A new display scheme in which SWIR, (NIR+GREEN)/2, RED bands display in RGB channels respectively, are found to be more suitable in forest fires monitoring. Under this scheme, both fire and smoke plume are clearly visible. The total radiance of the SWIR band consists of the reflected and the emitted radiances. We found that by comparing two areas, one with shadow and another without, the reflected radiance of the active can be estimated. With this, the temperature of the active fire is found to be about 53 °C.

REFERENCES

[1] S. C. Liew, O. K. Lim, L. K. Kwoh and H. Lim, "A study of the 1997 forest fires in South East Asia using SPOT quicklook mosaics", *Proc. 1998 Int. Geosci. Remote Sensing Symp.*, Vol. 2, 879-881, 1998.

[2] S. C. Liew, L. K. Kwoh, K. Padmanabhan, O. K. Lim and H. Lim, "Delineating land/forest fire burnt scars with ERS interferometric synthetic aperture radar",. *Geophysical Research Letters*, 26(16), 2409-2412.

[3] V. Trichon, D. Ducrot and J. P. Gastellu-Etchegorry, "SPOT4 potential for the monitoring of tropical vegetation. A case study on Sumatra", *Int. J. Remote Sensing,* 20(14), 2761-2785, 1999

STUDY ON THE RELATIONSHIP AMONG THE *MACHILUS* SPECTRAL BEHAVIOR AND LIGHT INTESITY AND PHYSIOLOGICAL ACTIVITY

Chinsu LIN
Assistant Professor, Department of Forestry
National Chiayi University
300 University Road, Chiayi (600)
Tel: (886)-5-2717476 Fax: (886)-5-2717467
Chinsu@mail.ncyu.edu.tw
TAIWAN

KEY WORDS: Spectral Behavior, Light Intensity, Photosynthetic Rate, *Machilus zuihoensis var. zuihoensis*, Remote Sensing

ABSTRACT: Spectral reflectance characteristic of plants was determined by many factors, such as leaf structure, pigment concentration, canopy structure, biomass, sunlight, atmospheric conditions, and so on. Among which plant parameters should be the most important bases for vegetative detection or monitoring senses. In this paper, one hardwood species, *Machilus zuihoensis var. zuihoensis* was selected to be research material. Reflected hemisphere irradiance was measured from five samples. Photosynthetic rate and light intensity were also measured in the same time of irradiance measurement. This study focuses to understand the relationship among the spectral behavior and light intensity and physiological activity, especially the photosynthesis. Spectral behavior for different wavelength was also analyzed. The results are considered to be benefit for natural resources monitoring or detecting by remote sensing.

1. INTRODUCTION

Multi-spectral data have been applied in natural resources researches for more than 20 years whereas their classification accuracy, in general cases, are not very high enough to satisfy the needs for planning the environmental and natural resources management. Especially for the cases of range area, spectral characteristics of vegetation become more sophisticated due to the terrain effect and vegetative variations, such as changeable crown density and its structure, and mixed trees in stand in a pixel, and so on. The spectral band width limitation of multi-spectral data now is overcome. Hyperspectral data that have very narrowed spectral intervals and coded as 2 bytes digital number, give us the chance for understanding the spectral behavior of targets. Vegetation, the living organism, may reflect the incident radiation according to their physical and physiological properties and hence it is more difficult to know how is the interaction between the light and vegetation in view of reflectance or reflected radiance – the major senses of remote sensing.

The process of plant uptake carbon dioxide from the air and water from the soil to produce nutrients for its growing is so call as photosynthesis and is one of the most important physiological activities of plant. This process takes place only in the existence of light. The reflected radiance of a plant is therefore related with the light intensity and photosynthetic rate and the organization of plant canopy, a group of branches and leaves. To understanding the interaction between the light and leaf physiological process, a tree named as *Machilus* was selected for measuring the reflected radiance from its leaf. Light intensity and photosynthetic rate are also measured in the same time of radiance measurement. In the mean while the concentration of chlorophyll is also analyzed in the laboratory.

2. MATERIALS AND METHODS

2.1 Materials and Instrument Description

Both *Lauraceae* and *Fagaceae* plants are the most important and dominant vegetation for the middle elevation mountainous area in Taiwan. ***Machilus zuihoensis var. zuihoensis***, a *Lauraceae* plant is one of the governmental assigned reforestation plants and hence several two-year old potted *Machilus* seedlings were selected as the study material. A portable spectroradiometer, LI-1800, is applied to obtain spectral radiation data of the plant. Figure 1 shows the LI-1800 optional diagram. The cosine receptor is designed to collect the radiant flux according to the cosine of the incident angle based on the Lambert's cosine law and accept radiation from all angles of a hemisphere. Therefore the LI-1800 measures the irradiance (watts.m^{-2}.nm^{-1}) under such consideration and is the case applied in this study. It also can be set to recording data in radiance (watts. m^{-2}.nm^{-1}.sr^{-1}).

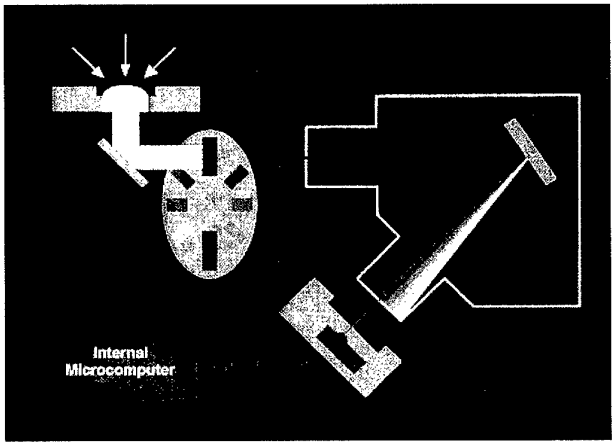


Figure 1. Operational diagram of LI-1800 spectroradiometer (adopted from LI-COR, 1989).

2.2 Configuration of Irradiance Measurement

For purifying the circumstances of reflected radiance measurements of vegetation, the remote cosine receptor and the LI-1800 is connected by a fiber probe and is settle to beneath the *Machilus* leaf to avoid the noises influence from canopy structure and background. Figure 2 depicts such configuration of the irradiance measurements. Because the measurements are made under plant canopies, it is therefore that what the machine recorded is irradiance and hence could reflect the leaf reflected irradiance amount. This study also adopted an accurate cosine correction for each measurement to avoid a significant error occurrence, that is dividing the cosine receptor scanned irradiance data (watts.m^{-2}.nm^{-1}) file by the instrument internal COSC file (LI-COR, 1989). Both photosynthetic photon flux density (PPDF) and illuminance (lux) is also calculated in each scan of leaf reflected irradiance. The value of PPDF and illuminance is then used for representing the photosynthetic rate of leaf and the light intensity from the hemisphere.



Figure 2. Configuration of leaf reflected irradiance measurement (adopted form LI-COR, 1989)

3. RESULT

3.1 Relationship between Photosynthetic Rate and Light Intensity

Relationship between leaf photosynthetic rate (Pn rate) and incident light intensity (Lux) was examined by regression method. The Pn rate could be more precisely estimated by light intensity in a parabolic regression equation in view of the determination coefficient (R^2) of the regression line showed in figure 3a (left plot). More robust relations of those two variables could be achieved by standardization method. Figure 3b (right plot) depicts such stronger relationship of both standardized Pn rate and light intensity. R^2 of the linear and the 2 orders polynomial equation is 0.8025 and 0.9225, which is large than the equations build from the original variables about 12 percent and 7 percent. Most important logically meaning of the standardized Pn rate and standardized light intensity relationship is that the polynomial regression line describes leaf Pn rate is increasing positively with the light intensity until the light intensity approaching a critical value where only little marginal effect of photosynthesis will happen. This is evident from the solid curvature line of figure 3b and is agree with the cases of Kramer and Kozlowski (1979).

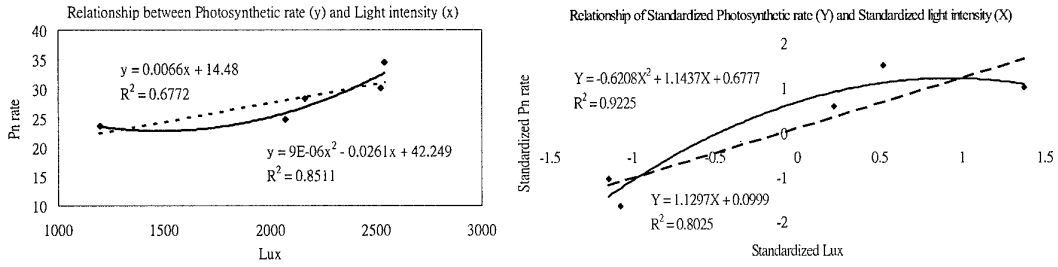


Figure 3. Relationships between the photosynthetic rate (Pn) of *Machilus* leaf and hemisphere light intensity (Lux). Left plot (a) and right plot (b) shows the fitted regression lines derived from the original variables, Pn and Lux, and their standardized variables.

3.2 Spectral Behavior of *Machilus* Leaf

The reflected irradiance (watts.m^{-2}.nm^{-1}) of *Machilus* leaf starting from 300 nm and ending at 1100 nm is recorded by a wavelength (λ) interval of 2 nm and is depicted in figure 4. Patterns of the reflected irradiance (RI) curves (peak-and-valley) around the wavelength of the five samples are almost identical to the ones of a healthy green leaf or vegetation (Lillesand and Kiefer, 1994) and also conform to the spectral irradiance pattern of reflected radiation (LI-COR, 1982).

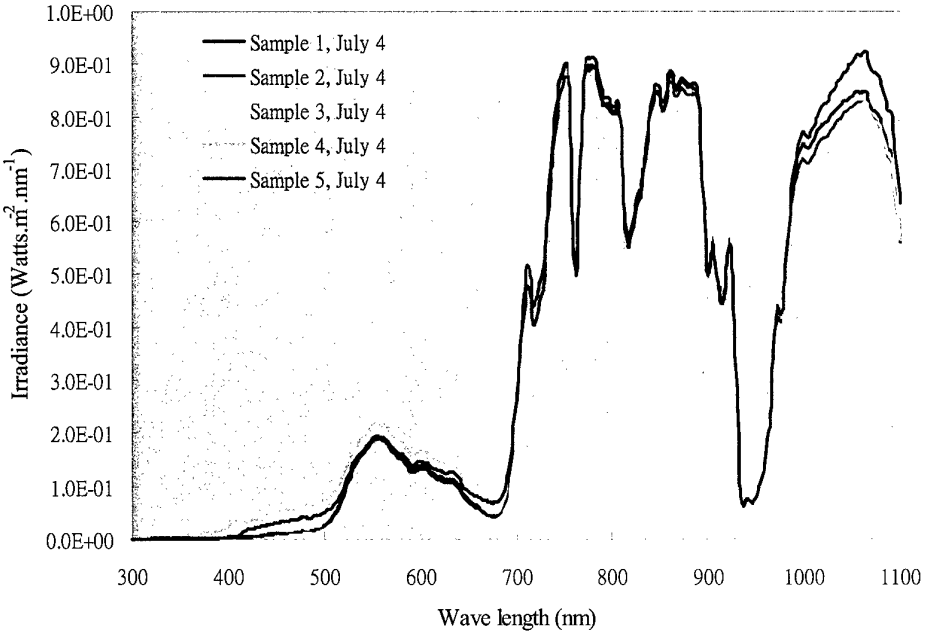


Figure 4. Reflected spectral irradiance curves of Machilus green leaves.

In briefly, leaf pigments absorb most of the incident blue ($\lambda \leq 500$ nm) and red (600 nm $\leq \lambda <$ 700 nm) energy that are known as the photon flux density for photosynthesis (Kramer and

Kozlowski, 1979). Significant RI Peak in the green is of course results from the color of leaf. The leaf RI increases dramatically in the infrared region (700 nm $\leq \lambda$). One noticeable phenomenon of RI curves is that there are several valley happened in the infrared region. Dips in RI curve occur at 760, 820, 900, 914, 940, and 1100 nm is not appeared in the reflectance curve of healthy vegetation (Lillesand and Kiefer, 1992).

3.3 Relationship among the Leaf Reflected Irradiance and Light Intensity and Photosynthetic Rate

Theoretically the squared correlation coefficient (r^2) of any two variables is identical to the coefficient of determination (R^2) of a simple linear regression equation fitted by those two variables (Eq. 1). This study therefore applied the correlation analysis method to examine if the leaf-reflected irradiance of a particular wavelength is correlated with light intensity and photosynthetic rate. A Student's ***t*** test is then used to examine if the correlation coefficient of these two variables is statistically significant under 5% significance level. The results also could be the evidence of what will the leaf-reflected irradiance depend on the wavelength variation.

$$r^2 = b^2 \frac{S_{xx}}{S_{yy}} = \frac{bS_{xy}}{S_{yy}} = \frac{SSR}{S_{yy}} = R^2 \tag{1}$$

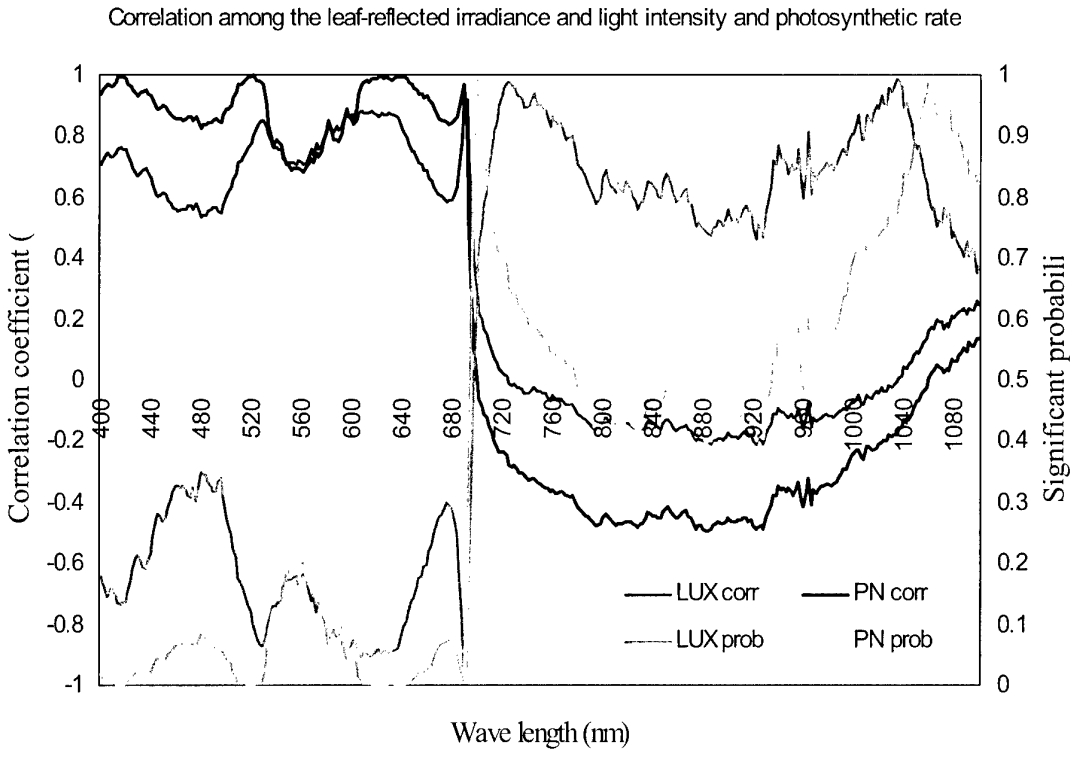


Figure 5. Relationship of the reflected irradiance and light intensity and that of the reflected irradiance and photosynthetic rate.

The correlation coefficient and its correspondingly significant probability of the leaf-reflected irradiance and light intensity (LUXcorr and LUXprob), and that ones of the leaf-reflected irradiance and photosynthetic rate (PNcorr and PNprob) for each wavebands are shown in figure 5. An interesting trend of these two correlation coefficient curves shows that a positive correlation exists in the visible area whereas a negative correlation exists in the infrared area. But the negative relationship should not be real for both case of light intensity and photosynthetic rate. Only the reflected irradiance in the range of 690-692 and 606-636 nm is significant correlated with light intensity and their correlation coefficient is about 0.90 and 0.85 respectively. While there are much of wavelength ranges (400-444, 500-532, 606-666, and 688-690 nm) whose reflected irradiance are significant correlated with photosynthetic rate and their correlation coefficients are correspondingly greater than 0.90.

4. DISCUSSION

The study results showed that leaf-reflected irradiance is significantly correlated with photosynthetic rate in partial wavelength intervals of blue, green, and red bands; and is also significantly correlated with light intensity in a relatively narrow bandwidth of red band. They both have showed the 690 nm band is a common position where the correlation between the leaf-reflected irradiance and light intensity and photosynthetic rate are statistically significant. Since the 690 nm band is located at the edge of visible and infrared bands, it could maybe widely used for vegetation researches with remote sensing techniques.

Another important result of this study is that the light intensity is not linearly correlated with leaf-reflected irradiance. This maybe give us a hint of that leaf-reflected irradiance is somewhat independent with light intensity but it should be well examined by additional new measurement or experiment to test if it will be same for the case of leaf radiance or reflectance. In the future we will also focus on studies to understand if there is a nonlinear relationship exist between the light intensity and leaf-reflected irradiance.

5. REFERENCES

Kramer, P. J. and T. T. Kozlowski. 1979. Physiology of Woody Plants. NY: Academic Press. 811pp.

LI-COR Inc. 1989. LI-1800 Portable Spectroradiometer Instruction Manual. Publication No. 8210-0030. Nebraska USA.

LI-COR Inc. 1982. Radiation Measurements and Instrumentation. Publication No. 8208-LM. Nebraska USA.

Lillesand T.M. and R.W. Kiefer. 1994. Remote Sensing and Image Interpretation. NY: John Wiley & Sons, USA.

ANALYSIS OF FRAGMENTATION AND ANTHROPOGENIC DISTURBANCES IN THE HIMALAYAN FORESTS: USE OF REMOTE SENSING AND GIS

Subrat Sharma, L.M.S. Palni
G.B. Pant Institute of Himalayan Environment & Development
Kosi-Katarmal, Almora 263 643, India
Fax: + 91 - 5962 – 31360; Email: prasad@nde.vsnl.net.in
&
P.S. Roy
Indian Institute of Remote Sensing
4, Kalidas Road, Dehradun 248 001, India
Fax: +91 - 135 – 741987; Email: psroy@del2.vsnl.net.in

KEY WORDS: District Almora, Forest, Fragmentation, Himalaya

ABSTRACT

The vastness and rugged "difficult to reach" nature of Himalayan terrain poses serious limitations on field observations; consequently field experimentation and information collection to develop regional planning is often difficult. Satellite remote sensing and GIS can be utilized to extract information through simple analyses and/or by the use of models to answer specific questions. Only limited attempts have been made to use these technologies in describing landscape dynamics for biodiversity management in the Himalaya. In the present approach forest vegetation has been explored using IRS 1C –LISS III FCC in an area of ~3167.5 km^2 (entire Almora district) and various landscape elements have been analysed. Forested area accounted for 42.2% of the total area. Most common vegetation type was pine forest (*Pinus roxburghii*), occupying 85.3% of the total forested area, but it was highly fragmentary in nature. Total 414 pine forest fragments were recorded over the entire landscape. Area of each patch varied from < 1 km^2 to 179 km^2; however, majority of fragments (77% of the total) were below 1 km^2. These smaller units are possible sites of pine forest "extinction" due to anthropogenic pressures. A greater shape index (1.1 - 9.2) was observed for pine forest fragments. Edge effect analysis of the pine forest fragments indicated that the impact area ranged from 19.9 ha to 855.7 ha. These areas are subject to microhabitat alterations without canopy cover loss. Human dependency on natural vegetation appeared to be the main cause of fragmentation. Disturbance index model revealed that about 34% of the total landscape area is under severe anthropogenic pressure as apparent from high index. RS & GIS based landscape approach is an emerging tool for identification of hot spots for biodiversity conservation in the mountains, and especially to appropriately include human dimension in the management planning.

INTRODUCTION

Mountain environment is characterized by its complexity. Large variations in climate, water characteristics, soil, and geology have, over millenia, produced a wealth of biological diversity in flora, fauna and microbes. The Himalaya are massive mountains that occupy over 1 million km^2. They produce a distinctive climate of their own and also influence the climate of much of the Asia. The Himalayan range contains some of the most spectacular biodiversity on earth, but much of it is under-explored and lacking in effective protection. The vastness and rugged "difficult to reach" nature of Himalayan terrain poses serious limitations on field observations; consequently field experimentation and information collection to develop regional planning is often difficult. There is a wide spread agreement that global biodiversity is being reduced at an accelerated rate (Myers, 1980) and current approaches to understand the landscape ecology are highly diverse. Landscape harbors all grades of biological hierarchy, from ecosystem level to

species and genes, that are targeted for biodiversity inventories and conservation (Noss & Harris, 1986). Landscape may also include agricultural, forested, protected and ecologically sensitive areas, which interact considerably (Forman & Godron, 1986), and upon which humans have a major influence (Naveh & Lieberman, 1990). Remote sensing can be used successfully to identify the frequency, boundaries, sizes and shapes of various landscape components (Scott et al., 1993). Use of satellite remote sensing in vegetation related studies was introduced around mid eighties in the Central Himalayan region (Singh et al., 1985, Tiwari et. al., 1985). The technology was used to identify landscape/landuse patterns (Singh et. al., 1984), and approaches were developed for mapping, monitoring & change detection (Rathore et al., 1997, Sahai & Kimothi, 1994). Only limited attempts have been made so far to use satellite remote sensing & GIS in describing landscape dynamics and for biodiversity management. Using such an approach Dinerstein (1998) has recently assessed the biological importance and status of habitats & ecosystems of the Himalaya to identify gaps in conservation and protection, and a total of 16 Himalayan ecoregions have been identified. Literature review indicates paucity on printed information on the loss of Himalayan biodiversity, related issues, and landscape studies on fragmentation. In this rational the present effort is to explore the vegetation status (major forest types) and the role of human habitation in a mountain landscape of the Indian Central Himalayan region with particular reference to landscape attributes and fragmentation in respect of a predominant pine (*Pinus roxburghii*) vegetation in the middle Himalaya.

STUDY AREA

The study area, District Almora, lies between 29°23'-30°00' N and 79°00'-80°05' E in the Indian Central Himalayan region (Fig. 1) and is one of the 13 hill districts of Uttaranchal State. Geographical extents of the district are spread in an area of about 3167 km^2, and majority of landscape geologically falls in the Lesser Himalayan belt, however, administrative boundaries also extend to Siwaliks (0.2 %) in the southwestern part. The district is inhabited by 836 thousands persons (1991 Census) with a population density of 282.9 persons per km^2.

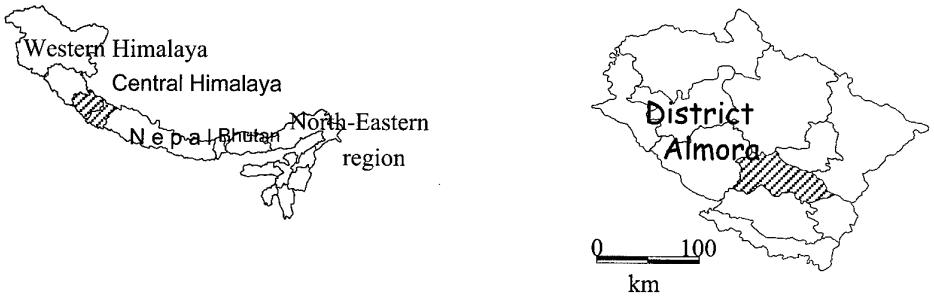


Figure 1. Location of Indian Central Himalayan region and district Almora.

METHODS

Attributes of any broad vegetation type that is structurally homogenous and distinct such as a forest or grassland, are readily inventoried with remote sensing. Using maps and remotely sensed data, with verification from careful ground truthing, it is possible to draw limits around vegetation types (Roy et al., 1985). IRS-1C, LISS-III false colour composite (FCC) of bands 2, 3 & 4 of January 1998 was used to identify various forest types and landuse/landcover classes. Visual interpretation (interpretation key is given in Table 1) was done followed by ground truthing, and interpreted details were transferred to the base map. Forest, Landuse/ Landcover and other thematic maps were digitized and different vector data layers were created in PC

ARC/INFO environment. Base map at 1:250,000 scale was prepared from Survey of India toposheet and information on settlements & primary road network was extracted from the same map. Road network was updated through a recent Survey of India map. Vector data layers were converted to raster data format with a cell size of 25x25 m (a pixel size class close to the spatial resolution of IRS-1C, LISS-III, i.e., 23.5 m) for the use of landscape analysis. Anthropogenic disturbances were measured as disturbance index (Anon., 1999) using a customised software (developed by I.I.R.S, Dehradun, India) and was computed by adopting a probabilistic weightage based linear combination of the landscape attributes.

Vegetation	Tone/Colour	Texture	Physiography	Phenology
Riverine	Medium Grey	Smooth	Island type or near to river, Lowest elevations	Deciduous
Sal	Dull Red	Smooth	Lower elevation	Green leaves
Pine	Dark Brown	Smooth	Middle elevation	Green Leaves
Oak	Brick Red	Smooth	Higher elevation	Green Leaves
Oak mixed Conifer	Red with Brown tinge	Uneven	Highest elevation	Green Leaves

Table 1: Interpretation Key for Major Forest Types using IRS 1C – LISS III FCC.

Shape index (Patton, 1975) was calculated for various forest fragments. Shape index (SI) includes perimeter analysis for each land unit (polygon) to find out edge interaction. A common feature of fragmentation is a sharp increase in the amount of induced habitat edge. The SI describes the deviation of each fragment from circularity (a perfectly circular fragment will have a SI value of 1.0 whereas all other shapes have higher values). SI was calculated using the formula: $SI = P/200\ [(\pi TA)^{0.5}]$ where TA = total area of the fragment (ha), and P = perimeter length (m). The area affected (due to edge impact) was computed (Laurance & Yensen, 1991) using equation:

$$AA_{adj} = AA \times 1 - \{[\ 0.265(AA/TA)]/SI^{1.5}\}$$

Where AA_{adj} = adjusted affected area of fragment, AA = computed affected area of fragment, TA = total area of fragment, SI = Shape Index of fragment. Remaining core area was calculated by the subtraction of affected area from the total area of fragment.

RESULTS & DISCUSSION

The forested area in the district Almora accounted for about 42% (1335.97 km^2) of the total area. An elevational difference between ~500m and > 2500m amsl in the mountainous landscape of district Almora has produced a diversity in forest vegetation (Table 2); however, majority of the landscape falls in the altitudinal zone (~1000–1800m) favourable for pine (*Pinus roxburghii*) dominance in the Central Himalayan region. It is apparent from the spatial distribution of different major forest types (Fig. 2) and area occupied by each type (Table 2) that pine dominated forests are preponderant in the entire landscape of the study area. Pine dominated forest accounts for about 85% (representing 1140.1 km^2) of the total forest while other forest types account for about 11% and 3.5% in case of oak (*Quercus* spp.) and sal (*Shorea robusta*) dominated vegetation, respectively. Riverine type in the lowest altitudinal range and oak-conifer type towards the highest altitudinal range are poorly represented on the district landscape.

While there is preponderance of pine forest, occurrence is very fragmentary in nature. A total of 414 forest patches of pine vegetation could be observed in the landscape (Table 3). The area occupied by each fragment varied between <1 km^2 and 179 km^2. The most noticeable feature is that 9% of the area occupied by pine vegetation is fragmented into a very large number (318,

accounting for about 77% of the total number of pine patches). The addition of further 67 patches (area between 1-4 km^2) the total area under this category enhances to 17%. This area analyses indicate that the vegetation fragmentation has reached an alarming stage because these small landunits are subject to further degradation and appear to be the possible sites of pine extinction. Smaller units are greater in number as reflected by the fact that fragments having area less than 4 km^2, account for ~ 91% of the total number of fragments. The area covered by these fragments represents ~ 17% of the total area under pine forest. Highly fragmented appearance of pine vegetation is mainly due to the diffused nature of human settlements throughout the landscape. Villagers consume vegetation as firewood and fodder (Singh et. al., 1984, Sharma & Singh, 1994). Functioning of a village ecosystem reveals that firewood accounts for almost hundred per cent of the cooking energy in the domestic sector, and village ecosystem imports about 16 units of energy from the forest to support one unit of agronomic production. To support agronomic production from 1 ha of cropland net primary production of 1 ha of good stocked forest is needed (Sharma & Singh, 1994).

Forest Type	Area (km^2)	% of the Forest	Major Tree Species
Riverine	3.49	0.3	*Acacia catechu, Dalbergia sisso*
Sal dominated	46.54	3.5	*Shorea robusta, Mallotus philippensis, Ehretia laevis, Adina cordifolia,*
Pine dominated	1140.10	85.3	*Pinus roxburghii, Pyrus pashia, Engelhardtia spicata, Myrica esculanta*
Oak dominated	142.82	10.7	*Quercus leucotrichophora, Quercus floribunda, Rhododendron arboreum, Lyonia ovalifolia*
Oak & Conifers	3.02	0.2	*Quercus semicarpifolia, Cupressus torulosa, Quercus floribunda, Rhododendron arboreum,*

Table 2: Major Forest Types and their attributes in District Almora.

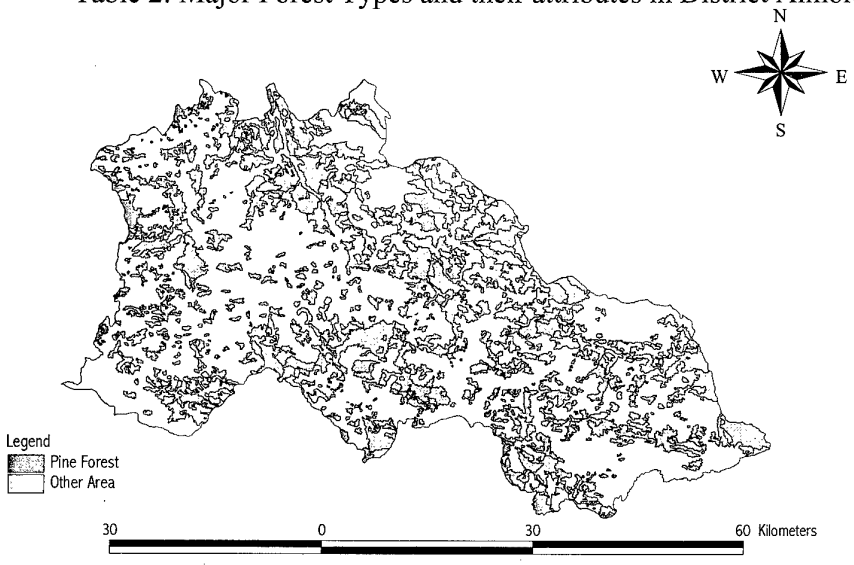


Figure 2: Spatial distribution of pine (*Pinus roxburghii*) forests in the district Almora.

The shape index among the various fragments ranged from 1.1 to 9.2. In general, it was observed that the smaller (in area) units had a low shape index than the larger units. For example, the smallest patches (having area < 1km^2) had a shape index close to one (ideal shape being circular), i.e., 1.1 – 2.2, while the largest vegetation patches had a high shape index (7.7 –

9.2). A high shape index indicates micro-environment interaction at the edge of a vegetation patch. The edge interaction analysis, upto10 m inside from the edge of a patch, indicated that among the various size classes area affected by the edge impact ranged between 2.3% to 8.5% of the total area. In total 3793.86 ha area (3.3%) of the pine vegetation was found to be subjected to alterations in micro-environment due to exposed edges. Severity of edge impact was greater in the patches of smaller size class than the patches of larger size class; however, shape deviation from circularity was much more in the latter in comparison to the former. However, unaffected area from the edge impact accounted for 96.7% of the total pine vegetation. Statistics of the disturbance index model revealed that only about 228 km^2 area on the entire landscape of the district was subject to no disturbance due to anthropogenic activities. At the district landscape 1299 km^2 area can be categorized as being highly disturbed, 1077 km^2 area as moderately disturbed, and ~560 km^2 area had a low disturbance due to anthropogenic reasons. Forests of the Central Himalayan region have been subjected to exploitation throughout the history. Anthropogenically induced disturbances greatly impact the regeneration and status of forests (Upreti et. al., 1984). Anthropogenic disturbances are reflected in the decline of the tree stocking density, e.g., between 1973 and 1989 forests having good crown cover (>60%) declined annually at a rate of 27.8 ha shrinking to the total of 292 ha from 736.32 ha in a watershed of Gaula river (Rathore *et al.* 1997).

Size Class (km^2)	Total number of fragments	Total Area (ha)	Range of Shape Index	Edge Effect upto 10 m		
				Affected Area (ha)	% of fragment size class	Core Area of size class (ha)
< 1 km^2	318	10087.57	1.1 – 2.2	855.66	8.5	9231.91
1 – 2	39	5287.12	1.2 – 2.9	292.64	5.5	4994.49
2 – 3	18	4376.11	1.6 – 2.8	201.11	4.6	4175.00
3 – 4	8	2821.32	1.7 – 2.7	117.49	4.2	2703.83
4 – 5	5	2261.33	1.7 – 3.0	91.03	4.0	2170.30
5 – 10	7	5289.56	1.8 - 3.4	186.88	3.5	5102.68
10 – 15	2	2237.56	2.3 - 4.1	76.06	3.4	2161.50
15 - 20	6	10151.25	1.7- 4.2	231.88	2.3	9919.37
21 – 25	1	2270.65	4.1	69.05	3.0	2201.60
25 – 30	2	5044.22	2.4 – 4.1	115.20	2.3	4929.01
30 – 100	6	35688.00	4.5 – 5.9	841.41	2.4	34846.59
100 – 200	2	28495.47	7.7 – 9.2	715.46	2.5	27780.01
Total	414	114010.17	1.1 – 9.2	3793.86	3.3	110216.30

Table 3: Landscape attributes of pine forest fragments in district Almora.

CONCLUSION

Pine (*Pinus roxburghii*) showed extensive presence on the entire region of the district Almora due to various reasons which may vary from favourable climate, ecology (colonizer due to early successional nature of species), abiotic (landslides) to biotic (preference for this species by the state forest department for revenue generation). However, this species had a diffused presence throughout the landscape it was found to be more fragmentary in areas having high concentration of human settlements. RS & GIS based landscape approach is an emerging tool for identification and conservation of biological hot spots. This has been illustrated in the present study particularly in view of the fragmented nature of vegetation in the mountains and with reference to appropriate inclusion of human dimension in the management planning.

ACKNOWLEDGEMENT:

SS is thankful to Prof. B.L. Deekshatulu, Director, CSSTE-AP, India for providing opportunity. This work forms a part of the project carried out for M.Tech. Degree Course at CSSTE-AP, sponsored by ICIMOD, Kathmandu, Nepal.

REFERENCES:

Anonymous, 1999. Project Manual for National Biodiversity Prioritization Programme. Indian Institute of Remote Sensing, Dehradun, India.

Dinerstein, E., 1998. A Biodiversity Assessment and Gap Analysis of the Himalayas. In: Proceedings of Ecoregional Co-operation for Biodiversity Conservation in the Himalaya. UNDP Publication, New York, USA, pp. 157-161.

Forman, R.T.T. & Godron, M., 1986. Landscape Ecology. John Wiley, New York.

Laurance, W.F. & Yensen, E., 1991. Predicting the impacts of edge effects in fragmented habitats. Biological Conservation, 55, pp. 77 – 92.

Myers, N., 1980. The problem of disappearing species: What can be done? AMBIO, 9(5), pp. 229-235.

Naveh, Z. & Lieberman, A.S., 1990. Landscape Ecology: theory and Applications. Springer-Verlag, New York.

Noss, R.F. & Harris, L.D. 1986. Nodes, networks and MUMs: Preserving diversity ata ll scales. Environmental Management, 10, pp. 299-309.

Patton, D.R. 1975. A diversity index for quantifying habitat edge. Wildl. Soc. Bull., 3, pp. 171-173.

Rathore, S.K.S., Singh, S.P., Singh, J.S., and Tiwari, A.K., 1997. Changes in forest cover in a Central Himalayan catchment: Inadequacy of assessment based on forest area alone. Journal of Environmental Management, 49, pp. 265-276.

Roy, P.S., Dutt, C.B.S., Jadhav, R.N., Ranganath, B.K., Murthy, M.S.R., Gharai, B., Lakshmi, V.U., Kandya, A.K., and Thakker, P.S., 1996. IRS-IC data utilization for forestry applications. Current Science, 70(7), pp. 606-613.

Sahai, B., and Kimothi, M.M., 1994. Remote Sensing of Nanda Devi Biosphere Reserve for biodiversity conservation. Proceedings of Seminar on Biodiversity Conservation, WWF, India. pp. 131-137.

Scott, J.M., Davis, F., Csuti, B., Noss, R., Butterfield, B., Groves, C., Anderson, J., Caicco, S., D'Erchia, F., Edwards, T.C., Ulliman, J. & Wright, R.G., 1993. Gap analysis: A geographical appraoch for protection of Biological Diversity. Wildlife Monograph, 123, pp. 1– 41.

Sharma, S., and Singh, S.P., 1994. Energy use pattern and sustainable development: A case study in rural landscape of the Central Himalaya. Landscape and Urban Planning, 29, pp. 19-24.

Singh, J.S., Tiwari, A.K., and Saxena A.K., 1985. Himalayan forests: A net source of carbon for Atmosphere. Environmental Conservation, 12, pp. 67-69.

Singh, J.S., Pandey, U. and Tiwari, A.K., 1984. Man and Forests: A Central Himalayan Case Study. AMBIO, 13, pp. 80-87.

Tiwari, A.K., Saxena, A.K., and Singh, J.S., 1985. Inventory of forest biomass for Indian Central Himalaya. In: Environmental Regeneration in Himalaya: Concepts and Strategies, edited by Singh, J.S., Gyanodaya Prakashan, Nainital, India, pp. 236-247

Upreti, N., Tewari, J.C. and Singh, S.P., 1985. The oak forest of the Kumaun Himalaya (India): Composition, diversity, and regeneration. Mountain Research & Development, 5(2), pp. 163-174.

MODELING LANDSCAPE CHANGES USING LOGIT MODELS

Li-Ta Hsu
Associate Professor, Department of Environmental Design
Hua Fan University
1 Huafan Rd., Shr-Ding, Taipei, 223
Tel: (886)-2-2663-2102 #4563 Fax: (886)-2-2663-2102 #4570
E-mail: lita@mail.ht.net.tw
TAIWAN

Chi-Chuan Cheng
Deputy Director
Yu-Ching Lai
Post Doctoral Researcher
Taiwan Forestry Research Institute
53 Nan Hai Rd., Taipei, 100
Tel: (886)-2-2303-9978 #1208 Fax: (886)-2-2375-4216
E-mail: ccchcng@serv.tfri.gov.tw
TAIWAN

KEY WORDS: landscape changes, Logit models

ABSTRACT: Detecting and monitoring landscape changes is an important issue of landscape ecology and ecosystem management. This study used two sets of aerial photographs taken in 1988 and 1996 to derive land cover maps of the Liukuei ecosystem management area. The two maps were compared to identify transitions among land cover types. GIS and logit models were used to examine the historic changes of the landscape, and to predict probabilities of landscape changes. Three kinds of explanatory variables, namely, environmental factors, spatial factors, and patch attributes, were examined. Environmental factors include elevations, slopes and aspects of the randomly selected places. Spatial factors include distances to roads, to streams, and to natural forests. Patch attributes include the sizes, perimeters, and shape indices of the patches where the samples were located. Maximum likelihood methods were used to estimate the parameters of binary and multinomial logit models. Results show that the most influential factors of landscape changes were elevations, slopes and distances to natural forests, whereas none of the patch attributes examined in the model were significant. In general, conifer and hardwood plantations located at lower elevations and near natural forests were more likely to become natural forests. Bare lands were more likely to occur on high elevation places near roads and with steep slopes. On the other hand, low elevation bare lands near natural forests and away from roads were more likely to be reclaimed by natural forests. These results can be used to project the probabilities of landscape changes spatially, and would be useful for guiding the management practices of the Liukuei ecosystem management area in the future.

1. INTRODUCTION

Landscape ecology studies the structure, function, and spatial pattern of landscapes (Forman and Godron 1986). In landscape ecology, landscape indices are often used to describe and analyze the landscape structure of a landscape. For examples, O'Neill et al. (1988), Li (1990), Turner (1990), Turner and Gardner (1991) used various landscape indices to quantify landscape structures. In analyzing landscape changes, regression models and Markov models are often used to analyze the distributional changes of a landscape at different points in time. For

instances, Alig (1986) used regression models to analyze the acreage changes of a forest landscape, Burnham (1973), Lindsay and Dunn (1979), and Muller and Middleton (1994) applied Markov models to study landscape changes. Another kind of landscape models is the spatial models. Spatial models of landscape changes focus on the spatial characteristics of landscape changes such as factors contributing to landscape changes, or variations in probabilities of landscape changes at different locations (Baker 1989). Distributional models such as Markov models and regression models can be modified into spatial, for example, Turner (1987) applied Markov probabilities to simulate spatial landscape changes using pixels. However, he suggested that because Markov models are non-spatial in nature, the probability in each pixed should be adjusted according to the conditions of its neighboring pixels. Another commonly used probabilistic spatial models are the probit or logit models. The principles of probit or logit models are similar to those of regression models. They can be used to analyze factors contributing to landscape changes, and use the results to predict probabilities of landscape changes at different spatial locations. Dale et al. (1993) used multinomial logit models to analyze the spatial pattern of deforestation in Brazil. In studies of land use changes, McMillen (1989)and Hsu (1996) further integrated logit models with economic theories, and used them to explore the spatial pattern of land use change. In Taiwan, there are also several literatures about monitoring landscape patterns, for example, Lin (1996) used Markov models and ridge regression models to model vegetation changes in Tainan, and Hsu and Cheng (2000) applied Markov models of predict long-term trends of landscape change in an ecosystem management area. However, until now, none of the literature has used probit or logit models in analyzing spatial landscape changes.

This study is a part of a long-term monitoring program carried out in Liukuei ecosystem management area. In this study, digital photogrammetry was used to generate land cover maps of the Liukuei ecosystem management area in 1988 and 1996. Logit models were used to examine the relationships between landscape changes and environmental factors. The results can provide useful information for the planning, monitoring of the landscape in the future.

2. MATERIAL AND METHODS

The study area, 'Liukuei ecosystem management area', is a part of the Liukuei experimental forest of the Taiwan Forestry Research Institute. Located at Maolin Township, Kaohsiung County, the study area encompasses seven forest compartments, and covers about 2500 ha. Elevation in the area ranges from 300m to 1800m, and the topography is up-sloped from southwest to northeast. The Shanping post and several nurseries are also located inside the area and are connected by service roads stretching throughout the area. Natural forests dominate 78% of the landscape, and man-made stands occupy the remaining 22%. Most of the man-made stands are coniferous plantations. On the other hand, natural forests consist of various broadleaf tree species, and some are mixed with conifers. Parts of the natural and man-made forests have recently undergone timber harvesting and reforestation. Therefore, some cut areas exist. In addition, there are some nonforested areas such as grasslands or bare lands resulted from landslides.

Aerial photographs taken in 1988 and 1996 were used to generate land cover maps of the study area. Positive films of the photographs were scanned into digital images. With several ground truth measurements, the images were subsequently rectified as orthogonal images with accurate positioning. Image pairs were then displayed as stereographs on computer screens, where features on the landscape were delineated and digitized. As a result, two sets of land cover map files were created in vector format (Fig.1).

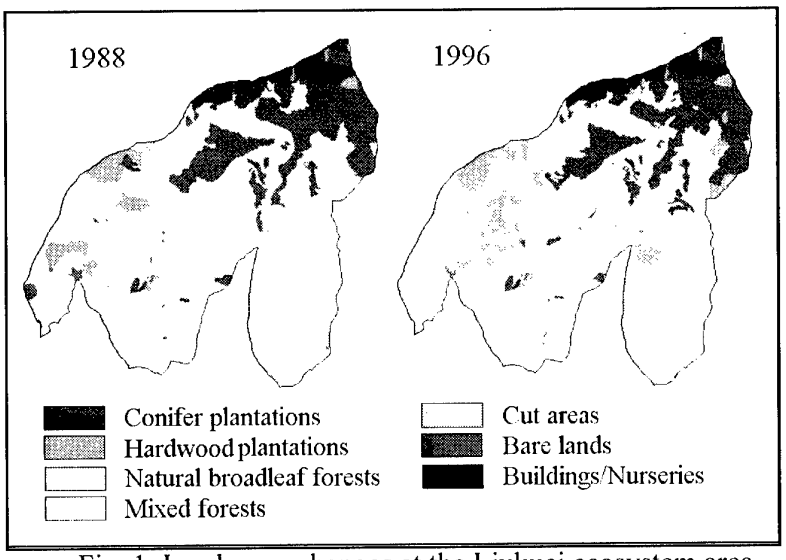


Fig. 1. Landscape changes at the Liukuei ecosystem area.

For each land cover patch, or polygon, its land cover type, area, and perimeter were recorded. The two maps were then overlaid together using a geographic information system to identify land cover changes during the time interval.

The purpose of this study is to develop a set of probabilistic models for predicting landscape changes spatially. Binomial and multinomial models were used to examine the factors contributing to landscape changes. Supposing the observed landscape changes were related to some exogenous factors x's, then, in multinomial logit models, the probability that a land cover type would become land cover type i , or Pn(i), can be written as:

$$P_n(i) = \frac{e^{\beta' x_{in}}}{\sum_{j \in C_n} e^{\beta' x_{jn}}} \qquad [1]$$

where $\beta' x_{in}$ is the vector of x's and their coefficients, $\beta' x_{jn}$ is the corresponding vector of every land cover type. When there are only two possible land cover types, the multinomial logit model is reduced to binomial logit model:

$$P(i) = \frac{1}{1 + e^{-\beta' x_i}} \qquad [2]$$

Factors examined in this study can be classified into three categories: locational factors, environmental factors, and patch characteristics. Locational factors include distance to roads (TOROAD), distance to streams (TOSTREAM), distance to natural breadleaf forests (TONATURE). Environmental factors elevations (ELEVATION), slopes (SLOPE), and aspects (ASPECT). Patch characteristics include patch size (SIZE), perimeter (PERI), patch shape index (SHAPE) and soil type (SOIL). In order to estimate logit models, sample points were randomly selected from the land cover maps. For each sample point, landscape change from 1988 and 1996, its associated environmental factors, and characteristics of its associated patch were recorded. Parameters in equation [1] and equation [2] were estimated using maximum likelihood method. To obtain the final models, backward selection was used to eliminate the least correlated variables step by step until the t-statistics of all parameters were statistically significant at ı.=0.05.

Statistical significance of a logit model can be tested using likelihood ratio test statistics, which follow Chi-square distribution with k degrees of freedom (k = number of parameters been estimated). Alternatively, the likelihood ratio index, orıÉ^2 can be used to examine the goodness of fit of a model. The likelihood ratio index is similar to the determinant coefficient (R^2) of a

regression model. $\rho^2 = 1$ when the model fits the observed data perfectly, and when $\rho^2 = 0$, it means that the included variables do not explain the observation at all.

3. RESULTS AND DISSCUSIONS

This study focused on landscape changes under natural conditions (without human interference), therefore, man-made modification such as cutting tract reforestation, forest roads, buildings and nurseries were not included in the analysis. Observed landscape changes from 1988 to 1996 included the following: (1) from coniferous plantations to coniferous plantations, natural forests, or bare lands, (2) from hardwood plantations to hardwood plantations or natural forests, (3) from natural forests to natural forests or bare lands, (4) from mixed forests to mixed forests, natural forests, or bare lands, (5) from bare lands to bare lands or natural forests. Among them, coniferous plantations and mixed forests included more than two possible ways of landscape changes, and therefore multinomial logit models were applied. For other land cover types including hardwood plantations, natural forests, and bare lands, binary logit models were used because they had exactly two possible ways of landscape changes.

The results of model fitting were shown in Table 1. Among the explanatory variables, the effects of locational factors and some of the environmental factors such as elevations and slopes were more significant. On the other hand, patch characteristics and aspects were not significant. Table 1 showed that for all the logit models, nether likelihood ratio test statistics, nor likelihood ratio indices (^{2}) were statistically significant. This is mainly because the landscape changes only consisted of a fairly small portion of the landscape. As a result, the models tend to underestimate the probabilities of a land cover type converting to other land cover types. Therefore, it would be difficult to judge which land cover type would a place convert according to e uation 1 and e uation 2 . However, comparisons show that for places where landscape changes did occur, their associated probabilities of land cover changes is significantly higher than other places. That is, despite that the models tends to underestimate the probabilities of landscape changes, the relative magnitudes of probabilities can be used to identify areas where landscape changes are more likely to occur.

The effects of explanatory variables on landscape changes can be inferred from the signs and magnitudes of coefficients shown in Table 1. The results showed that changes from coniferous plantation to natural forests or mixed forests were related to distances to natural forests and elevations. The closer the distance to natural forests, and the lower the elevation, the likelier a coniferous plantation would turn into natural forests or mixed forests. On the other hand, the occurrences of bare lands were related to elevations and slopes. Bare lands were more likely to occur on coniferous plantations at high elevations and with steep slopes. For mixed forests, the closer they were to natural forests, the likelier they would turn into natural forests, and the higher the elevation, the likelier they would remain as mixed forests. Similar to coniferous plantations, bare lands were also more likely to occur on mixed forests at high elevations and with steep slopes. For hardwood plantations, the conversions to natural forests were related to distances to natural forests, elevations, as well as distances to streams. Low elevation hardwood plantations near natural forests were more likely to become natural forests, but if they were near to the streams, the trends became less obvious. As to natural forests, bare lands were more likely to occur on forests near the roads and with steep slopes. In contrast, low elevation bare lands farther away from roads, and near natural forests were more likely to be reclaimed by natural forests.

Table 1. Results of the multinomial logit model for conifer plantations

Landscape changes from 1988 to 1996	Conifer plantations				Mixed forests			Hardwood plantations	Natural forests	Bare lands
	Conifer plantations	Natural forests	Mixed forests	Bare lands	Natural forests	Mixed forests	Bare lands	Natural forests	Bare lands	Natural forests
Sample proportion	81.93%	13.35%	2.95%	1.76%	42.24%	55.97%	1.79%	45.17%	0.36%	76.47%
Constant	-4.1416			-18.7055		-2.4230	-10.6943	43.1282	-6.8093	2.5744
TOROAD(10^2m)									-0.2448	0.4042
TOSTREAM(10^2m)								2.9274		
TONATURE(10^2m)		-2.2210	-1.4227		-4.2475			-1.4840		-2.3848
ELEVATION(10^1m)		-3.0595	-4.6397	5.1191		2.1656		-67.4428		-1.7874
SLOPE				0.0987			0.2542		0.0622	
Likelihood ratio test statistic		0.667				0.280		3.305	0.109	0.304
Likelihood ratio index (ρ^2)		0.284				0.131		0.781	0.053	0.141
Percent correctly predicted		83.30				66.12		93.05	99.64	80.67

The logit models can be used to spatially predict the landscape changes. Taking coniferous plantation as an example, the observed and model predicted landscape changes were compared in Fig. 2. The figures showed that, though not perfect, the model predicted landscape changes match the observed landscape changes fairly well.

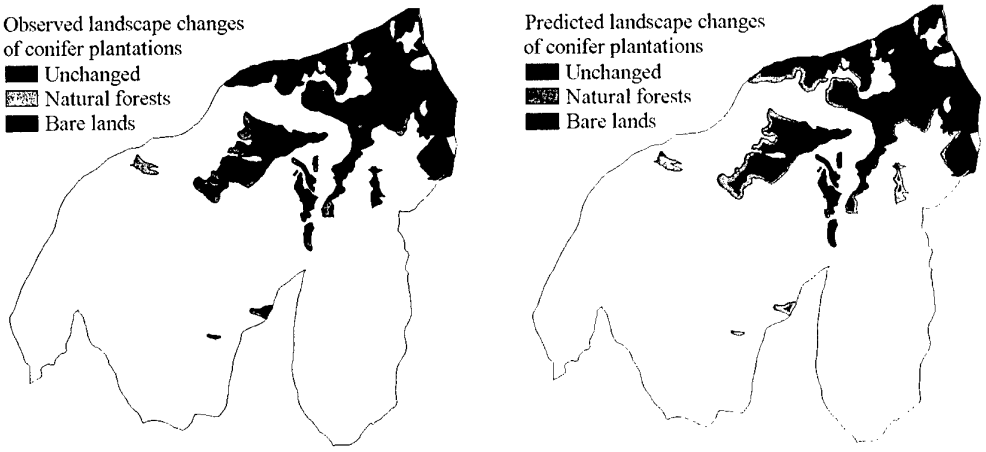


Fig. 2. Comparisons between the observed and model predicted landscape changes.

4. CONCLUSIONS

Several conclusions can be drawn from the results of this study:

(1) In analyzing factors contributing to landscape changes, topographic effects and edge effects appeared to be more influential than patch attributes. Whether a man-made plantation would turn into natural forests or not is largely determined by its distance to natural forests as well as its elevation. Whether a forested area would become bare lands or not depends on its slope. Factors that had the most significant effects included elevations, slopes, distances to natural forests, and distances to roads. On the other hand, bare lands with gentle slope and farther away from roads were more likely to recover into natural forests.

(2) Although logit models can be used to predict "what" land cover change would occur on a given place, but if the observed land cover changes only consist of a small portion of the landscape, the predicted probabilities of change will be under estimated. Therefore, it is not practical to use logit models for prediction in such cases. However, logit models are useful in comparing the relative likelihood of landscape change at different locations.

(3) In this study, factors affecting landscape change coincide with the a-priori expectation in general. One major advantage of logit models is that the extents of influences can be quantified and compared. Such comparisons can provide very useful information to decision maker in management planning.

REFERENCES

Baker, W. L., 1989. A review of models of landscape change. Landscape Ecology, 2(2), pp. 111-133.

Burnham, B. O., 1973. Markov intertemporal land use simulation model. Southern Journal of Agricultural Economics, 5, pp. 253-8.

Dale, V. H., O'Nell, R. V., Pedlowski, M., Southworth, F., 1993. Causes and effects of land-use change in central Rondônia, Brazil. Photogrametry Engineering & Remote Sensing, 59(6), pp. 997-1005.

Forman, R. T. T. , Godron, M., 1986. Landscape ecology. (NY): John Wiley and Sons. 619 p.

Hsu, L. T., 1996. Modeling land use change in human dominated landscapes: a case study of urbanization in an Indiana watershed [dissertation]. West Lafayette (IN): Purdue Univ. 255 p.

Hsu, L. T. , Cheng, C. C., 1999. Assessing landscape change in Liukuei ecosystem area using Markov model. Taiwan Journal of Forest Science, 15(1), pp. 41-49.

Li, H., 1990. Spatio-temporal pattern analysis of managed forest landscape: a simulation approach [dissertation]. Corvallis (OR): Oregon State Univ. 166 p.

Lin, J. S., 1996. Study on the change detection of ecological environment by using the remotely sensed data on vegetation ecosystem: an illustration of Tainan district [dissertation]. National Taiwan University. 252 p. [in Chinese with English summary]

Lindsay, B. E., Dunn, D. L., 1979. Land use projections under alternative policies: a transition matrix approach. J Northeastern Agricultural Economic Council 8(2), pp. 87-99.

McMillen, D. P., 1989. An empirical model of urban fringe land use. Land Economy, 65(2), pp. 138-45.

Muller, M. R., Middleton, J., 1994. A Markov model of land-use change dynamics in the Niagara Region, Ontario, Canada. Landscape Ecology, 9(2), pp.151-7.

O'Neill, R. V., Krummel, J. R., Gardner, R. H., Sugihara, G., Jackson, B., DeAngelis, D.L., Milne, B.T., Turner, M.G., Zygmunt, B., Christenser, S. W., Dale, V. H., Graham, R. L., 1988. Indices of landscape pattern. Landscape Ecology, 1, pp.153-162.

Turner, M. G., 1987. Spatial simulation landscape changes in Georgia: A comparison of 3 transition models. Landscape Ecology, 1(1), pp.29-36.

Turner, M. G., 1990. Spatial and temporal analysis of landscape patterns. Landscape Ecology, 4, pp.21-30.

Turner, M. G., Gardner, R. H., 1991. Quantitative methods in landscape ecology. Ecological Studies. Vol. 82. (NY): Springer-Verlag. 536 p.

IMPLEMENTATION OF A GEOGRAPHIC INFORMATION SYSTEM (GIS) TO DETERMINE WILDLIFE HABITAT QUALITY USING HABITAT SUITABILITY INDEX

YuChing Lai, Ph.D.
Post Doctor
Division of Forest Management
Taiwan Forestry Research Institute
53 Nan-Hai Road, Taipei 100
TAIWAN

Walter L. Mills, Jr., Ph.D.
Associate Professor of Forestry
Department of Forestry and Natural Resource
Purdue University
1159 Forestry Building, Room 110
West Lafayette, IN 47907-1159

Chi-Chuan Cheng
Deputy Director
Taiwan Forestry Research Institute
Council of Agriculture
53 Nanhai Rd., Taipei 100
TAIWAN

KEY WORDS: Geographic Information System (GIS), Habitat Suitability Index (HSI), Wildlife Habitat, Spatial Pattern

ABSTRACT: Habitat quality for many wildlife populations has a spatial component related to the arrangement of habitat elements across large geographic areas. There are a number of indices used to quantitatively describe the components of habitat assessment, yet, only a few of them incorporating spatial relationship in the model. Among these mathematical indices, habitat Suitability Index (HSI) models have been widely developed for use in habitat evaluation procedures (HEP). HEP, which is based on the assumption that habitat for a selected wildlife species can be described by a Habitat Suitability Index, can be used to document the quality and quantity of available habitat for a specific wildlife species. However, because of the difficult of quantifying spatial arrangement, HSI has ignored the spatial distribution of habitats. Geographic information system (GIS) provides wildlife managers and planners with techniques that can help overcome some of the problems inherent in developing, applying, and evaluating practical, spatially explicit habitat models. Given the desirability of deterministic results, seamless integration of data and analytical options available via GIS increases our ability to state, implement, test, and evaluate estimated or modeled habitat elements. This study examined possible ways to use the accumulated knowledge found in HSI to estimate the wildlife microhabitat quality across a landscape. In this study, GIS is used to generate parameters of HSI models, especially the spatial habitat parameters that are often of explicit importance for HSI models, incorporating spatial reasoning and constraints into HSI models, analyzing spatial patterns of habitat, and providing the mapping capability for converting stand-based information into maps of habitat. Species that occur in Missouri Ozark Forest Ecosystem with existing HSI

models are selected. A moving window the size of the home ranges of each species is applied to calculate the average value of each life requisites. In conclusion, implementing GIS in wildlife habitat assessment improves the use of HSI models by automating tasks, identifying areas where site-specific analyses were needed, and reducing the spatial and temporal complexity involved with integrating different resource perspectives.

1. INTRODUCTION

Ecosystem management appears to be the wave of the future. General program goals such as "maintain biodiversity", "maintain viable populations of all native species", and "protect representative natural communities" are often emphasized in ecosystem management (USDA 1994, Grumbine 1994, and Irland 1994). Tools for maintaining biodiversity and viable species populations are likely to be focused on providing habitats in an appropriate spatial and temporal arrangement. Therefore, vegetation management is a major tool for maintaining and restoring biodiversity and to achieve delisting or to avoid listing of threatened and endangered species (USDA 1994). There have been numerous attempts to assess habitat quality for particular species. Probably the most widely practiced in the United States is the Habitat Suitability Index (HSI), which together with the Habitat Evaluation Procedures (HEP) developed by the U.S. Fish and Wildlife Service, has frequently been used to assess habitat. It is also a useful monitoring tool for biodiversity at community-ecosystem level (Noss and Cooperrider 1994). However, it ignores the effects of immigration and spatial distribution of habitats (Carroll and Meffe 1994).
In this study, the possibility of using HSI for ecosystem management assessment will be tested. Species with existing HSI models will be use. Since the same procedure can be applied regardless of what species is used, more species could be used when, and if, appropriate HSI are developed. Point sample data combined with spatial data of the Missouri Ozark Forest Ecosystem Project (MOFEP) will be used to assess ecological organization at the community-ecosystem level in this study.

2. METHODOLOGY

2.1 Study Area

The Missouri Ozark Forest was located in southeastern Missouri Ozarks consists of 9,200 acres of mature upland oak-hickory and oak-pine forest communities. Collectively, these counties are 84% forested with large contiguous blocks of forests separated only by roads and streams. Compartment One of Missouri Ozark Forest Ecosystem Project (MOFEP) was selected for this study because it has the most detailed inventory data. It is 380 hectares (989 acres) in size and contained 62 stands. Seventy-six permanent sample plots are distributed among these stands. Dominant overstory species included pine (Pinus echinata), hickory , and oak.
A cluster plot design was used to collect data in order to investigate the effects of forest management on the composition and spatial distribution of woody and herbaceous vegetation. In this design, a 0.2 ha (0.49 ac.) circular plot was used to sample trees 11.4 cm (4.5 in) dbh and larger and to tally the total number of den trees. Four line intercepted 17.2 m (56.4 feet) in length were located within each 0.2 ha plot to measure the coverage of down dead woody material. Four circular 0.02 ha (0.05 ac.) plots were located within the larger plot to sample woody plants between 3.5 cm (1.5 in.) and 11.2 cm (4.4 in.) dbh. One 0.004 ha (0.01 ac) plot was placed within each 0.02 ha plot, sharing the same plot center, to sample vegetation taller than 1.0 m (3.3 feet) and less than 3.5 cm (1.5 inches) dbh. Four one square m (10.8 square feet) plots were located within each 0.02 ha plot to sample vegetation less than 1.0 m (3.3 feet) in height.

2.2 HSI Models selection

While hundreds of habitat suitability index models were available, the selected HSI represent those that were valid for the Missouri Ozark Highland and for which data was available. Eleven species were selected for this study including seven bird species and four mammals. The bird species were selected when either their breeding range or year-round range include the Missouri Ozark highland. They were barred owl (Strix varia) (Allen 1987), brown thrasher (Toxostoma rufum) (Cade 1986), downy woodpecker (Picoides pubescens) (Schroeder 1982), hairy woodpecker (Picoides villosus) (Sousa 1987), pileated woodpecker (Dryocopus pileatus) (Schroeder 1982), eastern wild turkey (Meleagris gallopavo sylvestris) (Schroeder 1985), and northern bobwhite (Colinus virginianus) (Schroeder 1985). Four mammal HSI models were selected, i.e., Bobcat (Felis rufus) (Boyle and Fendley 1987, Schwartz and Schwartz 1981), eastern cottontail (Sylvilagus floridanus) (Allen 1984, Schwartz and Schwartz 1981), gray squirrel (Sciurus carolinensis) (Allen 1982, Schwartz and Schwartz 1981), and fox squirrel (Sciurus niger) (Allen 1982, Schwartz and Schwartz 1981).
In most of these wildlife HSI models, more than one life requisite (for example, food, cover, and reproduction) was usually used (Table 1). Each of the life requisite was described by a set of habitat variables (Table 1).

Table 1. Attributes of selected specie

Attributes / Species	Home Range(ha)	Life Requisities	Variables
BARRED OWL	228.6	Reproduction	# of trees >51 cm dbh, mean dbh, Canopy cover
BOBCAT	100	Food	% by grass/forb-shrub
BROWN THRASHER	1	Food/cover/reproduction	Density, Canopy cover, Litter cover
DOWNY WOODPECKER	4	Food/reproduction	Basal area,# of snags >15cm dbh
EASTERN COTTONTAIL	4	Cover/	Herbaceous cover, Shrub cover, Canopy cover
FOX SQUIRREL	3.55	Food/cover	Canopy closure of hard mast trees, Distance to grain, mean dbh canopy cover, shrub cover
GRAY SQUIRREL	0.4	Food/cover	Canopy closure of mast trees, Distance of hard mast trees, canopy cover, mean dbh, shrub cover
HAIRY WOODPECKER	4	Cover/reproduction	Mean dbh, Canopy cover, Canopy closure of pine, # snags >25 cm dbh, mean dbh
N BOBWHITE	4.9	Food/cover/nesting	Canopy cover of preferred herbaceous plants, Litter cover, # pine or oak, canopy cover, herbaceous cover, mean hight of herbaceous canopy, grass herbaceous canopy, soil moisture regime
PILEATED WOODPECKER	136	Food/cover/reproduction	Canopy closure, # tree stumps, # tree >51 cm dbh, # snags >38 cm dbh, mean dbo of snags >38 cm dbh
TURKEY	29	Food/cover	Herbaceous cover, Mean hight of herbaceous canopy, Mean dbh of hard mast producing trees, # hard mast-producing trees, canopy coverage of soft mast-producing trees, shrub cover, shrub cover comprised of soft mast producing shrub, canopy closure

2.3 Automated HSI Model

The first step in developing the automated HSI model was to spatially join attribute data with stand and sample plot locations. Since stands were delineated mainly by their ecological land type and vegetation structure, it should be valid to treat stand as a homogeneous habitat area and to use stands as spatial boundary to expand point inventory data. Spatial Analyst was used to allocate the point sample plot attributes based on which stand polygons they fell in. Hence, an ecological site map was created to describe ecosystem information of each site. Stand polygons in Compartment One were then rasterized with cell size of 10 meter square. Habitat variables were extracted from the database according to requirements of each HSI models. Life requisite values of each species were then generated for each cell. A moving window the size of the

home ranges of each species was applied to calculate the average value of each life requisites. Different target species had different window size according to their home range (Table 1). For each cell in the grid ecological site map, the neighborhood-analysis function computed an average value based on the value of the cells within the home range.
Finally, for each species of interest a habitat unit map was generated. The final index of each species equaled the minimum value of each life requisite, cell by cell.

3. RESULTS

Four species was evaluated high in HSI values in Compartment One of Missouri Ozark Forest. Overall, gray squirrel had a relatively high HSI value in Compartment One (Figure 1). More than 80 percent of the area had HSI values higher than 0.5 (Table 2). The winter food life requisite had very high value in most of the cells. The cover requisite was lower mainly because the average dbh of overstory trees was too small. Eastern cottontail had very high HSI value for all of the cells (Figure 1). The successional stage of Compartment One was right where the optimum habitat the model described for eastern cottontail -- a forested landscape with middle shrub coverage and canopy coverage, and a relatively low nonwoody vegetation coverage. More than 85 percent of the cells had HSI values greater than 0.75 (Table 2). Bobcat also had high HSI value for all of the cells (Figure 1) mainly because the HSI model considered bobcat's prey, eastern cottontail and cotton rat, as the only life requisite, the result coincided with eastern cottontail. Most of the cells, more than 75 percent, in Compartment One had a HSI value higher than 0.5 (Table 2). Examination of the image (Figure 1) for bobcat showed that the higher value cells tend to form a continuous area. Compartment One was also evaluated high in all of the habitat variables of the downy woodpecker HSI model (Figure 1). Over 73 percent of the cells had HSI value larger than 0.5 with the high value distributed equally between range 0.5 – 0.75 and range 0.75 –1.00 (Table 2).

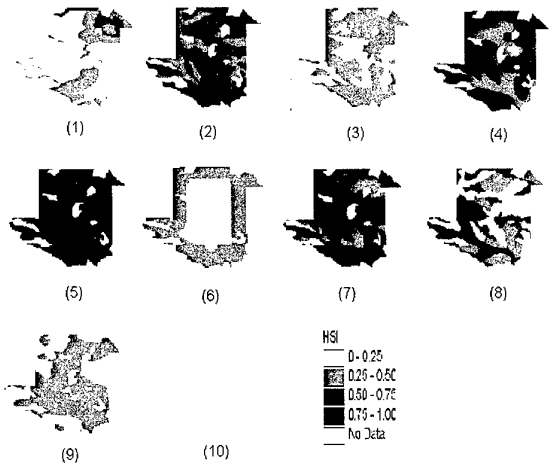


Figure 1. Habitat Suitability Index maps (1) barred owl (2) bobcat (3) brown thrasher (4) downy woodprcker (5) eastern cottontail (6) fox squirrel (7) gray squirrel (8) hairry woodpecker (9) northern bobwhite (10) pileated woodpecker (11) eastern wild turkey

Contrary to grat squirrel, fox squirrel was low in HSI. All of the cells had a HSI value for less than 0.5 (Figure 1). This was mainly due to the distance to available grain in this large forested area. Barred owl had low HSI value for most of the cells (Fig 1), more than 74 percent of the area. This result was a function of habitat variables which measured the number of big trees.

Brown thrasher also had low HSI values (Fig 1). The high HSI value cells occurred where the canopy coverage was lower. Eastern wild turkey was low on HSI values (Figure 1). About 95 percent of the cells had HSI value lower than 0.5 (Table 2). This was mainly because of the optimum herbaceous coverage for eastern wild turkey was not provided by Compartment One. Northern bobwhite required low, dense woody vegetation and grassy areas. Therefore, the HSI value of northern bobwhite was low in Compartment One. Pileated woodpecker had the lowest HSI value among the 11 selected species. It required mature, dense forest with large snags, which was not available in Compartment One (Figure 1).

The HSI value for the hairy woodpecker ranged from 0 to 1 (Figure 1). However, there was a big gap between the low value and high value cells. This was because of the number of very large snags per hectare required in the HSI model, a stand with a few large snags could have very high SI value while a stand with no large snags had a SI value of 0.

For each species, the factor that dominates the final HSI value differs. However, the species that are low in HSI and high in HSI have some common characteristics. For species that prefer open forests such as fox squirrel and turkey, the HSI value is low because Compartment One is a dense forest. Early successional species such as northern bobwhite and brown thrasher that require low dense woody vegetation with a less dense overstory canopy have low HSI values. The optimum habitat of later successional species such as pileated woodpecker, barred owl, and turkey requires more large trees then is currently provided by Compartment One.

Species with high HSI values tend to prefer mid-successional habitat. The optimum habitat of species such as downy woodpecker, eastern cottontail and gray squirrel require dense forest with nearly closed canopies, abundant understory cover with moderate shrub and herbaceous coverage (20-50%), and existence of some small snags.

However, there are species with very specific needs. The hairy woodpecker, for example, prefers fairly large snags and large trees and its HSI values vary widely over Compartment One (Figure1).

Table 2. Area of habitat evaluation

Species	Poor Habitat		Good Habitat	
	(Hectare)	(%)	(Hectare)	(%)
Barred owl	25,807	74.22	8,962	25.78
Bobcat	8,604	24.75	26,165	75.25
Brown thrasher	34,573	99.44	196	0.56
Down woodpecker	9,311	26.78	25,458	73.22
Eastern cottontail	0	0	34,769	100
Fox squirrel	34,769	100	0	0
Gray squirrel	5,528	15.90	29,241	84.10
Hairy woodpecker	19,015	54.69	15,754	45.31
Northern bobwhite	34,769	100	0	0
Pileated woodpecker	34,769	100	0	0
Turkey	32,937	94.73	1,832	5.27

5. CONCLUSIONS

A quantitative basis for management decisions may reduce the perception of subjective bias in decision making. This study provides a possible quantitative way to monitor management practices for ecosystem management by using HSI models. HSI models quantify habitat quality and permit consideration of wildlife along with other aspects of project planning, such as engineering and economics. They allow assessments of resultant changes in potential habitat quality and availability for selected wildlife species. This study's major contribution is the HIS incooperating spatial reseasoning and the redevelopment of spatially computed HSI. The use of

a moving window that represents an animal's home range enabled the spatial evaluation of the habitat condition home range by home range. Thus, the HSI value of the each cell reflects the habitat condition of each species' home range, not the condition of one pixel. The moving window approach assessed the conditions of the home range at each point within each stand. Therefore, the automated HSI is not an assessment of the forest condition at each point but an assessment of habitat conditions of the home range (moving window). Futhermore, HSI habitat map shows the spatial distribution of poor habitat areas that need management attention and the good habitat areas that the manager may want to be careful about when harvesting or other activities are implemented.

6. Bibliography

Allen, A.W. 1982. Habitat Suitability Index Models: Fox Squirrel. U.S. Dept. Int., Fish Wildl. Serv. FWS/OBS-82/10.18. 11pp.

Allen, A.W. 1982. Habitat Suitability Index Models: Gray Squirrel. U.S. Dept. Int., Fish Wildl. Serv. FWS/OBS-82/10.19. 11pp.

Allen, A.W. 1984. Habitat Suitability Index Models: Eastern Cottontail. U.S. Dept. Int., Fish Wildl. Serv. FWS/OBS-82/10.66. 23pp.

Allen, A.W. 1987. Habitat Suitability Index Models: Barred Owl. U.S. Dept. Int., Fish Wildl. Serv. FWS/OBS-82/10.143. 17pp.

Boyle, K.A., and T.T. Fendley. 1987. Habitat Suitability Index Models: Bobcat. U.S. Fist Wildl. Serv. Biol. Rep. 82(10.147). 16pp.

Cade, B.S. 1986. Habitat Suitability Index Models: Brown Thrasher. U.S. Dept. Int., Fish Wildl. Serv. FWS/OBS-82/10.118. 14pp.

Carroll, C. Ronald and Gary K. Meffe. 1994. Management to Meet Conservation Goals: Applications in Gary K. Meffe and C. Ronald Carroll, book, Principles of Conservation Biology.

Eaton, Stephen W. 1992. Wild Turkey. The birds of North America, No. 22. 21pp.

Grumbine, R. Edward. 1994. What is Ecosystem Management? Conservation Biology 8(1):27-38.

Irland Lloyd C. 1994. Getting from Here to There: Implementing Ecosystem Management on the Ground. J. of Forestry 92(8):12-17.

Noss, Reed F. and Allen Y. Cooperrider. 1994. Saving Nature's Legacy: Protecting and Restoring Biiodiversity. Island Press, Washington, D.C.

Schroeder, R.L. 1982. Habitat Suitability Index Models: Downy Woodpecker. U.S. Dept. Int., Fish Wildl. Serv. FWS/OBS-82/10.38. 10pp.

Schroeder, R.L. 1982. Habitat Suitability Index Models: Pileated Woodpecker. U.S. Dept. Int., Fish Wildl. Serv. FWS/OBS-82/10.39. 15pp.

Schroeder, R.L. 1985. Habitat Suitability Index Models: Eastern Wild Turkey. U.S. Dept. Int., Fish Wildl. Serv. FWS/OBS-82/10.106. 33pp.

Schroeder, R.L. 1985. Habitat Suitability Index Models: Northern Bobwhite. U.S. Dept. Int., Fish Wildl. Serv. FWS/OBS-82/10.104. 32pp.

Schwartz, Charles W., and Elizabeth R. Schwartz, 1981. The Wild Mammals of Missouri. University of Missouri Press and Missouri Department of Conservation, 356pp.

Sousa, Patrick J. 1987. Habitat Suitability Index Models: Hairy Woodpecker. U.S. Dept. Int., Fish Wildl. Serv. FWS/OBS-82/10.146. 19pp.

USDA. 1994. An Ecological Basis for Ecosystem Management. USDA Forest Service, General Technical Report RM-246. Washington DC. 22pp.

Whittaker, R. H. 1956. Vegetation of the Great Smoky Mountains. Ecol. Monogr. 26:1-80.

APPLICATION OF GIS TO MEASURE AND EVALUATE LANDSCAPE CHANGES

Chi-Chuan CHENG (Taiwan)
Deputy Director, Taiwan Forestry Research Institute
53, Nanhai Road, Taipei 100, Taiwan
Telephone: +886-2-23039978 Facsimile: +886-2-23757469
E-mail: ccchcng@serv.tfri.gov.tw
Jihn-Fa JAN (Taiwan)
Assistant Professor, Department of Geography
National Changhua University of Education
1, Jinn Der Road, Changhua 500, Taiwan
Telephone: +886-4-7232105 ext. 2825 Facsimile: +886-4-7211186
E-mail: jfjan@cc.ncue.edu.tw

KEY WORDS: GIS, landscape ecology, landscape diversity.

ABSTRACT: This study used the 'Liukuei ecosystem management area' of the Taiwan Forestry Research Institute as the study area. Geographic information systems were used to integrate indices of landscape structures to investigate the effects of management activities on the landscape. Forest type maps of the area in 1988 and 1996 were derived using digital photogrammetry and GIS. To analyze the effects of cutting and forest road building on the landscape, indices of landscape structure referring to landscape composition and landscape configuration were calculated. The results show that cutting and forest road building increased the numbers and types of patches. They not only directly altered the variety and abundance of the patches, but also indirectly affected landscape structure properties such as landscape diversity, evenness, and interspersion and juxtaposition. Several indices were compared, and it was found that the Shannon diversity performed better in distinguishing landscape changes. In addition, the effects of cutting and forest road building on the landscape were not significant based on the *t*-test result of the Shannon diversity index. This study reveals that integration of GIS and quantitative indices of landscape structure is a feasible and efficient approach for evaluating the effects of management activities on landscape.

1. INTRODUCTION

Landscape monitoring is a basis for studying forest landscape changes and validating theories of landscape ecology. Landscape ecology is a science that studies the relationships and mechanisms among landscape patches, i.e. a research focuses on the structure, function, and change of the landscape. However, to understand the function and change of the landscape, it is a prerequisite to quantify the landscape structure (O'Neill et al., 1988; Li, 1990; Turner, 1990; Turner and Gardner, 1991). Early studies on the quantification of landscape structure were mostly for special purpose or lack of analysis tools, thereby the results were limited (Turner, 1990). In recent years, the development of geographic information system (GIS) makes timely temporal and spatial information accessible. Moreover, its capability of spatial analysis and presentation makes it a useful tool for studying landscape spatial structure and landscape change analysis. Publications on the application of GIS in landscape research include: Burrough (1986), Cola (1989), Lam (1990), Rex and Malason (1990), and Olsen et al. (1993).

Integration of landscape ecology and GIS in landscape monitoring for forest management in Taiwan has become the main focus of researches recently. Wang (1998) and Cheng el al. (1999) used GIS and fractal dimension to monitor spatial variation of forest landscape. Huang (1997)

used Shannon index to monitor landscape diversity. However, publication concerning application of landscape index to evaluate the effects of cutting and forest road building on landscape structure and landscape changes has not been seen. Therefore, this study used digital photogrammetric technique to produce 1/5000 scale forest type maps of the 'Liukuei ecosystem management area' in 1988 and 1996. The objective was to apply GIS and quantitative indices of landscape structure to investigate the effects of cutting and forest roads building on landscape changes in the study site.

2. MATERIALS AND METHODS

2.1 Study area and materials

The 'Liukuei ecosystem management area' occupies about 2440 hectares. Approximately 75% of the area is covered with natural hardwood forest, whereas only a small portion of the area is plantation, within which *Taiwania cryptomerioides* is the most commonly planted species.

Two forest type maps (scale 1/5000) of 1988 and 1996 were produced using digital photogrammetric technique (as shown in Figure 1). A GIS database was established for quantitative analysis of the landscape structure. The software and hardware used in the study included a digital photogrammetric workstation, personal computers, ARC/INFO, ArcView GIS, and ERDAS IMAGINE.

2.2 Analysis methods

Quantification of landscape structure is a key element for studying landscape functions and changes. Therefore, this study applied GIS to calculate indices of the landscape structure using the forest type maps for 1988 and 1996, respectively. These indices were then used to analyze the landscape changes in the study area.

2.2.1 Quantification of landscape structure

A landscape can be characterized by its composition and configuration (Dunning *et al.*, 1992). Landscape composition refers to the variety and abundance of patch types within a landscape. Landscape configuration refers to the placement or spatial character of patches within a landscape. These two aspects can independently or jointly affect the ecological processes. This study followed the approach proposed by McGarigal and Marks (1994) to quantify the landscape structure. Several quantitative indices were used to measure landscape composition and landscape configuration for analyzing the effects of landscape changes.

Three indices were used to characterize the landscape composition, that is, landscape diversity, patch richness, and landscape evenness. The landscape diversity is often represented by three indices, which include Shannon diversity index (SHDI), Simpson diversity index (SIDI), and modified Simpson diversity index (MSIDI). Patch richness (PR) is simply the number of patch types. The landscape evenness is further described by Shannon evenness index (SHEI), Simpson evenness index (SIEI), and modified Simpson evenness index (MSIEI). For landscape configuration, this study used the interspersion and juxtaposition index (IJI) to illustrate the distribution characteristics of the landscape patches. Detailed definitions of these indices can be referred to McGarigal and Marks (1994).

2.2.2 Monitoring of landscape changes

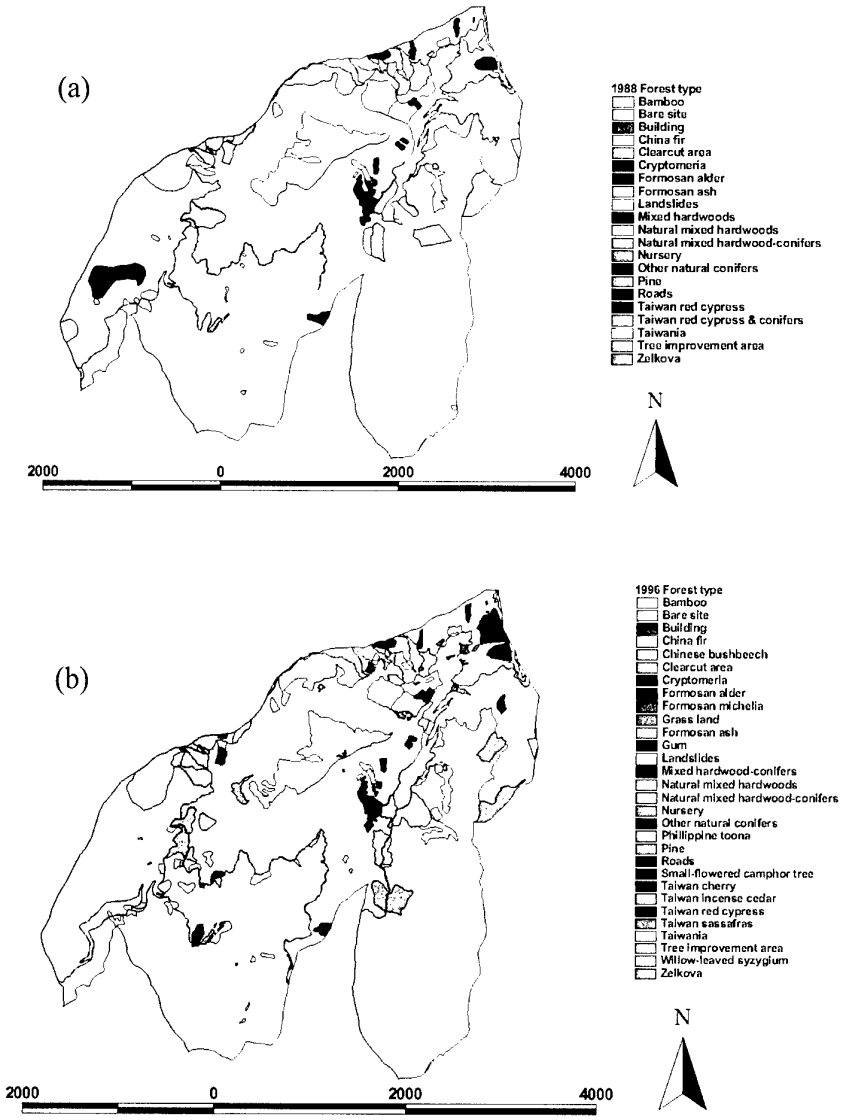


Figure 1. (a) Forest type map of 1988, (b) forest type map of 1996.

2.2.2.1 Analysis of landscape changes

Figure 1 illustrates the distribution of each forest type in1988 and 1996. The landscape is mostly composed of natural mixed hardwood forests, which can be regarded as the matrix of landscape. Resulting from human disturbances, plantations and forest roads can be treated as patches and corridors. From 1988 to 1996, it is apparent that management activities (e.g. plantations replanted after cutting and forest road building) were two major landscape changes. Therefore, this study used the aforementioned eight quantitative landscape structure indices to analyze the effects of cutting and forest road building on landscape changes.

2.2.2.2 Test of landscape changes

To understand the effects of cutting and forest road building on forest landscape changes, this study used the t-test method proposed by Magurran (1988) to examine the variation of landscape changes in the study area. This method was based on the Shannon diversity index. The equation of

t-test is as follows:

$$t = \frac{(H_1 - H_2)}{(VarH_1 + VarH_2)^{1/2}} \tag{1}$$

$$H_i = -\sum_{j=1}^{m_i} P_j \cdot \ln P_j - \frac{m_i - 1}{n_i} \tag{2}$$

where H_i is the Shannon diversity index of landscape i or stage i, m_i is the number of patch types, n_i is the number of patches, and P_j refers to the percentage of either the number of patch type j to the total number of patches, or the area of patch type j to the total area. The latter definition of P_j was used in this study. $VarH_i$ is the variance, and its equation and degree of freedom are as follows:

$$df = \frac{(VarH_1 + VarH_2)^2}{(VarH_1)^2 / n_1 + (VarH_2)^2 / n_2} \tag{3}$$

$$VarH_i = \frac{\sum_{j=1}^{m_i} P_j (\ln P_j)^2 - (\sum_{j=1}^{m_i} P_j \cdot \ln P_j)^2}{n_i} + \frac{m_i - 1}{2n_i^2} \tag{4}$$

3. RESULTS

The results of using GIS to quantify the landscape structure and eight quantitative indices to analyze the landscape changes were as Table 1. Table 1 depicts the quantitative indices of landscape structure derived from forest type maps of 1988 and 1996. The differences and the effects of cutting and forest road building on forest landscape of 1988 to 1996 were as follows:

(1) Cutting and forest road building resulted in increase of patch numbers (PN) from 104 to 249 and patch richness (PR) from 21 to 30.
(2) All the three landscape diversity indices (SHDI, SIDI, MSIDI) increased from 1988 to 1996, and SHDI had the largest increment among these three indices. The result reveals that the Shannon diversity index performed better in distinguishing landscape diversity.
(3) All the three evenness indices (SHEI, SIEI, MSIEI) decreased from 1988 to 1996, and SHEI had the largest decrement among these three indices. The result reveals that the patches within the landscape tended to distribute more unevenly after cutting and forest road building, but the difference was not significant.
(4) The interspersion and juxtaposition index (IJI), representing landscape configuration, decreased after cutting and forest road building. The difference in IJI is more prominent as compared to the indices of landscape diversity and landscape evenness. This reveals that the disturbance from cutting and forest road building resulted in more uneven distribution of adjacencies for the landscape configuration.

Table 1. Effects of cutting and forest road building on forest landscape from 1988 to 1996.

Index	1988 yr.	1996 yr.	Difference
PN	104	249	145
PR	21	30	9
SHDI	0.998	1.024	0.036
SIDI	0.427	0.432	0.005

MSIDI	0.558	0.566	0.008
SHEI	0.325	0.301	-0.024
SIEI	0.448	0.447	-0.001
MSIEI	0.184	0.166	-0.018
IJI	48.630	46.620	-2.010

To examine whether cutting and forest road building caused significant effects on landscape changes or not, a statistical method was needed to test the extent of landscape changes. Table 2 was obtained using t-test of Shannon diversity index at α=0.05. The results indicate that cutting and forest road building from 1988 to 1996 did not cause significant landscape changes in the study area.

Table 2. T-test results of Shannon diversity index.

t value	0.222
Degree of freedom	204
Test result	NS[1)]

[1)]NS: not significant at 5% significant level.

4. DISCUSSION

In this study, the forest type data obtained from 1988 and 1996 were used to quantify the landscape structure and to evaluate the effects of cutting and forest road building on landscape changes. The results were obtained based on: (1) the scale of forest type maps was 1/5000; (2) the maps were in vector format rather than raster format; (3) the P_j used for calculating landscape diversity and landscape evenness indices was defined as the percentage of the area of patch type *j* versus the total area. For different map scales, raster format maps, and defining P_i as the number of patches of type *j* versus total number of patches, the results need to be further studied and compared.

The quantitative indices of landscape composition can be used to analyze landscape changes. However, the landscape diversity indices had larger differences and more consistent results than the landscape evenness indices, and therefore are more suitable for landscape changes analysis. Among the three landscape diversity indices, the Shannon diversity index is most suitable for analysis.

The landscape structure indices including diversity indices, evenness indices, and interspersion and juxtaposition index were either slightly increased or decreased after cutting and forest road building. This implies that management activities can affect landscape changes. However, the t-test results of Shannon diversity indicate that effects of cutting and forest road building on landscape changes in the study area were not significant.

5. CONCLUSION

The study was concluded as follows:

(1) Application of GIS and quantitative indices of landscape structure in evaluating the effects of cutting and forest road building on landscape changes is a feasible and effective approach. This approach can be used for landscape planning and monitoring of the study area in the future.
(2) Management activities such as cutting and forest road building increased the numbers and

types of patches. They not only directly altered the variety and abundance of the patches, but also indirectly affected the landscape structure properties such as landscape diversity, evenness, and interspersion and juxtaposition. Several indices were compared, and it was found that landscape diversity indices had larger differences and more consistent results, and therefore they were more suitable for landscape changes analysis. In addition, among the three landscape diversity indices, the Shannon diversity index performed better in distinguishing landscape changes.

(3) From the t-test results of Shannon diversity index, cutting and forest road building did not cause significant effects on landscape changes in the study area. Therefore, from landscape perspective, management activities of the study area did not incur significant effects on the forest landscape up until 1996.

REFERENCE

Burrough, P.A., 1986. Principles of Geographic Information System for Earth Resources Assessment. Clarendon Press, Oxford, UK, 193 p.

Cheng, C.C., J.F. Jan, and L.T. Hsu, 1999. Application of fractal dimension in monitoring forest landscape structure and change. Taiwan Journal of Forest Science, 14 (4), pp. 397-407 [in Chinese with English summary].

Cola, L.D., 1989. Fractal analysis of a classified Landsat scene. Photogrammetric Engineering and Remote Sensing, 55 (5), pp. 601-610.

Dunning, J.B., B.J. Danielson, and H.R. Pulliam, 1992. Ecological processes that affect populations in complex landscape. Oikos, 65, pp. 169-175.

Huang, C.C., 1997. Study on landscape monitoring of forest: an illustration of Huisun Experimental Forest Station [dissertation]. National Chung-Hsing University, Taiwan, 161 p. [in Chinese with English summary].

Lam, NS-N., 1990. Description and measurement of Landsat TM image using fractals. Photogrammetric Engineering and Remote Sensing, 56 (2), pp. 187-195.

Li, H., 1990. Spatio-temporal pattern analysis of managed forest landscape: a simulation approach [dissertation]. Oregon State University, Corvallis, 166 p.

Magurran, A.E., 1988. Ecological diversity and its measurement. Princeton University Press, Princeton, NJ, 179 p.

McGarigal, K., and B.J. Marks, 1994. Spatial pattern analysis program for quantifying landscape structure. Dolores (CO): P.O. Box 606. 67 p.

Olsen, E.R., R.D. Ramsey, and D.S. Winn, 1993. A modified fractal dimension as a measure of landscape diversity. Photogrammetric Engineering and Remote Sensing, 59 (10), pp. 1517-1520.

O'Neill, R.V., J.R. Krummel, R.H. Gardner, G. Sugihara, B. Jackson, D.L. DeAngelis, B.T. Milne, M.G. Turner, B. Zygmunt, S.W. Christenser, V.H. Dale, and R.L. Graham, 1988. Indices of landscape pattern. Landscape Ecol 1, pp. 153-162.

Rex, K.D., and G.P. Malason, 1990. The fractal shape of riparian forest patches. Landscape Ecology, 4 (4), pp. 249-258.

Turner, M.G., 1990. Spatial and temporal analysis of landscape patterns. Landscape Ecol 4, pp. 21-30.

Turner, M.G., and R.H. Gardner, 1991. Quantitative methods in landscape ecology. Ecol Studies. Vol. 82. Springer-Verlag, New York, 536 p.

Wang, S.F., 1998. Application of geographic information system and fractal dimension in forest landscape spatial variation monitoring. [MSc thesis]. National Taiwan University, Taiwan. 73 p. [in Chinese with English summary].

GIS for Visual Impact Assessment

ZONGYU ZHANG, JIN YEU TSOU, and HUI LIN*
Department of Architecture, Geography*, The Chinese University of Hong Kong,
Shatin, Hong Kong, China
Emails:s992332@mailserv.cuhk.edu.hk, jinyeutsou@cuhk.edu.hk,& huilin@cuhk.edu.hk

Abstract

As an important component of urban landscape planning, visual impact assessment is mainly concerned with: A. the direct impacts of the development upon views of the landscape through intrusion or obstruction; B. the reactions of viewers who may be affected; C. the overall impact on visual amenity, which is often cumulated by plenty of minor process and can be range from degradation through to enhancement (IEATLI, 1995). In this article, the dichotomy of quantitative methods and 3D simulation for visual impact assessment are exposed based on the review of previous work and the characters of visual impact on urban landscape (Wherrett, 1996). Although these two methods are different greatly in software choosing and operational processes, they both aim at improving the preciseness and efficiency in capturing the impact to original landscape and public responses. The integration of both in one system is desired for visual impact assessment on urban landscape. Geography Information System (GIS) excels in the integration of quantitative and 3D simulation methods. The specifications for such a specific GIS are elicited. In includes the considerations on system functions, data management, project management, and user interface design. An experimental GIS system for visual impact assessment is also developed to test the feasibility of such integration.

Keywords: Visual impact assessment, urban landscape, GIS

1.Introduction:

The fast development of society accelerates the transformation or urban landscape. As an important facet of society and environment, the urban landscape's visual quality is attracting people's attention. To favour people's appreciation for high quality urban landscape, urban planners improve the visual sustainability in urban natural landscape and maintain valuable natural landscape resources with high visual quality in urban space . Urban visual landscape evaluation includes three major problems: the technical problem of how to visualise possible changes in the landscape; the theoretical problem of how to evaluate scenic beauty; and the administrative problem of how to integrate visual aspects in the planning process (Lange, 1994). In the past, planners emphasize on the analysis of people's preference on natural landscape and beauty degree evaluation of it (Wherrett, 1996). One the basic facets of urban landscape evaluation, visual impact assessment, however, have been overshadowed.

Visual impacts relate solely to changes in available views of the landscape, and the effects of those changes on people. They arise from the changes in land use, the development of buildings and structures, changes in land man-management, and less

commonly, the changes in production process and emissions. In addition, in the life of a project, many different sources of impact occur at various stages, that is during construction, operation, decommissioning and restoration. " Visual impact assessment is an important component of landscape planning and its part of process which seeks to provide the best 'environmental fit' for a development."(IEATLI, 1995)

3D simulation and quantitative analysis play important roles in the assessment of visual impact. Quantitative analysis for visual impact assessment includes view shed and indivisibility calculating. Its output can be projective maps, which are initiated from viewpoints within the development (inside looking out), or reflective mappings, which are initiated from viewpoints in the surrounding landscape (outside looking in). Objective of the former is to reveal the extent of visibility of the development to its surroundings. And the latter's objective is to determine whether, and to what extent, the development is visible from its surroundings. There have been few comprehensive programs to incorporate the visualization tools into environmental resource modeling system, nor to systematically evaluate the usefulness and applicability of such systems to agency and public decision making settings. In some areas there are comprehensive resource models, but lacking visualization capabilities in others there are well developed visualization tools but poor links to quantitative modeling (Orland, 1992a). Recently, situation seems the same. Homana developed specific Geographic Information Database for landscape evaluation (Homma et al, 1999). They utilized professional GIS software to accomplish the view shed and visibility precise calculating, but lacked in the simulation. Tsou integrated CAD, QuickTime VR and Visual Studio to assess the visual impact of the construction of one electronic substation, while did not analyze in quantitative (Tsou, 1999). Situation shows the importance of the integration of both simulation and quantitative analysis.

CAD software shows efficiency and effective in the complex scene simulation. It maps the image as texture to improve the vivid of simulation. The scene can also be animated into movies or high-resolution picture by so called ray-tracing technology. Recent developed technology called quick time VR is an image based panorama. By merging the documentation of the existing site environment with photos and QuickTime VR (QTVR) panoramas with CAD models, the future scene of that site can be rendered. Quick time VR allows some kinds of predefined interaction such as rambling in the virtual reality. Aimed at design assistant, CAD lacks in so called spatial analysis and precise simulation of 3D terrain. That makes the frequently computation of view shed analysis in visual impact a heavy task. Long as geo-analysis directed software, GIS excels in the spatial analysis. By the integration of both spatial analysis and 3D analysis modules in GIS, users are empowered to complete viewshed or visibility computation. The visual impact of new developed constructions or feature planning to specific features can be demonstrated by overlay the feature maps with view shed map. To those who only interested in 3D simulation, developers can customize GIS software with includes 3D-analysis extension to crater to their requirements. In addition, directed by so called engineering theory, GIS excels in project management. Which can also release those who work on visual impact assessment a lot. In this article, the integration of both simulation and quantitative analysis in a specific GIS for visual impact assessment will be discussed based on GIS's 3D analysis and spatial analysis extensions.

2.Specifications elicited for system design (Capturing the requirements)

It includes the considerations on database and user interface design, and emphasizes on project management, interactions between 2D analysis and 3D simulation, the integration of quantitative analysis and 3D simulation.

2.1 Function Requirements

The visual impact assessment of a proposed development addresses three types of issues: spatial, quantitative and qualitative. Spatial issues include where the development is visible from or, more specifically, what or whom it is visible to; quantitative issues include how much of the development is visible, how much of the surrounding area is affected, and to what degree; and qualitative issues include the visual character of the development and its compatibility with its surroundings. The first two issues can be due to the changes of the indivisibility for given development. The qualitative facet of the visual impact assessment lies more on people's subjective judgement and is hard to be quantified. In addition, the last one is also based on the outcome of the former two analyses. Homma et al (1999) utilized some specific mathematical model called Analytical Hierarchy Process (AHP) to assist the evaluation of visual impact from a designed garbage processing plant based on the prior viewshed analysis.

The principle of indivisibility states that visibility is determined in two ways either from the site or to the site. It includes both being viewed from outside of the development's boundaries and the outside view from the developing site to adjacent areas. In GIS's 3D analysis extension, they are both under the calculation of viewshed . Viewshed includes all visible or invisible area in the city from given viewpoints or view corridor (ESRI, 1997). View corridor means the corridor from the viewpoint to the scenery. In the urban area, view corridor often follows the route of roads, sidewalk of rivers, or some other linear. In landscape design, visibilities between scenery are often maintained for good visual effects. It is also necessary to maintain some visual relations between important landscapes in order to form the whole visual landscape effects. View corridor shows the dynamical characters of urban landscape. Different with static analysis of indivisibility calculation and its low efficiency in the demonstration of view corridor analysis, 3D simulation exhibits dynamically the variations of scenery when walking along the view corridor by animation. View corridors affect the layout and height of buildings. They also have effects on the layout of plant.

Besides the view shed and view corridor, there are also some other factors should be considered in design a specific GIS for visual impact assessment. In the city, areas show great differences in their magnitude of visual values. Even when it comes to a same building, some façades contribute more to its visual character. Those make it necessary to level constructions according to their visual values. And the visual impact of new constructions should also involve the parts which intercept with those prior parts.

2.3 Project Management

From the viewpoint of engineering, the process of urban planning or some other urban visual environment impacting projects can often be divided into three parts: capturing the requirements, feasibility analysis and design. Visual impact assessment often stands in the front part of them. It reveals the degrading or improvement of urban

planning projects to the original urban landscape. In the first stage of those projects, planners interview, poll or do some other investigations to infer the customers' requirements for the project, and form the project's norms and specifications. All limitations are analyzed in the following process to weigh the feasibility of that project. It includes the future expenses, national and regional polices, natural environment of the site and some other objective qualifications. The design is then modeled to simulate the future situation and also is assessed for its visual impacts. If those who concerned are satisfied with the design, planners can congratulate on their success; otherwise, they would have to repeat the whole process from beginning. Which often makes the whole project a lengthy and reciprocate process. And it also shows as an important part of the whole urban planning, visual impact assessment should be managed in projects.

GIS assists planners to quickly capture their customers' requirements for desired visual environment, even if people just have some vague pictures of what they want. Actually it is often hard for them to imagine the outcome of planners' design based on maps, and discussion or some other well-organized communications can often invigorate their inspiration for what visual environment they desire. GIS and the WWW are ever evolving technologies with the potential for public use allowing greater involvement in environmental decision making and "they can design GIS primarily for expert use or they can make them accessible to the lay professional and even to the general public". When connected with Internet, GIS grants people to live talk with all those who concerns the site planning. What's more, the web based GIS models the future scene of the planning site in either two-dimensional or three dimensional forms and broadcast them on web page, people can have a vivid impression on the outcome of the project. People can express their opinions by sending email or attend an online live chat and all those communications are logged and feedback to planners to rectify their design. All those contribute a lot to clarify and pinpoint people's subjective attitude to the impacted visual environment based on GIS's objective quantitative analysis and 3D simulation ability. The inner character for broadcasting to public of visual impact assessment desires more on web based GIS.

For the consideration of quickly prototyping, it is desired to integrate both the design and the evaluation modules into one system. But popular GIS system shows low efficiency and inhabit to those used to finish their design on CAD software. Import of data from another kind software challenges greatly the inter-operatibility of GIS. Although many popular GIS software, such as Arc/Info, Arcview or MapCAD, have specific extension for the import of CAD data, the semantics of data structure defined in GIS and CAD are differentiated. Thus makes it also important for developer to customize the imported data from other software to be GIS style. The reverse situation seems the same. The outcomes of visual impact assessment are often stored in the database as electronic maps. It needs to be reversed transformed into CAD or other software data format according to their semantics.

2.2 User Interface

Many commercial GIS software provides the allowance for developers to customized the user interface according to specific requirements. Following the current software's Window's style, the user interface of the specific GIS for visual
impact assessment should be graphical. However, the gap between the system and public still exits. It comes from the unfamiliarity between public and GIS. That challenges the

specific GIS for VIA not only in the system functions but also the user interface and system work style. The latter often contributes more to the public's acceptance for the specific system. In this article, a specific query language, which extends the SQL, is designed to facilitate planners in VIS process The extended SQL is aimed to be in oral style and accompanied by some jargon in VIA, which makes it easy to understand. Its architecture is transferred from standard SELECT-FROM-WHERE form into SELECT-FROM-WHERE-WHAT IF format. The input of query statement can be in text or visual design in customized Java Applet panel. The latter empowers user to interact with spatial objects on the displayed map while accomplishing the query statement. For example, to finish the query on visible area from given viewpoint, user can set up the view point in the WHERE clause by selecting its Id code in the candidate listbox or directly pinpoint it on the map. We map the specific spatial analysis for VIA into meta-operations of the extended SQL. It includes the viewpoint selecting, view shed analysis, and set operations. The user's interaction with themes or spatial objects on the map is also introduced into the SQL statement's formation. For instance, to answer 'what if' questions, system empowers user to do some editing operations on line or polygon objects in the active theme. The result will be included by the WHAT IF clause.

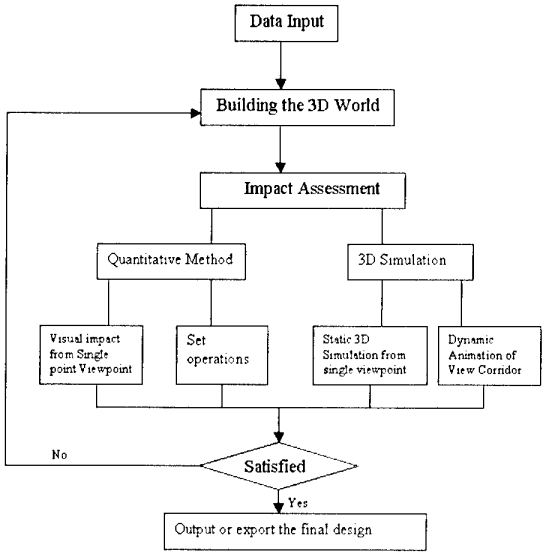
3. Case System

An experimental GIS system has been developed to test the method of integration of both quantitative method and 3D simulation for visual impact assessment by customizing the Arcview 3.1 with spatial analysis and 3D analysis extensions.

Spatial objects stored in the Database Management System (DBMS) are first classified according to their significance in global or local urban landscape. And also main façades of buildings, which contribute more to their scene character, are identified. The categorical system for the features can be listed as below:

Categorical	Contents
Natural landscape Resources	.Natural parks .Community gardens .Recreation facilities
Humanities landscape resources	. Scenic spot .Shrine and temple
Public utilities	.Public Office .Schools .Hospitals .Public Hall .Harbours
Resident Areas	.Residential quarters .Apartment houses
Public Transportation	.Main local road .National roads .Railway tracks
Planning project	.Draft of the constructions design .Reshaped Terrain

The assessment process can be diagrammed as following:



4. Preliminary finding and future work:

The experiment GIS system demonstrate the feasibility in the integration of both quantitative analysis and 3D simulation for VIA. It is illustrated by the identical viewpoint in both the two dimensional view for quantitative analysis and the 3D scene for simulation. The comprehensive utilization of set operations for visual impact detection effectively exposes the cumulative visual impacts. However, the system still shows its limitations and should be improved in the future.

1. The representation ability of GIS in three dimension for complex scene shows less vivid.
2. As mentioned before, VIA characterizes in its public. It is more desired to transfer the whole process from desktop to Internet. Currently, popular web GIS platform shows limit in provide complex analysis service and also lacks in 3D simulation.
3. Different from the popular computer aided architecture design software, GIS lacks the flexible toolkits to support design. Some minute edit tool such as changing spatial objects' positions, dimensions can also benefit a lot for quick design prototyping.

Reference:

Arcview 3D Analyst, 3D Surface Creation, Visualization, and Analysis. Environmental System Research Institute INC(ESRI) .

Institute of Environmental Assessment and The Landscape Institute (IEATLI), 1995 *Guidelines for Landscape and Visual Impact Assessment.* First Edition. London: E&FN SPON, and imprint of Chapman&Hall.

Homma, R., IKI,K., Morozumi, M., and Morisaki, T. 1999. Geographic Information Database for Landscape Evaluation. Proceedings of the Fourth Conference on Computer Aided Architecture Design Research in Asia. Shanghai Scientific and Technological Literature Publishing House.

JEFF W.T.Kan, BENNY K.M.CHOW, and JIN-YEU,TSOU,1999. Visual Impact evaluation of electricity substation architecture. Proceedings of the Fourth Conference on Computer Aided Architecture Design Research in Asia. Shanghai Scientific and Technological Literature Publishing House.

Lange, E. 1994 Integration of computerized visual simulation and visual assessment in environmental planning. *Landscape and Urban Planning, 30, PP99-112.*

Orland,B.(1992a) Data Visualization Techniques in Envrionmental Management. *Landscape and Urban Planning, 21, 237-244.*

Orland, B.(1994) Visualization techniques for incorporation in forest planning geographic information systems. *Landscape and Urban Planning, 30,83-97.*

Wherrett, J.R., 1996. Visual Impact Assessment. *Visualization Techniques for Landscape Evaluation Literature Review.* http://bamboo.mluri.sari.ac.uk/~jo/litrev/chapters.html.

The 21st Asian Conference on Remote Sensing
December 4-8, 2000 Taipei, TAIWAN

INTEGRATION AND APPLICATION OF SOCIO-ECONOMIC AND ENVIRONMENTAL DATA WITHIN GIS FOR DEVELOPMENT STUDY IN THAILAND

Tran Hung, Yoshifumi Yasuoka
Institute of Industrial Science, University of Tokyo
4-6-1 Komaba, Meguro-ku, Tokyo 153-8505, Japan
Tel: +81-3-5452-6415 Fax: +81-3-5452-6410 E-mail: tranhung@iis.u-tokyo.ac.jp

KEYWORDS: GIS, Information Integration, Development Study, Thailand

ABSTRACT: Effective decision-making often requires information on various aspects of regional development, which is not so easily obtained, especially in developing countries. Beside the data paucity, the socio-economic information is very different in their geographic properties to those relating to the physical world. This paper presents a set of combined GIS procedures to integrate up-to-date information from remotely sensed data with demographic and socio-economic data in order to create a comprehensive spatial database for two fast-growing suburban areas in Thailand (Chiang Mai – Lamphun and Pathum Thani areas). Issues, which arise in the integration of disparate data sets such as scale and modifiable area unit problems, are addressed. Then, with a combination of logical and statistical operations, reliable data variables are derived to monitor and represent underlying factors of regional development in the study areas. An example of spatial modeling on urban-rural interactions demonstrates how the unified set of spatial and spatialized socio-economic variables can be used to gain insights into regional development problems. The paper also discusses other potential uses of the integrated database. The results of these case studies show that *socioinformatics* overcome the "data barriers" problem and can be successful in the developing world.

1. INTRODUCTION

Up-to-date and reliable information is vital for the management of a region's human and natural resources and for dealing with regional development decisions that have a spatial context (Klosterman, 1995). A comprehensive information base could reduce uncertainty and enhance decision-making. Managers and policy makers may wish to integrate social, economic and environmental data in order to formulate strategic development plans (Kliskey, 1995). In developing countries, however, the *data barriers* are still obvious due to both institutional and technical reasons. As institutional issues are being recognized and governments start to invest millions of dollars in collecting data, the data management and usage are still far from satisfactory level. Information on various aspects of regional development – social, economic and environmental data – is originally collected for different purposes, at different scales, at different time frames and with different underlying assumptions about the nature of the phenomena. This creates technical difficulties to the integration of social and environmental data, and explains the scarcity of successful empirical researches on regional development analysis in developing countries.

Recent technological advances in geographic information system (GIS) have made it possible to manipulate large amounts of geographic data and construct the topological structure underlying complicated spatial phenomena. As about 80-90% of data collected and used for regional and environmental information systems are related to geography (Huxhold, 1991), GIS provides such an integrated computing environment for social and environmental data integration. This

paper addresses the data integration problem in regional development studies in Thailand. Results of spatial analysis are also presented to illustrate the usefulness of integrated spatial GIS database in gaining insights into regional development problems in Chiang Mai – Lamphun and Pathum Thani areas, Thailand. The data integration presented in this paper was conducted on the 'loose integration' between GIS (Arc/Info, Imagine) and developed Visual FoxPro routines.

2. DATA INTEGRATION ISSUES

Originally, social, economic and environmental data are collected for different purposes, at different scales, and with different underlying assumptions about the nature of the phenomena. The subjects of environmental data often exhibit continuous spatial variation (e.g., elevation, soils, precipitation, and temperature) while social phenomena tend to be more spatially discrete (e.g., people, farms, factories and administrative units). The spatial physio-graphic data are normally available in the map forms from various mapping and surveying agencies. With rapid advances of remote sensing technologies during the last two decades, satellite imagery provides accurate and up-to-date information of the land surface, making the integration of remotely sensed data with other environmental and socio-economic data sets beneficial. However, in order to produce regional empirical models of urban-rural interactions, social and environmental data must be in a common format.

A variety of approaches to integrating social and environmental data exist namely: full integration, loose integration and parallel analysis. Among them, the loose integration appears to take most advantages of GIS systems (e.g., overlay and regional characterization techniques) while provide enough flexibility to a user (mainly planners or managers) in deriving information at desired administrative units (Brown, 1996). Conversions between areal units or the creation of new areal units, which represent the intersection of two sets of units, provide mechanisms for comparing disparate data. Data collected and aggregated to some spatial aggregation unit (e.g., Thailand's tambols) can be converted from those units to other spatial units through a variety of approaches. Areal interpolation can be carried out using techniques outlined by Tobler (1979), Flowerdew and Green (1989), and Goodchild *et al.* (1993). A common assumption for many of these methods is that the density of the count variable, or the value of a density variable, is constant throughout each of the units. As spatial units defined for environmental data are nearly always designed to be internally homogenous to some degree (e.g., soil units, land cover types), while socio-economic units are nearly always the product of some political process; they are administrative units. That so-called *modifiable area unit (MAU) problem* may create biases towards one set of data. Thus, before data integration, the internal heterogeneity of administrative units should be investigated and remedial measures should be considered.

3. FRAMEWORK FOR DATA INTEGRATION IN THAILAND

3.1 Data Collection and Database Building

With regional development issues in the focus, data in Chiang Mai – Lamphun and Pathum Thani areas, Thailand were collected from various government offices in the form of physio-graphic data (e.g., topographic, administrative, land-use, industrial locations as well as transportation network maps) and socio-economic indicators. Satellite data of different dates (1986, 1989, 1993, 1999 for Pathum Thani and 1986, 1994 for Chiang Mai – Lamphun areas) were used to provide up-to-date land cover and land use information. The image processing procedures were used to classify georeferenced remotely sensed images and to produce updated classified land-use maps and transportations networks maps in raster format (ERDAS Imagine). The detailed image processing procedures were discussed in Tran (1998). The spatial physio-

graphic data sets from paper maps were classified, digitized and fed into vector GIS (Arc/Info). The classified images were, then, integrated with other environmental and societal data sets through raster-to-vector data conversion to update and build time series data. As the loose data integration approach was used in this research, data were managed in both raster and vector format and convert from one to another when data analysis required.

The major source for socio-economic data is the National Rural Development Database (NRD-2C), which provides surveyed data at village level after each two years from 1986 composing of more than 100 economic and social indicators. The data were also collected from other government documents, statistical records at provincial and municipal offices. They were selected, reclassified and combined based on the basic administrative unit IDs – village code number in dBase IV format. A program in Visual FoxPro was written to automate the process of extracting, normalizing and combining socio-economic indicators including population, income, education, health, natural environmental conditions, services, agriculture and industrial activities, work force, capital investment, employment, etc. (Tran, 1998).

3.2 Integrated GIS Database Management

As data management in GIS facilitates the integration of diverse data sets and determines the analyses possible with those data, some data transformation routines were built in this research to facilitate the conversion of physio-graphic and socio-economic data to a common spatial structure (e.g., set of areal units). The spatial physio-graphic data in GIS database were to summarize/regionalize by administrative units in order to be compatible with socio-economic data.

Modifiable area unit problem: To choose desirable aggregation units criteria on within-unit variance and spatial autocorrelation index were used. In the case of Chiang Mai – Lamphun area, two possible regionalizations on the basis of aggregated villages were examined for 1036 selected villages: by *amphoe* or by *tambol*. The internal variation in each of the spatial units (*regions*) was measured using the average coefficient of variation of test variable (village population density in 1994). The between regions variation was calculated as the coefficient of variation of all regional population values (*Coefficient of Variation = Standard Deviation / Mean*).

Table 1 Comparative study of variations for different variables on various levels of aggregation of population density in 1994 data.

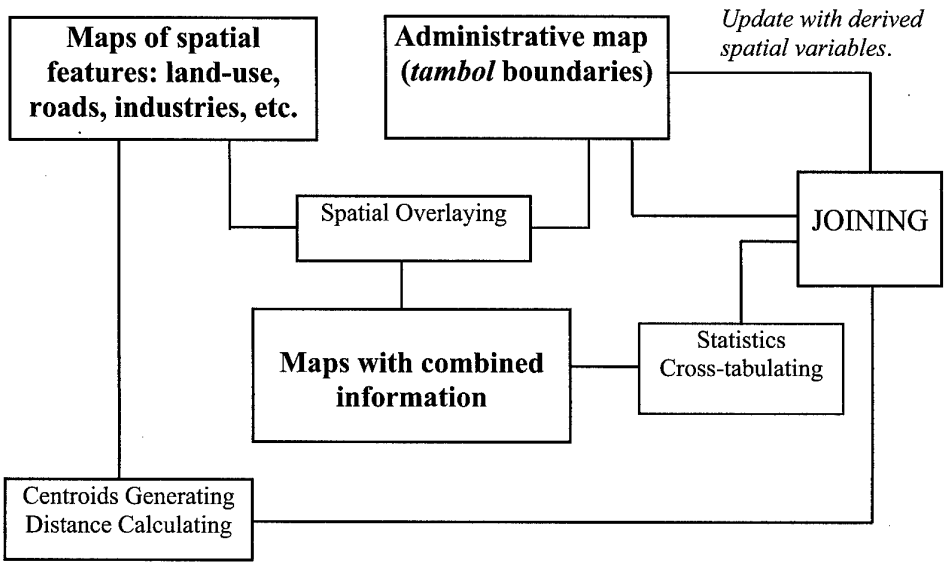
Regionalization Level	No.	Within-unit Coeff. of Variance	Between-unit Coeff. of Variance	Moran Coefficient
Villages	1036	N / A	28.52	N / A
Tambols (sub-district)	146	24.23	29.39	0.4441
Amphoes (district)	16	41.47	33.54	0.7104

The results reported in Table 1 indicated that *amphoes* have higher within-regions rather than between-regions variation of population density and much higher Moran coefficient of autocorrelation as compared to *tambols*. This showed that the aggregation at *amphoe* level would increase the loss of spatial information, leaving the *tambol* level as the desirable level of aggregation (basic spatial unit) for data integration.

Compilation of socio-economic data: The socio-economic data were aggregated from village to *tambol* level, and were normalized as relative shares of the total population of each respective *tambol*, in order to further reduce the effect of unequal sizes of *tambol*.

Creating Spatial Indicators within GIS: The spatial physio-graphic data such as land use types, road networks, irrigation networks, industrial factories were aggregated to tambol level using spatial overlay and logical-statistical analysis functions in GIS (Arc/Info). Some accessibility measures such as distance from residential areas to nearest roads and nearest factories were derived through GIS spatial joins functions utilizing the locational information of data. The common summarizing/regionalizing procedures are presented in Figure 1.

Figure 1 GIS procedure to regionalize the spatial physio-graphic indicators into *tambol* level from Chiang Mai - Lamphun spatial database.



Comprehensive spatial GIS database: With all aggregated socio-economic data and regionalized spatial physio-graphic data to common tambol level, the GIS join function through a key item – *tambol* ID – was used to complete the spatial GIS databases for Chiang Mai – Lamphun and Pathum Thani areas. The GIS databases, thus, containing comprehensive spatial information characterizing development states of the Chiang Mai – Lamphun area (in 1986 and 1994) and Pathum Thani area (in 1979, 1989 and 1999) for each tambol in terms of:

- *spatial physio-graphic data*: % of urban land-use, industrial land-use, agricultural land-use, road length density, irrigation length density, median distance from industrial land to closest residential areas, median distance from residential area to the nearest road;
- *demographic aspect*: population density; *economic aspect*: average household property taxes, travel time to nearest town and commercial center, % of farmer, per capita number of vehicles, number of factories, per capita industrial capital investment, % factory employees, average household income, % people working far from home; and *social aspect*: level of primary education, secondary education, illiterate rate, etc.

3.3. Spatial Data Analysis

The resulting spatial data sets in unique format are useful for further empirical analysis of regional spatial development patterns using various multivariate statistical and spatial statistical analysis techniques. With these databases, policy makers can easily explore data and their spatial coincidences at locations of interest, visualize spatial patterns in economic, social and demographic aspects at times of interest, visualize time trend of regional development based on social / environmental indicators of interest, and create various tambol development index based on combined indicators for planning and management. On the other hand, with more sophisticated analysis and modeling tools, researchers could go further in analysis to gain insights into regional development problems. As an example to illustrate the utilization of the derived GIS databases, below is a spatial model of urban-rural interactions in Chiang Mai – Lamphun area, Thailand. As rural labor outflow (in form of *% of Working-out Population* variable) indicates job attraction of urban centers as well as the excess of free labor released from the agricultural sector, it could represent the intensity of urban-rural linkages, as a result of regional development. The spatial regression techniques were adopted to produce the final spatial-lag regression model of urban-rural interactions in Chiang Mai – Lamphun area in 1994 as shown in Table 2. It confirmed significant urban-rural disparity and important roles of industrial establishments and infrastructure development in regional labor migration in Chiang Mai – Lamphun area. The detailed modeling process and its interpretation are beyond the scope of this paper; they were discussed in Tran (1998). Some results in analyzing urban-rural interactions using the integrated GIS database in Pathum Thani area will be discussed in the presentation.

Table 2 Results of spatial-lag regression analysis to study the urban-rural interactions in Chiang Mai- Lamphun area in 1994.

Response Variable: *ln(Working-out Population + 1)*
pseudo R^2 = 0.4921 Log-likelihood = -88.428 AIC = 122.855

Variable	Coefficients	Std. Err.	z-value	Prob
Lagged variable of *Ln(Working-out Population+1)*	0.0497432	0.0126568	3.930157	0.000085
Constant	1.39591	0.232631	6.000540	0.000000
Rural-Urban Indicator	0.464627	0.187835	2.473583	0.013377
Neg. Accessibility Measures	-0.322413	0.0597546	-5.395623	0.000000
Pop. Density	-9.88531E-05	5.02207E-05	-1.968374	0.049025
Lagged variable of Industrialization index	0.186305	0.105104	1.772585	0.076297

Regression Diagnostics
Breusch-Pagan (heteroskedasticity) = 36.347 (p = 0.000)
Lagrange Multiplier test (spatial error dependence) = 1.966 (p = 0.125)

4. CONCLUDING REMARKS

The paper has indicated that GIS is a useful technical tool in integrating social and environmental data for regional development studies in Thailand. With decentralization planning on increase in Thailand, these comprehensive GIS databases at tambol level could provide needed details to local decision makers at the newly-created administrative level – Tambol Administrative Organization (TAO). The results of these case studies showed that

socioinformatics overcome the "data barriers" problem and can be successful in the developing world. Furthermore, with the developed spatial databases, GIS can serve as an efficient technical vehicle for spatial analysis and spatial modeling functions to gain insights into regional development problems, e.g., to evaluate development impacts in the past, and to enhance regional development strategies through facilitating various scenarios. Some theoretical issues on data integration, however, remain to be further addressed as an important area of future research. The data integration framework described in this paper can be also extended into various regional environmental impacts researches.

REFERENCES

Brown, D.G., 1996. Spatial statistics and GIS applied to internal migration in Rwanda, Central Africa. In Arlinghaus S. L., Practical Handbook of Spatial Statistics. New York: CRC Press Inc., pp. 149-173.

Flowerdew, R., and Green, M. (1989). Statistical methods for inference between incompatible zonal systems. In M.F. Goodchild and S. Gopal, Accuracy of Spatial Databases. London: Taylor and Francis, pp. 239-247.

Goodchild, M.F., Anselin, L., and Deichmann, U. 1993. A framework for the areal interpolation of socioeconomic data. Environment and Planning A, Vol. 25, pp. 383-397.

Huxhold W.E., 1991. Introduction to Urban Geographic Information Systems. New York: Oxford University Press Inc.

Kliskey A.D., 1995. The role and functionality of GIS as a planning tool in natural-resource management. Computer, Environment and Urban Systems, vol. 19, No. 1, pp. 15-22.

Klosterman R.E., 1995. The appropriateness of geographic information systems for regional planning in the developing world. Computer, Environment and Urban Systems, vol. 19, No. 1, pp. 1-13.

Tobler, W. 1979. Smooth pycnophylactic interpolation for geographical regions. Journal of the American Statistical Association, Vol. 74(367), pp. 519-536.

Tran H., 1998. Integrating GIS with spatial data analysis to study the development impacts of urbanisation and industrialisation: Case study of Chiang Mai - Lamphun area, Thailand. Ph.D. Dissertation No. SR-98-3, Asian Institute of Technology, Bangkok, Thailand.

HARNESSING INFORMATION TECHNOLOGY FOR (GEO)MANAGEMENT AND DECISION-MAKING

ROWENA BASSI QUIAMBAO
Philippine Institute of Volcanology & Seismology
C.P. Garcia Street, University of the Philippines, Diliman, Quezon City 1101
PHILIPPINES
Tel: (632) 426 14 68 to 79/Fax: (632) 920 70 58, 927 45 24
weng@phivolcs.dost.gov.ph

KEY WORDS: geoinformation, infrastructure, quality management, information technology, decision-making

ABSTRACT

The use and access of **Geo**Information (GI) at an affordable cost demand the creation of an infrastructure. Creating a **Geo**Information **I**nfrastructure (GII) requires consideration, if not total solution, of the most basic issues on its design. Optimal utilization of the incessant and radical **I**nformation **T**echnology (IT) should be geared towards the facility of the flow of information from the sources to the users. With the influx of multitudes of GI, there is a requirement to develop a GII for the information-based society. Geoinformation companies in the government are providing GI as their public service. Such an organization is known as a **Geo**Information **U**tility (GIU). For whatever type of geoinformation service, a GIU needs to consider the proper use of IT. This entails the thorough examination of the dimensions of its overall quality - data and organizational or institutional. Such scrutiny of the overall quality of a GIU should lead to its better procedures. With a better overall performance by the providers of the GI, the users will be able to obtain optimum data. The proliferation of high-quality geoinformation leads to rapid and reliable decision-making. The GI-based society should be well supported by existing GIUs, which, in turn, comprises part of the entire GII. The workable solutions to GI-related problems should put the society or country in a position capable of sustainable national development.

1 INTRODUCTION

Information is a vital component of managerial and/or decision-making activities because it provides the answers to specific questions arising from problems within a system. The system is composed of people, hardware, software, and programs organized to perform and accomplish a specific set of functions or applications. In order to accomplish a specific question and function within an organization, for example, the people in the organization make use of the available hardware, software, and procedures to come up with the information needed. Good management of production process within an organization is highly reliable on efficient and effective use of information. It has been known that information technology (IT) is a key resource for modern, business-oriented organization although it is a costly resource. Good results from a decision-making process can be attributed to the generation of a good information. Thus, there exists a high dependency between information quality and information system development. It can be said, therefore, that a critical success factor for an organization is the methodology used to develop the information system.

Most geoinformation specialists have agreed that there is a requirement to develop a GeoInformation Infrastructure (GII) for the information-based society. The design of a GII requires commitment and involvement from the GI community, users and providers of data, the public and private sectors, the academic community, the professionals working in the field and also from responsible politicians and top civil servants (Berends, 1996).

2 THE GII

Several definitions for the phrase "GeoInformation Infrastructure" have been written and published that stating one definition here would seem to invalidate the others. Thus, it would be more appropriate and fitting to mention some characteristic elements of a GII as used in the literatures. GII has been taken to include various software, hardware, human resources, the actual spatial data, policies, agreements, standards, administrations, management, the knowledge and the technology to make all of these elements to work together in the pursuit of the objectives of its design. A GII serves the purpose of facilitating the efficient access and responsible use of geoinformation at an affordable cost. It enables the capability of transporting large quantities of data at high speed. It is interesting to note that most of the professionals in the geoinformation field recognize the importance of the human element in the definition of a GII (Latimer). They acknowledge the necessity of the technicians that keep the GI system going, the professionals that show how to use the system and software, the community that supports the purchase of the hardware and the professional support (politicians and civil servants) that share ideas and problems.

With the establishment of a GII, several problems on the use, access, cost, availability, accuracy, reliability, and acceptability of the geoinformation could be solved or even just remedied. The technical, institutional and economical matters related to geoinformation are to be resolved with the proper management of a GII.

It is a common eventuality that individual organizations are forced to duplicate efforts in acquiring geoinformation that are already in existence in other organizations without a working information infrastructure. The results are staggering in terms of economic loss, wasteful duplication of efforts, loss of information sharing and loss of data integration capability in support of decision-making activities (Sharifi, 1993).

3 ISSUES RELATED TO THE DESIGN OF A GII

3.1 Technical Issues

Information Technology (IT) products form important building blocks for using geographic information. The technology concerns computers, software, techniques, and networks working all together. The rapid development of electronic data communication gave new impulses to GII and created fresh opportunities (Berends, 1996). There is a need to continuously research and develop on the necessary technology for building and using effectively the GII. Included in this are the application testing of the infrastructure, what system to buy, the compatibility with other systems and data, which data is the best and which data to use. Included in the technical viewpoint of the design of a GII is the issue on structural aspects of geoinformation. It involves relationships between terrain features, their thematic attributes, and their geometry. A feature classification system could be established such that the three key characteristics of a geoinformation - terrain feature, thematic attribute, and geometry - will be efficiently defined

and interrelated. Furthermore, the linkage between thematic data to geometric data could be resolved (Molenaar, 1991).

In response to the technical issues on how to meet the increasing demands of building an infrastructure, there has been suggestions to design the infrastructure modularly and add to it as necessary using technology which precludes the need to redesign and reengineer after each upgrade (Infrastructure Question #4, Internet article).

3.2 Institutional Issues

When institutional issues on the design of a GII are taken, this involves a multi-dimensional perspective. Questions on the following topics are common in the discussion of institutional issues:

1) the organizations' policies, functions and mandates;
2) inter- and intra-relation of the organization with others; and
3) education and training of human resources.

Included in the policy structure of an organization are the issues on access, usage, and distribution of the GI products; research and development programs; and legislation issues. The concept of building an infrastructure to support specific objectives must be made with guiding policies. It should be established in order to perform certain functions based on written mandates. It is similar to justifying the ends by the means.

External issues concern the access and usage of the geoinformation (who are allowed to participate in the access and use of the geoinformation?); the definition of a user and a provider (who is supposed to give, use and provide the geoinformation?); and management/ministerial concerns on the relationship with outside organizations or individuals.

The GII should be able to address institutional issues within the (members of the) system, or internal issues, and outside the system, or external issues. Internal issues are organizational ones some of which are as follows:

1) bureaucracy which blocks the flow of information;
2) resistance to change by personnel due to ignorance and worry on costs rather than increasing benefits;
3) redundancy due to overlapping functions;
4) incapability of specialists to address details of a project; and
5) underestimation of the need for expertise.

In the definition of a GII, the human element has been given its due recognition and importance. It is, therefore, a relevant issue to include in the design of a GII the education and training of human resources. A well-educated and trained staff is essential in the success of a GII. The concept of a participatory learning from every level of an organization to the"Geoinformation School" must be implemented right from the senior management level down to the administrative support level. Education and training in the GI school of thought should not be regarded as too costly, too time-consuming, and too risky that it will not be implemented nor even be considered at all.

It is often a question of whether the members are complying with the jobs that they are supposed to perform and whether they do their jobs in such a way that the standards are followed (Groot, lecture on GII, 1996).

3.3 Economical Issues

It has been noted as a common factor for the success of national economies and cross border regional economies the dependence on the capacity to access and use in a multidisciplinary way large amounts of data, statistics and spatially-referenced information (Sharifi, 1993). In itself, the term "infrastructure" is used as the capital investment needed to create the structures and services to make access to and use of geographic information efficiently possible (Groot, 1990). In this sense, economic issues are relevant to be considered and solved for the design of a GII.

Cost and benefit analysis of the whole GII entails the economic issues such as developmental, operational and maintenance cost of the system. It is imperative to define the source of funding and/or financing to be utilized in the design of a GII. With the cost issues resolved, tangible and intangible benefits could be obtained leading to fewer tasks and people involved, information being more rapidly available, higher quality of goods and services, more conclusive and rapid decisions, and better-used information.

4 ON GEOINFORMATION UTILITY AND QUALITY MANAGEMENT

A definition of a Geoinformation Utility (GIU) is given as "an infrastructure set up for the efficient distribution of data/information to enhance its availability, accessibility and use at an affordable cost" (Addai, 1995). There are certain characteristics of a GIU to perform well in terms of: 1) adhering to the objectives, mandates, duties, and responsibilities; 2) its users' requirements; and 3) the existing issues and constraints that are binding to the utility.

In a study by Wang and Strong, a hierarchical framework for organizing data quality dimensions was developed which captures the aspects of data quality that are important to data consumers. The four dimensions of data quality that are important to data consumers are as follows:

1) **Intrinsic** data quality which denotes that data have quality in their own right;
2) **Contextual** data quality which highlights the requirement that data quality must be considered within the context at hand;
3) **Representational** data quality which includes aspects related to the format of the data and meaning of data; and
4) **Accessibility** data quality, which answers the question on the extent to which data are available or obtainable.

Categories or dimensions relating to the organizational or institutional structure, procedure, and set-up of an organization also point to its overall quality management scheme. Examples of these are: 1) establishment of communication protocol; 2) commercialization of products and services; and 3) proper management and maintenance of the Geographic Information System (GIS). These categories or dimensions can be grouped under organizational or institutional quality. Hence, the framework on categorizing the quality of the geoinformation for a GIU is illustrated best in Figure 1 (Quiambao, 2000).

5 ON DECISION-MAKING

Decision-making has acquired a convenient tool in the access of the needed data through advancements in the information technology. Individual autonomous databases have been integrated at various proportions by the advent of advances in digital technology. Sharing of geoinformation has become possible as newer and more sophisticated computer systems and networks are being designed. These are among the cumulative, positive results of the great big

bandwagon of information technology. All around the world, users and providers of spatial data have either started to embark on discussions about geoinformation or are about to start. It is becoming a national concern in most countries due to the fact that the groups involved are concerned with national matters as much as with their own local problems.

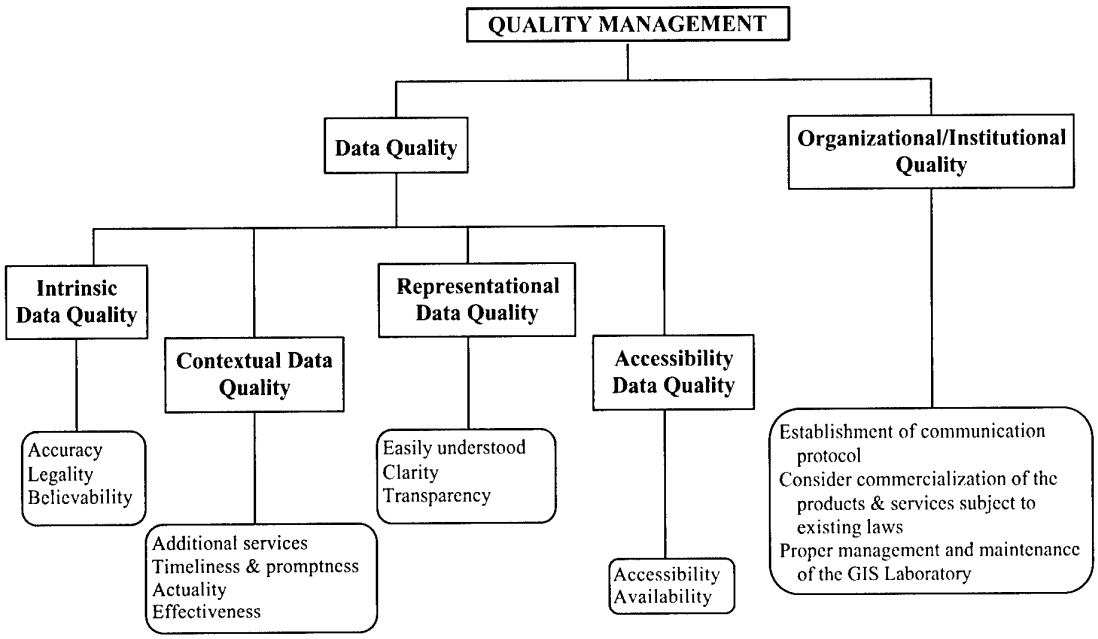


Figure 1. A Conceptual Framework of Quality Management for a Geoinformation Utility (GIU) (modified after Quiambao, 2000)

Proper utilization of geoinformation leads toward an effective management of an information system. With high-quality geoinformation on hand, it is a valuable input for decision-making tasks. The results obtained from decision tasks prove to be of equal effect whether for a small organization or for the national-level entity. That result is basically just between two judgements - the good and the bad. Good benefits result from a good decision. And the inverse is true for a bad decision. The demands incorporated in arriving at a good decision are quite high such that improved techniques have to be used to arrive at one. The consequences of the results from decisions are becoming more and more daunting as the overall quality of the geoinformation becomes less and less.

Some applications of generated geoinformation that is used as a tool for decision-making include selection of sites suitable for some purposes; assessment of land areas for hazard protection scheme; classification of satellite images for land evaluation; and even simple comparison of geoinformation attributes, both in time-related and quality-related dimensions.

6 CONCLUSIONS

The need to develop a workable framework for the integration of the geoinformation based on the requirements, needs, and resources of the users and providers is answered by the establishment of a GeoInformation Infrastructure. The design of a GII is a multi-layering of technical, institutional and economic aspects. It could not be achieved by just considering one or two main issues but by an integrated and collaborative analysis of all the three concerns.

The technical know-how of running a geoinformation system could not be guaranteed to ensure success if the institutional structures and mechanisms of its development, operation and

maintenance will not be properly implemented as well as the provision of the needed economic and financial support.

A GeoInformation Utility (GIU) should be able to provide better service if, first and foremost, the requirements by the users of its GI products will be satisfied. The basis for the performance of a GIU and its quality management relies heavily on the users' end. On this context, there is a need for a GIU to satisfy the requirements of the users of its GI products in order for it to function as a better GIU.

The quality management of a GIU encompasses issues ranging from technical, institutional, social, economic, legal, political, managerial, and educational. These issues are all relevant to the quality of the information; to the quality of the processes which these information are obtained and produced; to the quality of the way all the procedures involved are handled: and to the overall quality of a GIU as a service-organization, as a group of people. Problems to these issues should be well identified and resolved.

Emerging as an important tool for decision-making, proper utilization and management of information technology should be well supported by the existing GeoInformation Utilities.

REFERENCES

Addai, P.A., 1995. Selection of an Optimum Methodology for the Development and Maintenance of GeoInformation Utility. ITC, MSc. Thesis, Enschede, The Netherlands.

Berends, J. & Kok, B., 1996. How to Raise Political Support for the Development of a National GeoInformation Infrastructure. In: Proceedings of Second Joint European Conference & Exhibition on Geographical Information, Barcelona, Spain, Volume 2.

Groot, R., 1990. From Geodesy to Geomatics: A Challenge of Information Society.

Groot, R. Lecture on GII, ITC, 19 February 1996.

Infrastructure question #4. Internet article.

Latimer, E., Mississippi State University, Summary of Infrastructure-Question 1. Internet article.

Molenaar, M., 1991. Status and problems of geographical information systems. The necessity of a geoinformation theory. ISPRS J. Photogrammetry. Remote Sensing, volume 46, pp.85-103.

Quiambao, R. B., Quality Management of a Geoinformation Utility: the Users' Perspective. In: Proceedings of the 19th Congress of the International Society of Photogrammetry and Remote Sensing (ISPRS), Amsterdam, The Netherlands, 16-23 July 2000.

Sharifi, M.A., Groot, R., GIS Infrastructure: An Essential Element of Successful Development and Transfer of GIS Technology. In: Proceedings of the 14th Asian Conference on Remote Sensing (ACRS), Tehran, Iran, 10-17th October 1993.

Wang, R.Y. and Strong, D.M., Spring 1996. Beyond Accuracy: What Data Quality Means to Data Consumers. Journal of Management Information Systems, volume 12, number 4, pp.5-34.

GIS DATABASE OF THE ENVIRONMENTAL INFORMATION

Author(s): Sharav MUNKHTUYA, Batjantsan ENKHTSETSEG (Mongolia)

Name:	Sharav Munkhtuya
Title:	GIS Specialist
Affiliation/Institution:	Information and Computer Center of Ministry of Nature and Environment
Mailing Address:	Information and Computer Center of Ministry of Nature and Environment, Ulaanbaatar 11, Khudaldaany Gudamj 5, Mongolia
Country:	Mongolia
Telephone:	976-1-329984 **Facsimile:** 976-1-329968
E-mail:	mtt@magicnet.mn mtuya@yahoo.com

Name:	Batjantsan Enkhtsetseg
Title:	GIS Specialist
Affiliation/Institution:	Information and Computer Center of Ministry of Nature and Environment
Mailing Address:	Information and Computer Center of Ministry of Nature and Environment, Ulaanbaatar 11, Khudaldaany Gudamj 5, Mongolia
Country:	Mongolia
Telephone:	976-1-329984 **Facsimile:** 976-1-329968
E-mail:	mtt@magicnet.mn enkheeb@hotmail.com

KEY WORDS:

ICC – Information and Computer Center
MNE – Ministry of Nature and Environment
GIS – Geographic Information System

ABSTRACT

In this paper we will present description of Mongolian Environmental GIS database design and some results on implementation of database establishment. The Environmental GIS database is a important part of Mongolian Environmental database project, which is supervised by the Ministry of Nature and Environment (MNE) of Mongolia and implemented by the Information and Computer Center (ICC) of the MNE.

The Environmental GIS Database has 4 categories, such as global, national, provincial (aimag) and local.

a. Global level database includes 1:1 000 000 and lower scale maps
b. National level database includes maps with the scale of 1:1 000 000 up to 1:100 000
c. Provincial level database includes regional and aimag area maps with the scale of 1:200 000 up to 1:50 000 scale
d. Local level database includes maps of 1:50 000 scale and higher.

For the first two categories the Mongolia has quite amount of various thematic maps, however most of them is old and not updated. Basic topographical map of Mongolia has 1:100000 scale and last update were made in 1970's. The ICC completed GIS database with 1:1 000 000 scale

thematic maps. Same time also is working with provincial and local levels entering various maps on demand of users. In ICC uses Arc/Info, Arcview GIS system and PCI, ERDAS and IDRSI image processing systems on SUN, VAX, Silicon Graphics Workstations and PCs.

INTRODUCTION

Mongolia is situated in Central Asia. Different regions of the country differ considerably from each other by structure of relief and elevation. The medium elevation of the territory is 1580 m above the sea level. About 9.7% is a forest, 75.8 % is a grassland, 1% is water and 0.4 % is an urban of the country. There are nearly 540 rivers and 3000 lakes, but they are situated in the north half of the country. Such geographic traits of Mongolia determine the severe nature, sharp continental climate and frequently unfavorable weather conditions. The country has extensive natural resources, minerals, fossil fuels, forests and vast areas of grassland, much of which is suitable for grazing livestock. As yet, the major portion of these resources is untapped. Mongolia with its nomadic animal husbandry is one of the most dependent countries from nature and climate. The global warming and climate change problems are affecting to the land cover changes. Different kind of natural disasters such as drought, flood, heavy winter (zud), land degradation, desertification or steppe and forest fires also has influences on land cover changes. Extensive exploitation in mining, increasing number of livestock, preparation of timber wood is causing land and pasture degradation, deforestation.

The comprehensive data and information about natural resources, environmental state is essential for the policy on sustainable development of our country and well living of our nation. Understanding it the Ministry of Nature and Environment has a item in its **key objectives**, which says: "*Maintain database on land, underground resources, water, forest, atmosphere, flora and fauna; organize the implementation of ecological policy on protection and proper use of the above resources*".

The establishment of Environmental Information System, which can supply by information about nature and environment to the user community starting from policy makers, through the business people ending on everyone, is an important factor to achieve above mentioned objective. Such Environmental Information System should include components like Information Database, Network and Tools for analyzing and decision support. One important part of the Environmental Information Database is a Geographic Information Database.

The Information and Computer Center of the Ministry for Nature and Environment is an executing organization for creation of Environmental Information Database including GIS component. Establishment of GIS database includes following steps such as investigation of existing information sources, ongoing activities, selection and collection of maps, prioritizing and entering into GIS, evaluation, updating and documentation. Since 1930's in Mongolia started to produce various topographic and thematic maps with different scale by Mongolian scientists jointly with others specially soviet scientists in the field of geology, geography, geomorphology, hydrology, landuse, forestry, climatology, archeology and ecosystem etc. Because of size our territory information amount is very huge and most of maps are not updated and old.

STRUCTURE OF GEOGRAPHIC INFORMATION DATABASE

The Geographic Information Database of the Environmental Information has 3 levels such as national, regional and local. The national level includes all the thematic maps of 1:500,000 scale and above, regional level will have maps of 1:100,000 and above and local level includes maps of 1:100,000 scale and below. But scale of maps in each level will depend from the existence of source information, its accuracy, actuality and quality. First step of implementation is entering all thematic maps of 1:1,000,000 scale for the National level database and meantime for other levels maps will be entered under the request. The attribute information of maps is in Mongolian language and many of them are in Russian. So our database will have attributes in Mongolian, Russian and English. In case of topographic map Mongolia has 1:100,000 scale, which is made by former Soviet Union specialists, and has a 1024 sheets. This map will be basis of National and Regional level geographic information database.

GIS HARDWARE AND SOFTWARE

The ICC has ArcInfo 7.03 GIS systems on platforms Sun Sparcstation 20, Vaxstation 90 and ArcView 3.1 on PC and PCI image processing system on Silicon Graphics Indy workstations. GIS system includes also Calcomp 9500 digitizer, HP designjet 750c plotter, Calcomp Classic pen plotter, and A4 size scanner. Those systems are used for the Geographic Information Database.

CURRENT STATUS OF GEOGRAPHIC INFORMATION DATABASE

The lists of GIS database are in Table1 and Table2, examples of existing maps in database are shown in Figure 1 and Figure 2.

Table 1. National level database

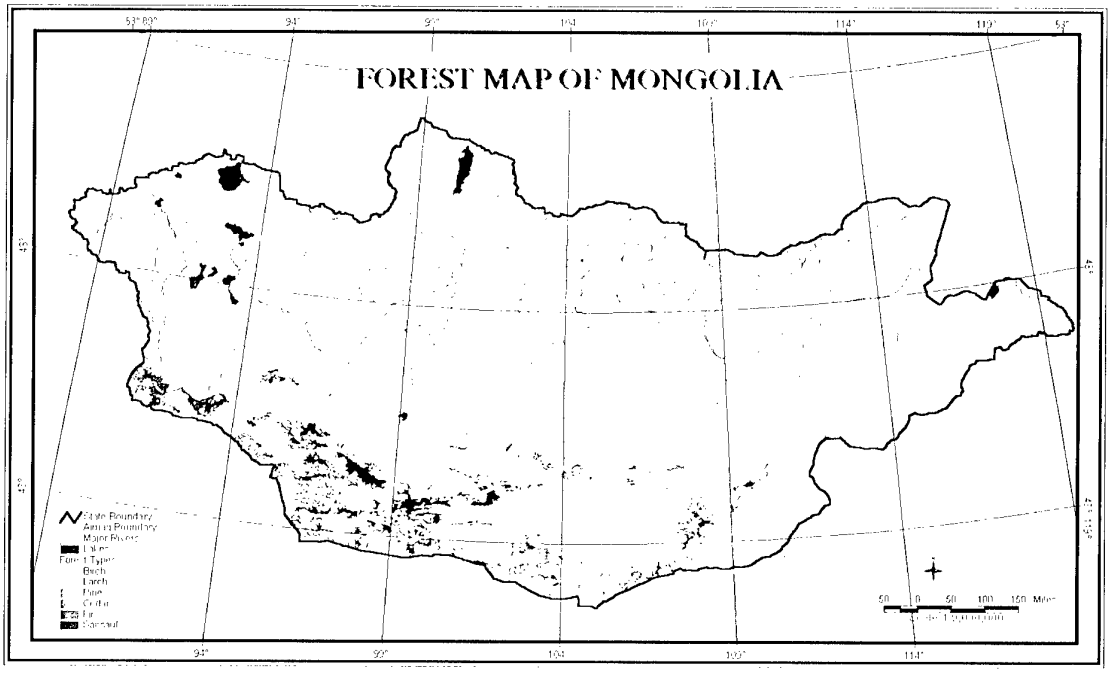
No.	Map	Scale	Data type	Original authors	Year of the release
1	Administrative boundaries and centers	1:500 000	Polygon, line point		1999
2	Vegetation	1:1 000 000	polygon	Russian & Mongolian Scientists	1981
3	Fodder resource	1:1 000 000	polygon	B.Dashnyam	1981
4	Soil type	1:1 000 000	polygon	- " -	1981
5	Underground water	1:1 000 000	polygon	- " -	1981
6	Landscape	1:1 000 000	polygon	- " -	1981
7	Geological structure	1:1 000 000	polygon	- " -	1981
8	Forest	1:1 000 000	polygon	V.I.Sukhikh, N.Gombojav, Ts.Bolooj	1981
9	Ecosystem	1:1 000 000	polygon	Gunin (Russia)	1990
10	Protected areas	1:1 000 000	polygon	PA Admin. Of MNE	1999
11	Haying& grassland map	1: 1 000 000		Buyanorshih	1995

12	Vegetation map	1:1 500 000	polygon	A.A.Unatov, B.Dashnyam	1961
13	Distribution of Mammals	1:6 000 000	polygon		
14	Paleogenic period	1:6 000 000	polygon		
15	Jurassic period	1:6 000 000	polygon		
16	Endemic plants	1:9 000 000	point		
17	Medical plants	1:9 000 000	point		
18	Fish	1:9 000 000	polygon		
19	Rare mammals	1:9 000 000	polygon		
20	Rare birds	1:9 000 000	polygon		
21	Number of mammal species	1:9 000 000	polygon		
22	Insect groups	1:9 000 000	polygon		
23	Vegetation regionalization map	1:10 000 000	polygon	A.A.Unatov, B.Dashnyam renewed by N.Olziihutag	(1979) (1984).
24	Soil-geographic zonation	1:12 000 000	polygon		

Table 2. Regional and local level database

No	Map	Scale	Original authors	Coverage
1	Topographic maps	1:100 000		Uvs lake hollow, Khan Khentii region, Selenge aimag, Some parts of Tuv aimag, Ulaanbaatar city, Khuvsgul National Park
2	Vegetation maps	1:25 000		Gorkhi-Terelj Khustai
3	Soil map	1:25 000		Gorkhi-Terelj Khustai
4	Water	1:25 000		Khustai
5	Forest	1:50 000		Khuder sum (Selenge aimag)
6	Pasture and fodder	1:200 000		Selenge aimag
7	Underground water	1:1 000 000		Selenge, Tuv

Figure 1. Example of National Level GIS Database



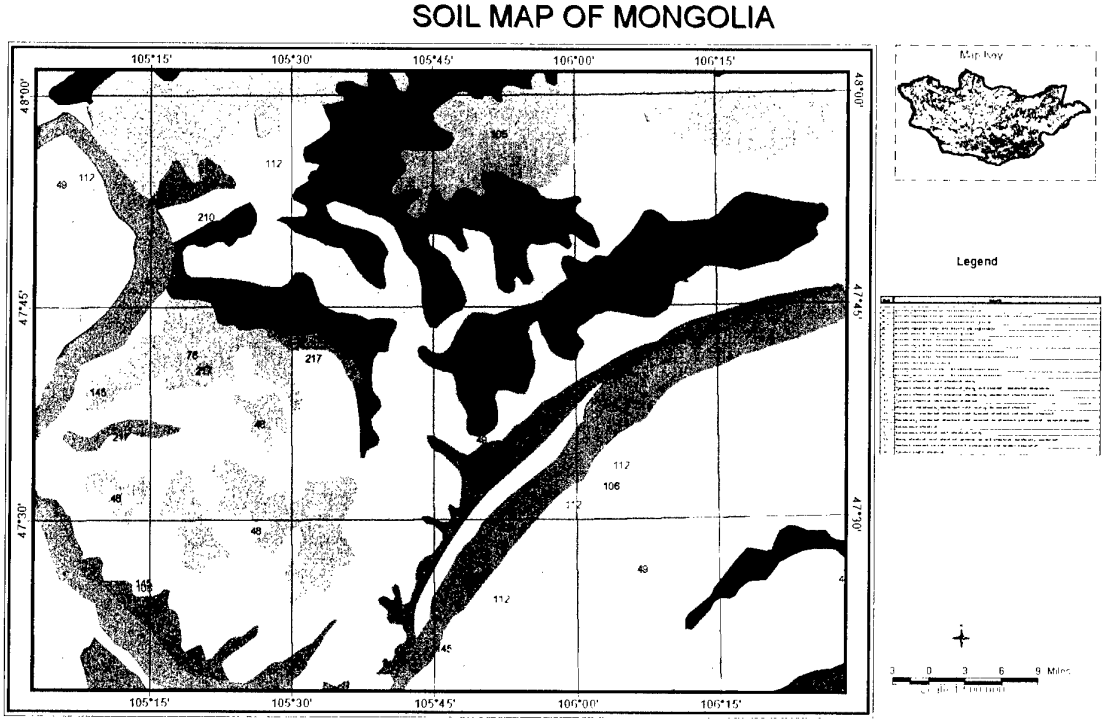
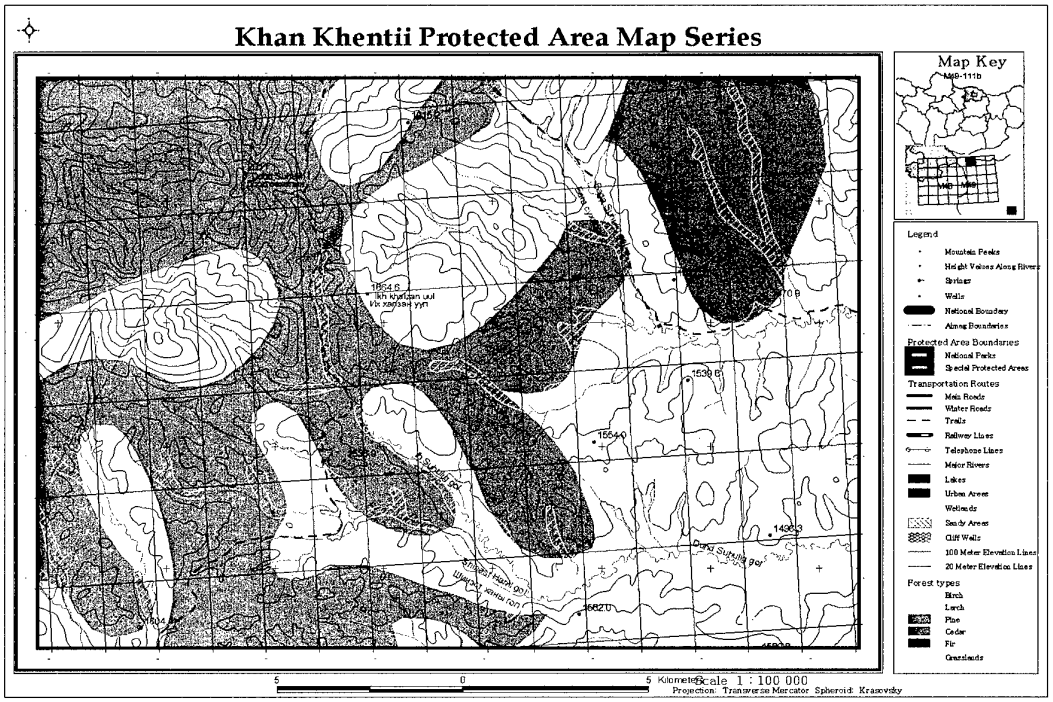
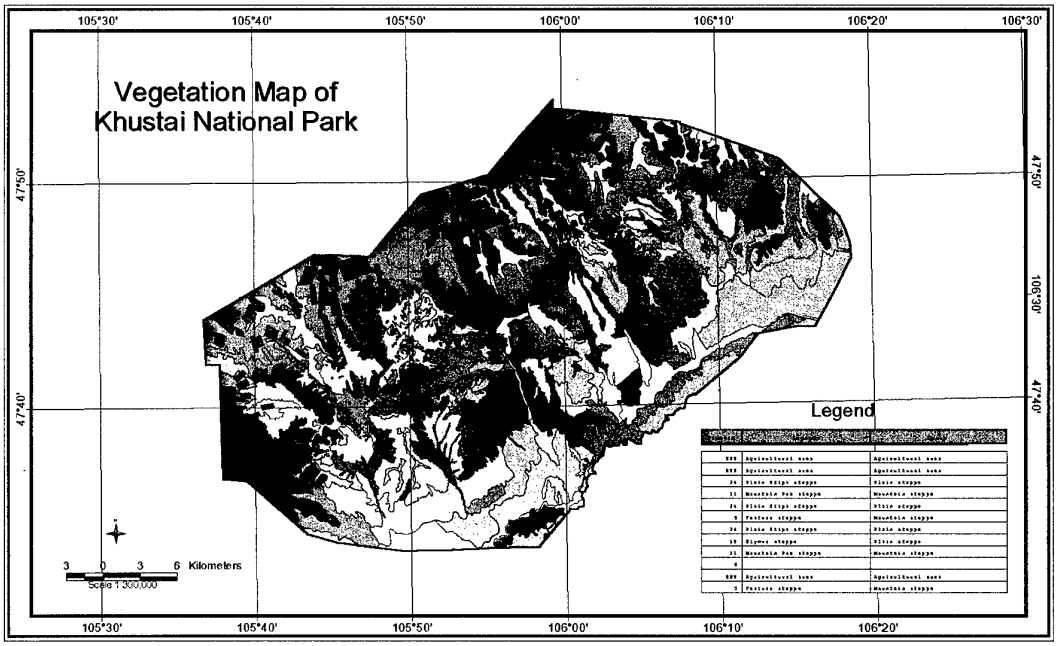


Figure 2. Example of Regional and Local Level GIS Database





APPLICATION OF GEOINFORMATICS ON MOUNTAIN LAND HAZARD MAPPING: A CASE OF ANNAPURNA HIMALAYAS, CENTRAL NEPAL

KRISHNA POUDEL
Department of Geography, Tribhuvan University, Prithwi Narayan Campus, Pokhara, Nepal
P.O. Box 214, Pokhara, Fax ++977-61-25200, e-mail: gislab@pngeog.mos.com.np

KEY WORDS: Mountain, Instability, Landslide, Human welfare, Sustainable development.

ABSTRACT

Nearly one-fifth of the world's land surface is under the mountainous topography. There is a grievous coincidence of weak and vulnerable poor people, limited availability of resources, and fragile surface conditions, which causes the processes or conditions that may initiate and are often the main, immediate causes of damage. For the betterment of the human lives and their welfare, it needs to give the appropriate knowledge about the possibilities of hazard and to provide them the better alternatives. For the analysis two different methods have been applied. The method-1 is designed to give a general spatial association of different factors of the surface. The method-2 is applied for the computation of the Landslide Susceptibility Score (LSS). Based on these methods, the possible hazard prone areas of the region have been delineated. 13.8 percent of the 304 total settlement units of region are over the very high hazard-prone parcels. Field verification also confirmed the results depicted from the map analysis.

1. INTRODUCTION

Nearly one-fifth of the world's land surface is under the mountainous topography. Weak geological structure, steep and rugged surface, high altitude variation along with seasonal monsoon triggers result the high degree of fragility in the whole Himalayan territory (Bhandary, 1987: 1-88). Even under those fragile parcels of land a significant number of people are residing and adapting atypical socioeconomic activities. Those people are eking out their life support-bases from those fragile units of land. There is a grievous coincidence of weak and vulnerable poor people, limited availability of resources, and fragile surface conditions, which causes the processes or conditions that may initiate and are often the main, immediate causes of damage. Landslide is one of the most visible and commonly perceived destructive phenomena of most of the hill-slope in the mountain watersheds. For the betterment of the human lives of those who are residing over such surface conditions needs to provide appropriate knowledge about the possibilities of probable hazards and to give them the better alternatives in their conventional activities which might be essential steps for the human welfare and sustainable development. Present study is designed to identify the fragile parcel of land of mountainous topography in a micro spatial scale and suggestion have been made to reduce the possibilities of human vulnerability on those specific units.

2. STUDY AREA

The study is concentrated on the upper part of the four perennial river basins Modi, Seti, Madi and Mardi of Annapurna Himalayan Range, Central Nepal. Geographically the region is extending from 28°13' north to 28°37' north latitude, and 83°43' east to 84°16'east longitude (Figure 1). The region

covers an area of 1450 square kilometers. The area is extending nearly from 600 m asl at the lower part to 8000 m asl at the higher ridge. The area includes human settlement zone at the lower part, seasonal grazing at the middle part and permanent snow cover at the upper part.

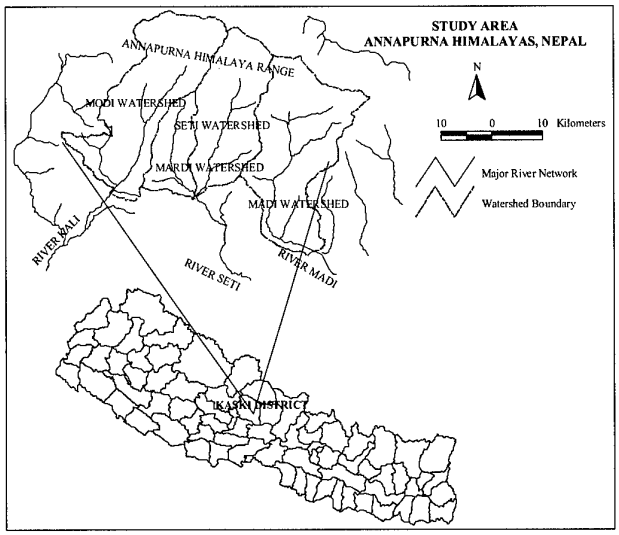


FIGURE 1

Geomorphology of the region is characterized by the morphometry of the major river network systems. Upper part of the four major rivers and their numerous tributaries drain the area. The permanent stream network depicted in the 1:63,360 scale topographic map with 100 ft (30.56m) contour interval have been digitized in ARC/INFO PC-based vector GIS and calculated some morphometric parameters of the region (Table 1).

Table 1
Morphometric Characteristics of the Watersheds

CHARACTERISTICS	WATERSHEDS*			
	MODI	SETI	MADI	MARDI
Area (km^2)	476.92	342.63	502.31	140.69
Perimeter (km)	125.4	87.01	118.16	58.17
Number of stream segments	1236	1090	1543	377
Order of trunk river	5^{TH}	6^{TH}	6^{TH}	5^{TH}
Length of the trunk river (km)	31.62	27.06	28.70	12.03
Total length of stream segments (km)	1057.76	896.55	1239.23	373.81
Mean length of 1^{st} order stream (meter)	733.98	701.48	741.42	888.25
Average drainage density (m/km^2)	2217.91	2616.69	2467.07	2656.99
Mean bifurcation ratio ($R_b = N_U/N_{U+1}$)	5.7	4.071	4.282	4.183
Mean length ratio ($R_L = L_U/L_{U-1}$)	2.911	4.5	3.053	2.10

* Only the upper parts of the basins have been delineated
Source: Computed from the base-map

3. METHODOLOGY

For the assessment of the terrain two different methods (method – 1 and method – 2) are applied. The method – 1 is designed to give a general spatial association of different factors, which are perceived as major determinants of the surface fragility as well as database available in the case of Himalayan

watersheds. Eleven different map layers including geological lineament, lithology, altitude, relief ratio, slope inclination, soil, land use, stream frequency, drainage density, aspect and rainfall zone, and seventy-five classes of these factors have been considered (Table 2).

Table 2
Terrain Factors, Class Code and Description

Map Layers	CLASS CODE									
	1	2	3	4	5	6	7	8	9	10
1. Aspect	Flat	N	N-E	E	S-E	S	S-W	W	N-W	-
2. Relief Ratio	Very Low	Low	Medium	High	Very high	-	-	-	-	-
3. Drainage Density	Very Low	Low	Medium	High	Very high	-	-	-	-	-
4. Elevation	< 1000m	1000-2000	2000-3000	3000-4000	4000-5000	5000-6000	6000-7000	>7000m	-	-
5. Stream Frequency	Very Low	Low	Medium	High	VeryHigh	-	-	-	-	-
6.Geological Structure	Himal	Naudanda	Seti	Ghanpo	Others	-	-	-	-	-
7.Distance from lineament	Form.	form.	Form.	kh Form.						
8. Land use	Very Close	Close	Far	Very Far	-	-	-	-	-	-
9. Soil	Agriculture	Forest	Bush	Grazing	Landslide	Sand	Rock	Snow/ice	-	-
10. Slope	Recent	Ancient	sloping	Sloping	PastGlaci.	PastGlaci.	High	No Data	-	-
11.Rainfall Zone (mm)	Alluvial	Lake/river	<30°	>30 °	in Use	no Use	Himalay	-	-	-
	< 10°	10° - 20°	20°-30°	30°-40°	40°-50°	50°-60°	>60°	-	-	-
	500-1000	1000-1500	1500-2000	2000-2500	2500-3000	3000-3500	3500-4000	4000-4500	4500-5000	>5000

All these classes were scored in a sequential order of possibility of failure according to the procedure in general scale of regional mapping (Marsh 1978). Certain weight has been assigned to them accordingly (Table 3). Annapurna Region has been classified into five respective classes of potential geomorphic hazard units.

Table 3
Terrain Factors and Score Assigned (Method – 1)

Map Layers	CLASS CODE										Weight	Total Score
	1	2	3	4	5	6	7	8	9	10		
1. Aspect	0.1	0.1	0.5	1	2.5	2.5	2	0.8	0.5	0	7	70
2. Relief Ratio	0.3	0.7	2	3	4	0	0	0	0	0	10	100
3. Drainage Density	0.3	0.7	2	3	4	0	0	0	0	0	12	120
4. Elevation	0.5	1	1.5	1.8	2.2	3	3	3	0	0	2	20
5. Stream Frequency	0.3	0.7	2	3	4	0	0	0	0	0	12	120
6. Geological Structure	2	0.5	4	1.4	1	0	0	0	0	0	5	50
7. Distance from lineament	4	3	2	1	0	0	0	0	0	0	10	100
8. Land use	2.2	0.1	1.5	1	3.5	0.5	1	0.2	0	0	10	100
9. Soil	0.2	0.3	3	3.5	2	0.5	0.3	0.2	0	0	8	80
10. Slope	0.2	0.8	1	1.5	1.8	2.2	2.5	0	0	0	12	120
11. Rainfall Zone	0.1	0.2	0.5	0.7	0.8	1	1.2	2	3	3.5	12	120

The method – 2 is applied based on the previous studies made on this field. In this method, Landslide Susceptibility Score (LSS) has been calculated as suggested in the studies (Aniya, 1985: 102-114; Sarkar, Kanungo and Mehrotra, 1995: 301-309; Dhakal, Amada, and Aniya, 1999: 3-16). Accordingly:

Landslide Susceptibility Score (LSS) = R (L)/R (A)

Where, R (L) = a ratio of the landslide area in a particular class of a factor to the total landslide area

R (A) = a ratio of the area belonging to that particular class to the total study area

A score greater than 1 suggests that the class contributes to landslide, whereas a score smaller than 1 implies the class inhibits landsliding. In this procedures seventy-five different classes of eleven factors in total were considered. However, there were fifteen classes having null score (Table 4). The LSS of each class of the factors were linked with the vector coverage. That coverage was later on overlaid with each other to obtain the cumulative score. The score of overlaid layers were added linearly.

Table 4
Landslide Susceptibility Score (Method - 2)

Class code	Aspect	Relief ratio	Elevation	Slope	Geologic structure	Geologic lineament	Land use	Soil	Rainfall zone	Drainage density	Stream frequency
1	0.49	0	1.875	0.1	1.75	2.514	0.187	0	0	0.808	0.733
2	0.958	1.773	1.236	0.526	0.21	1.103	0.026	0	0	0.565	1.433
3	1.477	1.049	2.881	0.781	1.212	1.175	0.774	1.405	0	0.715	0.622
4	1.964	0.771	0.129	1.053	4.074	0.579	0.107	1.421	0.204	1.562	2.25
5	0.806	1.24	0	1.644	0.719		3.218	1.469	1.992	1.2	1.056
6	0.696		0	0.834			0.252	1.592	0.629		
7	0.843		0	0.987			0	0.897	1.895		
8	0.769		0				0	0	0.177		
9	0.492								0.023		
10									0		
11									0		

What is generally considered is the high susceptible parcel that accounts for higher score and the lesser susceptible parcel is the vice versa. The range of LSS obtained is classified into five zones of relative instability. Theoretical potentiality of the terrain instability is further verified by overlaying the existing landslide maps on the result of both method-1 and method-2 and calculated the LSS. Finally overlaying the potential hazard map with settlement and cultivation land has given the coincidence of possible hazard and vulnerability of human life and property.

4. RESULT AND DISCUSSION

Based on the analysis of method –1, about five percent of the total area of the region is under the very high potential hazard zone, whereas only 0.2 percent area of the total is in the very low potential hazard zone. Distribution of the proportion of total area of the region is skewed towards the potentially high hazard prone classes (Table 5). The analysis reveals that the Madi watershed has the maximum share of its area under the very high potential hazard zone. This follows the Mardi watershed. Though the Modi and Seti have smallest share on very high potential hazard zones, the share of high zone has considerably large proportion. The extension of very low potential hazard area is less than one percent to all watersheds. The pattern of distribution is normal to some extent, but it is skewed towards the very high potential hazard class in all four watersheds under studied. According to method –2, the highest susceptible score is delimited to the lithological structure of the Ghan-Pokhara Formation. This group of lithology is consisting the black carbonaceous slates, green shales and grayish shales, white dolomitic limestone and limestone. This group is closely associated at the MCT zone of the region. Therefore, the geological structure seems very fragile. Again the second highest LSS is concentrated in close proximity to the geological fault line, therefore, the landsliding phenomena in the region are closely associated with weak geological structure.

Table 5
Distribution of Potential Hazard Area in Different Watersheds (Method –1)

(Area in percentage of the total)

Class	Hazard Class	Modi	Seti	Madi	Mardi	Total of the Region
1	Very Low	0.08	0.11	0.25	0.06	0.2
2	Low	29.42	19.40	22.66	5.44	22.5
3	Medium	43.46	48.15	35.74	59.98	43.4
4	High	25.72	29.85	32.26	30.49	29.4
5	Very High	1.31	2.50	9.09	4.03	4.5
Total		100	100	100	100	100

Source: Computed from the Analyzed Map

According to this procedure, extensive area of the region is located within low and medium instability zones. Very low and very high susceptible zones have considerably small proportion of the total area. This analysis reveals that the Madi watershed has the highest proportion of its area under high and very high susceptible zones (Table 6). The proportion of areal distribution is quite small in very low susceptible zones of all watersheds. The large area is in the medium class of all watersheds. This analysis also shows a higher fragility at the Madi watershed. The Mardi watershed has a good proportion of land in lesser fragility classes. But, the Seti and Modi are in between trend.

Table 6
Distribution of Potential Hazard Area in Different Watersheds (Method –2)

(Area in percentage of the total)

Class	Hazard Class	Modi	Seti	Madi	Mardi	Total of the Region
1	Very Low	0.26	0.15	0.20	0.00	0. 80
2	Low	52.29	50.8	34.90	27.51	43.29
3	Medium	43.92	43.38	51.55	65.71	48.20
4	High	3.53	5.63	13.32	6.78	7.70
5	Very High	0	0	0.02	0.00	0.01
Total		100	100	100	100	100

Source: Computation from the Map

According to this procedure, the method-1 has the highest failure rate at class five followed by class four to smaller class respectively. But at the method – 2, the failure rate is the highest one at class four and very small value at class third. And, the other classes have null score (Table 7).

Table 7
Comparative Failure Rate Analysis (Method – 1 and Method – 2)

Class	Method_1			Mehtod_2		
	R/L	R/A	LSS	R/L	R/A	LSS
1	0	0.002	0	0	.008	0
2	0.044	0.225	0.196	0	0.433	0
3	0.331	0.435	0.761	0.177	0.482	0.367
4	0.478	0.294	1.626	0.821	0.077	10.660
5	0.144	0.045	3.200	0	0	0

From the analysis of LSS, the method –1 seems to be quite a better indicator to depict the landslide hazard of the mountain region. However, the method –2 also has a good concentration of the high LSS at the fourth class. On the whole, the region has considerable area under the high fragility. Which shows that the resources over the region are in delicate situation in terms of its terrain condition. The analysis depicted that the result of method – 1 has quite uniform pattern, and it seems that the spatial

character explains appropriately. In the regional scale, this technique tends to give convincing answer. Even for the comparison of LSS with the result of Method –1, it has given a better result. For the planning point of view, the settlement of the region has therefore, been overlaid over the possible hazard-prone areas resulted through the method-1.

According to this procedure, the spatial locations of 13.8 % settlements out of 304 settlements of the region are falling at the very high possible hazard-prone zone. Similarly, 37 %, 44.4 %, and 4.9 % settlements are located at high, medium and low hazard-prone areas respectively. The very low hazard-prone class has no settlement location. It might be because of tiny extension. Among these settlements Modi watershed has 5 settlements (i.e. Kimrong Khola, Uri, Yumle, Tallogaun in Ghandruk VDC, and Landruk, Dhawa and Lumle Bikas area in Lumle VDC). In Seti watershed 6 settlements (i.e. Meprang, Chyanglung, Khaimarang and Chipleti in Sardikhola VDC, Ghamtara and Khahare in Machhapuchhre VDC) are there. In Madi watershed, there are 25 settlements, which are in very high hazard-prone zone. Among them most vulnerable are Taprang, Khilang, Uppallo Namarjung, Pakhagaun of Saimarang VDC, Ghartidanda of Bhachok VDC, and Harse of Mijuredanda VDC. In Mardi watershed 4 settlements are in this zone, which are Kuji, Patikhola, Armalakot and Kamsekhorphedi.

The result depicted from the map analysis was further tried to verify during the field visit from January to March 2000. Generally the terrain instability is viewed under the direct observation of the concentration of landslide scars, topsoil loss and dissection of surface of the terrain. Among the four watersheds under studied, the Madi has a greater number of landslides with extensive coverage. In this watershed, Saimarang, Taprang, and Uppallo Namarjung were the most affected parts. The second large concentration of the landslide was in Modi watershed. Tanchok and Landruk village of Lumle VDC, Kyomrong Khola, Uri, and Kimche of Ghandruk VDC were the most affected area of that watershed. The severity of landslide in Seti watershed was not clearly visible. The catchment of Idi Khola has a large concentration in Mardi watershed. In terms of severity and loss of property, Madi watershed was the most affected ones. Causes of instability seems to its natural reasons, however, the human activities in the region were inducing to the natural processes. Khet terraces and open grazing were the most common location of the concentration of big slides. Maintenance activities of agricultural terraces were not properly done. Open grazing on abandoned agricultural terraces was further worsening the situation. Having abandoned the transhumance pasturing systems, concentration of livestock units near the human settlement was causing further deterioration the situation of land degradation. The process shows that the terrain of mountain watersheds is degrading severely even though the human population is less dense and also is reducing through out-migration. For the mitigation and preparedness, the settlements situated at the very high hazard-prone zone require the prompt attention. Precisely an operation plan is, thus, indispensable to human welfare and sustainable development in the region.

References

Aniya, M., 1985. Landslide Susceptibility Mapping in the Amahta River Basin, Japan. Annals of the Association of American Geographers, 75 (1), pp. 102 -114.

Bhandary, R.K., 1987. Slope Instability in the Fragile Himalaya and Strategy for Development. Indian Geophysical Journal. 17, pp. 1 – 88.

Dhakal, A.S., Amada, T. and Aniya, M., 1999. Landslide Hazard Mapping and the Application of GIS in the Kulekhani Watershed, Nepal. Mountain Research and Development, 19 (1), pp. 3 -16.

Marsh, M. W., 1978. Environmental Analysis for Land Use and Site Planning. Mcgraw-Hill Book Company, New York, p.241

Sarkar, S., Kanungo, D. P. and Mehrotra, G. S., 1995. Landslide Hazard Zonation: A Case Study in Garhwal Himalaya, India. Mountain Research and Development, 15 (4), pp. 301 -309.

A Surface Interpolation for Large-scale Representation of Terrain in An Urban Area

Yohko Shimura*, Shaobo Huang** and Ryosuke Shibasaki*
*Center for Spatial Information Science, University of Tokyo
**Center for Environmental Remote Sensing Center, Chiba University
4-6-1, Meguro-ku, Komaba, Tokyo 153-8505 Japan
tel:+81-3-5452-6417 fax:+81-3-5452-6417

E-mail : yshimura@iis.u-tokyo.ac.jp

KEY WORDS : urban space, triangulated irregular network (TIN), surface interpolation, three dimensional (3D) representation, boundary representation (BR) model

ABSTRACT : Urban terrain surfaces have geometric characteristics such as discontinuities in terms of elevation and slope gradient. By introducing boundary representation (BR)model to the terrain surface representation instead of conventional 2.5D type representation, such characteristics can be easily handled, though how to provide elevation data for the BR model efficiently is still an open question. With this background, this paper presents a surface interpolation method to represent terrain surface in urban space suitably. Through an example of the representation of terrain surface, it is demonstrated that the proposed surface interpolation method can be efficiently applied.

1.Introduction

Nowadays, the information society is growing dramatically. In a "flood of information", one of the key issues is how to organize data to extract useful information. By focusing the time and spatial position/extent that those data are referring to, we can analyze various types of data and information and uncover the hidden structure behind them. The movement that combines 3D CAD (Computer Aided Design) design data with survey data in GIS is becoming more active to improve efficiency in information distribution and sharing in urban planning, infrastructure construction and facility management.

It is very important to manage and utilize urban information in 3D GIS for urban disasters and urban designs, while we have kept road networks and buildings as 2D information. It is expected that 3D mapping technologies will be applied to many fields especially in car navigation system, urban planning, urban disaster.

Representation of terrain surface, especially large-scale detailed representation is a basis of urban 3D data because the height of buildings are determined against the terrain surface and the terrain surfaces play important roles in a number of simulations such as traffic simulation, flooding simulation etc.

Though urban terrain surface have geometric characters such as discontinuities in terms of elevation and slope gradient, terrain surface are conventionally interpolated based on an assumption that the surface is smoothly undulating. Many commercial GIS packages provide

terrain surface interpolation methods as such. But if the terrain surface is interpolated based on such assumption, it is disable to represent urban space in 3D suitably.

On the other hand, calculating a large amount of coordinate data is necessary to represent 3D geographic objects and buildings in urban area. The surface in urban space has so complicated shapes that a large amount of elevation points are needed. With this reason, the method is necessity to interpolate the surface efficiently with both least and easily sampled points

This paper presents an improved interpolation method to represent terrain surface in an urban space in 3D, considering three basic requirements for 3D representation model of urban space as follows; (1) Ease of representation of a variety of geographic objects in urban space; (2) Efficiency in building and updating 3D special database; (3) Compatibility with existing map data and 3D presentation system

2. Existing interpolation methods

It needs much amount of points to represent urban spaces in 3D.But it's not easy to assign data to such amount of points respectively. Generally after sampling spatial data on the ground, unknown points about spatial characteristics are interpolated the value which is the most plausible between data points

A. Thiessen polygons

This method is based on the assumption that the best information is given by the nearest sampled point. This method is best for nominal data with a two dimensional array, but the level of accuracy on information in each polygon is not homogeneous because the size and shape of each polygon depends on sample layout.

B. Trend surface analysis

This method is to fit a surface (e.g. polynomial surface) by least squares through data points. This is the simplest method to describe long-large variations but the trend surface is very susceptible to outliers in the data.

C. B-splines

This method uses spline functions. They are piecewise functions fitted to small number of points exactly, while the same time ensuring that the joints between part of the curve and another are continuous.

D. Method using moving average

This method estimates values at un-sampled locations by the average of those of neighboring points. This method depends on the range of definition about ' around ' and the distribution of sampled points.

E. Kriging

This method is based on the assumption that statistical nature of variation can be expressed by the sum of three major components as follow; (1) a structural components (associated with a constant mean value or a constant trend) ; (2) a randam, spatially correlated

component ; (3) a random noise. This method needs more computing time but usually yields quantitatively better results.

F. Universal Kriging

This method is an "improved" method to express local drifts based on Kriging as universal interpolation method. Universal Kriging enables to include the nature of ' drift ' in a structual component in Kriging.

However, these methods (Method using moving average , Kriging, Universal Kriging) represent terrain surface smoothly. Therefore, these can't represent geometrical discontinuous such as break lines and step lines suitably.

3. The outline of surface interpolation methods

Existing surface interpolation methods usually assume that terrain surfaces are smooth. But the discontinuities of slopes and elevations are often the case in urban areas. The examples of discontinuities are shown in figure3-1

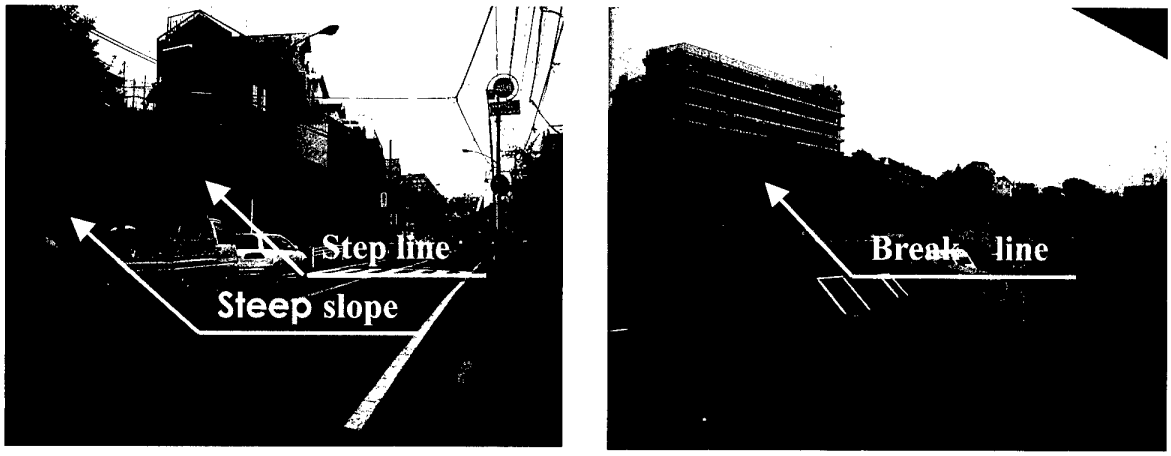


figure3-1 the example of discontinuities

In the large-scale representation of urban terrain surfaces, such discontinuity have to be represented faithfully, while smooth surface representation may cause no serious problems in small scale representation of urban areas. The conventional surface interpolation methods can be used for the smallest scale representation of rural terrain area, though they cannot be directly applied into large scale representation to urban terrain surfaces.

This paper presents an improved interpolation method for large scale urban terrain surface representation to avoid such artifacts using road surface elevation data and boundary data which can be easily acquired both with air-based and ground-based surveying methods.The method allows us to take into account geometric characteristics or constraints such as discontinuity of elevation and slope gradients, smooth changes of road surface elevation. Interpolated surfaces are represented by triangular plane patches (TIN representation).

The smoother terrain surfaces are, the larger the sum of the square of inner-products of unit normal vectors of neighbouring triangular planes is. The surfaces are interpolated so as to

maximize the sum of the square of inner-products of unit normal vectors of neighbouring triangular planes in urban space under such constraint conditions as keeping discontinuity of elevation and slope gradients at specified locations.

The basic process of the surface interpolation is shown in figure3-2. The surface interpolation process consists of five parts as follow.

1) 3D coordinates (x, y, z) of selected elevation points (known points) and 2D coordinates (x, y,) of the rest (unknown points) are given.
2) The geometric constraint conditions or structural features such as break lines and step lines are given. Additional constraint conditions can be added such that ground floor of buildings is flat (all points constituting the boundary should have identical elevation values).
3) TIN network is generated based on Delaunay triangulation so as to include break lines and step lines as edges in the TIN network.
4) Estimate of a road network are estimated through the "smooth" surface interpolation.
5) Elevations of terrain surfaces are estimated in each block respectively taking the geometric constraints conditions into account.

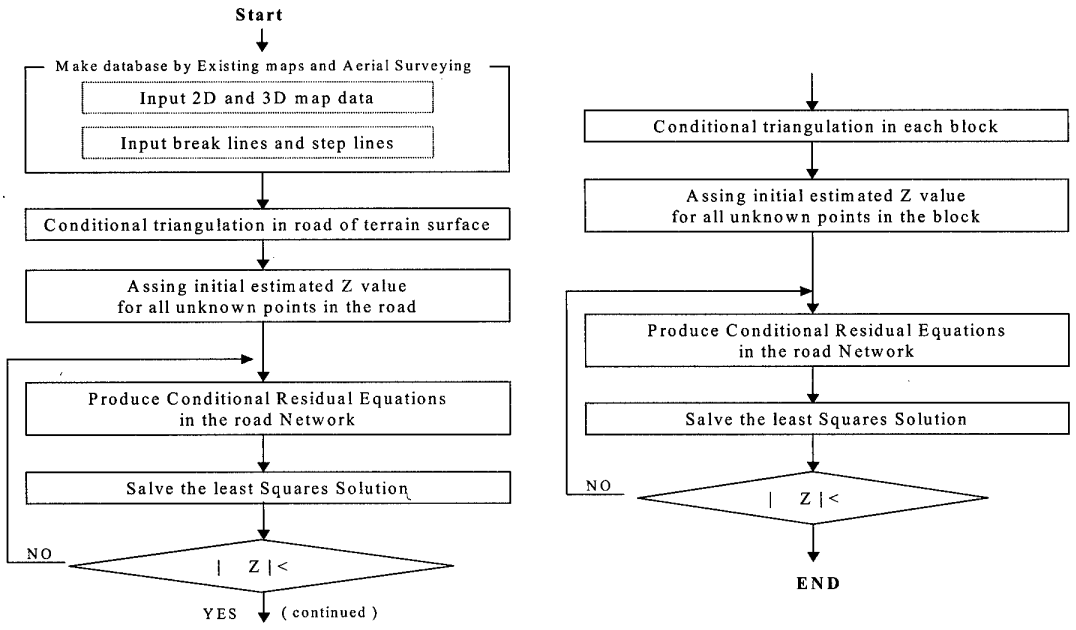


figure3-2 the basis process of surface interpolation

4. The case study in ROPPONGI area and its conclusion

A example of the surface interpolation has been made in ROPPONGI area around ROPPONGI and NOGIZAKA station in Tokyo, Japan. The range of study area in about 300m by 700m.There are about fifty blocks in the area. And more than 500buildings and other man-made objects are located in its terrain surface. In its 2D mapping data, more than twenty thousands points and edges are existing..



figure 4-1 the air-bone picture in ROPPOMGI

This area has much geographical characters such as surfaces cutting into the ground, residential area which have many break lines, avenues which are smoothly undulating. The detailed results of the case study will be presented at the conference.

5. Conclusion

The terrain surface in urban areas have geographic characters such as discontinuities in terms of elevation and steepness of slopes. Under these geometric conditions, the proposed surface interpolation enables us to estimate Z values of spatial objects from some observed elevation data and save much time and labor in modeling 3D spatial objects in an urban space.

Comparing between the surface conditions of urban area by air-born sueveying and the representation of urban area by both this improved and conventional method, this example suggests that this proposed surface interpolation method represents urban space in 3D more suitably than conventional one.

References:

(1) P.A.Burrough, Principle of Geographical Information System for Land Resources Assessment, Clarenden Press, Oxford, 1986

(2) J.Raper, Three Dimensional Applications in Geographic Information, 1989, Dept. of Geography, Taylor and Francis Ltd. 1989

(3) R.Shibasaki and Huang Shaobo, The Representation of Terrain Surface and Its Interpolation Method for large Scale Digital Maps in An Urban Area, symposium of japan Society of Photogrametric and Remote Sensing, tokyo, May. 1992

DYNAMIC SPATIAL MODELING USING ROS AND CARRYING CAPACITY FOR ECOTOURISM MANAGEMENT

Kampanart PIYATHAMRONGCHAI and Nitin K. TRIPATHI
Space Technology Applications and Research
School of Advanced Technology
Asian Institute of Technology
PO Box 4 Klongluang, Pathumthani, 12120
Tel(66)-2-524-6392, Fax (66)-2-524-5597
E-mail: kampanart@nu.ac.th, nitinkt@ait.ac.th
THAILAND

KEY WORDS: Dynamic, Spatial, Tourism, Carrying Capacity, GIS, ROS

ABSTRACT: In general, any geographic phenomena are visually depicted as 'static' map with 'static' spatial model. This paper presents how the time variable can be combined to give more information to the spatial model and how to implement the dynamic map with dynamic spatial model. The recreation opportunity spectrum (ROS) framework is a method to identify the tourism carrying capacity (CC). It is modeled spatially as well as dynamically.

Conceptually, there are four steps to implement the dynamic spatial modeling for tourism carrying capacity including computer simulation, spatial analysis, DSM interfacing and verification. Avenue script on ArcView GIS package was used to implement. The simulation of traveling of tourists is implemented based on parameters such as route for tourist, speed of car and stopping time in each facility from field observation. The spatial analysis dynamically applies to the ROS and CC evaluation using cartographic modeling. Three settings are layered and weight scores defined including physical, managerial and social. The programs developed are generally interactive with dialogue interface. User can flexibly set up different scenarios for supporting the decision.

For the result, sequential ROS class maps, CC exceed maps and the CC exceed level can be generated. The information obtained from the analysis in this work will be useful to control the impact of tourism on each facility of the Phuhinlongkhla National park and provide more comfort to the tourist.

1. INTRODUCTION

"A great part of the challenge of modeling interactions between natural and social processes has to do with the fact that processes in these systems result in complex temporal-spatial behavior" (Itami, 1994)

Geographic phenomena are depicted as a 'static' map displaying information of the real world. The static-maps can be produced using the geographic information system (GIS) as a powerful tool to create complex spatial model. Efficiently, cartographic modeling with overlay and weight procedure is still a popular method to offer visual information from many layers of map represented any geographical features or events.

Static-maps are depiction of land use or other information at a particular time but geographic process are dynamically. Time-based approach is nowadays included to many fields of researches. Spatial modeling is one of research fields that undertake the need of the time. The spatio-temporal approach is provided due to the merits of information given from time applied

to spatial model. The temporal GIS database is also set up. Then the 'dynamic spatial modeling' framework that uses both of time and spatial information to create any models give different results and is implemented.

There are three fold frameworks applying in this study. Firstly, computer simulation is performed. The key features of simulation are input, algorithms and output (Maquire 1989). In this study, the computer simulation is developed collecting parameters from traveling of tourists in the park. Those parameters are applied using some basic concept of system dynamic. Secondly, cartographic modeling technique is set as spatial modeling in this study. GIS package nowaday provides a lot of spatial operations is chosen as tool for spatial analysis. The third aspect, tourism carrying capacity (CC) is a spatially dynamic application. The impact of visitors traveling in Phuhin Longkhla National Park is simulated and evaluated. Recreation Opportunity Spectrum (ROS) framwork was defined in this study.

2. DYNAMIC SPATIAL MODELING IMPLEMENTATION

The questionaires were designed for collecting the information: general information, satisfaction to the tourist place of tourist and the most important is time spending information. Those raw data from field survey were analysed.

Two practical frameworks were integrated included computer simulation and spatial modeling applying for tourism carrying capacity. This section explains the detail of each procedure to implement.

2.1 Computer Simulation

Step 1 Map layers preparation. Both three possible routes for car and walking simulation were defined. Algorithm for assigning and merging routes from existing road and walking trail was designed and developed.

Step 2 Tourist parameter. For generating tourist parameters to the simulation, the range of time, which tourists start to travel in the park, was defined. The range of time was taken as randomly for programming. Each tourist group adopts random number of people for that group.

Step 3 Movement algorithm. Route maps prepared in UTM coordinate system was converted to percent unit. For example total length of a route is equal to 10,000 meters. 10,000 meters was converted to 100 percent. According to the speed of car and distance to move the object, the step in percent unit can be calculated. The current position of a moving object was updated with the step when the time calculated from the speed was changed.

Step 4 Stop and time spending algorithm. Time spending information from field observation is important for this step. The range of time spending can be calculated from mean and the standard deviation of time spending. While the movement algorithm is running and the moving object passes a tourist point, random stopping time is defined. The object stops at that point until the stopping time finish.

Step 5 Output generation. Time stamp to output the simulation information can be defined such as 15 minutes. The algorithm for generating two types of output was designed included text file and variable used for spatial analysis.

2.2 Spatial Analysis

The spatial model was applied based on the attribute-based approach. Algorithms and programming codes were developed purpose for creating and adjusting the value inside the spatial database. The main input for spatial analysis is from computer simulation. Steps for complete spatial analysis part is shown follows.

Step 1 Defining weight and ROS class map generation. According to the ROS framework, there are three conditons: physical managerial and social. For the weight given, the physical and managerial conditions were determined as static. On the other hand, the social condition, the weight is set as dynamic based on the number of visitors obtained from the simulation part. Initial stage of ROS class map can be created using GIS overlay method without social weight score.

Step 2 Algorithm for recalculating the ROS class and CC exceed class. Each time stamp, each tourist point has different amount of tourists. Social weight score can be computed according to the number of visitors. For ROS score updating, the attribute-based model was performed in this step. The algorithm to access the ROS attribute to get ROS score was performed. Initial stage ROS score is updated from social weight score and reclassified to 5 classes of ROS.

For CC exceed map, the initial stage ROS class and updated ROS class were accessed. Based on CC concept, the ROS class change matrix was created.

Step 3 Output generation. The algorithm to create the ROS class and CC exceed maps in sequential files was developed. Quantitatively, the area-based approach was applied to calculate the CC exceed level. The text file is created for writing the CC exceed level in time stamp.

2.3 Dynamic spatial modeling interfacing

Integrating the two main procedures, computer simulation and spatial analysis, graphic user interface (GUI) was designed. Consequently, input, adjustable parameters, and alternative output were proposed and programmed connecting to the main module.

2.4 Simulation and model testing

For testing the DSM, different scenarios can be set up for evaluating the result the simulation and spatial model. Variety for number of groups, range of people per group and the social weight parameter method were defined.

3. RESULT AND DISCUSSION

Much of programming coded lines were written re-conceptualizing the framework in the last section. The visual result provided the ROS class maps and carrying capacity (CC) exceed maps,

which were generated over the time simulation. Quantitatively, an index used for indentifying the exceeding of carrying capacity was generated in form of text file.

Testing of models with different scenarios in the real world was performed. Different number of visitor groups and different range of number of people per group scenarios can be set up. For instance, the simulation results are shown as graphs in Figure 1. Figure 1 a) demonstrates the increasing range of time to use Third world tourist area. And Figure 1 b) illustrates the Lanhintaek group traveling that if there are a few group, the traveling will be discretely. However, this area tend to incessant use, the time period changed from 45 minute – 2 hours to be 45 minutes to after 8 hours passing.

Figure 2 represents the ROS class map and CC exceed map of 50 group compare with 100 tourist group in Phuhin Longkhla National Park after 6 hours of simulation. Figure 2 b) and d) illustrate the CC exceed map created based on the acceptable change of ROS class map (Figure 2 a) and b) respectively). More groups travel in the National Park cause more impact to tourist points.

CC exceed map not only visually represents the impact of tourists over the time, but also can be used to calculate the CC exceed level. The result shows an index of carrying capacity of any tourist point and peak period time. Figure 3 depicts graphs created using the information of CC exceed level index and peak period time. Park manager can define the level of acceptable, for instance, the acceptable level is equal to 3 as shown as cross dotted-line in Figure 3

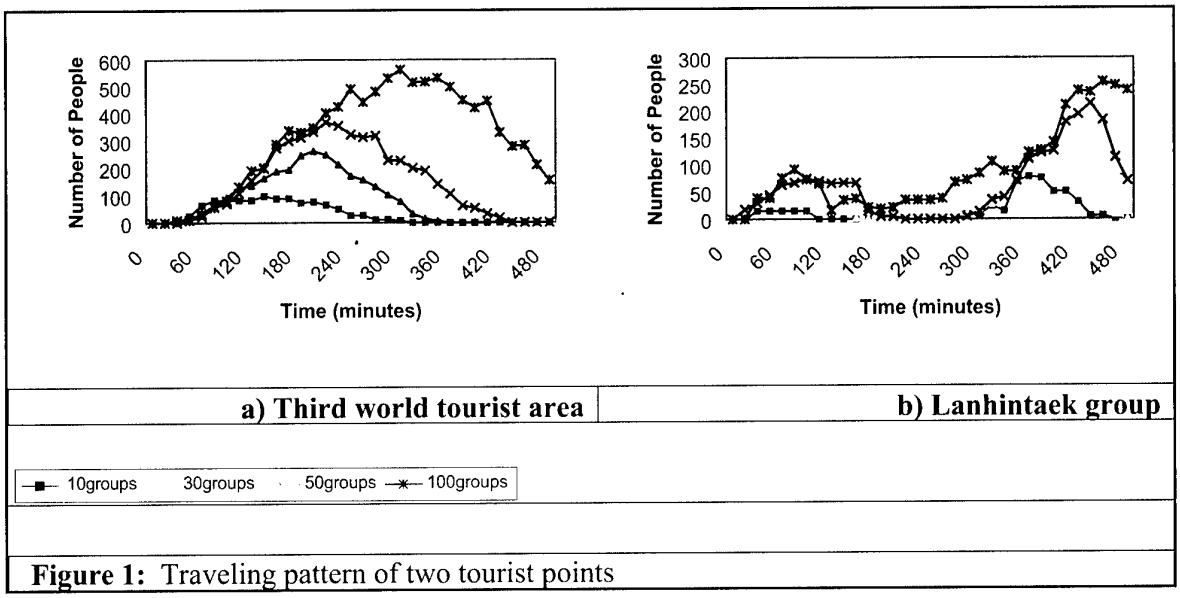


Figure 1: Traveling pattern of two tourist points

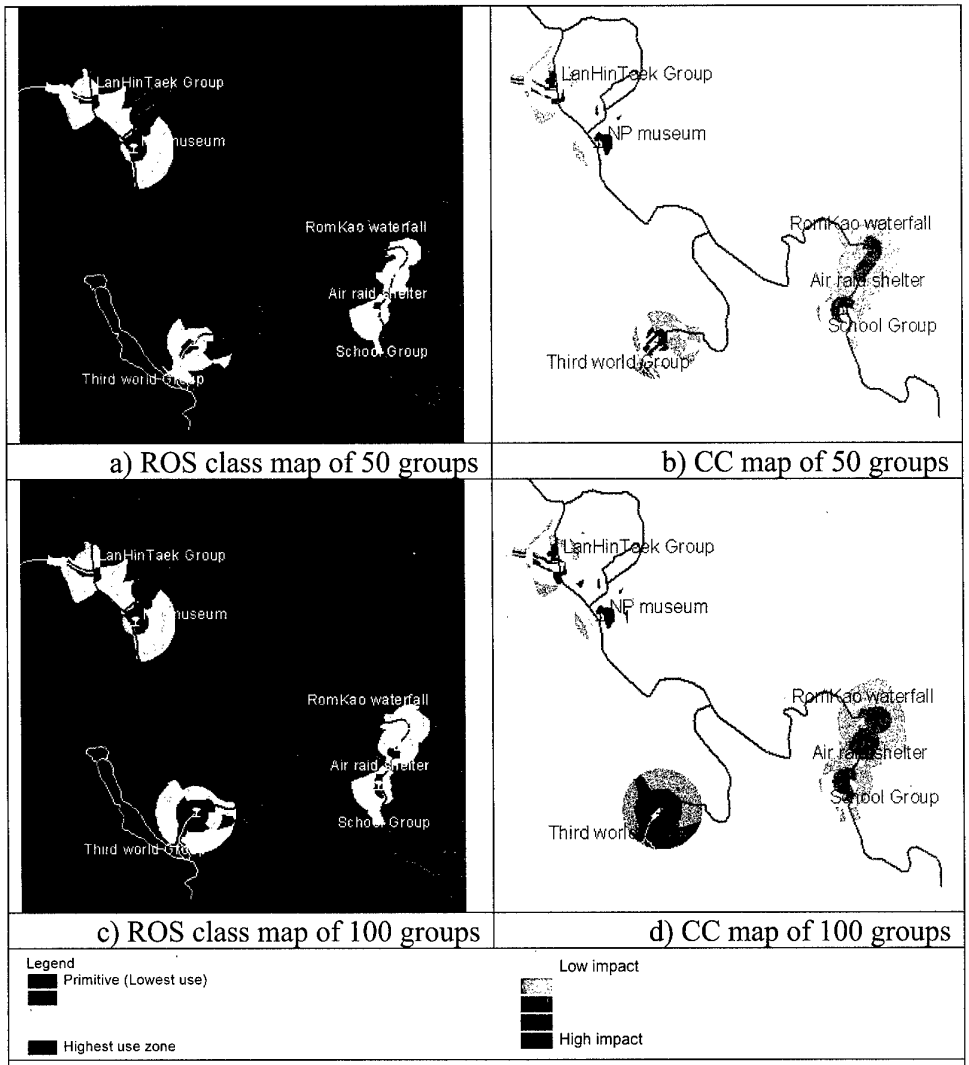


Figure 2: ROS class and CC map after 6 hours of 50 and 100 groups simulation

4. SUMMARY AND CONCLUSION

Dynamic spatial modeling (DSM) offers clear view of 'where' and 'when' a phenomena occurs. This study represented the integration of computer simulation and spatial analysis. Computer simulation yields the real time information of number of visitors in each tourist point. Integrating spatial analysis yields more closely to the impact of tourist to the natural resource.

The attribute-based approach is more easier and faster to manage the information. Linking of attribute table to the spatial is useful for visualization in form of map and graph.

Nowaday, GIS softwares are equipped with the programming interface. Therefore, the simulation program can be performed using only one package. It will be very useful and effective technology.

DSM for Tourism Carrying Capacity can answer questions for example, "where is the area which has exceeded the carrying capacity at 1.00pm?" and "How does the exceed in this area is comparable to another at 2.00pm?" etc. These scenarios are very useful for ecotourism management. The result from this study will provide necessary CC exceed information for better management of tourist places.

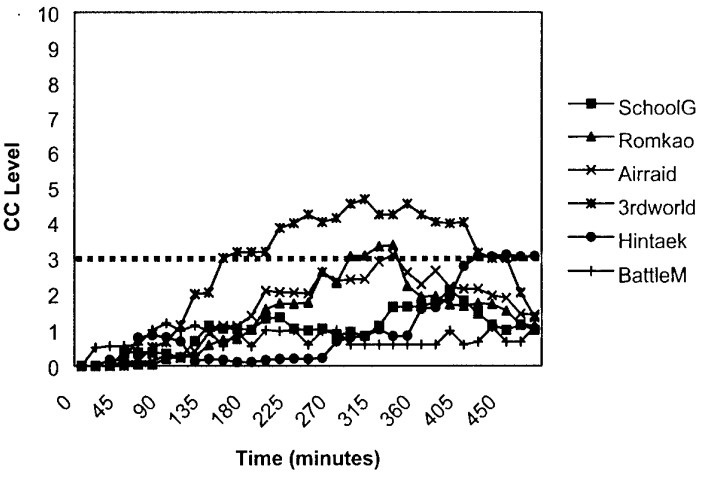


Figure 3: Graph illustrates the CC exceed level of 100 groups simulation

5. REFERENCE

Aronoff, S. 1993 Geographic Information Systems: A Management Perspective. WDL Publications, Canada.

Itami, R.M. 1994 Simulating spatial dynamics: Cellular automata theory. *Landscape and Urban Planning*, 30:27-47.

Maquire, D.J. 1989. Computers in Geography. Longman Group Limited, Honk Kong.

Payne, R.J., Carr, A., and Cline, E 1997 Assessing Visitor Opportunities in Two National Parks. School of Outdoor Recreation, Parks & Tourism Lakehead University, Thunder Bay, Ontario Canada [WWW document] URL http://parkscanada.pch.gc.ca/library/Ros/english/tdm_e.htm

Yuan, M. 1996 Temporal GIS and Spatio-Temporal modeling. [WWW document] URL http://ncgia.ucsb.edu/conf/SANTA_FE_CD-ROM/sf_papers/yuan_may/may.html

A CASE-BASED URBAN PLANNING SUPPORT SYSTEM USING AN INTEGRATED COMBINATION OF GEOGRAPHICAL INFORMATION SYSTEMS AND REMOTE SENSING

Ko-Wan Tsou

Associate professor, Department of Urban Planning,

National Cheng-Kung University, Tainan, Taiwan

Tel: (886)6-2757575#54232; Fax: (886)6-2754943

E-mail: uptkw@mail.ncku.edu.tw

Yao-Lin Chang

Candidate of Dr. Degree, Department of Urban Planning,

National Cheng-Kung University, Tainan, Taiwan

Tel: (886)6-2342373#34; Fax: (886)6-2754943

E-mail: yaolin@ntcp.up.ncku.edu.tw

Yu-Ting Hung

Candidate of Dr. Degree, Department of Urban Planning,

National Cheng-Kung University, Tainan , Taiwan

Tel: (886)6-2342373#34; Fax: (886)6-2754943

E-mail: eva@ntcp.up.ncku.edu.tw

TAIWAN

KEY WORDS: Case-based urban planning support system (CBUPSS), GIS

ABSTRACT: Case-based support system (CBSS) is an innovated knowledge-based system (KBS). CBSS makes data more accessible by organizing it as a set of examples from past experience that can be generalized and applied to current problems. CBSS has been successfully applied to a wide variety of domains, including systems for architectural design, site planning, environmental design, and engineering structural design. This paper proposes a conceptual framework for developing case-based urban planning support system (CBUPSS)

that can structure and retrieve old cases accurately and efficiently. The conceptual framework employs a combination of GIS and RS to structure spatial case information and provide experiential planning solutions. The usefulness evaluation of historical cases is further carried out by the comparison of original spatial plan and recent land use pattern. The RS imagery is used to map recent land use pattern. Furthermore, we build a prototype CBUPSS to demonstrate the implementation of the conceptual framework.

1. Introduction

Most current KBS for urban planning are limited to deal with its well-structured aspect and fall short in dealing with flexibility and fuzziness in the alternative design. Case-Base Reasoning (CBR) was suggested as a promising way to overcome the difficulties in applying KBS to urban planning (Shi & Yeh, 1999). The fundamental philosophy of CBR is to use previous similar cases to solve problems or design new cases. Furthermore, rather than dismantling expert knowledge, this system emphasizes solving ill-structured problems on the basis of previous case study. It can, thus, partly improve the restriction on the knowledge expression of the conventional KBS. CBSS are a type of KBS based on CBR. CBSS also assume that people tend to adopt previous problem-solving pattern as the ground base and then make appropriate modifications to tackle new problems. In retrospect, the general planning practice emphasizes the significance of planning experience. The nature of planning experience is an accumulation of case-based comparison. It has many similarities with the principle of CBSS. Therefore, this article has trying to construct a CBUPSS to support the work of alternative design in urban planning.

Moreover, we can see that in the historical development of support system the procurement of expertise is the key element to the success of system. On case-based support system, how to efficiently procure the case used by the expert to solve the problems and to control the behavior and pattern of the case used is the key point of system development. It also carries out survey analysis to planners by experimental approach to initially sum up the behavior design and presentation procedure of planning case procurement to the reference of virtual system construction.

2. Framework of CBUPSS

When the urban planners face with a problem, them often utilize their past experiences and knowledge to help them understand the issues. When CBUPSS is operating, a case analysis is required from existing case-based knowledge to induct and retain the predecessor's experiences and make it become the short cut to find out the answer. Therefore, the operating procedure of a CBUPSS is generally including as follows: (1) identifying the problem as a new case; (2) picking up the case which had been solved with similar situations from current database; (3) comparing the current cases with the existing cases then revising it; (4) determining the optimal alternative; (5) storing the new case into database, etc. (See Figure 1). Operating through these procedures, the system could search for the past example which had most similarities with current problems and modifying them to present the best alternative.

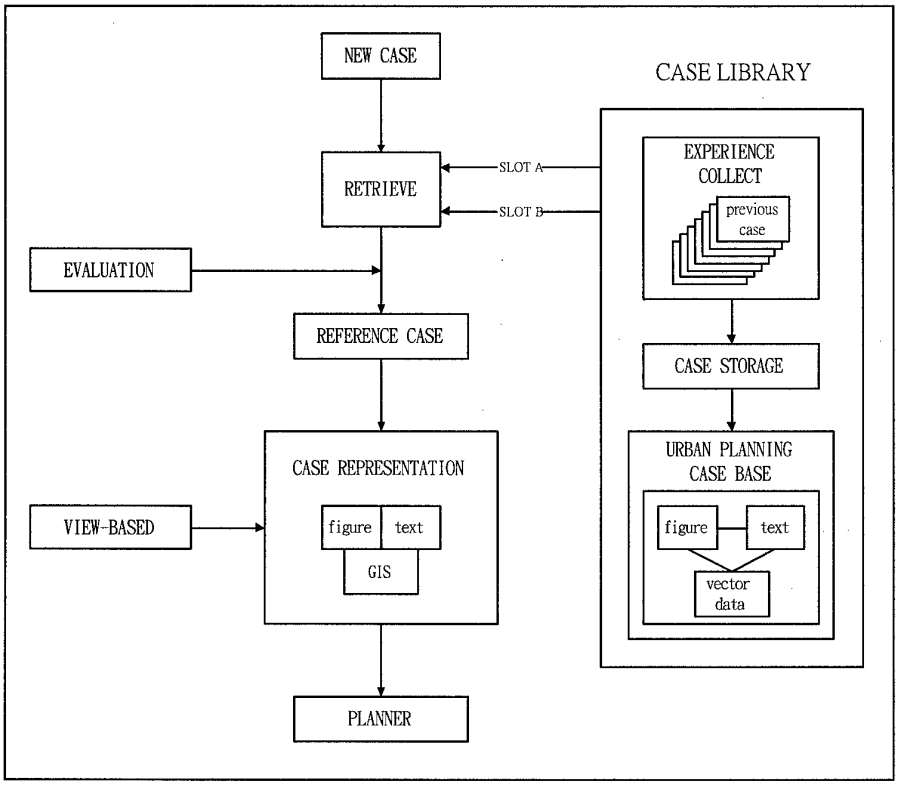


Figure 1 The Procedure for Building a CBUPSS.

3. Case Library and a Prototype System

3.1 Case Library

The case library is the knowledge base and core of a CBUPSS. Basically, the requirements for contents and information formats of urban planing case are complicated. The descriptions of themes like planning circumstances, plan alternatives, and plan evaluation except requiring text information, it also requires descriptions of photo images, charts, and related geographic information. More over, most of the planners are used to utilizing graphs to understand pertinent information and outcomes of planning sites. Therefore, case descriptions must combine texts with graphs.

The integrated-information of urban planning cases that offered by the combination of GIS and RS in the producing of graphs using artificial cut to mince the real world entity into pieces. This method adopts geometric objects (point, line, plane), topological relation, classification attribute and area image to accomplish case's description method. Features of planning cases can be categorized as:

(1) Describing attributes information of spatial characteristics of feature by statistical information.

(2) Describing spatial information and the degree of urban development obtained from the relativity of objects in the planning coverage and RS by users.

(3) Describing attributes information of non-spatial characteristics of feature mainly to express the significance of planning feature in planning.

(4) Describing relations of non-spatial characteristics of feature to elaborate non-spatial relationship with other features.

3.2 A Prototype CBUPSS

3.2.1 Searching for Reference Cases

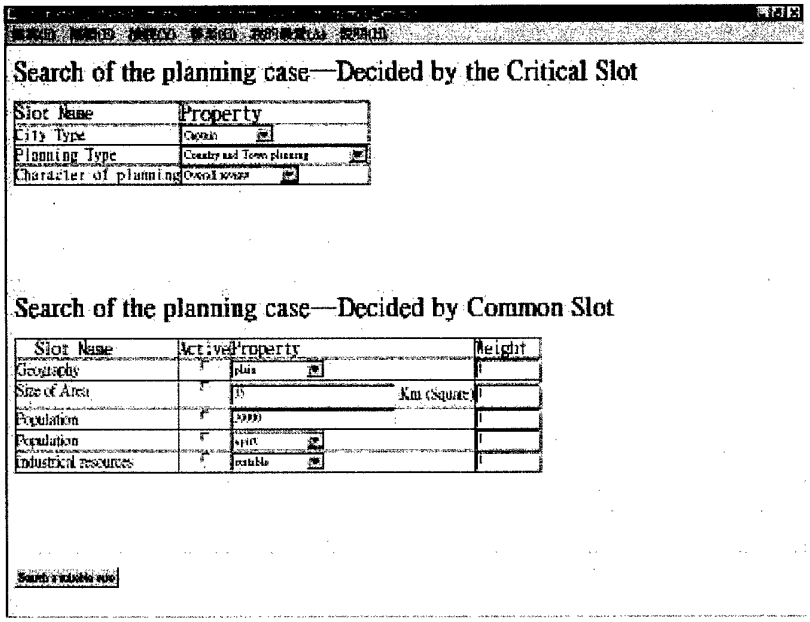


Figure 2 The Compilation of Slot Search in the Prototype CBUPSS

3.2.2 The Representation of Searching Results

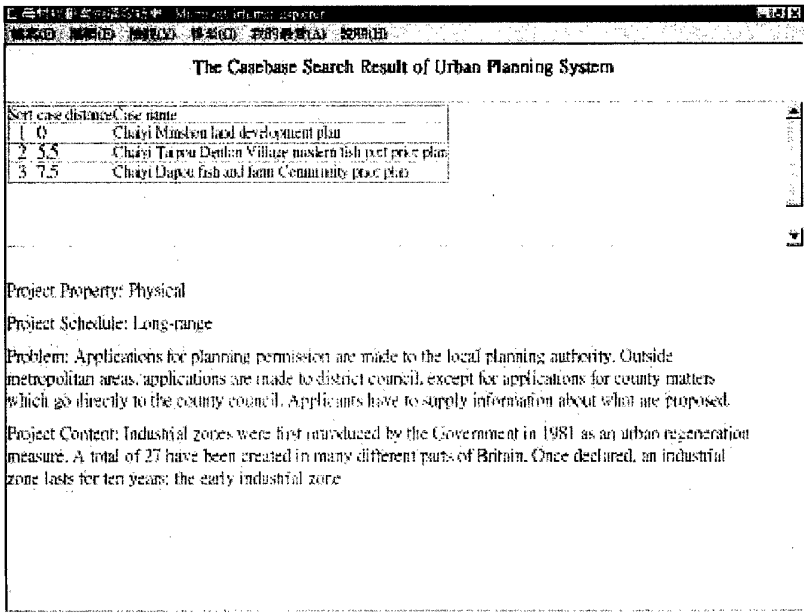


Figure 3 The Search Results of the Prototype CBUPSS

3.2.3 The Content Representation of Selected Cases

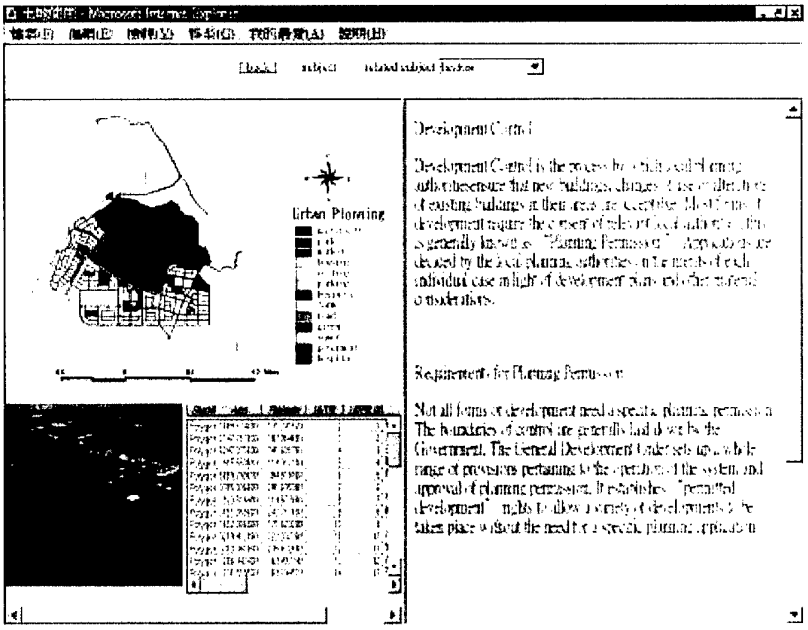


Figure 4 The Content Representation of the Prototype CBUPSS

4. Conclusions

This paper proposes a conceptual framework for developing CBUPSS that can structure and retrieve old cases accurately and efficiently. CBUPSS with a combination of GIS and RS to structure spatial case information are suggested as a promising way to overcome those difficulties in applying KBS to alternative design in urban planning.

5.Reference

Reference for Journals:

Shi, X. and Yeh, A. G. O., 1999, The integration of case-based systems and GIS in development control, Environment and Planning B: Planning and Design, 26, pp.345-364.

An Implementation of 3D GIS on web

Tien-Yin Chou* , Lan-Kun Chung** 、Wen-Yuan Ku*** 、Wei-Yuan Lo***
*Director, **Lecturer, ***Researcher of GIS Center, Feng Chia University
Tel:886-4-4516669 Fax:886-4-4519278
Email:msie@gis.fcu.edu.tw
Taiwan

Keywords: *3D GIS, VR, VRML*

Abstracts:3D GIS is the best way to display and exposure the z-value of the spatial object and let the analyst or decision maker to recognize the shape of these spatial objects, and web-based 3D GIS is also a hot topic since 1997. To accomplish the goal of 3D GIS on web, VRML is always discussed and implemented, but traditional VR emphasizes the expression of the object or scene, and usually ignores the attribute data behind the spatial object. This research introduce a solution to convert the 2D spatial data to VRML and keep the attribute data anyway, so that user can just browse a 3D scene on a browser and query the attribute data of each spatial object.

I.Introduction

It would be a tendency that GIS more internet and data more vision . Nowadays , we can find many successful GIS website in internet , for example : Taiwan Map (www.map.com.tw) 、EasyMap of Taichung (www.easymap.com.tw)..... but all of them only can display geographic information to user by 2D , and cannot present more close real world to user . At present , GIS vision only can use by PC and less to use in internet , the reason is to use 3D technology in WEB GIS till have many problems not solved yet .

The research follow the tendency of GIS , and base on the subject of internet and data vision to study 3D GIS ON WEB solution . We expect can have more edification for the people who are interested in GIS technology research .

II.Review of 3D GIS on web

At presently, the research of 3D GIS on Web is base on VRML (Virtual Reality Modeling Language). It's take account of two factors：

1. VRML is a platform independent file format for sharing 3D worlds on the Web. VRML browsers or plug-ins are available for all major platforms. User may find browsers and other VRML tools for their system. And they could view 3D scenes on the web.
2. Reduce the load of researcher.

In general, it's not an easy work to design a good drafting engine for the domain

of three-dimensional graphics. The development of VRML is an exciting piece of news. It's an unnecessary work to waste time on drafting engine. Developers only need to consider converting 2D data format into VRML format and they will accomplish the purpose about 3D GIS on Web.

The technique of 3D GIS on Web has evolved in two ways：

The first method： converts the 3D scene into a set of files in VRML format with GIS software.

Bo Huang, who studies in The Chinese University of Hong Kong, have made a study of ArcView with its 3D Analysis and Internet Map Server. Mr. Huang developed a complete application, GeoVR, by these two extensions. If users connect the home page serve 3D GIS functions, they could convert 2D data format of the area they allocated into VRML format and return to their computer immediately.

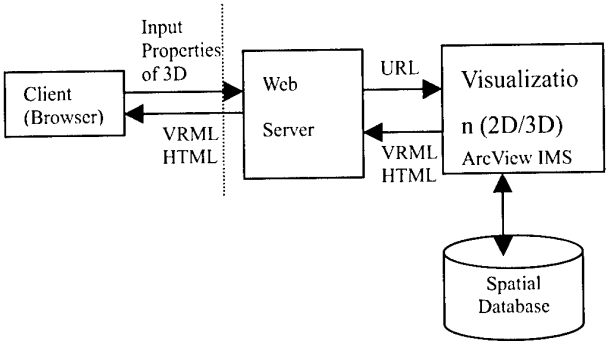


Fig 1. Bo Huang's Structure

It spends the shortest time to generate a 3D GIS with this method. But there are two chief defects：

(1) We have to expend large sums of money in purchasing 3D Analyst and Internet Map Server extension.

(2) We can export a 3D scene to the VRML files by ArcView 3D Analyst. But each independent spatial object of this theme is treated as a unique object, and therefore couldn't be queried by users.

The second method：converts the 3D scene into a set of files in VRML format with CAD software.

To solve the above-mentioned problems, Scott A. Carson brought up an idea. He applied some software and data format like Adobe Illustrator to convert a GIS data to a 2D data format VRML. And then use the extrusion tool of MetaCreations Ray Dream Studio to extrude the building. Last, save the file into VRML format and link attribute data to every object manually.

Then, we followed Carson's method to reform the processes for generating a VRML file. The following are these steps:

(1) Export a polygon shape file (ex. school's layout) to *.ai format.

(2) In Adobe Illustrator, export *.ai format to *.eps format.

(3) In 3D Studio Max, import this .eps file and extrude every building manually and then export to VRML

(4) Link attribute data to every object manually.

After testing, our result confirmed Carson's method is capable of solve a part of these problems. People can generate a real 3D GIS and manipulate even query each spatial object via Internet. We are very excited to learn the skill. But we also have some opinions about the 3D GIS on Web with Carson's method :

(1) It seems to be a sticky process. And we must extrude every object manually.

(2) It never mentioned the method of link attribute data.

III.Research Topics

This research aims at the bottleneck of 3D GIS on web, i.e. transfer 2D GIS data to VRML and keep their attribute data concurrently, the research topics are as follows:

1. VRML and 2D GIS data structure analysis
2. Transfer 2D GIS data to VRML

This topic focus on the method which can present each 3D spatial object in a economical way

3. Keep the attribute data during the process of transferring 2D GIS data to VRML

This topic is the most important issue in this research, because a complete GIS data is consisted of spatial and attribute data.

IV. Research Result

1. The solution of 2D to 3D problem

How to translate 2D object into 3D object is one of the bottlenecks on 3D GIS ON WEB research. Therefore, we analyzed this problem carefully and bring up our ideas. The analysis step is as follows:

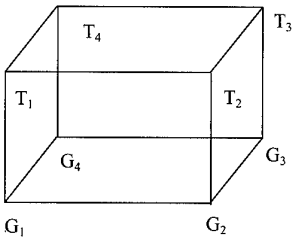


Fig 2. 3D object diagram

(1)Node defined

On the GIS, the spatial data are saved in SHAPE field and consisted of nodes. These nodes can record values of the X and Y coordinate, but cannot record Z coordinate. In general, the Z coordinate is stored on the attribute table. Therefore, we

must create and define node structure and give the value of X, Y and Z coordinates into these nodes on all 3D Objects.

Define node structure:

$G_i = \{x,y,z|where\ x,y,z\ belong\ R\}$

G_i is represent the bottom node of 3D object

$H_i = \{0,0,h|where\ h\ belong\ \}$

H_i is represent 3D object's height value.

$T_i = N_i + H_i$

T_i is represent the top node of 3D object

(2)Face defined

When all nodes of the 3D object are defined completed, we starting to define the face of the 3D object. The face define can divided into there section:

Define the 3D object's bottom face:

$Bottom = \{G_1,G_2,G_3,\ldots,G_i\}$

Define the 3D object's top face:

$Top = \{T_1,T_2,T_3,\ldots,T_i\}$

Define the 3D object's edge face:

$Edgej = \{G_j,G_{j+1},T_{j+1},T_j\}$

For reduce complexity, we using four nodes to make a side face.

(3)3D Algorithm

When the nodes and faces are defined completed. Finally, we start to design the 3D algorithm.

```
begin
 for i:=1 to nNode
        LinkG(G_i,G_i+1)
        LinkT(T_i,T_i+1)
        LinkS(G_j,G_j+1,T_j+1,T_j)
 end
end
```

2. The solution of the attribute data problem

Because VRML cannot access data from Server's database directly. Therefore, we must apply other technology, such as ASP or CGI that can be access data form

Server's database and to solve this problem.

This study will be saved the GIS attribute data on the Microsoft Access database and writing an ASP program to connect this database, and using VRML ***Anchor*** node to group of every 3D Object. By using Anchor's Field ***url***, we can define link URL of the 3D Object. For example,

Anchor{

children Shape{ geometry Box{} }

url "http://wyku/vrml.asp?table=attribute&object=ObjectNo"

}

When user clicked the 3D Object, browser will be connecting to this URL. Because ASP is running on the Server, so we can query this Object's attribute data from server's database.

3. Automatic Translation Interface

In order to confirm the practicable of method with our research, we integrated our study result to program the Automatic Translation Interface(ATI), the ATI structure is as follows:

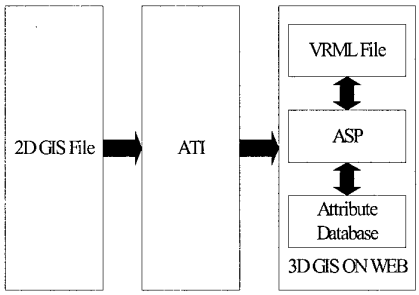


Fig 3. ATI structure

When 2D GIS File is improved into ATI, we can set translation area, the ATI will analyze nodes of all 2D object and translate into VRML format. In the same time with translation, ATI will be exported every 2D object's attribute data into database, and add a link on every 3D VRML object.

4.Example

For testing ATI, we made of choice the first campus of Feng Chia University for our experiment. We imported the 2D campus file into ATI(see. Fig4) and the result is very perfect. ATI exported a VRML file that the size is only 50 KB and every building is independent.

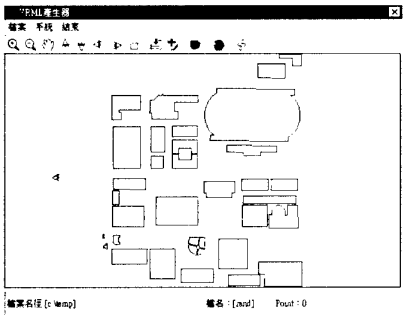


Fig 4. First campus in ATI

User can connect to our 3D GIS web site(***http://rand.gis.fcu.edu.tw/3DGIS***) to visit this VRML scene and query every building attribute data. This result proves our method of this study is practicable.

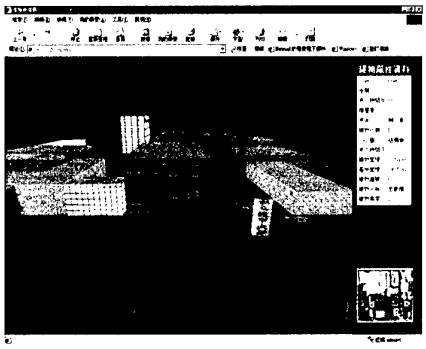


Fig 5. First campus VRML scene

V.Conclusion

This research resolve the bottleneck of 3D GIS on web, i.e. transfer 2D GIS data to VRML and keep their attribute data concurrently, this is just a beginning, and there are several problems should be discussed:

1. It decreases the speed of browsing VRML scene when VRML scene has a large size, binary VRML format will be a good solution for decreasing the presently ASCII VRML format.
2. How to query a spatial object not only by mouse click, but also by object attribute is next phase to research.
3. The result shows the building objects by cube, i.e., the 3D shape of a building is based on its 2D shape, and extrude with its attribute related to its height, it's a simple way to display a spatial object, but also ignore the real figuration of itself, how to present a spatial object with its original figuration is worth to study in the field of 3D GIS on web.

References

1. Bo Huang, Hui Lin,1999. GeoVR: a web-based tool for virtual reality presentation from 2D GIS data, Computers and Geosciences 2591999), p1167-p1175.

The Management System Development of Campus Facility Information using Web-based GIS

Myung-Hee Jo · Sung-Joong Park · Mal-Suk Kim · Yun-Won Jo
Department of Geodetic Engineering, Kyungil University
33 Buho-ri, Hayang-up, Kyungsan-si, Kyungsan bukdo, 712-701, Korea
Tel) +82-53-850-7312, Fax) +82-53-854-1272
Email : mhjo@bear.kyungil.ac.kr, sjpark@tksun.aiit.or.kr
sukkim@cuth.cataegu.ac.kr, gerry@purple.knu.ac.kr

KEY WORDS: Web-based GIS, Facility Information Management, Intranet, GUI

Abstract

This paper, which deals with the developmental result of university facility management system using GIS, is to verify the developmental process of this system and merits of GIS facility management system. It makes possible for GIS facility management, as a discipline in this paper, to put together the facility managers' works in offices and physical workspaces. Thus, they can administer and manager spatial data and attribute data more effectively and systemically.

Moreover, anyone, even doesn't have any knowledge of computer, can easily operate, input and modify data because GIS facility management system introduced in this paper is implemented and focused on the GUI(Graphic User Interface) effectively.To implement this study, many kinds of drawing layer in campus facility and building including surrounding area. In addition, Oracle Server was used for client and server environment and develop the GUI needed for operating GIS facility management system using Map Object 2.0 GIS S/W and Visual Basic 6.0. To develop the web based GIS for campus-life information system, IMS(Internet Map Server) was applied to integrate GIS and Internet.

INTRODUCTION

The definition of Internet GIS (Geographic Information System) is that input, manipulation, analysis, output of geographic data can work on Internet.

Recently the use of Internet GIS (Geographic Information System), which is geared with Internet and GIS, is on the increase because of services of GIS data on web, non-limitation of platform, low cost of installation, and extension of it.

Shin. S.Y(1999) installed the stream information using Internet GIS for water analysis, Andrew Evans(1999) and Keng-Pin Chang(1997) constructed system based on web for each public democratic involvement and Community Participation.

The purpose of this paper is to develop the Management System of Campus Facility Information using Web-based GIS so that the limitation of use for only domestic users in specific area under LAN environment overcomes. In addition, it makes to verify the efficiency of this system as comparing with traditional facility management system. Moreover, even general users can grasp geographic information visually by searching spatial data with its attribute data. Furthermore, the technology to search of spatial data on network is needed.

DATA AND METHOD

The surrounded area of Kyung-il University and Ha-yang town for study is selected. And then the information of this area was installed and constructed on Internet GIS.

Most of all database including various and detail spatial data and its attribute should be built in GIS DB.

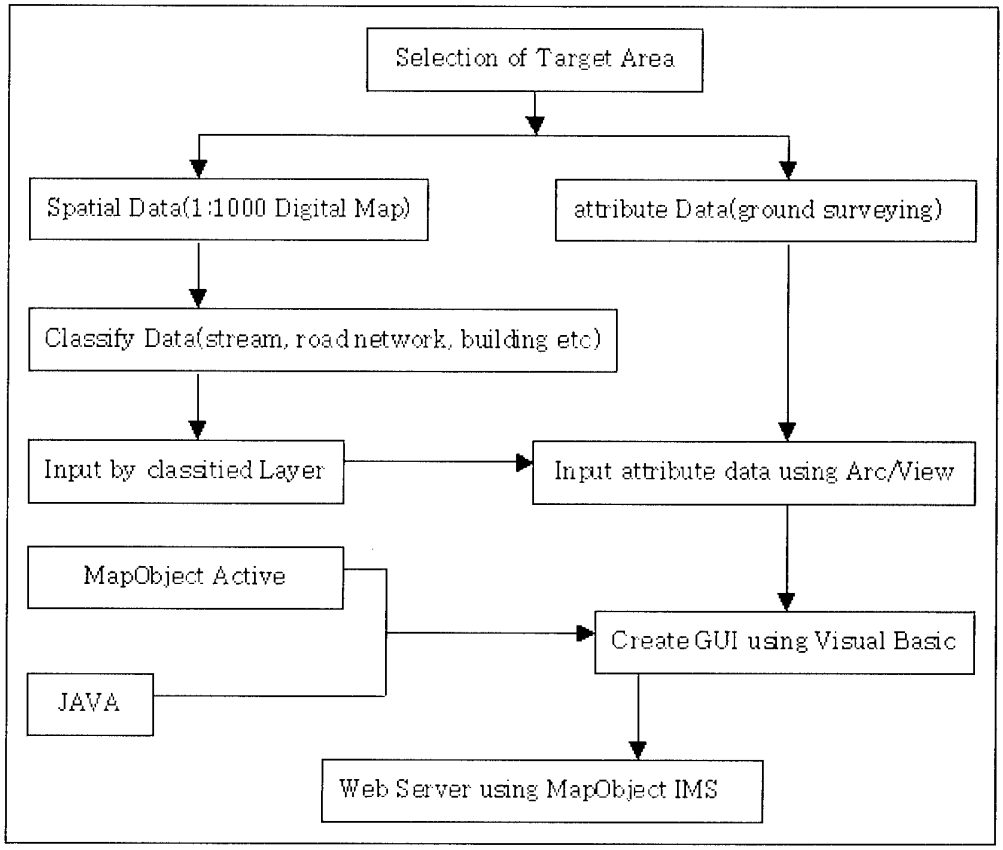


Figure 1. the study flow

The spatial data is classified as stream layer, road layer, and buildings layer based on 1:1000 digital map and has .shp file format on ArcView 3.1. For the attribute data, information of each building such as name and phone number etc. is regarded and input to shape file.

Moreover, GIS facility management system introduced in this paper, which is focused on the GUI(Graphic User Interface), is implemented on Map Object 2.0 GIS S/W and Visual Basic 6.0 and use JAVA language to show the result on web-browser.

Also, it is linked with MapObject IMS(Internet Map Server) to integrate GIS and Internet. The web server to manage spatial data and attribute data is setup on Windows NT 4.0 workstation and Microsoft Explorer for client is installed on Pentium PC.Fig.1 shows the flow of research.

The most important thing to regard when design user interface is to specify function for suitable operations. The general functions for Management System of Facility Information are movement, magnification, reduction, searching, and viewing the attribute.

GIS ActiveX control could be called small size GIS programming, having the ability of computation and transmission, and its own graphic interface. Also, it can be added to any types of application.
The operation of this is similar to other plug-in program. This module is stored at sever and forwarded to web-browser in case of need. When web-browser realize GIS data, this module operates ActiveX control, which is referenced HTML. Map Object IMS is working in above way. Fig.2 presents the implementation diagram of the Internet GIS.

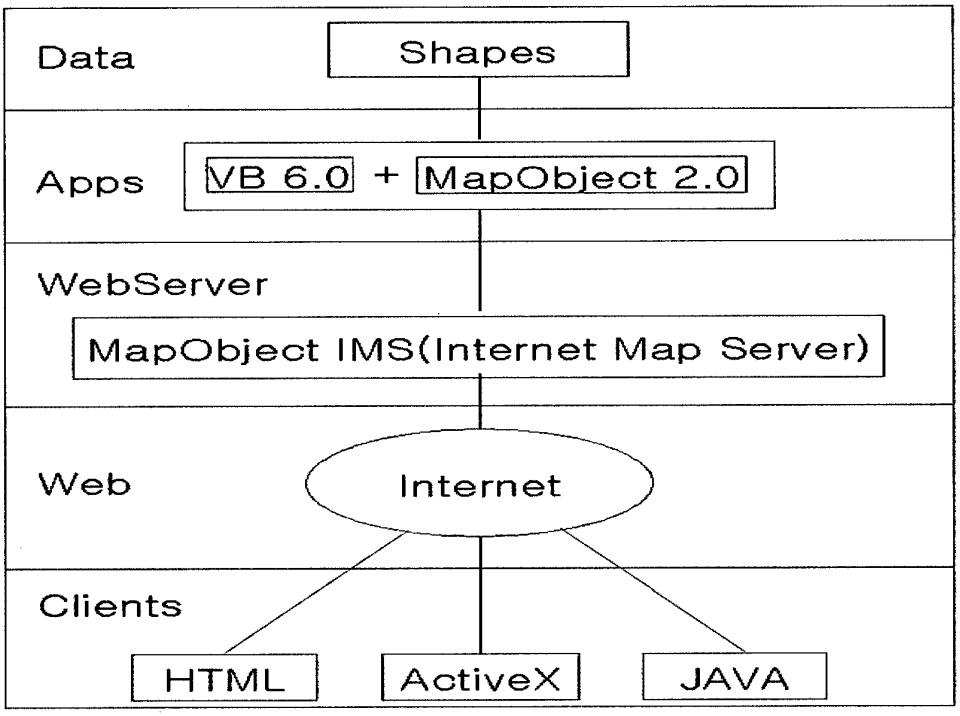


Figure 2. Implementation diagram of the Internet GIS

As shown in Fig.2, HTML, Java, ActiveX are used to access to spatial data on Internet and to process. Finally, the result of processing is shown on web-browser in raster type.
Fig. 3 and Fig.4 shows the result of our Management System of Facility Information based on Web.

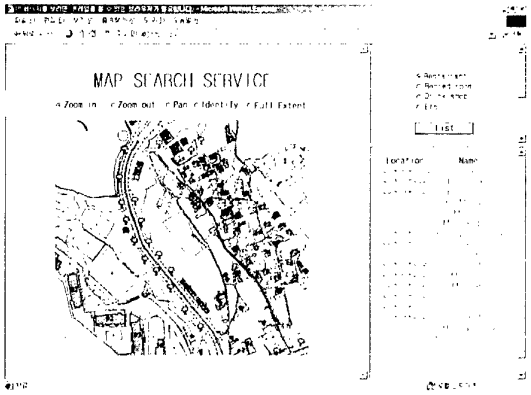


Figure 3. the list of facility information

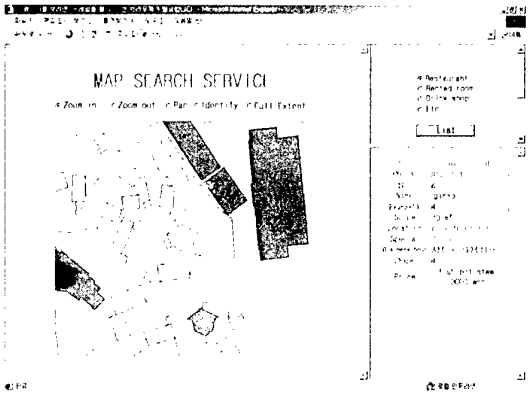


Figure 4. the view of facility information

The Fig. 5 script tells you that the transmitting data to web browser through Web Link object in Map Object.

```
WebLink1.WriteString "<td align='center' width='150'><p>name</td></tr>" & vbCrLf
    If Not f_identifyRecs.EOF Then
Dim fld As Object
Dim i As Integer
        For i = 1 To f_identifyRecs.Count     '<-increase I until f_identifyRecs
WebLink1.WriteString "<tr><td align='center' width='100'><p>" & f_identifyRecs.Fields
                        ("Location").ValueAsString & " </td>" & vbCrLf
                        '<- list the attribute of location
WebLink1.WriteString"<td align='center' width='150'><p><a href = 'http://park/scripts/
    esrimap.dll?name=tour&cmd=find&layername=" & layername & "&findstr=" &
                f_identifyRecs.Fields("name").ValueAsString & "' target='map'>" &
          f_identifyRecs.Fields("name").ValueAsString & "</a> </td></tr>" & vbCrLf
    f_identifyRecs.MoveNext    '<- list the attribute of name
      Next
End If
```

Figure 5. The script with weblink object

CONCLUSION

In this paper Management System of Facility Information based on Web is implemented so many people can share these GIS data. This system performs perfect searching so this system is expected to use in many ways.

This research shows that Web-based GIS is a useful vehicle for accessing distributed spatial data and conducting GIS processing and spatial modeling among a particular user community by removing geographical and physical constraints to involvement and reducing the need for users to own the data or software system. This study also gives us a research insight into the applicability of Web-based GIS in developing open spatial decision supporting systems where a decision-making process in solving spatial problems demands significant input from the public. The GIS research community is looking for new challenges in future developments of Web-based GIS in terms of users, developers, and institutions.

REFERENCES

Young-Joo Lee, "The Bank location decision support system based on the web using GIS" 1999.12, Masters Thesis, University at Kyungpook Department of Geographic Information.

Kidong Bu Ilsu Jun Namsik Won,"Developing a viewer for raster map with vector information in the web environment", 1999.11, Proceedings of the 99 KAGIS Fall Meeting, The Korean Association of Geographic Information Studies

Ki-Dong Bu, "A Study on developing GIS User Interface using OLE Automation", Journal of The Korean Association of Geographic Information Studies. Vol 1. No 1, 1999. 5, p.66

Jong-Sung Sunwoo, "A Study on a data sharing standard for Internet GIS", 1998, NGIS Report, Korean National Computerization Agency

Ki-Dong Bu Myung-Hee Jo Kwang-Joo Kim Jun-Suk Seu, "Construction and evaluation of bank marketing database using Geographic Information Systems", 1998, Proceedings of the 98 KAGIS Fall Meeting, The Korean Association of Geographic Information Studies.

Berger,Blaine H. "The Web enabling of spatial information technologies", 1997, GIS97, Conference Proceedings.

Zhong-Ren Peng, "An Assessment of the development of Internet GIS", 1997, Abstract for URISA '97

Zhuang, V. "Spatial engines drive Web-based GIS". 1997.GIS World 10(10):54-58.

Thoen, B. "Interactive mapping and GIS Thrive on the Web". 1995. GIS World 8(10):58-59.

Usery, E. L., J.C. Seong and B.W. Jun., "Implementing GIS Software over the World-Wide-Web". Proceedings of ASPRS-RTI 98 Annual Conference, Tampa, FL, Mar. 31-Apr. 3, 1998, pp.623-629.

Keng-Pin Chang, "The Design of a web-based Geographic Information System for community participation" 1997, Masters Thesis, University at Buffalo Department of Geography, August

Evans, A.J., Kingston, R., Carver, S., and Turton, I., "Web-based GIS used to enhance public democratic involvement", 1999, Proceedings of the 4th International Conference on GeoComputation.

Karimi, H. 1996. Open computing GIS: An effective, affordable approach to solving spatial problems. GIS World 7(3)

Jun, B.W. 1998. Integration of GIS with the World Wide Web (WWW) using Java. paper presented at 13th Annual Meeting of the Southeastern Geography Student Conference, Feb. 6-7, 1998, Athens, GA, USA.

INFORMATION TECHNOLOGY AND NATURAL DISASTER MANAGEMENT IN INDIA

Dr. Alok Gupta
Research Associate
National Centre for Disaster Management (NCDM)
Indian Institute of Public Administration
I.P. Estate, Ring Road, New Delhi-110002 (INDIA) Tel.: 91-11-3317309, 3716509,
FAX: 91-11- 3358629, 3319954, E-mail: alokncdm@usa.net

KEYWORDS: GIS, Remote Sensing, Warning and Forecasting, Financial and Administrative Arrangements.

ABSTRACT: It may be observed that advancement in Information Technology in the form of Internet, GIS, Remote Sensing, satellite communication, etc. can help a great deal in planning and implementation of hazards reduction measures. GIS can improve the quality and power of analysis of natural hazards assessments, guide development activities and assist planners in the selection of mitigation measures and in the implementation of emergency preparedness and response action. Remote Sensing, on the other hand, as a tool can very effectively contribute towards identification of hazardous areas, monitor the planet for its changes on a real time basis and give early warning to many impending disasters. Communication satellites have become vital for providing emergency communication and timely relief measures. Integration of space technology inputs into natural disaster monitoring and mitigation mechanisms is critical for hazard reduction. It is absolutely necessary to create awareness amongst the public as well as decision makers for allocating resources for appropriate investments in information technology. In this paper an attempt has been made to highlight the role of information technology in management of natural disasters in India.

1. INTRODUCTION

It is a well known fact that natural disasters strikes countries, both developed and developing, causing enormous destruction and creating human sufferings and producing negative impacts on national economies. Due to diverse geo-climatic conditions prevalent in different parts of the globe, different types of natural disasters like floods, droughts, earthquakes, cyclones, landslides, volcanoes, etc. strikes according to the vulnerability of the area. India is considered as the world's most disaster prone country. It has witnessed devastating natural disasters in recent past like droughts, floods, cyclones, earthquakes, landslides, etc.

2. NATURAL DISASTERS IN INDIA

India is a large country and prone to a number of natural hazards. Among all the natural disasters that country faces, river floods are the most frequent and often devastating. The shortfall in the rainfall cause droughts or drought like situation in various parts of the country. The country has faced some severe earthquakes causing widespread damage to the life and property. India has a coastline of about 8000 km which is prone to very severe cyclonic formations in the Arabian Sea and Bay of Bengal. Another major problem faced by the country is in the form of landslides and avalanches.

With an increase in the perception towards spreading a culture of prevention in the disaster management scenario, considerable emphasis is now being placed on research and development activities in the area of information technology for disaster preparedness and prevention. This has brought in a significant positive change even though the multitude and frequency of disasters in the country has increased.

3. APPLICATION OF INFORMATION TECHNOLOGY IN DISASTER MANAGEMENT

Though it is not possible to completely avoid the natural disasters, but the sufferings can be minimised by creating proper awareness of the likely disasters and its impact by developing a suitable warning system, disaster preparedness and management of disasters through application of information technology tools. The changing trends have opened up a large number of scientific and technological resources and skills to reduce disaster risk. The IT tools are discussed below:-

3.1 GIS and Remote Sensing

GIS provides a tool for effective and efficient storage and manipulation of remotely sensed data and other spatial and non-spatial data types for both scientific management and policy oriented information. This can be used to facilitate measurement, mapping, monitoring and modelling of variety of data types related to natural phenomenon. The specific GIS application in the field of Risk Assessment are:- **Hazard Mapping** to show earthquake, landslides, floods or fire hazards. Thses map could be created for cities, districts or even for the entire country and tropical cyclone **Threat Maps** are used by meteorological departments to improve the quality of the tropical storm warning services and quickly communicate the risk to the people likely to get affected by the cyclone.

Remote sensing makes observation of any object from a distance and without coming into actual contact. Remote sensing can gather data much faster than ground based observation, can cover large area at one time to give a synoptic view. Remote sensing comprises **Aerial Remote Sensing which** is the process of recording information, such as photographs and images from sensor on aircrafts and **Satellite Remote Sensing which** consists of several satellite remote sensing system which can be used to integrate natural hazard assessments into development planning studies.These are: Landsat, SPOT Satellite, Satellite Radar System, Advanced Very High Resolution Radio. Some application of GIS and Remote Sensing in various disasters are as follows:-

3.1.1 Drought: GIS and Remote Sensing can be used in drought relief management such as early warnings of drought conditions will help to plan out the strategies to organise relief work. Satellite data may be used to target potential ground water sites for taking up well-digging programmes. Satellite data provides valuable tools for evaluating areas subject to desertification. Film transparencies, photographs and digital data can be used for the purpose of locating, assessing and monitoring deterioration of natural conditions in a given area.

3.1.2 Earthquake: GIS and Remote Sensing can be used for preparing seismic hazards maps in order to assess the exact nature of risks.

3.1.3 Floods: Satellite data can be effectively used for mapping and monitoring the flood inundated areas, flood damage assessment, flood hazard zoning and post-flood survey of rivers configuration and protection works.

3.1.4 Landslides: Landslide zonation map comprise a map demarcating the stretches or area of varying degree of anticipated slope stability or instability. The map has an inbuilt element of forecasting and is hence of probabilistic nature. Depending upon the methodology adopted

and the comprehensiveness of the input data used, a landslide hazard zonation map able to provide help concerning location,-extent of the slop area likely to be affected, and rate of mass movement of the slope mass.

3.1.5 Search and Rescue: GIS can be used in carrying out search and rescue operations in a more effective manner by identifying areas that are disasters prone and zoning them accordingly to risk magnitudes.

3.2 Internet

In the present era of electronic communication, the internet provides a useful platform for disaster mitigation communications. Launching of a well defined web site is a very cost-effective means of making an intra-national and international presence felt. It provides a new and potentially revolutionary option for the rapid, automatic, and global dissemination of disaster information. A number of individuals and groups, including several national meteorological services, are experimenting with the Internet for real-time dissemination of weather observation, forecasts, satellite and other data. In the most critical phase of natural disasters electronic communication have provided the most effective and in some instances perhaps the only means of communication with the outside world.

4 WARNING AND FORECASTING SYSTEM

An advance system of forecasting, monitoring and issuing early warnings plays the most significant role in determining whether a natural hazard will assume disastrous proportions or not. The country have the following forecasting systems:

4.1 Indian Meteorological Department (IMD)

IMD provides cyclone warnings from the Area Cyclone Warning Centres (ACWCs) It has developed the necessary infrastructure to originate and disseminate the cyclone warnings at appropriate levels. It has made operational a satellite based communication system called Cyclone Warning Dissemination System for direct dissemination of cyclone warnings to the cyclone prone coastal areas. IMD runs operationally a Limited-area Analysis and Forecast System (LAFS), based on an Optimal Interpretation (OI) analysis and a limited area Primitive Equation (PE) model, to provide numerical guidance.

4.2 National Remote Sensing Agency(NRSA)

Long term drought proofing programmes on the natural resources of the district have been greatly helped by the use of satellite data obtained by NRSA. Satellite data can be used very effectively for mapping and monitoring the flood inundated areas, flood damage assessment, flood hazard zoning and past flood survey of river configuration and protection works.

4.3 Seismological Observations

Seismological observations in the country are made through ***national network of 36 seismic*** stations operated by the IMD, which is the nodal agency. These stations have collected data over long periods of time.

4.4 Warning System for Drought

The National Agricultural Drought Assessment and Management System (NADAMS) has been developed by the Department of Space for the Department of Agriculture and Cooperation, and is primarily based on monitoring of vegetation status through National Oceanic and Atmospheric Administration (NOAA) Advanced Very High Resolution (AVHR) data. The drought assessment is based on a comparative evaluation of satellite observed green

vegetation cover (both area and greenness) of a district in any specific time period, with that of any similar period in previous years.

4.5 Flood Forecasting

Flood forecasts and warnings are issued by the Central Water Commission (CWC) , Ministry of Water Resources. These are used for alerting the public and for taking appropriate measures by concerned administrative and state engineering agencies in the flood hazard mitigation. Information is gathered from the CWC's vast network of Forecasting Stations on various rivers in the country.

4.6 Cyclone Tracking

Information on cyclone warnings is furnished on a real-time basis to the control room set up in the Ministry of Agriculture, Government of India. High-power Cyclone Detection Radars (CDRs) that are installed along the coastal belt of India have proved to be a very useful tool to the cyclone warning work. These radars can locate and track approaching Tropical Cyclones within a range of 400 km. Satellite imagery received from weather satellite is extensively used in detecting the development and movement of Tropical Cyclones over oceanic regions, particularly when they are beyond the range of the coastal radars. The existing mode of dissemination of cyclone warnings to various government officials is through high priority telegrams, telephones, telex and fax.

5. FINANCIAL ARRANGEMENTS FOR NATURAL DISASTER IN INDIA

Natural Disasters are huge economic burdens on developing economies such as India. Every year huge amount of resources are mobilised for rescue, relief and rehabilitation works following natural disaster occurrences. The Central Government plays a major role as far as mobilisation of financial resources are concerned. A scheme called **Calamity Relief Fund (CRF)** has been constituted for each state with contribution from the Central and State Government to undertake relief and rehabilitation measures .This enable the states to manage and provide for calamity relief on their own by drawing upon the resources available with a fund constituted for that purpose separately for each state. In addition to CRF, a **National Fund for Calamity Relief (NFCR)** has been created to deal with hazards of rare severity managed by a National Calamity Relief Committee (NCRC). The State Governments are required to submit memoranda for this purpose giving details of damage and destruction and the cost of relief and rehabilitation. On receipt of these memoranda, the Government of India decides on an individual basis whether a Central Team is required to be deputed to assess the situation.

6. ADMINISTRATIVE STRUCTURE OF DISASTER MANAGEMENT IN INDIA

The **Department of Agriculture and Cooperation (DAC)** in the Ministry of Agriculture, Government of India, is the nodal department for all matters concerning natural disasters relief at the Centre. The **National Contingency Action Plan (CAP)** facilitates launching of relief and rescue operations without delay. There are various committees at the national level for disaster management such as ***Cabinet Committee*** for effective implementation of relief measures in the wake of natural calamity; ***National Crisis Management Committee*** at the national level headed by the Cabinet Secretary who is in charge of various types of disasters and supporting ministries as members; ***Crisis Management Group*** reviews various measures required for dealing with a natural disaster, and coordinates activities of the Central ministries and the State Governments pertaining to

disaster preparedness and relief and obtains information from nodal officers on measures relating to the above. **Figure 1** shows the Interaction Pattern in the Government.

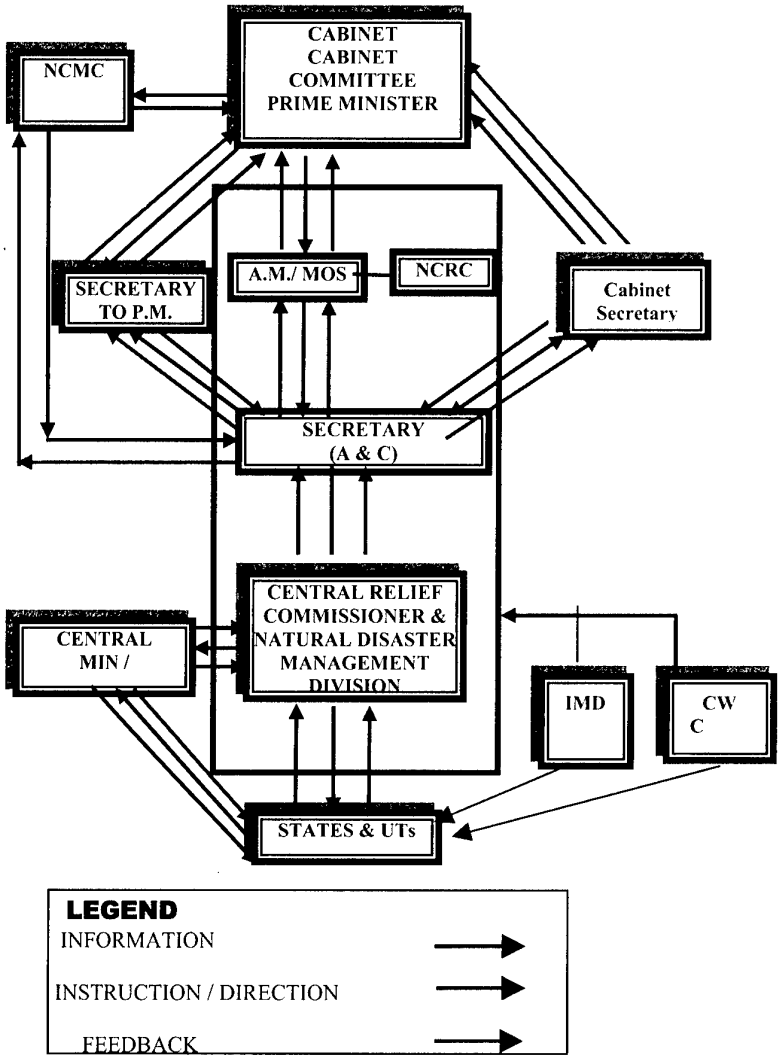


Figure 1:Natural Hazards - The Interaction Pattern in the Government

The State Governments are autonomous in organising relief operations in the event of natural disaster and a long-term preparedness / rehabilitation measures. The State Governments efforts are supplemented by Central Government. There is a **State Crisis Management Group (SCMC)** under the Chairmanship of Chief Secretary/Relief Commissioner to take into consideration the infrastructure and guidance received, from time to time, from Government of India and formulate action plans for dealing with different natural disasters.There is a **State Level Control Room** set up whenever a disaster situation develops.

States are further divided into districts, each headed by the District Collector (also known as the District Magistrate or Deputy Commissioner), who is the focal point at the district level for directing, supervising and monitoring relief measures for disaster and for preparation of district level plans. The Collector exercises coordinating and supervisory powers over functionaries of all the departments at the District level. The relief measures are reviewed by the ***District Relief Committee*** consisting of official and no-official members, including local legislators and members of parliament. In the wake of Natural disasters, a

Control Room is set up in the District for day-to-day monitoring of the rescue and relief operations on a continuing basis.

The Collector/Deputy Commissioner maintains close liaison with the Central Government authorities in the districts, namely, Army, Air Force an Navy, Ministry of Water Resources, etc., who supplement the effort of the District Administration in the rescue and relief operation.They also co-ordinates all voluntary efforts by mobilising the non-government organisations capable of working in such situations.

The **armed forces** of the country have played a vital role during disaster emergencies providing prompt relief to the victims even in the most inaccessible and remote areas of the country. The organisational strength of the armed forces with their disciplined and systematised approach, and with their skills in technical and human resource management make them indispensable for such emergency situations. India having a federal structure the integrated disaster management mechanism exists within the government framework.

8. CONCLUSIONS

It may be observed that advancement in Information Technology in the form of Internet, GIS, Remote Sensing, Satellite communication, etc. can help a great deal in planning and implementation of hazards reduction. For maximum benefit, new technologies for public communication should be made use and natural disaster mitigation messages should be conveyed through these measures. GIS can improve the quality and power of analysis of natural hazards assessments, guide development activities and assist planners in the selection of mitigation measures and in the implementation of emergency preparedness and response action. Remote Sensing, on the other hand, as a tool can very effectively contribute towards identification of hazardous areas, monitor the planet for its changes on a real time basis and give early warning to many impending disasters.Communication satellites have become vital for providing emergency communication and timely relief measures. Integration of space technology inputs into natural disaster monitoring and mitigation mechanisms is critical for hazard reduction. It is absolutely necessary to create awareness amongst the public as well as decision makers for allocating resources for appropriate investments in information technology. Awareness and training in Information technology in a much grater measure is required to develop human resources, particularly in the developing countries, who are chronically suffer from natural disasters.

The disasters usually occur in the well-defined areas, even though the community does not know the coping mechanism for the disaster. The disaster mitigation programmes must be extensively taken up covering various aspects at national level to minimise the disaster damages. There should be a greater emphasis on development of new technologies in disaster mitigation. The disaster preparedness and awareness is the only effective way of mitigating the impact of future disasters.

8. REFERENCES

-Sinha, Anil & Sharma, Vinod K., (1999),*Culture of Prevention,* Government of India, Ministry of Agriculture, Natural Disaster Management Division, New Delhi.

-Mandal, G. S. (1999), Forecasting and Warning Systems for Cyclones in India, *Shelter*, October, 1999, pp. 24-26.

-Sinha, Anil (1999), Relief Administration and Capacity Building for Coping Mechanism towards Disaster Reduction, *Shelter*, October, 1999, pp. 9-12.

Detection of Disaster Damage Using Changes of City Lights with DMSP/OLS Data in Asia Pacific Region

Izumi NAGATANI*, Genya SAITO**, Masafumi KODAMA*, Xianfang SONG**
and Chris ELVIDGE***
* Computer Center for AFFR, MAFF, Tsukuba, Japan
2-1-2 Kannondai, Tsukuba, Ibaraki, 305-8604, JAPAN
** National Institute of Agro-Environmental Science, MAFF
3-1-1 Kannondai, Tsukuba, Ibaraki, 305-8604, JAPAN
***NOAA National Geophysical Data Center
325 Broadway, Boulder, Colorado 80303 USA

KEY WORDS: Disaster Mitigation, Satellite Image, Network, Database System, DMSP/OLS

ABSTRACT: This research is a part of ANDES (Asia Pacific Network for Disaster Mitigation using Earth Observation Satellite) project. The objective of this project is to detect and inform disasters in Asia-Pacific region as soon as possible by using satellite data and high-capacity network systems.
The disaster damage of volcano eruption of Mt Usu, Hokkaido, Japan was detected using the city lights data of DMSP/OLS.

1. Introduction

Now, as global environmental changes such as global warming, anomalous climatic changes, desertification and others are facing urgently to the mankind. They cause serious problems on water, food and energy supporting mankind life. To understand the mechanisms of global environmental change is important and to develop the system of early detecting and warning disasters using satellites is required.
In order to detect and inform disasters in Asia Pacific region as soon as possible, Asia Pacific Network for Disaster Mitigation using Earth Observation Satellite (ANDES) project was started on October 1, 1998 (Kodama,2000, Saito,1999, Song,2000). The ANDES project has executed four study themes, which are Real-time Archiving, Forest Fire, Agriculture Disaster, and Heavy Rain.
It is well known that the meteorological satellite sensors have an ability to detect wildfires (Elvidge,1997). Recently, the meteorological satellite data are tried to use for detection of disaster damage (Takashima,2000). ANDES project are trying to use them for practical utility functions of the detection and early warning system.
The main satellite data used for this project are NOAA/AVHRR, GMS, DMSP/OLS, and

TRMM. These data are processed and archived in the Satellite Image Database System for Agriculture, Forestry and Fisheries (SIDaB), which is managed by Computer Center for Agriculture, Forestry and Fisheries Research, the Ministry of Agriculture, Forestry and Fisheries (MAFF), Japan.

DMSP/OLS are suitable for the early identification of earthquake damage area (Hayashi,2000), because that DMSP/OLS possesses a wide swath, high overpass frequency, and high sensitivity for night-time observations in its visible-near infrared waveband (0.47 to 0.95 um).

In March, 2000, The volcanic eruption occurred at Mt.Usu in Hokkaido Japan. There were many influences on human activities. About four thousands people were forced the evacuation for about one month and there were electric power failures in over two thousands houses. The disaster damage will be detected using city lights data by DMSP/OLS.

2. Outline of SIDaB

This research is using SIDaB, therefore the outline of SIDaB will be described at first.

SIDaB is Satellite Image Database System in AFF. Using this system, the user could search and download freely satellite images as he wants through internet. The user could select data easily by menu of times span, area, and also format of data. This system is not only for the researchers in MAFF, Japan, but also for the ordinary person in MAFF and other administrative, environment and disaster prevention agency in Asia and all over world.

SIDaB have collected earth observation and meteorological satellite data and stored from the institutes of MAFF, the relation agencies and institutes of overseas using median of DAT or network. The using network is following.

a. Receiving of transmitting of data between the institutes of MAFF using Japan Gigabit Network (JGN)
b. Receiving of transmitting of data between overseas using Network of APAN.
c. Receiving of transmitting of data between domestic agencies and MAFF using Inter-Ministry Research Information network (IMnet).

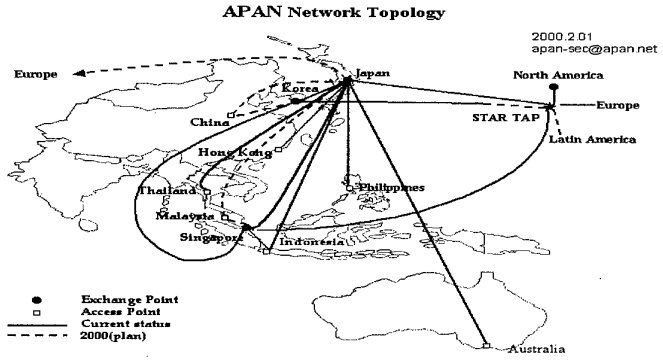


Fig. 1 The Map of APAN Network

The meteorological satellite data, NOAA/AVHRR, GMS, DMSP/OLS, and the tropical rainfall measuring mission TRMM are archived in the SIDaB system. These data has been transferred in real-time or near real-time data from each receiving station or data provider using high performance network to the Computer Center for AFFR, MAFF, Japan.

3. Detection of disaster using DMSP/OLS

3.1 DMSP/OLS data

The U.S. Air Force Defense Meteorological Satellite Program (DMSP) Operational Linescan System (OLS) data are received and used at operational centers on a continual basis in USA. The data are sent daily to the National Geophysical Data Center (NGDC), located in Boulder, Colorado, USA for creation of an archive. From Boulder, Colorado, these data are transferred in semi real time to the Computer Center for Agriculture, Forestry and Fisheries Research (AFFR), MAFF, Japan.

DMSP/OLS is designed for cloud imaging with two spectral bands, visible-near infrared (0.47-0.95 um) and thermal infrared, at 2.7 km resolution and swath of 3000 km. This instrument can also detect faint sources of visible-near infrared emission such as city lights, wildfire, fishing boats and so on.

Four satellites (F12, F13, F14 and F15) data are archived in SIDaB system. Here is a exsample of daily composite image(Fig. 2).

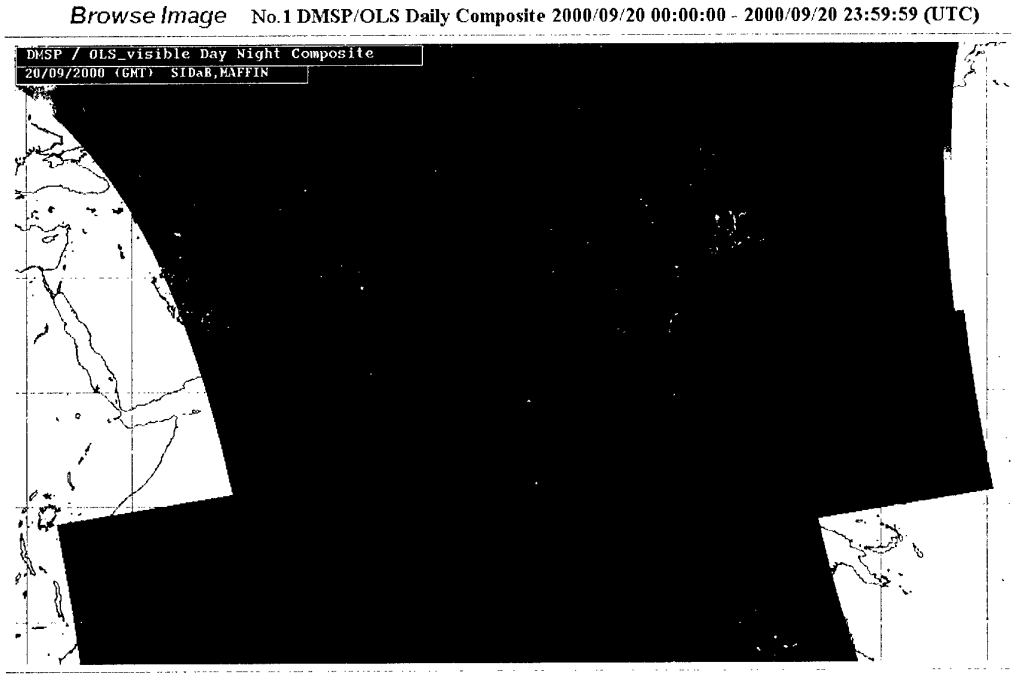


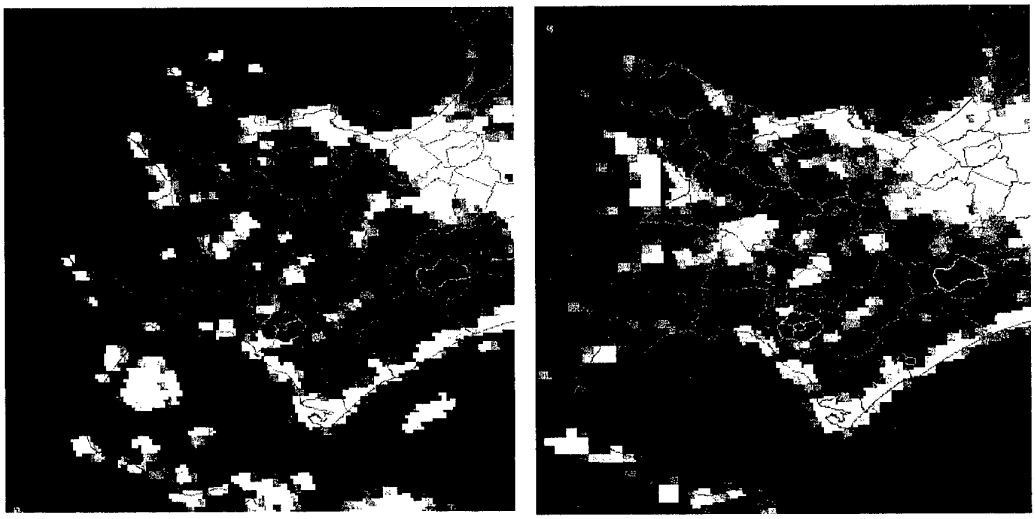
Fig.2 Example of DMSP/OLS Daily Composite image

3.2 Mt. Usu eruption

Mt. Usu volcano, located at Hokkaido, north of Japan, explored on 31 March, 2000. ANDES project tried to detect this eruption's damage area using DMSP/OLS data.

Kohiyama (Hayashi,2000) proposed a method to estimate the impacted area of the earthquake using visible-near infrared imagery. In this method, it is assumed that the brightness of the impacted area would decrease when the buildings collapsed or blackout occurred due to the earthquake. Thus, the impacted areas where brightness decreased significantly after the earthquake compared with before the earthquake were estimated.

Using this method, we studied Usu volcanic disaster and confirmed the ability of DMSP/OLS to detect disaster damage. Two DMSP/OLS data were used, one was acquired on 10 October, 1999, as the pre-event imagery and another was acquired on 4 April, 2000, as the post-event imagery (Fig. 3). These data were acquired with high visible band gain settings under new moon nights. The volcanic eruption influenced areas were estimated according to difference of visible-near infrared emissions between of the pre-event imagery and of the post-event imagery. The estimated image (Fig. 4) shows that there are significant reductions in nighttime lights at Toyako Hot Spring and in Date City. Indeed there are severe ash flows after Usu volcanic eruption around there.



(a) (b)

Fig.3 DMSP/OLS visible-near infrared images before(a) and after(b) the volcanic eruption

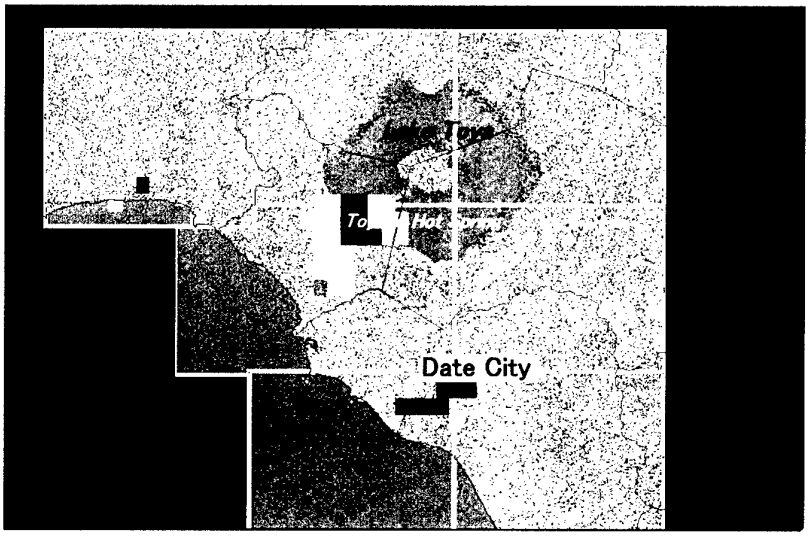


Fig. 4 The estimated impacted area of eruption of Usu volcano

4. Conclusions

The influenced areas of volcanic eruption were able to estimated, though the resolution of DMSP/OLS is coarse. It means that DMSP/OLS is suitable for detection not only of big earthquake area but also of volcanic eruption, as influencing to human activities.
ANDES project is trying to detect any disaster's damage using SIDaB. DMSP/OLS is useful for early detection of disaster, however digital value of visible-near infrared are saturated in heavy lightning area such as Tokyo or Osaka, even Sapporo city. It is hard to detect disaster damage in such area. Therefore, to detect disaster damage more effectively, we recommend using DMSP/OLS and other satellites.

Acknowledgement

This study is financially supported by Research and Development for Applying Advanced Computational Science and Technology of Japan Science and Technology Corporation.

References

Elvidge, C.D., K.E.Baugh, E.A.Kihn, H.W.Kroehl, and E.R.Davis, 1997. Mapping City Lights with Nighttime Data from the DMSP Operational Linescan System. Photogrammetric Engineering and Remote Sensing, 63, pp.727-734.

Hayashi, H., S.Hashitera, M.Kohiyama, M.Matsuoka, N.Maki, H.Fujita, C.D.Elvidge, 2000. International Collaboration for the Early Damaged Area Estimation System Using DMSP/OLS Nighttime Images. Proceedings of IEEE 2000 International Geoscience and Remote Sensing Symposium.(CD-ROM)

Kodama, M. and X.Song, 2000. Constructing for satellite image database system in AFF. Proceedings of the 28th Conference of the Remote Sensing Society of Japan. pp.259-260. (in Japanese).

Saito, G., M.dama, and X.Song, 1999. The remote sensing search system, Proceeding of 2nd CEReS Symposium on Environmental Remote Sensing. pp.143-148. (in Japanese)

Song, X., and M.Kodama, 2000. Application of satellite image database system in AFF. Proceedings of the 28th Conference of the Remote Sensing Society of Japan. pp.257-258. (in Japanese).

Takashima,M., H.Hayashi, H.Kimura, and M.Kohiyama, 2000. Earthquake Damaged Area Estimation Using DMSP/OLS Night-time Imagery - Application for Hanshin-Awaji Earthquake. Proceedings of IEEE 2000 International Geoscience and Remote Sensing Symposium. (CD-ROM)

HIGH RESOLUTION REMOTE SENSING DATA & GIS TECHNIQUES IN UPDATION OF INFRASTRUCTURE DETAILS FOR FLOOD DAMAGE ASSESSMENT - A CASE STUDY

YK Srivastava, Binod Doley*, DK Pal, RK Das, S Sudhakar, S Adiga *** KV Venkatachary***, SK Srivastava*****

Regional Remote Sensing Service Centre, ISRO, Department of Space, IIT – Campus, Kharagpur – 721 302, West Bengal, India, Phone: (O) 91-3222-55644, (R) 91-3222-78225, Fax: 91-3222-77210, E-mail: srivastava_yk@yahoo.com

*** SRF in Indian Agricultural Research Institute, New Delhi, India.**
**** Presently working under government of Botswana.**
*****Department of Space, ISRO Headquarters, Bangalore, India.**

KEY WORD: Infrastructure, GIS, Remote Sensing, Flood Damage, Brahmaputra River, Disaster, IRS –1C /1D, LISS –III, PAN

ABSTRACT

There are several natural disasters occurring throughout the world round the year and causing huge loss to the lives, property and natural resources. Assessment of damage caused by these disasters needs to be carried out accurately in minimum possible time frame. Space technology is one of the best-suited means for the assessment of damage brought about by natural disasters. Remote sensing satellites provide synoptic view, repetitive coverage and high-resolution images. This advanced high-resolution sensor technology has provided immense scope to the earth resource scientists world-wide for mapping and analysis of earth surface feature details using Remote Sensing and Geographic Information System (RS & GIS). India is among several countries in the world, which face severe problem of floods every year particularly in the river basin of Ganga-Brahmaputra.

Considering the seriousness of the flood problem, Department of Space / Govt. of India has taken very important step to develop and implement an effective Disaster Management System (DMS). One of major activities under DMS is to provide flood damage assessment and to assist in flood mitigation/ protection work. North – Eastern part of India and especially the Assam State is most prone to flood due to its delicate geographic location in the Bramhaputra valley. The mighty river Brahmaputra travels approximately 720 km in Assam from east to west with its perennial flood menace during monsoon that affects almost 20 districts out of a total 24 districts in the state of Assam. Marigaon district of Assam, which is taken as the case study is one of the worst affected districts. Almost 60 % of the district get inundated during flood season causing untold human sufferings and heavy loss to animal lives, property and natural resources worth several million rupees. Indian Remote Sensing Satellite (IRS) – 1C / 1D high resolution PAN, LISS- III, WiFS data and topographic maps on 1: 50,000 scale are used in carrying out this study. Initially digital map database is prepared for geometric rectification of PAN, LISS-III and WiFS data. Further this map database is utilised in digitizing infrastructure details. Merged products of PAN+LISS- III are generated and used for extraction of infrastructure details in GIS environment, i.e., settlements, metal and unmetal roads/ cart tracks, rails, embankments/ dykes and causeway. Apart from infrastructure details, natural features were also digitized, i.e., drainage, ox-bow lakes, streams, river, river islands, tanks and reserve forests boundaries. WiFS data is used for extraction of flood layer and the resultant flood layer is used along with all infrastructure layers to intersect the inundated area and assess the damage.

Classified landuse/ landcover (level III) map generated from LISS – III data is used to assess the damage to agricultural crops.

1. INTRODUCTION

Almost all the countries in the world are prone to one or more forms of disasters viz. earthquakes, cyclones, volcanic eruptions, drought, landslides, flood etc. India is among several countries in the world that faces multiple facets of such disaster almost every year. The region, facing floods during monsoon is often subjected to severe drought during lean season. Northern and North-East part of India which fall under Bramhaputra – Ganga river basin is prone to floods. Floods in these areas directly or indirectly affect the economy of the country either in the form of natural resources, lives, property or infrastructures such as houses, roads, railways, pipelines, electricity and telecom network.

Bramhaputra River is among the largest rivers in the world. This river originates from the glacier of east Manasarovar and travels nearly 1100 km across the Tibet before entering in India through the eastern part of Arunachal Pradesh. After another 226 km of mountainous journey in Arunachal Pradesh, this mighty river enters in Assam State near Pasighat and travel 720 km in the state from east to west direction and finally leaves Assam at Dhubri district to enter Bangladesh. Bramhaputra River is almost 2880 km long from its origin to out falls in Bay of Bengal. Floods in Brahmaputra River have been aggravated due to frequent change in river course, bed topography and heavy sedimentation load. As reported by the state Govt. that during August – September 1998 people of Assam State have experienced one of the most devastating flood conditions after 1950. This flood had affected a total of 50,000 population, 16,000 houses in 5,126 villages of 21 districts and claimed nearly 156 lives and inundated 2.21 lakh hectares of crop area for about two weeks (*DMS Report phase-1 January1999*).

In recent years, this has been observed and proved that the space technology is the only means for the mapping, analysing of flood affected area and for providing earliest information to various agencies for carrying out relief rehabilitation measures and for restoration of normalcy. Because, today remote sensing satellites are equipped with high-resolution sensors that can provide finer details of ground with synoptic view and repetitive coverage (*Venkatachary KV et al 1999).*

Disaster Management System (DMS) conceived by the Department of Space / Govt. of India has been playing a very important and effective role towards flood damage assessment and providing assistance in flood mitigation/ protection work. Infrastructure details on 1: 50,000 scale topographic maps particularly in these areas where floods and migration of river channel are very common, are invariably out dated and over a period of 30 –35 years no updation has been done. If updated, these details can play very important role in assessment of damage. It is very difficult to assess the damage in total without having current information of infrastructure details. Therefore it was decided under DMS project to obtain current information of the infrastructure details using both existing maps on 1:50,000 scale as preliminary base and high resolution panchromatic remote sensing data of IRS – 1C /1D for updation of such details. IRS – 1C /1D, LISS – III data are used for generation of landuse / landcover map for assessment of crop damage. The present study has been carried out with following objectives.

(i) To assess the utility and capability of IRS 1C / 1D high resolution data for mapping of infrastructure details such as metal and unmetal roads/ cart tracks, settlements, railways and causeways.

(ii) To monitor changes in natural feature using existing topographic maps and IRS 1C / 1D high-resolution data.

(iii) To undertake damage assessment of 1998 flood.

2. STUDY AREA

Marigoan district of Assam State is taken up for this study as this district is severely affected by the floods almost every year. It is covered in 7 topographic maps on 1:50,000 scale and has an area of 1522 Sq. km. The general climate of the district is hot and moist except in the months of December and January. The average temperature of the district is 35^0 C with an average humidity of 70% - 80% but in peak summer temperature rises to $37^0 - 40^0$ C during May-June. The average annual rainfall is about 200 cm.

3. DATA USED

1. IRS –1C, LISS –III data path / row no. 111/53 of 19 February &18 December, 1998
2. IRS –1C PAN data path / row no. 111 /53 B & D of 28 March, 1998
3. IRS –1C WiFS data of 8 September, 1998
4. Topographic maps on 1:50,000 scale
5. Village boundary map

4. DETAILS OF INVESTIGATIONS

In the present study digital image processing has been carried out using ERDAS IMAGINE and EASI/ PACE image processing software. The former is used for creation of digital map database, rectification of PAN, LISS –III, WiFS data, while the later is used for classification of LISS – III data and fusion of LISS –III+ PAN data. Digitization of infrastructure layers, natural features and integration of thematic layer with satellite data is carried out using ARC/ INFO software.

4.1 PREPARATION OF DIGITAL MAP DATA BASE

A digital map database is created on 1:50,000 scale topomaps covering Marigoan district using 200 Dots Per Inch (DPI) with corresponding resolution on maps 0.127 mm which is equivalent to 6.35 m on the ground. Though at least 400 DPI is recommended but keeping in mined the computer memory space requirement with respect to 400 DPI and the utility of digital map database, 200 DPI has been accepted as a trade-off. Moreover, 200 DPI corresponds to a spatial resolution of 6.35 in the ground (*Das RK et al 1999*). This database fulfill the requirement of compatibility with IRS –1C PAN data of 5.8 m. All digital maps are geo corrected and mosaiced and one uniform base is prepared for district extraction and digitization of infrastructure and other details for updation and change detection.

4.2 GEOMETRIC RECTIFICATION OF IRS –1C PAN AND LISS- III DATA

Pixels of raw / unrectified satellite image does not have appropriate geometry and uniform scale hence it cannot be used for mapping purpose. After rectification process is performed, each pixel in the image can be referenced not only by its row and column position but also in degree, feet or meter in a standard map projection system. There are several ways and techniques to convert raw image into map but where micro or sub micro level mapping has to be carried out using high-resolution images, it is advantageous to rectify satellite image using Ground Control Points (GCPs) from large-scale topomaps as base for rectification.

Digital map database has been used for the geometric rectification of IRS –1C PAN data. A second degree polynomial model is utilized to establish the transformation between the image and map leading to Root Mean Square Error (RMSE) of about 35 m (which is 15 –25 m with respect to GCP). Each GCP is taken on cultural features, because cultural features are unlikely to change in course of time. Two IRS –1C PAN scenes are used in this district which are geometrically rectified and then mosaiced for district image extraction and updation. These rectified PAN scenes are utilized as base for rectification of LISS – III data.

4.3 FUSION OF IRS –1C PAN + LISS – III DATA

The advancement in digital image processing has provided additional tools such as data fusion or data merging. IHS to RGB transformation method is used for the fusion of two different sensor data. This method delivers best color output by merging high-spatial resolution single band black & white data with low-resolution multispectral data. Here, in this study IRS –1C PAN (electromagnetic spectrum range 0.50 – 0.75) single band black & white data with 5.8 m spatial resolution and IRS –1C LISS – III multispectral data with 23.5 m resolution are used for fusion. Spatial resolution of both PAN and LISS – III data are rounded off to 6 m and 23 m respectively for calculation of scale factor. LISS – III sensor (electromagnetic spectrum range 0.52 – 1.70 micrometer) have 4 bands, i.e., band 1 – Green, 2 – Red, 3 – Near Infrared and band 4 – Short wave Infrared. As short wave infrared band with very coarse spatial resolution is not useful for mapping of infrastructure details hence band 1,2,3 are taken for fusing with PAN data. The fused/ merged output is in 6 m resolution with three RGB viewing image channels (Figure-1).

4.4 DIGITIZATION OF INFRASTRUCTURE/ NATURAL FEATURE DETAILS

Infrastructure details which are required to be updated such as settlements, road network (unmetal & metal), railways, embankments/ dykes, etc., are digitized in ARC / INFO software environment using digital map database. Other than infrastructure natural features such as reserve forest boundaries, drainage, water bodies, river islands, etc., are also digitized to study the changes occurred in last 30 to 35 years. Separate layer is prepared for each feature with assigning proper attributes.

4.5 UPDATION OF INFRASTRUCTURE/ NATURAL FEATURE DETAILS

All the layers digitized using digital map database are overlaid on fused image with 6 m resolution (FCC) and changes are incorporated in respective layers (Figure- 5). During the process of updation, it has been experienced that some features that are linear in nature can be updated using single band PAN data. But complexity arises when features are non-linear and there is possibility of mixing with other features. PAN data has various tones of black & white and some times it is very difficult to fix the boundaries between one object and the other. Whereas fused data offers more shades of color and enable the interpreter to separate out subtle differences in objects because of change in color tone. It may be noted that human eye can distinguish easily more shades of color than shades of gray tone in black & white. Therefore, it can be safely stated here that fused data is always more useful than black & white PAN data for mapping of such details if multispectral data of high-resolution is not available.

4.6 PREPARATION OF FLOOD LAYER

Generally SAR data is used for preparation of inundation flood layer, since getting cloud free optical RS data during monsoon season is difficult. It is a coincidence that cloud free data of IRS 1C WiFS data was available. RADARSAT data, which is being used under DMS study for flood inundation layer is very costly as compared to IRS 1C WiFS data. Therefore, an attempt has been made to use WiFS data for preparation of flood inundation layer. WiFS data has spatial resolution of 188 m with 810 km swath. WiFS image covers a vast area of 810 km stretch would have needed huge amount of digital map database for rectification. Hence rectified LISS – III data is used for the rectification of WiFS data. Another aspect is of its resolution; WiFS data does not contain finer details of which cultural features are normally used as GCP for rectification. After rectification, two bands WiFS data is segmented to create flood layer and this is used to report damage for the individual districts. A single WiFS scene covers the entire Brahmaputra valley in the state of Assam.

4.7 LANDUSE / LANDCOVER MAP GENERATION

Process of generating landuse/ landcover map is done by classifying each pixel of image through assigning training areas about different features that are sought to be classified. MXL supervised classification technique is used in this study for classification of IRS – 1C LISS – III two season data. Main objective of generation of landuse/ landcover map and use of two season data is to assess the damage caused by floods to standing crops.

4.8 FLOOD DAMAGE ASSESSEMENT

Flood inundation layer extracted from WiFS data is intersected with landuse/ landcover map for agricultural area and infrastructure layers for assessment of damage. The derived result shows that an area of 915 sq. km was inundated during 1998 flood. This includes an agricultural area of 51,068 ha. During two weeks inundation has affected 28,028 ha crop area and other infrastructure such as road network and settlements. (Figure- 4).

5. RESULTS AND DISCUSSION

National highways, metal/ unmetal roads are very well detectable on the fused image except those areas where these features are surrounded by the thick vegetation cover. In some places where unmetal roads are narrow and curved, resembled like cart tracks. Therefore, limited ground verification is essential. Railway tracks are clearly visible, as they are straight. Mapping of embankments/ dykes is not very difficult, as they are located beside the banks of the river or big water reservoir. Often they become part of the road network as metal/ unmetal roads are laid over them. Natural features like forest, river, water tanks, oxbow lakes and drainage network have very sharp boundaries hence they are mapped very well.

Mapping and monitoring with reference to infrastructure details, it is worthwhile to mention that today remote sensing, GIS and digital image processing have emerged as powerful tool. No doubt, the way this technology is advancing it is going to play very effective role for real time mapping and analysis of such natural disasters. In 30 – 35 years so many changes have taken place in this district either in form of change in river course or infrastructure (Figure 2, 3 A & B), but local authorities are still dependent on existing topographic maps which are absolutely out dated. If these maps are updated, several aspects of management by the concerned departments can be streamlined. The experience reveals that no other cost-effective inputs are available at present for carrying out such work. Therefore IRS –1C /1D high-resolution images are best suited in context with mapping and monitoring of damage caused by natural disasters. The utility of Remote Sensing and GIS has been realized and people are switching over to this space

technology instead of using age-old techniques for mapping and management of natural resources. High-resolution Remote Sensing data and GIS help in integrating multi-parameter spatial information for generating locale-specific plans (*Kasturirangan K 1995*). Some important infrastructure details that are derived from the study are presented in Table 1.

Table 1. Derived results of infrastructure details

Sl. No.	Infrastructure Details	Derived Results	Inundated during 1998 flood	Engulfed by the Bramhaputra River*
1	Road metal	269 km	86 km	42 km approx.
2	Road unmetal	1723 km	1055 km	138 km approx.
3	Total villages	662	414	59
4	Settlement area	190 sq. km	87 sq. km	30 sq. km
5	No. of Islands	17		
6	Area of Islands	13 sq. km		
7	Area under RF	80 sq. km		
8	Area of District	1522 sq. km		
9	Area affected	915 sq. km		

**** Remote Sensing satellite data of 1998 shows that Bramhaputra River has changed its course during the period of 30 – 35 years. It has shifted 114.6 sq. km inside of Marigoan district. This has resulted in engulfing of above infrastructure details which are present in the topomaps surveyed in 1965 –67.***

ACKNOWLEDGEMENTS

The first author is very much grateful to Dr V M Chowdhary, Mr. A Mondal, Mr.S K Tumala, Mr. S K Paul, Dr Kalpana Tiwari, Mr. K Rajesh and Mr. D. Chakraborty Scientists of RRSSC – Kharagpur for their support and help. Mr. Uday Kumar, JRF is also acknowledged for his support in various stages of the study.

REFERENCES

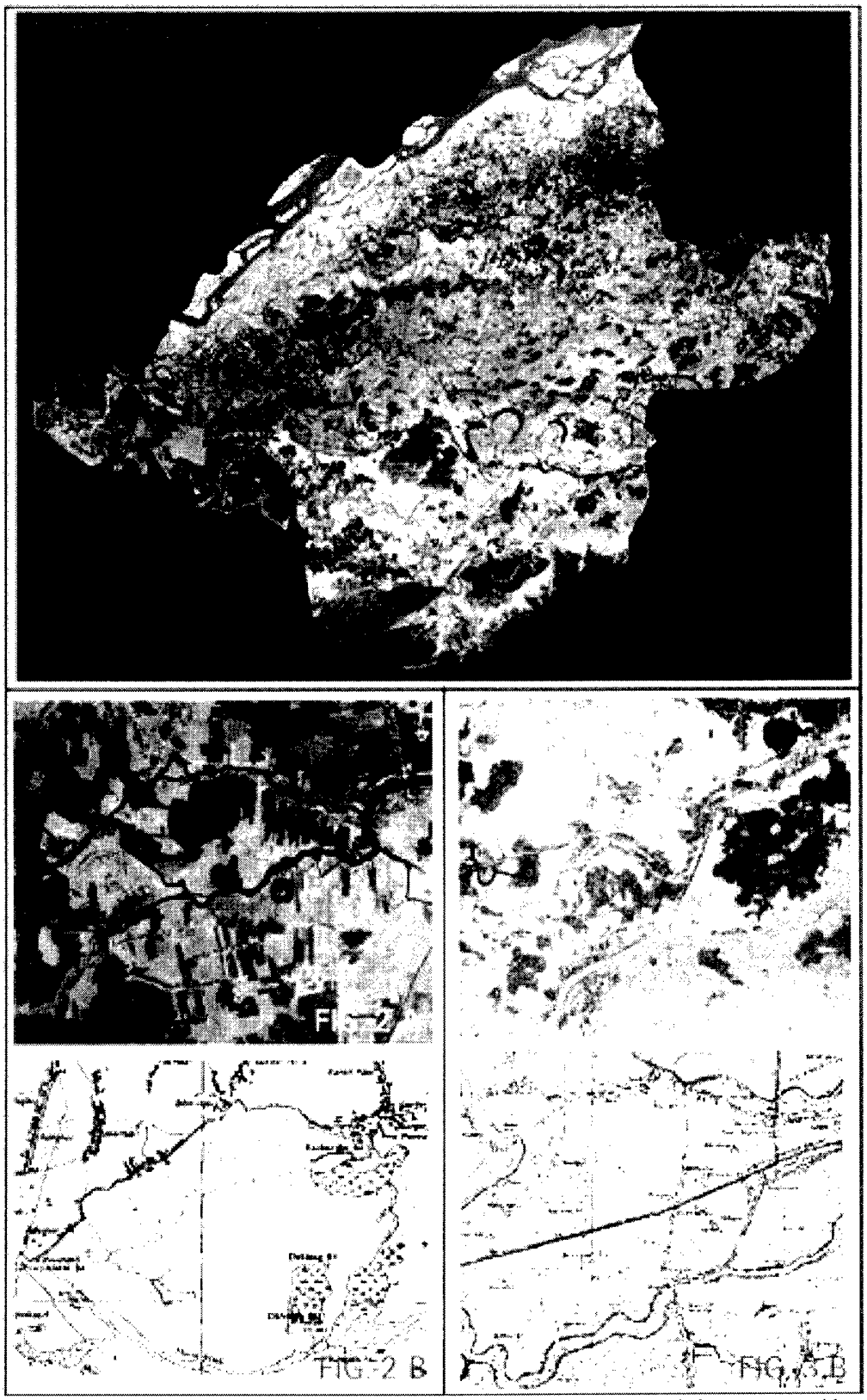
1. Binod Doley and YK Srivastava (January 2000) "Remote Sensing and GIS techniques in updation of infrastructure detail for flood damage assessment of Marigaon district, Assam" M.Tech. Project report, BIT, Ranchi, India.

2. Kasturirangan K (1995) "Remote Sensing in India – Present scenario and future thrusts" Photonirvachak. Vol. 23. No. 1

3. Venkatachary KV, Rangarajan S, Nageswara Rao PP and Srivastava S K (1999) "Remote Sensing Application for Natural Disaster Management: Retrospective and Perspective" ISRS National Symposium and Remote Sensing Application. Bangalore, India.

4. Project Report of Task Force on Damage Assessment due to flood in Brahmaputra Basin in Assam State (phase –1), January 1999,DMS office, ISRO Bangalore. India.

5. Das RK, Mondal A, Paul SK, Pal DK and Srinivasa Kumar T. (1999) "Mapping of some infrastructure details from IRS IC/ ID high resolution images for Lakhimpur District of Brahmaputra valley –an Experiment". INCA conference, Goa, India.



Figures 2A and 3A are current satellite data showing changes in natural and infrastructures with compare to topographic maps (Figures 2B and 3B) surveyed in 1965 – 1967.

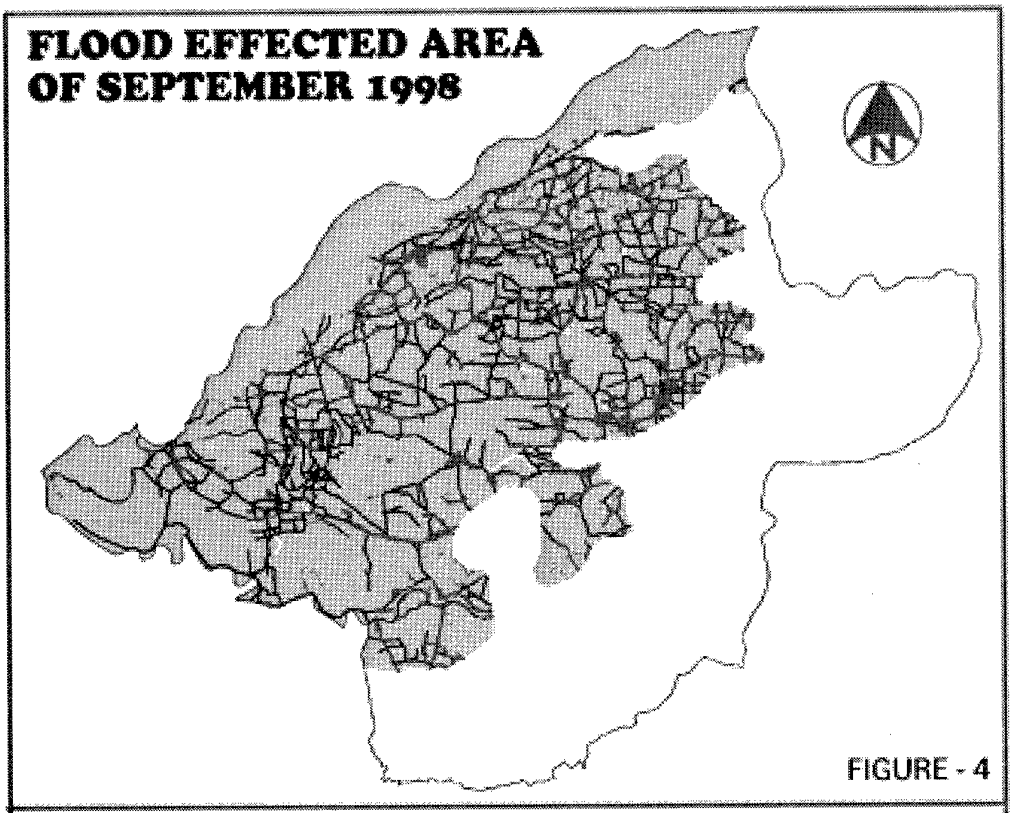


FIGURE - 4

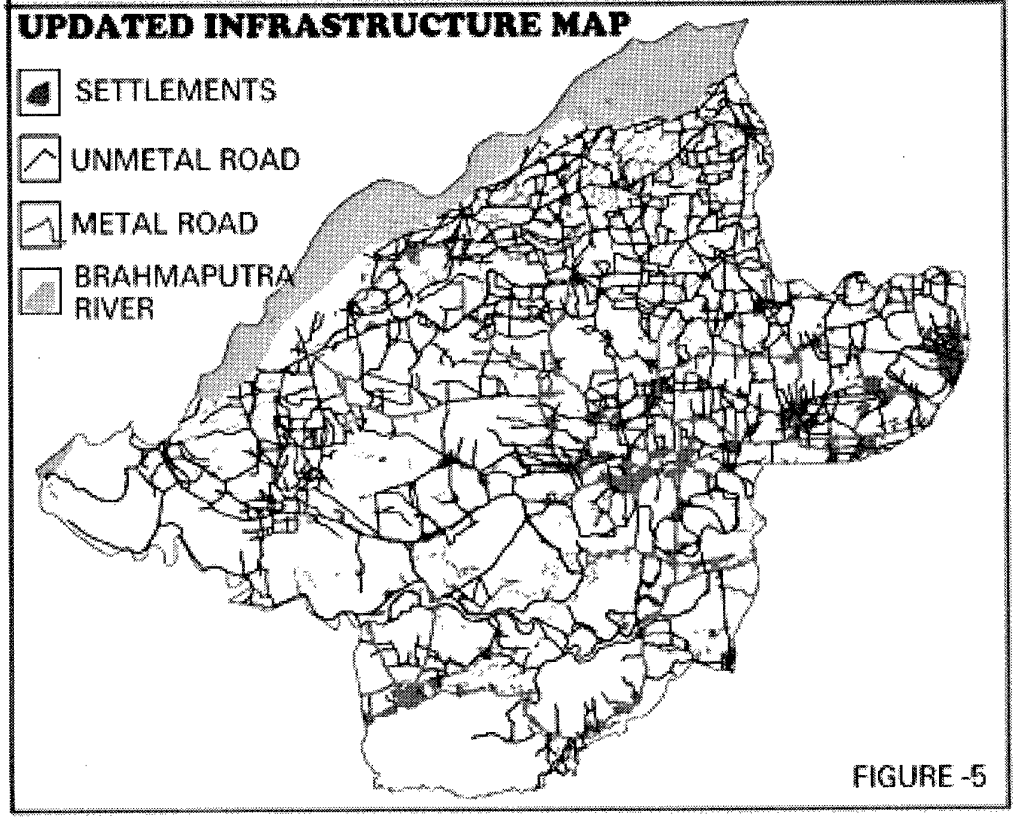


FIGURE -5

Visualization of Water Levels from JERS-1 SAR Images Using Strong Scatters - Phitsanulok, Thailand -

Takako Sakurai-Amano
Invited Scientist, Earth Observation Research Center/NASDA
1-9-9 Roppongi, Minato-ku, Tokyo, 106-0032
TEL: +81-3-3224-7021 FAX: +81-3-3224-7052
E-mail: takako@eorc.nasda.go.jp
JAPAN

KEYWORDS: seasonal water level, narrow water channels, isolated strong scatterers, JERS-1 SAR, Thai rice growing area

ABSTRACT: We recently developed a method for detecting and visualizing narrow rivers in Amazon forests from 3-look JERS-1 SAR images using isolated strong scatterers. In this study, we extend this concept to flood-stricken regions and examine whether we can detect the rise in the water level of narrow water channels prior to large-scale flooding. If we can monitor the area regularly by L-band SAR, our method can be used as to warn against flooding danger on a regional scale. We apply the method to a series of thirteen 4-look JERS-1 SAR images of a Thai rice-growing area observed between February 19, 1995 and August 18, 1998. The results are: Rain zones can be detected as diffuse bright areas; Many water channels that are not visible in dry seasons become visible in rainy seasons. This means that the rise in water level can be observed before the land is actually flooded.

1. INTRODUCTION

SAR can be used to observe flooded areas even in bad weather. However, current methods in SAR image interpretation rely on the detection of substantial changes in the size of very dark open water areas or bright under-the-canopy water areas, meaning that flooding can be detected only after the fact.

We have recently developed a method for detecting and visualizing narrow rivers in Amazon forests from 3-look JERS-1 SAR images. This method takes advantage of the spatial pattern of very strong scatterers lined up intermittently (a few hundred meters apart) along the radar-facing shoreline (Sakurai-Amano *et al*, 2000a). We applied the method to detect the seasonal water levels of tropical forests in the Amazon and Zaire using 4 look JERS-1 SAR images (Sakurai-Amano *et al.* 2000b and 2000c)

In this study, we extend the original idea to a flood stricken area where there are many man-made objects, though in certain cases the method suffers from the interference from them. We investigate whether we could detect the rise in the water level of narrow water channels prior to large-scale flooding. We then apply the method to a series of thirteen 4-look JERS-1 SAR images of a Thai rice-growing area.

2. METHOD

Our method consists of the following three steps:

(1) **Speckle reduction**. Combining the SFP filter and the enhanced SFP filter, we can preserve very dark features and bright small features, while reducing speckle noise in general (Sakurai-Amano and Iisaka,1999). The user specified constant of the Enhanced SFP filter for level 2.1 JERS-1 images was set to 6000, a slightly lower value than the peak values of the histograms. The constant k for integrating two SFP filtered images was set to 5800.
(2) **The Moving sum** of absolute differences is taken between each pixel and its surrounding pixels. Thus we can emphasize isolated strong scatterers.
(3) **Low pass filtering to visualize waterways**. We could say that the resulting images show densely populated areas of isolated strong scatterers (hereafter we call the images "isolated scatterers' maps"). These areas are the narrow open rivers in tropical forests. In this paper's case, they may be rivers and flooded areas.

The details of our method was described in a previous paper (Sakurai-Amano *et al.*, 2000a).

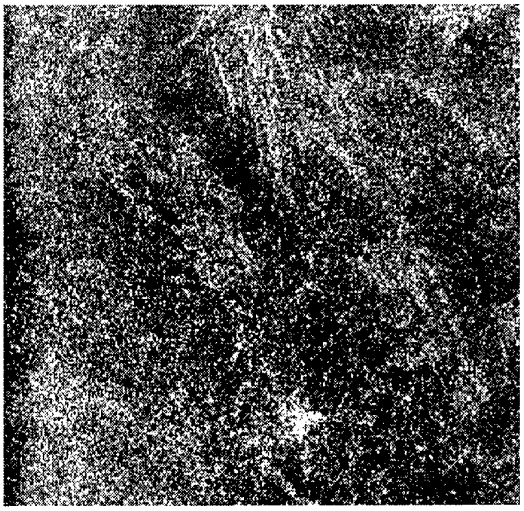
3. DATA

We used thirteen level 2.1 JERS-1 SAR images (©MITI/NASDA) observed between February 19,1995 and August 18,1998 and two corresponding JERS-1 VNIR data (©MITI/NASDA) of Phitsanulok, Thailand (D128-272, Descending Path=128, Row=272). Large rice fields in the northern Thai plain surround Phitsanulok, about 380 km north of Bangkok.

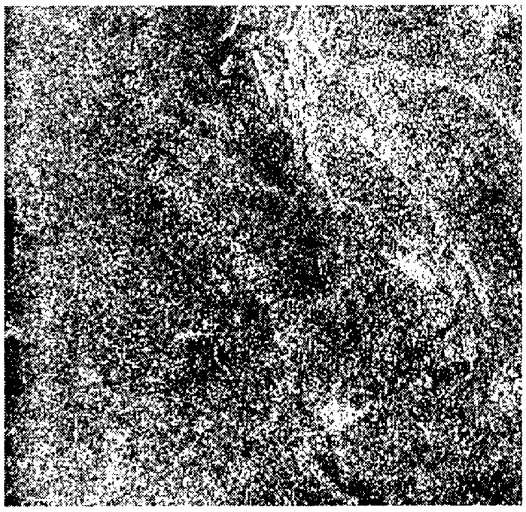
4. RESULTS AND DISCUSSION

Figure 1 shows SAR images of the entire scene of D128-272 near Phitsanulok, observed on January 10,1998 and May 22,1998. We selected those two images as examples of images of dry seasons and rainy seasons respectively. The city of Phitsanulok appears as a very bright area almost at the center of the bottom of the images. There are mountain ranges at the center top and right of the image. We see bright inundated wooded areas along the winding river flowing nearly vertically through the city and a tributary bending to the right near the city to a mountain range. Most of the other areas are rice fields.

Examining all thirteen images, we find that the rainy season's SAR images have more bright scatterers than the dry season's images, as shown in Figure 1. In the rainy season, many right angled objects of bright material along or near rivers are surrounded by flood water, the image resulting from the rising and bounce back of the specularly reflected microwave from the water surface to the satellite antenna. However, floods and the river water rise cannot explain the relatively even increase of the scatterers through the entire scene. Our interpretation is that since this is an area of natural drainage, water stays on the ground after rain for some time, and therefore millions of tiny water pools are created during the rainy season, each only a few m^2 and with a depth of less than a few cm. These tiny water pools in front of the objects with right orientation also specularly reflect microwaves, and so the objects bounce microwaves back to the satellite. The rainy season's SAR images of this area are therefore brighter than dry season's images.



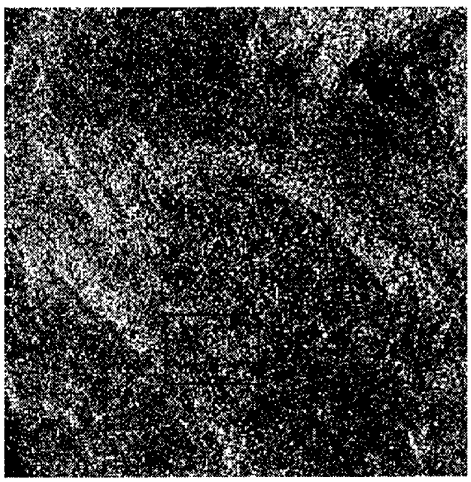
98/01/10



98/05/22

Figure 1. 4-look JERS-1 SAR images of the entire scene D128-272 observed on 98/01/10 and 98/05/22.

Examine the SAR image in more detail. Figure 2(a) shows the original SAR of the upper right (North East) quarter of the entire D128-272 scene observed in January, 1998. Figure 2(b) is the isolated scatterers' map of the corresponding area. While we can easily see a winding river in the lower half of the scatterers' map, it is not very easy to detect the corresponding river in the original SAR image because the various terrain covers have different backscattering intensities. The isolated scatterers' map, shown in figure 2(b), reduces the differences in ground cover. Mountain ridges are still visible on the map but there are substantially reduced bright areas compared to those in the original SAR images.



(a) SAR data

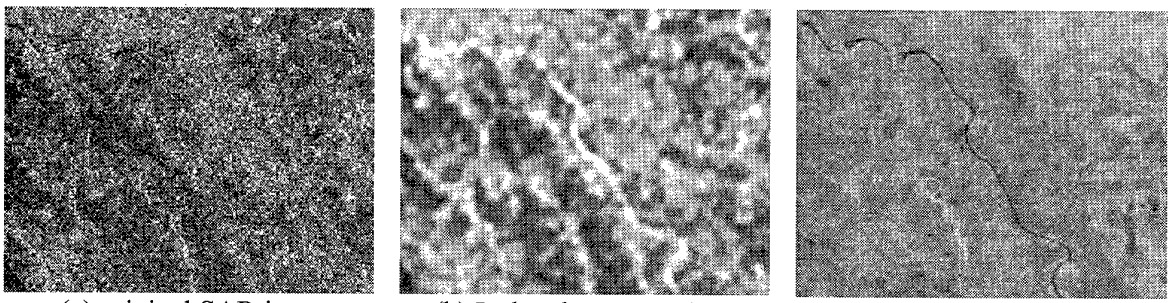


(b) Isolated scatterers' map

Figure 2. SAR image and the corresponding isolated scatterers' map.

Figure 3 shows the full resolution images of the rectangular area marked in figure 2(a). Since the width of the river is about ~50m as estimated from VNIR data, we can detect the river in the

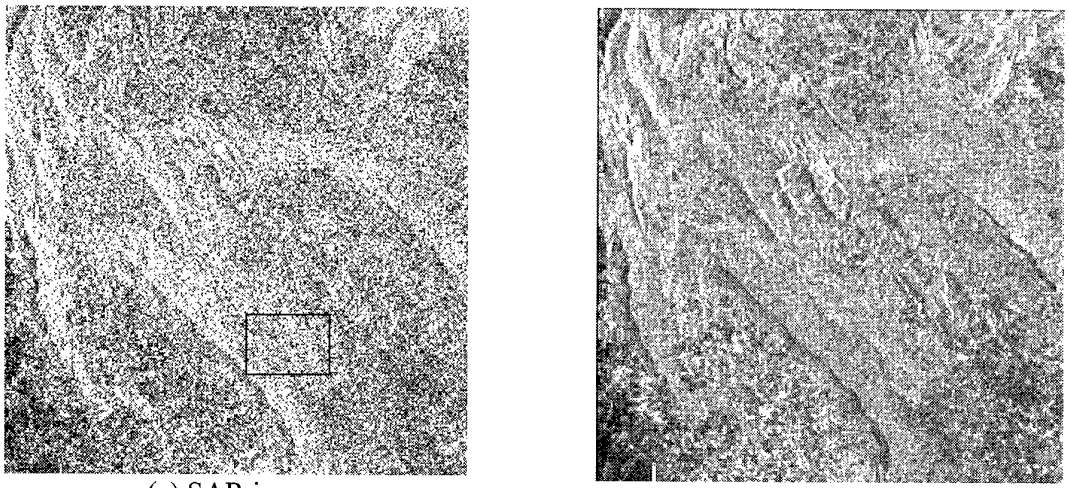
original SAR image visually. However, we can easily detect the river in the map as the brightest winding linear feature that closely corresponds to the river in the near IR image of the VNIR data (see figure 3(c)), although the map also shows extra bright features.



(a) original SAR image (b) Isolated scatterers' map (c) near IR image

Figure 3. Full resolution images of the small rectangle area shown in Figure 2(a)

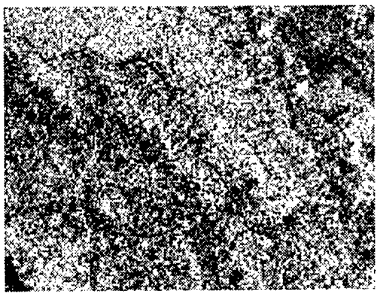
Figure 4 shows the upper-right-quarter of the SAR image observed in May 1998. Both the SAR image and the corresponding scatterers' map are brighter everywhere when compared to those of January, as previously mentioned.



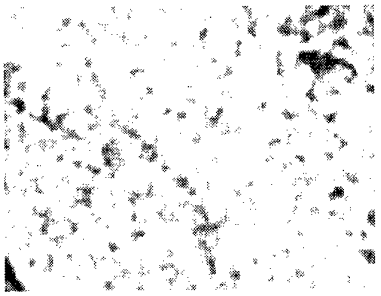
(a) SAR image (b) Isolated scatterers' map

Figure 4. SAR image and scatterers' map obtained from data observed in May,1998

Figure 5 shows the full resolution images of the area shown in Figure 3 (also marked in figure 4(a)). There is no corresponding VNIR data. In this case, the river appears more clearly and slightly wider against the bright background in the SAR image, although we cannot easily see the entire water level picture. On the other hand, we cannot easily distinguish the river from the surrounding area in the scatterers' map because scatterers are everywhere and rivers do not particularly stand out in such situations. However, we can easily grab the entire picture of water level rises from the isolated scatterers' map.



(a) SAR image



(b) Isolated scatterers' map

Figure 5. Full resolution images from the data observed in May,1998.

Figure 6 shows the scatterers' maps from November 27, 1997 to August 18, 1998. Those maps roughly indicate the water levels during this period. Examine the lower left quarter of the images. The number of bright fine features slightly increases from November to January and February. But these features increase significantly in May, indicating that the rainy season has begun. In July, the background becomes brighter and some very dark areas appear, indicating that the water gathers to lower places. In August, most of the bright fine features are gone. We interpret this to mean that water levels in narrow channels are lower than that in July, although it is still raining.

5. CONCLUSION

We can roughly estimate water levels in narrow channels and wet areas of Thai rice-growing areas from JERS-1 SAR images using isolated strong scatterers' maps. Although original SAR images may be better for examining water levels on a pixel-by-pixel basis in certain conditions, the isolated scatterers' map is superior for grabbing the entire water level picture at one time. We expect that the regional scale estimate for water levels could easily be obtained using these isolated scatterers' maps.

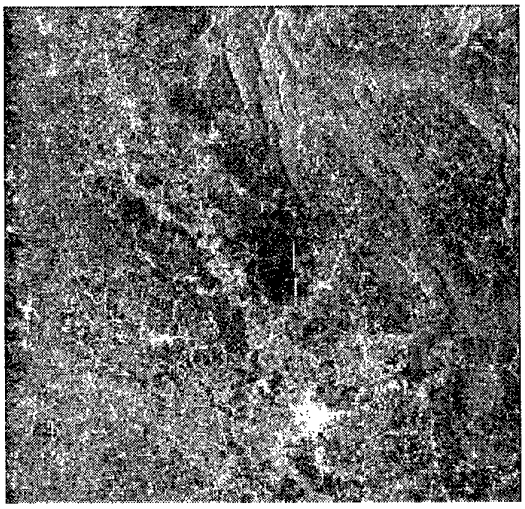
6. REFERENCES

Sakurai-Amano, T., Iisaka, J., and Takagi M., 2000a. Detection of Narrow Open-water Channels from JERS-1 SAR Images of Amazon Forests. In: Proceedings of SPIE's Second International Asia-Pacific Symposium on Remote Sensing of the Atmosphere, Environment, and Space, 9-12 October 2000, Sendai, Japan.

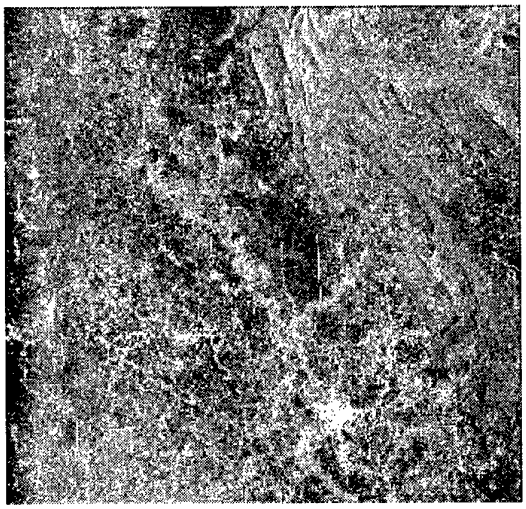
Sakurai-Amano, T., Nakasugi, and Takagi, M., 2000b. Detection of Seasonal Water Levels in Amazon Forests from JERS-1 SAR images. In: Proceedings of Japan Society of Remote sensing, November, 2000, Nara, Japan.

Sakurai-Amano, T., Yoshioka, T., and Takagi, M., 2000c. Dry and wet season water levels in Zaire detected from JERS-1 SAR images. In: Proceedings of Japan Society of Remote sensing, November, 2000, Nara, Japan.

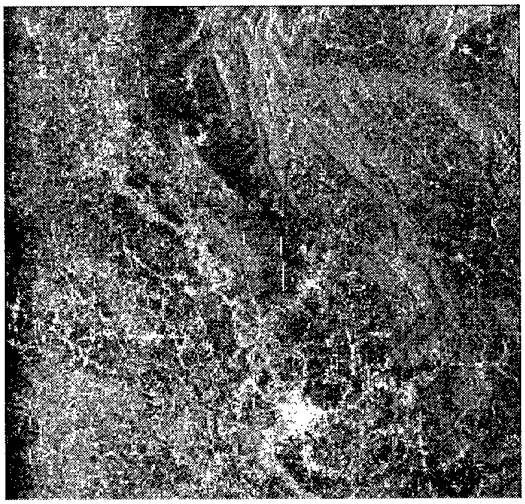
Sakurai-Amano, T., and Iisaka, J., 1999. Speckle Reduction of SAR images for small Feature Extraction. J. Japan Soc. of Photogrammetry and Remote Sensing, Vol.38, N0.3, pp.32-43.



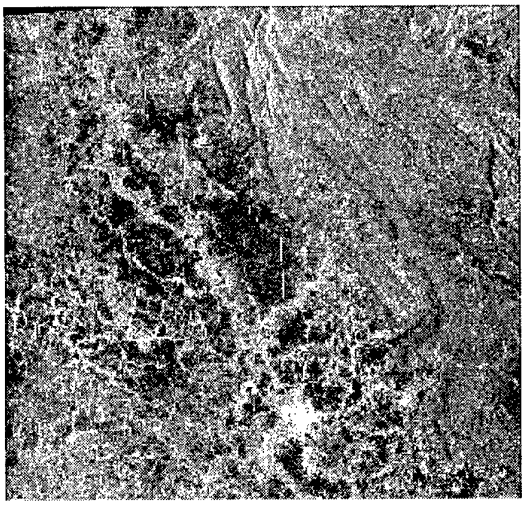
1997/11/27



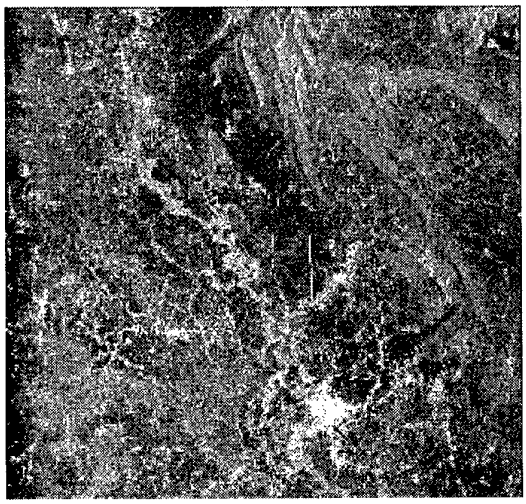
1998/05/22



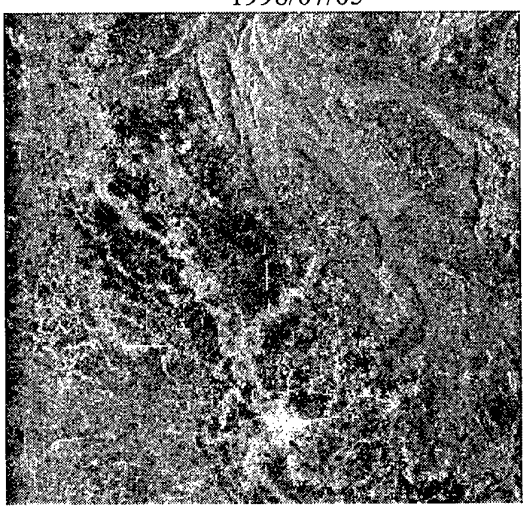
1998/01/10



1998/07/05



1998/02/23



1998/08/18

Figure 6. Seasonal change of water levels indicated in the series of scatterers maps.

DROUGHT AND VEGETATAION MONITORING IN THE ARID AND SEMI-ARID REGIONS OF THE MONGOLIA USING REMOTE SENSING AND GROUND DATA

Yu. Bayarjargal [1], Ts. Adyasuren[2] and Sh. Munkhtuya[3]
[1]Remote Sensing Lab., J.Blaustein Institute for Desert Research, Ben Gurion University, Sede Boqer-84990, ISRAEL
Tel: +972-7-6596856, Fax: +972-7-6596805; E-mail: yub@bgumail.bgu.ac.il
[2]National Committee of the Combat Desertification, Ministry for Nature and the Environment,
[3]National Remote Sensing Center, Ministry for Nature and the Environment, MONGOLIA

KEY WORDS: Drought, land surface temperature, vegetation index

ABSTRACT: The Gobi Desert and the Desert Steppe regions of the Central Asia within an area of approximately 60% of the country's territory of Mongolia are naturally the main part of the grazing livestock husbandry. The natural disasters such as drought and heavy snowfall states are often observed there. Over this regions drought occurs on an average of once every two or three years. Short-term operational detecting and monitoring of the natural hazards as well as droughts over large territory will contribute to meeting requirements of the economical development of the country. Coarse spatial resolution, high temporal frequency satellite data from the NOAA/AVHRR based technology and methods are widely used to monitor vegetation cover and drought episode throughout the world. This paper presents some results of detection of drought-affected regions by calculating the Normalized Difference Vegetation Index (NDVI) and the Land Surface Temperature (LST) values of the drought and wet years. The NDVI-LST space based drought indicator was tested and by use of this indicator can be detect and operationally monitor of drought distribution over the territory of the country.

1. INTRODUCTION

Mongolia has expansive areas (almost 90%) of natural grasslands and current dominant industry in the agricultural sector of the country is the nomadic livestock husbandry which is highly dependent upon the conditions and changes in nature and the environment during the four seasons of a year. Almost 99% of the Gobi Desert and Desert Steppe - arid and semi-arid zone are used as natural pasture. In the above-mentioned vast Gobi Desert and Desert Steppe area are often occur the natural disasters such as drought and heavy snowfall states. Over this regions drought occurs on an average of once every two or three years and the heavy snowfalls occurs every 5 to 6 years and once every 2 to 3 years covering half and quarter of country's territory, respectively (Shiirevdamba, 1998). The summer frequent droughts and severe winter's forces are intensifying desertification in arid, semi-arid and sub-humid areas of Mongolia. Coarse spatial resolution, high temporal frequency satellite data from the Advanced Very High Resolution Radiometer (AVHRR) operated by the National Oceanic Atmospheric Administration (NOAA) based technology and methods are widely used to monitor vegetation cover and drought events throughout the world (Goward *et al.,* 1985; Walsh, 1987; Reed, 1993; Kogan, 1997; Karnieli 1999). In Mongolia, several studies involving the use of the NOAA/AVHRR data have been published. Most of them had concerned with determining vegetation cover study (Oyun *et al.,* 1994; Adyasuren and Bayarjargal, 1995; Bayarjargal, 1995). Recently, Adyasuren and Bayarjargal (1995) mapped drought conditions of the Central Asian zone based on the multi-temporal Global Vegetation Index data from 1982-1987 and noticed that when a drought events occur in the Mongolian Gobi Desert zone, the Normalized Difference Vegetation Index (NDVI) values became to a low values, 0.0-0.05 units, same as

value of the extra-arid land - Taklimakan Desert. As mentioned, previous works have introduced that the AVHRR derived NDVI images are useful for analysing spatial vegetation pattern and for assessing vegetation dynamics. However, from a synoptic point of view is required to improve the vegetation cover and dynamic estimation technology as well as to assess the impact of natural drought and its overall extent in space and time, especially in the Gobi Desert and the Steppe area of the Mongolia.

2. CLIMATE DESCRIPTION OF STUDY AREA

Mongolia is a land-locked country which covers an area of 1.5 million square kilometers on the southernmost fringe of the Great Siberian boreal forest and the northernmost Central Asian deserts and vast steppes. The main characteristics of the climate of Mongolia are sunny days, long and cold winters. The average mean air temperature in the warmest month is 15-20°C in the north, and 20-25°C in the south of Mongolia. In the Gobi Desert and Steppe zones, the summer continues over 3 months. The maximum summer air temperature can reach anywhere 35-39°C in the north and 38-41°C in the south. The total annual precipitation in mountainous regions averages to about 400 mm, in the steppe 150-250 mm and in the desert-steppe less than 100 mm. About 85 to 90 per cent of the precipitation falls during the three summer months (Shiirevdamba, 1998). The number of rainy days decreases from north to south. The temporal and spatial distribution of precipitation in Mongolia is variable. There is very little precipitation at the beginning of the growing season but much more in the second half of the season when cool air starts to spread around the country. This variation has considerable effects on the growth of several spring plants. Summer, autumn and winter precipitation is a source of soil moisture but it is insufficient for vegetation to thrive in this country.

3. METHODOLOGY

In order to carry out the study, we classified the territory of Mongolia into four dryness zones such as the humid, the sub-humid, the semi-arid and the arid zone, by NDVI data, vegetation types and as well as according with desertification and geobotanic maps (Kharin *et. al.,* 2000; Shiirevdanba, 1998). The fourteen plots shown in figure 1 have been chosen which are corresponds to the arid and semi-arid zones. Monthly total rainfall data and monthly composite of the NDVI and LST data for the period April to September of 1992-1995 were used. Prolonged drought, which has been affecting arid and the semi-arid areas, as well as high land surface temperatures which are reached in summer with June and July. The original images from the NOAA/NASA Pathfinder AVHRR Land Data Set, which have been monthly composite and 8 km spatial data, were derived. Prior to analysis, the images were geometrically corrected to a master image using a ground control points and applying a first order transformation into Geographic Projection. The NDVI data calculated from AVHRR channel-1 and channel-2 reflectances and the NDVI is has been shown to be highly correlated with vegetation parameters such as green-leaf biomass and green-leaf area and, hence, is of considerable value for vegetation discrimination (Justice et al. 1985). The NDVI defined mathematically as NDVI=[NIR-R]/[NIR+R], where R and NIR are the radiance or reflectances in the red and the near-infrared spectral channels, respectively (Rouse et al. 1974). The LST computed from AVHRR channel-4 and channel-5 brightness temperatures through the split window methods for land surfaces (Price, 1984; Kerr et al., 1992; Qin and Karnieli, 1999). The LST is correlative to evapotranspiration since it is highly controlled by the radiation received at the surface and the latent heat flux from the surface to atmosphere. This heat loss is responsible to the LST. The NDVI and the LST maximum value composites (MVC; Holben, 1986) were

produced from all the images available within the monthly periods for the four study years. The MVC minimizes the effects of atmosphere, scan angle, and cloud contamination (Lambin and Ehrlich, 1996).
In this study we were tested NDVI-LST space based drought indicators which are developed by Karnieli (1999). Also we were developed drought monitoring indicators based on normalization method in the NDVI-LST space of a local area.

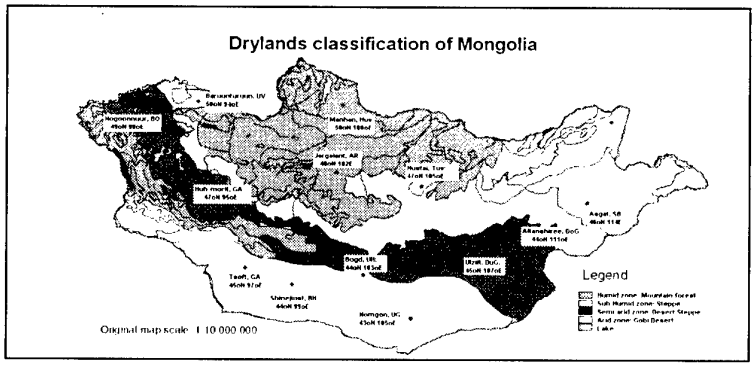


Figure 1. Dryness zone classification of the Mongolia (based Kharin *et. al.*,2000 and Shiirevdanba, 1998). Thirteen plots position are used for drought estimation.

4. ANALYSIS AND RESULTS

The warm seasonally (from April to September) temporal analysis of the arid and the semi-arid areas in the NDVI-LST space were performed on the NDVI and LST data sets for the selected four years. In the summer of 1992 and in the summer and fall of 1995 were severe droughts within the whole territory of the Mongolia. The average summer air temperatures were 19°C and 18°C in the 1992 and 1995, respectively. The average total rainfalls were 52 and 76 mm in the arid area and 100 and 114 mm in the semi-arid area in the summer of 1992 and 1995, respectively. In 1996, the worst year in Mongolian history, altogether 417 forests and steppe fires (over 10.5 million hectare) occurred due to dryness - as effects of sever drought which occurred in the fall of 1995. The other two years were relatively wet years–1993 and 1994 with rainfalls 100 and 75 mm in the arid and 155 and 142 mm in the semi-arid zone, respectively. From the warm months temporal variations of the NDVI and LST on the some plots of the arid and semi-arid zones presented in figure 2 and it might be noticed that the a lower NDVI and a higher LST values occurs on the dry years and a higher NDVI and a lower LST values occur on the wet years, respectively, on the both arid and semi-arid areas.
In order to discover any relations in the warm seasonal NDVI, LST and total rainfall the correlation coefficients were performed in the different dryness zones (Table 1). As can be seen from table 1, the correlations between of those parameters vary in throughout the dryness zones. On this table, two directions of warm seasonal variations of the NDVI, LST and total rainfall values: *(i)* for arid zone, characterized by a both negative relations of the NDVI with LST and rainfall, respectively and *(ii)* for other dryness zones, a relations of NDVI-LST and NDVI-rainfall are positive and increases from semi-arid zone (low latitude) to humid zone (high latitude). But only the correlation of LST and Rainfall were almost equal and positive in whole territory, during the vegetation growing period. An interesting conclusion from table 1 and figure 2 is that, in the whole territory, most of the temporal variability during the warm period in ecological characteristics depends a local condition (i.e., land cover type, landform, local climate, latitude).

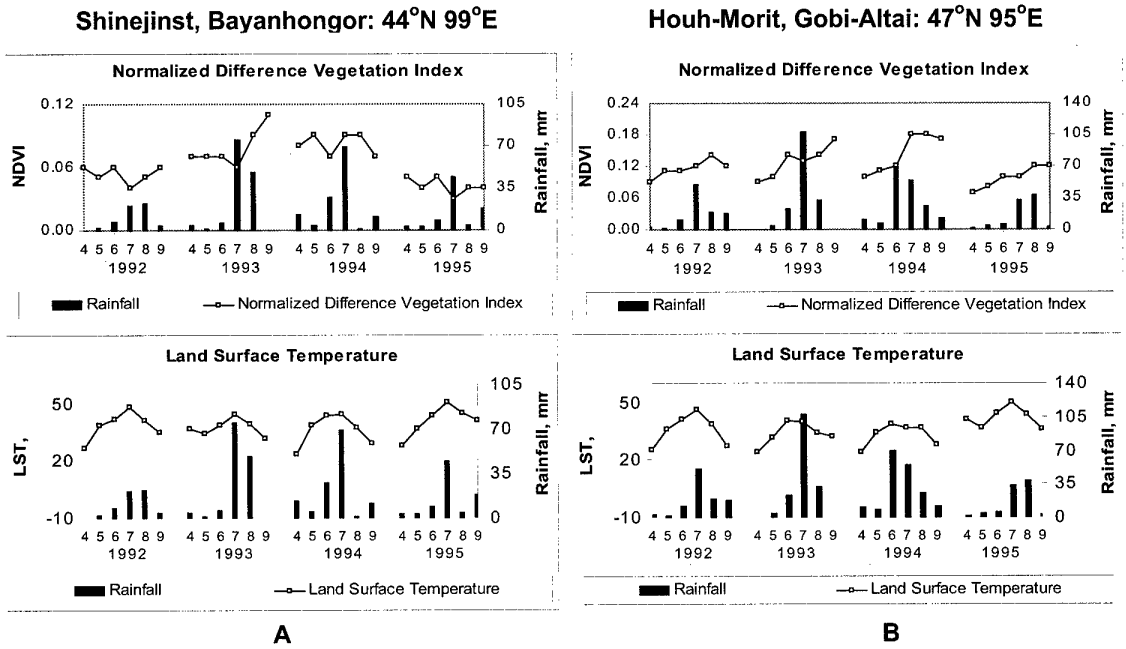


Figure 2. Warm months temporal variations of the NDVI and LST on the sample plots correspond to arid (A) and the semi-arid (B) zones.

Table 1. Correlation coefficients between the NDVI, LST and the total Rainfall on the different dryness zones in the warm (April to September) seasons.

Conditions		Dryness zone			
		Arid	Semi-Arid	Sub-Humid	Humid
Wet years (1993, 1994)	NDVI and LST	-0.10	0.35	0.36	0.50
	NDVI and Rainfall	-0.20	0.36	0.54	0.76
	LST and Rainfall	0.75	0.61	0.51	0.59
Drought years (1992, 1995)	NDVI and LST	-0.35	0.14	0.44	0.56
	NDVI and Rainfall	-0.27	0.17	0.57	0.73
	LST and Rainfall	0.69	0.69	0.66	0.74

Most suitable method for estimate local a condition in any case is establishing a "normal" value. We may considered that the NDVI and LST of 1993 are used as a "normal" years and calculated as:

$$NDVI_{differenced} = [NDVI_{1993} - NDVI_i]/NDVI_{1993}$$
$$LST_{differenced} = [LST_{1993} - LST_i]/LST_{1993}$$

where $NDVI_{differenced}$ and $LST_{differenced}$ are subtracted values from a year of normal precipitation - 1993. $NDVI_i$ and LST_i are values of any particular year. In order to characterize the drought years, warm seasonal time trajectories of the "differenced" two products were applied for other drought occurred and wet years and some selected points from arid and semi-arid area illustrated in the Figure 3. Due to moisture stress on the vegetation, NDVI/LST values recorded in the dry years should be lower/higher than those values recorded in a "normal" year; therefore drought occurred areas will have high/low $NDVI_{differenced}$ / $LST_{differenced}$ values. Bottom part of Figure 3 shows that the mean values and the line connected between the maximum $LST_{differenced}$ with minimum $NDVI_{differenced}$ and minimum $LST_{differenced}$ with maximum $NDVI_{differenced}$ values. It might be seen that the drought occurred years, 1992 and 1995; lines and mean values are very similar terms of position and angle in the both arid and semi-arid zones. The mean value and the line - connected maximum and minimum values of the calculated $NDVI_{differenced}$ and $LST_{differenced}$ were used as indicators for detecting and monitor drought events. The lines of the drought years' are steeper and shorter, whereas the wet (1994) years lines are gentler and longer.

The mean values of the $NDVI_{differenced}$ and $LST_{differenced}$ of drought years' are always located in the lower-right part of the NDVI-LST space-system, i.e., they have a positive $NDVI_{differenced}$ and the negative $LST_{differenced}$ value in the drought year. In the opposite, wet year's mean values are positioned in the upper-left part in throughout the arid and the semi-arid zones.

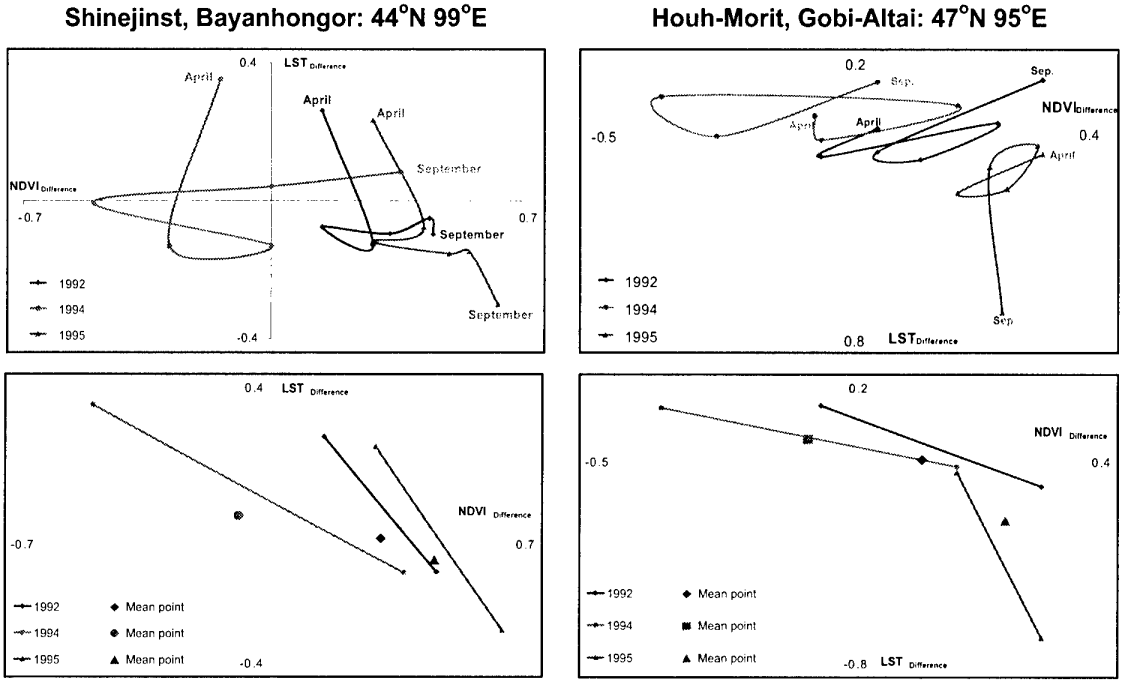


Figure 3. Warm seasonal time trajectories (upper part) of the $NDVI_{dirrerenced}$ vs. $LST_{dirrerenced}$ (subtracted from1993) for drought years (1992 and 1995) and the wet year (1994) on the sample plots correspond to arid area (A) and semi-arid (B) zones. The lines (bottom part) connected between the maximum $LST_{differenced}$ with minimum $NDVI_{differenced}$ and minimum $LST_{differenced}$ with maximum $NDVI_{differenced}$ values correspond to upper parts.

5. SUMMARY AND CONCLUTIONS

Several previous investigations have shown that the multi-temporal NOAA-AVHRR based NDVI and LST are suitable study for land cover classification in Africa, climate variability in southern Sahel, deforestation of Central African evergreen forest, and for quantify droughts in sparse vegetated area of the Negev Desert. All of those area located in relatively low latitude when there were drastic negative relations between those two parameters. We get such kind of relations in the middle latitude area, such as in the Gobi Desert arid area. But in the semi-arid area in the middle latitude we could discover positive relations between those two parameters. Based on differenced method we found a drought indicator – well suitable in the arid and semi-arid area of Mongolia. Due to moisture stress on the vegetation, NDVI (LST) value recorded in the dry years should be lower (higher) than those values recorded in a "normal" year; therefore in drought occurred areas, drought indicator - $NDVI_{differenced}$ ($LST_{differenced}$) values will be high (low) than normal and wet years. It is concluded that the AVHRR based NDVI and LST can provide valuable information for drought detecting and monitoring by operationally.

ACKNOWLEDGEMENTS

The authors would like to thank to Dr. Arnon Karnieli of the Remote Sensing Laboratory of the J. Blaustein Institute for Desert Research (BIDR) for his discussions, comments and assistance for able to present this paper on the ACRS-2000. We would also like to thank Ph.D. Q. Zhihao, Spatial Modelling Center of the Sweden for his suggestion and assistance for calculating the LST on study area.

REFERENCES

Adyasuren, Ts., and Yu. Bayarjargal, 1992. Studies of Vegetation Change on the Territory of Mongolia using AVHRR and Meteorological Ground Data. *Proceedings of the 13th Asian Conference on Remote Sensing*, Ulaanbaatar, Mongolia, D-9.

Adyasuren, Ts., and Yu. Bayarjargal, 1995. Vegetation & Drought Monitoring Using Sattelite & Ground Data. International Seminar on Space Informatics for Sus. Devel.: Grassland Monitoring & Management. Ulaanbaatar, 20 June, Mongolia.

Bayarjargal, Yu., 1995. Estimation of grassland primary production and carrying capacity at the Hustain-Nuruu Nature Reserve. *Project Final Report*, Ulaanbaatar, pp.15.

Goward, S. N., C. J. Tucker, and D. G. Dye, 1985. North American vegetation patterns observed with the NOAA-7 Advanced Very High Resolution Radiometer. *Vegetation,* 64:3-14.

Holben, B.N., 1986. Characteristics of maximum-value composite images from temporal AVHRR data, *Int. J. Remote Sensing,* 7:1417-1434.

Justice, C.O., J.R.G. Townshend, B.N. Holben, and C.J. Tucker, 1985. Analysis of the phenology of global vegetation using meteorological satellite data, *Int. J. Remote Sensing,* 6:1271-1318.

Karnieli, A., 1999. Space monitoring of Soil and Vegetation Dynamics in the Negev Desert (Israel), (in press International Journal of Remote Sensing)

Kerr, Y.H., Lagourde, J.P., and J. Imbernon, 1992. Accurate land surface temperature retrieval from AVHRR data with use of an improved split window algorithm *Remote Sens. Environ.* 41, pp. 197-209.

Kharin, N., R. Tateishi and H. Harahsheh, 2000. A New Desertification Map of Asia. *Desertification Control Bulletin,* 36, pp. 5-17.

Kogan, F. N., 1997. Global Drought Watch from Space. *Bulletin of the American Meteorology Society,* 78, 621-636.

Lambin, E. F., and D. Ehrlich, 1996. The surface temperature-vegetation index space for land cover and land-cover change analysis. *International Journal of Remote Sensing,* 17:463-487.

Oyun, R., Bayarjargal, Yu., and M. Enkhbayar, 1994. Development of methodology for estimation of grassland primary production at the Hustain NN.R.. Fin.report, Ulanbaatar, pp. 80.

Price, J. C., 1984. Land surface temperature measurements from the split windows channels of the NOAA-7 AHVRR. *Journal of Geophysical Research*, 89:7231-7237.

Qin, Zh., and A. Karnieli, 1999. Progress in the remote sensing of land surface temperature and ground emissivity using NOAA-AVHRR data. *Int. J. Remote Sensing,* 20 (12): 2367-2393.

Reed, B.C., 1993. Using remote sensing and GIS for analyzing landscape/drought interaction. *Int. J. Remote Sensing,* 14(18): 3489-3503.

Rouse, J. W., Haas, R. H., Schell, J. A., Deering, D. W., and J. C. Harlan, 1974. Monitoring the Vernal Advancements and Retroradation (Greenwave Effect) of Nature Vegetation. NASA/GSFC Final Report, NASA, Greenbelt, MD, 371 pp.

Shiirevdamba, Ts., 1998. Biological Diversity in Mongolia, *First National Report, Ministry for Nature and the Environment,* 'Admon' printing house, Ulaanbaatar, Mongolia, pp. 106.

Walsh, J. S., 1987. Comparison of NOAA AVHRR Data to Meteorological Drought Indices. *Photogrammetric Engineering and Remote Sensing*, 53(8), 1069-1074.

Integrating Remote Sensing and GIS for Fire Hazard Categorization & Resource Allocation.

A case study of Bathurst, New South Wales, Australia.

Sunil Bhaskar
School of Geography, Faculty of Science and Technology
University of New South Wales, 2052, Kensington
Australia
Tel: +61-02-9385 5537
Fax: +61-02-9313 7878
Email: z2240167@student.unsw.edu.au

ABSTRACT

'Fire hazard categorization' is vital for emergency planning in order to minimize loss of lives and property. Recording hazard levels help in understanding the spatial distribution of fire susceptibility and vulnerable areas and assist in the 'Allocation' and 'Mobilization' of dynamic resources. Insitu field surveys are carried out to determine fire hazard categories in New South Wales. Although reasonably accurate, this method of classifying hazards is time consuming, not very accurate and most importantly does not permit spatial analysis. It also leaves out important important variables that need to be considered for a comprehensive hazard categorization. This paper examines the integration of high-resolution orthorectified aerial photoimages with GIS in order to develop a methodology to generate fire hazard categories. It also examines the choice of an appropriate 'spatial unit' to record and compare hazard categories in a given region for the effective management of dynamic resources.
Author keywords: Fire hazard categorization, dynamic resources, spatial unit, spatial analysis.

INTRODUCTION

Fire hazards cause widescale destruction within no time and are the scourge of modern civilization. Although fire hazards cannot be avoided totally, they can be studied within the spatial context for better preparedness and mitigation. It is vital that hazard levels be generated in order to understand the spatiality of fire hazards and enable distribution of the minimal dynamic resources in a balanced manner.

The present method of generating fire hazard categories is by an insitu field survey method where a physical assessment of structures is carried out and recorded on every Unit Survey Squares (USS) derived from the 1 km square Australian mapping grid (Corporate Strategy Group, 1996). This structure is then related to a detailed descriptive table (Table 1) that scales the hazard from low to very high or special hazard. This method of classifying hazards is beset with a few issues that need to be addressed. Emergency services need current information to make on the spot decisions. Data acquisition by insitu field survey does not capture the current spatial details on landuse or usefunctions of structures and involves too many man-hours and finance.
The current approach is focussed on the identification of hazards based on inventory, alone which has a legislative attraction. The neglect of spatial context and potential population exposure can also pinpoint to the technical and engineering focus of many working in this area, operating within a traditional 'hazard

perspective' concentrating on ensuring the integrity of on-site safety systems and finding engineering solutions to accident prevention (Rayner S, 1992). Spatial context can be an important factor in determining the scale of potential harm but has often been neglected in setting of criteria or thresholds which determine levels of risk management attention (Gordon et al , 2000). Recent perspective on natural hazards also emphasize the wider spatial and social context within which disasters are experienced. The concept of vulnerability has been particularly important, encompassing the physical relationship between hazards and communities at risk, accident preparedness and mitigation and the social geography of potentially affected populations (Blakie et al, 1994).
Other factors, such as preparedness of communities in different locations and the social characteristics of different groups within communities at risk, are also important and need to be incorporated into a more complete analysis of 'human ecology of endangerment' (Hewitt K, 1997).

STUDY AREA AND DATA COLLECTION

The city of Bathurst is chosen for the study since it has a mixed type of landuse and is representative of a considerable part of the New South Wales province. Bathurst is located approximately 210 kms to the west of Sydney and is a growing industrial city. The other study area of Hornsby has a residential-bushland interface. It is believed that the benefits of the study in these two sites will be extrapolated to most of New South Wales.
High-resolution orthorectified color aerial photo images exposed in 1998, september are used mainly for visualization and synoptic capture of data. All the other vector layers were a mix of point, line and polygon features and carried information about the land parcels, important location and demographic features. The datasets were matched to a single coordinate system and spheroid so that they could be overlaid and analyzed. An attempt is also made here to address the issue of GIS data redundancy and data sharing within alike government and non-governmental agencies. Demographic variables like age of people and number of dwelling were extracted from the 1996 census data.

METHODOLOGY AND ANALYSIS

Most of the modeling tasks were performed on multiple GIS packages including ArcInfo version 8.0.2, MapInfo and ArcView and the supervised classification was carried out with an Image Analysis software ENVI. The major task apart from mapping the fire hazards in the city of Bathurst was to develop a methodology that could be replicated easily over the entire state. The local environment plan (LEPs) was overlaid on the image for arriving at the broad land-use classes. Variables of demographic data like age, number and type of dwellings gave a description of the proximity of people and structures to the fire hazards. The location of 'Special Hazards' was one of the main nonstructural hazard criteria in identifying the location of 'Special Hazards' for each spatial unit. The density, size of the roof area, proximity of use functions of structures, measure of compactness was calculated separately for each spatial unit before arriving at the different scales of fire hazards. The roof area was calculated by training sites on the raster image and performing a supervised classification using the maximum likelihood method. Several classes of concrete, bitumen, terracotta roof were identified on the RGB colour composite image. A raster to vector conversion created polygons for all the different features. These were transferred to a GIS platform for further analysis. Several spatial units were considered for the choice of the most appropriate spatial unit like the census collectors unit, the 250 by 250 and 500 by 500 metre grid, and land parcels. Emphasis was not restricted to the geometric aspects of the spatial unit for GIS analysis but also on the conceptual aspects of spatial unit for hazard categorization. The total built up area for the

basic spatial unit (BSU) was calculated to arrive at a measure of the congestion, which gives a measure of the difficulty of 'Fire containment'. The study selected data sets that were already available within the state of New South Wales, so that the methodology could be replicated easily.

SCOPE AND DISCUSSIONS

Fire hazards levels should incorporate other variables also since the true definition of hazard will necessarily incorporate location of dangerous sites as well as the community who may be affected by the hazard. Location is an important variable for understanding the spatial distribution of fire hazards but a wider perspective needs to taken to classify and categorize hazards. An understanding of fire hazard must encompass the threat posed by the physical structure, the geographical setting of the region, the community in the vicinity at risk. In the true sense the magnitude of a hazard that classifies it into a major or minor one will be determined by numerous factors but chiefly by the type of structure Chemical Plant, Nuclear reactor, Industries etc and the number of people living in the proximity of that area. The 250 by 250 m good areal unit provides a good basis for comparing the hazard level in one region to that of another. Spatial distribution of fire hazards can be synoptically captured by current remotely sensed data in a short period of time.

RESULTS

A methodology to categorize fire hazards was developed integrating remotely sensed raster data with cartographic vector data GIS and a spatial database to store and analyze fire hazards in the city of Bathurst, NSW, Australia was developed on a consistent and continuous coordinate system. Datasets that are available with all the councils within New South Wales were used selectively to devise the methodology so that it could be applied to other parts of the New South Wales State. The 250 x 250 metre grid was found to be the most appropriate 'areal unit' for the purpose of 'Hazard Categorization' and allocation of dynamic resources.

ACKNOWLEDGMENTS

The study is a part of an ongoing joint project between the New South Wales Fire Brigades and the University of New South Wales supported by a scholarship from the New South Wales Fire Brigades and the author is particularly grateful to Trevor Neal, Dr Bruno Parolin and Professor Barry Garner for their advise.

REFERENCES

1. Corporate Strategy Group, "Hazard Categorization Project", The New South Wales Fire Brigades.1996.

2. K.Hewitt, "Regions of risk: a geographical introduction to disasters Longman, Harlow, U.K. 1997.

3. P.T. Blakie,T.Cannon, I.Davis, B.Wisner "At risk:natural hazards,people`s vulnerability and disasters.

London:Routledge 1994.

4. S.Rayner, "Cultural theory and risk analysis". In: S.Krimsky, and D.Golding, Editors, "Social

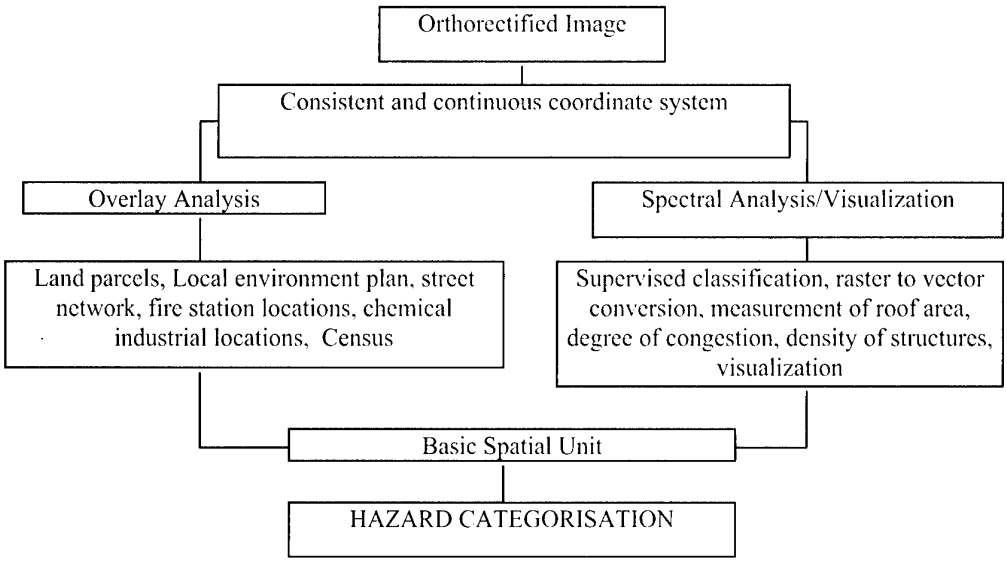
Theories of risk" Praeger, Westport,CT. 1992.

5. W.Gordon,J.Mooney,D Pratts "The People and the Hazard: the spatial context of major accident hazard management in Britain", Vol 20 pp119-235, 2000

Table 1. (Source: NSWFB project)
HAZARD CATEGORIES

General Hazard Type	Specific Hazard Category	Map Colour Code	Brief description of hazard
Special Hazard	Category 1	Red	A site that poses extreme hazards for people, property or environment, eg some hospitals and aged hostels, major lpg depots, chemical plants, oil refinery, etc.
Intermediate	Category 2	Orange	May include some high hazard residential-but basically high hazard industrial/commercial occupancies with a high level of structural density within the Unit Survey Square.
	Category 3	Yellow	May include some high hazard residential-but basically high hazard industrial/commercial occupanc's with low to moderate level of structural activity.
Low or base level hazard	Category 4	Dark green	A fully developed area of residential and low hazard industrial/commercial occupancies.
	Category 5	Light green	A partially developed area of residential and low hazard industrial/commercial occupancies

Fig 2. WORK PROCESS



LANDSLIDES TRIGGERED BY THE CHI-CHI EARTHQUAKE

Hsuan-Wu Liao[1], Chyi-Tyi Lee[2]
[1] Mr., Institute of Geophysics
[2] Professor, Institute of Applied Geology
National Central University
32045 Chung-Li, Taiwan
Tel: +886-3-4253334 Fax: +886-3-4223357
E-mail: swliao@gis.geo.ncu.edu.tw, ct@gis.geo.ncu.edu.tw
TAIWAN

KEY WORDS: Landslides, Earthquake, SPOT, GIS

ABSTRACT

A large number of landslides were triggered by the Chi-Chi Earthquake (M_L7.3) on September 21, 1999. These landslides have been mapped from SPOT images in this study. By using GIS (Geographic Information System) as a tool, we construct a GIS table of landslides triggered by the earthquake and analyze their characteristics, including types, distribution, areas and numbers, ...etc. The distribution and areas of landslides have been compared with the distance to earthquake foci, distance to faults, distance to roads, distance to rivers, rock types, hill slopes and slope directions.

There were 9272 larger landslides (area greater than 625 square meters or 4 pixels on a SPOT image) occurred during earthquake shaking. The total area of landslides is 127.8 square kilometers. There were 8843 landslides located within the area of PGA value 250 gal and above. These landslides were distributed in an ellipse-shaped region with the major axis striking NNE, coinciding with the trend of regional faults.

Statistics shows the following results: (1) Landslides most located within the area that PGA greater than 250 gal, especially within the area that PGA greater than 300 gal. (2) A lot of landslides occurred within 20 km from the fault rupture plane. The most distant landslide locates at about 60 to 70 km away from the fault rupture plane. (3) The Toukoshan Formation, The Chinshui Shale and the Tachien Sandstone were more easily influenced by the earthquake shaking, especially at Huoyenshan Facies of the Toukoshan Formation. (4) Slopes with inclination larger than 100% involve more landslides. (5) At the hanging wall, most landslides locate at S and SE facing slopes. At the footwall, most collapsed slopes face to S, SE and SW, whereas slopes facing to other directions were not so seriously damaged. It shows that the movement of the faulting during the Chi-Chi earthquake was from SE to NW.

INTRODUCTION

At 1:47 a.m. local time on September 21, 1999, an M_L7.3 earthquake struck the central Taiwan. The hypocenter located at a depth of 8 km beneath the Chi-Chi area. The surface rupture was along the existing Chelungpu fault. High peak ground accelerations were recorded over a broad region. The strong ground shaking induced not only considerable structural damages but also thousands of landslides.

We documented about 9000 landslides triggered by the Chi-Chi earthquake. This article

provides a preliminary result, including a brief description of how we mapped the landslides, an overview of landslides distribution, and basic statistics of some factors that associated with landslides. Detailed analyses will be completed in the future study.

METHOD

This study utilized the use of SPOT satellite images and aerial photographs to identify the landslides. MapInfo GIS software was used to digitize the location and extent of landslides. Numbers and areas of landslides triggered by the Chi-Chi earthquake were then calculated. Spatial functions in GIS were used to analyze the relationship among the landslide distribution and factors that triggered the landslides.

MAPPING THE LANDSLIDES

The Chi-Chi earthquake provides a good opportunity for studying of earthquake triggered landslides. Since the influenced area was large, SPOT satellite images are used to identify the landslides. Areas that were covered by cloud were re-examined by using aerial photographs. Landslide maps before the Chi-Chi earthquake and after the earthquake were identified separately. The images used are only 6 days after the earthquake on September 26 and 27, and about 5 months before the earthquake on April 1.

We compared the location and extent of the landslides between two maps, and then separated the landslides that were really triggered by the Chi-Chi earthquake. We obeyed the following principles:

(1) Landslides that can be found on both maps before and after the Chi-Chi earthquake are assumed triggered by the earthquake.
(2) Landslides that can be found only on the map after the earthquake were assumed triggered by the earthquake.
(3) Landslides that can be found on the map before the earthquake but cannot be found at the map after the earthquake are assumed not triggered by Chi-Chi earthquake.

Combining the data we got from satellite images, aerial photographs and field check, a landslides map triggered by Chi-Chi earthquake were prepared (Figure 1). The Chi-Chi earthquake triggered over 9000 landslides, which are larger than 625 square meters in area or are more than 4 pixels in a SPOT image. These landslides distribute in an ellipse-shaped region with the major axis striking NNE, coinciding with the trend of regional faults.

CHARACTERISTICS OF LANDSLIDES AND DISCUSSION

This study analyzed some relations between the landslide distribution and the factors that influence the landslide. The results are discussed as follows.

Distance to earthquake epicenter

Main shock and aftershocks locations were acquired from the Central Weather Bureau. We calculate the distance between the epicenter of main shock and the edge of a landslide. We found that most landslides occurred within 30 km from the epicenter. There are few landslides occurred over 60 km from the epicenter. The greatest distance between the landslide and the epicenter is 117 kilometers, which is smaller than the result of Keefer (1984). (Figure 2)

Distance to the fault rupture plane

We used fault rupture plane (Cheng et al., 2000) to calculate the distances between

landslides and the fault plane. We found that most landslides occurred in the distance of 20 km from the fault plane. Landslides occurred in the distance large than 30 km are rare. The greatest distance between the landslide and the fault rupture plane ranged from 60 to 70 km, which is also smaller than the result of Keefer (1984). (Figure 3)

Intensity of ground shaking

We compare landslides and earthquake intensity map. We found that landslides usually occurred at the area of PGA greater than 250 gals. Areas of PGA less than 250 gals contain fewer landslides. This result is similar with some other researches.

Characteristic of the Geologic formation

Geologic conditions have great influences on landslides. This study used the 1:250000 geologic map of Taiwan from the Central Geological Survey as base map and also 1:100000 geologic maps of Maioli, Taichung and Chiai from the Chinese Petroleum Corporation for detail examinations. We found that the Toukoshan Formation, Chinsui Shale and the Tachien Sandstone were more easily influenced by the earthquake shaking, especially at Huoyenshan Facies. Because these stratums are weak, the resistances against ground shaking are relatively low.

Distance to rivers

The erosion of the rivers will make the slopes become unstable. Drainages from 1:25000 topographic maps were extracted to a GIS layer. By using buffer analysis inside the MapInfo GIS, we found that a large number of landslides happened in the distance of 300 meters from the drainage channels.

Distance to Roads

The appearances of road represent human activities that accelerate the erosion rate. This study also extracted roadways from 1:25000 topographic maps into GIS. By applying the same process we found landslides at the distance less than 80 meters from the road are more than the landslides at the distance between 80 meters and 200 meters. But much more landslides were located outside the vicinities of roadways.

Slope Angle

Slope angle is the most important factor controls the landslide occurrence. Slope angle map was calculated from the 40 meters resolution digital terrain model (DTM). We found that the slopes inclination larger than 100% involve much more landslides.

Slope Orientation.

Earthquake shaking may have preferred orientation. Therefore, landslides may occur more frequently at slopes facing to certain direction. This study extracted slope direction from DTM. We found that at the hangingwall, most S and SE facing slopes collapsed. Meanwhile, slopes at the footwall collapsed mostly at S, SE and SW direction. Slopes facing to other directions were not so seriously damaged. It shows that the movement direction of the Chelungpu fault was from SE to NW.

CONCLUSION

There were 9272 larger landslides (area greater than 625 square meters or 4 pixels on a SPOT image) occurred during earthquake shaking. The total area of landslides is 127.8 square kilometers. There were 8843 landslides located within the area of PGA value 250 gal and above. These landslides were distributed in an ellipse-shaped region with the major axis striking NNE, coinciding with the trend of regional faults.

Statistics shows the following results: (1) most landslides locate within the area of PGA greater than 250 gal, especially within the area of PGA greater than 300 gal. (2) The majority of the landslides occurred within a distance of 20 kilometers from the fault rupture plane. The greatest distance from the fault rupture plane is about 60 to 70 km. (3) The Toukoshan Formation, the Chinsui Shale and the Tachien Sandstone were more easily influenced by the ground shaking, especially at Huoyenshan Facies of the Toukoshan Formation. (4) Slopes with gradient larger than 100% involved with more landslides. (5) At the hangingwall, most landslides occurred at S and SE facing slopes. At the footwall, most landslides concentrated at S, SE and SW facing slopes, whereas slopes facing to other directions were not so seriously damaged. It shows that the movement of the faulting during the Chi-Chi earthquake was from SE to NW.

REFERENCE

Keefer, D. K. (1984) Landslides caused by earthquakes: *Geol. Soc. Amer. Bull.*, **95**, 406-421.

Cheng, C.T., Lee, C.T., and Tsai, Y.B. (2000) Fault rupture plane and attenuation model associated with the 1999 Chi-Chi earthquake. *Proceedings of the 2000 Annual Meeting of the Geological Society of China*, 21-23. (in Chinese)

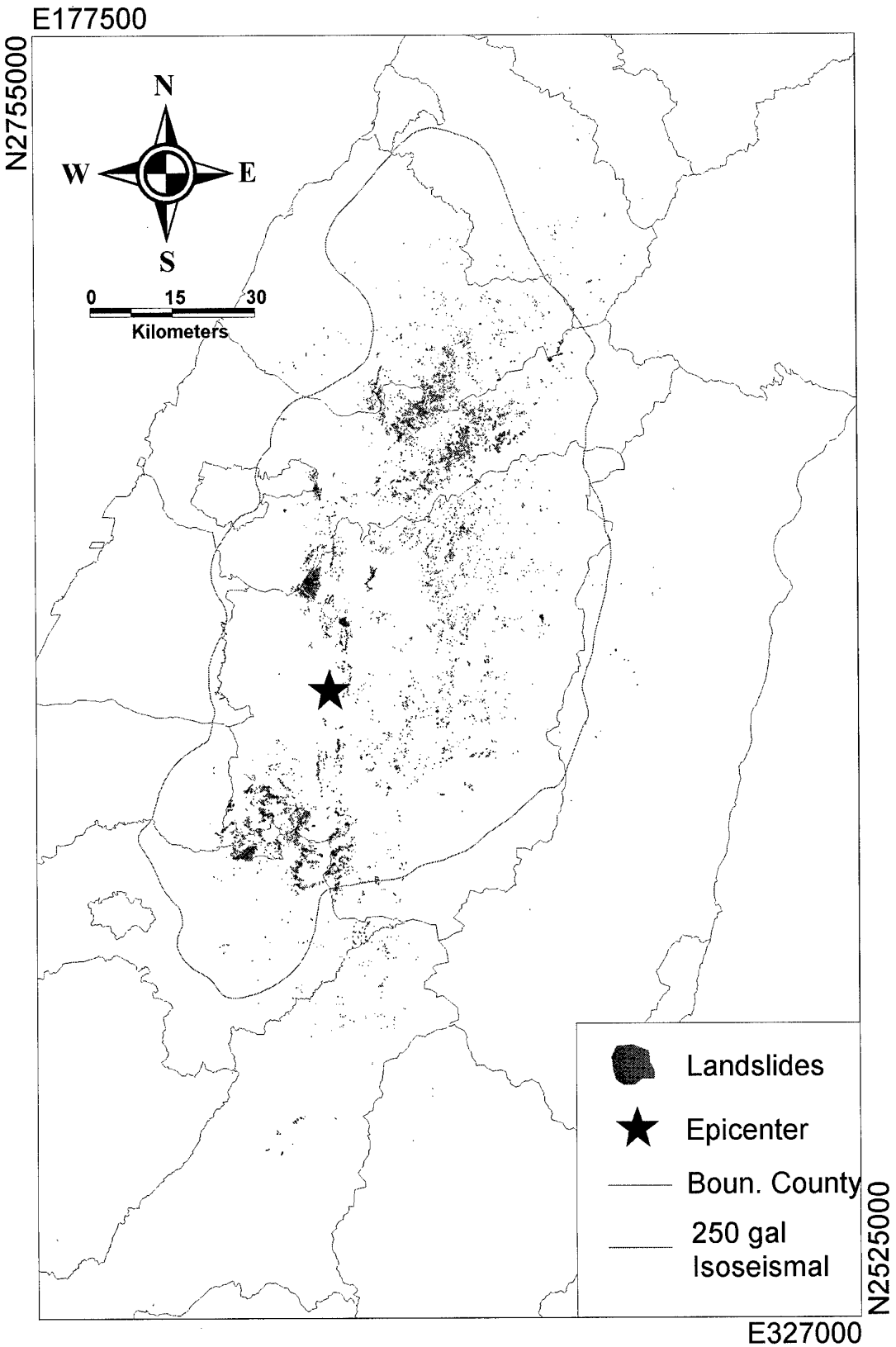


Figure 1 Landslides triggered by the Chi-Chi Earthquake

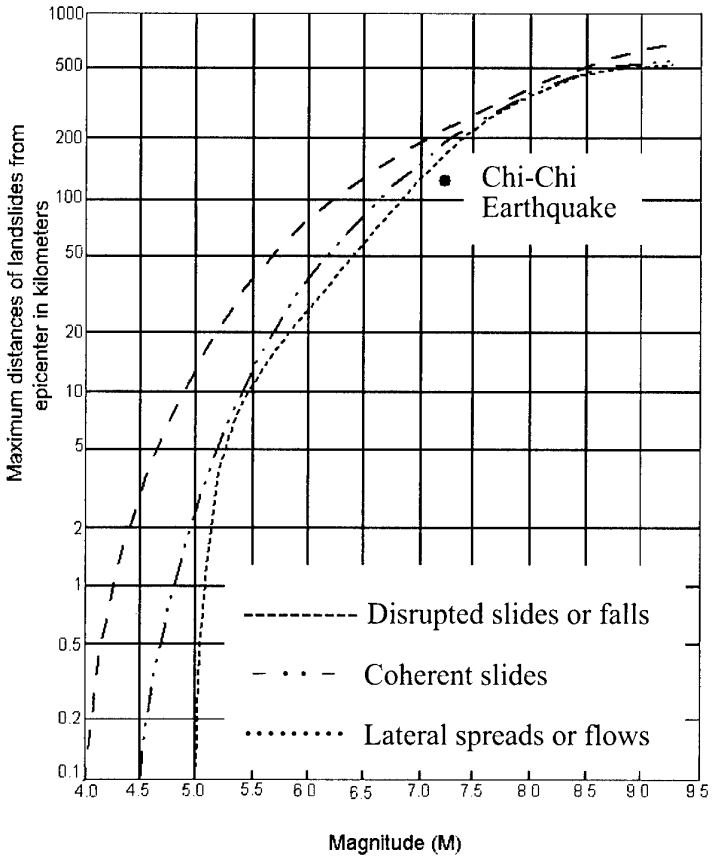


Figure 2 Maximum distances of landslides from epicenter and magnitude relation

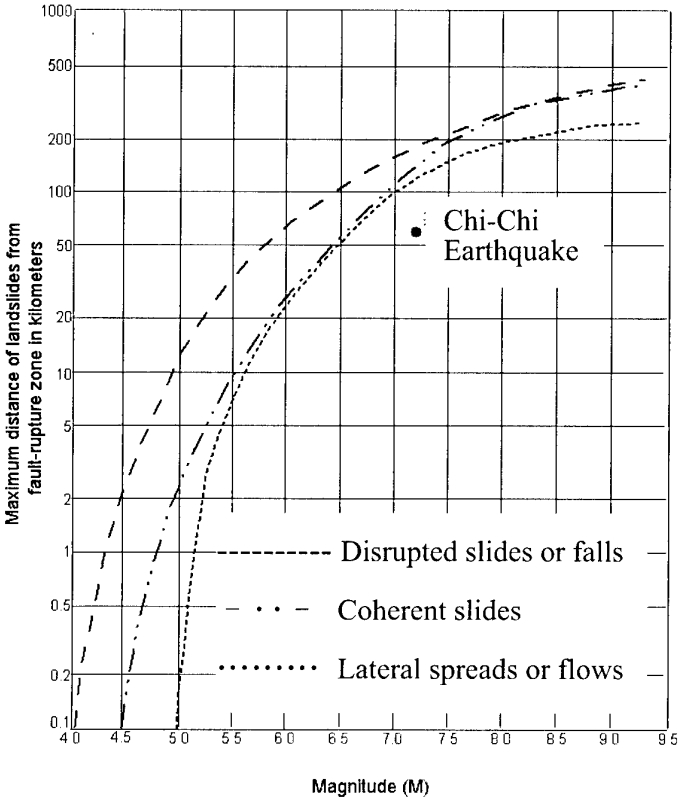


Figure 3 Maximum distances of landslides from fault rupture zone

Development of GIS-Based Building Damage Database for the 1995 Kobe Earthquake

Koichiro UMEMURA, Osamu MURAO, and Fumio YAMAZAKI

Institute of Industrial Science, University of Tokyo
4-6-1 Komaba, Meguro-ku, Tokyo, 153-8505
Tel: (81)-3-5452-6388 Fax: (81)-3-5452-6389
E-mail: umemura@rattle.iis.u-tokyo.ac.jp
JAPAN

KEY WORDS: the 1995 Kobe Earthquake, Building Damage Database, GIS, Digitized Data

ABSTRACT: After the 1995 Kobe Earthquake, local governments and an organization consisted of Architectural Institute of Japan (AIJ) and City Planning Institute of Japan (CPIJ) carried out building damage surveys. Each organization made the damage database according to its own criteria. In this study, a more detailed database of damaged buildings in Nishinomiya City was developed by matching two different data sets. One of them is the building damage data surveyed by Nishinomiya City Government in Hyogo prefecture, and other one is conducted by the organization of AIJ and CPIJ and digitized by Building Research Institute (BRI). By the matching, it would be possible to utilize the detailed inventory by the former survey and the unified standard of damage assessment in the wide damaged area by the latter. This database can be used to analyze the building damage in regard to the structural type and construction period. As a result, using the damage ratio in each district and the ground motion distribution, better fragility curves can be constructed.

1. INTRODUCTION

After the 1995 Kobe Earthquake, local governments and an organization consisted of AIJ and CPIJ, carried out many building damage surveys for different purposes. They made summary reports of those surveys, and BRI and Nishinomiya City Government digitized the spatial data with the result of building damage assessment. The digitized data in the damaged area can be used effectively for the researches on urban safety planning or earthquake engineering, and the recent computer technology enables us to deal with various GIS data. The structure of the digitized GIS data is different according to the organization. Besides, each of the conducted survey has own characteristics and the databases were constructed accordingly. In this study, a more detailed database of building damage in Nishinomiya City was developed by matching two different data sets. One of them is the building damage data surveyed by Nishinomiya City Government in Hyogo prefecture. Another one is conducted by the organization of AIJ and CPIJ, and digitized by BRI. Using the results from this study, the fragility curves for buildings can be constructed more accurately comparing the two data sets.

2. BUILDING DAMAGE DATA

The two data sets of building damage in Nishinomiya City were used in this study. One of them was the building damage data that had been investigated by Nishinomiya City Government, and another one was surveyed by the organization of AIJ and CPIJ and digitized by BRI (BRI 1996).

2.1 Building Damage Data by Nishinomiya City Government

This data set was investigated by the Nishinomiya City Government just after the Kobe Earthquake. The main purpose of the damage survey was its use for the property tax reduction. The result of the survey was also used for the distribution of the donated money from people to the victims, and for grasping the damaged area. Therefore, the standard of the damage assessment was intended for the residents. Two staff members of the local government examined and judged how much buildings were damaged by visual observation from inside and outside. This survey was carried out for two weeks after the earthquake. The classification of building damage was divided into three levels, i.e., "heavy damage", "moderate damage", and "slight damage" including "no damage". According to the damage levels, the property tax was reduced by 100%, 50%, and 10%, respectively (Murao and Yamazaki, 1999). Table 1 shows the comparison of the building data by Nishinomiya City Government and by BRI. Remarkable characteristics of the Nishinomiya data set are more detailed "structural type", including "roof type" and "construction period". These factors are very significant to construct fragility curves. The center of each building is shown as point data (Figure 1). The coordinate system is fifth of JPN.

Table 1: Comparison of the Building Data by Nishinomiya City and by BRI

	Nishinomiya data	BRI data
Area	Nishinomiya city	7 cities 3 towns
Total number	155,442	443,000
Damage classification	3 categories	5 categories
Structural type	9 categories	3 categories
Building use	62 categories	6 categories
Roof type	10 categories	-
Stories of building		-
Construction period		-
Coordinate system	5th of JPN	6th of JPN
Shape	point	polygon

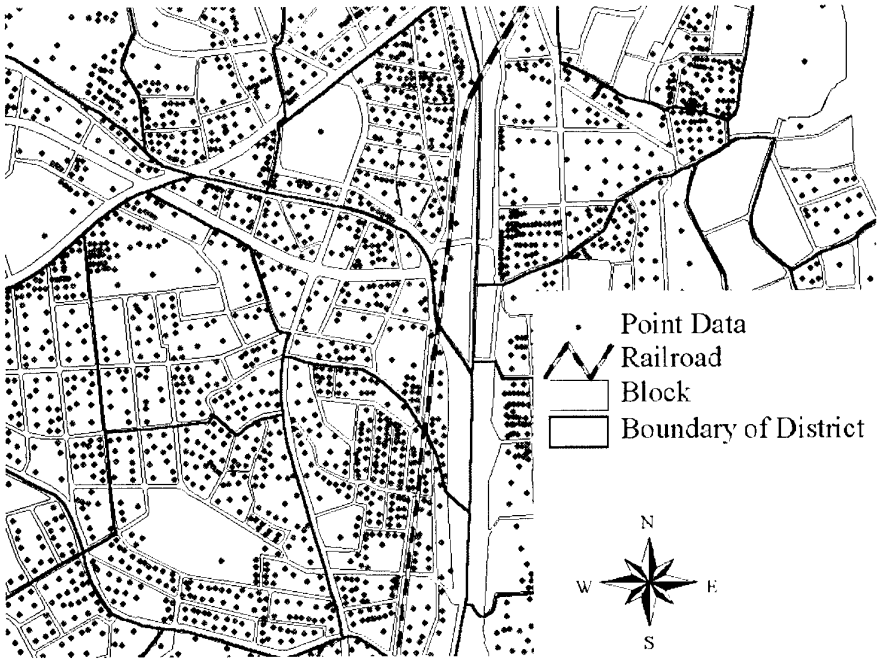
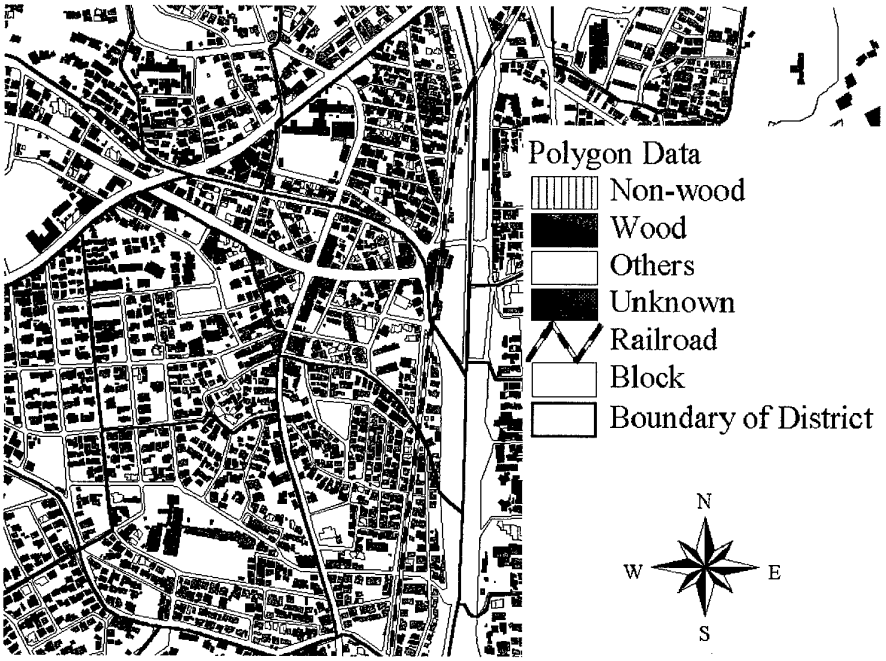


Figure 1: Point Data of Buildings by Nishinomiya City

2.2 Building Damage Data by BRI

This survey was carried out by professionals, researchers, and volunteer students who major in Architecture or City Planning. After the investigation, City Planning section of Hyogo prefecture conducted a further survey with the same method to supplement data in insufficient areas. The survey was conducted not only in Nishinomiya City but also in other cities: Kawanishi, Itami, Takarazuka, Amagasaki, Kobe and Awaji Island, to grasp the comprehensive damaged area due to the earthquake. The aim of the survey was for future academic contribution. Therefore, the assessment of the building damage was more strict and the method of the survey was more technical than that of local governments. The damage was classified into 5 categories, i.e., "collapse or heavy damage", "moderate damage", "slight damage", "no damage", and "burned". However, each building was evaluated by visual observation from outside of the building, so that the inventory does not contain "roof type" and " construction period", and the classification of "non-wooden buildings" in "structural type" is not divided. Figure 2 shows the polygon data of buildings in the BRI's GIS database. The coordinate system is sixth of JPN.

Figure 2: Polygon Data of Buildings by BRI



3. MATCHING THE DIFFERENT DATA SETS

3.1 Pretreatment

First, the authors had to make the Nishinomiya data (Data-1) and the BRI data (Data-2) with the same coordinate system. The coordinates of Data-1 were transformed from the fifth coordinate system of JPN to the sixth. Next, the regions of the both data sets were compared to extract the researched area for the database as shown in Figure 3. While the whole area of Nishinomiya City was made as the target of Data-1 because of the purpose for the tax reduction, the area for the Data-2 was limited. As a result, the south area of the City was extracted as the research object. One problem of the matching was that overlapped point data had existed for one building in Data-1 because the data were constructed based on the household unit. It was necessary to integrate these multiple point data into one.

3.2 Integration by the Positional Relationship

To integrate the both spatial data sets, only a spatial positional relationship was considered. Firstly, the point data of Data-1 inside the polygon data of Data-2 was extracted as shown in Figure 4. Secondly, in the other data except for the above, the distances between the points and polygons were calculated, and a point located within 3m from a polygon was matched with it as shown in Figure 5. The shortest distance is the perpendicular distance between a point and an edge of polygons or the distance between a point and a corner of polygons. Figure 6 shows the method to calculate the shortest distance. After that, these matched data were printed out on a paper, and they were compared with a detailed map.

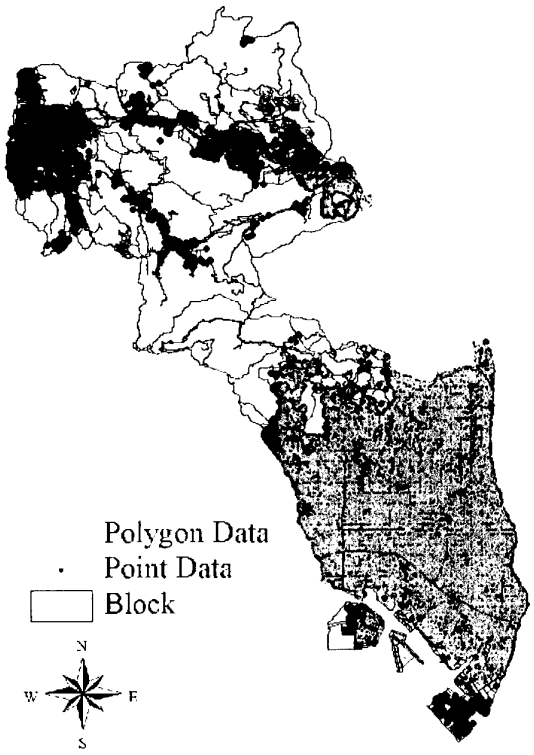


Figure 3: The Area of Nishinomiya City Covered by the Two Data Sets

3.3 Processing of Overlapped Data

In case of being more than two points inside one polygon as shown in Figure 7, these multiple overlapped data were integrated into one data set considering the building use. The reason of the overlapped points was mostly due to the difference in dealing with attachment buildings, such as garages or warehouses. The cause of it was considered and these additional data were omitted from the viewpoint of the building use. In addition, this process is carried out considering the construction period, structural type, and damage classification. Figure 8 shows the flowchart of the matching process.

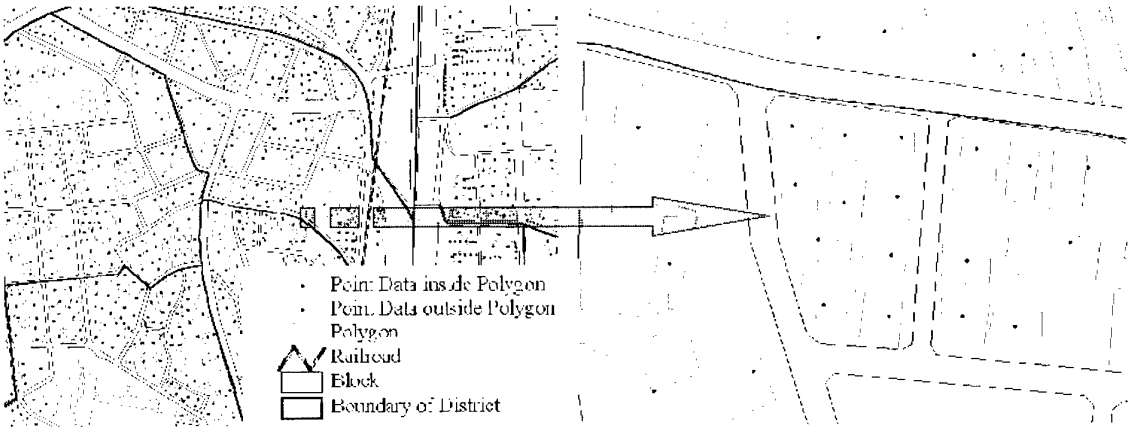


Figure 4: Matching of the Point Data inside Polygons

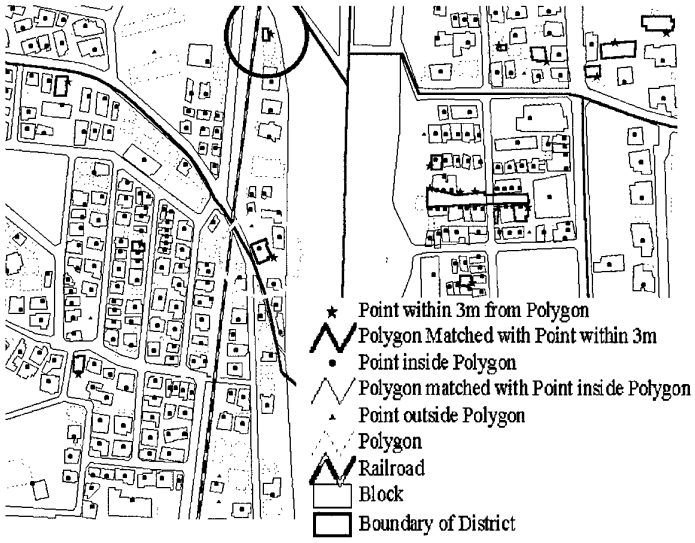


Figure 5: Matching of Point Data within 3m from Polygons of Buildings

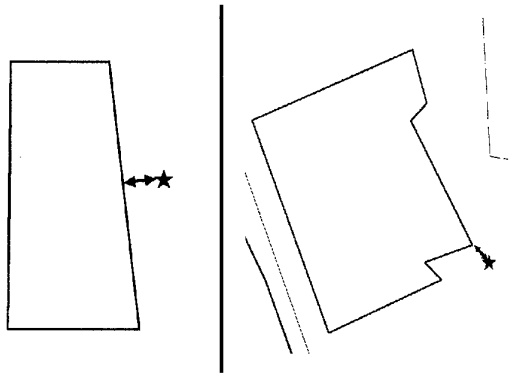


Figure 6: Method to Calculate the Shortest Distance between a Point and a Polygon

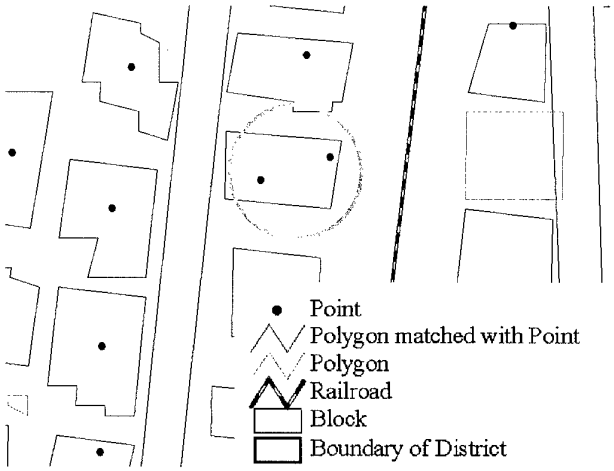


Figure 7: Integration of Overlapped Point Data Considering the Building Use

4 CONCLUSION

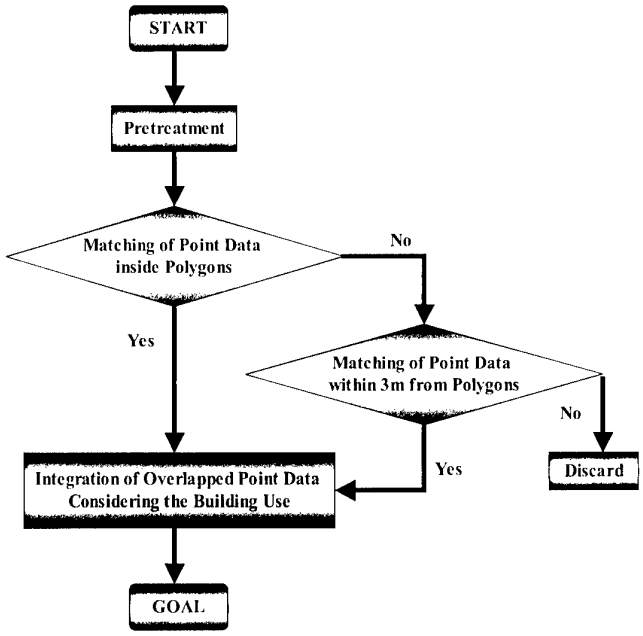


Figure 8: Flow Chart of Matching

In this paper, the process to match the different building damage data sets due to the Kobe Earthquake and the importance of it were described. The authors developed this building damage database by matching Nishinomiya Government data and BRI data to supplement insufficient items. The former contains the detailed inventory, i.e., structural type (wooden, RC, steel, light-gauged steel, etc.), roof type of wooden buildings, construction period. On the other hand, the BRI data based on the survey by AIJ and CPIJ is intended for academic contribution. Fragility curves for buildings in Japan have been constructed by some researchers (e.g., Yamaguchi and Yamazaki, 2000) based on the data from the 1995 Kobe Earthquake. However, some of them are based on the tax reduction data with detailed inventory, while the others are based on the BRI data without detailed information on buildings. After the development of the GIS-based building damage database, fragility curves, which are impossible to create without matching the different data sets, can be constructed considering both the detailed building characteristics and rigorous damage classification.

ACKNOWLEDGEMENTS

The digitized spatial data used in this paper were provided by Building Research Institute and Nishinomiya City Government.

REFERENCES

Building Research Institute. 1996. Final Report of Damage Survey of the 1995 Hyogoken-Nanbu Earthquake (in Japanese).

Murao, O., and F. Yamazaki. 1999. Comparison of building damage evaluation by local governments after the 1995 Hyogoken-Nanbu Earthquake. *Journal of Architecture, Planning and Environmental Engineering* 515, pp.187-194.

Yamaguchi, N., and F. Yamazaki. 2000. Fragility curves for buildings in Japan based on damage surveys after the 1995 Kobe Earthquake. *Proceedings of the 12th World Conference on Earthquake Engineering*. Auckland, New Zealand, 8p, CD-ROM

AIRBORNE THERMAL IR REMOTE SENSING OF LUSHAN GEOTHERMAL FIELD

Chi-nan WU and Ta-Ko CHEN
Manager, Researcher, Remote Sensing Lab
Energy & Resources Labs, ITRI
Bldg 24, 195-6 Sec4, CHUNG HSING RD.
CHUTUNG HSINCHU 310,
Tel : (886)-3-5915465 Fax : (886)-3-5820038
E-mail : 690398@itri.org.tw
TAIWAN

KEY WORDS : Airborne MSS, Thermal IR, Brightness Temperature

ABSTRACT : Airborne DS-1260 MSS thermal infrared (TIR) data were used to analyze the surface temperature distribution of Lushan Geothermal Field. The main purpose is focused on detecting the geothermal outcrops for assisting the route planning of Central Cross-island Expressway, as it's deemed that a geothermal outcrop should be 500 meters away from the Expressway. TIR data were acquired in the early morning with pixel size about 9.5 meter, which were pre-processed to remove S-bend and aspect ratio effects, and GCPs were adopted to geometrically correct the image using 3'rd order polynomial equation. Vector data such as the existing roads and the planned route were also digitized to overlay with the image for the convenience of image interpretation and field check. The data quality of TIR data was evaluated by S/N and NEDT, and brightness temperature of each pixel was calibrated using plank's equation and blackbody temperatures. The resulting thermal imagery were ground-checked and interpreted, and it's found that those hot spots ($\geq 22°C$) were all irrelevant to geothermal activity, instead, they were owing to metal roofed houses, residential buildings or bare rocks located on the sunshine slope. On the other hand, the temperature of geothermal outcrops was between 19 to 21°C. It's because of the relatively coarse pixel size, small scale hot spring seepage and atmospheric absorption that the sensed geothermal temperature was lower than the actual temperature, consequently, a hot spring outcrop is not necessary appearing as higher temperature in a thermal image. Some thermal anomaly areas were located, while owing to the view angle effect or canopy shaded effect, a few small scale geothermal seepage were ignored by the TIR image, Fortunately, they are all located at a distance more than 500 meters from the planned Expressway.

1. INTRODUCTION

Airborne thermal Infrared (IR) data were adopted to analyze the surface temperature distribution of Lushan Geothermal Field from Wushe to Yunhai in central Taiwan. The main purpose is focused on detecting the hot spring activities, which will be helpful for the planning of Central Cross-island Expressway. As the hot spring areas are usually geological weak zone, the expressway should be 500 meters away from those areas. Besides, the acquired imagery could be used as ancillary data for the investigation of landslides and geology of the area. This work is a part of geological investigation during the planning stage of the Expressway, integrated by United Geotech Inc. and sponsored by National Highway Construction Bureau.

2. DATA ACQUISITION

2.1 Scanner System

A Daedalus DS-1260 Multispectral Scanner (MSS) was used to acquire the desired remotely sensed data. DS-1260 MSS can record eleven channels of image data Simultaneously, including a thermal IR channel using a MCT or InSb detector. Thermal IR channel receives the spontaneous radiation from ground surface and it is good for temperature analysis, while the other channels receive reflected energy from the Sun, which are helpful for surface imaging. During the airborne mission, 12 channels of imagery data are recorded with a High Density Digital Tape (HDDT), the 12'nd channel also records the same thermal IR data as the 1 1'st channel but with different signal gain.

2.2 Mission Planning

(a) Target area : Lushan Area, from Yunhai to Wushe. Coordinates, TM 2 (262000, 2658000) to (275000, 2661000)

(b) Detectors : 10-channel DE 160 Spectrometer and DE 237 MCT detector. Table 1 Shows the spectral channels of the detectors.

(c) Scan line : 716 pixels, 1 byte/pixel.

(d) Field of view : 85.92°, i. e., 2.1 milli-radian/pixel.

(e) Ground resolution : within 10 meters.

(f) Flight altitude : <5762 meter for the elevation of 1000m as at Lushan.

(g) Scanning time : predawn or early morning in order to avoid the heating effect of sunlight.

Channel #	Wavelength (μm)	Channel #	wavelength (μm)
1	0.38～0.42	6	0.60～0.65
2	0.42～0.45	7	0.65～0.69
3	0.45～0.50	8	0.70～0.75
4	0.50～0.55	9	0.80～0.89
5	0.55～0.60	10	0.92～1.10
		11	8.0～14.0

Table 1. Spectral channels of DS-1260 MSS

2.3 Data Acquisition

The airborne imagery of the target area were acquired at AM 7:35 Aug. 19, 1996 with a scan rate of 25 scans/sec. During the flight, the temperature of 2 reference blackbodies was set at 10.9 and 26.4°C, respectively. The flight altitude was 18,000 ft and flight direction was 265°. As a result, 3640 scan lines were recorded, and each line contains 736 bytes of data including 20 bytes of ancillary data such as blackbody temperatures and their corresponding digital numbers (DN), gains, etc., for calibration.

3. DATA PROCESSING

3.1 Pre-processing

(a) Reformatting

The acquired imagery data in HDDT were transferred to hard disk and their data format were transformed from band interleaved (IL) to band sequential (BSQ), which are ready for the following consecutive processing.

(b) S-bend Correction

According to the imaging geometry, the panoramic effect in the image was removed. After this operation the pixel number per line is changed from 716 to 888 pixels/line.

(c) Aspect Ratio Correction

Three parameters i. e., Scan rate, ground resolution and flight speed were used to estimate the aspect ratio of the acquired imagery. For the elevation of 1000 meters as at Lushan, the computed aspect ratio is 2.77, consequently, integer 2 was adopted to minimize the aspect ratio effect. In other words, an image line is extracted from every two lines of original image.

3.2 Geometric Correction

Refer to 1:10,000 photographic base map, ground control points (GCP) were selected and their conjugate pixels were also identified in the image. A derived three order polynomial equation was then used to perform geometric correction of the acquired image, trying to fit the image as close as possible to the map.

3.3 Vector Data Digitizing

The existing roads in Lushan area and the planned route of Central Cross-island Expressway were digitized, those vector data were then overlaid on the thermal anomaly image which would be helpful for locating positions during field check and image interpretation.

4. THERMAL IR DATA CALIBRATION

4.1 Data Quality Evaluation

For the acquired thermal image, the recorded blackbody temperatures and their corresponding DN were checked to evaluate data quality. It was found that the calibration parameters of channel 11 were very unstable during flight mission. Consequently, channel 12 data were selected, in lieu of channel 11, for the following processing and analysis. In channel 12, the recorded calibration parameters were relatively stable, while its gain is 0.5 instead of 1.0 in channel 11.

However, the calibration parameters of some image lines are still unstable in channel 12 data, in such case the average value of the corresponding parameters of the neighboring two lines is adopted to replace the unstable one.

4.2 Radiometric Calibration

According to blackbody temperatures and their corresponding DN, Plank's equation was used to calibrate thermal IR data. The DN value was then transformed to radiance. Signal to noise (S/N) ratio of the thermal image was also calculated and was as high as 17.36, and its noise equivalent delta T (NEDT) was 0.98 °C. These values indicate that the quality of channel 12 was acceptable.

4.3 Brightness Temperature Calculation

A radiance to temperature conversion table obtained from the above steps was adopted to calculate the brightness temperature (BT) of each pixel of the image. Table 2 lists the count of temperature distribution. The statistics are : mean BT 15.56 °C, Standard deviation 2.13°C and mode at 16°C.

BT (°C)	# pixel	BT (°C)	# pixel	BT (°C)	# pixel
4	94	14	284667	24	343
5	2390	15	244170	25	190
6	1501	16	341608	26	55
7	987	17	228066	27	34
8	2147	18	209711	28	13
9	6294	19	60446	29	5
10	11668	20	16234	30	2
11	24564	21	8987	31	1
12	64178	22	3088	32	0
13	103652	23	1056	33	1

Table 2. BT Distribution in Lushan Area

By field check and comparison with base maps, it was found that those " hot spots" with BT>27°C were all located at the slope lands of Chinjin Farm and NTU Experimental Farm and they were irrelevant to geothermal activity. Instead, those thermal effects were owing to metal roofed houses or residential buildings.

5. HARDCOPIES GENERATION

5.1 False Color Composite

After contrast enhancement, images of MSS channel 4, 6, and 9, i. e. green, orange and reflected IR bands, were composite (B/G/R) for hard copy output. Such a false color composite (FCC) simulates a IR photograph for surface feature interpretation..

5.2 Pseudo-color Image of Brightness Temperature

The temperature image was transformed to a pseudo-color image in which each color represents a specific temperature range. However, owing to the atmospheric absorption effect, usually the derived BT is lower than the actual surface temperature ; also, it must be realized that the pixel temperature represents the average temperature in a area covered by that pixel. In this case the pixel coverage is about 10mx 10m on the ground.

5.3 Thematic Map of Thermal Anomaly

Although the image generated in 5.2 shows the surface BT of every pixel in Lushan area, it's difficult to identity where are the pixels with higher temperature in that map. In order to distinguish "hot spots" or "hot area", the pixels with temperature greater than 19°C were extracted and overlaid on the MSS 4/6/9 FCC to generate a thermal anomaly image , in which yellow represents 20~21°C, green represents 22~23°C and red for the pixels with temperature great than 23°C (Fig.1).

6. FIELD CHECK

Field checks were carried out twice to verify the "ground truth" in Feb. and Apr. 1997. Those hot spots within 1 km along the planned route, if accessible, were checked to see if they were related to hot spring activity.

7. RESULTS AND INTERPRETATION

In Fig. 1 the background image displayed is MSS 4/6/9 FCC, while the BT anomalies are shown in yellow, green and red colors which represent 20~21°C, 22~23°C and $\geq$24°C BT, respectively.
In MSS 4/6/9 FCC image, deep blue area is the water body of Wanda Reservoir. Light blue represents bare lands including landslides, cultivated land, road and shallow water riverbed. These surface features have similar spectral signature and consequently they appear as similar color. Pinky and reddish color indicate vegetation including forest, grass land, orchards and vegetable patches. Dark area is shadow which enhance the rugged terrain. However within some shadow area some dark greenish spots still can be seen, which were landslides or cultivated land.

Most of the high temperature anomalies were scattered on the sunshine slope, they were roadside buildings, landslides and cultivated land. The local environment is that there are many metal roofed houses in Lushan, Chinjin and Wushe, and many hotels and outdoor swimming pools locate at Lushan Spring Area. All these landuses appeared as hot spots in thermal image. It's found that all hot spots with BT>27°C were located at the dense developed area around Chinjin Farm and NTU Experimental Farm, and they were irrelevant to geothermal activity. As for bare land, the dry bare rocks had higher temperature and appeared as red, while debris had lower temperature and appeared as green or yellow color.

Lushan area is a geothermal field in the metamorphic terrain and is the typical location of Lushan Formation. Lushan is located at the middle member of Lushan Formation, the Yuanfen Member, and is sandstone-dominated. On the other hand, the Chunyang Spring Area to its west is located at the lower Chunyang Member, which is slate-dominated (Chang and Lee, 1980 ; Fan and Lee, 1994). Fractures and joints in the brittle Lushan F. are common and produce important secondary porosity for geothermal water. Geothermal water move upwards along the fractures and usually appear on the riverbed. For this reason, the detection of geothermal activities had been focused on the river valley of Talowanshi river, Mahaipushi River and a creek near Chunyang.

In Fig. 1, to the south of Muansan mountain there are many hot spots scattering and extending more than 1 km along the riverbank of Talowanshi R. This area has become a famous recreation area. However those hot spots were all buildings and outdoor swimming pools and their spring water are all from Spring Head located at 1 km upstream or from private geothermal borehole. The place 1.5 km upstream from here and on the left riverbank near PA18 borehole, there are two yellow hot spots in Fig.1 (S1). After field checks it's confirmed that they were spring outcrops. During field checks upstream along Talowanshi R. we had also found that many small spring water seepages appeared on the left riverbed, however their coverage were too small to detect in thermal image. Yellow spot N1 on the right riverbank there was also a hot spot near PA 19 borehole and below a silt arrester, during field checks we had found it was a big iron-tank. The L1 hot spot was a landslide on a steep slope where did not has any geothermal activity. Another hot area near PA20 borehole was also a landslide (L2), where Highway 14 passes by. Other hot spots such as L3 and L4 in Fig. 1 are too difficult to reach, they are also interpreted as landslide according to their spectral signature.

At 3km downstream of Talowanshi R. from Lushan it is Chungyang. The yellow spot (S2) at the intersection of Talowanshi R. and a creek had been verified as a geothermal outcrop during field check. L5 and L6 were also hot areas located at 700m and 1km upstream of that creek. On the way to check these two areas, more than ten spring seepages were found, however they could not be identified in the thermal image because of their small size. L5 was a landslide having strong geothermal activity, as we could see hot water were tapped and piped outside to hotels. Around L5 some spring seepages were also found. L6 was also a landslide, while some spring seepages appear on the other side of the creek. It is concluded that the riverbed of that creek has strong geothermal activity underlain.

In Fig. 1 there is not a hot spot at all appearing along the riverbed of Mahaipushi R. However hot water and steam seepage points were really existing at 400m upstream of the river. When we lowered the BT of color coding to 19°C and displayed the pixels having this BT as cyanine color, the hot spot S3 of this outcrop appeared. From the results it is clear that a spring outcrop is not necessarily appearing as higher temperature in a thermal image because of mixed pixel effect.

8. SUMMARY AND CONCLUSION

Airborne Thermal IR data were adopted to analyze the surface temperature of Lushan area during the planning phase of Central Cross-island Expressway. Results show that the sensed BT of spring outcrops was in between 19 to 21°C, and all the surface features with BT great than 21°C were bare land or buildings, the former includes landslides and cultivated patches. It's owing to the mixed pixel effect and atmospheric absorption that the sensed temperature of geothermal was lower than it's actual temperature.

The thermal anomaly areas and their surface feature near the planned route of Central Cross-island Expressway are listed as the following:

During two field checks, more than 10 geothermal spring seepages were found in both valley of Talowanshi R. and a creek near Chungyang. However, because these outcrops are small scale, seeping on the hill wall or covered by canopy, they were not sendsed by the thermal image.

Spring outcrop :
- S1 : Near PA19 borehole, on the left riverbed of Talowanshi R.
- S2 : At the intersection of Talowanshi R. and a creek near Chungyang.
- S3 : At 400m upstream of Mahaipushi R.

Landslide :
- L1 : At 300m upstream from PA19 borehole, on the left riverbed of Talowanshi R.
- L2 : To the north of PA20 borehole, where Highway 14 passes by.
- L3 : 800m upstream from L1, on a slope land and to the right of Talowanshi R.
- L4 : On a slope land near PA21 borehole.
- L5 : At 700m upstream of the creek near Chunyang, also the source of spring water piped to hotels.
- L6 : At 1 km upstream of the creek near chunyang.

One of the criteria for planning the route of the Expressway is that any thermal outcrop should not be within 500 meters from the route. Fortunately, this study shows the criterion is thoroughly fulfilled.

9. REFERENCES

Chang, P. T. and C. S. Lee, 1980. Geological Investigation of Lushan GEOTHERMAL Field, Central Taiwan. Geothermal Resources Council TRANSACTIONS Vol. 4, pp.109-112.

Fan, C. and H. C. Lee, 1994. Report on the Re-evaluation of National Geothermal Resources in Taiwan. ERL/ITRI, Sponsored by MOEA, Taiwan.

Wu, C., 1993. FY93 Report on The data Conversion of Airborne MSS Data. ERL/ITRI, Sponsored by COA, Taiwan.

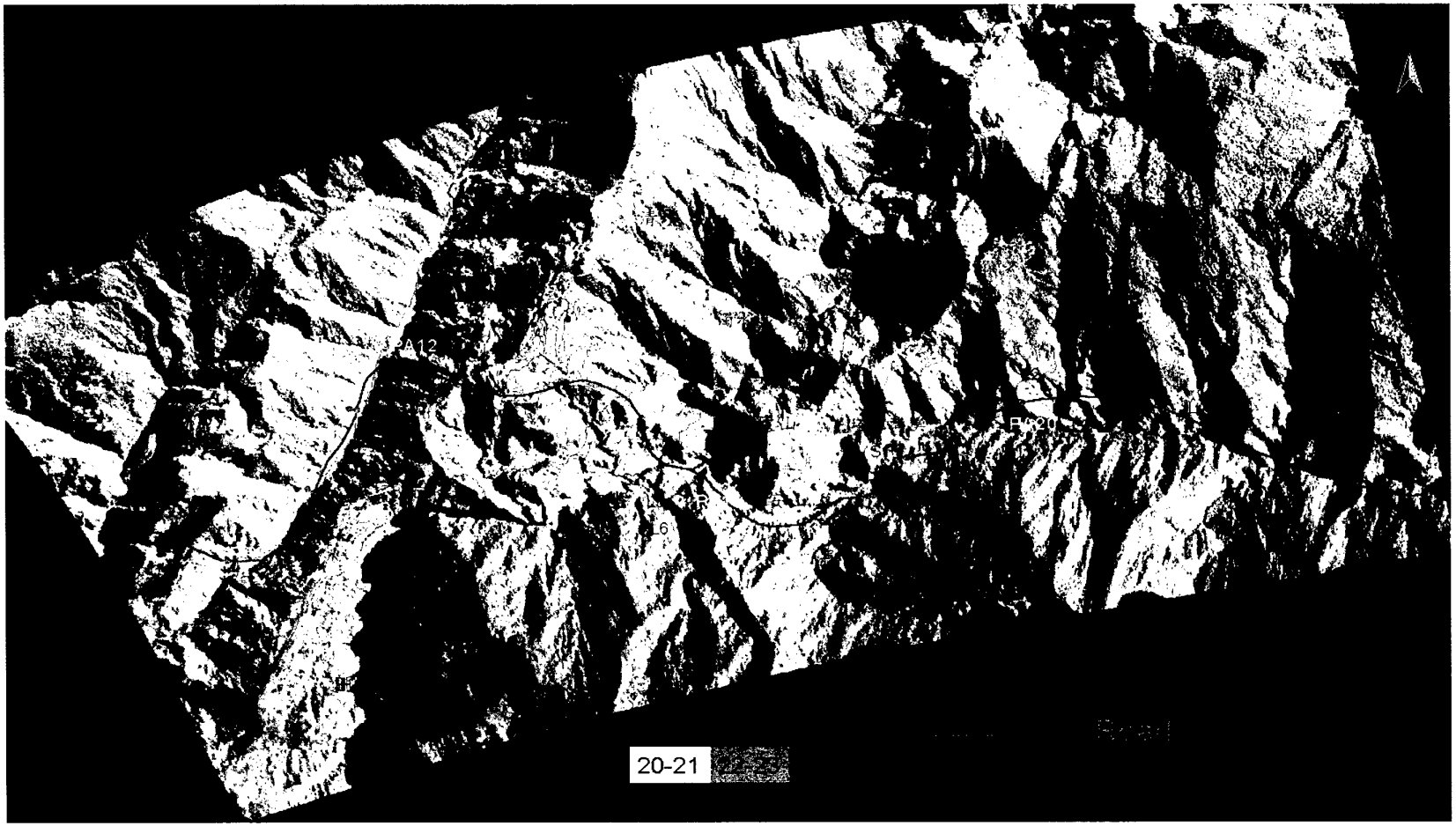


Fig 1. Thermal anomaly Image of Lushan Geothermal Field

The 21st Asian Conference on Remote Sensing
December 4-8, 2000 Taipei, TAIWAN

AUTOMATED DETECTION OF BUILDING DAMAGE DUE TO RECENT EARTHQUAKES USING AERIAL TELEVISION IMAGES

Hajime MITOMI, Fumio YAMAZAKI and Masashi MATSUOKA
Earthquake Disaster Mitigation Research Center, RIKEN
2465-1 Mikiyama, Miki, Hyogo 673-0433, Japan.
Tel: +81-794-83-6632 Fax: +81-794-83-6695
E-mail: mitomi@miki.riken.go.jp

KEY WORDS: Image Processing, Building Damage, Texture Analysis, the 1999 Kocaeli Earthquake, the 1999 Chi-Chi Earthquake

ABSTRACT: The characteristics of severely damaged buildings were examined by image processing of aerial television images taken after the 1999 Kocaeli, Turkey and the 1999 Chi-Chi, Taiwan earthquakes. In image processing, color indices and edge elements were used for the extractions of information on damaged buildings. After pixels indicating damaged buildings were detected on the basis of these characteristics, the texture analysis of the image was attempted. The result of the texture analysis was compared with the results of visual inspection. Using this approach, collapsed buildings were properly identified. The automated damage detection method proposed here can be used efficiently in emergency management shortly after a large-scale natural disaster.

1. INTRODUCTION

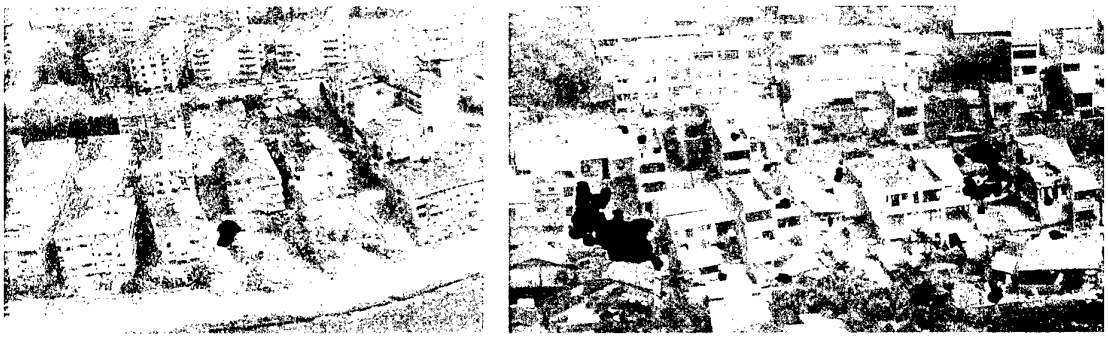
After the 1995 Hyogoken-Nanbu (Kobe) earthquake, the delay of initial measures by central and local governments was pointed out. It is important to estimate and grasp damage situations during the early stage of recovery activity without depending on information sent from the interiors of the stricken area. Several methods for gathering information on damage from outside of the stricken area are available, such as aerial television imagery, aerial photography and satellite imagery. Aerial television images and photographs, which have higher spatial resolution than satellite images, were visually inspected (Hasegawa et al., 2000a; Ogawa and Yamazaki, 2000). Although the severely damaged buildings could be visually inspected, a significant amount of time was required for visual interpretation. Therefore, Koga et al. (1998) and Hasegawa et al. (2000b) carried out preliminary studies on automated damage detection using image processing. In particular, Hasegawa et al. (2000b) examined the characteristics of aerial images of severely damaged wooden buildings taken by high-definition television (HDTV) cameras operated by the Japan Broadcasting Corporation (NHK) after the Kobe earthquake, and we developed a method of automated damage detection based only on the post event images. The damage distribution extracted using the proposed method agreed relatively well with the ground truth data and the results of visual inspection of the HDTV images. In this paper, we report the results obtained by applying the method proposed by Hasegawa et al. (2000b) to the 1999 Kocaeli, Turkey and the 1999 Chi-Chi, Taiwan earthquakes.

2. DAMAGE DETECTION METHOD

In the damage detection method proposed by Hasegawa et al. (2000b), the characteristics of damage to wooden buildings were defined based on hue, saturation, brightness (intensity) and edge elements. Using the threshold values of these parameters, the typical areas were classified into damaged and undamaged pixels. Texture analysis was then carried out on these pixels and the damaged buildings were identified. The steps of the automated detection method (described

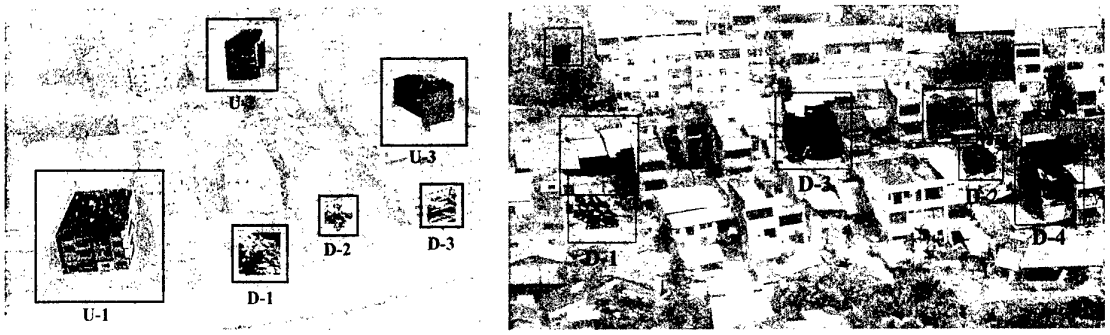
as the Kobe method) are as follows:

1. Some training data are selected from typical damaged and undamaged wooden buildings in a HDTV image.
2. The intensities of edge elements are calculated by a general gradient filter with a 3 x 3 pixel window and are allocated to one byte (256) value.
3. The pixels with the edge intensity value between 32 and 90 are selected.
4. The variances in the edge intensity are evaluated for the area of 7 x 7 pixels and are allocated to one byte value for the center pixel.
5. The pixels with the variance between 0 and 30 are selected.
6. The relative frequencies of color indices such as hue, saturation and intensity (HSI) are also calculated using the RGB values and are allocated values from 0-360 degrees for hue and one byte values for saturation and intensity.
7. The pixel, which contains the range of 92-148 degrees (this color range is from red to yellow) for hue, 0-90 for saturation, and 0-175 for intensity, are selected.
8. The local density of the selected pixels (described as *Rpx*) is calculated by texture analysis. For the texture analysis, 31 x 31 to 63 x 63 pixel windows are selected to be proportional to the image scale, depending on the location of the area in the image.
9. The pixel blocks whose density values are smaller than 14%, and larger than or equal to 14% are assigned as belonging to undamaged and collapsed buildings, respectively.



(a) Golcuk, Turkey (b) Chungliao, Taiwan

Figure 1: Results of automated damage detection by the Kobe method



(a) Golcuk, Turkey (b) Chungliao, Taiwan

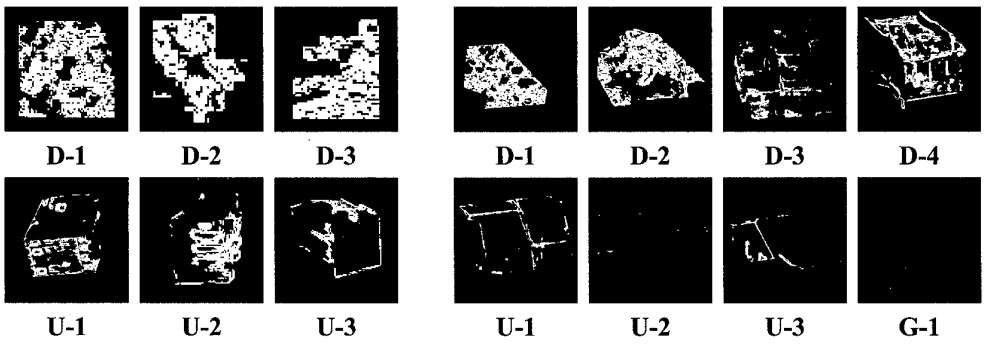
Figure 2: Training data used in this study

3. APPLICATION TO THE RECENT EARTHQUAKES

The Kocaeli, Turkey and the Chi-Chi, Taiwan earthquakes occurred on August 17, 1999 and September 21, 1999, respectively (Earthquake Disaster Mitigation Research Center, 2000a,b). The Japanese Geotechnical Society captured images of stricken areas, a few weeks after the Turkey earthquake using a digital video camera from a helicopter. Two and four days after the Taiwan earthquake, NHK captured images of severely damaged areas using a HDTV camera from a helicopter. In this study, we used images taken at Golcuk in Turkey and Chungliao in Taiwan, which had suffered severe damage after the earthquakes. We applied the Kobe method to images taken in Turkey and Taiwan, as shown in Figure 1. The damage areas extracted from the Turkey image was much smaller than the actual distribution of damaged buildings, although more accurate information on building debris was extracted in the Taiwan image. Because some factors attaching the images may be different, such as the influence of sunshine, built environment and so on, whereas damage distribution in the case of the Taiwan image may fortunately be similar to the built environment of the Kobe image used by Hasegawa et al. (2000b). We selected training data and threshold values for each image in order to obtain an extracted damage distribution close to the actual damage situation. Figure 2 and Table 1 represent the selected training data and threshold values for each image of the Turkey and the Taiwan earthquakes. In this study, training data were also selected for moderately damaged buildings, such as D-3 in Turkey, D-3 and D-4 in Taiwan. Damaged pixels were then extracted

Table 1: Threshold values of image characteristics for three earthquakes

Characteristics	Range of threshold values		
	Kobe	Turkey	Taiwan
Hue (degree)	92 - 148	0 - 360	14 - 148
Saturation	0 - 90	16 - 95	25 - 109
Intensity	0 - 175	63 - 176	52 - 170
Edge intensity	32 - 90	15 - 103	14 - 70
Variance of edge intensity	0 - 30	5 - 77	1-25



(a) Golcuk, Turkey (b) Chungliao, Taiwan

Figure 3: Pixels satisfying the threshold values for the selected small areas in Figure 2. The identified pixels (white area) from each image corresponds mostly to "collapsed" buildings while the shaded gray-color pixels indicate mostly "undamaged" buildings

from the training data in combination with these threshold values for each case, as shown in Figure 3. Table 2 presents the ratios between total and extracted pixels for all the training data. In this table, the differences in the ratios between damaged and undamaged training data are observed, although the ratios for damaged training data are not particularly high.

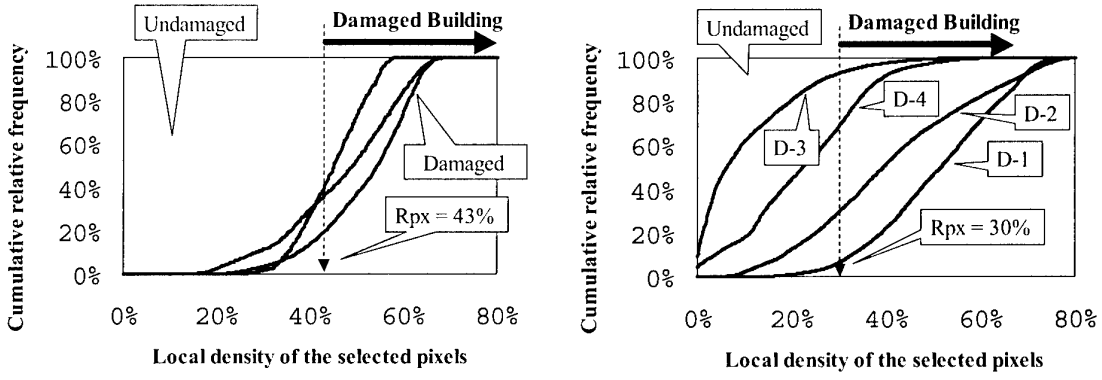
Table 2: Number of pixels and ratio of extraction in the training data of the two earthquakes

(a) Golcuk, Turkey Image

Training data	Characteristics of the training data	Number of pixels		Ratio of extraction (%)
		total	extracted	
D-1	Debris of collapsed building	3,969	2,187	55.1
D-2	Debris of collapsed building	1,334	815	61.1
D-3	Damage of outside wall with collapsed balcony	1,499	1,062	70.8
U-1	Undamaged building	12,841	2,812	21.9
U-2	Outside wall of undamaged building	3,894	1,186	30.5
U-3	Outside wall of undamaged building	5,464	838	15.3

(b) Chungliao, Taiwan Image

Training data	Characteristics of the training data	Number of pixels		Ratio of extraction (%)
		total	extracted	
D-1	Debris of collapsed wooden building	11,196	6,734	60.1
D-2	Collapsed wooden building	6,729	3,409	50.7
D-3	Damaged buildinig with sound outside wall	27,734	3,351	12.1
D-4	Damaged buildinig with sound outside wall	20,661	5,292	25.6
U-1	Undamaged wooden building	25,033	1,732	6.9
U-2	Roof tiles of undamaged wooden building	6,494	29	0.4
U-3	Undamaged wooden building	11,002	626	5.7
G-1	Green color of woods and leaves	3,025	0	0.0



(a) Golcuk, Turkey (b) Chungliao, Taiwan

Figure 4: Cumulative relative frequencies versus local density of the selected pixels in a 31 x 31 pixel window for the texture analysis

A 31 x 31 pixel window as the minimum size for the Kobe method was used for the texture analysis. Then, to determine the *Rpx* for the texture analysis, cumulative relative frequencies were plotted against *Rpx* for each training data, as shown in Figure 4. The *Rpx* values for the Turkey and the Taiwan images were set to 43% and 30%, respectively, because damaged and undamaged training data could be roughly distinguished by these values. Figure 5 shows distributions of the extracted damage area for these values. The result for the Turkey image is much better than that using the Kobe method, because more pixels representing building debris and collapsed buildings were extracted by this study. In addition, the result for the Taiwan image is slightly better than that using the Kobe method.



(a) Golcuk, Turkey



(b) Chungliao, Taiwan

Figure 5: Building damage distribution obtained by the automated detection using the threshold values in Table 1

4. CONCLUSIONS

Automated detection of damaged buildings was carried out by the image processing of aerial images taken after the 1999 Kocaeli, Turkey and Chi-Chi, Taiwan earthquakes. In the proposed Kobe method, characteristics of the damage to wooden buildings selected as training data were defined on the basis of hue, saturation, intensity, edge intensity and variance of edge intensity, and their threshold values were established. A threshold value for a texture analysis was also determined for estimating the distribution of damaged buildings, after the damaged pixels were extracted. The damage distribution obtained by the Kobe method for the Turkey image was not in particularly good agreement with the actual damage scale, although the result of the Taiwan image was not so bad. We found that it was difficult to use the same threshold values for all the images because of the difference in some factors, such as the influence of sunshine, built environment, and so on. Therefore, the different threshold values for the image characteristics and the texture analysis were estimated for each image. The distribution results for the extracted areas were better than those obtained by the Kobe method.

The distribution of severely damage buildings was estimated by the image characteristics and texture analysis, whose threshold values were empirically determined. In order to establish more general methodologies and threshold values, the authors intend to perform further case studies in the near future.

ACKNOWLEDGMENTS

The digital video images and the HDTV images taken in Turkey and Taiwan were provided by Dr. N. Yoshida of Sato Kogyo Co., Ltd., and the Japan Broadcasting Corporation, respectively.

REFERENCES

Earthquake Disaster Mitigation Research Center, 2000a. Report on the Kocaeli, Turkey Earthquake of August 17, 1999, EDM Technical Report, No.6.

Earthquake Disaster Mitigation Research Center, 2000b. Report on the Chi-Chi, Taiwan Earthquake of September 21, 1999, EDM Technical Report, No.7.

Hasegawa, H., Yamazaki, F., Matsuoka, M. and Sekimoto, I., 2000a. Extraction of Building Damage due to Earthquakes Using Aerial Television Images, Proceedings of the 12th World Conference on Earthquake Engineering, No. 1722, CD-ROM.

Hasegawa, H., Aoki, H., Yamazaki, F. Matsuoka, M. and Sekimoto, I., 2000b. Automated Detection of Damaged Buildings Using Aerial HDTV Images, Proceedings of the IEEE 2000 International Geoscience and Remote Sensing Symposium, IEEE, CD-ROM.

Koga, K., Miura, F. and Nozawa, M., 1998. Image Analysis for Damage Estimation of Building due to Earthquake, Proceedings of the 3rd Symposium on the Mitigation of Urban Disasters by Near-Field Earthquakes, pp. 417-418 (in Japanese).

Ogawa, N. and Yamazaki, F., 2000. Photo-Interpretation of Building Damage due to Earthquakes Using Aerial Photographs, Proceedings of the 12th World Conference on Earthquake Engineering , No. 1906, CD-ROM.

The 21st Asian Conference on Remote Sensing
December 4-8, 2000 Taipei, TAIWAN

VALIDITY STUDY OF EDES APPLICATION TO TAIWAN CHI-CHI EARTHQUAKE DISASTER

Masayuki KOHIYAMA, Haruo HAYASHI, Norio MAKI, Shin HASHITERA
Earthquake Disaster Mitigation Research Center, RIKEN
2465-1 Mikiyama, Miki, Hyogo, 673-0433, Japan
Tel: (81)-794-83-6623 Fax: (81)-794-83-6695
E-mail: kohiyama@miki.riken.go.jp

KEY WORDS: Damaged Area Estimation, DMSP/OLS, Radiance Calibration, Taiwan Chi-Chi Earthquake Disaster, Electric Load

ABSTRACT: The authors are developing the Early Damaged Area Estimation System (EDES), which provides the information as to the estimated impacted areas after any significant earthquake based on nighttime lights observed by the Defense Meteorological Satellite Program (DMSP) Operational Linescan System (OLS). The estimation method is based on the detection of significant reductions or loss of lights in nighttime images following the event, for it can be expected that city lights will observably decrease after a large earthquake. In the 1999 Taiwan Chi-Chi Earthquake Disaster, there was a countrywide power cut due to the damage of the transmission facilities in Chungliao and Tienlun. The post-event image seems to reflect this influence in appearance compared with a pre-event image, but the further investigation is needed because the gain setting of OLS changes along with lunar phase and elevation, and visible-near infrared (VNIR) band imagery only provides relative light intensity. This paper presents a new method to estimate damaged areas based on a radiance-calibrated image and a method to estimate gain and radiance of observed VNIR imagery, and the validity of the estimation result of EDES application to the Chi-Chi Earthquake is discussed using the electric load data before and after the earthquake.

1. INTRODUCTION

In order to support emergency response after an earthquake, we are developing the Early Damaged Area Estimation System (EDES), which disseminates spatial information of estimated damaged areas using Defense Meteorological Satellite Program (DMSP) Operational Linescan System (OLS) nighttime imagery (Hayashi et al., 2000). The estimation method is basically based on significant test of lights decreases more than normal fluctuation. But the sensor gain of OLS is controlled to generate consistent imagery of clouds at all scan angles for air navigation of United States Air Force, and the gain values are not open to the public. OLS visible-near infrared (VNIR) images are observed with different gain values in the different moon situations, and their digital numbers (DNs) only provide relative light intensities in the same observed scene. For all that, it can be assumed that the gain setting is almost the same in a similar moon situation, and we proposed image selection criteria to compare a pre-event image (PreI) and post-event image (PostI) (Kohiyama et al., 2000).
Elvidge et al. (1997) created the stable lights image (SLI), which is a map of VNIR emission sources based on cloud-free observations from 1994 to 1995 under low lunar illumination conditions. We improved the damaged area estimation method using artificial PreI derived from SLI in order to prevent cloud influence in PreI (Kohiyama et al., 2000). Elvidge et al. (1999) produced the radiance calibrated nighttime lights image (RCI), which was assembled observation data of three levels of gain setting from 1996 to 1997. It is revealed that calculated radiance from RCI is highly correlated to population and electric power consumption of states in

the United States because of broader dynamic range and higher expressive power of urban areas than SLI, which has saturated data in many urban areas. In this paper, we propose a new method of damaged area estimation using artificial PreI derived from RCI and a method to estimate gain and radiance of observed VNIR imagery, and verify the estimation result based on the relation of electric load and radiance of nighttime imagery before and after the Chi-Chi, Taiwan Earthquake of September 21, 1999.

2. NIGHTTIME IMAGES BEFORE AND AFTER CHI-CHI EARTHQUAKE

Heavy typhoon clouds covered Taiwan Island around the earthquake onset day, and we chose the image on September 23, 1999 (lunar age: 13.6), which has little cloud influence, to detect lights reductions. As a-month-before images all have cloud contamination, the July-24-1999 (lunar age: 11.4) image was selected as a PreI. DMSP passed over the center of Taiwan (23.8°N) at 20:47 on July 24 and at 20:09 on September 23, respectively. Fortunately, this 38-minute time lag makes lunar elevations of two images more similar. Figures 1 and 2 show the VNIR PreI and PostI ranging from 15°N to 30°N latitude and from 115°E to 130°E longitude. Thermal infrared (TIR) band images are shown in figures 3 and 4.



Figure 1 Pre-event VNIR image
(July 24, 1999)

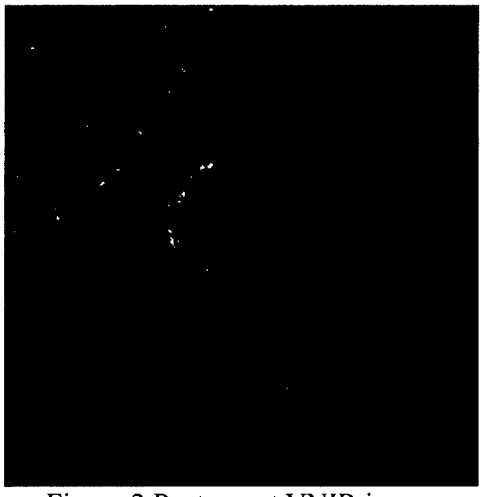


Figure 2 Post-event VNIR image
(September 23, 1999)

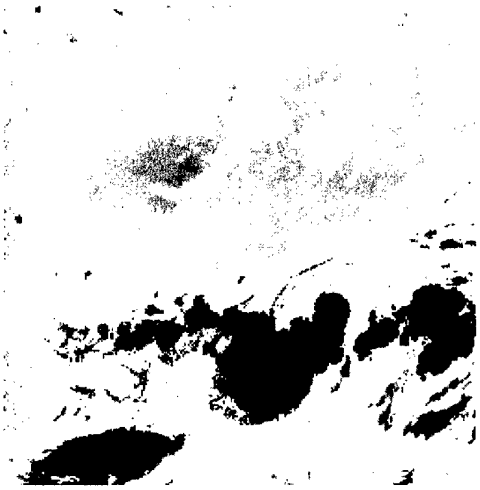


Figure 3 Pre-event TIR image
(July 24, 1999)

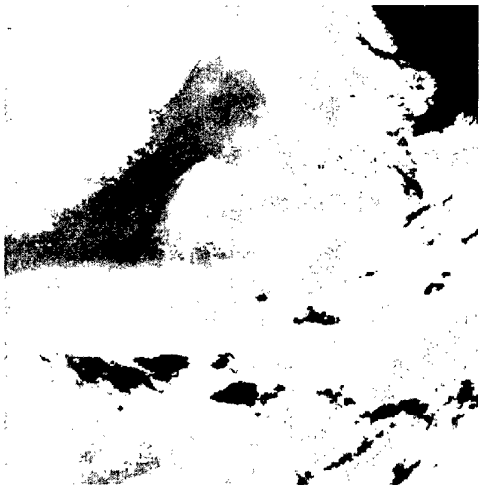


Figure 4 Post-event TIR image
(September 23, 1999)

3. DAMAGED AREA ESTIMATION USING RADIANCE CALIBRATED IMAGE

The relationship between the OLS VNIR band gain G (dB), digital numbers D_V, and observed radiances R (W/cm^2/sr/μm) derived from the preflight sensor calibration are depicted by Elvidge et al. (1999). The following equations are derived from the relationship graph:

$$G = -20 \log_{10} R + a \log_{10} D_V - C_1 \ \text{(dB) where} \ a = \frac{38}{\log_{10} 63} \approx 21.1 \ \text{and} \ C_1 = 143. \quad (1)$$

$$R = D_R^{\frac{3}{2}} \times 10^{-10} \ \text{(W/cm}^2\text{/sr/μm)} \quad (2)$$

Equation (2) shows the relation between RCI DN D_R and radiances R (W/cm^2/sr/μm).
Kohiyama et al. (2000) proposed a method to evaluate a PreI using SLI, but the estimation result corresponds only qualitatively to the result based on an observed PreI. We replicate the method using RCI instead of SLI. The relation D_V-D_R can be derived from equations (1) and (2):

$$D_V = f(G) \cdot D_R^{\frac{30}{a}} \approx f(G) \cdot D_R^{1.4} \ \text{where} \ f(G) = 10^{\frac{G+C3}{a}}, C_3 = 57. \quad (3)$$

We conducted regression analysis to evaluate the D_V-D_R function using the same sample dataset that was selected in the function evaluation using SLI. The regression curve $D_V = 0.171 D_R^{1.4}$ has the correlation factor 0.749, which is greater than that of regression curve using SLI, 0.631. The estimated damaged areas based on the observed PreI, SLI and RCI are shown in figures 5, 6 and 7, respectively. In the figures, red and yellow areas indicate exceeding 97.5 % and 85 % probability points of the normal distribution derived from histograms of D_V differences between PreI and PostI. Gray areas show VNIR band saturation in PostI. Estimated results using RCI resembles to that based on observed PreI better than results using SLI especially around Koahsiung.

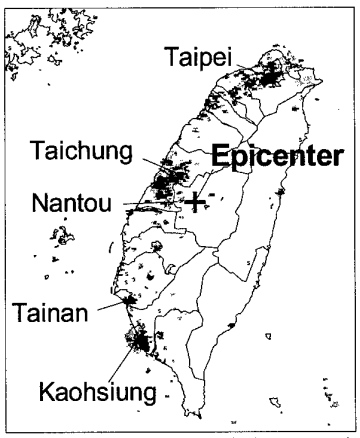


Figure 5 Estimated damaged areas based on observed PreI

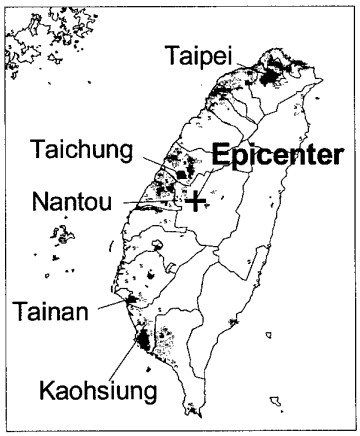


Figure 6 Estimated damaged areas based on SLI

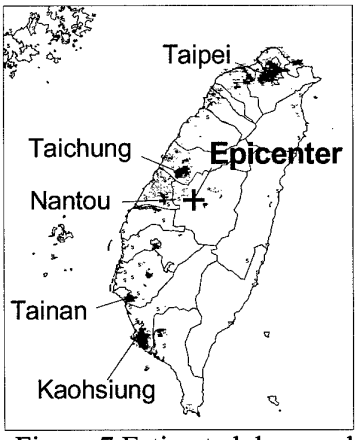


Figure 7 Estimated damaged areas based on RCI

4. ELECTRIC LOAD DATA BEFORE AND AFTER CHI-CHI EARTHQUAKE

We obtained electric load (EL) data in Taiwan on July 23 and from September 21 to 23, 1999. The date of pre-event data is different from that of satellite imagery (July 24, 1999), but the difference is enough short to be assumed negligible. The time series data of three aggregation areas are provided as post-event data. As for pre-event data, the time series data of the total

system load and peak loads of three aggregation areas are provided. We estimated the satellite-crossing-time load of each area based on the peak load ratio of each area. Figures 8 and 9 show the EL data before and after the earthquake. The estimated loads are plotted in Figure 8. The aggregation areas of pre-event data shown in figure 10 are different from those of post-event data shown in figure 11.

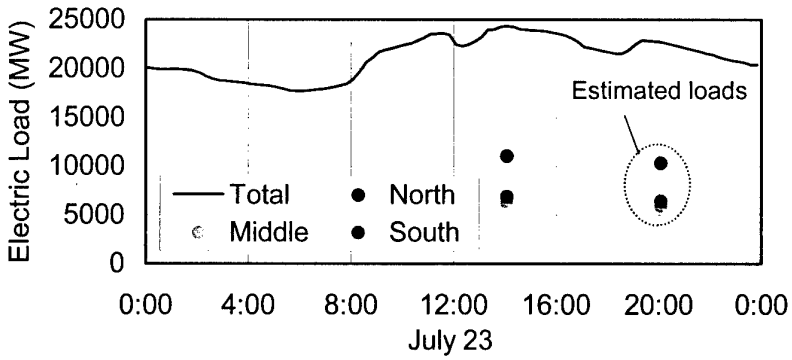


Figure 8 Electric load data on July 23, 1999

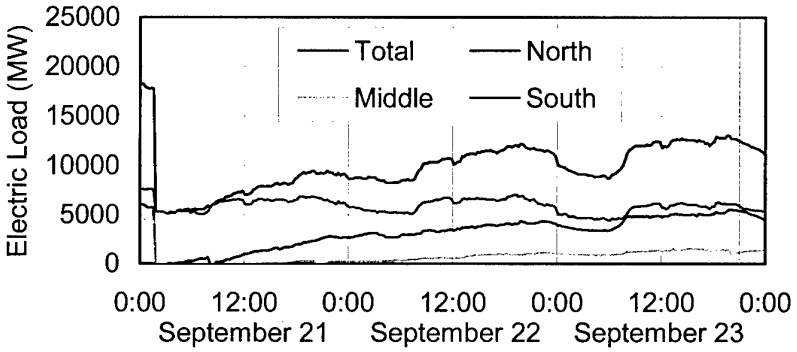


Figure 9 Electric load data from September 21 to 23, 1999

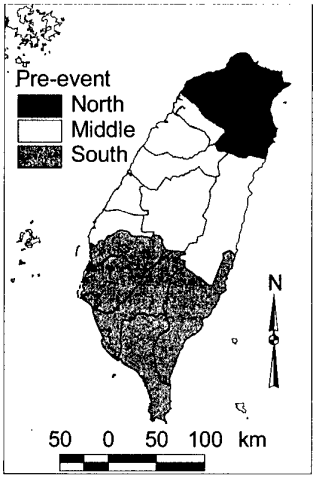


Figure 10 Aggregation areas on July 23, 1999

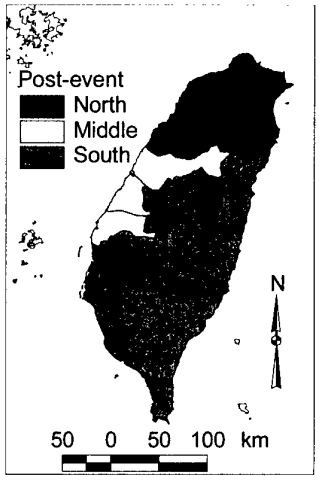


Figure 11 Aggregation areas on September 21 to 23, 1999

5. GAIN AND RADIANCE ESTIMATION METHOD

If the observation year of VNIR image is near RCI creation years, that is, there are few changes of light emission source between observed image and RCI, the gain G can be estimated based on D_R in edges of D_V-saturated areas (that means D_V equals to 63) using the following equation:

$$G = -30 \log_{10} D_R + C_2 \ \text{(dB)}, \quad C_2 = 95. \tag{4}$$

Generally, D_V saturates in highly urbanized cities and D_V starts to saturate in peripherals of cities. The D_R contour lines become longer along with the distance from centers of cities, which should have larger D_R. Thus, D_R in edges of D_V-saturated areas is the largest in pixel number. This D_R can be found as the mode of histogram of D_R in areas where D_V equals to 63. When G is given, R can be expressed by D_V from (1) as follows:

$$R = b(G) \cdot D_V^{\frac{a}{20}} \approx b(G) \cdot D_V^{1.06} \ \text{(W/cm}^2\text{/sr/μm) where} \ \ b(G) = -\frac{G + C_1}{20}. \tag{5}$$

6. GAIN ESTIMATION BEFORE AND AFTER THE EARTHQUAKE

Figures 12 and 13 are histograms of D_R in D_V-saturated areas of the PreI and PostI shown in figures 1 and 2, respectively. The area ranging from 30°N to 40°N latitude and from 129°E to 143°E longitude, which covers Taiwan, is excluded from sample datasets to eliminate the earthquake influence. Conditions: D_V, D_S and $D_R > 0$ are used to select urban areas where D_S is DN of SLI. To eliminate cloud influence, a condition: $D_T > 219$ (corresponding to 20°C) where D_T is DN of TIR band, is also used. Estimated gains are shown in Table 1.

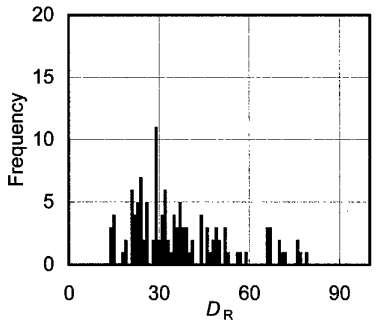


Figure 12 Histogram of D_R in D_V-saturated areas of pre-event image

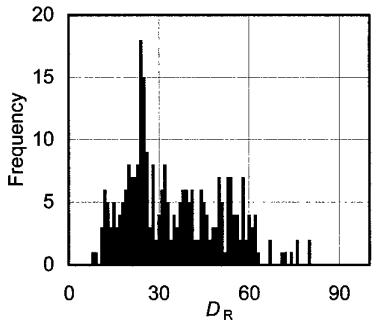


Figure 13 Histogram of D_R in D_V-saturated areas of post-event image

Table 1 Estimated gains of pre- and post-event images

Visible-Near infrared Image	Mode of D_R Histogram	Estimated Gain (dB)
July 24, 1999	29	51.1
September 23, 1999	24	53.6

7. VERIFICATION OF ESTIMATED DAMAGED AREAS

Figure 14 shows the relation between cumulative radiances (CRs) and ELs in Taiwan. CRs directly calculated from RCI are also plotted with pre-event ELs. Evaluated CR of an observed

PreI can be smaller than that of RCI because large radiances cannot be expressed due to D_V saturation. Though the north aggregation area become larger in area after the event, the EL become smaller. There was power cut and restriction of power supply due to the damage of the extra-high voltage transmission facilities in Chungliao and Tienlun. The fact that CR becomes smaller proves the lights decrease in this area. Similarly, the south area become larger in area and the EL is smaller after the event. This indicates there was the reduction or loss of lights in Nantou or Hualien County, which are the increment parts of south aggregation areas. These results support the validity of the estimation results of EDES.

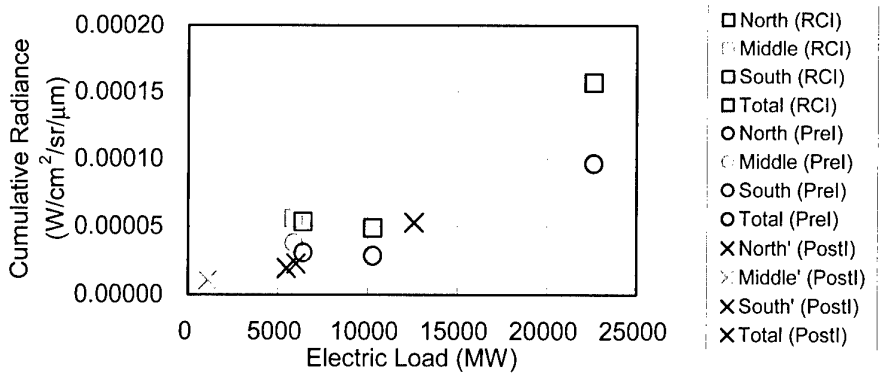


Figure 14 Cumulative radiances and electric loads in Taiwan

8. CONCLUSIONS

Radiance calibrated nighttime image can be used to evaluate an artificial pre-event image better than stable lights image. Estimation method of gain and radiance of VNIR image using radiance calibrated image is proposed. The relation between the cumulative radiance and electric load in Taiwan before and after the Chi-Chi Earthquake reflects the power cut due to the damage of transmission facilities, and this supports the validity of the estimation results of EDES.

ACKNOWLEDGEMENTS

We wish to thank National Oceanic and Atmospheric Administration's National Geophysical Data Center for DMSP/OLS images, SLI and RCI, and also Taiwan Power Company for electric load data before and after the Chi-Chi Earthquake.

REFERENCES

Elvidge, C. D. et al. 1997, Mapping City Lights With Nighttime Data from the DMSP Operational Linescan System, Photogrammetric Engineering & Remote Sensing, Vol. 63, No. 6, pp. 727-734.

Elvidge, C. D., et al., 1999, Radiance Calibration of DMSP-OLS Low-Light Imaging Data of Human Settlements, Remote Sensing of Environment, Vol. 68, pp. 77-88.

Hayashi, H. et al., 2000, International Collaboration for the Early Damaged Area Estimation System Using DMSP/OLS Nighttime Images, Proceedings of IEEE 2000 International Geoscience and Remote Sensing Symposium.

Kohiyama, M. et al., 2000, Development of Early Damaged Area Estimation System (EDES) Using DMSP/OLS Nighttime Imagery, Journal of the Institute of Social Safety Science, No. 2 (in press, in Japanese).

ASIA PACIFIC NETWORK FOR DISASTER MITIGATION USING EARTH OBSERVATION SATELLITE (ANDES) (1) - FOREST FIRE DETECTION

Taro SHINMURA (shinmura@cc.affrc.go.jp)*, Haruo SAWADA**, Izumi NAGATANI***
(Japan)

*, ** World Forest Monitoring Research Team, Forestry and Forest Products Research Institute, Japan (FFPRI), 1 Matsunosato, Kukizaki, Ibaraki, 305-8687 Japan
*, *** Research and Development Applying Advanced Computational Science and Technology, Japan Science and Technology Corporation (JST-ACT)
*** Computer Center of Agriculture, Forestry and Fisheries Research

KEY WORDS: disaster mitigation, earth observation satellite, forest fire, real time system, NOAA

ABSTRACT

The High Resolution Picture Transmission (HRPT) data of Advanced Very High Resolution Radiometer (AVHRR) aboard the National Oceanic and Atmospheric Administration (NOAA) Polar Orbiting Environmental Satellites (POES) are received in Japan and Thailand, and these data are transferred in real time to the computer center of Agriculture, Forestry and Fisheries research in Tsukuba. Real time fire detecting system has been processing AVHRR data covering most of East and Southeast Asian countries and detecting thermal spots since May 2000. Products of this system with Defense Meteorological Satellite Program (DMSP) fire products shows the locations of thermal spots and they are put on the web site. In 2000, the number of thermal spot increased explosively in March and July. In Thailand and neighboring countries, and in Indonesia, the number of thermal spots reached maximum in March and July, respectively. It is because March and July is in dry season severally. Time-series analysis shows that almost all thermal spots disappeared within a day in and around Thailand, and each cluster of the spots consisted less than ten. But in Indonesia, thermal spots sometimes appeared several days in same position and clusters of such spots consisted more than ten. The former pattern shows the thermal spots are controlled fire, and the latter one is potentially uncontrollable or wild fire.

1. INTRODUCTION

Severe natural disasters are often cause by global climate changes and they are becoming worse, and damage of human activities is increasing. Flooding, drought and big forest fire are the main natural disasters in East and East Asian countries. Therefore, It is strongly required to establish systems for mitigating these natural disasters. ANDES project supported by ACT-JST and started since 1998 aims to develop the operational systems for mitigating the disasters. In this paper, as parts of this project, Tropical Rain Measuring Mission (TRMM) real time system and real time fire detecting system using NOAA/AVHRR data and DMSP/OLS data and its products are introduced, and analysis of fire products are discussed.

2. ANDES PROJECT

ANDES project (http://www.affrc.go.jp/ANDES/) is an international project on research and development applying advanced computational science and technology, cooperative project of Forestry and Forest Products Research Institute, National Institute of Agricultural Environment Study, Meteorological Research Institute, Computer Center for Agriculture, Forestry and Fisheries Research, National Space Development Agency and Japan Science and Technology Corporation (JST). The objective of this project is to detect and inform disasters in Asia-Pacific region as soon as possible by using satellite data and high-capacity network systems. The following four study themes are executed, 1) to develop a real time archiving and delivering system of satellite data, 2) to detect fire and create fire risk map for forest fire mitigation, 3) to detect flood and create drought risk map for agricultural disaster mitigation, 4) to evaluate the data of TRMM for heavy rain disaster mitigation.

The main satellite data used for this project are NOAA/AVHRR and GMS for forest fire and agricultural disaster, DMSP/OLS for forest fire and TRMM for heavy rain. High-resolution satellite data are also used for observing the situation of the study area according to the necessity. The NOAA/AVHRR data are received in Japan and Thailand and these data are transferred in real time to the computer center of Agriculture, Forestry and Fisheries research in Tsukuba. The DMSP/OLS data and TRMM data are also transferred to the center from USA through the network. These data are processed and archived in the Satellite Image Database (SIDaB) system (http://rms1.agsearch.agropedia.affrc.go.jp/menu_en.html), which is managed by the computer center. As for the NOAA/AVHRR, the nighttime data are used for detecting the hot spot and the daytime data are used for monitoring vegetation condition in global

scale. The SIDaB system automatically generates both the weekly composite images and the ten-days' composite image of East Asia region. From the ten-days' composite image, we analyze the vegetation condition and create the terrain images for being used with other disaster products as the base image. The data of global geographic information in Asia Pacific area, such as the Digital Chart of the World (DCW), the global Digital Elevation Model (DEM: 30 arc second), the FAO digital soil maps and meteorological data are also used for producing disaster maps and risk maps. This project aims to develop the operational systems for mitigating the disasters. Therefore, the project has close relations with related institutions in other countries, especially with governmental disaster management units and network specialties.

3. ANDES TRMM REAL TIME SYSTEM

TRMM is a joint mission between NASA and the National Space Development Agency (NASDA) of Japan designed to monitor and study tropical rainfall and the associated release of energy that helps to power the global atmospheric circulation shaping both weather and climate around the globe. Observatory carries five instruments. It includes the first space-borne Precipitation Radar (PR), the TRMM Microwave Imager (TMI), a Visible and Infrared Scanner (VIRS), a Cloud and Earth Radiant Energy System (CERES), and a Lightning Imaging Sensor (LIS).

SIDaB system has been receiving real time PR and TMI data from Goddard Space Flight Center (GSFC)/NASA since Oct 1999 using highly advanced network link. This link mainly consists of Asia-Pacific Advanced Network (APAN) nodes (NASA Integrated Services Network (NISN) => TransPAC =>Inter-Ministry Research Information network (IM-net) => Ministry of Agriculture, Forestry and Fisheries Information Network (MAFFIN)).

This system processes heavy rain images (using TRMM Science Data and Information System TSDIS Orbit Viewer) and images are renewed in every thirty minutes (http://betleh.cc.affrc.go.jp/~shinmura/trmm/). SIDaB system archives heavy rain images and past images can be easily referred. Figure 1, a) and b) show precipitation images produced by this system. Precipitation on the sea is difficult to be measured by ground radar, but TRMM measures precipitation for both land and sea area in higher resolution (4km) as Figure 1, c). Such information will help weather forecasting and mitigation of torrents on the sea and island, and in the area without highly advanced meteorological equipments

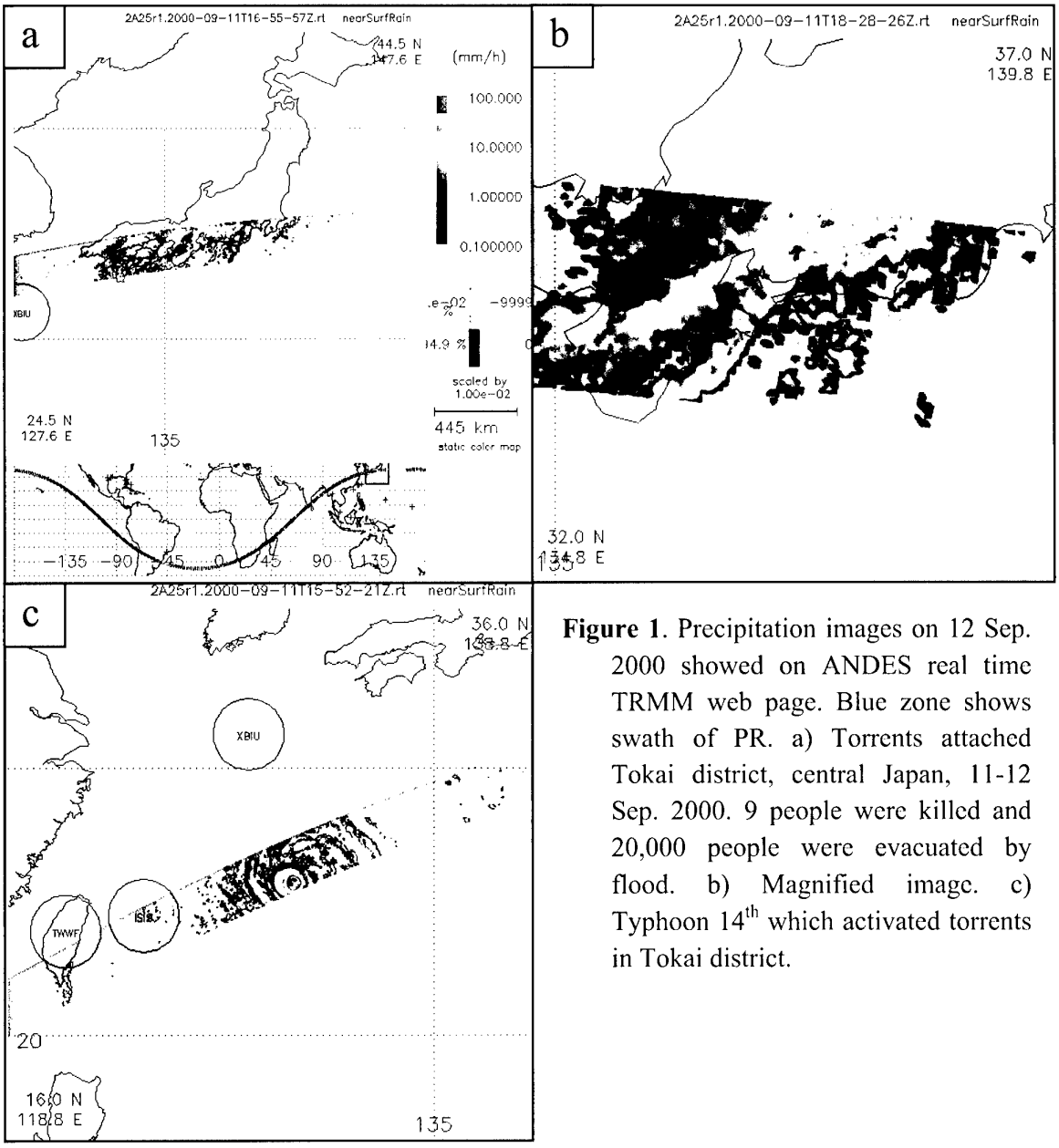


Figure 1. Precipitation images on 12 Sep. 2000 showed on ANDES real time TRMM web page. Blue zone shows swath of PR. a) Torrents attached Tokai district, central Japan, 11-12 Sep. 2000. 9 people were killed and 20,000 people were evacuated by flood. b) Magnified image. c) Typhoon 14th which activated torrents in Tokai district.

4. FOREST FIRE DETECTING IN EAST ASIA

In the Southeast Asian region, wild fire and artificially made fire for farming sometimes became large and uncontrollable, and damaged human activities and health. Information for such fire is needed as soon as possible. NOAA/AVHRR data is useful for fire detecting because NOAA POES frequently and widely observe ground. The data is processed and thermal spots which are possible fire are detected in our system. NOAA/AVHRR HRPT data received at Asian Institute of Technology (AIT), Thailand, covering this region is transferred in real time to the computer center of Agriculture,

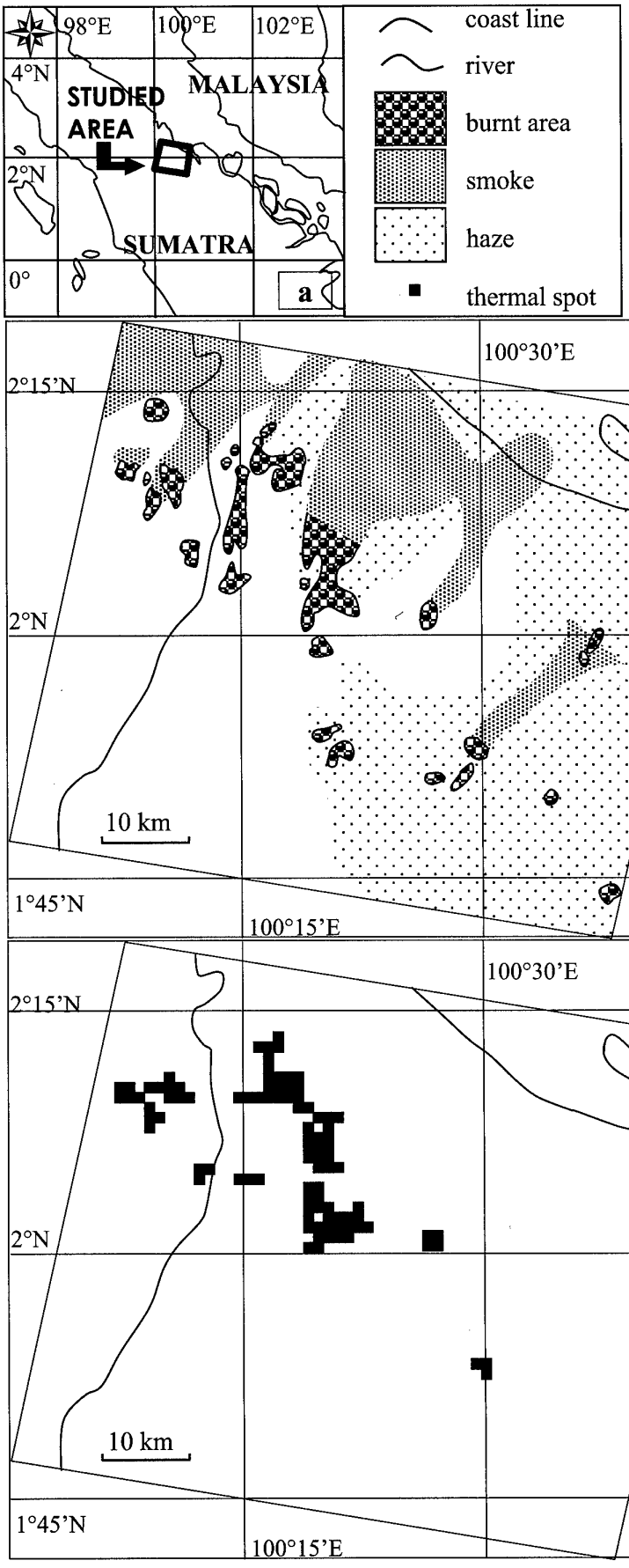


Figure 2. Images of big fire monitored by 2 earth observation satellites in Riau province in Sumatra, Indonesia, July 13, 2000.

a) Legends and index map.

b) Distributions of burnt area, smoke and haze cause by big fire recognized by using SPOT image. Some burnt areas eject smoke and they still burns or smolders. The other areas are already ceased eject smoke and they are hot but does not burn. Smokes spread forward NNE direction and this shows wind direction. Right half are covered with haze which may be produced another areas in Sumatra.

c) Distributions of thermal spots detected by the ANDES system. Most of all areas which eject smoke (in picture b and meaning "burns") are detected as thermal spots.

Forestry and Fisheries research in Tsukuba through highly advanced network links (Science Information Network (SINET) and IM-net). Shiogama, Yokohama and Ishigaki stations in Japan receive NOAA/AVHRR HRPT data and send through MAFFIN network to the computer center. These data covering most of East and Southeast Asian countries, are processed by the real time fire detecting system. Mainly nighttime data is used for detecting thermal spots, because channel 3 data of AVHRR is not affected by day light, cloud and heated surface by the sun directly. This system uses simple threshold as "T3 > 310K" for detecting thermal spots and this was verified by comparing with high-resolution images of SPOT satellite (Figure 2). AIT data just covers Indonesia, in which haze sometimes caused by big fire and damages closing area. Although this area is often covered with noises which are made at the beginning of receiving and these makes pseudo thermal spots, they are removed by geometrical method in the system.

In the system, both thermal spots of NOAA/AVHRR and fire products of DMSP/OLS data are showed with SPOT/vegetation ten-day's composite using LMF method (Sawada, 1999). Thermal spots sometimes include remanent noises and show heated point which has remanent heat of sun light. DMSP/OLS detects only light and this supports AVHRR thermal spots data for separating these pseudo thermal spots. Real time fire products process three kinds of satellites data and the final images are put on the ANDES web site early next morning. Real time fire detecting system does not only detect thermal spots but also checks time-series of the spots. When a thermal spot is detected on a same place (accuracy is about 1km), the system records and informs by email where and how long the continuous spot exists. Because continuous thermal spots mean big or uncontrolled fire. In fact, in July 2000, in Sumatra, Indonesia, number of detected thermal spots rapidly increased, and many spots continued (5 days in maximum). As shown in figure 2, the area where continuous thermal spots sited, spots distributes as cluster and it consists of more than ten spots, and big fires occurred and they made haze and smokes over several ten kilo meters. On the contrary, in March 2000, in and around Thailand, the number of thermal spots reached maximum. But almost all thermal spots disappeared within a day, and they distributes separately. This means fires in this region were almost controlled and they did not grew dangerous fires.

REFERENCES

Sawada, Y., Mitsuzuka, N., Sawada, H., 1999. Classification of vegetation types by time series data analysis of vegetation index. Proceedings of the 27th conference of Remote Sensing Society of Japan, pp.73-74.

A NEURAL NETWORK MODEL FOR ESTIMATING SURFACE CHLOROPHYLL AND SEDIMENT CONTENT AT THE LAKE KASUMI GAURA OF JAPAN

Pranab Jyoti BARUAH
Hydraulic and Hydrodynamic Laboratory , Institute of Engineering Mechanics and Systems
University of Tsukuba, Tsukuba, Ibaraki 305 8573, Japan
Tel : +81-298-502589, Fax: +81-298-502572, E-MAIL: p.j.baruah@nies.go.jp

Masayuki TAMURA
Information Processing and Analysis System, Social and Environmental Systems Division
National Institute for Environmental Studies, 16-2 Onogawa ,Tsukuba 305 0053, Japan
Tel : +81-298-502479, Fax : +81-298-502572, E-MAIL: m-tamura@nies.go.jp

Kazuo OKI
Biological and Environmental Information Laboratory, Graduate School of Agricultural and Life Sciences
University of Tokyo, Yayoi 1-1-1, Bunkyo-ku, Tokyo 113 8657, Japan
Tel : +81-3-5841-8101, E-MAIL : agrioki@m.ecc.u-tokyo.ac.jp

Hitoshi Nishimura
Hydraulic and Hydrodynamic Laboratory , Institute of Engineering Mechanics and Systems
University of Tsukuba, Tsukuba, Ibaraki 305 8573, Japan
Tel/Fax : +81-298-535254, E-MAIL: nishimura@surface.kz.tsukuba.ac.jp

KEYWORDS: Neural Network, Chlorophyll-a, Suspended Solid, Back propagation, CASI.

ABSTRACT: Two important parameters for monitoring water quality of inland water bodies are the concentrations of Chlorophyll a (Chl.a) and Suspended Sediment (SS) in the surface water. Due to the optically complex nature of inland water with high turbidity and dissolved organic matter this task becomes quite difficult in comparison to Case-I water. Neural Network have proven its ability successfully in modeling a variety of geophysical transfer function. A Back-Propagation Neural Network (BPNN) model with one hidden layer is employed for modeling the transfer function between the chlorophyll a and sediment concentrations and in situ upward reflectance radiance taken with a spectro-radiometer at the Lake *Kasumi Gaura* of Japan. The inputs to the network model are the in-situ upward radiance taken all over the Lake *Kasumi Gaura* and the outputs are the concentrations of Chl.a and SS. The trained and validated model is used to get the spatial distribution of Chl.a and sediment concentrations at the lake *Kasumi Gaura* using CASI(*Compact Airborne Spectrographic Imager*) imagery. The Neural Network model was able to model the transfer function to a much higher accuracy than multiple regression analysis. In case of Chl.a estimation, the RMS error for the neural network was 8.29μg/l, whereas the same for regression analysis were 26.498.29μg/l.. However, in case of estimation of SS by regression RMS errors was 3.94mg/l, whereas by Neural Network RMS error came out to be 2.90mg/l..

1. INTRODUCTION :

Lake Kasumi Gaura is the second largest lake in Japan located about 60 km northeast of Tokyo.. It is a monomictic lake with average depth of about 4 m.. It faces acute problems of eutrophication and heavy sedimentation every year. The lake houses several important cities/towns around its bank which effect or are being effected by the water quality of the same. Keeping in view this very important fact and other, it becomes necessary to parameterize and estimate the water quality parameters as accurately as possible for effective and correct investigation of the present situation and possible solutions. The main factors effecting the water quality of lakes include the concentrations of Chlorophyll-a(Chl.a) and Suspended Solid(SS). This study tries to find a way to effectively estimate these two water quality parameters in the

Lake Kasumi Gaura. Present day remote sensing makes it possible to monitor the Chl.a and SS concentration in wide spatial scale. Oki(1997) have developed spatial concentration maps for Chl.a and SS in Lake Kasumi Gaura using Landsat-TM and regression analysis. The authors believed that, conventional techniques like regression can not model the transfer function effectively in complex waters. The study is a result to eliminate this very drawback.

This study employs Neural Networks (NN) as a tool for effectively model the transfer function of Chlorophyll and Suspended Solid in the water of Lake Kasumi Gaura. The model is then is used in CASI image taken at the lake to get the picture of Chl.a and SS distribution.

2. IN SITU DATA:

Water Quality samples for concentrations of Chl.a and SS were collected in the waters of Lake Kasumi Gaura by Oki(1997) for a total of 29 locations spread over the lake. Out of these 29 data set, data for 20 locations were collected on 10th Sept., 1993, 6 locations were collected on 22nd of April, 1994 and the data at remaining 3 locations were collected on 5th of September, 1996, coinciding with the CASI flight over the lake. Measurements of water leaving radiance reflectance at the water surface were also done at all the 29 locations with a spectro-radiometer.

3. NEURAL NETWORKS:

3.1 Background:

The idea of Neural Networks (NN) came from the basic structure of functioning of the human brain. In the modern field of science and engineering, NN has strengthened their importance with numerous applications ranging from pattern recognition, fields of classification etc. There are different kind of NN available depending on the task to be performed. In this study the neural network used is *Multi layer Feed-Forward* type employing back-propagation of Error, simply called *Back-Propagation Neural Network.(BPNN)*. Fig.1 Shows the fundamental building block for a back propagation network.. A set of inputs is applied is applied to the network. Each of these is multiplied by a weight, and the products are

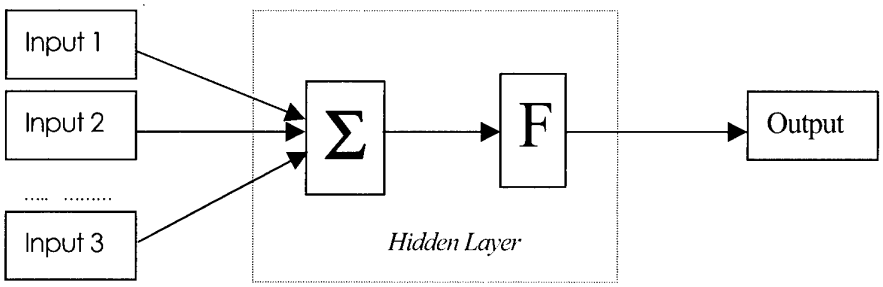


Figure 1 Artificial Neuron with Activation Function.

summed up. The summation is termed as NET and must be calculated for each neuron(the hidden layer/output layer nodes). After NET is calculated, an activation function F is applied to modify it, thereby producing the signal OUT. This output OUT is compared with the target output provided to the network and the difference(error) is back-propagated to modify the weights in the network. This

process of *learning* continues until the error minimizes to a desired value. The present form of back propagation algorithm is developed by Rumelhart et al.(1986).

3.2 Procedure of Study:

This section gives an outline of the general procedure to carry out the modeling with neural networks.

I. The NN model in this study have several inputs of upward radiance reflectance and a single output of either Chl.a or SS concentration. Out of the 29 data set available, 20 of them is selected as training data to the network and the rest is used as validation data for examining the performance of the *trained* model. Selection of training data is done by first arranging the entire data set in decreasing order of Chl.a (or SS) concentration and then, starting from the top, picking up every two values and leaving one as validation data.

II. Upward radiance reflectance data taken with the spectro-radiometer is available for the wavelength range [400-848]nm with an interval of 2nm. Six sets of combinations of wavelengths that best represent the concentration of Chl.a and SS are selected as listed below. Input and validation data set for all the 6 combinations are created.

Combination set 1:	440 674 676 700 724 726	[nm] : 6 inputs (reflectance)
Combination set 2:	440 675 700 725	[nm] : 4 inputs (reflectance)
Combination set 3:	440 675 676 700	[nm] : 4 inputs (reflectance)
Combination set 4:	675 676 700 725	[nm] : 4 inputs (reflectance)
Combination set 5:	442 444 446 674 676 678 700 720 740 760	[nm]: 10 inputs (reflectance)
Combination set 6:	442 446 452 672 678 682 700 720 740 760	[nm]: 10 inputs (reflectance)

III. The NN model in this study uses only one hidden layer. It has been proven that any function, no matter how complex, can be represented by a neural network with one hidden layer (Masters, 1993). The activation function (F) used is the *binary sigmoid* (Fig.2) with slope parameter 'g'. All the data output data are scaled in the range [0.1,0.9] to match with the range of activation function, [0,1]. Training of the NN model is performed on data for each Combination set with varying number of hidden layer nodes to find the best one giving faster learning and better convergence. Training rate is varied as the training progresses starting with a value of 0.3. The training error is measured with study *Mean Square Error (MSE)* [Eqn.1]. It is found that, the NN overfits the training values if training is performed until the MSE flattens down. Hence, the RMS (root-mean-square) error of the training testing set (in our case, the validation set) is calculated in each pass of

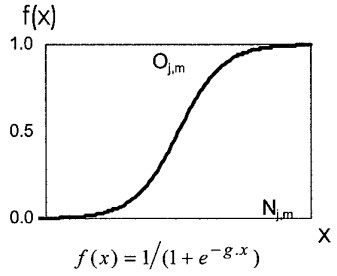


Figure 2. Binary Sigmoid Function

$$MSE = \frac{1}{n}\sum_{i=0}^{n-1}(t_i - o_i)^2 \qquad (1)$$

t_i: target output
o_i: network output
n: training iteration.

training and the training is terminated as soon as it reaches the minimum. Slope parameter 'g' is kept

constant throughout the training at 3. Finally, the trained model is subjected to the validation data set.

4. RESULTS AND APPLICATION:

4.1 Regression Analysis:

To compare the ability of neural networks with conventional methods of water quality estimation Multiple regression analysis is performed on all the combinations of data. The dependent variable is either the concentration of Chl.a or SS and the independent variable being the upward radiance reflectance values used as training data in case of NN. Also, the coefficient of determination (R^2) and the error in the dependent parameter estimate [the root mean square (RMS) error in this study] have been calculated for both the regression and NN.

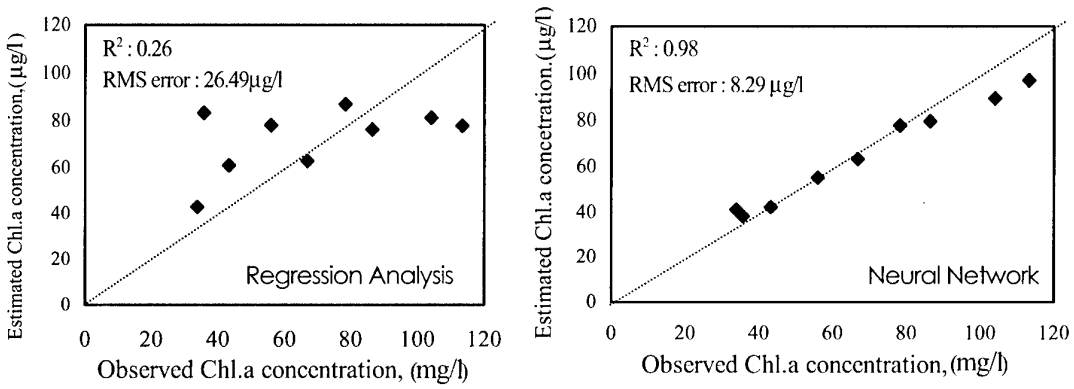


Figure 3. Observed .vs. Estimated Chl.a concentration by Regression Analysis and Neural Network

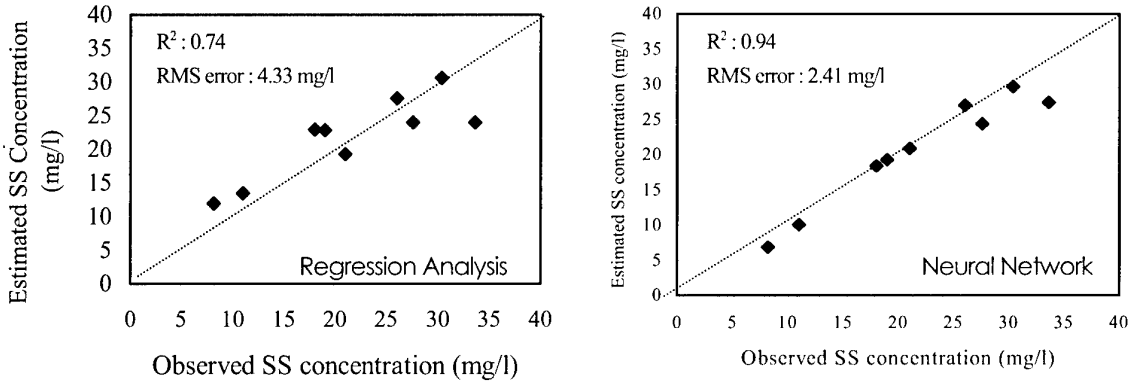


Figure 4. Observed .vs. Estimated SS concentration by Regression Analysis and Neural Network

As a whole for all the combinations, while estimating Chl.a, the RMS error for regression comes out to be 3-4 times than that of NN. However, the difference of RMS errors was not much in case of estimation of SS and NN showing up with better performance. The results (for all combinations) show that, the NN could not predict the high Chl.a concentration quite satisfactorily as expected. This may be due to limited

number of data set used in this study or because of the complex behavior of the lake water containing other components contributing to the lake water color such as Chromophoric Dissolved Oxygen Material(CDOM). Combination set 6 and Combination set1 gave best results in predicting the Chl.a and SS concentration respectively for the validation data set.

The trained and validated NN model of Combination set 6 is selected for application to CASI data. Figure 3 and figure 4 shows the NN and regression results for the same with corresponding RMS error and R^2 values.

4.2 Application to CASI image:

CASI (Compact Airborne Spectrographic Imager) image of lake Kasumi Gaura was taken on 5th of Sept, 1996. It has 96 layers(bands) with spatial resolution of 5m x 3.5 m. 1 CASI DN = 0.001SRU. Data for 10 layers, namely 6, 7, 8, 47, 48, 49, 52, 55, 59 and 62 are sorted out for estimation of Chl-a and SS, as their central wavelengths coincide with that of the Combination set 6 selected for application. To convert the radiance values to reflectance values (to apply the NN model), regression is done between radiance and reflectance values for 3 locations over the lake (plus one on the ground/concrete), the in-situ data for which was taken on the same as CASI. With this regression all the radiance values are converted to corresponding reflectance for input to the NN model. Mean radiance of a 5 x 5 pixel area in the CASI image is taken for representation of each point. Figure 6 in the next page show the spatial distribution of Chl.a and SS concentration in the lake Kasumi Gaura estimated by the NN model.

In a same similar manner, the NN model can be applied to other satellite sensor images such as Landsat TM to get a better and bigger picture of distribution of Chl-a and SS at the lake site.

5. CONCLUSION:

The Neural Network model was able to model the transfer function to a much higher accuracy than multiple regression analysis as expected. The performance of the NN model varies with varying number of hidden layer nodes. The model could not represent the higher values of Chl-a satisfactorily. For a more effective and accurate model to represent the water quality of the site under investigation, the author proposes collection of larger data set including measurements of other primary components believed to contribute to the lake water color such Chromophoric dissolved oxygen material(CDOM) in coincidence with overpass of modern satellite sensor(such as Landsat TM or SeaWIFS).

References:

Keiner, L.E. and Yan, X.H., 1998. A Neural Network Model for Estimating Sea Surface Chlorophyll and Sediments from Thematic Mapper Imagery. Remote Sensing of Environment, Elsevier, 66:153-165.

Masters, T, 1993. Practical Neural Network Recipes in C++. Academis Press, 491pp.

Oki, H, 1997. Study of Lake basin Land use and its Impact on Lake Water Quality. Doctoral Thesis, University of Tsukuba Library, 141pp.

Rumelhart, D., Hinton, G.E., and Williams, R.J., 1986a. Learning Representations by back-propagating errors. Nature (London), 323, pp533-536.

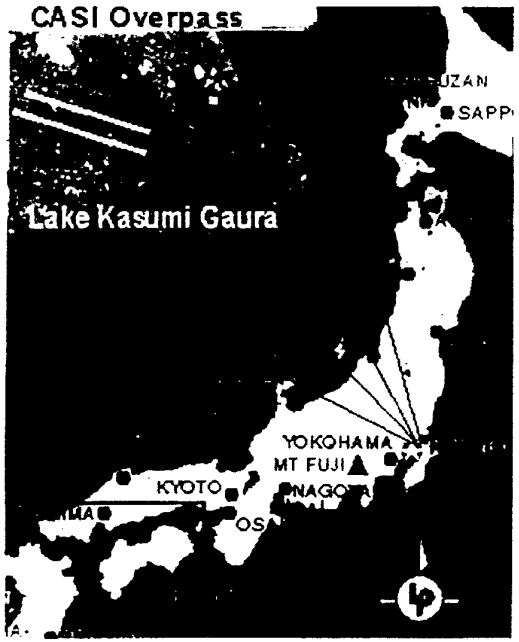


Figure 5. Location of Lake Kasumi Gaura showing the CASI Overpass (two white lines on the lake)

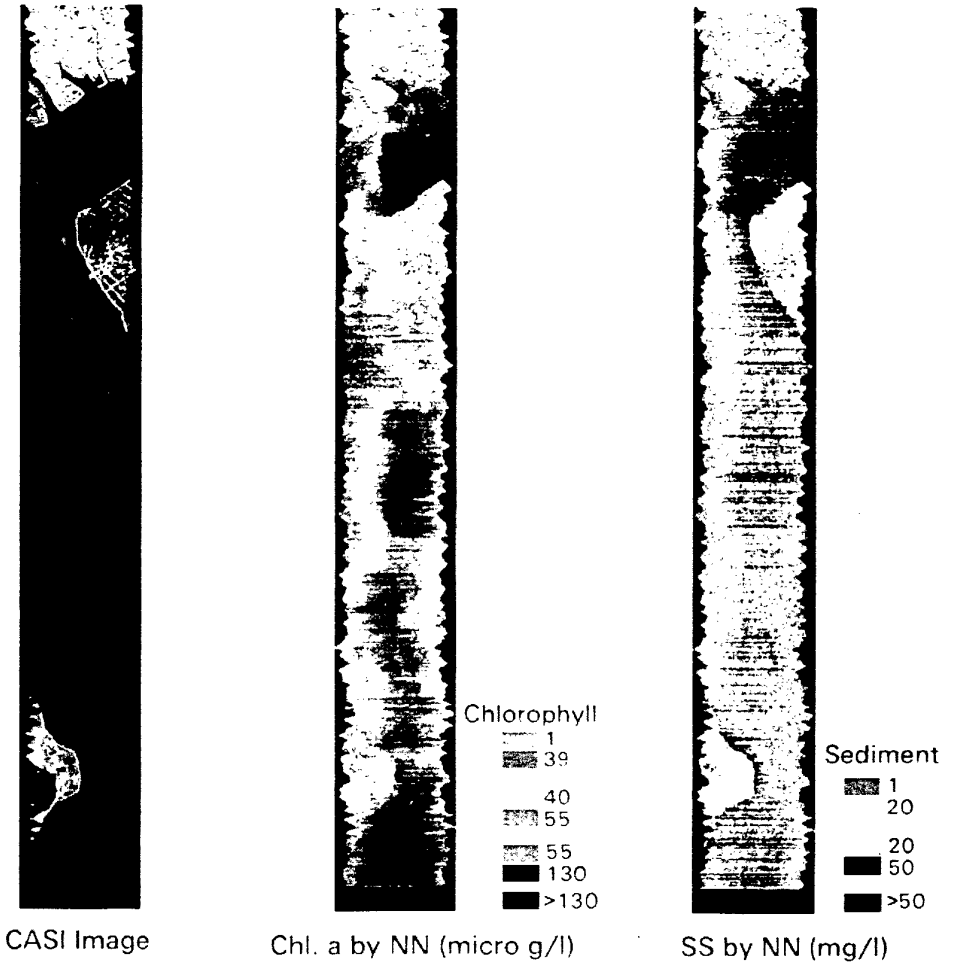


Figure 6. Estimated Chl.a and SS concentration by Neural Network at the Lake Kasumi Gaura using CASI Image.

URBAN IMAGE ANALYSIS USING ADAPTIVE RESONANCE THEORY

Supoj MONGKOLWORAPHOL, Yuttapong RANGSANSERI and Punya THITIMAJSHIMA

Department of Telecommunications Engineering, Faculty of Engineering
King Mongkut's Institute of Technology Ladkrabang, Bangkok 10520
Tel: (66-2) 326-9967, Fax: (66-2) 326-9086
E-mail: Supoj.mongkolworaphol@compaq.com, {ktpunya, kryuttha}@kmitl.ac.th
THAILAND

KEY WORD: Urban Image Analysis, Adaptive Resonance Theory, Neural Network

ABSTRACT: In this paper multispectral images of an urban environment are analyzed and interpreted by means of a neural network approach. In particular, the advantages found by using Adaptive Resonance Theory network of the data are shown and commented. We used the ART2 structure accepts floating-point data, so that each input can be for each pixel directly the vector of the gray level values at each band. This choice is due to the attempt to simplify algorithm as much as possible. Experiments carried out with JERS-1 images will be given.

1. INTRODUCTION

The analysis of urban structure is gaining more and more interest, due to the fact that this kind of study may be useful for a number of applications, e.g. settlement detection, population estimation, mapping of land use and changes, assessment of urban activities on the landscape. In particular, remote sensing has a growing importance in this field; indeed, it gives the possibility to observe at difference scales and without interference the urban environment at rates that are clearly impossible for a study on the ground. Computer-aided classification of earth terrain based on the segmentation of remotely sensed image, e.g., Landsat, JERS-1, ADEOS, and SPOT, has provided an alternate, effective method for the above mapping purpose. Adaptive Resonance Theory (ART) architecture is neural networks that carry out stable self-organization of recognition codes for arbitrary sequence of input pattern. Adaptive Resonance Theory first emerged from an analysis of the instabilities inherent in feed forward adaptive coding structure (Grossberg, 1976a, 1976b). More recent work has led to the development of three classes of ART neural network architecture, specified as system differential equations: ART1 and ART2 (Carpenter, 1991). By especially ART2 self-organizes recognition categories for arbitrary sequences of either binary or analog inputs. ART2 is designed to perform for continuous-valued input vectors the same type of tasks as ART1 does for binary input vectors. The differences between ART2 and ART1 reflect the modifications need to accommodate patterns with continuous-valued components. The more complex F1 field of ART2 is necessary because continuous-valued input vector may be arbitrarily close together. The F1 field in ART2 includes a combination of normalization and noise suppression, in addition to the comparison of the bottom-up and top-down signals needed for the reset mechanism.

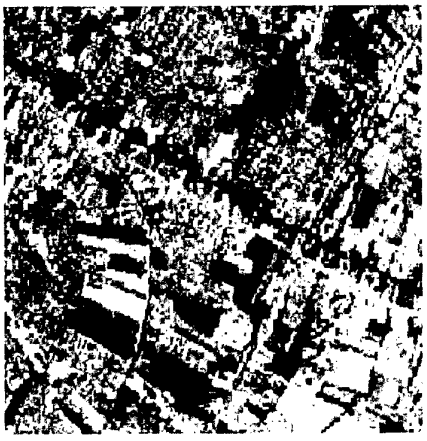


Figure 1: ADEOS image of. Bangkok area.

2. THE ART2 NEURAL ALGORITHM

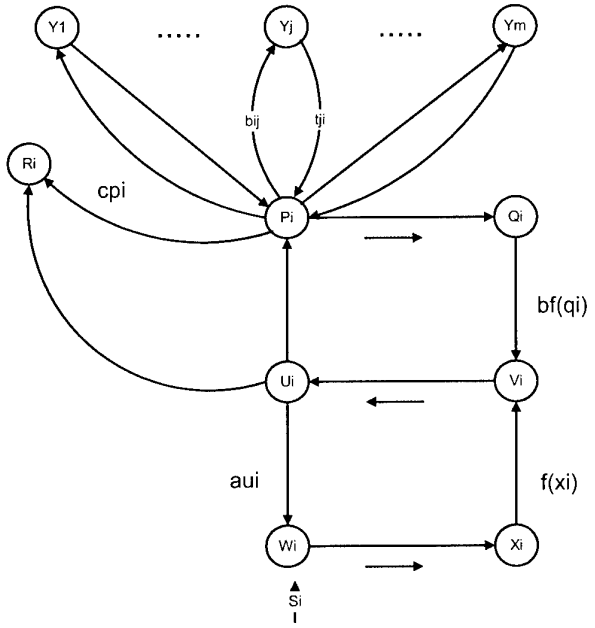


Figure 2: Typical ART2 architecture.

The ART2 architecture (Carpenter, 1991), (Fausett, 1994), which consists of two main modules: the attentional and the orienting modules. The attentional module is further divided into two fields: an input representation field F1 and a category representation field F2. F1 consist of (w, x, v, u, p, and q), each having n neural. The F2 field contains only one layer, which is denote by **Y** and serves as a competitive layer. There are top-down and bottom-up full connections between F1 and F2. Pattern prototypes are to be preserved on these connections. The input signal is S = (S1,...,Si,...,Sn) continues to be sent while all of the sections to be described are performed. At the beginning of a learning trail, all activation is set to zero. The computation within the F1 layer can be thought of as originating with the computation of the activation of unit Ui (the activation of unit Vi normalized to

approximately unit length). Next, a signal is sent from each unit Ui to its associated units Wi and Pi. The activation of units Wi and Pi are then computed. Unit Wi sum the signal it received from Ui and the input signal Si. Pi sum the signal it receives from Ui and the top-down signal it receives if there is an active F2 unit. The activation of Xi and Qi are normalized version of the signal at Wi and Pi. An activation function is applied at each of units before the signal is sent to Vi. Vi then sums the signals if receives concurrently from Xi and Qi; this completes one cycle of updating the F1 layer.

The activates of the F1 layer are formulated, respectively, as

$$u_i = \frac{v_i}{e+\| V \|}, \quad x_i = \frac{w_i}{e+\| W \|}, \quad q_i = \frac{p_i}{e+\| P \|},$$
$$w_i = s_i + au_i, \quad p_i = u_i + dt_{Ji}, \quad v_i = f(x_i) + bf(q_i), \tag{1}$$

$$ri = \frac{ui + cpi}{e+\| U \| + c \| P \|} \tag{2}$$

After the activation of the F1 units have reached equilibrium, the Pi units sent their signals to the F2 layer, where the winner-take-all competition chooses the candidate cluster unit to learn the input pattern. The units Ui and Pi in the F1 layer also send signal to the corresponding reset unit Ri. The reset mechanism can check for a reset each time it receives signal from Pi and Ui, which aggregates the activities of Pi and Ui and transmits the result to the vigilance parameter. Vigilance parameter then decides whether or not a reset signal is emitted to the layer **Y** in field F2. There are also gain control units in the network. They normalize activity patterns over layers. (Fausett , 1994)

We propose an unsupervised approach to the neural classification of the source images. This choice is due to the attempt to simplify as mush as possible the detection of the urban features by the automatic analysis of the data. Therefore, we look for competitive algorithms suitable for the task. We need neural networks able to aggregate data in consistent clusters. The ART2 neural algorithm respectively, as

Step0. Initial parameter
Step1. Perform the specified number of training
Step2. For each input vector update F1unit
Step3. Update F1 unit activation again
Step4. Compute signals to F2 units
Step5. Check for reset
Step6. Perform the specified of learning iterations
Step7. Update weights for wining unit
Step8. Update F1 unit again
Step9. Test stopping condition for weight update
Step10. Test stopping condition for number of training

3. EXPERIMENTAL RESAULTS



Figure 3: Classification result of the area in Fig 1.

The classification was applied to a three-band image of Bangkok (Fig. 1). The image was recorded by the ADEOS satellite. We applied the previously presented neural classification algorithm to this data set by OPS image the result are completely satisfying. The neural classification starts by applying an ART network looking for spectral aggregation of the pixel. The three-band data are aggregate an input vector in order to match the ability of ART networks to discriminated against different pattern. Fig. 3 presents spectral classification result obtained by the ART2 algorithm and we found very difficult to tune the network parameters to obtain satisfying result.

4. CONCLUSION

This work simplifies and completes the ART approach to remote sensing data analysis introduced in (Silva, 1997). We apply the methodology to urban environments and multiband data introduce a clustering step to solve class redundancy and high lightening the advantages and disadvantages of data analysis. The results presented, corresponding to a part of data, are satisfying, and it can be using to analysis another image for classification by computer-aided.

5. ACKNOWLEDGEMENT

The authors wish to thank the National Research Council of Thailand (NRCT) for providing the satellite image data

REFERECNES

Carpenter A. G., Grossberg S. and Rosen. B. D., 1991. ART 2-A:, an adaptive resonance algorithm for rapid category learning and recognition. neural network, (4), pp. 493-504.

Fausett L., 1994. Fundamentals of Neural Network Architecture Algorithm and Application. Prentice-Hall.

Silva S. and Caetano M., 1997. Using Artificial Recurrent Neural Nets to Identify Spectral and Spatial Pattern for Satellite Imagery Classification of Urban Area. In: Neurocomputation in Remote Sensing Data Analysis, I. Kanellopoulos et al. (eds.), Springer: Berlin, pp. 151-159.

COLOR IMAGE ENHANCEMENT BASED ON SEGMENTATION REGION HISTOGRAM EQUALIZATION

Sakreya. CHITWONG, Fusak CHEEVASUVIT, Kobchai DEJHAN and Somsak MITATHA

Faculty of Engineering and Research Center for Communication and Information Technology, King Mongkut's Institute of Technology Ladkrabang, Ladkrabang, Bangkok 10520, Thailand.
Tel : 66-2-3269967, 66-2-3269081, Fax : 66-2-3269086
E-mail : kobchai@telelan.telecom.kmitl.ac.th

KEY WORDS : edge preserving smoothing, local and global histogram equalization, segmentation, graph theory

ABSTRACT: Histogram modification is a classical method for image enhancement, especially histogram equalization. Histogram equalization method is a self-acting process since it does not request any information, just only the probability of each intensity level of image. However, the enhanced image is obtained by the global area histogram equalization will cause an effect of intensity saturation in some areas. This defeat is appeared because of the process attempted to merge the adjacent gray levels together in order to flatten the histogram. To reduce the mentioned defeat, a method of local area histogram equalization is proposed. First, the original image will be partitioned into small areas by using graph theory, since the graph theory gives high accurately boundaries of region. The histogram of all pixels in each segmented region will be equalized independently. The method of segmented region histogram equalization will be applied to each scene of multi-spectral satellite imageries. The enhanced color image can be accomplished by assigning the color of red, green and blue to 3 different spectral images. The resulting of obtained color image from the proposed method is obviously shown the details more than the traditional method.

1. INTRODUCTION

The enhancement techniques are employed in order to increase the contrast of an image. Therefore, the distinction of features in the scene can be easily performed by visualization. This will augment the efficiency of image classification and interpretation. Generally, an image can be enhanced by spreading out the range of scene illumination. This procedure is called contrast stretch. If the ranges of gray values are uniformly prolonged, the process will be called linear contrast stretch. The disadvantage of the linear contrast stretch is that a number of gray levels are equally assigned to the unusually appeared gray levels as to the often appeared gray levels. This effect still causes the ambiguous distinction of the similar features. To overcome the mention defect, the process of histogram equalization is applied. The process tries to assigned more number of gray levels to the frequency appeared gray levels. The enhanced image obtained from the global area histogram equalization will cause an effect of intensity saturation in darkness area and whiteness areas. This drawback is appeared because of the process attempted to agglomerate the adjacent gray levels together in order to flatten the histogram. To overcome this defect, we proposed a method of local area histogram equalization. The process will be, first partitioned the original image into small area by graph theory. Then the histogram of each segmented region will be equalized independently. This process is applied to the multispectral images. The color image enhancement will be obtained by encoding the color of red, green and blue to three different spectral images. The detail of the proposed algorithm can be described as the following paragraph.

2. IMAGE SEGMENTATION BY GRAPH THEORY

The aim of image segmentation is to divide the scene into significance regions. The adjacent similar pixels will be grouped together into the same region. Then the interested objects will be isolated from each and other. Therefore the segmented image can be applied to widely application such as feature classification, object detection, motion estimation, data compression etc. However the noise pixels always presented in an image. These noises will cause an ambiguity in feature classification by segmented image, since the isolated small regions will be spread out over the interested features. So the edge preserving smoothing method of (S. Chitwong, et al., 2000) will be applied to cancel these noise pixels. The smoothing algorithm not only eliminates the noise but also accentuate the boundaries of the separated region. For obtaining the high accurate region's boundaries in the segmented image , the segmentation via graph theory (O.J. Morris,et al., 1986) has been chosen. The segmentation procedure can be manifested as the following steps.

1) Mapping one by one of each pixel in image onto a vertex of graph, where the gray level of the pixel is the vertex weight of the graph. The mapping result can be shown in Fig. 1.

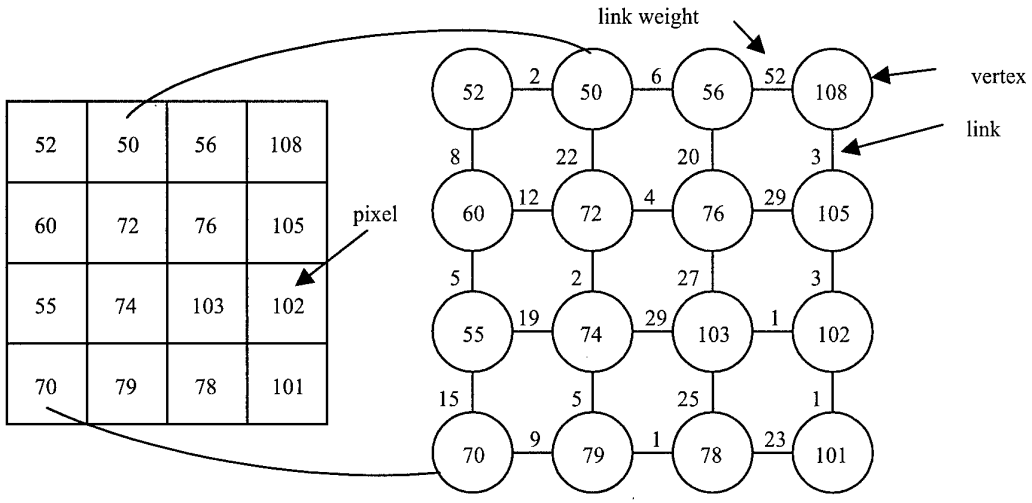


Fig. 1 Image and corresponding graph

2) Each pixel will be linked to its neighbour in 4 perpendicular directions and each link weight is obtained by the absolute different of vertex weight between two connected vertices.

3) Merge two adjacent vertices together to form an homogeneous region. The link weight is used to verify the resemblance of the adjacent pixels. The average value of merging vertices will be assigned to the pixel group and the concerned link weight will be recalculated.

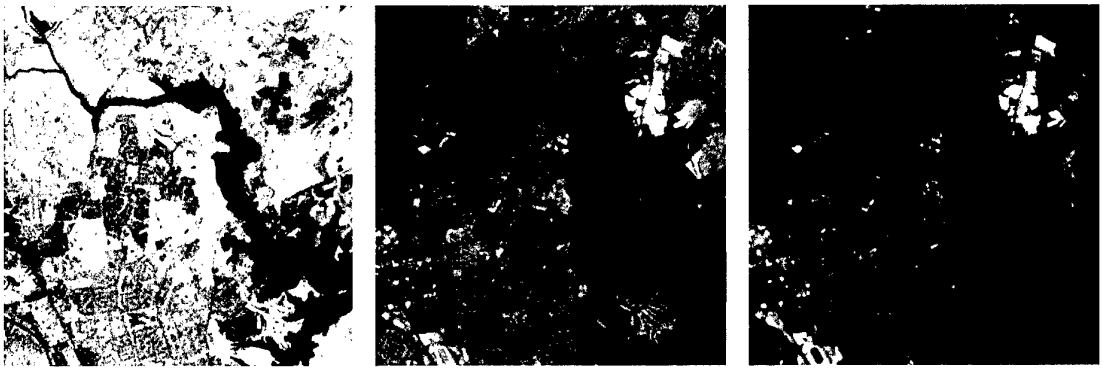
4) For obtaining M+1 segmented regions in the image, the last M links will be cut.

3. HISTOGRAM EQUALIZATION

The histogram equalization is applied in order to improve the contrast of image. Therefore, the histogram of each segmented region will be modified by local histogram equalization process in order to reduce the effect of intensity saturation which obtained from the global histogram equalization.

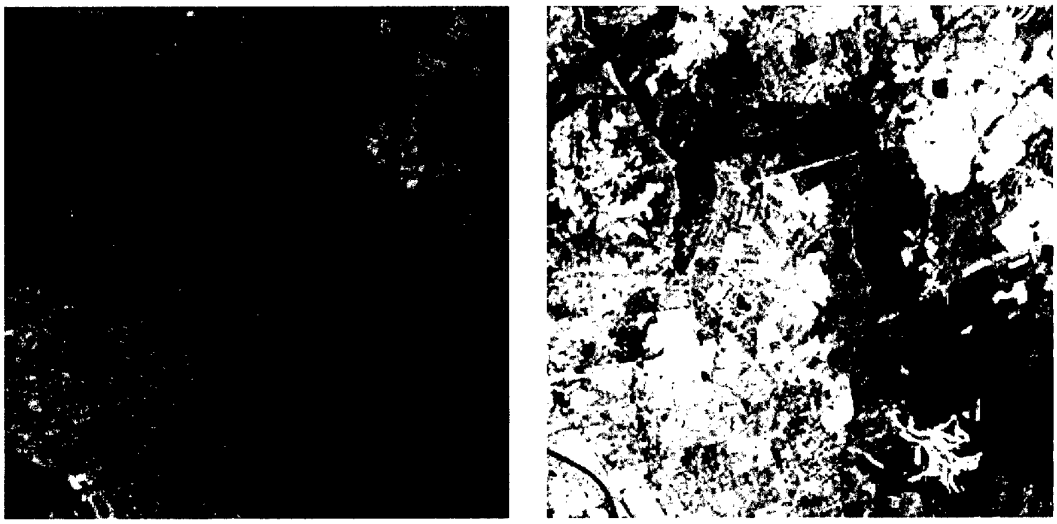
4. IMPLEMENTATION RESULT

The edge preserving smoothing process is applied to the original images Fig. 2. The graph theory is employed for segmenting the images of Fig.2. The histogram of each segmented region will be equalized independently. By assigning the color red, green and blue to processed image. The result of color image enhancement is shown in Fig.3(a). While the traditional method of global histogram equalization is presented in Fig.3(b).



(a) band 4 (b) band 5 (c) band 6

Fig.2 Original TM image



(a) (b)

Fig.3 Colour image
(a) Colour image from local area histogram equalization
(b) Colour image from global histogram equalization

5. CONCLUSION

Histogram equalization is powerful method for increasing the contrast of image. The enhanced image will give the full dynamic range of histogram. However, the global histogram equalization process tries to merge the adjacent gray levels together in order to force the uniformity of number of pixels in each appeared gray levels. Consequently, the intensity saturation will be presented in darkness regions and whiteness region. Also the pixels located in the border of two regions which are not too different in gray levels will be grouped together.

But, for our propose, we separate out these two regions first and then exploit the histogram equalization to each region independently. Therefore, the mentioned defects can be overcome.

REFERENCES

P.W. Fung, K.K. Ly, and Y. Attikiouzed, 1988. Automatic segmentation of biomedical image. Proc ICASSP, pp. 882-885.

F. Tomita and S. Tsuji, 1977. Extraction of multiple regions by smoothing in selected neighbourhood. IEEE Trans. System Man and Cybernetics SMC-7, pp. 107-109.

M. Nagao and T. Matsuyama, 1979. Edge preserving smoothing. Computer Graphics and Image Processing, vol.9, pp. 374-407.

S. Chitwong, F. Cheevasuvit, K. Dejhan, S. Mitatha, C. Nokyoo and T. Paungma, 2000 Segmentation on Edge Preserving Smoothing Image based on Graph Theory. Proceeding of IGARSS 2000, July.

S.L. Horowitz and T. Pavlidis, 1974. Picture segmentation by a directed split-and-merge procedure. Proc. 2nd Int. Joint Conf. on Pattern Recognition, pp. 424-433.

F. Cheevasuvit, H. Maitre and D. Vidal-Madjar, 1986. A robust method for picture segmentation based on a split-and-merge procedure. Computer Vision, Graphics and image processing, vol. 34, pp. 268-281.

J.B. Jun Kruskal, 1956. On the shortest spanning subtree of a graph and the travelling saleman problem. Proc. Am. Math. Soc., vol. 7, pp. 48-50.

D. Cheriton and R.E. Tarjan, 1967. Finding minimum spanning trees. SIAM J. Comput., vol. 5, pp. 724-742.

O.J. Morris, M.de J. Lee, and A.G. Constantinides, 1986. Graph theory for image analysis : an approach based on the shortest spanning tree. Proc. IEE, vol. 133, pt. F, no. 2, pp.146-15.

O.J. Morris, M.de J.Lee, and A.G. Constantinides, 1986. A unified method for segmentation and edge detection using graph theory. Proc. ICASSP, pp. 2051-2054.

The 21st Asian Conference on Remote Sensing
December 4-8, 2000 Taipei, TAIWAN

Parallel Computing in Remote Sensing Data Processing

Chao-Tung Yang* Chi-Chu Hung
Associate Researcher Satellite Analyst
Ground System Section
National Space Program Office
Hsinchu, Taiwan
Tel: +886-3-5784208 ext. 1563 Fax: +886-3-5779058
e-mail: ctyang@nspo.gov.tw

KEY WORDS: Parallel Computing, Clustering, Speedup, Remote Sensing

ABSTRACT: There are a growing number of people who want to use remotely sensed data and GIS data. What is needed is a large-scale processing and storage system that provides high bandwidth at low cost. Scalable computing clusters, ranging from a cluster of (homogeneous or heterogeneous) PCs or workstations, to SMPs, are rapidly becoming the standard platforms for high-performance and large-scale computing. To utilize the resources of a parallel computer, a problem had to be algorithmically expressed as comprising a set of concurrently executing sub-problems or tasks. To utilize the parallelism of cluster of SMPs, we present the basic programming techniques by using PVM to implement a message-passing program. The matrix multiplication and parallel ray tracing problems are illustrated and the experiments are also demonstrated on our Linux SMPs cluster. The experimental results show that our Linux/PVM cluster can achieve high speedups for applications.

1 Introduction

There are a growing number of people who want to use remotely sensed data and GIS data. The different applications that they want to required increasing amounts of spatial, temporal, and spectral resolution. Some users, for example, are satisfied with a single image a day, while others require many images an hour. The ROCSAT-2 is the second space program initiated by National Space Program Office (NSPO) of National Science Council (NSC), the Republic of China. The ROCSAT-2 Satellite is a three-axis stabilized satellite to be launched by a small expendable launch vehicle into a sun-synchronous orbit. The primary goals of this mission are remote sensing applications for natural disaster evaluation, agriculture application, urban planning, environmental monitoring, and ocean surveillance over Taiwan area and its surrounding oceans.

The Image Processing System (IPS) refers to the Contractor-furnished hardware and software that provide the full capabilities for the reception, archival, cataloging, user query, and processing of the remote sensing image data. The IPS will be used to receive, process, and archive the bit sync remote sensing image data from the X-band Antenna System (XAS) of NSPO. The XAS is dedicated for receiving the high-rate link of the earth remote sensing data from ROCSAT-2 satellite, and has the capability of receiving downlink data rate up to 320Mbps. It will also be expanded to receive data from other remote sensing satellites. Generally, IPS has configuration to receive satellite data like that depicted in Figure 1. Remote sensing data comes to the IPS via either a satellite link or some other high-speed network and is placed into mass storage. Users can then process the data through some of interface.

What is needed is a large-scale processing and storage system that provides high bandwidth at low cost. Scalable distributed memory systems and massively parallel processors generally do not fit the latter criterion. A cluster is type of parallel and distributed processing system, which consists of a collection of interconnected stand-alone computers working together as a single, integrated computing resource [1, 2, 3]. A computer node can be a single or multiprocessor system (PCs, workstations, or SMPs) with memory, I/O facilities, and an operating system. A cluster generally refers to two or more computers (nodes) connected together. The nodes can exist in a single cabinet or be physical separated and connected via a LAN. An interconnected (LAN-based) cluster of computers can appear as a single system to users and applications. Cluster nodes work collectively as a single computing resource and fill the conventional role of using each node as an independent machine. A cluster computing system is a compromise between a massively parallel processing system and a distributed system. An MPP system node typically cannot serve as a standalone computer; a

*Corresponding author. e-mail: ctyang@nspo.gov.tw, Phone: +886-3-57842080 ext. 1563, Fax: +886-3-5779058.

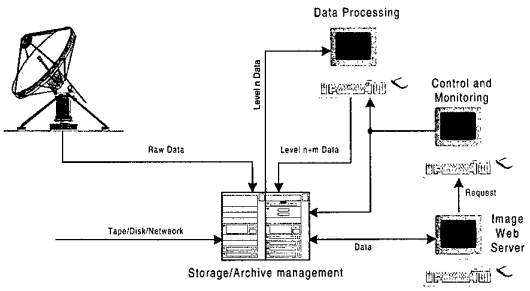


Figure 1: System Architecture of IPS.

cluster node usually contains its own disk and complete operating systems, and therefore, also can handle interactive jobs. In a distributed system, nodes can serve only as individual resources while a cluster presents a single system to the user.

In recent years, the performance of commodity-off-the-shelf (COTS) components, such as processor, memory, hard disk, and networking technology, has improved tremendously. Free operating systems, such as Linux and Free-BSD, are available and well supported. Several industry-standard parallel programming environments, such as PVM [5], MPI, and OpenMP, are also available for, and are well-suited to, building clusters at considerably lower costs. Such a system can provide a cost-effective way to gain features and benefits (fast and reliable services) that have historically been found only on more expensive proprietary shared memory systems. The main attractiveness of such system is that they are built using affordable, low-cost, commodity hardware (such as Pentium PCs), fast LAN such as Myrinet, and standard software computers such as MPI, and PVM parallel programming environments. These systems are scalable, i.e., they can be tuned to available budget and computational needs and allow efficient execution of both demanding sequential and parallel applications.

RSS (Ground System Section) currently operates and maintains an experimental Linux SMP cluster (SMP PC machines running the Linux operating system) which is available as a computing resource for test users [6]. The Ground's Linux SMP cluster (LSC) machines are operated as a unit, sharing networking, file servers, and other peripherals. This cluster is used to run both serial and parallel jobs. In this paper, an experimental environment for remote sensing and telemetry application development on a cluster is proposed. The cluster would provide a mechanism for the scientist or engineer to utilize high-performance computer systems without requiring extensive programming knowledge [7].

As the growing volume of satellite data increases with the growing number of users who want to process the data, there is a need to move away from the traditional computer to more powerful supercomputers. The cost, however, of these computers generally places a constraint on the types of users. Clusters of parallel computers provide a good ratio of cost-to-performance and it is within this framework that we design LSC. LSC is aimed at making it easy to process large amounts of satellite data quickly. This is accomplished through an environment tailed towards design of parallel component-based software that can easily be connected and gain high-performance.

2 An Example: Matrix Multiplication

The most commonly used program as shown in Figure 2 in parallel processing has a uniform workload. Since matrix `a` rows and matrix `b` columns are referenced constantly, and the elements of both matrices are not modified, a local cache if available will be very useful to the system. This algorithm requires n^3 multiplications and n^3 additions, leading to a sequential time complexity of $O(n^3)$.

```
for (i = 0; i < N; i++) /* can be parallelized */
    for (j = 0; j < M; j++) { /* can be parallelizd */
        c[i][j] = 0;
        for (k = 0; k < P; k++)
            c[i][j] = c[i][j] + a[i][k] * b[k][j];
    }
```

Figure 2: A kernel of Matrix Multiplication.

The serial program computes a result matrix result by multiplying two input matrices, `a` and `b`. Matrix `a` consists of N rows by P columns and matrix `b` contains P rows by M columns. These sizes yield a result matrix `c` of N rows by M columns. The serial version of the program was quite straightforward.

Let's consider what we need to change in order to use PVM. The first activity is to partition the problem so each slave can work on its own assignment in parallel. For matrix multiplication, the smallest sensible unit of work is the computation of one element in the result matrix. It is possible to divide the work into even smaller chunks, but any finer division would not be useful. For example, the number of processor is not enough to process, i.e., n^2 processors are needed.

The matrix multiplication algorithm is implemented in PVM using the master-slave paradigm. The master task is called `master_mm_pvm`, and the slave tasks are called `slave_mm_pvm`. The master reads in the input data, which includes the number of slaves to be spawned, nTasks. After registering with PVM and receiving a *taskid* or *tid*, it spawns $nTasks$ instances of the slave program `slave_mm_pvm` and then distributes the input graph information to each of them. As a result of the spawn function, the master obtains the *tids* of each of the slaves. Since each slave needs to work on a distinct subset of the set of matrix elements, they need to be assigned instance IDs in the range $(0, ..., nTask - 1)$. The *tids* assigned to them by the PVM library do not lie in this range, so the master needs to assign the instance IDs to the slaves and send that information along with the input matrix. The slaves also need to know the total number of slaves in the program, and this information is passed on to them by the master process as an argument to the spawn function since, unlike the instance IDs, this number is the same for all $nTasks$ slaves.

To send the input data and instance ID information, the master process packs these into the active send buffer, and then invokes the send function. It then waits to receive partial results from each of the slaves. the slaves register with the PVM environment, and then wait for input data from the master, using a wildcard in the receive function to receive a message from any source. Once a message is received, each slave determines the master's *tid* from the received message buffer properties. Alternatively, the slaves could have determined the master's *tid* by calling the `pvm_parent()` function, which they could have used as the source in their receive function. On receiving the message from the master that contains the input matrix, a slave unpacks this data from the active receive buffer. Each slave then works on its input partition, and send its partial results to the master when it is done. Then the master collects these partial results into an output matrix and outputs the results.

In the slave program, we keep the basic structure of the sequential program intact. But now the routine to multiply the two matrices, the main program of `slave_mm_pvm` does not do the actual work itself, only performs the loop partition for each individual portion. Instead, the slave program calls a function `matrix_multiple` to perform real matrix multiplication. The individual slaves each then perform a portion of the matrix multiplication as shown in Figure 3.

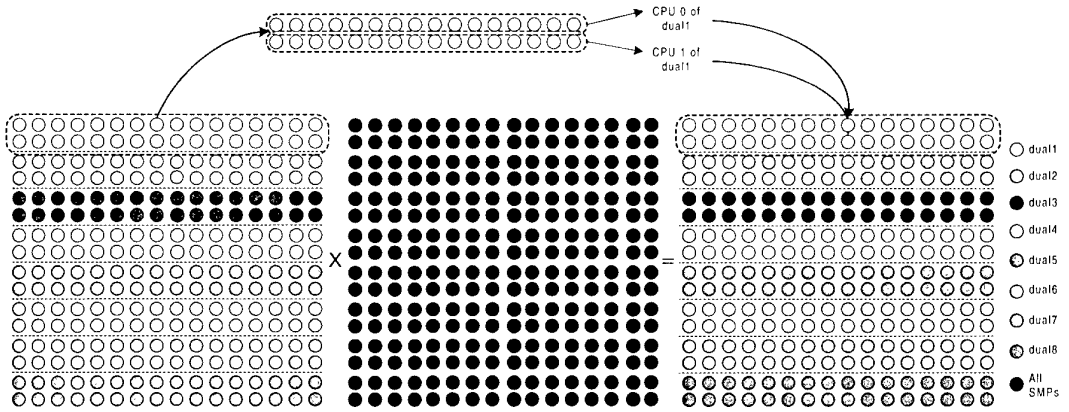


Figure 3: The block version of partitioning.

3 Experimental Result

Our SMP cluster is shown in Figure 4 that consists of nine PC-based multiprocessors connected by a switched Hub with Fast Ethernet interface. There are one server node and eight computing nodes. The server node has two

Intel Pentium-!!! 667MHz processors and 256MBytes of shared local memory. Each computing node has two Celeron processors and 196MBytes of shared local memory. Each Pentium-!!! has 32K on-chip instruction and data caches (L1 cache), a 256K on-chip four-way second-level cache with full speed of CPU. Each Celeron also has 32K on-chip instruction and data caches (L1 cache), a 128K on-chip four-way second-level cache with full speed of CPU. The individual processors are rated at 495MHz, and the system bus has a clock rate of 110 MHz.

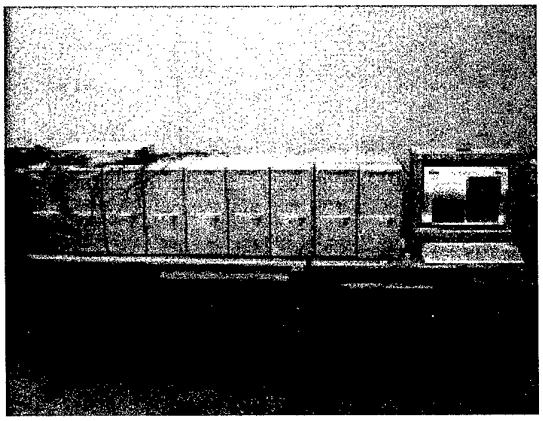


Figure 4: The snapshot of SMP-based cluster.

3.1 Matrix Multiplication Results

The matrix multiplication was run with forking of different numbers of tasks to demonstrate the speedup. The problem sizes were 256×256, 512×512, 768×768, 1024×1024, and 1280×1280 in our experiments. It is well known, the speedup can be defined as $\frac{ts}{tp}$, where t_s is the execution time using serial program, and t_p is the execution time using multiprocessor. The execution time on dual2 (2 CPUs), dual2~3 (4 CPUs), dual2~4 (6 CPUs), dual2~5 (8 CPUs), and dual2~9 (16 CPUs), were listed in Figure 5, respectively. The corresponding speedup of different problem size by varying the number of slave programs were shown in Figure 6. Since matrix multiplication was a uniform workload application, the highest speedup was obtained about 10.89 (1280×1280) by using our SMP cluster with 16 processors. We also found that the speedups were closed when creating two slave programs on one dual processor machine and two slaves program on two SMPs respectively.

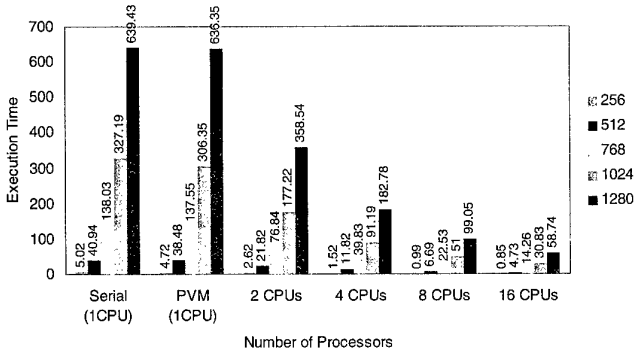


Figure 5: Execution time (sec.) of SMP cluster with different number of tasks (slave programs).

3.2 PVMPOV Cluster Benchmark Results

Pov-ray is a multi-platform, freeware ray tracer [4]. Many people have modified its source code to produce special "unofficial" versions. One of these unofficial versions is PVMPOV, which enables POVray to run on a Linux cluster.

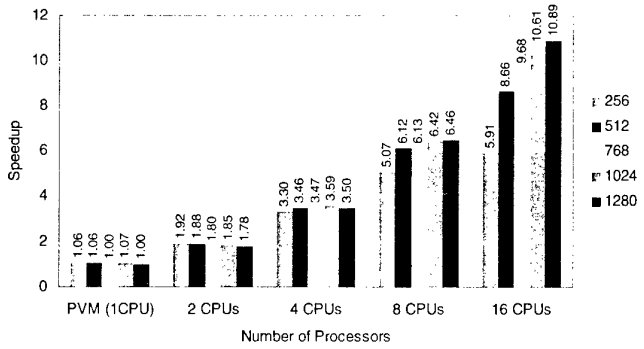


Figure 6: Speedup of SMP cluster with different number of tasks (slave programs).

With the cluster configured, runs the following command to begin the ray tracing and generates the image file as shown in Figure 7:

```
./pvmpov +iskyvase.pov +w640 +h480 +FT +v1 -x -d +a0.300 -q9 -mv2.0 -b1000
-nw32 -nh32 -nt4 -L/home/gs17/pvmpov3\_1e\_1/povray31/include
```

This is the benchmark option command-line with the exception of the `-nw` and `-nh` switches, which are specific to PVMPOV and define the size of image each of the slaves will be working on. The `-nt` switch is specific to the number of tasks will be running. For example, `-nt4` will start four tasks, one for each machine. The messages on the screen should show that slaves were successfully started. When completed, PVMPOV will display the slave statistics as well as the total render time. Using single processor mode of a dual processor machine for processing 1600×1280 image, the render time was 369 seconds. Using both CPU's on a single machine reduced the render time to 190 seconds. Adding the second machine with dual CPU's dropped the time to 99 seconds. Using out SMP cluster (16 processors) further reduced the time to 27 seconds. The execution time on dual2, dual2~3, dual2~4, dual2~5, and dual2~9, were shown in Figure 8, respectively. The corresponding speedup of different problem size by varying the number of task (option: -nt) were shown in Figure 9. The high speedup were gained about 1.94 (1600×1280) on dual2, and 3.73 (1600×1280) using both dual2 and dual3. The highest speedup was obtained about 13.67 (1600×1280) by using our SMP cluster with 16 processors.



Figure 7: The skyvase.tga genreated form PVMPOV.

4 Conclusion and Future Work

Scalable computing clusters, ranging from a cluster of (homogeneous or heterogeneous) PCs or workstations, to SMPs, are rapidly becoming the standard platforms for high-performance and large-scale computing. It is believed that message-passing programming is the most obvious approach to help programmer to take advantage of clustering

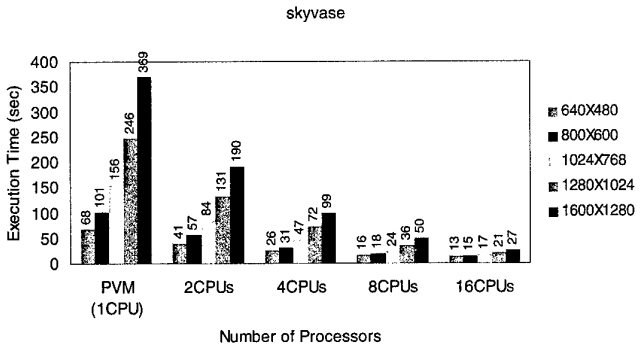


Figure 8: Execution time (sec.) of SMP cluster with different number of tasks (slave programs).

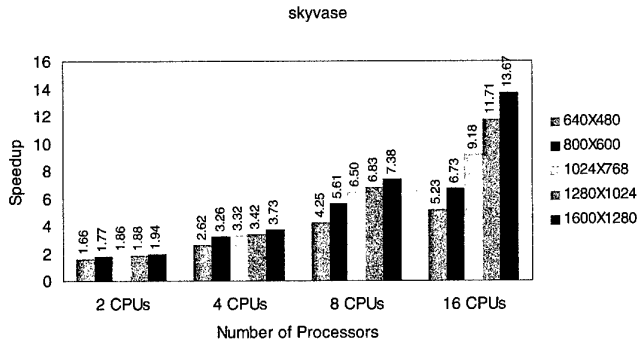


Figure 9: Speedup of SMP cluster with different number of tasks.

symmetric multiprocessors (SMP) parallelism. In this paper, we present the basic programming techniques by using Linux/PVM to implement a PVM program. The matrix multiplication and parallel ray tracing problems are illustrated and the experiments are also demonstrated on our Linux SMPs cluster. The experimental results showed that the highest speedup were 10.89 and 13.67 respectively for matrix multiplication and PVMPOV, when the number of processors is 16, by creating 16 tasks on SMPs cluster. The results of this study will make theoretical and technical contributions to the design of a PVM program on a Linux SMP clusters for remote sensing data processing.

References

[1] R. Buyya, *High Performance Cluster Computing: System and Architectures*, Vol. 1, Prentice Hall PTR, NJ, 1999.

[2] R. Buyya, *High Performance Cluster Computing: Programming and Applications*, Vol. 2, Prentice Hall PTR, NJ, 1999.

[3] G. F. Pfister, *In Search of Clusters*, Prentice Hall PTR, NJ, 1998.

[4] `http://www.haveland.com/povbench/`, POVBENCH — The Official Home Page.

[5] `http://www.epm.ornl.gov/pvm/`, PVM — Parallel Virtual Machine.

[6] T. L. Sterling, J. Salmon, D. J. Backer, and D. F. Savarese, *How to Build a Beowulf: A Guide to the Implementation and Application of PC Clusters*, 2nd Printing, MIT Press, Cambridge, Massachusetts, USA, 1999.

[7] B. Wilkinson and M. Allen, *Parallel Programming: Techniques and Applications Using Networked Workstations and Parallel Computers*, Prentice Hall PTR, NJ, 1999.

Using Complete Polarimetric Information in Fuzzy Neural Classification of SAR Image Based on Complex Gaussian Distribution

Chia-Tang CHEN[1] and K. S. CHEN[1,2]
[1]Institute of Space Science
[2]Center for Space and Remote Sensing Research
National Central University
Chung-Li, TAIWAN

KEY WORDS: Polarimetric, Fuzzy, Neural Network, SAR, Classification

ABSTRACT: This paper develops a supervised algorithm by incorporating the polarimetric statistics into a fuzzy dynamic neural network (Chen et al., 1996)(Tzeng and Chen, 1997) using a multilook complete polarimetric information. The method makes use of inherent statistical properties of the polarimetric data and hence the information is fully explored. A set of P-L-C-band images acquired by JPL airsar during the PACRIM'96 campaign were used as test images. Validation and effeteness of the proposed scheme were able to demonstrate the utilization of complete polarimetric information. It has been shown that with complete polarimetric data, the fuzzy neural network has substantially reduced its training time and improved the classification accuracy as well. A Lee polarimetric filter was applied to reduce speckle level while preserving the polarimetric properties and is proven to be useful to improve the classification accuracy. The approach also demonstrates the adaptability and flexibility for high dimensional feature vectors such as the complete polarimetric presented here.

1. INTRODUCTION

In classification of SAR image, three linear polarized data (diagonal term of covariance matrix) is often used and a proper classification results could be obtained (Chen, 1996; Tzeng, 1997). As stated in (Lee et al., 2000), there are basically three approaches: 1) algorithms based on image processing techniques, 2) algorithms based on a statistical model, and 3) algorithms based on em wave scattering mechanisms. Approach 1) can be supervised or unsupervised, while 2) and 3) are devised to be supervised only. Supervised and unsupervised algorithms are complementary to each other; each has its own advantages and disadvantages, depending on their purposes and applications. In all image classifications, still only partial polarimetric data are mostly often utilized. Hence, one has not yet taken full advantage of polarimetric data. This certainly does not necessarily mean that partial polarimetric data is not sufficient for the applications cited there. However, it may miss some important information that is embedded in the off-diagonal term of covariance matrix. For this purpose, a neural fuzzy classifier based on Wishart distribution for fully polarimetric SAR is demonstrated in this paper.

2. POLARIMETRIC SAR IMAGE

2.1 Statistical Properties

A polarimetric SAR records the matrix *S*. A scattering matrix ***S*** is a relationship between the incident field and the scattering field

$$\begin{bmatrix} E_v^s \\ E_h^s \end{bmatrix} = \frac{e^{jkr}}{r} \begin{bmatrix} S_{vv} & S_{vh} \\ S_{hv} & S_{hh} \end{bmatrix} \begin{bmatrix} E_v^i \\ E_h^i \end{bmatrix} = \frac{e^{jkr}}{r} S \begin{bmatrix} E_v^i \\ E_h^i \end{bmatrix} \tag{1}$$

where the subscripts in *S* denote the polarized states, and k is incident wavenumber, r the range from radar antenna to target center. With the complex scattering matrix *S* available, the interactions of radar waves and target medium can be fully described in the sense of complete polarization response. For simplicity, a complex vector v may be defined by elements of *S* as

$$v = [S_{vv} \quad S_{vh} \quad S_{hv} \quad S_{hh}]^T \tag{2}$$

where T denotes the matrix transpose and q the dimension of v, $q = 4$ for bistatic case and $q = 3$ for backscatter case by duality theorem stating $S_{vh} = S_{hv}$ for a reciprocal medium. SAR is a coherent imager and thus unavoidably suffers from speckle noise. This degrades image quality. Thus, SAR images are usually multi-look processed by averaging several neighboring one-look pixels. For polarimetric SAR system, it requires averaging several one-look covariance matrices

$$Z = \frac{1}{n} \sum_{i=1}^{n} v_i v_i^T \tag{3}$$

where v_i is i^{th} look elements vector in Eq. (3), n is number of looks, Z is a Hermitian matrix. The statistics of the Z has a complex Wishart distribution [Lee, 2000)

$$P_n(Z) = \frac{n^{qn} |Z|^{n-q} \exp[-nTr(C^{-1}Z)]}{Q(n,q)|C|^n} \tag{4}$$

$$Q(n,q) = \pi^{(1/2)q(q-1)} \Gamma(n) \cdots \Gamma(n-q+1) \tag{5}$$

where $C = < Z >$ denotes the feature covariance matrix and $< >$ the ensemble average.

2.2 Polarimetric Speckle Filter

SAR image records the scattered echoes from the scatterers within the illuminating cell. It causes speckle phenomena. To obtain better classification results, the despeckle procedure is performed before the SAR image is applied for classification. A new despeckle technology proposed and proven well suited for fully polarimetric SAR data [Lee, 1999] is applied in filtering the speckle of the SAR image in this study.

3. A STATISTICAL FUZZY NEURAL CLASSIFIER

3.1 Fuzzy Clustering

In the fuzzy c-means algorithm, the position of a class or cluster center is found to be the average of the positions of all the patterns in that cluster, based on minimizing the sum of the

variances of all variables i within a domain D for each pattern in each cluster l. And membership function μ_{li}, is introduced to weight the distance measure and to define the problem of finding the fuzzy c-partitions with a fuzzy index m, $m \in [1,\infty)$. That is, to adjust the position of , the cluster center, by minimizing the fuzzy c-means functional

$$J(U,\Omega)=\sum_{i=1}^{N}\sum_{l=1}^{L}(\mu_{li})^m d^2(x_i,\omega_l) \tag{6}$$

where

$$U=\begin{bmatrix} \mu_{11} & \mu_{12} & \mu_{13} & & \mu_{1N} \\ \mu_{21} & \mu_{22} & \mu_{23} & \cdots & \mu_{2N} \\ \mu_{31} & \mu_{32} & \mu_{33} & & \\ & \vdots & & \ddots & \\ \mu_{L1} & \mu_{L2} & \mu_{L3} & & \mu_{LN} \end{bmatrix} \tag{7}$$

is a fuzzy c-partition of X, $X=(x_1,x_2,\cdots,x_N)$ is a set of training N vector, and μ_{li} is the membership of the ith pattern to lth cluster; $\Omega=(\omega_1,\omega_2,\cdots,\omega_L)$ is the cluster center of X; In [Bezdek, 1987), the distance measure is defined by $d^2(x_i,\omega_l)=\|x_i-\omega_l\|^2$ where $\|\ \|$ denotes the matrix norm. In order to incorporate the statistical information of SAR, the distance in fuzzy c-means functional is replaced by the following form

$$d(Z_i,\omega_l)=n\left[\ln|C_l|+Tr(C_l^{-1}Z_i)\right]-\ln[P(l)] \tag{8}$$

where ω_l is class center of the l-th class, C_l is the feature covariance matrix of class l, and Tr denotes the trace of a matrix. Without *a prori* information, an equal probability for each class is assumed. To merge multifrequency data, a linear combination leads to a similar distance measure as

$$d_{li}=d(Z_i,\omega_l)=\sum_{j=1}^{K}\left[\ln|C_l(j)|+Tr(C_l^{-1}(j)Z_i(j))\right] \tag{9}$$

where $C_l(j)$ and $Z_i(j)$ are the feature matrix and the covariance matrix for *j-th* band, and K is the total number of frequency bands.

Differentiating $J(U,\Omega)$ with respect to ω_l, μ_{li} and applying the constrain

$$\sum_{l}\mu_{li}=1\forall i \tag{10}$$

to find the minimum of $J(U,\Omega)$, we obtain

$$\omega_l=\frac{\sum_{i=1}^{N}(\mu_{li})^m Z_i}{\sum_{i=1}^{N}(\mu_{li})^m},\forall l \tag{11}$$

and

$$\mu_{li} = \left[\sum_{k=1}^{L} \left\{ \frac{d_{li}}{d_{lk}} \right\}^{2/(m-1)} \right]^{-1} ; \forall l, i \qquad (12)$$

In fuzzy c-means algorithm, the fuzzy membership is obtained by iterative procedure of Equation (11) and (12).

3.2 Neural Implementation

The classification scheme used in this study is a neural network, called dynamic learning neural network (DLNN). DLNN has been applied in many applications. Such a neural network plays the role of connecting the input feature vector of SAR and the output membership vector. The input-output relationship can be simply expressed as

$$y = Wx \qquad (13)$$

where y is the output nodes and x is the input nodes. In this study, they are the membership vector of each pixel to a specific class and the feature vector of SAR, respectively. W is the weighting matrix of neural network. And the weighting matrix W is tuned by training process. By the use of the fuzzy membership vector as the output, DLNN becomes a fuzzy neural network (FDL)[Tzeng and Chen, 1997].

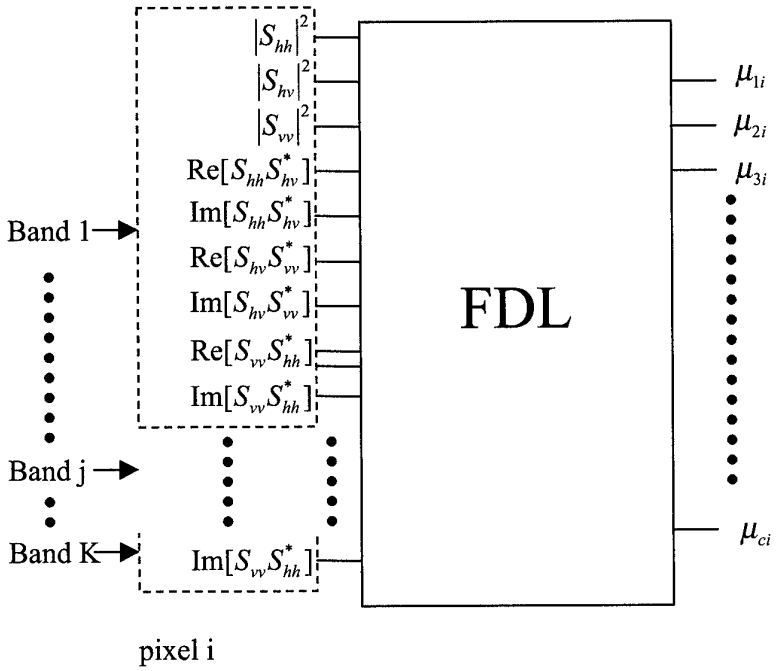


Fig.1 Configuration Setup of FDL

The training process is a standard procedure for a supervised neural network. The necessary training set is formed by a set of input information and desire output. For purpose of using complete polarimetric information, the input data is the covariance matrix, and the desire output is the corresponding membership vector. The training set must be sufficient and non-ambiguous. Fig. 1 shows the configuration of the neural network.

4. TEST DATA AND RESULTS

The test data used in the study the L-band polarimetric SAR of San Francisco acquired by JPL AIRSAR. The image size is 1024x900 pixels. The land covers were classified into four class; they are ocean, tree (the park and the hill), urban and grass (the playground and ball park). Fig. 2 shows the un-filtered and filtered SAR image of San Francisco. To train the neural network, totally 1600 pixels training set is chosen from location of each class for training. For comparison, four setups using different inputs were devised, as given in Table 1.

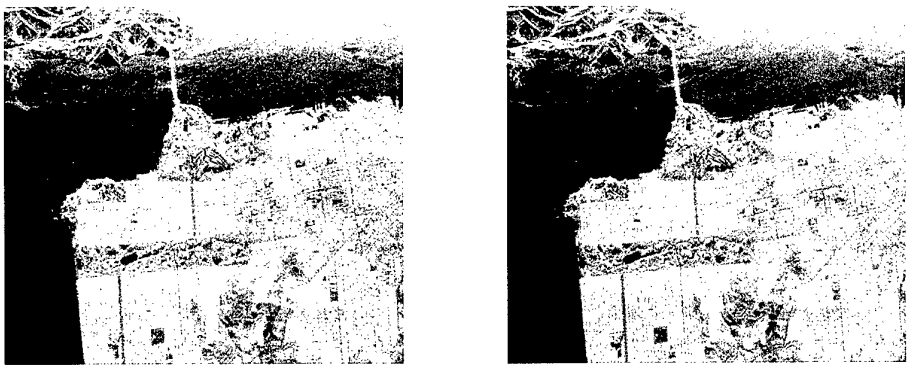
Setup	A	B	C	D
Input Channel	Covariance Matrix	HH, HV, VV	Covariance Matrix	Covariance Matrix
Classifier	Minimum distance	FDL	FDL	FDL
Distance Measure	Based on Wishart Distribution	Euclidean distance	Euclidean distance	Based on Wishart Distribution
Fuzzy	no	yes	yes	yes

Table 1 The setup of test

Setup A and D used Wishart distribution as distance measure, while Setup B and C are to used to test the suitability of Euclidean to covariance matrix containing the polarimetric information. Fig.3 shows the final classification results with four different setups. It is observed that the Euclidean distance, devised in Setup B and C, confuses the FDL due to the ambiguity of the off-diagonal terms in polarimetric covariance matrix,; Setup A performs classification well but lack of the fuzzy information in it; Setup B uses only three linear polarizations (diagonal term in covariance matrix) information for classification, and loses some important information contained in off-diagonal term. Setup D uses the covariance matrix and applies the Wishart Distribution in fuzzy c-means iterations. Among the four setup, Setup D clearly outperforms the other three. From the network learning curves (not shown here) of all setups, it is also indicated that Setup D convergence much faster than the rest of setups. It means that by using the Wishart distribution in FDL, the algorithm could quickly hit the class center, and at the same time speed the learn rate.

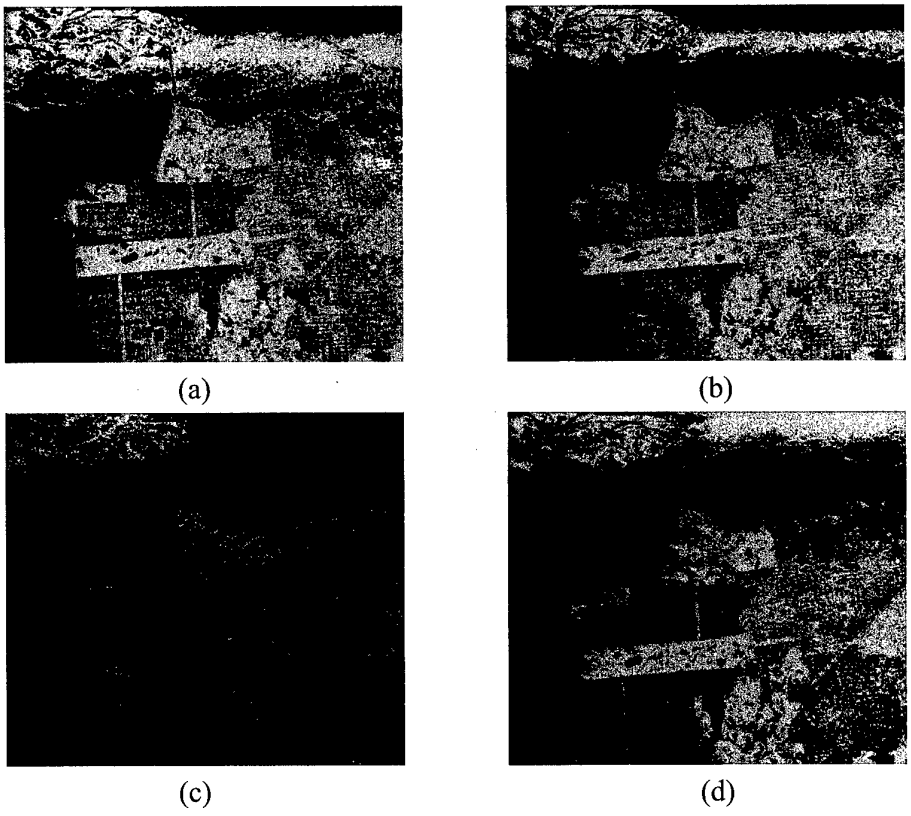
5. CONCLUSION

A classification scheme for fully polarimetric SAR imagery data based on a dynamic fuzzy neural network has been proposed and its effectiveness and efficiency has been demonstrated. Complete polarimetric matrix can be easily formed as an n-tuple vector data as inputs to the network and all polarimetric information are naturally implicitly contained in the network. In conclusion, a fuzzy neural network-based classification method has been successfully developed to take advantage of fully polarimetric SAR.



(a) (b)

Fig. 2 SAR image of San Francisco: (a)unfiltered (b) filtered



(a) (b)

(c) (d)

Fig.3 The classification results: (a) setup A, (b) setup B, (c) setup C, and (d) setup D.

REFERENCE

Bezdek, J. C., 1987. Pattern Recognition with Fuzzy Objective Function Algorithms. Plenum Press. New York

Chen, K. S., W.P. Huang, D.W. Tsay and F. Amar, 1996. Classification of multifrequency polarimetric SAR image using a dynamic learning neural network. IEEE Transactions on Geoscience and Remote Sensing, 34(3), pp. 814-820.

Lee, J. S. et al., 2000. Terrain Classification Using Polarimetric SAR Data – An Overview. PIERS2000, Boston, USA.

Tzeng, Y. C. and K. S. Chen, 1997. A fuzzy neural network for SAR image classification. IEEE Trans. Geoscience and Remote Sensing, 36(2), pp.301-307.

Comparative study on model fitting methods for object extraction

Masafumi NAKAGAWA, Huijing ZHAO, Ryosuke SHIBASAKI
Graduate School of Frontier Sciences, Shibasaki lab.
University of Tokyo
4-6-1 Komaba, Meguro-ku, Tokyo, 153-8505
Tel: (81)-3-5452-6417 Fax: (81)-3-5452-6417
E-mail: mnaka@iis.u-tokyo.ac.jp
JAPAN

KEY WORDS: SNAKE, Fitting, High resolution image, Residential maps update

ABSTRACT

It is expected that spatial data with various forms and content will be used in city in the future. It is advantageous to integrate various source data to generate urban spatial information. For instance, laser scanner has only limited resolution, though it can acquire three dimensional data directly. On the other hand, CCD image has very high resolution and conveys useful information for recognizing object though stereo matching methods are necessary for the extraction of 3D shape and the reliability is not sufficiently high for the automation. The integration of laser scanner and CCD sensor may enable to automate three dimensional spatial data generation with high resolution.

Model fitting methods attract attention as a method of integrating various sensor data for object recognition. The model fitting methods usually prepare models which describe the characteristics of the object with several parameters to generate a hypothesis, and selects a model which maximizes the agreement to obtained multi-sensor data, and simultaneously decides the parameter values of the model. However, enough examination is not performed on the characteristics of various model fitting methods, though a variety of methods are proposed in terms of the definition of an objective function necessary for deciding the model parameter and those of constraint conditions.

In this research, the building extraction from the high-resolution satellite image was assumed to be an example, and the techniques of the model fitting were compared under different conditions in terms of accuracy and reliability, etc.

1 INTRODUCTION

Model fitting methods attract attention as a technique to extract an object from various data of the image etc. The model fitting methods usually apply models which describe the characteristics (e.g. shape, texture) of the object with several parameters to generate a hypothesis, and selects a model which maximizes the agreement to obtained multi-sensor data, and simultaneously decides the parameter values of the model. However, enough examination is not performed on their characteristics of various model fitting methods, though a variety of methods are proposed in terms of the definition of an objective function necessary for deciding the model parameter and those of constraint conditions.

The purpose of this paper is to compare and to characterize model fitting methods ay applying them to high-resolution satellite image data to extract building outline. Success rate of extracting the building outline is used as an indicator.

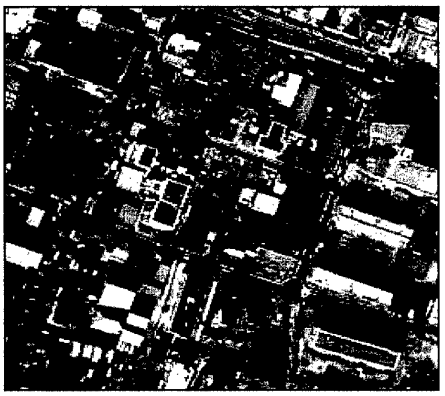
First of all, the building samples in an urban area are chosen in this image, and those samples are classified into two classes; buildings that can be extracted successfully and the other that fail to be extracted (Chapter 2). For the buildings that cannot be easily extracted, the initial model position/shape is changed so that the initial value dependency of the fitting results can be analyzed (Chapter 3). In addition,

range of parameter values which make model fitting succeed is searched for by changing the parameter and forms of the energy function and the constraint conditions of SNAKE, and generality of the sensitibity analysis is examined.

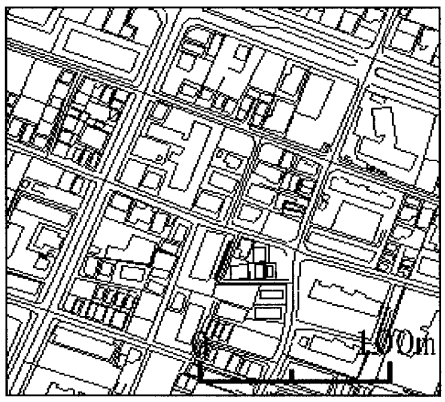
1-1 Test data

In this research, high-resolution satellite image (IKONOS) and the existing residential maps (Zenrin Map; vector data) of Kobe City are used. This is a typical case with the urban area in Japan.

- Figure 1-1: IKONOS image(1999)-



- Figure 1-2: Zenrin Map-



1-2 SNAKE

Here, Polygonal SNAKE which one of the authors proposed based on [Fua 1996] is used. SNAKE is initialized at first by using the map data. Next, each line is moved in parallel to maximize the average of edge intensity along SNAKE lines. The edge intensity is defined as a cross-sectional gradient of the gray value of the edge-enhanced image. The following functions are used for SNAKE.

$$E_{total} = {}_1E_{internal} + {}_2E_{external} \rightarrow \text{maximize} \quad \text{(equation 1)}$$

$E_{internal}$; Paragraph that Internal energy is evaluated
$E_{external}$; Paragraph that External energy is evaluated
ω_1 ; Weight of internal energy ω_2 ; Weight of external energy

ω_1 =1.000000 and ω_2=0.250000 are set from the experience as default value. Besides this, it is set as Scale Space=5 and Search Segment Number=5, and assumed default value. Scale space is distance between SNAKE's points. And Search Segment Number is range where SNAKE searchs optimum point. Basically, the fitting is done by these values. These parameter values are changed when the fitting fail with the default value, and the value which the fitting success is recorded.

1-3 Evaluation of fitting errors

Quantitative evaluation of the fitting errors was not made because the purpose of this study is to identify conditions affecting the success or failure of the model fitting. The success or failure is determined by visual inspection.

2 Experiment of model fitting (SNAKE) using existing map data as an initial value

Building in dense urban areas are chosen as samples, and the model fitting (SNAKE) using an existing map to set up initial models is conducted. IKONOS image was geocoded to overlay with the existing

1/2500 digital maps. Example results of the fitting experiment are shown in Figure 1-3~Figures 1-7. Factors greatly affecting the fitting success in the experiment are summarized as follows.

•Distance between initial location/shape of the model and edge location in the image

•Contrast or intensity of the edge

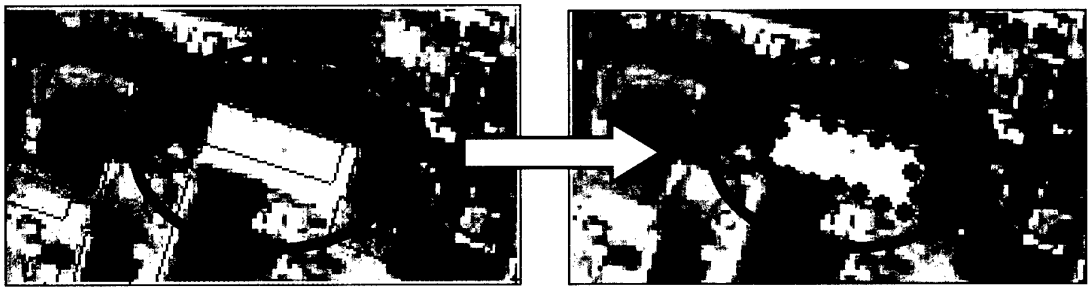
•Three dimensional complexities of buildings

2-1 Distance between initial location/shape of the model and edge location in the image

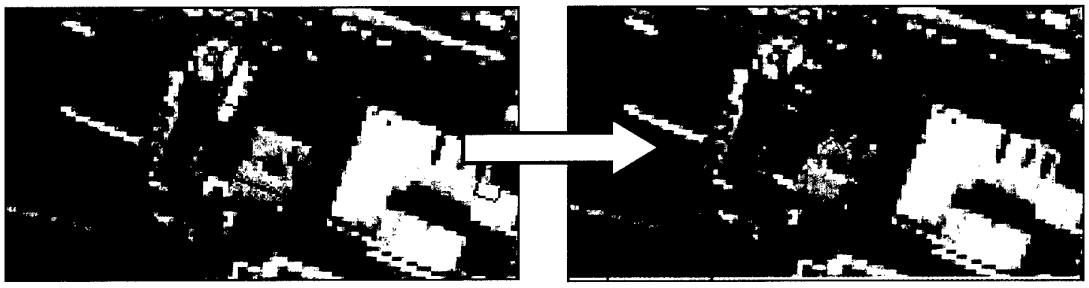
The building whose shape and position in the existing map agree well to edges in the image have higher rate of success of the fitting. Figure 2-1 shows typical examples. On the other hands, the fitting fails for a rebuilt building as shown in Figure 2-2, which suggests that newly built buildings after a building is demolished can be detected. Here, it can be concluded that agreement of the shape and the position of existing building boundary data and the image is important for the model fitting, though further experiments are needed for the quantitative evaluation. Since the IKONOS image used in this research is an oblique image, the height of the building has caused horizontal shift of the building boundary data which results in the failure of the model fitting.

In the following figures, the existing residential map data is drawn by blue line, the result of processing with SNAKE is drawn by blue line connected in a blue point.

- Figure 2-1: initial value and image: success example-



-Figure 2-2: initial value and image: failure example-



2-2 Contrast of edges

If buildings have edges with good contrast and connectivity in the edge image, model fitting tend to succeed. On the other hands, it is likely that the model fitting fail for the buildings where the edge contrast is low and the connectivity of the edge is poor. Especially, when there are trees adjacent to the building or shadow on north side of building, they are recognized as parts of the building, and SNAKE

edges tend to be caught by those other edges. However, there is a tendency that a good result is obtained easily when roof color is white. It is due to stronger contrast of white roofs to building shadow and ground color. In addition, the experiment suggests that distance to the adjacent buildings also influences. Figure 2-3 and Figure 2-4 show the edge map in the building in Figure 2-1 and Figure 2-2. When the edge contrast and connectivity is good, SNAKE edge can follow neatly along the edge.

- Figure 2-3: Edge image: Good contrast-



- Figure 2-4: edge image: Poor contrast and connectivity-

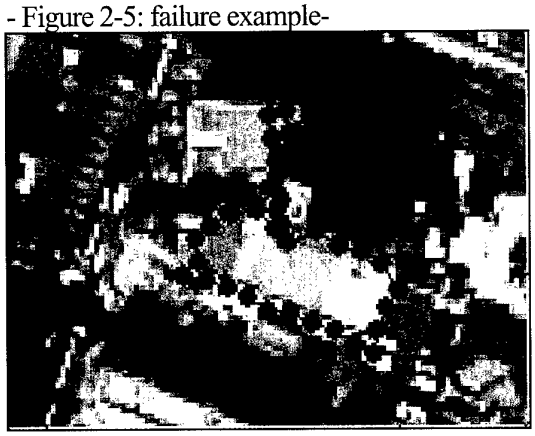


2-3 Three dimensional complexity

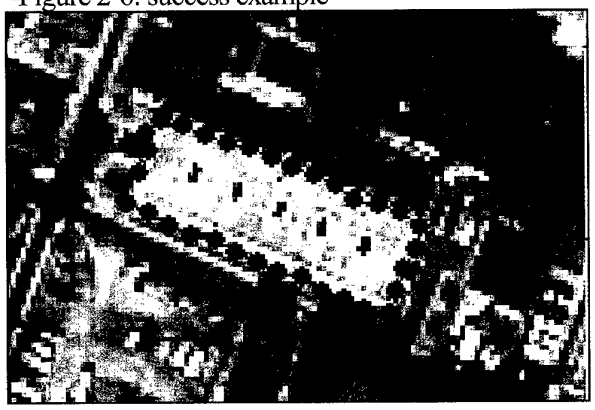
In case of deck, model fitting usually succeed, because the roof has homogenous color, while gable roofs may not be successfully extracted, because north side of the roof are regarded as the shadow of the buildings.

In case of a building consisting of different structures (composite building), the height of the building roof is not homogenous, which generate edges with complicated shapes not consistent with the building boundary data in 2D maps. Typical success and the failure example are shown in Figure 2-5 and Figure 2-6.

- Figure 2-5: failure example-



-Figure 2-6: success example-



2-4 Iteration number

It was examined whether there is a correlation between success/failure of the fitting and iteration number. Iteration number is total times that points move with SNAKE.

When targeted building is quadrangle (node number is 4), there is a tendency that the fitting succeeds if the iteration number is ten or less, but there is a tendency that the fitting fails when it was a lot of from ten. This value might be helpful in the classification of the success or the failure o the fitting.

3 Dependency on initial values

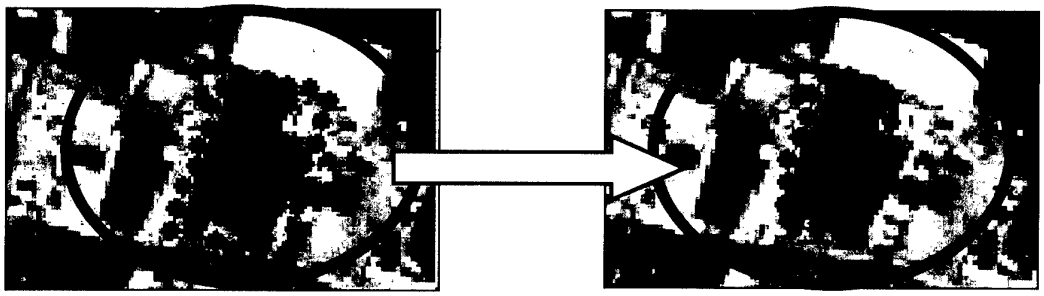
Especially, for the building where the fitting does not succeed in Chapter 2, the initial value in terms of the distance with "Correct answer" is changed to see how or whether the fitting results fail. Thus the initial value dependency of the fitting result is analyzed. Here, the initial value of the vector data is recreated along the rooftop side on the building in the IKONOS image.

Moreover, the similar procedure is applied to the buildings not recorded in the existing residential maps, that is, new buildings. As for SNAKE, the initial value dependency is thought to be high as a result. The following two examples are typical examples of showing the dependency.

3-1 For edge map

If the initial value is not appropriate, the fitting does not often succeed. When the building is overcrowded or the trees are grown in surroundings, SNAKE is pulled to the edge of surrounding features. However, when the initial value is given on the outline in the building again, a good result is obtained. Figure 3-1 shows an example of giving the initial value, and the success in the fitting.

- Figure 3-1: building overcrowdedness and success example-



-The first fitting results-

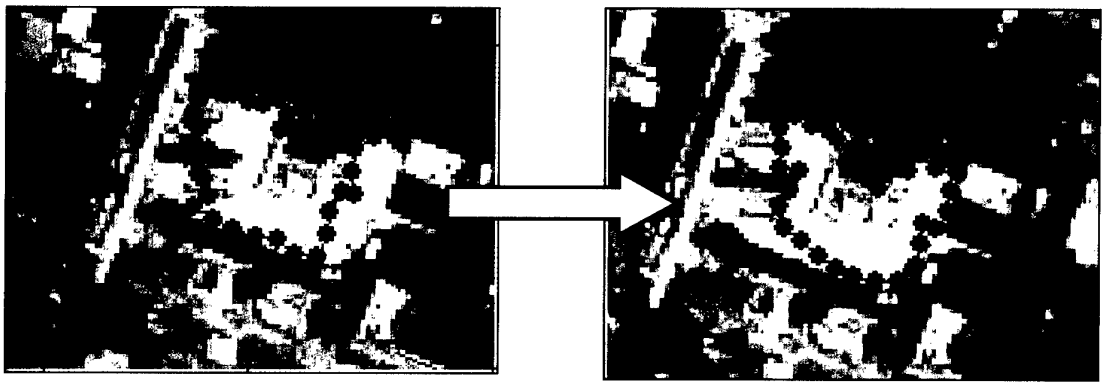
-Second fitting trial by changing the initial values-

3-2 For high building

An oblique photograph caused the shift in the location of the building roof shape. The fitting is able to have done well when there is a difference in the color of the wall and the rooftop.

Oppositely, when the color of the wall and the rooftop are almost the same, the fitting usually fails. It is thought that this is due to the poor contrast. So, when the entire wall is shadowed, the fitting can succeed. Figure 3-2 shows horizontal displacement of the initial value, and the example of the success of the fitting changing the initial value.

-Figure 3-2: high building-



-The first fitting results-

-Second fitting trial by changing the initial values-

4 Change in parameter values of energy function

By changing the parameters of the energy equation of SNAKE, more appropriate values or range of values are searched for so that SNAKE can fit the feature better.

For the cases where the fitting failed by the method of Chapter 2 and Chapter 3, the values of parameter $\omega 1$ and $\omega 2$ of the energy equation (equation 1) are changed. By monitoring the relation of these parameter and the movement of SNAKE in changing the parameter values, a suitable value is examined for the fitting. Moreover, the value of the parameter obtained for this research is inputted to the energy equation again to see the behavior of Snake for the building cases in Chapter 2. Detailed results will be reported in the conference.

5 CONCLUSIONS

In this research, it is examined through numerical experiments what conditions are preferable for the success and can cause the failure of the fitting taking the building model and using the high-resolution satellite image as examples.

The conditions are summarized as follows;

. Accurate initial values (map data).

. Clear edge image.

Especially, it is understood that the result of the fitting changes greatly depending on the initial values. The presence of a strong peripheral edge is important for the success of the fitting, too. However, there is room for conducting more quantitative analysis on the influences of the initial values. These results suggest the following procedure of applying SNAKE for revising spatial database using aerial or space images.

First of all, the model fitting is done using the out-of-dated digital map; The initial value is inputted for the one not having succeeded, and the fitting of the model can be tried again; For the one failed again, detailed vector data is made manually; It is thought that an automation and efficiency improvement can be achieved by depending on a series of work like these for the extraction of the building outline.

If an appropriate edge map etc. are made, updating the existing residential maps data will become easier, though it is still problematic to find the building which should be renewed.

REFERENCES

MICHAEL KASS, ANDREW WITKIN, and DEMETRI TERZOPOULOS, 1988. Snakes (Active Contour Models). International Journal of Computer Vision, pp321-331.

SOME ADVANCED TECHNIQUES FOR SPOT 4 XI DATA HANDLING

Nguyen Dinh Duong
Le Kim Thoa
Nguyen Thanh Hoan
Environmental Remote Sensing Laboratory
Institute of Geography, Hoang Quoc Viet Rd., Cau Giay, Hanoi, Vietnam
Phone: 84-4-7562417, Fax: 84-4-8361192, Email: duong.nd@hn.vnn.vn

KEY WORDS: SPOT 4 XI, Land cover, Automated classification, Color composite

ABSTRACT: The SPOT 4 satellite with short wave infrared band provides a new data source for environmental monitoring and natural resource management. The authors carried out research to develop a new methodology which can fully exploit the advantages of the short wave infrared band. Two issues will be reported in this paper: automated land cover classification and a new color composite model.

The conventional classification methods (supervised or unsupervised) are based on statistical models which use mean vectors, standard deviation and distances such as Euclidean or Mahalannobis as the major classifiers. Different land cover objects have different spectral reflectance properties that can be visualized as a spectral reflectance curve, so it is possible to use this curve as one of the principal measures for classification. The automated classification method developed by the authors uses this spectral reflectance curve along with other quantitative values such as band ratio and band differences for classification. The classification algorithm which is based on graphical analysis of the spectral reflectance curve (GASC) works well with LANDSAT TM data that has 7 spectral bands. SPOT 4 is equipped with a new short wave infrared band at 1.5 μm that provides higher spectral resolution and enhanced sensitivity for leaf moisture content and canopy structure. These improvement is essential for successful application of the GASC algorithm to SPOT 4 XI data in automated classification of land cover. In this paper the authors report on the preliminary results of automated classification using SPOT 4 XI data scene 277/329 acquired on April 24, 2000 near to Hochiminh City, Vietnam.

SPOT 4 XI with 4 spectral bands provides 24 different color composites using the RGB model. Each RGB color composite enhances certain land cover characteristics. However, none of them is capable to display information available in all 4 spectral bands. In this paper the authors report experiment to develop a color composite using all 4 spectral bands. This new color composite is based on data transformation from 4 dimensional conic vector space into 3 dimensional orthogonal space. The transformed components are converted to IHS and RGB space using common algorithms. The new color composite provides more information than any of the conventional ones. The visualized image is an excellent tool for vegetation study and water and infrastructure mapping.

I. INTRODUCTION

The SPOT 4 satellite has been launched successfully into orbit on Mar. 24, 1998. From that date the new sensor HRVIR provided new image data for natural resource management and environment monitoring. With new spectral band in short wave infrared region 1.5 – 1.7 μm the HRVIR sensor has broadened application of SPOT data because the SWIR band is particularly sensitive to soil moisture content, vegetation cover and leaf moisture content. The conventional methodology for processing and analysis of multi-spectral remote sensing data, of course, still can be used for SPOT 4 data. However, there is a potential of development of new technique which will help to fully exploit advantages of all four spectral bands of HRVIR sensor. In this

paper the authors will present research results on automated classification of land cover and a new color composite model for SPOT 4 XI data. This methodology has been developed in the Environmental Remote Sensing Laboratory, Institute of Geography, Vietnam. SPOT 4 data has been provided by the Satellite Remote Sensing Laboratory, National Central University, Taiwan in the framework of Visiting Scientist Programme.

II. SPOT 4 XI DATA

Image data of SPOT 4 HRVIR is provided in two modes: XS - multispectral mode without SWIR and XI – multispectral mode with SWIR. Depending on processing level, different preprocessing is applied, however, the detector radiometric equalization (MTF enhancement and optional digital dynamic stretching)is always applied for SPOT 4 raw data. Because of variation of ground radiance condition HRVIR sensor applies several gain modes to achieve the best dynamic range of data. Absolute calibration coefficients can be retrieved in the header record of CAP format to compute equivalent radiance at the input of the HRVIR instrument. The gain mode is applied differently for different scenes and different bands of the same scene. This arrangement has caused saturation of image data for some highly reflected objects such as cloud, sand, construction and even bare soil. From this point of view one can expect proper usage of SPOT 4 XI data for interpretation or classification of objects which are not too dark or too bright. Absolute calibration coefficients of some SPOT 4 scenes are shown on Table 1. While gain coefficients for the first three bands are relatively low, band 4 has always very high value of gain coefficient. It is maybe the main reason for digital value saturation of highly reflected objects in band 4. For comparison, digital values of some land cover objects have been read out and shown on Table 2. When compare these values we can see that low reflectance objects

Table 1: Absolute calibration coefficients

Scene number	Gain / Offset			
	Band 1	Band 2	Band 3	Band 4
277/329 2000/03/01	1.93500 / 0.0	2.28786 / 0.0	2.45268 / 0.0	13.31878 / 0.0
278/321 2000/04/22	1.29258 / 0.0	1.01000 / 0.0	1.08000 / 0.0	8.79000 / 0.0
278/320 2000/04/22	1.29258 / 0.0	1.01000 / 0.0	1.08000 / 0.0	8.79000 / 0.0

Table 2: Digital values of some land cover objects

Objects	Scene 277/329				Scene 278/321			
	Band 1	Band 2	Band 3	Band 4	Band 1	Band 2	Band 3	Band 4
Cloud	254	254	254	254	254	254	168	207
Sand	215	254	199	254	133	150	74	139
Bare soil	170	198	133	254	178	214	112	186
Turbid water	96	96	33	17	94	87	20	28
Clear water	67	48	24	33	54	36	8	17

such as turbid or clear water are sensed correctly in dynamic range of one byte integer for both scenes 277/329 and 278/321. However, due to different gain mode some saturation occurred for bare soil and sand in scene 277/329 (high gain mode) while in the scene 278/321 (normal gain mode) they are still in right values. Cloud is always saturated in all gain modes. Readers should

be noticed that the right dynamic range of SPOT 4 digital values is from 1 to 254. This fact should be taken into consideration in digital processing SPOT 4 data

III. AUTOMATED CLASSIFICATION OF LAND COVER USING SPOT 4 HRVIR DATA

The conventional classification methods (supervised or unsupervised) are based on statistical models which use mean vectors, standard deviation and distances such as Euclidean or Mahalannobis as the major classifiers. Different land cover objects have different spectral reflectance properties that can be visualized as a spectral reflectance curve, so it is possible to use this curve as one of the principal measures for classification (Nguyen Dinh Duong, 1997). The automated classification method developed by the authors uses this spectral reflectance curve along with other quantitative values such as band ratio and band differences for classification. The classification algorithm which is based on graphical analysis of the spectral reflectance curve (GASC) works well with LANDSAT TM data that has 6 spectral bands in visible region. SPOT 4 is equipped with a new short wave infrared band at 1.5 μm that provides higher spectral resolution and enhanced sensitivity for leaf moisture content and canopy structure. These improvement is essential for successful application of the GASC algorithm to SPOT 4 XI data in automated classification of land cover. SPOT 4 XI data of scene 277/329 acquired on April 24, 2000 near to Hochiminh City, Vietnam has been chosen as a study area.



Figure 1. False color composite of the study area

The study area is located in south of Vietnam near to Hochiminh City. Its landscape is dominated by features of coastal zone: mangrove forest, wetland agricultural activities. The scene covers also a part of Mekong river's delta which is well known as area of highly productive rice cultivation. On the upper right quarter of the scene are the famous rubber plantation farms. Hochiminh City is located on the upper left part of the image. Land cover categories are enough diverse for land cover classification. The scene is partly cloudy from the middle towards the top. Standard false color composite of the study area is shown on Figure 1.

For automated classification a module named as GASC_G07.F90 has been used. This program was developed based on GASC algorithm (Nguyen Dinh Duong 1997, 1998). For this study area a digital legend of 23 land cover categories was developed. In this legend each land cover is described by a set of image invariants (Nguyen Dinh Duong, 2000) composed of: Spectral curve modulation, total reflected radiance index TRRI, band ratios and difference of normalized spectral values. Major land cover categories such as forest, mangrove of different coverage

density, rice crop, water body etc. has been automatically extracted using GASC_G07 module. On the Figure 2 is classification result of the study area.

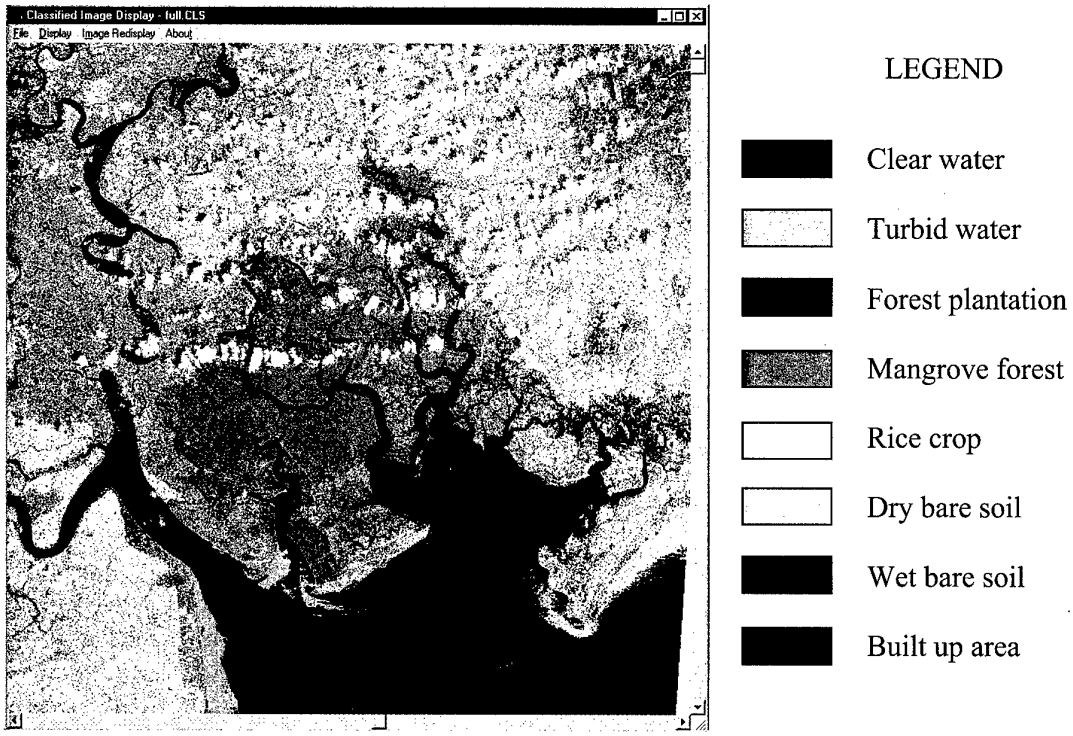


Figure 2. Result of automated land cover classification

By visual comparison of classification result on the Figure 2 and standard color composite on Figure 1 we can recognize advantages of the proposed approach. Water body is extracted very precisely. Different vegetation types and its distribution has been correctly classified. Mangrove forest, forest plantation (rubber), shrub and grass land including rice crop are possible to be automatically extracted using information derived only from the image data. Bare soil of different level of moisture content is also well identified. Built up area such as urban and housing area is extracted reliably, however, some thin cloud is misclassified into this class. Thick cloud is subject of classification without any doubt, but cloud shadow remains as one of weak point of the GASC algorithm. One of disadvantages of application of different gain modes during observation is needed absolute calibration and working with image data in real number instead integer values which will slow down obviously overall computation performance of the program.

IV. A NEW COLOR COMPOSITE MODEL FOR SPOT 4 HRVIR DATA

SPOT 4 XI with 4 spectral bands provides 24 different color composites using the RGB model. Each RGB color composite enhances certain land cover characteristics. However, none of them is capable to display information available in all 4 spectral bands. The authors have conducted an experiment to develop a color composite using all 4 spectral bands. This new color composite is based on data transformation from 4 dimensional conic vector space into 3 dimensional orthogonal space.

In general, there is possibility to transform data from n to 3 dimension space. Some degradation of data quality, of course, can be found in the result, however, experiments have confirmed that

the visualized transformed data show more information than any of the conventional three band color composites. The transformation can be made using the following equation:

$$\begin{bmatrix} a_1 & . & . & . & a_n \\ b_1 & . & . & . & b_n \\ c_1 & . & . & . & c_n \end{bmatrix} \times \begin{pmatrix} p_1 \\ . \\ . \\ . \\ p_n \end{pmatrix} = \begin{pmatrix} p_1' & p_2' & p_3' \end{pmatrix}$$

Where p_i is original image digital count and p'_i is transformed value. The coefficients a_1, a_n, b_1, b_n, c_1, c_n can be computed using different transformation model. In this case the authors used 4 dimensional conic vector space to transform data from 4 to 3 dimension space. For the case of SPOT 4 data the transformation is done by the following equation:

$$\begin{bmatrix} -0.866025 & +0.000000 & +0.866025 & +0.000000 \\ +0.000000 & +0.866025 & +0.000000 & -0.866025 \\ +0.500000 & +0.500000 & +0.500000 & +0.500000 \end{bmatrix} \times \begin{pmatrix} p_1 \\ p_2 \\ p_3 \\ p_4 \end{pmatrix} = \begin{pmatrix} p_1' \\ p_2' \\ p_3' \end{pmatrix}$$

Because the transformed components are in achromatic space so it is necessary to convert them to IHS and RGB space for color visualization. The conversion can be done by any of common HIS-RGB algorithms. The new color composite provides more information than any of the conventional ones. The visualized image is an excellent tool for vegetation study and water and infrastructure mapping. Conversion of transformed components p'_i into I,H,S system is done by formulas:

$$I = \sqrt{p_1'^2 + p_2'^2 + p_3'^2}$$

$$H = Arc\tan\left|\frac{p_2'}{p_1'}\right|$$

$$S = Arc\tan\left(\frac{\sqrt{p_1'^2 + p_2'^2}}{p_3'}\right)$$



Figure 3. New color composite of SPOT 4 XI data

On the Figure 3 is color composite created by this approach. This conversion has been applied for all pixel vectors in the image. Absolute calibration could be applied to ensure stability of the output color. To obtain specifically desired color, some offset of H could be added. When comparing this image with color composite on Figure 1 we could see that the new color composite is much more better than the standard one. When a composite is made by assigning component 1 to blue, component 2 to green and component 3 to red color respectively, vegetation is displayed always in green,

water in blue like in true color mode. Therefore the authors has named it as quasi-true color composite. Because of existence of the SWIR band which is not much impacted by atmospheric water vapor and aerosol so the final image is much more clear with higher contrast than the conventional one. Many land cover types such as urban, turbid water, bare soil that have similar color in standard color composite are very easy to be recognized each from other in the new color composite.

V. CONCLUSION

From this research we could make some conclusions:

- The SPOT 4 XI data with new SWIR band is excellent information source for land cover mapping and environmental research.
- Some saturation is found out in the SWIR band for cloud and bright ground objects. This occurs mostly for image data received in high gain mode.
- The graphical analysis of spectral reflectance curve (GASC) algorithm can be applied for automated classification of SPOT 4 XI data.
- Due to different gain mode of SPOT 4 data, absolute calibration should be applied before classification and image invariant used for digital description of land cover must be computed using absolutely calibrated pixel vector.
- It is possible to create new color composite using all four SPOT 4 XI bands by transformation matrix given in the paper. The visualized image provides more information than the conventional standard color composite and enhances many land cover objects. The new color composite is suitable for vegetation study, water body and infrastructure mapping.

ACKNOWLEDGEMENT

The authors would like to acknowledge the Satellite Remote Sensing Laboratory, NCU of Taiwan for providing SPOT 4 data. The authors also thank the Fundamental Research Programme of Vietnam for funding the research.

Reference

SPOT IMAGE: The SPOT Scene Standard Digital Product Format S4-ST-73=01-SI

Nguyen Dinh Duong. Graphical Analysis of Spectral Reflectance Curve. Proceedings of the 18th Asian Conference on Remote Sensing. 20 – 24 October 1997, Kualalumpur Malaysia.

Nguyen Dinh Duong. Total Reflected Radiance Index- An Index to Support Land Cover Classification. Proceedings of the 19th Asian Conference on Remote Sensing. 16 – 20 November 1998, Manila, Philippines

Nguyen Dinh Duong. Land Cover Category Definition by Image Invariants for Automated Classification. International Archives of Photogrammetry and Remote Sensing. Vol. XXXIII, Part B7/3, Commission VII. ISPRS 2000 Amsterdam, the Netherlands.

The Analytic of Remotely Sensed Digital Image

Li Xianhua[1,2,4], Zhang Dengrong[1], Yu Gelong[3], Lin Hui[4],Shihuosheng[4]

(Zhejiang University, Hangzhou, 310027)[1]

(Chinese Eastern Normal University, Shanghai 260032)[2]

(Agricultural Remote Sensing Center of Sichuan Province)[3]

(Hongkong Chinese University)[4]

Abstract

A method to disintegrate digital remotely sensed image is discussed in this paper. By which the information in original remotely sensed data can be disintegrated point by point into three components--solar direct illuminance (SDI), sky-scattering illuminnce (SSI) and atmospheric path radiance(APR). Because it is the result of the interaction of the natural spectral components with ground features and the atmosphere, the three components images play a more powerful role than the normal original remotely sensed data in the quantification inversion research of ground radiation energy, atmospheric environment condition, and remote sensing image pattern recognition.

Key Word: Remote Sensing, Digital Image, Analytic

1.Introduction

[1]The concept of image disintegration is widely used in remotely sensed digital image processing such as: to disintegrate panchromatic image into different band image according to spectral wavelength, to disintegrate image into high and low frequency parts by filter, to disintegrate image into the sum of wave element by Fourier transform and wavelet analysis Wavelet, and the mixed pixel disintegration etc...They are all effective method in remotely sensed image sensed image into three respective component images representing solar illuminance, sky-scattering illuminance and atmospheric brightness by the support of GIS will be discussed in the following.

2.Interaction of Terrain, Natural Spectrum and Remotely Sensed Data

The quantification relationships between remotely sensed data and natural spectrum and composition of ground pixel, and the quantification relationships between remotely sensed value of different band component pixel and slope direction and gradient of ground surface of the pixel is the bases of disintegration of remotely sensed digital image.

2.1 The quantitive relationships between remotely sensed data and ground illuminance and pixel natural spectral illuminance.

The quantitative relationships are as following:

$$E_{ij} = E_{Sij} + E_{Dij}$$

国家自然科学基金（49971057）.Chinese National Key-important Basic Research Plan (49971057).

$$DN_{ij} = K \bullet E_{ij} \bullet \tau_{ij} \bullet \gamma_{ij} \Big/ \pi + K \bullet N_{Aij}$$

$$DN_{ij} = K \bullet (E_{Sij} + E_{Dij}) \bullet \tau_{ij} \bullet \gamma_{ij} \Big/ \pi + K \bullet N_{Aij} = D_{Sij} + D_{Dij} + D_{Aij} \quad - \qquad (1)$$

where, K is the intrinsic ration in MSS system; γ_{ij} and τ_{ij} is the ground spectral reflectance and the atmospheric spectral transmissivity of the pixel respectively; E_{Sij} is the pixel's solar illuminance (PSIOP); E_{Dij} is sky-scattering illuminance (SSI); N_{Aij} is atmospheric brightness (AB); E_{Sij}, E_{Dij} and E_{Aij} are the corresponding remotely sensed component value of the pixel respectively.

2.2 The Quantitative Relationship Between the Pixel's Illuminances on the Slope and Respective Remotely Sensed Data

2.2.1 The Relationship between PSIOS and the respective Remotely Sensed Data

As shown in Figure 1, given a solar elevation, the solar point-blank luminous flux on the pixel's slope aspect, ϕ_{ij} , is F_{ij} times of the solar point-blank luminous flux on the horizontal projective aspect, ϕ'_{ij}

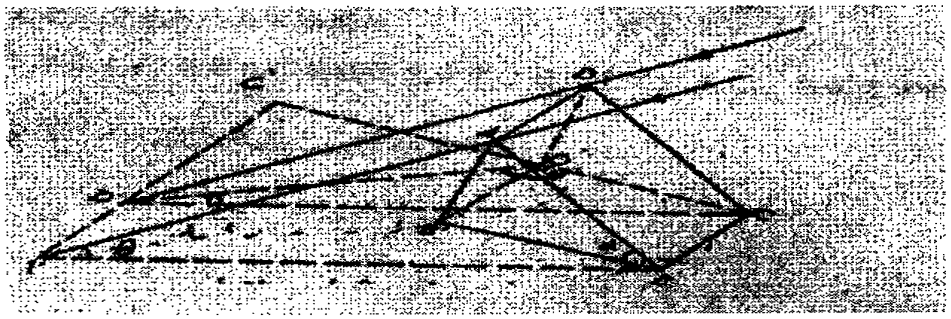


fig 1 The solar direct luminous flux on the slope aspect and the horizontal projective aspect

$$\phi_{ij} = F_{ij} \bullet \phi' \bullet S_{ij}$$

$$F_{ij} = 1 - tg\alpha_{ij} \bullet ctg\theta_{ij} \bullet Cos\omega_{ij}$$

$$\phi_{Sij} = (1 - tg\alpha_{ij} \bullet ctg\theta_{ij} \bullet Cos\omega_{ij}) \bullet \phi'_{Sij}$$

$$\omega_{ij} = Al_{ij} - Ae_{ij} \qquad (2)$$

Where, α_{ij}, θ_{ij} Al_{ij} and Ae_{ij} are respectively the pixel's ground sloped angle, the solar

elevation, the slope aspect and the sun azimuth angle. Because there is relationship between pixel's slope aspect area S_{ij} and its horizontal projective aspect area S'_{ij} as following.

$$S_{ij} = S'_{ij} / Cos\alpha_{ij}$$

We have the pixel's slope aspect luminous as:

$$E_{Sij} = \phi_{Sij} / S_{ij} = F_{ij} \bullet \phi' \bullet S_{ij} \bullet Cos\alpha_{ij} / S'_{ij} = F_{ij} \bullet Cos\alpha_{ij} \bullet E'_{Sij} \quad (3)$$

Where E'_{Sij} is the pixel's horizontal projective aspect luminous.

And the pixel's slope aspect remotely sensed data value can be:

$$D_{Sij} = K \bullet E_{ij} \bullet \tau_{ij} \bullet \gamma_{ij} / \pi = K \bullet E_{ij} \bullet \tau_{ij} \bullet \gamma_{ij} \bullet Cos\alpha_{ij} \bullet E'_{ij} / \pi = F_{ij} \bullet Cos\alpha_{ij} \bullet D'_{Sij}$$

2.2.2 The pixel's sky-scattering light illuminance on the slope aspect and its remotely sensed data value

As shown in Figure 2[2], a given pixel there have relationslhip between the pixel's sky light

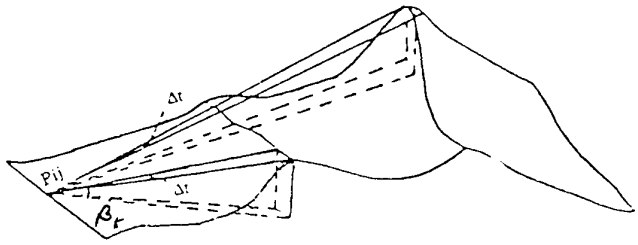


Fig 2 The sky-scattering light shielded model by the surrounding terrain factors

illuminance on the slope aspect (E_{Dij}) where P $_{ij}$ is shielded by the suround landform and the pixel's sky light illuminance E'_{Dij} where P_{ij} is on flat and widen terrain condition as:

$$E_{Dij} = E_{Dij} \bullet G_{ij}$$

$$G_{ij} = 1 - 2/n\pi \bullet \Sigma \beta_k \qquad n = 2\pi / \Delta t \qquad (4)$$

Where, β_k is the terrain-shielding angle of pixel in the K th aspect on a digital topographic map.

Δt is the azimuth increment.

In a similar way, there have:

$$D = G_{ij} Cos\alpha_{ij} E'_{Dij} K\tau_{ij}\gamma_{ij} / \pi = G_{ij} Cos\alpha_{ij} D'_{Dij} \qquad (5)$$

2.2.3 The quantitative relationship of pixel's remotely sensed components between solar direct light and sky-scattering light illuminance

The quantitative relation between pixel's remotely sensed components of solar direct light D_{ij} and remotely sensed components of sky-scattering light illuminance D_{ij} depends on the ratio of the horizontal projective aspect component of the sky-scattering light illuminance (E'_{ij}) to the solar direct light (E'_{Sij}) on the pixel's slope aspect surface (What is called scatter to direct ratio(SDR)).

$$L_{ij} = E'_{Dij} \Big/ E'_{Sij}$$

$$D_{Dij} = (D_{Nij} - D_{Aij}) G_{ij} L_{ij} \Big/ (F_{ij} + G_{ij} L_{ij})$$

According to (4) and (5) equation, we have,

$$L_{ij} = D'_{Dij} \Big/ D'_{Sij} = D_{Dij} F_{ij} Cos\alpha_{ij} \Big/ (D_{Sij} G_{ij} Cos\alpha_{ij}) = D_{Dij} F_{ij} \Big/ D_{Sij} G_{ij} \qquad (6)$$

3 The scatter to direct ratio(SDR) and the remotely sensed data value of atmospheric path radiance (APR)

In horizontal direction, the spatial change of sky-scattering light illuminance to the solar direct light (SDR) and he remotely sensed data value of atmospheric path radiance, have such properties as low-frequency and continuousness. Thus, the horizontal component of a certain pixel point can be interpolated by digital surface simulation. According to the distance-weighted interpolation algorithm, We can get the following expression:

$$D_{Aij}(L_{ij}) = \Sigma D_{Ak}(L_k)/S_k \Big/ \Sigma(1/SK)$$

Where D_{Ak} and L_k are seperately defined as the satellite-ground synchronous observational pixel's remotely sensed data value of APR and SDR on the =ground surface in Kth small region; And S_k is the distance from the Kth observation point to the pixel P_{ij} .

The compute algorithm of the remotely sensed data value of pixel P_k of APR is presented in Reference[3]:

$$D_{Ak} = DN_1 - \gamma_1 (DN_1 - DN_2)/(\gamma_1 - \gamma_2)$$

Where, DN_1, DN_2 respectively refers to the pixel's remotely sensed data value of two different neighboring ground features, γ_1, γ_2 is their reflectivity. And n is the number of actual-measured discrete ground observation points.

4 Disintegration of pixel's remotely sensed data value

As we review equation (1) and equation(6), we can get the following expression that presents the relationship between the original remotely sense data (DN_{ij}) and the remotely sensed component of solar direct light D_{Sij} of pixels;

$$D_{Sij} = DN_{ij} - D_{Aij})F_{ij} \Big/ (F_{ij} + G_{ij}L_{ij}) \qquad (7)$$

In the similar way, the relationship between the original remotely sensed data (DN_{ij}) and the remotely sensed component of sky-scattering light illuminance D_{Dij} of pixels

$$D_{Dij} = (DN_{ij} - D_{Aij}) * G_{ij} * L_{ij} / (F_{ij} + G_{ij} * L_{ij}) \qquad (8)$$

Suppose the Band 4 original data value on a remotely sensed image are as follows;
DN=112,DA=7, L=0.19, AL=173°,A_c=-135°,G=1-0.33=0.67

$\theta = 32^\circ, \alpha = 27^\circ$

Then :

F=1-tg$\alpha * ctg\theta * \cos\omega$ =1-tg27° * $ctg31^\circ * \cos(173^\circ + 135^\circ)$ =1.331

$$D_S = (DN - D_A)F/(F + G \bullet L) = (112 - 7) \bullet 1.331/(1.331 + 0.67 \times 0.19) \approx 96$$

$$DD = (DN - D_A) \bullet F \bullet L/(F + G \bullet L) = (112 - 7) \times 0.19 \times 0.67/(1.331 + 0.67 \times 0.19) \approx 9$$

Because pixel's remotely sensed data value of APR(D_{Aij}) depend on the atmospheric conditions and have no relationship with the ground features, the expression (DN_{ij}-DD_{ij})in the equations is the atmospheric correction in traditional remotely sensed image processing.

For the sake of simplification, all above discussion is based upon the assumption that the surface is of Lambertian feature. But the conclusive expressions are also appropriate for the non-Lambertian surface, because the coefficients, F_{ij}, G_{ij} and G_{ij} in the equation are computed directly based on the equimultiple change of the same pixel's ground irradiance (the directions of incidence and reflection are same either on natural ground surface or on horizontal ground surface), don't involve the directional reflection.

5.Composition and Decomposition of Remotely sensed digital image

Being Have the expression of pixel's remotely sensed data value with the three components of the solar direct light, sly-scattering light illuminance and atmospheric path radiance, we can now resolve the original remotely sensed digital image light illuminance (SSI) image and atmospheric path radiance(APR) image.

Suppose the original remotely sensed image is defined as:

$G(i, j) \qquad i = 1,2,....,n; \qquad j = 1,2,.....n.$

The solar direct illuminance (SDI) image is defined as:

$G_S(i,j)$ $i=1,2,....,n;$ $j=1,2,.....n.$

The sky-scattering light illuminance (SSI) image is defined as:

$G_D(i,j)$ $i=1,2,....,n;$ $j=1,2,.....n.$

The atmospheric path radiance(APR) image is defined as:

$G_A(i,j)$ $i=1,2,....,n;$ $j=1,2,.....n.$

then

$$G(i,j)=DN_{ij}$$

$$G_S(i,j)=INT[(DN_{ij}-D_{Aij})F_{ij}/(F_{ij}+G_{ij}\bullet L_{ij})]$$

$$G_D(i,j)=INT[(DN_{ij}-D_{Aij})\bullet L_{ij}\bullet F_{ij}/(F_{ij}+G_{ij}\bullet L_{ij})]$$

$$G_A(i,j)=INT[\Sigma(DAK/SK)\Sigma(1/SK)]$$

$$F_{ij}=1-tg\alpha_{ij}\bullet ctg\theta_{ij}\bullet Cos\omega_{ij}$$

$$\Omega_{ij}=Al_{ij}-Ae_{ij} \qquad L=E'_{Dij}/E'_{Sij}=D'_{Dij}/D'_{Sij}$$

$$N=2\pi/\Delta t \qquad G_{ij}=1-(2/n\pi)\bullet\Sigma\beta k$$

$$G(i,j)=G_S(i,j)+G_D(i,j)+G_A(i,j)$$

Where i=1,2.....,n; j=1,2.....,m.

The image composition and decomposition can be realized by the above calculation point by point.

For the sun light is a kind of strong-directional non-polarized light, the SDI image can be used in research of direction reflection of ground surface features. The sky-scattering light is anisotropic random polarized, its corresponding remotely sensed image, which is free from shadow disturb, can be applied in research of computer identification and classification. The remotely represents the difference of atmospheric environment monitoring.

In conclusion, the different kind of components of natural light shows different characters. The analytic of remotely sensed image plays a unique powerful role in the research of remote sensing mechanism, and ground surface radiant energy quantitative analysis.

Reference

1.Li Xianhua, Correction of Terrain Influence in remote sensing Information, Journal of Topography, May, 1986,15(2)

2.Li Xianhua, Calculation and emendation of diffusion irradiant energy of Remotely sensed Data on upland condition, Remote sensing Technique and Application,Mar,1992,7(1).

3 Li Xianhua, Inversion Calculation of the Pixel's Surface Reflectivity of the remotely sensed data , Environmental Remote Sensing, Dec, 1993,8(4)

THE STATISTICAL CORRELATION WITH INVARIANT MOMENTS FOR GEOMETRIC CORRECTION IMPROVEMENT

Sompong WISETPHANICHKIJ, Kobchai DEJHAN, Somkid HANPIPATPONGSA,
Fusak CHEEVASUVIT, Somsak MITATHA, Chanchai PIENVIJARNPONG*,
Chatcharin SOONYEEKAN**

Faculty of Engineering and Reserch Center for Communication and Information Technology,
King Mongkut's Institute of Technology Ladkrabang, Ladkrabang,
Bangkok 10520, Thailand.
Tel : 66-2-3269967, 66-2-3269081, Fax : 66-2-3269086
E-mail : kobchai@telelan.telecom.kmitl.ac.th
* National Research Council of Thailand,
MOS-I Receiving Ground Station, Ladkrabang, Bangkok 10520, Thailand.
** Aeronautical Radio of Thailand,
102 Ngamduplee, Tungmahamek, Bangkok 10120, Thailand.

KEY WORDS: Statistical Correlation, Geometric Correction

ABSTRACT: The systematic and non-systematic (or random) distortions are major causes of geometric distortion on remote sensing images. The reliableness of all applications usage lay down on geometric correction methods. The precision method is images registration with ground control points, but the assigned GCPs position on the corrupted images with interference noise and burry cloud coverage is difficult and bore some task. Therefore, this paper presents a method to assign automatic GCPs by using image registration method based on sequential similarity detection algorithm (SSDAs) technique, called statistic correlation measurement. The subimage around GCPs are selected and applied with invariant moments method as prototype image to assign a precise positions of GCPs are without translation, rotation and scale change problems. The above sub-images will be applied with whitening filter, that are the results of statistic correlation measurement analysis under the assumption of Markov-process before image registration, geometric transformation and resampling to carry out a precision geometric correction.

1. INTRODUCTION

The systematic and non-systematic (or random) distortions are geometric distortion that appear on satellite image and necessary to correct before using. With the ground control points(GCPs), the precision of geometric correction will be done. The corrupted-image with cloud coverage and noise make mapping between GCPs and coincident areas on the image diffculty. To automatic register the sub-image around GCP from the improved image acting as prototype image to assign the positions of GCPs for the improving satellite image, the correlation will also be used in order to obtain the precision and accuracy. The geometric correction process geometrically converts the image coordinates from (x,y) to $(\hat{x}, \hat{y})$, where corrected coordinates without geometrical distortion are expressed by $(\hat{x}, \hat{y})$ and input image corrdinates by (x,y). For Precision geometric correction could be preformed the image to image registration that one image is refered to be the reference image and assumed to be of good quality, i.e., no clound to present, contrast is good and geometrical distortion are negligible. The search (input) image, on the other hand, is relatively unknown quality. Some fog/clound cover may be present along with geometrical distortion. The important issue to achieve such process is the way to select the ground control point (GCP), which should be evident on both images or topographic map, time invariance and spread through out the image. For the sake of two images of the same scene

cannot be meaningfully compared. Principal among these are cross-correlation, normalized cross-correlation as shown in eq.1 and minimum distance cirteria (Webber, 1973).

$$R(u,v) = \frac{\sum_{j=1}^{J}\sum_{k=1}^{K} f_1(j,k) f_2(j-u,k-v)}{\left[\sum_{j=1}^{J}\sum_{k=1}^{K} f_1^2(j,k) \sum_{j=1}^{J}\sum_{k=1}^{K} f_2^2(j-u,k-v)\right]^{1/2}} \quad (1)$$

where (j,k) are indices in a JxK point window area W, that is located within an MxN point search area S.

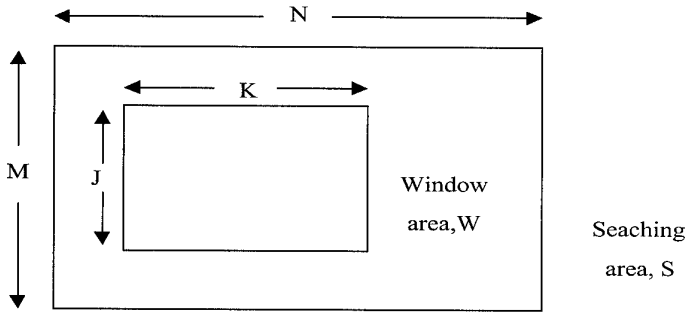


Figure 1. Relationship between search and window areas.

With translation, rotation and scale chane problems, the window sub-images around GCPs are selected from corrected image and appiled with non-variant moments technique to carry out the precise positions of GCPs in searching area in un-corrected image as mention in section 3. Then, the window sub-image will be applied with whitening fillter based on statistical correlatrion technique.

2. STATISTICAL CORRELATION MEASURE

Let f_1 and f_2 are search and window images that come form the same scene. The elements of f_1 (j,k) and f_2(j,k) will be highly correlated spatially. So, the conventional correlation measure, it is relatively difficult to distinguish the peak of R(u,v). With the spatially filtering to decorrelate or "whiten", this problem will be removed.

Let the column vector Q and P represent the image function f_1(j,k) and f_2(j,k), repectively, scaned in a vertical raster fashion.

$$Q = \begin{bmatrix} f_1(1,1) \\ f_1(2,1) \\ \vdots \\ f_1(J,1) \\ f_1(J,2) \\ \vdots \\ f_1(J,K) \end{bmatrix} \quad \text{and} \quad P_{u,v} = \begin{bmatrix} f_2(u+1,v+1) \\ f_2(u+2,v+1) \\ \vdots \\ f_2(u+J,v+1) \\ f_2(u+J,v+2) \\ \vdots \\ f_2(u+J,v+K) \end{bmatrix} \quad (2)$$

So the whitening filtered images matrix are

$$A = [H_Q]^{-1} Q \quad \text{and} \quad B_{u,v} = [H_P]^{-1} P_{u,v} \quad (3)$$

where H_Q and H_P are obtained by a factorization of the image covariance matrices.

$$C_Q = H_Q H_Q^{\,T} \quad \text{and} \quad C_P = H_P H_P^{\,T} \quad (4)$$

Hence,

$$H_Q = E_Q \Lambda_Q^{\frac{1}{2}} \quad \text{and} \quad H_P = E_P \Lambda_P^{\frac{1}{2}} \quad (5)$$

where Λ_Q and Λ_P are diagonal matrices containing eigen values along the diagonal, E_Q and E_P are composed of eigen vactors arranging in corresponding column form on each eigen values in Λ_Q and Λ_P

The basic correlation operation (eq. 1) is now preformed on the whitened vector A and B, yielding the statistical correlation measure.

$$R_s(u,v) = \frac{A^T B_{u,v}}{\left[(A^T A)(B_{u,v}{}^T B_{u,v})\right]^{1/2}} \tag{6}$$

which can be reduced to

$$R_s(u,v) = \frac{[GQ]^T P_{u,v}}{\left[([GQ]^T [GQ])(P_{u,v}{}^T P_{u,v})\right]^{1/2}} \tag{7}$$

where $G = (C_T)^{-1}$

Under the assumption of Markov Process Image, that is , the row and column image elements are assumed to be samples of Markov process (Pratt, 1972). Hence, the image covariance matrix, C is given by

$$C = \begin{bmatrix} 1 & \rho & \rho^2 & \cdots & \rho^{JK} \\ \rho & 1 & \rho & \cdots & \rho^{JK-1} \\ \rho^2 & \rho & 1 & \cdots & \rho^{JK-2} \\ \rho^{JK} & & & & 1 \end{bmatrix}_{JK \times JK} \tag{8}$$

where JxK is size of window area (Figure 1) and ρ is the adjacent element correlation. The eigen values and eigen vectors can be found recursively and whitening filter become to (Arcess, 1970):

$$G = C^{-1} = \frac{1}{(1-\rho^2)} \begin{bmatrix} -1 & -\rho & 0 & 0 & \cdots & 0 \\ -\rho & (1+\rho^2) & -\rho & 0 & \cdots & 0 \\ 0 & -\rho & (1+\rho^2) & -\rho & \cdots & 0 \\ \vdots & & & & & \vdots \\ 0 & \cdots & & & 0 & -\rho & 1 \end{bmatrix} \tag{9}$$

Multiplication of the image vector(Q) by whitening filter (G) is equivalent to convolving the image $f_1(j,k)$ with the two dimensional function (Pratt, 1974)

$$D_{jk} = \begin{bmatrix} 0 & 0 & 0 & 0 & 0 \\ 0 & \rho^2 & -\rho(1+\rho^2) & \rho^2 & 0 \\ 0 & -\rho(1+\rho^2) & (1+\rho^2)^2 & -\rho(1+\rho^2) & 0 \\ 0 & \rho^2 & -\rho(1+\rho^2) & \rho^2 & 0 \\ 0 & 0 & 0 & 0 & 0 \end{bmatrix} \tag{10}$$

If the images are complety spatially unrelated, the ρ = 0. the whitening filter becomes

$$D_{jk} = \begin{bmatrix} 0 & 0 & 0 \\ 0 & 1 & 0 \\ 0 & 0 & 0 \end{bmatrix} \tag{11}$$

Hence, the statistical measure reduce to the simple correlation measure. At the other extreme, is correlation factor ρ = 1, thus

$$D_{jk} = \begin{bmatrix} 0 & 0 & 0 & 0 & 0 \\ 0 & 1 & -2 & 1 & 0 \\ 0 & -2 & 4 & -2 & 0 \\ 0 & 1 & -2 & 1 & 0 \\ 0 & 0 & 0 & 0 & 0 \end{bmatrix} \tag{12}$$

whereas, form as spatial discrete differentiation operation. Thus, while the images are highy correlated, the statistical correlation measure concentrates on the edge outline comparison between the two scenes.

3. AN INVARIANT MOMENTS CONSIDERATION

The 2-D continuous function f(x,y), the moment of order (p+q) is

$$m_{pq} = \int_{-\infty}^{\infty}\int_{-\infty}^{\infty} x^p y^q f(x,y)dxdy \tag{13}$$

The central moments is

$$\mu_{pq} = \int_{-\infty}^{\infty}\int_{-\infty}^{\infty} (x-\bar{x})^p (y-\bar{y})^q f(x,y)dxdy \tag{14}$$

where

$$\bar{x} = \frac{m_{10}}{m_{00}}; \qquad \bar{y} = \frac{m_{01}}{m_{00}}$$

For digital image, the central moments is

$$\mu_{pq} = \sum_x \sum_y (x-\bar{x})^p (y-\bar{y})^q f(x,y) \tag{15}$$

The 3 order central moments are

$$\mu_{00} = m_{00},\ \mu_{10} = 0, \mu_{01} = 0, \mu_{20} = m_{20} - \bar{x}m_{10},\ \mu_{02} = m_{02} - \bar{x}m_{01},\ \mu_{11} = m_{11} - \bar{y}m_{10}$$
$$\mu_{12} = m_{12} - 2\bar{y}m_{11} - \bar{x}m_{02} + 2\overline{y^2}m_{10},\ \mu_{21} = m_{21} - 2\bar{x}m_{11} - \bar{y}m_{20} + 2\overline{x^2}m_{01},$$
$$\mu_{30} = m_{30} - 3\bar{x}m_{20} + 2m_{10}\overline{x^2} \text{ and } \mu_{03} = m_{03} - 3\bar{y}m_{02} + 2m_{01}\overline{y^2} \tag{16}$$

So, A set of invariant moments is

$$\phi_1 = \eta_{20} + \eta_{02},\ \phi_2 = (\eta_{20} - \eta_{02})^2 + 4\eta_{11}^2,\ \phi_3 = (\eta_{30} - \eta_{12})^2 + (3\eta_{21} - \eta_{03})^2 \tag{17}$$

4. GEOMETRIC TRASFORMATION

The geometric transfoemation in this paper using the bilinear transformation method for image restoration.The image,f is given with pixel coordinates (x,y) undergoes geometric distortion to produce an image g with coordinates $(\hat{x}, \hat{y})$. This transformation can be expressed as follow:

$$\hat{x} = r(x,y) \text{ and } \hat{y} = s(x,y)$$

where r(x,y) and s(x,y) repesent the spatial transformation that produced the geometrically corrected image $g(\hat{x}, \hat{y})$. Suppose that the geometric distortion process within the quadrifateral regions is modeled by a pair of bilinear equations. sothat,

$$r(x,y) = C_1 x + C_2 y + C_3 xy + C_4 \tag{18}$$

and

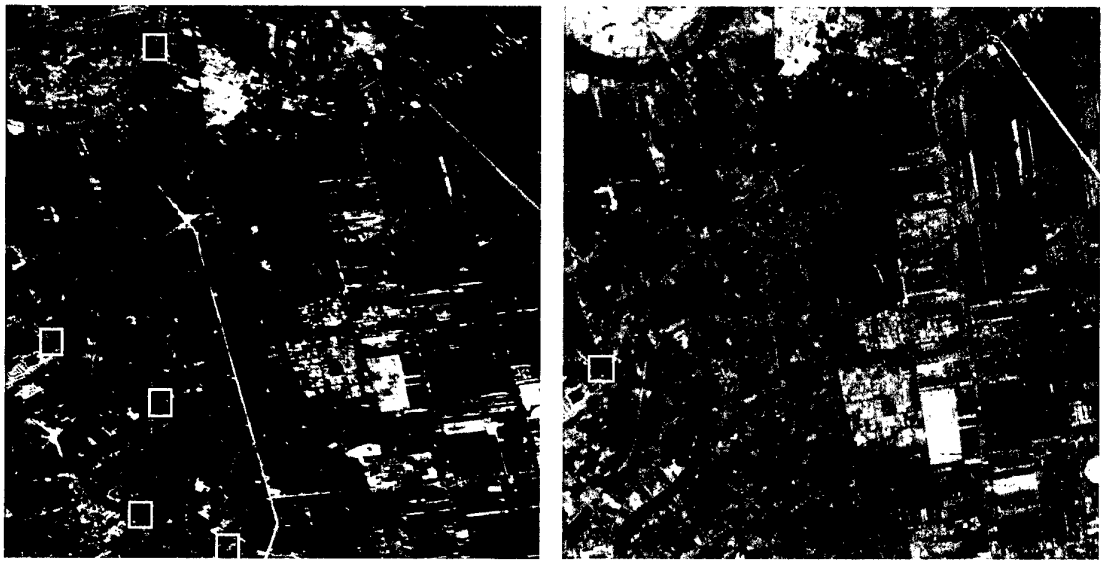
$$s(x,y) = C_5 x + C_6 y + C_7 xy + C_8 \tag{19}$$

The resampling for noninteger value of $\hat{x}$ and $\hat{y}$ according to the coefficients C_i will be interferren with bilinear interpolation for gray level interpolation, which can be express as

$$v(\hat{x}, \hat{y}) = ax + by + cxy + d \tag{20}$$

5. EXAMPLE OF GEOMETRIC CORRECTION WITH STATISTICAL CORRELATION MEASURE TECHNIQUE BASED-ON INVARAINT MOMENT CRITERIA

For completly geometric correction, frist step is choosed for searching areas and window areas, where cover on the points as expected tobe ground control point (GCP). Fig 2(a) and 2(b) show full scence OPS image around north of Bangkok which are acquired by JERS-1 on Jan, 29, 1997 and Dec, 10, 1995, respectively. Evenmore, Fig2(b) has been corrected by GICS, image processing system installed in Ladkrabang Ground station and used as reference image.



(a) raw data January 29,1997 (b) geometric corrected December 10,1995

Figure 2 North of Bangkok OPS images

Figure 3 shows window sub-image, where selected from corrected image (Figure 2b). Whileas, Figure 4 shows corresponding searching area from uncorrected image (Figure 2a) that has almost same correlation value and difficultly distinguish the correct area.



Figure 3 Typical window area



(a) (b) (c) (d)

Figure 4 Seaching area with the almost-same correlation value.

Second step, to apply the invaraint moment calculation to such images and the results as shown in table 2. The window image has nearest value with Figure4C. After applying the statistical correlation as mentied before on a pair of sub scence to find out the best-correction point, R_s (u,v) peakes. Figure 5 shows the searching areaes, where are decorrelated by whitening filter (G) with $\rho = 0, 0.5, 0.9$ and 1, respectively.



a. **b.** **c.** **d.**

Figure 5 Simulation results of Static correlation measurement with $\rho = 0, 0.5, 0.9$ and 1

Figure 5 shows simulation results of correlation measure with $\rho = 0, 0.5, 0.9$ and 1. The peak of sub images are referred as ground control points (GCPs) and used for geometric transformation with bilinear technique. The gray level interpolation, then it has been performed with bilinear interpolation in last step and final result of geometric correction has shown in Figure 6.



Figure 6 Final result of geometric correction image.

Moment invariants

Invariant (Log)	ϕ_1	ϕ_2	ϕ_3	ϕ_4	ϕ_5	ϕ_6	ϕ_7
Figure 3 window image	7.15	18.65	22.74	23.04	38.98	30.65	38.84
Figure 4(a)	6.14	10.71	14.36	13.42	45.35	38.36	48.95
Figure 4(b)	5.65	23.30	16.61	17.35	33.12	40.85	32.53
Figure 4(c)	7.23	17.44	23.57	23.19	39.06	31.07	39.32
Figure 4(d)	8.36	22.81	24.06	26.37	51.17	46.14	52.91

6. CONCLUSION

The basic developed correlation shows easierly distinguish the peaks of $R_s(u,v)$ with statistical correlation technique. By using the invaraint moment, it is easy to get rid of the ambiguous same correntlation value. Finally, after re-applying the statistical correlation with the result as $R_s(u,v)$ peaks sharply at the correct point, that bring to the reliable automatically geometic correction based on image to image registation.

REFERENCE

Webber, W.F., 1973. Techniques for Image Registration. IEEE Conf. on Machine Processing of Remotely Sensed Data, pp. 1B.1 - 1B.7.

Pratt, W. K., 1974. Correlation Techniques of Image Registration. IEEE Trans.Aerosp. Electron.Syst., Vol AES-10, pp.353-358.

Arcess, A., Mengert, P.H. and Trombini, E.W., 1970. Image Detection through Bipolar Correlation. IEEE Trans. Information Theory, Vol.IT-16, pp.534-541.

Gonzalez, R. C. and Woods, R.E., 1993. Digital Image Processing. Addison-Wesley Publishing Company, USA.

Pratt, W.K., 1972. Generalized Wiener Filtering Computation Techniques. IEEE Trans. Computer, Vol. C-21, pp. 636-641.

Wisetphanichkij, S., Dejhan, K., Cheevasuvit, F., Mitatha, S., Hanpipatpongsa, S., Pienvijarnpong, C. and Soonyeekan, S., 1998. An Improvement of Geometric Correction of Satellite Image. Proc. of the 19th Asian Conference on Remote Sensing (ACRS'98).

OPTIMIZATION OF ACTIVE AND PASSIVE REMOTE SENSING SYSTEMS USING INFORMATIONAL CRITERION

Asadov Hikmat Hamid oglu
Chief of department of Special Space Device Development Bureau of
Azerbaijan National Aerospace Agency
370087, Azerbaijan, Baku, Azadlig av., 159
Tel.: +99450 - 629388

KEY WORDS: Optimization, Dimension Remote sensing, Theorem, Optical channel

ABSTRACT: Questions related with optimization of systems of active remote sensing (lidars, radars, sonars etc.) taking into account of energetic losses of sensing signal in the investigated medium are considered in first part of this submission. Physical model of such systems, envisaging energetic losses is considered.

It is shown, that mathematical model of remote sensing process, according which signal, reflected from the n - th border doesn't contain influence of previous reflections from $n-1$ borders, could be obtained from considered physical model. In this case, signal reflected from n - th border will contain of influence of systematic energetic losses in homogenous layers of the investigated object.

Theorems, optimizing grade regimes of system's output signals when correction of fading is carried out and is not carried out are proved.

In second part of this submission grounding of synthesis of optimal passive remote sensing systems is given. As a result of held research it was shown, that optimum value of band width of radiometers is existed within transparent wavelength band 3 - 5 mcm.

1. OPTIMIZATION OF ACTIVE REMOTE, SENSING SYSTEMS

1.1. Principle of the measuring systems dimension lowering

Criterion of effectiveness of any class of measuring systems, could be expressed by functional

$$U = F(X, Y)$$

where $X = (x_1, x_2, \ldots, x_n)$ - vector, characterizing system's parameters, which could be managed; $Y = (y_1, y_2, ..., y_n)$ - vector, composed of non - managed parameters of a system.

If according to the principle of measuring system's dimension lowering [1], we assume, that vector $X = (x_1, x_2, \ldots, x_n)$ characterizes determined class of n - dimensioned systems, so any specific lowering of $X's$ dimension will characterize some subclass of such systems. For lowering of $X's$ dimension we suppose, that some components of vector X are not independent and managed by other independent components of vector X. Thus, vector X is substituted by

two vectors: X_1 - independent or managing one, and X_2 - dependent, or managed one. The criterion of effectiveness for such systems is functional of following type

$$U_1 = F(X_1, X_2, Y)$$

In common case, designating above dependence as $X_2 = \varphi(X_1)$ we obtain

$$U_1 = F[X_1, \varphi(X_1), Y] \quad (1)$$

Therefore, the task of synthesis is lead to the searching of maximum of functional (1) for subclass of systems.

It should be noted, that two variants synthesis of subclasses are possible: 1. Function $\varphi(X_1)$ is unknown and should be determined [1]; 2. function $\varphi(X_1)$ is known [2].

In this submission we consider the second variant of synthesis applied for active and passive systems of remote sensing.

1.2. Model of researched object

A multilayered model, consisting of n - number of various homogenous layers is accepted as a basic model of studied object of active remote sensing. We assume, that sensing signal loses its own energy as a result of two processes:

1. Reflections from mutual border of any two various contiguous homogenous layers.
2. Fading in homogenous layers of studied object.

Working principle of the considered systems is explained by figure 1, where numbers mean: 1 - light emitter; 2 - studied objects; 3 - receiver.

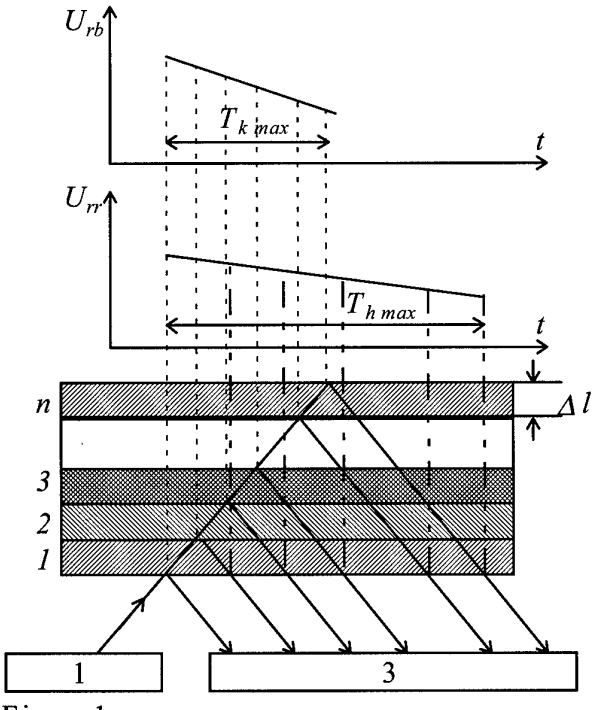


Figure 1

Figure explaining work principle of active remote sensing.

Now we assess the value of the signal in the output of such systems. If could be shown, that signal reflected from n - th border could be assessed using formula:

$$U_{r_n}=U_0 \cdot d_0 \prod_{i=1}^{n-1} d_i \prod_{i=1}^{n-1} (1-k_i) \cdot k_n$$

where d_0 - coefficient indicating fading of signal during its propagation till object;
d_i - fading in i - th homogenous layer; k_i - coefficient of reflection from i - th border.

We could assume, that signals are corrected by multilication to the coefficients

$$P_i = \frac{1}{\prod_{i=1}^{n-1} (1-k_i)}$$

In this case signal from n - th border is calculated as

$$U_{rn}=U_0 \, d_0 \left[\prod_{i=1}^{n-1} d_i \right] k_n \qquad (2)$$

Thus, corrected model fully keeps informativeness, because, information of signal reflected from n - th border is characterized by coefficient k_n .

1.3. Application of the measuring system's dimension lowering principle.

As it could be shown from formula (2) active systems of remote sensing are typical representatives of informational systems class with fading of signal. In order to synthesize an according subclass, now we consider major parameters of such systems, which could be interconnected:

$T_{k\,max}$ - maximum duration of signal, reflected from mutual borders of layers;

$T_{h_{max}}$ - duration of holding of signal, during which signal, is faded.

Obvioully, that

$$T_{h_{max}} = 2\, T_{k\,max};$$
$$T_{h_{min}} = 0; \;\; T_{k\,min} = 0$$

As a result, averaged value of T_h could be assessed as

$$T_{h\,av} = \frac{T_{h_{max}} + T_{h_{min}}}{2} = T_{k\,max}$$

Thus, dimension of such a system could be lowered, if we accept that $T_{hav} = T_k$.

Now we analuse two cases of influence of energetic lossess to the informational characteristics of such systems:

1) Fading of signal is not taken into account, when number of separable grandes of signal is determined;

2) Fading of signal is taken into account during aforesaid process.

Now we prove two following theorems, according to above cases.

Theorem 1: When correction of energetic losses is lacking in a system of active remote sensing, maximum amount of information could be reached at the output of system, if two - grade regime of output signal is chosen.

Prove: We use linear equivalent system of above one. Weight function $h(t)$, determined as reaction of a system to the input signal with one - grade amplitude is used as common charateristic.

Output signal of considered systems is determined as

$$U_{out}=U_{in}\cdot h(t)$$

Number of grade in output signal

$$m=\frac{U_{out.max}}{2\,U_{in\,max}\cdot|h'|\,T_h}+1=\frac{U_{out.max}}{2\,U_{in\,max}\cdot|h'|\,\Delta t\cdot n}+1$$

Where Δt - time period of passing of sensing light beam through layer of an object by thickness Δl. We consider the amount of information containing in received signal as a criterion of quality.

$$M=n\,log_2\,m=n\,log_2\left[\frac{U_{out.max}}{2\,U_{in\,max}|h'|\,\Delta t\cdot n}+1\right] \qquad (3)$$

In order to investigate function (3) for extremum, we obtain its first derivative and equate it to zero. As a result we obtain following equation:

$$ln(1+x)=\frac{1}{1+\frac{1}{x}} \qquad (4)$$

Where $x=\dfrac{U_{out\,max}}{2\,U_{in\,max}|h'|\,\Delta t\,n}$.

Solution of transcendental equation (4) gives us $x\approx 0{,}8$, which conforms to $m=2$.

Thus, theorem 1 is proved.

Theorem 2. Maximum amount of output information could be reached in the systems of active remote sensing where correction of systemayic energetic losses (fading) is corrected, if multigrade regime of output signal is closen.

Prove: Correction of fading of received signal leads us to the fact, that number of separable grades in it could be assessed as

$$m=\frac{U_{out.max}\cdot h(t)}{\sigma}+1$$

Where σ - noise of the system, including noise of receiver.

Consequently, amount of information in the output signal could be determined as

$$M=n\,log_2\left[\frac{U_{out.max}\left[1-|h'|\,n\,\Delta t\right]}{\sigma}+1\right] \qquad (5)$$

Investigating function (5) for maximum, we obtain its first derivative on *n* and equate it to sero. As a result we receive following equation

$$log_2\left[1+\psi_0(1-\beta)\right]=\frac{\psi_0\,\beta}{1+\psi_0(1-\beta)} \qquad (6)$$

Where: $\beta = n\cdot|h'|\,\Delta t$.

For example, if $\psi_0 = 30$, so $\beta = 0{,}7$, and $m = 10$.

Thus, theorem 2 is proved.

2. OPTIMIZATION OF PASSIVE REMOTE SENSING SYSTEMS

In the second part of this submission we consider passive systems of remote sensing, where Solar radiation is used. Systematic decreasing of Solar's radition intensity in spectral band make it possible to express the spectral dependence of ratio signal/noise ψ as

$$\psi = \psi_0 + \psi'(\lambda - \lambda_0)$$

Where $\psi_0 = \psi(\lambda = \lambda_0)$; $\lambda_0 = 3\ mcm$.

In this case quantity of information is assessed as

$$M = \frac{\lambda_\Sigma}{\Delta\lambda} log_2\left[\psi_0 + 1 + \psi(\lambda - \lambda_0)\right] \qquad (7)$$

Where λ_Σ - parameter, characterizing total width of transparant window of passing of atmospehere, used for passive sensing within band $(\lambda - \lambda_0)$; $\Delta\lambda$ - width of the one spectral channel.

In order to syntesize the optimal system we use aforesaid principle lowering of dimension. We assume, that regularity of dependency between parameters λ_Σ and $(\lambda - \lambda_0)$, i.e. function $\lambda_\Sigma = f(\lambda - \lambda_0)$ is known. In first approach we assume linear type of said function $\lambda_\Sigma = k(\lambda - \lambda_0)$, and designating $\lambda_1 = \lambda - \lambda_0$ we have

$$M = \frac{k\cdot\lambda_1}{\Delta\lambda}\cdot log_2\left[1+\psi_0+\psi'\lambda_1\right] \qquad (8)$$

In order to investigate function (8) for maximum on λ_1, we use above rule and obtain following equation

$$log_2(\psi_0 + 1 + \psi'\lambda_1) = \frac{k\,\lambda_1\cdot\psi'}{ln\,2(\psi_0 + 1 + \psi'\,\lambda_1)} \qquad (9)$$

If we receive conditionally even distribution of noises in spectral band 3 - 5 mcm, equal to $10^{-5}\frac{W\,t}{cm^2\ mcm}$, and presence of following fuction for hypothetical optical - electronic channel of radiometer in said spectral band

$$\psi(\lambda) = 111 - 50\,\lambda_1, \qquad (10)$$

then solution of (9) taking into account of (10), when $\psi_0 = 111$, $\psi' = 50$; $k = 1$ give us $\lambda_1 \approx 1{,}7\,mcm$.

Thus, held analysis make it possible to conclude that there is possibility of existence of optimum spectral band width, within 3 - 5 mcm where maximum amount of authentic information is attained.

Reference

1. Asadov H.H. 2000. Synthesis of one subclass of measuring systems on the basis of dimension lowering principle. Baku, Proceedings of Azerbaijan Technical University, v. VIII., ¹ 1, p. 51 - 54.
2. Asadov H.H. 1982. Optimization of the process of registration on electron - beam tube. Moscow, Journal "Radiotechnics", ¹ 2, p. 64 - 66.

MULTISPECTRAL IMAGE COMPRESSION USING FCM-BASED VECTOR QUANTIZATION

Uthai SANGTHONGPRAOW and Yuttapong RANGSANSERI

Department of Telecommunications Engineering, Faculty of Engineering
King Mongkut's Institute of Technology Ladkrabang, Bangkok 10520
Tel: (66-2)326-9967, Fax: (66-2)326-9086
E-mail: mr_uthai@hotmail.com, kryuttha@kmitl.ac.th
THAILAND

KEY WORDS: Image Compression, Vector Quantization, FCM

ABSTRACT: Image compression is the process of reducing the number of bits required to represent an image. Vector Quantization method (VQ) is a method to deal with this operation. With this method a set of data points is encoded by a reduced set of reference vectors (the codebook). VQ is useful in compressing data that arises in wide range applications and it can achieve better compression performance than any conventional coding techniques which based on the encoding of scalar quantities. This paper presents a multispectral image compression method using Vector Quantization technique based on Fuzzy c-Means (FCM). In this method we first use FCM algorithm to generate a good initial codebook. A modified version of FCM is used to reduce the computational time. Experimental results are shown to illustrate the performance of the proposed method.

1. INTRODUCTION

Image Compression is a process of reducing the number of bits required to represent an image. There are several methods to compress an image data. One popular method is Vector Quantization (VQ). VQ was used for compressing data in wide range applications, including image processing (Gray, 1984), (Nasrabadi, 1988), speech processing (Makhoul, 1985), facsimile transmission (Netravali, 1980) and weather satellites (Elachi, 1987). In this method the training vectors in the image are encoded by a reduced set of reference vectors (the codebook). From rate distortion theory, it can be shown that VQ can achieve better compression performance than any conventional coding technique which based on the encoding of scalar quantities (Gray, 1984). The objective of VQ is to design the codebook. An optimum VQ system is that one uses a codebook that yields the least average distortion of the reconstructed image. Other methods for designing codebooks have been proposed in (Linde, 1980), (Hsieh, 1992), (Hsieh, 1991), (Wu, 1994). The most popular one is the LBG algorithm (Linde, 1980). In this paper we use FCM to design the codebook in Vector Quantization process. The major problem of this method is the huge execution time in the FCM process. So, this paper will also present the modification on the FCM algorithm that can reduce the execution time in each iteration.

2. FUZZY C-MEANS CLUSTERING TECHNIQUE

The fuzzy c-means (FCM) algorithm (Bezdek, 1984) is an iterative clustering method that used to partition a data set. The objective of FCM segmentation is to compute the cluster centers and generate the class membership matrix (Zadeh, 1965). This class membership matrix is a cxN

matrix, where c is the number of groups and N is the number of samples of image in n-space. Each column of the class membership matrix is the distribution of the class attribute of its corresponding sample. Each row of the class membership matrix is the membership value of each sample to be a member of that particular cluster.

An optimal fuzzy c-partition is one that minimizes the generalized least-squared errors function. We can explain the fuzzy clustering by the following equation.

$$\text{Minimize: } \text{Jm (U,v)} = \sum_{k=1}^{N}\sum_{i=1}^{c}(u_{ki})^m \| y_k - v_i \|^2 A$$

Where : $Y = \{y_1, y_2, y_3, \ldots, y_N\} \subset R^n$ is the data set,
c is the number of clusters in Y: $2 \le c < n$,
m is a weighting exponent: $1 \le m < \infty$,
$U = \{u_{ki}\}$ is the fuzzy c-partition of Y,
$\|y_k - v_i\|A$ is an induced a-norm on R^n, and,
A is a positive-definite (nxn) weight matrix.

The weighting exponent m has the effect of reducing the squared distance error by an amount that depends on the observation's membership in the cluster. As $m \rightarrow 1$, the partitions that minimize J_m become increasingly hard. Conversely, higher values of m tend to soften a samples cluster membership, and the partition becomes increasingly blurred. Generally m must be selected by experimental means.

The first step of FCM algorithm is generate an initial random membership matrix and use this random membership matrix as weight of each samples to belong to each cluster. Then computes the centroid of each cluster. The new cluster centers are used to update the membership matrix. The updated membership matrix is compared with the previous ones. If the difference is greater than some threshold, then another iteration is computed, otherwise the algorithm is stopped. The algorithm is shown below. The notation $x^{(t)}$ signifies the value of variable x at iteration t.

The FCM Algorithm

1. set value for c, A, m, ε, and the loop counter $t = 1$
2. create a random Nxc membership matrix U
3. compute each cluster centroid by equation

$$v_i^{(t)} = \sum_{k=1}^{N}(u_{ki}^{(t)})^m y_k / \sum_{k=1}^{N}(u_{ki}^{(t)})^m \qquad (1)$$

4. update the membership matrix by equation

$$u_{ki}^{(t+1)} = \left(\sum_{j=1}^{c} \left(\frac{d_{ki}}{d_{kj}} \right)^{\frac{2}{m-1}} \right)^{-1} \qquad (2)$$

where $d_{ki} = \| y_k - v_i^{(t)} \| A$

5. If $\max \left\{ \left| u_{ki}^{(t)} - u_{ki}^{(t-1)} \right| \right\} > \varepsilon$ increment t and go to step 3.

3. THE MODIFIED FUZZY C-MEANS ALGORITHM

From equation (1) we can find that each cluster center v_i is computed as the weighted average of samples in the data set Y. The weight used for each sample is that sample's membership in the i^{th} cluster. In the original algorithm this is computed by performing a pass over the entire data set and membership matrix.

The following describes an improvement to the algorithm whereby the computation of cluster centers is performed in sequence with the membership matrix updating. This effectively eliminates an entire pass of the data set. The outcome is not a decrease in the number of iterations required for convergence, but decrease in the time of each iteration.

We maintain two extra data structures, a cxn matrix, P = $\{p_i\}$, and a vector q of length c. We can obtain these two matrix from the first iteration when the random membership matrix is created. If we represent the numerator and denominator of equation (1) by P and q, respectively, then keep them as initial values. So now the equation (1) is replaced by equation (3)

$$v_i = p_i / q_{.i} \tag{3}$$

where p_i is a vector of length n, and $q_{.i}$ is a scalar. The dot-i subscript is used to avoid confusion between vectors and scalars.

Each time an element u_{ki} of the membership matrix is computed there is an increment in the numerator of equation (1), that is an increase in p_i of

$$\left(\left(u_{ki}^{(t+1)}\right)^m - \left(u_{ki}^{(t)}\right)^m\right) y_k \tag{4}$$

And an increment in the denominator of equation (1), that is, an increase in $q_{.i}$ of

$$\left(u_{ki}^{(t+1)}\right)^m - \left(u_{ki}^{(t)}\right)^m \tag{5}$$

These increments are accumulated into P and q respectively as the membership matrix is updated. At the beginning of the next iteration the new cluster centers are again computed by equation (3).

The Modified FCM algorithm

1. set values for c, A, m, ε, and loop counter t=1
2. create a random Nxc membership matrix $U^{(t)}$
3. initialize data structures P and q using equation (1)
4. compute c cluster centers using equation (3)
5. update the membership matrix using equation (2) as each membership is computed, increment the corresponding element of P and q using equation (4) and equation (5)
6. if max $\left\{u_{ki}^{(t)} - u_{ki}^{(t-1)}\right\} > \varepsilon$ increment t and go to step 4.

4. FCM-BASED VECTOR QUANTIZATION

In this paper, FCM process is used to calculate the reference vector or average vector from each cluster. The output of this process is a membership matrix and a set of reference vectors that used to design the vector quantization codebook. The training vector will be encoded with this codebook. The algorithm of this compression method is shown in Figure 1.

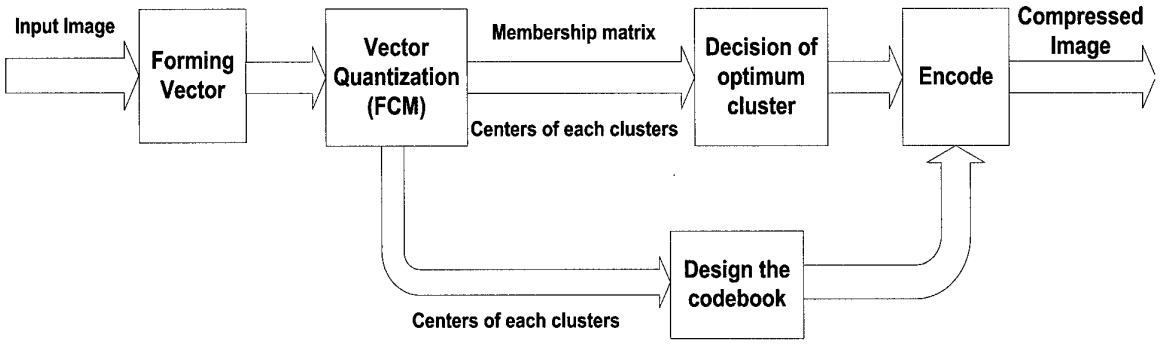


Figure 1: Block diagram of the proposed method.

The evaluation was performed by using the following measures:

$$bpp(number\ of\ bits\ per\ pixel) = \frac{Encoded\ number\ of\ bits}{Number\ of\ pixels} \tag{6}$$

$$PSNR(Peak\ Signal\ to\ noise\ ratio) = 10\log_{10}\left[\frac{255^2}{MSE}\right][dB] \tag{7}$$

$$MSE(Mean\ square\ error) = \frac{1}{3MxN}\sum_{i=0}^{M-1}\sum_{j=0}^{N-1}\sum_{k=1}^{3}\{x_k(j,i) - \hat{x}_k(j,i)\}^2 \tag{8}$$

5. EXPERIMENTAL RESULTS

The proposed image compression algorithm was implemented using Matlab. Several multispectral images were used in experimental. Table 1 shows the experimental results when applied to a three-band (24 bits) image, size of 256x256 pixels. The input image size is 196 Kbyte. The experiments were carried out with the number of clusters of 4, 16 and 64.

Table 1: Experimental results.

Number of clusters	bpp	PSNR (dB)	MSE
4	2.0016	22.0651	404.1790
16	4.068	27.4127	117.9196
64	6.0293	31.2498	48.7638

6. CONCLUSION

The experimental result shown that the proposed method can compress the multispectral image data. The compressibility of this method and the image distortion from quantizing process depends on the number of clusters used in FCM process. The major problem of this method is the execution time spent in clustering process caused by the computation complexity of FCM algorithm even we use the modified version of FCM.

REFERENCES

Bezdek, J.C., Ehrlich, R., and Full, W., 1984. FCM : The fuzzy c-means clustering algorithm. Computers and Geosciences, 10, pp. 191-203.

Elachi, C., 1987. Introduction to The Physics of Remote Sensing. Intersciences, New York.

Gray, R.M., 1984. Vector quantization. IEEE ASSP Magazine, 1(2), pp. 4-29.

Hsieh, C.H., 1992. DCT based codebook design for vector quantization of images. IEEE Trans. Circuits and Systems, 2, pp. 40-1-409.

Hsieh, C.H., Lu. P.C. and Chung. J.C., 1991. Fast codebook generation algorithm for vector quantization of images. Pattern Recogn. Lett., 12, pp. 605-609.

Linde, Y., Buzo, A. and Gray, R.M., 1980. An algorithm for vector quantization design. IEEE Trans. Commun., 28, pp. 84-95.

Makhoul, J., Roucos, S. and Gish, H., 1985. Vector quantization in speech coding, Proc. IEEE, 73(11), pp. 1551-1588.

Nasrabadi, N. and King, R.A., 1988. Image coding using vector quantization: A review. IEEE Trans. Commun., 36(8), pp. 957-971.

Netravali, A.N. and Mounts F.W., 1980. Ordering techniques for facsimile coding: A review. Proc. IEEE, 68, pp. 796-807.

Wu, X. and Guan, L., 1994. Acceleration of the LBG algorithm. IEEE Trans. Commun., 42, pp. 1518-1523.

Zadeh, L.A, 1965. Fuzzy sets. Information and Control, 8, pp. 338-353.

The 21st Asian Conference on Remote Sensing
December 4-8, 2000 Taipei, TAIWAN

COMPARISON OF TWO TEXTURE FEATURES FOR MULTISPECTRAL IMAGERY ANALYSIS

Pornphan DULYAKARN, Yuttapong RANGSANSERI, and Punya THITIMAJSHIMA

Department of Telecommunications Engineering, Faculty of Engineering,
King Mongkut's Institute of Technology Ladkrabang, Bangkok, 10520
Tel: (66-2)-326-9967 Fax: (66-2)-326-9086
E-mail: doll_dulya@hotmail.com, {kryuttha, ktpunya}@kmitl.ac.th
THAILAND

KEY WORDS: Gray-level Co-occurrence Matrix, Fourier Transform, Texture Analysis Neural Network, Multispectral Image

ABSTRACT: Two feature extraction methods, gray-level co-occurrence matrix and Fourier transform, are compared for land cover classification, which is viewed as texture of the image. Comparing results between these two texture features show that feature derived from the gray-level co-occurrence matrix give the better result than Fourier transform. With these features, supervised classification is carried out by the multi-layer perceptron (MLP) neural network using the back-propagation (BP) algorithm

1. INTRODUCTION

Texture is one of the most important defining characteristics of an image. It is characterized by the spatial distribution of gray levels in a neighborhood (Jain et al., 1995). In order to capture the spatial dependence of gray-level values which contribute to the perception of texture, a two-dimensional dependence texture analysis matrix are discussed for texture consideration. Since texture shows its characteristics by both each pixel and pixel values. There are many approaches using for texture classification. The gray-level co-occurrence matrix seems to be a well-know statistical technique for feature extraction. However, there is a different statistical technique using the absolute differences between pairs of gray levels in an image segment that is the classification measures from the Fourier spectrum of image segments.

Texture features derived from gray-level co-occurrence matrix and Fourier transform are used to be input data for unsupervised classification. By this experiment, multilayer perceptron (MLP) neural network using the back-propagation (BP) algorithm is chosen to be the classification algorithm.

2. TEXTURE FEATURES

Feature extractions acquired by this experiment are derived from the two methods. That are gray-level co-occurrence matrix and Fourier transform, which are the kinds of statistical methods. The more details of these texture analyses are shown by the following subheadings.

2.1 Gray-level Co-occurrence Matrix

Gray-level co-occurrence matrix is the two dimensional matrix of joint probabilities $P_{d,r}(i,j)$ between pairs of pixels, separated by a distance, d, in a given direction, r. It is popular in texture description and based on the repeated occurrence of some gray level configuration in the texture; this configuration varies rapidly with distance in fine textures, slowly in coarse textures (Haralick et al., 1973).

Finding texture features from gray-level co-occurrence matrix for texture classification in this experiment are based on these criteria:

Energy:

$$\sum_i \sum_j P_{d,r}^2(i,j) \tag{1}$$

Entropy:

$$\sum_i \sum_j P_{d,r}(i,j) \log P_{d,r}(i,j) \tag{2}$$

Contrast: (typically $k = 2$, $\lambda = 1$)

$$\sum_i \sum_j |i-j|^k P_{d,r}^{\lambda}(i,j) \tag{3}$$

Homogeneity:

$$\sum_i \sum_j \frac{P_{d,r}(i,j)}{|i-j|} \tag{4}$$

2.2 Fourier Transform

This classification measures from the Fourier spectrum of image segments require the calculation of the fast Fourier transform (FFT) for each segment and the definition of features in terms of the amplitudes of the spatial frequencies. The discrete Fourier transform $F(u_n,v_m)$ of a digitized image segment $f(x_j,y_k)$ of size $N_1 \times N_2$ is defined by

$$F(u_n, v_m) = \sum_{x_j=0}^{N_1-1} \sum_{y_k=0}^{N_2-1} \exp(2\pi i u_n x_j / N_1) \cdot \exp(2\pi i v_m y_k / N_2) f(x_j, y_k) \tag{5}$$

where u_n and v_m are the discrete spatial frequencies
x_j and y_k are pixel positions
$i = \sqrt{-1}$

The set of features based on the power spectrum consists of four statistical measures. If $|F(j,k)|$ is the matrix containing the amplitudes of the spectrum and N is the number of frequency components then these measures are given by (Augusteijn et al. 1995)

$$\text{Maximum Magnitude} = \max\left[|F(j,k)| : (j,k) \neq (0,0)\right] \tag{6}$$

$$\text{Average Magnitude } (A_M) = \sum_{j,k} |F(j,k)| / N \tag{7}$$

$$\text{Energy of Magnitude} = \left[\sum_{j,k} |F(j,k)|^2\right] \tag{8}$$

$$\text{Variance of Magnitude} = \sum_{j,k} \left[|F(j,k)| - A_M\right]^2 / N \tag{9}$$

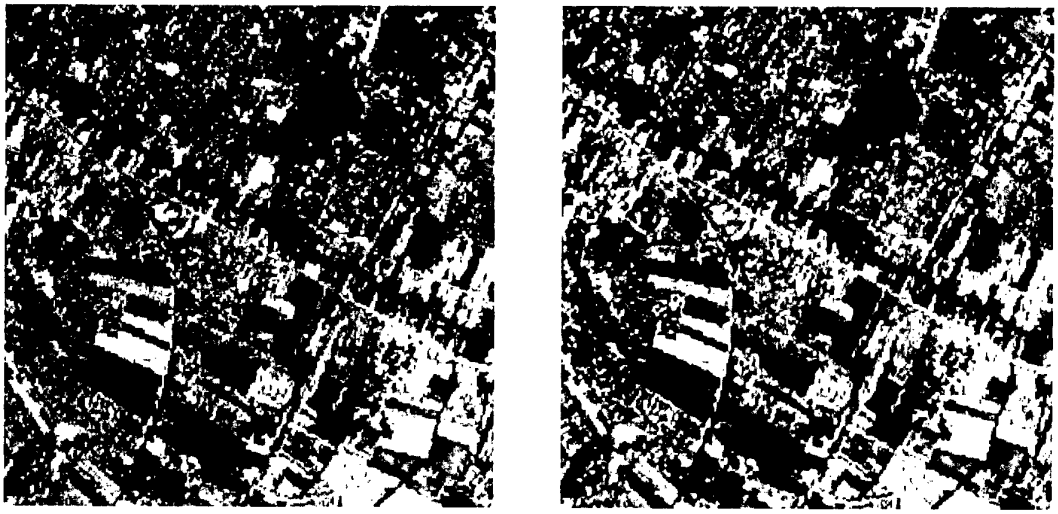
3. NEURAL NETWORK CLASSIFICATION

Multi-layer perceptrons are feed-forward networks with one or more layers of nodes between the input and output nodes. These additional layers contain hidden units or nodes that are not directly connected to both the input and output nodes. The capabilities of multi-layer perceptrons stem from the nonlinearities used within nodes. The behavior of a multi-layer network with nonlinear units is complex. A multi-layer network can be trained with a back-propagation learning algorithm (Rumelhart et al., 1986). Learning via back-propagation involves the presentation of pairs of input and output vectors. The actual output for a given vector is compared with the desired or target output. If there is no difference, no weights are changed; otherwise, the weights are adjusted to reduce the difference. This learning method essentially uses a gradient search technique to minimize the cost function that is equal to the mean square difference between the desired and actual outputs. The network is initialized by setting random weights and thresholds, and the weights are updated with each iteration to minimize the mean squared error.

The back-propagation training algorithm is an iterative gradient algorithm designed to minimize the mean square error between the actual output of a multi-layer feed-forward perceptron and the desired output. It requires continuous differentiable non-linearities. (Dulyakarn et al., 2000).

4. EXPERIMENTAL RESULTS

The multispectral image used in this experiment is ADEOS, which composes of 3 bands in the size of 256×256 pixels. This tested area, in Figure 1(a), is a region of Bangkok, Thailand. This image must be removed or decorrelates an interband correlation before using this data to be an input data by using Karhunen Loève Transform (KLT) (Dulyakarn et al., 1999). The transformed image is shown in Figure 1(b). Using the two textural analyses, gray-level co-occurrence matrix and Fourier transform, by giving the detail in the above subheading we can calculate two texture features. The supervised classification, multi-layer perceptron using back-propagation algorithm, is applied for classifying in this research. The classification results considered from two texture features are compared and shown in Table 1. The classified images can be compared by noticing from Table 1 and concluded that the texture feature using gray-level co-occurrence matrix give the result better than Fourier transform.



(a) (b)

Figure 1 The ADEOS acquired from the region of Bangkok, Thailand.
(a) An original multispectral image.
(b) The first principal component image resulted from KLT.

Table 1 Classification results.

Class	Number of Tested Pixels	Gray-level Co-occurrence Matrix (%)	Fourier Transform (%)
1	1273	85.53	81.34
2	773	76.45	74.16
3	782	70.47	67.58

5. CONCLUSION

A comparative study between two texture features derived from gray-level co-occurrence matrix and Fourier transform has been proposed. The experimental results displayed in percentage of correct classifications make the evidence that the texture analysis using gray-level co-occurrence matrix method provides the better result than texture feature derived from Fourier transform.

ACKNOWLEDGEMENT

The authors wish to thank the National Research council of Thailand (NRCT) for providing the satellite image data.

REFERENCES

Augusteijn, M. F., Clemens, L. E., and Shaw, K. A., 1995. Performance evaluation of texture measures for ground cover identification in satellite images by means of a neural network classifier. IEEE Trans. Geoscience and Remote Sensing, 33(3), pp. 616-626.

Dulyakarn, P., Rangsanseri, Y., and Thitimajshima, P., 1999. Segmentation of multispectral images based on multithresholding. In: 2nd International Symposium on Operationalization of Remote Sensing, The Netherlands.

Dulyakarn, P., Rangsanseri, Y., and Thitimajshima, P., 2000. Textural classification of urban environment using gray-level co-occurrence matrix approach. In 2nd International Conference on Earth Observation and Environmental Information, Cairo, Egypt.

Haralick, R. M., Shanmugam, K., and Dinstein, I., 1973. Textural features for image classification. IEEE Trans. Syst., Man, Cybern., SMC-3, pp. 610-621.

Jain, R., Kasturi, R., and Schunck, B. G., 1995. Machine Vision. Mc Graw-Hill International Editions, pp. 234-239.

Sonka, M., Hlavac, V., and Boyle, R., 1993. Image Processing, Analysis, and Machine Vision. Chapman & Hall Inc., pp. 482-485.

Image Analysis of Remote Sensing Data Integrating Spectral and Spatial Features of Objects

Joji IISAKA and Takako SAKURAI-AMANO*
Pacific Forestry Centre, Natural Resources Canada
506 West Burnside Road, Victoria, BC. V8Y 2N3
E-mail: jiisaka@pfc.forestry.ca
Canada
*The Earth Observation Research Centre/NASDA
Roppongi First Building, 13F
1-9-9 Roppongi, Minato-Ku, Tokyo 106-0032
E-mail: takako@eorc.nasda.go.jp
JAPAN

Keywords: TM images analysis, object recognition, spatial information extraction, application of fractal dimension, pixel swapping, image analysis of remote sensing

ABSTRACT: Digital image analysis techniques have been and are being used widely in remote sensing assuming that each terrain surface category is characterised with spectral signature observed by remote sensors.

Even with the remote sensing images of medium coarse resolution such as Landsat TM data, integration of spatial information is expected to assist and to improve the image analysis of remote sensing data.

This paper will describe and demonstrate a method, named as" Pixel swapping", to analyse remote sensing images in a unified way, integrating spatial information extraction as well as spectral information.

After a brief introduction of the method, some application to identify terrain objects like roads in the forest are demonstrated utilising the spatial information of objects.

1. INTRODUCTION

With remote sensing images such as LANDSAT TM data, most of digital analyses are applied through pixel-by pixel basis, assuming that each ground cover objects has their specific spectral characteristics.

The conventional digital image processing techniques, based on the field theoretic approach, have many advantages in numeric and analytical calculation such as filtering the signals and classifying terrain covers using multi-spectral characteristics of objects, but they are not so capable to handle spatial and geometrical information.(J. Richard, 1994, J. Jensen, 1995).

On the other hand, the mathematical morphology, based on a set theoretical approach, provides better capability with morphological processing of objects, but week in numeric and quantitative treatment of objects. Thus, more powerful functions to handle spatial feature extraction for remote sensing are required.

2. SPATIAL INFORMATION EXTRACTION FOR REMOTE SENSING

As an extension of conventional image processing and mathematical morphology, It has been proposed a method to process spatial information in an image.(J.Iisaka,1989, 1998, 1999, 2000, and J. Iisaka, et al, 1993 and 1994)

2.1 Image Computing through Pixel Swapping.

An image is defined as a function image intensity field I with parameters of a coordinate pair, x and y as:

$$I = f(x, y) \tag{2.1}$$

For a digital image, the set of co-ordinate value, X, is a finite set, and the function (2.1) is a projection of a set X to an element of a pixel value set, a, and can be denoted as:

$$I = \{(x, a(x) : x \in X)\} \tag{2.2}$$

Here, a is a set of the pixel values

This equation can be rewritten again using two points, dividing it into two terms as

$$a(x_i) = \lfloor \{a(x_i) + a(x_j)\}/2 + \{a(x_i) - a(x_j)\}/2 \rfloor \tag{2.3}$$

This means that an image is composed with two components, one represents an additive term between a pixel at the co-ordinate x_i and another pixel at the co-ordinate x_j and the other represents a subtractive term between them.
Let's demote the first term as

$I_+ = \{(x, \{a(x_i) + a(x_j)\}/2 : x \in X)\}$ and the second term as

$$I_- = \{(x, \{a(x_i) - a(x_j)\}/2 : x \in X)\} \tag{2.4}$$

Then, an image, I, is presented as

$$I = I_+ + I_- \tag{2.5}$$

The selection of a pixel pair between pixel i and j is arbitrary. A homogenous flat image can be identified if the image is not affected against any pair of pixels in that image, and if the image is not affected against any pixel pair arranged in the horizontal direction, but affected against other directions, the image may include horizontal objects. In this way, a strategy for pixel pair selection defines the spatial feature of interest.
Foe simplicity, let's select the counter pixel j to be paired with a focusing pixel i from the adjacent eight neighbour pixels and take a sum of them.

$$a(x_i) = \frac{1}{2n}\left\{\left[\sum_{j=1}^{n}\{a(x_i) + a(x_j)\}\right] + \left[\sum_{j=1}^{n}\{a(x_i) - a(x_j)\}\right]\right\} \tag{2.6}$$

Here, n is the number of pairs.

The first term corresponds to a weighted image smoothing function, and the second terms is same as the eight neighbour Laplacian edge detection kernel, which are ordinary treated separately through conventional image processing. As the operations described in the above have dilation (or erosion) effects to the objects, it would be necessary to eliminate these effects.

The simplest and most fundamental application it to identify the objects in terms of spatial entities as point-like, line-like and region-like objects. Other immediate application of the method is to detect the spatial feature points such as line-start and end points, vertices or corner points, or branch-points and line crossing points.

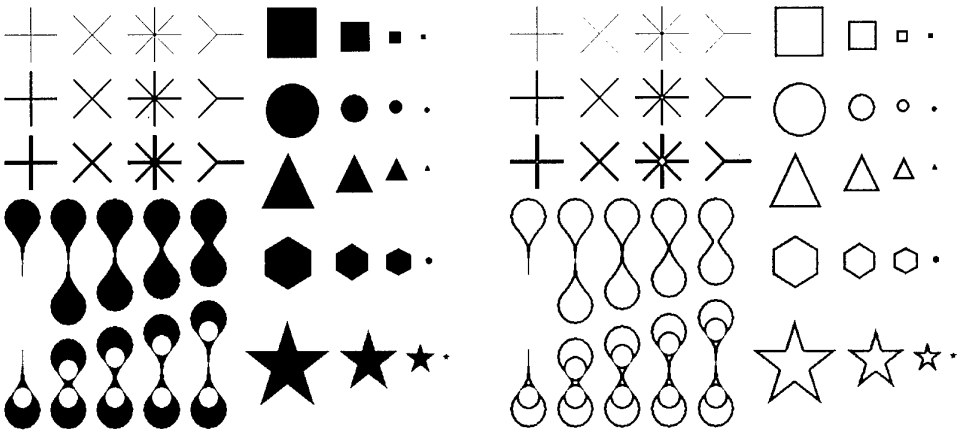


Figure 1. A test image with ideal shapes and the result of pixel swapping , using a 7x7 circular kernel. The image is divided into inner regions (yellow), boundaries (red), and lines (blue).

3. ROAD DETCTION FROM LANDSATA TM IMAGES:

The road network development in the forest indicates an expansion of human activities, and it is highly related to the man-made disturbances to forest ecology and forest growth. Therefore, monitoring of these changes from space is one of important applications for remote sensing. Forest clear-cut patches appear as area-like objects in remote sensing, and it has been investigated in the previous work (J. Iisaka and et al.1995), here the line-like objects are focussed.

The following sections illustrate some direct application of the pixel swapping method to analyse remote sensing data integrating spatial and spectral information of terrain objects.

3.1. Automated line-like object detection.

Image slicing is the most popular method to extract specific objects for many image-processing applications. This threshold value is ordinary determined at locations of peaks or valleys of the histogram of pixel values distribution, or interactively by operators of image analysis. As long as the targets have specific pixel value range and are well separated in the histogram, this method extracts the target objects very well. With multispectral images, the target objects are well identified based on the spectral similarity in spectral space, and the threshold is selected from spectral similarity.

Unfortunately, most terrain covers observed in conventional remote sensing such, as Landsat TM data are not well separated in spectral space except few objects like water. Therefore, simple threshold values are difficult to select solely from the histograms.

Problem are not only separability among objects, but some objects may have several threshold levels, because the radiometric values are affected by the objects of their neighbour or background objects in that sensor resolution cell.

It is assumed that the roads and trails appear as line-like objects and brighter than other object in a scene.

For simplicity, TM brightness image is used as the roads and trails mostly appear as bright objects in a TM scene. The brightness image is created by combining the TM visible bands, TM band 1, TM band 2 and TM band 3, which is illustrated in Figure 2.Figure 2 TM Brightness

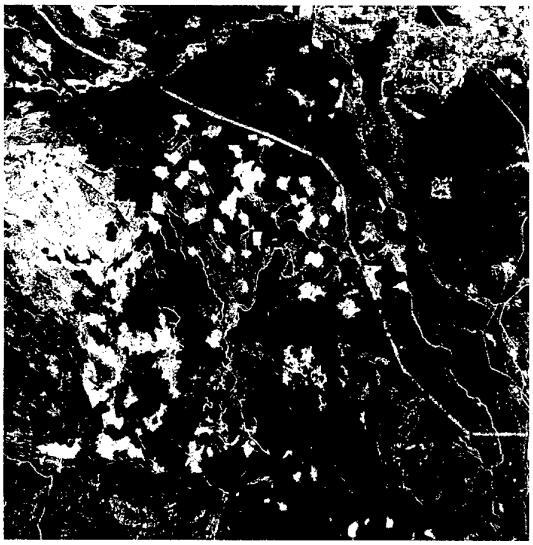


Figure 2. Image of Study Area: Watershed of Greater Victoria, BC, Canada

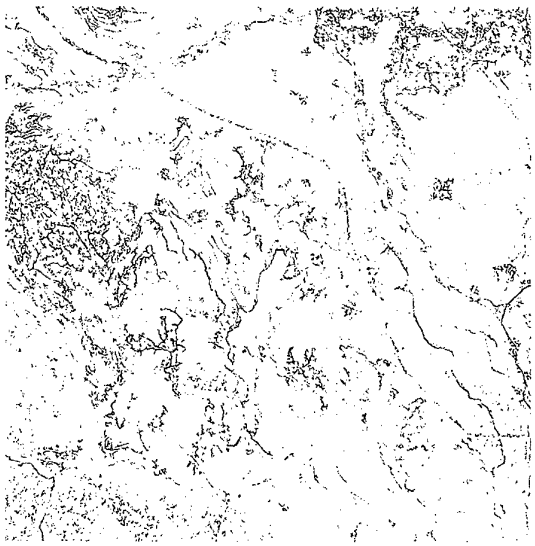


Figure 3. The Result of Line-like Object Detection

This brightness image is sliced at various thresholds starting from the maximum pixel value in the scene decreasing it with a fixed interval. With the highest threshold, no objects are extracted. With the intermediate threshold between the maximum and minimum pixel values, some objects appear as point-like objects, region like object or line-like objects. Figure 3 shows the objects extracted at the threshold that generates the maximum number of pixels for the line-like patterns.

The first experiment was conducted as follows: 1) Create a series of binary images sliced at every grey level. 2) Each binary image is processed by the pixel swapping method, and each pixel is labelled as a point, a line, or a region. 3) Then, extract only the objects labelled as line-like objects and store these results. 4) Repeat the above procedure to the image of the next slice level. 5) The result image for line-like objects is "ORed" with the previous results.

As seen in the Figure 3, many shorter line-segments are detected in the vegetated areas, and they might be the features generated by the topographic effects or tree height variability in the forest.

3.2 MODVI and Vegetation Mask

These small line-like features in the forest can be masked out using vegetation indices derived from remote sensing data.

Although the NDVI (Normalised Difference Vegetation Index: C. Tucker, 1979) is widely used as a vegetation index, it is not so reliable against radiometric environment of remote sensing. In this experiment, the MODVI (The modified Vegetation Index) is adopted in this experiment, as the MODVI is less affected by the atmospheric and solar illumination conditions. (J. Iisaka and et al. 1999, and J. Iisaka, 2000)

The MODVI is estimated by the following equation.

$$MODVI = \frac{D4 - W4}{D3 - W3} \qquad (3.1)$$

Here, W (W3, W4) is estimated from the spectral values of darkest objects in TM band 3 and band 4 images, and D3 and D4 is the pixel values of TM band 3 and 4, respectively.

3.3 Fractal Based line-like Object Detection.

It is more convenient if an algorithm is able to identify the line-like object independent to the pixel values or contrast among neighbour pixels. Most of objects observed in nature are not so simple like straight lines or ploy-lines. Rather, they are characterised by fractal dimensions. As the fractal dimension of line-like objects never exceeds 2, no matter how complex they are, fractal measures can be applied to delineate line-like objects.

Let i and j be the indices of scales (the swapping window sizes) , and denote the results of pixel swapping as S_i and S_j. The fractal dimension (local fractal dimension) D can be estimated from the following equation.(J. Iisaka, 1998,1999)

$$D = \frac{\log(S_i / S_j)}{\log(i / j)} \qquad (3.2)$$

In Figure 4, each pixel represents the local fractal dimension (windows sizes were 3x3 and 5x 5).
Therefore, it is necessary to threshold the fractal image between "1 or greater than 1" and "less than 2".

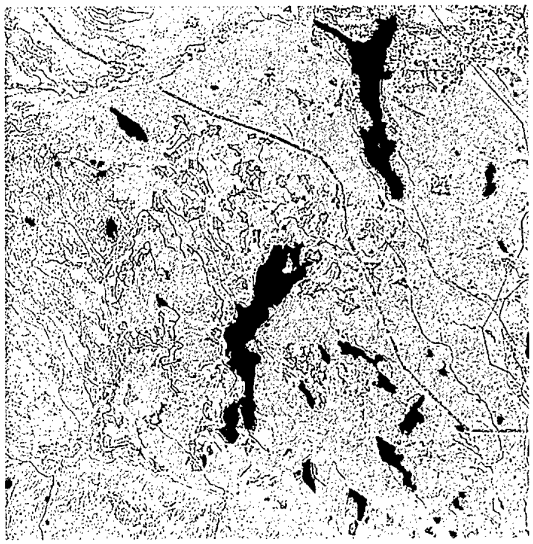


Figure 4 Fractal Image derived from the rightness image (see Figure 2.)



Figure 5 Road detected in less vegetated areas

The Figure 5 is the result of roads in less vegetated areas derived using the TM data, and overlaid with TM false colour image of the study area.

4. SUMMARY AND COCLUSIONS

It was demonstrated that terrain cover objects with specific spatial objects, roads and trails in the forest were detected well through integration of spatial and spectral information. It was also demonstrated that the method, the pixel swapping, worked well to extract spatial features of terrain objects for remote sensing.

More complex and sophisticate post processing is definitely required to create the similar feature like conventionally maps provide. This is the main subject for the future study.

5. REFERENCES

1) Joji Iisaka, "Automated Detection of man-made Disturbances in the Forest From Remotely Sensed Images", Proceeding of the 2nd International Conference on Geospatial Information in Agriculture and Forestry, 10-12 January, 2000, Lake Buena Vista, FL, USA, pp. II-135-322.

2) Joji Iisaka and Takako Sakurai-Amano, "A new Vegetation Index for Remote Sensing", Proceeding of the 115th symposium of the Korean Society of Remote Sensing and the Workshop of Environment Monitoring from Space for East Asia, Nov.3-5, 1999, Kangnung, Korea, 1:256-261.

3) Joji Iisaka, " A Unified Image Computing Method for Spectral and Spatial Feature Extraction form Remotely Sensed Imagery," the Proceeding of SPIE Symposium on Non-linear Image Processing IX, San Jose, California, USA, pp.232-239, January 26-27, 1998.

4) Joji Iisaka, Etsuko Amano and Takako Amano, " Automated forest clear cut detection from TM data" , Proceedings of the 26th Annual Symposium of Remote Sensing of Environment, Vancouver, Canada, pp.67-70, March 1996.

5) Joji Iisaka and Takako Sakurai-Amano, "Terrain Feature Recognition for SAR Imagery employing Spatial Attributes of Targets," In the Proceedings of the ISPRS Commission III Symposium, SPIE Vol. 2357, pp.399-408, September 5-9, 1994.

7) Joji Iisaka and Takako Sakurai-Amano, " Spatial Association Analysis for Radar Image Interpretation," In the Proceeding of the IGARSS'93, Tokyo, Japan, pp.1200-1203, August 18-21 1993.

8) Joji Iisaka, "Structural Spatial Information Extraction form Remotely sensed data," In the Proceeding of the IGARSS'89, Vancouver, Canada, pp.1224-1227, July 10-14 1989.

9) Compton J. Tucker, "Red and Photographic infrared Linear combinations for monitoring vegetation," Remote sensing of Environment, Vol.8 (2), pp.127-150 (May 1979).

10) John A. Richards, "Remote Sensing Digital Image Analysis: An Introduction," Springer Verlag, New York, USA; ISBN: 0387582193, edition September 1994.

11) John R. Jensen, Introductory Digital Image Processing: A Remote Sensing Perspective, August 24, 1995, Prentice Hall, New Jersey, USA; ISBN: 0132058405.

A NEW APPROACH FOR AUTOMATIC DETERMINATION OF EDGE CENTER LINES IN A DIGITAL IMAGE

Jaan-Rong TSAY
Assistant Professor, Department of Surveying Engineering
National Cheng Kung University
1 University Road, Tainan ,Taiwan
Tel: (886)-6-2370876 ext. 838 Fax: (886)-6-2375764
E-mail: tsayjr@mail.ncku.edu.tw
TAIWAN

KEY WORDS: Digital Image, Edge Center Line, Gradient Operator, Wavelets, Zero-Crossing

ABSTRACT: Firstly, this paper proposes a set of new symmetric gradient operators. They were derived from the wavelet theory and some well-known compactly supported orthonormal wavelets. Some tests are done using digital images. They conclude that such operators are really better edge-detectors e.g. than the Sobel ones. Secondly, a new approach for automatic determination of edge center lines in a digital image is presented. It integrates these new wavelet-based gradient operators with the general zero-crossing principle. Test results show apparently that it can automatically determine all center edge-lines of one pixel width.

1. INTRODUCTION

At present, edge features are often used in different kinds of image-based techniques, e.g. photogrammetry, remote sensing, computer vision, image understanding and so on. Based on those edge features, geometrical, physical-radiometric and semantic data and information as well can be extracted semi- or even full-automatically by different algorithms, where digital or digitized images are the main input data. In the field of image processing, there are already many different kinds of operators and methods for detecting three basic types of discontinuities: points, lines, and edges. For detail, please see e.g. (Gonzalez and Woods, 1993). In this paper, an alternative new method for automatic edge detection in an image is presented.

The section 2 describes briefly the mathematical derivation and presents a set of new gradient operators. Some tests and analyses are also given there. In section 3, a new approach for automatic determination of edge center lines is given. Some preliminary test results are analyzed in section 4. Conclusions are made in section 5.

2. A SET OF NEW GRADIENT OPERATORS

2.1 Brief Depiction on Mathematical Derivations

If a signal f exists in a so-called *Hilbert space*, it can be represented in a linear form based on orthonormal bases. For instance, the space of square-summable sequences and the space of square-integrable functions depicted in (Vetterli and Kovacevic, 1995) are two examples of the so-called Hilbert spaces. The compactly supported Daubechies wavelets proposed in (Daubechies, 1988) are examples of orthonormal bases. The theory for multiresolution signal decomposition was firstly presented in (Mallat, 1989). It was derived based on those signals f in a Hilbert space. The signal component $A_j f$ of f in a resolution space V_j is so defined that it has the property of minimal error energy, i.e. $\int \left(A_j f(t) - f(t)\right)^2 dt$ is minimal. Herewith, all coefficients in the linear representation are defined. $A_j f$ can be further decomposed into two orthogonal components $A_{j-1} f$ and $D_{j-1} f$. They exist in two V_j 's subsets. One is a coarser resolution space V_{j-1} than V_j. The other one is the orthogonal complement of V_{j-1} in V_j. It is a so-called wavelet space and denoted by O_{j-1}. On all equidistant dyadic grid points stated in (Rioul and Duhamel, 1992; Jawerth and Sweldens, 1994), the decomposition derives the basic mathematical formulas of image decomposition shown in (Mallat, 1989). (Tsay, 1996) gave a more user-friendly formulas for image decomposition and image reconstruction. If the first derivatives of those wavelet bases used in that decomposition exist, a new gradient operator can be derived from the derivative values on all dyadic grid points. In case that Daubechies wavelets are used, these operators are defined as follows (Tsay, 1998):

$$\beta_m = -\sqrt{2}\sum_n \left\{\lambda(n)\cdot h_{m+n} + \xi(n)\cdot(-1)^{m+n}\cdot h_{(2N-1)-(m+n)}\right\} \quad (1)$$

where β_m is the m-th element of the operator; h_k is the k-th low-pass filter coefficient of the Daubechies wavelet; $\lambda(u) = 2^{-1}\int_{-\infty}^{+\infty}\phi\left(\frac{t+u}{2}\right)\phi'(t)dt$; $\xi(u) = 2^{-1}\int_{-\infty}^{+\infty}\psi\left(\frac{t+u}{2} - N + 1\right)\phi'(t)dt$; N is the order of Daubechies wavelets; ϕ and ψ are the father and mother wavelet of Daubechies, respectively. Table 1 shows the new gradient operators derived from the Daubechies wavelets of order N = 3 (1) 10. These new gradient operators are to be named as "*Daubechies operators*" in this paper.

2.2 New Symmetrical Gradient Operators

Apparently, they are symmetrical gradient operators. Moreover, it is verified that the operators determined by the *asymmetric* Daubechies wavelets are the same with the ones determined by the *least asymmetric* Daubechies wavelets of the same order N.

Table 1. New gradient operators derived from the Daubechies wavelets of order N = 3 (1) 10, where β_0=0 and the other β_m-coefficients are equal to zero (|m|>2N+1) or they are insignificant coefficients with $|\beta_m| < 10^{-6}$ (|m|≤2N+1).

	m	$\beta_m = -\beta_{-m}$		m	$\beta_m = -\beta_{-m}$
N=3	1	0.745205	N=7	1	0.868744
	2	-0.145205		2	-0.282965
	3	0.014612		3	0.090189
	4	0.000342		4	-0.022687
				5	0.003881
				6	-0.000337
				7	-0.000004
				8	0.000002
N=4	1	0.793010	N=8	1	0.883446
	2	-0.191999		2	-0.303259
	3	0.033580		3	0.106364
	4	-0.002224		4	-0.031290
	5	-0.000172		5	0.006958
	6	0.000001		6	-0.001032
				7	0.000077
N=5	1	0.825906	N=9	1	0.895316
	2	-0.228820		2	-0.320312
	3	0.053353		3	0.120954
	4	-0.007461		4	-0.039953
	5	0.000239		5	0.010617
	6	0.000054		6	-0.002103
				7	0.000278
				8	-0.000020
N=6	1	0.850137	N=10	1	0.905071
	2	-0.258553		2	-0.334784
	3	0.072441		3	0.134055
	4	-0.014546		4	-0.048427
	5	0.001589		5	0.014669
	6	-0.000004		6	-0.003526
	7	-0.000012		7	0.000631
				8	-0.000077
				9	0.000005

2.3 Test Results

Figure 1 shows an image of the national monument "Anping Fort" in Tainan, Taiwan, and its gradient images computed by the Sobel operators (Gonzalez and Woods, 1993) and by the Daubechies operators of order N=3 and N=10, respectively. In the same manner as common practice, the gradient is approximated with absolute values (Gonzalez and Woods, 1993). In all computations of gradients, all operators are normalized so that $\sum \beta_m = 1$. Figure 2 expresses the mean, RMS (=root mean square) value, and maximum of gradients of the "Anping Fort" image. Apparently, the gradients computed by the Daubechies operators of N=3 (1) 10 have larger mean, RMS and maximal gradients than the ones determined by the Sobel operators. There exists a distinct effect. For example, Figure 3 illustrates an image of a Chinese character 'dragon' and its gradient images. Daubechies operators can extract much finer edges than the Sobel operators. Moreover, the center lines of all edges determined by both Daubechies and Sobel operators are the same. Figure 4 illustrates an example. The edges computed by the Daubechies operator of order N=3 are located in the centers of the edges computed by the Sobel operators.

In other words, the proposed *Daubechies operators* are new ones for gradient computation. Test results show that they can extract unbiased and finer edges, e.g. than the Sobel operators.



(a) (b) (c) (d)

Figure 1. (a) an image of Anping Fort in Tainan, Taiwan, and its gradient images computed by the Sobel operators (b), the *Daubechies operator* of order N=3 (c) and N=10 (d), respectively.

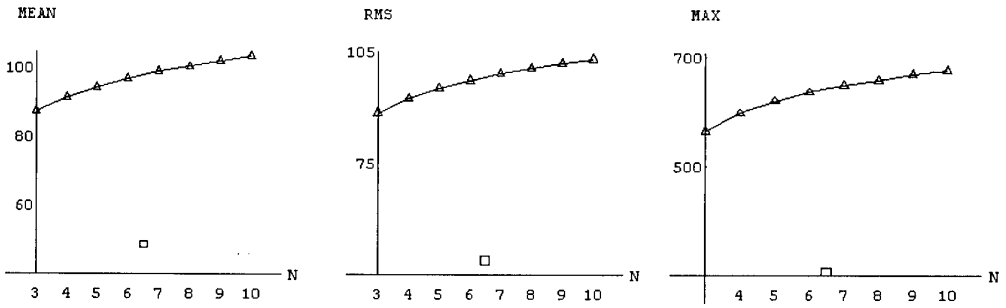


Figure 2. mean values (left), RMS (middle) and maximum (right) of gradients of the "Anping Fort" image shown in Figure 1 computed by the Daubechies operator of N = 3 (1) 10, where the square denotes the ones determined by the Sobel operators.



(a) (b) (c) (d)

Figure 3. (a) an image of a Chinese character "dragon" and its gradient images computed by the Sobel operator (b), Daubechies operators of N=3 (c) and N=10 (d), respectively.



Figure 4. The edges computed by the Daubechies operator of order N=3 (white center lines) are located in the center of the edges computed by the Sobel operators (dark boundary lines).

3. A NEW APPROACH FOR AUTOMATIC DETERMINATION OF EDGE CENTER LINES

The above-mentioned superior characteristics of the Daubechies operators are further integrated with the principle of *zero-crossing* for a much more effective edge detection. A new approach for automatic determination of edge centers is thus developed.

Input image data

Compute the estimation of image noise

Wavelet-Based Low-Pass Filtering, if it is needed

Select a Daubechies operator of order N

Compute the first derivatives G' by the Daubechies operator

Compute the second derivatives G" by the Daubechies operator with respect to G'

Locate each edge by zero-crossing of second derivatives

Linking edge pixels

Output all extracted edges

Figure 5. A new algorithm for automatic determination of edge center lines in an image.

Figure 5 illustrates briefly the entire computation algorithm. It utilizes the zero-crossing principles and the new gradient operators. Firstly, a digital image is given. If necessary, the image can be then low-pass filtered e.g. by low-pass filters of the compactly supported orthonormal Daubechies wavelets. It should reduce the image noise and cause no or as little blurring effect as possible. After low-pass filtering, one should select a Daubechies operator of order N. Preliminary tests show that, for the purpose of edge detection, there is no significant difference in those edges extracted by different order of Daubechies operators. Nevertheless, it should and will be further studied.

In the next steps, the first derivatives G' are computed by the Daubechies operators. Then, the second derivatives G" are computed by the same Daubechies operators but with respect to the first derivatives G'. Now, each edge is automatically detected by zero-crossing of the second derivatives. All pixels are detected as a pixel on an edge and are denoted as black pixels, abbreviated as B-pixels, if the following conditions exist:

(if G' > s0 and G" decreases from positive to negative numbers) or
(if G' < s0 and G" increases from negative to positive numbers) (2)

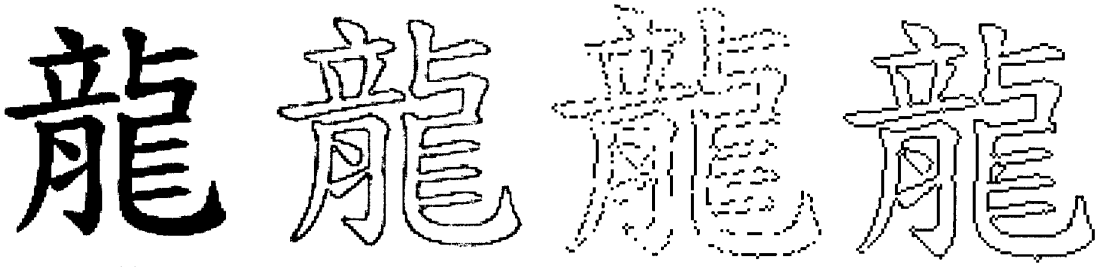
where s0 is a positive real number. Until now, all test results show that the edge detection is done very well and correctly if s0 is equal to the root mean square values of first derivatives.

Because a digital image often has locally blurred edges, only incomplete edges as shown in Figure 6 are generated by the above-mentioned processes. In order to generate successfully as complete edges as possible, we utilize a rule to link edge pixels. The rule is almost the same as the two principal properties used for establishing similarity of edge pixels in this kind of analysis. They are (1) the strength of the response of the gradient operator used to produce the edge pixel, and (2) the direction of the gradient that is often defined by $\tan^{-1}(G'_Y / G'_X)$(Gonzalez and Woods, 1993). The detailed description about this rule will be published soon.

4. TEST RESULTS

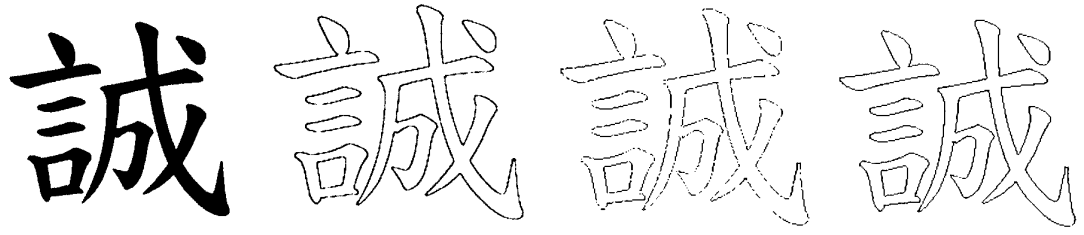
Figure 6 shows some test results, where a blurred image of the Chinese character "dragon" is used as a test image. Its gradient image (Figure 6(b)) shows a complete but thick edges. In general, one concludes from these test results together with all of other tests that the Daubechies operator extracts edges with line width of about 2-3 pixels that is finer than the ones with line width of c.a. 4-5 pixels produced by the Sobel operator. Figure 6(c) shows apparently that the wavelet-based zero-crossing approach will produce some disjointed edges if no edge linking operation is done. Nevertheless, almost all disjointed edge center line segments are connected with each other very well if the edge linking operation is done after the zero-crossing approach is completed. Each edge has the width of 1 pixel. Figure 6(d) shows also some defects, e.g. incorrect edge linking exists in the right area. In contrast against that, Figure 7 shows another complete successful example. In short, an effective edge linking operation should be further studied.

Moreover, some 'noise-like' B-pixels (black edge pixels) shall appear, if a small threshold s0 (e.g. 0.05RMS) is used. RMS denotes the root mean square value of the derivatives. For example, wrong B-pixels appear on the lower right region of Figure 6(c).



(a) (b) (c) (d)

Figure 6. an original image (a), its complete but thick edges represented by its gradient image computed by Daubechies operator of N=3 (b), disjointed thin edges produced by the wavelet-based zero-crossing approach without edge linking process (c), and complete and thin edges (edge width = 1pixel) produced by the proposed approach with edge linking operations, where there are some incorrectly linked edges.



(a) (b) (c) (d)

Figure 7. an original image of the Chinese character 'honesty' (a), its gradient image computed by the Daubechies operator (b), its edge image produced by the wavelet-based zero-crossing approach without edge linking (c), and with the edge linking operations (d), where the Daubechies wavelet of order N=3 is used and edge linking is completely successfully done.

5. CONCLUSIONS

This paper presents a set of new symmetrical gradient operators. In this paper, they are named as "Daubechies operators". It is verified that the operators determined by the asymmetric Daubechies wavelets are the same with the ones determined by the least asymmetric Daubechies wavelets of the same order N. They provide alternatives for gradient computation. Test results show that they can extract much finer edges than the Sobel operators. The edge width is generally c.a. 2-3 pixels and 4-5 pixels, if edges are represented by first derivatives determined by the Daubechies operators and the Sobel operators, respectively. Moreover, the center lines of all edges determined by both Daubechies and Sobel operators are the same.

Disjointed edges are often generated in a blurred image. In order to generate successfully as complete edges as possible, the approach also utilizes a rule to link edge pixels. The rule adopts two principal properties: (1) the strength of the response of the gradient operator used to produce the edge pixels, and (2) the direction of the gradient. The detailed description about this rule will be published soon.

All tests show that the wavelet-based zero-crossing approach with edge linking operations is really available for edge extraction. It can produce successfully complete edges with a width of one pixel.

Preliminary tests show that there is no significant difference in those edges extracted by different order of Daubechies operators. Nevertheless, it should and will be further studied.

Incorrect edge linking often appears in locally blurred edges. An effective edge linking operation should be further studied.

The mathematical models and algorithms proposed in this paper can also be utilized to represent a general curve/line on a 2D plane or in a 3D space, e.g. see (Tsay, 2000). The concepts might and will be further extended to represent a multi-valued 3D surface.

REFERENCE

Daubechies, I., 1988. Orthonormal bases of compactly supported wavelets. Comm. Pure Appl. Math., 41, pp. 909-996.

Daubechies, I., 1992. Ten Lectures on Wavelets. SIAM (=Society for Industrial and Applied Mathematics, Philadelphia, Pennsylvania, pp. 167-213.

Gonzalez, R.C., and Woods, R.E,, 1993. Digital Image Processing. Addison Wesley, pp. 161-221 and pp. 414-443.

Jawerth, B., and Sweldens, W., 1994. An Overview of Wavelet Based Multiresolution Analyses. SIAM Reviews, pp. 1-39.

Mallat, S.G., 1989. A Theory for Multiresolution Signal Decomposition: The Wavelet Representation. IEEE Transaction on Pattern Analysis and Machine Intelligence, Vol. 11, No. 7, pp. 674-693.

Rioul, O., and Duhamel, P., 1992. Fast Algorithms for Discrete and Continuous Wavelets Transforms. IEEE Transactions on Information Theory, Vol. 38, No. 2, pp. 569-586.

Tsay, J.R., 1996. Wavelets fuer das Facetten-Stereosehen. DGK (=Deutsche Geodaetische Kommission), Reihe C, Dissertation, Heft No. 454, Munich, Germany, pp. 53-57.

Tsay, J.R., 1998. A New Algorithm for Surface Determination Based on Wavelets and its Practical Application. PE&RS, Vol. 64, No. 12, pp. 1179-1188.

Tsay, J.R., 2000. DWT-based representation of a multi-valued line function. To be presented in the Technical University Darmstadt, Germany.

Vetterli, M., and Kovacevic, J., 1995. Wavelets and Subband Coding. Prentice Hall, pp. 20-25.

GEOMETRIC REGISTRATION METHOD FOR 10-DAY COMPOSITE AVHRR DATA FOR ASIAN REGION

Ts. Purevdorj and R.Yokoyama
Department of Computer Science, Faculty of Engineering, Iwate University, Japan
Email: dorj@cis.iwate-u.ac.jp and yokoyama@cis.iwate-u.ac.jp

ABSTRACT. This paper describes a geometric registration method for compositing AVHRR images. In the method, we consider two problems to improve geometric registration accuracy. The first is a development of automated detection procedure for GCPs locations in AVHRR imagery. The second is to develop image to map registration procedure for fine correction. Using the existing and developed methods, the geometric registration is carried out in two stages. In the first stage-correction, an accuracy of AVHRR image navigation is increased by automated technique of GCPs identification and correction of terrain elevation. In the second, the navigated AVHRR image is overlaid on reference coastline image for determination offsets and a final correction is carried out by registration of the navigated image to fixed reference image. This method was implemented by using "C" under UNIX operating system in HP workstation and has been operationally used for geometric registration of AVHRR composite data without operator intervention. The registration software package is applicable to any pre-processed AVHRR data for fine geometric correction.

KEYWORDS: AVHRR, geometric correction, registration, GCP, matching, edge line

1. INTRODUCTION

The availability of daily Advanced Very High Resolution Radiometer (AVHRR) imagery which covers very large regions has been shown to be useful for monitoring global and continental environmental conditions. AVHRR imagery has major advantages such as high frequent overpass and wide scanning provide the chance of producing cloud free images by compositing AVHRR images collected in regular intervals (3). However, for users of the data, it has been often showed difficult to pre-process and produce multi-temporal AVHRR composite data set. One of the most difficult problems in the compositing process is to provide high accuracy of geometric correction for each individual scene to be composited.

This paper considers improvements on geometric correction in two ways and designing full registration system for AVHRR composite data. The first improvement is the increase of systematic correction accuracy using automated detection procedure of GCPs locations in AVHRR imagery and elevation data. The second is to develop an automated image registration of navigated AVHRR images to fixed map image.

2. METHOD

The approach of accurate geometric registration used in the compositing AVHRR data consists of two-stage correction procedures. In the first stage of correction is to calculate ground location of the image pixels using an orbital model and it includes two steps: identification of GCPs and AVHRR image navigation. The second stage correction is motivated by the need to increase multitemporal positional accuracy of the navigated images for compositing requirement and it includes estimation of navigation accuracy, determination of mapping function and resampling. A flow of geometric registration method for composite AVHRR data set is shown in Figure 1. In the registration approach, we use PaNDA package for image navigation procedure and the rest of all steps were developed.

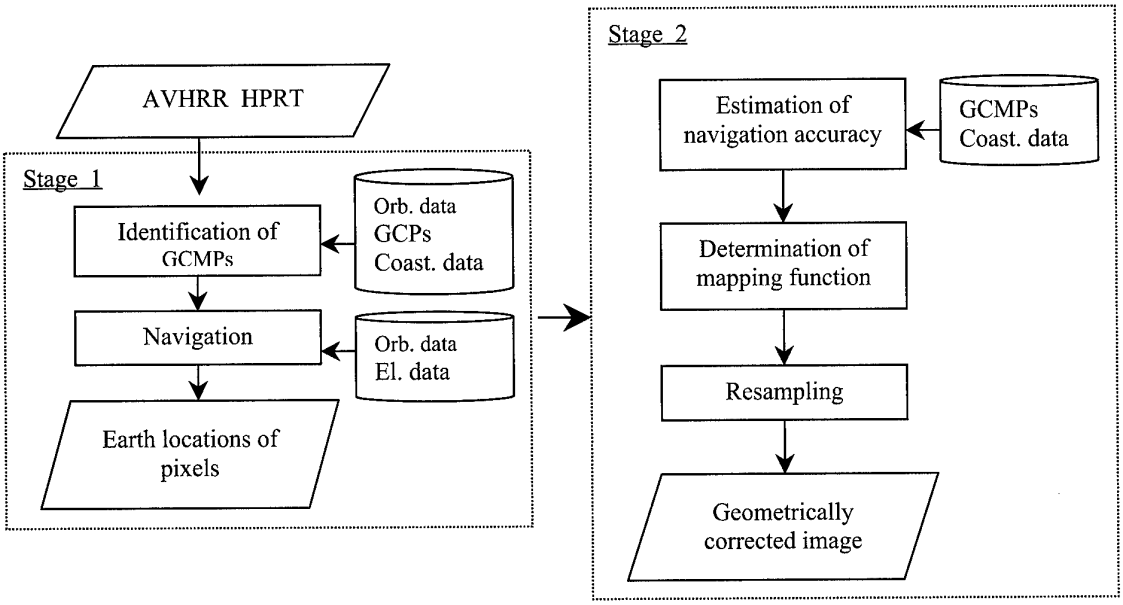


Figure 1. Processing steps for geometric registration of AVHRR data

3. DEVELOPMENT OF GEOGRAPHICAL DATABASE

The registration procedure developed requires the use of geographical database consisting of GCPs data set, ground control matching pattern (GCMP), reference overlay image of geographic features such as coastline and rivers and elevation data. Therefore, these geographical databases were created in the software development stage.

The geographical database used in the geometric registration includes coastline vector data, elevation data, and library of GCPs and GCMPs. These data are used to precise identification of GCPs positions in satellite and ground projections, and accurate matching of shape similarity. The coastline vector data were created from Digital Chart of the World (DCW). However, the vector data created from only DCW does not fully satisfy our requirement, because data for rivers are not available in DCW. When image to map registration is used, the digital data for rivers are extremely important where lakes or coastal data are not available. Therefore, the hydrological feature of rivers was generated from water mask data (EROS DATA Center) and added to the vector data. Each of the points included in the vector data, has latitude, longitude and elevation values.

The coastline vector data was converted to reference overlay image of coastline. GCPs data set was created from the reference overlay image by selecting easily detectable and most suitable locations for matching procedure. Using the reference overlay image, land and water mask image had been created and then it was used to generate bitmap image chips with 32 by 32 pixels size for pattern matching of shape similarity. Each of these chips is assigned GCP location, which we are referred to as GCMP.

The digital elevation data used for correction for terrain elevation were generated from GTOPO30 according to whole coverage area of the final composite data set.

4. FIRST-STAGE CORRECTION

4.1. Identification of GCPs locations in AVHRR imagery

The shifts of GCPs locations in AVHRR image from the corresponding locations in the reference overlay image is determined by matching image window of edge line derived from AVHRR image with binary template image extracted from the reference overlay image. We

refer these images as to searching window and reference window respectively and they are created using same ground point selected from the GCP data set.

The reference window of edge line is created in the following way. Before the matching procedure, once the reference overlay image had been created in satellite projection from the coastline vector data described in section 3. The reference overlay image includes coast and shorelines of the area, which is exactly same as whole coverage area of the raw AVHRR imagery. Then the reference window of 32 by 32 binary data is extracted from the reference overlay image centered GCP position.

The searching window from raw AVHRR imagery is created in the following way. At first, an image window of 64 by 64 data is extracted from raw AVHRR channel 1, 2 and corresponding pixel numbers centered at selected GCP position (Figure 2, 2nd and 3rd columns). The channel 1 and 2 were calibrated and a suitability of the image window for the subsequent matching process is tested by cloudiness and sensor scan angle.

A searching window of edge line for the matching is created from the image window by edge extraction using NDVI value, an adaptive thresholding and filtering. Thus three searching windows of edge line for each GCP were produced: first one by NDVI value (Figure 2, 4-th column) and second one by spatial filtering method (Figure 2, 5-th column) and third one by optimal thresholding method (Figure 2, 6-th column). In the searching window, cloudy pixels belonging to edge line are not used for matching.

After the reference window and searching windows had been generated, a similarity between the two windows is determined by image correlation procedure. In the result of image correlation procedure, the location of selected GCP was determined simultaneously in the three searching windows and the searching window with maximum correlation coefficient was selected (Figure 2, the area where best match occurs is marked by small window in the searching windows).

4.2 AVHRR image navigation

A final step of first stage correction is the conversion of each line and sample numbers of raw AVHRR imagery to corresponding earth locations. In this step, a set of GCPs determined by automated image matching, were used for adjustment of orbital parameters and satellite attitude correction. Then the conversion procedure is realized by indirect navigation method using PaNDA package (1,2). However, PaNDA package does not consider elevation effect in image navigation procedure because elevation data were not adapted to the package. The analysis showed that if an elevation is not considered for in the image navigation procedure, registration errors for off-nadir pixels can occur up to 4 pixels in high land areas. Therefore, elevation data created from GTOPO 30 were added to the PaNDA and earth location of each pixel of AVHRR imagery was calculated considering elevation effect in image navigation. Thus, first stage correction results in determining line and sample numbers of satellite image for given latitude and longitude of Plate Carree projection coordinate system. The navigation procedure is also used to compute sun-target geometry angles for each pixel.

5. SECOND-STAGE CORRECTION

Error evaluation of calculated ground locations of raw imagery showed that AVHRR image navigation does not work well over the whole image. Moreover, test composite data produced from the images corrected by only first-stage correction procedure showed that navigation accuracy does not satisfy compositing requirement and it was easily observed that small lakes and rivers were significant blurred in the composite image. Therefore, in order to achieve satisfactory accuracy for multitemporal compositing, it was necessary to register the each navigated image to fixed map overlay image. This reason motivates to develop second stage correction that is carried out in three steps: estimation of navigation accuracy, determination of mapping function and resampling.

5.1 Determination of navigation accuracy

A positional accuracy of the navigated image is determined by the correspondence between the reference overlay image and the navigated image. The correspondence is established by precise matching GCMPs as reference windows with searching windows in Plate Carree projection. The reference window in this step is the land and water surface pattern surrounding the center point of GCP. The GCMPs (Figure 2, A1~F1) described in section 3 are used as reference window in the pattern matching procedure. Simultaneously, an image window of 64 by 64 size centered at the same location as for the GCMP, is produced from raw imagery referring calculated ground location points. Then the image window is used to generate searching window of binary data of "1" for land or "0" for water (Figure 2, A3~F5). Then, the image correlation method described in section 4.1, is applied to match the reference and searching windows. The result of the matching procedure is a set of GCPs locations both in the navigated and reference overlay images. Thus, the set of GCPs selected allows estimating navigation errors and they are used for determination mapping function for final correction.

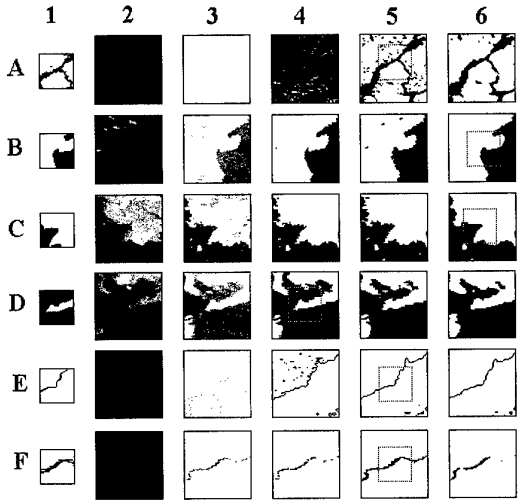


Figure 2. GCMP's and searching windows used in matching. 1-GCMP's, 2, 3- Ch2 and NDVI image windows extracted from raw AVHRR data, 4,5,6- searching windows extracted by NDVI, filtering and adaptive threshold value respectively.

5.2 Determination mapping function and resampling

The resampling process includes two steps. The first is determination of polynomial mapping function. Applying least square method to the set of GCPs selected in previous step, the polynomial mapping functions of degree two is established and they are formulated as following:

$$x_i = a_0 + a_1*X_i + a_2*Y_i + a_3*X_i*Y_i + a_4*X_i^2 + a_5*Y_i^2$$

$$y_i = b_0 + b_1*X_i + b_2*Y_i + b_3*X_i*Y_i + b_4*X_i^2 + b_5*Y_i^2$$

where x_i and y_i correspond to a point in the navigated image, X_i and Y_i correspond to a point in the corrected image. Using the set of GCMPs, the unknown coefficients a_0~a_5 and b_0~b_5 were determined by minimizing the sum of squared errors using least-squares technique.

Using the mapping functions, the resampling procedure is carried out in the final step. The resampling is performed by transformation of pixel locations in the navigated image to corresponding locations in the resulting output image. In the transformation, nearest neighbour interpolation technique is used.

6. EVALUATION OF ERRORS IN REGISTRATION ACCURACY

It is reasonable to measure geometric correction quality for all over image by RMSE obtained from the GCPs different from those used to determine the mapping functions. Therefore we used the estimation approach in which the accuracy of the geometric registration method was evaluated by calculation RMSE and mean deviations of the GCMPs for samples and lines when a geometrically corrected image was overlaid on the reference overlay image. The reference overlay image was generated from the geographical database. For test, we used AVHRR HPRT data acquired from August 1 to August 10 of 1999 at Ulaanbaatar (Mongolia). In the first experiment, RMSE and mean deviations of pixels and lines were estimated from the image that is not corrected by terrain elevation and GCPs. The result is compared with the accuracy of the image corrected by terrain elevation and GCPs (Table 1). The RMSE is represented by

$$RMSE = \frac{\sum_{i=1}^{n} \sqrt{(x_i^0 - x_i^1)^2 + (y_i^0 + y_i^1)^2}}{n}$$

and mean deviation for pixels (X_Dev) and lines (Y_Dev) calculated by

$$X_Dev = \frac{\sum_{i=1}^{n} \sqrt{(x_i^0 - x_i^1)^2}}{n}$$

$$Y_Dev = \frac{\sum_{i=1}^{n} \sqrt{(y_i^0 - y_i^1)^2}}{n}$$

where x_i^0 and y_i^0 are pixel and line number of i-th GCMP detected in AVHRR imagery, x_i^1 and y_i^1 are corresponding pixel and line number in the map overlay image, n is the number of GCMPs.

In the second test, two-stage correction was carried out for the each single scene and daily mosaic images were produced. Then RMSE and mean deviations were estimated from the daily mosaic images (Table 1). Table 1 clearly showed that GCPs matching result and terrain correction give significant improvement in the first stage of geometric correction. However, it can be seen that accuracy of the first stage correction is not sufficient for compositing requirement. Comparison of two-stage correction result shows that fine correction allows getting images with much better accuracy than the images performed by only first-stage correction.

Table 1. RMSE comparison of the correction steps for daily composite images

Day	Syst. Corr.	Stage-one	Stage-two
1	17.534	3.918	1.679
2	16.283	4.254	1.873
3	15.412	5.236	2.134
4	15.207	4.692	1.580
5	14.735	5.399	2.463
6	15.783	3.899	2.238
7	17.496	4.697	1.628
8	16.786	5.184	1.826
9	14.428	5.428	2.176
10	14.746	5.876	1.876

Table 2. RMSE comparison of the correction steps for 10-day composite image

	Syst. Corr.	Stage-one	Stage-two
GCP	25	168	168
X_DEV.	7.28	3.301	1.598
Y_DEV.	12.16	2.863	0.963
RMSE	14.063	4.701	1.969

In the third experiment, 10-day composite image was produced from the daily mosaic images and the accuracy of the geometric registration was evaluated (Table 2). The composite image of 14400 pixels and 6000 lines covers area between 50.0 and 170.0 degree of longitude and 30.0 and 80.0 degree of latitude. The number of GCPs actually used for the evaluation was 166. The result shows that RMSE was 1.969. Mean deviations for sample and line were 1.598 and 0.963 respectively. The result shows that the correction methodology gives relatively good accuracy in the along-track direction, but the across-track error can not reach to one pixel accuracy. We consider two factors, which decrease RMSE and mean deviation value. The first is that the errors detected in off-nadir pixels of the image or in the end of scenes specially in North Polar region, were larger than other ones. The second factor is that the accuracy of the DCW and water mask data used for reference overlay image is still not high. Because it was visually detectable when the reference image is overlaid on the composite image. The third is that ordinary least square method was applied to determining mapping functions which can not take count local distortions.

CONCLUSIONS

A full automatic method of geometric registration used of AVHRR data has been presented. This approach based on two-stage correction algorithm has been used in the geometric registration of composite AVHRR data set for Asian region with satisfactory result. The increase of registration accuracy of AVHRR imagery has been achieved by two improvements. In the first, an accuracy of AVHRR image navigation using PaNDA package is improved by accurate identification of GCPs and terrain correction. In the second, AVHRR image navigation accuracy is estimated and a final correction is carried out by registration of the navigated images to fixed reference image. Realizing this algorithm, we developed the registration software in "C" and implemented it under UNIX operating system in HP workstation. This software has been operationally used for geometric registration of AVHRR data and it is applicable to pre-processed AVHRR data for fine geometric correction without any operator intervention.

The development of the composite data set has been shown that registration of AVHRR data for large area with subpixel accuracy is somewhat difficult in practical realization. The difficulties have arisen due to several problems discussed in previous sections: inaccuracies in navigation model and coast and shoreline data, also some errors in orbital parameters. Specially, these problems are very important to resulting accuracy when operational registration system has been used and they are long-term issues for the increase registration accuracy.

In spite of the existing difficulties, we consider some way to improve present accuracy in the future. The overlay of the coastline image on AVHRR imagery showed that there are non-uniform shifts across the whole navigated image. In this case the use of ordinary polynomial mapping function for image transformation determined by least-squares technique may not enough to get more higher accuracy because a local geometric distortions are equally averaged for all over the image. Therefore, utilization of mapping functions, which is sensitive to local distortions, is one of the possible ways to improve the overall registration accuracy.

References

1. Hashimoto, T. and Murai, C., 1993, geometric correction of NOAA AVHRR Imagery in accordance with the number of GCPs, Journal of the Japan Society of Photogrammetry and Remote Sensing, 13.

2. PaNDA User Manual, 1998.

3. Yokoyama, R., Lei, L., Purevdorj, Ts. and Tanba, S., 2000, AVHRR 10-day Mosaic Composite Image Data Set for Asian Region, Journal of the Japan Society of Photogrammetry and Remote Sensing, Vol. 39, No.1, 33-38

FEATURE EXTRACTION IN RESIDENTIAL AREAS BY KNOWLEDGE MODELLING

Hsi-min Chao
Email:hmchao@seed.net.tw

John C. Trinder
University of New South Wales
Email: j.trinder@unsw.edu.au

KEY WORDS: Digital Photogrammetry, Feature Extraction, Knowledge Modelling, Image Understanding

ABSTRACT

The study describes the procedure of digital image processing, and interpretation approaches to the sample image for object recognition. A classified section on an aerial image obtained by texture analysis is input as a potential residential area for further interpretation. Both linear (**1D**) and regional (**2D**) features are extracted from the classified section, based on image segmentation in terms of the degree to which their statistical, geometrical, and physical properties matched to rooftops and roads that mostly appeared in residential areas.

Linear features are detected first using Canny's method. The derived edge map is then defined for straight lines and vector information, such as line equation and intersection angle by the Hough Transform. Areal features are extracted and numbered through thresholding and coding techniques,based on relevantfactors, such as physical surfaces, size and scale, and housing density. These potential house blobs can also be located by computing the centroid thus providing vector information.

Rooftop extraction rate is studied by comparison of ground truth and roof blob number. An improved thresholding extracts 60% rooftops in the study. Knowledge required for the identification of rooftops and roads are discussed.

Representating and modelling for residential areas are based oncharacteristics of houses and streets, for example, roof chains and road intersections. Syntactic patterns that form the relations between identified features needs to be further studied. An early model of housing area is proposed and tested whether they fit the extracted features and relations between features for the purpose of image understanding.

INTRODUCTION

This research on digital photogrammetry studies some functions in computer vision technology and their performance when applied to photogrammetric mapping. It is based on Marr's vision theory of the primal sketch and image representation, with consideration to both physical (brightness) and psychological (human vision) factors in digital image analysis. The objectives are thus to develop the procedures and techniques that will support the processes of feature extraction and recognition of cartographic features in digital aerial images.

The process of segmentation partitions an input image into its constituent parts. The output of the segmentation stage usually consists of pixels constituting either the boundary of a region or all the points in the region itself. In either case, converting the raster data into a mathematical form suitable for computer processing is necessary. Three types of segmentation methods, histogram, discontinuity, and similarity, are used in practice.

Object representation is an essential process for transforming raw image data into a suitable geometric form for subsequent computer processing. Most cartographic features are usually identifiable in aerial photographs by a human interpreter. The geometric representation of objects in terms of their extracted linear and regional features can provide information for computer based description of the image contents.

The term "representation" in this study has two broad usages: one is to present different image processing stages for the mathematical description of objects, as indicated in [Marr 1982] and [Ballard and Brown 1982]; the other is to describe programmed human knowledge i.e. knowledge representation.

Marr [1982] stated that although human vision delivers a shape description of an object from one image, it is almost certainly impossible to do this in only one step, which leads to *the idea of a sequence of representations*, starting with descriptions that could be obtained straight from an image, but actually are carefully designed to gradually facilitate the subsequent recovery of an object's physical characteristics and mathematical properties about its shape, size etc.

Three vision representational stages are introduced by Marr [1982]:

1. **2D representation** or **primal sketch** --- the representation of the properties of a two-dimensional image, such as intensity changes and local two-dimensional geometry.
2. **2.5D representation** --- the representation of the properties of visible surfaces in a viewer-centred coordinate system, such as the surface orientation, distance from the viewer, and discontinuities in these quantities; the surface reflectances; and some coarse descriptions of the prevailing illumination.
3. **3D representation** --- an object-centred representation of the **3D** structure and of the organisation of the viewed shape, together with some description of its surface properties.

The role of knowledge is displayed in **Figure 1**, showing four basic representational categories in computer vision.

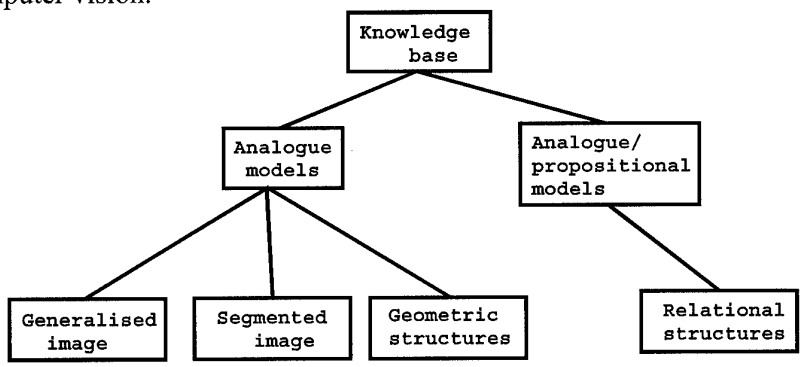


Figure 1 The knowledge base of a complex computer vision system, showing the four basic representational categories. [Ballard and Brown 1982]

PRE-PROCESSING

The significant topics included in pre-processing for this sudy are, the creation and comparison of multi-resolution images, and texture description and modelling, for residential areas. The image understanding system in the study provides a data structure for images used in different stages for specific projects. Texture measures derived by the co-occurrence matrix have resulted in a suitable method of classification on multi-resolution images [Chao and Trinder 1997]. Linear and areal features, such as rooftops and straight roads are extracted respectively for the purposes of segmentation, representation, and recognition.

FEATURE EXTRACTION

'Features', as described in Sowmya and Trinder [2000], can have different meanings in

photogrammetry and computer vision. In this paper , 'features' refer to lines, road crossings, corners, blobs, regions. The extraction procedure involves both linear (road boundaries) and regional (roof blobs) features. Roof groups form the main part of the process, but houses are not the only elements in residential areas. Important co-existing linear features, most probably straight roads, must also be considered.

Edge Detection of Road Boundaries

The Hough Transform (HT) is used to extract straight lines from an edge segmented image (or edge map). The edge map of a residential area is still very complex, so it is difficult to recognise a road network without knowing the location and number of roads. The advantage of using HT is that no prior knowledge of line position is needed. It works even for imperfect edge maps [Hough 1962]. HT pre-processing is carried out using a Canny edge detector.[Canny 1986] It has been shown by Chao and Trinder [1997] that low resolution images simplified the information content, both physically and geometrically, but fail to represent some details. Therefore, high resolution images were chosen for road detection.

Grey level edges reflect the steepness of the intensity changes. To enhance the linear elements on the extracted edge map, an appropriate threshold was selected by the human operator, to ensure the best contrast and quality of linear features. The input image to the HT is the edge map derived from the edge detection process. The output image presents all the detected linear elements in binary mode. The actual straight lines identified by this method which is based on low levelknowledge are presented in **Figure 3** [Chao 1999].

Roof Group Extraction

Rooftop extraction is based on image intensities. House density studies by Forster and Jones [1988] and Ng [1990] have been applied to determine a suitable threshold for the extraction of roof blobs and to assess the number of houses in an area. According to Forster and Jones [1988], rooftops reflect approximately 15% of the visible light, but are not necessarily with high intensity. This means that approximately 15% of pixels in a black and white image of a residential area will be related to buildings. Three rates in close arithmetic sequence5%, 8%, 12% , were used to test the extraction of an appropriate number of roof topbright blobs, .

Output images from these 3 P-tile thresholds based on extraction rates of 5%, 8%, 12% , are then combined by adding the new images together. This shows that the number of roof blobs in the new image is more than is obtained in any of the three independent images. Hence the total number of roof blobs can be increased and the rooftop extraction rate improved. This is because some blobs that appeared in the 5% extraction rate image did not necessarily appear in the other extracted images. **Table 1** shows that the accuracy of the rooftop extraction rate can be increased from 27 percent to 42 percent, up to 60 percent, when the extraction percentage is increased. However, this also increases the number of erroneous blobs, as indicated in **Table 1**. Therefore, shape representation techniques, (e.g. elongatedness and compactness,) are needed for accurate rooftop extraction and recognition. Results for accepted regions are demonstrated in **Figure 3**. Better accuracy of extraction is expected to be achieved when higher percentages are used.

Building shape representation is a major issue in **3D** building reconstruction and visualisation processes. For precise single building reconstruction, a scale larger than 1/8,000 is required. However, a scale of 1/8,000 might provide a better display of the surrounds and associated information, such as the house density, and the housing patterns in a typical residential area.

House density percentage	Extracted blobs	Extracted correct blobs	Extracted but error	Accumulated correct blobs (accuracy)
5%	19	19	0	19 (27%)
8%	30	28	2	30 (42%)
12%	47	38	9	42 (60%)

Table 1 Results of rooftop extraction based on 3 different extraction levels.The total house number of ground truth is counted to 70.

KNOWLEDGE MODELLING FOR FEATURE EXTRACTION

Semantic Information of Major Residential Objects

Knowledge representation and modelling have been important topics in object recognition. For the contextual study of residential areas, some related factors are considered as follows:

1. **Co-existence** relates possible objects in a specific class. In this study objects such as houses, roads, trees, grasslands , all appear in a typical residential area.
2. **Adjacency**, derived from the region adjacency graph in Sonka et al. [1993], is expressed by the distance between individual objects, but it can also be explained by geometric relationships such as, neighbour of, next to, part of, contains, above, below, inside, outside, vertical, horizontal, parallel to, etc. as suggested in Guelch et al. [1990].
3. A **Relational structure** is based on semantic knowledge in terms of **is_a, a_kind_of**. It therefore, provides a *meaning* or a physical object for matching a symbol to an object.

Semantic Knowledge Supporting Image Processing

This section concerns the verification of the previous relational structure, a hypothetical model for the analysis of a residential sub-image. A flowchart, presenting different levels of dependence and independence in the context of the sub-image is shown in **Figure 2**. This is a proposed early image understanding procedure, that includes four basic parts:

1. Image processing for pre-processing, data structure, and segmentation.
2. Unary independent context (or low level context) for representation.
3. Unary dependent context (or middle level context) for representation, and classification.
4. Binary dependent context (or high level context) for recognition, and image understanding.

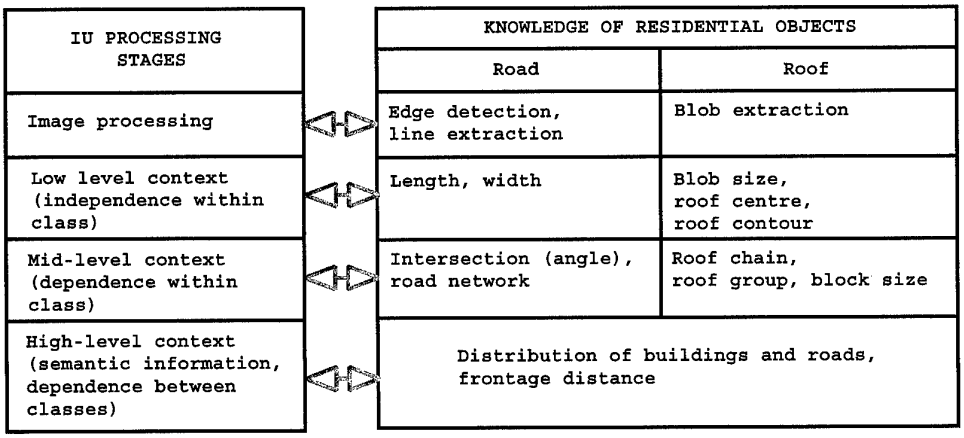


Figure 2 A proposed IU system utilising both context and knowledge for residential areas recognition at different stages and with corresponding results.

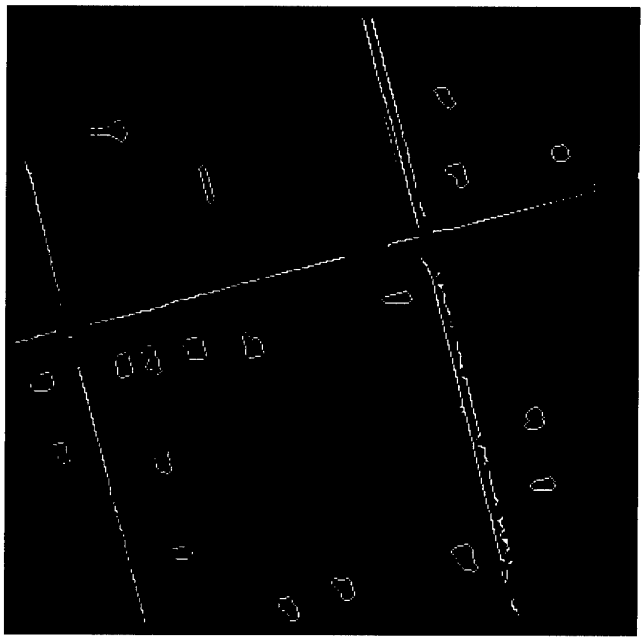


Figure 3 Results of a test of the co-existence and adjacency of two residential objects, housing and road boundaries. The merging of housing and road patterns results in a reasonable distribution and contextual view of a typical residential area. This binary image is a result of 5% value for house reflectance and line detection. The original image scale = 1/8,000, with a resolution = 1m/pixel, image size (x:y) = 386 x 374 pixels, from Wellington, NSW.

To understand residential areas, both roofs and roads are extracted and partly identified by their descriptors. The use of road and roof maps for context considerations can lead to better identification of the objects in the residential cell. The IU system in **Figure 2** shows how different levels of contextual information are processed in the study. The extracted features and recognised objects in a residential model derived from the proposed IU system is shown in **Figure 3**.

CONCLUDING REMARKS

A quality "primal sketch" is important for giving both global and local information image understanding. A global primal sketch (texture) provides grouping for classification purposes, while a local primal sketch (edge and line detection) provides correctly selected objects for recognition and an object-based contextual network.

The rate of house reflectance in images of residential areas for visible light is between 13% to 15%. The procedure in this study commenced with a rooftop extraction rated of 5% and varied to a rate of 12%. An intermediate rate is also recommended for extra blob information. However, for the use of only one rate, 5% is suggested, as there is a minimum of error in the extraction process, as shown in **Table 1**.

Low level forms of knowledge (descriptors or features), and domain knowledge (binary contextual relation) are designed for recognition methods, and have proven to be both logical and feasible. The paper has proposed a semantic network for determining residential patterns support as a photogrammetric IU system, which has been tested successfully on one example. a .

This example of residential area recognition by knowledge representation techniques based on semantic networks shows that domain knowledge is necessary to address the adjacency, co-

existence, and relational structures between different objects and classes.

ACKNOWLEDGEMENTS
This research is mainly financially supported by Chung-Cheng Institute of Technology, Taiwan, Republic of China.

REFERENCES

Ballard, D.H., Brown, C.M. 1982. Computer Vision, Prentice-Hall INC.

Chao, H., Trinder, J. 1997. Texture Parameter Analysis on Residential Area, 1st Trans Tasman Surveyors Conference Technical Papers, pp. 23-1/23-9, Newcastle, NSW

Chao, H. 1999. Road Boundary Segmentation and Representation of Residential Areas in Digital Aerial Imagery, The 18th Symposium on Science and Technology of Surveying and Mapping, pp.807/813, I-Lan, Taiwan

Canny, J.F. 1986. A Computational Approach to Edge Detection, PAMI Vol.8, No.4, pp. 679/698

Forster, B.C., Jones, C. 1988. Urban Density Monitoring Using High Resolution Spaceborne Systems, IAPRS, Comm VII, Vol.27, pp. 189/195

Guelch, E, Axelsson P, Stokes J, 1990. Object Description and Precise Localisation of Prescribed Objects in Digital Images. IAPRS Vol.28, part 3, pp. 221/233, ISPRS Com. III Symposium, Wuhan

Hough, P.V.C. 1962. A Method and Means for Recognizing Complex Patterns, U.S. Patent 3,069,654

Marr, D. 1982. Vision, W.H. Freeman and Company

Ng, T.K. 1990. Predicting Residential Housing Density and Housing Size with Satellite Imagery Using Simplified Models, Research Project Report, Master of Engineering Science, University of New South Wales, Sydney, Australia

Sonka, M., Hlavac, V., Boyle, R. 1993. Image Processing, Analysis and Machine Vision, Chapman and Hall Computing

Sowmya, A., Trinder, J. 2000. Modelling and Representation Issues in Automated Feature Extraction from Aerial and Satellite Images, ISPRS Journal of Photogrammetry and Remote Sensing 55(2000) pp.34/47

Subband SAR Image Coding by using Quadtree Decomposition on Variable Block Truncation Code

Amnach KHAWNE, Somchai OMSIN, Suthichai NOPPANAKEEPONG
and Krit WONGRUJIRA
Student, Student, Doctor and Lecturer, Telecommunication Engineering
King Mongkut Institute of Technology Ladkrabang
3 Moo 2 chalongkrung rd. Ladkrabang Bongkok Thailand 10520 Tel. (662) – 737-2500
Ext. 3354 E-mail address s2061037@kmitl.ac.th

KEY WORDS: Synthetic aperture radar, Subband coding, Block Truncation code, Quadtree decomposition

ABSTRACT: This paper proposes a subband synthetic aperture radar (SAR) image coding by using variable block truncation code, which is assisted by quadtree decomposition (QT) technique to divide image data. Quadtree decomposition is a simple technique for ordering an image data to hierarchical levels. This technique is partitioning an image into variable-sized blocks based on a quadtee structure, that the data in each subblock-size will be homogeneous. Quadtree decomposition will optimize a block for coding by setting up variable block sizes. Therefore, memory and process times are reduced when compared with fixed-block truncation code and absolute moment block truncation coding. The subband image coding is based on the decomposition of a signal into narrow band by a set of parallel filters. This paper uses the 16-band separable subband filter based on the quadrature mirror filter (QMF) by using the separable 2-D QMF, which allows the aliasing to be removed in the reconstruction signal. The coefficients are obtained from each subband and encoded by a classified priority, that is the lower subband having more information than the higher subband. It should be coded with a small block size. In this case, we choose the minimum block equal to 1x1 and the maximum block size is 16x16. For the higher subband, we choose 4x4 minimum block and 16x16 maximum block. The lower subband, especially a part of approximation can be coded with the small block size, but a part of details can be coded large block than the approximation. A combination of both techniques improves the minimum mean square error and image quality.

I.INTRODUCTION

Block truncation code (BTC) is the simple technique that is firstly introduced by Delp and Mitchell [1,2]. It is an efficient image coding method that has been adapted to obtain the statistical properties of the block in image compression. This algorithm, the image is firstly divided into non-overlap blocks. The BTC output data set is including of the binary bit plane, which defines the quantization level of each pixel, and two-reconstruction level values, determined by the mean and standard deviation of the block x_i. Where $i=1$ to m, q is the number of pixels with values greater thean or equal to the transmitted mean μ, the two output levels a and b from the quantizer for each block are given by

$$a = \bar{X} - \bar{\sigma}\sqrt{\frac{q}{m-q}} \quad \text{for } x_i < \bar{X} \tag{1}$$

$$b = \bar{X} + \bar{\sigma}\sqrt{\frac{m-q}{q}} \quad \text{for } x_i \geq \bar{X} \tag{2}$$

where $\overline{X}$ is the sample mean and $\overline{\sigma}$ is the standard deviation that is

$$\overline{X} = \frac{1}{m}\sum_{i=1}^{m} x_i \tag{3}$$

$$\overline{\sigma} = \left\{\frac{1}{m}\sum_{i=1}^{m} x_i^2 - \overline{X}^2\right\}^{\frac{1}{2}} \tag{4}$$

In addition, the BTC method is a fixed-based method, that inefficiency for coding. We have the method for dividing an image into varieties of the small block. The pixel in the block is homogeneous called quadtree decomposition (QT) [3,4]. This QT is efficiency than fixed block, especially used for coding SAR image. This paper proposes the combination of subband coding and variable block truncation code.

Section II introduces the subband coding of images. Section III describes the quadtree decomposition method. Section IV describes the combination between the quadtree decomposition method and block truncation code. Simulation result and conclusion are given in section V and VI

II. SUBBAND IMAGE CODING

Subband coding [5] is the most important to obtain high bit-rate compression as illustrate in Fig 1. This figure shows the transform using the two-channel filter bank. The part of the system on the left of the dotted line is the analysis part, and the part of the right is the synthesis part. In the analysis stage, the input data signal is processed by the analysis filter bank consisting of the time-invariant linear with transfer function $H_0(z), H_1(z)$, such that H_0 is lowpass and H_1 is highpass filter respectively.

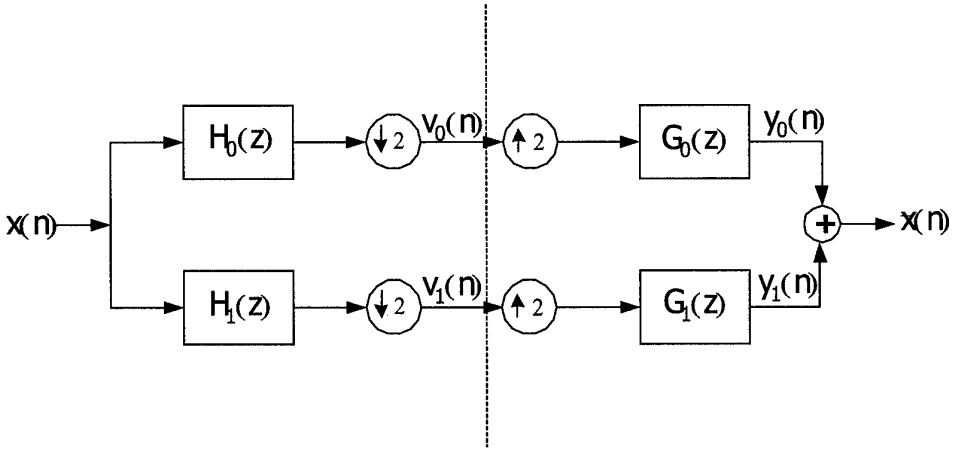


Figure 1. General two-channel subband coding system

The basic two-channel system in Figure 1 should be designed so that if no compression takes places, the system output will be equal to the translation of the system input. This is called the perfect reconstruction condition or PR-QMF [6,7]. We identify of the two conditions for perfect reconstruction. One condition is removed distortion and the other is removed alising. The signal $x(n)$ can be perfectly reconstructed if the analysis and systhesis filters satisfy the conditions (5), (6), (7), (8).

$$G_0(z) = -H_1(-z) \tag{5}$$
$$G_1(z) = H_0(-z) \tag{6}$$
$$H_1(z) = z^{-(N-1)} H_0(-z^{-1}) \tag{7}$$
$$H_0(z)H_0(z^{-1}) + H_0(-z)H_0(-z^{-1}) = 1 \tag{8}$$

III. QUADTREE DECOMPOSITION

Quadtree Decompostion (QT) [3,4] is the analysis technique that involves subdividing the image into blocks that are more homogeneous than the image itself. This technique works by dividing the square image into four equal-sized squared blocks by determining the criterion and then testing each block to meet same criterion of homogeneity. If block meets the criterion, it is not divided any further. If it does not meet the criterion, it is subdivided again into four blocks, and the test criterion is applied to those blocks. This process is repeated iteratively until each block meets the criterion. The result may have blocks of several different sizes. In the Figure 2 illustrates the result of QT

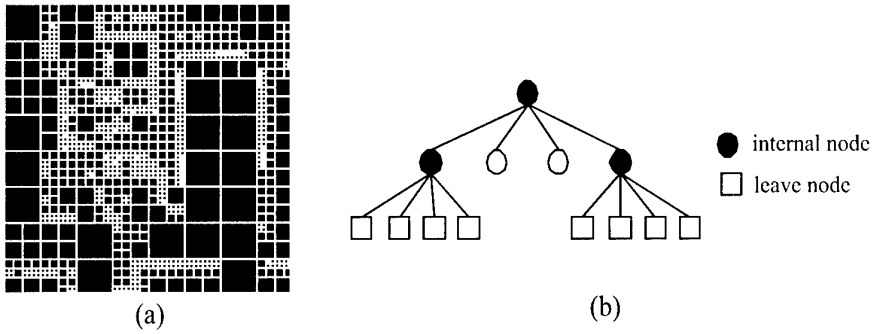


Figure 2. quadtree decomposition. (a) quadtree decompostion an image.
(b) Tree structure of quadtree

The quadtree is the tree structure in which each internal node has four branches emanating form it. In the other words, each node in the quadtree has either four children as illustrated in Figure 3. The four children of a particular parent node represent the four subblocks obtained by splitting the parent block into four equal-sized square blocks. In this case, all of leave nodes are compressed by BTC method, described in the next section.

IV. SUBBAND AND VARIABLE BLOCK TRUNCATION CODE (VBTC)

Image was reduced noise and pre-processed method will be divided into subband. In this case, we used the subband to 16 subbands as shown in Figure 3. for coding. Each subband is filtered and downsampled from filter bank stage and then is divided into small block by quadtree decomposition. The leave node of quadtree can be coded by setting the priority and coded by using VBTC [3,4] method. Subbands are defined as inter-subband and intra-subband [5] for arrangement the subband to coding. The Classification as inter-subband or intra-subband depends on whether they have the same parent source signal. In this case, subband HHLL and HHHH are the intra-subband because both of there are generated from the same parent source signal subband HH. Subband HHLL and LLLL are inter-subbands because their parent source signals are subband HH and LL, respectively

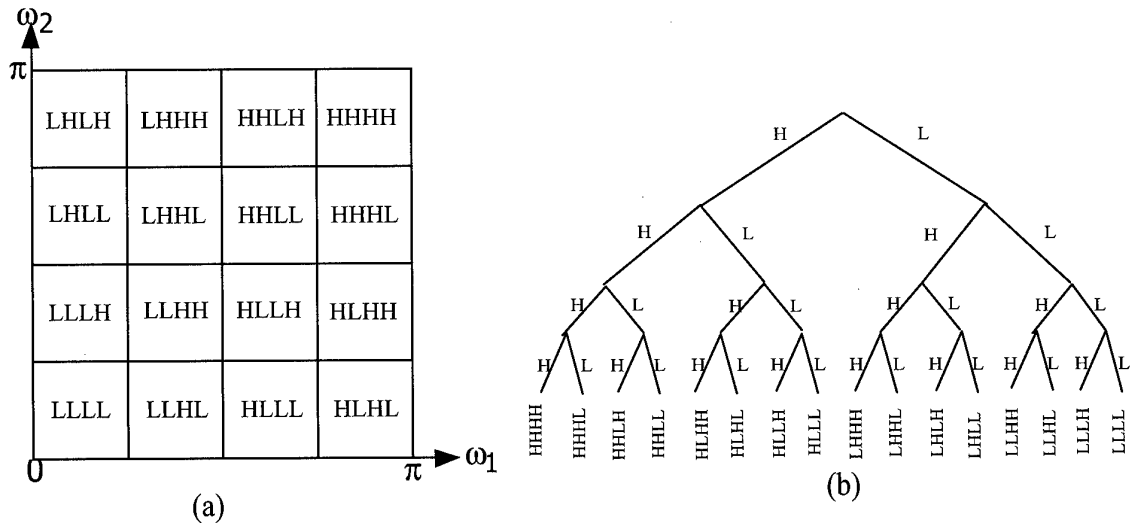


Figure 3. (a) 16 subbands structure, (b) Tree structure 16 subbands

V. SIMULATIONS AND RESULTS

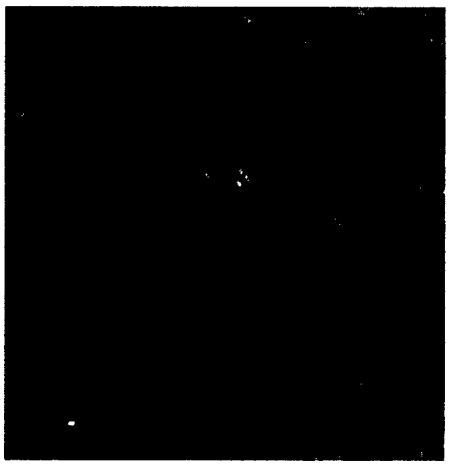
In the experiment the original SAR images, with size 512 x 512 show in Fig. 4. (a),(c). It is divided by the QT method and differently encoded by VBTC for every leave node of the QT. The results are shown in Fig. 4. (b),(d). In Fig. 4 (b), SAR image are reconstructed and measured then evaluate mean square error and peak signal to noise ratio. This technique gives higher of peak signal to noise ratio than the BTC technique and can be reduced the processing time. Compression ratio depends on as a defined of the threshold in a quad tree technique. Table 1. illustrate a process time, mean square error (MSE) and peak signal to noise ratio (PSNR)of each image. The MSE and PSNR in the compression are expressed as

$$MSE = \frac{1}{MN}\sum_{i=1}^{M}\sum_{j=1}^{N}[x(i,j)-x(i,j)]^2 \tag{9}$$

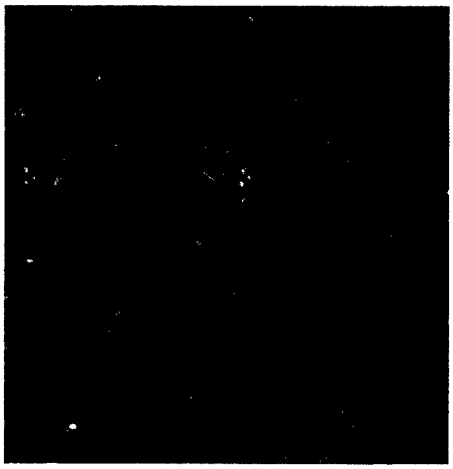
$$PSNR = 10\log_{10}\frac{(2^n-1)^2}{MSE} \tag{10}$$

image	Bit Rate	MSE(dB)	PSNR	Subband encoded with [1x1] , {2x2}	Times (Sec.)
Tm4	1.2813	44.2823	31.6684	[LLLL,LHLL,HLLL]	353.94
Tm4	0.4553	43.4394	31.6684	[LLLL,LHLL,HLLL]	321.1
Sanfran	2.875	17.7568	35.6371	[LLLL,LLHLLHLL,HLLL]	1349
Sanfran	0.8748	17.2611	35.6855	[LLLL,LLHLLHLL,HLLL]	842.44
Sar3	3.0625	40.0997	32.0033	[LLLL,LLHLLHLL,HLLL],{LLLH,LLH H}	1430
Sar3	0.9788	39.3096	32.1858	[LLLL,LLHLLHLL,HLLL],{LLLH,LLH H}	850.03

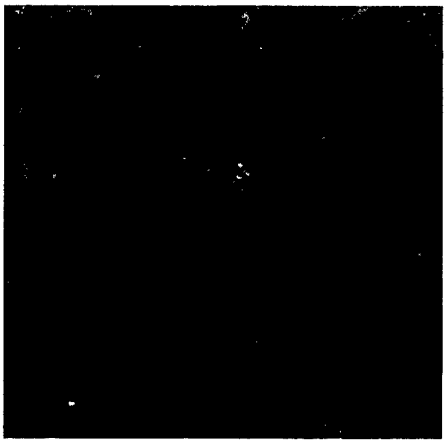
Table 1. Simulations and results



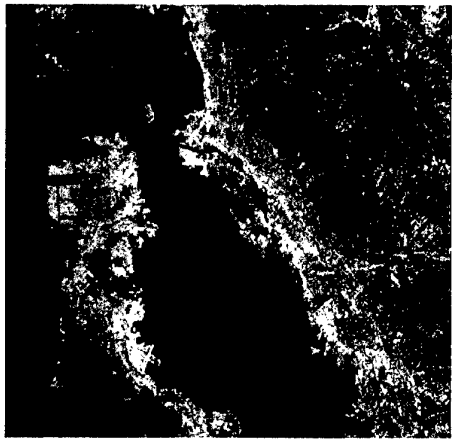
(a) Original Tm4. image



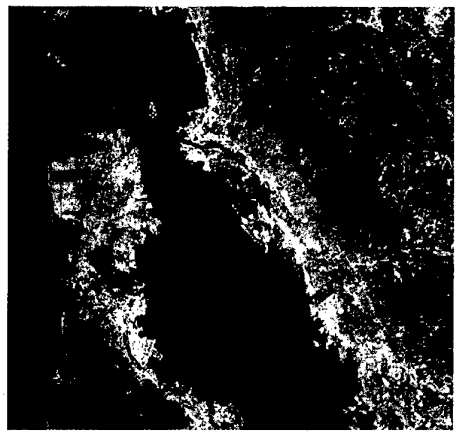
(b) 0.8748 bpp ; PSNR 35.6855 dB.



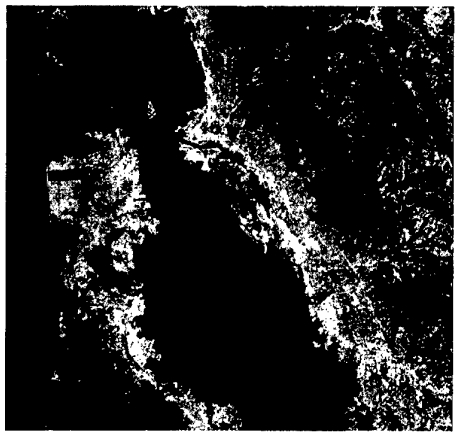
(d) 1.2813 bpp, PSNR = 31.6684



(e) Original sanfran image

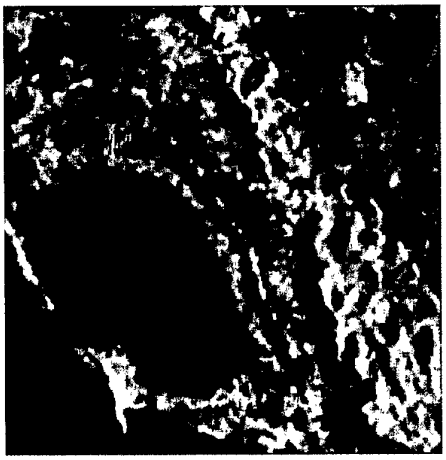


(f) 0.9166 bpp, PSNR = 28.2613

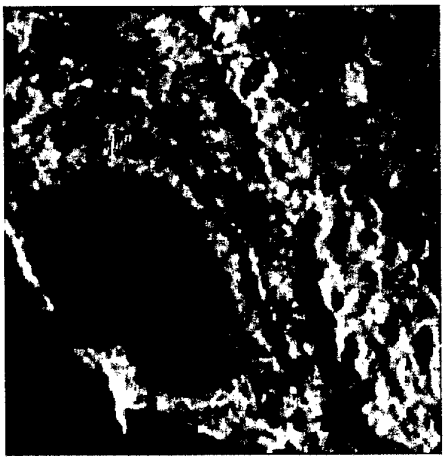


(g) 2.8750 bpp, PSNR = 28.1818

Figure 4. (a),(e) Original SAR images , (d),(g) Reconstruction by subband BTC and (f),(b) Reconstruction by subband VBTC



(h) Original sar3 image



(i) 0.9788 bpp, PSNR = 32.1858

Figure 4. (con't.) (h) Original sar3, (i) Reconstruction by subband VBTC

VI. CONCLUSIONS

Subband SAR image coding by using the variable block truncation coding (VBTC) is more efficient than using Fixed Block Truncation code that is reduced the processing time for compression a SAR image. VBTC technique can be classified data in an image into group that is homogeneous in a group of data. Data in each group is divided by QT decomposition, which is optimal for encoding by using VBTC encoder. Disadvantage of VBTC technique is the threshold selection in the quadtree stage. These thresholds are the criterion for dividing the image into block. If we select the maximum threshold which is obtained most large of blocks and a few blocks for coding. We will get the high compression rate, but the low quality of reconstruction image. In other word, reconstruction image is high quality, but low compression rate. Good pre-filter are required to reduce noise before compressive procedure that are obtained high quality of the reconstruction image.

VII. REFERENCES

[1] Delp, E. J., and Mitchell, O. R., 1991, Moment Preserving Quantization, IEEE Transactions on Communications, Vol. 39, pp. 1549-1558.

[2] Delp, E. J., Saenz, M., and Salama, P., 2000, Block Truncation Coding (BTC), Handbook of Image and Video Processing, edited by Bovik A. C., Academic Press, pp. 176-181.

[3] Long Wen Chang, and Ching Yang Wang, 1999, Image Compression Using Optimal Variable Block Truncation Coding, Multimedia Signal Processing, 1999, IEEE 3rd Workshop on, 1999, pp. 413-418.

[4] Mohamed Kamel, Sun C. T., and Lian Guan, 1991, Image Compression by Variable Block Truancation Coding with Optimal Threshold, IEEE Transactions on Signal Processing. Vol. 39, No. 1, pp. 208-212.

[5] Kai-Krung Ma, and Sarah A. Rajala, 1991, Subband Coding of Digital Images Using Absolute Moment Block Truncation, IEEE Transactions on Acoustics, Speech, and Signal Processing, 1991. ICASSP-91., International Conference on, 1991 Vol. 4, pp. 2645-2648.

[6] Martin Vetterli, and Cormac Harley, 1992, Wavelets and Filter Banks: Theory and Dsign, IEEE Transactions on Signal Processing, Vol. 40, No. 9, pp. 2207-2232.

[7] Strang G., and Ngnyen T., 1996, Wavelet and Filter Banks, M.A., edited by Wellesley-Cambridge Press, pp. 103-113.

Optimal Polarization for Contrast Enhancement in Polarimetric SAR Using Genetic Algorithm

Ruey-Long SU[1], K.S.CHEN[1], Jiancheng SHI[2]
[1]Institute of Space Science
National Central University
Chung-Li, Taiwan
[2]ICESS, University of California
Santa Barbara, CA, USA

KEY WORDS: polarimetric matched filter, genetic algorithm, SAR

ABSTRACTS: The optimal use of polarimetric scattering information provided by fully polarimetric synthetic aperture radar (SAR) is useful for discriminating between different terrain covers. Conventionally, eigenanalysis is used to synthesize a polarimetric matched filter (PMF) image that maximizes the contrast between the features of interest, but it involves many algebraic operations and can get one contrast ratio for any two classes at one time. This paper describes the application of genetic algorithm (GA) to the contrast enhancement. It obtains all contrast ratios characterizing the best discrimination for any two among all possible classes simultaneously. After using an L-band fully polarimetric SAR image as a test data, it shows that the proposed method is very effective and promising.

1. Introduction

Remote sensing imagery data are known for their high degree of complexity and irregularity, especially for SAR image. Moreover, there are usually many natural and man-made targets resulting in extremely difficult in the task of segmentation, classification, and detection. The problem of optimization of polarimetric contrast enhancement has been attracting attention in recent years [1-7]. The main purpose is to choose the polarization states that enhances the desired target versus the undesired target (clutter). What we can control is the polarization states of the transmitter and the receiver. For example, Teti et al. [3] used polarimetric matched filter (PMF) technique based on eigenanalysis to enhance image contrast in selected regions to improve detection and classification of flooded regions. Yang et al. [4] developed a numerical method for solving the optimal problem of contrast enhancement. However, the polarimetric techniques reported abovementioned for target discrimination have been limited to the special case of two targets because of the complex nature of the optimization problem. In reality, there are more than two possible targets of interest involving the discrimination process. This motivates us to use stochastic-base search method to handle problems with targets more than two so as to enhance the operation efficiency and yet remain effective.

Two stochastic-base optimization procedures that can deal a large number of discrete parameters are simulated annealing and genetic algorithm (GA). In recent years, applications of GA to a variety of optimization problems in electromagnetics have been successfully demonstrated [7-11]. It's optimization is global in the sense that it has random components that test for solutions outside the current minimum, while the algorithm converges. In particular, GA is much better at dealing with solution spaces having discontinuities, constrained parameters, and/or a large number of dimensions with many local maxima.

Traditional optimization algorithms search for the best solution, using gradients and/or random guesses. Gradient methods have the disadvantages of getting stuck in local minimum, requiring gradient calculations, working on only continuous parameters, and being limited to optimizing a few parameters. Random-search methods do not require gradient calculations, but being a blind-search and tend to be slow. In addition, GA is easy to program and is able avoid the mathematical rigor of traditional optimization methods.

In this paper, we utilize GA to search for a pair of optimal polarimetric states so that at these polarization states the contrast ratio between two classes in SAR image is maximmum. Besides, it can get all contrast ratios for any two classes simultaneously subject to the sum of all individual contrast ratios being maximum. The results also provide an excellent preprocess for subsequent image classification, if desired.

2. Genetic Algorithm

This section begins with a brief overview of GA, followed by a description of a step-by-step implementation. More details on GA can be found in [9][11][12] and references cited there. The goal of the GA is essentially to find a set of parameters that maximize (or minimize) the output of a function (or process). A typical flow diagram of a simple GA optimizer is presented in Figure 1.

2.1 Parameters Encoding

Encoding is a transformation from the parameter space (also called *phenotype*) to the gene space (also called *genotype*). Genes in the chromosome represent the coded parameters. Usually, a binary coding is utilized. For example, if the chromosome has three parameters (said var1, var2, var3) to be optimized and use three bits for each parameter, then the chromosome might be written as

Chromosome	→	1	1	0	0	0	1	1	0	0
Parameters	→		var1			var2			var3	

2.2 Population Initialization

If there are M populations in a generation, 1 or 0 is randomly selected for each bit to form a chromosome and consequently construct M chromosomes that represent possible solution of var1, var2, and var3. This randomness guarantees the diversity of population of possible solutions.

Chromosome 1	→	1	1	0	0	0	1	1	0	0
Chromosome 2	→	0	1	1	1	1	1	0	1	0
Chromosome M	→	1	0	0	0	1	1	1	0	1

2.3 Fitness Calculation

Each chromosome has a cost value, founded by evaluating a fitness function, or object function. Fitness evaluation involves decoding of the chromosomes to produce the parameters that are associated with the individual. If a GA tool is available, the good fitness function is the only portion that a user must provide and in general the most difficult part of the whole processes. The fitness value in this example can be expressed as

$$fitness = f(var1,\ var2,\ var3) \tag{1}$$

2.4 Reproduction

Reproduction, also called selection, shows the influence of the fitness value to GA. Although, fitness is the merit of goodness of an individual, reproduction cannot be executed only by selecting the best individual, because the best individual may not be very close to the optimal solution, especially in the very early generation. In order to avoid the problem of premature convergence, some individuals with relative low fitness value must be preserved to ensure that genes possessed by these individuals are not lost prematurely. The selection operator can either be stochastic or deterministic.

2.5 Crossover

The most productive step in GA before convergence is crossover. It stems from the idea

that by exchanging information between two chromosomes may produce a new better chromosome. One-point and two-point crossover methods are the most popular.The probability of individuals chosen to attend crossover during each generation is specified by the parameter $p_{crossover}$(typically 0.6---1.0). After crossover, the total number of chromosomes remains constant.

parent 1 → 1 1 0 0 0 ***1 1 0 0***
parent 2 → 0 1 1 1 1 ***1 0 1 0***

offspring 1 → 1 1 0 0 0 ***1 0 1 0***
offspring 2 → 0 1 1 1 1 ***1 1 0 0***

2.6 Mutation

In order to maintain a more diverse population among the new generations, the mutation that provides a means for exploring new portions of the solution space is needed. Probability of bit mutation should be kept low enough so that the highly fit chromosomes are not destroyed. Typically, on the order of $p_{mutation}$=0.01 of the total bits mutate per generation.

Chromosome before mutation → 0 1 1 1 ***1*** 1 0 1 0
Chromosome after mutation → 0 1 1 1 ***0*** 1 0 1 0

3. Polarimetric Matched Filter

In this paper, the optimal polarization filter algorithm developed by Swartz et al. [1] was used to select the optimal polarizations between two different classes. A brief discussion of the polarimetric SAR and optimal filter is given below.

For a give set of antenna polarizations, the scattered power can be expressed in terms of the scattering matrix for the target

$$P = \left| a^r \bullet S a^t \right|^2 \tag{2}$$

Where a^m denotes antenna polarizations in the transmitting and receiving mode, i.e.,

$$a^m = \frac{E^m}{\left| E^m \right|} \tag{3}$$

m = t(transmitted), r (received), and

$$S = \begin{bmatrix} S_{hh} & S_{hv} \\ S_{vh} & S_{vv} \end{bmatrix} \tag{4}$$

Equation (2) can be rewritten according to the definition given in [1] as

$$P = \left| F^+ X \right|^2 \tag{5}$$

In case of backscattering, $S_{hv} = S_{vh}$, then

$$F = \begin{bmatrix} F_{hh} \\ F_{hv} \\ F_{vv} \end{bmatrix} = \begin{bmatrix} a_h^t a_h^r \\ a_h^t a_v^r \\ a_v^t a_v^r \end{bmatrix}, X = \begin{bmatrix} S_{hh} \\ S_{hv} \\ S_{vv} \end{bmatrix} \tag{6}$$

Equation (5) may be expressed in the form P =F$^+$ hCF, where C is the covariance matrix of the terrain cover assumed to be statistically distributed, defined by [1]

$$C = \left\langle XX^+ \right\rangle = \begin{bmatrix} S_{hh}S_{hh}^* & S_{hh}S_{hv}^* & S_{hh}S_{vv}^* \\ S_{hv}S_{hh}^* & S_{hv}S_{hv}^* & S_{hv}S_{vv}^* \\ S_{vv}S_{hh}^* & S_{vv}S_{hv}^* & S_{vv}S_{vv}^* \end{bmatrix} \tag{7}$$

where means ensemble average operation and * the complex conjugate.

In [1], the contrast ratio between class A and B is defined as

$$r_{A/B} = \frac{F^+ \bullet C_A F}{F^+ \bullet C_B F} \tag{8}$$

To maximize $r_{A/B}$ above, the Lagrange multiplier method is used.

Making use of Lagrange multiplier concept leads to the eigen-equation

$$C_A F = \lambda (C_B F) \tag{9}$$

Since F represents the optimum matched filter, we now want to calculate the corresponding transmitting and receiving antenna polarizations. In[1], each a^m was solved but involves tedious algebraic operations. Indeed, Chen et al. [2] derived an analytical equations to get antenna polarization angles for transmitter and receiver directly and effectively. it can be readily shown that what is needed are the following ratios

$$Q^t = \frac{C_1 C_2 \pm \sqrt{C_1^2 C_2^2 - 4C_1 C_2}}{2C_1} = |Q^t| e^{-j\delta_t} \tag{10}$$

$$Q^r = C_2 - \frac{C_1 C_2 \pm \sqrt{C_1^2 C_2^2 - 4C_1 C_2}}{2C_1} = |Q^r| e^{-j\delta_r} \tag{11}$$

where $\delta_m = \phi_v - \phi_h$; $Q^t = a^t_v / a^t_h$, $Q^r = a^r_v / a^r_h$; $C_1 = F_{hv}/F_{vv}$, $C_2 = F_{hv}/F_{hh}$.

At this point, it should be remembered that in general a polarization vector can be transformed into a normalized Stokes vector and related to orientation ψ and ellipticity χ angles. It turns out that we can simply find the polarization angles in terms of Q^t and Q^r

$$\tan 2\psi_m = \frac{2|Q^m| \cos\delta_m}{1 - |Q^m|^2}, \sin 2\chi_m = \frac{2|Q^m| \sin\delta_m}{1 + |Q^m|^2} \tag{12}$$

4. Implementation and results

Unlike tedious algebraic operations used in Lagrange method, GA is trying to find parameters directly. Referring to elements in eigenvector found through Lagrange method, equation (6) can be rewritten to

$$F = \begin{bmatrix} F_{hh} \\ F_{hv} \\ F_{vv} \end{bmatrix} = \begin{bmatrix} R_{hh} + iI_{hh} \\ R_{hv} + iI_{hv} \\ R_{vv} + iI_{vv} \end{bmatrix} \tag{13}$$

where R_{xx} and I_{xx} are real numbers representing real part and imagery part, respectively.

It can be seen that in this problem there are six parameters to be found to meet the criteria that the contrast ratio between any two classes is maximum.

In this paper, we compare optimal matched filter ***F***'s that are found from the Lagrange method and the GA respectively. The test data is an L-band four-look fully polarimetric image over the San Francisco Bay area required by the JPL airsar system. This image has been widely used in the past as a testing image. The original image is shown in Figure 2. Three classes may be identified by visualization : open water, park area, and urban city.

For comparison, optimal polarizations determined by these two methods and linear polarizations were summarized in Table 1. Obviously, it can be shown that optimal polarization has higher contrast ratios than linear polarization, as expected, and GA provides an alternative to solving optimal polarization problem. The fitness function to be maximized in this case is

$$fitness = r_{\text{Urban/Ocean}} \text{ or } r_{\text{Park/Ocean}} \text{ or } r_{\text{Urban/Park}} \tag{14}$$

In addition to get an optimal polarization to discriminate any two classes in an image at one time, GA can also determine an optimal polarization characterizing the best discrimination

for any two among all possible classes simultaneously. The fitness function to be maximized in this case is

$$fitness = r_{\text{Urban/Ocean}} + r_{\text{Park/Ocean}} + r_{\text{Urban/Park}} \quad (15)$$

It should be pointed out that although GA slightly degrades the overall performance when compared to those obtained individually and sequentially, it is much more computationally efficient, as observed in Table 1. This should be regarded as a more practical approach particularly when there are many classes of interest in an image. Table 2 listed polarization angles and corresponding final chromosome for the case.

5. Conclusions

Assuming that the polarimetric responses of all the classes in the image are known *a priori*, determination of polarization states of the transmitter and the receiver for maximizing the contrast ratios between any two classes was presented in this paper. As compared to conventional method, GA shows the ability to provide another and even convenient way to solve optimal polarization problem. It can get all contrast ratios characterizing the best discrimination for any two among all possible classes individually and simultaneously.

It must be emphasized at this point that GA may not always be the best method to deal with all optimal problems in hand, but it has obvious advantage that it seems to find globally optimal solutions without requiring a great deal of information about the solution space. In some sense, it searches for a solution like an engineer learns from experiments and trial-and-error. That makes GA useful for solving problems that were solved experimentally and empirically in the past.

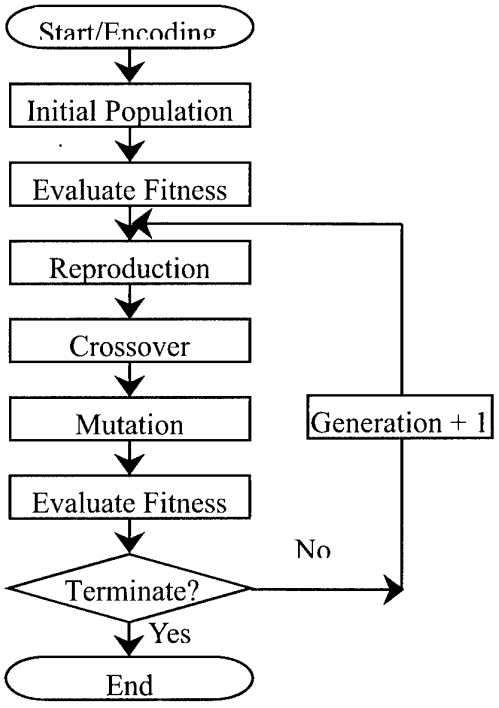


Figure 1.Flow diagram of GA



Figure 2. L-band SAR image of the San Francisco

Polarization/class	Urban/Ocean	Park/Ocean	Urban/Park
Optimal- Lagrange	28.5990 dB	19.1451 dB	9.5674 dB
Optimal-GA	28.5988 dB	19.1449 dB	9.5674 dB
Linear-HH	15.1013 dB	7.3075 dB	7.7938 dB
Linear-HV	20.3604 dB	17.2547 dB	3.1057 dB
Linear-VV	9.4340 dB	4.2362 dB	5.1978 dB
GA(simultaneously)	28.5988 dB	19.0547 dB	9.5441 dB

Table 1. contrast ratios for different polarizations.

ϕ_t	-26.25°
χ_t	-1.73°
ϕ_r	-40.90°
χ_r	3.67°
Chromosome	000100010011111101000010100111110001010011001100010100011100

Table 2. Polarization angles and solution chromosome for simultaneous case

6. Reference

[1] A. A. Swartz, H. A. Yueh, J. A. Kong, L. M. Novak, and R. T. Shin, "Optimal polarizations for achieving maximum contrast in radar images," J. Geophys. Res.,93, pp.15252-15260, 1987

[2] K. S. Chen, D. H. Tsay, W. P. Huang, and Y. C. Tzeng, "Remote Sensing Image Segmentation Using a Kalman Filter-Trained Neural Network," International Journal of Imaging Systems and Technology, Vol. 7, pp. 141-148, 1996

[3] J. G. Teti, Jr., F. J. llsemann, J. S. Verdi, W.–M. Boerner, and S. K. Krasznay, "Application of the Polarimetric Matched Image Filter to the Assessment of SAR Data from the Mississippi Flood Region," Geoscience and Remote Sensing Symposium, Vol. 3, pp.1368 –1370, 1994

[4] Jian Yang, Yoshio Yamaguchi, Wolfgang-Martin Boerner, and Shiming Lin, "Numerical Methods for solving the Optimal Problem of Contrast Enhancement," IEEE Transactions on Geoscience and Remote Sensing, Vol. 38, No. 2, pp.965-971, 2000

[5] L. M. Novak, M.C. Burl, and W. W. Irving, "Optimal Polarimetric Processing for Enhanced Target Detection," IEEE Transactions on Aerospace and Electronic Systems, Vol. 29, No. 1, pp.234-244, 1993

[6] Fawwaz T. Ulaby and Charles Elachi, "Radar Polarimetry for Geoscience Applications," Artech House, 1990.

[7] Kamal Sarabandi and Eric S. Li, "Characterization of Optimum Polarization for Multiple Target Discrimination Using Genetic Algorithms," IEEE Transactions on Antennas and Propagation, Vol. 45, No. 12, pp.1810-1817, 1997

[8] Randy L. Haupt, "Thinned Arrays Using Genetic Algorithms," IEEE Transactions on Antennas and Propagation, Vol. 42, No. 7, pp.993-999, 1994

[9] Randy L. Haupt, "An Introduction to Genetic Algorithm for Electromagnetics," IEEE Antennas and Propagation Magazine, Vol.37, No.2, pp.7-15, 1995

[10] Eric A. Jones and William T. Jones, "Design of Yagi-Uda Antennas Using Genetic Algorithms," IEEE Transactions on Antennas and Propagation, Vol. 45, No. 9, pp.1386-1392, 1997

[11] J. Michael Johnson and Yahya Rahmat-Samii, "Genetic Algorithms in Engineering Electromagnetics," IEEE Antennas and Propagation Magazine, Vol. 39, No. 4, pp.7-21, 1997

[12] Goldberg, D. E, "GENETIC ALGORITHM in Search, Optimization and Machine Learning," Addison-Wesley, 1989.

The 21st Asian Conference on Remote Sensing
December 4-8, 2000 Taipei, TAIWAN

A REFLECTANCE RETRIEVAL ALGORITHM FOR LANDSAT TM SATELLITE IMAGE

C. H. Liu
Assistant Professor, Department of Management Information System,
Transworld Junior College of Commerce,
88 Yen-shan Rd., Touliu, Yunlin, Taiwan 640
Tel: 886-5-5570866-3351 Fax:886-5-5570869
E-mail: chliu@mail.tit.edu.tw
TAIWAN

E. F. Vermote
Associate Research Scientist, NASA's Goddard Space Flight Center
Code 922 Greenbelt, MD 20771
Tel: (301) 614-5521 Fax: (301) 614-5269
E-mail: eric@kratmos.gsfc.nasa.gov
USA

KEY WORDS: atmospheric correction model, reflectance, aerosol optical depth

ABSTRACT: An blockwise approached atmospheric correction model (BACM) for correcting non-uniform aerosol effect is developed in this paper. By using the dense dark vegetation, non-uniform aerosol optical depth can be retrieved in every specified block of image. Three Landsat TM images in LTER sites including two Hog Island images of uniform aerosol effect and one Madison of non-uniform aerosol effect are used to testify BACM. The results show that the mean errors of retrieved aerosol optical depths in these three images are 0.14 and 0.05 in TM1 and TM3 bands by comparing the field measurements from AERONET. Higher aerosol optical depth (τ (TM1)=0.84) in the hazier region is derived compared with lower value (τ (TM1)=0.62) in the clearer region of Madison scene. Non-uniform aerosol effect is then well corrected. Although in lack of field measurement, typical bare soil and vegetation reflectance can be retrieved even in the very hazy region (visibility~5km) of the scene after atmospheric correction.

1. INTRODUCTION

Quantitative analysis of remotely sensed data relies on the accurate correction of atmospheric effect, since modulation of the atmosphere impedes many applications of multi-temporal satellite images, such as agriculture monitoring (Hill and Sturm, 1991), land-cover change, remote sensing of surface albedo and classification (Liu 1995). Therefore, it is indispensable to convert the digital count of satellite image to surface reflectance which is reasonably independent of atmosphere and better related to the surface characteristics (Moran et al., 1992).

Dense dark vegetation (DDV) algorithm for land is now the most widely used method (Liu et al., 1996; Richter, 1996) to retrieve aerosol optical depth, because of the stable and low reflectance in the visible bands. This algorithm is not very satisfactory, since the normalized difference vegetation index (NDVI) used to select DDV is affected by the aerosol and thus tends to select pixels with low aerosol concentration given similar surface reflectance (Holben, 1992; Kaufman and Tanre, 1992). Based on the less sensitivity to aerosol scattering in longer wavelength (e.g. mid-IR 2.2 mm or 3.7 mm) and still sensitive to surface characteristics, global remote sensing of aerosol and subsequent atmospheric correction procedure for AVHRR and future EOS-MODIS has been developed (for details, see (Kaufman and Tanre, 1992; Kaufman et al., 1997)). Alternative way to correct the non-uniform aerosol effect by DDV algorithm from NDVI is to partition the remote sensing image into blocks (or sectors,(Richter, 1996)), which are assumed with uniform aerosol.

In this paper, a blockwise approach Atmospheric Correction Model (BACM) is developed to correct the non-uniform aerosol effect of Landsat TM images. Evaluation of retrieved aerosol optical depths is made possible by comparison with the field measurements from AERONET (Holben et al., 1997). .

2. ATMOSPHERIC CORRECTION MODEL FOR NON-UNIFORM AEROSOL EFFECT

To correct the non-uniform aerosol effect, Blockwise approached Atmospheric Correction Model (BACM) is developed. Those include geometry (sun and sensor), date, image (e.g., blocksize to correct non-uniform aerosol effect, window size to correct adjacency effect), sensor (absolute radiometric calibration coefficients to convert the

DC to radiance), molecule (scattering and absorption optical depths), aerosol (refractive index, Junge parameter and size range) and DDV assumption (f1, f2, f3 and ρ ddv in blue and red for Landsat TM, or green and red for SPOT HRV). At first, the total image is divided to Nx*Ny blocks where uniform aerosol effect is assumed in every block. The fractions f1* and f2* in every block are then equal to f1/(Nx*Ny) and f2/(Nx*Ny) respectively. DCddv for retrieving the aerosol optical depths in TM1 and TM3 bands in every block are then determined by using the three parameters f1, f2 and f3 (e.g. 0.2, 0.5 and 0.01). Look-up table (LUT) between digital count and aerosol optical depth at assumed surface reflectances ρ ddv (0.01 and 0.02 in blue and red bands, respectively) is used to derive aerosol optical depth by determined DCddv for every block. Angstrom formula is used to interpolate the aerosol optical depths in the other TM bands. Surface reflectance image with uniform target assumption can be obtained through LUT between digital count and surface reflectance at derived aerosol optical depths. In practice, spherical albedo ρ s, total upward transmittance T(μ v), upward diffuse transmittance td(μ v) and upward beam transmittance exp(- τ / μ v) are computed and stored for every block to correct the adjacency effect (equation 15, (Liu, 1995)). Window size is specified about 1 km, which is approximately the same as Richter (1996).

3. DATA DESCRIPTION

Three subseted Landsat TM images (1000*1000 pixels) which are the test sites of NSF LTER (National Science Foundation, Long-Term Ecological Research) project are used to testify the model. Two images scanned in July 12 and July 28 1993 are located in Hog Island (HI), the other one scanned in June 22 1995 is located in Madison (MD). Their solar zenith angles are all about 30.50. The sunphotometer-measured aerosol optical depths which are available from the AERONET (Holben et al., 1997) denote that HI-12jul93 image with τ (TM1)=0.69 is much hazier than HI-28jul93 with τ (TM1)=0.25 (table 1). HI scenes are all in uniform atmospheric effect, whereas MD scene shows non-uniform aerosol effect (hazier in the lower part). HI scenes contain near sea-shore oceans and most of agricultural lands combined with crops and bare soils. The MD scene contains different landcovers, such as forest, lake, urban and bare soil.

4. RESULTS AND DISCUSSIONS

Table 1 shows the derived aerosol optical depths (with / without iteration) and their errors $\Delta \tau$ to the field-measurements in TM1 and TM3 bands. Highly abnormal derived n (> 4.0) by using the υ iterative procedure results large $\Delta \tau$ (-0.14~0.36) in TM1 band. Reasonable υ should be in range of 2 (dust) ~ 4 (smoke) (Kaufman and Tanre 1992). Mean errors of $\Delta \tau$ by iterated method are 0.25 and 0.12 in TM1 and TM3 bands which are larger than non-iterated method (0.14 and 0.05). In evaluating the accuracy of retrieved τ in MD-22jun95 scene with non-uniform aerosol effect, the retrieved τ s of central four blocks are averaged (table 2). The ranges of retrieved τ (TM1) and τ (TM3) are 0.62~0.84 and 0.29~0.53 respectively, which account for the spatial variation of aerosol concentrations in MD-22jun95 scene. Retrieved aerosol optical depths are larger in lower part of image than upper part (e.g 0.82 and 0.62 in lower left and upper left corner in TM 1 band), which are also conforming to diverse haziness of MD-22jun95 scene. After atmospheric correction, the non-uniform aerosol effect is well removed.

After above discussions, therefore, the accuracies of retrieved aerosol optical depth (i.e. 0.14 and 0.05 in TM 1 and TM 3 bands) should be satisfactory, since the error of retrieved surface reflectance is about 0.01~0.02 as shown in the previous study (Kaufman and Tanre, 1992).

Although surface reflectance measurements are not available, the typical bare soil and vegetation reflectance spectra can be obtained after atmospheric correction even in the very hazy part (e.g. τ (TM1)=0.84, visibility~5km) of the MD-22jun95 (figure 1).

5. CONCLUSION

An atmospheric correction model (BACM) is developed for correcting the non-uniform aerosol effect of Landsat TM images by using the blockwise approach. A sensitivity study of aerosol characteristics such as optical depth, single scattering albedo, phase function and Junge parameter has shown that large error of retrieved aerosol optical depth (~0.3) can be caused due to the error of derived Junge parameter in the iterative procedure. Therefore, a fixed model is used.

The results show that the accuracies of the retrieved aerosol optical depths are encouraging ($\Delta \tau$ <0.2), by comparing the error of retrieved surface reflectance (0.01~0.02) made in the previous study. Non-uniform aerosol effect of image is also well corrected. After atmospheric correction, typical bare soil and vegetation

reflectance spectra can be acquired.

The major limitation of BACM is the requirement of DDV target in scene and a priori knowledge of blocksize to perform correction of non-uniform aerosol effect. The errors of retrieved aerosol optical depth and surface reflectance will be increased, if the image covers less dense and dark target, such as in semi-arid area. Blockwise approach will be less satisfactory, if the aerosol distribution on image is highly non-uniform, such as plume. Therefore, more studies should be done to assess the algorithm.

ACKNOWLEDGMENT

This work is supported by both post-doctoral scholarship from Ministry of Education of Taiwan and NSF LTER project of US.

REFERENCES

Hill, J., and Sturm, B., 1991, Radiometric correction multitemporal thematic mapper data for use in agricultural land-cover classification and vegetation monitoring. International Journal of Remote Sensing, 12, 1471-1491.

Holben, B. N., Vermote, E., Kaufman, Y. J., Tanre, D., and Kalb, V., 1992, Aerosol retrieval over land from AVHRR data-application for atmospheric correction. IEEE. Transactions on Geoscience and Remote Sensing, 30, 212-222.

Holben, B. N., Eck, T. F., Slutsker, I., Tanre, D., Buis, J. P., Setzer, A., Vermote, E., Reagan, J. A., Kaufman, Y. J., Nakajima, T., and Lavenu, 1997, Multi-band automatic sun and sky scanning radiometer system for measurement of aerosols. Remote Sensing of Environment, forthcoming.

Kaufman, Y. J., 1984, Atmospheric effects on remote sensing of surface reflectance. SPIE-Society of Photo-Optical Instrumentation Engineers, 475, 20-33.

Kaufman, Y. J., and Tanre, D., 1992, Atmospheric resistant vegetation index (ARVI) for EOS-MODIS. IEEE. Transactions on Geoscience and Remote Sensing, 30, 261-270.

Kaufman, Y. J., Tanre, D., Remer, L. A., Vermote, E. F., Chu, A., and Holben, B. N., 1997, Operational remote sensing of tropospheric aerosol over the land from EOS-MODIS. Journal of Geophysical Research-Atmosphere , *102*(14), 17051-17068.

Liu C. H., 1995, Radiometric correction of SPOT satellite imageries. Ph. D. dissertation, National Central University, Taiwan, 172pp.

Liu, C. H., and Chen, A. J., 1995, An improved spectral knowledge for multi-temporal image classification-a case study of urban area. Proceedings of the International Geoscience and Remote Sensing Symposium, Firenze, Italy, 10-14 July 1995 (Piscataway, NJ:IEEE), pp.1279-1281.

Liu, C. H., Chen, A. J., and Liu, G. R., 1996, An image-based retrieval algorithm of aerosol characteristics and surface reflectance for satellite images. International Journal of Remote Sensing, 17, 3477-3500.

Moran, M. S., Jackson, R. D., Slater, P. N., and Teillet, P. M., 1992, Evaluation of simplified procedures for retrieval of land surface reflectance factors from satellite sensor output. Remote Sensing of Environment, 41, 169-184.

Richter, R., 1996, A spatially adaptive fast atmospheric correction algorithm. International Journal of Remote Sensing, 17, 1201-1214.

Vermote, E., 1995, Atmospheric correction software for Landsat 5 Thematic Mapper data set. NASA/GSFC, Technical Report, 89p.

Vermote, E. F., Tanre, D., Deuze, J. L., Herman, M. and Morcrette, J., 1997, Second simulation of the satellite signal in the solar spectrum, 6S: an overview. IEEE. Transactions on Geoscience and Remote Sensing, 35, 675-686.

Table 1. Comparison of image-derived aerosol optical depths (with / without iterated) and their errors $\Delta\tau$ to the field-measurement (AERONET) in TM1 and TM3 bands. High $\Delta\tau$ in TM1 band from iterated method is due to the abnormally high image-derived n which is also listed. HI, MD are abbreviations of Hog-Island and Madison sites respectively. Mean errors of retrieved τ by iterated method are 0.25 and 0.12 in TM1 and TM3 bands as well as 0.14 and 0.05 by non-iterated method, respectively.

Site-Date	Field Measurement		$\Delta\tau$						
			Iteration[a]			No Iteration[b]		TMSAC[d]	
	TM1	TM3	TM1	TM3	υ	TM1	TM3	TM1	TM3
HI-12jul93	0.69	0.43	-0.25	-0.19	4.0	0.09	-0.02	0.08	0.06
HI-28jul93	0.25	0.15	0.36	-0.03	7.2	0.19	-0.03	0.11	0.01
MD-22jun95[c]	0.56	0.25	-0.14	-0.14	4.0	0.13	0.1	0.11	0.14

[a] is the iterative procedure by iterating the Junge parameter υ with initial υ =3.0 (Liu et al. 1996).

[b] υ is set to 3.3 which corresponds to continental model.

[c] derived aerosol optical depth is the average value of the central four blocks. See table 2 and context.

[d] ρ_7/ρ_1=2.4, ρ_7/ρ_3=1.35 for pixels selected ρ_7=[0.015,0.05] (see context).

Table 2. Retrieved aerosol optical depths in TM1 and TM3 bands for every block of MD-22jun95 image which contains non-uniform aerosol effect. Values in parenthesis are (τ (TM1), τ (TM3)) respectively.

(0.62,0.29)	(0.62,0.29)	(0.64,0.37)	(0.64,0.37)
(0.64,0.33)	(0.64,0.33)	(0.66,0.33)	(0.64,0.33)
(0.74,0.45)	(0.70,0.37)	(0.70,0.37)	(0.72,0.37)
(0.82,0.49)	(0.84,0.53)	(0.82,0.49)	(0.82,0.49)

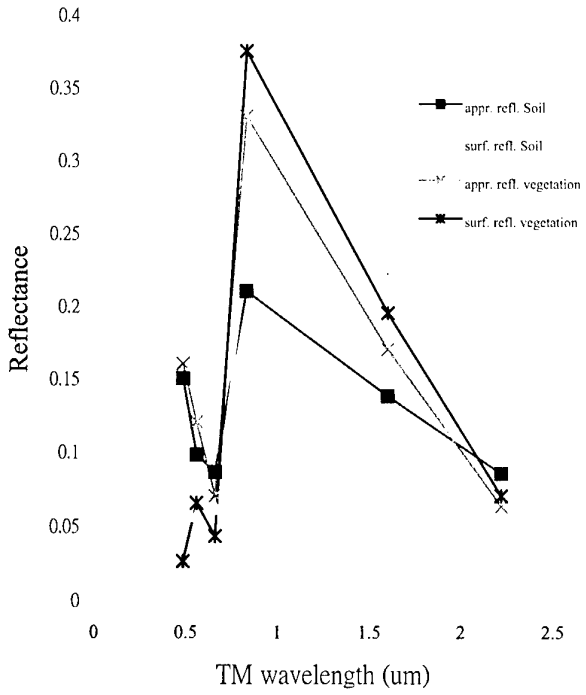


Figure 1. The apparent and surface reflectance spectra of bare soil and vegetation extracted from the very hazy part (visibility~5km) of MD-22jun95 scene.

The 21st Asian Conference on Remote Sensing
December 4-8, 2000 Taipei, TAIWAN

A SYNERGISTIC AUTOMATIC CLUSTERING TECHNIQUE (SYNERACT) FOR MULTISPECTRAL IMAGE ANALYSIS

Kai-Yi Huang
Associate Professor, Department of Forestry,
National Chung-Hsing University,
250 Kuo-Kuang Road, Taichung, Taiwan 402
Tel: +886-4-2854663; Fax: +886-4-2873628
E-mail: kyhuang@dragon.nchu.edu.tw

KEY WORDS: Remote Sensing, Clustering Algorithm, Unsupervised Classification

ABSTRACT

ISODATA has been widely used in unsupervised and supervised classification. However, it requires the analyst to have *a priori* knowledge about the data for specifying input parameters. The beginner will spend much time on determining those parameters by trial and error. It is time-consuming because of its iterative process. The study aimed to develop a synergistic automatic clustering technique (SYNERACT) that combined the hierarchical descending and K-means clustering procedures to avoid limitations with ISODATA. They were compared according to classification accuracy and efficiency using two-date video images. An inappropriate seed assignment for ISODATA was shown to significantly reduce accuracies. In contrast, SYNERACT was required to specify only two parameters. It determined the locations of the initial clusters automatically from the data, thereby avoiding those limitations. Because SYNERACT passed through the data set in times largely fewer than ISODATA did, SYNERACT was much faster than ISODATA. SYNERACT also matched ISODATA in accuracy. Accordingly, SYNERACT was a suitable alternative for ISODATA in the multispectral image analysis.

1. INTRODUCTION

Multispectral image classification is one of the most often used techniques for extracting information from remotely sensed data of the Earth, which can be performed by unsupervised classification using clustering (Jensen, 1996). Clustering performs the valuable function of identifying some of the unique classes but with very small areal extent that might not be initially apparent to the analyst applying a supervised classifier. Therefore, the clustering method seems to be a much more practical approach for information extraction (Viovy, 2000). There are two main families of clustering methods: the Iterative Self-Organizing Data Analysis Techniques (ISODATA) clustering and hierarchical clustering approaches (Viovy, 2000).

The ISODATA (or K-means) algorithm is a widely used clustering method to partition the image data in the multispectral space into a number of spectral classes (Jensen, 1996). This type of clustering algorithms, however, suffers from several limitations. One of the limitations is that ISODATA requires the user to specify the number of clusters beforehand. The second limitation is that it requires the user to specify the starting positions of these clusters through an educated guess. The clustering starts with a set of arbitrarily selected pixels as cluster centers with exception no two may be the same (Swain, 1978). The choice of the initial locations of the cluster centers is not critical, but it will evidently affect the time it takes to reach a final, acceptable result (Richards, 1993). It does not matter where the initial cluster centers are located, as long as enough number of iterations is allowed (ERDAS, 1997). Because no guidance is available in general, a logical procedure is adopted in LARSYS (Richards, 1993). The initial cluster centers are chosen evenly distributed along the diagonal axis in the multidimensional feature space. This is a line from the origin to the point corresponding to the maximum digital number in each spectral component. Other similar procedures used in ISODATA have been proposed in Jensen (1996) and ERDAS (1997). However, few studies have investigated the problem for the past years about how random choice of the initial cluster centers and those procedures proposed by ERDAS (1997) and Jensen (1996) may affect final classification results. The study thus will examine this very important but apparently neglected problem.

The third limitation associated with ISODATA is its processing speed. ISODATA is computationally intensive when processing large data sets since, at each iterative step, all pixels in the whole data set must be checked against every cluster center. Furthermore, this method tends to suffer from performance degradation as the number of bands, the number of pixels, or the number of clusters

increases (Richards, 1993; Viovy, 2000).

The second type of clustering methods that does not require the analyst to specify the number of clusters beforehand is hierarchical clustering (Richards, 1993). As pointed out by Richards (1993), a divisive hierarchical clustering (or hierarchical descending) algorithm has been developed in which the data are initialized as a single cluster that is progressively subdivided. This method is more computationally intensive and is rarely used in remote sensing image analysis since usually a large number of pixels are involved.

The goal of this study was to develop a synergistic automatic clustering technique (SYNERACT) that combined both hierarchical descending and K-means approaches to avoid before-mentioned limitations associated with ISODATA. The study attempted to accomplish the three specific objectives using two-date video image data. The first objective was to develop SYNERACT based on hyperplane, dynamical (iterative optimization) clustering principles, and binary tree. The second one was to compare SYNERACT with ISODATA in terms of classification accuracy and efficiency. The third one was to show that SYNERACT was very fast and well suited to act as a substitute for ISODATA in remote sensing applications, which was opposite to the ideas suggested by Richards (1993).

2. STUDY AREA AND MATERIALS

The study area was located near Weslaco in Hidalgo county, Texas. It was a completely randomized block designed field experiment consisting of plots of the following surface features: (1) cotton, (2) cantaloupe, (3) sorghum, (4) johnsongrass, (5) pigweed, and (6) bare soil (Figure 1). Each of the 24 plots (six treatments and four replications) measured 7.11 m by 9.14 m, making the total site dimension 42.67 m by 36.56 m (Richardson *et al.*, 1985). However, the fourth row (drawn with dash line) was excluded from the study due to damage of this portion of the video data file.

The two-date video image data were acquired on 31 May and 24 July 1983 near noon on moderately sunny days from an altitude of 900 m. The video imaging system used to collect data for the study is described in detail in Richardson *et al.* (1985). Spectral bands 1-4 were acquired on 24 July; spectral bands 5-8 were acquired on 31 May. Channels 1 and 5 were blue bands (420 to 430 nm), Channels 2 and 6 were red bands (640 to 670 nm), channels 3 and 7 were yellow-green bands (520 to 550 nm), and channels 4 and 8 were near-infrared bands (850 to 890 nm). Multiple-date image normalization using regression (Jensen, 1996) was performed to radiometrically correct the data set used in the study since atmospheric effects probably affected pixel brightness values of the two-date video image data. Accuracy assessment was performed over 18 plots from row 1 to row 3 in the experimental field with the exception of row 4.

3. METHOD AND RATIONALE

SYNERACT in fact combines the concepts of hyperplane, iterative optimization clustering and binary tree. The hyperplane divides a cluster into two clusters of smaller size and computes their means. The iterative optimization clustering procedure (IOCP) is based on estimating some reasonable assignment of the pixel vectors into candidate clusters and moving them from one cluster to another in such a way that an objective function is minimized (Richards, 1993). The binary tree is a useful data structure that can store the clusters successively generated from each split. SYNERACT treats all of the image pixels as a single cluster. The single cluster is placed at the root of a binary tree firstly, and then is progressively subdivided. At each split, the algorithm will attempt to divide each cluster defined at the previous split into two clusters of smaller size and to compute their centers. IOCP is then performed. Each split is tested for relevance *a posteriori*. Two clusters of smaller size generated from each split by a hyperplane are placed at the left and right subtree nodes, respectively. If the test fails, the cluster will no longer be split in further separation. The cluster is called stabilized. This process continues until all clusters are stabilized.

3.1 Definition of a Hyperplane

To appreciate the development of SYNERACT, it is required to understand the concept of hyperplane. The family of linear discriminant functions (Nilsson, 1965) can be expressed in the form as follows:

$$f(\mathbf{X}) = W_1 * X_1 + W_2 * X_2 + \ldots + W_n * X_n + W_{n+1}, \qquad (1)$$

where $W_1, W_2, \ldots, W_n, W_{n+1}$ are weighting coefficients. f is a linear function of the components of an augmented column vector **X**.

A simple linear separation is performed by a linear discriminant function that partitions the feature space into two regions. The linear discriminant function can be viewed as a separating surface in which the simplest form is a hyperplane (Nilsson, 1965). A hyperplane partitions the feature space into two regions defined as:

$$f(\mathbf{X}) = \mathbf{W} \cdot \mathbf{X} > 0 \quad \text{and} \quad f(\mathbf{X}) = \mathbf{W} \cdot \mathbf{X} \leqq 0, \tag{2}$$

where $\mathbf{W} = [W_1, W_2, \ldots, W_n, W_{n+1}]$, $\mathbf{X}^t = [X_1, X_2, \ldots, X_n, 1]$, and n = dimension of the feature space.

Assume that there is a cluster in the feature space. A weight vector **W** is viewed to implement a linear separating surface (hyperplane) to divide a cluster in the feature space into two clusters of smaller size (children). The augmented pixel vectors of the one child-cluster have a positive dot product value with **W**, while the other child-cluster consists of pixels (lying on the other side of **W**) that have a zero or negative dot product value with **W**. The former is categorized as S_1 and the latter is categorized as S_2. Centers of the two sets are computed according to all of the pixels in the two sets, respectively. The sets of parent cluster (S) and two child-clusters ($S_1$and S_2) can be defined as:

$$S_1 = \{\mathbf{X} \varepsilon S | \mathbf{W} \cdot \mathbf{X} > 0\}; \quad S_2 = \{\mathbf{X} \varepsilon S | \mathbf{W} \cdot \mathbf{X} \leqq 0\}; \quad S = S_1 \cup S_2.$$

3.2 Generation of a Hyperplane

An augmented pixel vector is defined as:

$$\mathbf{X} = [\mathbf{V}^t, 1]^t, \quad \text{where} \quad \mathbf{V}^t = [V_1, V_2, \ldots, V_n]. \tag{3}$$

The process of generating a weight vector is illustrated in Figure 2. Let the pixels be augmented and expressed by the general column vector **X**. One pixel **P** is chosen from this cluster so that $|\mathbf{P} - \mathbf{C}| > |\mathbf{X} - \mathbf{C}|$ for all **X**, where **C** is an arbitrarily chosen position vector in the feature space. Let **C** be the grand mean vector computed from all of the pixels in a single cluster. Under this condition, **P** and **C** define a line from the grand mean **C** to the farthest pixel **P**. Assume that there is a single cluster in the two-dimensional feature space consisting of two spectrally distinct clusters of smaller size represented by **U** and **V**, respectively so that $\{\mathbf{X}\} = \{\mathbf{U}\} \cup \{\mathbf{V}\}$, $\mathbf{P} \varepsilon \{\mathbf{X}\}$. Assume further that **P** comes from {**U**} and is denoted by **U***, $\mathbf{U}^* = \mathbf{P}$. The next step is to find all of **V** so that $(\mathbf{V} - \mathbf{C}) \cdot (\mathbf{U}^* - \mathbf{C}) \leqq 0$, $\{\mathbf{V}\} \subset \{\mathbf{X}\}$. Find $\mathbf{V}_1^*$ or $\mathbf{V}_2^*$ from {**V**} so that $\mathbf{V}_1^*$ must satisfy $|(\mathbf{V}_1^* - \mathbf{C}) \cdot (\mathbf{U}^* - \mathbf{C})| = 0$ and $\mathbf{V}_2^*$ must satisfy $|(\mathbf{V}_2^* - \mathbf{C}) \cdot (\mathbf{U}^* - \mathbf{C})| < |(\mathbf{V} - \mathbf{C}) \cdot (\mathbf{U}^* - \mathbf{C})|$. Since the brightness value of each pixel in remotely sensed data is recorded as an integer, $\mathbf{V}_1^*$ cannot always be found in all cases. Thus $\mathbf{V}_2^*$ having the biggest negative dot product value is used as an alternative of $\mathbf{V}_1^*$. Lines perpendicular to $(\mathbf{U}^* - \mathbf{C})$ and passing through $\mathbf{V}_1^*$ or $\mathbf{V}_2^*$ will be hyperplanes (weight vectors) separating {**U**} and {**V**}, as shown in Figure 2. According to the concept of the single-sided decision surface proposed by Lee and Richards (1984), these two hyperplanes (weight vectors) are defined by equations shown as follows:

$$\mathbf{W}_1 = [(\mathbf{U}^* - \mathbf{C})^t, \mathbf{V}_1^* \cdot (\mathbf{U}^* - \mathbf{C})]^t \tag{4}$$

$$\mathbf{W}_2 = [(\mathbf{U}^* - \mathbf{C})^t, \mathbf{V}_2^* \cdot (\mathbf{U}^* - \mathbf{C})]^t \tag{5}$$

3.3 Test for Relevance of Splitting

SYNERACT will split each cluster formed at the previous separation into two clusters of smaller size. The splitting process is theoretically continued until there is only one pixel in each cluster. Therefore, this process must be controlled by two input parameters, including the maximum number of clusters to be considered (C_{max}) and the minimum percentage of pixels allowed in a single cluster (P%). Each split is tested for these two parameters *a posteriori* in order that a homogeneous cluster will not be split inappropriately. Since each cluster is the basis for an information class, C_{max} will become the maximum number of classes to be formed. Some clusters with number of pixels less than P% can be eliminated, leaving less than C_{max} clusters. The pixels in these discarded clusters will be reassigned to an alternative cluster.

4. RESULTS AND DISCUSSION

The two-date video image data used for testing two clustering algorithms had eight bands mentioned in section 2. The total number of band combinations (i.e. ${}_8C_8 +, \ldots, + {}_8C_1$) was equal to 255. The band combination of 2, 3, 4, and 8 with best separability was chosen for the test using the program module Separability \ Euclidean Distance Measure in ERDAS Imagine 8.3.1 software.

4.1 Influences of Initial Seed Assignment

Table 1 presents the classification results of ISODATA using six sets of initial cluster centers randomly generated. Overall accuracies varied from the lowest 65% to the highest 85% for six sets of initial seeds randomly generated. Clearly, the choice of the initial locations of the cluster centers was critical, because it evidently affected final classification results. This outcome was contrary to the ideas proposed by Richards (1993) and ERDAS (1997).

This study also applied the procedure of initial seed assignment proposed by Jensen (1996) and ERDAS (1997) to specify the initial locations of the cluster centers required by ISODATA. Table 1 also presents the classification results generated from ISODATA using five initial seed allocations. In this case, $\mu \pm 1 * \sigma$ had the best overall accuracy (93%) and $\mu \pm 5 * \sigma$ had the lowest overall accuracy (75%), where μ is the mean vector and σ is standard deviation; however, the analyst would have to spend much of his time on 'try and see' to determine an optimal number of standard deviations for other cases.

4.2 Efficiency

4.2.1 Processing Speed

Table 2 presents the lengths of computational time of two clustering algorithms varied with the number of pixels in the data set they processed and the number of clusters generated. The lengths of computational time spent by ISODATA were 6-39 (T_I/T_S) times as long as those spent by SYNERACT, as the number of pixels increased from 3,400 to 17,640 and the number of clusters was set 16. Table 3 presents the lengths of computational time of two clustering algorithms varied with different band combinations. The lengths of computational time spent by ISODATA were 6-12 (T_I/T_S) times as long as those spent by SYNERACT, as the number of bands varied between two and eight.

4.2.2 Ease of Use

A sophisticated ISODATA algorithm described by Jensen (1996) normally requires the analyst to specify seven parameters. The ISODATA program of ERDAS Imagine software requires the user to specify four parameters identical to some of parameters proposed by Jensen and to initialize cluster means along a diagonal axis or principal axis, but skips splitting and merging parameters. In contrast, SYNERACT developed in the study required the analyst to specify only two parameters already mentioned in section 3. Moreover, it eliminated the need for *a priori* estimates on the locations of the initial clusters. Accordingly, SYNERACT was more users-friendly for the beginner than ISODATA.

4.3 Classification Accuracy

Table 4 presents the overall accuracies and the accuracies of individual categories of the two clustering approaches. The overall accuracy (92%) of SYNERACT was only about 1% lower than that of ISODATA (93%); this difference was probably due to chance. Accordingly, SYNERACT and ISODATA were equally matched in classification accuracy.

5. CONCLUSIONS

SYNERACT required a minimum of user input with only two parameters, thereby reducing the load of specifying other complex parameters by trial and error on the beginner. By comparison, ISODATA was not users-friendly since it required the analyst to specify many input parameters, particularly the starting positions of the initial clusters. This study showed that an inappropriate choice of this parameter for ISODATA significantly reduced final classification accuracies. This outcome obviously was opposite to the ideas stated by Richards (1993) and ERDAS (1997). In contrast, SYNERACT had the ability to determine this parameter automatically from the data set itself, and thus avoided the adverse effect on a final clustering. SYNERACT was very fast, whereas ISODATA was time-consuming. SYNERACT had the capability to compete with ISODATA in classification accuracy. In sum, this study showed that SYNERACT was really efficient and well suited to serve as an alternative of

ISODATA for applications in remote sensing image analysis involving a large data set, which was opposite to the thoughts proposed by Richards (1993).

REFERENCES

ERDAS, 1997. ERDAS Field Guide. ERDAS, Inc., Atlanta, Georgia, pp. 225-229.

Jensen, J. R., 1996. Introductory Digital Image Processing--A Remote Sensing Perspective. Prentice Hall, Inc., New Jersey, pp. 197-256.

Lee, T., and J. A. Richards, 1984. Piecewise linear classification using seniority logic committee methods with application of remote sensing. Pattern Recognition, 17(4), pp. 453-464.

Nilsson, N. J., 1965. Learning Machines. McGraw-Hill Book Co., New York, pp. 15-27.

Richards, J. A., 1993. Remote Sensing Digital Image Analysis: An Introduction. Springer-Verlag, Berlin, German, pp. 229-244, 265-291.

Richardson, A. J., R. M. Menges, and P. R. Nixon, 1985. Distinguishing weed from crop plants using video remote sensing. Photogrammetric Engineering & Remote Sensing, 51(11), pp. 1785-1790.

Swain, P. H., 1978, Fundamentals of Pattern Recognition in Remote Sensing. In: the Remote Sensing: the Quantitative Approach, edited by Swain, P. H. and Davis, S. M., McGraw-Hill Book Co., New York, pp. 136-187.

Viovy, N., 2000. Automatic classification of time series (ACTS): a new clustering method for remote sensing time series. International Journal of Remote Sensing, 21(6), pp. 1537-1560.

Table 1. Classification Accuracies of ISODATA Using Six Sets of Randomly Generated Initial Seeds and five sets of ERDAS's Initial Seed Assignment.

Random Seed Assignment		ERDAS's Initial Seed Assignment	
Set	Overall Accuracy (%)	No. of Standard Deviation (σ)	Overall Accuracy (%)
1	83	1	93
2	80	2	88
3	70	3	80
4	76	4	75
5	65	5	75
6	85	—	—

Table 2. The Lengths of Processing Time Spent by SYNERACT and ISODATA for Different Number of Pixels.

		SYNERACT		ISODATA		
No. of Pixels	*No.* of Clusters	T_S (Second)	*No.* of Iterations	T_I (Second)	*No.* of Iterations	T_I / T_S
3400	16	3.1	6	17.2	24	6
6460	16	5.1	5	55.1	42	11
9499	16	7.0	10	84.6	45	12
12284	16	8.8	7	258.4	105	29
17640	16	12.3	7	478.7	138	39

Table 3. The Lengths of Processing Time Spent by SYNERACT and ISODATA for Seven Sets of Band Combinations.

	SYNERACT		ISODATA		
Band Combination	T_S (Second)	*No.* of Iterations	T_I (Second)	*No.* of Iterations	T_I / T_S
2 3 4 8	7.0	10	84.7	45	12
2 3 4 5 8	8.0	4	74.8	33	9
1 2 3 4 5 8	10.6	8	93.2	35	9
1 2 3 4 5 6 8	12.1	8	69.0	22	6
1 2 3 4 5 6 7 8	13.3	8	92.0	26	7

Table 4. Classification Accuracies of the SYNERACT and ISODATA Methods.

Land-cover Type	Accuracy (%) of SYNERACT	Accuracy (%) of ISODATA
Cotton	90	93
Soil	97	97
Johnsongrass	86	93
Cantaloupe	95	95
Pigweed	91	85
Sorghum	90	93
Overall Accuracy	92	93

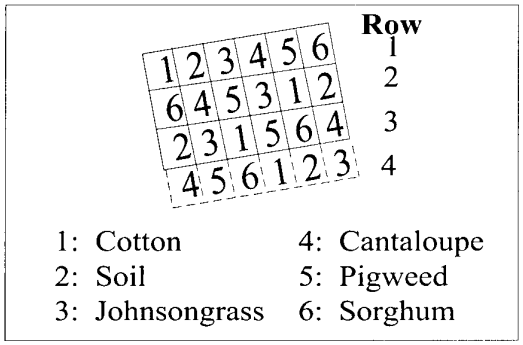


Figure 1. Plot Identification Map of the Study Area (Not Drawn on the Scale).

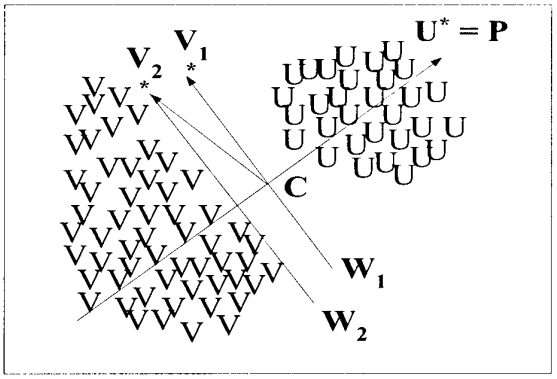


Figure 2. A Two-dimensional, Hypothetical Case with Two Clusters Illustrates the Process of Generating the Weight Vector W_1 or W_2 That Implements a Hyperplane of Hierarchical Descending Clustering.

AN EFFICIENT ARTIFICIAL NEURAL NETWORK TRAINING METHOD THROUGH INDUCED LEARNING RETARDATION: INHIBITED BRAIN LEARNING

Joel C. Bandibas
(Research Center, Cavite State University, Philippines)
Research Fellow, Land Evaluation and Development Laboratory
NGRI, Senbonmatsu, Nishinasuno, Tochigi Prefecture, 329-2739 Japan
Tel. 0081-287-377246 Fax: 0081-287-366629 email: bandibas@ngri.affrc.go.jp

Kazunori Kohyama
Head, Land Evaluation and Development Laboratory
NGRI, Senbonmatsu, Nishinasuno, Tochigi Prefecture, Japan
Email: kohyama@ngri.affrc.go.jp

KEY WORDS: Artificial Neural Network Satellite Image Inhibited Brain Learning

ABSTRACT

This study focuses on the development of a training scheme to make a large artificial neural network learn faster during training. This involves the identification of the few connection weights in the neural network that are too "greedy" to change during training. It is assumed that these few units "monopolize" the modeling of the information classes in satellite images. The hugely unequal participation of the neural network units during training is assumed to be the reason for the network's difficulty to learn. This study formulates a training scheme by which the changes of the connection weights of the most active units are temporarily inhibited when they reached a predetermined deviation limit. A set of connection weight deviation limit and maximum number of connection weights to be inhibited is formulated. The procedure induces a temporary retardation of the artificial neural network to learn. Through this, the most active units' "monopoly" in the modeling of the information classes is minimized giving the less active ones higher chances of participating in the modeling process. This results to faster training speed and a more accurate artificial neural network. The training procedure is termed inhibited brain learning.
The developed training method is tested using a Landsat TM data of the study site in Nishinasuno, Tochigi Prefecture, Japan with 7 land cover types. The results show that the developed training scheme is more than two times faster than the conventional training method. The fastest training speed obtained using the inhibited brain learning method is 2495 iterations. The conventional training method requires 8239 and 6495 iterations for the small and large artificial neural networks, respectively. Furthermore, the trained artificial neural network using the developed procedure is more accurate (90.5 %) compared to the accuracy of the small network (82.0%) and the large network (88.3%), both trained using the conventional method.

INTRODUCTION

The modeling of the human brain has always been motivated by its high performance in complex cognitive tasks like visual and auditory pattern recognition. One of the products of this effort is the development of artificial neural network (ANN) computing for satellite image classification, where training of the ANN is the core of the modeling process. Although ANN-based satellite image

classification methods are more robust than conventional statistical approaches, difficulties in their use relate to their long training time (Kavzoglu and Mather, 1999). The process is computationally expensive making the use of ANN in remote sensing impractical.

The search for the ANN computing method that is both efficient and accurate has been the object of research of the practitioners of ANN computing. Previous research works primarily focused on the determination of the most appropriate ANN architecture and size that result to higher efficiency during training. Indeed, ANN efficiency is related to its architecture (Kanellopoulos and Wilkinson, 1997). However, designing the best ANN architecture and size that learns fast during training is a difficult balancing task. In general, large networks take longer time to learn than the smaller ones. Faster learning smaller networks might be able to generalize and accurate when processing smaller number of information classes in satellite images, but they are inaccurate for processing data with large number of training patterns (Kavzoglu and Mather, 1999). Furthermore, smaller networks are also inaccurate when the information classes involved have high intra-class spectral variability. On the other hand, slower learning large networks are very accurate to identify training data and are capable of processing large number of training patterns. They can also cope well with satellite images where the information classes are spectrally heterogeneous. However, they have poor generalization capability (Karnin, 1990) and are proven to be inaccurate during the actual classification.

The high intra-class spectral variability of information classes in satellite images is more of a rule than an exception. Consequently, the use of a relatively large ANN for satellite image classification can be advantageous if it can be made efficient during training and accurate during the actual classification. This study aims at making a large ANN learns faster during training and improves its capability to generalize. This study successfully formulates a training scheme by which the ANN is induced to learn faster. The procedure also enables the ANN to generalize better making it more accurate during the actual classification. The training scheme is termed inhibited brain learning (IBL).

METHODS

Inhibited Brain Learning

IBL is a training scheme by which the change of values of the connection weights of the most active ANN units is temporarily inhibited during training. The development of IBL training scheme is based from following assumptions:

- In large networks, some connection weights are too "greedy" to change during training compared to the majority of the connections.
- These few "greedy" units "monopolize" the modeling of the information classes in the training data.
- Temporarily inhibiting the changes of these "greedy" units during training will increase the participation of the less active units in the modeling of the information classes in the training data.

In this study, IBL method was implemented in a very straightforward way. The scheme involves the "clamp and release" approach and consists of three major steps which are as follows:

1. Identification of the "greedy" connection weights (most active units) during the initial stage of training.
2. Inhibit the change of the values of the active units during training through "clamping" when they reached a set deviation limit.
3. Releasing the "clamped" connection weights when their number reaches a set limit.

The "Clamp and Release" (CAR) Approach

CAR was implemented to minimize the "monopolistic" tendency of the most active connection weights of the ANN during training. To achieve this goal, the values of the connections of the most active units have to be inhibited (clamped) from changing after reaching a predetermined deviation limit. Once these values are clamped, the error can just be minimized through the changes of the values of the less active unclamped units. Obviously, the number of clamped connection weights increases as the training proceeds as more units will reach the deviation limit. Definitely, learning will be significantly retarded if majority of the units will already be clamped. A limit then has to be established as to how many connections are to be clamped. Once this limit is reached, clamping will be stopped and all the clamped connections will be released. Figure 1 shows an example of the clamping sequence of the ANN units connections during training.

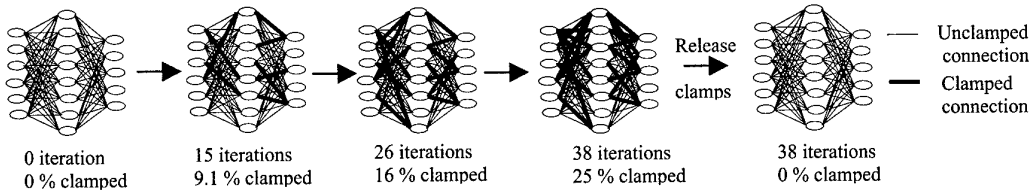


Figure 1. The clamp and release sequence during training of ANN with 25 percent clamped connection limit.

Connection Weights Deviation and Clamped Connections limits

CAR can just be implemented if the connection weights deviation and clamped connections limits are earlier determined. In this study, a series of experiments were conducted to determine the two important parameters to be used for the IBL. The values of the deviation limits used in this experiment, expressed in percent change of the initial values of the connection weights ranges from 25% to 300% at 25 % interval. On the other hand, the values of the clamped connection limits, expressed as percentage of the total number of connections of the ANN, ranges from 5% to 90% at 5% interval.

A Landsat TM data covering an area of 230 km^2 was used for this experiment. The study area was located in Nishinasuno, Tochigi Prefecture, Japan. Training and test pixels were obtained through actual field visit of the study area. Seven land cover classes were considered in this study and they were the following: 1.) buildup areas; 2.) grassland; 3.) deciduous forest; 4.) coniferous forest; 5.) rice field; 6.) river and ; 7.) pond/dam.

Artificial Neural Network Structure

A multi-layer perceptron trained by the back-propagation algorithm (Rumelhart et al., 1986) using the gradient descent training method was used in this experiment. The ANN has one hidden layer

with 30 nodes. The input layer has 5 nodes used to accommodate the 5 TM bands (bands 1 to 5) and the output layer consisted of 7 nodes reflecting the 7 land cover classes. For comparison purposes, two ANN of different sizes were trained using the conventional method and served as controls. The first ANN (control a) is a small network with 15 nodes in the middle layer and the second one (control b) has the same size as the networks trained using IBL. In this study, all ANN training were stopped after the trained networks reached an accuracy of at least 90% using the training data.

RESULTS AND DISCUSSION

Training Speed

The results of the different training runs to determine the best combination of the deviation and clamped percentage limits that can give the fastest training time is shown in figure 2. Each line in figure 2 represents a deviation limit and shows the change in the number of iterations as the percentage of clamped connection increases. The two straight horizontal lines represent the number of iterations using the conventional training method (controls). It is very evident from the graph that most of the points are below the horizontal lines indicating that the IBL method results to faster training speed compared to the conventional one. Table 1 shows the fastest training speed of 2417 iterations (54.4 seconds) using the connection weight deviation and clamped connection limits of 225% and 15%, respectively. The conventional training method required 8239 iterations (101.6 seconds) and 6495 iterations (148.8 seconds) for the small ANN (Control a) and big ANN (Control b), respectively. The results also show that using the IBL, large ANN learn faster compared to the smaller ANN trained using the conventional method.

The effect of the clamped connection percentage is very evident in the experiment. The results show that training speeds were faster at clamped connection limits ranging from 15 to 45 percent. On the other hand, training speed did not significantly change when the clamped connection limits were 10 or lower at all levels of deviation limits. This indicates that only few active connections were identified at this level hence the effect on the training speed was minimal. On the other hand, training speed started to significantly decrease as the number of clamped connections goes beyond 85 percent. This result suggests that once the number of clamped connections reaches a critical mass, learning retardation will become very significant for only very few unclamped connections will be left to change to reduce the error.

The fastest training speeds were obtained at higher deviation limits and lower clamped connection limits. As indicated in figure 2, deviation limits ranging from 175 to 250 percent with clamped connection limits values ranging from 15 to 20 percent generated the best result. On the other hand, lower deviation limits generally yielded longer training time. This is because lower deviation limit will make connection weights that changes slightly qualify to be clamped. Consequently, more units will be clamped at the early stage of training which result to the significant retardation of the neural network to learn. On the other hand, higher deviation limits just allow connection weights that change significantly faster than most connection to be clamped. Because of this, the combination of higher deviation and lower clamped connection limits is sufficient to inhibit the changes of the "monopolistic" few connections in the ANN while giving more time for the less active units to participate in the error reduction process.

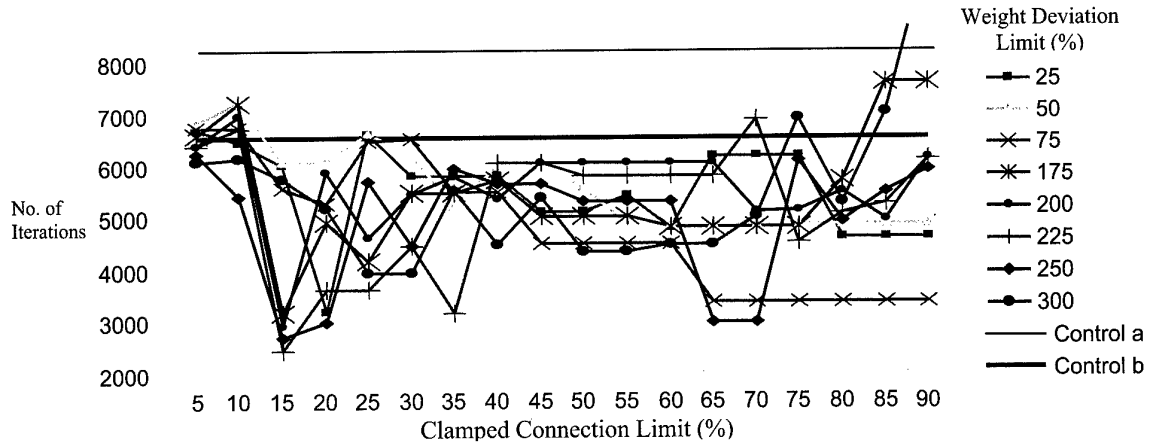


Figure 2. ANN training speed using different weight deviation and clamped connection limits values.

Accuracy

Artificial neural network accuracy is always related to its ability to generalize. Generalization is the ability of the neural network to interpolate and extrapolate data that it has not seen before (Atkinson and Tatnall, 1997). One of the most important factors that effect the ANN generalization capability is training time. The longer a network is trained the better it classifies the training data, but the more likely it is to fail in the classification of new data because it may become over-specific (Kavzoglu and Mather, 1999). In this study, the combination of deviation limits and clamped percentage limits that resulted to the shortest training time were determined. The accuracy of the trained networks obtained from these limit settings were investigated whether the shortened training time also resulted to the improvement of the network's ability to generalize.

Table 1 shows the combination of deviation and clamped connection limits that resulted to the fastest training speeds in the experiment. The training speeds and accuracy obtained using the conventional training method are also included for comparison. The results show that IBL method with deviation limits ranging from 175 to 250 percent with 15 % clamped percentage limit resulted to training speeds more than twice as fast as the controls. It also shows that using the IBL, the ANN's accuracy to identify test pixels is greater than those trained using the conventional method. These results indicate that with shortened training time, the ability of the ANN to generalize also improves. Furthermore, the large ANN trained using the IBL can generalize better than the small ANN trained using the conventional method. Figure 3 shows two classified images using trained ANN employing the conventional and the IBL training methods.

Table 1. Trained ANN accuracy using the combinations of weight deviation and clamped connection limits that resulted to the fastest training speeds.

Weight Deviation Limit (%)	Clamped Connection Limit (%)	Number of iterations	Training Time (seconds)	Accuracy (%)
control a (small ANN)	control a	8239	101.6	82.0
control b	control b	6495	148.8	88.3
175	15	3135	75.5	89.1
200	15	2893	66.1	89.4
225	15	2417	54.4	90.0
250	15	2670	59.9	89.4

CONCLUSIONS

The inhibited brain learning training method proved to be a very simple, effective and promising procedure for training artificial neural network. The procedure significantly increased the training speed of a large network. Furthermore, the tendency of a large artificial neural network to be over specific, hence have less generalizing capability, was avoided through reduced training time. The procedure generated a trained large network that can generalize and more accurate for satellite image classification.

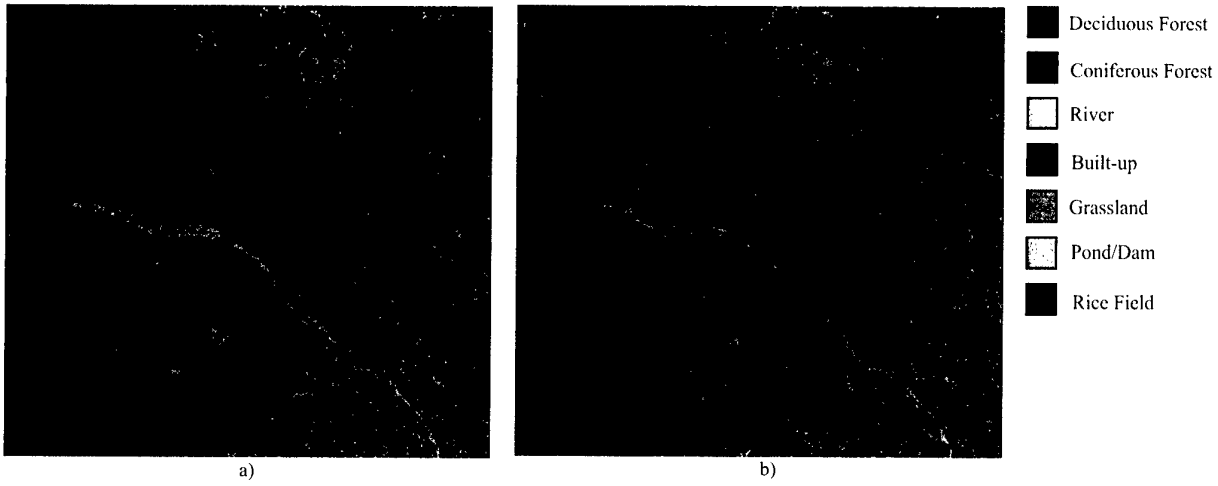


Figure 3. Classified satellite image using the trained ANN. Image ***a*** was generated using conventional training ANN method (control b) and image ***b*** using IBL with 225 % deviation and 15 % clamped connection limits, respectively.

REFERENCES

Atkinson, P.M., and Tatnall, A.R.L., 1997. Neural networks in remote sensing, International Journal of Remote Sensing, 18 (4), pp. 699-709.

Kanellopoulos, I., and Wilkinson, G.G., 1997. Strategies and best practice for neural network image classification, International Journal of Remote Sensing, 18 (4), pp. 711-725.

Karnin, E.D., 1990. A simple procedure for pruning back-propagation trained neural networks, IEEE Transactions on Neural Networks, 1, pp. 239-242.

Kavsoglu, T., and Mather, P.M., 1999. Pruning artificial neural networks: an example using land cover classification of multi-sensor images, International Journal of Remote Sensing, 20 (14), pp. 2787-2803.

Rumelhart, D.E., Hinton,G.E., and Williams, R.J., 1986. Learning internal representations by error propagation. In: Parallel Distributed Processing: Explorations in the Microstructure of Cognition, Volume 1: Foundations, edited by Rumelhart, D.E., McLelland, J.L., and the PDP Research Group (Cambridge, Massachusetts: MIT Press), pp. 318-362.

FLOODED AREA ASSESSMENT WITH FUSED MULTI-SPECTRAL MULTI-SENSOR BY USING TEXTURE FEATURE ANALYSIS AND NEURAL NETWORK CLASSIFICATION

Kobchai DEJHAN, Sompong WISETPHANICHKIJ,
Prasit KERDYOU, Fusak CHEEVASUVIT, Somsak MITATHA,
Chanchai PIENVIJARNPONG*, Chatcharin SOONYEEKAN**

Faculty of Engineering and Research Center for Communication and Information Technology,
King Mongkut's Institute of Technology Ladkrabang, Ladkrabang, Bangkok 10520, Thailand.
Tel : 66-2-3269967, 66-2-3269081, Fax : 66-2-3269086
E-mail : kobchai@telelan.telecom.kmitl.ac.th

* National Research Council of Thailand,
MOS-I Receiving Ground Station, Ladkrabang, Bangkok 10520, Thailand.

** Aeronautical Radio of Thailand,
102 Ngamduplee, Tungmahamek, Bangkok 10120, Thailand.

KEY WORDS: flood, multi-spectral, multi-sensor, texture feature, neural network

ABSTRACT: In recent tens year, there have exist significant natural environment changes, especially in a country covered by monsoon climate as a tropical area. The environmental management, planning and monitoring must be done to avoid a recurrent disaster. Multi-temporal images are used to detect the environment changing, while the multi-spectral images provide necessary information for land cover interpretation. To conveniently assess the flooded area, radar images act as the flood monitoring due to the properties of all weathers, day-and-night and capability of cloud-piercing. Therefore, multi-sensors of such images are merged to hold each superior characteristics by using image fusion technique, as shown in this paper. The classification and interpretation for flooded area identification of fused images based on the texture analysis and neural network classification. These comprehensive method shows the efficient investigation and assessment the unupdated area.

1. INTRODUCTION

There are several efforts to monitor and assess flood area. Especially, the monsoon regions are suddenly inundated by flash flood caused by the storm and others natural hazard. Several techniques have been applied to estimate the flood area. To investigate and identify the damage areas.

The radar image uses the back-scattering wave technique in the antenna direction gives two evidence results, discontinuity/roughness of the object surface and the object absorption depending on the moisture. Therefore, SAR images are efficiently flood detection. However, the classification and interpretation of SAR image are quite difficult with low precision because its mechanism is quite different from multi-spectral image. Texture feature analysis in section 2 shows comprehensive methodology to describe such data.

As the multi-spectral images provide necessary information for land cover interpretation. The fusion details of an effective exploiting the complimentary nature of these different data types, especially the SAR–optical image have the clearly different characteristics. Therefore, the dominant data addition of multi-spectral image into SAR image will make the data analysis to be comfortable and easy.



Figure 1 JERS-1 SAR image acquired on June 03,1997, Surat Thani province.

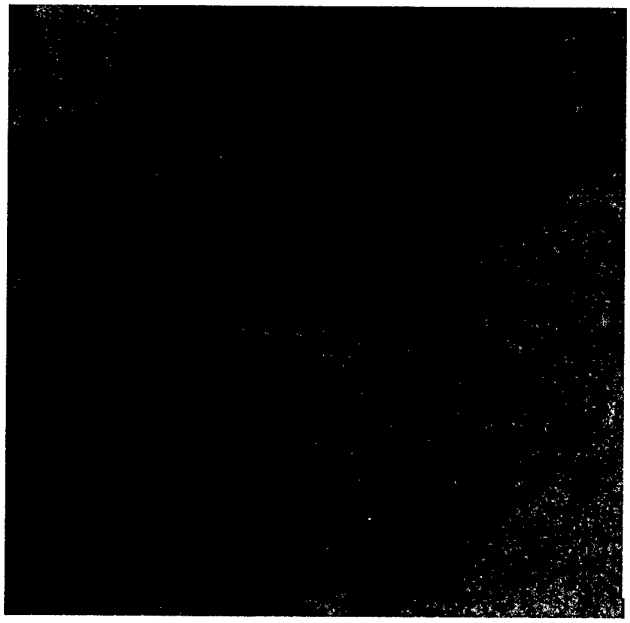


Figure 2 JERS-1 SAR image acquired on August 30,1997.

This paper have been adopted this technique to perform the flood area classification. The mixed data of SAR and OPS (optical sensor) obtained from JERS-1 satellite in the flood period of central area of Thailand as study region. This region is water hole with flooding. JERS-1 SAR data acquired on June 03, 1997 and August 30, 1997 were taken before and during flood hazard from the tropical storm Zita, in Surat Thani province, were used. Because of its cloud penetration capability as shown in Fig.1 and 2, respectively. Fusion these images with JERS-1 OPS data acquired on March 14, 1997 were performed to distinguish flood area. Using the wavelet decomposition based on low wavelet coefficient of SAR image is included with OPS image, the wave absorption from the object moisture is combined with the other physical data as mention in section 3.

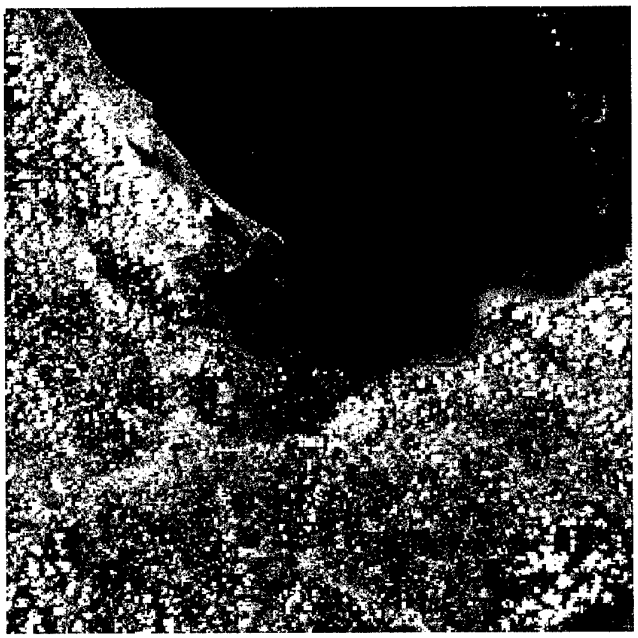


Figure 3 JERS-1 OPS data acquired on March 14,1997.

To study the flood assessment, the image classification is used as a revolutionary computing methodology known as the multi-layer perception (MLP) neural network based on the back propagation (BP) algorithm suitably for multi-spectral image as shown in section 4. The fused image and texture content are applied to this mechanism. Thus, the classification and analysis of flood area will be high resolution and high accuracy. The results and conclusion are presented in last section.

2. TEXTURE CONTENT

The textural information is assumed to be contained in the overall, or average, spatial relationship among gray levels for a particular image. Although no formal definition of texture exists, intuitively this descriptor provides the measures of properties, such as smoothness, coarseness and regularity. The three-principle approaches use to describe the texture context are statistical, structural and spectral. The statistical approaches use to be descriptor of spatial relationships and yield characterizations of textures as smooth, coarse, grainy, and so on. This spatial relation is considered to be the covariance of pixel values as a function of distance and direction between pixels. Such information can be extracted from an image using gray-tone spatial-dependence matrices or co-occurrence matrices (Wisetphanichkij, 1999). Let Z be a random variable denoting discrete image intensity, P be a position operator and let A be a k*k matrix whose element a_{ij} is the number of times that points with gray level z_i occur (in the position specified by P, relative to points with gray level z_j, with $1 \leq i, j \leq k$. The co-occurrence matrix (A) can be constructed as follow;

1. The numbers of different pixel values (z_i) are determined.
2. These pixel values are ranked (k) smallest to largest.
3. The digital image is scanned in the direction noted (P-operator) to determine the frequency with which one of these pixel values follows another.
4. Each entry in matrix (A) is divided by n, the number of pixels in the image satisfying P, let this resultant matrix be called co-occurrence matrix (C).

To analyze a co-occurrence matrix (C) in order to categorize the texture, the statistical parameters as a set of descriptors are computed as follows.

1. maximum probability,

$$\max_{i,j}(C_{ij}) \tag{1}$$

2. Second-order inverse element difference moment.

$$\sum_i \sum_j (i-j)^2 C_{ij} \tag{2}$$

3. Frist-order inverse element difference moment,

$$\sum_i \sum_j \frac{C_{ij}}{(i-j)^2} \tag{3}$$

4. Entropy

$$\sum_i \sum_j C_{ij} \log(C_{ij}) \tag{4}$$

5. Uniformity

$$\sum_i \sum_j C_{ij}^2 \tag{5}$$

3. IMAGE FUSION

The image fusion can be divided into two classes: spatial domain method and spectral domain method. The last method is used in most application, such as color space transformation. In this paper, the IHS (Intensity-Hue-Saturation) model will be used as a color space and the image fusion is done as follow:

1. The RGB color space of OPS image is transformed to the IHS model [3]:

$$I = \frac{R+G+B}{3} \tag{6}$$

$$S = 1 - \frac{3}{R+G+B}[\min(R,G,B)] \tag{7}$$

and

$$H = \cos^{-1}\left\{\frac{\frac{1}{2}[(R-G)+(R-B)]}{(R-G)^2+(R-B)(G-B)^2}\right\} \tag{8}$$

2. The different gray value of pixel in the black-white of two SAR images (g1 and g2) are added into the OPS image intensity:

$$I' = I + |g_1 - g_2| \tag{9}$$

The last term of the above equation is the different of before and during flood. The flood area will be emphasized and non-flood area will be depressed. Adding this term to intensity component in IHS mode means transferring of flood area data to OPS image.

3. The IHS model is inversely transformed to the RGB space and ready to classify in the further.

4. NEURAL NETWORK CLASSIFICATION

In this paper, the multi-layer perceptron (MLP) neural network based on back propagation (BP) algorithm is used as classifier, which consists of set of nodes arranged in multiple layers with connection only between node in adjacent layer by weights. The input informations are presented at input layer as the input vector. The output vector is the processed information, that are retrieved at the output layer. The hidden layers stand between these two-layers. A schematic of a three-layer MLP model is shown in Fig 4 and used in this paper.

In this work the nonlinear function, Sigmoid function given in Eq.(12), is used to determine the output state:

$$f(x_i) = \frac{1}{1+e^{-x_j}} \tag{12}$$

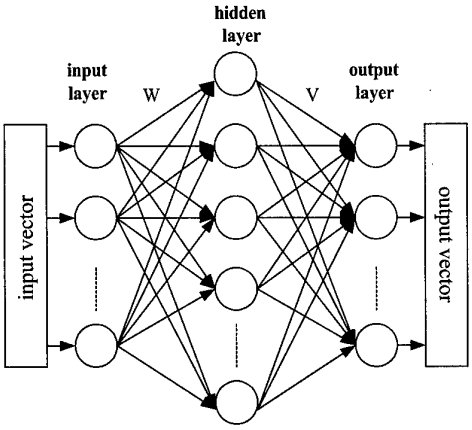


Figure 4 The 3 - layer (MLP) model of neural network.

5. METHODOLOGY AND RESULTS.

5.1 Method

Pre-processing/image preparation

- The SAR data obtains 16 bit and are reduced to 8 bits in order to obtain 256 values of intensity by using linear scaling.
- From wavelet decomposition [5], the low wavelet coefficient of SAR images will be used within two reasons, to remove the speckle noise and continue the proper data for applying to neural network training algorithm.
- The 12.5m x 12.5m resolution of SAR data were reduced to 25m x 25m in the same order of OPS resolution. All image should be registered and geometric corrected.

Texture content extraction

- Follow the instructions as in section 2 with P-operator "one pixel to the right and one pixel below", co-occurrence matrix can be constructed.
- Using statistical parameters, only second-order element difference moment and entropy as a set of descriptors to reduce input node of MLP neural network and save calculation time. The first descriptor represents the value of the variogram at a lag distance as a P-position operator that is applied to develop the co-occurrence matrix. The second descriptor is a measure of randomness, achieving its highest value while all elements of co-occurrence matrix are equal.

Images fusion and classification

- Data fusion technique as mentioned in section 3, is used as shown in Fig.5.
- After pre-processing satellite image prepares then applying to neural network classification. Two kind of texture content will be added in to two last input nodes of network to increase classification accuracy.

5.2 Results

Table 1. The result of flood assessment by neural network classification with data fusion.

Classification	Water	Cloud	Urban		Vegetation		Bare soil	
			Flood	Non-flood	Flood	Non-flood	Flood	Non-flood
Result/testing (pixel)	478/500	47/50	45/50	43/50	44/50	90/100	44/50	89/100
Correction %	95.6	94.0	90.0	86.0	88.0	90.0	88.0	89.0

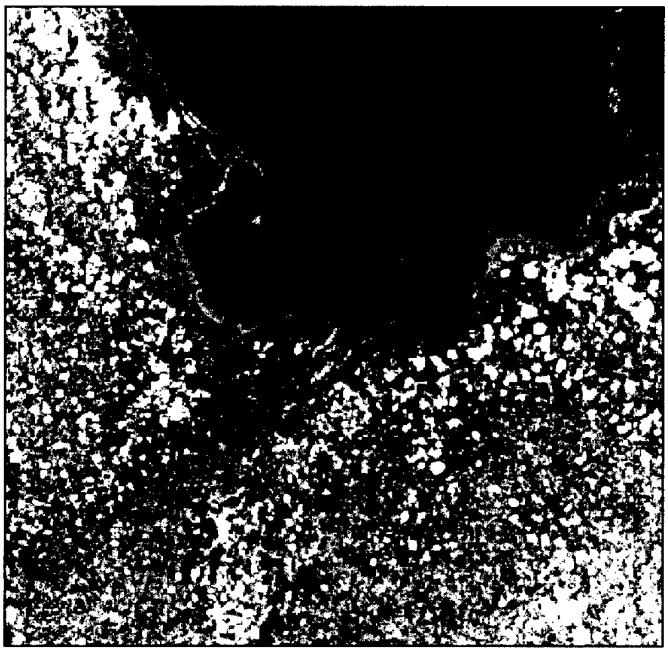


Figure 5 Fused image for flood area assessment.

6. CONCLUSION

As results, above method show effectiveness and efficiency of multi-temporal SAR data, which are very useful for flood assessment and monitoring. The SAR texture content helps us to identify a flood area. While as the OPS data provide the necessary information for land cover interpretation with the highly reliable result.

ACKNOWLEDGEMENT

The ground truth informations are kindly supported by Office of Agricultural Economics, Ministry of Agriculture, Royal Thai Government.

REFERENCES

Xiaomei, Y., and Chenghu, Z., 1998. Recognition of Flooded Area in Radar Image Using Texture Feature Analysis. Proc. of 19th Asian Conference on Remote Sensing (ACRS'98), Manila, Philipines, pp. P22-1 – P22-6.

Carr, J. R., 1998. The Semivariogram in Comparison to the Co-Occurrence Matrix for Classification of Image Texture. IEEE Trans. Geoscience and Remote Sensing, Vol.36, No.6, pp.1945-1952.

Wisetphanichkij, S., Dejhan, K., Cheevasuvit, F., Mitatha, S., Arungsrisangchai, I., Yimman, S., Pienvijarnpong, C., Soonyeekan, C. and Chanwutitum, J., 1999. A fusion approach of multispectral with SAR image for flood area analysis. Proc.of the 20th Asian Conference on Remote Sensing (ACRS'99), Hong Kong, China, pp.53-58.

Wisetphanichkij, S., Dejhan, K., Cheevasuvit, F., Mitatha, S., Netbut, C., Pienvijarnpong, C., Soonyeekan, C. and Chanwutitum, J., 1999. Multi-temporal cloud removing based on image fusion with additive wavelet decomposition Proc. of the 20th Asian Conference on Remote Sensing (ACRS'99), Hong Kong, China, pp.1109-1114.

ACCURACY IMPROVEMENT OF THE LAND COVER CLASSIFICATION BY USING TRUNCATED NORMAL DISTRIBUTION

Tsukasa Hosomura (Japan)
Professor, Department of Information and Arts
Tokyo Denki University
Ishizaka, Hatoyama-machi, Hiki-gun, Saitama , 350-0394
Tel: +81-492-96-2911, Fax: +81-492-96-5311,
E-mail: hosomura@ia.dendai.ac.jp
JAPAN

KEY WORDS: fused image, test site, verification

ABSTRACT: In this paper, in order to improve the classification accuracy training data screening and truncated normal distribution maximum likelihood classification are adopted. We verify these techniques are effective measures for the improvement in the classification accuracy.

1. Introduction

Generally classified result is changed by how to get the training data in the land cover classification using unsupervised algorithm. As the training data are extracted by the human interpretation, pixels including errors are extracted. Therefore, it becomes the classification accuracy lower. By removing the extracted pixels including errors, the classification accuracy will be improved. The normal distribution is assumed for the distribution of each class in the maximum likelihood classification. But actual distribution is different from normal distribution. The misclassification decreases by removing the tail of each class in which the misclassification seems to increase, and the classification accuracy will be improved. In this paper, in order to improve the classification accuracy training data screening and truncated normal distribution maximum likelihood classification are adopted. We verify these techniques are effective measures for the improvement in the classification accuracy. The distribution profile of training data is examined. Probability density function of each class is recalculated after removing the tail of each distribution. In other words, the distribution with large standard deviation converts into small distribution profile. Instead of the normal distribution in the case of maximum likelihood method, truncated normal distribution is used in truncated normal distribution maximum likelihood classification. Classification accuracy will be calculated by comparing test site data and classified result. As a result of the experiment, it is confirmed that screening of training data and truncated normal distribution maximum likelihood classification are effective measures for the classification accuracy improvement.

2. The screening of the training data

With the screening of the training data, the distribution profile of normalized training data is examined, and probability density function is recalculated after excluding the pixels, which cause misclassification. There are two methods for screening.

(1) The pixel was removed when pixel value exist in the tail of training data distribution at least one band.

(2) The pixel is removed when pixel value exist in the tail of training data distribution at all bands

3. Maximum likelihood classification using the truncated normal distribution

3.1 Outline of the truncated normal distribution

Truncated normal distribution is made from normal distribution by truncating the tail of the distribution. The probability distribution function of truncated normal distribution is defined in equation (3.2) using A(α) of following equation (3.1).

$$A(\alpha)=\int_{\mu-\alpha}^{\mu+\alpha}\frac{1}{\sqrt{2\pi}\sigma}e^{-\frac{(x-\mu)^2}{2\sigma^2}}dx \tag{3.1}$$

$$f(x,\alpha)=\begin{cases}\dfrac{1}{A(\alpha)}\cdot\dfrac{1}{\sqrt{2\pi}\sigma}e^{-\frac{(x-\mu)^2}{2\sigma^2}} \\ 0\end{cases} \tag{3.2}$$

In the maximum likelihood classification normal distribution is used for the distribution of the population of each class. Classification result differs by the distribution profile. Generally, a region of the class from mean value of each class is decided by standard deviation. The region of each class is decided by the coefficient of this standard deviation σ. The classification accuracy will be improved by removing the part of the tail of normal distribution in each class. The part of the tail is mixel region of the distribution profile, and the misclassification will be decreased. In other words, by accurately classifying the part of the tail, the improvement of the classification accuracy can be expected. The number of undiscriminant pixels increase, when the coefficient of σ is decreased. The number of undiscriminant pixels decrease, when the coefficient of σ is increased.

4. Experiments

Object image used in this study is fused image of panchromatic image of SPOT and 2,3,4 band of Landsat/TM. The classification was carried out in 50 classes, and each category was finally integrated to 7 classes, housing area, grassland, paddy field, coniferous forest, bare ground, water body and shadow.

4.1 Maximum likelihood classification using truncated normal distribution

The range of ($\mu - 2\sigma$, $\mu + 2\sigma$, μ: mean value, σ: standard deviation) in normal distribution contains about 95%. Normal distribution was truncated in this range. Truncated normal distribution was created.

4.2 Maximum likelihood classification by the screening of the training data

There are two following types for the screening of the training data

The pixel was removed when pixel value exist in the tail of training data distribution at least one band.

The pixel is removed when pixel value exist in the tail of training data distribution at all bands In this study, screening object is made to be the data in which the data does not come in within (μ-2σ, μ+2σ μ : Mean value σ : Standard deviation) in each class. Maximum likelihood classification was implemented by using screening and screening .

4.3 Maximum likelihood classification using the both methods

Classification accuracy using both methods of the maximum likelihood classification of the training data using screening and truncated normal distribution proposed in this paper.

5. Result

Standard classification accuracy must be prepared to confirm the improvement of classification accuracy. Multisensor fusion image of the Landsat/TM 3 bands and SPOT panchromatic image was used. The maximum likelihood classification result for this image is used as the standard classification accuracy. The classification result is shown in Table 1.

Table 1 Accuracy of classification result

Maximum likelihood classification	59.0%
Truncated normal distribution classification	75.1%
Screening	60.9%
Screening	62.7%
Classification accuracy using both methods	76.1%.

As a result of the experiment, classification using both methods obtained the highest classification accuracy compared with independently used method. And, there was seldom undiscriminant pixel. There was no category where the classification accuracy became 10% or less on the each classification category.

6. Conclusion

The screening of training data and maximum likelihood classification using truncated normal distribution, which are techniques of the classification accuracy improvement proposed in this paper, improve classification accuracy. Especially the latter is good method for reducing number of pixels in the undiscriminant class. It also improves the classification accuracy more. It is effective measures for the classification accuracy improvement. And the technique by using both methods improves classification accuracy evidently. In this paper, satellite image of 3 bands of the 30m resolutions was used as object image. If the object image is different from the image used in this experiment, obtained result will be changed. Therefore, we should verify another case, for example different sensor, different time, different resolution and so on.

SELF-ORGANIZING FEATURE MAP FOR MULTI-SPECTRAL SPOT LAND COVER CLASSIFICATION

Jen-Hon Luo, Lecturer and PH. D Candidate
Department of Electronic Engineering, Ming-Hsin Institute of Technology
1 Hsin-Hsing Road Hsin-Fong, Hsin-Chu, Taiwan
jhluo@ip.csie.ncu.edu.tw
(886) 3-4227151 ext. 7864
Din-Chang Tseng, Professor
Institute of Computer Science and Information Engineering,
National Central University, Chungli
TAIWAN

KEY WORDS: Texture, Self-Organizing Feature Map (SOFM), Learning Vector Quantization (LVQ) network, Land Cover Classification.

ABSTRACT: Most of the remote sensing images have the so-called texture patterns. This makes texture feature extraction and classification techniques play important roles in the remote sensing image processing. Traditional statistical classification methods suffer from the assumption that the probability distribution must be normal distribution in practice. Recently, many non-parametric neural networks have been successfully used in the field of remote sensing classification. We apply a new category classification method to SPOT scene land cover classification. This is a three-stage mechanism. First, use a spatial filter for multi-spectral feature extraction. Secondly, employ a supervised non-parametric self-organizing feature map (SOFM) for pattern similarity learning, then a Learning Vector Quantization (LVQ) network with the trained SOFM as its hidden layer is used to classify the land covers. From experimental results, we can see that the proposed method obtains superior results compared to traditional maximum likelihood (MLH) and other methods.

INTRODUCTION

With the growing number of remote sensing imagery and the extensive use of the geographic databases, there is a need to develop tools for efficient extraction of information, and intelligent search and manipulation of the image database. Therefore, the potential use of the accumulated images can be fully realized. The required techniques include feature extraction, segmentation, and classification. That most of the remote sensing senses have the so-called texture patterns makes texture feature extraction, segmentation, and classification techniques play pivotal roles in the field of remote sensing image processing.

The classification method consists of two types: supervised and unsupervised. The maximum likelihood (MLH) (Andrews, 1972) method has often been applied to

category classification of remote sensing data as the supervised classification method and has very good results in many applications. In practice, the discrimination function of MLH method works under the assumption that the probability distribution for each category is an n-dimensional normal distribution where n denotes the number of spectral bands. However, the probability distribution of real data for each category does not always follow a normal distribution that is essential to a conventional MLH method.

Therefore, a non-parametric classification method, neural networks, becomes important for real data processing. The network architectures and signal processes used to model neural systems can roughly be divided into three categories: feed-forward networks, feedback networks, and self-organizing networks.

1. Feed-forward networks transform sets of input signals into sets of output signals. The desired input output transformation is usually determined by external, supervised adjustment of the system parameters.
2. In feedback networks, the output information defines the initial activity state of a feedback system, and after state transitions the asymptote final state is identified as the outcome of the computation.
3. In the third category, neighboring cells in a neural network compare in their activities by means of mutual lateral interactions, and develop adaptively into specific detectors of different signal patterns. In this category, learning is called competitive, unsupervised, or self-organizing map.

In this article, a window mask is used to extract texture pattern features, and a self-organizing feature maps (SOFM) is proposed to learn the pattern similarity in the feature space, then a Learning Vector Quantization (LVQ) network with the trained SOFM as its hidden layer is used to classified the test images.

SELF-ORGANIZING FEATURE MAP (SOFM)

SOFM based on competitive learning is a topology-preserving map (Kohonen, 1982, 84), and can be adjusted to approach the probability distribution of the inputs (Zheng, 1996). In a topology-preserving map, neurons located physically next to each other will respond to input vectors of classes that are likewise next to each other. By this method, large-dimensional input vectors can project down on the two-dimensional map in a way that still maintains the natural order of the input vectors.

1. The SOFM Learning Algorithm

During the training period, each neuron with a positive activity within the

neighborhood of the winning neuron participates in the learning process. A winning processing element is determined for each input vector based on the similarity between the input vector and the weight vector.

Let us denote the input vector, X, as follow:

$$X = [x_1, x_2, ..., x_p]^T \tag{1}$$

The weight vector, W_j, corresponding to output layer neuron j can be written:

$$W_j = [w_{j1}, w_{j2}, ..., w_{jp}]^T \quad j = 1, 2, \ldots, N \tag{2}$$

The winning neuron can be determined by

$$c = \arg\min_i \{\|X - W_i\|\} \tag{3}$$

, the index c refers to the winning neuron.

If c is the winning neuron, $N_c(t)$ is the list of neuron indices that make up the neighborhood. $N_c(t)$ is a decreasing function of discrete time (i.e., iteration). It means the size of the neighborhood is decreased as training iterations go on. Then, the weight-update equations are:

$$W_i(t+1) = \begin{cases} W_i(t) + \alpha(t)(X - W_i(t)), & i \in N_c(t) \\ W_i(t), & i \notin N_c(t) \end{cases} \tag{4}$$

In the relaxation process, the so-called learning-rate factor, $\alpha(t)$, has a very central role. It can be liner, exponential, or inversely proportional to t. For convergence it is necessary that $\alpha(t) \to 0$ when $t \to \infty$. For instance, $\alpha(t) = 0.9(1 - t/1000)$ may be a reasonable choice.

EXPERIMENTS AND RESULTS

The study site, Tung-shih farm, is located at E/N (159000, 2602950) as left up corner, and (164000,2597950) as right down corner. It is an experimental farm belonging to Taiwan Sugar Corporation. The 3-band (G, R, and IR) SPOT image over the study area was received on 1994, at the receiving station of the Center for Space and remote Sensing research at the NCU campus and was further processed to produce a geocoded image on a 2° TM coordinate system. Fig. 1(a) shows the pseudo color image (composed by SPOT XS3, XS2, and XS1 as R, G, and B.) of the size 400 x 400 pixels of the test site covering approximately 5km x 5km. The field is divided into 400 meters by 100 meters square blocks. As an experimental farm, it maintains complete records for land truth reference. These two reasons make the farm an ideal

place for image processing test site.

We take the three bands value of each pixel (*xs1, xs2, xs3*) as the spectral feature vector of each pixel, and $(\mu_d(i,j), \delta_d(i,j), \beta_d(i,j))$ as the spatial feature vector of pixel $p(i,j)$ where $\mu_d(i,j)$ is the mean, $\delta_d(i,j)$ is the standard deviation, and $\beta_d(i,j)$ is the difference between the maximum and minimum values of the pixels in a window of size $2d+1$ and centered at (i, j).

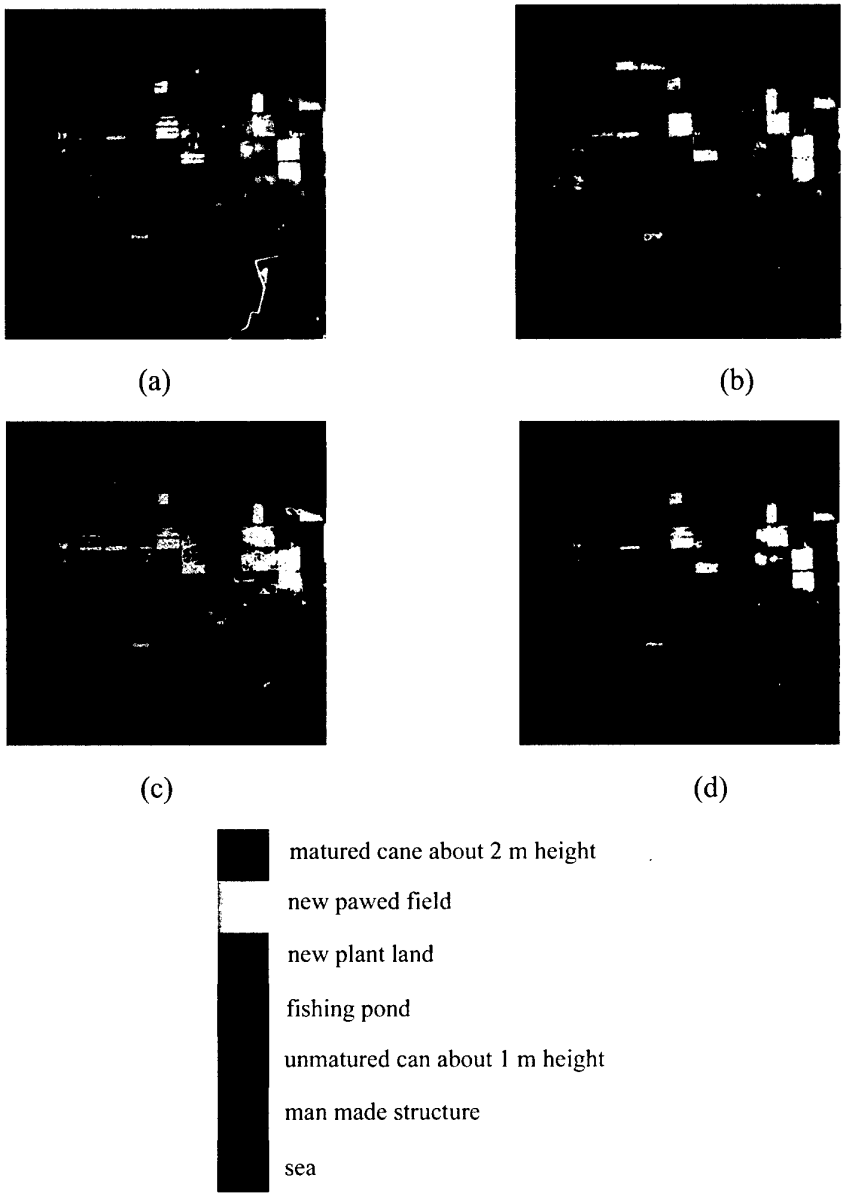


Fig. 1(a) SPOT pseudo color image (copyright@CNES 1996), (b) MLC classified image using spectral information only, (c) MLC classified image using (μ,σ,β) spatial information, (d) SOM classified image using (μ,σ,β) spatial information, and (e) the color coding map for classification results.

Fig. 3(b) is the classified image of (a) by MLC method uses spectral information as feature vectors, Fig. 3(c) is the classified image of (a) by MLC method uses spatial information as feature vectors, and Fig. 3(d) is the classified image of (a) by SOFM method uses spatial information as feature vectors. Fig. 3(e) is the color coding map for classification results.

Table 1. MLC classification matrix uses spectral features only, table 2. MLC classification matrix uses spatial features, and table 3. SOM classification matrix uses spatial features.

Table 1 MLC classification matrix using spectral features.

Class	1	2	3	4	5	6	7	Producer's purity (%)
1	2312	2	23	0	163	0	0	92.5
2	16	2141	6	0	282	55	0	85.6
3	30	10	2116	0	309	35	0	84.6
4	50	0	59	2070	0	0	321	82.8
5	302	214	405	0	1503	76	0	60.1
6	0	24	115	0	87	2274	0	91
7	6	0	18	37	0	0	2439	97.6
User's purity (%)	85.1	89.5	77.2	98.2	64.2	93.2	88.4	

Overall purity=84.9%, K coefficient=0.824

Table 2 MLC classification matrix using spatial features.

Class	1	2	3	4	5	6	7	Producer's purity (%)
1	2322	0	0	0	178	0	0	92.9
2	0	2347	0	0	138	15	0	93.9
3	6	0	1760	0	662	73	5	74.4
4	64	0	3	2366	41	0	26	94.6
5	63	2	176	0	2254	5	0	90.1
6	0	68	37	0	132	2263	0	90.5
7	49	0	24	0	75	0	2352	94.1
User's purity (%)	93	97.1	88.3	100	64.8	96.1	98.7	

Overall purity=90%, K coefficient=0.88

Table 3 SOM classification matrix using spatial features.

Class	1	2	3	4	5	6	7	Producer's purity (%)
1	2348	0	0	0	152	0	0	93.9
2	8	2408	25	0	59	0	0	96.3
3	18	0	2361	0	121	0	0	94.4
4	75	0	21	2378	3	0	23	95.1
5	75	3	215	0	2207	0	0	88.3
6	3	47	110	0	45	2295	0	91.8
7	148	0	34	0	0	0	2310	92.4
User's purity (%)	87.8	98	85.4	99.7	85.3	100	99.0	

Overall purity=93.2%, K coefficient=0.921

CONCLUSIONS

A large variety of back-propagation methods are used to train the networks. The convergence of a learning process is sensitive to the selection of a training data set, and the learning method often requires a large number of iterations and much computational time. The method is a black box approach that is difficult to give physical meaning to weights connecting the neurons. The utility of the SOFM lies mainly in its fairly rapid convergence, it can capture the probability distribution of the inputs, and it is easy to interpret. From the experiments, it gets pretty good results compared to other methods.

REFERENCE

Andrews, H. C., 1972. Introduction to Mathematical Techniques in Pattern Recognition. Wiley, N. Y.

Kohonen, T., 1982. Self-organized formation of topologically correct feature maps. Biol. Cybern., vol. 43, pp. 59-69.

Kohonen, Teuvo, 1984. Self-Organization and Associative Memory. volume 8 of Springer Series in Information Sciences, Springer, New York, pp. 184-189.

Zheng,Yi and Greenleaf, James F, 1996. The effect of concave and convex weight adjustments on self-organizing Maps. IEEE Trans. Neural Networks, vol. 7, no. 1, pp. 87-96.

DEVELOPMENT OF DATA SET FOR ANALYSIS OF LANDSAT TM IMAGES USING WWW BROWSER AND SPREADSHEET

Kiyotada SATO
Ichinoseki National College of Technology
Takanashi,Hagisyo,Ichinoseki-shi,Iwate
021-8511,JAPAN
Tel:(81)-191-24-4738 Fax: (81) -191-24-2146
satok@ichinoseki.ac.jp

Ryuzo YOKOYAMA
Iwate University
Ueda 4-3-5,Morioka,Iwate
020-8511,JAPAN
Tel:(81)-19-621-6478 Fax: (81) –19-621-1170
Yokoyama@cis.iwate-u.ac.jp

KEYWORDS: Remote sensing education, WWW browser, Spreadsheet, VBA macros

ABSTRACT: We have developed a data set for education of Landsat TM images using WWW browser and spreadsheet. The data set includes images for display and CSV numerical data for calculation. The CSV data are calculated using Microsoft EXCEL spreadsheet. The result can be displayed as a thematic map with VBA macros. All of the data set has created automatically using UNIX shell.

1. INTRODUCTION

Recently, variety satellite imageries and digital maps have been available. However, those data are not necessarily used actively for education purpose. One of the reasons, there is no adequate data set and calculation techniques using personal computer. Therefore we developed a data set for education of remote sensing image analysis. The data set includes image and numerical data of TM, topographical map and vegetation map. The images are displayed with WWW browser online or offline. Some of the images are converted to Comma-Separated Values (CSV) numerical format data. The CSV data are calculated with Microsoft EXCEL spreadsheet. The result of the calculation can be displayed as a thematic map using Microsoft EXCEL Visual Basic for Applications (VBA) macros developed by us.

The data set require preliminary operation skills of a WWW browser and a spreadsheet. In the near future, the skills will be taught at any school. The data set using WWW browser and spreadsheet will be appropriate style for remote sensing education.

2. IMAGE DATA AND ITS DISPLAY

2.1 Image data

All images in the data set are made in JPEG format for full color display by any WWW browser. The images are geometrically corrected and projected by UTM and 30m resolution (Iikura, 1998). There are 17 images, those are

1) Landsat TM images:
   Band 1,2,3,4,5 and 7 images
   Natural colored image (Band 3=Red, 2=Green, 1=Blue)
   Pseudo colored image (Band 4= Red, 5=Green, 6=Blue)
2) Topographical maps:
   Digital elevation model (DEM)
   Slope angle map calculated by DEM
   Aspect angle map calculated by DEM
   Sunlight incidence angle map calculated by above data and incidence and zenith angle
   1:50000 geographical map
3) Vegetation maps:
   Vegetation map edited by Japan Environmental Agency
   Land cover map made from above vegetation map
   Automatic classification land cover map

In the vegetation maps, The land cover map (7-merged vegetation map) is made from the vegetation map which merge into grass, conifer leaf forest, broadleaf forest, paddy, town, water and unclassified. The automatic classification land cover map (ACAI) is made from cluster image by ISODATA unsupervised classification to get maximum value of a classification accuracy (Sato, 1999). We suppose the map shows detailed land covers.

2.2 Link structure of the images

There are three types of the image size for browsing. We call those images "Layer1", "Layer2" and "Layer3". Fig.1 shows link structure of the images.

Layer1 shows a wide area image of Iwate prefecture of Japan, where longitude is from 141 to 141.996 and latitude is from 38.823 to 39.833. Layer1 image use only assignment to Layer2 area by WWW browser.

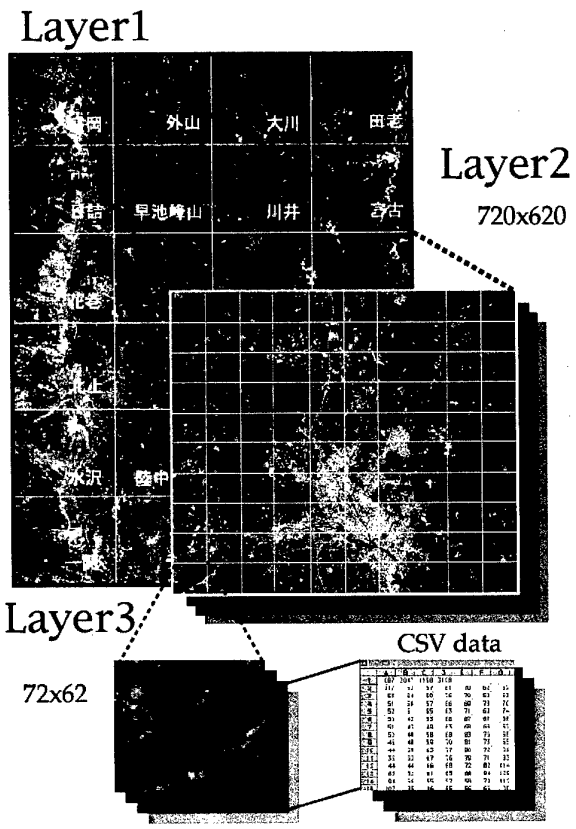


Fig.1 Link structure of the images

There are 17 Layer2 images in the data set. The image size of the Layer2 is 720x620 pixel. The size and location coincide with 1:50000 geographical map issued by the Geographical Survey Institute of Japan. Each of Layer2 images is divided into 10x10 grid for assignment Layer3 image using WWW browser. The size of Layer3 images is 72x62 pixel. The images are icons for WWW browser. A selection of the image will start of loading the corresponding CVS data.
The Layer2 and Layer3 images have statistics data, minimum, maximum, mean and standard deviation. The Layer3 statistics data are displayed besides the images as Figure.2.

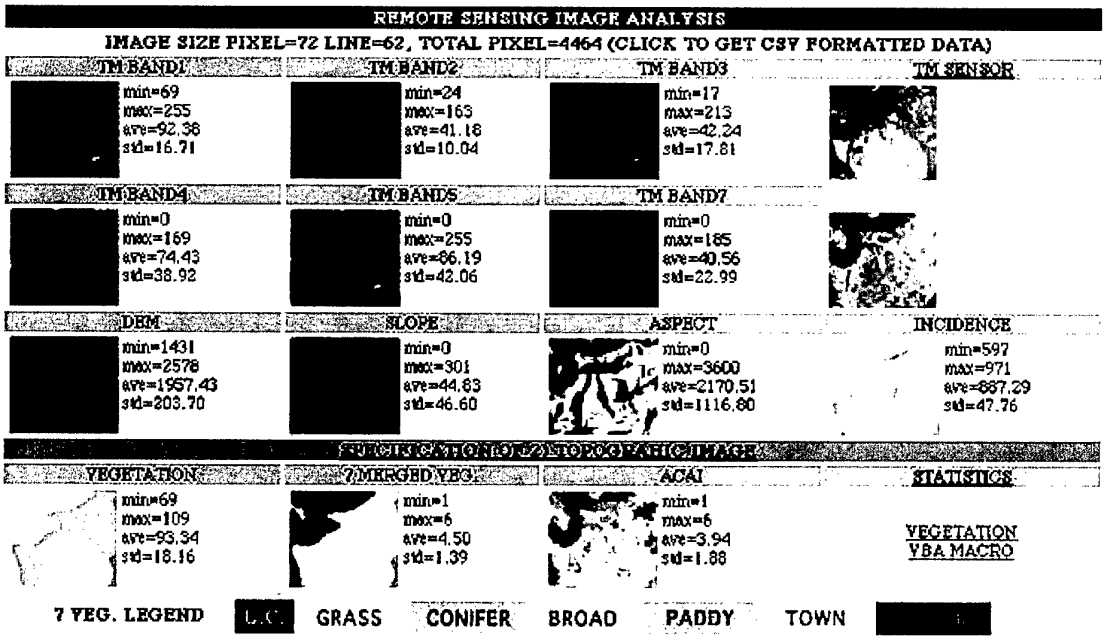


Fig.2 Layer3 images using WWW browser

3. CSV DATA AND ITS CALCULATION

3.1 Numerical value of the data set

There are two types of the CSV data. Those are

1) 1 byte length integer

TM band 1,2,3,4,5 and 7

Vegetation map,7-merged vegetation map and Automatic classification land cover map

2) 2 bytes length integer (multiplied by 10)

DEM with 0.1m resolution

Slope angle map, Aspect angle map, Sunlight incidence angle map with 0.1degree resolution

These CSV data will be read by Microsoft EXCEL automatically, and displayed the numerical values on the spreadsheet if the WWW browser setup so.

3.2 VBA macros

The CVS data on the spreadsheet will display or calculate using Microsoft EXCEL. The result of the calculation can be displayed as a thematic map using VBA macros. Table1 shows the VBA macro names and their operations.

Table 1 VBA macro operation for image display

MACRO NAME	OPERATION
Shift right	Insert two columns at left side of Layer3 data
Legend set	Setup two values and paint colors for conditional formatting
Paint	Conditional formatting of cell colors
Minimum size	Reduction image size to minimum of cells
Recover size	Normal cell size recover
Half size	Reduction image size to half of normal
Shift left	Delete setup values and colors area

In order to display of thematic map, macros sequence as follows.

1) The CVS data on the spreadsheet will be right shifted by execution of "Shift right" macro.
2) "Legend set" macro will setup legend colors and initial values, minimum, average and maximum value of the CVS data. These initial values and legend colors can change.
3) "Paint" macro will color paint to the CVS data area according to the setup values. The macro will be colored quickly by conditional formatting operation. If setup values are outside of the CVS data, the cell color will be white.
4) "Minimum size" macro will show a reduction size image. Fig.3 shows an example of the minimum size image display.
5) "Recover size" macro will recover cell size at the loading CSV data, and "Half size" macro will display at half size of the image.

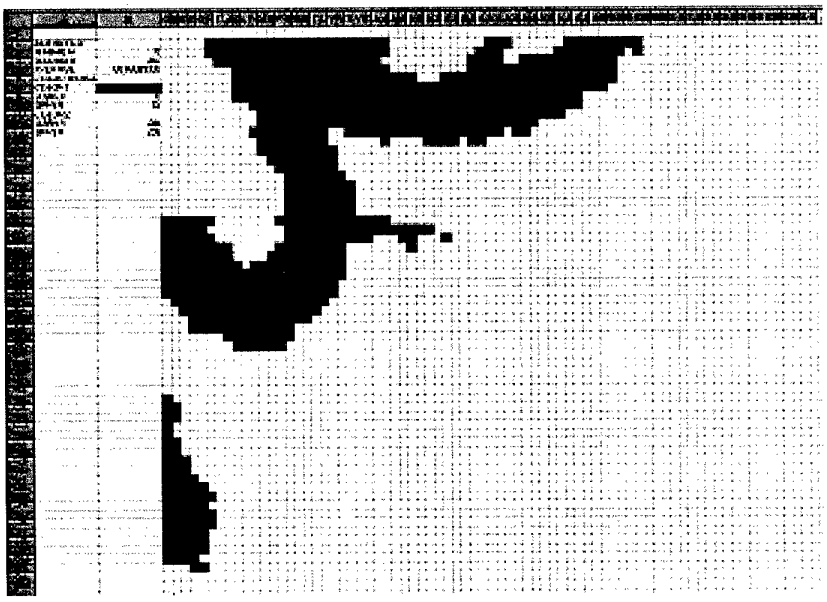


Fig.3 Image display by VBA macro function

4. CREATE OF THE DATA SET

The data set is created automatically using a UNIX shell command. The command readout data from the geometrical corrected 4350 x 6800 pixel image of TM, topographical maps and vegetation maps. All of the images are converted to JPEG format, all of the texts are written by HTML format. All of the Layer2 images are drawn grid line. Then make a hundred subdirectories to save of Layer3 data. Each of the Layer3 subdirectory includes 16 images, 13 CSV data, and some text files. All of a Layer2 data set will creates less then 25 minutes using the HP 9000/C240.

5. CONCLUSION

We developed data sets of useful for remote sensing education. The data set has been using at a college and others. However, the data set does not assist a guide of elementary knowledge for remote sensing. An explanation of this guide is necessary for practical use of the data set.
Internet WWW browser and Microsoft EXCEL have been utilized by many people. In order to promote of remote sensing education, the tools can not ignore. This paper showed useful data set using the tools.

REFERENCES

Iikura, Y., Yokoyama, Y., 1998, Ortho-rectification of Landsat TM imagery and its evaluation. Journal of the Japan Society of Photogrammetry and Remote Sensing, Vol.37, No.4, pp. 12-22

Sato, K., Iikura, Y. and Yokoyama, R., 1999,Automatic category assignment of satellite images using vegetation map. Journal of Remote Sensing Society of Japan, Vol.19 No.4,pp. 40-48

" Survey Department of Nepal : today and tomorrow "

Krishna Raj Adhikary
Survey Department
Nepal

Abstract

Survey Department of Nepal is a government agency under the Ministry of Land Reform and Management. Originating from 1957, the mission of Survey Department is to give support for creating and efficient and sustainable use of Land Information including maps and related product documents. Changing in society and changing in technology affects us all, we need to anticipate and plan for change in the needs of those who depend upon our land information, maps with related product document and services. To meet the user needs, attempts have been made to have resources for development of new products and services by introducing the new technology like GPS and digital system in some of the surveying and mapping activities including Geographical/Land information system.

1. Twenty five years in retrospective

Understanding change in surveying and mapping activities requires interpretation of the present in terms of the past. Knowing change in the past will prepare us for the future.

In Nepal, the history of surveying and mapping activities excluding cadastral survey is not so long. Surveying and mapping activities up to 1970's AD was mainly concentrated on the preparation of cadastral maps and related documents. They are prepared as an island map without the use of national geodetic controls. The purpose of preparing total land holding and the collection of revenue according to the types and areas of the holdings.

The Geodetic Survey and Topographical Survey in Nepal was established during 1970's. The initiation to define the spheroid with projection system and the national datum of the country was taken during those period. Earlier the system of map projection and preparation of topographical maps were all done with the help of Survey of India through Colombo Plan agreement. The ground control system were prepared by extrapolating the trigonometric control network system of India and adjacent countries.

Survey Department was established, as a department status of the His Majesty's Government of Nepal, on 1975 AD. Topographical Survey, Geodetic Survey, Cadastral Survey and Survey Training Centre are the main branches of the department. Looking at the state of surveying and mapping, aviaries function were carried out by the different branches of the Department during past twenty five years.

What are the major changes on the field of surveying and mapping activities during past twenty five years of time ? There are a number of specific development which are changing the faces of Survey Department.

* **Cadastral Survey :**

- Establishment of napigoswara and preparation of cadastral maps/documents in national level 1964 AD.
- Completion of a series of cadastral maps of cultivated areas for all the seventy five district of Nepal.

* **Geodetic Survey :**

- Establishment of Geodetic survey 1971 AD.
- Establishment of higher and lower order national Geodetic control network.
- Establishment of lower order national levelling net work.
- Establishment of observatory tower, base stations, gravity station and laplace station.

* **Survey Training :**

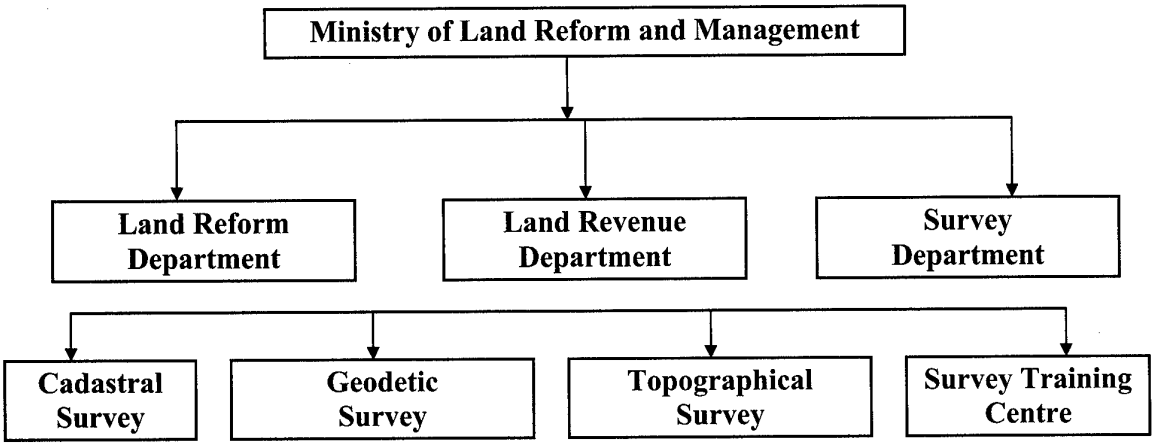
- Establishment of Survey training centre 1969 AD.
- Production of different level of survey technicians (Basic, junior and supervisory level).
- Updating knowledge on surveying and mapping techniques for working surveyors by refresher courses on various subjects.

* **Topographic Survey :**

- Establishment of topographical survey 1976 AD.
- Establishment of aerial survey lab, installation of photogrammetry, cartography and printing equipments.
- Preparation of aerial photos of whole kingdom of Nepal (1979 and 1992 AD) at 1:50,000 scale.
- Preparation of Land use maps (at 1:50000 scale) and subsequent report of whole kingdom of Nepal 1980 AD.
- Preparation of topographic base maps (1:25000 and 1:50000 scale) of whole kingdom of Nepal except some portion of north western region of Nepal.
- Preparation of Nepal China International boundary maps (1979 AD).
- Preparation of large scale maps of specific regions of the country.

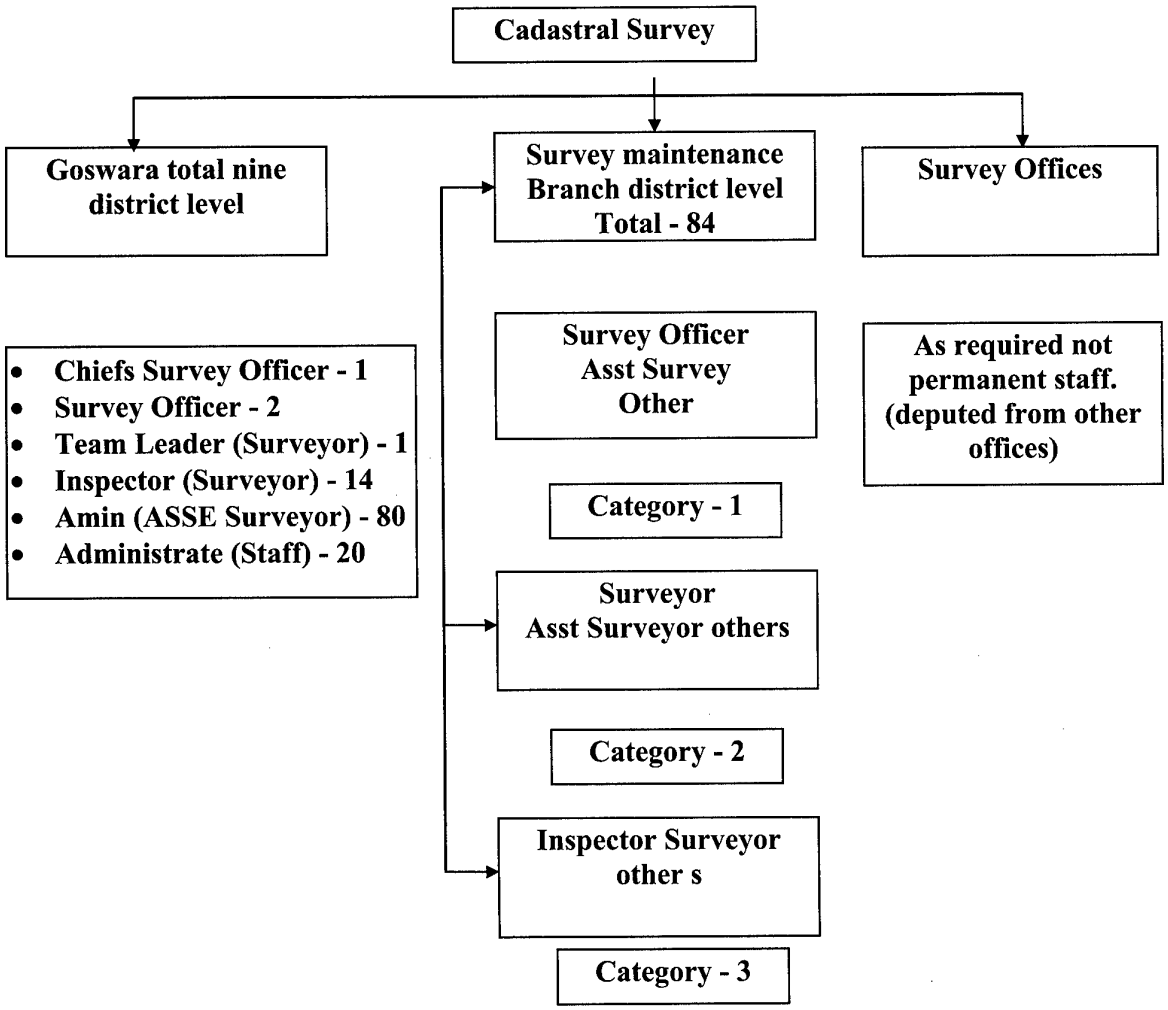
2. Organisational structure

The survey department is one of the three departments of the ministry of Land Reform and Management.

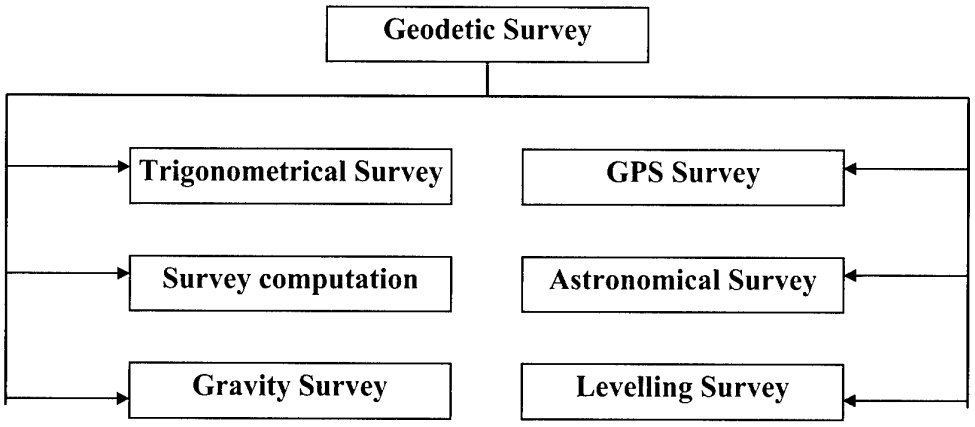


Survey department has four different branches. The activities of the department are :

- Establishment of national network of horizontal and vertical control points.
- Prepare and update topographic base maps and other types of maps.
- Prepare and update topographic base maps and other types of maps.
- Human resource development in the field of surveying and mapping.
- To conduct and monitor the surveying and mapping activities of the country.

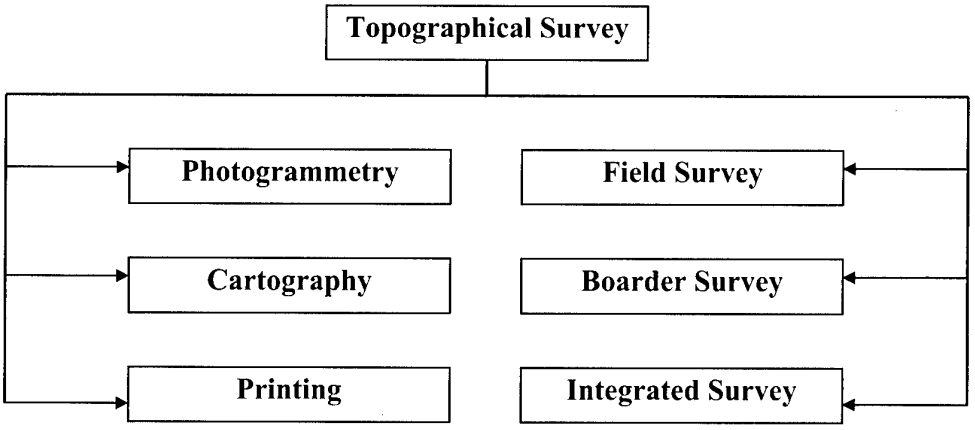


Geodetic Survey Branch of Survey Department has different sub-branches e.g. Trigonometrical gravity, GPS, Astronomical, Levelling and Survey Computation.

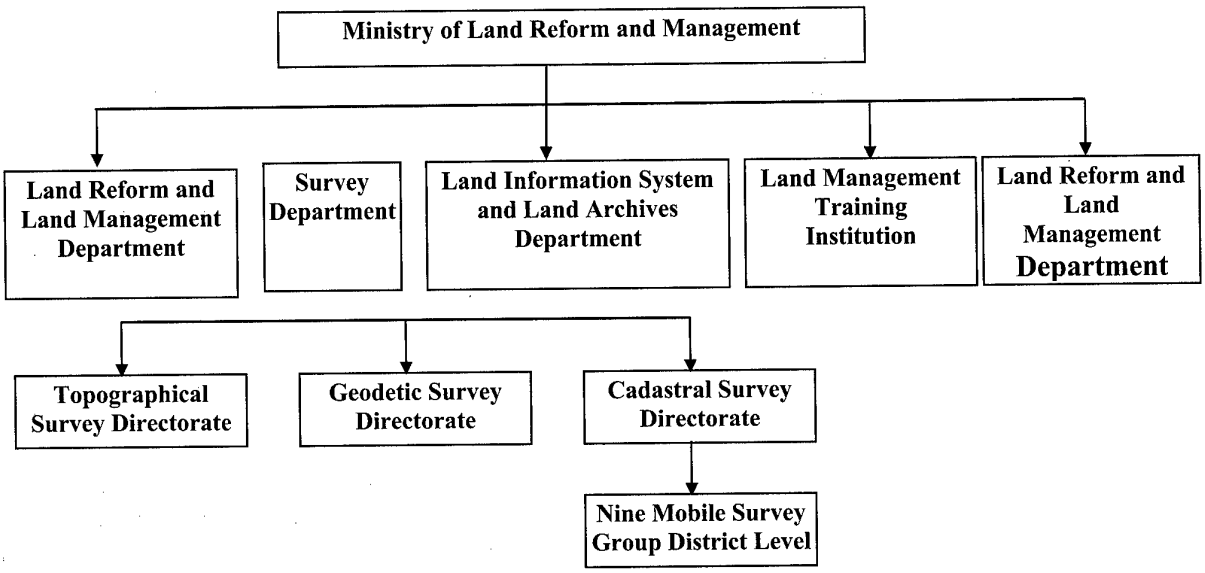


Similarly, topographical survey has the following sub-branches

Photogrammetry, Field survey, Cartography, Printing, Boarder survey, and Integrated survey.



Recently, His Majesty's Government has initiated to have an organisational restructuring an efficient and effective organisation. The proposed organisation of the ministry is :



The proposal is to merge survey maintenance offices of Survey Department and district Land Revenue offices in one office. Survey Training Centre will act as Land Management Training Institution under the Ministry with the departmental status.

Land information system and Land archives department will newly be established in order to have an integrated Land information system with central level archived. The name of the Land revenue department will be changed as Land reform and Land management department after merging Land reform department into Land revenue department.

3. Technical development

Today surveyors are familiar with a new generation of surveying equipment and techniques. Traditional system of surveying and mapping has been replaced to semi-modern or modern techniques who can be characterised as "black box technology"

Giving results in real time and in digital form. Many of the surveying activities including field operation have been using "Push of Bottom" System with limited use of knowledge and experiences of the survey professionals. This technical evolution in our profession has influenced the instrumentation and techniques used in surveying and mapping. In Nepal, plane table surveying for cadastral survey is still popular. More than 2000 surveyors are still working on this technology. However, topographical surveying is carried out using aerial photos with photogrammetric analogue plotter and Geodetic surveying is still using triangulation traversing by theodolite and distance meter. Higher order geodetic controls and precision levelling works is carried out by precise theodolite and levels.

Attempts, to automate and make the surveying and mapping process more efficient, have also been going on for considerable time e.g. the use of digital mapping on cadastral, GPS methods for control points determination and use of computers for geographic land information system etc.

GPS methods for control points

Global positioning system (GPS) was used in the production of topographical base map on the Eastern Nepal Topographical base maps at 1:25 000 scale in the plane and 1:50 000 scale at the mountain. The aerial photography was taken with the help of kinematics GPS techniques in order to have the minimum control for the aerial triangulation singular on an unaccusable Himalayas part of the country. Similarly, the same method was used for the Western Nepal Topographical Mapping Project.

The extension of ground control for large scale cadastral maps is also carried out by GPS methods.

National topographic data base

The utilisation of digital geographic information has been growing fast in all sectors of the society of the world. Also, in Nepal this has given a great influence to the different organisations as well as in some of the sector of society. Recently, survey department has already prepared the specifications for geographic information service and national topographic data base in order to ensure the homogeneous quality and availability of needed geographic information with this national data base standard. Survey department runs its digital mapping applications on environment. Survey department is utilising cadcore/Tracer software for on-screen vectorsing and ARC/ Info as their editing and map use software. ARC/Info data base is used as data storage format. Digital geographic information is also used in producing graphic maps. The objective of the product specification is to ensure the sufficient information content for the user and the specification for topographic maps in scale 1:25 000 and 1:50 000 are aiming to fulfil the needs of users, as most updated maps of most of the regions of the country is easily available.

Reference

- Specification for Geographic Information Service and National Topographic Database Survey Department, June, 1999.

- National Mapping Issues and Strategies
  Survey Department, July, 2000

- Introduction to Survey Department
  A Report

The 21st Asian Conference on Remote Sensing
December 4-8, 2000 Taipei, TAIWAN

TELLING STORIES OF JIN-SHAN-MIANN ADJACENT TO HSINCHU SCIENCE-BASED INDUSTRIAL PARK ON A SIMULATED ROCSAT-2 IMAGE

Ku-Yu Chang
National Chu-Pei High School,
Hsinchu, Taiwan

Chih-Li Chang
Senior Researcher, National Space Program Office
8F, 9 Prosperity 1st Road Science-Based Industrial Park
Hsinchu, Taiwan, 300
Tel: 886-3-5784208 ext. 8461, Fax: 886-3-5799972
Email: CLChang@nspo.gov.tw

KEY WORDS: ROCSAT-2, Space Image Simulation, Jin-Shan-Miann, Hsinchu Science-Based Industrial Park (SBIP)

ABSTRACT: Space images started civil uses since Landsat satellite was launched in 1972 and were mostly utilized by government agents. The civil uses were soon expanded to many fields of science, engineering and education; nevertheless personal use of the space image is the goal of the application for the remote sensing satellite. The paper describes a study of combining a space image and the stories of the spots on the image. Part of the paper was the result of the assignment of the history course. It demonstrates an excellent personal use of the space image.

The authors live in an area called Jin-Shan-Miann (JSM) adjacent to Hsinchu Science-Based Industrial Park (SBIP). The SBIP, nicknamed Taiwan's "Silicon Valley", is famous with semiconductor, PC computer, and related high-tech industries. Many famous worldwide companies are located there, such as, Taiwan Semiconductor Manufacturing Company (TSMC) and Acer Inc. On the other hand, the JSM was bright in the past but is faded now. The authors collected the stories and the image of the spots of JSM and tried to connect the old history and true spots with a simulated ROCSAT-2 image. The five stories were collected about JSM including Jin-Shan Temple, Kang-Lun Temple, Cool Water Stream, Huangs' House, and the oldest tree of Hsinchu City. The area of interest was selected and cut out from an air-borne image. The resolution is re-sampled in two-meter to generate an ROCSAT-2 image that will be available in late 2003. Furthermore, the simulated image was value-added with overlapping, marking and annotating. Since the space image provides plenty of information of the spots and the connections between those. It is then an excellent medium in the near future for students or the public to recognize and familiarize the area where he or she lives.

1. INTRODUCTION

Space images started civil uses since Landsat satellite was launched in 1972 and were mostly utilized by government agents. The space images take advantages of continuous archive of long history, global coverage, latest timing, and wide size. The civil uses were soon expanded to many fields of science, engineering and education; nevertheless personal use of the space image is the goal of the application for the remote sensing satellite.

Taiwan started the applications of the space image since 1974 and receiving space images from space in 1994. For educational applications in Taiwan, some SPOT images were collected to introduce the landscapes of Taiwan by professors and journalists (Wang 1998c). A junior high school teacher used SPOT images as supplementary materials in her earth science class (Kueng, 1998c). The user community grew up very fast over the recent years. Consequently, National Space Program Office, the official space organization of Taiwan, proposed a space imaging satellite in 1997. A pilot project, called

"Investigation on the Requirements and Applications of Remote Sensing Satellite", was carried on during September 1997 and February 1998 (ERL/ITRI 1998a). The requirements were surveyed among the local users for the first baseline of user needs. After intensive discussion, the system requirements were finalized and filed in the Request for Proposal for an open bid. Matra Marconi Space (Astrium) won the spacecraft, a satellite without the science payload, in 1999 after bid competition. The satellite development passed the system design review in March 2000 and preliminary design review in June 2000. The satellite is scheduled to launch in 2003. The main characteristics of the satellite are as shown in Table 1.

	Panchromatic	**Multispectral**
Mission		
Altitude	891 km	
Spectral Bands	One Panchromatic Band	Four bands: B1, B2, B3, B4
GSD	2 m @ Nadir	8m @ Nadir
Swath width	24 km @ Nadir	
Registration	After on-ground processing	
SL pointing capability	Roll & Pitch +/- 45°	
Optical Sub-Assembly		
Focal length	2896 mm	
Pupil Diameter	600 mm - F/N = 4.83	
Type	Cassegrain type with refractive Corrector	
Focal Plane Assembly		
CCD	TH 7834	THX 31547 Quad-linear CCD
Integration Time	0.308 ms	1.232 ms
Processing rate	10 Mpixels/s	5 Mpixels/s
Data Processing		
Pixel encoding	12 bits (*)	12 bits (*)
Compression ratio	2.8 & 3.8	1.7 & 3.8

(*) 8 bits are selected after encoding.

Table 1: Some specifications of ROCSAT-2 remote sensing satellite in the preliminary design phase (Astrium, 2000a)

2. JIN-SHAN-MIANN

The Jin-Shan-Miann area is a community area rather than an administrative area. The Jin-Shan Temple is in the center of the area. It includes a big part of the present Hsinchu City and Hsinchu County. Most of the residences in this area are Hakkaness. T here are lots of historic sites in this little area, and five of them will be introduced later in this article.

3. ROCSAT-2 SIMULATED IMAGE

To simulate an ROCSAT-2 image with two-meter resolution, one can find two sources with finer resolution, such as Ikonos and aerial images. The aerial photos have been used for estimation of rice production and inventory of rice parcels regularly. The aerial image can be selected for any place in Taiwan and digitized from the aerial photo. There are several sets of aerial photos of whole Taiwan for the different time. On the other hand, the total coverage of the Ikonos image is limited in the existing archive for Ikonos was launched into the mission orbit last year. But, Ikonos is available for ordering a

new imaging task of a specified area. The cost is cheaper for an aerial image than Ikonos. Because the aerial image of the Jin-Shan-Miann is available in the existing archive and the copied were widely used here; it serves as the source for the ROCSAT-2 simulated image. A digitized file of the aerial photo of the target, taken in 1993, was selected. Thanks to some powerful tools, the interest of region were re-sized and the resolution was re-sampled in two meters. The interested spots were properly identified, marked and annotated on the image.

When you go to the spot marked on the simulated image, you may have some difficulty recognizing it. Because the space or aerial image is viewed from top and the image may be too old to match the latest land use. The new picture of the real scene is helpful for the visitor. To take the best shot of the spots, the authors visited the spots and took pictures of them again. Each digital picture was overlapped on the simulated ROCSAT-2 image near the mark of the spot. Finally, some main roads, landmarks and scale were annotated in the simulated image to complete a tourism map. The simulated image is shown as Figure 1.

The first four spots are very closed each other in a simulated image covering area about 1.5 square kilometers. The fifth spot is far away from them and does not shown in the image.

4. STORIES OF FIVE SPOTS

The authors live in an area called Jin-Shan-Miann (JSM) adjacent to Hsinchu Science-Based Industrial Park (SBIP). The SBIP, nicknamed Taiwan's "Silicon Valley", is famous with semiconductor, PC computer, and related high-tech industries. Many famous worldwide companies are located there, such as, Taiwan Semiconductor Manufacturing Company (TSMC) and Acer Inc. On the other hand, the JSM was bright in the past but is faded now. The authors collected the stories and the image of the spots of JSM.

First let's take a look at the two hundred-year-old Jin-Shan Temple (translation: Golden Hill Temple), because of it's old history, the temple went through many wars and historical events, yet it survived. Worshipers come from everywhere to worship the temple and ask for blessings (Chang 2000b).

Heritages of the temple reveal the evidences of the historical events that happened to the temple and even to the city. For example, on one of the octagon limestone pillar outside the temple is a little blob of concrete. Underneath the concrete is a bullet hole, which was caused during a battle between the Taiwanese and Japanese about a hundred years ago. Unfortunately a few years ago, the unique hole was sealed with concrete by the staff of the temple without valuing its historical significance. As years passed, many other historical heritages were also destroyed. Including the original clay shaped Buddha, which was brought to Taiwan from China about 150 years ago. For unknown reasons, in 1996 the temple threw the Buddha into the Do-Jan Stream. Taking its place is a wood carved Buddha which we see today.

During the war the Jin-Shan Temple served not only as a shelter to people' s soul but also their body, which lead to being burned by the Japanese. So most of what we see now is from reconstruction after the war and modification in 1985. Even then, there is still a lot of historic value in it, worthwhile for us to learn about.

The next site is a little temple unnoticed by many people because of its size and location. The little Kang-Lun Temple is located on a little hilltop embraced by two two hundred-year-old trees, one on each side. Don't underestimate this little temple, it was once the landmark of Jin-Shan area, because back then it could be seen by the naked eye from 20 km far away. Now high buildings block the view, yet the little temple carries on its job of protecting the residences nearby.

The third site is a stream named Cool Water Stream. The spring water that runs in it was sweet and pure, and it was once called the "Spiritual Springs ", many poets were attracted to come and wrote poems while drinking tea made with the water. So there are quite a few literature works about Cool Water Stream. But in 1980 SBIP used the water from the stream to fill a man made lake called Jin-Shin Lake, and what' s left of the stream was turned into the SBIP's industrial ditch. How pathetic! A once poetic stream now sacrificed to being the industries' ditch.

Although the source of the Cool Water Stream is difficult to identify now, the outlet from Jinq-Shin Lake is located at the north of the lake. The stream is beside the first part of Lane 525 of Section 1 of Guang-Fuh Road, intersects with the Guang-Fuh Road, and flows continually northward.

The next site is a seventy-year old house, this is where the Huangs live, and it is called the Huangs' House, located at 15 Lane 335, Section 1, Guang-Fuh Road. The Huang family was famous in Hsin-chu for its Hsin-Fu-Hsing pottery factory. At that time, it mainly produced red tiles, red bricks, jars, urns, basins and tombstones. Hsin-Fu-Hsing's red tiles and red bricks were the best construction materials in the entire Hsinchu area. Back then, most houses in Chin-Shan-Mien and the surrounding areas used Hsin-Fu-Hsing's products for their roof, floor and wall. The roof tiles used on the Huangs' House are red tiles from Hsin-Fu-Hsing. Even after several decades, their colors are still bright and have almost no visible green moss.

Across the road from the Huang House is a sixty-nine years old sandalwood tree, it was planted when their first grandson was born. That elder grandson who still lives in the Huang House is also sixty-nine years old now. So this sight is named Huangs' House and sandalwood tree.

Last, but not least is another old tree. This camphor tree is now three hundred years old as shown in the Figure 2. It is said that the hillsides of Jan-Shan Mean was once almost covered by camphor trees, but after years of over development this is the only camphor tree left from the past. The tree is 25 meters tall and can be surrounded by three people' s arms open! This is the oldest tree in all of Hsin-chu City!

The Taiwan High Speed Rail was originally planned to go over the old tree, so it had to be cut down. Many residences objected, and signed a petition to save the tree. This petition aroused the attention of the president of Taiwan High Speed Rail, Miss Ji In, and she decided to change the plan in order to protect this priceless old tree. All of the Jin-Shan Miann residents really appreciate the decision.

5. CONCLUSIONS

The applications of the space image are versatile. This paper shows a personal application of the remote sensing satellite. The five stories were collected about JSM including Jin-Shan Temple, Kang-Lun Temple, Cool Water Stream, Huangs' House, and the oldest tree of Hsin-chu City for a school assignment. The area of interest was selected and cut out from an air-borne image. The resolution is re-sampled in two-meter to generate an ROCSAT-2 image that will be available in late 2003. Furthermore, the simulated image was value-added with overlapping, marking and annotating. Since the space image provides plenty of information of the spots and the connections between those. It is then an excellent medium in the near future for students or the public to recognize and familiarize the area where they live.

REFERENCES

Astrium, May 2000a, Remote Sensing Instrument Design Report, NSPO-CDRL-021a, p.9

Chang, K. Y., 2000b, Assignment Report (in Chinese): National Chu-Pei High School, Chu-Pei City

ERL/ITRI, 1998a, Investigation on the requirements and application of remote sensing satellite (Final Report), Report no: 06-3-87-W007

Kueng, H. M., 1998b, An Application of Satellite Remote Sensing Image In Junior High Education, paper presented at The Seventh Resource Satellite Application Conference, National Central University, Chung-Li

Wang, S., 1998c. Looking at Taiwan (in Chinese). Da-di publication company, Taipei

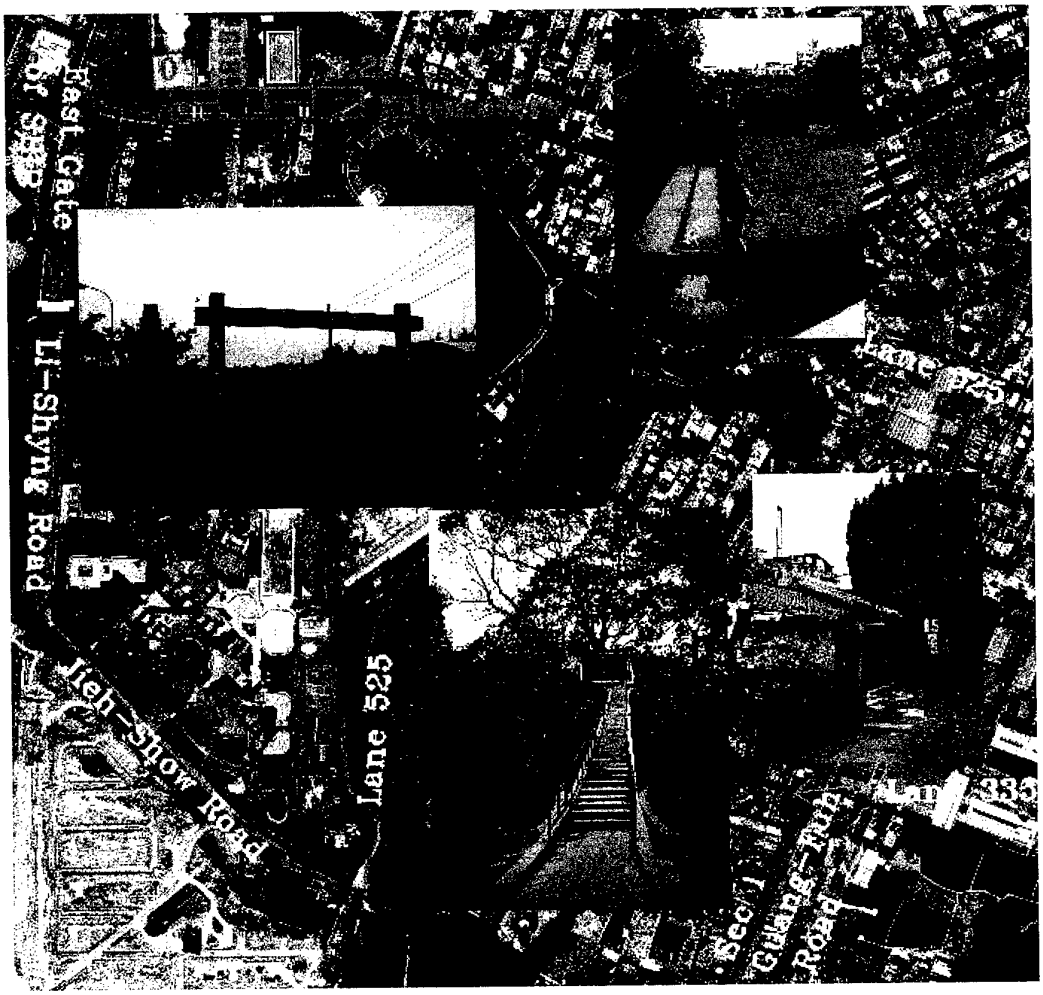


Figure 1: ROCSAT-2 Simulated Image of Jin-Shan-Miann Adjacent to SBIP

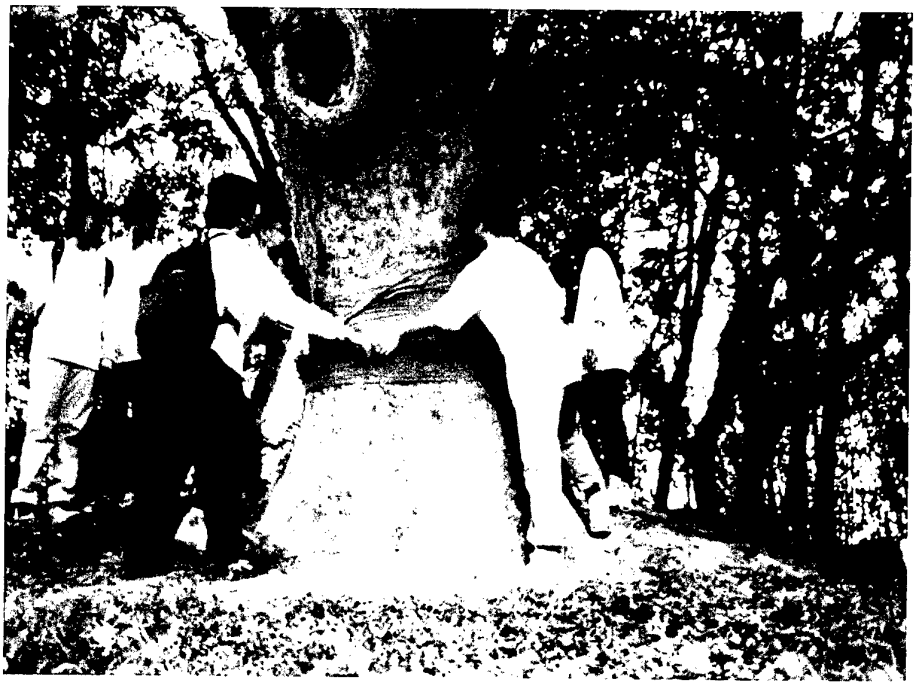


Figure 2: The oldest tree of the Hsinchu City

DETERMINATION OF ORIGINAL SIZE OF THE ABHAYAGIRIYA STUPA

Siri Diyupathi DAMPEGAMA
Senior Lecturer / Superintendent of Surveys
Institute of Surveying & Mapping.
Tele: +94-57-23015 Fax: +94-57-22004
E-mail:ism_surv@sri.lanka.net
Sri Lanka.

KEY WORDS: Size of Stupa, Least Squares

ABSTRACT: This paper presents an approach developed to determine the original size of the ruined Abhayagiriya stupa built between 89 to 77 BC. Determination of the radius and the centre of the stupa was computed using the mixed model observation equations of general least square principle. The radius of the stupa was determined by taking the coordinates of the old plasters available on the outer surface of the dome. Observations were taken with respect to a three dimensional cartesian coordinate system. Measurements were taken by precise Electromagnetic Distance Measuring (EDM) equipment and the coordinate controls were made by Global Positioning System (GPS). Radius and the centre of the stupa were computed to an accuracy of ±5cm due to the advance technology utilized in field procedure and the computation methodology. The centre of the spire (Koth Kerella) was also determined using the same technology. The shape to be determined by best fitting curve to the old plaster / bricks existing on the stupa.

INTRODUCTION

Abhayagiriya stupa was erected by King Valagambahu between years 89 to 77 BC. This is one of the largest religious structure of the world during its construction period. The Abahayagiriya stupa was situated at the city of Anuradhapura in the north central province of Sri Lanka.The initial stupa built by king Valagambahu was much smaller than the present monument and no records were available about its initial dimension. But it was considerably enlarged by successive kings such as king Gajabahu I who has restored guard houses at the four entrances between years 112-134 AD. At present the outer surface of the dome is completely deteriorated due to weathering. But several small patches of original outer plaster are existing in the dome and preserved by the Archeological Department and Central Cultural Fund.
The following procedure was adopted in order to determine the radius of the stupa using the available remaining plaster and bricks of the original stupa.

PROCEDURE

After careful investigation of the stupa it was decided to obtain rectangular cartesian coordinates of all points connected to the new conformal grid coordinate system used by the Sri Lanka Survey Department. Control stations were established using precise Global Positioning System. This was done by four LEICA SR 399 geodetic type GPS receivers. Eight control stations were established around the stupa using above technique. In addition to the GPS control stations seven additional control points were established using Electro Magnetic Distance Measuring technology (EDM). A SOKKIA SET 3B digital total station was used in order to pick up the coordinate of the dome plaster and the points identified as on original structure of the stupa. Six circles at the base of the stupa were identified in order to compute the radius and the coordinates of the centre of the stupa as follows.

1. Circle constructed by stones on the stone paved terrace around the base of the stupa. (Salapathala Maluwa)
2. Circle formed by the stone basement of the lower Pesawa. (Welikonda.)
3. Circle formed by the top of first Pesawa.
4. Circle formed by the top of second Pesawa.
5. Circle formed by the top of third Pesawa.
6. All existing old plaster patches of the lower part of the dome.

Another five circles formed by undisturbed old work on the spire (Koth Kerella) were also identified to compute the centre at the top of the stupa in order to check the verticality.

Coordinates of all points identified as original construction were picked up by SOKKIA SET 3B total station to the accuracy of ± (5mm + 3ppm.). This instrument is capable of storing the coordinates digitally and the coordinates were down loaded to a computer for post processing.

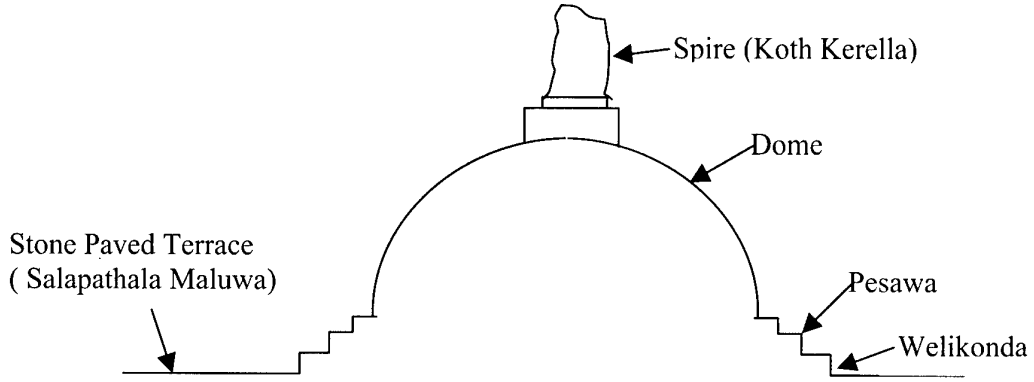


Diagram 1. Cross Section of Stupa.

MATHEMATICAL MODEL

The observed points are on concentric circles with their centres at the centre of the stupa. The mathematical equation of the circle (equation 1 below) was taken as the model to construct observation equations.

$$x^2 + y^2 - 2gx - 2fy + C = 0 \quad \text{——} \quad (1)$$

The radius of the circle is given by,

$$r = (g^2 + f^2 - C)^{1/2} \quad \text{——} \quad (2)$$

where,

g = North coordinate of the centre
f = East coordinate of the centre

According to equation (1) above, parameters g, f & C could be computed if coordinates of three points on the circumference of the circle are known. When more than three points are available on the circle, the best fitting circle which passing through the points can be obtain by the least square adjustment. As the coordinates are also contaminated by random errors the general least square solution with mixed observation equation model was selected to compute the parameters of best fitting circle.

The number of points available on the circumference of each circle near the base is shown in table 1.

Circle	Description	No.
C	Stone circle on Salapathala Maluwa.	22
D	Circle on Welikonda.	27
E	Circle on first Pesawa.	19
F	Circle on second Pesawa.	20
G	Circle on third Pesawa.	19
H	Circle formed by plaster on the dome.	29

Table 1 Descriptions & number of Points of Circles at the Base of Stupa

The observation equation for the circle after linearizing using Taylor series and neglecting 2nd and higher orders is in the form of equation (3).

$$\begin{pmatrix} 2(x_1-\overset{\circ}{g}) & 2(y_1-\overset{\circ}{f}) \end{pmatrix}\begin{pmatrix} V_x \\ V_y \end{pmatrix}+\begin{pmatrix} -2x_1 & -2y_1 & 1 \end{pmatrix}\begin{pmatrix} dg \\ df \\ dC \end{pmatrix}=-\overset{\circ}{f}$$

Equation 3.

$$P=\left(BQB^T\right)^{-1}_{nxn}$$
$$X=\left(J^TPJ\right)^{-1}\left(J^TPK\right)_{3x1}$$
$$V=JX-K$$

$\overset{o}{C}$ - Approximte 'C' value of the circle

V - Residual matrix

X - Corrections to approximate g, f & C

$\overset{o}{f}$ - Approximate north coordinate of the Center

$\overset{o}{g}$ - Approximate east coordinate of the Center

x_i - North coordinate of a point on circumference

y_i - East coordinate of a point on circumference

$$B=\begin{pmatrix} 2(x_1-\overset{o}{g}) & 2(y_1-\overset{o}{f}) & 0 & 0 & \cdots\cdots & 0 & 0 \\ 0 & 0 & 2(x_2-\overset{o}{g}) & 2(y_2-\overset{o}{f}) & \cdots\cdots & 0 & 0 \\ . & . & . & . & \cdots\cdots & . & . \\ . & . & . & . & \cdots\cdots & . & . \\ 0 & 0 & 0 & 0 & \cdots\cdots & 2(x_n-\overset{o}{g}) & 2(y_n-\overset{o}{g}) \end{pmatrix}_{nx2n}$$

Adjusted parameters could be obtained from the following equations.

Equation 4. Co-efficient matrix of coordinates x & y

$$J = \begin{pmatrix} -2x_1 & -2y_1 & 1 \\ -2x_2 & -2y_2 & 1 \\ . & . & . \\ . & . & . \\ -2x_n & -2y_n & 1 \end{pmatrix}_{nx3}$$

Equation 5. Coefficient matrix of *dg, df & dC*

$$K = \begin{pmatrix} -x_1^2 - y_1^2 + 2g\overset{o}{x}_1 + 2f\overset{o}{y}_1 - \overset{o}{C} \\ -x_2^2 - y_2^2 + 2g\overset{o}{x}_2 + 2f\overset{o}{y}_2 - \overset{o}{C} \\ . \\ . \\ -x_n^2 - y_n^2 + 2g\overset{o}{x}_n + 2f\overset{o}{y}_n - \overset{o}{C} \end{pmatrix}_{nx1}$$

Equation 6. Approximate Equation of the circle

$$Q = \begin{pmatrix} \sigma_{x_1}^2 & & & \\ & \sigma_{y_1}^2 & 0 & \\ & & . & \\ & & . & \\ & 0 & \sigma_{x_n}^2 & \\ & & & \sigma_{y_n}^2 \end{pmatrix}_{2nx2n}$$

Equation 7. Variance matrix

Due to the neglection of the second and higher orders of the Taylor series, results obtained by the above equations to be iterated until it reached to the specified tolerance levels.

COMPUTATION

A computer programme was specially developed to solve the above equations due to the complex nature of the calculation and the iterative process. Hence a computer programme was developed to execute the above calculations using FORTRAN77 scientific programming language. All calculations were carried out in double precision mode (up to sixteen decimal places) to maintain required accuracy.

RESULTS

Parameters of the best fitting circles after least squares adjustment are shown in table 2. Adopted ±1mm tolerance level was reached within three iterations. The parameters of the best fitting circles after least squares adjustment was given in table 2. Small variances of the results clearly indicate the high accuracy levels maintained in the field procedure. The mean of the centres of the six circles around the base was the best probable value of the centre of the stupa, which is having following co-ordinates.

North co-ordinate of the centre = 1538.7017±0.05
East co-ordinate of the centre = 8315.1568±0.05
The height to the top of the spire from the Salapathala Maluwa is 73 m.

Position	Northing	σ^2	Easting	σ^2	Radius	σ^2
Circle – C Salapathala Maluwa	1538.6418	.0009	8315.1474	.0009	58.0190	.0005
Circle – D Welikonda	1538.7398	.0005	8315.2033	.0004	54.6777	.0002
Circle – E Top of 1st Pesawa	1538.6880	.0008	8315.1778	.0026	54.3918	.0011
Circle – F Top of 2nd Pesawa	1538.6345	.0007	8315.0412	.0018	52.5900	.0011
Circle – G Top of 3rd Pesawa	1538.7376	.0007	8315.1581	.0027	50.9446	.0011
Circle – H Old plaster on dome	1538.7684	.0017	8315.2131	.0006	48.6349	.0006
Circle – K Old bricks on spire	1537.7774	.0001	8315.0454	.0001	5.9020	.0001
Circle – L On spire	1537.7545	$4x10^{-5}$	8315.0414	$4x10^{-5}$	5.7787	$2x10^{-5}$
Circle – M On spire	1537.8186	.0002	8315.0510	.0002	4.7397	.0001
Circle – N On spire	1537.7963	.0001	8315.0400	$1x10^{-5}$	4.7081	$5x10^{-5}$
Circle – P Top of the spire	1538.7058		8315.1797		1.7713	

All values are in meters. σ^2 - Variance

Table 2. Centre co-ordinates and the radius of each circle

CONCLUSION

The above results clearly show that the centre of the original dome was setout to an accuracy of ± 20 cm. These measurements are independent from the centre of the Koth Kerella. The centre of the Koth Kerella is approximately one meter south to the centre of the dome. Surprisingly the centre of the top of the ruined spire (Circle P) is within ±2cm to the computed coordinates of the centre. This procedure can be adopted to find out the original size of any other large monuments very accurately.

REFERENCES

Dampegama, S.D.P.J., 1999. Interim Report of Abhayagiriya Stupa Survey Stage I
Smithers, J.G., Architectural Remains, Anuradhapura, Sri Lanka.
Urho A. Uotila , 1986. Notes On Adjustment Computations.

REMOTE SENSING ACTIVITIES OF NASDA IN SOUTHEAST ASIA

Eiichi MUTO
Director, NASDA Bangkok Office
RM.1312, B.B.BLDG., 54 Asoke RD., Sukhumvit 21, Bangkok 10110
Tel: (66)-2-260-7026 Fax: (66)-2-260-7027
E-mail: nasdatha@ksc15.th.com
THAILAND

KEY WORDS: Remote Sensing, Southeast Asia, NASDA, Development, Earth Observation

ABSTRACT: National Space Development Agency of Japan (NASDA) was established 31 years ago to act as the nucleus for the development of space and to promote the peaceful use of space. NASDA is responsible for the following tasks:

- Development of satellites (including space experiments and the space station) and launch vehicles, launching and tracking the craft.
- Development of methods, facilities and equipment required for the above.

NASDA is developing earth observation satellites, such as ADEOS-II and ALOS. ADEOS-II is being developed to help answer question on the global environment; a theme of common concern to all humanity. ALOS is a satellite following JERS-1 and ADEOS, which will utilize advanced land observing technology. ALOS will be used for cartography, regional observation, disaster monitoring and resource surveying. ALOS has three remote-sensing instruments: the Panchromatic Remote-sensing Instrument for Stereo Mapping (PRISM) for digital elevation mapping, the Advanced Visible and Near Infrared Radiometer type 2 (AVNIR-2) for precise land coverage observation, and the Phased Array type L-band Synthetic Aperture Radar (PALSAR) for day-and-night and all-weather land observation.

NASDA is conducting the pilot projects for public use in cooperation with related governmental agencies in Thailand and Indonesia. Purpose of the pilot projects is to promote operational data use for governmental and administrative purposes through data analysis technologies development. In the pilot projects, we are developing and researching particular application for each participating agency, and we are expecting that the results should be useful in the governmental activities. The results from the pilot projects could be reflected to the design of future earth observation satellite program in Japan.

NASDA organizes some seminars and training programs in cooperation with related organizations.

1. INTRODUCTION

National Space Development Agency of Japan (NASDA) was established 31 years ago, under the National Space Development Agency Law, to act as the nucleus for the development of space and to promote the peaceful use of space. NASDA is responsible for the following tasks, based on the Japanese Space Development Program enacted by the Prime Minister:

- Development of satellites (including space experiments and the space station) and launch vehicles, launching and tracking the craft.
- Development of methods, facilities and equipment required for the above.

This paper presents the outline of the remote sensing activities of NASDA in the Southeast Asia.

2. DEVELOPMENT OF EARTH OBSERVATION SATELLITES

NASDA is developing earth observation satellites, such as ADEOS-II and ALOS. ADEOS-II is being developed to help answer question on the global environment; a theme of common concern to all humanity. ALOS is a satellite following JERS-1 and ADEOS, which will utilize advanced land observing technology. ALOS will be used for cartography, regional observation, disaster monitoring and resource surveying. ALOS has three remote-sensing instruments: the Panchromatic Remote-sensing Instrument for Stereo Mapping (PRISM) for digital elevation mapping, the Advanced Visible and Near Infrared Radiometer type 2 (AVNIR-2) for precise land coverage observation, and the Phased Array type L-band Synthetic Aperture Radar (PALSAR) for day-and-night and all-weather land observation.

2.1 ADEOS-II

The Advanced Earth Observing Satellite II (ADEOS-II) is the satellite which will take over ADEOS's observation mission of monitoring frequent climate changes occurring in the world, expansion of the ozone holes, and global environmental changes, as well as investigating the causes of these phenomena.
ADEOS-II is equipped with two core sensors; AMSR for the observation of various physical content concerning water cycling regardless of day and night, and GLI for the observation of many field such as ocean, land and cloud with high precision, with the combination of other instruments developed by domestic and overseas organization. They include a scattering meter (Sea Winds, NASA/JPL), ILAS-II an improved spectrometer for measuring infrared radiation at the edge of the atmosphere (Environmental Agency), and POLDER, an earth surface reflection measuring device from CNES.
ADEOS-II is expected to acquire the data necessary to understand the circulation of water and energy, and the circulation of carbon in order to contribute to study the global environmental changes including seizing the mechanism of global environmental changes.
Main Characteristics of ADEOS-II are as follows.

Dimension
Main body Approx. 5 × 4 × 4m (X-axis × Y-axis × Z-axis)
Solar Array Paddle Approx. 3 × 24m

Weight
Total Weight Approx. 3500kg
Mission Instrument Weight Approx. 1200kg

Power
5000W (EOL)

Life
Designed Life 3 years
Propellant For 5 years

Orbit

Category	Sun-synchronous sub-recurrent orbit
Altitude	802.9km
Inclination	98.62deg.
Period	101min.
Recurrent Period	4 days
Local Sun Time	AM 10:30±15

Launch	
Launch Vehicle	H-IIA Rocket
Launch Site	Tanegashima Space Center
Launch Period	2001 (Fiscal Year)

2.2 ALOS

The Advanced Land Observing Satellite (ALOS) is a Satellite following the Japanese Earth Resources Satellite-1 (JERS-1) and Advanced Earth Observing Satellite (ADEOS) which will utilize advanced land observing technology, The ALOS will be used for cartography, regional observation, disaster monitoring, and resource surveying.
The ALOS has three remote-sensing instruments: the Panchromatic Remote-sensing Instrument for Stereo Mapping (PRISM) for digital elevation mapping, the Advanced Visible and Near Infrared Radiometer type 2 (AVNIR-2) for precise land coverage observation, and the Phased Array type L-band Synthetic Aperture Radar (PALSAR) for day-and-night and all-weather land observation. The ALOS will be launched by an H-IIA launch vehicle from the Tanegashima Space Center in 2003.

2.2.1 Main Characteristics: Main Characteristics of ALOS are as follows.
Launch:
Japanese fiscal year 2003 / H-IIA Launch Vehicle
Tanegashima Space Center

Life:
3 - 5 years

Orbit:
Altitude=Approx. 700km, Sun-Synchronous Subrecurrent,
Inclination=Approx. 98deg., Period=Approx. 99min.,
Recurrent Perid=Approx. 45day,
Local time at Descending Node=10:30AM+-15min.

Weight:
Approx. 3,850kg (at lift-off)

Power:
Approx. 7000W (EOL)

2.2.2 PRISM: Panchromatic Remote-sensing Instrument for Stereo Mapping (PRISM) is a panchromatic radiometer with 2.5-meter spatial resolution. In order to obtain terrain data including elevation, the PRISM has three telescopes for forward, nadir and backward view.

Precise land information can be obtained frequently by the PRISM.
Major Specifications of PRISM are as follows.
Observation Band 0.52 - 0.77μm (Forward-Nadir-Backward)
Base/Height ratio 1.0
S/N 70
Spatial Resolution (IFOV) 2.5m (3.57μrad)
MTF 0.20
Swath Width 35km
Pointing Angle +-1.5deg. (cross track)

2.2.3 AVNIR-2: Advanced Visible and Near Infrared Radiometer type 2 (AVNIR-2) is a visible and near infrared radiometer for observing land and coastal zones and provides better spatial land coverage maps and land-use classification maps for monitoring regional environment.
The instrument has a cross track pointing function for disaster monitoring.
Major Specifications of AVNIR-2 are as follows.
Observation Band ch1: 0.42 - 0.50μm, ch2: 0.52 - 0.60μm,
ch3: 0.61 - 0.69μm, ch4: 0.76 - 0.89μm
S/N 200
Spatial Resolution 10m
MTF ch1 - 3: 0.25, ch4: 0.20
Swath Width 70km
Pointing Angle +-40deg. (cross track)

2.2.4 PALSAR: Phased Array type L-band Synthetic Aperture Radar (PALSAR) is an active microwave sensor for cloud-free and day-and-night land observation and provides higher performance than the JERS-1's SAR. The sensor has a beam steerable in elevation and the ScanSAR mode, which allows us to obtain a wider swath than conventional SARs. The development of the PALSAR is a joint project between NASDA and Japan Resources Observation System Organization (JAROS).
Major Specifications of PALSAR are as follows.

Observation Mode	Fine Resolution Mode	ScanSAR Mode
Frequency	L-band	
Polarization	HH or VV (option: HV or VH)	
Spatial Resolution	10m (2 looks)	
	20m (4 looks)	100m
Swath Width	70km	250 - 360km
		(3 - 5scans)
Off-nadir Angle	18 - 48deg.	

3. PILOT PROJECTS

Under the bilateral agreement between the Royal Thai government and the government of Japan, National Research Council of Thailand(NRCT) and NASDA have managed the ground receiving station for MOS-1, JERS-1 satellites at Lad Krabang area in Bangkok in order to receive, process and distribute Japanese satellite data to their coverage region since 1987. In this context, NASDA has started the first pilot projects for public use in Thailand and added projects in Indonesia.
Purpose of the pilot projects is to promote operational data use for governmental and administrative purposes through data analysis technologies development. In the pilot

projects, we are developing and researching particular application for each participating agency, and we are expecting that the results should be useful in the governmental activities.
The results from the pilot projects could be reflected to the design of future earth observation satellite program in Japan.

4. TRAINING

4.1 AIT Training Program

Under contract with NASDA, in cooperation with Asian Institute of Technology (AIT), Remote Sensing Technology Center of Japan (RESTEC) has five training courses in a year at AIT campus in Bangkok, Thailand (two weeks, 15-20 participants) and some other places (one week, 20-40 participants). The purpose of the training program is mainly to promote the continuous use of data from Japanese Earth observation satellites, such as JERS-1 and ADEOS, which will contribute to the development of this region.
The first course, Remote Sensing & Geographic Information System, was held in 1995 at AIT. Caravan style training and SAR data application training were added as new options in 1997.
The objectives of these courses are as follows;

- To provide the trainees from Asia and Pacific with advanced GIS with a focus on the integration with Japanese satellite data such as JERS-1 OPS and ADEOS AVNIR in the operational applications.
- To provide application techniques of JERS-1 SAR data recognizing that SAR data are supplementary to optical data when there is cloud cover and when there is only one data source, particularly in the rainy and flood seasons.
- To maximize the efficiency of training by providing application techniques in remote sensing and GIS in local and/or regional aspects to encourage technical transfer.

4.2 Regional Seminar on Earth Observation for Tropical Eco-system Management

This seminar has been conducted by NASDA and UNESCAP since 1992 in cooperation with RESTEC. The main objective of this seminar is to share our experience and knowledge on remote sensing and Geographical Information System (GIS) applications for sustainable ecosystem management in the Asia-Pacific region. Participants are decision-makers, planners and technical users from Asian and Pacific region. The content includes the seminar on the application of RS and GIS for tropical ecosystem management(two days), field trip survey for understanding of tropical ecosystem dynamics (one day), computer hands-on training on digital image analysis for RS and GIS (two days).
This seminar has been held in eight different countries of the Asian and Pacific region: Thailand in 1992, Malaysia in 1993, Indonesia in 1994, Philippines in 1995, Fiji in 1996, Vietnam in 1997, Bangladesh in 1998 and Myanmar in 1999. The ninth Regional Seminar on Earth Observation for Tropical Eco-system Management is scheduled to take place at Khao Yai National Park, Thailand from 20 to 24 November 2000.

5. CONCLUSION

These activities contribute to the capacity-building of the related countries of this region. NASDA will continue this kind of effort.

The Educational Function of Satellite Imagery

Shi-Ming Lu
Editor-in-Chief,
The Earth Geographic Publishing Co., Ltd.
2F No.16, Lane 130, Min Chuan Road, Hsin-Tien, Taipei, Taiwan
Tel: 886-2-22181506 ext 501 Fax: 886-2-22186837

Abstract

Over the past decade, the world has seen a very rapid development in satellite imaging technology and its applications. Satellite imagery has also become an increasing important tool for education, especially in geography related fields. Taiwan is no exception in this regard. This paper will present a general picture of the recent development of satellite imagery being used as a tool for education in Taiwan. The paper will comprise the following major parts: 1. How to read a satellite image, 2.Various presentation forms of satellite images, 3. Satellite image exhibitions, 4.Mobil cargo exhibition of satellite images, 5.Satellite image in weather news broadcasting, 6. Satellite image in publications.

The 21st Asian Conference on Remote Sensing
December 4-8, 2000 Taipei, TAIWAN

DESERTIFICATION MAPPING OF WEST ASIA
-A GIS and Remote Sensing Application-

Hussein Harahsheh and Ryutaro Tateishi
Center for Environmental Remote Sensing (CEReS), Chiba University
1-33 Yayoi-cho, Inage-ku, Chiba 263, Japan
Fax: +81-43-290-3857
Email: hussein@ceres.cr.chiba-u.ac.jp / tateishi@ceres.cr.chiba-u.ac.jp

KEY WORDS: Remote sensing, GIS, Desertification, Assessment, Mapping

ABSTRACT: In the context of the constitution of environmental GIS database of west Asia, satellite remote sensing and GIS technology were applied as essential tools to address important aspects of environmental monitoring. A multi-temporal analysis of satellite derived monthly vegetation index data allows to create a land cover map of the study area. The land cover map with satellite images of NOAA AVHRR formed the basic elements of the environmental GIS database. The GIS is constructed in such way to envelop all necessary environmental layers (soil, geology, rainfall, elevation, temperature, moisture, albedo...etc). These layers were digitized and geo-coded to fit with latitude and longitude coordinates system as well as with the original satellite images representing the study area. Based on this environmental GIS database a desertification assessment and mapping was achieved. In order to analyze the desertification phenomena and other environmental parameters in the study area a layer of Environmental Mapping Units (EMUs) was prepared. The EMUs layer was formed using the land units layer, land cover classes and country area. Several desertification maps were produced, which reflect the desertification types persist in the study area: wind erosion, water erosion, vegetation degradation and salinization are the basic desertification maps, others are combinations of these basic maps. In term of statistic analysis 31% of the total land area (6.615 million km2) is considered as sand or sand dune, and not included in our analysis of desertification. About 27% has a slight to moderate desertification and 42% of the total land area is facing a severe to very severe desertification.

1. INTRODUCTION

Environment is considered as a worldwide phenomenon, which is characterized with sensitive equilibrium between its components; water, air and soil. The changes that take place in many areas of the world, as a result of human and other natural activities, could have the greatest impact on the environment.

The main goal of this research is to enable countries affected by desertification and drought to be associated with the generation of knowledge and techniques related to remote sensing and GIS, which are needed to solve their specifics problems in field of desertification control. And thus, to contribute to a better natural resources management and economic development.

2. Land cover of West Asia

The main land cover types occurring in the study area are listed in **Table 1.** Where we note that about 30% of the studied area (6653037 km^2) are desert or desert rangeland and 32% is sand or sand dune. Followed by the permanent rangeland or marginal land, which represent 20% of the study area. The forest coverage constitutes 3.5% of the study area. The agriculture activity is divided into two main forms: irrigation activity and arable land, which represent 5.2% and 8% of the study area respectively.

3.0 Methodology

The environmental studies involved many types of parameters and variables, which are all dependant on each other, these variables could be related to water, land, atmosphere and people. So an integrated approach used remote sensing and GIS is the best methodology to take in consideration all aspects of environmental study, which is the case in this study.

Figure 1: land cover map of West Asia

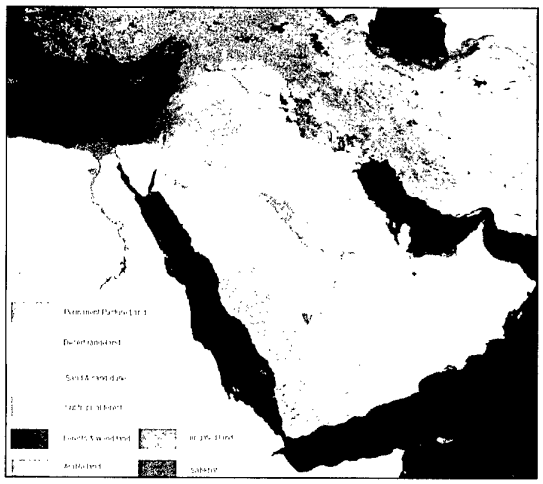


Table 1: Land cover of the study area

Land cover type	Area	
	Km 2	%
Internal water bodies	38075.62	0.57
forest	181884.17	2.73
Desert rangeland	1992924.18	29.96
Sabkhat	27735.61	0.42
Irrigated land	345700.26	5.20
Arable land	534283.16	8.03
Sand & sand dune	2124799.22	31.94
Permanent pasture	1349280.29	20.28
Subtropical forest	58355.10	0.88
Total	6653037.61	100.00

4. ENVIRONMENTAL GIS DATABASE

The aim of this part of study is to construct a Geographic Information System containing environmental parameters influencing the regional and global changes, with focus on desertification/ land degradation problems in West Asia. More than 70 layers of information were collected or calculated then geo-referenced and entered into the GIS system.

These layers belong to five types of data:

1- land cover, natural vegetation and ecosystems maps

2- Soil types and derived soil properties (texture, organic matter, PH, Nitrogen %, ...)

3- Climatic data: includes rainfall (average of 50 years), potential evapotranspitation, aridity index and air temperature.

4- Topographic data: digital elevation model (DEM) and derived data such slop, aspect , shaded relief, drainage network and elevation zones.

5- Satellite data: 10-days composite data set of NOAA AVHRR 1 km resolution covering the period from April 1992 through March 1993 and others data on the period of 1995 and 1996. Monthly NDVI data, Average NDVI, Land surface temperature and albedo Vegetation condition Index (VCI =(NDVI – $NDVI_{MIN}$)/($NDVI_{MAX}$-$NDVI_{MIN}$)), etc.

6- Land degradation and desertification layers (Wind erosion, vegetation degradation...)

7- Socio-economic data

5. Environmental Mapping units – EMUs-

In order to construct the database for the prepared GIS layers, it is very important that this database represents a set of polygons or units describing the environmental characteristics of such units, we called this Environmental Mapping Units-EMUs-. This is called also Desertification Mapping Units (DMUs) when it is related to desertification mapping. Here we choose three factors to build up the database units: soil units, land cover classes and country area. In total we obtained 502 EMUs, which represent unique physical mapping unit, unique land cover class and belong to

one country. Under the "Idrisi software" GIS and database structure, we extracted all the information from the GIS layer based on the EMUs, then information filled in to the database.

6. Desertification assessment and Mapping

6.1 Introduction

The problem of desertification in arid and semi arid areas has a long history through the past centuries. It has always been an overlap of long-term changes in climate and human activities. With the rising population and, therefore, growth in consumption of the very limited resources, scope and intensity of interface with ecosystems by human activities grow rapidly, leading to sever degradation of vegetation, soil and water resources, which compose the natural resources of human existence. In fact United Nations by its organizations defined the desertification as the land degradation of dry, semi dry and dry humid lands caused by human activities and natural causes. This study emphasizes on desertification processes, causes and indicators occurring in west Asia, then desertification mapping, assessment and monitoring.

6.2 General Criteria of desertification assessment

Criteria for desertification assessment must take in consideration the local conditions of the study area. These conditions should be investigated through field observations, with the help of remote sensing tools. The results of such investigation can be interpreted according to the type and degree of desertification. The types of desertification considered in this study are as follows: Vegetation cover degradation, wind erosion, water erosion and soil salinization

Criteria for the assessment and small scale mapping of desertification were developed for each land use type. The following categories of land use were identified: forest/woodland, rangeland and meadow, dry agriculture and irrigation agriculture. Because absolute figures of these characteristics vary from region to region, the criteria are given in relative figures (for example, percentage of the area covered with moving sand dunes or vegetation) (Kharin, 1999). Examples of criteria used for desertification assessment are: Plant community, percentage of climax species, decrease of total plant cover, loss of forage on rangeland, percentage of area covered with sand dunes, type of water erosion in percentage, Removal of topsoil horizon of arable land, Blow-outs of the area, loss of yield of main crop in percentage, Salinity of ground water, salinization, Salinity of irrigation water, Salt accumulation. For developing the criteria, desertification maps and experimental data collected in study area were used, as well as literature sources. We should be clear that these criteria are still more theoretical and the application is not always possible. To some degree of accuracy we could used some of these criteria, and some times we used criteria, which are related and have linear relationship with these criteria mentioned on above.

6.3 Desertification Assessment and Mapping

6.3.1 Methodology

The assessment of desertification, which we fixed in four forms: vegetation degradation, water erosion, wind erosion and salinization, needs the combination of several factors or criteria. This could be achieved only by the use of GIS tools. Generally we have a scatter information about criteria of desertification, which are distributed over the study area, and to extend these information over whole the study area we developed linear models with one or two variables. So we have generally for each criterion an image layer in which its gray level values represent different degrees of importance of the criterion. This methodology makes the combination of criteria within the GIS framework logic and easy. The final result of each desertification map has

to forms one with range of 0-255 values and another one with four degrees of desertification: slight, moderate, severe and finally very severe degree of desertification, this make it easier to interpret the results. The method of mapping will be explained for each type of desertification separately.

6.3.2 Vegetation degradation mapping

For the vegetation degradation mapping we consider the two main indicators or factors: decrease of forage productivity and decrease of the percent of vegetation cover. The analysis of vegetation degradation was achieved through the following steps:

Step1: Decrease of forage productivity:

As we mentioned above there is a general decrease of production of dry matter for livestock. To convert what we have of information about the decrease of forage, we consider that this decreasing could be linked to two variables: the intensity of livestock and the vegetation index (NDVI). We defined the intensity of livestock as the number of heads per hectare of area (rangeland area). We calculated this intensity for the year of 1961 and 1999, and so we obtained two layers map of livestock intensity, then the difference of two periods give an indicator of the increasing of intensity of livestock. Here we assume that this situation reflects the intensity of overgrazing, a phenomena, which is considered to be the most important cause of vegetation degradation and consequently of desertification.

By a multiple regression calculation we obtained the following model:

$$F = 68.45 + 1.744 * L - 333.46 * NDVI$$

F: Decrease of forage in percentage
L: increase of livestock intensity
NDVI: Normalized difference vegetation index (NOAA AVHRR data 1km resolution, average of the period April 1992 through march 1993)

Using this model we calculated the first indicator image of vegetation degradation. This indicator was divided into four classes according to the criteria of desertification assessment.

Step2: Decreasing of vegetation cover percentage

The percentage of vegetation cover decrease is highly related to the Normalized Difference Vegetation Index (NDVI). In this study we used a model developed by Purevdorj (1998) to calculate the vegetation cover percent from the NDVI:

$$\text{Vegetation Cover (\%)} = -4.337 - 3.733 * NDVI + 161.968 * NDVI^2$$

The calculation was achieved for two periods on 1980s and 1990s. For the period of 1980s, we used an average of five years data of NOAA AVHRR 8km resolution, and for the second period the 1km NOAA AVHRR of the period of April 1992 through March 1993. Then the decrease on vegetation cover percent image was obtained by the difference of the two periods. The output image was scaled to values between 0 and 100, then divided into four classes according to criteria.

Step3: Integration of indicators

The decrease of forage productivity image and the decrease on vegetation cover percent image were combined to produce by overlapping the vegetation degradation image. This result contained 16 combinations possible, which were reduced to four classes by a decision rule from slight degree of degradation to very severe degree of degradation see **Table 2** and **Figure 2**.

6.3.3 Soil Erosion and Salinity

in the same way as vegetation degradation, the wind erosion, water erosion and salinity maps were achieved, but with different criteria and paprameters.

Figure 2: Vegetation degradation

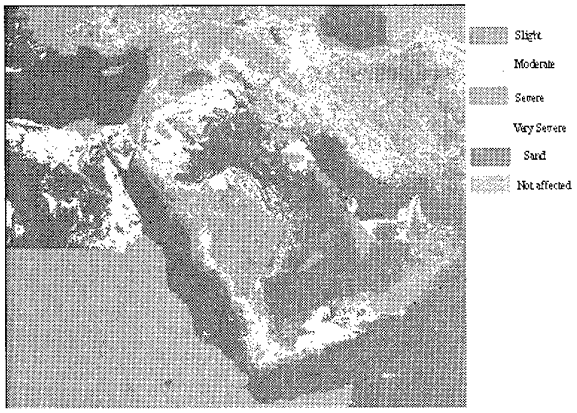


Table 2: Vegetation degradation of West Asia

Class	vegetation degradation	
	Area km2	Area %
Slight vegetation degradation	584673.31	8.84
Moderate vegetation degradation	1271677.13	19.22
Severe vegetation degradation	2071623.13	31.32
Very severe vegetation degradation	562964.94	8.51
Sand	2124023.75	32.11
Total land area	6614962	100.00

6.3.4 Synthetic map of desertification

There are many methods to integrate these results; here we adopted a procedure that gives an important result in all its systematic steps:

Step 1: As the wind erosion and water erosion are considered to have the same effect and shape, which is soil erosion, so we integrated the wind erosion and water erosion in one maps, which has originally 16 combinations of "soil erosion classes". In this step we need to take decisions to group these combinations into four classes of importance regarding soil erosion.

Step 2: The soil erosion affects directly the vegetation cover, and it is consider as main cause for vegetation degradation. Therefore in this step we integrated the result of step 1 with the vegetation degradation map obtained previously in the same manner as in step 1, and we obtained an intermediate desertification map with four classes explaining the degrees of desertification.

Step 3: Finally we integrate the result of step 2 with the salinization map, this combination gives 16 classes as a logic operation of intersection. Then these classes are grouped into the final classes of desertification **(Table 3)**. **Figure 3** show the final map of desertification in West Asia.

5.4.6 Desertification Assessment

The total studied land area is about 6.46 millions square kilometers, 33 percent are classified as sand or sand dune land, and generally located in extra arid environment, which is theoretically excluded from desertification assessment. But we included the sand area, which is under irrigation activity as part of salinization assessment.

The study shows that 55% of West Asia is affected by moderate to severe soil erosion, which represents about 3.58 millions square kilometer. This area losses of its topsoil material from 50 to 150 tones per hectare per year. The vegetation degradation statistics show that it has the same range of importance as soil erosion, in fact 50 % of land are subject to moderate to severe vegetation degradation. Here we can clearly interpret the loss of topsoil by the degradation of vegetation cover, which is important factor to prevent the removal of topsoil material. The salinization mapping shows an important distribution severe and very severe salinization in the irrigated areas and others areas, which have problems of waterlogging and increase of water table level (world atlas, 92). **Table 3** shows that about 266,000 km2 are affected by severe and very severe salinization, which constitute a 75% of the potential of irrigation area in West Asia.

Figure 3: Desertification map of West Asia

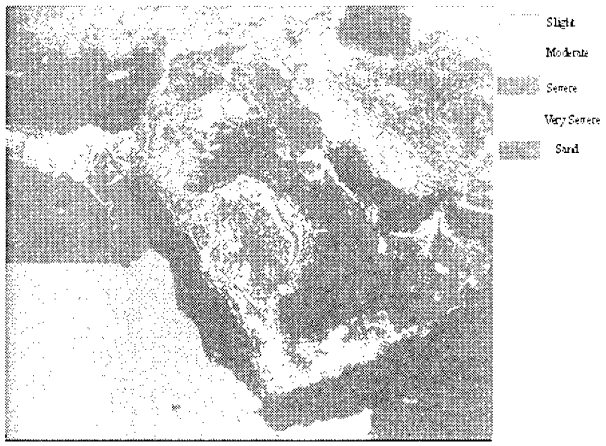


Table 3: Desertification classes in West Asia

Desertification type Class	Desertification status	
	Area km2	Area %
Non affected area	0.00	0.00
Slight	367205	5.55
Moderate	1314427	19.87
Severe	2146005	32.44
Very severe	719233	10.87
Sand	2068092.38	31.26
Total land area	6614962	100.00

In **Table 3**, we have the general estimation for desertification in West Asia. It is supposed that all the area is subject of desertification as we mentioned previously, mainly by vegetation degradation process followed by water erosion process, even the very severe water erosion is lees that 5%. Wind erosion dos not affect 16%, and 22% are slightly affected by wind erosion. So we conclude that 6% of land area in West Asia is slightly desertified, 21% is moderately desertified, 31% is severely desertified and 11% is very severely desertified. Without doubt these results show the gravity of desertification problem in the study area.

Conclusion

We found a big lack in desertification mapping techniques using remote sensing and GIS. And few studies were conducted to map desertification using such tools and methodology. An Integrated Approach is utmost important for desertification study, which reflect the complexity of desertification process. So the desertification assessment in this study is the output of a combination of social factors, economic factors, climatic factors and physical factors. Development of standard methods and criteria is needed for desertification studies. Also there is some lack in the definition of desertification, and needs some improvement, where it is important to include the socio-economic factors when the delineation of area susceptible to desertification.
Finally the statistic results of this study show the gravity of desertification problems in all levels. It is supposed that all the area is subject to desertification, mainly by vegetation degradation process, where 40% of study area is severely and very severely affected by vegetation degradation, followed by wind erosion process (27% severe and very severe wind erosion). So we conclude that 6% of land area in West Asia is slightly desertified, 21% is moderately desertified, 31% is severely desertified and 11% is very severely desertified. Without doubt these results show the gravity of desertification problem in the study area.

References:

Porevdorj T, The estimation of percent green vegetation cover using AVHRR data-Application to Mongolian grassland-, 1998, Graduate School of Science and Technology/Chiba University.
Tubengen Atlas of Middle East, Tubengen University, Stuttgart, Germany, 1978-1987. 30 p.
World atlas of desertification. UNEP, 1992, 69 p.

Development for Data Base for Eco-System Changes and Emission Changes of GHG Using Remote Sensing and GIS in Sumatra Island, Indonesia

Lilik Budi Prasetyo*, Genya SAITO** and Haruo TSURUTA**
*Bogor Agriculture University, Indonesia,
**National Institute of Agro-Environmental Sciences, Japan

KEY WORDS: Remote Sensing, Greenhouse effect gases, Database, Land cover changes

ABSTRACT: Using LANDSAT/TM data, we determined land cover changes of Pasir Mayang area, Sumatra from 1993 to 1999. The database of GHG flux measurement and land cover changes was developed, and we estimated above carbon and GHG

1. Introduction

Deforestation, conversion of forest into non-forest land cover, especially in tropical forest area has been an international concern. It was estimated that tropical forest was deforested by 6 – 16.8 million hectares per year (Grainger, 1993; Barbier etc., 1991; Myers, 1994). Since forest hold the most carbon in terrestrial ecosystem, such changes give significant impact on the net increase of atmospheric carbon. In addition, land cover changes result in greenhouse effect gases (GHG: CO_2, N_2O, CH_4) dynamics.

GHG emission of soil surface is influenced by several factors such as land cover types, climatic factors, biological factors and physical environment factors. Emission measurements usually are conducted at a point location, therefore problem arise when emission estimation will be used for scaling up into a broader areas. The objectives of this research was at the development of spatial database using GIS and remote sensing to assist the regional estimation of aboveground carbon stock loss and soil surface GHG emission changes caused by land cover changes. We studyed land cover and GHG changes between 1992 to 1999 of Pasir Mayang area as a case study.

2. Research method

2.1. Development GHG database at Pasir Manyang area

Using LANDSAT/TM data, we determined land cover of Pasir Mayang area in 1993, 1995 and 1999. Pasir Manyang area is 84,000ha as 35km (east to west) and 24km (north to south), and is represented in Fig. 1 and 2. The estimation of total above ground carbon stock in this area was calculated by multiplying the value of ha by total area of each land cover. The same method was applied for calculating the total emission of GHG. Database was developed using ARC/Info and remote sensing analysis was performed using ERDAS/Imagine.

2.2 Biomass estimation (Above ground carbon stock)

Weight of sample components of the tree *i.e.* timbers, stems, branches, twigs, leaves and roots of primary forest, secondary forest and logged over forest were estimated by using equation developed by Kira and Iwata (1989). Tree biomass for one hectare plot was calculated by multiplying biomass of each tree with the number of tree per hectare.

2.3 Soil GHG flux measurement

Flux of carbon dioxide, nitrous oxide and methane from soil surface were measured at various land cover types in order to obtain the estimates of GHG emissions by the ground survey group of our collaboration project of Indonesia and Japan. The GHG flux measurement points were illustrated on LANDSAT/TM image in Fig. 2.

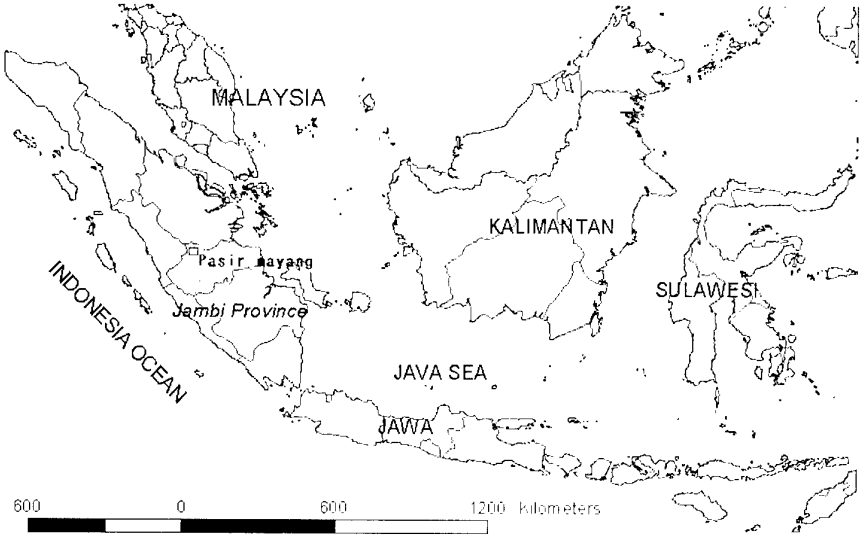


Fig. 1 Pasir Mayang area and Jambi Province

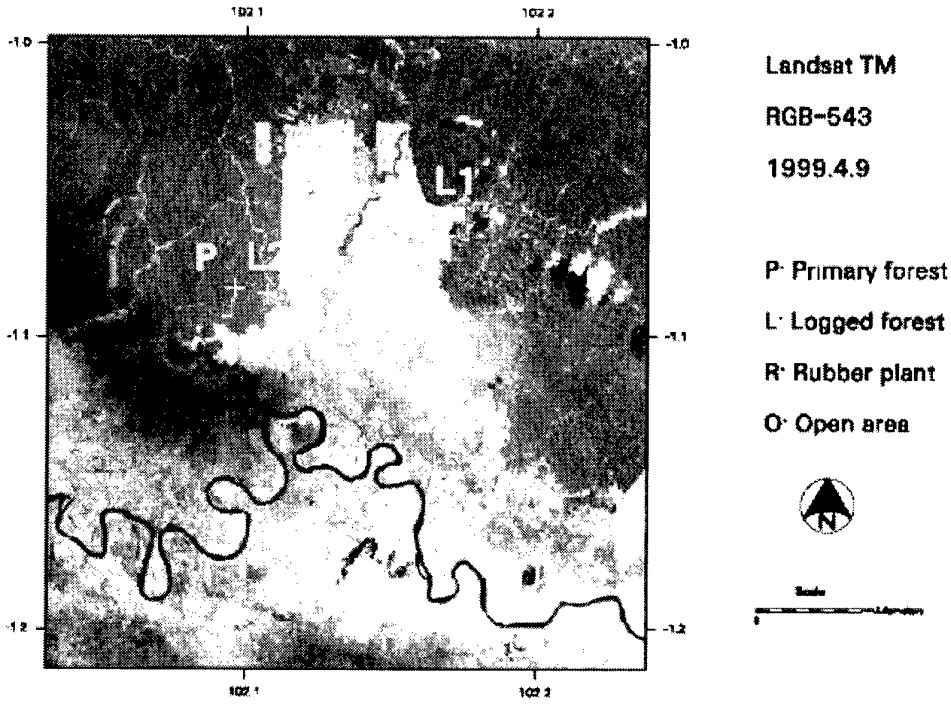
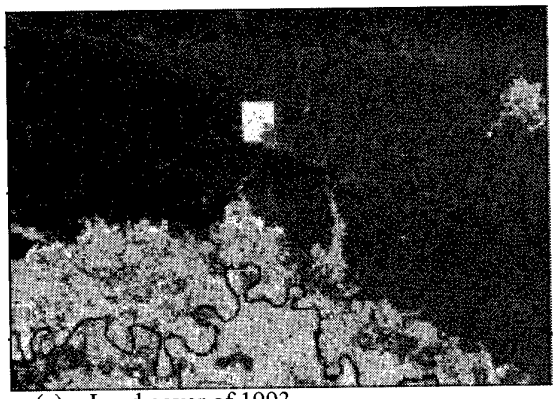


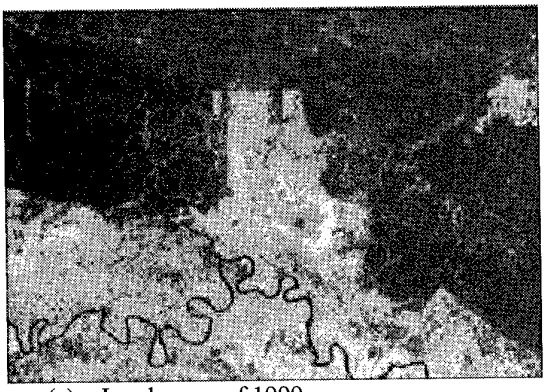
Fig. 2 Used LANDSAT/TM image and the points of GHG flux measurement



(a) Land cover of 1993



(b) Land cover of 1995



(c) Land cover of 1999

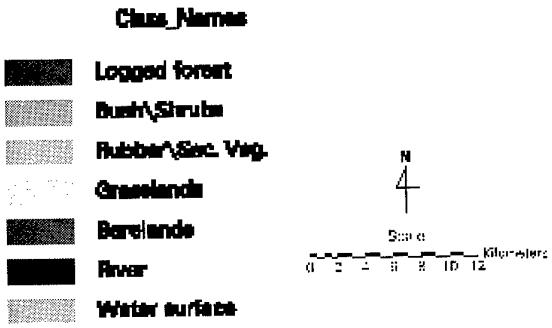


Fig. 3 Land cover maps of Pasir Manyang area and changes in 1993, 1995 and 1999

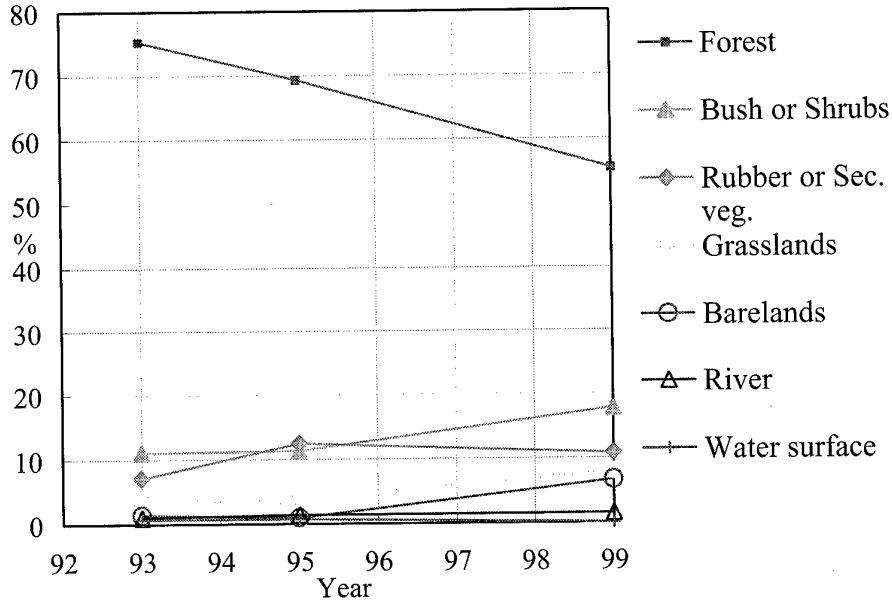


Fig. 4 Land cover changes in Pasir Mayang

3. Results and Discussion

The land cover maps of Pasir Mayang area in 1993, 1995 and 1999 were indicated in Fig. 3. Estimation of above ground carbon stock was calculated by multiplying the unit value by total area of each land cover using the land cover maps of Pasir Mayang area. The same method was applied for calculating the total emission of GHG. These results are shown as table 1, 2 and 3. Forest was the most dominant land-cover in Pasir Mayang, followed by rubber/secondary vegetation, bush/shrubs, grassland and bare land (clear cut area) (Fig. 4).

Between 1993-1995, forest area decreased of about 5,000ha, while rubber/secondary and bush/shrubs land increased. Due to this, above ground carbon stock of the area decreased from 10.2 million ton to 9.6 million ton, or have loss of about 0.7 million ton. Between 1995-1999, forest area decreased of about 12,000ha, and also rubber/secondary and bush/shrubs land increased. Due to this, above ground carbon stock of the area decreased from 9.6 million ton to 7.8 million ton, or have loss of about 1.8 million ton.

GHG flux of soil varies depend on type the site condition and season. The values of each unit were based on flux measurement conducted in November 1997 in several points of Pasir Mayang area (Fig.2). The calculation results of total flux based on 1993, 1995 and 1999 land cover data for major land cover presented in Fig. 4. Comparison of the total GHG flux of the three periods of time studies could not be performed since there are still no information on GHG flux of soil surface under cash crops plantation and secondary forest. However, it seems that the conversion of natural forest will cause on the decrease of methane gas absorption and induce the increase of nitrous oxide and carbon dioxide flux emission as Fig.5.

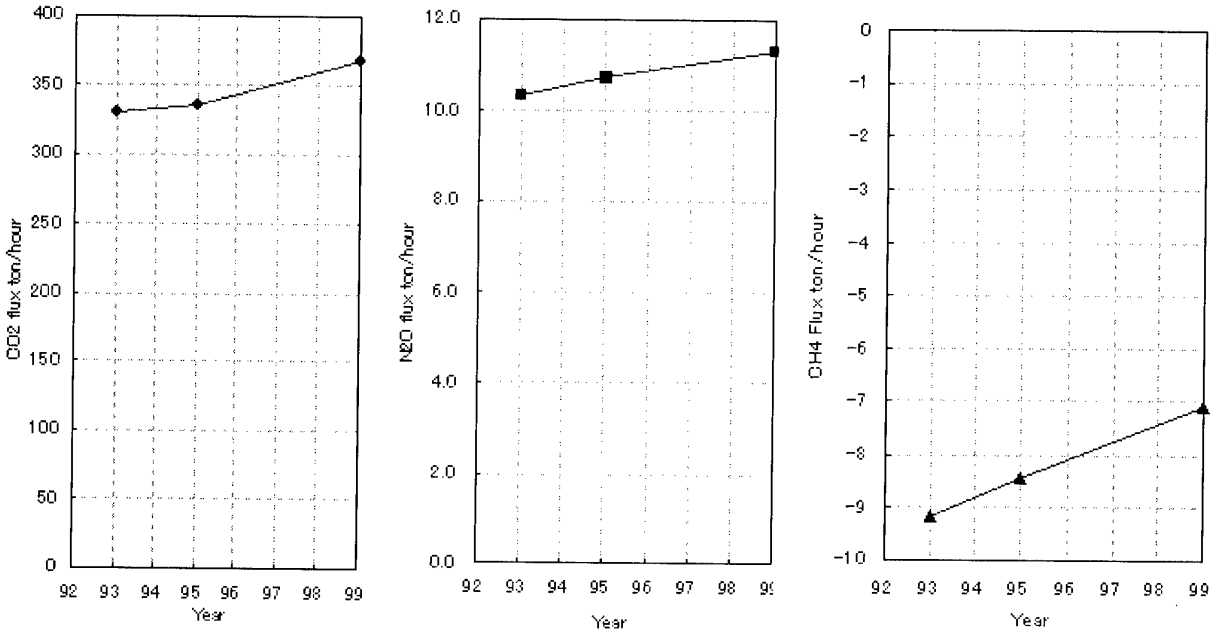


Fig. 5 GHG flux changes in Pasir Mayang area between 1993 and 1999

Table 1 Above carbon stock and total GHG flux in Pasir Mayang area on 1993

	Area		Carbon stock		CO2		N2O		CH4	
	ha	(%)	Ton/ha	Total ton	mg/m2/h	ton/hour	mg/m2/h	ton/hour	mg/m2/h	ton/hour
Forest	63,239	75.3	155.2	9,814,615	352.3	222.8	10.7	6.8	-14.33	-9.1
Bush or Shrubs	9,230	11.0	15.0	138,446	580.7	53.6	20.0	1.8	-0.04	0.0
Rubber or Sec ve	5,996	7.1	35.5	212,858	473.6	28.4	20.3	1.2	-0.02	0.0
Grasslands	2,888	3.4	6.0	17,325	603.6	17.4	11.0	0.3	0	0.0
Barelands	1,146	1.4	0.0	0	624.9	7.2	13.4	0.2	-7.42	-0.1
River	892	1.1								
Water surface	610	0.7								
Total	84,000	100.0		10,183,244		329.4		10.3		-9.2

Note : Above ground biomass was estimated using the data of BIOTROP, Indonesia.

The calculation of GHG fluxes was based on mean value of 10 months (10 time) measurement.

The measurements were made in Jan., Feb., Mar., June, July, Aug., Sep., Oct., Nov. and Dec

Table 2 Above carbon stock and total GHG flux in Pasir Mayang area on 1995

	Area		Carbon stock		CO2		N2O		CH4	
	ha	(%)	Ton/ha	Total ton	mg/m2/h	ton/hour	mg/m2/h	ton/hour	mg/m2/h	ton/hour
Forest	58,283	69.4	155.2	9,045,444	352.3	205.3	10.7	6.2	-14.33	-8.4
Bush or Shrubs	9,480	11.3	15.0	142,204	580.7	55.1	20.0	1.9	-0.04	0.0
Rubber or Sec ve	10,459	12.5	35.5	371,286	473.6	49.5	20.3	2.1	-0.02	0.0
Grasslands	3,212	3.8	6.0	19,271	603.6	19.4	11.0	0.4	0	0.0
Bare lands	811	1.0	0.0	0	624.9	5.1	13.4	0.1	-7.42	-0.1
River	1,145	1.4								
Water surface	611	0.7								
Total	84,000	100.0		9,578,204		334.4		10.7		-8.4

Note : Same as table 1.

Table 3 Above carbon stock and total GHG flux in Pasir Mayang area on 1999

	Area		Carbon stock		CO2		N2O		CH4	
	ha	(%)	Ton/ha	Total ton	mg/m2/h	ton/hour	mg/m2/h	ton/hour	mg/m2/h	ton/hour
Forest	46,560	55.4	155.2	7,226,034	352.3	164.0	10.7	5.0	-14.33	-6.7
Bush or Shrubs	14,936	17.8	15.0	224,036	580.7	86.7	20.0	3.0	-0.04	0.0
Rubber or Sec ve	9,010	10.7	35.5	319,864	473.6	42.7	20.3	1.8	-0.02	0.0
Grasslands	6,638	7.9	6.0	39,827	603.6	40.1	11.0	0.7	0	0.0
Bare lands	5,577	6.6	0.0	0	624.9	34.9	13.4	0.7	-7.42	-0.4
River	1,259	1.5		0						
Water surface	21	0.0		0						
Total	84,000	100.0		7,809,761		368.4		11.3		-7.1

Note : Same as table 1.

References

Adger., W. Neil and K. Brown. 1994. Land-use and the causes of global warming, John Wiley & Sons. New York. 271 p

Ball, D. and R. Babbage. 1989. Geographical information system; defense application, New South Wales. Macathur Press. 257 p

Bappeda Jambi. 1985 and 1988. Jambi province statistics, Bappeda (in Indonesian)

Barbier, E.B, Joanne C. B. and A. Markandya. 1991. The economic of tropical deforestation, Ambio 20 (2): 55 -58

Burrough, A. 1986. Principles of geographical information system for land resources assessment, Oxford, Clarendon Press. Oxford, 193 p

Houghton, J. T., et. al. Greenhouse gas inventory reference manual, page 5.1-5.74

Ikeda, H., Okamoto, K., and Fukuhara, M., 1994. Estimation of carbon budgets in croplands using Landsat TM data, Proceedings of the 7th IUAPPA Regional Conference on Air Pollution and Waste Issues, Taipei. I, 139-146.

Khalil, M. A. K., R. A. Rasmussen, M.X. Wang and L. Ren. 1991. Methane emissions from rice fields in China, Environ. Sci. Tech. 25: 979-981

Kira, Tatuo and Keiji Iwata.1989. Nature and Life in Southeast Asia, Volume IV, Fauna and Flora Research society, Kyoto, Japan.

Mahmood, N. et. al. 1991. Characterization of environmental changes using remote sensing technique - A case study applied to Klang valley area -, Application of remote sensing in Asia and Oceania - Environmental change monitoring.. (Murai eds) Asian Assoc. on Remote Sensing

Maguire, J. et. al. 1991. Geographical information system; principles and application, New York. John Wiley and Sons Inc. 588p

Myers, N. 1994. Tropical deforestation, rates and pattern in the causes of tropical deforestation (Brown, K. and D.W. Pearce eds.) England, UCL Press, pp 27-40

MODELING THE EFFECTS OF RECENT LAND USE CHANGE ON THE CARBON CYCLE IN THE ZHU JIANG DELTA REGION OF SOUTHERN CHINA

Dennis G. DYE
Senior Research Scientist
Frontier Research System for Global Change, Institute for Global Change Research
Sumitomo Hamamatsu-cho Bldg., 4F, Minato-ku, Tokyo 105-0013
Tel: (81)-3-5404-7850 (ext. 236) Fax: (81)-3-5405-4150
E-mail: dye@frontier.esto.or.jp
JAPAN

Thomas HINCHLIFFE*, Graduate Student
Curtis E. WOODCOCK**, Professor
*Department of Geography and **Environmental Science Program
Boston University, 675 Commonwealth Ave., Boston, MA 02215
USA

KEY WORDS: net primary production, biomass, carbon cycle, land use change

ABSTRACT: We investigated the effects of recent land use change (1988-1996) in the Zhu Jiang Delta region, People's Republic of China, on two components of the terrestrial carbon cycle: net primary production (NPP) and ecosystem carbon storage. The analysis employed a mechanistic model of NPP in combination with satellite-derived and reported environmental and ecological data. Our analysis shows that land use change in the 9-year study period significantly altered the terrestrial ecosystem component of the regional carbon cycle. The annual amount of atmospheric carbon assimilated into phytomass through NPP was reduced by approximately $155 \cdot 10^4$ t C (–7.5%). More than half of this reduction is attributed to the loss of cultivated land. Vegetation removal and soil disturbance by the expansion of urban areas reduced the amount of carbon stored in terrestrial ecosystems by $792 \cdot 10^4$ t C, of which approximately 72% came from phytomass. The carbon released by land use change, however, is only 5.3% of the carbon emissions from fossil fuel combustion for the same area and time, suggesting relatively small significance for the overall carbon budget of the ZJDR.

1. INTRODUCTION

Terrestrial ecosystems mediate the exchange of carbon between the atmosphere and the terrestrial biosphere through photosynthesis, respiration, decomposition, and combustion. They also comprise a major carbon reservoir by storing carbon in biomass, decaying organic matter, and soils. Land use and land use change by humans can alter ecosystem performance in these roles, which may alter regional and global carbon budgets.

Recent satellite-based studies indicate that land use change in the People's Republic of China, as in many parts of the developing world, is occurring at unprecedented rates. The land use changes result from a combination of driving forces, including population growth, migration, economic development, and government policies (e.g., Seto, 2000; Kikuchi et al., 1997). In the Zhu Jiang Delta region (ZJDR) of Guangdong Province during the period from 1988 to 1996, urban areas increased by over 300%, while natural and agricultural land areas declined by approximately 6% and 10%, respectively (Fig. 1). We investigated the effects of these changes

in the ZJDR on two components of the terrestrial carbon cycle: net primary production (NPP) and ecosystem carbon storage. Our analysis employed a mechanistic model of NPP in combination with satellite-derived and reported environmental and ecological data.

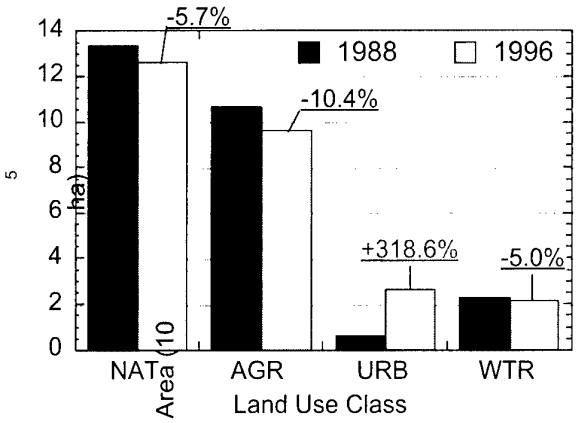


Figure 1. The spatial extent of major land use types in Zhu Jiang Delta region for years 1988 and 1996 as determined by the satellite analysis of Seto et al. (2000). Labels refer to natural vegetation (NAT), agriculture (AGR), urban (URB), and water (WTR) land use classes.

2. BACKGROUND AND METHODS

2.1 Description of the Study Area

The study area encompasses the Zhu Jiang River Delta region (ZJDR) in Guangdong Province, People's Republic of China. The boundaries correspond to the Landsat Thematic Mapper scene used in the land use change analysis (Seto et al., 2000). The area covers 2.7 x 10^6 ha, or approximately 15% of the total area of Guangdong Province. The natural, potential vegetation of the region is predominantly evergreen broadleaved forest (Zhao, 1994).

Over much of the study area, the observed vegetation deviates substantially from the climatic potential. The differences reflect current and historical patterns of intensive land use by humans (Li and Liu, 1994). We focussed our analysis on two of the three non-water land use classes in the Seto et al. (2000) study: natural vegetation (NAT) and agriculture (AGR). We assumed that NPP in the urban (URB) land use class was negligible.

2.2 Modeling NPP with Satellite Data

We used a simple light-use efficiency (LUE) model to estimate NPP (e.g., Waring and Running, 1998; Sheriff et al., 1995). The basic form of the LUE model can be expressed as:

$$NPP = f \cdot \varepsilon \cdot FPAR \cdot S. \quad (1)$$

The S term is the amount of PAR incident above vegetation canopy (MJ m^{-2}). FPAR is a dimensionless term that accounts for the efficiency with which PAR is absorbed by the green, photosynthetic elements of the canopy. The product of S and FPAR determines the amount of vegetation-absorbed PAR (APAR, MJ m^{-2}). The ε parameter equals the gross or net amount of plant dry matter produced per unit of APAR (g MJ^{-1}). The f term is a dimensionless factor that accounts for any reduction in ε resulting from environmental constraints (e.g., Prince, 1991).

An important feature the LUE model is that the variables S, FPAR, and f can be estimated using existing satellite remote sensing techniques (Goward and Dye, 1996). We validated the model results by comparing them with NPP figures reported in the research literature for comparable ecosystems and environmental conditions.

2.3 Data Sources

2.3.1 Net Primary Production. We used monthly average normalized difference vegetation index (NDVI) data to estimate FPAR, based on the empirical relationship employed by Ruimy et al. (1994). The NDVI data were from the NOAA/NASA Pathfinder AVHRR Land (PAL) data set (Agbu and James, 1994). Monthly PAR data were from the satellite-derived data set described by Dye and Shibasaki (1995). The spatial resolution of the NDVI and PAR data sets were 8 km and 100 km, respectively. We set the ε value for NAT to 1.39 g MJ, based on field data from Peng and Zhang (1995). We set ε for AGR to 1.74 g MJ^{-1}, which is value given by Ruimy et al. (1994) for tropical cultivation. Based on available climate data, we assumed that environmental constraints in our study area were negligible and set the value of f in Equation (1) to 1. We referred to the 30 m land use maps from Seto et al. (2000) to select sample locations in the course resolution FPAR images to represent the NAT and AGR land use classes. From the sample data we produced time series of monthly FPAR and PAR values for input to the NPP model.

2.3.2 Carbon Storage. Our estimates of the carbon content of soils in the ZJDR are based on data reported by Cai (1996). We estimated carbon storage in phytomass in NAT by referring to data given by Chen et al. (1993) and other published sources. For AGR, we referred to data reported by Atjay et al. (1977). The carbon storage data were specified on a per-unit-area basis (density). In the current analysis we assume the carbon densities associated with the land use classes remain fixed at their specified levels during the study period.

2.4 Estimating Regional Effects

To estimate the regional effects of land use change we assumed that ecosystem NPP and carbon storage were spatially homogeneous within the land use classes. We calculated regional changes by multiplying the area-based NPP and carbon storage values by the total land area lost or gained for each land use class.

3. RESULTS

3.1 Validation of NPP Model Results

Based on the observed range of values from field studies reported in the literature, we specified high, medium, and low NPP estimates for NAT and AGR. For NAT, our model estimate of NPP differs from the medium field estimate by +13% (20.5 and 18.2 t DM ha^{-1} yr^{-1}, respectively). The high quality of the field data used in the NAT comparison strengthens our confidence that our model estimate of NPP is reasonably accurate for NAT. The results suggest that the model was moderately successful in estimating NPP for AGR. Because of shortcomings in the reported data for AGR, caution is necessary when interpreting the AGR comparison results.

3.2 Effects of Land Use Change on NPP

The NPP analysis indicates that land use change in the ZJDR between 1988 and 1996 reduced the annual amount of atmospheric C assimilated into phytomass by approximately 1.55 Mt (-7.5%) (Table 1). More than half (55%) of this reduction is attributable to the loss of agricultural land.

Table 1. LUE model results showing NPP (rate and regional total) for 1988 and 1996, and the net change, ΔNPP_{tot}. Conversion from dry matter (DM) to carbon assumes .45 g C per g DM.

Land Use Class	NPP ($t\ C\ ha^{-1}\ yr^{-1}$)	NPP_{tot} ($10^4\ t\ C\ yr^{-1}$)		ΔNPP_{tot}	
		1988	1996	($10^4\ t\ C\ yr^{-1}$)	(%)
NAT	9.3	1247.8	1177.2	-70.6 (45.4%)	-5.7
AGR	7.6	813.5	728.7	-84.8 (54.6%)	-10.4
Total		2061.3	1905.9	-155.4 (100%)	-7.5%

Table 2. Soil organic carbon (OC) density estimates from the literature, and results from our analysis on the effects of land use change (1988-1996) on regional total soil OC storage.

Land Use Class	Soil OC density[a]			Net change in OC Content (10^4 t C)		
	high	med	low	high	med	low
NAT	121.5	87.2	52.9	-273.4	-196.2	-119.0
AGR	65.4	52.1	38.7	-36.6	-29.1	-21.7
Total				-310.0	-225.3	-140.7

[a]Based on values from Cai (1996).

Table 3. Net change in regional total phytomass (988-1996) based on estimates from reported field data and land use change (Fig. 1).

Land Use Class	Net change in Phytomass (10^4 t C)		
	high	med	low
NAT	-1347.3	-464.5	-269.1
AGR	-203.4	-101.9	-0.3
Total	-1550.7	-566.4	-269.4

3.3 Effects of Land use Change on Carbon Storage

Our results indicate that conversion of natural and agricultural land to urban uses in the ZJDR from 1988 to 1996 is the source of a release of between $140 \cdot 10^4$ and $310 \cdot 10^4$ tons of soil organic C, with a medium estimate of $225 \cdot 10^4$ tons (Table 2). These figures account for the expected cumulative release during the 20 years following conversion. Patterns of carbon loss observed

in studies of cultivated soils (Schlesinger et al., 2000) suggest that the majority of the carbon would be released in the several years immediately following conversion.

Our medium estimate for carbon lost from phytomass is $566 \cdot 10^4$ tons; the majority (82%) of this was from natural vegetation (Table 3). Phytomass accounted for about 72% of the total of $792 \cdot 10^4$ tons of carbon released (medium estimate).

4. DISCUSSION AND CONCLUSION

Land use change in the Zhu Jiang Delta region between 1988 and 1996 affected the regional carbon cycle by reducing both the annual rate of NPP and the size of the terrestrial carbon reservoir. The dominant mode of land use change underlying this effect involved the conversion of vegetated land areas (natural and cultivated) to urban uses (Fig. 1). In some types of land use change where vegetation is removed from the landscape (e.g., deforestation, swidden agriculture), NPP can rebound through secondary growth. Vegetation-to-urban land use conversion, however, causes a sustained reduction in the capacity the landscape to assimilate atmospheric CO_2. Thus the observed 7.5% decline in annual NPP is a measure of the reduction in the total photosynthetic capacity and carbon sequestration potential of terrestrial ecosystems in ZJDR.

Vegetation removal and soil disturbance in the expansion of urban areas reduced the amount of carbon stored in existing phytomass and soils by an estimated $792 \cdot 10^4$ t C. In the absence of a compensatory increase in NPP and biomass through secondary growth, this result represents a sustained reduction in the potential size of the terrestrial carbon pool in the ZJDR. The future course of the socio-economic driving forces that influence the rates and modes of land use change in the region (Seto, 2000), in combination with potential climate change, will determine whether these effects become exacerbated or diminished in the coming decades.

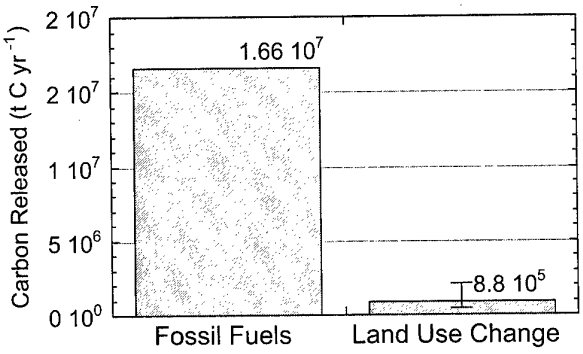


Figure 2. Estimated total amount of carbon released in the ZJDR study area as a result of fossil fuel energy use (1996) and land cover change (annual average, 1988-1996).

Our analysis shows that recent land use change caused significant modifications to the terrestrial ecosystem component of the regional carbon budget in the ZJDR. It is instructive to compare our estimates of carbon released from ZJDR ecosystems to carbon emissions from fossil fuel combustion for the same area and time (Fig. 2). We used energy consumption data to estimate the carbon emissions from fossil fuels for Guangdong Province in 1996 (SSB, 1998). We adjusted this figure to our study area based on the fraction of the 1996 Guangdong gross domestic product (GDP) generated within the area (K. Seto, personal communication). The results indicate that fossil fuel combustion in our ZJDR study area in 1996 emitted about $1.7 \cdot 10^7$

tons of carbon, which is two orders of magnitude greater than the average annual amount of carbon released as a result of land use change in the ZJDR ($8.8 \cdot 10^5$ t C). Despite significant effects for the terrestrial ecosystems, the role of land use change in the overall carbon budget of the ZJDR is small (5.3%) relative to fossil fuel-based energy consumption.

5. REFERENCES

Agbu, P.A., and M.E. James. 1994. NOAA/NASA Pathfinder AVHRR Land Data Set User's Manual. Goddard Distributed Active Archive Center, NASA Goddard Space Flight Center, Greenbelt.

Cai, Z, 1996. Effect of land use on organic carbon storage in soils in eastern China. Water, Air and Soil Pollution, 91, pp. 383-393.

Dye, D.G., and Shibasaki, R., 1995. Intercomparison of global PAR data sets. Geophysical Research Letters, 22(15), pp. 2013-2016.

Goward, S.N., and Dye, D.G., 1996. Global biospheric monitoring with remote sensing. In: The Use of Remote Sensing in the Modeling of Forest Productivity, H.L. Gholz, K. Nakane, and H. Shimoda, eds., Dordrecht, The Netherlands: Kluwer Acad. Publ., pp. 241-272

Kikuchi, T., Zhan, G., Guo, H., 1997. Land use changes and their driving forces in the Beijing metropolitan area, China. Geographical Reports of Tokyo Metro. Univ., 32, p. 43.

Li, W., and Liu, Y., 1994. Land use and land cover change in China. Journal of Chinese Geography, 4(3-4), pp. 25-40.

Peng, S., and Zhang, Z., 1995. Biomass, productivity of climax vegetation on Dinghu Mountains, Guangdong, China. Science in China (Series B), 38(1), pp. 67-73.

Prince, S.D., 1991. Satellite remote sensing of primary production: comparison of results for Sahelian grasslands, 1981-1988. International Journal of Remote Sensing, 12, pp.1301-1312.

Ruimy, A., Sugier, B., and Dedieu, G., 1994. Journal of Geophysical Research, 99(D3), 5263-5283.

Schlesinger, W.H., Winkler, J.P., and Megonigal, J.P., 2000. Soils and the global carbon cycle. In: T.M.L. Wigley and D.S. Schimel, eds., The Carbon Cycle, New York: Cambridge Press, pp. 93-114.

Seto, K.C, Woodcock, C.E., Song, C., Huang, X., Lue, J., and Kaufmann, R.K., 2000. Monitoring land-use change in the Pearl River Delta using Landsat TM. Submitted to International Journal of Remote Sensing.

Seto, K.C., 2000. Monitoring and modeling land-use change in the Pearl River Delta, China, using satellite imagery and socioeconomic data. Ph.D. thesis, Dept. of Geography, Boston University.

Sheriff, D.W., Margolis, H.A., Kaufmann, M.R., and Reich, P.B., 1995. Resource use efficiency. In: Resource Physiology of Conifers, W.K. Smith and T.M. Hinckley, eds., New York: Academic Press, pp 143-177.

STB, 1998. China Energy Statistical Yearbook, 1991-1996. Dept. of Industrial and Transportation Statistics, State Statistical Bureau, People's Republic of China, China Statistical Publishing House, Beijing.

Waring, R.H., and Running, S.W., 1998. Forest Ecosystems: Analysis at Multiple Scales. New York: Academic Press, 370 pp.

Zhao, S., 1994. Geography of China. John Wiley & Sons, New York, 332 pp.

SATELLITE OBSERVATION OF MIGRATION ROUTES AND HABITATS OF MIGRATORY BIRDS LIVING IN WETLANDS IN EAST ASIA

Masayuki TAMURA
Social and Environmental Systems Division
National Institute for Environmental Studies
Japan Environmental Agency
16-2 Onogawa, Tsukuba, Ibaraki, 305-0053 Japan
Tel: (81)298-50-2479, Fax: (81)298-50-2572
E-mail: m-tamura@nies.go.jp

Hiroyoshi HIGUCHI
Laboratory of Biodiversity Science
School of Agriculture and Life Sciences
University of Tokyo
1-1-1 Yayoi, Bunkyo-ku, Tokyo, 113-8657 Japan
Tel: (81)3-5841-7541, FAX: (81)3-5841-8192
E-mail: higuchi@uf.a.u-tokyo.ac.jp

KEY WORDS: Argos system, red-crowned crane, oriental white stork, remote sensing, Landsat/TM

ABSTRACT: Migration routes and habitats of red-crowned cranes and oriental white storks were studied by two kinds of satellite-based observation techniques, i.e. satellite tracking and remote sensing techniques. By the former we obtained bird location data; by the latter we investigated habitat ecosystem conditions. By combining these two techniques we analyzed the relationship between ground conditions and habitation patterns of wetland migratory birds. In the summer of 1999 small platform transmitter terminals were set on six red-crowned cranes and six oriental white storks in the wetlands along the Amur River in the Russian Far East. Their migration routes to wintering sites in China were tracked by using the satellite tracking technique. Locations of important places for breeding, stopover and wintering have been extracted from the migration data. Satellite remote sensing technique was used for investigating ground environmental conditions. The relationship between wetland ecosystems and habitation patterns of migratory birds was investigated.

1. INTRODUCTION

Recently wetlands are being recognized as important ecosystems for the conservation of

biodiversity. They support wide variety of flora and fauna and serve as habitats for many kinds of creatures including migratory birds. However wetlands are disappearing at a rapid rate in East Asia due to human activities such as agricultural, residential, and industrial developments (Hussain, 1994). The decrease and environmental deterioration of wetlands are bringing quite a few species of migratory birds to face the danger of extinction. For the conservation of wetland ecosystems and wetland migratory birds, it is urgently needed to understand the actual situation of the decrease and environmental destruction of wetlands and to investigate the relationship between wetland ecosystems and habitation patterns of migratory birds.

In this study a satellite tracking system (Argos system, http://www.argosinc.com/) was used to pursue migration routes of two species of migratory birds, i.e. red-crowned cranes and oriental white storks, both of which are in danger of extinction. They can serve as good indicators of the conservation state of wetlands because they stand at the top of the wetland food chains. The satellite tracking data were used to extract locations of important places for breeding, stopover and wintering. We then used satellite images (NOAA/AVHRR and Landsat/TM images) for investigating the distribution and environmental conditions of the wetlands in East Asia. The relationship between wetland ecosystems and habitation patterns of migratory birds was analyzed by combining remotely sensed images and satellite tracking data of bird locations.

2. SATELLITE TRACKING OF MIGRATION ROUTES

In the summer of 1999 small platform transmitter terminals (PTT) were set on six red-crowned cranes and six oriental white storks in the wetland areas along the Amur River in the Russian Far East. Figure 1 shows the capture points. Their migration routes from the breeding sites in the Amur Basin to the wintering sites in China were tracked by the Argos system. The accuracy of the Argos system is indicated by the location class (Table 1). Basically we only used the data with the location classes higher than 1, which means the error of an estimated bird location is less than 1 km.

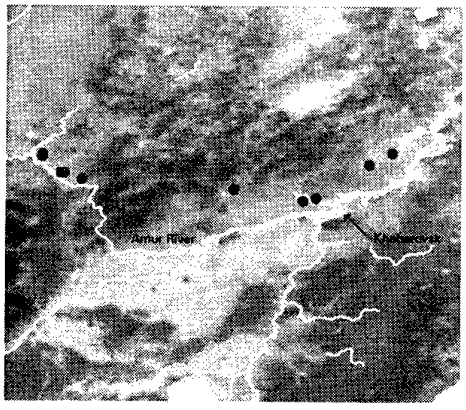
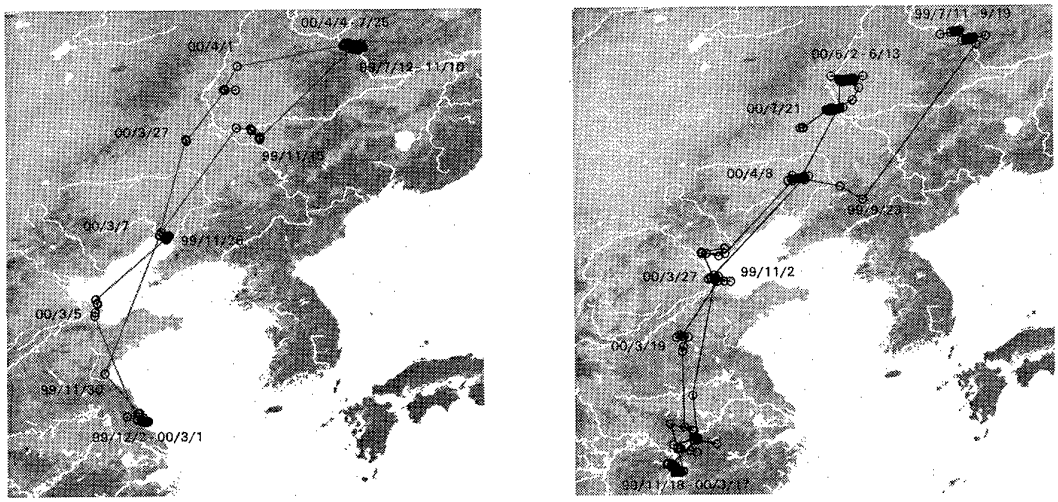


Fig. 1. Capture points. (Red: red-crowned cranes, Blue: oriental white storks).

Table 1 Accuracy of the Argos system (http://www.argosinc.com/).

Location Class	Estimated accuracy in latitude and longitude
3	≤150m
2	150m<accuracy<350m
1	350m<accuracy<1000m
0	>1000m
A	no estimate of location accuracy
B	no estimate of location accuracy
Z	(invalid locations)



(a) 21502 (b) 20821

Fig. 2. Migration routes of a red-crowned crane 21502 and an oriental white stork 20821.

Table 2 (a) Migration data in autumn 1999.

ID	Species	Departure	Arrival	Days	Destination
20819	Red-crowned crane	99/11/11	99/11/17	6	Yancheng marsh
21502	Red-crowned crane	99/11/10	99/12/02	22	Yancheng marsh
20820	Oriental white stork	-	99/12/07	-	Poyang lake
20821	Oriental white stork	99/09/19	99/11/18	70	Poyang lake
20823	Oriental white stork	99/08/21	99/12/10	111	Poyang lake

Table 2 (b) Migration data in spring 2000.

ID	Species	Departure	Arrival	Days	Destination
21502	Red-crowned crane	00/03/01	00/04/04	34	Arkhara lowland
20821	Oriental white stork	00/03/17	00/05/02	47	Zhalong marsh

Among the twelve captured birds, we have succeeded in tracking the migration routes of two red-crowned cranes and three oriental white storks to their wintering sites in China. Moreover for one red-crowned crane and one oriental white stork the PTT's continued to function until the summer of 2000 and we could track the entire round-trip migration routes between their breeding sites in Russia and wintering sites in China (Figs. 2 (a) and (b)). Table 2 (a) and (b)

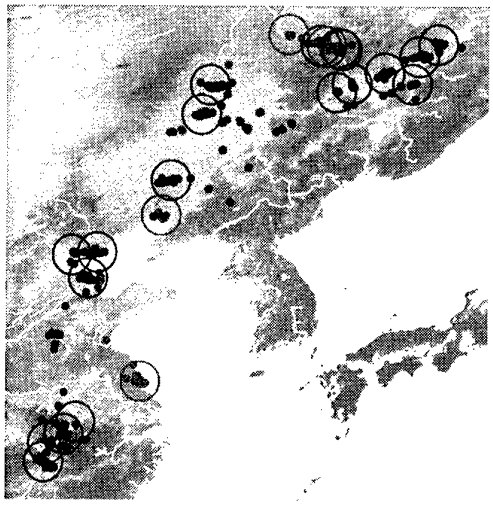


Fig. 3. Important habitats. (Red: red-crowned crane, Blue: oriental white stork).

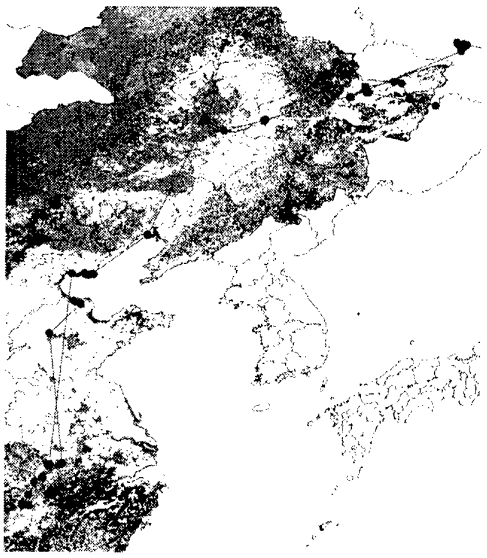


Fig. 4. Land cover map of China with a migration route of an oriental white stork 20823.

summarizes individual migration data in autumn 1999 and spring 2000 respectively. From the bird location data we can extract important habitats of red-crowned cranes and oriental white storks for breeding, stopover and wintering. Figure 3 shows the locations of important habitats where birds stayed more than 10 days.

3. ANALYSIS OF HABITAT CONDITIONS USING SATELLITE IMAGERY

To investigate the ground conditions of bird habitats we used satellite images. Figure 4 shows a part of a Chinese land cover map produced from NOAA/AVHRR and Landsat/TM images by Luo Di of the Institute of Remote Sensing Applications, Chinese Academy of Science. We overlaid bird locations on this map and studied in what kinds of land cover types the birds liked to stay. In Figure 4 the migration route of an oriental white stork (ID: 20823) is indicated as an example. Figure 5 shows the number of location data obtained at each of six land-cover types for two red-crowned cranes and three oriental white storks. We note that four out of five birds were found more frequently in farmlands than in wetlands. This frequent use of farmlands may be causing some friction with human activities in China. We also note that red-crowned cranes were found more frequently in grasslands than oriental white storks. This may be explained by the fact that the former is omnivorous while the latter is carnivorous.

To obtain detailed information on the wetland ecosystems we used Landsat/TM images. Figure 6 shows the result of land-cover classification using a TM image (path:116, row:26) in Arkhara Lowland, which lies along the Amur River around the Arkhara River confluence in the

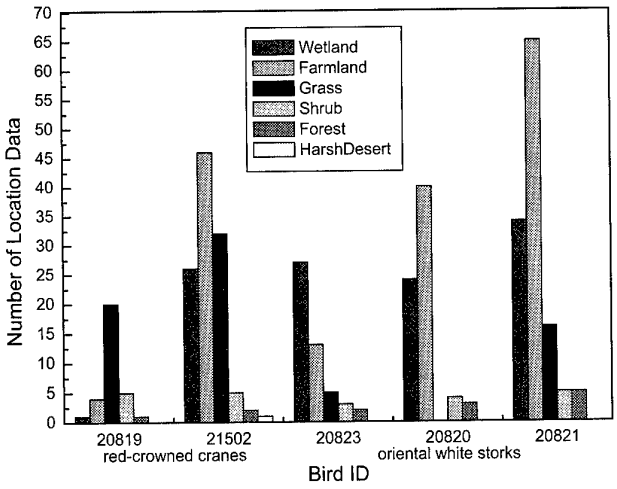


Fig. 5. Bird locations in China.

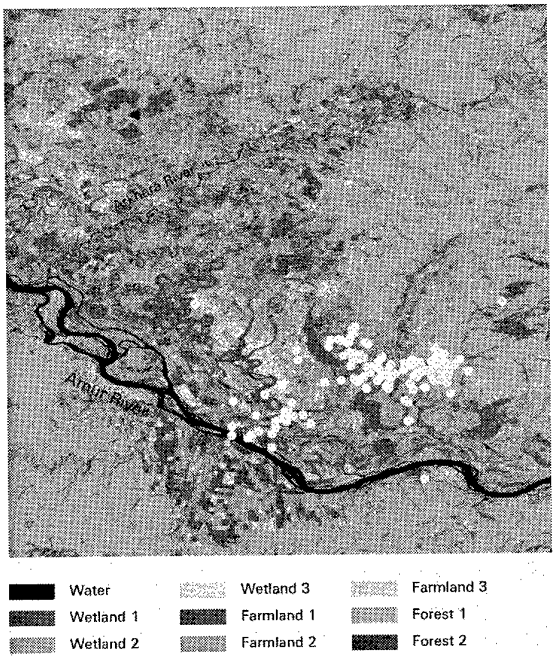


Fig. 6. Land-cover map of Arkhara Loeland in the Russian Far East.

Russian Far East. The Arkhara lowland includes the Khingan Nature Reserve and Ganukan Landscape Refuge, which were registered as a Ramsar Convention site in 1994. The wetland area was classified into three categories, the wettest part with sedges and reeds (Wetland 1), the modestly wet part with sedges and grasses (Wetland 2), and the dry part with various kinds of grasses (Wetlnad 3). Location data of one red-crowned crane (ID: 21502) and one oriental white stork (ID: 20821) were overlaid on the land-cover classification map. (In Figure 6 only the location data of the crane 21502 are shown for clarity.) Figure 7 shows the number of location

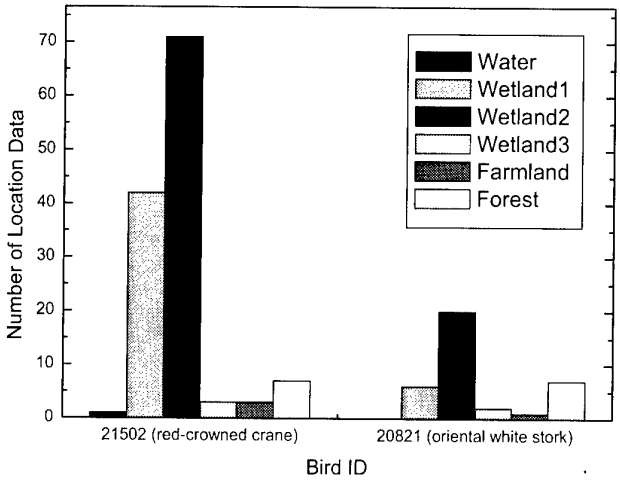


Fig. 7 Bird locations in Arkhara Lowland in the Russian Far East.

data obtained at each of six land-cover types for two birds. We see that both birds mostly stayed in wetland 1 and 2. We hence can say that these two wetland types are most important ecosystems for the habitation of both a red-crowned crane and an oriental white stork.

4. CONCLUSIONS

Migration routes and habitats of red-crowned cranes and oriental white storks were studied by two kinds of satellite observation techniques, i.e. satellite tracking and remote sensing techniques. By the former we obtained bird location data; by the latter we investigated habitat ecosystem conditions. By combining these two techniques we analyzed the relationship between ground conditions and habitation patterns of wetland migratory birds. The followings are major results of this study:

- Important habitats of red-crowned cranes and oriental white storks were extracted during their migration from the breeding sites in the Amur Basin to the wintering sites in China.
- It was found that both kinds of birds frequently stayed in farmlands during their migration in China.
- The wetland ecosystems of Arkhara Lowland in the Russian Far East were classified into three categories, and both kinds of birds mostly stayed in wetland types 1 and 2.

REFERENCE

Hussain, S. A. (1994) The present status of wetland conservation in Asia. In: *The Future of Cranes and Wetlands*, edited by Higuchi, H. and Minton, J., Wild Bird Society of Japan, Tokyo, pp. 15-25.

AN OPERATIONAL APPROACH FOR MAPPING BUSHFIRE HISTORY IN THE TROPICAL SAVANNAS OF NORTHERN AUSTRALIA

Yue ZHANG [1] Peter WHITEHEAD [2] Waqar AHMAD [3] Carl Menges [4]

[1]*PhD Student,* [2]*Director of KCTWM and A/Prof.,* [3]*Senior Lecturer,* [4] *Research Associate*
Cooperative Research Centre for Sustainable Development of Tropical Savannas
[1,2] *Australian Research Council Key Centre for Tropical Wildlife Management*
[3,4] *RS/GIS Lab, Faculty of Science, Information Technology & Education*
Northern Territory University, Darwin, NT 0909, Australia
Telephone Number: +61 8 8946 6894 Facsimile Number: +61 8 8946 7088
E-mail: yue.zhang@ntu.edu.au

KEY WORDS: interactive approach, DEM, bush fire mapping, savannas, Australia

ABSTRACT Tropical savannas occupy one third of Australia's landmass, and are composed of dense grasslands and scattered trees. Both deliberately lit and natural wildfire sweep across the vast monsoonal savannas of northern Australia each year and the consequence of these modern fire regimes can be catastrophic for fire-sensitive plants and animals. This paper presents an interactive methodology which improves the mapping accuracy for mapping fire history from Landsat Thematic Mapper data of an area with typical savanna landscape characteristics of northern Australia. A satellite image captured in the middle dry season of the year 2000 was used. With the visible red, NIR and MIR bands, an unsupervised digital image classification was carried out to delineate the burnt patches. These patches were labelled by using field knowledge as well as by on-screen assessment of the raw data and signature files for previously confirmed fire scars. Spectral overlap between fire scars, water bodies, shadows and miscellaneous geological features was observed and was eliminated by using of a binary spatial mask and the Digital Elevation Model (DEM). The validity of the fire mapping was assessed with the help of field data as well as using a high spatial resolution IKONOS image acquired at the time of the TM data recording.

1. Introduction

Wildfire has been considered as one of the major landscape characteristics in the Australian tropical savannas. Earlier studies have estimated that over 50% of the savannas in some regions of northern Australia are burnt during the 7-month (May-November) dry season each year (Press 1988). Even in Kakadu National Park, a United Nation's World Heritage property, an average of 55% of lowland savanna habitats and 28% of habitats occupying both sandstone plateau and riverine landforms has been burnt each year (Russell-Smith *et al.* 1997). Depending on a variety of purposes of management and conservation, dry season fire is ignited to reduce the level of flammable fuel loads, to encourage 'green pick' for cattle and kangaroos, and to create patchy mosaics of burnt and unburnt country to help developing habitat diversity (Jacklyn and Russell-Smith 1998). However, the bulk of late dry season uncontrolled wildfire sweeping across the Northern Territory of Australia, are catastrophic for fire-sensitive flora and fauna to be the consequence of such contemporary fire regimes. To add the understanding of the savanna landscape structure and dynamics, fire scars mapping has been carried out using satellite images (Russell-Smith *et al.* 1997).

Acquired in various geometric, radiometric and spectral resolutions, satellite remotely sensed data, multi-temporal or single post-fire, have been processed successfully to map burnt scars, species affected and post-fire recovery (Chuvieco and Congalton 1988, Pereira *et al.* 1997). Various fire-mapping methods have been developed and applied, but most of these focus on the areas where vegetation distribution and topographic features are comparatively uniform. However, when mapping bush fire in tropical savannas, such as in northern Australia, spectral overlaps between fire scars and terrain shadows, water bodies, unburnt canopies, and vegetation regrowth in burnt area create substantial difficulties in separating and discriminating fire classes. Russell-Smith *et al.* (1997) utilized the hard copies of Landsat MSS data to define the fire scars. In this study, an interactive fire mapping method that improves the accuracy of bush fire mapping and helps overcome these problems of separation and discrimination was developed for this special landscape type in the Australian tropical savanna.

2. Study area

The study area is located on the tropical savannas with typical landscape features in the Top End of the Northern Territory, Australia, which is bounded by longitudes 131°48'E, 132°27'E and by latitudes 13°41'S, 14°17' (Figure 1).

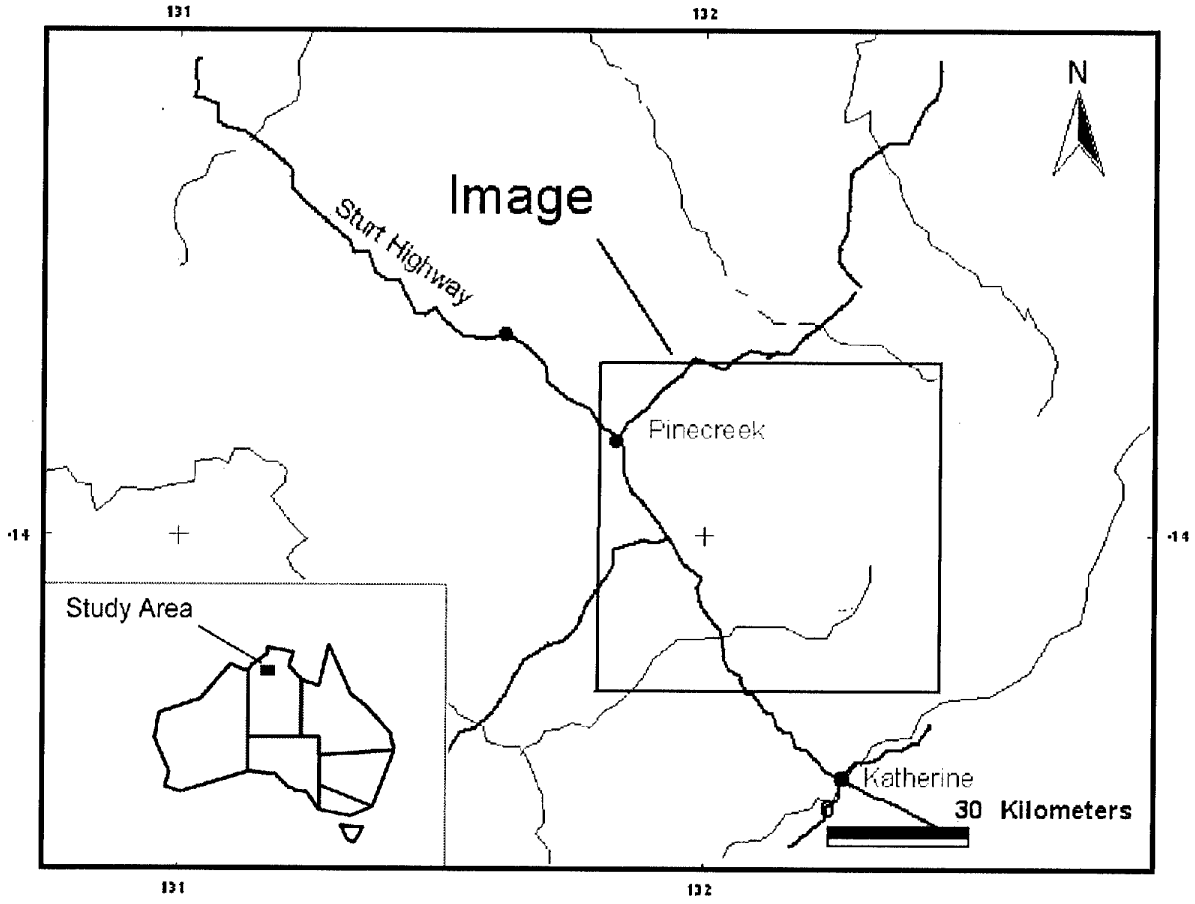


Figure 1. Location of the Study Area (Yinberrie Hills, Northern Territory, Australia)

The study area occupies the west part of Nitmiluk National Park and is close to the southwest boundary of Kakadu National Park that is inscribed in the World Heritage list for both its cultural and natural values. The major land uses in terms of area are Aboriginal land, pastoralism and nature reserves. The regional climate is characterised seasonally by rainfall with over 90% occurring in the summer wet season (from November to March). The average rainfall is 1 200 mm. Maximum daily temperatures average above 30°C over the year (Russell-Smith et al 1995). The wildfire pattern in the study area is characterised in terms of burning period during the dry season. The rugged Arnhem Land plateau exists in the east part of the study area with an elevation below 400 m. An undulating Cainozoic plain stretches away from the plateau margins and is composed of weathered and coarse-grained sediments (Williams 1991). An open forest/woodland type dominated by *Eucalyptus spp.* over a typically grassy understorey is the main vegetation type, while other freshwater floodplain communities ranging from sedgelands to open forests dominated by *Melaleuca spp.* distribute along the creeks in lowlands (Wilson *et al.* 1990, Russell-Smith 1995).

3. Methodology

In this project, one georeferenced Landsat Thematic Mapper image was acquired in June 2000 to demonstrate an operational method for the accurate mapping of fire scars that can be employed to extract a fire history for the past decade using this data. The accuracy assessment is based on field data and an IKONOS high-resolution data acquired within one week of the Landsat data. A 9-second Digital Elevation Model (DEM) acquired from Australian Survey and Land Information Group was available for the study area.

The interactive approach developed here employs a two-tired approach as can be seen in the flow diagram (Fig 2). On one hand, a conventional pixel-based, spectral classification is carried out to identify potential fire areas. On the other hand, areas that can be recognized as fire scars by the operator are manually delineated to provide the coverage of definite fire areas. The spectral classification is based on an unsupervised ISODATA algorithm of Landsat TM bands 3,4, and 5 generating 100 spectral classes. Considering that vegetation is highly sensitive to fire, the visible red, NIR and MIR bands were used in the image classification process, since this band combination has widely been used as a standard in vegetation studies (Conese and Maselli 1993). Each of the resulting classes is displayed on top of the false colour composite and assessed as being a fire scar or other land cover. This process is supported by available field data and the DEM to indicate potential water bodies and shadow areas. The classes are then aggregated to a binary image containing a value of '1' for all pixels that are potentially affected by fire. The manual delineation of definite fire areas was achieved by digitising the boundaries from the enhanced false colour composite with the help of field knowledge and the DEM. The boundary of fire patches was followed as closely as possible, attempting to eliminate shadows, water bodies, and other topographic features that may spectrally overlap with fire signatures. The digitised map was converted to a binary image with a value of '1' for the identified fire areas. The final fire map is produced by multiplying the binary maps from the classification and manual masking process.

In this project, two types of data were used to carry out accuracy assessment. Ground-truthing data were collected by recording fire locations and its coordinates in each 50 m interval by walking along four transects of 5 km length each set up uniformly in the study area. This fieldwork was carried out at the time of Landsat TM image acquisition. A total of three hundred field observations was used to

assess the overall accuracy rate of fire mapping. Additionally, five hundred random points were tested on the high spatial resolution IKONOS data.

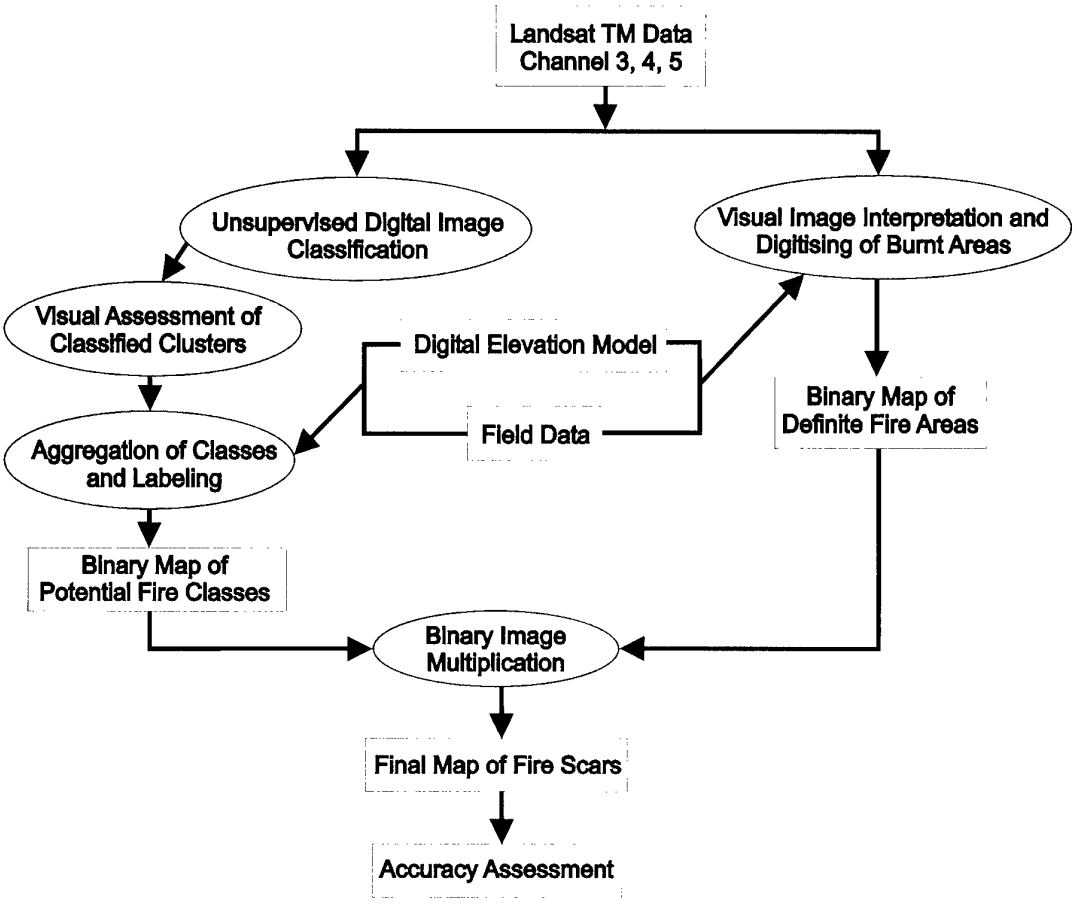


Figure 2. Flow chart of image processing steps for fire mapping in Australian savannas

4. Results and Discussion

The unsupervised spectral classification resulted in extensive confusion between fire classes, water bodies, shadows, and other topographic features such as mixed pixels in catchment areas where vegetation signatures are dominated by standing water. A more detailed classification, possibly using more spectral bands could be implemented, but there is doubt as to whether the problem could be solved. The real difficulty in this task is the nature of the fire scars to be mapped. Within the study area, the frequent fire events throughout the dry season lead to a great spectral variation to be tackled in the classification process. The fires in this environment burn the dry grass, but leave the sparse tree canopies unaffected. Thus the spectral signature is a mixture of the canopies and the burnt grasses, which are black at first, but rapidly, become lighter as the ash disperses, and eventually show signs of re-growth. For this reason, a relatively large number of spectral classes were generated to minimise the spectral overlap, but a more sophisticated classification methodology was not followed as its main goal is to become operational for the mapping of long-term fire history. The binary map of potential fire classes is shown in figure 3A.

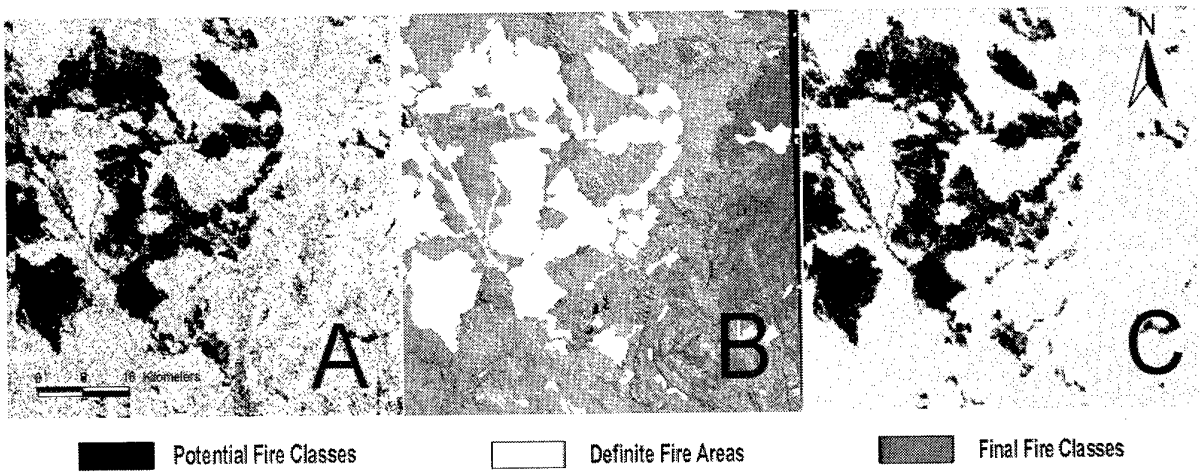


Figure 3. Binary maps of (A) potential fire classes, (B) definite fire areas, and (C) the final map of fire scars. The false colour composite is shown for reference.

Rather than attempting to devise a sophisticated classification methodology that may work well in some cases, the problem of spectral overlap was solved by utilizing the operator's knowledge of the study area and image interpretation. Manually digitising of fire scars has the major disadvantage of being time consuming, but on the other hand, it yields great accuracy in recognition, especially in conjunction with ancillary data and multiple images that are available for fire history mapping. Having a multi-temporal view allows recognition of permanent landscape features. There is a possibility that very small fire events of less than 10 pixels may be missed, but such events would be very rare in this environment. The problem in relying on this methodology is the accurate boundary delineation. To trace the outline accurately increases the time requirement very rapidly. For this methodology, it is important to be accurate in eliminating image elements that may be confused with fires. However, the boundaries do not have to be very accurate where distinct land cover features adjoin, as the spectral classification will resolve this boundary with the best accuracy possible for the data resolution.

The accuracy of the final map was 91% and 94% according to field data and IKONOS data respectively. Even though the overall accuracy rate assessed by IKONOS data was reduced because of some errors occurred in the visual interpretation, this method could be an easy and extensive approach for accuracy assessment. Some of the errors can be attributed to the time difference between the acquisition of Landsat TM image and the IKONOS data as there is a distinct possibility of several fire events occurring in a single week during the middle dry season. The methodology developed is subjective as it depends on operator knowledge, and moderately time intensive depending on the number of fire events present in the data, but it is robust as no radiometric corrections are required and produces highly accurate and reliable results. This is of great importance for fire history mapping, as there is no available ground truth for past image dates.

5. Acknowledgment

This study is a part of Yue Zhang's PhD project supported by Australian Cooperative Research Centre for Sustainable Development of Tropical Savannas and Australian Research Council Key Centre for Tropical Wildlife Management. Parks and Wildlife Commission of Northern Territory,

Australia, funded acquisition of images. We are grateful for these supports. Thanks should also go to Mr Joshua Forner, Mr Craig Hempel, and Mr Andrew Edwards, for their field help and suggestions.

6. References

Chuvieco, E., and Congalton, R. G., 1988. Mapping and inventory of forest fires from digital processing of TM data. Geocarto International, 4, 41-53.

Conese C., and Maselli F., 1993. Selection of optimum bands from TM scenes through mutual information analysis. ISPRS Journal of Photogrammetry & Remote Sensing. 48, 2-11.

Jacklyn, P. and Russell-Smith, J., 1998. Proceedings from the North Australia Fire Management Workshop, Tropical Savannas CRC, Darwin, pp. 1-40.

Pereira, J. M. C., Chuvieco, E., Beaudoin, A., and Desbois, N., 1997. Remote sensing of burned areas. In: A review of remote sensing methods for the study of large wildland fires, edited by E. Chuvieco, Alcala de Henares, Spain, pp. 127-183.

Press, A. J., 1988. Comparisons of the extent of fire in different land management systems in the Top End of the Northern Territory. Proceedings of the Ecological Society of Australia. 15, 167-175

Russell-Smith, J., Needham, S., and Brock, J., 1995. The physical environment. In: Kakadu: Natural and Cultural Heritage and Management, edited by A. Press, A. J. Lea, A. Webb and A. J. Graham, Australian Nature Conservation Agency and North Australia Research Unit, Australian National University, Darwin, pp. 94-126

Russell-Smith, J., Ryan, P., and Durieu, R., 1997. A LANDSAT MSS-derived fire history of Kakadu National Park, monsoonal northern Australia, 1980-94: seasonal extent, frequency and patchiness. Journal of Applied Ecology, 34: 748-766.

Williams, M. A. J., 1991. Evolution of the landscape. In; Monsoonal Australia: Landscape, Ecology and Man in the Northern Lowlands, edited by C. D. Haynes, M. G. Ridpath and M. A. J. Williams, Balkema, The Netherlands, pp. 5-17

Wilson, B. A., Brocklehurst, P. S., Clark, M. J., and Dickinson, K. J. M., 1990. Vegetation survey of the Northern Territory, Technical Report No. 49, Conservation Commission of the Northern Territory, Darwin, Australia.

RELATIONSHIP BETWEEN CANOPY BRDF AND PHYSICAL PARAMETERS OF 3-D STRUCTURE OF VEGETAION IN NORTHERN WETLANDS IN JAPAN

Michiru MIYAMOTO*, Kunihiko YOSHINO**, Keiji KUSHIDA***(JAPAN)

* Ms., Graduate School of Agricultural and Life Sciences, Biological Environmental Engineering, University of Tokyo
1-1-1 Yayoi, Bunkyo-Ku, Tokyo, 113-8657
Tel: +81-3-5841-5370 Fax: +81-3-5841-8169
E-mail: aa07102@mail.ecc.u-tokyo.ac.jp, michiru521@hotmail.com
** Assistant Prof., Institute of Policy and Planning Science, Tsukuba University
1-1-1 Tennou-dai, Tsukuba, Ibaraki, 305-8573
Tel: +81-298-53-5005 Fax: +81-298-55-3849
E-mail: sky@shako.sk.tsukuba.ac.jp
*** Assistant teacher., Institute of Low Temp. Sci. Hokkaido University
Sapporo, 060-0819
Tel: +81-011-706-5490 Fax: +81-011-706-7142
E-mail: kkushida@pop.sk.lowtem.hokudai.ac.jp

KEY WORDS: Wetland Vegetation, Productive 3-D Structure, Multi Angles, Spectral Reflectance, Vegetation Indices

ABSTRUCT: The canopy spectral reflectance at multi angles and the 3-D structures of vegetation were measured in "Kushiro wetland" and " Akkeshiko - Bekanberushi Wetland" located in the eastern part of Hokkaido; the north island of Japan in the summer of 1998. Our purpose of this research was to clarify the characteristics of spectral reflectance and to develop the algorithm according to the wave bands and the band ratio with multi angles effective to the classification and the estimation biomass used cross - near range R.S.

We clarified the relationship of the spectral reflectance and each 3-D biomass layer structure specific to the wetland vegetation. The bi-band ratio of reflectance and the LAD (Leaf Area Density) - SLA (Specific Leaf Area) and the productive structure by the stratified clip method was measured. And we specified the canopy layer structure by the observation at not only the nadir angle but also the plural angles from± 15° to ± 45° range.

The values with remarkable difference could be seen at multi angle rather than nadir, and also infrared rather than red range, especially among the similar vegetation canopies located in the transition moor. While we could not find out any effectively different values for the classification among the fens and the transition moors in G/NIR, R/NIR, and NDVI, though the effectiveness of those could be seen in only bog *Muskege* and the fen and the transition - moor mixed with shrub. On the other hand, G/R and VI were effective to them classify. The spectral reflectance of the canopies depended on their canopy 3-D structures and their dominant vegetation types. Selecting the specific wave bands and their band ratio observed at multi - plural angle with cross - near range R.S. data was effective for the estimation of the biomass and the classification of wetland vegetation.

1. INTRODUCTION

The estimation of CH_4 flux at each wetland vegetation in global wide range is in urgent necessity for the study of the influence of the global warming. From the local point of view, it is necessary to grasp the vegetation distributions in wide range to understand the extension of the migration belt and the biodiversity to preserve the wetland vegetation.

So many researchers are trying to classify vegetation in wetlands using satellite or aeroplane .S. in order to make vegetation maps. Recently, the spectral reflectance of vegetation canopy measured at multi angles has a lot of information of canopy structure as well as species types. However the precision of classification of wetland vegetation based on R.S. is not enough for the reason why the wetland vegetation has the complicated layer structure and its specific characteristics especially situated in bog and transition mixed vegetation. Our goal of this research is to develop the algorithms and make it clear the relationship of the characteristics of the spectral reflectance measured at plural angles and the 3 - D layer biomass structure.

2. STUDY AREA

The research was carried out at typical fen, transitional, bog vegetation in Akkeshiko Bekkanberushi wetland, and Akanuma in Kushiro wetland, eastern part in Hokkaido(**Fig.1**). The former is the second largest and the latter is the largest wetland in Japan and they have been registered in the list of wetlands of international importance. Especially, the bog in Akkeshiko Bekkanberushi wetland is known as the academically precious existence with little artificial impact. The concrete investigation site was peat bog in which the Sphagnum moss piled up located in the confluence point of Toraibetsu River and Bekkanberushi River and where precious alpine plant develops (site A - C) and the fen besides Taibetsu River (site D) (**Fig.2**). In Kushiro at the bog right bank of Kushiro River (site E - G), the fen along the walk street inside the wetland (site H, I) and the transitional moor paralleled old railway (site J). This researchwas carried out in June and July, 1998.

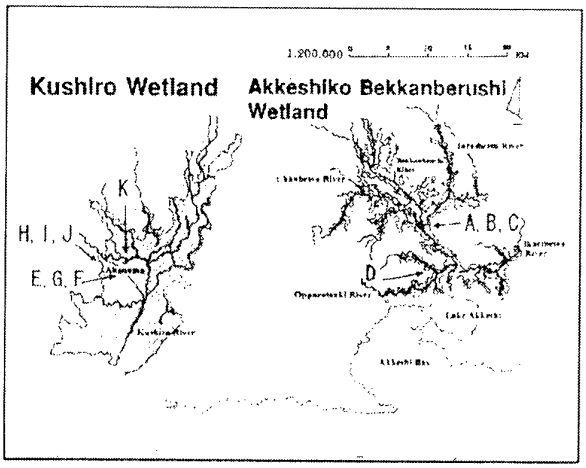


Fig.1 Study Area Kushiro Wetland:
Site E-G: Bog, located in the right bank of the embankment , Site H: Transitional moor, along the walking wooden street, Site J: Fen, along the walking wooden street, Site K: Bog, around the southern part of the Akanuma Swamp
Akkeshiko Bekkanberushi Wetland:
Site A-C: Transitional moor, the confluence site of Bekkanberushi, River and Traibetsu River, Site D: Fen, the lower current area of Traibetsu River

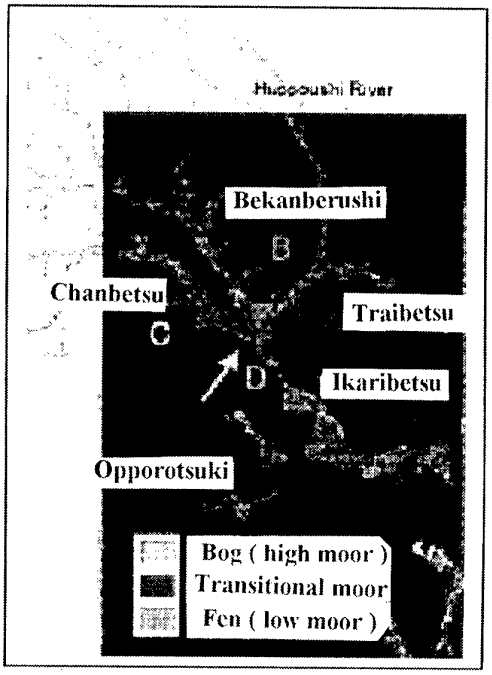


Fig.2 Akkeshiko Bekkanberushi Wetland
Landsat TM , Aug 17, 1998

2. 2 Measurement of Vegetation Research and Biomass

The vegetation research and the biomass were measured. Since the layer structure is complicated, the productive structure figure were made with the combination of dominant

species and other species. Each 0.5m× 0.5m quadrat was set based on the simple random sampling method. We measured occurrence, dominance, sociability, vegetation cover, and height above the ground for herbaceous layer, moss layer, bush layer. Each vegetation photos in the quadrate were taken above two m high from the canopy by using long pole carried with two steel cameras and optical tube sensor on the top. Based on the stratified clip technique, the biomass measurement was carried by cutting down from the top of the plant community in every 10cm interval. The dry mass were measured (48 hours at 80 degrees) after they were diffrenciated in photosynthesis organ (assimilatory organ ; lamina) and non-photosynthesis organ (non- assimilatory organ ; stem, spike, petiole, flower) on each 10 cm layer and the species. Leaf Area Index {LAI: all leaf area (cm^2) / 0.5m× 0.5m quadrat} and Leaf Area Density (LAD: all leaf area (cm^2) / 0.5m× 0.5m quadrat / 10 cm layer) were also measured. And we examined the relationship between LAD - SLA in each layer to specify the two dimension data of each biomass and leaf area.

1.) In order to grasp features of the spatial distribution of classification and stratification of the biomass, LAD was concerned.
2.) So as to understand the layer unit of biomass characteristics, Specific Leaf Area { SLA: dry weight (g) / leaf area (cm) / 10cm layer } was measured.

2. 3 Measurement of Canopy Spectral Reflectance

The spectral reflectance energy intensity from the vegetation was measured with zenith, ± 15° ,± 30° , ± 45° angle on both chief plane and perpendicular plane. Three repetitions were taken for the measurement (**Fig 3**) The bidirectional spectral reflectance two meter above the canopy were measurement by using VIS - IR portable spectrometer, SD - 1000 made by Ocean Optics Co. Ltd (**Table.1**) set on the long pole. Each 1m× 1m quadrat was set for the measurement. As to the reflectance of the reference, they were calculated from the ratio with energy intensity of reflectance on the object using standard albedo board. Before the spectral measurement, the solar altitude, solar azimuth, time, background value from the sensor energy were researched. Actually in the field, since the sub sensor receive the solar incident energy several times as much as that of the master sensor. Therefore, we reduced the amount of the incident energy from the sun by either shortening integral time or setting the filter of cutting specific wave bands and we narrowed the slit to avoid the saturation.

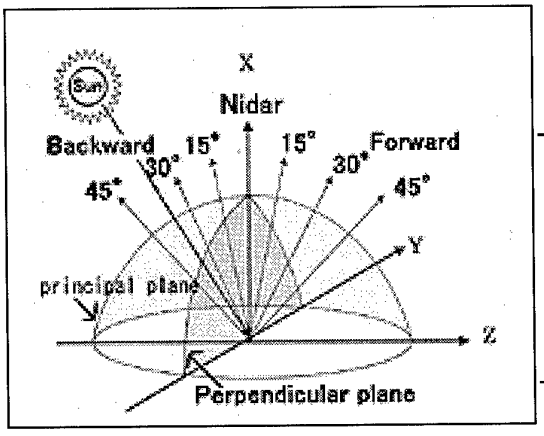


Table.1 VIS-NIR spectrometer SD-1000, Ocean Optics CO. Lted.

Wavelength (nm)	400~900
Resolution (nm)	2~3
Sampling interval (nm)	1
Optical angle (degree)	25
Measurement time(second)	10
Detecter number (times)	1100 (Si)

Fig. 3 BRDF measurement The spectral reflectance energy intensity from the vegetation was measured with zenith, ±15°,±30°, ±45°angle on both chief plane (X-Z coodinate axis) and perpendicular plane (X-Y coodinate axis).

The ideal value from the measurement wavelength range was limited in 400 - 900nm because of the accuracy of the spectrometer SD - 1000. In this study, the diffuser board, with obscured glass on the standard albedo board was used. It enabled us to remove the effect of the dependence of the angular noise. The vegetation index (NDVI: normalized difference vegetation, VI: simple vegetation index) and each band ratio (G / NIR: green / near infrared, R / NIR: red / near infrared, R / G: red / green) were calculated from the spectral signature obtained from single band, green (530 - 550nm), red (650 - 670nm), near infrared (760 - 810nm) respectively at each site. We examined the relationship between LAI and the spectral signature with multi angle observation and detected the specific observation angle which is sensitive to the significant classification for each vegetation.

3. RESULS

3.1 vegetation research

The 46 species was identified according to the vegetation research. They are 16, 9, 21 in the low, transitional, high moor respectively. We could classify the 6 types hierarchy through the A - H site. Two types of fen (*Phleum* - *Carex* in the field stratum and *Alunus* - *Chamaedaphune* in the shrubby stratum), three types of transitional moor (*Phleum – Carex, Thelypteris* in the field stratum and *Chamaedaphune* in the shrubby stratum) and three types of bog (*Carex* in the field stratum, the alpine plants in the dwarf shrub stratum and *Sphagnum* in the lichen bog stratum)

3.2 Productive Structure and Relationships between LAD and SLA

3.2.1 Productive Structure Diagram: So far as the productive structure diagram is concerned, the similar tendency could be seen between D and G site dominated *Carex* and between A and H dominated *Phleum*. That is to say, the more lower layer the more biomass gradually tend to increase while *Phleum* type is rapidly tend to increase. The Sphagnum moss community in the site C, the biomass of the lower layer showed more large value.

3.2.2 LAD and SLA : The area of leaf area in each 10cm layer unit was divided as dominant species and other species. The correlation and regression line among leaf area and height above the ground in each 10cm layer unit and dry weight was taken. Compared to the dominant species and other species, they showed converse tendency in dry weight and the leaf area each other. Namely, the monocotyledon type showed that the more lower layer the more dry weight increase though the *Phleum* dominated type and other broad leaved herb type decrease.

From the point of view of the LAD - SLA, there similar characteristics could be seen between site D and G (*Phleum* and *Carex* dominated in the low-moor), site H and A (*Carex* dominated in the transitional moor along with the high moor), site E and C (*Carex* , shrub, and alpine plants dominated), respectively. That is, we could classifier 3 types of the relationship between LAD and SLA which is represented semicircle type in the site D - G, straight line type in the site H - A type and dispersion type in the site C - E type (**Fig. 4 , 5**).

3.3 Characteristics of Multi Angle Spectral Signature and Classification of Wetland Vegetation

The spectral reflectance was less than 15% in the visible range and 20 - 40% in the near infrared at the high moor vegetation. In the fen and transitional moor, less than 20 % in the visible range and 60 - 80% in the near infrared range. According to the angle observed from the nadir to $\pm$ 45° , it clarified that the increase of the reflectance at visible range is more than 5% and that of the near infrared is about 20% in each vegetation type. That could be effective within

the near infrared on the transitional vegetation.

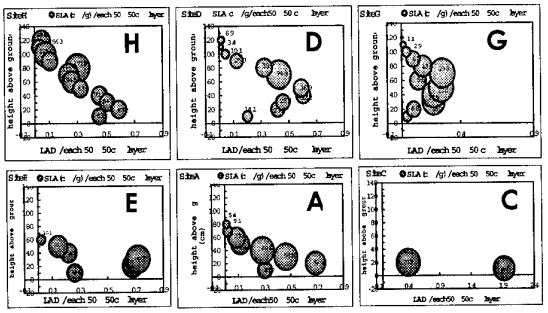


Fig. 4 The relationships between LAD and SLA among each vegetation type.
LAD : leaf area (cm2) / 10cm layer / 50×50 (cm2), SLA : leaf area (cm2) / dry weight (g) / 10cm layer/50×50(cm2)

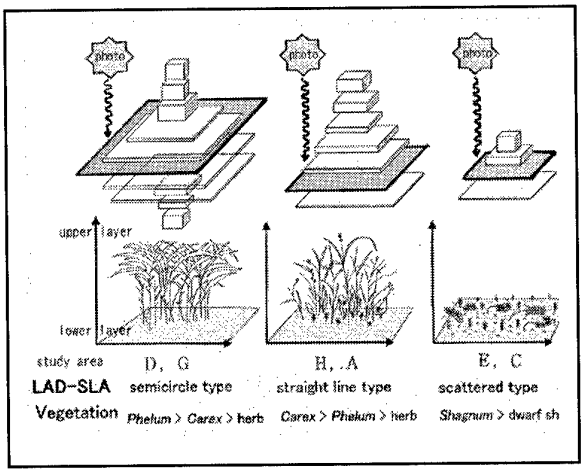


Fig. 5 Illustration for relationship between LAD-SLA and each biomass layer structure

3.3.1 Multi Angle Spectral Reflectance Measured at Single Bands: At first the spectral reflectance in the Green band (530 -550nm), the Red band (650 - 670nm), and the NIR band (760 - 810nm), were measured with multi angular. From the NIR and Green band point of view, we could not classifier the each spectral reflectance but could discriminate the difference by the measurement of the oblique forward 15° - 45° . Especially, it was very effective to discrimination of *Sphagnum* moss. In addition to that, it was also effective to the classification for the vegetation mixed with shrub. For concrete, when the shrub, *Chamaedafune* invaded to *Carex* vegetation, the reflectance of *Carex* vegetation became small. That is to say, we could extract the spectral reflectance of the vegetation mixed the shrub stratum, especially 10% in the Green band, 40% in the NIR band. The processing of the calculation of the band ratio for the spectral reflectance, NDVI and VI were effective to extract the typical three wetland vegetation type measured at ± 15° rather than nadir angle. In addition to that, in Red/NIR, Green/NIR and NDVI, we could not find the effective differences except for the *Sphagnum* moss group, site C however effective to the vegetation mixed with *Sphagnum* and the shrub (**Fig.6**).

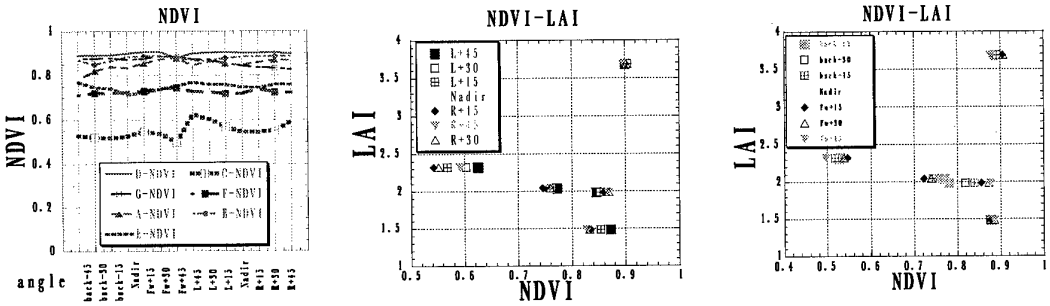


Fig.6 NDVI and its relationship with LAI measured at multi angles at each vegetation

3.3.2 Relationships between Band Ratio and LAI: By selecting the effective and specific band ratio and vegetation indices with multi angles to discriminate each vegetation, it was possible to classifier the specific wetland vegetation by using the spectral data measured at 2m high above the canopy. It proved that even in the case that the difference of LAI was slight though the band ratio was actually quite different or the case that the difference of band ratio was similar though the LAI was quite different, the measurement at not only multi angles but also the nadir angle was very effective to the classification.

4. DISCUSSION

4.1 Classification of Wetland Vegetation Concerning Canopy Productive Structure and Multi Angle Spectral Signature

It was obviously easy to extract such as *Sphagnum* from other vegetation without multi spectral measurement and was enough for only nadir angle. However, for the vegetation which had the similar kinds of canopy, such as both *phleum* and *Carex* were the first dominant species and the second dominant species were mixed with other herb species, multi angular measurement was evidently effective to discriminate from other similar kinds of vegetation. In addition to that, taking biomass into considerations, it is distinctly effective to compare and discriminate following type of vegetation. The vegetation with different spectral signature though the actual biomass was quite similar and the vegetation with quite different biomass though the actual reflectance was similar. It was verified that the multi spectral measurement was effective to the classification of the vegetation whose canopy has similar herb stratum. When we grasp wide range of wetland vegetation, we will be able to understand and estimate the spatial arrangement of the vegetation community by specifying the indefinite spectral signature in detail. As one of the basic technique of the remote sensing of vegetation, it appeals that it is important to clarify the physical relationship between the biological data including biomass and spectral signature with multi observation for verifying the effectiveness of remote sensing data. In the near future, it seems that the focus are making on the various spectral principles applied for the remote sensing data for the analysis of the research in order to clarify the spectral characteristics relating to the function of the ecosystem.

5. CONCLUSIONS

Following three statements are concluded in this study.

1.) Each productive structure was specified by the relationship between LAD- SLA in each layer.

2.) The characteristic of spectral signature measured at multi angle was clarified.

3.) By clarifying the relationship between the effective band ratio, it became clearly possible to classify the specific types of wetland vegetation especially herb stratum, mixed shrub stratum, and the only moss vegetation and by selecting specific vegetation index and observation angle, it became remarkably possible to estimate the biomass in each vegetation type in detail.

6. REFERENCES

1. Asrar, G., Kanemasu, E.T., Miller, G.P., and weiser, R.L., 1986. Light interception and leaf area estimates from measurements of grass canopy reflectance. *IEEE Trans. Geosci.remote Sens.*GE-24:76-82

2. Christensen, S., and Goudriaan, J.,1993. Deriving Light Interception and Biomass from Spectral Reflectance Ratio, *Remote Sens.Environ.*43:87-95.

3. Watson R. T., Zinyowera, C. Z., and Moss, R. H.,1996. 'Climate Change1995': Impacts, Adaptations and Mitigation of Climate Change: Scientific-Technical Analyses, Working Group II to the Second Assessment Report of the Intergovernmental Panel on Climate Change, Intergovernmental Panel on Climate Change, Cambridge University Press

ISBN 957-02-7241-4